Raghu V. Prakash
R. Suresh Kumar
Atikukke Nagesha
Gomathy Sasikala
Arun Kumar Bhaduri   *Editors*

Structural Integrity Assessment

Proceedings of ICONS 2018

Springer

Lecture Notes in Mechanical Engineering

Raghu V. Prakash · R. Suresh Kumar ·
Atikukke Nagesha · Gomathy Sasikala ·
Arun Kumar Bhaduri
Editors

Structural Integrity Assessment

Proceedings of ICONS 2018

Springer

Editors
Raghu V. Prakash
Department of Mechanical Engineering
Indian Institute of Technology Madras
Chennai, Tamil Nadu, India

Atikukke Nagesha
Materials Development and Technology
Division
Indira Gandhi Centre for Atomic Research
Kalpakkam, Tamil Nadu, India

Arun Kumar Bhaduri
Indira Gandhi Centre for Atomic Research
Kalpakkam, Tamil Nadu, India

R. Suresh Kumar
Reactor Design Group
Indira Gandhi Centre for Atomic Research
Kalpakkam, Tamil Nadu, India

Gomathy Sasikala
Materials Development and Technology
Division
Indira Gandhi Centre for Atomic Research
Kalpakkam, Tamil Nadu, India

Foreword

It gives me great pleasure to write this foreword for the proceedings of Second International Conference on Structural Integrity, ICONS 2018, held at IIT Madras, Chennai, during December 14–17, 2018. We owe a gratitude to Prof. Raghu Prakash and Dr. Sasikala for their valiant efforts to ensure that the conference was a success and papers presented and offered for publication were of high quality. Congratulations to the entire Organizing Committee for a job well done!
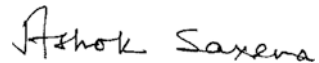
We all understand that premature and abrupt fracture has been and continues to be an important and complex problem in structures that bear loads and face extreme environments during service. Many approaches have been adopted to tackle this phenomenon from the beginning of civilization. For the past one and a half centuries, the goal of achieving structural integrity has frequently brought together scientists and engineers from disciplines ranging from engineering mechanics and mathematics, materials science and engineering, nondestructive testing, and physics under one umbrella. There lie the benefits of the conferences such as ICONS. These conferences report the developments in theoretical and experimental fracture mechanics and contribute immensely to the understanding of deformation and the underlying damage mechanisms, the latest developments in computational tools for

structural integrity assessments, and in sensors and systems for nondestructively inspecting structural components. The developments in these fields have now evolved to the point that it is no longer necessary to conduct expensive and time-consuming, full-scale testing of pressure vessels, aircraft structures, components of rotating machinery, and medical devices and implants to prove that they are adequately designed to resist sudden failures. All that can be done using the principles of "Design by Analysis" enabled by the progress in structural integrity research.

The rapid progress in the multidisciplinary field of structural integrity is largely due to conferences such as ICONS 2018 that attract scientists and engineers working on the different aspects of understanding and preventing fracture in components. The participants have an opportunity to share their ideas with their colleagues from the allied disciplines paving the way to leverage each other's successes to benefit industry that is engaged in designing more efficient and high-performance energy conversion machinery and transportation systems. ICONS 2018 attracted 70 peer-reviewed papers that run the entire gamut of structural integrity-related topics and is a significant contribution to the field.

As one who has spent almost 50 years in fracture research, I deeply appreciate the high quality of the papers that were a part of the conference and are included in the proceedings. About 200 delegates participated in ICONS 2018, and 7 plenary lectures and 23 invited/keynote lectures were presented in 4 parallel sessions spread over 3 days of the conference. One of the features of this conference that I found to be of note was a "Young/Future Researchers of Structural Integrity Research" session.

I wish to extend my best wishes to the entire Organizing Committee for an excellent conference. The leadership of Dr. Sasikala and Prof. Raghu Prakash as conference co-chairs deserves special mention, and I thank the speakers and delegates of the conference for their role in its success.

Ashok Saxena

April 2019   Ashok Saxena
Distinguished Professor and Dean Emeritus
Department of Mechanical Engineering
University of Arkansas, Fayetteville, AR, USA

Executive Chair, ICF-15, Atlanta, Georgia, USA
President, Indian Structural Integrity Society (InSIS), (2015–2018)
Vice-President, ICF Council (2009–2013)
asaxena@uark.edu

Preface

This book contains selected papers from the presentations made at the Second Quadrennial International Conference on Structural Integrity (ICONS 2018) held at IIT Madras, Chennai, during December 14–17, 2018. The conference was organized jointly by the Society for Failure Analysis (Chennai Chapter) and Indira Gandhi Centre for Atomic Research (IGCAR) along with Indian Structural Integrity Society (InSIS), Indian Institute of Science, Bangalore, and Indian Institute of Technology Madras, Chennai; further, the conference was endorsed by the Italian Group of Fracture (IGF).

The conference attracted the delegates from six countries (Egypt, France, Germany, Italy, Japan, and Singapore) in addition to nearly 200 delegates from India. The program comprised 7 plenary talks, 23 invited presentations, and 132 contributed papers and spread over 3 days in 4 parallel sessions. In addition, about 70 papers were presented as posters—mostly by research scholars—and the best posters were chosen by a panel of experts for the awards. One of the key aspects of this conference was the Young Researchers panel discussion—to identify future directions for structural integrity research in India, roles and responsibilities of the younger generation over the next decade, and how they harmonize their research with the rest of the world to be global players. The panel comprised scientists, academics from leading IITs (Bombay, Delhi, Madras, and Roorkee), and R&D laboratories (DAE/NPCIL, IGCAR, GTRE/DRDO, and CSIR-SERC, Chennai.).

ICONS 2018 focused on all aspects relating to structural integrity—including fatigue and fracture mechanics; creep and creep–fatigue interactions; structural health and condition monitoring; failure analysis; experimental techniques; computational and numerical fracture mechanics; metals, composites, and new-generation materials; life extension; advanced structural materials; design and stress analysis; reliability and regulatory aspects. The application domains covered bio-engineering, aerospace structures, civil engineering structures, power plants, and transportation. The timing of the conference is apt and coincided with India's efforts toward design, development, and realization of advanced ultra-supercritical power plants and "Make in India" mission. ICONS 2018 brought together practicing engineers and scientists from the nuclear, aerospace, defense, chemical, and

oil industries, apart from faculty and research scholars from IISc, IITs, NITs, and other academic institutions.

The conference was sponsored by several agencies such as Department of Atomic Energy; Office of the Principal Scientific Advisor, Government of India; Department of Science and Technology; RUMUL, Switzerland, Walter+Bai, Switzerland, and Kammrath & Weiss, Germany—all three companies are represented by ABS Instruments, Chennai; Zwick Roell, Germany; Star Testing Systems, Mumbai; BiSS Research, Bangalore; Productive Technologies Limited, New Delhi; apart from many other sponsors.

This conference provided a platform for young researchers, practicing scientists and engineers to disseminate their knowledge and learn from each other to play a collective role in solving complex problems of structural integrity and safety assurance. We hope that this tradition will continue and that the Quadrennial ICONS conferences will play a key role in advancing knowledge in this critical domain of structural integrity.

The high quality of the selected papers in this book is due to the hard work put in by all the authors, reviewers, and volunteers, and we acknowledge their support. We hope this volume will serve as a good reference for practicing researchers, budding engineers, and scientists working in the domain of structural integrity. We wish to place on record the support received from various committees of this conference.

Chennai, India	Raghu V. Prakash
Kalpakkam, India	R. Suresh Kumar
Kalpakkam, India	Atikukke Nagesha
Kalpakkam, India	Gomathy Sasikala
Kalpakkam, India	Arun Kumar Bhaduri

Contents

About the Editors

Raghu V. Prakash is a Professor in the Department of Mechanical Engineering, Indian Institute of Technology Madras (IIT Madras) where he specializes in new product design and the assessment of structural integrity and remaining life prediction of critical components used in transportation and energy sectors. He has developed test systems for use in academia, R&D and industry during his tenure as Technical Director at BiSS Research, Bangalore and teaches courses relating to product design and structural integrity assessment at IIT Madras. He serves in the editorial boards of multiple journals including the Journal of Structural Longevity, Frattura ed Integrità Strutturale (IGF Journal), Journal of Life Cycle Reliability and Safety Engineering, and is a member of several technical societies. He has won several prestigious awards and recognition for his work, including the Binani Gold Medal (Indian Institute of Metals).

R. Suresh Kumar is currently affiliated with the Indira Gandhi Centre For Atomic Research (IGCAR). His research focuses on the theoretical and experimental aspects of structural integrity assessment and life extension of power plants. He has received his Bachelor's in Mechanical Engineering from Kerala University and Master's from the Department of Applied Mechanics, Indian Institute of Technology Madras, Chennai. He is a life time member of several technical societies, and is a recipient of numerous awards including the DAE Scientific and Technical Excellence Award (2013).

Atikukke Nagesha currently heads the Fatigue Studies Section in the Metallurgy and Materials Group at IGCAR and is an Associate Professor in the Homi Bhabha National Institute. Dr. Nagesha published more than 80 papers in journals and conference proceedings. He received the DAE Science and Technology Excellence award for his contributions to understanding the thermomechanical fatigue and creep-fatigue interaction behavior of reactor structural materials, as well as for his contribution towards the development of India-specific reduced activation ferritic-martensitic (IN-RAFM) steel and nitrogen-enhanced 316LN SS for reactor applications.

Gomathy Sasikala is currently the Head of the Materials Development and Technology Division at IGCAR and a Professor in the Homi Bhabha National Institute, Mumbai. Prof. Sasikala's research interests lie in understanding deformation, damage and fracture under creep and fatigue, fracture mechanics, fatigue crack growth, creep crack growth. She has published more than 230 research articles in reputed journals and proceedings, 7 chapters to edited books, and edited two books. She is a life member of several professional societies, and has served as an editor of Transactions of the Indian Institute of Metals and has been recognized for her outstanding contributions as a reviewer to several international journals.

Arun Kumar Bhaduri is the Director of IGCAR and a senior Professor at Homi Bhabha National Institute. He pilots the design and technology development of sodium-cooled fast reactors and its associated fuel cycle for the second stage of India's nuclear power programme, and anchors the development of materials and their fabrication technologies for Indian programmes on sodium-cooled fast reactors, fusion reactors and advanced ultra-supercritical thermal power. He specializes in the field of materials joining, and has published more than 650 research articles in reputed journals and conferences and holds 2 international patents. He has received numerous awards and recognitions, including the *Jaeger Lecture Award* (International Institute of Welding), the *GD Birla Gold Medal* (Indian Institute of Metals); *Carl von Bach Commemorative Medal* (MPA University of Stuttgart, Germany) and the *Metallurgist of the Year Award* (Ministry of Steel, Government of India).

Part I
Plenary Talks

Towards Improved Modeling of Variable-Amplitude Fatigue Crack Growth—Theory and Fractographic Validation

R. Sunder

Abstract A multi-mechanism load interaction model is proposed, that accounts for crack closure, crack-tip blunting and near-tip residual stress. It is validated for microscopic consistency using as reference, fatigue failures obtained under a specially designed programmed adaptation of the TWIST load spectrum. The programmed load sequence was rendered in two statistically identical versions, but suitably arranged to induce vastly different load interaction effects that cannot be distinguished by conventional models. Load levels were selected to ensure residual fatigue life from 10^6 to over 10^7 cycles. Microscopic consistency was verified by comparing actual fatigue crack extension in individual steps of the load sequences with expectations from the model. The study focused on long duration spectrum load fatigue response that presents practical interest in engineering application. The study reveals the need for more advanced testing practices than what are currently employed, specifically to handle fatigue thresholds reflective of service loading and crack growth rates under controlled near-tip stress conditions.

Keywords TWIST load spectrum · Microscopic consistency · Multi-mechanism model · Near-tip residual stress

1 Introduction

Around the same time that the Linear Damage Accumulation Rule was proposed by Miner [1], Gassner performed path-breaking experiments on aircraft structures under programmed loads simulating service load spectra [2]. He demonstrated that fatigue damage from loads of different magnitude does not lend itself to linear summation and concluded that to be useful in engineering application, fatigue data must be obtained under conditions simulating service conditions. Indeed, damage sum under variable-amplitude loading has been found to vary between 0.1 and 10

R. Sunder (✉)
BISS (P) Ltd., Bengaluru, India
e-mail: rs@biss.in

[3]. Not surprisingly, safety-critical transport vehicle structures are qualified through laboratory testing under loads that represent actual usage.

A large fraction of fatigue life in service is consumed by early crack growth. Early experiments by Schijve et al. revealed a large and systematic variation in fatigue crack growth life due to rearrangement of the sequence of loads in a load spectrum, whilst keeping spectrum statistical parameters unchanged [4]. This underscores the importance of understanding how fatigue cracks respond to service load spectra.

Most laboratory fatigue testing continues to be performed under constant amplitude loading. Driven by this "market", most commercial test automation software caters to constant amplitude fatigue testing, and this in turn also may incline researchers towards such loading conditions. Standard practices such as ASTM E606, E466, and E647 prescribe tight control of constant loading magnitude as one of the measures of ensuring reproducible test results. The section in ASTM E647 on decreasing ΔK stipulates extremely gradual rates of cyclic unloading specifically in order to avoid sequence effects that can retard crack growth. Ironically, while fatigue may be extremely sensitive to load sequence effects, the reproducibility of such effects ensures repeatability of test data that compares favorably with that constant amplitude data. Therefore, reproducibility of test data cannot serve as an argument in support of experiments under constant amplitude loading. One may argue that it is difficult to extrapolate variable-amplitude test data to a different load sequence, or even modifications of the same sequence. The gap remaining to be bridged may lie in lack of systematized understanding of load interaction mechanisms, leading to a structured process of their characterization, preferably from first principles. The nature of this gap precludes its closure through more constant amplitude experiments. In the meantime, engineering practice relies on analytical modeling to account for load interaction effects, backed up by inflated safety factors in the design and necessarily followed up by component level and full-scale testing under simulated conditions of expected usage.

This paper attempts to describe a multi-mechanism model of fatigue crack growth that explains and accounts for known load interaction phenomena in a manner that is amenable to analytical modeling. The microscopic consistency of the model is validated through specially designed experiments. The next section is a critical review of available load interaction models to estimate variable amplitude fatigue crack growth and an explanation of the significance of near-tip residual stress in atmospheric fatigue. This is followed by a summary of previous work to validate the new understanding about the role of near-tip residual stress and its characterization, leading up to a multi-mechanism model of variable-amplitude fatigue crack growth. A major part of this paper is devoted to the description of experiments to verify the new model for microscopic consistency. As this work was restricted to a model material in the form of 2024-T3 Al–Cu alloy, the paper concludes with a recommendation for a new testing practice that may assist in enhancing the practical value of test data obtained on other materials.

2   Critical Review of Load Interaction Models

Several load interaction mechanisms are involved in causing retardation and acceleration effects under variable-amplitude loading [5, 6]. Their modeling has remained an active area of research. Models in the industrial application are typically built around Elber's crack closure model [7], around Wheeler's [8] or Willenborg's [9] residual stress models, or, around a combination of the two. Elber's model is based on his discovery that the plastically stretched crack wake can close even during tensile unloading, thereby reducing the effective range of the applied load cycle. Obviously, as the fatigue crack grows into the much larger monotonic plastic zone created by a tensile overload, crack closure will increase, leading to retarded crack growth. Innumerable closure models and their adaptations followed the pioneering work of Newman in analytical modeling of closure [10]. However, if one assumes that a closed crack cannot respond to load variation, closure cannot explain the significant effect of underloads in the tensile region. For closure to evolve, some crack extension into a newly formed overload plastic zone. But retardation is not always delayed.

The Wheeler and Willenborg models are conceptually flawed. In assuming that the crack-tip residual stress effect is attributable to the monotonic plastic zone, these models essentially simulate the consequences of crack closure, albeit, foregoing the ability to explain the phenomenon of delayed retardation after a tensile overload [11, 12]. If they were to model some other mechanism, its effect would need to be synergistic and shown to add up to deliver results that neither can independently explain. But as a rule, either one or the other model is typically considered adequate to account for load interaction effects, implying either that the other "does the same thing", or, maybe simply irrelevant. Another possibility is that an exaggerated estimate of one effect compensates for ignoring the other.

We now know that the residual stress effect in fatigue crack growth works in two distinctly different ways [13]. One may identify these as the "far-field" and the "near-field" components, but not in the sense sometimes implied in the literature [14]. The far-field component via the monotonic plastic zone and due to material and structural processing parameters such as cold working, welding, differences in thermal expansion between elements of built-up structures, etc., impacts fatigue crack closure in much the same manner as stress ratio under constant amplitude loading. The superposed effect of all elastic residual stress fields combined with applied external loading is what is seen by the fatigue crack. The near field component is driven by the mechanics of crack-tip cyclic stress–strain hysteresis and its effect on cyclic environmental action [15]. Thus, near-tip residual stress after the previous cycle determines crack-tip diffusion kinetics during the rising portion of the next cycle, impacting instantaneous material resistance to micro fracture of

crack-tip surface layers.[1] Therefore, by the very nature of its operative mechanism, near field residual stress affects atmospheric near-threshold resistance to crack extension. The closure affects crack-tip mechanics. Near-tip residual stress affects material resistance to local premature fracture by "instantaneous environmental action". Specifically, ΔK_{th}, is affected, as will be shown below, because, in atmospheric fatigue, near-tip stress moderates crack-tip surface diffusion, that in turn a few atomic layers at a time. This effect diminishes with increasing slip component and totally disappears in high vacuum [19].

One may speculate, that the well-known effect of mean stress on fatigue limit may well be the direct result of the sensitivity of ΔK_{th} to a certain "near-tip mean stress" in early fatigue crack growth.

The fatigue crack tip being a singularity, crack-tip stress will exhibit hysteretic load sequence sensitivity even in the early stages of fatigue crack growth. This may extend right down to small (surface) cracks of microstructural magnitude and in high cycle/very high cycle/gigacycle fatigue where near-threshold conditions prevail to extended crack size. Importantly, near-tip stress exhibits "cycle-sequenced sensitivity", whereby, near-tip residual stress upon unloading will always be sensitive to load history. It follows, that ΔK_{th} under a pseudo-random load sequence can vary from cycle to cycle. ΔK_{th} is cycle-sequenced sensitive.

Cycle-sequence sensitivity does not require a crack extension. The effect will be seen right up to growth rate levels where a crack extension is less sensitive to the environment and more to slip. These observations were confirmed by a series of experiments involving specially designed simple variable-amplitude sequences in air and also in vacuum that illustrate the role of crack-tip diffusion kinetics of active species, i.e., hydrogen from moisture in air and oxygen at elevated temperature and specifically, the effect on it of near-tip residual stress and significantly, the absence of such effect in high vacuum.

One must note that the potential significance of surface diffusion kinetics in controlling near-threshold response has been well known for a long time [20–22]. What was not appreciated earlier, is the moderating effect of near-tip residual stress on diffusion kinetics and the associated variation in ΔK_{th}.

One may wonder why the obvious connection between load history and the "physics and chemistry" around the fatigue crack-tip was overlooked for so long. One possibility may be the propensity in fracture mechanics analyses to assume the

---

[1]Reference [15] alludes to a mechanism of Brittle Micro Fracture (BMF) on the assumption that hydrogen released by reaction of moisture with nascent, highly stressed crack tip surface layers diffuses into and embrittles them, inhibiting slip and thereby leading to fracture. This model has been questioned by evidence of crack extension by slip in Al-alloys even at very low crack growth rates of atmospheric fatigue [16]. More recent studies on steel indeed show that hydrogen promotes rather than inhibits slip, albeit in a highly localized manner [17]. If hydrogen indeed acts as an agent of strain localization, large inhomogeneity in the onset of slip will lead to reduction in the number of slip planes and hence to a sharper crack tip even if the material may be ductile. This may explain the tendency of the fatigue crack tip to be sharper in corrosive medium [18] than in air. Obviously, a high degree of strain localization leads to the same consequence as brittle fracture, with the exception that the fracture occurs in shear rather than tension.

crack-tip response to be elastic—ideally plastic. Such simplification leads to the belief that crack-tip stress ratio will always be R = −1, irrespective of applied stress ratio. Indeed, with increasing crack-tip cyclic plastic strain as under the Paris Regime, the near-tip stress ratio may tend towards minus unity and render near-tip stress less sensitive to load history. Importantly, with increasing growth rate, the relative contribution of crack-tip surface phenomena will diminish that may also explain the diminishing effect of environment and cycle frequency at growth rates above 10^{-3} mm/cycle.

3 Summary of Previous Work

Engineering application of the new understanding required two additional inputs. First, an analytical model is required to describe the mechanics of cycle-by-cycle crack-tip inelastic stress response as a function of applied stress intensity history. This involves an extension of the conventional application of Linear Elastic Fracture Mechanics (LEFM) in order to account for the reality of near-tip cyclic stress and applied stress intensity not being uniquely related at any instant, (except at peak value of K_{max}).[2] Second, it is necessary to establish the relationship between (computed) near-tip residual stress and (instantaneous) ΔK_{th}. This demands a deviation from standard practice such as ASTM E647 that stipulate test conditions that essentially result in reproducible and more or less identical near-tip residual stress. Instead, a procedure is required that will enforce user specifiable values of near-tip residual stress over a sufficiently vast range, representative of service load history.

Methods were developed to meet the two additional requirements in a manner that renders them to adaptation as standard practice [23]. A simple analytical procedure was developed to model near-tip inelastic stress response as a function of applied stress intensity. The procedure is modeled after the Local Stress–Strain approach to describe inelastic stress–strain at a notch [24–27]. In order to characterize ΔK_{th} as a function of controlled near-tip residual stress, a fully automated fatigue crack growth test system was developed that employs a decreasing ΔK algorithm but with P_{max} = Const and with programmable periodic slow overloads and underloads designed to leave behind controlled and computable magnitude of near-tip residual stress (see Fig. 1). The system allows accelerated generation of the relationship between ΔK_{th} and near-tip residual stress, σ^* by virtue of high-frequency baseline cycling. P_{max} being constant and with the periodic overload/underload sequence controlling near-tip residual stress, rate of decrease of ΔK is rendered practically irrelevant. As a consequence, threshold (no growth)

---

[2]This is not to suggest that LEFM is unsuitable for fatigue crack growth analysis. Just as monotonic and cyclic plastic zone size are computed as a unique function of applied stress intensity, near-tip inelastic stress response can also be computed from K. It is the unique correlation between the two that retains validity of LEFM approach.

conditions are met within a few mm of crack extension using much higher rates of decrease of ΔK than are permissible per ASTM E647. This allows multiple ΔK_{th} values to be obtained on a single compact tension specimen as seen from individual data sets in Fig. 1c.

The factor of five variations in ΔK_{th} as a function of near-tip residual stress underscores the significance of the sensitivity of atmospheric near-threshold fatigue behavior to load sequence. Given the underlying physics of the relationship, one may expect a similar relationship to exist for other materials and for other environments as well. Thus, the data in Fig. 1c are likely to shift to the right with decreasing partial pressure of moisture at room temperature. They may shift to the left with increasing test frequency as less time is available under the loading half-cycle for surface diffusion to saturate. Expectations along the same lines may apply with regard to fatigue response at elevated temperature.

Extension of the emergent understanding to engineering application proceeded in a stage-wise manner. The entire effort including this study was built around quantitative fractography of discernible crack extension between unambiguously identifiable markers that also served to create the desired magnitude of near-tip residual stress. For this reason, most of the work was performed on 2024-T3 Al–Cu alloy. This is a model material that practically ensures reproducible striation and marker patterns, practically with "digital precision" as was established in early work [28]. First, a number of specially designed experiments confirmed the existence of the near-tip residual stress effect and its significance and did so in a manner that precluded the effect of other load interaction mechanisms [29–31]. These experiments also confirmed the presence and synergistic action of fatigue crack closure.
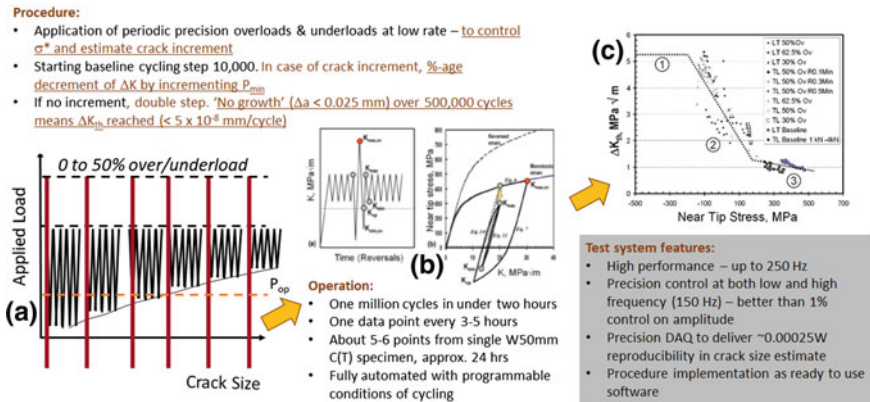
Fig. 1 Procedure to determine the relationship between threshold stress intensity and near tip residual stress. **a** Type of loading used in threshold testing involves periodic controlled overloads between baseline cycling of programmable duration and diminishing range. **b** Near-tip residual stress is determined for the next block of baseline cycling (**c**) ΔK_{th} is determined from no growth conditions. Note the factor of five variations in its value as a function of σ^*

The second set of experiments was devoted to establishing the relationship (summarized by Fig. 1c) between computed near-tip residual stress and ΔK_{th}. The third set of experiments was designed around this relationship. The goal was to induce either crack arrest or crack growth exclusively through identical overloads but by manipulating load sequence to cause vastly different near-tip stress [32, 33]. Figure 2 shows a typical fractograph from one of the experiments, whose content cannot be explained by any of the models that are currently in practical use. These experiments illustrated the sensitivity of post-overload growth rate to the magnitude of underloads that followed the tensile overload. The degree of sensitivity was backed up by computed values of near-tip residual stress. The computations, as well as fractographic evidence, showed the relative insensitivity of post-overload crack growth to the magnitude of underload preceding the overload. Last, but not the least, the experiments clearly showed that crack-tip blunting upon application of an overload briefly eliminates closure by rendering the crack fully open. This has been shown by other authors as well, but in a different context. In our experiments, complete closure recovery was seen to be rapid and consistently within about 1% of crack extension in terms of overload plastic zone size. This was irrespective of the extent of crack extension after the previous overload. This suggests that closure transients caused by crack-tip blunting can be numerically simulated. This possibility led to the development of a multi-mechanism model to simulate fatigue crack growth under programmed block loading involving periodic overloads, etc. A brief description of the analytical procedure is forthcoming.
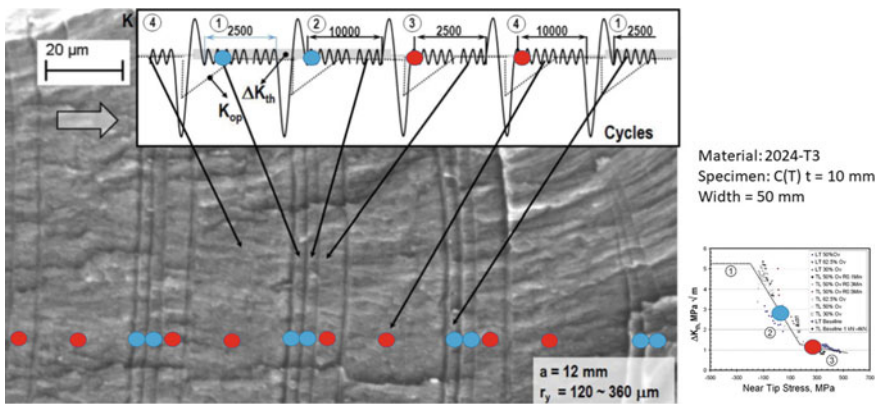
Fig. 2 Typical fractography from specially designed experiment to validate a new understanding of the relationship between threshold stress intensity and near-tip residual stress. Magnitude and duration of baseline cycling were specially designed between differently sequenced periodic overloads to demonstrate controlled crack arrest and propagation. This experiment revealed the consequences of crack-tip blunting that enforces delayed crack arrest after closure recovery [32]

4   Scope of Present Study

The fourth set of experiments was designed with two objectives. The first objective was to check the capability of the new model to correctly simulate crack growth under adaptations of the well-known TWIST load spectrum, engineered to test quality of estimates under extended residual life of the order of ten million cycles and above, with high induced sequence sensitive variability in growth rates that arguably cannot be explained by any of the models currently in use. The second objective was to check the new model for "microscopic" consistency, i.e., the ability to not only correctly estimate average growth rates, but also the relative contribution of individual load levels in the load spectrum. Considering that the TWIST spectrum contains a healthy spread of different load amplitudes, all of which contribute to damage, microscopic consistency may serve as an assurance that the model is better equipped to handle differences between load spectra as well as extreme differences induced by load sequence.

5   The SuperTWIST Load Spectrum

The Transport WIng STandard (TWIST) load spectrum has served as a reference for fatigue testing over long duration cycling [34]. It contains almost half a million load cycles in 8 incremental amplitudes corresponding to actual statistics of gust loading over 5,000 flights with as many ground-to-air cycles included. The smallest amplitudes at levels 1, 2, 3 each carry a 10% increment with respect to the 1 g mean load of the spectrum. As statistics of smaller gusts increase exponentially with an asymptotic decrease in amplitude, each of the levels 1–3 correspondingly decreases in cycle count (frequency of occurrence) by one order of magnitude over the previous level. Thus, over 5,000 flights, there are about 450,000 cycles of level 1, 45,000 of level 2 and 4,500 of level 3.

TWIST was chosen for the present study because it shows an almost log-linear increase of damage sum in both crack growth as well as cumulative fatigue with increasing frequency of occurrence (decreasing magnitude) of load cycles [35, 36]. This means that each load amplitude down to the smallest one contributes to fatigue damage, with reducing magnitude more than made up by vastly increasing frequency of occurrence. By implication, any omission of smaller load levels to speed up testing will inevitably lead to exaggerated life estimates in terms of flights. Tests under MiniTWIST [37] showed a dramatic increase in residual life over TWIST. This is in contrast to MiniFALSTAFF spectrum that shows hardly any change from the (full) FALSTAFF. FALSTAFF is a combat aircraft load spectrum. It has been shown that in the FALSTAFF spectrum, over 90% of the damage is from less than 10% of the load cycles, suggesting that combat aircraft load spectra like FALSTAFF are not the best candidates to evaluate the quality of modeling [37]. This is because the sequence of large cycles determines the extent of damage under

the smaller ones. The reverse does not apply. From the viewpoint of evaluating fatigue models, load histories immune to sequence effects are not valuable. By the same token, one must conclude that the omission of load cycles below Level 1 in the TWIST spectrum must have come at the price of ignoring a vital statistic of gust loads. To test the multi-mechanism model for its ability to correctly interpret the effect of load sequence under near-threshold conditions, one more load level, Level 0 was inserted into the spectrum, hence the name SuperTWIST. Level 0 carries half the amplitude and $10\times$ of the cycle count of Level 1 in keeping with the statistical trend of smaller gust loads. Thus, SuperTWIST has a total duration of about 5 million cycles over 5,000 flights.

The TWIST spectrum is intended for pseudo-random flight-by-flight application in laboratory testing. However, such testing is not suitable for assessing the relative contribution of individual load levels to damage, except by elimination (omission) over repeat tests that requires much effort. The experience with quantitative fractography using specially programmed load sequences served as a motivation to adopt the same technique to investigate fatigue response to the SuperTWIST spectrum. With this objective, two versions of programmed load sequences were derived from SuperTWIST. The two versions were intended to be statistically identical, but with major cycles sequenced differently to produce contrasting response given new understanding of the near-tip residual stress effect.

Design of the new programmed load sequence involved reconciliation of contradictory requirements. All cycles of a given level, except the major ones, were consolidated into a single step. Quantitative fractography demands appearance on the fracture surface of crack extension from multiple applications of the load program. Their multiple appearances underscore visible, reproducible and more or less equal crack extension from each application. At the same time, crack extension from individual steps in the block must be clearly discernible to eliminate confusion in quantitative analyses. In achieving these objectives, the main goal of allowing the targeted load interaction to be representative of actual service conditions should not be compromised beyond acceptable proportions. As an example, converting all 5,000 flights into a single block may be an unacceptable deviation from the reality of flight-by-flight occurrence. Besides, the sizeable crack extension over a single application of such a block would render fractography impossible.

Figure 3 shows the two resultant programmed block load spectra, SuperTWIST-LoHi, and SuperTWIST-HiLo that served our experiments. These represent 50 flights and contain about 50,000 cycles (50,014 to be precise). In order to account for the associated statistics, the TWIST spectrum was truncated from the 8th down to the 5th load level. Thus four load cycles at level 5 were available for the purpose of marking and "engineering" sequence effects. However, there are five steps in the program. To work around this problem, cycles at level 3 are sequenced immediately after level 4. As these two steps are more or less of the same magnitude, they are applied without a marker in between. There was also the possibility that being of sufficiently large magnitude (Level 3 represents the Ground-to-Air cycle between flights), these cycles would leave behind discernible striations for differentiation.
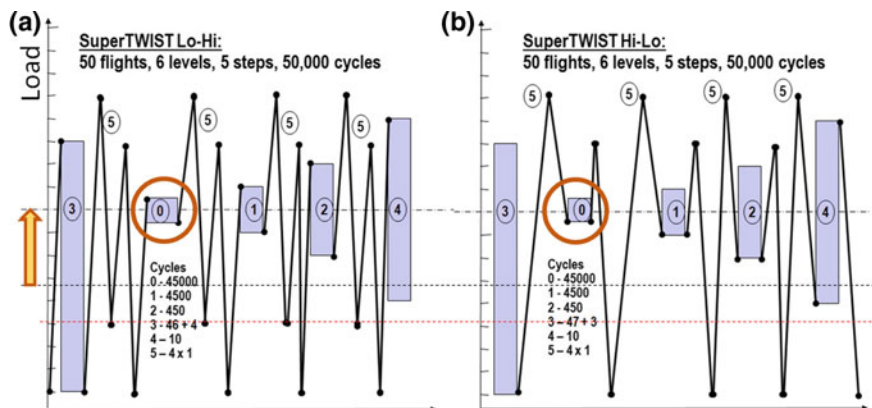
Fig. 3 a LoHi and **b** HiLo renditions of the SuperTWIST load spectrum representing a total of 50 flights. Note the difference in the transition from one step to the other in the two sequences. Step 0 was added to investigate the role of a large number of very small amplitude cycles that are normally omitted to reduce test duration. In (**a**) all steps are arranged to be on the rising half of major cycles. The reverse applies to (**b**)

The LoHi and HiLo versions of SuperTWIST may appear identical at first glance. Even Level 5 "overloads" that also serve as markers are in the same position in both sequences. What makes the two drastically different is the manner of transition between each occurrence of Level 5 and the smaller amplitude step of cycles that follows it. The design of the two sequences is intended to highlight the potential effect of the transition on near-tip residual stress over the following step in a manner that ought to be similar to what was reported in earlier work. This also represents an acid test of the new multi-mechanism model, a test, unlikely to be passed by conventional modeling schemes that cannot arguably sense any difference between the two load sequences. After all, neither crack closure nor overload plastic zone size would be affected by the transients in question. Crack-tip blunting occurs as a consequence of an increment in K_{max} by comparison to the previous cycling that caused crack extension. Therefore, the effect of crack-tip blunting by way of removal of closure immediately following the application of maximum (marker) load at Level 5 may be assumed to be similar in both cases. Recovery of closure following the marker loads is driven exclusively by crack increment during the following step and may be deemed similar across all the steps and over the two sequences. This was shown in previous work that indicated an approximate 1% of crack extension into the monotonic plastic zone to be adequate for closure recovery from blunting.

In this study, the SuperTWIST sequence was applied with an upward offset of the load program such that all minimum loads rise into tension. The offset is marked on Fig. 3. The upwards offset in load raises the stress ratio of all load cycles and reduces the significance of crack closure as a load interaction mechanism. Four more tests were performed without offset to simulate conditions closer to the actual

TWIST sequence. Two of these tests were at a maximum load of 5 kN and another two at 3.5 kN. Fractographic analysis of these four tests is the subject of a separate study. However, it may be noted that the trends in growth rates varied between LoHi and HiLo sequences in the same manner as the first two whose description is forthcoming.

6   Experimental Procedure

The tests were performed on 50 mm wide and 4.95 thick C(T) specimens cut for crack orientation in the L-T direction from 2024-T3 Al-alloy sheet material. The clevis grips used in testing carried roller bearings to permit compressive loads. A 0.3 wide wire notch cut to crack size of 11.5 mm served as the crack initiator. Testing under spectrum loading commenced without prior fatigue pre-cracking.

The tests were performed on a BISS Nano 25 kN test system using TestBuilder software to program the required load sequence. A Crack Mouth Opening Displacement (CMOD) gauge enabled periodic automatic recording of COD versus Load at low cycling frequency of 0.1 Hz. This operation coincided with the application of the Level 5 marker load cycles. The crack growth curve was later constructed from unloading compliance estimates. The tests were performed without interruption on 24/7 basis and were remotely monitored at all times using the BISS-IOT software, Cycling frequency under the SuperTWIST sequence was varied between 3 and 20 Hz depending on load amplitude in individual steps. Real-time adaptive control ensured cyclic loading accuracy was well within 2%. This ensured consistency of marker and striation spacings observed during microscopic observations of the fatigue fracture surface.

One test was performed under the Lo-Hi sequence, the other under HiLo. In both tests, the maximum load corresponding to Level 5 was set to 4 kN.

7   Analytical Procedure

Figure 4 summarizes the analytical process to compute fatigue crack growth under spectrum loading. It is built on the following premises:

1. The fatigue crack extends only during the rising load half-cycle
2. ΔK_{th} is determined by near-tip residual stress at the commencement of the rising load half-cycle. Near-tip residual stress is determined using the procedure described in [23] by simulating near-tip inelastic hysteretic stress response assuming a fully open crack (from blunting) and ignoring the effect of crack extension on near-tip response.
3. Crack extension over the loading half-cycle will depend on ΔK_{th}, the excursion in K from K_{op} to K_{max} and the proximity of K_{max} to K_c. It is determined from the
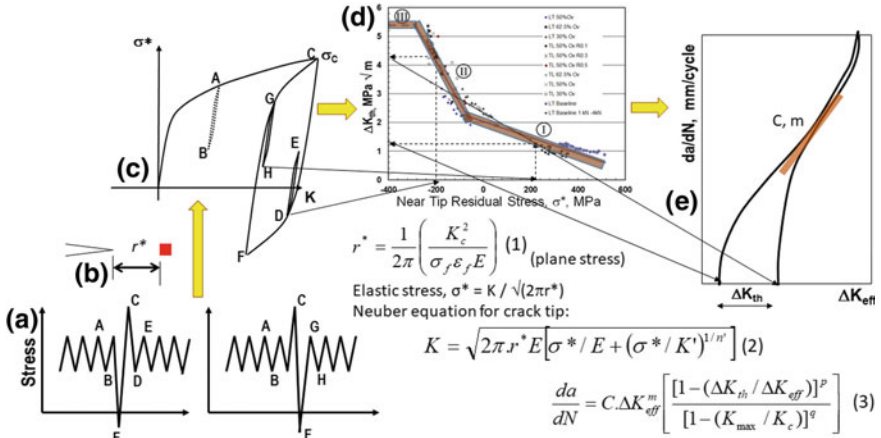
Fig. 4 Schematic of the analytical procedure. Load sequence as in (**a**) can be converted for a point as in (**b**) into local stress versus K-history (**c**). **d** This relationship is used to translate computed near-tip stress into threshold stress intensity so it can be used to compute crack growth rate from Eq (3)

equations that appear in Fig. 4. The figure summarizes the connection between applied sequence (Fig. 4a), leading through near-tip point (Fig. 4b, Eq. 1) stress simulation (Fig. 4c and Eq. 2) to estimate applicable ΔK_{th} for the next cycle (or step) and on to the growth rate equation (Eq. 3 in Fig. 4) schematically shown in Fig. 4c.

4. In the event the monotonic plastic zone over the rising load half-cycle exceeds current (residual) zone size by more than 1%, crack-tip blunting is assumed and the crack is treated to be fully open over the following load cycles with Kop returning to its stable value over an increment of 1% of new monotonic plastic zone.

5. K_{op} is deemed to consist of two components that are computed from the "Elber constants", k_1 and k_2 (see Fig. 5). The "minimum" component is associated with K_{max} that would induce the current monotonic plastic zone. The second component is treated as a cycle-dependent variable determined exclusively from the ratio of K_{min} in the previous unloading half-cycle to the K_{max} "associated with current monotonic plastic zone". The exception is crack-tip blunting, upon which, K_{op} will linearly recover from zero with crack increment as explained earlier and simulated by an attenuation coefficient increasing from 0 to 1 with crack increment.

Constants C, m and K_c for the crack growth rate equation were determined from a few constant amplitude tests. "p" and "q" were assumed to be unity. Crack closure constants were adopted from previous tests on the same material of representative thickness and to match a limited set of test data from different stress ratio [32]. ΔK_{th}

Fig. 5 Calculation of crack closure load for individual steps in the load spectrum

was assumed to be governed by the relationship established in previous work as shown in Fig. 4d. That study was on the same material and specimen type.

Using the above procedure, estimates were made of near-tip residual stress at the commencement of each of the five steps in the sequence. In doing so, it was assumed that the application of P_{MAX} induces crack-tip blunting given the crack increment in the previous step. These estimates were made at a crack increment of 1 mm. For each of the computed residual stress value, the associated ΔK_{th} was estimated. This enabled the calculation of fatigue crack extension in each step after accounting for crack closure. In calculating crack closure, the effect of blunting was ignored on the consideration of a negligible effect of the transition zone of closure recovery.

Tabulated values of near-tip residual stress, crack opening load, ΔK_{th} and ΔK_{eff} for individual steps as a function of crack size permitted their consideration whilst studying actual crack extension as seen from fractographs. This is the essence of check for microconsistency of the analytical model employed.

8   Results and Discussion

The specimen subject to the Lo-Hi sequence failed after 4,500,000 cycles, which represents 100 blocks or 5,000 flights. The one tested under the HiLo sequence failed after 13,500,000 cycles that correspond to 300 blocks or 15,000 flights.

Considering that commercial transport aircraft are typically inspected after every 5,000–10,000 h of operation, and considering the initial crack size of 11.5 mm, the residual life as seen in the two tests appears to conform to a range of practical interest. Given satisfaction of this rudimentary criterion of relevance, one may assume that the forthcoming discussion pertains to parameters of practical relevance.

Fracture surfaces from the tests performed under offset SuperTWIST LoHi and HiLo sequences were subject to fractographic analysis on Scanning Electron Microscopes (SEM). Typical fractographs along with results of supporting analytical effort appear below. All the fractographs were obtained from the mid-thickness region that offers good clarity and whose coverage in terms of reproducible pictures extends to within 0.5 mm of either specimen surface.

The quality of fractographic marking was adequate to identify individual steps without any ambiguity using a simple process. To start with, the four Level 5 marker loads left behind well-defined striations in all cases. Fortunately, in case of the TWIST spectrum, and given the choice of material, reference load levels corresponding to residual life range of practical interest are evidently associated with Level 5 load ranges falling strictly into the Paris Regime. This leaves behind extremely well-defined and unambiguous marker bands. First, the band corresponding to Steps 4, 3 is identified. This is easy in most cases because of the distinct striation patterns produced by the 56-odd cycles that suggest affinity with the Paris Regime, where growth rate is in the range 10^{-4} to 10^{-3} mm/cycle. Using this band as a reference to the bands associated with sequentially placed steps 0, 1, 2 that follow can be readily identified. These are separated by clearly discernible striations associated with the marker (over) loads at Level 5. Further proof of correct identification is by way of repeatability of the band patterns corresponding to repeat blocks of loading.

A distinct feature of this fractographic study is the remarkable reproducibility of the morphology of the fracture surface that is uniquely associated with the growth rate. Thus, Steps 0 and 1 without exception "belong to" the near-threshold regime of growth rates below 10^{-5} mm/cycle. Step 2 showed growth rates that straddled the near-threshold and Paris Regime, while Steps 3, 4 were always in the Paris Regime.

Figure 6 shows a fractograph obtained under SuperTWISTLo-Hi at the crack size of 13 mm, where crack growth rate is of the order of about 1.5 mm per 1000 flights. Even at this region of a low rate of fatigue, Step 0 accounts for a third of crack extension, even though the load level is considered too small to be part of the standardized TWIST spectrum. The computed value of ΔK_{th} for this point is 1.3 MPa$\sqrt{m}$, while applied ΔK_{eff} is 1.76 MPa$\sqrt{m}$. As seen from the fractograph, Steps 0 and 1 together account for 60% of crack extension under the Lo-Hi rendering of the SuperTWIST spectrum. It is interesting to note that Step 1 is omitted in MiniTWIST. Such omissions are often based on considerations of fatigue limit and ΔK_{th}. Indeed, the growth rate in Step 0 is as low as 6.6×10^{-7} mm/cycle. Obviously, even at such low growth rates, provided there are a sufficient number of load cycles, they will advance the crack significantly, particularly if adverse sequence effects induce reduced ΔK_{th} as seen in Fig. 6. Adding to this, real-life effects of far reduced cycling frequency, of environmental exposure, etc., and it would follow, that assessment of ΔK_{th} under realistic conditions is extremely important to engineering practice.

The fractograph in Fig. 7 is from the crack size of 25 mm, where individual bands are still discernible, though the crack is extending over 0.3 mm over a single block which exceeds grain size. Though the crack has accelerated by about an order
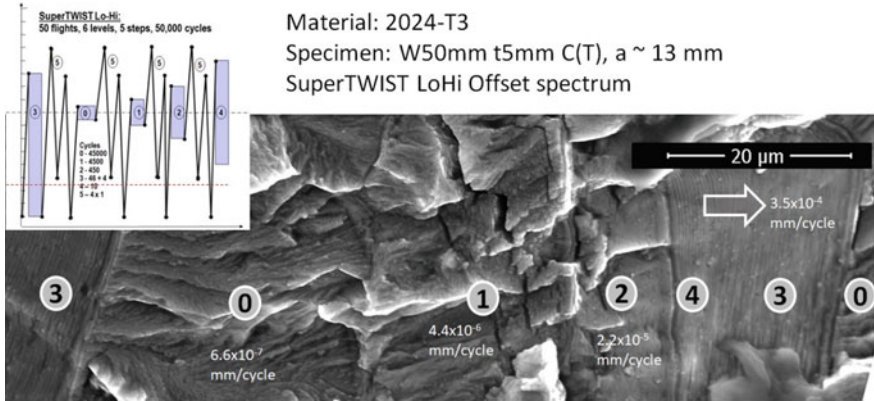
Fig. 6 Fractograph obtained under SuperTWIST Lo-Hi spectrum at a $\sim$ 13 mm
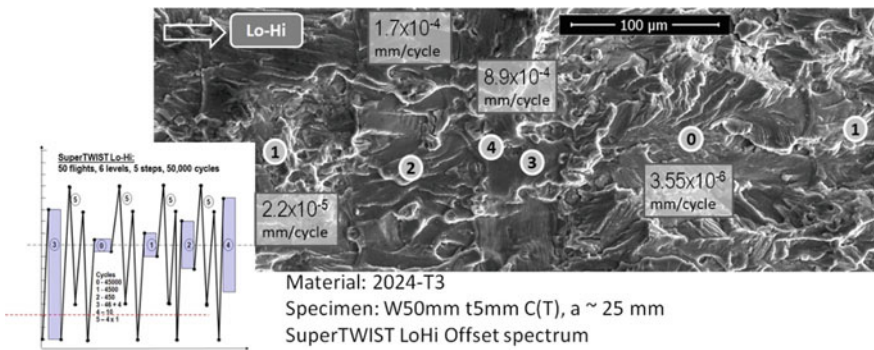
Fig. 7 Fractograph obtained under SuperTWIST Lo-Hi spectrum at a $\sim$ 25 mm

of magnitude, the distribution of crack extension across the steps 0, 1, 2 has remained more or less unchanged. However, crack extension in Step 2 noticeably exceeds that in Steps 3, 4, which is the opposite of Fig. 6. Note that at this point, with $\Delta K_{eff} \sim 9.5$ MPa$\sqrt{m}$, Step 2 has "graduated" into the Paris Regime, whose slope is much lower than over the near-threshold region. Thus, because Steps 3, 4 are still in the Paris Regime, they have not been able to accelerate crack growth beyond what would follow from a slope of about m = 2.4. One may, therefore, attribute the change in proportions to the migration of one step from one crack extension mechanism to another.

Figure 8 shows fractographs from the specimen subject to the SuperTWIST sequence in HiLo rendering. Two typical fractographs from this test appear in the figure, one from the crack size of 14 mm and the other from 23 mm. In stark contrast with the LoHi sequence, crack extension in Steps 0, 1 and 2 is highly retarded under the HiLo sequence. Crack extension under Step 0 is so marginal at less than a fraction of a micron over 45,000 cycles, suggesting a growth rate much
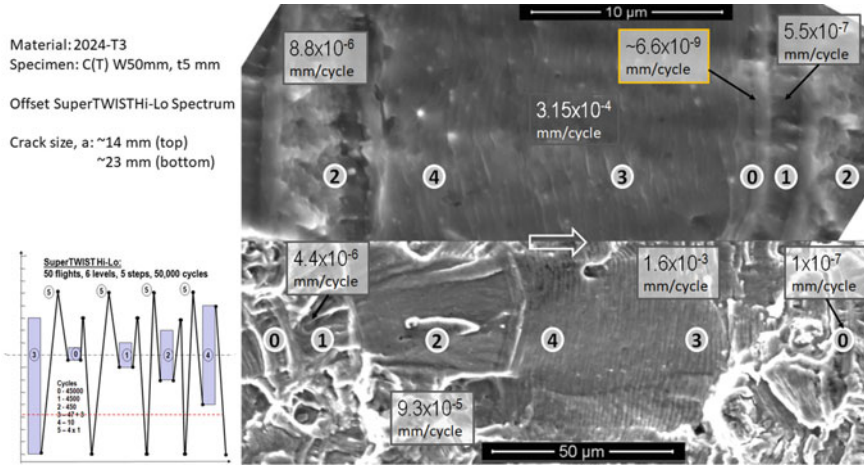
Fig. 8 Fractograph obtained under SuperTWIST Hi-Lo spectrum at crack sizes 14 (top) and 23 (bottom) mm

less than 10^{-8} mm/cycle even though $\Delta K_{eff} \sim 1.8$ MPa√m, a virtual crack arrest. Interestingly, the growth rate in Step 0 does not appreciably increase even at the crack size of 23 mm and $\Delta K_{eff} \sim 2.5$ MPa√m. Interestingly if at smaller crack length, crack extension in Step 2 was less than a fourth of that in Steps 3, 4, at 23 mm, it has increased in proportion to almost 70% of Steps 3, 4. Judging from the growth rate and fracture morphology, the reason seems to be the same as in the case of the LoHi sequence, and, associated with the transition of Step 2 into the Paris Regime. This also implies, that the favorable HiLo sequence does not do much to retard crack growth in Step 2 once baseline ΔK_{eff} crosses a certain value. Indeed, at this point, is in excess of 17 MPa√m and may be too far removed from the maximum possible ΔK_{th} of 5.5 MPa√m to be influenced by it. One may point out, that other known load interaction mechanisms cannot possibly explain this differentiation in fatigue response with increasing ΔK (or growth rate).

Note that the bottom fractograph shows clear signs of local quasi-static crack growth component arising out of strain localization at secondary particulates at bands from Step 1 and towards the end of Step 3. These, however, have absolutely no impact whatsoever on the retarded crack extension over Step 0 in the immediate vicinity. From a modeling perspective, the implication may follow, that in modeling near-threshold fatigue crack growth, while one needs to scrupulously account for sequence effects on ΔK_{th}, there will be little or no influence from either crack extension or local surface morphology as affected by other load cycles.

In an attempt to put fatigue response under LoHi and HiLo renditions into proper perspective, a composite picture was built using fractographs from the two failures at approximately 17 mm crack size. The resultant picture appears as Fig. 9. For ready comparison, a cropped fractography from the HiLo test is placed as an inset into the LoHi fractograph, taking care to ensure that crack extension over Steps 3, 4
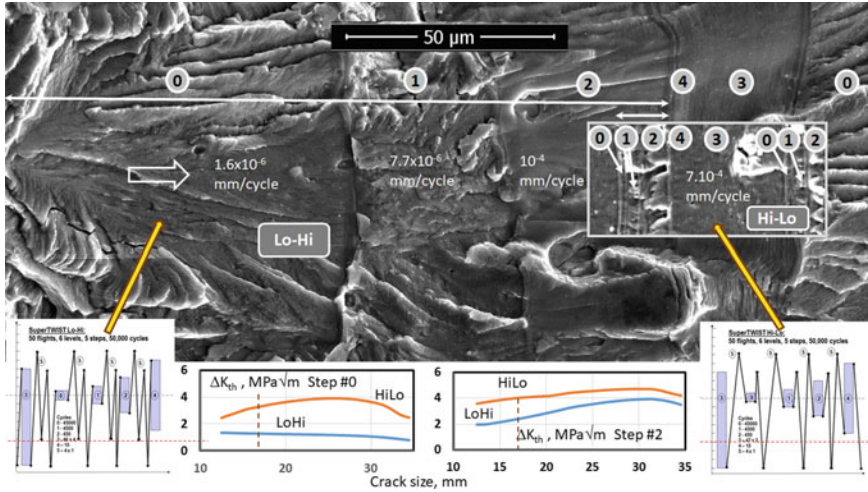
Fig. 9 Superposed fractographic images from LoHi and HiLo renderings SuperTWIST LoHi and HiLo renderings at a $\sim$ 17 mm

coincides in the two fractographs. This provides a readily assessable perspective about the differences in fatigue response to the two sequence renditions. It also provides an opportunity to judge the emergent multi-mechanism model for its microscopic consistency.

The almost $10\times$ difference in crack extension over Steps 0, 1, 2 between the LoHi and HiLo renditions is striking. Interestingly, at this crack size, even though Step 2 in the LoHi rendering appears to be on the verge of the Paris Regime, crack extension over the step is about $4\times$ greater than under the HiLo rendering. $\Delta K_{eff} \sim 12$ MPa$\sqrt{m}$ at this point. From the computer simulated values of ΔK_{th} for the two sequences shown at the bottom of the figure, it would follow that the $2\times$ difference in ΔK_{th} over Step 2 between the two sequences may explain the $4\times$ difference in growth rate. It was noted earlier that at $\Delta K_{eff} \sim 17$ MPa$\sqrt{m}$ the difference appears to turn negligible.

Figure 10 illustrates the difference between near-tip stress response to the applied K sequence associated with the SuperTWIST LoHi and HiLo renditions. On the assumption of blunting by application of Level 5 marker load, and, by retaining just one cycle in all the steps, the near-tip stress versus applied K response is plotted for the two sequences. The circles pinpoint load, K and local stress values associated with the commencement of the loading half-cycle of Step 0. The ΔK_{th} associated with this stress can be seen to also dramatically vary depending on how the preceding higher loads affected local hysteretic inelastic stress. The loops associated with the other Steps are also seen in the figure, albeit not so clearly in case of the HiLo sequence.

Figure 11 summarizes computed near-tip stress as a function of crack size over Steps 0 and 2 in the two tests and also the associated variation in ΔK_{th} with crack
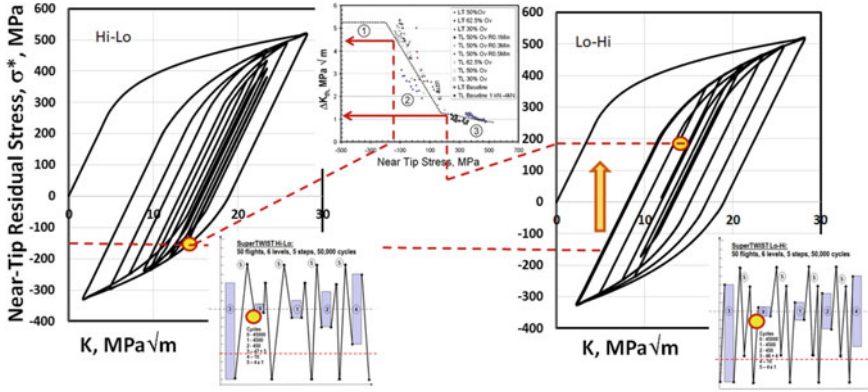
Fig. 10 Typical computed near-tip stress response to offset SuperTWIST HiLo and LoHi load sequence arrangements. Actual near-tip stresses at crack size 13 mm shown as circles for Step 0 under the two sequences. Note the vast associated difference in near-tip stress
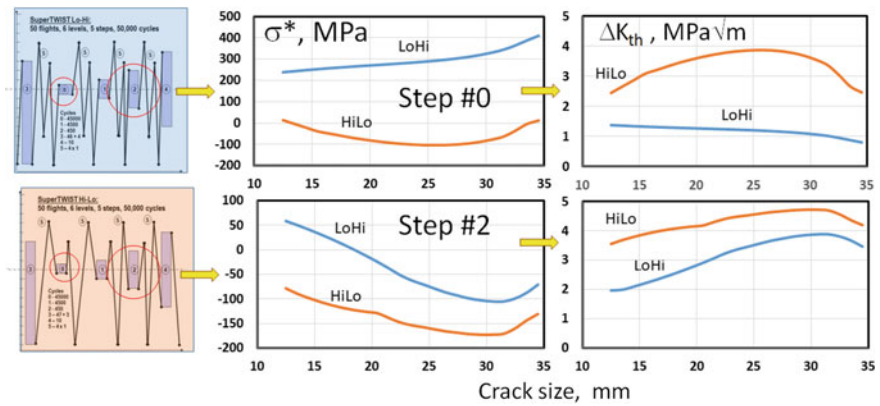
Fig. 11 Computed near-tip stress and threshold stress intensity as a function of crack length for Steps 0 and 2

size. In the case of the HiLo sequence, steady decrease into compression in near-tip residual stress with increasing crack size (applied K) is associated with the increasing extent of elastic unloading towards the commencement from a minimum of Steps 0 and 2. This, in turn, causes a steady increase with crack size in ΔK_{th} and may explain why extreme retardation in Steps 0, 1, 2 persists even if crack size and K-levels may be increasing. However, with the onset of reverse yield during unloading, the process also reverses. Unfortunately, it was not possible to obtain discernible marker band patterns at very high crack growth rates to throw more light on this aspect.

9 Summary and Future Work

This study is the first attempt to validate the multi-mechanism model against a long duration load spectrum of practical interest that was modified to enable a check for microscopic consistency, i.e., the ability of the model to correctly reproduce relative contribution of cycles over a range of load levels and over a range of stress intensity covering crack growth interval of practical value. The emphasis in this verification was to confirm the ability of the model to handle the near-threshold region extending down from the Paris Regime starting at 10^{-4} mm/cycle. This is but the beginning of a long and demanding process directed at fine-tuning modeling approach and more importantly, the process of determining the many constants required for modeling in a manner that can be deemed reproducible.

The need for much more improvement to modeling is underscored by Fig. 12 that compares estimated and experimental average crack growth rates. The data are for six spectrum load tests under SuperTWIST HiLo and LoHi sequences, including four without offset and at two different load levels. In terms of residual life, estimates and experimental results were well within 30% of each other. However, as seen from Fig. 12, errors in terms of crack growth were substantial and call for improvement. The motivation for future work in advancing the new approach of modeling near-tip stress response to account for the unavoidable physics of environmental action stems from other potential areas of its deployment. The potential and opportunity are schematically described in Fig. 13.

The load sequence shown in Fig. 13a presents much interest in engineering applications in stress corrosion cracking and elevated temperature cracking both due to hot corrosion as well as creep [38]. The direct link between near-tip stress and diffusion processes that relate to these problems underscore the potential of

Fig. 12 Comparison of estimated and actual crack growth rates from all six tests
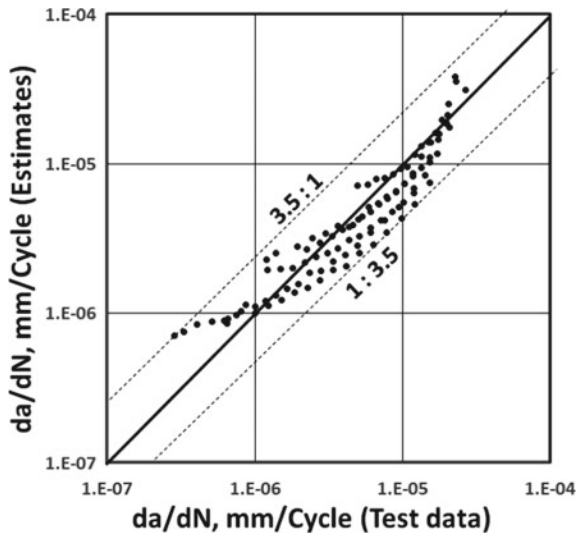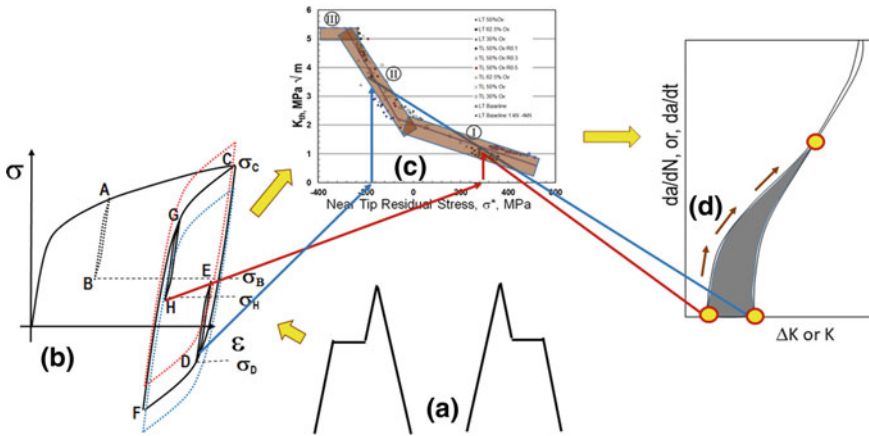
Fig. 13 Schematic of potential for modeling the influence of dwell time and material softening/
hardening effects on thresholds for crack extension

modeling these processes by translating applied K-history to near-tip stress
response. In doing so, constitutive models of material can be used to model
inevitable time-dependent shifts in near-tip response as schematically illustrated by
the dotted loops in Fig. 13b. Obviously, near-tip stress will affect the thresholds for
creep crack growth, for corrosion crack growth as well as for sustained load
cracking at elevated temperature. Much work and innovative practices are required
to required to establish the relationships between these parameters and the key
parameter that controls the near-tip physics of the processes of interest in the form
shown in Fig. 13c.

Much remains to be done with regard to the (literally) gray area shown in
Fig. 13d. There isn't a proven relationship between da/dN and ΔK_{eff} to cover the
gray area between circles shown. A standard practice needs to be developed that
can deliver such a relationship in a reproducible manner. The arrows in the figure
indicate the shape of a curve based on standard decreasing-K testing per ASTM
E647. What is required is a relationship that would relate da/dN to ΔK_{eff} in the
interim between and the Paris Regime, given instantaneous near-tip residual stress.
Improved modeling of the gray area is likely to considerably improve the quanti-
tative aspect of residual life estimates.

The value of r* was chosen from the convenience of modeling. It is not clear
whether this parameter should be treated as constant. And assuming it indeed is one,
whether there may be a more rational definition for it and for the relationship
between local stress at the point and applied K. In this regard, one can at this
juncture be certain only about the procedure that was used to relate σ* to ΔK_{th}. The
validity of that procedure is borne out by the close correlation between the two as
demonstrated by a whole series of tests. This in itself may serve as a motivation to
advance the new approach.

References

1. M.A. Miner, Cumulative damage in fatigue. Trans. ASME J. Appl. Mech. **12**, A159–A164 (1945)
2. E. Gassner, Strength experiments under cyclic loading in aircraft structures. Luftwissen **6**, 61–64 (1939) [in German]
3. W. Schuetz, *A History of Fatigue* (DVM, Germany, 2008), p. 88
4. J. Schijve, Effect of load sequences on crack propagation under random and program loading. Eng. Fract. Mech. **5**, 269–280 (1973)
5. J. Schijve, Observations on the prediction of fatigue crack growth propagation under variable amplitude loading, in *ASTM STP*, vol. 595 (American Society for Testing and Materials, Philadelphia, PA, 1976), pp. 3–23
6. M. Skorupa, Load interaction effects during fatigue crack growth under variable amplitude loading. A literature review. Part II: Qualitative interpretation. Fatigue Fract. Eng. Mater. Struct. **22**, 905–926 (1999)
7. W. Elber, The significance of fatigue crack closure, in *ASTM STP*, vol. 486 (ASTM, Philadelphia, 1971), pp. 230–242
8. O.E. Wheeler, Spectrum loading and crack growth. ASME J. Basic Eng. 94 (1971)
9. J. Willenborg, R.H. Engle, H.A. Wood, *A Crack Growth Retardation Model Based on Effective Stress Concepts* (AFFDL-TM-71-1 FBR, WPAFB, OH, 1971)
10. J.C. Newman, A crack-closure model for predicting fatigue crack growth under aircraft spectrum loading. Methods and models for predicting fatigue crack growth under random loading, in *ASTM STP*, vol. 748, ed. by J.B. Chang, C.M. Hudson (1981), pp. 53–84
11. W.J. Mills, R.W. Hertzberg, The effect of sheet thickness on fatigue crack retardation in 2024-T3 aluminum alloy. Eng. Fract. Mech. **7**, 705–711 (1975)
12. M.R. Ling, J. Schijve, Fractographic analysis of crack growth and shear Lip development under simple variable-amplitude loading. Fatigue Fract. Eng. Mater. Struct. **13**, 443–456 (1990)
13. R. Sunder, Unraveling the science of variable-amplitude fatigue. J. ASTM Int. **9**(1), Paper ID JAI103940 (2012). Also, ASTM Special Technical Publication **1546**, 20–64 (2012)
14. C.M. Ward-Close, A.F. Blom, R.O. Ritchie, Mechanisms associated with transient fatigue crack growth under variable-amplitude loading: an experimental and numerical study. Eng. Fract. Mech. **32**(4), 613–638 (1989)
15. R. Sunder, Fatigue crack growth as a consequence of environment-enhanced brittle-micro fracture. Fatigue Fract. Eng. Mater. Struct. **28**(3), 289–300 (2005)
16. Y. Ro, S.R. Agnew, G.H. Bray, R.P. Gangloff, Environment-exposure-dependent fatigue crack growth kinetics for Al-Cu-Mg/Li. Mater. Sci. Eng. A **468–470**, 88–97 (2007)
17. Y. Murakami, T. Kanezaki, Y. Mine, S. Matsuoka, Hydrogen embrittlement mechanism in fatigue of austenetic stainless steels. Metall. Mater. Trans. A **39**, 1327 (2008)
18. E. Gach, R. Pippan, Cyclic crack tip deformation—the influence of environment, in *Proceedings of the Tenth International Conference on Fracture, International Congress of Fracture*, Hawaii, Dec 2001 [Paper ICF 100420OR]
19. R. Sunder, W.J. Porter, N.E. Ashbaugh, The role of air in fatigue load interaction. Fatigue Fract. Eng. Mater. Struct. **26**, 1–16 (2003)
20. C.Q. Bowles, The role of environment, frequency and wave shape during fatigue crack growth of aluminum alloys, Ph.D. thesis, Report No. LR-270, Delft Univ. of Technology, Delft, The Netherlands, 1978

21. J. Petit, G. Henaff, C. Sarrazin-Baudoux, *Mechanisms and Modeling of Near-Threshold Fatigue Crack Propagation, Fatigue Crack Growth Thresholds, Endurance Limits and Design*, vol. 1372, ed. J.C. Newman, Jr., R.S. Piascik, ASTM Spec. Tech. Publ. (American Society for Testing and Materials, West Conshohocken, PA, 2000)
22. F.J. Bradshaw, C. Wheeler, The effect of gaseous environment and fatigue frequency on the growth of fatigue cracks in some aluminium alloys. Int. J Fract. Mech. **6**, 255–268 (1969)
23. R. Sunder, Characterization of threshold stress intensity as a function of near-tip residual stress: theory, experiment, and applications. Mater. Perform. Charact. (ASTM J.) **4**(2), 105–130 (2015)
24. H. Neuber, Kerbspannungslehre [*Theory of Notch Stresses*] (1937), ed. J.W. Edwards (Springer, Berlin, Ann Arbor, MI, 1946)
25. W. Ramberg, W.R. Osgood, Description of stress-strain curves by three parameters, Technical Report No. 902, National Advisory Committee for Aeronautics, Washington, D.C., 1943
26. R.M. Wetzel, A method for fatigue damage analysis, Ph.D. thesis, Dept. of Civil Engineering, Univ. of Waterloo, ON, Canada, 1971
27. *SAE Fatigue Design Handbook*, 3rd ed., AE-22 (Society for Automotive Engineers, Warrendale, PA, 1977)
28. R. Sunder, *Binary Coded Event Registration on Fatigue Fracture Surfaces.* J. Soc. Env. Eng. (SEECO, London 1983), p. 197
29. R. Sunder, Effect of periodic overloads on fatigue thresholds in Al-alloys, in *Fatigue and Fracture Mechanics: 34th Volume, ASTM STP 1461*, ed. by S.R. Daniewicz, J.C. Newman, K.H. Schwalbe (ASTM International, West Conshohocken, PA, 2005), pp. 557–572
30. R. Sunder, Fractographic reassessment of the significance of fatigue crack closure, in *Fatigue and Fracture Mechanics: 34th Volume, ASTM STP 1461*, ed. by S.R. Daniewicz, J.C. Newman, K.-H. Schwalbe (ASTM International, West Conshohocken, PA, 2005), pp. 22–39
31. R. Sunder, On the hysteretic nature of variable-amplitude fatigue crack growth. Int. J. Fatigue **27**, 1494–1498 (2005)
32. R. Sunder, A. Andronik, A. Biakov, E. Eremin, S. Panin, A. Savkin, Combined action of crack closure and residual stress under periodic overloads: a fractographic analysis. Int. J. Fatigue **82**, 667–675 (2016)
33. R. Sunder, A. Biakov, A. Eremin, S. Panin, Synergy of crack closure, near-tip residual stress and crack-tip blunting in crack growth under periodic overloads—a fractographic study. Int. J. Fatigue **93**, 18–29 (2016)
34. J.B. de Jonge, D. Schutz, H. Lowak, J. Schijve, *A Standardized Load Sequence for Flight Simulation Tests on Transport Aircraft Wing Structures*, Report No. NLR TR 73029U, National Aerospace Laboratory (NLR), Amsterdam, The Netherlands, 1973
35. R. Sunder, *Contribution of Individual Load Cycles to Fatigue Crack Growth under Aircraft Spectrum Loading,* ed. by M.R. Mitchell, R.W. Landgraf, ASTM STP 1122 (1992), pp. 176–190
36. R. Sunder, Contribution of individual spectrum cycles to damage in notch crack initiation, ASTM STP 1211, in *Short and Long Cracks*, ed. by M.R. Mitchell, R.W. Landgraf (1993), pp. 19–29
37. H. Lowak, J.B. de Jonge, T. Franz, D. Shuetz, *Mini-TWIST: A Shortened Versoon of TWIST*, NLR Report MP 79018U (National Aerospace Laboratory, Amsterdam, 1979)
38. R.J.H. Wanhill, *Significance of Dwell Cracking for IN718 Turbine Discs*, NLR-TO-99392 (National Aerospace Laboratory NLR, 1999)

Cyclic Strain Localization Assessment by Advanced Microscopies

Jean-Bernard Vogt, Jérémie Bouquerel and Ingrid Proriol Serre

Abstract The paper reports our interesting results gained during these last years about the role of microstructure on strain localization of three different types of metallic alloys. The benefit of using advanced techniques (TEM, AFM, SEM-ECCI) is pointed out. Strain gradient and strain localization at microscopic scale and strain partition at mesoscopic scale are discussed and allow explanations for crack initiation site, precipitate dissolution or cyclic accommodation.

Keywords Dislocation structure · Precipitate dissolution · Plasticity partition · Crack initiation

List of Symbols

LCF	Low cycle fatigue
$\Delta\varepsilon_t$	Total strain variation
AFM	Atomic force microscope
SEM	Scanning electron microscope
TEM	Transmission electron microscope
cECCI	Controlled Electron Channeling Contrast Imaging
EBSD	Electron Back-Scatter Diffraction
KAM	Kernel Average Misorientation
GROD	Grain Reference Orientation Deviation

J.-B. Vogt (✉) · J. Bouquerel · I. Proriol Serre
Univ. Lille, CNRS, INRA, ENSCL, UMR 8207 - UMET - Unité Matériaux et Transformations, F-59000 Lille, France
e-mail: jean-bernard.vogt@univ-lille.fr

1 Introduction

Materials subjected to cyclic loading end up fracturing by fatigue. Even for very low applied stresses, beyond the yield stress, fatigue failure is expected as is pointed out by the studies on very high cycle fatigue (VHCF) [1]. Localized and cumulated strain, even if very small at each cycle, is the starting point of crack initiation. A microstructural inhomogeneity, present before (e.g. inclusion) or formed during fatigue (e.g. persistent slip band) or an external defect (e.g. scratch) can be responsible for strain or stress localization. For very smooth specimen or components, fatigue crack initiation takes place in general at the external surface and sometimes under the surface for VHCF. In low cycle fatigue (LCF), the loading at each cycle can be high enough to deform plastically a large number of grains. For metallic alloys subjected to LCF, the accumulation of plastic strain results in formation of dislocations structures which configuration depends on loading conditions (temperature, strain range, strain rate…) and on metallurgical features of the material (chemical composition, phase, stacking fault energy…). The partition and the localization of plasticity reflected by the analysis of the dislocations arrangements affect as well fatigue resistance as stress–strain relation of materials. It is therefore important to identify the zones of high deformation at the mesoscopic and microscopic scales.

The objective of the paper is to report our interesting results gained during these last years about the role of microstructure on cyclic strain localization of three different types of metallic alloys. Moreover, the benefit of using advanced techniques, especially atomic force microscopy (AFM), transmission electron microscopy (TEM) and scanning electron microscopy (SEM) equipped with an EBSD detector will be pointed out. AFM has been employed for careful analysis of slip traces at the surface of the fatigued specimen while TEM and SEM have been employed for dislocations imaging or crystallographic purposes.

2 Experimental

2.1 Materials

The selected materials for which the link between the microstructure and the fatigue response needed to be clarified and required advanced microscopies are a Fe–3Si steel, a Cu–Ni–Si alloy and a duplex stainless steel. Their metallurgical features are hereafter described and more details can be found in [2–6].

At first, a non-oriented silicon steel (2.88% Si 0.003% C 0.1% Mn 0.45% Al) provided in thin sheet, 350 µm in thickness is investigated. It exhibits a ferritic structure with a wide grain size distribution but determined by the intercept method as 75 µm.

The second example concerns the CuNi2Si (CW111C) alloy, solution treated around 950 °C for 2 h, hot formed, rapidly quenched and finally aged at a

temperature between 450 and 500 °C for a duration between 2 and 4 h. The grains had a size ranging from 20 to 50 μm and contained disc-like δ-Ni_2Si nano precipitates

Finally, a high nitrogen duplex stainless steel (25% Cr 3.7% Ni 3.5% Mo 0.5% Mn 0.22% Si 0.25% N) heat-treated at 1070 °C for 20 min then water quenched is presented. The volumic fraction of phases was 49% of ferrite and 51% of austenite randomly distributed. The mean grain diameter was 6.5 (±2.7) μm for γ and 10 (±6.2) μm for α.

2.2 Mechanical Testing

All these materials were fatigued at room temperature using a servo controlled fatigue machine. LCF tests were performed under total strain control by using a 10 mm gauge extensometer directly attached on the specimen. A triangular waveform, a fully push–pull mode ($R_\varepsilon = -1$), a total strain variation ($\Delta\varepsilon_t$) value included between 0.6 and 1.5%, and a constant strain rate of 4×10^{-3} s^{-1} have been selected as testing parameters.

2.3 Microscopies

The advanced microscopies comprised a Veeco Nanoscope III AFM with a silicon nitride pyramidal tip (angle equal to 35°, radius of curvature inferior to 15 nm) employed in contact mode and a Digital III AFM in tapping mode with a Veeco anisotropic pyramidal tip. MPP-11100 (front angle 15°, back angle 25°, side angle 17.5° and radius of curvature inferior to 10 nm).

EBSD analyses were carried out on a FEI Quanta 400 SEM fitted with an Oxford Instruments Aztec EDS/EBSD system. The EBSD patterns were acquired with a NordlysNano detector. TEM observations were performed on a Philips CM30 or on a FEI Tecnai G2-20 equipped with the ASTARTM acquisition system.

3 Results and Discussion

3.1 Strain Gradient in a Fe–3Si Steel

The evolution of the stress amplitude with the number of cycles of the Fe-3Si steel is reported in Fig. 1. It is characterized by a very short transient period (of about 10 cycles) followed by a rapid hardening stage and then a moderate rate hardening stage. For the test performed at $\Delta\varepsilon_t = 0.3\%$, the evolution is almost constant with a

Fig. 1 Evolution of the stress
amplitude with the number of
cycles
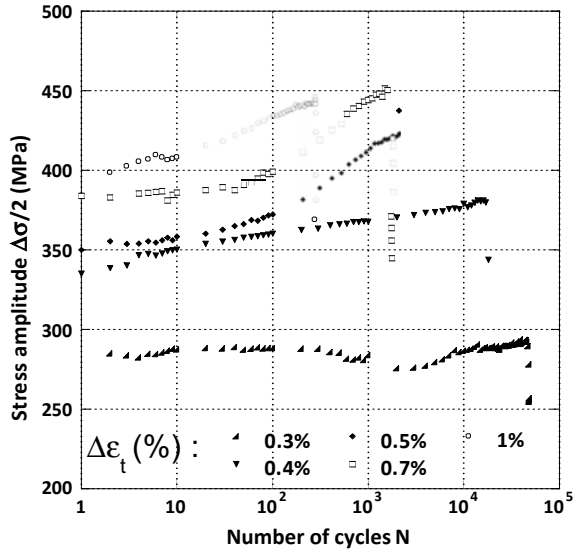
Fig. 2 SEM image of a
sample after fatigue $\Delta\varepsilon_t = 1\%$
showing intergranular crack
initiation
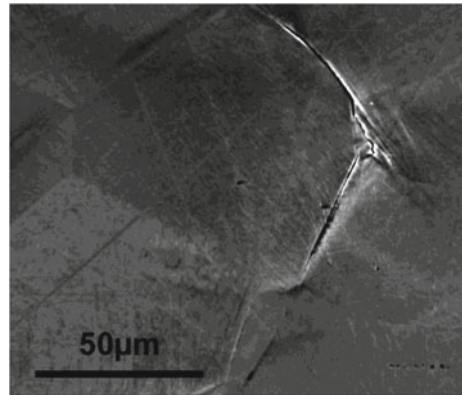
stress value lower than the yield stress. For the higher strain amplitudes test
($\Delta\varepsilon_t > 0.5\%$), the transition between the high and low hardening rate periods
represents about 30% of the fatigue life.

SEM observations of the surface of the polished fatigue samples revealed the
effect of the strain variation on crack initiation sites. Below $\Delta\varepsilon_t = 0.7\%$, crack
initiation is mainly transgranular while above $\Delta\varepsilon_t = 0.7\%$, crack initiation is
intergranular (Fig. 2). At $\Delta\varepsilon_t = 0.7\%$, mixed crack initiation mode is observed.

The evolution of the dislocation structures was studied by cECCI on samples
fatigued at $\Delta\varepsilon_t = 0.5\%$ and $\Delta\varepsilon_t = 1\%$ for different life fractions. At $\Delta\varepsilon_t = 0.5\%$,
elongated jogged dislocations were found within the grain with only one slip
system activated for the first percentages of the fatigue life. Then, later on
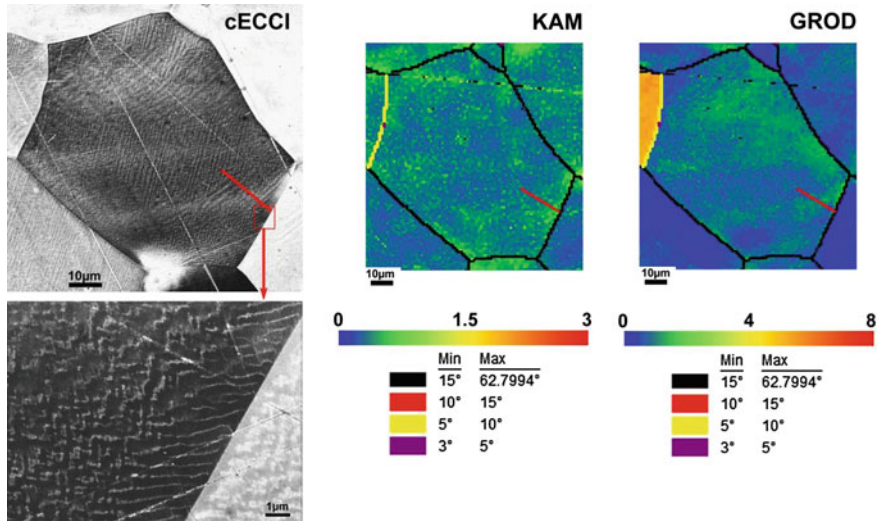
Fig. 3 cECCI image of a sample loaded at $\Delta\varepsilon_t = 1\%$ with KAM and GROD maps of the corresponding grain, the red line within the grain corresponds to the misorientation profile

(80% lifetime), shorter jogged dislocations were visible and 2 slip systems were activated. No typical dislocation arrangements were observed and the strain was accommodated by quasi-reversible motion of dislocations.

The cECCI observations (strengthened by TEM investigations) show that at $\Delta\varepsilon_t = 1\%$ dislocation structure formation has already started after 10 cycles. Dislocations bundles and condensed walls could be observed but they were located near the grain boundaries while the grain interior contained fewer dislocations. Moreover, there was double glide of screw dislocations in the channels between the walls. Slip activity and dislocation structuration were not homogeneous within the grain. After 178 cycles and after failure (Fig. 3), the wall structure consisted of more compact and thinner walls formed near the grain boundaries while at the same time, a vein structure and a diffuse wall structure were observed in the grain interior. These dislocation structures were already observed at N = 50 and N = 100 cycles. The strain gradient visible on cECCI images is also confirmed with EBSD data processing. The local strain level in the present Fe–3Si steel is pointed out by means of the kernel average misorientation (KAM) and grain reference orientation deviation (GROD). KAM calculates the average misorientation between a pixel i and its neighbors provided that the misorientation does not exceed 5°, thus the incorporation of High Angle Grain Boundary (HAGB) is avoided. GROD is based on the misorientation between a reference point of that grain and the other points. The reference point can be the mean misorientation of the grain or the point of the grain where the KAM is the lowest. KAM and GROD maps reveal strain localization at grain boundaries, and this reflects intergranular crack initiation (Fig. 3). The first strength of this approach is to be useful for the prediction of crack initiation mode in

general. The second strength is to be able to distinguish the two types of dislocation configurations, the vein-channel structure and the wall-channel inside a grain while the misorientation between these two dislocation structures was evaluated at about 1°.

Based on the literature [7] concerning the metallurgical properties of the material and based on the present observations, it is reasonable to assume that in the as-received material, short-range order between Fe and Si atoms exists which can be destroyed by cyclic plasticity. For low strain amplitudes, dislocation sources are activated within the grain and dislocation slip is planar which is encountered in short range ordered alloys. The dislocation glide length is restricted by the high friction effect caused by Fe–Si clusters but it is enough to accommodate the required strain in a quasi-reversible regime. Crack initiation is transgranular. For high strain amplitudes, the plastic strain and the cumulative strain are high enough to modify the Fe–Si short-range order which decreases its restricted effect on plasticity. Dislocations are more mobile and the stress concentration at grain boundaries is high enough to trigger plasticity in a narrow adjacent band whose activity decreases in the grain interior. The investigation suggests that grains accommodate the strain in an individual way and that dislocation glide through grains is difficult. This leads to incompatibility effects producing intergranular stresses and thus intergranular strain localization and finally intergranular crack initiation.

3.2 Strain Localization in a Precipitation Hardened Cu–Ni–Si Alloy

The evolution of the stress amplitude with the number of cycles of the Cu–Ni–Si alloy is reported in Fig. 4. For the high total strain variation tests ($\Delta\varepsilon_t = 1.2$ and 1.5%), the fatigue life of the alloy can be divided into four parts. At the beginning of the test, a hardening behavior is observed during the first 50 cycles. This step is followed by a primary softening behavior, until 20% of the fatigue life fraction. Then, a secondary softening step with a lower intensity occurs until 90% of the fatigue life fraction. In the end, the last 10% of the fatigue life fraction are attributed to the propagation of the main crack in the bulk. At lower total strain variation ($\Delta\varepsilon_t = 0.8$%), no hardening stage is observed at the beginning of the test and the alloy continuously softens during the cyclic loading at a rate close to the second softening step at high total strain variation. Moreover, at the lowest tested total strain variation ($\Delta\varepsilon_t = 0.6$%), the softening effect is very slight. Therefore, for the considered conditions, the material exhibits no real stable state during the cyclic loading The graphical representation of the total, the plastic and the elastic strain variations (respectively $\Delta\varepsilon_t$, $\Delta\varepsilon_p$ and $\Delta\varepsilon_e$) with the fatigue life are presented in Fig. 5. The Manson-Coffin relation (plastic strain range versus fatigue life) must be considered according to two regimes ($\Delta\varepsilon_t \leq 1$% or $\Delta\varepsilon_t > 1$%) while only one regime can be considered for the Basquin relation (elastic strain range versus fatigue life).

Fig. 4 Evolution of the stress amplitude with the number of cycles
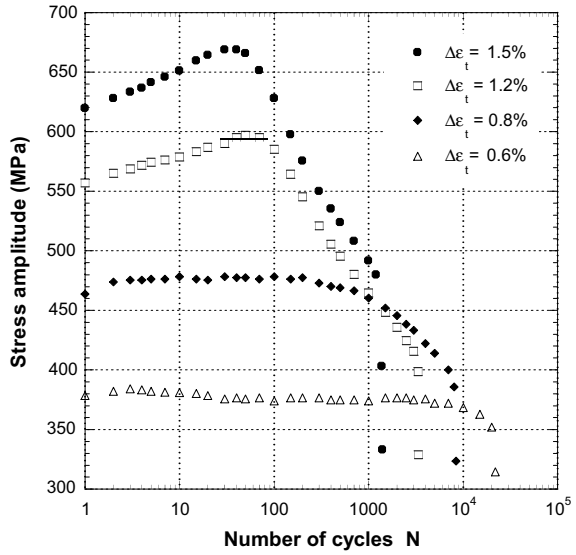
Fig. 5 Evolution of the strain variation with the number of cycles to failure
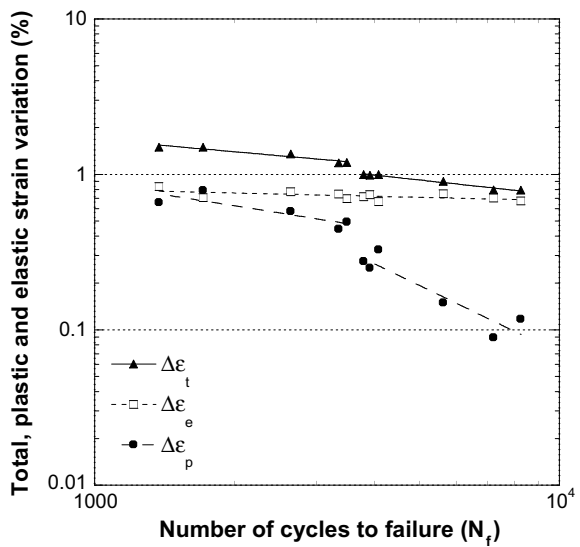
Globally, the grains were featuring two kinds of deformation structures. The first one is shown in Fig. 6a, where some grains contained a high density of dislocations segments or debris next to the δ-Ni_2Si precipitates but dislocations remained isolated and did not rearrange into a low energy dislocation structure. In addition, some dislocations appear to be pinned between two precipitates.
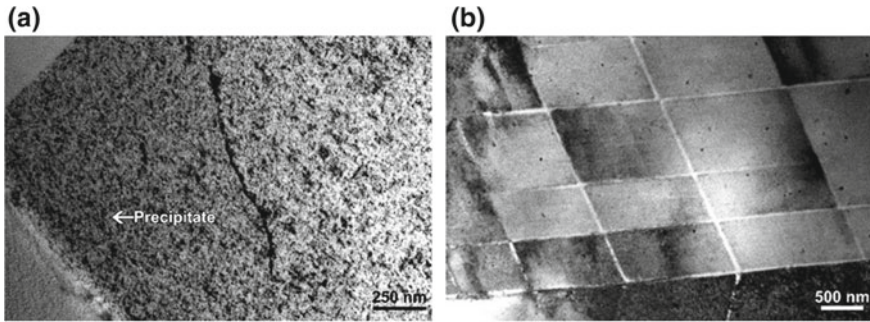
Fig. 6 TEM observations of fatigued Cu–Ni–Si specimens after failure at $\Delta\varepsilon_t = 0.6\%$ (**a**) and at **b** after failure at $\Delta\varepsilon_t = 1.5\%$ showing bands without precipitates

The alloy fatigued at $\Delta\varepsilon_t = 0.6\%$ had all the grains with this structure observed in Fig. 6a. For the other specimens tested at strain ranges higher than $\Delta\varepsilon_t = 0.6\%$, in addition to the former observations, the other grains were decorated with a grid pattern of white bands as shown in Fig. 6b.

The more the specimen was strained, the higher was the amount of grains presenting this pattern. These bands crossed the entire grain from grain boundary to opposite one and propagated from neighbouring grains or twins. Close observations showed that they were free of precipitates. The nature of the white precipitate-free bands has been determined using the ACOM-TEM technique. A zone 4 μm^2 in area including precipitate-free bands was scanned at a 5 nm step with the ASTAR^{TM} software. Figure 7a is virtual bright field image and Fig. 7b is the inverse pole figure for copper crystals.

No misorientation was pointed out between the band and the matrix, or was below the angular resolution of the system, evaluated at 1° with the selected experimental conditions. It is therefore clearly concluded that these precipitate-free bands are not deformation twins but intensive slip bands. The assigned deformation was so high that most of all the grains were activated and accommodated large plastic strain. The number of involved dislocations was high, had a limited mean free path for gliding because of the high density of nanoscale δ-Ni$_2$Si precipitates. Dislocations-dislocations and dislocations-precipitates interactions occurred resulting in a strong hardening. At the same time, precipitates piled up by dislocations and thus were subjected to increasing shear stress. When it exceeded the critical value for shearing (here after 50 first cycles, the cyclic peak stress), then precipitates were cut providing a path for dislocations. The blocked dislocations can, therefore, escape leading to stress relaxation and to the observed strong primary cyclic softening. A strong localisation of plastic deformation occurred in narrow bands similar to that observed in Cu–Co alloys [8] e.g. which behaved as persistent slip bands in pure copper. Therefore, due to successive cutting of δ-Ni$_2$Si
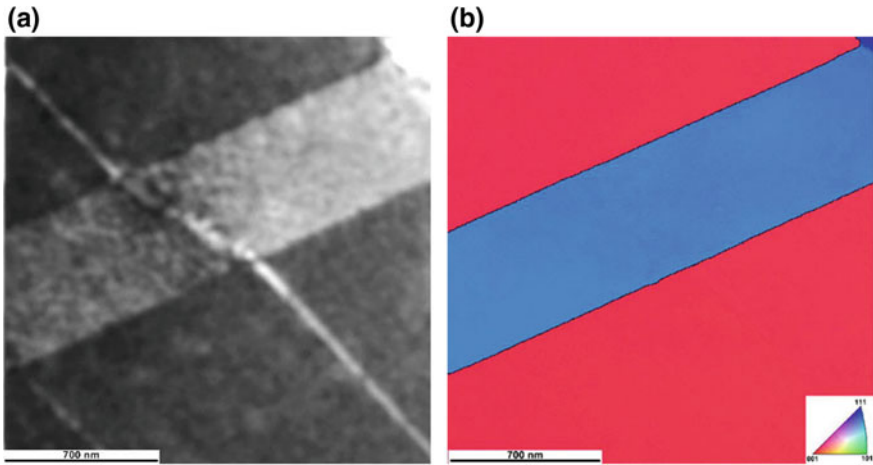
Fig. 7 ACOM-TEM virtual bright-field image (**a**) and corresponding inverse pole figure map (**b**) of a zone scanned with a 5 nm step containing precipitate-free bands

by the dislocations going forward and backward in the softening stage, precipitates were reduced under the critical size of stability, leading to their dissolution into the matrix and finally to the formation of precipitate-free bands.

3.3 Partition of Cyclic Deformation in the Duplex Stainless Steel

When a multi-phased material is subjected to cyclic loading, the partition of the plasticity in each of these phases determine the macroscopic response and the fatigue resistance of the material. This is also the case for the duplex stainless steel (DSS) [9]. The objective of this part is to explain the cyclic accommodation of a DSS subjected to LCF at high strain range ($\Delta\varepsilon_t = 1.6\%$) from AFM investigation of the surface topography created in the two phases. The evolution of the stress amplitude consists of an initial hardening during 5 cycles followed by a softening, and of a period of quasi stabilization (see Fig. 8).

At first, it was necessary to identify the topography resulting from cyclic plasticity (Fig. 9). In the austenitic phase of the studied DSS, the slip markings consist of rectilinear slip lines (height less than 20 nm), ribbon-like extrusions (height between 20–75 nm and up to 100 nm) or a mixed morphology (extrusion beginning along the slip lines).

However, in the ferritic phase, the formation of slip markings originated not only from the bulk properties of the ferrite but was also assisted by the neighbouring austenite. Curvilinear slip traces (less than 10 nm in height) and other persistent slip markings more typical of cyclic deformation such as rectilinear band-like extrusions

Fig. 8 Evolution of the stress amplitude with the fatigue life fraction—$\Delta\varepsilon_t = 1.6\%$
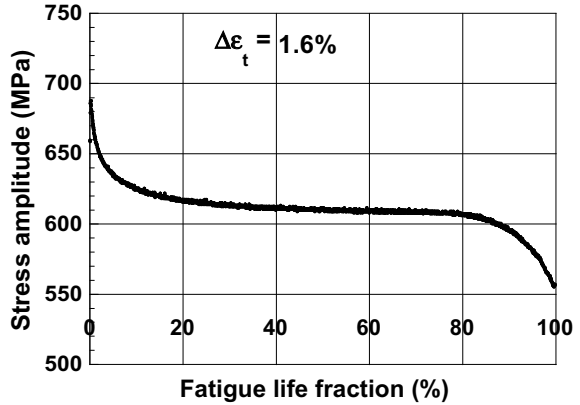
Fig. 9 AFM micrograph showing slip markings (CL: cord like extrusion EX: ribbon like extrusion, RA: rugged area SL: slip line)
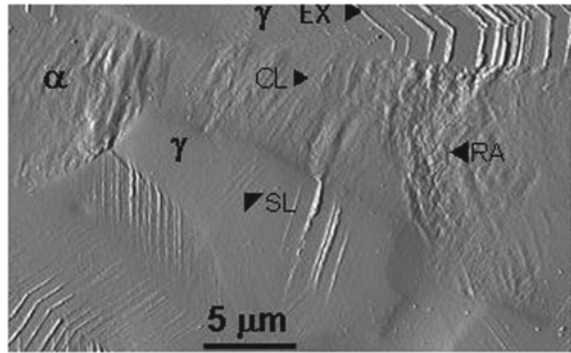
and curvilinear cord-like extrusions (height between 17 and 26 nm) and "rugged" areas were observed.

In austenite, surface modifications started to develop early in fatigue life (near 40% of active grains after 5 cycles). The grain activity almost increased during the very first 3.5% of fatigue life and then remained more or less stable with 80% of active grains in average. The situation in ferrite is different since the surface activity during the first percentages of the fatigue life is weak and then increases progressively to reach nearly 90% of the grains (Fig. 10).

It is interesting to note that in both phases slip bands are growing during cycling, even in austenite though ferrite accepts to contribute later in the fatigue life than austenite.

The detailed AFM study of surface relief in DSS cycled at $\Delta\varepsilon_t = 1.6\%$ allows us to conclude that the two phases of the DSS contribute to the cyclic plastic deformation. In terms of stress evolution, the initial hardening-softening period up to 25% of the fatigue life reflects a self-austenitic response related to well-formed extrusions. From that point, a real contribution of the ferritic phase seems to take place even though topographic changes are noticeable since 3.5% of the fatigue life.
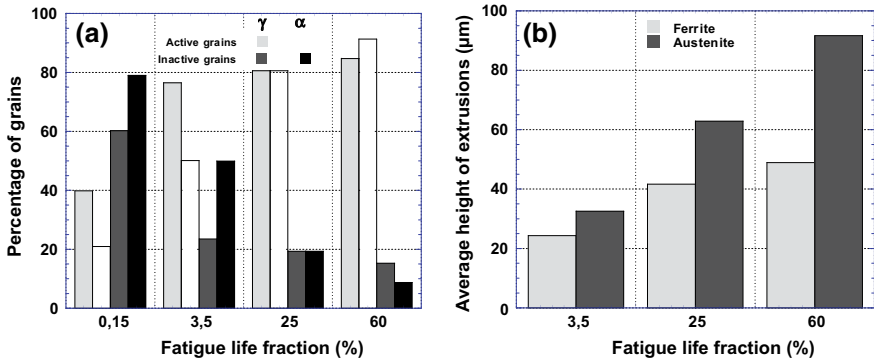
Fig. 10 Evolution of the plasticity partition versus fatigue life fraction in α and γ grains of the DSS in terms of active and inactive grains (**a**) and of average in height of extrusions (**b**)

This allows concluding that the cyclic accommodation by the two phases is a progressive process in which ferrite compensates the vanishing action of austenite in the accommodation mechanism.

4   Conclusions

The present paper shows that employing advanced microscopies under specific conditions, sometimes unusual, allow providing clear explanations of a macroscopic mechanical response.

References

1. B. Pyttel, D. Schwerdt, C. Berger, Int. J. Fatigue **33**, 49 (2011)
2. C. Schayes, J. Bouquerel, J.-B. Vogt, F. Palleschi, S. Zaefferer, Mater. Charact. **115**, 61 (2016)
3. C. Schayes, J.-B. Vogt, J. Bouquerel, F. Palleschi, S. Zaefferer, Int. J. Fatigue **82**, 530 (2016)
4. M. Delbove, J.-B. Vogt, J. Bouquerel, T. Soreau, F. Primaux, Int. J. Fatigue **92**, 313 (2016)
5. J. Bouquerel, M. Delbove, J.-B. Vogt, Mater. Charact. (to appear)
6. D. Salazar, I. Serre, J.-B. Vogt, in *Proceedings of the 6th International Conference on Low Cycle Fatigue and Plasticityc* (Deutscher Verband für Materialforschung und–prüfung e.V., 2008), p. 85
7. D. Ruiz, T. Ros-Yañez, RE. Vandenberghe, Y. Houbaert, in *Proceedings Conference on Industrial Applications of the Mössbauer Effect* (AIP, 2005), p. 331
8. D. Steiner, R. Beddoe, V. Gerold, G. Kostorz, R. Schmelczer, Scr. Metall. **17**, 733 (1983)
9. A. Mateo, L. Llanes, L. Iturgoyen, M. Anglada, Acta Mater. **44**, 1143 (1996)

Part II
Invited Talks

Analysis of Subcritical Crack Growth Using Kitagawa–Takahashi Diagram

K. Sadananda, A. Viswanathan and M. Nani Babu

Abstract Fundamental concepts governing crack initiation and growth in metals and alloys are presented. Cracks being high-energy defects require very high stresses for their initiation and growth. Griffith's equation shows that the stress needed for initiation of an elastic crack is inversely proportional to the square root of its length. For elastic–plastic crack, based on the Orowan equation, the needed stresses are even higher. Hence, cracks normally nucleate at stress concentrations, either preexisting or in situ generated. In this paper, we analyze the fundamentals of crack initiation and growth contributing to fracture in materials using the modified Kitagawa–Takahashi diagram. The analysis, in principle, is applicable for all subcritical crack growth processes in materials.

1 Introduction

The components in service are subjected to static and/or dynamic mechanical forces in inert or aggressive chemical environments. Mechanical failures occur ultimately by crack initiation and growth processes. Crack initiation and growth are governed by the applied mechanical and chemical crack tip driving forces overcoming the opposing material resistance. Material resistance can be enhanced by the material-design approaches involving judicious selection of materials, alloying elements, heat treatments, and processing conditions. Quantification of mechanical forces involves knowledge of the applied forces and the specimen/component loading conditions which, in principle, can be determined. The quantification of

K. Sadananda (✉)
Technical Data Analysis Inc., 3190 Fairview Park, Falls Church, VA 22043, USA
e-mail: kuntimaddisada@yahoo.com

A. Viswanathan
225 Valerie Lane, Wayne, PA 19087, USA

M. Nani Babu
Metallurgy and Materials Group, Materials Development Technology Division, Indira Gandhi Centre for Atomic Research, HBNI, Kalpakkam 603102, India

chemical forces affecting kinetics of crack initiation and growth is complicated because many engineering materials are microstructurally inhomogeneous, by design. Therefore, they are subjected to localized galvanic forces, in addition to other types of embrittling factors that cause stress corrosion, changes in the passivation kinetics, hydrogen embrittlement, etc. While many of these factors have been extensively studied, there has been no consensus in terms of how to quantify them for life prediction. Several models and life prediction methodologies [see, for example, Refs. 1–7] have been presented in the literature approximating the crack tip kinetics in material-component systems in service.

Here, we will examine the crack tip driving forces needed to overcome the material resistance, and methods to quantify them for life prediction, using experimental data. We assume, for simplicity, the validity of linear elastic fracture mechanics and the principle of similitude which can be stated as "*equal crack tip driving forces cause equal crack growth rates*." This principle of similitude forms the basis for extending material test data to components in service assuming that environmental and loading conditions and the mechanism of crack growth remain same.

We have also analyzed initiation and the growth of the elastic–plastic cracks using the discrete dislocation models [8]. Our results show that their behaviors are similar to that of an elastic crack. Mechanical and mechanical equivalent of chemical forces are defined that are useful for estimating the life of a component in service, without the need of knowing the details of the chemical reactions at the crack tip. Failure diagrams have been developed based on the modification of the classical Kitagawa–Takahashi diagram [9] that bridges the behaviors of smooth and fracture mechanics specimens [10–13]. Connections between crack initiation, growth, arrest, and overload fracture can all be established via these failure diagrams. These diagrams can be applied for engineering components in service for diagnostic and prognostic purposes.

2 Elastic Crack

To appreciate the fundamental concepts involved, we start with an elastic crack as described by Griffith [1] and Lawn [7], Fig. 1a. Many of these concepts discussed are not new but are implicit in Griffith's analysis. When a crack forms in a body under a constant, uniform applied stress, σ_y, the increase in the surface energy is compensated by the strain energy released in forming the crack. The total energy, E_T, as a function of crack size reaches a peak corresponding to an unstable equilibrium condition, Fig. 1b. If the stress remains constant, then the crack that formed expands with acceleration. The total crack tip driving force is proportional to the gradient in the potential energy of the system, and which can be expressed as Griffith condition given by
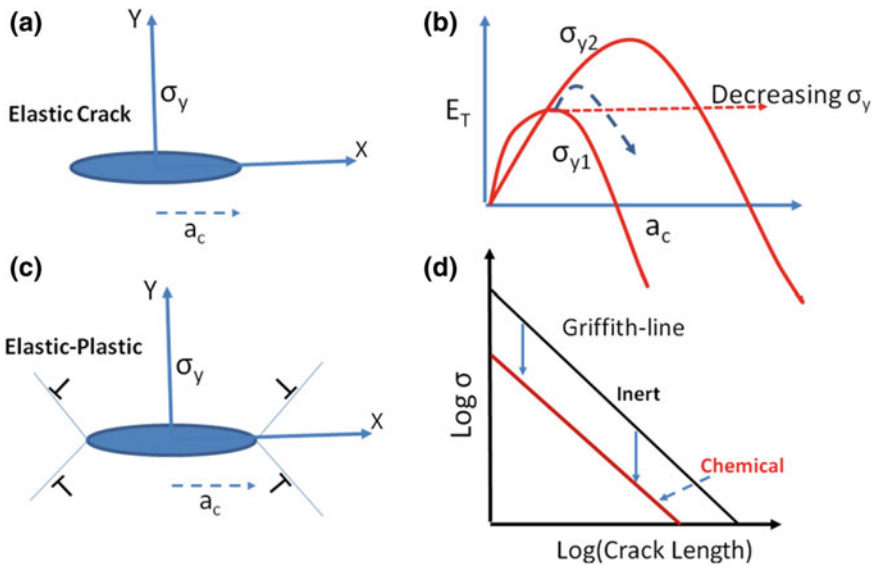
Fig. 1 **a** Elastic crack, **b** energy versus crack length, Griffith condition, **c** elastic–plastic crack, **d** stress versus crack length

$$\sigma_y = \sqrt{2E\gamma/\pi a} \tag{1}$$

where E is the total energy, γ is surface energy and **a** is the crack length. If the applied stress is lower, correspondingly the peak in the energy occurs at a larger $\mathbf{a_c}$ value.

As a thought experiment, suppose we decrease applied σ_y slowly just after the Griffith's condition is reached, then the subsequent rate of decrease in the total energy will be reduced. That forces the crack that is formed to expand with reduced acceleration. Continuing the thought experiment, if the stress is decreased infinitesimally but continuously keeping the total energy constant at the Griffith condition, then we have a case where crack grows maintaining quasi-equilibrium steady-state. In a way, we have established a subcritical crack growth condition. To accomplish such a quasi-equilibrium growth of a nucleated crack, the stress has to follow the Griffith condition stated above, as the crack length increases. Figure 1d shows the stress versus crack length plot in log–log coordinates and the slope of the line will be 0.5.

If there is an aggressive environment, then we can simply think of the role of the environment is to effectively reduce the surface energy, γ, thereby reducing the Griffith stress above. For such a simple scenario, the Griffith stress will be reduced and Griffith line in Fig. 1d will be below that of the inert line. For the elastic–plastic case, as in Fig. 1c, to compensate for the plastic work, the equivalent Griffith line will be above that of the elastic-crackline. The slope for the elastic–elastic case can

be different from 0.5 depending on the nature of the plastic work. Using discrete dislocation models, it was shown [8] that for the growth of a continuous elastic–plastic crack, log stress versus crack length relation will remain linear, but with the slope decreasing from 0.5, depending on the ratio of friction stress (yield stress) to the applied stress. It was also shown that the effect of hydrogen is to reduce the plasticity effect depending on the hydrogen concentration or indirectly depending on the degree of embrittlement.

2.1 Propagating and Non-propagating Cracks

Figure 1d also provides another insight into the mechanics of crack initiation and growth. From the figure as well as Eq. 1, it is obvious that as the crack size decreases the required stress to nucleate a crack approaches infinity. Hence for an incipient crack to nucleate in an otherwise prefect crystal is not possible. Stress concentrations either preexisting or in situ created by plastic flow are required. The plastic flow results in shear bands, dislocation pile-ups, etc., with their characteristic stress fields and stress gradients. We term all of them as "internal stresses" differentiating them from the externally applied stresses. These internal stresses could be in situ generated by inhomogeneous deformations or residual stresses due to previous operations. Only the stresses that are of tensile nature help in accentuating the initiation and growth processes. The material toughness depends on the extent of the plastic flow needed for the initiation and subsequent growth of the cracks. All internal stresses are self-equilibrating to keep the specimen in equilibrium, implying that there will be associated stress gradients.

Examination of Fig. 1d shows that for a Griffith crack to grow, the stress gradient should be at least as given by the corresponding Griffith equation. If the stresses and gradients matched with Griffith's line, then the initiated crack will grow at quasi-equilibrium state until unstable fracture occurs. Likewise, if the gradients are too sharp such that the stresses fall below Griffith's line then the arrest of the propagating crack occurs. The crack may not collapse and heal if the environment present has oxidized the nascent surfaces. Nevertheless, the cracks become non-propagating. Non-propagating crack conditions are encountered under fatigue for cracks that are growing near sharp notches, resulting in fatigue notch stress concentration factor, K_F, being different from the elastic notch stress concentration factor, K_t. Near the sharp notches, the stress gradients are steep, and hence the nucleated crack becomes non-propagating when the stresses fall below that required for propagation. Similarly, if the stress gradients are such that the stresses are above the crack growth line, then a nucleated crack accelerates.

Likewise, if the materials ahead of the crack tip strain-hardens during crack growth, then the material resistance to the growth increases. In that case, the Griffith line shifts to higher stresses. Hence, for the strain-hardening material, the crack growth can be insured only by increasing required applied stresses. The increased stress required to sustain the growth due to material strain hardening is generally

called resistance-curve (R-curve), and R-curve behavior has been observed under monotonic as well as fatigue load conditions [14, 15]. Finally, based on the above discussion, Fig. 1d also implies that crack initiation and growth involve not only the magnitude of the applied stress but also the required stress gradients depending on the nature of the crack, i.e., elastic, elastic–plastic, etc.

2.2 Kitagawa–Takahashi Diagram

The well-known Kitagawa–Takahashi (KT) diagram [9] forms an important tool in connecting the behavior of a smooth specimen to the cracked specimen. Figure 2a provides the original KT diagram. In this figure, σ_0 defines the endurance stress for a smooth specimen (stress needed for 10^7 cycles or more). The authors found that the endurance stress remains the same for cracked specimens if the crack length is less than a critical crack length, a_{kt}. For crack length longer than a_{kt}, the required applied stress for failure is the same as that for long cracks. Thus, the endurance of the cracked specimen approaches the limiting value of the smooth specimen, the value indicated by an arrow in the log–log plot. Implication of the plot is that cracks smaller than **a_{kt}** behave differently from the long cracks. This led to several explanations starting from the breakdown of the Principle of Similitude discussed earlier, plasticity induced crack closure responsible for this breakdown, critical distance approach, etc.

However, there is an inherent dichotomy involved here since as per Eq. 1 the required stress for crack initiation and growth of an insipient crack should increase inversely with the square root of the crack length, and while the Kitagawa–Takahashi diagram shows that the endurances of the specimens approach a constant value as that the smooth specimen endurance, almost independent of crack length. This dichotomy is resolved if we consider that the fatigue involves significant number of cycles which generate internal fatigue damage that contributes to the required internal stresses that compensate the applied stresses for the initiation and growth. Hence, there is no similitude breakdown if we include internal stresses that aid the applied stresses in computing the total crack tip driving force. Internal stresses are difficult to determine as they depend on the distribution of the dislocations involved. Nevertheless, their existence and their role during the crack initiation are unquestionable.

Based on these principles, and also the consideration that fatigue involves two load parameters involving $\Delta\sigma$ and σ_{max} for smooth specimen and ΔK and K_{max} for fracture mechanics specimens, we have modified the KT diagram defining, in the process, the internal stress triangle as shown in Fig. 2b. Normally the internal stresses are of monotonic type and contribute via the K_{max} parameter inherent in our approach. The internal stress triangle defines the additional stresses and stress gradients required to sustain the initiation and growth of short cracks at the imposed applied stresses. By considering the role of the internal stresses, we have also preserved the principle of similitude and could explain the fatigue crack growth
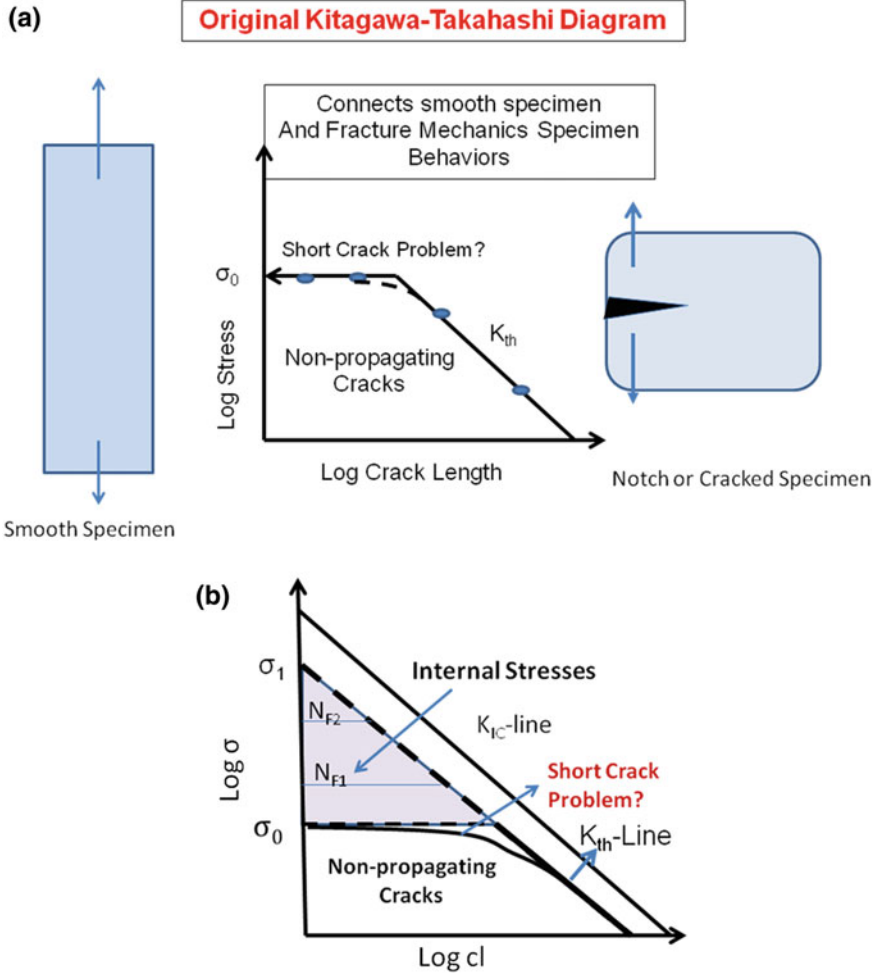
Fig. 2 **a** Original Kitagawa diagram connecting the smooth specimen behavior to the behavior of the fracture mechanics specimen, **b** the modified KT diagram. The crack line is extrapolated, and the internal stress triangle is defined. σ_0 can be endurance stress for a smooth specimen. N_{F1} and N_{F2} define the stresses required for fatigue cycles less than the endurance limit. σ_1 can be monotonic fracture stress, in a way, defining failure stress for one or half fatigue cycle

process without resorting any extrinsic factors, such as crack closure. The analysis has also been applied [13] to the cracks initiated at notches accounting both propagating and non-propagating cracks, and why or how the fatigue notch stress concentration factor, K_F deviates from the elastic notch stress concentration factor, K_t. The internal stresses are introduced, for example, via the formation of intrusions and extrusions, etc. in an otherwise smooth specimen [16].

3 Application of the Modified KT Diagram

We can now easily apply the modification to the stress crack length diagram in Fig. 1d. This is shown in Fig. 3. The Griffith-lines for elastic or environmentally assisted or elastic–plastic crack growth is shown in the figure along with the superimposed behavior of smooth specimens. One can, in principle, define the internal stress triangle that quantifies the additional in situ generated minimum stresses and their gradients required to ensure crack initiation and growth. This process is applicable for all cases where crack initiation and growth involved. The size of the internal stress triangle gets reduced as the yield stress of the material (or endurance stress for fatigue sample) increases and approaches the fracture stress of the specimen. Even at fracture stress, local plasticity or chemical forces are needed to meet the crack line for the initiation and growth of an incipient crack. In the following, we present some application of the above principles and the KT diagram to account for the subcritical crack growth.

3.1 Application to Subcritical Crack Growth

Figures 4 and 5 show the application of the modified KT diagram to growth of fatigue crack growth. The short and long crack growth data were collected by Airforce [17]. Using the short crack lengths and the applied stresses the internal stresses involved were computed using the long crack growth data as the reference. The total stresses (applied + internal) can be plotted considering that such addition is justified under linear elastic formulations, and these are shown as a function of crack length in Fig. 5. It is recognized that the KT diagram provides only the crack length and stress, and therefore crack growth rates cannot be seen. It is also important to note that internal stresses are very difficult to compute or estimate except for simple dislocation pile-ups or distributions. Here they are computed using the long crack growth rate data as the reference by invoking the principle of similitude that equal crack tip driving forces give equal crack growth rates. We use

Fig. 3 Crack growth conditions in Fig. 1d represented similar to the modified Kitagawa–Takahashi diagram
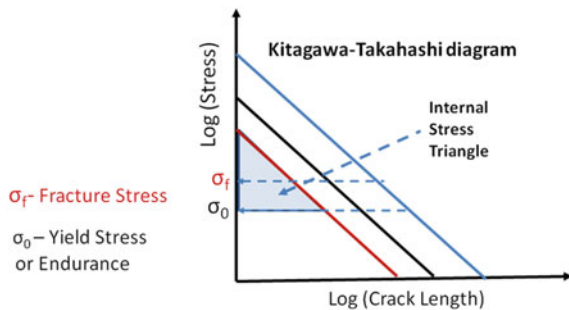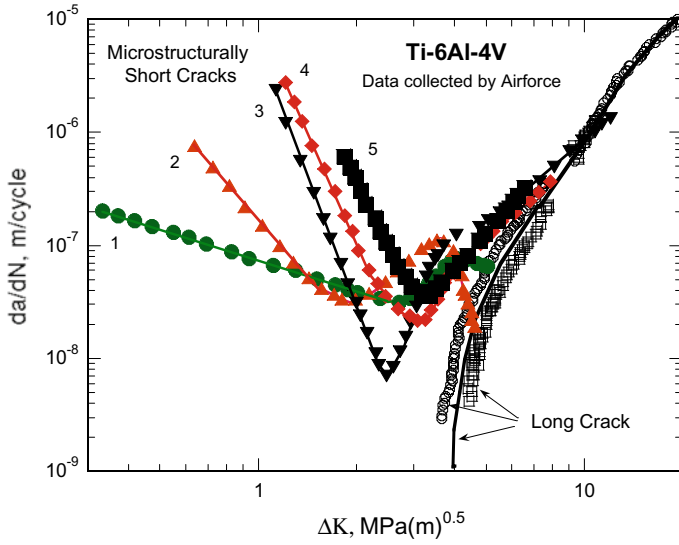
Fig. 4 Behavior of microstructurally short cracks in relation to that of long cracks. Data collected by Airforce
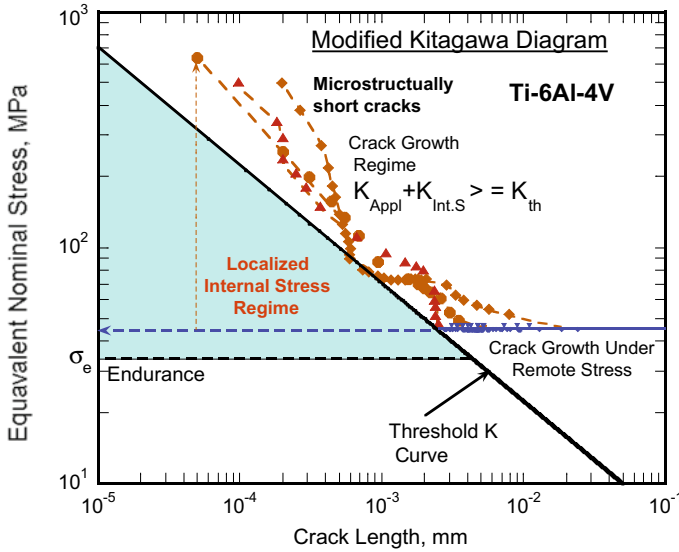
Fig. 5 Representation of the short crack growth data in Fig. 4 in the form of KT diagram, defining the internal stress triangle. The applied stresses and gradients exceed the minimum required for continuous crack growth

this methodology to compute both mechanical forces as well as mechanical equivalent of chemical forces that contribute to the total crack tip driving force.

3.2 Application to Stress Corrosion

While the original KT diagram was developed for crack growth under fatigue, we can extend it to stress corrosion crack growth as shown in Fig. 6. The inserts in the figure show schematically the limiting behavior of smooth specimens in a corrosive environment. For a given concentration, the time to failure increases with decreasing stress approaching a limiting threshold value, σ_{th} for that concentration. The σ_{th} value decreases as a function of concentration and reaches another limiting value σ_{th}^* for that material and corrosive medium. The σ_{th}^* is similar to the endurance value in fatigue and σ_{th} value is equivalent to stress to cause failure at stresses higher than the endurance limit. In addition, the figures also indicate that chemical environment can only accentuate the failure process, and without the minimum stress, σ_{th}^* failure cannot occur for any concentration. In essence, one can define the operating chemical forces in terms of equivalent mechanical forces needed for failure. On that basis, modified KT diagram can be plotted as shown in Fig. 6. In principle, we can define using this diagram the mechanical equivalent of chemical internal stresses and their gradients required for continuous crack growth under stress corrosion. Many of these concepts are new and there is not much of experimental work to validate these concepts. Figure 7 shows some data generated by Hiroshi and Mura for 4340 steel in H_2SO_4 solution [18]. The results follow the KT diagram within the experimental errors.

Fig. 6 The modified Kitagawa–Takahashi diagram for stress corrosion crack growth
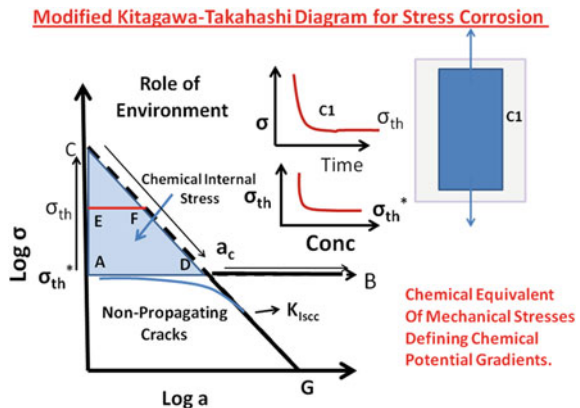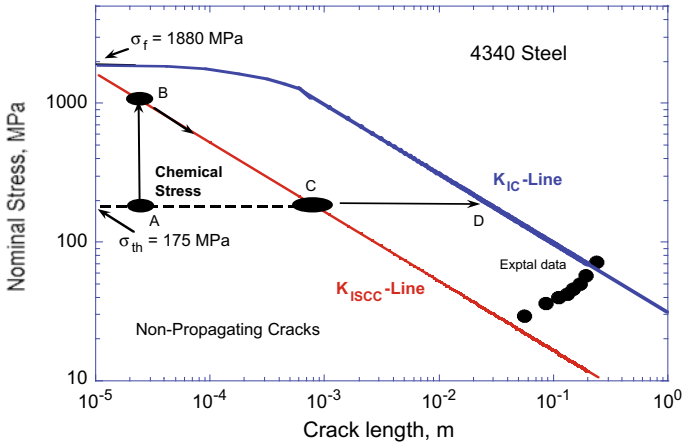
Fig. 7 Analysis of stress corrosion data of Hiroshi and Mura on 4340 steel tested under H_2SO_4 solution

3.3 Application to Corrosion-Fatigue

In principle, we can extend this concept to any subcritical crack growth. Here we show only the schematic diagram for corrosion-fatigue where we are now combining the fatigue and stress corrosion concepts into one diagram. There are thresholds for fatigue and thresholds for stress corrosion. In combining these, we can assume linear summations, if applicable. Otherwise one has to determine experimentally the thresholds for combined loads before such combined KT diagram is considered. The modified KT diagram for Corrosion-Fatigue is shown in Fig. 8. There is no data available in the literature that can be used to extract the needed information to plot in terms of the modified KT diagram.

Fig. 8 The modified Kitagawa–Takahashi diagram for corrosion-fatigue
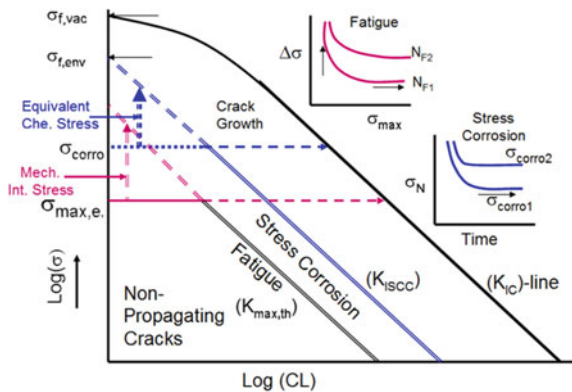
4 Summary and Conclusions

Analysis of crack initiation and growth behavior is analyzed using the fundamental concepts and applying the well-known Kitagawa–Takahashi diagram. By modifying the KT diagram we can account the existence of in situ generated internal stresses that augment applied stresses. The modified KT diagram is used to determine the magnitude of the internal stresses and their gradients needed for initiation and growth of subcritical cracks under fatigue, stress corrosion, corrosion-fatigue.

References

1. A.A. Griffith, The phenomena of fracture and flow in solids. Philos. Trans. R. Soc. Lond. A **221**, 163 (1921)
2. E. Orowan, Zurkristallplastizitt. III: ber den mechanismus des gleitvorganges. Z. Phys. Hadron. Nucl. **89**(9), 634 (1934)
3. G.R. Irwin, Crack-extension force for a part-through crack in a plate. J. Appl. Mech. **29**, 651 (1962)
4. R.W. Lardner, Bilby-Cottrell-Swinden model for a growing crack with residuals stresses. Proc. R. Soc. Lond. 1098 (1970)
5. R.A. Oriani, Hydrogen embrittlement of steel. Annu. Rev. Mater. Sci. **8**, 327 (1978)
6. M.H. Kamdar, in *Chapter 9, Treatise on Materials Science and Technology*, ed. by C.L. Briant, S.K. Benerji, vol. 25 (Academic Press, New York, NY, 1983), p. 361
7. B.R. Lawn, *Fracture of Brittle Solids*, 2nd edn., Cambridge Solid State Science Series (Cambridge, UK, 1993)
8. I. Adlakha, K. Sadananda, K.N. Solanki, Discrete dislocation modeling of stress corrosion cracking in an iron. Corros. Rev. **33**, 467 (2015)
9. H. Kitagawa, S. Takahashi, Applicability of fracture mechanics to a very small crack or the cracks in the early stage, in *Second International Conference on Mechanical Behavior of Materials,* Metals Park, Ohio (ASM, 1976), p. 627
10. K. Sadananda, Failure diagram and chemical driving forces for subcritical crack growth. Metall. Mater. Trans. **44A**, 1190 (2012)
11. K. Sadananda, S. Sarkar, Modified Kitagawa diagram and transition from crack nucleation to crack propagation. Metall. Mater. Trans. **44A**, 1175 (2013)
12. K. Sadananda, A.K. Vasudevan, Review of environmental cracking. Metall. Mater. Trans. **42A**, 279 (2011)
13. K. Sadananda, A. Arcari, A.K. Vasudevan, Does a nucleated crack propagate. Eng. Frac. Mech. **176**, 144 (2017)
14. R.M. Mcmeeking, A.G. Evens, Mechanics of transformation toughening in brittle materials. J. Am. Ceram. Soc. **65**, 242 (1982)
15. R.O. Ritchie, Mechanisms of fatigue-crack propagation in ductile and brittle solids. Int. J. Fract. **100**, 55 (1999)
16. D.E. Witmer, G.C. Farrington, C. Laird, Changes in strain localization behavior induced by fatigue in inert environments. Acta Metall. **35**, 1895 (1987)
17. Airforce Report, *Improved High Cycle Fatigue Life Prediction*, UDRI Industry team, UDR-TR-1999-0079 (2001)
18. Y. Hirose, T. Mura, Crack nucleation and propagation of corrosion fatigue in high strength steel. Eng. Fract. Mech. **22**, 859 (1985)

Surprising Corrosion Failures of Standard and Special Stainless Steels and Nickel Base Alloys in Chemical Process Environments

K. Elayaperumal

Abstract Stainless steels are well known for their corrosion resistance. Austenitic Stainless Steels of the '300' series are known as Standard Austenitic Stainless Steels and are very much used for chemical process equipment utilizing their good corrosion resistance to most of the popular chemical environments with not very severe corrosive conditions. Unfortunately their corrosion resistance fails in severe corrosive situations such as high chlorides, high temperatures, highly reducing conditions, presence of residual stress, presence of microstructural inhomogeneities, etc. For such cases, special stainless steels such as Super Austenitic Stainless Steels and Duplex Stainless Steels and Nickel Base Alloys are developed. These are popularly known as CRAs (Corrosion Resistant Alloys). This paper deals with four real-time case studies of unusual surprising corrosion failures of standard stainless steel such as 316(L) SS, duplex stainless steel and a nickel base alloy, all analyzed by the author himself. The cases discussed involve the following types of corrosion: general high uniform corrosion by process impurities, stress corrosion cracking, crevice corrosion and improper weld corrosion. The environments involved are inorganic acid, waste streams, sea water, and marine atmosphere. Each case would be illustrated giving the process conditions, the circumstances which led to the failure, the mode of failure, and the recommendations for remedial measures.

Keywords Stainless steels · Nickel alloy · Crevice corrosion · Stress corrosion cracking

K. Elayaperumal (✉)
C-20, Melur Meadows, Kumaran Kundru Village, Pogalur-Vadavalli Post, via Mettupalayam, Coimbatore District 641697, Tamil Nadu, India
e-mail: keperumal@gmail.com

1   Introduction

Stainless steels and Nickel base alloys are well known for their corrosion resistance. Austenitic Stainless Steels of the '300' series are known as Standard Austenitic Stainless Steels and are very much used for chemical process equipment utilizing their good corrosion resistance to most of the popular chemical environments with not very severe corrosive conditions. Unfortunately, their corrosion resistance fails in severe corrosive situations such as high chlorides, high temperatures, highly reducing conditions, presence of residual stress, presence of microstructural inhomogeneities, etc. For such cases, special stainless steels and nickel base alloys are developed. These are classified under three categories: Super Austenitic Stainless Steels, Duplex Stainless Steels, and Nickel base alloys. These latter materials are popularly known as CRAs (Corrosion Resistance Alloys).

The latter also fail if the corrosive situations exceed beyond the resistive limits of each grade of special stainless steel. This paper would present detailed real-time case histories of surprising unusual Corrosion Failures of both standard and certain CRAs in chemical process environments, analyzed by the author himself. The alloys under discussion have shown premature failures of the following forms/types of corrosion. 1. Corrosion due to impurities in acids, Stress Corrosion Cracking by chlorides, crevice corrosion, and weld porosity corrosion. The environments involved are inorganic acids, waste water, sea water and Oil and Gas process media. Each case would be illustrated giving the process conditions, the circumstances which led to the failure, the mode of failure, and the recommendations for remedial measures.

2   Case 1: Corrosion of 316L SS Pipeline by Impurities in Acids

The subject pipeline is used to transport phosphoric acid from ships to an NPK plant producing composite NPK fertilizer. The pipeline showed leaks starting from fourth month of service. The leaks were from both parent metal and butt-weld joints. Ultrasonic wall thickness readings conducted throughout the pipeline after 15 months of operation showed unacceptably very low thickness values throughout the pipeline indicating that the pipeline is corroding on the inside surface at highly unacceptable rates.

The pipeline is made of several sections of longitudinally welded pipe of Type 316L Stainless Steel of 18 in. OD and 5 mm WT manufactured as per ASTM specification A-258 Class 1. The received sections are butt welded at the plant site to a total length of about 2.7 km from the ship unloading point in the seaport to the storage tank at the plant site. Elbows are of higher thickness of same 316L SS bought from different source and butt welded at the site.

Phosphoric acid produced through the wet process (WPA) is being obtained from different sources through ships which unload the acid into the subject pipeline at the port ship terminal. The maximum unloading temperature is 50 °C. The acid, being made through the wet process contains many impurities. From corrosion and erosion point of view, sulfuric acid, chloride, fluoride and suspended solids are of concern. The other impurities are oxides of iron, aluminum, calcium, and magnesium. The chemical analysis for every shipment was obtained and recorded against the supplier source, date, quantity, etc.

Ultrasonic wall thickness measurements conducted at various points along the pipeline, including elbows and inlet lines (totally 280 locations) along the pipeline indicated that in all places measured, the corrosion rate was coming to very high values, 1.00 mm/year to as high as 2.40 mm/year. These values are much higher than the maximum accepted value of 0.10 mm/year for stainless steels for such applications. These are very high values and continuation of this trend is very dangerous.

From the removed pipe portions, three representative sections were cut and closely examined on the cleaned inside surface. Among these three sections, one contained one of the leaked butt-weld joints along with the nearby pipe inside surface. The following are the observations.

Photographs 1 and 2 show the typical appearance of the inside surface. The surface is that of stainless steel affected by corrosion by reducing acids such as sulfuric acid, phosphoric acid and dilute hydrochloric acid, all accelerated by the fluoride impurity. The surface contained very sharp flow marks running in different directions. This is typical of fluoride accelerated corrosion. In present case, fluoride has been present in the processed WPA ranging from a minimum of 0.11% from one source (Low F) to as high as 1.68% from another source (High F).

The fluoride content in the High F source acid has been much higher than those from other sources. The former ranged from a minimum of 0.35% to a maximum of 1.68%. Both are not acceptable. On the other hand in the acids from other sources, the fluoride ranged from 0.11 to 0.69%, the lower values acceptable. A summary comparison of chemical analysis of the acids received from High F with those received from other sources Low F, is shown in Table 1.

It can be clearly seen that the content of corrosive impurities is quite high in the High F source as compared to other sources. Hence, the High F acid is the cause of excessive corrosion observed.

It is diagnosed from the above observations that the unacceptably high corrosion rates experienced by the subject pipeline are due to the high fluoride impurity present in the acid received from the High F source which contained as high as 1.68% fluorides.

From literature study, one can notice the strong influence of fluoride addition on phosphoric acid corrosion of Type 316(L) SS that at 60 °C, corrosion rate crosses steeply the mark of 0.2 mm/year at about 0.3% Fluoride. Fluoride from the High F source has been always above this limit of about 0.3%.

Photograph 1 Typical appearance of the corroded inside surface on and near the weld joint

Photograph 2 Typical appearance of the corroded inside parent metal surface

Table 1 Comparison of impurity levels in phosphoric acid

Source	% H$_2$SO$_4$	Chloride (ppm)	% Fluoride
Low F, Min	0.80	16	0.11
Low F, Max	5.84	354	0.69
High F, Min	1.59	96	0.35
High F, Max	2.91	740	1.68

2.1 Recommendations for Remedial Measures

1. The acid from the High F source has to be stopped immediately until the supplier is ready to provide acid with very low fluoride impurity.
2. As a long term plan, after working out cost/performance ratio, a stainless steel much superior to Type 316L SS with respect to corrosion by impure WPA can be chosen as pipe MOC. A good proven material in this respect is Alloy 28, one of the super austenitic stainless steels, proven for WPA service. Cost–performance ratio would be lower for Alloy 28 as compared to 316L SS. There would be many operational advantages, overcoming the initial high cost.

3 Case 2: Stress Corrosion Cracking of 316SS Seamless Heat Exchanger Tubes

The subject tubes are of size 25.4 mm OD × 1.6 mm WT × 6 M long and 45 in number as per A-213/Type 316SS, cold finished seamless, annealed and white pickled. They form the tubes of a shell and tube heat exchanger. 7 tubes out of 45 were said to have leaked after about 3 months of service. This is a premature failure and hence the present detailed study was undertaken to arrive at the cause of the premature failure and to make recommendations for remedial measures.

Photographs 3 and 4 show a sample cut from one of the leaked tubes. **Through and through cracks**, visible on both outside and inside surfaces, and **thick black coating only on the inside surface** can be seen. One can also notice that **crack is wider on the inside surface** than that on the outside surface. All the seven leaked tubes were said to have shown similar features.

The above features represent localized corrosion cracking phenomenon and not a general uniform corrosion phenomenon, attributable to deficiency, if any, in chemical composition and mechanical properties of the tubes.

Photographs 5 and 6 show metallurgical microstructures across the wall of the tube at the cracked positions.

The following features are noticeable from these photographs:

- The general structure is that of properly annealed austenitic stainless steel. 316SS is one such austenitic stainless steel.
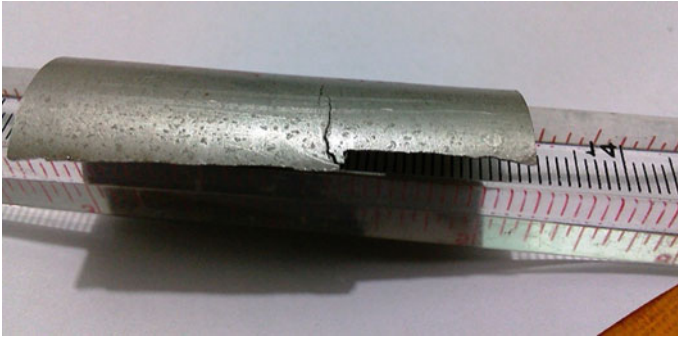
Photograph 3 Crack as seen on the outside surface of the tube

Photograph 4 Black adherent coating on the inside surface of the tube along with a bunch of cracks

- There are cracks **initiated on the inside surface** and propagated toward the outside surface.
- Cracks have **initiated at multiple locations** on the inside surface, not one isolated place.
- Cracks have propagated toward the outside surface in a **transgranular manner** (cutting across grains and not necessarily only through grain boundaries).
- Cracks have taken a **branched manner (tree-like branches)** while propagating from inside to outside surface across the wall thickness of the tube.

All the above features are representative of **Chloride Stress Corrosion Cracking of Austenitic Stainless Steel (CSCC)**. In the present case, the cracks have initiated on the inside surface of the tubes.
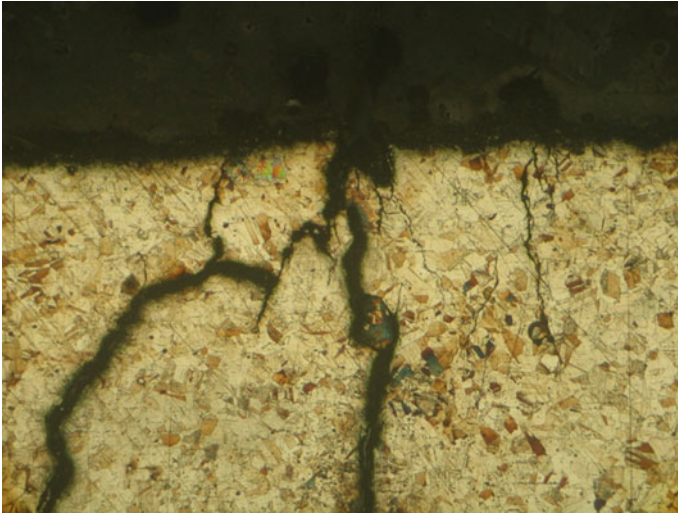
Photograph 5 Cracks starting from the inside surface of the tube wall. Multiple initiation points can be seen. (100X)
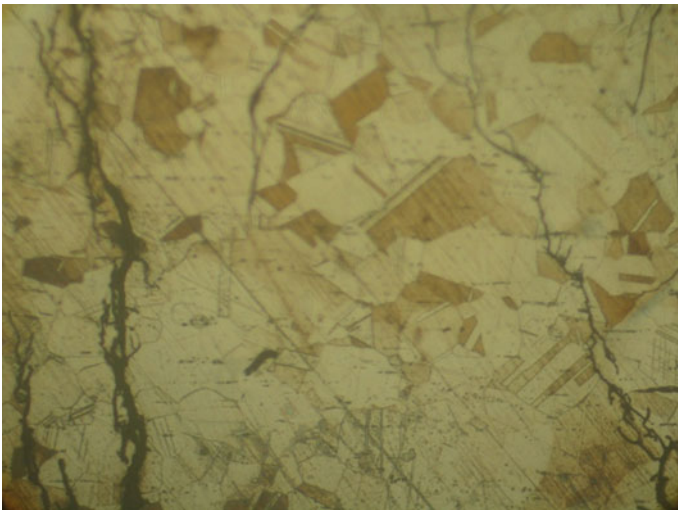
Photograph 6 Cracks showing transgranular nature (cutting across the grains) and branching like tree branches while propagating. The general structure is that of any fully annealed austenitic stainless steel including 316 SS. (200X)

The following are the end-use service conditions to which the particular heat exchanger was subjected to.

Shell side: Thermic fluid (hot oil) entering at temperature 175 °C and leaving at 160 °C at a pressure of 4.5 kg/cm^2. This fluid acts as a source of heat, transferring heat across the wall of the tube, giving heat to the inside fluid.
Tube side: Industrial wastewater of 40,000 ppm total dissolved salts (TDS) getting heated from 110 to 130 °C at a pressure of 6 kg/cm^2. In this process part of the water is converted to steam which is used as a heat source in downstream multiple effect heat exchangers.

The previously mentioned observations made physically on cut samples and on metallurgical microstructures are explainable on the basis of the above information.

The black coating seen on the inside surface is due to high concentration waste products (much higher than the stated 40,000 ppm) remaining in contact of the inside surface of the tube after a considerable portion of the water evaporates and goes out as steam.

Thermic fluid is pure oil without any aqueous base dissolved salts. Hence, there is no black coating on the outside (shell side) surface of the tubes.

In industrial wastewaters, chlorides are invariably present in appreciable quantities. Chloride even in small ppm level leads to CSCC in stainless steels at temperatures above about 50 °C.

The stress required for CSCC can be either externally applied like high-pressure boiler tubes or internally existing residual stress even in annealed tubes. The level of such stress required for CSCC to occur (in the presence of chloride) is quite low, a small percentage (even 2 or 3%) of the Allowable Stress as per ASME is sufficient. For a heat exchanger tube, such small amount of residual stress can occur throughout the length as a result of high-pressure hydro testing during manufacture or locally near expanded tube ends or near baffle positions through non-noticeable vibrations. This level of stress in a heat exchanger varies from tube to tube. Hence, only 7 tubes out of 45 failed.

CSCC also requires a time factor to initiate and to completely propagate to leakage depending upon the actual level of stress present, wall thickness value, the amount of chloride present and also the operating temperature. In this case, it has taken about three months for the complete propagation of the crack to the point of leakage.

Crack or any other failure occurring due to any manufacturing defect, including tube quality or tube manufacturing step, should have occurred at a single location, without multiple locations, and almost immediately, within a few days of operation, not 3 months.

3.1 Diagnostic Conclusion

The tubes have failed due to the phenomenon called Chloride Stress Corrosion Cracking to which fully austenitic stainless steels such as 316SS are highly susceptible. The necessary chloride in the present case is from concentrated industrial wastewater present in contact with the inside surface of the tubes after partial evaporation of the wastewater to steam.

3.2 Recommendations for Remedial Measures

For the specified service condition of the subject heat exchanger, namely evaporation of industrial wastewater at about 130 °C, 316SS is not the right material of construction (MOC). The right material would be Duplex Stainless Steel 2205 if the temperatures can be maintained below 130 °C and Duplex Stainless Steel 2507 if the tube wall temperature on the wastewater side exceeds well above 130 °C.

4 Case 3: Localized Corrosion of Duplex Stainless Steel in Sea Water

A debris filter upstream of a seawater condenser cooler in a coastal based thermal power plant showed premature unusual corrosion problem in the fasteners within a very short time of 3 months of erection and commissioning. A sample of the corroded fastener collected from the affected filter was taken for detailed testing and analysis.

The main internal components of the subject filter, mainly the screen and the fasteners and other supporting components, other than the outer shell, which are in contact with flowing seawater, were said to be made of Duplex Stainless Steel 2205. The inside surface of the outer shell was rubber lined.

Practically all fasteners were found to be **severely corroded at the bolt threaded surfaces only**. No corrosion was said to have occurred on the filter screen itself and other components of the interior except the threading of the fastener bolts. Filter screen contains conical sections of Duplex SS sheets in which holes of very small diameter are drilled to allow seawater to pass through but to retain debris materials.

Photo 7a shows a corroded fastener sample (M-10 size) given for detailed analysis. Photo 7b shows a corroded one more fastener still remaining in the filter.

One can notice heavy corrosion on the threaded portion and absence of any corrosion on the bolt head. Such is the case for all the corroded fasteners seen at this site.
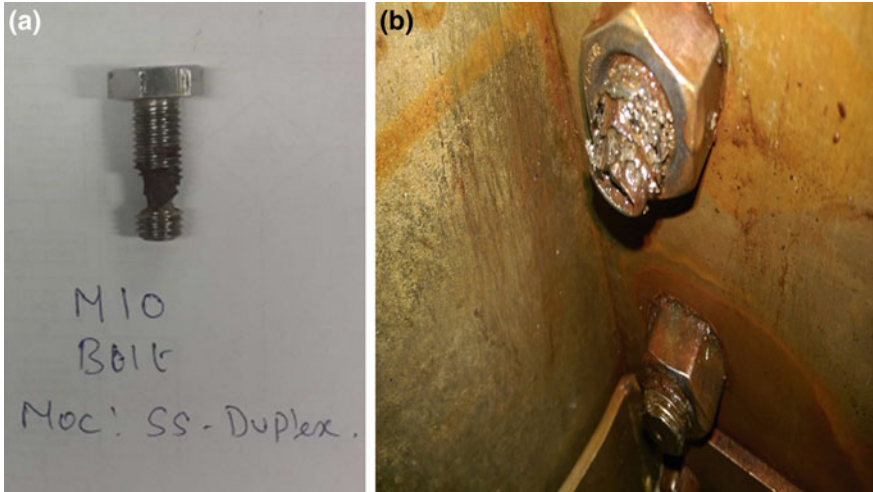
Photograph 7 a Bolt Sample given for detailed analysis. **b** Corroded Fastener still remaining in the filter

Photograph 8 Close macroscopic view of the sample as seen through a stereo microscope

Photo 8 shows a close macroscopic view of the sample, as seen through a stereo microscope. One can notice severe corrosion on a certain portion of the threaded portion. Photographs 9 and 10 show in some detail the nature of corrosion as seen through stereomicroscope under higher magnifications. There is practically nil or very little corrosion on the trough portions and high corrosion on the valleys of the threading.

Through Scanning Electron Microscopic observations, one could notice that there are corrosion products adhering to the valley portions and absence of such

Photograph 9 Close view of a corroded nut where troughs are free from corrosion
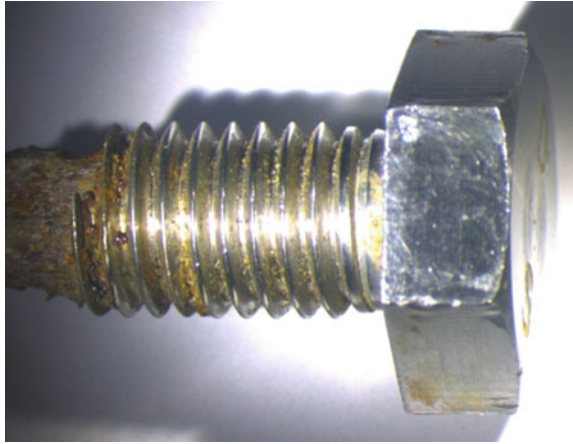
Photograph 10 Close view of a corroded nut where valleys are corroded
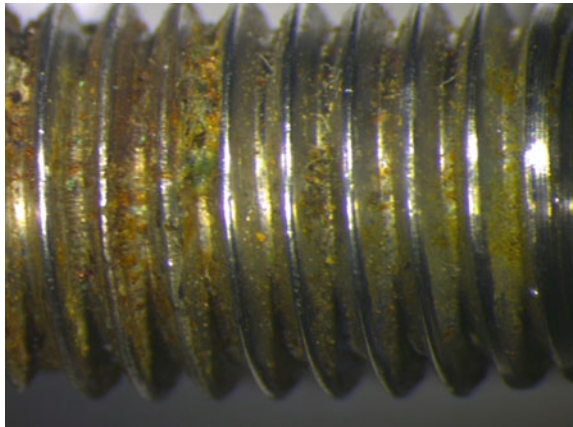
corrosion products on the trough portions. One could also notice alternate bands of corroded areas. These are typical of corrosion in duplex stainless steel.

Through Optical Microscopy observations also it was confirmed that troughs are not corroded and there has been the initiation of corrosion in the valley portions only. Photograph 11 shows a typical optical micrograph showing localized corrosion on the valley portion.

- EDAX (ENERGY DISPERSIVE ANALYSIS OF X-RAYS) results also indicated that preferential corrosion has occurred mostly in the valleys and to a lesser extent in the troughs by showing much high oxygen (oxide) and chlorine (chloride) contents only on the valley portions and not on the trough portions.

Photograph 11 Optical
Micrograph of a cross section
of a corroded nut showing
localized corrosion on the
valley portion
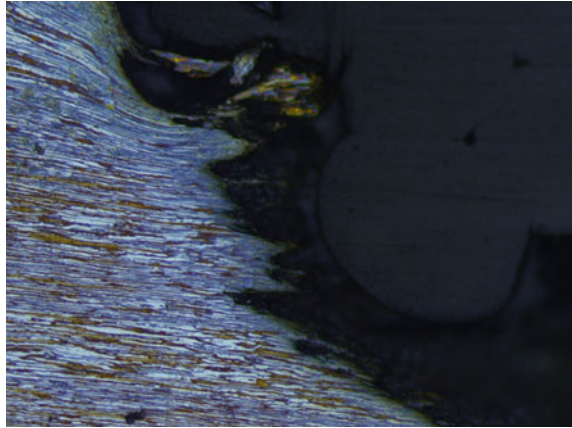
4.1 Inferences and Analysis

Among the above input observations and sample test results, the following are the
important inferences relevant to the study:

- Preferential corrosion has occurred only on localized place such as bolt
  threading.
- There is no corrosion on the main body of the Debris Filter (DF), punched
  screens, even though the MOC for both screen and fasteners is the same namely
  DSS.
- SEM pictures and Optical Metallographic photographs confirm the preferential
  corrosion on the valleys of the bolt turnings and not much on the trough.

The above observations lead to the following inference. DSS has not experienced
any general uniform corrosion by the flowing seawater, but it has experienced
localized corrosion. Among the localized corrosion by sea water, pitting corrosion
and crevice corrosion are the usual ones. In this particular case *crevice corrosion*
rather than pitting corrosion has occurred on the bolt head threading.

The usual laboratory measure of resistance to crevice corrosion is the critical
crevice corrosion temperature, or CCCT, which is the highest temperature at which
an alloy resists crevice corrosion in a given environment.

Crevice corrosion resistance as measured by the ferric chloride test relates, to a
degree, to performance in seawater. Here are the results (Table below) for a number
of alloys: temperatures for initiation of crevice corrosion in ferric chloride
($FeCl_3 \cdot 6H_3O$)10% $FeCl_3 \cdot 6H_2O$, per ASTM G48 Practice B, (PRE) N = Cr + 3.3%
Mo + 30% N:

CCCT IN FeCl$_3$:

Alloy	Mo (%)	Temp (°C)	Pitting resistance equivalent (PRE), N
316L	2.1	−3	23
317L	3.2	2	29
2205	3.1	20	38
317LMN	4.4	20	34
904L	4.4	25	35
2507	4.0	35	47
625	9.0	55	51
C-276	15.4	55	66

From the above table one can get the following inferences with respect to crevice corrosion:

- 316L SS is inferior to DSS 2205.
- 2205 is inferior to super DSS 2507.
- Nickel alloys 625 and C-276 are much better than DSS.

The above results are with respect to Ferric Chloride solution which is somewhat considered equivalent to seawater with respect to corrosion tendency, both general corrosion and localized crevice corrosion. Further, chlorination of seawater, which is practiced in all power stations for killing bio-organisms, unfortunately, increases the tendency for crevice corrosion. In other words, chlorinated sea water is more corrosive than plain sea water. Here again, the high Mo and high Ni alloys are better than 2205 DSS with respect to crevice corrosion.

4.2 Diagnostic Conclusions

It is concluded from this study that the bolts suffered localized crevice corrosion along the threading of the bolt head fasteners by the chlorinated sea water. Within the threading flow of seawater is restricted and leads to some level of stagnancy of the sea water, which is the most important condition for crevice corrosion. Wherever sea water is flowing freely like through the perforated screens and along the bolt heads no corrosion, both general and localized, occurs. Some corrosion observed on bolt heads is actually propagation of crevice corrosion from the inside threading rather than corrosion by outside flowing sea water.

4.3 Recommendations for Remedial Measures

Though somewhat more expensive, it is recommended that the bolts and nuts be made of duplex stainless steel DSS 2507 or nickel base alloy Inconel 625, which are shown to be much better than DSS 2205 in ASTM Standard Ferric Chloride tests.

5 Case Study 4: Localized Corrosion of Incoloy 825 Cooler Tubes

Air Fin Coolers made of nickel base alloy, Incoloy 825, after commissioning, showed leaks after about 9 months of intermittent service. The coolers are made of seamless tubes nickel base alloy Incoloy 825 (ASME SB 163 UNSN08825), and are of size 25.4 mm OD $\times$ 1.65 mm WT $\times$ approx 10 M long, 250 numbers per cooler. The coolers cool compressed hot process hydrocarbon gas flowing on the inside by atmospheric air circulating on the outside surface of the tubes.

The hot compressed hydrocarbon process gas enters the cooler tube inside at a temperature of 135 °C and at a pressure of 27.8 barg, gets cooled while passing through the tube by the surrounding air and leaves the tube at an outlet temperature of 57 °C. The process gas is basically a mixture of hydrocarbons with small amount of inorganic gases. From corrosion point of view, the stream contains H_2O 3.06 mol%, CO_2 3.72 mol%, and H_2S 4.18 mol%. As per NACE specification MR0175, the gas is sour gas and the MOC used to carry the gas at the design/operating temperature of the coolers should satisfy the "sour gas" condition and Incoloy 825 does satisfy the sour gas condition.

Leaks were experienced through the smell of H_2S gas coming out of the two external row tubes through pinhole leaks at two distinct isolated places. Other than these isolated localized leaks, there is no other leak in the balance of the tubes.

Photo 12 The as received cut sample from the leaked tubes
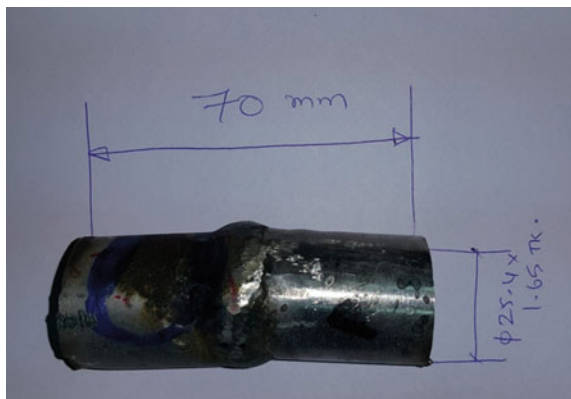
After shutting down, the leaking tubes were removed and a small portion containing the leaky spot in the middle was cut and removed from the leaked tubes for detailed study.

5.1   Sample Description

Photo 12 shows the sample as received, keeping the butt weld approximately in the middle. The left side is toward the header and the right side toward the first baffle.

On the left portion, there is a dark rough patchy surface covering part of the parent metal and part of the weld. This patch showed some remnants of weld spatter, a bunch of fine pores, mechanical ground marks and a fine single pore in the bottom of the ground portion close to the weld. Leak has occurred through this last mentioned pore.

On the right-hand side, toward the baffle portion of the tube, one can see relative brightness and smoothness, but with marks of weld spatter.

Photo 13 above shows the inside surface of the above sample. The hole through which leak has occurred can be seen clearly on the right half of the cross section of the tube sample. One can see a circular patch of burnt-like dark surface surrounding the hole with a shiny circular outline. A weld burnt out area can be seen on the left portion of the sample.

From the inputs so far, process and incident inputs, one can make the following inferences/observations:

1. Neither the inside process fluid nor the outside atmospheric air has led to any fast major corrosion problem which could have been the primary cause of leakage.

Photo 13   The inside surface of the cut sample, as received

2. The fact that only three tubes leaked out of the total of 750 tubes used indicate that there is no overall quality deficiency with respect to the cooler tubes and with respect to process operational parameters.
3. The leakage is associated with a highly localized quality problem associated with some repair welding work done sometime after installing and before commissioning.
4. There are visible defects on the repair weld, like weld splatter, nonuniform ripples and fine porosities both on the inside surface and outside surface of the weld.

Observations through stereomicroscope: There are some repairs done on the original butt weld. These repair welds gave rise to porosities both on the inside and outside surfaces. These pores got interconnected through corrosion by the hot humid air entering the pores from outside atmosphere contact with the OD surface resulting in leaks.

5.2 Scanning Electron Microscopic Examinations (SEM) at High Magnifications

SEM micrographs at very high magnifications (a few thousand times) of the various places at and near the affected areas (repair welds) confirmed the presence of the below-mentioned defects which were seen earlier under stereomicroscopes and also shown crack morphology in the final leaked area near the inside pinhole. The following are the specific ones:

1. Weld spatters;
2. Shrinkage of the repair weld;
3. Final leaked portion on the inside surface is more of linear wide crack with branches rather than a circular corrosion pit;
4. High-density fine porosities, some of these interconnected through fine cracks;
5. Slag inclusions;
6. General oxidation corrosion product, rust patches;
7. Multiple cracking on the inside surface surrounding the leaked crack/hole.

5.3 EDAX/ESCA Analysis During SEM Examination

These give elemental chemical analysis at selected points along with SEM examination. The analyses at varying places of the repair weld near the leaked crack gave the following observations:

1. Presence of Ni, Cr, Fe, Mo, Cu, Ti, C and impurity elements such as Mn, Si, S, P, and Al. In certain places, the proportion of these elements matches with that expected of specification, but at other places it does not.
2. Presence of oxygen, indicating oxidation during welding, insufficient purity of the shielding gas argon.
3. Presence of Ca, Mg, Na, and Cl, indicating outside marine moisture entering the porosities and pits, corroding and propagating them to a small ligament thickness before final fracture and leakage.

Outside marine moisture containing the usual waterborne elements such as calcium and magnesium and marine atmosphere sodium chloride have entered the fine porosities and corroded them to the final point of fracture.

5.4 Diagnostic Conclusion

Incoloy-825 is a suitable material of construction for the service condition (compressed warm sour gas inside and atmospheric air outside) to which the subject air coolers have been designed, fabricated and put into service. In general, the three coolers have given satisfactory service except three localized leaks shown by 3 tubes out of 750 tubes after about 6–8 months of service.

In the affected tubes, there has been some un-recorded necessity for doing repair welding to be done near the first butt weld area near the gas entry end. The repair welding has been defective and resulted in porosities and interconnected cavities. During operation, the hot humid marine atmosphere air in contact with the outside surface of the tubes near the hot gas entry end of the cooler has entered these pores, condensed and remained stagnant inside the pores. This hot moisture has corroded the pores and deepened them and gave rise to leak.

6 General Conclusions

The cases presented above are grouped as **surprising** because of the following reason. All the stated materials come under the so-called CRAs, Corrosion Resistant Alloys. 316(L) Stainless Steel, Duplex Stainless Steel and Incoloy-825 have been chosen as the appropriate material of construction (MOC) for the stated services. But the operational transients/variants are not expected in the design stage. The variants discussed in the paper are the following:

1. Presence of high quantity of fluoride in phosphoric acid;
2. Chloride getting concentrated in the wastewater when evaporation occurs;
3. Certain Susceptibility to Crevice Corrosion in seawater of duplex stainless steel;

4. Defective unplanned repair weld and the resultant corrosion within the weld defects.

These unexpected variations have resulted in unexpected failures. Hence, the above cases are termed **surprising failures**.

The remedial measures vary from case to case. Anticipate the impurity effects and take appropriate measures like using acids of fewer impurities or change the MOC to resist the impurity effect. Anticipate chloride increase during wastewater heating and choose proper MOC. Anticipate crevice corrosion within the threading of the bolts and choose proper MOC. Ensure good quality welds as per the standards even for repair welds. These measures would prevent similar failures in the future and prevent recurrence of huge production downtime losses.

Modelling of Low Cycle Fatigue Failure Through Damage Mechanics

A. K. Asraff, S. Sheela, Reeba Jacob, Krishnajith Jayamani S. Sarath Chandran Nair and J. Cyric

Abstract The classical Gurson–Tvergaard–Needleman (GTN) model has been used for the damage modelling of metallic and non-metallic materials with great success. Damage mechanisms such as void nucleation, void growth and void coalescence under monotonic loading have been considered in this model. Because of its popularity and generality, this model has been implemented in almost all popular non-linear finite element analysis codes. However, this model has not been used much for cyclic loading situations. The application of GTN model for a cyclically loaded structure is attempted here. The well-known Chaboche cyclic plastic model has been combined with the GTN model to investigate the cyclic growth of voids in a copper base alloy which is used in a liquid rocket engine thrust chamber. This combined model which has been implemented in ANSYS code would be useful in the direct computation of low cycle fatigue life of structures undergoing high cyclic plastic deformations such as double walled rocket thrust chambers.

Keywords GTN model · Damage · Chaboche · Copper · ANSYS · LCF

1 Introduction

Thrust chamber is one of the most important subsystems of a liquid propellant rocket engine. Liquid fuel and oxidizer are mixed and ignited here to develop the thrust which is used as the propulsive force for the rocket. During combustion, the chamber will be subjected to severe mechanical and thermal loads taking its inner wall into the plastic state [1]. Repeated operation of the engine induces low cycle fatigue (LCF) in the inner wall material, which will be generally of a high

A. K. Asraff (✉) · S. Sheela · R. Jacob · K. J. S. Sarath Chandran Nair · J. Cyric
Structural Dynamics & Analysis Group, Mechanical Design & Analysis Entity, Liquid
Propulsion Systems Centre, Indian Space Research Organisation, Valiamala, Trivandrum,
India
e-mail: akasraff@yahoo.com

conductive material like copper alloy. The tensile properties of the alloy are evaluated from monotonic tension tests [2] and LCF properties from cyclic tests [3]. The true stress–strain properties are computed by an extrapolation technique [4]. Constitutive modelling of the alloy is done using the multilinear Isotropic hardening plasticity model in ANSYS (Version 16.0) general purpose finite element analysis code [5]. During large-scale yielding, pre-existing voids in the material grow, fresh voids nucleate and adjacent voids coalesce to form a macro crack [6]. Growth of this macro crack under continued loading will lead to ductile failure of the material. The Gurson–Tvergaard–Needleman modelling of the copper alloy, which involves calibration of nine parameters, has been done from simple tension tests on smooth tensile specimens [7–11].

A combination of the Chaboche non-linear kinematic hardening model [12–16] and Voce non-linear isotropic hardening model [17] has the unique capability to simulate complex processes accompanying cyclic plasticity such as cyclic hardening/softening and its stabilization as well as ratcheting [18]. Chaboche modelling involves calibration of seven parameters while Voce model requires calibration of four more parameters, all done based on low cycle fatigue tests. Calibration of the model is done for the copper alloy from smooth round LCF test specimens [19, 20].

Finally, material damage parameters have been incorporated into the Chaboche–Voce model by combining it with the GTN model, wherein cyclic growth of voids in the material is simulated. The potential use of this model is that low cycle fatigue behaviour of a material can be directly computed from a cyclic stress analysis in which fatigue failure is indicated by high growth of void volume fraction at a particular load cycle. The combined GTN–Chaboche–Voce model has been applied here for ultra-low cycle fatigue life prediction of a round notched bar under cycling loading. This combined model would be useful in the direct computation of low cycle fatigue life of structures undergoing cyclic plastic deformations [21, 22].

The objectives of the study are: (i) to evaluate the tensile properties of copper alloy used in a double walled rocket engine thrust chamber using a computerized Universal Testing Machine, (ii) to evaluate the cyclic yielding characteristics of the copper alloy by conducting low cycle fatigue tests on round smooth specimens, (iii) to perform the Gurson–Tvergaard–Needleman-based micromechanical modelling of the copper alloy from tension tests and finite element simulations, (iv) to perform cyclic plasticity modelling of the copper alloy using Chaboche and Voce models from cyclic stress analysis of a simple block and low cycle fatigue tests conducted on smooth round LCF specimens, (v) to develop a cyclic void growth model of the copper alloy by combining the above cyclic plasticity and micromechanical models and (vi) to apply the cyclic void growth model for fatigue life prediction of a round notched bar.

2 Experimental Investigations

Experimental investigations are carried out in an INSTRON 8862 electromechanical UTM at room temperature. Photograph of the machine is shown in Fig. 1. Salient features of the machine are listed below:

- Load frame rated to 100 kN.
- Induction heating system.
- Water cooled environment chamber.
- Test temperature range: 30–1400 °C.

2.1 Tension Test of Copper Alloy

Round smooth tension test specimens are fabricated and tested in the UTM as per the relevant ASTM standards [2]. Dimensioned drawing for the specimen is given in Fig. 2. The yield strength obtained from these tests is noted. Photographs of a specimen before and after test are shown in Fig. 3 and Fig. 4, respectively. The stress–strain curve, yield and ultimate strengths, percentage elongation, and percentage reduction in area of each specimen are recorded from the tests.

Fig. 1 Photograph of Universal Testing Machine
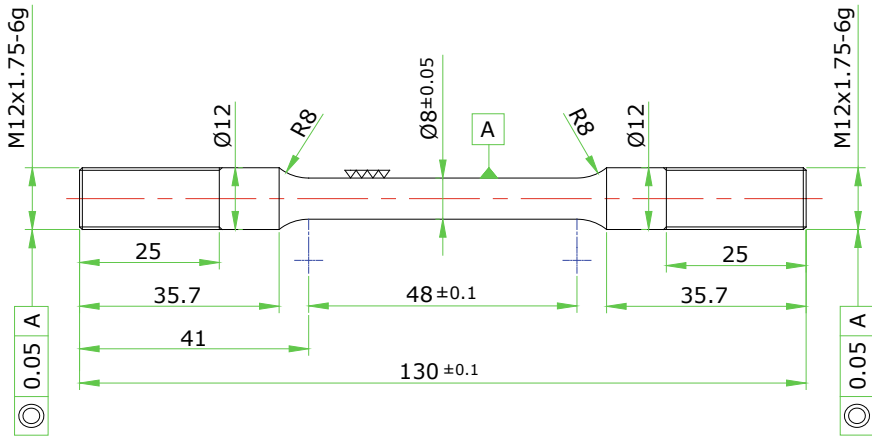
Fig. 2 Drawing of tension test specimen [10]

Fig. 3 Specimen before testing

Fig. 4 Specimen after testing

2.2 LCF Testing of Copper Alloy

Round smooth threaded LCF test specimens are prepared and tested in a Universal Testing Machine as per ASTM E-606 standards [3]. Sketch of the specimen is shown in Fig. 5. Photographs of a specimen before and after testing are shown in Fig. 6 and Fig. 7, respectively. The cyclic stress–strain curve, evolution of peak tensile and compressive stress with cycling and number of cycles to failure for each specimen are recorded from the tests.
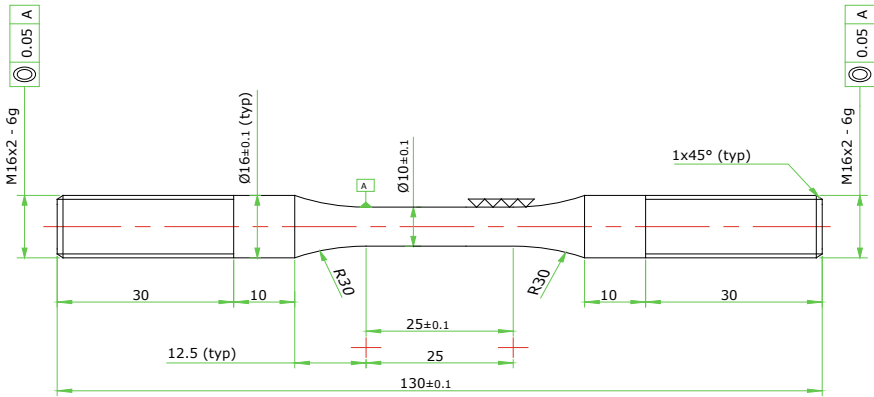
Fig. 5 Sketch of LCF test specimen [11]

Fig. 6 Specimen before testing

Fig. 7 Specimen after testing

3 Constitutive Modelling of Copper Alloy

3.1 True Stress–Strain Modelling

True stress–strain modelling of the copper alloy is done using an extrapolation technique [4]. True stress–strain relationship in the plastic range is given by the expression

$$\sigma = K\varepsilon^n \tag{1}$$

where K is the strength coefficient = 421.7 MPa, n is the strain hardening exponent = 0.283 at room temperature.

In order to perform stress analysis of this alloy, it is required to input its true stress–strain characteristics to the finite element analysis software employed. Material model used is the well-known Multilinear Isotropic hardening (MISO) plasticity model.

3.2 Micromechanical Modelling

The Gurson–Tvergaard–Needleman model is used for micromechanical modelling which considers a damage parameter, f to describe the damage (amount of voids) in the material. The plastic potential function for this model is given by

$$\phi = \frac{\sigma_e^2}{\sigma_y^2} + 3f^* q_1 \cosh\left(\frac{3q_2\sigma_m}{2\sigma_y}\right) - 1 - q_3(f^*)^2 = 0 \tag{2}$$

where f^* is the effective void volume fraction considering coalescence effects.

$$
\begin{aligned}
f^* &= f & \text{if } f \leqslant f_c \\
f^* &= f_c + \frac{\frac{1}{q_1} - f_c}{f_f - f_c}(f - f_c) & \text{if } f > f_c
\end{aligned}
\tag{3}
$$

where f is the void volume fraction, f_c is the critical void volume fraction and f_f is the void volume fraction at rupture [7–9].

3.3 Cyclic Plasticity Modelling

For cyclic plasticity modelling of the material, the following material models are used: (i) Chaboche model, which is a non-linear kinematic hardening model to represent the stabilized cyclic stress–strain hysteresis loop of the material and (ii) Voce model, which is a non-linear isotropic hardening model to represent cyclic hardening characteristics of the material.

3.3.1 Chaboche Model

The classical linear kinematic hardening model, originally proposed by Prager, which is suited for bilinear stress–strain behaviour, is given below

$$d\alpha = Cd\varepsilon^p \tag{4}$$

where $d\alpha$ is the incremental deviatoric backstress tensor, C is the constant of proportionality and $d\varepsilon^p$ is the incremental equivalent plastic strain tensor. However, to model smooth non-linear stress–strain behaviour of materials, the Chaboche model, as given below, is commonly used

$$d\alpha_{ij} = \frac{2}{3}Cd\varepsilon_{ij}^p - \gamma\alpha dp \tag{5}$$

where α is the backstress, dp is the accumulated plastic strain and C, γ are the material parameters. A third order Chaboche model is found sufficient for common materials and hence used for the current idealization as given below

$$\alpha = \sum_{i=1}^{3} \alpha_i \tag{6}$$

This model requires six parameters C_1, γ_1, C_2, γ_2, C_3, γ_3 evaluated from a saturated stress–strain hysteresis loop of the material [12–15].

3.3.2 Voce Model

This model is used for materials exhibiting a smooth exponential transition from the linear elastic region to a final constant linear strain hardening slope. It is given below

$$\sigma_y = k + R_0\varepsilon^p + R_\infty(1 - e^{-b\varepsilon^p}) \tag{7}$$

where σ_y is the yield strength, ε_p is the plastic strain, k is the elastic limit or initial yield point, R_o is the slope of linear plastic region at high strain levels and R_∞ is the stress intercept [17].

4 Calibration of GTN Parameters

In order to evaluate the Gurson–Tvergaard–Needleman parameters of the copper alloy, a parametric finite element analysis of the tension test specimen is done using the ANSYS_APDL finite element analysis code [5]. Stress analysis is done with combined MISO and GTN models.

Figure 8a shows the idealized zone of the specimen for which axisymmetric FE modelling is adopted. Four-noded axisymmetric solid element PLANE182 is used
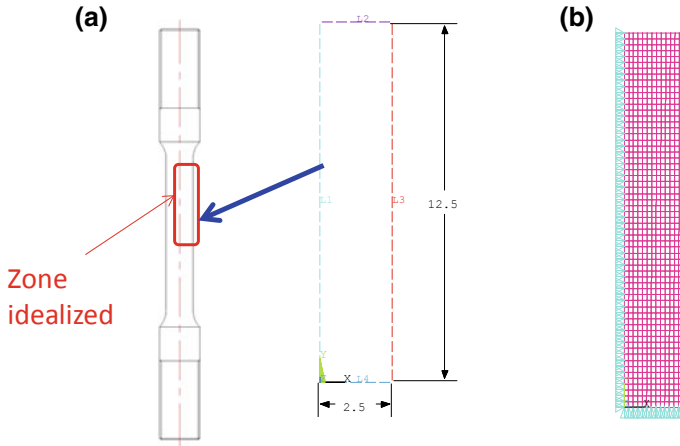
Fig. 8 a Idealized zone of specimen **b** FE model of specimen

Fig. 9 Comparison of engineering stress strain graphs from test and analysis
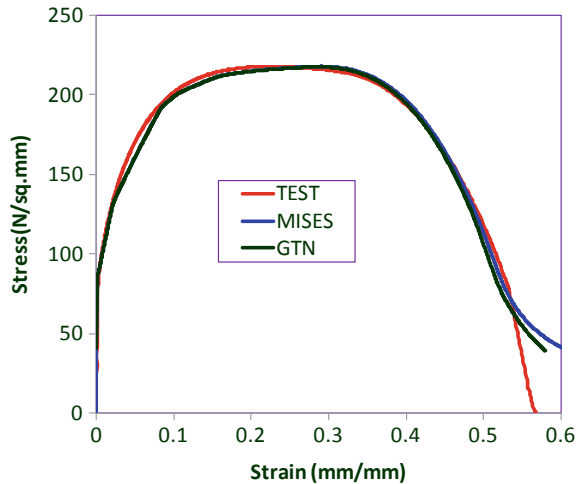
to mesh the model. Considering the symmetry of the specimen, only half of the gauge length portion is modelled and meshed as shown in Fig. 8b.

GTN analysis trials of the tension test specimen are done by changing Gurson parameters to get values matching with experimental results. Comparison of the engineering stress–strain graph for specimen from test and simulation is shown in Fig. 9. The calibrated GTN parameters are given in Table 1. Contour plot of growth porosity and nucleation porosity at failure are shown in Fig. 10.

Table 1 Calibrated GTN parameters of copper alloy

σ_{ys}^2 (N/mm)	f_0	q_1	q_2	q_3	f_N	ε_N	S_N	f_c	f_f
86	0.0001	1.5	1	2.25	0.001	0.1	0.27	0.1	0.2
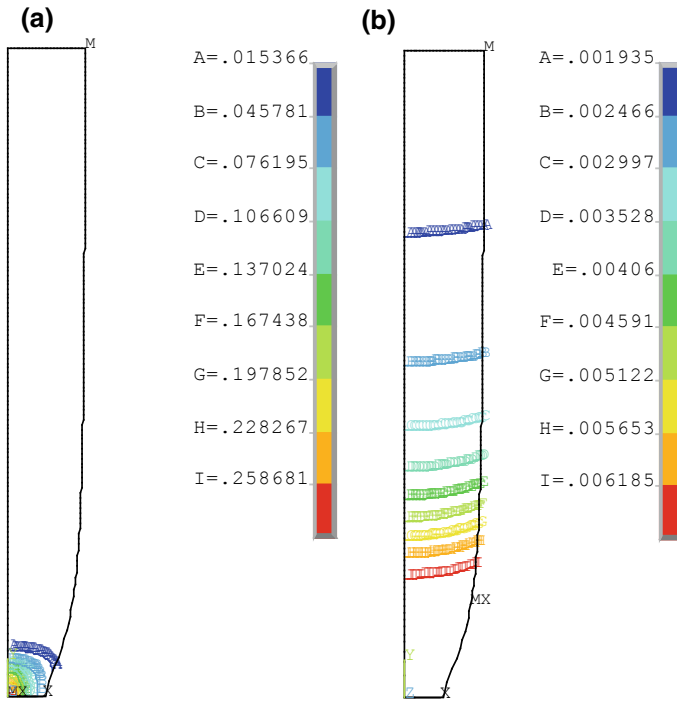
Fig. 10 Contour plots of **a** growth porosity **b** nucleation porosity

5 Calibration of Chaboche and Voce Model Parameters

Detailed steps of calibration of the Chaboche and Voce model parameters based on the work of Budahazy and Dunai [18] are given below:

- *Step 1*: From the raw data obtained from a low cycle fatigue test, the cyclic stress–strain graph is plotted, which showed cyclic hardening initially and saturation after a certain number of cycles, as in Fig. 11.
- *Step 2*: The evolution of peak tensile yield stress in each cycle is plotted next, as shown in Fig. 12. The cycle after which hardening stabilizes can be found out from this curve.

Fig. 11 Cyclic stress–strain graph of round smooth copper alloy specimen
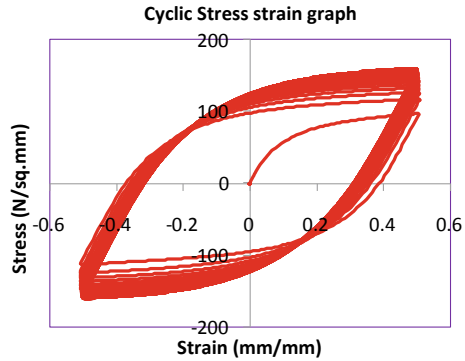
Fig. 12 Evolution of peak tensile yield stress in each cycle
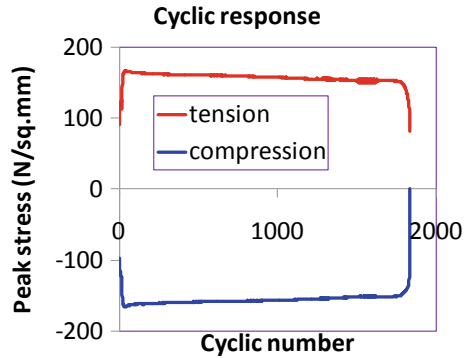
- *Step 3*: The initial Chaboche model parameters are taken from the first stabilized hysteresis graph from LCF test results, which consists of three zones: (I) a linear elastic region (II) a curvilinear transition from elastic to plastic region and (III) a gently sloping hardening region at large plastic strains. C_1 is taken as the slope at the beginning of region II, C_2 as the slope at the middle of region II and C_3 as the slope of region III. γ_1 is taken as the rate at which C_1 reduces (decays) to C_2, γ_2 is the rate at which C_2 decays to C_3 and γ_3 is the rate at which C_3 decays These three parameters are evaluated by trial and error as explained in the next step.
- *Step 4*: A new simple, intuitive and elegant method is introduced here for calibration of Chaboche/Voce parameters based on cyclic analysis of a simple block (idealized using a single 8-noded solid element, SOLID185 in ANSYS, with appropriate symmetry boundary conditions).

  Finite element model of the block is given in Fig. 13. The procedure consists of trial and error cyclic stress analysis of the block under uniaxial displacement controlled loading using the Chaboche constitutive model directly in ANSYS.
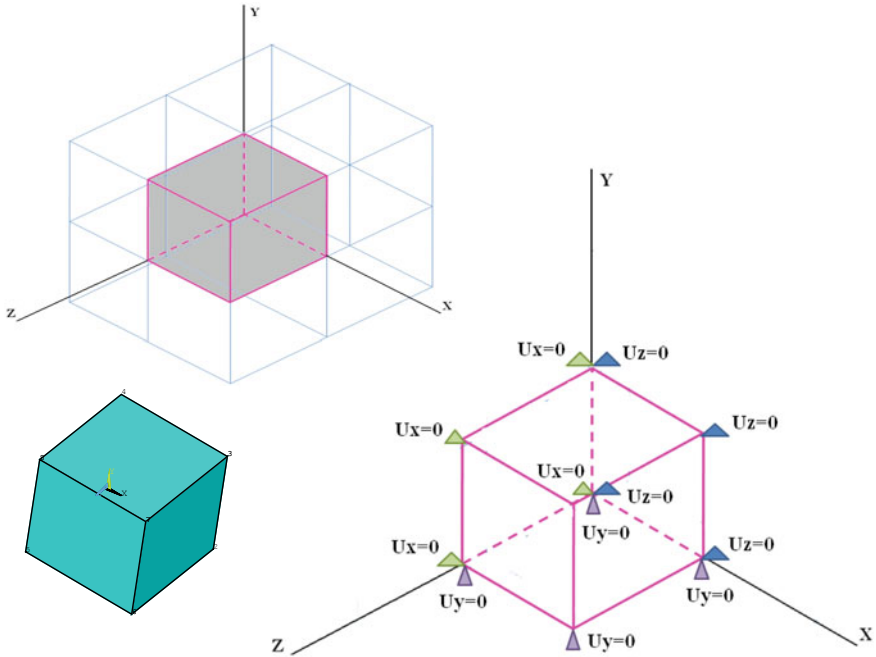
Fig. 13 FE model of simple block

Fig. 14 Comparison of Chaboche graph with test graph
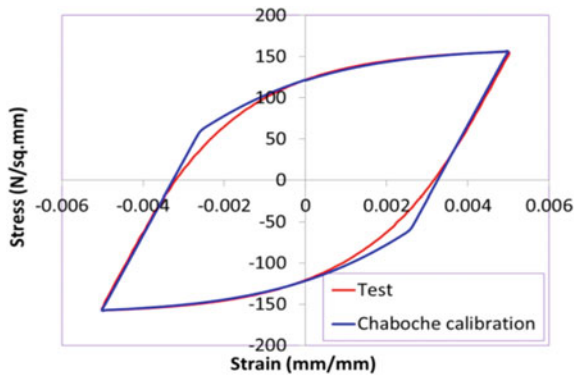
The parameters are varied in each trial, till the computed cyclic response matches well with the experimental one. No ratcheting effects are, however, considered here. Comparison of Chaboche graph with test graph is shown in Fig. 14 and Table 2 gives calibrated Chaboche parameters of copper alloy at room temperature.

Table 2 Calibrated Chaboche parameters for copper alloy at room temperature

Parameter	σ_o	C_1	γ_1	C_2	γ_2	C_3	γ_3
Value	86	2 e5	8 e4	2.6 e4	5 e2	1 e2	5

Table 3 Calibrated Voce parameters for copper alloy at room temperature

Parameter	K	R_o	B	R_∞
Value	50	0	10	70

Fig. 15 Cyclic stress–strain graph of smooth LCF specimen from test data
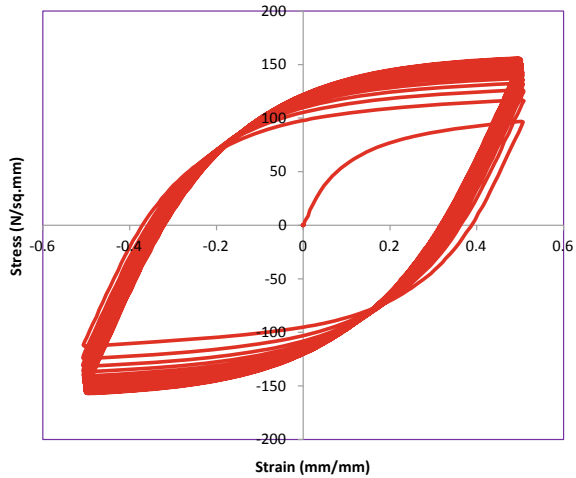
- *Step 5*: The peak yield stress versus cycle number graph obtained from Step 2 is approximately transformed into a Voce graph (which is a stress vs. strain graph) by trial and error. Since the hardening of the material stabilizes after a few cycles, the slope R_0 would be zero. Only one parameter, b has to be fit from the above curve, again based on trial and error. R_α is taken as the difference between the stabilized yield stress and initial peak yield stress, k.

  Table 3 gives the calibrated Voce parameters for the copper alloy. Figure 12 and Fig. 13 give the cyclic response of smooth LCF specimen from test data and simulations.

- *Step 6*: Chaboche and Voce models are now combined and the combined model is calibrated with the test graph. Cyclic stress–strain graph of smooth LCF specimen from test data and analysis results are given in Fig. 15 and Fig. 16, respectively.

Fig. 16 Cyclic stress–strain graph of smooth LCF specimen from analysis
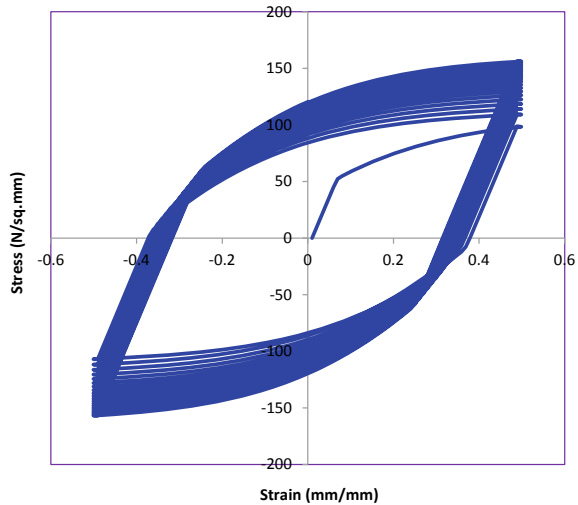
6 Combination of Chaboche, Voce and GTN Models

When the number of cycles to fatigue failure is less than 100, the type of failure is called Ultra-Low Cycle Fatigue (ULCF) wherein the failure surface resembles that of tensile failure. ULCF is found to be primarily due to cyclic void growth which can be simulated using a combination of cyclic plasticity model (Chaboche + Voce model) and micromechanical model (GTN model). Cyclic void growth modelling in ANSYS is based on the work of Besson and Guillemer-Neel [21]. This model can compute the cycle-by-cycle growth of porosity in a material. Fatigue failure is indicated by the void growth becoming suddenly high in a particular cycle. The following points are worth noting in this regard:

1. During tensile phase of cyclic load, voids will grow.
2. During compressive phase of load, voids will shrink.
3. When loading is kept constant, void growth will be zero.

To combine the Gurson model with Chaboche kinematic hardening model, the original Gurson plastic potential function has been modified as [5]

$$f(\sigma, \sigma_y) = \left(\frac{\overline{\sigma}_e}{\overline{\sigma}_y}\right)^2 + 2f^* \cosh\left(\frac{3q_2\sigma_m}{2\overline{\sigma}_y}\right) - \left(1 + q_3 f^{*2}\right) = 0 \qquad (8)$$

where $f(\sigma, \sigma_y)$ is the modified Gurson plastic potential function, $\overline{\sigma}_e$ is the von Mises equivalent modified stress, $\overline{\sigma}_y$ is the modified yield stress, which is a function of the modified back stress given by

$$\alpha_{eff} = \left(1 - \sqrt{q_3}f^{*2}\right)\alpha \tag{9}$$

where α is the kinematic hardening back stress. Then, the modified equivalent stress is given by

$$\bar{\sigma} = \sigma - \alpha_{eff} \tag{10}$$

and the modified yield stress is given by

$$\bar{\sigma}_y = \sigma_y + \sqrt{\frac{3}{2}\left[\alpha_{eff} - \frac{1}{3}trace\left(\alpha_{eff}\right)\right] : \left[\alpha_{eff} - \frac{1}{3}trace\left(\alpha_{eff}\right)\right]} \tag{11}$$

7 Cyclic Void Growth Modelling

Cyclic void growth modelling in a round notched bar at room temperature is done by combining Chaboche, Voce and GTN model. Schematic diagram of a round notched bar is shown in Fig. 17.

Figure 18 and 19 show the cyclic meridional stress–strain graph and evolution of total porosity at notch root during cycling respectively.

The total porosity is found to increase significantly after seven cycles which indicates that cyclic failure of notched bar due to void growth would occur after the seventh cycle. This is due to the local high deformations, stresses and strains at the notch root. The combined Gurson–Chaboche–Voce model is able to capture the ultra-low cycle fatigue failure of the material at the notch root.

Fig. 17 Schematic diagram of a round notched bar
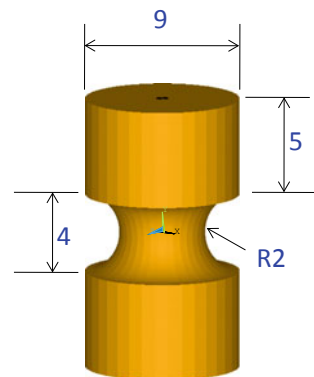
Fig. 18 Cyclic stress–strain graph at notch root
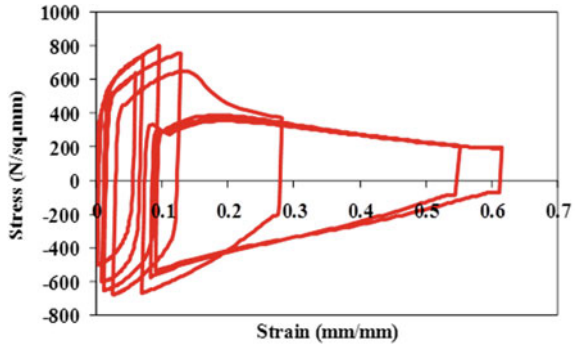
Fig. 19 Evolution of total porosity at notch root during cycling
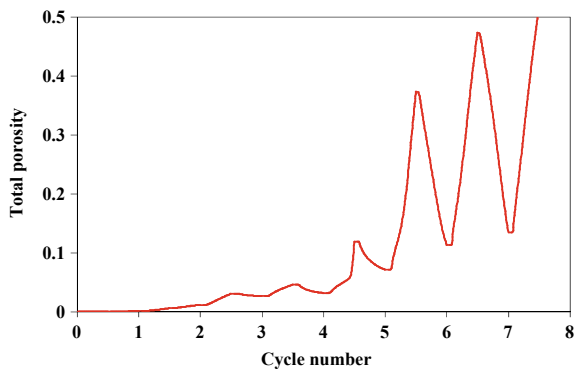
8 Conclusions

From the experiment and analysis results, it is seen that the GTN graph is closer to the test curve than the MISO graph for all the specimens, showing the superiority of the GTN model over the MISO model in predicting ductile failure of the copper alloy. The Chaboche–Voce cyclic plasticity model gave good match with LCF test results. Combined Gurson–Chaboche–Voce model is able to capture the ultra-low cycle fatigue failure of the material at the root of the round notched bar. Cyclic void growth due to fatigue loading is found to increase by a large amount after the seventh cycle indicating fatigue failure could occur after seven cycles.

References

1. A.K. Asraff, R.K. Eapen, Cyclic stress analysis of a rocket engine thrust chamber using Chaboche constitutive model, in *Proceedings of the National Conference on Frontiers in Mechanical Engineering* (2014), pp. 1–7
2. ASTM-E8, Tensile testing of metals, in *American Society for Testing and Materials,* Philadelphia, USA (2008), pp. 1–25
3. ASTM-E606, Low cycle fatigue testing of metals, in *American Society for Testing and Materials,* Philadelphia, USA (2007), pp. 1–30
4. D. Roylance, *Stress Strain Curves* (Department of Materials Science and Engineering, Massachusetts Institute of Technology, Cambridge, 2001)
5. Anonymous, *ANSYS-Engineering Analysis System, Release 11.0,* "Theory, Procedures and Element Reference Manuals" (2009)
6. A.L. Gurson, Continuum theory of ductile rupture by void nucleation and growth: Part I—Yield criteria and flow rules for porous ductile media. Trans. ASME J. Eng. Mater. Technol. 2–15 (1977)
7. A. Needleman, V. Tvergaard, An analysis of ductile rupture in notched bars. J. Mech. Phys. Solids **32**, 461–490 (1984)
8. Z.L. Zhang, A complete Gurson model, in *Nonlinear Fracture and Damage Mechanics*, ed. by M.H. Alibadi (WIT Press, Southampton, UK, 2001), pp. 223–248
9. P.F. Liu, J.Y. Zheng, Finite element analysis of tensile behaviour of ductile steel with defects. ASM Int. 212–217 (2010)
10. A.K. Asraff, S. Sheela, S. Sam, R. Muthukumar, Amruth, Micromechanical modelling of a copper alloy, Paper No. C1, in *Proceedings of 2nd National Conference on Recent Advances in Civil Engineering*, Saintgits College of Engineering, Kottayam, Kerala (2013)
11. T.S. Thomas, A.K. Asraff, M.G. Airin, Damage modelling of highly ductile copper alloy. Int. J. Emerg. Technol. Adv. Eng. **4**, 538–545 (2013)
12. J.L. Chaboche, On some modifications of kinematic hardening to improve the description of ratcheting effects. Int. J. Plast **7**, 661–678 (1991)
13. S. Bari, T. Hassn, An advancement in cyclic plasticity modeling for multiaxial ratcheting simulation. Int. J. Plast. 873–894 (2002)
14. H. Jarrahzadeh, S. Shahrooi, Examination of cyclic plasticity models uniaxial loading by finite elements method. Int. J. Appl. Mech. **21**, 133–140 (2013)
15. P.M. Rezaiee, S. Sinaie, On the calibration of the Chaboche hardening model and a modified hardening rule for uniaxial ratcheting prediction. Int. J. Solids Struct. **46**, 3009–3017 (2009)
16. A.K. Asraff, R.K. Eapen, S. Anand, Cyclic stress analysis of a rocket engine thrust chamber using Chaboche constitutive model, in *Proceedings of the National Conference on Frontiers in Mechanical Engineering,* Mar Baselios College of Engineering & Technology, Trivandrum (2015)
17. E. Voce, A practical strain hardening function. Metallurgia 219–225 (1955)
18. V. Budahazy, L. Dunai, Parameter-refreshed Chaboche model for mild steel cyclic plasticity behaviour. Period. Polytech. 139–155 (2013)
19. A. Babu, A.K. Asraff, N. Philip, Fatigue life prediction of a rocket combustion chamber. IOSR J. Mech. Civ. Eng. 11 12–10 (2014)
20. A.K. Asraff, A. Paul, A. Mathew, S. Sheela, S. Savithri, Cyclic stress analysis of a rocket engine thrust chamber using Chaboche, Voce and Creep constitutive models, in *Proceedings of the 7th International Conference on Creep, Fatigue and Creep-Fatigue Interaction,* IGCAR, Kalpakkam (2016)
21. J. Besson, C. Guillemer-Neel, An extension of the Green and Gurson models to kinematic hardening. Mech. Mater. **35**, 1–18 (2003)
22. D. Steglich, A. Pirondi, N. Bonora, W. Brocks, Micromechanical modelling of cyclic plasticity incorporating damage. Int. J. Solids Struct. **42**, 337–351 (2005)

Part III
Advanced Materials and Processes

Influence of Stacking Sequence on Mechanical Properties and Vibration Characteristics of Glass/Carbon Hybrid Plates with Different Fabric Areal Densities

R. Murugan, R. Ramesh and K. Padmanabhan

Abstract In the present study, the stacking sequence effects of woven fabric Glass/Carbon hybrid composite laminates on mechanical behaviour and free vibration characteristics were investigated. For understanding and analysing the influence of stacking sequence, the laminates were made with different fabric areal densities. Four layered Glass/Carbon hybrid laminates with two different fundamental stacking sequences were fabricated. In the first-type laminate (GCCG), two glass fabrics were placed in the outer layers and two carbon fabrics were kept as inner layers. For the second-type laminate (CGGC), two carbon fabrics were preferred as outer layers. Three different fabric areal densities such as 200, 400 and 600 g/m^2 were considered in the fabrication of laminates for understanding the effect of fabric areal densities. All the laminates were fabricated at prescribed fibre volume fraction using compression moulding machine. The composite samples were tested for the mechanical properties namely tensile, compression and flexural properties. Vibration characteristics such as modal frequency and material damping of hybrid composite plates were measured by impulse hammer excitation method in free–free end condition. Appreciable variation in flexural modulus is noticed by controlling the stacking sequence of hybrid laminate and only a limited influence was noticed over the tensile and compressive behaviour. Free vibration of hybrid plates exhibited fundamentally modified characteristics in accordance with the layering sequence and areal densities. This variation in flexural modulus and modal response is observed to be considerable for all the fabric areal densities and stacking sequences of hybrid laminates fabricated and tested.

R. Murugan (✉)
Department of Mechanical Engineering, Panimalar Institute of Technology, Chennai 600123, Tamil Nadu, India
e-mail: saimurugan1973@gmail.com

R. Ramesh
Department of Mechanical Engineering, Sri Venkateswara College of Engineering, Pennalur, Sriperumbudur 602117, Tamil Nadu, India

K. Padmanabhan
School of Mechanical Engineering, VIT University, Vellore 632014, Tamil Nadu, India

1 Introduction

Woven fabric composites are popular in automotive and aircraft applications because of their excellent integrity and conformability and more balanced properties in the fabric plane. Nevertheless, the composite structures asked for very good passive damping to mitigate the amplitude of vibration caused during the dynamic service conditions [1]. The ability of a material to dissipate elastic–strain energy during mechanical vibration is measured as damping capacity. Many investigations were performed on evaluation of material damping of dedicated glass fibre laminates using impulse excitation method under free–free end condition in the past. Experimental evaluation of damping for glass composite laminates by controlling fibre orientation and laminate configuration was studied extensively [2, 3]. Bledzki et al. [4] investigated the elastic properties of unidirectional glass laminates by a mixed numerical/experimental method using the vibration test of plates. Jean Marie Berthelot et al. [5] found that the stacking sequence had significant effect on free vibration characteristics of E-glass and Kevlar hybrid composite laminate. Investigation by Ahmed Maher et al. [6] on vibration damping in composite structures showed that the orientation angle of the outer laminate have significant effects on the modal parameters of the composite compared with the inner laminate. From the experimental study on damping characteristics of orthotropic composites laminates using impulse excitation method, Abderrahim et al. [7] observed that friction between the warp fibres and weft fibres of the orthotropic laminates significantly contributes to increase in damping. Zeki Kiral et al. [8] confirmed that the stacking sequence influences the natural frequencies of a composite beam under free vibration.

There are only limited studies on evaluation of mechanical properties of woven fabric Glass/Carbon hybrid composite laminates. Saka et al. [9] studied the tensile strength of woven fabric Glass/Carbon hybrid composites analytically and experimentally. Youjiang Wang et al. [10] showed that fibre type and the weaving structure of the reinforcement had a strong effect on tension, flexure, compression, and short beam shear strength of Glass/Kevlar-woven fabric composites. Abot et al. [11] determined the mechanical properties of satin weave Carbon/epoxy composite experimentally under quasi-static loading condition and found that the elastic modulus in tension/compression is approximately equal to half of the elastic modulus of the unidirectional composite. Huang Gu [12] showed that the strength of the multilayer laminates was proportional to the increased number of layers of the laminate. Based on the previous study, it is understood that hybrid composite laminates made of glass and carbon fibres offer very good mechanical properties with 50% of carbon fibre reinforcement and proper control of the stacking sequence of glass and carbon fibre layers.

Detailed literature review revealed that hybridization of glass and carbon fibres in a composite laminate is the best way for achieving good damping performance. The current investigation aims for understanding and analysing the stacking sequence effect of two synthetic fibres, glass and carbon, on mechanical behaviour and free vibration characteristics.

2 Fabrication of Glass/Carbon Hybrid Composite Laminates with Various Fabric Areal Densities

All the hybrid laminates considered for the study were fabricated by hand lay-up method. E-glass and T300 carbon plain woven fabrics of three different areal densities of 200, 400 and 600 g/m^2 were used as reinforcement. LY556 grade epoxy resin along with HY951 hardener was used as matrix. In order to achieve good mechanical properties, all composite specimen were fabricated with a uniform volume fraction of $v_f = 0.5$. The casting was cured in compression moulding machine at room temperature.

All the cured laminates were cut by sawing machine tool into 250×250 mm size plates for free vibration study. Figure 1 shows the four-layered Glass/Carbon hybrid composite plates made by hand layup technique. Two different stacking sequences H1 and H2 were preferred in fabricating hybrid laminates. The arrangements H1, H2 was preferred in fabrication to possess balanced elastic modulus in both longitudinal and transverse directions of the plate. H1 (GCCG) laminate was made by preferring two inner layers as carbon fabrics and two outer layers with glass fabrics. For H2 (CGGC) arrangement, the two outer layers are carbon fabrics and two inner layers are glass fabrics. Figure 1 shows the photographic image of Glass/Carbon hybrid samples with different fabric areal densities fabricated by hand layup method. Table 1 shows the average dimensions, moment of inertia and symbol used for all composite plates considered.

Fig. 1 Image showing hybrid samples with different fabric areal densities fabricated by hand layup method
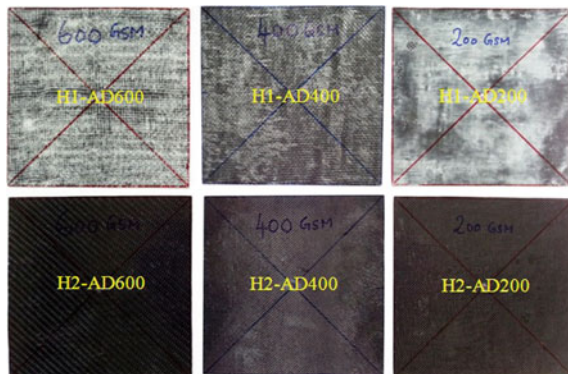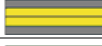
Table 1 Dimensions, moment of inertia, layering sequence and symbol used for Glass/Carbon hybrid composite laminates with three different fabric areal densities considered

Symbol	Fabric areal density [g/m^2]	Preferred layer sequence of laminate		Average dimensions of laminate ($l*w*t$) [mm]	Average MOI (I) [mm^4]
H1-AD200	200	GCCG		250.4 × 250.6 × 1.0	20.88
H2-AD200		CGGC			
H1-AD400	400	GCCG		250.3 × 250.2 × 1.8	121.6
H2-AD400		CGGC			
H1-AD600	600	GCCG		250.2 × 250.5 × 2.4	288.58
H2-AD600		CGGC			

3   Experimental Testing Procedure

3.1   Evaluation of Mechanical Properties of Glass/Carbon Hybrid Laminates with Different Fabric Areal Densities

To verify the final fibre volume fraction of the Glass/Carbon hybrid laminate, resin burn out test was carried out for all hybrid samples fabricated and it was found to be v_f = 0.5 with less than 5% variation. Tensile, compressive and flexural properties of fabricated laminates were evaluated as indicated by ASTM standards. Table 2 reports the test specimen sizes preferred for various mechanical testing and testing rates, where t is the average thickness of composite specimen which is reported in Table 1. Tests were performed at room temperature on a closed loop servohydraulic testing machine (INSTRON® make). Figure 1 shows the images of Glass/Carbon hybrid composite specimens during tensile test, compression test and flexural test conducted on INSTRON®machine (Fig. 2).

Table 2 Geometry of test specimen and feed rate according to ASTM standard for evaluating mechanical properties

Description	Test standard	Specimen size [mm]	Testing rate [mm/min]
Tensile test	ASTM D3039	250 × 25 × t*	1.25
Compression test	ASTM D3410	37 × 6.25 × t*	1.0
Flexural test	ASTM D790	63 × 12.5 × t*	1.2

*t = average thickness of specimen and its corresponding values are stated in Table 1
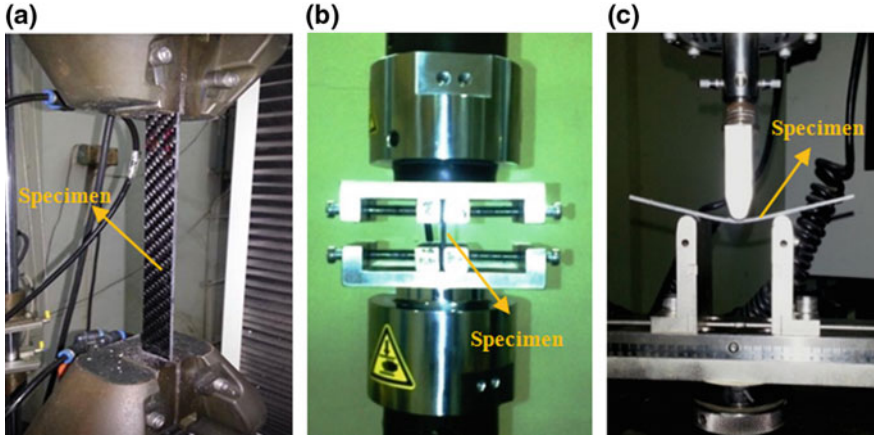
Fig. 2 Images showing Glass/Carbon hybrid composite specimens under (**a**) tensile test (**b**) compression test and (**c**) flexural test conducted on INSTRON®machine

3.2 Free Vibration Testing of Glass/Carbon Hybrid Plates by Impulse Excitation Method

The experimental setup used for measuring free vibration response of composite plates is shown in Fig. 3. Free–free end condition is preferred for modal analysis of Glass/Carbon hybrid composite plates H1 and H2 in order to eliminate the effect of damping due to the supports [13]. Figure 2 shows the experimental setup with quasi-static table arrangement for the free vibration test. The Glass/Carbon hybrid composite plates were freely suspended from the quasi-static table by thin steel wires. The plate samples carrying larger surface to thickness ratio were preferred for evaluating the material damping property. An impact hammer (B&K Type 5800B4)
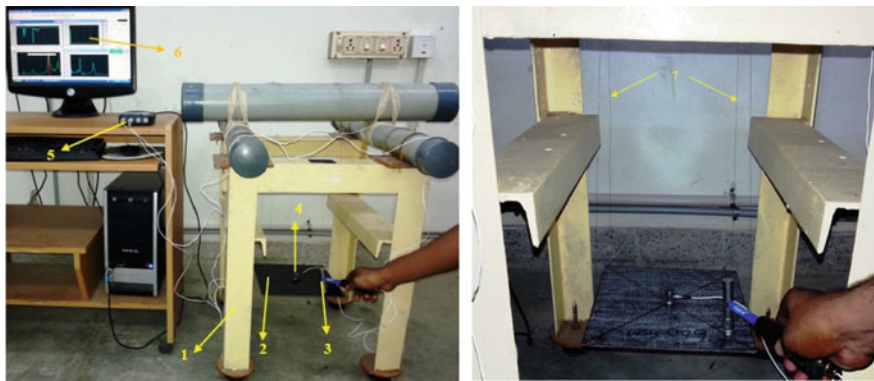
Fig. 3 Image showing experimental test setup for vibration measurement of hybrid composite plate (1) quasi-static table (2) composite specimen (3) impact hammer (4) accelerometer (5) data acquisition card (6) PC with RT Pro software showing FRF (7) thin steel wire

with a load cell was used to excite the structure. The piezoelectric transducer with very low self-weight of 2.7 g (B&K Type 3273A2) was considered for measuring the vibration response of plate specimen to eliminate the add on mass effect as specified in literature [14]. The signals of the impact hammer and the accelerometer were amplified and digitized through a high-speed data acquisition card (B&K Type Photon+) and finally processed using FFT software (RT Pro Photon+), to obtain FRFs of the accelerance (acceleration/force) of the tested component. The measured FRFs were used to extract the modal damping and frequency values of each vibration mode. The loss factor, a measure of damping, of the hybrid composite laminates were evaluated from FRF plot using half power bandwidth method as per ASTM standard procedure [15].

4   Results and Discussion

4.1   Mechanical Properties of Glass/Carbon Hybrid Composite Laminates

Table 3 shows the results obtained by performing tensile test on hybrid composite samples made of three different areal densities of 200, 400 and 600 g/m². Among the two hybrid laminates, there is only marginal variation in tensile strength for different fabric areal density as shown in Table 3. Since the four layers of hybrid laminates equally share the tensile load the difference in tensile modulus is marginal. In earlier investigation, Pandya et al. [16] also confirmed that the hybrid laminate with outer Glass layer and inner Carbon layer gives higher ultimate tensile strength.

In compression test, the elastic strength and elastic modulus of specimen were considerably low as compared to tensile loading. The combined resistance of layers to axial push load is observed to be poor. Table 4 shows the experimental compressive strength and compression modulus and its corresponding variation for specimen with two different layering H1 and H2. Further analysis reveals that the stacking sequence influences the resisting performance of specimen in compression

Table 3 Variation in tensile strength and tensile modulus of hybrid laminates against fabric areal density

Fabric areal density (g/m²)	Tensile strength [MPa]		Tensile modulus [MPa] $\times 10^2$		% of variation in tensile modulus of H1 against H2
	H1	H2	H1	H2	
AD 200	286.4	275.5	139.9	142.7	2.01
AD 400	342.6	338.0	121.1	126.0	4.07
AD 600	413.6	410.4	114.7	119.6	4.28

Table 4 Variation in compressive strength and compression modulus of hybrid laminates against fabric areal density

Fabric areal density (g/m^2)	Compressive strength [MPa]		Compression modulus [GPa]		% of variation in compression modulus of H1 against H2
	H1	H2	H1	H2	
AD 200	169.5	157.1	4.19	3.79	9.23
AD 400	203.2	194.0	4.79	4.26	10.44
AD 600	250.1	241.0	5.44	4.76	12.50

to some extent. There is an increase in compression modulus in the range of 10% for H1 specimen as compared to H2 layered specimen as shown in Table 4. The increased core strength of specimen, H1, is beneficial in axial compression loading. This similar characteristic behaviour was noted in all preferred fabric areal density with different in strength performance for varying areal density, as expected. Previously Zhang et al. [17] also concluded that altering the stacking sequence in a hybrid composite would enhance the compression strength due to the bridging effect of different fibre layers.

Flexural properties of a composite laminate are primarily controlled by the nature of enveloping layer which is in direct contact with bending load. Table 5 shows the experimental results obtained by conducting flexural test on hybrid composite samples made of three different areal densities. There is a considerable flexural strength variation between hybrid laminates H1 and H2 in all three fabric areal density levels. H2 layer arrangement has flexural modulus value 46% higher than that of H1 arrangement in all three fabric areal densities considered as shown in Table 5. This characteristic behaviour is due to more resistance offered by the high modulus Carbon fibre present in outer layer.

For all hybrid laminates, flexural rigidity, the product of flexural modulus and area moment of inertia of cross section were evaluated. The variation in the flexural rigidity of hybrid laminates for three different areal densities is shown in Fig. 4. The layer arrangement H2 offered a noticeable increase in flexural rigidity than the other arrangement H1. Control of stacking sequence with two different elastic moduli of synthetic fibres resulted in laminates with different strength arrangement and higher areal density of fibre offers high resistance against bending load. Earlier

Table 5 Variation in flexural strength and flexural modulus of hybrid laminates against fabric areal density

Fabric areal density (g/m^2)	Flexural strength [MPa]		Flexural modulus [GPa]		% of variation in flexural modulus of H2 against H1
	H1	H2	H1	H2	
AD 200	314.4	324.6	16.83	31.75	47.01
AD 400	393.0	405.8	19.05	33.35	42.88
AD 600	491.2	507.2	21.23	42.08	49.55

Fig. 4 Variation of flexural rigidity of hybrid laminates H1 and H2 for three different fabric areal densities
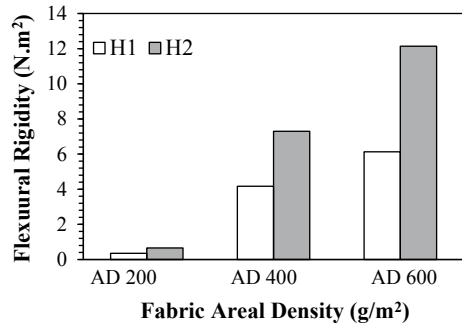
experimental investigation conducted by Ary Subagia et al. [18] stated that placing high stiffness fibre away from the neutral axis of the laminate and the low stiffness fibre at the neutral axis, will enhance the flexural modulus significantly and which also confirm the present characteristic study.

4.2 Frequency Response Function of Hybrid Composite Plates

Figure 5a, b, c show frequency response plots of hybrid composite plates, H1 and H2 made of three fabric areal densities, 200, 400 and 600 g/m^2, respectively. In all
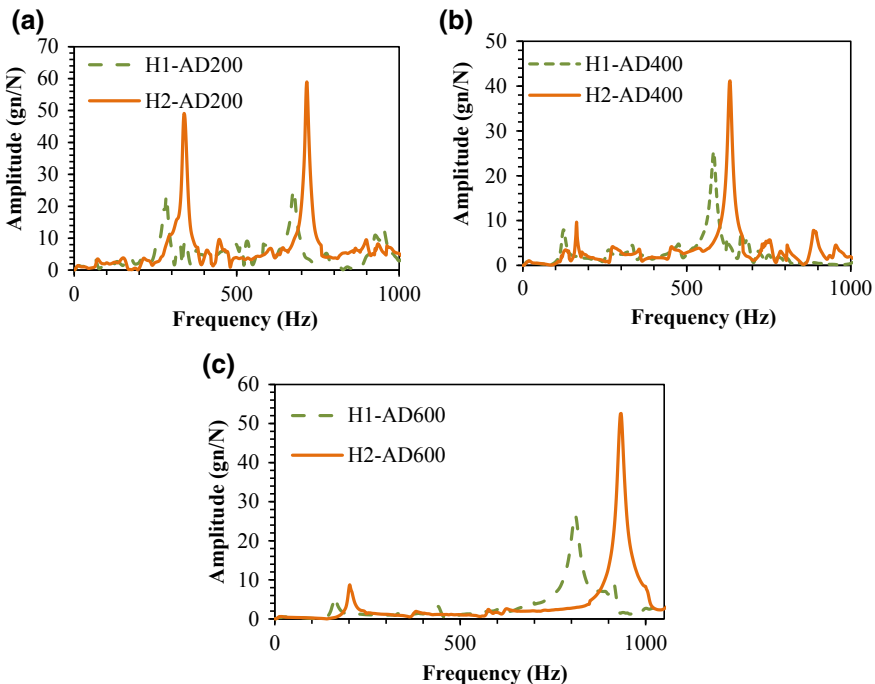
Fig. 5 Comparison of FRF plot of H1, H2 hybrid plates made of (**a**) 200 g/m^2 areal density (**b**) 400 g/m^2 areal density (**c**) 600 g/m^2 areal density for the range of 0–1000 Hz

three areal density plates tested, the spectrum of H1 plate has relatively less amplitude at all successive resonance sets which illustrate improved damping performance. Loss factor values of various composite plates listed in Table 7 also confirms this attribute. Earlier Ingle et al. also confirmed that less amplitude in vibration spectrum indicates high damping in material [19]. Further, free vibration response of H1 hybrid plate shows modified amplitude over the other hybrid arrangement, H2. The different natural frequency values of carbon and glass fabric layers interplied in hybrid plates together promotes the improved amplitude under free vibration.

4.3 Analysis of Modal Frequency and Its Respective Damping

Figure 6a, b, c show the variation in modal frequency values among hybrid composite plates in successive transverse modes for different areal densities considered.
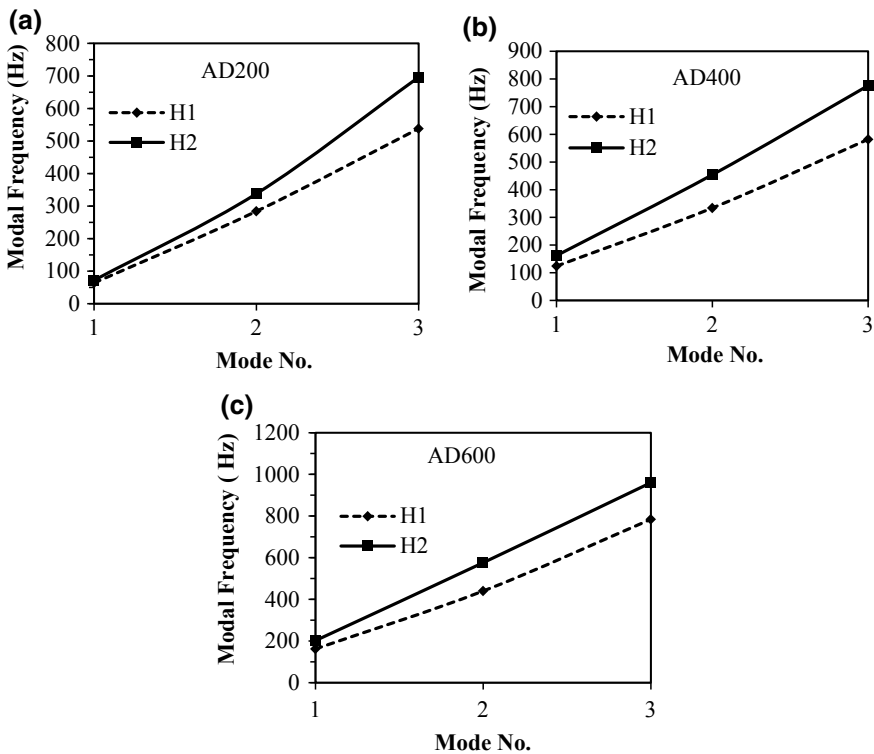
Fig. 6 Variation in modal frequency values in successive transverse modes of hybrid composite plates with **a** 200 g/m^2 areal density **b** 400 g/m^2 areal density **c** 600 g/m^2 areal density

Table 6 Loss factors of hybrid composite plates of three different areal densities tested under free end condition

Mode	AD 200		AD 400		AD 600	
	H1	H2	H1	H2	H1	H2
1	0.059	0.057	0.047	0.033	0.031	0.03
2	0.028	0.027	0.025	0.019	0.017	0.016
3	0.018	0.018	0.012	0.012	0.013	0.012

H2 hybrid plate showed higher resonant frequencies than H1 layer arrangement, in all modes of vibration. The stacking sequence of hybrid plate influences the vibration characteristics and among hybrids, H2 layer arrangement exhibited improved vibration performance by offering higher resonant frequency level than the other layer arrangement H1. The higher flexural strength of H2 plate, as reported in the previous section, than H1 arrangement caused this modification.

Loss factor for the first three modes arrived from experimentally recorded FRF function of hybrid composite plates are reported in Table 6. Table 6 reveals that change of fabric areal density in a composite laminate appreciably modifies the loss factor values. This tendency might be due to modified elastic energy restoring and retrieval capacity in deformation of plate under free vibrating force. Further, there is consistency in material damping under the control of stacking sequence over each plate made of different areal density of fibre in epoxy matrix.

5   Conclusions

The influence of stacking sequence of Glass/Carbon hybrid layered laminate on mechanical properties and free vibration characteristics were experimentally carried out for different fabric areal density levels. Increase in areal density of fibre in fabricated laminates with the same volume fraction, showed a significant increase in mechanical properties as expected. In hybrid laminates, strength arrangement across the layers, by controlling with different fundamental modulus of fibre, significantly modified the compressive and flexural behaviour.

The free vibration characteristics at successive modes were experimentally evaluated for Glass/Carbon hybrid plates, made of three different areal densities under impulse excitation method. Vibration responses of hybrid composite plates are significantly influenced by its stacking sequence. The difference in natural frequency of Carbon and Glass fabric layers interplied in the plate facilitated to modified free vibration characteristics with minimal variation in material damping. Hybrid layering arrangement, CGGC (H2), showed increased modal frequency values in all successive modes than the other hybrid arrangement, GCCG (H1). Similar vibration characteristic behaviours were observed for different fabric areal

densities considered. The effective layering sequence is established as reference layering arrangement in making bulk structure to facilitate good dynamic stability.

References

1. P.K. Mallick, *Fibre Reinforced Composites, Materials and Manufacturing and Design* (CRC Press, Taylor & Francis Group, 2008)
2. R.F. Gibson, J. Mater. Eng. Perform. **1**, 11 (1992)
3. R. Chandra, S.P. Singh, K. Gupta, J. Compos. Tech. Res. **25**, 1 (2003)
4. A.K. Bledzki, A. Kessler, R. Rikards, A. Chate, Compos. Sci. Technol. **59**, 2015 (1999)
5. J.M. Berthelot, M. Assarar, Y. Sefrani, A. El Mahi, Compos. Struct. **85**, 189 (2008)
6. A. Maher, F. Ramadan, M. Ferra, Compos. Struct. **46**, 163 (1999)
7. A. El Mahi, M. Assarar, Y. Sefrani, J.-M. Berthelot, Compos.: Part B **39**, 1069 (2008)
8. Z. Kiral, L. Malgaca, M. Akdag, B.G. Kiral, J. Compos. Mater. **43**, 2943 (2009)
9. K. Saka, J. Harding, Composites **21**, 439 (1990)
10. Y. Wang, J. Li, D. Zhao, **5**, 1159 (1995)
11. J.L. Abot, A. Yasmin, A.J. Jacobsen, I.M. Daniel, Compos. Sci. Technol. **64**, 263 (2004)
12. G. Huang, Mater. Des. **28**, 704 (2007)
13. D.J. Ewins, *Modal Testing: Theory, Practice and Application* (Research Studies Press, Hertfordshire, 2000)
14. A.D. Karle, S.K. Bhoite, A.B. Amale, Int. J. Eng. Res. Appl. **4**(6), 207 (2014)
15. ASTM Standard E756-05, *Standard Test Method for Measuring Vibration Damping Properties of Materials* (ASTM International, West Conshohocken, PA, 2005)
16. K.S. Pandya, C. Veerraju, N.K. Naik, *Mater. Des.* **32**, 4094 (2011)
17. J. Zhang, K. Chaisombat, S. He, C.H. Wang, Mater. Des. **36**, 75 (2012)
18. I.A. Subagia, Y. Kim, L.D. Tijing, C.S. Kim, H.K. Shon, Compos.: Part B **58**, 251 (2014)
19. R.B. Ingle, B.B. Ahuja, Compos. Sci. Technol. **66**, 604 (2006)

Process Parameter Optimization of A-TIG Welding on P22 Steel

A. R. Pavan, B. Arivazhagan and M. Vasudevan

Abstract In the present study, the Activated Tungsten Inert Gas (A-TIG) welding process parameters for welding of 2.25Cr-1Mo (P22) steel have been optimized to attain desired weld bead geometry. Before fabricating weld joints, it is essential to understand the effect of A-TIG welding process parameters in producing quality weld joints. It is proposed to employ the Response Surface Methodology (RSM) of the design of experiments (DOE) approach to determine the optimum parameters in P22 steel weld joint. First, using RSM, a design matrix will be generated by considering various input variables such as welding current, arc gap, torch velocity and electrode tip angle and the output responses such as depth of penetration (DOP), bead area and heat-affected zone (HAZ) width. Further, regression models were generated to correlate the input variables and output responses. The optimum process parameters to obtain the desired DOP, bead area and HAZ width have been determined mainly by utilizing the regression equations and the desirability approach. The Root Mean Square Error (RMSE) of the predicted and measured DOP, HAZ width, and bead area was minimum 0.2571 mm, 0.1776 mm and 6.628 mm^2, respectively. TIG current from 235 to 270 A, arc gap from 2.2 to 2.9 mm and welding speed from 60 to 75 mm/min is obtained from RSM analysis as an optimum process parameter. The study manifest that there is an excellent agreement between the predicted and measured values.

Keywords P22 steel · A-TIG welding · Depth of penetration and response surface methodology

A. R. Pavan
Homi Bhabha National Institute, Mumbai, India
e-mail: pavanar@igcar.gov.in

B. Arivazhagan · M. Vasudevan (✉)
Metallurgy and Materials Group, Indira Gandhi Centre for Atomic Research, Kalpakkam 603102, Tamil Nadu, India
e-mail: dev@igcar.gov.in

1 Introduction

During fabrication of engineering components, welding is a major joining method employed. Therefore, joining and employing the Cr–Mo ferrite steels in severe servicing conditions will affect its lifetime [1, 2]. Thus, joining is an essential method involved in the fabrication of engineering components, where welding is employed to coalesce two metals through fusion. Welding introduces very complex thermal cycle, which results in introducing residual stresses in the material [3]. This often leads to distortion, brittle fracture, and hydrogen embrittlement. This can overcome by proper choice of the welding process.

Fabrication of thicker weld joints using conventional TIG welding process requires joint (groove) preparation, filler material and needs multiple numbers of welding passes. On the other hand, A-TIG welding has enhanced the performance and productivity by threefold [4]. In this technique, the flux is prepared using fine particles of strong deoxidizers dissolved in acetone to form a paste and applied over the joint. During welding, the flux disintegrates to produce oxygen that alters the flow of the molten pool called Marangoni convection eventually to yield an increased DOP [5]. The oxygen content increases the surface tension gradient eventually this increases the depth to width ratio [5]. The A-TIG welding process helps in achieving high productivity [6], lower residual stress and distortion [7].

In the present work, the objective is to determine optimum A-TIG welding parameters to obtain the desired weld shape in P22 steel. For optimizing all independent variables such as current (A), welding speed (mm/min), and Arc gap (mm) the most widely used method is RSM. The main advantage of RSM is it mainly reduces human efforts in achieving the desired output with a minimum number of experiments.

RSM is a useful method to control the input parameters for obtaining the desired response. The output response for respective inputs is analyzed by a series of experiments by using the DOE approach. Central Composite Design (CCD) is the well-known method in RSM, which uses the properties of rotatability to determine the factors. Eventually, the optimum response can be graphically analyzed using contour plots.

Several authors have used the RSM tool to optimize the input variables. Vasantharaja et al. [8] have efficiently correlated the generated model solutions with experimental values and found the actual parameters required to join the 10 mm thick RAFM steel by using A-TIG welding. Nanda et al. [9] demonstrated the influence of the A-TIG welding parameters on the weld geometry of duplex stainless steel alloy 2205. Benyounis et al. [10] successfully demonstrated how the laser power and welding speed alters the geometry of the weld bead and also showed how to get efficient welds exhibiting good mechanical properties with optimized parameters. Ragavendran et al. [11] reported the influence of TIG current and laser power on DOP and finally arrived at a set of optimum parameters to join 5.6 mm thick type 316 LN steel plates. However, there is not much literature available on the multi-response process parameter optimization for joining of P22

steels using A-TIG welding. In the present study, we have tried to determine the best possible parameter for A-TIG welding of P22 steels eventually to attain desired DOP, HAZ width and minimum weld bead area, also called multi-response optimization. By using the design of experiments software, CCD is used to generate the design matrix for carrying out the experiments. The optimized parameters have been verified through experiments.

2 Experimental

P22 plates of dimension $300 \times 120 \times 10$ mm was used in the preparation of bead-on-plate welds. The P22 steel chemical composition is given in Table 1.

A tungsten electrode (dia.3.2 mm) with a 60° tip angle was employed to generate the arc. Argon is used to prevent the oxidation at the flow rate of 10 L/min. The generated design matrix is shown in Table 3. The three input variables were varied at five-level in CCD, with eight factorial points ($2^3 = 8$), six center points, and six-star points collectively to get 20 number of data sets as shown in Tables 2 and 3. The 20 number of small specimens were extracted from the weld plate which is polished and finally etched using 10% nitric acid dissolved in ethanol. The region of interest from weld bead geometry is analyzed using an optical microscope. The respective details are then given to the Design expert for further analysis which is presented in Table 3.

3 Results and Discussion

Significance tests are conducted by portioning the variability of a data set also referred to as analysis of variance (ANOVA). Here the main objective is to fit the model to attain the desired response; to get optimum weld bead geometry by

Table 1 P22 Steel chemical composition

Element	C	Mn	Si	Cr	Mo	Cu	Ni	P	S
Weight (%)	0.15	0.5	0.2	2.25	1	0.05	0.2	0.02	0.02

Table 2 Process parameters varied at five levels

Parameters	Unit	Level 2	Level 1	Level 0	Level 1	Level 2
Current	A	100	141.54	200	259.46	300
Arc gap	mm	1	1.41	2	2.59	3
Torch speed	mm/min	60	72.16	90	107.84	120

Table 3 Generated Design Matrix with the Experimentally Measured Responses

Run	Type	Factor 1 A: current (A)	Factor 2 B: arc gap (mm)	Factor 3 C: torch speed (mm/min)	Response 1 DOP (mm)	Response 2 HAZ width (mm)	Response 3 bead area (mm^2)
1	Axial	200	2	60	4.73	1.452	31.648
2	Axial	300	2	90	5.333	3.01	35.428
3	Fact	140.54	2.59	72.16	2.936	1.14	14.556
4	Fact	259.46	2.59	72.16	6.303	2.9	37.53
5	Center	200	2	90	4.47	1.472	23.247
6	Center	200	2	90	4.904	1.367	24.004
7	Axial	200	2	120	3.943	1.424	20.863
8	Center	200	2	90	4.892	1.567	25.371
9	Fact	140.54	1.41	107.84	4.943	1.73	18.533
10	Fact	259.46	1.41	107.84	3.587	1.621	23.5
11	Fact	140.54	2.59	107.84	2.798	1.405	13.192
12	Center	200	2	90	5.063	1.608	25.21
13	Axial	100	2	90	2.016	1.18	4.943
14	Center	200	2	90	4.987	1.52	25.171
15	Fact	140.54	1.41	72.16	3.517	1.268	20.556
16	Axial	200	1	90	4.873	1.875	29.461
17	Axial	200	3	90	4.457	2.161	25.845
18	Fact	259.46	1.41	72.16	5.322	2.25	43.711
19	Fact	259.46	2.59	107.84	4.222	2.47	28.791
20	Center	200	2	90	5.172	1.409	23.878

developing the polynomial equations between the independent variables and responses RSM is the key tool utilized.

RSM effectively utilizes the independent variables to fit the numerical model. A polynomial regression Eq. (1) is generated to demonstrate the optimum response.

$$Y = b_0 + b_1x_1 + b_2x_2 + b_3x_3 + b_4x_1^2 + b_5x_2^2 + b_6x_3^2 + b_7x_1x_2 + b_8x_1x_3 + b_9x_2x_3$$

(1)

Here, b_0 constant; b_1 to b_9 represents the coefficients. The terms X_1, X_2, X_3, X_1^2, X_2^2, X_3^2, X_1X_2, X_1X_3 and X_2X_3 correspond to the process parameters. Previously in some of literatures reported, similar analysis procedure was carried out [8].

ANOVA determines the significance level of the process parameters and its interaction level. The adjusted R-squared value decides the fitness of the model. The model is adequate when the adjusted R-squared is nearly equal to one. The Model F-value of 24.47, 62.69, and 66.18 for DOP, HAZ width and weld bead area, respectively suggests the significance of the model. The model terms are significant

Table 4 ANOVA for DOP

Source	Sum of squares	df	Mean square	F value	p-value Prob > F	
Model	19.05	9	2.12	24.47	<0.0001	Significant
A-current	8.57	1	8.57	99.08	<0.0001	
B-arc gap	0.24	1	0.24	2.77	0.1269	
C-torch speed	1.09	1	1.09	12.56	0.0053	
AB	2.36	1	2.36	27.25	2.36	
AC	3.26	1	3.26	37.65	3.26	
BC	0.46	1	0.46	5.27	0.46	
A2	2.72	1	2.72	31.42	2.72	
B2	0.10	1	0.10	1.18	0.10	
C2	0.58	1	0.58	6.68	0.58	
Residual	0.86	10	0.086			
Lack of fit	0.57	5	0.11	1.96	0.2383	Not significant
Pure error	0.29	5	0.058			
Cor total	19.92	19				

R-Squared- 0.9566; Adj R-Squared 0.9175; Pred R-Squared 0.7457; Adeq Precision 20.211

only when the "Prob > F" value is less than 0.050. ANOVA analysis for the DOP, HAZ width and weld bead area responses are shown in Tables 4, 5 and 6.

The value of Adeq Precision estimates the signal to noise ratio, and the value of Adeq Precision greater than 4 is advisable. Moreover, in this model, for DOP, HAZ width and weld bead area are 20.211. 27.669, and 33.251, respectively, indicate the adequacy of the signal in the model. The regression equation derived by using all input variables such as Current (A), Arc gap (B), and Torch speed (C) that represents the response surface is given as follows:

$$DOP = +4.91 + 0.79 \times A - 0.13 \times B - 0.28 \times C + 0.54 \times A \times B - 0.64 \times A \times C$$
$$- 0.24 \times B \times C - 0.43 \times A^2 - 0.084 \times B^2 - 0.20 \times C^2$$

$$(2)$$

$$HAZ\,Width = +1.49 + 0.50 \times A + 0.11 \times B - 0.028 \times C + 0.24 \times A \times B - 0.22 \times A \times C$$
$$+ 2.5E - 004 \times B \times C + 0.21 \times A^2 + 0.18 \times B^2 - 0.024 \times C^2$$

$$(3)$$

$$Bead\,Area = +24.47 + 8.64 \times A - 1.34 \times B - 3.70 \times C + 1.31 \times A \times B - 3.20 \times A \times C$$
$$+ 1.52 \times B \times C - 1.45 \times A^2 + 1.19 \times B + 0.70 \times C^2$$

$$(4)$$

Table 5 ANOVA for HAZ width

Source	Sum of squares	df	Mean square	F value	p-value Prob > F	
Model	5.47	9	0.61	62.69	<0.0001	Significant
A-current	3.36	1	3.36	346.62	<0.0001	
B-arc gap	0.17	1	0.17	17.60	0.0018	
C-torch speed	0.011	1	0.011	1.08	0.3221	
AB	0.48	1	0.48	49.11	0.48	
AC	0.40	1	0.40	41.11	0.40	
BC	5.0E-7	1	5.0E-007	5.16E-5	5.0E-7	
A^2	0.63	1	0.63	64.67	0.63	
B^2	0.47	1	0.47	48.90	0.47	
C^2	8.07E-3	1	8.07E-3	0.83	8.07E-3	
Residual	0.097	10	9.70E-3			
Lack of fit	0.054	5	0.011	1.27	0.4004	Not significant
Pure error	0.043	5	8.55E-3			
Cor total	5.57	19				

R-Squared- 0.95826; Adj R-Squared 0.9669; Pred R-Squared 0.9095; Adeq Precision 27.669

Table 6 ANOVA for bead area

Source	Sum of squares	df	Mean square	F value	p-value Prob > F	
Model	1407.62	9	156.40	66.18	<0.0001	Significant
A-current	1018.95	1	1018.95	431.17	<0.0001	
B-arc Gap	24.55	1	24.55	10.39	0.0091	
C-torch Speed	186.55	1	186.55	78.94	<0.0001	
AB	13.65	1	13.65	5.78	13.65	
AC	81.68	1	81.68	34.56	81.68	
BC	18.40	1	18.40	7.78	18.40	
A^2	30.20	1	30.20	12.78	30.20	
B^2	20.49	1	20.49	8.67	20.49	
C^2	7.03	1	7.03	2.97	7.03	
Residual	23.63	10	2.36			
Lack of fit	19.72	5	3.94	5.04	0.0502	Not significant
Pure error	3.91	5	0.78			
Cor total	1431.25	19				

R-Squared- 0.9835, Adj R-Squared 0.91686, Pred R-Squared 0.8754, Adeq Precision 33.251
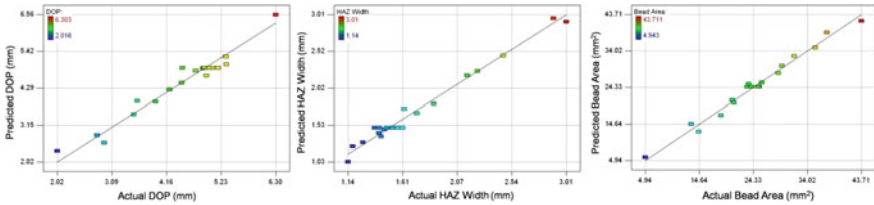
Fig. 1 Predicted versus actual responses

The above equations (Eqs. (2), (3) and (4)) will be used in the desirability analysis to achieve the optimum result. The predicted versus actual value of the obtained response variable is depicted in Fig. 1. Actual values show good agreement with the predicted model values. Here, current (A), Arc gap (B), and Torch speed (C) and the interaction factors of AB, AC, BC, A^2, B^2, and C^2 are recommended to be the significant model terms.

3.1 Interaction of Input Variables on DOP

From ANOVA, the input variables and its interaction showed prominent effects on the output. The effect of the parameter on the outcome can be determined by the generated models. Process parameters, interaction effects can be examined by keeping the third parameter at the central level. The interactions between current, arc gap and torch speed on DOP are presented in Fig. 1, which is derived from the mathematical model shown in Eq. (1). The interaction plots between the input variables suggest that DOP is mainly controlled by current, which is clear from the ANOVA Table 4. With an increase in welding current (100–300 A) DOP increases. Similarly, the DOP increases with the decrease in welding speed (120–60 mm/min) due to a decrease in supplied heat input. Lower welding speed and high current results higher DOP. Also, it can be noted that the influence of current is more to increase DOP compared to all other parameters which can be seen in Table 4 (Fig. 2).

3.2 Interaction of Input Variables on HAZ Width

The interaction of current, torch speed, and arc gap on HAZ width are shown in Fig. 3a. It is evident from the figure that, as the current increases HAZ width increases. HAZ width depends on the TIG current and welding speed. At higher current and lower speed, HAZ width is more. As the speed increases from a certain
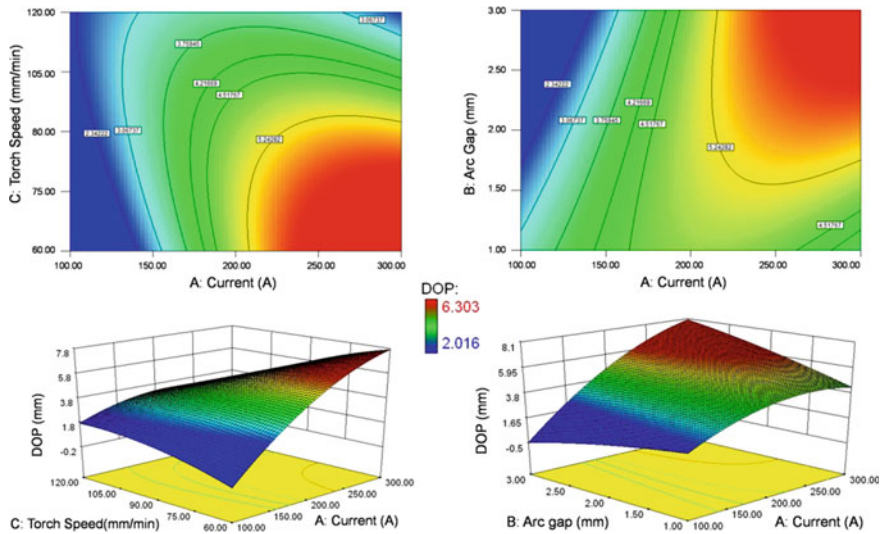
Fig. 2 Interaction between current, arc gap, and torch speed on DOP

limit (>90 mm/min), the HAZ width drastically decreases. This apparently indicates that heat flow into the base material depends on both current and torch speed. Also, it can be noted that as the arc gap increases the HAZ width increases due to the rise in heat input.

3.3 Interaction of Input Variables on Bead Area

TIG current monitors the bead area. When current is at a lower level, the obtained bead width is small, which lead to a decrease in, weld cross-sectional area. As current increases depth to width ratio increases which lead to increased weld bead area. However, higher TIG current and lower welding speed lead to maximum weld cross-sectional area (Fig. 3b).

Optimization of process parameter uses numerical and graphical approach by choosing the target for all process variables and output. Numerical approach couples all necessary targets to get a desirable response. In graphical technique optimization with varying responses, the software interprets the region with the help of a CCD model. Where the defined region gives the range of optimized parameter and the shaded regions on the overlay plot meet the proposed criteria.

For joining the thick sections of P22 steel using A-TIG welding, the primary objective is to achieve maximum DOP, targeted HAZ width and to get minimum
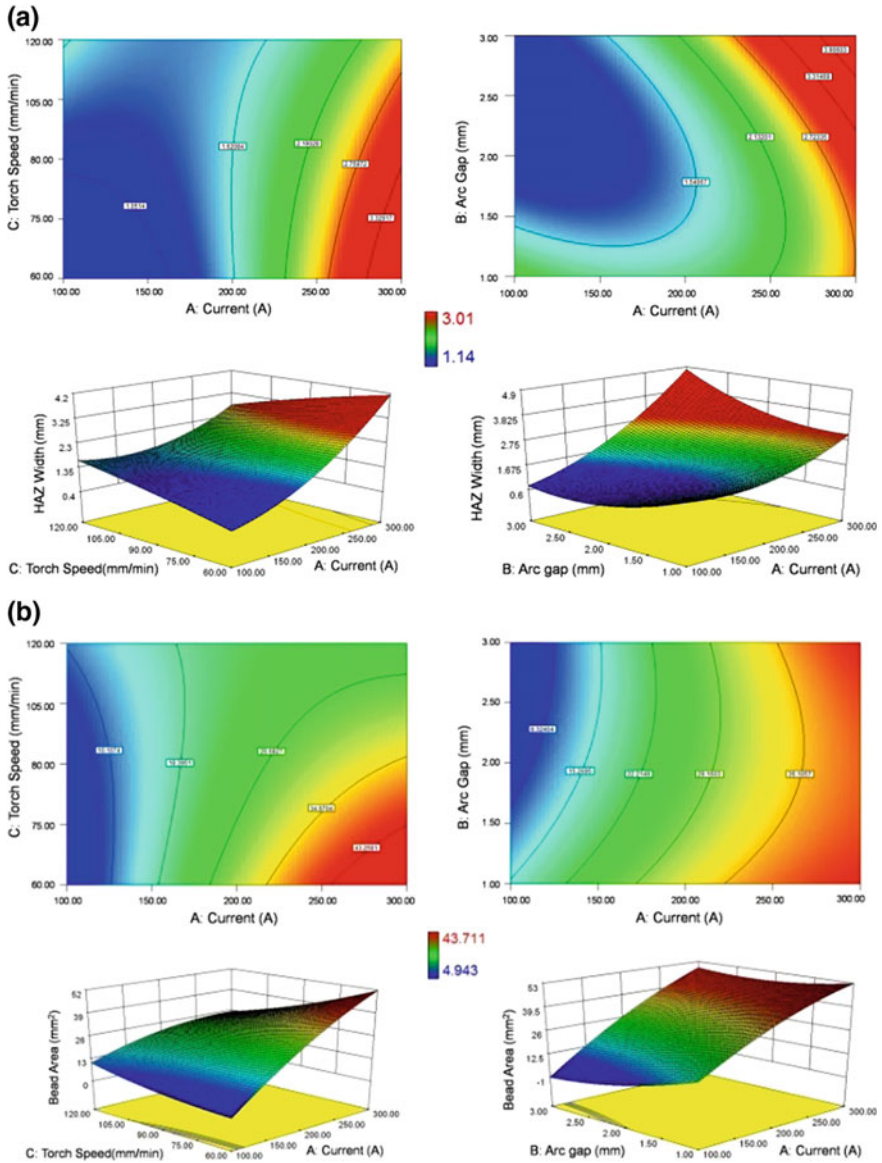
Fig. 3 The interaction between current, arc gap, and torch speed. **a** HAZ width, **b** bead area

bead area in other words, high depth to width ratio. In order to achieve targeted and the optimum result, the multi-objective optimization is necessary. Achieving full DOP during welding of thicker (10–12 mm) materials is necessary to improve the weld metal properties; hence the goal is set as maximizing the DOP, whereas the HAZ width and bead area was kept in range. Several numbers of solutions were

Table 7 Multi-response optimization criteria

Constraints						
Name	Goal	Lower limit	Upper limit	Lower weight	Upper weight	Importance
Current	Is in range	200	300	1	1	5
Arc gap	Is in range	1	3	1	1	5
Torch speed	Is in range	60	100	1	1	5
DOP	Maximize	2.016	6.303	1	1	5
HAZ width	Is in range	1	3	1	1	5
Bead area	Is in range	4	45	1	1	5
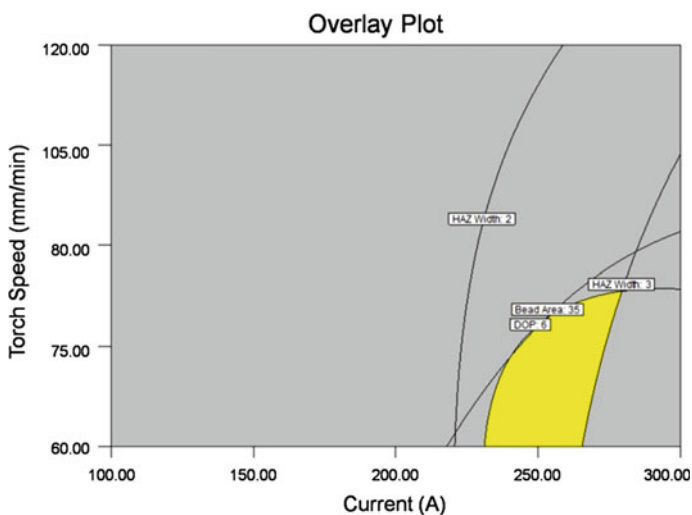
Fig. 4 The overlay plot shows the optimum welding process parameters

produced depending on the target as shown in Table 7. RSM determined 37 solutions with respect to all three process parameters (input variables) to obtain maximum DOP and keeping the values of responses HAZ width, bead area in-range. Also, for easy understanding, graphically, the optimized results were displayed as overlay contour plots. The colored region on the contour plot (Fig. 4) meets the proposed desired criteria.

Table 8 Validation of predicted values

Sl. N0.	Current (A)	Arc gap (mm)	Torch speed (mm/min)	DOP (mm)		HAZ (mm)		Bead area (mm²)	
				Pred.	Exp.	Pred.	Exp.	Pred.	Exp.
1	262.29	2.38	60.58	6.785	6.440	2.915	3.21	44.350	48.22
2	246.84	2.77	63.40	6.695	6.569	2.959	3.10	39.862	47.74
3	234.99	2.89	60.02	6.464	6.234	2.850	2.83	38.399	41.32
4	270.67	2.18	71.94	6.311	6.034	2.786	2.91	40.701	48.22
Root Mean Square Error (RMSE)				0.2571		0.1776		6.628	

3.4 Validation of the Model

The objective of this work is to achieve maximum DOP; hence, the predicted optimum solutions, determined by the model are validated by carrying out the experiments. Randomly, five sets of parameters are taken from the determined solutions for performing the validation experiments as shown in Table 8. The experimentally obtained actual DOP, HAZ width, and bead area values are presented in Table 8 and was found to be in good agreement with the predicted values.

4 Conclusion

The RMSE of the predicted and measured DOP, HAZ width, and bead area was very less. Hence, RSM successfully optimized the A-TIG welding process parameters for attaining the desired weld geometry. It has been found that TIG current has a major effect on the output responses compared to that of other input variables. TIG current from 235 to 270 A, arc gap from 2.2 to 2.9 mm and welding speed from 60 to 75 mm/min is obtained from RSM as an optimum process parameter. The predicted value is successfully confirmed by performing bead-on-plate experiments. The predicted result showed reasonable agreement with the experimentally measured values.

Annexure

Table 9 presents the data resulting from an investigation into the effect of three variables current (A), arc gap (B) and torch speed (C) with the respective response depth of penetration (DOP) (y). To improve the optimization process design of experiment was chosen. At first, numbers of experiments were defined based on the most important variables. The quadratic model was used to fit the result to current, arc gap and temperature.

Table 9 Experimental design matrix for response DOP with natural and coded variables

Run	Type	A			B			
		Factor 1 A: current (A)	Factor 2 B: arc gap (mm)	Factor 3 C: torch speed (mm/min)	x_1	x_2	x_3	y Response DOP (mm)
1	Axial	200	2	60	0	0	−1.681	4.73
2	Axial	300	2	90	1.681	0	0	5.333
3	Fact	140.54	2.59	72.16	−1	1	−1	2.936
4	Fact	259.46	2.59	72.16	1	1	−1	6.303
5	Center	200	2	90	0	0	0	4.47
6	Center	200	2	90	0	0	0	4.904
7	Axial	200	2	120	0	0	1.681	3.943
8	Center	200	2	90	0	0	0	4.892
9	Fact	140.54	1.41	107.84	−1	−1	1	4.943
10	Fact	259.46	1.41	107.84	1	−1	1	3.587
11	Fact	140.54	2.59	107.84	−1	1	1	2.798
12	Center	200	2	90	0	0	0	5.063
13	Axial	100	2	90	−1.681	0	0	2.016
14	Center	200	2	90	0	0	0	4.987
15	Fact	140.54	1.41	72.16	−1	−1	−1	3.517
16	Axial	200	1	90	0	−1.681	0	4.873
17	Axial	200	3	90	0	1.681	0	4.457
18	Fact	259.46	1.41	72.16	1	−1	−1	5.322
19	Fact	259.46	2.59	107.84	1	1	1	4.222
20	Center	200	2	90	0	0	0	5.172

Levels used for A, B and C are shown in Table 1, panel A (natural variables). Panel B shows the levels in terms of coded variables x_1, x_2 and x_3

Quadratic equation for this model is shown in Eq. 5

$$Y = b_0 + b_1x_1 + b_2x_2 + b_3x_3 + b_4x_1^2 + b_5x_2^2 + b_6x_3^2 + b_7x_1x_2 + b_8x_1x_3 + b_9x_2x_3$$

(5)

This optimization process is performed using central composite design (CCD), and it is most widely used for fitting a second-order response surface. The CCD consists of 8 runs at the corners of a square, 6 axial runs and 6 runs at the center of the square and overall 20 runs. In terms of the coded variables the corners of the square are $(x_1, x_2, x_3) = (−1, −1, −1), (−1, 1, −1), (1, 1, −1), (−1, −1, 1), (1, −1, 1), (−1, 1, 1), (1, −1, −1)$ and $(1, 1, 1)$; the axial runs are at $(x_1, x_2, x_3) = (0, 0, −1.681), (1.681, 0, 0), (0, 0, 1.681), (−1.681, 0, 0), (0, −1.681, 0)$ and $(0, 1.681, 0)$ the center points are at $(x_1, x_2, x_3) = (0, 0, 0)$. The second-order model can be fitted using the coded variables.

The coefficients of b_0 to b_9 can be estimated by using the methods of least squares, $\mathbf{b} = (\mathbf{X^1X})^{-1}\mathbf{X^1y}$

For a second-order model with 20 sets of the experiment, the matrix of independent variables X and y vector for this data is

$$
X = \begin{pmatrix}
& x_1 & x_2 & x_3 & x_1^2 & x_2^2 & x_3^2 & x_1x_2 & x_1x_3 & x_2x_3 \\
1 & 0 & 0 & -1.681 & 0 & 0 & 2.828 & 0 & 0 & 0 \\
1 & -1.681 & 0 & 0 & 2.828 & 0 & 0 & 0 & 0 & 0 \\
1 & -1 & 1 & -1 & 1 & 1 & 1 & -1 & 1 & -1 \\
1 & 1 & 1 & -1 & 1 & 1 & 1 & 1 & -1 & -1 \\
1 & 0 & 0 & 0 & 0 & 0 & 0 & 0 & 0 & 0 \\
1 & 0 & 0 & 0 & 0 & 0 & 0 & 0 & 0 & 0 \\
1 & 0 & 0 & 1.681 & 0 & 0 & 2.828 & 0 & 0 & 0 \\
1 & 0 & 0 & 0 & 0 & 0 & 0 & 0 & 0 & 0 \\
1 & -1 & -1 & 1 & 1 & 1 & 1 & 1 & -1 & -1 \\
1 & 1 & -1 & 1 & 1 & 1 & 1 & -1 & 1 & -1 \\
1 & -1 & 1 & 1 & 1 & 1 & 1 & -1 & -1 & 1 \\
1 & 0 & 0 & 0 & 0 & 0 & 0 & 0 & 0 & 0 \\
1 & -1.681 & 0 & 0 & 2.828 & 0 & 0 & 0 & 0 & 0 \\
1 & 0 & 0 & 0 & 0 & 0 & 0 & 0 & 0 & 0 \\
1 & -1 & -1 & -1 & 1 & 1 & 1 & 1 & 1 & 1 \\
1 & 0 & -1.681 & 0 & 0 & 2.828 & 0 & 0 & 0 & 0 \\
1 & 0 & -1.681 & 0 & 0 & 2.828 & 0 & 0 & 0 & 0 \\
1 & 1 & -1 & -1 & 1 & 1 & 1 & -1 & -1 & 1 \\
1 & 1 & 1 & 1 & 1 & 1 & 1 & 1 & 1 & 1 \\
1 & 0 & 0 & 0 & 0 & 0 & 0 & 0 & 0 & 0
\end{pmatrix}
\quad Y = \begin{pmatrix}
4.72 \\ 5.333 \\ 2.936 \\ 6.303 \\ 4.47 \\ 4.904 \\ 3.943 \\ 4.892 \\ 4.943 \\ 3.587 \\ 2.798 \\ 5.063 \\ 2.016 \\ 4.987 \\ 3.517 \\ 4.873 \\ 4.457 \\ 5.322 \\ 4.222 \\ 5.172
\end{pmatrix}
$$

And From, $b = (X^1X)^{-1}X^1y$

$$
X^1.X = \begin{pmatrix}
20 & 0 & 0 & 0 & 13.657 & 13.657 & 13.657 & 0 \\
0 & 13.657 & 0 & 0 & 0 & 0 & 0 & 0 \\
0 & 0 & 13.657 & 0 & 0 & 0 & 0 & 0 \\
0 & 0 & 0 & 13.657 & 0 & 0 & 0 & 0 \\
13.657 & 0 & 0 & 0 & 24 & 8 & 8 & 0 \\
13.657 & 0 & 0 & 0 & 8 & 24 & 8 & 0 \\
13.657 & 0 & 0 & 0 & 8 & 8 & 24 & 0 \\
0 & 0 & 0 & 0 & 0 & 0 & 0 & 8 \\
0 & 0 & 0 & 0 & 0 & 0 & 0 & 0 \\
0 & 0 & 0 & 0 & 0 & 0 & 0 & 0
\end{pmatrix}
$$

$$
X^1.y = \begin{pmatrix}
88.46 \\ 10.81 \\ -1.80 \\ -3.85 \\ 54.41 \\ 60.01 \\ 58.15 \\ 4.34 \\ -5.10 \\ -1.91
\end{pmatrix}
\quad b = \begin{pmatrix}
4.91 \\ 0.79 \\ -0.13 \\ -0.28 \\ -0.43 \\ -0.08 \\ -0.20 \\ -0.54 \\ -0.63 \\ -0.23
\end{pmatrix}
$$

Therefore, the Eq. 5 can be written as shown below,

y = 4.91 + 0.79x₁−0.13x₂−0.28x₃ + 0.54x₁x₂−0.63x₁x₃−0.23x₂x₃−0.43x₁²−0.08x₂²−0.20x₃²

In terms of natural variables, the model is

y = 4.91 + 0.79A−0.13B−0.28C + 0.54AB−0.64AC−0.24BC −0.43A²−0.08B²−0.20C²

Steps involved in the analysis of variance (ANOVA)

The sequence of steps involved in doing analysis of variance (ANOVA) is explained below. The ANOVA for different responses are shown in Table 4, 5 and 6 which contains the output of Design Expert. Generally, computer software will be used to fit a response surface model and to construct the contour plots. ANOVA for the selected quadratic model is an overall summary for the full model with all interactions and main effects.

Step 1: computing the sum of squares

The model sum of squares is

$$SS_{model} = SS_A + SS_B + SS_C + SS_{AB} + SS_{AC} + SS_{BC} + SS_A^2 + SS_B^2 + SS_C^2$$

$$SS_{total} = \sum (X - X^1)^2$$

$$SS_{residual} = SS_{total} - SS_{model}$$

X—Response, X^1—average of X.

Step 2: computing the degrees of freedom (DF)

$$DF = N{-}1$$

N is a number of observations.

Step 3: computing the mean squares (MS)

$$MS = SS/DF$$

$F = MS_{model}/MS_{residual}$

The F ratio is the ratio of two mean square values. If the null hypothesis is true, then F will have a value close to 1.0. The P value is computed from the F ratio which is computed from the ANOVA table. For each ANOVA table, various R^2 value is presented

$$R^2 = SS_{model}/SS_{total}, R_{adj}^2$$
$$= (SS_{residal}/DF_{residual})/(SS_{total}/DF_{total}) \text{ and } R_{pred}^2 1{-}PRESS/SS_{total}$$

PRESS = prediction error sum of squares

Step 4: a significance test

After, all the above steps are completed, the results provided in table format.

References

1. R.C. Reed, H.K.D.H. Bhadeshia, A simple model for multipass steel welds. Acta Metall. Mater. **42**, 3663–3678 (1994)
2. A. Al-Mazrouee, R.K.S. Raman, R.N. Ibrahim, Effect of post weld heat treatment on the oxide scaling of Cr–Mo steel weldments. J. Mater. Process. Technol. **164**, 964–970 (2005)
3. H. Singh, A. Singh, G.A. Singh, *Review on Residual Stress Analysis of Thick Wall Welded Pressure Vessel*, vol. 2 (2013), pp. 1–7
4. B. Arivazhagan, M. Vasudevan, Studies on A-TIG welding of 2.25Cr-1Mo (P22) steel. J. Manuf. Process. **18**, 55–59 (2015)
5. A. Berthier, P. Paillard, M. Carin, F. Valensi, S. Pellerin, TIG and A-TIG welding experimental investigations and comparison to simulation. Sci. Technol. Weld. Join. **17**, 609–615 (2012)
6. M. Vasudevan, A.K. Bhaduri, B. Raj, K.P. Rao, Genetic-algorithm-based computational models for optimizing the process parameters of A-TIG welding to achieve target bead geometry in type 304 L(N) and 316 L(N) stainless steels. Mater. Manuf. Process. **22**, 641–649 (2007)
7. V. Maduraimuthu, M. Vasudevan, V. Muthupandi, A.K. Bhaduri, T. Jayakumar, Effect of activated flux on the microstructure, mechanical properties, and residual stresses of modified 9Cr-1Mo steel weld joints. Metall. Mater. Trans. B **43**, 123–132 (2012)
8. P. Vasantharaja, M. Vasudevan, Optimization of A-TIG welding process parameters for RAFM steel using response surface methodology. *Proc. Inst. Mech. Eng., Part L: J. Mater.: Des. Appl.* **0**, 1–16 (2016)
9. N.N. Korra, M. Vasudevan, K. Balasubramanian, Optimization of A-TIG welding of duplex stainless steel alloy 2205 based on response surface methodology and experimental validation. *Proc. Inst. Mech. Eng., Part L: J. Mater.: Des. Appl.* **0**, 1–10 (2015)
10. K.Y. Benyounis, A.G. Olabi, M. Hashmi, Multi-response optimization of CO_2 laser-welding process of austenitic stainless steel. *Opt. Laser Technol.* **40**, 76–87 (2008)
11. M. Ragavendran et al., Optimization of hybrid laser–TIG welding of 316LN steel using response surface methodology (RSM). Opt. Lasers Eng. **94**, 27–36 (2017)

Influence of Thermomechanical Treatment in Austenitic and Ferritic Fields on Tensile Properties of Reduced Activation Ferritic–Martensitic Steel

P. Prakash, J. Vanaja, G. V. Prasad Reddy, K. Laha and G. V. S. Nageswara Rao

Abstract In the present study, reduced activation ferritic–martensitic steel subjected to thermomechanical treatment (TMT), in austenitic phase field and ferritic phase field, was evaluated for tensile properties (at temperatures 300–923 K) and compared with those under normalized and tempered (N+T) condition. The steel subjected to TMT in austenitic phase field consists of fully tempered martensitic structure and that subjected to TMT in ferritic phase field consists of the fully ferritic structure within prior austenite grain boundaries (PAGBs) after tempering treatment. In the case of TMT in austenitic phase field, allotriomorphic ferrite was also observed along the PAGBs of steel. The tempered martensite of TMT steels is decorated with the increased population of finer precipitates of $M_{23}C_6$ and MX-type compared to the N+T condition. The TMT process improved the strength properties of the steel over the N+T condition without compromising the ductility of the material. Interestingly, the steel subjected to TMT in austenitic phase field resulted in higher yield and ultimate tensile strengths compared to that in ferritic phase field. The improved tensile properties of the steel in TMT condition, over N+T condition, is thus attributed to the microstructural features such as the increase in dislocation density and the increased population of fine $M_{23}C_6$ and MX-type precipitates in TMT steel.

Keywords Reduced activation ferritic–martensitic steel · Thermomechanical treatment · Electron microscopy · Tensile properties

P. Prakash · G. V. S. Nageswara Rao (✉)
Department of Metallurgical and Materials Engineering, National Institute of Technology Warangal, Warangal 506004, Telangana, India
e-mail: gvsnr@nitw.ac.in

J. Vanaja · G. V. Prasad Reddy
Indira Gandhi Centre for Atomic Research, Kalpakkam 603102, Tamilnadu, India

G. V. Prasad Reddy
Homi Bhabha National Institute, Kalpakkam 603102, Tamilnadu, India

K. Laha
Department of Atomic Energy, AUSC Mission Directorate, Noida 201305, Uttar Pradesh, India

115

1 Introduction

Reduced activation ferritic–martensitic (RAFM) steels are considered as primary structural materials for the fabrication of test blanket module (TBM) in fusion reactors. These steels primarily contain (in wt%): 9–12% Cr, $\sim 0.1\%$ C, 1–2% W, 0.18–0.22% V and 0.02–0.18% Ta [1]. RAFM steels have become popular because of their high resistance to radiation-induced swelling [2], high thermal conductivity [3], resistance to helium embrittlement [4] and good structural stability [5]. These steels are conventionally used in normalized and tempered (N+T) condition. In this condition, the microstructure consists of tempered martensite, within prior austenite grains, decorated with Cr-rich $M_{23}C_6$ carbides and MX-type precipitates and hence provides a good combination of strength and ductility (i.e. toughness). However, prolonged exposure at high temperatures induces microstructural instability (coarsening of precipitates, formation of new precipitates, widening and recovery of lath structure, etc.) in these steels and seriously impair their mechanical properties (tensile, charpy, fracture toughness, low cycle fatigue, creep, etc.). Significant efforts have been underway to improve microstructural stability and high-temperature mechanical properties of RAFM steels by several researchers. The optimization of W and Ta contents [5], effect of tungsten [6], tantalum and carbon [7], isothermal heat treatment [8] and austenitization temperature [9, 10] on microstructure, tensile and creep properties have been studied in detail. Precipitation of very fine and thermally stable MX carbonitrides can be expected by thermomechanical treatment (TMT). The dislocation substructures produced upon TMT process in the austenite/ferrite phase field is expected to facilitate the precipitation of nano-sized MX carbonitrides particles by providing the nucleation sites. Earlier investigation on modified 9Cr-1Mo steel showed enhanced precipitation of MX type of precipitates over $M_{23}C_6$ upon TMT and reported an increase in creep deformation resistance and rupture life [11]. Most of the research on RAFM steel is focused on the normalization and tempering heat treatment condition and on the adjustment of chemical composition for improving the specific mechanical properties [12–14]. It must be emphasized that very limited research has been carried out using TMT for improvement of tensile and creep properties of RAFM steel [7, 11]. In the present investigation, an attempt has been made to understand the role of TMT on microstructural stability and size distribution of $M_{23}C_6$ and MX precipitates and the resulting tensile properties. TMT in austenitic and ferritic phase fields has been applied to RAFM steel and corresponding microstructure, bulk hardness, tensile properties at room and elevated temperatures were evaluated. Tensile flow behaviour of RAFM steel in N+T and TMT conditions were analysed using Voce's constitutive equation. Efforts have also made to correlate the microstructural observations with tensile properties and also with the best fit of Voce's constitutive parameters.

2 Experimental

The material used in the present study is reduced activation ferritic martensitic (RAFM) steel and the major alloying elements (in wt%) in RAFM steel are: Fe-9.04Cr-0.08C-1.01W-0.06Ta-0.22V-0.55Mn. The steel was received in normalized (1253 K for 30 min) and tempered (1033 K for 90 min) condition, and is designated as N+T. The steel was then subjected to a controlled TMT by warm rolling in two different phase fields, viz. austenitic and ferritic phase fields. For this, the steel was re-austenitized at 1423 K for 10 min, to convert all tempered martensite to austenite and dissolve the existing precipitates [9, 10], and then air cooled to the warm-rolling temperature of 973 K. In austenitic phase field condition, the steel was warm rolled at 973 K in four controlled passes to achieve 25% reduction in thickness. The warm rolling was followed by ageing at the same temperature (973 K) and then air cooled to the room temperature. In ferritic phase field condition, re-austenitized steel plate was soaked (aged) at 973 K for 120 min to fully convert the austenitic phase into ferritic phase and then the steel was warm rolled to achieve 25% reduction in thickness. Subsequently, the steel was cooled to room temperature. In both the cases, the whole TMT process was completed in 10 min. This includes reheating of the plate to rolling temperature after each pass. Each pass is completed in 10 s and four passes in 40 s and the average strain rate is $6.25 \times 10^{-3} \, s^{-1}$. The authors have carried out 15, 25, 40 and 50% reductions on P91 steel and observed that the best combination of strength and ductility was achieved at 25% reduction in thickness. Hence, for RAFM steel also, the same 25% reduction was used in the present study. Further, it is known in the literature that higher percentage of deformations can cause recrystallization. The air cooled steels in both the TMT conditions, are finally subjected to tempering at 1033 K for 90 min, and hereafter, they are designed as AF-TMT25 (for austenitic phase filed TMT steel) and FF-TMT25 (for ferritic phase field TMT steel).

The microstructural investigations were carried out using optical microscope and scanning electron microscope techniques. The hardness of the steel was determined by macro Vickers hardness tester using 10 kg load and 15 s dwell time. Tensile tests were carried out at a strain rate of $3 \times 10^{-4} \, s^{-1}$ in the temperature range 300–923 K for all the three conditions of steel.

3 Results and Discussion

3.1 Microstructure

The microstructural features of RAFM steel in N+T, AF-TMT25 and FF-TMT25 conditions are depicted in Fig. 1a–f. While the steel in N+T (Fig. 1a) and AF-TMT25 (Fig. 1c) conditions shows a tempered martensitic structure, the steel in FF-TMT25 condition (Fig. 1e) exhibited fully ferritic phase. Further, the prior
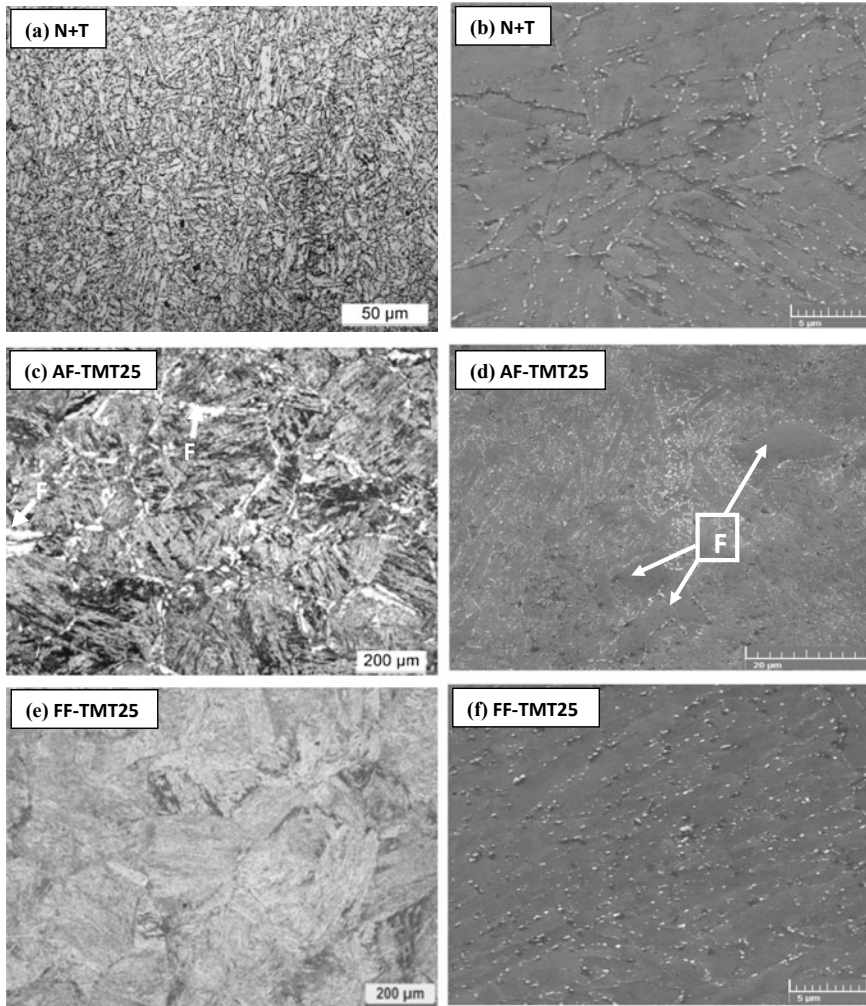
Fig. 1 Optical (**a**, **c** and **e**) and SEM (**b**, **d** and **f**) micrographs of RAFM steel, (**a–b**) N+T; (**c–d**) AF-TMT25; (**e–f**) FF-TMT25

austenite grain (PAG) size in N+T steel is observed to be within 15 ± 2 μm, whereas it is about 175 ± 13 μm and 150 ± 20 μm in AF-TMT25 and FF-TMT25 conditions respectively. This is attributed to the re-austenitization of the steel, prior to TMT, which causes dissolution of most of the existing precipitates thereby leading to grain coarsening. Grain coarsening up on TMT was also reported earlier in grade 91 steel [15]. Apart from this, the steel in AF-TMT25 condition (Fig. 1c) contains allotriomorphic ferrite along the PAGBs and traces of idiomorphic ferrite within PAGBs [16–19], in contrast to the fully ferritic structure in FF-TMT25 steel. The existence of ferrite in AF-TMT25 and FF-TMT25 conditions was also

confirmed by microhardness measurements. The imposed mechanical deformation during TMT and subsequent ageing time might have led to the formation of ferrite along the PAGBs of the AF-TMT25 steel [18, 20].

Typical tempered martensitic structure decorated with coarse $M_{23}C_6$ precipitates along the PAGBs and lath boundaries and fine MX precipitates along with the laths and within the matrix have been observed in N+T condition (Fig. 1b), the latter, however, is difficult to visualize clearly in the SEM images in Fig. 1. Based on the studies of Fernandez et al. [21], the larger precipitates are of $M_{23}C_6$ and the finer ones are of MX type. Similar microstructural features were also reported by several researchers [6, 8, 18, 22] in similar or other ferritic–martensitic steels. The TMT of the steel refines the above mentioned microstructural features of N+T steel, such as refinement of lath structure, precipitate size and number density (Fig. 1d, f). The width of the martensite lath is observed to be around 272 nm in N+T steel, whereas it is refined to 179 nm in AF-TMT25 steel [18]. The size of the $M_{23}C_6$ and MX precipitates are observed to be 50–150 and 20–50 nm in N+T steel, whereas their size has been refined to 30–100 and 5–30 nm in AF-TMT25 and FF-TMT25 conditions [6, 18, 22]. It can be clearly discerned, from Fig. 1d, f, that both the TMT processed steels (AF-TMT25 and FF-TMT25) shows a large density of fine precipitates, compared to the steel in N+T condition. This can be ascribed to the development of high density of dislocations and refined lath sizes up on TMT. In the case of AF-TMT25 steel, the dislocations and refined lath structure act as preferential sites for the nucleation of fine and large number of MX precipitates, and refined laths for $M_{23}C_6$ precipitates. In contrast, the steel in FF-TMT25 condition (Fig. 1f) shows a large amount of finer precipitates compared to the other two conditions. This could be accredited to the enhanced diffusion of elemental constituents of precipitates to the nucleation sites in the ferrite matrix [16, 19]. The high dislocation accumulation indeed is the primary reason for fine and high density of precipitates in FF-TMT25. However, it must be mentioned that the source of dislocations in AF-TMT25 case arises from TMT deformation plus austenite to martensite transformation and thus dislocation density in AF-TMT25 case would usually be higher than that in FF-TMT25 case as the source of dislocations is only TMT deformation in the latter case. TMT deformation in FF-TMT25 case inherently promotes easy cross-slip and thus could increase the associated large density of dislocation tangled networks which possesses high internal stresses. The latter enhances the density of nucleation sites to which rapid diffusion of solute elements assisted by pipe diffusion and open structure of BCC causes large density of finer precipitates. Coarsening is not observed, probably due to the large density of nucleation sites and depletion of required solute concentrations.

3.2   Bulk Hardness

The hardness values of the RAFM steel in N+T, AF-TMT25 and FF-TMT25 conditions are found to be 206 ± 2, 222 ± 2 and 198 ± 3 HV, respectively. The

higher hardness of the steel in AF-TMT25 condition can be attributed to the development of high dislocation density and lath interface volume that generates an abundant amount of finer $M_{23}C_6$ and MX precipitates. Although, the steel in FF-TMT25 condition too possess high dislocation density and numerous numbers of fine precipitates, lower hardness can be ascribed to its softer ferrite matrix after TMT in ferritic phase field.

3.3 Tensile Properties

The tensile stress–strain curves of all the steels displayed a smooth monotonic behaviour without any serrations. The representative engineering stress–engineering strain curves for the temperatures 300 and 673 K for all three conditions of the steel is compared in Fig. 2. The steel in AF-TMT25 condition depicted higher strength values at all test temperatures than the other two conditions. This can be corroborated with the microstructural refinement explained in Sect. 3.1. An important effect of TMT can be noticed in Fig. 2, i.e. an improvement in total strain to failure (e_f) in comparison to that in N+T condition, in spite of higher strength values of the steel in AF-TMT25 and FF-TMT25 conditions. While the steel in AF-TMT25 condition exhibited higher e_f values up to 623 K, the steel in FF-TMT25 condition exhibited higher e_f values even beyond 623 K.

The yield strength (YS) and ultimate tensile strength (UTS) decreased with increasing temperature in all the conditions of steel (Fig. 3a, b). The steel in AF-TMT25 condition exhibited higher YS and UTS than the steel in the remaining two conditions at all temperatures. This is attributed to the existence of typical martensitic structure decorated with higher amounts of fine precipitates of $M_{23}C_6$ and MX type (Fig. 1d). The fine and numerous amounts of precipitates create

Fig. 2 Engineering stress versus engineering strain curves of RAFM steel in N+T, AF-TMT25 and FF-TMT25 condition, tensile tested at 300 and 673 K using a strain rate of 3×10^{-4} s^{-1}
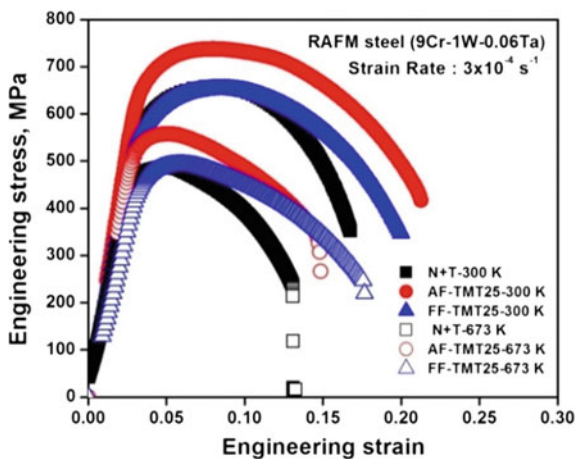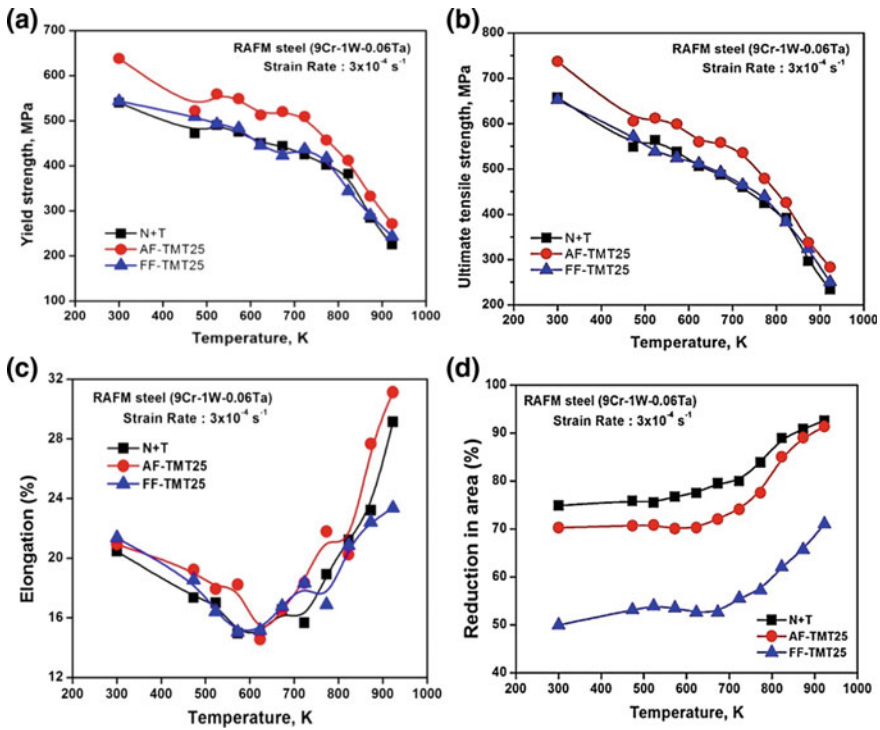
Fig. 3 Variation of **a** YS, **b** UTS, **c** percent elongation and **d** percent reduction in area with temperature of RAFM steel in N+T, AF-TMT25 and FF-TMT25 condition

obstacles to the movement of dislocations thereby increasing the strength of the steel. Although, the steel in FF-TMT25 condition possess substantial amount of fine precipitates, because of its fully ferritic structure (soft and ductile), it exhibits lower values of YS and UTS than the steel in AF-TMT25 condition, but marginally higher than those of N+T steel. On the whole, the steel in AF-TMT25 condition showed better YS and UTS than that in N+T and FF-TMT25 conditions. From YS and UTS plots (Fig. 3a, b), a mild plateau region can be noticed in the temperature range of 473–723 K, and beyond 723 K a rapid fall in YS and UTS can be observed for all three conditions of the steel.

The basic idea of applying TMT to the steel is to improve the strength without affecting the ductility, while in the other strengthening techniques either of the property has to compromise. The present study is the first attempt to increase the microstuctural stability and strength which is successfully achieved, though only 10% increase in strength is noticed. However, further studies are in progress to enhance the strength above 10%. The tempered martensitic structure in TMT condition is stable at least up to 773 K, and also at slightly elevated temps. as reported in our earlier study [18]. However, it is planned to increase the strength of TMT steel in the present study up to the temperature of 873 K. Higher percentage

reductions may lead to recrystallization of the material and hence reduce the mechanical properties of the material.

The % elongation and the % reduction in area plots (Fig. 3c, d) for all the three conditions of the RAFM steel depict similar trends, i.e. slight decrease between 300 and 473 K, followed by a dip in the temperature range of 473–723 K with a drastic increase in ductility parameters beyond 723 K. While the steel in AF-TMT25 condition exhibited a higher percent elongation than the steel in N+T and FF-TMT25 conditions, the steel in N+T condition showed slightly better % elongation than the steel in FF-TMT25 condition. In case of % reduction in area, the steel in FF-TMT25 condition exhibited lower values; whereas N+T steel showed higher values and the steel in AF-TMT25 condition showed intermediate values. On the whole, the presence of mild plateau region in YS and UTS plots (Fig. 3a, b) and a dip in % elongation and % reduction in area plots (Fig. 3c, d) at the intermediate temperatures indicate the existence of dynamic strain ageing (DSA) in all conditions of the steel. Though both %elongation and %reduction in area are ductility parameters, they represent different characteristics of the material. An important feature to be observed from Fig. 2 is the post necking elongation which is extended in TMT steels. Further, a detailed observation of stress drop profile in the post necking region (of tensile stress–strain curves) at all the test temperatures (not presented here), revealed rapid rate of stress drop in the order: N+T > AF-TMT25 > FF-TMT25. As the post necking elongation is localized and since the stress drop during post necking elongation and the reduction in area are directly proportional to each other, the % reduction in area for the three material conditions also follows the above order. The FF-TMT25 condition thus exhibits the lowest % reduction in area.

3.4 Tensile Flow Behaviour

The flow behaviour of the steels can be best understood by fitting the Voce's constitutive equation to the true stress-true plastic strain curves. Several investigators applied the applicability of Voce's equations to the ferritic–martensitic steels in normalized and tempered conditions [6, 18, 22]. This equation predicts the upper limit of degree of strain hardening of the material precisely [18] and it is best applicable to the materials which have a tendency to achieve the saturation stress at higher strains. In the present study, this constitutive equation is applied to the RAFM steel in two TMT conditions and the results were compared with the steel in N+T condition. The Voce's constitutive equation is expressed as [6, 18].

$$\sigma = \sigma_s - (\sigma_s - \sigma_i) \exp\left[\frac{-(\varepsilon_i - \varepsilon)}{\varepsilon_c}\right] \tag{1}$$

where σ_S is the saturation stress, σ_i and ε_i are true stress and true plastic strain at the onset of plastic deformation, respectively and ε_c is a constant. For condition $\varepsilon_i = 0$, Eq. (1) reduces to

$$\sigma = \sigma_s - (\sigma_s - \sigma_i)\exp(n_v\varepsilon) \qquad (2)$$

with three constants σ_s, σ_i and $n_v = -(1/\varepsilon_c)$.

The variation of Voce's parameter, n_v, as a function of temperature is plotted in Fig. 4 and it clearly demonstrates a two-slope behaviour in all conditions of the steel. Initially, n_v values gradually decrease up to a temperature of 723 K followed by rapid decrease. The drastic fall in the n_v values with increasing temperature implies the acceleration of recovery. The change in slope of n_v versus temperature plot implies the change in deformation mechanism. At lower temperatures cross-slip mechanism dominates and the n_v values associated with this are relatively high, whereas at higher temperatures, the change in controlling mechanism from cross-slip to climb and sub-boundary migration leads to very low n_v values [6, 18]. This trend is observed in all conditions of the steel in the present study. The calculated n_v values are in line with those reported in the literature [6, 18, 24, 25]. The n_v values for Cr–Mo steels of type P9 steel with 0.42% Si, P91, 2.5Cr-1Mo and RAFM steels are presented in Table 1. Higher n_v values can be seen in the steel in FF-TMT25 condition above 723 K compared to N+T and AF-TMT25 (Fig. 4) conditions. This indicates that the recovery mechanism accelerates in N+T and AF-TMT25 conditions at higher temperatures compared to FF-TMT25 condition. It must be mentioned that the N+T condition of steel, in general, exhibit higher
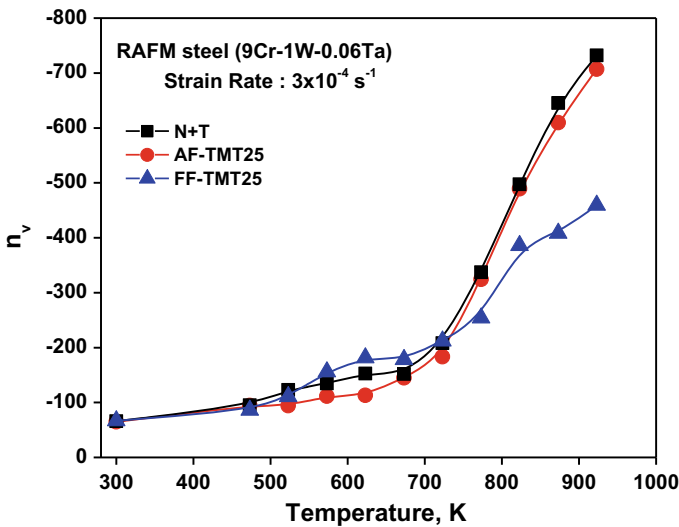
Fig. 4 Variation of Voce's parameter, n_v as a function of temperature for RAFM steel in different conditions

Table 1 n_v values for typical steels

Steel	n_v at RT	n_v at 873 K	Ref.
9Cr–1Mo (P9) with 0.42%Si	−49	−828	[24]
P92	−40	−320	[25]
RAFM (N+T)	−66	−645	[6]
RAFM (AF−TMT25)	−65	−610	[18]
RAFM (FF-TMT25)	−67	−408	Present study

recovery rates due to its unstable microstructure because of coarse lath martensite and precipitates ($M_{23}C_6$ and MX) as mentioned in Sect. 3.1. In addition, the steel possess free mobile dislocations (formed during martensite formation), which further enhances the recovery rates by thermally activated deformation through cross-slip and climb of dislocation. The lower recovery rates in FF-TMT25, at high temperatures, could be attributed to the finer distribution of $M_{23}C_6$ and MX precipitates over large density of dislocation tangled networks. Though FF-TMT25 steel inherently promotes faster diffusion, the observed recovery rates remain low (at high temperatures) indicating the higher stability of refined microstructure.

3.5 Prediction of Strength Properties from Voce Constitutive Equation

Voce's constitutive equation can be applied to ascertain Voce's parameters such as initial stress (σ_i) and saturation stress (σ_s). Initial stress is the stress at the beginning of the plastic strain and this can be correlated with the experimental YS (σ_{YS}), whereas as the saturation stress is the stress at which the work hardening rate ($d\sigma/d\varepsilon$) becomes zero at peak stress in the stress–strain curve and this can be compared with the experimental UTS (σ_{UTS}). The comparisons of experimental YS with Voce's initial stress and the experimental UTS with Voce's saturation stress are presented in Fig. 5a, b respectively. It can be perceived from these figures that the YS (σ_{YS}) can be linearly related with initial stress (σ_i) (Fig. 5a) with R^2 value of 0.962, whereas the UTS (σ_{UTS}) can be linearly connected with saturation stress (σ_s) (Fig. 5b) with R^2 value of 0.99 irrespective of the TMT applied to RAFM steel in different phase fields. Similar results were also reported by Vanaja et al. [6] for the ferritic–martensitic steel in N+T condition and Ganesan et al. [23] for the 316 LN austenitic stainless steel in solution annealed and quenched condition.
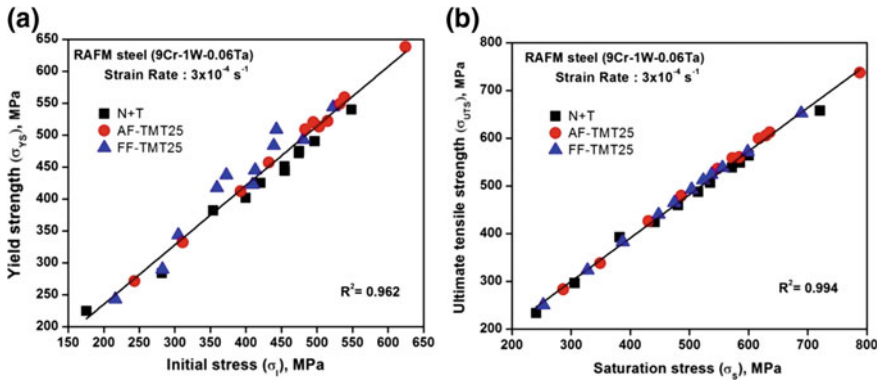
Fig. 5 Comparison of **a** experimental YS (σ_{YS}) with Voce initial stress (σ_i) and **b** experimental UTS (σ_{UTS}) with Voce saturation stress (σ_s) for RAFM steel in N+T, AF-TMT25 and FF-TMT25 conditions

4 Conclusions

In the present investigation, the impact of thermomechanical treatment in austentic phase (AF-TMT25) and ferritic phase (FF-TMT25) fields on microstructural and mechanical properties of RAFM steel was studied and the results were compared with the same steel in N+T condition. The following inferences were obtained:

(1) The steel in N+T and AF-TMT25 conditions shows a tempered martensitic structure, in comparison to fully ferritic phase in FF-TMT25 condition. In addition, the steel in AF-TMT25 condition revealed the presence of allotri-omorphic ferrite along the PAGBs.

(2) TMT of the steel resulted in refinement of the lath structure and precipitates and increase in number density of the precipitates. The width of the martensite lath is around 272 nm in N+T steel, whereas it is refined to 179 nm in AF-TMT25 steel. The $M_{23}C_6$ and MX precipitates were refined from 50–150 to 20–50 nm in N+T steel, to 30–100 and 5–30 nm in TMT steels.

(3) The steel in AF-TMT25 condition exhibited higher YS and UTS than the steel in the remaining two conditions. However, the YS and UTS of steel in FF-TMT25 condition are marginally higher than the steel in N+T condition.

(4) The steel in AF-TMT25 condition exhibited a higher % elongation than the steel in N+T and FF-TMT25 conditions. The % reduction in area varied in the order: N+T > AF-TMT25 > FF-TMT25.

(5) The steel in N+T and AF-TMT25 conditions is found to undergo more thermal recovery at high temperatures (above 723 K) compared to FF-TMT25 condition.

(6) The tensile flow behaviour of RAFM steel in all three conditions was well described by Voce's equation. Experimental YS and UTS varied linearly with

initial stress (σ_i) and saturation stress (σ_s), respectively, with $R^2 \geq 0.962$, irrespective of the TMT in different phase fields.

(7) The most significant effect of TMT is the improvement in strength properties without loss of ductility, particularly in the case of the RAFM steel in AF-TMT25 condition.

References

1. R.L. Klueh, D.R. Harries, *ASME, Philadelphia*, 5 (2001)
2. A. Kohyama, Y. Kohno, K. Asakura, H. Kayano, J. Nucl. Mater. **212–215**(1), 684–689 (1994)
3. N. Baluc, R. Schaublin, P. Spatig, M. Victoria, Nucl. Fusion **44**, 56–61 (2004)
4. T. Jayakumar, M.D. Mathew, K. Laha, Procedia Eng. **55**, 259–270 (2013)
5. K. Laha, S. Saroja, A. Moitra, R. Sandhya, M.D. Mathew, T. Jayakumar, J. Nucl. Mater. **439**, 41–50 (2013)
6. J. Vanaja, K. Laha, M. Nandagopal, Shiju Sam, M.D. Mathew, T. Jayakuma, E. Rajendra Kumar, J. Nucl. Mater. **433**, 412–418 (2013)
7. L. Tan, Y. Yang, J.T. Busby, J. Nucl. Mater. **442**, S13–S17 (2013)
8. K.S. Chandravathi, C.S. Sasmal, K. Laha, P. Parameswaran, M. Nandagopal, V.D. Vijayanand, M.D. Mathew, T. Jayakumar, E. Rajendra Kumar, J. Nucl. Mater. **435** 128–136 (2013)
9. R. Ravikirana, S. Mythili, S. Raju, T. Saroja, E. Jayakumar, Rajendrakumar. Mater. Char. **84**, 196–204 (2013)
10. S. Raju, B. Jeya Ganesh, Arun Kumar, R. Mythili, S. Saroja, E. Mohandas, M. Vijayalakshmi, K.B.S. Rao, Baldev Raj, J. Nucl. Mater. **389**, 385–393 (2009)
11. R.L. Klueh, N. Hashimoto, P.J. Maziasz, Sci. Mater. **53**, 275–280 (2005)
12. K.S. Chandravathi, Kinkar Laha, C.S. Sasmal, P. Parameswaran, M. Nandagopal, H.M. Tailor, M.D. Mathew, T. Jayakumar, E. Rrajendra Kumar, Metall. Mater. Trans A **45A**, 4280–4292 (2014)
13. J. Vanaja, Kinkar Laha, M.D. Mathew, Metall. Mater. Trans A **45A**, 5076–5084 (2014)
14. J. Vanaja, K. Laha, Metall. Mater. Trans A **46**(10), 4669–4679 (2015)
15. T. Sakthivel, P. Shruti, P. Parameswaran, G.V.S. Nageswara Rao, K. Laha, T. Srinivasa Rao, Trans. Indian Inst. Metall. **70**(5), 1177–1182 (2017)
16. T. Furuhara, J. Yamaguchi N. Sugita, G. Miyamoto, T. Maki, ISIJ Int. 43, 1630–1639 (2003)
17. Matthias Nohrer, Walter Mayer, Sophie Primig, Sabine Zamberger, Ernst Kozeschnik, Harald Leitner, Metall. Mater. Trans. A **45A**, 4210–4219 (2014)
18. P. Prakash, J. Vanaja, N. Srinivasan, P. Parameswaran, G.V.S. Nageswara Rao, K. Laha, Mater. Sci. Eng. A **724**, 171–180 (2018
19. S.K. Sahay, H.K.D.H. Bhadeshia, R.W.K. Honeycombe, Mater. Sci. Eng., A **157**, 101–105 (1992)
20. A. Benjamin, Shassere, Yukinori Yamamoto, Sudarsanam Suresh Babu, Metall. Mater. Trans. A **47A**, 2190 (2016)
21. P. Fernandez, A.M. Lancha, J. Lapena, M. Hernandez-Mayoral, Fusion Eng. Des. **58–59**, 787–792 (2001)

22. Prakash, J. Vanaja, K. Laha, G.V.S. Nageswara Rao, *IOP conference series: materials science and engineering* **338** (2018) 012027
23. V. Ganesan, K. Laha, P. Parameswaran, M. Nandagopal, M.D. Mathew, Mater. High Temp. **32**, 4 (2015)
24. J. Christopher, B.K. Choudhary, E. Isaac Samuel, V.S. Srinivasan, M.D. Mathew, Mater. Sci. Eng. A **528** (2011) 6589–6595
25. G. Sainath, B.K. Choudhary, J. Christopher, E. Isaac Samuel, V.S. Srinivasan, M.D. Mathew, Int. J. Pres. Ves. Pip. **132–133** (2015) 1–9

Improvement on High-Temperature Mechanical Properties of Modified 9Cr-1Mo Steel Through Intermediate Hot Rolling

S. S. Samant, I. V. Singh and R. N. Singh

Abstract Modified 9Cr-1Mo steel is a candidate material for high-temperature ($\sim$650 °C) application in the development of Generation-IV nuclear reactors. In the present investigation, intermediate hot rolling on modified 9Cr-1Mo steel have been performed in austenitic phase (1050 °C) and below austenitic phase (550 °C). Intermediate hot rolling including normalization at elevated temperature (1150 °C), followed by tempering (700 °C) is employed to refine its lath structure and improve precipitation state. The modified 9Cr-1Mo steel rolled at 1050 °C with 30% deformation showed improvement on both strength and toughness, which may be attributed to increase in area fraction of $M_{23}C_6$/MX precipitates and higher dislocation density. A typical mode of tensile fracture with radial cracks and axial splitting is observed in the testing temperature between −196 and 20 °C. These cracks are caused by a high fracture stress generated in perpendicular direction during necking since stress triaxiality increases as necking is deepened. However, such radial cracks are found completely absent in the test temperature between 100 and 650 °C.

Keywords Modified 9Cr-1Mo steel · Hot rolling · High-temperature mechanical properties

1 Introduction

As per the increasing demand for energy, International Atomic Energy Agency (IAEA) proposed Generation IV nuclear reactors. These reactors include fast water cooled (Supercritical Water Reactor—SCWR), gas cooled (Very High-Temperature

S. S. Samant (✉) · I. V. Singh
Department of Mechanical and Industrial Engineering, IIT Roorkee, Roorkee 247667, Uttarakhand, India
e-mail: sanjaysama@gmail.com

R. N. Singh
Mechanical Metallurgy Division, Bhabha Atomic Research Centre, Trombay, Mumbai 400085, India

Reactor—VHTR) and liquid metal cooled (Sodium and Lead Fast Reactor-Na-LMR and Pb-LMR) reactors [1]. To meet the challenges of this new generation (Generation IV) nuclear reactors, steels are being developed for high operating temperatures (i.e., 650 °C). Ferritic–martensitic-modified 9Cr-1Mo steel (P91) has been considered a candidate material for steam generator, secondary piping and fuel subassembly tubes over austenitic steels due to its low coefficient of thermal expansion, very high thermal conductivity and high void swelling resistance in irradiated condition [2, 3].

Since the modified 9Cr-1Mo steel has been considered for steam generator and secondary pipes, high-temperature strength and toughness are also very important besides good creep and corrosion resistance properties. Extensive studies have been investigated to deal with the relationship between the microstructures and the mechanical strength of modified 9Cr-1Mo steel [4–6]. Kim et al. [5] reported the hot rolling either at 1050 or 950 °C increases the number density of secondary V-rich MX precipitates that causes improvement in high-temperature mechanical property. In martensitic steel, increase in toughness is obtained due to recovery of dislocations and laths [6]. High angle boundaries such as packets and blocks are more effective to hinder cleavage crack propagation rather than low angle boundaries (lath martensite) [7]. Ferritic–martensitic steels are strengthened by various types of uniformly dispersed particles such as $M_{23}C_6$ carbide and MX carbo nitrides (VN, NbC). $M_{23}C_6$ type precipitates are formed during tempering and located at grain boundaries and subgrain boundaries. In order to improve mechanical properties, many researchers have used various processing techniques such as hot rolling, cryo rolling, equal channel angular extrusion and other severe plastic deformation techniques (SPD). Few researchers have reported the effect of these SPD techniques on high-temperature mechanical behavior of P91 steel. Still, detailed investigation is required to find out the effect of SPD techniques and other heat treatment procedures on high-temperature mechanical behavior. Tempering temperature and rolling temperature can play an important role in the microstructure. Therefore, objective of the present study is to investigate the effect of intermediate rolling temperature (i.e., 1050 and 550 °C) and tempering temperature on high-temperature strength and toughness of modified 9Cr-1Mo steel.

2 Materials and Experimental Details

The modified 9Cr-1Mo steel plate (500 mm × 250 mm × 30 mm) was received from the Bhabha Atomic Research Center (BARC) Mumbai, India in the form of normalized and tempered condition. The elemental composition of this material is given in Table 1. Blanks of $50 \times 20 \times 22$ mm^3 size were sectioned from the as-received plate. These blanks were austenitized at 1150 °C for 1 h to eliminate the prior history of microstructure. After austenitizing at 1150 °C and air cooling, blanks normalized at 1050 °C and tempered at two different temperature (i.e., 750 and 700 °C). These two processes are abbreviated as N1050-T750 and

N1050-T700, respectively. Blanks subjected to intermediate rolling (i.e., 1050 and 550 °C) after austenitizing at 1150 °C for 1 h and subsequent tempering at 700 °C were abbreviated as R1050-T700 and R550-T700, respectively. Heat treatment and intermediate rolling schedule adopted in this study are presented in Fig. 1.

After heat treatment and intermediate rolling process, tensile tests were conducted on MTS machine at a strain rate of $4 \times 10^{-4} \, s^{-1}$ at a room temperature (i.e., 20 °C) and 650 °C as per ASTM E8/E21. Subsize tensile specimens were prepared with 16 mm gauge length and 4 mm gauge diameter. Samples were soaked for 30 min at test temperature to attain thermal equilibrium. The microstructural examination of steel was carried out using an optical microscope and Quanta 200 Field-emission scanning electron microscope. Samples were etched using Villella's reagent solution (1 g picric acid + 5 ml hydrochloric acid + 100 ml ethanol). Transmission electron microscopy was carried out using FP5022 Tecnai 20S on normalized and tempered samples to reveal lath structure and dislocations.

3 Results and Discussion

In the following section, the effect of tempering and intermediate rolling on microstructural and mechanical behavior of modified 9Cr-1Mo steel are described.

Table 1 Chemical composition of modified 9Cr-1Mo steel plate in wt%

Element	C	Cr	Mn	Mo	Nb	V	Si
wt%	0.104	8.76	0.49	0.98	0.08	0.20	0.19
Element	Co	W	Al	Ni	N	Fe	–
wt%	0.015	0.02	0.02	0.28	0.02	Balance	–
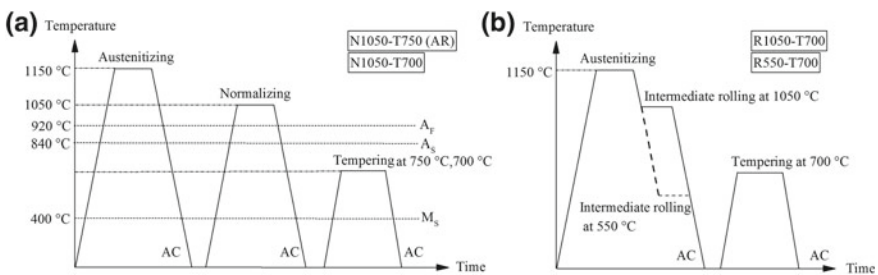
Fig. 1 Schematic diagram represents the heat treatment and rolling schedules employed in the present study, where A_S Austenite start temp., A_F Austenite finish temp., M_S Martensite start temp., and *AC* Air cooling

3.1 Characterization of Microstructure

The optical micrographs and SEM micrographs of the heat-treated and rolled samples are shown in Figs. 2 and 3. The micrographs exhibit complete tempered martensitic lath structure with different morphologies such as prior austenite grains, packets, blocks, and laths. It is the tendency of modified 9Cr-1Mo steel is to form martensite even if it is cooled in air. The variation in prior austenite grain size with respect to the processing conditions are presented in Table 2. The marginal effect of tempering temperature on grain size is noticed. However, intermediate rolling (R550-T700) caused a reduction in grain size up to ~ 8.2 μm. In order to estimate the particle size and area fraction of different precipitates M_{23}(Cr, Mo, Fe)C_6 and M (Nb, V)X(C, N), FE-SEM micrographs (at high magnification, i.e., 50kX) for different heat-treated and rolled samples were obtained (shown in Fig. 3). Reduction in tempering temperature from 750 to 700 °C restricted the growth of precipitates and led to the distribution of fine $M_{23}C_6$ and MX precipitates along the prior austenite grain boundaries and within martensite lath.

In the as-received (AR) condition, area fraction of precipitates found to be $\sim 21.76\%$. However, a small decrease in tempering temperature (i.e., 700 °C) caused a reduction in area fraction of precipitates up to 19.95%. Whereas sample
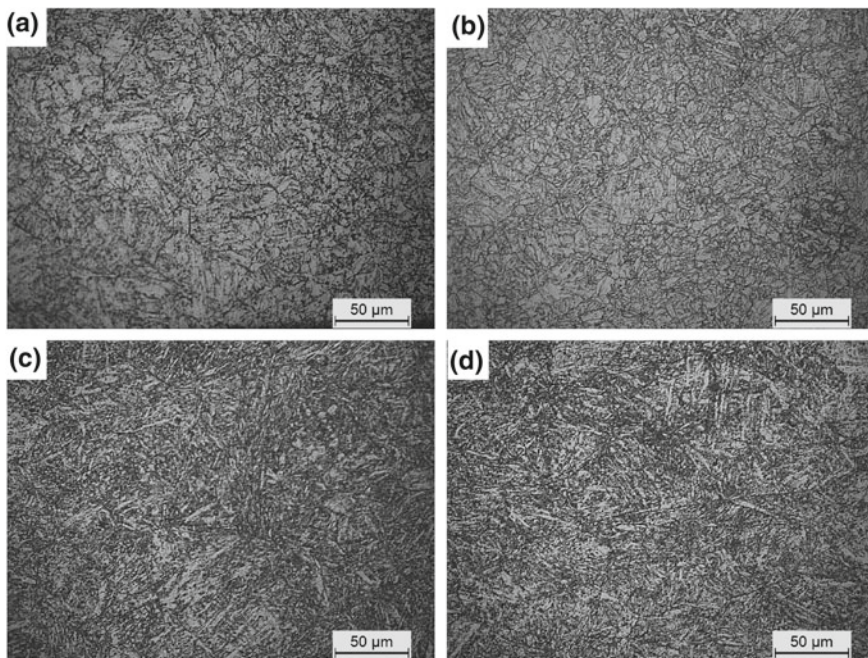
Fig. 2 Optical micrographs of modified 9Cr-1Mo steel in heat treated and rolled conditions **a** N1050-T750, **b** N1050-T700, **c** R1050-T700 and **d** R550-T700
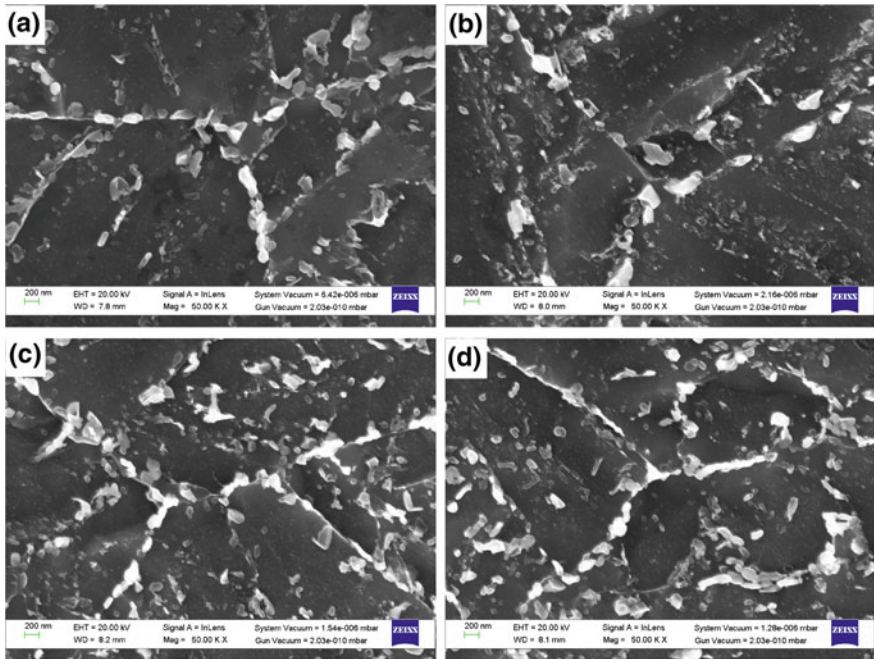
Fig. 3 SEM micrographs of modified 9Cr-1Mo steel at 50kX showing precipitates in **a** N1050-T750, **b** N1050-T700, **c** R1050-T700, **d** R550-T700 samples

Table 2 Variation in PAGS, YS and Toughness of modified 9Cr-1Mo steel plate of investigated samples

Sample	PAGS (µm)	Yield strength (MPa)		Elongation (%)		Toughness (J)
		At 20 °C	At 650 °C	At 20 °C	At 650 °C	
N1050-T750	15.2 ± 3.2	670	254	21.9	32.5	159
N1050-T700	14.1 ± 4.8	820	410	18.2	24.0	136
R1050-T700	10.3 ± 1.9	876	449	17.9	22.0	123
R550-T700	8.2 ± 2.5	928	485	17.2	21.1	103

rolled at R550-T700 and R1050-T700 condition show improvement in area fraction of precipitates as compared to normalized and tempered samples. Maximum area fraction of precipitates was observed in R550-T700 followed by R1050-T700, N1050-T750 and N1050-T700 sample (Fig. 4). The small size of precipitates are known to have better pinning effect and prevent the movement of dislocations at elevated temperature, which lead to an increase in mechanical strength. At elevated temperature, higher rate of self-diffusion of iron atoms and gliding of dislocations
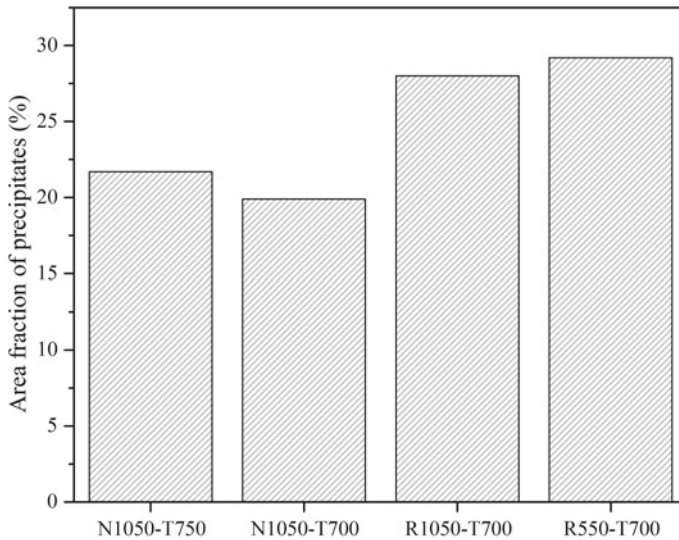
Fig. 4 Variation of area fraction of precipitates in heat treated and rolled conditions

cause deformation and formations of vacancies. Therefore, higher area fraction of fine precipitates will provide improvement in mechanical strength at elevated temperature.

TEM images of samples normalized and tempered (i.e., N1050-T750 and N1050-T700) are shown in Fig. 5. In the as-received condition of material, lath width is obtained about $\sim$208 nm. With the decrease in tempering temperature (N1050-T700), lath width decreased up to $\sim$137 nm. It shows higher tempering temperature causes recovery of lath martensite and dislocation density.

3.2 Tensile Properties and Impact Toughness of Investigated Samples

Figure 6 shows the engineering stress and plastic strain plots of heat-treated and thermomechanical processed samples of modified 9Cr-1Mo steel and their corresponding mechanical properties presented in Table 2. In case of N1050-T700, an increase in yield strength (22% at 20 °C and 61% at 650 °C) is observed with the reduction in tempering temperature in comparison to the as-received (N1050-T750) condition of the material. Reduction in tempering temperature limits the growth of precipitates as evident from SEM image (Fig. 3) and lead to the distribution of fine $M_{23}C_6$ and MX precipitates along the prior austenite grain boundaries and within martensitic lath. However, with the increase in tempering temperature, recovery of martensite lath and dislocation density are observed. The sample rolled in
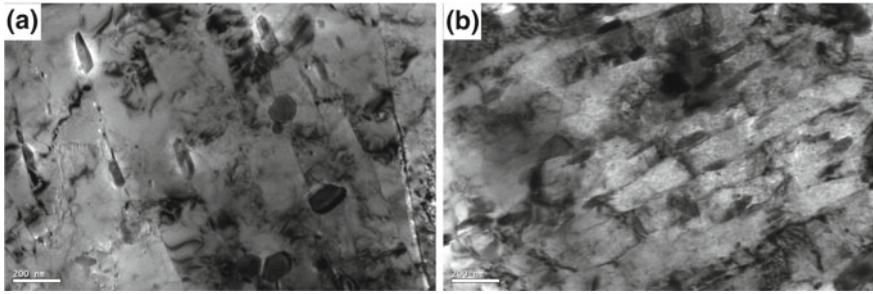
Fig. 5 Bright field TEM micrographs of modified 9Cr-1Mo steel in normalized and tempered conditions **a** N1050-T750, **b** N1050-T700
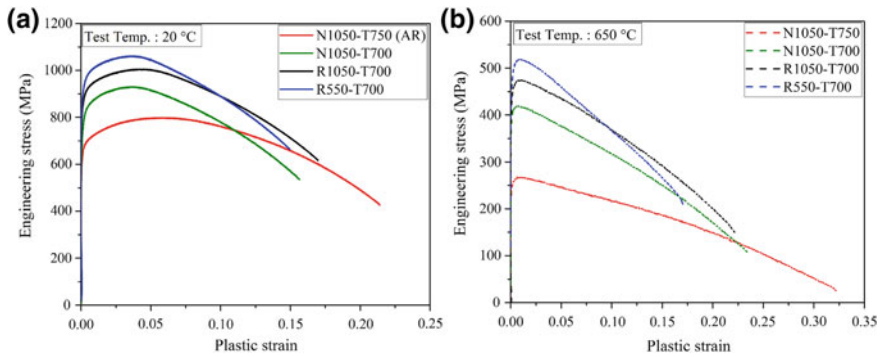
Fig. 6 Plot of Engineering stress-plastic strain of modified 9Cr-1Mo steel in heat-treated and rolled conditions at test temperature **a** 20 °C and **b** 650 °C

R550-T700 condition shows increased in yield strength by 39% at 20 °C and 91% at 650 °C in comparison to as-received condition. However, percentage elongation is reduced by 21% at 20 °C and 35% at 650 °C. It shows combined effect of precipitation strengthening and strain hardening is more effective for improvement in yield strength (YS) at elevated temperature.

Variation in impact toughness for heat-treated and rolled samples corresponding to room temperature (RT) are presented in Table 2. In as-received condition, the impact toughness was measured about 159 J. It was observed that with the decrease in tempering temperature (i.e., N1050-T700), impact toughness decreased up to 14.5% in comparison to N1050-T750 condition. The reduction in impact toughness is mainly attributed to an increase in dislocation density of the material.

3.3 Effect of Microstructure on Tensile Properties and Impact Toughness

In the past, various studies have been conducted to investigate the effect of grain size, packet size, block size, lath width on the mechanical behavior of metallic materials [4–6]. Yan et al. [8] reported that increase in tempering temperature causes recovery of lath martensite and dislocation density resulting in improvement in toughness of the material. Similar behavior is observed in the present study. Reduction in tempering temperature from 750 to 700 °C causes reduction in impact toughness from 159 to 136 J. However, 61% increase in yield strength was observed at test temperature of 650 °C as compared to N1050-T750 condition. It shows modified 9Cr-1Mo steel is more susceptible to precipitation hardening. In addition to this, prior austenite grain size (PAGS) is known to have a minor effect on strength of the modified 9Cr-1Mo steel [9]. At elevated temperature, distribution of fine precipitates prevent the movement of dislocation and lead to an improvement in mechanical strength. Therefore, the presence of higher area fraction of fine precipitates causes improvement in mechanical strength. Chatterjee et al. [7] reported that precipitate fraction increase with the decrease in rolling temperature. Similar behavior of precipitates area fraction was observed in Fig. 4. Sample rolled at R1050-T700 is found to have the best combination of yield strength and toughness.

3.4 Fracture Surface Morphology of Tensile Samples

The fractographs of the investigated sample corresponding to RT and 650 °C are shown in Fig. 7. A typical fracture behavior with radial cracks and axial splitting can be seen in normalized and tempered specimens tested at RT. However, such radial cracks and axial splitting are completely absent at 650 °C. Sample tested at 650 °C exhibit cup and cone fracture. Fracture surface of rolled sample shows deep cracks along rolling direction. There are various factors such as strain rate, test temperature, processing technique, and stress triaxiality, etc., which may affect the typical fracture mode (axial splitting and radial cracks). To find out the effect of test temperature on radial cracks and axial splitting, tensile tests were conducted at −196, 20, 100, and 200 °C in as-received condition of the material. Fracture surfaces of as-received condition of modified 9Cr-1Mo steel at different test temperatures are shown in Fig. 8. Axial splitting was dominant in between −196 and 20 °C. However, only radial cracks appeared above 100 °C. These cracks are possibly occurred due to high fracture stress generated in perpendicular direction during necking since stress triaxiality increases as necking is deepened. This fracture analysis ensure that test temperature and rolling influences the typical radial cracks and axial splitting type of fracture.
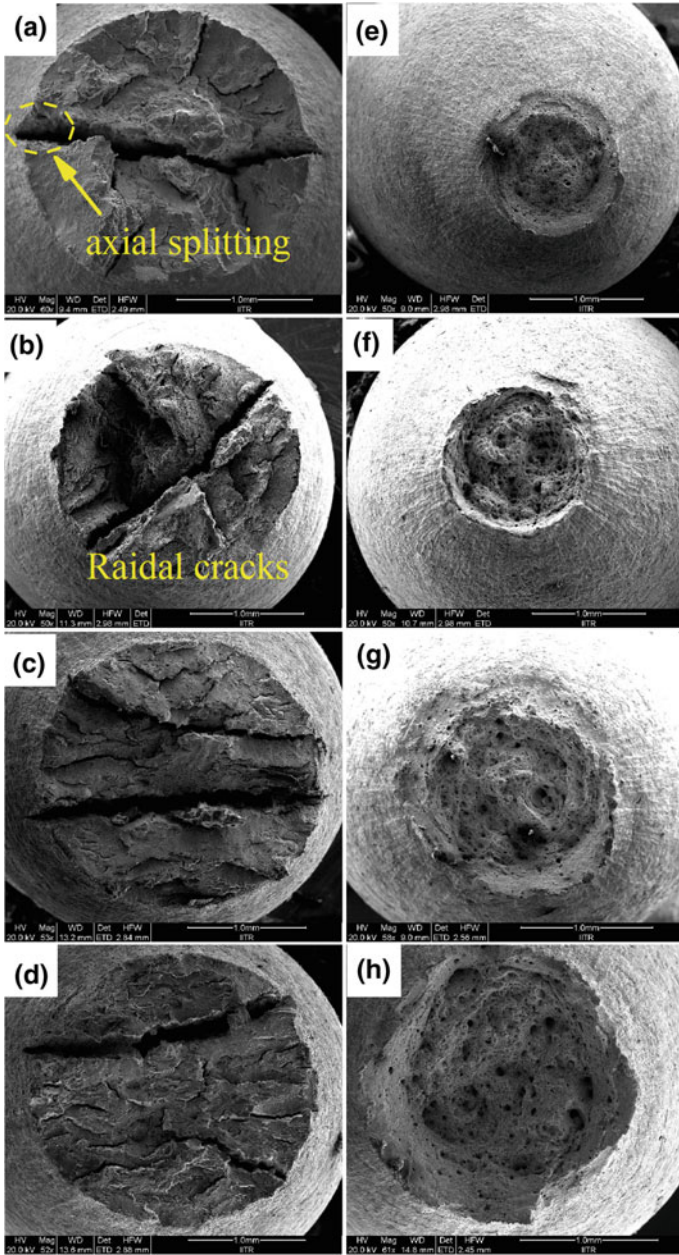
Fig. 7 Fractographs showing fracture surfaces **a** N1050-T750 at RT, **b** N1050-T700 at RT, **c** R1050-T700 at RT, **d** R550-T700 at RT, **e** N1050-T750 at 650 °C, **f** N1050-T700 at 650 °C, **g** R1050-T700 at 650 °C and **h** R550-T700 at 650 °C
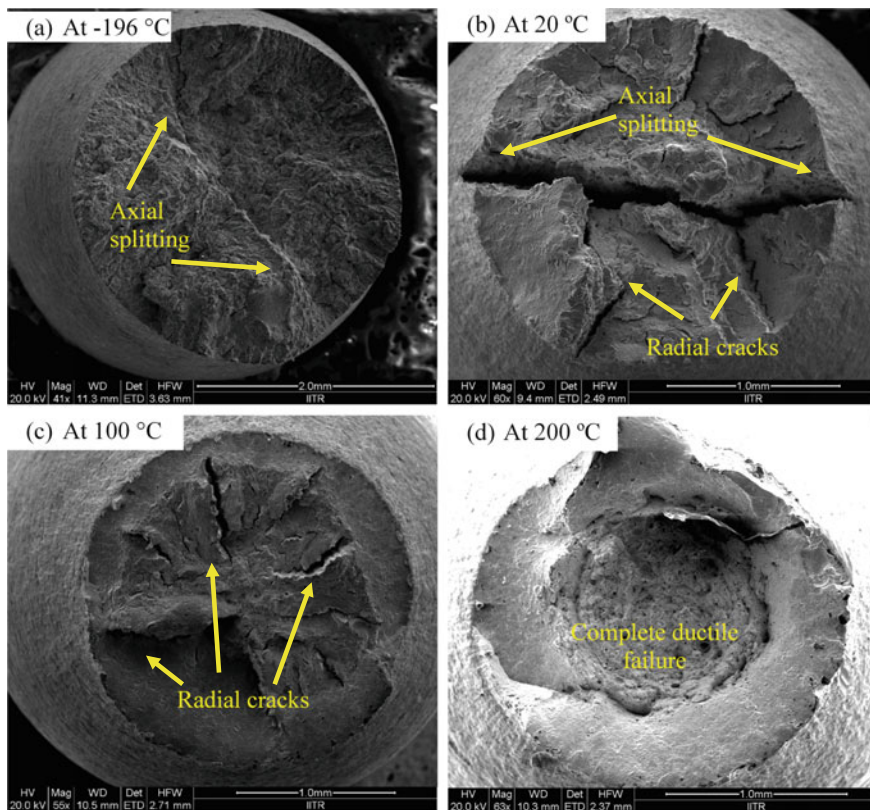
Fig. 8 Fractographs of as-received modified 9Cr-1Mo steel tested at **a** −196 °C, **b** 20 °C, **c** 100 °C and **d** 200 °C at a strain rate of 10^{-4} s^{-1}

4 Conclusions

Based on the present investigation, the following conclusions are drawn:

- With the decrease in tempering temperature from 750 to 700 °C, the toughness of the modified 9Cr-1Mo steel decreases. This may be due to an increase in the dislocation density and less recovery of martensitic lath.
- Combined effect of intermediate rolling at 1050 °C and tempering at 700 °C provides strain hardening and precipitation strengthening, which leads to improvement in high-temperature strength and toughness. Increased area fraction of precipitates and high dislocation density are observed at R1050-T700 as compared to as-received condition.
- Modified 9Cr-1Mo steel exhibits a typical mode of fracture with axial splitting and radial cracks. Test temperature and hot rolling are the factors that assist radial crack type fracture.

References

1. S.J. Zinkle, G.S. Was, Materials challenges in nuclear energy. Acta Mater. **61**, 735–758 (2013)
2. R.L. Klueh, A.T. Nelson, Ferritic/martensitic steels for next-generation reactors. J. Nucl. Mater. **371**, 37–52 (2007)
3. R.L. Klueh, D.S. Gelles, S. Jitsukawa, A. Kimura, G.R. Odette, B. Van der Schaaf, M. Victoria, Ferritic/martensitic steels—overview of recent results. J. Nucl. Mater. **307–311**, 455–465 (2002)
4. M. Song, C. Sun, Z. Fan, Y. Chen, R. Zhu, K.Y. Yu, K.T. Hartwig, H. Wang, X. Zhang, A roadmap for tailoring the strength and ductility of ferritic/martensitic T91 steel via thermo-mechanical treatment. Acta Mater. **112**, 361–377 (2016)
5. J.H. Kim, J.H. Baek, S.H. Kim, C.B. Lee, K.S. Na, S.J. Kim, Effect of hot rolling process on the mechanical and microstructural property of the 9Cr-1Mo steel. Ann. Nucl. Energy **38**, 2397–2403 (2011)
6. Y. Dong, Y. Lu, Effects of tungsten addition on the microstructure and mechanical properties of near-eutectic $AlCoCrFeNi_2$ high-entropy alloy. J. Mater. Eng. Perform. **27**, 109–115 (2018)
7. A. Chatterjee, D. Chakrabarti, A. Moitra, R. Mitra, A.K. Bhaduri, Effect of deformation temperature on the ductile-brittle transition behavior of a modified 9Cr-1Mo steel. Mater. Sci. Eng., A **630**, 58–70 (2015)
8. P. Yan, Z. Liu, H. Bao, Y. Weng, W. Liu, Effect of tempering temperature on the toughness of 9Cr-3W-3Co martensitic heat resistant steel. Mater. Des. **54**, 874–879 (2014)
9. A. Chatterjee, D. Chakrabarti, A. Moitra, R. Mitra, A.K. Bhaduri, Effect of normalization temperatures on ductile-brittle transition temperature of a modified 9Cr-1Mo steel. Mater. Sci. Eng. A **618**, 219–231 (2014)

Effect of Aging Heat Treatment on the Microstructure of Gas Tungsten Arc-Welded Inconel Superalloy 718

G. Ravi, N. Murugan, R. Arulmani and Gopal Magadi

Abstract The precipitation hardenable nickel-based superalloys are widely used in aerospace, power plants, oil, and gas industries due to their excellent high-temperature strength and remarkable hot corrosion resistance. Though it is weldable, the required properties such as hardness, resistance to fracture, corrosion, etc., depends upon the weld microstructure which is to be obtained by various heat treatment methods. In the present investigation, the influence of aging heat treatment on gas tungsten arc-welded microstructure of alloy 718 was studied. The aging heat treatment was carried out at 780 °C for 1 h, 4.5 h and 8 h and air cooled to enhance the properties of the weld metal. After heat treatment, the welded samples were characterized using an optical microscope (OM), field emission scanning electron microscope (FESEM), transmission electron microscopy (TEM), and microhardness tester. The effect of heat treatment time on the microstructure was evaluated. Gamma prime (γ'), gamma double prime (γ'') and the primary carbides of MC, $M_{23}C_6$ were observed in the HAZ and grain boundaries. It was observed that with the increase in aging time microhardness was significantly increased. The mechanical bend test was carried out to evaluate the ductility of the weld metal in the heat-treated conditions. On aging at 780 °C for 8 h, the ductility of the weld metal was found to be good and the microstructure depicted the reduction of laves phases and NbC in weld fusion zone and higher amount of γ'' resulting is higher strength and hardness.

Keywords Inconel 718 · Gas tungsten arc welding (GTAW) · Aging heat treatment · Microstructure and vickers microhardness (HV)

G. Ravi (✉) · N. Murugan
Department of Robotics and Automation Engineering, PSG College of Technology,
Coimbatore 641004, Tamil Nadu, India
e-mail: ganesanravi.87@gmail.com

R. Arulmani
Cameron Manufacturing India Pvt. Ltd, Coimbatore 641014, India

G. Magadi
Cameron International Corporation, Houston, TX, USA

1 Introduction

Nickel-based superalloy alloy 718 is mostly used in power and valve industries owing to the excellent corrosion and wear resistance at high temperatures. It also exhibits good resistance to stress corrosion cracking and strain age cracking. It is mainly strengthened by gamma prime γ' Ni (Al, Ti), and gamma double prime γ'' (Ni_3Nb) precipitates which are formed at aging temperature range of 650–850 °C on the aging heat treatment process [1–6]. Therefore the aging temperature should not exceed 810 °C to obtain optimum strength in Ni–Fe based alloy [5]. The amount of γ'' precipitate formed at a temperature range of 700–850 °C is 4 times higher than that of γ' phase resulting in enhanced strength [7, 8]. On increasing the aging time at above 850 °C aging temperature, γ'' will be changed into δ phase, which will reduce mechanical strength and microhardness [6]; above this temperature, the precipitates are dissolved in the material.

Numerous types of welding processes are applied to join nickel-based superalloy namely, gas tungsten arc welding (GTAW), gas metal arc welding (GMAW), laser beam welding, electron beam welding, etc. Laser and electron beam welding processes are used to join Inconel 718 alloys especially in the aerospace and automotive industries to have reduced heat input, distortion, and heat-affected zone (HAZ) area [9]. Most of the works reported were on studies on microstructures, weld defects, and mechanical properties of Inconel 718 alloy [10–12]. It was reported that use of pulsed current (PC) in gas tungsten arc welding (GTAW) of solution treated and aged Inconel 718 alloy resulted in reduction of % of volume fraction of laves phases and Nb segregation in the weld metal causing improved mechanical properties compared to that joined by the constant current (CC) GTAW [13]. The amounts of Nb segregation and laves phases in the weld metal were less in electron beam welded 718 alloys compared to that of GTA welded after the cyclic post-weld heat treatment (PWHT) process [14].

It can be summarized that most of the research work carried out on the aging heat treatment process was focused on analyzing the mechanical properties or microstructures at the temperature range of 500–750 °C, aiming to increase strength in the high-temperature alloy. To the best of the knowledge of the authors, no broad investigation on the effect of aging heat treatment at a temperature of 780 °C at different aging timings have not yet reported in GTA-welded Ni-based superalloy Inconel 718 in aged condition. In the present research work, 6 mm thick Inconel 718 plates were welded by gas tungsten arc welding and aged at different aging timings. The effect of aging heat treatment on the metallurgical characterization and mechanical properties of GTA welded Inconel 718 has been studied.

2 Experimental Procedure

2.1 Material

Inconel superalloy 718 received in the aged condition in the form of a circular disc of diameter 250 mm and 6 mm thickness was used as the base material. Three plates having a width of 70 mm were prepared from the base disc and in each plate, a V-groove with 70° groove angle and depth of 5 mm was machined by wire cut EDM process. Alloy 718 was deposited in the V-grooves by gas tungsten arc welding (GTAW) process using a filler rod ERNiFeCr-2 of size 2.4 mm diameter and length of 1 m. The chemical composition of the base metal and filler rod and the GTAW process parameters are presented in Tables 1 and 2, respectively. The same GTAW process parameter was used to deposit weld metal on the V-Grooves of three plates using pure argon shielding and the welded plates are shown in Fig. 1. The quality of the welded plates was tested with 100% X-ray radiography test and no defects were found.

Table 1 Chemical composition of the base metal and the filler metal (in wt%)

Elements	Ni+Co	Cr	Fe	Nb+Ta	Mo	Ti	Al	Cu	Si
Base metal	52.94+0.15	18.12	Bal	4.87	2.92	0.95	0.34	0.063	0.20
Filler rod	53.56	18.65	17.9	5.05	2.95	0.97	0.59	0.08	0.001

Table 2 The GTA welding process parameter

Sl. no	Current (A)	Voltage (V)	Welding speed (cm/min)	Shielding gas flow rate (lit/min)	Purging gas flow rate (lit/min)
1	150	14	10	12	5

Fig. 1 GTA-welded Inconel 718 plates
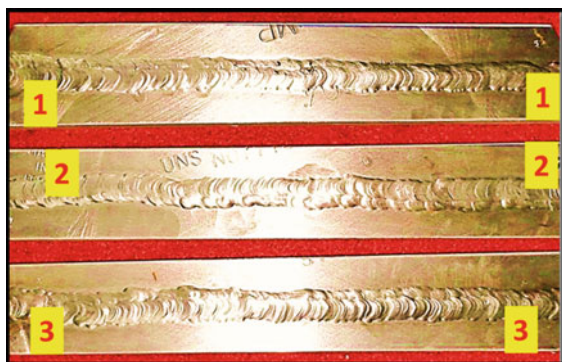
2.2   Heat Treatment

The heat treatment setup consisted of an electrical muffle furnace for heating to a maximum temperature of 1500 °C. The time and temperature were controlled by a Eurotherm controller and R-type thermocouples. The three GTA welded plates were heated up to a temperature of 780 °C as recommended by Special Metal Corporation [15] and the first plate (S_1) was held for 1 h, the second plate (S_2) for 4.5 h, and third plate (S_3) for 8 h, and all the plates were separately cooled to room temperature in air. The heat treatment cycle adopted for the three plates is shown in Fig. 2.

2.3   Metallographic Examination

After heat treatment, the welded plates were cut transverse to the welding direction and samples of size 15 mm × 10 mm × 6 mm were prepared from each plate for macro and microstructural analysis. The cut samples were prepared as per the standard metallographic procedure using different abrasive grade papers (from 400 to 1500 SiC) and diamond paste up to 1 μ to obtain mirror finish surface. The samples were etched with a Super Kalling's (5 ml H_2O_2 + 60 ml HCL + 6 g $CuCl_2$) etchant to reveal the microstructure under optical microscope (OM), field emission and scanning electron microscope (FESEM) and to identify various elements present in the phases using EDS. The etched sample of the welded specimen was presented in Fig. 3. Samples were prepared as per standard procedure from each welded plates for transmission electron microscopy (TEM) analyses.

Fig. 2 Heat treatment cycles applied for welded plates
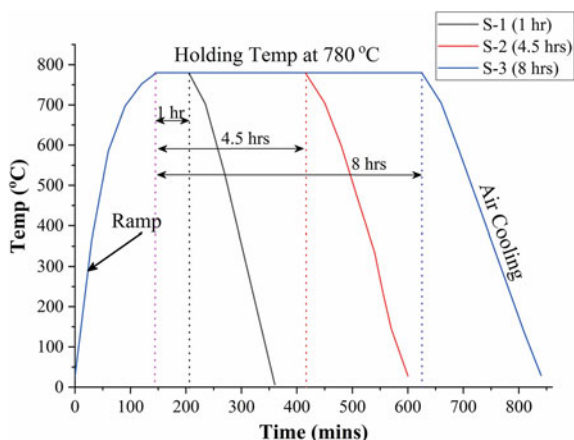
Fig. 3 Typical weld cross section of Inconel 718
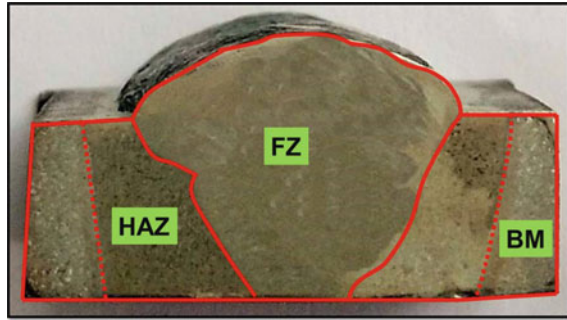
3 Result and Discussion

3.1 Microstructure of Aged GTA Welded Inconel 718 Alloy

After aging heat treatment, the microstructures of heat-affected zone (HAZ) and weld metals were obtained for the three samples using optical microscope and presented in Fig. 4. From the figure, it is found that the grains are coarser when the holding time increases. The measured average grain sizes of HAZ of the heat-treated samples were ASTM #5.5, #4.5, and #4, respectively for S_1, S_2, and S_3. There were no microfissures on HAZ and fusion line in GTA welded plates. The average volume fractions of laves phases present in dendritic and interdendritic regions were calculated with the help of Image processing software Metal Plus and presented in Table 3. It is also observed from Fig. 4 that laves particles are finer with the increase in aging time at the aging temperature of 780 °C.

Fig. 4 Optical microstructures of fusion zone (FZ) and HAZ of heat-treated alloy 718: **a, b**—S_1 (1 h), **c, d**—S_2 (4.5 h) and **e, f**—S_3 (8 h)

Table 3 Estimation of volume fraction in weld fusion zone of heat-treated samples

Samples	Avg. laves particles (% of volume fraction)
S$_1$—1 h	22.5 ± 5
S$_2$—4 h 30 min	20.1 ± 2
S$_3$—8 h	18.5 ± 1

The microstructures of the heat-treated samples were observed under field emission scanning electron microscope (FESEM) to identify the phases like laves phases, Niobium, and gamma matrix in the weld fusion zone. Figure 5 shows the presence of laves particles in the weld fusion zone aged at different aging time. It was reported that the direct aging (DA) heat treatment had not produced any change in laves phase and Nb segregation in weld zone, but only on post-weld solution treatment (PWST) at above 980 °C laves phase and Nb segregation can dissolve not completely. In some case of PWST at a range of (860–955 °C), the δ precipitates were formed, after 955 °C solution treated and aging (STA) treatment is required to decrease the amount of δ phase precipitates by a cyclic treatment [12, 13]. The Nb segregation and laves particles are relatively less in sample S$_3$ compared to S$_2$ and S$_1$ samples. However, the Nb is a highly refractory element, which will segregate in the interdendritic region during the solidification process and undesirable phases like laves can form only in welding. Laves is a hexagonally close-packed phase (HCP) formed in the weld metals due to microsegregation of alloying elements like Nb, Ti, Mo, etc. The MC carbides are irregular with blocky morphology and located in the interdendritic region as shown in Fig. 5a, b. It was reported that the morphologies of M$_{23}$C$_6$ carbides were distributed evenly at grain boundaries, on increasing aging temperature and the amounts of M$_{23}$C$_6$ carbides were decreased and appeared nonuniformly at a temperature of 810–840 °C. γ′ phases are coarser with spherical morphology with increasing temperature and holding time and the γ′ particles were evenly distributed resulting in increasing the microhardness at a temperature of 810 °C [5]. The γ″ phase being the strengthening precipitate of alloy 718 has disc-like shaped coherent with γ′ precipitates. It was reported that the

Fig. 5 FESEM microstructures of fusion zone of heat-treated alloy 718: **a**—S$_1$ (1 h), **b**— S$_2$ (4.5 h) and **c**—S$_3$ (8 h)

respective volume fraction of the γ' and γ'' precipitates and the clustering of Al/Ti and Nb suggested that γ'' nucleated prior to γ' during aging at 706 °C for this alloy [3].

EDS spectrums analyses were performed at different points in the weld fusion zone in all three aged samples to identify laves phases, Niobium carbide (NbC) and gamma matrix and typical EDS spectrum and the corresponding elemental analysis are presented respectively in Fig. 6 and Table 4. The niobium segregation and laves phases present in the weld metal strongly influenced to reduce the strength of the GTA welded alloy compared to that of the EB and laser welded alloy 718 [12]. They are present in S_2 and S_3 samples less than S_1 leading to more γ'' in the weld fusion zone of the heat-treated alloy 718.

Figure 7 illustrates higher magnification TEM micrographs showing the γ'' precipitates present in both the heat-treated samples S_2 and S_3. However, it is found that on aging heat treatment at a temperature of 750 °C for 4 h the γ'' precipitates were formed on the γ' precipitates and increased in hardness [11]. It is reported that on longer duration of aging time for longer thermal exposure temperature from (700 to 900 °C) range, the γ'' phase seems to transform to the elongated structure of delta phases (δ) [2, 6].

Where the gamma double prime (γ'') precipitate increases significantly the hardness also increases and improves the strength of the weld metals as shown in Fig. 8b, c. The hardness is increased in sample S_2 and S_3 due to the presence of gamma double prime (γ'') precipitates in alloy 718 after the aging heat treatment.
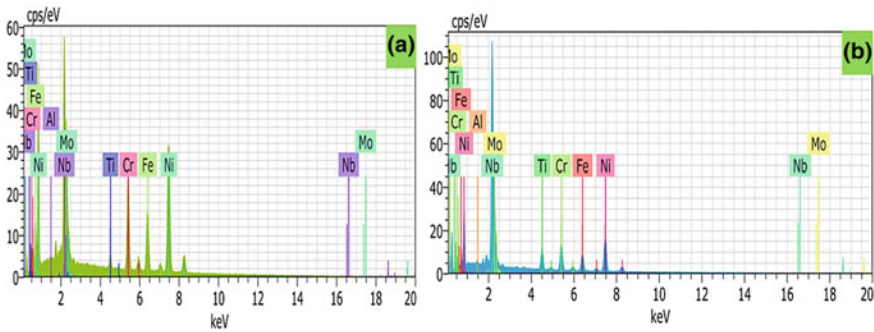
Fig. 6 Typical EDS spectrum of EDS analysis of GTA weld **a** Laves phases, **b** NbC

Table 4 Composition of phases obtained by EDS analysis of GTA-welded Inconel alloy 718

Spectrum	Elements (wt%)								
	Ni	Cr	Fe	Nb	Mo	Ti	Al	Si	C
Matrix	53.25	18.50	19.61	4.35	2.65	1.01	0.95	0.05	0.08
Laves	34.39	11.74	9.54	19.80	5.53	1.45	0.03	–	–
NbC	10.55	4.14	3.38	59.45	0.57	4.57	0.30	0.10	16.8
Dendrite	49.95	18.69	18.85	4.28	2.95	1.01	1.59	0.08	1.6
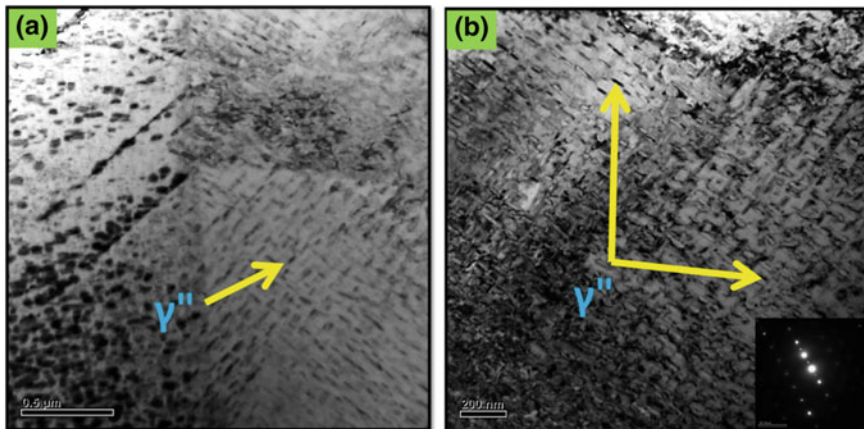
Fig. 7 TEM microstructures of fusion zone of heat-treated alloy 718: arrowhead showing the γ'' precipitates in samples: **a**—S_2 (4.5 h) and **b**—S_3 (8 h)

On sample S_2 the presence of γ'' precipitates are lower than that of sample S_3, where the aging time increases the amount of γ'' precipitates will increase and increase in the hardness values. From the result, the main strengthening phase of γ'' precipitates will occur at a temperature of 780 °C in short duration time of 4–8 h, respectively.

4   Mechanical Testing

4.1   Vickers Microhardness

Microhardness measurements were taken in the transverses direction i.e. perpendicular to the welding direction in heat-treated samples S_1, S_2, and S_3 and the hardness profile is shown in Fig. 8. Table 5 presents the average microhardness values of three aged samples and the base metal microhardness was approximately

Fig. 8 Microhardness profile of PWH treated samples (S_1–S_3)
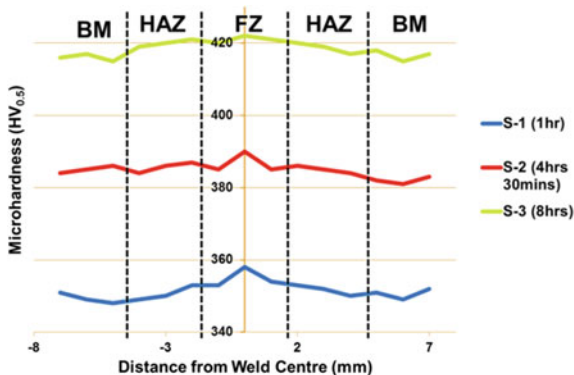
Table 5 Average Vickers microhardness values

Aging heat treatment timings	Fusion zone (FZ)	Heat-affected zone (HAZ)	Base metal (BM)
S_1—1 h	358 ± 4	355 ± 3	345 ± 2
S_2—4 h 30 min	390 ± 3	386 ± 4	380 ± 2
S_3—8 h	421 ± 3	418 ± 3	412 ± 1

378 HV received in aged condition. From the table, it is observed that microhardness of all the zones tends to increase with the aging time. The maximum hardness values attained in the S_3 sample is 421 ± 3, where the aging time increases simultaneously the amount of γ'' precipitates also increases. Also, it is found that the γ'' precipitates are not formed in the weld fusion zone. It was reported that with the increase in aging temperature the hardness decreases with the increasing aging time [5]. It is clear that the weld metal exhibits higher hardness in the weld fusion zone at a temperature of 780 °C for an aging time of 8 h.

4.2 Face Bend Test

Face bend test results are shown in Fig. 9. Cracks were observed in S_1 sample, which is due to the presence of large no. of Nb segregation and laves phases in the weld fusion zone that reduce the ductility of the metal as shown in Fig. 9a. After aging heat treatment of alloy 718, the more amount of γ'' precipitates present in S_2 and S_3 increased the hardness and ductility of the weld fusion zone and passed the bend test as shown in Fig. 8b, c. The ductility may be due to less amount of laves phase and NbC and less segregation of Nb on aging at the higher aging time.
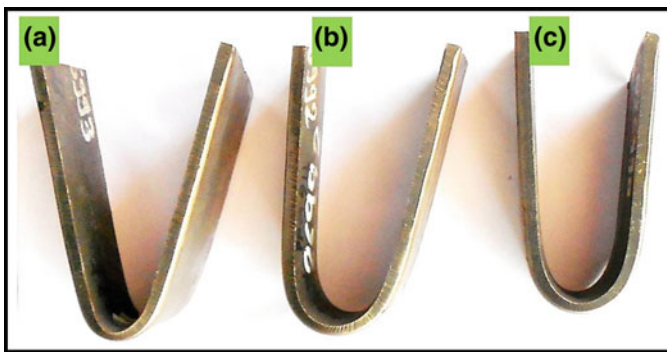
Fig. 9 Mechanical face bent samples: **a**—S_1 (1 h) **b**—S_2 (4.5 h) and **c**—S_3 (8 h)

5 Conclusion

In the present research work, 6 mm thick nickel alloy Inconel 718 was welded by GTAW and post-weld aging heat treatment was carried out at 780 °C for different aging time and the effect of aging time on microstructures on weld metal and HAZ was investigated. The following conclusions are drawn:

1. Higher the aging time up to 8 h at 780 °C, higher the microhardness and finer the weld metal microstructure resulting in adequate ductility. Higher the aging time up to 8 h less is Nb segregation and amount of laves particles in the weld metal resulting enhanced amount of γ'' precipitates leading to higher strength.
2. At 780 °C aging temperature, more γ'' precipitates occured in weld metal at 4.5 h and 8 h aging time and the microhardness was found to be (390 HV) and (421 HV) respectively compared to the base metal.

References

1. A. Lingenfelter, Welding of Inconel 718: a historical overview, ed. by E.A. Loria, *Conference Proceedings on Superalloy 718—Metallurgy and Applications*, TMS-AIME, Warrendale (1989), pp. 673–683
2. C. Slama, M. Abdellaoui, Structural characterization of the aged Inconel 718. J. Alloy. Compd. **306**, 277–284 (2000)
3. T. Alam, M. Chaturvedi, S.P. Ringer, J.M. Cairney, Precipitation and clustering in the early stages of aging in Inconel 718. Mater. Sci. Eng. A **527**, 7770–7774 (2010)
4. C.T. Sims, S.N. Stoloff, W.C. Hagel, Superalloys II, *High-Temperature Materials for Aerospace and Industrial Power* (Wiley, New York, 1987)
5. Zhao, X., Dang, Y., Yin, H., Jintao, L., Yuan, Y., Yang, Z., Yan, J.: Effect of heat treatment on the microstructure of a Ni–Fe based superalloy for advanced ultra-supercritical power plant applications. Progress in Natural Science: Materials International **26**, 204–209 (2016)
6. P. Maj, B. AdamczykCieslak, M. Slesik, J. Mizera, T. Pieja, J. Sieniawski, T. Gancarczyk, S. Dudek, The precipitation processes and mechanical properties of aged Inconel 718 alloy after annealing. Arch. Metall. Mater. **62**(3), 1695–1702 (2017)
7. R. Cozar, A. Pineau, Morphology of γ' and γ'' precipitates and thermal stability of Inconel 718 type alloys. Metall. Trans **4**, 47–59 (1973)
8. A.E. Marsh, Aerospace forgings—materials, processes, products. Metallurgical January, 10–20 (1982)
9. J.K. Hong, N.K. Park, J.H. Park, I.S. Eom, Microstructure and mechanical properties of Inconel 718 welds by CO_2 laser welding. J. Mater. Process. Technol. **20I**, 515–520 (2008)
10. A.K. Abdul Jawwad, M. Strangwood, C.L. Davis, Microstructural modification in full penetration and partial penetration electron beam welds in Inconel 718 (IN-718) and its effect on fatigue crack initiation. Metall. Trans. A **36A**, 1237–1247 (2005)
11. K.R. Vishwakarma, N.L. Richards, M.C. Chaturvedi, HAZ micro fissuring in EB welded ALLVAC 718 plus alloy, in *Proceedings of Superalloy 718, 625 and Derivatives*, pp. 637–647 (2005)
12. G.D. Janaki Ram, A. Venugopal Reddy, K. Prasad Rao, G. Madhusudhan Reddy, Microstructure and mechanical properties of Inconel 718 electron beam welds. J. Mater. Sci. Technol. **21**, 1132–1138 (2005)

13. G.D. Janaki Ram, A. Venugopal Reddy, K. Prasad Rao, G. Madhusudhan Reddy, Improvement in stress rupture properties of Inconel 718 gas tungsten arc welds using current pulsing. J. Mater. Sci. **40**, 1497–1500 (2005)
14. X. Cao, B. Rivaux, M. Jahazi, J. Cuddy, A. Birur, Effect of pre and post-weld heat treatment on metallurgical and tensile properties of Inconel 718 alloy butt joints welded using 4 kW Nd: YAG laser. J. Mater. Sci. **44**, 4557–4571 (2009)
15. Technical Data Sheet: Inconel Alloy 718. Special Metals Corporation (2007)

Effectiveness of Polyurea Coated Steel Plates in Blast Mitigation in Vehicles

Agesh Markose and C. Lakshmana Rao

Abstract Increasing terror attacks and development of improvised explosive devices (IEDs) has resulted in the development of protective structures for armoured personnel vehicles (APV). Protective members like flat steel plates are susceptible to damage due to blast load and have been already explored. As an improvement, composite plate having steel with coatings of hyperplastic materials like polyurea, for enhancing the blast mitigation, is being explored. These coated metallic plates can deflect away and absorb a major part of the blast load. One of the objectives of this work is to develop numerical methods for blast loading of structures using Abaqus explicit and validate the results against published results. These validated methods can be used for assessing the effectiveness of protective structures like V-plate with polyurea coating under blast loading. In this work, the main focus is on numerical simulation of the mechanical response of the V-shaped plate. The validation studies cover blast load generation and its interaction with V-shaped plates with and without polyurea coatings and its comparison with results reported in the literature. It is observed that blast functions can adequately model the shock waves generated in the blast loading. The latter part studies the impulse transmitted and deformations. The numerical work was carried out with a full-scale V-shaped plate made of mild steel (and having a projected dimension of about 2500×2500 mm), having polyurea coatings of 16 mm, 16×2 mm and 16×4 mm thickness. The impulse transmitted to the base structure was compared with a V-plate without coating and reduction in the transmitted impulse was observed. It is assumed that the above results may be helpful in obtaining optimized plate designs.

Keywords Armoured personnel carriers · Blast loading · V-shaped plate · Transmitted impulse

A. Markose (✉) · C. Lakshmana Rao
Department of Applied Mechanics, IIT Madras, Madras 600036, Tamilnadu, India
e-mail: ageshmarkose@gmail.com

1 Introduction

New and improvised explosive devices in the form of land mines are widely used in war-affected zones. The armoured personnel vehicles (APV), which are the only means of transportation under those situations are always under threat from those landmines. The effectiveness of the APV to resist blast loads depends on the metallic plates used as blast mitigation structures. These coated metallic plates can deflect away and absorb a major part of the blast load. Hence, net impulse transferred to the vehicle crew is significantly reduced thus enhancing their security. APV like South African Casspir are known to use V-shaped plates as blast mitigation structures. These plates are made from the armoured steel. Latest research has also highlighted the use of sandwich structures, using hyperplastic materials like polyurea for the above purpose as given in [1, 2]. Polyurea is an elastic polymer formed by the rapid chemical reaction between isocyanates and amines. Polyurea coatings have been found to have resistance to fragmentation, impact loads and ballistic loads along with blast mitigating capacity. These materials when applied as an external coating on the metals plate are seen to improve the blast-resistant property of the shaped plates.

Yuen et al. [3] and Agesh et al. [4] have conducted experimental, as well as, numerical investigation of shaped plates under blast loading. From the literature review, it is seen that the V-shaped plates are more effective in mitigating the blast loads as compared to flat plates. Roland et al. [5] has proposed that the energy absorption capacity of the polyurea layer is due to the transition from rubbery state to the glassy state during deformation. We see that while the adequate focus is given for the case of shaped plate's research on the response of the polyurea-coated V-plates under blast loading is inadequate.

The first part of the study focuses on the development and validation of numerical models, for obtaining the response of flat plates coated with polyurea subjected to blast loading. The second part of the work focus on the response of full-scale V-plate under blast loading from explosives. In all the cases, a comparison of response of the plate with and without the polyurea coating is carried out.

In the present paper, the objectives are as follows:

1. To develop a numerical model for simulating the response of metallic plates with polyurea coating and validate the published results.
2. To use the validated model to assess the effectiveness of polyurea-coated plates in reducing the transmitted impulse and forces in vehicle hulls.

The response parameters simulated are the midpoint displacement and the force or impulse transmitted to the boundaries. The parameters under consideration are (a) mass of the explosive and (b) coating thickness.

2 Problem Description and Numerical Modelling

APV like Casspir used metallic hull as protection against blast loading. The hull, fitted under the vehicle floor is made from armoured steel plates which are bent in a V shape. These plates provide sufficient protection to the crew from land mines as well as other explosive hazards. The blast-resistant capacity of the plate depends on the capacity of the plate to (a) absorb a part of the energy and (b) deflect part of the explosive load away from the hull. A schematic diagram of the shaped plate used for the numerical simulation is shown in along with the hull in Fig. 1.

The focus of our analysis is on the structural part and hence, a simplified blast model is assumed. The parameters under consideration are (a) mass of the explosive and (b) thickness of the coating. The 3D numerical study is conducted with Abaqus version 6.12. The model dimensions and materials are given in Table 1.
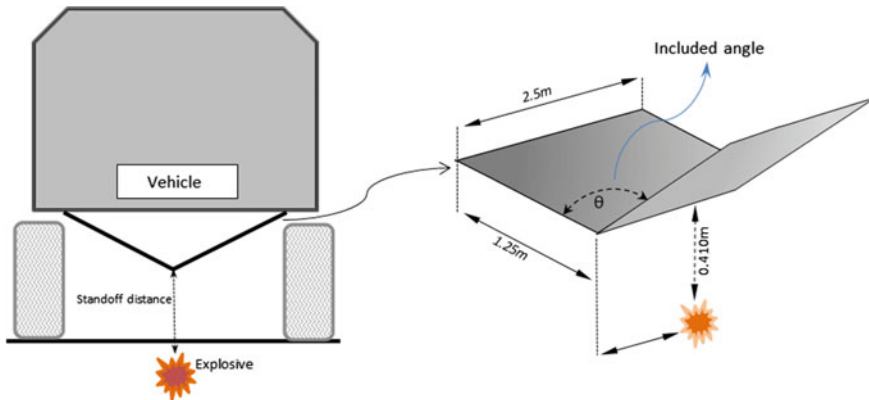
Fig. 1 Schematic illustrating the V-shaped hull fitted to the vehicle hull [4]

Table 1 Model dimensions [1, 4]

	Parameters of flat plate for validation	Parameters of the full-scale V-plate
Dimensions of projected area	1000 × 1000 mm	2500 × 2500 mm
Standoff distance	10 mm	410 mm
Plate thickness	4–6 mm	16.66 mm
Plate material	Bluescope XLERPLATE 350 grade.	Mild steel
Polyurea thickness	7.7 mm,15.7 mm	16.6 mm, 16.6 × 2 mm, 16.6 × 4 mm
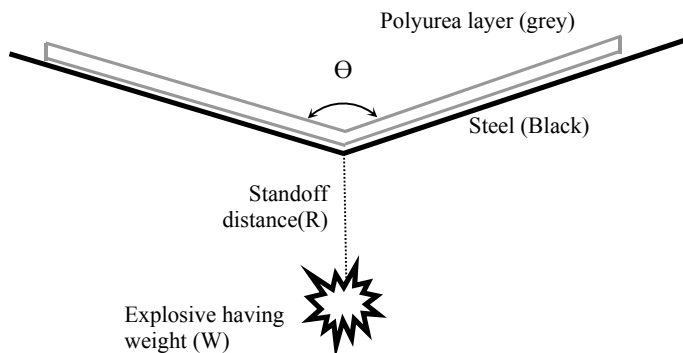
Fig. 2 Schematic cross section of typical coated V-plate

2.1 Geometric Modelling and Meshing

The plate angle of 145° has been selected based on a recommendation from the numerical study conducted by the authors as given in [4]. A plate of 2500 × 2500 × 16.6 mm has been selected. The analysis is carried out on a full model rather than a half or quarter symmetrical model. It is due to the reason that the full model can capture the structural instabilities which may not be symmetrical. The 3D model is created with Abaqus and discretized using Lagrangian elements. The solid elements defined in Abaqus have been used for the simulation of the plates under blast loading conditions. The first-order solid elements (C3D8R that is, continuum three-dimensional 8-node reduced integration), which have minimal shear and volume locking effect has been used for modelling the steel plate. The solid elements are preferred over the lesser time-consuming shell elements since the limitations imposed by the Mindlin shell theory can be avoided. First-order solid element C3D8R (three-dimensional 8 node reduced integration element) has been used for modelling the hyperelastic material polyurea. Similar elements have been used previously in Ackland et al. [1], for modelling these materials under impulsive loading. The interaction between plate and polyurea layer is modelled in Abaqus with the help of built-in cohesive layer. A schematic cross section of the coated V-plate is shown in Fig. 2.

2.2 Material Modelling

The V-shaped plate has been modelled with mild steel although armoured steel, which is a preferred choice for military applications. The Johnson–Cook material

model which is dependent on the strain rate has been used in the calculation of finite deformations. The von Mises flow stress given by Johnson et al. [6] is expressed as

$$\sigma = [A + B\varepsilon^n][1 + Cln\dot{\varepsilon}^*][1 - T^{*m}] \tag{1}$$

Here, ε is the equivalent plastic strain, $\dot{\varepsilon}^* = \frac{\dot{\varepsilon}}{\dot{\varepsilon}_0}$ is the dimensionless plastic strain rate and $\dot{\varepsilon}_0$ is the reference strain rate. T^* is the homologus temperature. The constants A, B n, C and m in the equation may be determined by fitting the flow stress data, based on static and dynamic tests.

All the material parameters for steel in the Johnson–Cook elastoplastic model have been evaluated by Iqbal et al. [7] and is presented in Table 2. The polyurea layer is assumed to obey the Mooney–Rivlin hyperplastic material model and the constants have been taken from Ackland et al. [1]. The hyperelastic strain energy function can be expressed as a two-parameter Mooney–Rivlin model as

$$\psi = C_{10}(I_1 - 3) + C_{01}(I_2 - 3) + \frac{1}{d}1(J - 1)^2 \tag{2}$$

Here, C01 and C10 are material constants, I1 and I2 are the first and second invariant of the deformation tensor, J is the determinant of the elastic deformation gradient and d is the material incompressibility factor. The value of C_{10} = 875.2 kPa, C_{01} = 6321.3 kPa and $d = 4 \times 10^{-7}$ (kPa)$^{-1}$.

The cohesive elements representing the adhesive undergoes failure under the forces existing between the plate and polyurea layer. The failure in cohesive layer is modelled with principal stress failure model. The strength parameters of the model have been taken from the [1].

Table 2 Properties of mild steel presented in Iqbal et al. [7]

Description	Notation	Numerical value
Modulus of elasticity	E(GPa)	203
Poisson ratio	v	0.33
Density	ρ(Kg/m^3)	7850
Yield stress	A(MPa)	304.33
Strain hardening constant	B(MPa)	422.007
	n	0.345
Viscous effect	C	0.0156
Thermal softening constant	m	0.87
Reference strain rate	$\dot{\varepsilon}_0$	0.0001 s^{-1}
Melting temperature	Θ_{melt}(K)	1800
Transition temperature	$\Theta_{transition}$(K)	293

2.3 Blast Load Modelling

The explosive charge upon detonation generates a shock wave propagating towards outer direction with a sudden jump in the field parameters (like particle velocity, density, pressure and internal energy) across the shock front. The shock wave exerts a pressure, P_s which is much higher than ambient pressure, P_a and the difference of these pressures is denoted by blast overpressure, $(P_s\text{-}P_a)$. The shock wave has a positive and negative phase associated with it and can be represented as shown in Fig. 3.

The pressure time history of the blast wave can be represented by the modified Friedlander equation [8].

$$p(t) = (p_s - p_a)1 - \frac{t - t_a}{t_d} e^{\frac{-(t-t_a)}{\theta}} \tag{3}$$

Here, t_a is the time of arrival, t_d is the duration of the positive phase and θ is the decay constant.

In the numerical work, blast loading is generated by the built-in blast generation function Conwep. Conwep is an empirical equation for calculating the shock wave pressure acting on the surfaces. Adisak Showichen [9] has given a brief description about Conwep. Conwep loading on different structures like flat plates, circular plates and honeycomb structures have given results, which is consistent with experiments [10].
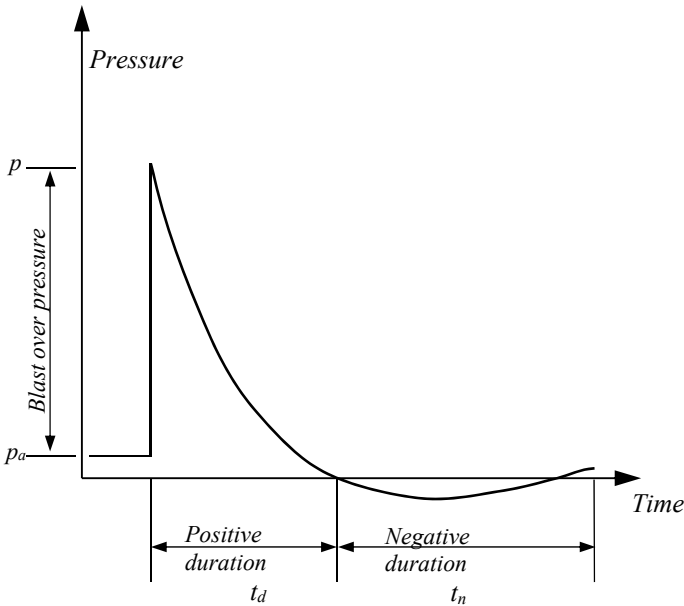
Fig. 3 Typical pressure time history of a blast wave

The imparted impulse (I) is be obtained by integrating the pressure acting with respect to the time duration of the loading.

$$I = \int_0^{t_d} P dt \qquad (4)$$

Here, P represents the applied pressure due to blast loading function Conwep and t_d is the duration of loading.

3 Results and Discussion

In the first part of the study, the parameters like deformation of the plate and polyurea layer were simulated and compared with the experimental result given in Ackland et al. [1]. A mesh convergence study was conducted on the plates subjected to Conwep loading. The mesh size for the scaled down model was varied as, 0.006, 0.003 and 0.001 m. The mesh size for the scaled down model was selected as 0.002 m. Figure 4a shows the comparison between the deformation contours of 6 mm flat plate where the numerical results are compared with experiments conducted on the same plates by Ackland et al. [1]. Figure 4b shows the deformation contour of a 5 mm polyurea-coated plate. It is seen that reasonable results are obtained by using Conwep blast functions and the hyperelastic material models.

From the comparison, it is seen that the numerical model is able to capture the experimental trends fairly accurately for the coated plate. The higher deflection seen in numerical simulations needs to be investigated further. Figure 5 shows the comparison of midpoint deflections from the experiment as reported in [1], and numerical curves. The deflection of the 6 mm thick metallic plate, as well as that of the polyurea layer coating on a 5 mm plate has been plotted. It is seen that the plate deflection reported from the experiment [1] is closely matching with the numerical
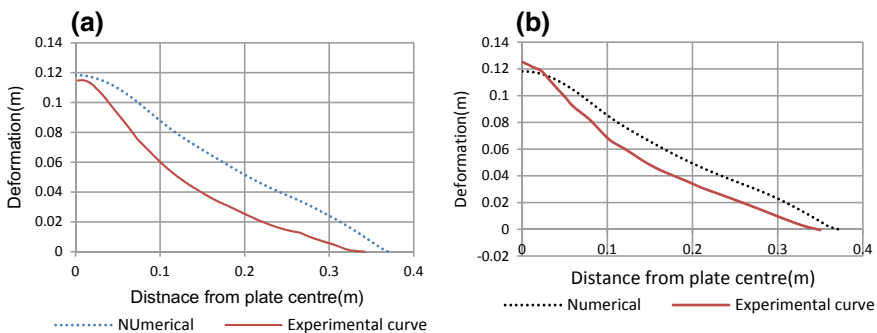
Fig. 4 a Deformation contour of 6 mm bare plate. b Deformation contour of 5 mm plate coated with polyurea
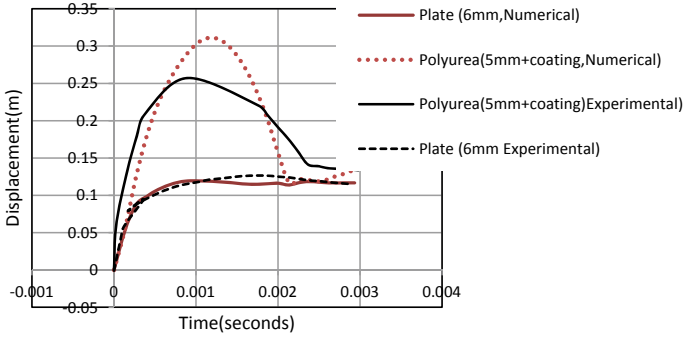
Fig. 5 Deformation of 6 mm bare plate and 5 mm plate coated with polyurea

simulation. The extremely high values of the polyurea layer in Fig. 5 seem to suggest that there is a debonding that's taking place between the steel and polymer. The polyurea layer detaches from the metallic plate due to the momentum transfer from the metallic plate. The debonding occurs when the maximum principal stress at the interface reaches the strength of the bond. The debonding area originates from the point of maximum impact load and radially expands in the form of a circle. This continues till the transferred momentum is fully converted into elastic strain energy. Once the expansion stops, the polyurea layer falls back into the metallic plate which has already undergone plastic expansion. The difference in the displacements may be attributed to the inherent variations in the Conwep load functions and loads in the experiment.

The effectiveness of the polyurea coating has been studied by considering a bare plate of 16 mm thickness and plates with varying polyurea coating thicknesses (16 mm, 16 × 2 mm and 16 × 4 mm). The polyurea layer is supposed to absorb and dissipate the energy from the steel plate. The deflection of the plate and polyurea has to be confined within the limits to avoid damage to the passenger cabin. This could be possible by increasing the weight/thickness of the polyurea layer, and is also in line with the thickness range followed in Ref. [1]. The force transmitted to the base structure for the bare and coated plates for same mass of the explosives has been studied and the results are shown in Fig. 6. The graph is drawn for bare plate of 16 mm and for 16 mm plates with various coating thickness, (SS1a is bare plate), (SSP1a has 16 × 2 mm coating) and (SSP31a has 16 × 4 mm coating). The above figure shows that the maximum force has a decreasing trend with an increase in coating thickness.

Figures 7 and 8 shows the deformation of the plates for varying massof the explosive. It is seen that deformation decreases with the increase of the thickness of polyurea. The reduction of about 25% is observed for 16 mm coatings. For the 64 mm coatings, a reduction of about 78% is obtained.

The plots for the impulse transmitted for various thickness of the polyurea layer is shown in Figs. 9 and 10. It is seen that the impulse reduction increases as the thickness of the polyurea layer increases. It is seen that the coating with 16 mm
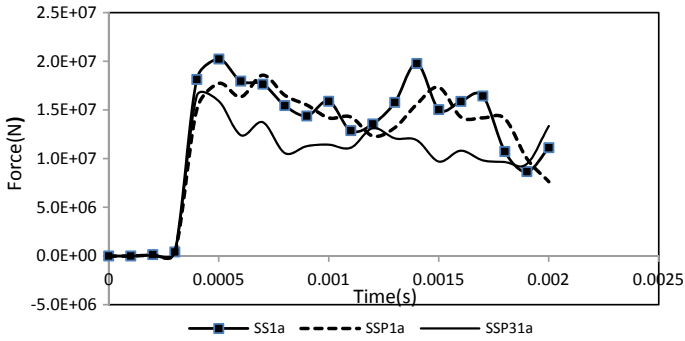
Fig. 6 Force exerted on the plates with different coating thickness

Fig. 7 Deformation plots for 16 mm plates
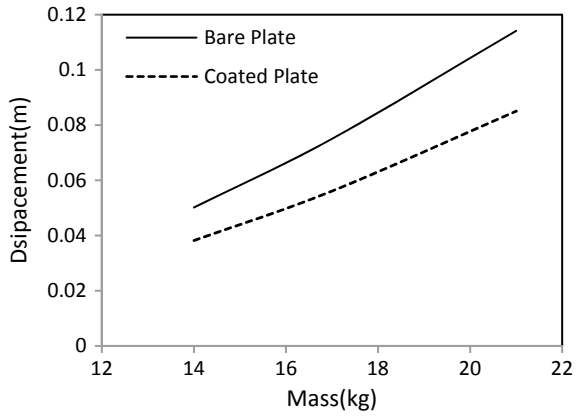
Fig. 8 Deformation plots for 16 mm plate with 64 mm coating
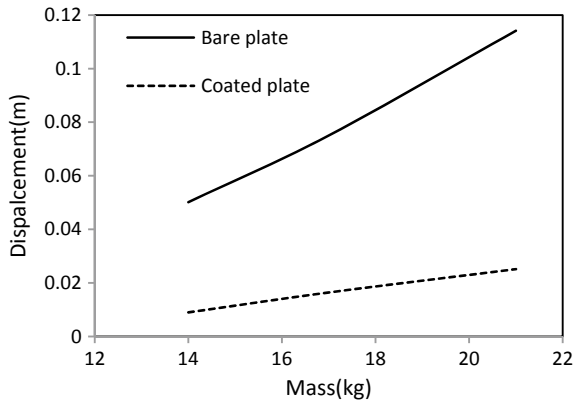
Fig. 9 Impulse plots for 16 mm plate with 16 mm coating
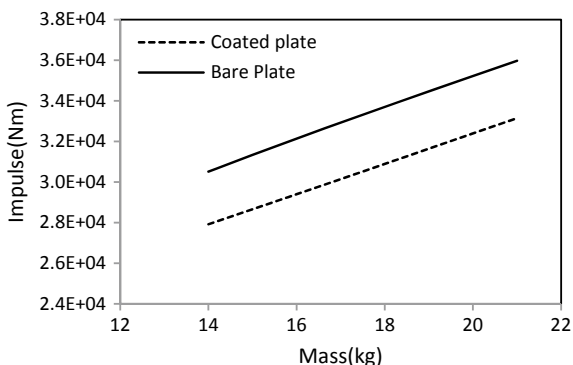
Fig. 10 Impulse plots for 16 mm plate with 64 mm coating
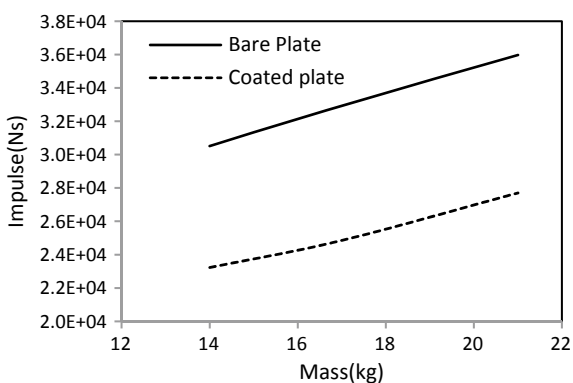
polyurea reduces the impulse by about 9% while the maximum thickness of 64 mm polyurea gives a reduction of about 25%.

The profile of the bare plate as well as the coated plate along the centre line, after loading is shown in Fig. 11. It is clear that at sufficiently high explosive loads, the coating undergoes debonding and as a result, it undergoes stretching. Hence, a part of the energy is utilized for increasing the total energy of the coating and hence better dissipation.

It has to be observed that the coatings are applied on the back face of the plate. This is in line with the results in Ref. [1], which shows no improvement in the blast resistance, either for front side coating or for sandwich configuration where poly-urea layer is sandwiched between metal plates. It was seen from simulations that increasing the mass of the explosives results in complete detachment of the poly-urea layer. Hence, the energy is channelized towards imparting momentum to the polyurea plate rather than an increase in the deformations and likely fracture under
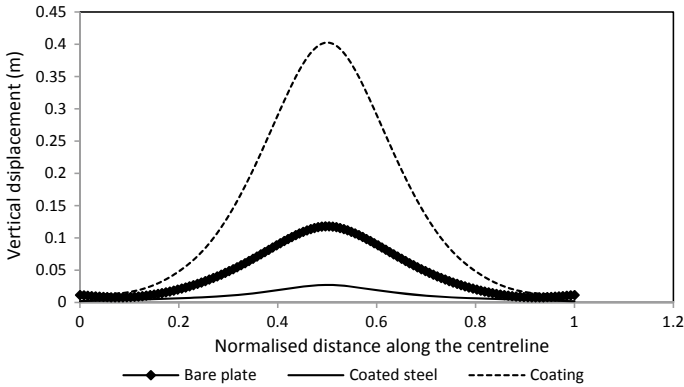
Fig. 11 Displacment contours for the bare plate and the coated plate

the present value of bond strength of the adhesive. Other parameters like temperature may affect the performance but the scope of such analysis is limited by the availability of parameters.

4   Conclusions

This paper presents a numerical approach for evaluating the response of full-scale V-shaped plate under blast loading. The proposed numerical method is validated by using the experimental results from other investigators. The following conclusions can be drawn:

- The deformation of coated and uncoated plate goes on increasing with an increase in charge mass.
- The bare plates when coated with a layer of polyurea can reduce the deformation and impulse transmitted to the base structure.
- The variation of the imparted impulse was studied and it is seen that there is a linear variation of the imparted impulse with the mass of the charge. Transmitted impulse is seen to increase with the increase in mass of the explosive.
- The variation of the displacement with time is seen to be slightly non-linear for the range of the mass of explosives. Displacement is seen to decrease with the increase in thickness of the coating.
- The deformation contours indicate that there is debonding between the steel and polyurea layer which leads to better dissipation of energy.

References

1. K. Ackland, C. Anderson, T. Ngo, Int. J. Impact Eng. **51**, 13 (2013)
2. M.R. Amini, J. Simon, S. Nemat-Nasser, Mech. Mater. **42**, 615 (2010)
3. C.K. Yuen, G.S Langdon, G.N. Nurick, E.G. Pickering, V.H. Balden, Int J. Impact Eng. **46**, 97 (2012)
4. M. Agesh, C.L. Rao, Thin Walled Struct. **115**, 12 (2017)
5. C.M. Roland, J.N. Twigg, Y. Vu, P.H. Mott, Polymer **48**, 574 (2007)
6. G.R. Johnson, W.H. Cook, In: *Proceedings of the 7th Symposium on Ballistics*, Hauge, Netherlands, p. 541 (1983)
7. M.A. Iqbal, K. Senthil, P. Bhargava, N.K. Gupta, Int. J. Impact Eng **78**, 98 (2015)
8. W.E. Baker, *Explosions in Air*. University of Texas Press, Austin, TX (1973)
9. A. Showichen, *Numerical analysis of vehicle bottom structures subjected to anti-tank mine explosions*. Ph.D. Thesis, Cranfield University, UK (2008)
10. T.F. Henchie, S.C.K. Yuen, G.N. Nurick, N. Ranwaha, B.H. Balden, Int. J. Impact Eng. **74**, 36 (2014)

Evolution of Tribological Properties of Cast Al–10Zn–2Mg Alloy Subjected to Severe Plastic Deformation

G. K. Manjunath, G. V. Preetham Kumar and K. Udaya Bhat

Abstract In the current investigation, tribological behaviour of the cast Al–10Zn–2Mg alloy processed by severe plastic deformation (SPD) technique was studied. In this work, one of the SPD techniques, equal channel angular pressing (ECAP) was adopted as a processing tool. ECAP was carried out in route B_C and processing was attempted at the lowest temperature. After ECAP, grain structure of the material was refined and considerable improvement in the microhardness of the alloy was perceived. Mainly, wear resistance of the alloy material was enhanced with successive ECAP passes. Coefficient of friction of the alloy material was decreased with successive ECAP passes. Wear resistance of the alloy was decreased with a rise in the applied load and the sliding speed. Both at low and high load condition, abrasive wear was noticed in as-cast and homogenized specimens. Whereas in ECAPed specimens, in addition to abrasive wear, oxidation wear and adhesive wear were observed in low load and it changes to abrasive wear at high load. In the ECAPed specimens, at low load transfer of iron particles from the steel disc surface to the specimen surface was identified.

Keywords Wear · Al–Zn–Mg alloy · SPD · ECAP · Wear mechanism

G. K. Manjunath · G. V. Preetham Kumar · K. Udaya Bhat (✉)
Department of Metallurgical and Materials Engineering, National Institute
of Technology Karnataka, Srinivasnagar P.O., Surathkal, Mangalore 575025, India
e-mail: udayabhatk@gmail.com

G. K. Manjunath
e-mail: manjugk2001@gmail.com

G. V. Preetham Kumar
e-mail: pkphd@hotmail.com

1 Introduction

Aluminium alloys are considered as a reliable material in the field of engineering applications. The Al–Zn–Mg alloys are acknowledged as the hardest and strongest alloys amongst aluminium alloys family [1]. Al–Zn–Mg alloys have earned wide appreciation in the development of lightweight equipment where high strength to weight ratio is an essential criterion [2]. However, poor ductility and low wear resistance of these alloys in cast condition obstruct its utilization in industries. Wear is identified as an important property in the design and manufacture of engineering equipment. Wear resistance capability of a material can be enhanced by strengthening the material [3]. Strength of the material can be enhanced by grain refinement through various severe plastic deformation (SPD) techniques. Among various SPD techniques, equal channel angular pressing (ECAP) is more attractive because of its simplicity [4]. ECAP was first introduced in 1972 by Segal, later during the 1990s, this process gained attention to develop ultra-fine-grained materials [5]. In ECAP process, the specimen is pushed through two channels which are intersecting at an angle (Φ). Large volume of shear strain is generated in the specimen as it crosses the intersecting line of two channels, which in turn causes grain size to decrease considerably along with the generation of large amount dislocations. The speciality of the ECAP is that after processing, the cross section of the specimen is unchanged so the same specimen could be processed repetitively to achieve higher grain refinement [6].

Numerous literature were reported on the implementation of the SPD process to Al–Zn–Mg alloys, particularly to identify the impact of the SPD process on the mechanical properties and evolution of microstructure [7–9]. In spite of that, wear study of the Al–Zn–Mg alloys processed by SPD techniques have not gained much consideration. In order to get optimal usage of the SPD processed alloys and materials, it is required to study the tribological properties of these materials. Since UFG materials processed by SPD techniques possess high strength and hardness [10]. They are expected to have good wear resistance. From the limited available literature on the tribological behaviour of the SPD processed materials, both favourable and unfavourable effects were observed [11]. So it is necessary to study the effect of ECAP on the tribological properties of Al–Zn–Mg alloys. It is very interesting to investigate the tribological performance of the SPD processed Al–Zn–Mg alloys. In this regard, in the present work, tribological properties of the ECAP processed cast Al–10Zn–2Mg alloy was studied and the consequence of ECAP on the tribological behaviour of the material was investigated. The composition of the material selected in the current investigation closely matches the composition of the Al 7034 alloy. This alloy is presently used in the fabrication of the lightweight structures [12].

2 Experimental

The material studied in the current investigation was prepared through a gravity casting technique. The procedure for the specimen preparation by gravity casting technique is described in our previous report [13]. The composition of the cast material was checked through optical emission spectroscopy (OES). Results obtained through OES technique is presented in Table 1. As-cast material was treated with a homogenization process at 753 K for 20 h. For ECAP, homogenized material was machined to Ø 15.9 mm and 80 mm height rods. The ECAP was carried out in a split die having channel diameter of 16 mm. The channels of the die are interconnecting at an angle (Φ) of 120º and having an external arc of curvature (Ψ) of 30º. With these angles, in each pass, a stain of 0.667 is imposed on the specimen. ECAP was attempted to carry out at the lowest possible temperature in route B_C and at a speed ≈ 0.5 mm/sec. Molybdenum disulphide was coated on the specimen surface and in the die channels to control friction during processing. A separate heating arrangement was used for heating the die assembly to the necessary temperature and the same temperature is retained while processing.

Microstructure of the specimens was studied by using scanning electron microscope (SEM) and energy dispersive spectroscopy (EDS) was carried out to check the chemical composition of the precipitates. For microstructural study, the specimens were polished using a sequence of silicon carbide abrasive papers followed by cloth polishing using aluminium oxide particles and distilled water. Lastly, specimens were etched using Keller's reagent. Microhardness was measured by using Vickers microhardness tester. The Vickers microhardness (Hv) was obtained by imposing a load of 50 gm for 15 s. Dry sliding wear tests were conducted in pin on disc arrangement at ambient temperature. To carry out wear tests, processed and unprocessed specimens were machined to cylindrical pins of Ø10 mm and 28 mm height. Specimens were made to slide against EN31 steel disc having a hardness of 62 HRc. Prior to wear test, specimen and the disc were washed with acetone. To investigate the wear resistance capability of the alloy material, wear tests were conducted at different loads and sliding speeds. These conditions are presented in Table 2. In all conditions, wear tests were done for a span of 1000 m and in a circular track of Ø 120 mm. The wear resistance was measured by weight loss method.

Table 1 Composition the material verified through optical emission spectroscopy

Element	Al	Zn	Mg	Fe	Mn	Si	Zr	Cu	Ti	Ni	Cr	Pb
Weight (%)	87.3	10.1	2.1	0.23	0.074	0.16	0.005	0.022	0.003	0.002	0.002	0.002

Table 2 Wear test conditions

	C1	C2	C3	C4
Load (N)	19.62	19.62	39.24	39.24
Sliding speed (m/s)	1	2	1	2

The coefficient of friction was obtained through frictional force and load data documented in the controller. The surface morphology and the quantitative elemental analysis of the worn surfaces of the specimens were done in SEM.

3 Results and Discussion

The literature on various SPD process indicates that more refined grain structure could be achieved by processing the material at the lowest possible temperature [14]. On this detail, the material was attempted to process at the lowest temperature. Processing was unsuccessful in the first pass itself at room temperature, 373 and 398 K. At 423 and 448 K, the material fruitfully processed in the first pass and they cracked during the second pass in route B_C. At 473 K, the material was fruitfully processed up to four passes in route B_C without crack. This was the lowest possible temperature at which the material might be fruitfully processed in route B_C without fail up to four passes. In this section, results related to the material ECAP processed at 423 and 473 K is presented.

3.1 Microstructure

Figure 1 presents the microstructure of the material in various conditions. In as-cast state, the microstructure is composed of dendrites and the precipitates were
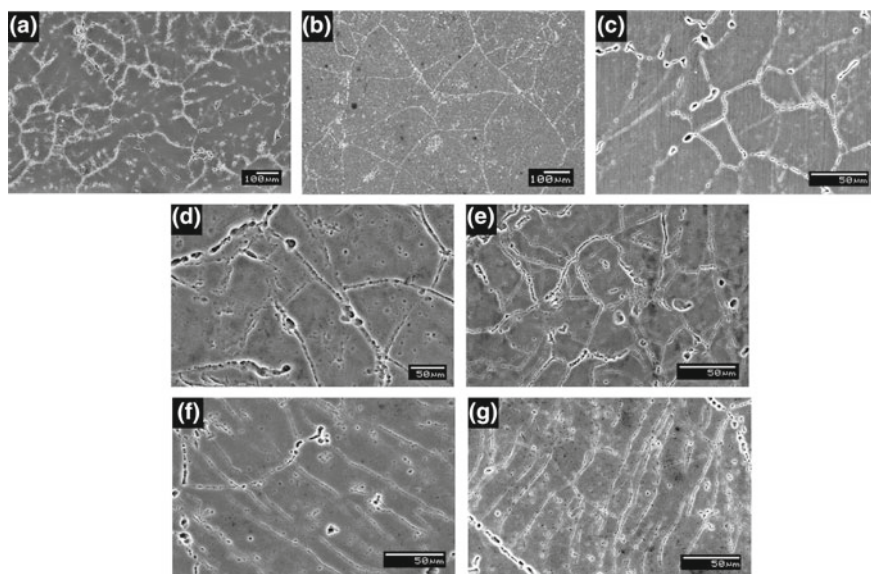
Fig. 1 SEM micrographs of the material **a** as-cast, **b** homogenized, **c** 1 pass at 423 K, **d** 1 pass at 473 K **e** 2 pass at 473 K, **f** 3 pass at 473 K and **g** 4 pass at 473 K

observed in the inter-dendritic spaces as shown in Fig. 1a. Size of the dendrites measured in this condition is approximately equal to 280 μm. The precipitates in the inter-dendritic spaces were identified as η' phase ($MgZn_2$) precipitates [15]. The composition of the precipitates was also confirmed through SEM-EDS analysis. The EDS report is presented in Fig. 2. After homogenization, large-size grains approximately equal to 260 μm replaced the dendritic structure and the precipitates in the inter-dendritic spaces were almost dissolved in the base material as shown in Fig. 1b. After ECAP, grain structure of the material was refined. After one pass ECAP at 423 K, the grain size of the material was approximately decreased to 60 μm as shown in Fig. 1c. Also, precipitates were observed nearby grain boundaries. After ECAP at 473 K, the grain size was decreased to 75 μm in the first pass, 40 μm in the second pass, 20 μm in the third pass and 8 μm in the fourth pass as shown in Fig. 1d, e, f and g, respectively. The detailed investigation of the microstructure evolution after ECAP processing of this material was presented in our earlier work [16, 17]. Figure 3 presents the morphology of the precipitates in the material. In as-cast condition, large flake-shaped precipitates were noticed as

Element	Weight %
Mg K	3.14
Al K	90.05
Zn K	6.81
Total	100.00

0 Cnts   0.000 keV   Det: Element-C2B
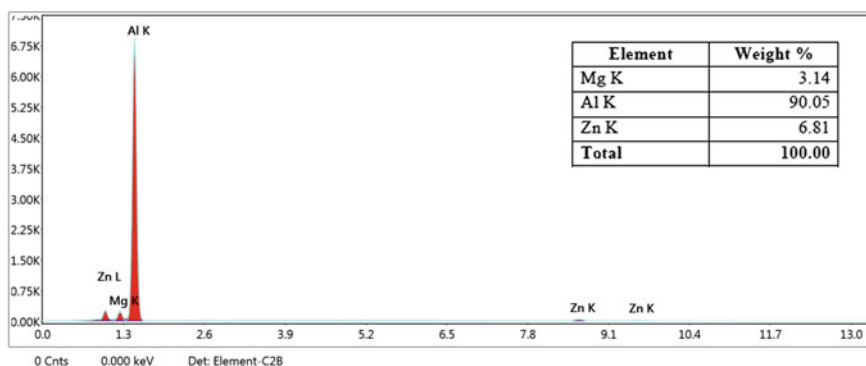
Fig. 2 EDS report of the material in as-cast condition
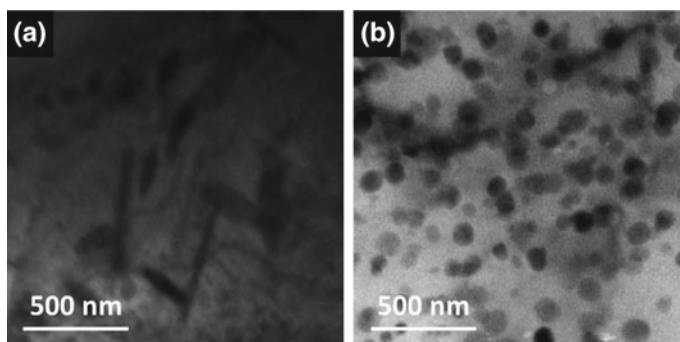
Fig. 3 TEM micrographs of the material **a** as-cast and **b** 4 pass at 473 K

shown in Fig. 3a. After four passes at 473 K, fine spherical-shaped precipitates were noticed. Also, these precipitates were uniformly distributed in the alloy as shown in Fig. 3b.

3.2 Microhardness

Table 3 displays the microhardness of the alloy material in different conditions. In as-cast state, the microhardness of the material is 144 Hv. After homogenization, the microhardness of the alloy material is improved to 155 Hv (8% improvement from the as-cast state). Significant improvement in the microhardness of the material was perceived after ECAP. After one pass ECAP at 423 K, the microhardness of the alloy material was improved to 216 Hv (50% improvement from the as-cast state) [16]. After ECAP at 473 K, the microhardness of the alloy material was enhanced to 204, 223, 232 and 240 Hv in the first, second, third and fourth passes, respectively. After ECAP processing at 473 K, the microhardness was increased by 42, 55, 61 and 67% in the first, second, third and fourth passes, correspondingly from the as-cast state [17]. Improvement in the microhardness of the alloy material after ECAP is owing to the grain refinement, work hardening of the material due to the development of high-density dislocations and formation of high angle grain boundaries [18].

3.3 Wear Properties

3.3.1 Wear Rate

Table 4 displays wear rate of the material in different conditions. The wear rate presented is in the magnitude of 10^{-3} mm^3/m. It is noticed that wear rate is lower in

Table 3 Microhardness (Hv) of the material in different conditions

As-cast	Homogenized	1 pass (423 K)	1 pass (473 K)	2 pass (473 K)	3 pass (473 K)	4 pass (473 K)
144	155	216	204	223	232	240

Table 4 Wear rate of the material in different conditions

	Wear rate (10^{-3} mm^3/m)			
	C1	C2	C3	C4
As-cast	2.169	2.589	3.009	3.394
Homogenized	1.889	2.274	2.799	3.149
1 pass (423 K)	1.365	1.819	2.239	2.589
1 pass (473 K)	1.470	1.924	2.344	2.694
2 pass (473 K)	1.190	1.540	2.064	2.379
3 pass (473 K)	0.945	1.295	1.819	2.169
4 pass (473 K)	0.805	1.120	1.610	1.889

ECAPed specimens in contrast to the as-cast and the homogenized specimens. Also, the wear rate decreased with successive ECAP passes. A decrease in wear rate in the ECAP processed specimens is credited to decrease in the grain size, rise in the microhardness of the alloy material and uniform distribution of the finer size spherical-shaped precipitates in the alloy after ECAP. But, wear resistance of the ECAPed material was decreased with a rise in the load applied and sliding speed. Even though the wear resistance of the ECAPed material was decreased with a rise in the load applied and sliding speed, in all conditions, ECAP processed specimens show superior wear resistance in contrast to the as-cast and the homogenized specimens. The behaviour of increase in the wear resistance of the alloy material after ECAP is consistent with the previous reports on cast Al-7Si material processed by SPD [19]. It was observed that wear rate is comparatively less in one ECAP pass material processed at 423 K in contrast to the one ECAP pass material processed at 473 K. This is owing to the more hardness perceived in the material when processed at 423 K in contrast to the material processed at 473 K.

3.3.2 Coefficient of Friction (μ)

Table 5 displays the coefficient of friction of the material in different conditions. It is noticed that coefficient of friction is lower in ECAP processed specimens in contrast to the as-cast and the homogenized specimens. Also, the coefficient of friction decreased with successive ECAP passes. Decrease in the coefficient of friction in the ECAP processed specimens is attributed to the decrease in the grain size of the material and formation of homogenized microstructure after ECAP processing. But, the coefficient of friction of the ECAPed material increased with a rise in the load and the sliding speed. Even though the coefficient of friction of the ECAPed material increased with a rise in the load and the sliding speed, in all conditions, ECAP processed specimens possess less coefficient of friction in contrast to the as-cast and the homogenized specimens. The behaviour of decrease in the coefficient of friction of the alloy material after ECAP is consistent with the previous reports on aluminium–bronze material processed by SPD [3].

Table 5 Coefficient of friction (μ) of the material in different conditions

	Coefficient of friction (μ)			
	C1	C2	C3	C4
As-cast	0.35	0.4	0.46	0.5
Homogenized	0.33	0.38	0.44	0.48
1 pass (423 K)	0.26	0.31	0.38	0.42
1 pass (473 K)	0.28	0.32	0.4	0.44
2 pass (473 K)	0.25	0.3	0.38	0.42
3 pass (473 K)	0.24	0.29	0.37	0.41
4 pass (473 K)	0.23	0.28	0.36	0.4

3.4 Wear Surface Morphology

Figure 4 displays the SEM micrographs and EDS report of the worn surfaces of the material in different conditions, after wear test conducted at condition C1. The worn surfaces of the as-cast and homogenized samples were comprised of delamination areas and scratches formed due to the separation of the specimen material in the shape of debris, resulting in abrasive wear as shown in Fig. 4a and b. In the EDS report of the as-cast and homogenized specimens, a small trace of oxygen was perceived. But its consequence on the oxide layer growth was not perceived in SEM micrographs. Figure 4c and d shows the worn surface of the material after one pass ECAP at 423 K and 473 K, respectively. It is noticed that in addition to material delamination, scratches and ploughing; at few locations sticking of the worn particles was also observed. Hence, it is presumed that both adhesive and abrasive wear mechanisms were perceived in the first pass specimen processed at 423 K and 473 K, respectively. In the EDS report, the existence of oxygen content was perceived in the adhered debris. The existence of oxygen indicates the oxide layer

Al	Zn	Mg	O	Fe
76.18	8.11	2.28	11.49	2.28

Al	Zn	Mg	O	Fe
75.03	7.37	2.04	14.65	0.91

Al	Zn	Mg	O	Fe
51.20	7.20	1.39	16.77	23.44

Al	Zn	Mg	O	Fe
44.44	4.78	1.18	22.60	27.00

Al	Zn	Mg	O	Fe
41.30	5.09	1.33	22.04	30.25

Al	Zn	Mg	O	Fe
40.49	4.54	1.19	21.04	32.75

Al	Zn	Mg	O	Fe
35.30	6.46	1.02	22.54	34.67

Fig. 4 SEM micrographs and EDS report of the worn surfaces of the material after wear test conducted at condition C1 **a** as-cast and **b** homogenized**, c** 1 pass at 423 K, **d** 1 pass at 473 K **e** 2 pass at 473 K, **f** 3 pass at 473 K and **g** 4 pass at 473 K (EDS report is collected from the marked area)

growth on the worn surface. Thus, in addition to adhesive and abrasive wear; oxidation wear is too perceived. The presence of iron on the adhered debris indicates that the transfer of the iron elements from the steel disc to the specimen surface. This is owing to the increase in the hardness of the material after ECAP [20]. The adhesion effect is comparatively more in one ECAP pass material processed at 423 K in contrast to the one ECAP pass material processed at 473 K. This is owing to the more hardness perceived in the material when processed at 423 K in contrast to the material processed at 473 K. Figure 4e, f and g show the worn surface of the material after second, third and fourth passses ECAP at 473 K, respectively. It is observed that with successive ECAP passes sticking of the worn particles to the surface of the specimen is increased. Subsequently, delamination and abrasion marks on the worn surfaces were decreased with successive ECAP passes. Consequently, wear mechanism has changed from abrasive wear to adhesive wear with successive ECAP passes. In the EDS report, it is noticed that the transfer of iron elements from steel disc to the specimen surface increased with successive ECAP passes. This is owing to the increase in the hardness of the material with successive ECAP passes. With successive ECAP passes, oxide layer formation on the worn surface also increased. Thus, with successive ECAP passes, the intensity of oxidation wear also increased.

Figure 5 displays the SEM micrographs and EDS report of the worn surfaces of the material in different conditions, after wear test conducted at condition C4. The worn surfaces of the as-cast and the homogenized specimens were heavily damaged as displayed in Fig. 5a and b, correspondingly. Ploughing grooves were extended longitudinally towards the sliding direction. The existence of continuous wear scars and scratch marks on the worn surfaces shows the presence of abrasive wear in as-cast and homogenized specimens. In the EDS report, a large amount of aluminium and zinc traces were observed. Also, negligible traces of oxygen were observed. But, oxide layer growth was not perceived in SEM micrographs. Figure 5c and d shows the worn surface of the material after one pass ECAP at 423 K and 473 K, respectively. Comparatively shallow and narrow grooves were, observed in contrast to the as-cast and the homogenized specimens, this is owing to the increase in the hardness of the alloy after ECAP. In the EDS report, a small trace of oxygen was observed but oxide layer growth was not perceived in SEM micrographs. Adhesion of wear debris is also not observed in the SEM micrographs. Hence, it is presumed that in this condition, abrasive wear mechanism was observed in the first pass specimen processed at 423 K and 473 K, respectively. Figure 5e, f and g show the worn surface of the material after second, third and fourth passses ECAP at 473 K, respectively. It is observed that with successive ECAP passes mild wear tracks with fairly smooth surfaces were perceived. This is owing to the increase in the hardness of the material after ECAP. Sticking of the worn particles is also not perceived in the second, third and fourth pass specimens.
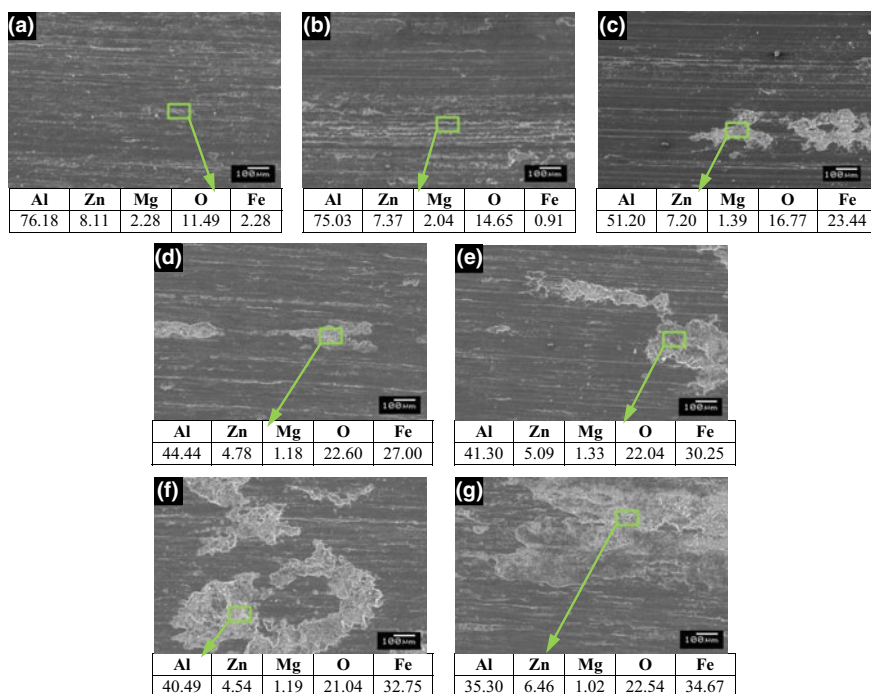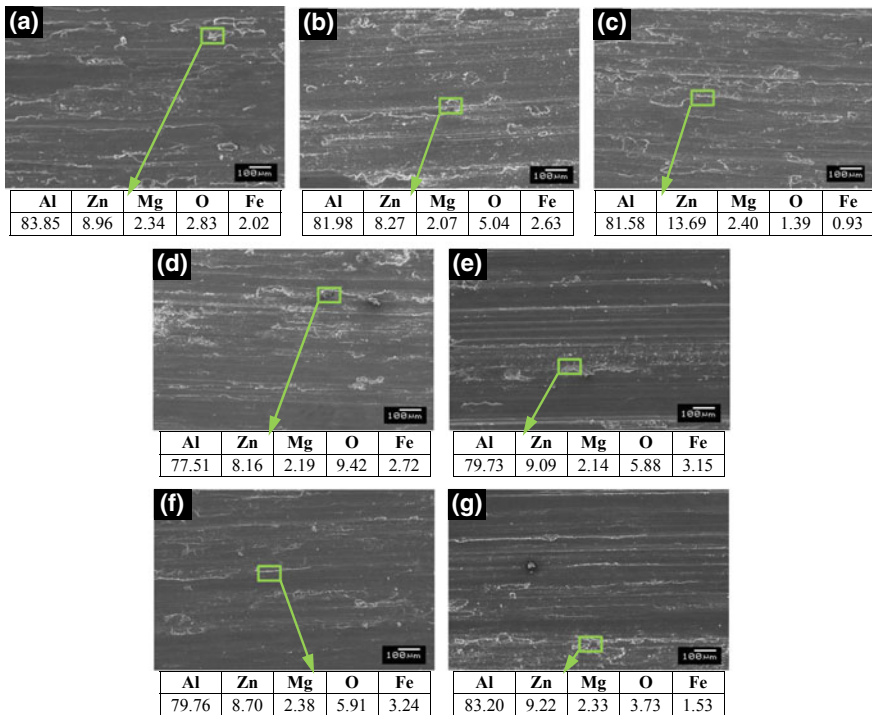
Fig. 5 SEM micrographs and EDS report of the worn surfaces of the material after wear test conducted at condition C4 **a** as-cast and **b** homogenized, **c** 1 pass at 423 K, **d** 1 pass at 473 K **e** 2 pass at 473 K, **f** 3 pass at 473 K and **g** 4 pass at 473 K (EDS report is collected from the marked area)

As, in this condition of the wear test, the applied load and sliding speed both are higher, due to which worn particles might have been separated from the worn surfaces. Thus, in this condition, abrasive wear is the predominant wear mechanism perceived in ECAPed specimens. In the EDS report, a little trace of oxygen was perceived. But, its consequence on the oxide layer growth was not perceived in SEM micrographs.

4 Conclusions

Following conclusions were drawn from the current investigation.

- After ECAP, grain structure of the material was significantly refined and significant improvement in the microhardness of the alloy material was perceived.

- Wear resistance of the alloy material was enhanced with successive ECAP passes. Specimens processed at 423 K possess better wear resistance compared to the specimens processed at 473 K.
- Irrespective of the load, abrasive wear was perceived in the as-cast and homogenized specimens. Whereas in the ECAPed specimens, at lower load, along with abrasive wear; adhesive wear and oxidation wear were also perceived. At higher load, only abrasive wear was perceived.
- In the ECAP processed specimens, at lower load, transfer of iron elements from the steel disc surface to the specimen surface was perceived.

REFERENCES

 1. M. Kutz, *Mechanical Engineers Handbook: Materials and Mechanical Design* (Wiley, New Jersey, 2006)
 2. M.H. Shaeri, M.T. Salehi, S.H. Seyyedein, M.R. Abutalebi, J.K. Park, Mater. Des. **57**, 250 (2014)
 3. L.L. Gao, X.H. Cheng, Wear **265**, 986 (2008)
 4. R.Z. Valiev, T.G. Langdon, Prog. Mater Sci. **51**, 881 (2006)
 5. V.M. Segal, Mater. Sci. Eng. A **271**, 322 (1999)
 6. Y.T. Zehetbauer, M.J. Zhu, *Bulk Nanostructured Materials* (Wiley-VCH, Weinheim, 2009)
 7. Z. Horita, T. Fujinami, M. Nemoto, T.G. Langdon, J. Mater. Process. Technol. **117**, 288 (2001)
 8. I. Nikulin, R. Kaibyshev, T. Sakai, Mater. Sci. Eng. A **407**, 62 (2005)
 9. Z.L. Ning, S. Guo, F.Y. Cao, G.J. Wang, Z.C. Li, J.F. Sun, J. Mater. Sci. **45**, 3023 (2010)
10. R.Z. Valiev, R.K. Islamgaliev, I.V. Alexandrov, Prog. Mater Sci. **45**, 103 (2000)
11. N. Gao, C.T. Wang, R.J.K. Wood, T.G. Langdon, J. Mater. Sci. **47**, 4779 (2012)
12. C. Xu, T.G. Langdon, Mater. Sci. Eng. A **410–411**, 398 (2005)
13. G.K. Manjunath, G.V. Preetham Kumar, K. Udaya Bhat, Trans. Indian Inst. Met. **70,** 833 (2017)
14. A. Goloborodko, O. Sitdikov, R. Kaibyshev, H. Miura, T. Sakai, Mater. Sci. Eng. A **381**, 121 (2004)
15. S. Zhang, W. Hu, R. Berghammer, G. Gottstein, Acta Mater. **58**, 6695 (2010)
16. G.K. Manjunath, G.V. Preetham Kumar, K. Udaya Bhat, AIP Conf. Proc. **1943**, 020067 (2018)
17. G.K. Manjunath, K. Udaya Bhat, G.V. Preetham Kumar, Metallogr. Microstruct. Anal. **7**, 77 (2018)
18. L.J. Zheng, H.X. Li, M.F. Hashmi, C.Q. Chen, Y. Zhang, M.G. Zeng, J. Mater. Process. Technol. **171**, 100 (2006)
19. M.I.A.E. Aal, H.S. Kim, Mater. Des. **53**, 373 (2014)
20. M.I.A.E. Aal, N.E. Mahallawy, F.A. Shehata, M.A.E. Hameed, E.Y. Yoon, H.S. Kim, Mater. Sci. Eng. A **527**, 3726 (2010)

Finite Difference-Based Conduction Model of Weld Pool for Laser and TIG Welding

B. Vikas Kumar Reddy, S. Murugan, A. V. G. Reddy, A. C. Wali and D. Srivastava

Abstract In the present work, a heat conduction-based model has been developed for simulating the molten region of a welded joint of stainless steel clad tube with an end plug. Both TIG welding and Laser welding processes are considered. This model has employed the finite difference method to discretize the differential equations of heat conduction. Explicit scheme has been used to determine the temperature at each nodal point, which will depend on the temperatures of the surrounding nodal points and the heat transfer with the ambient. The resulting simultaneous linear equations have been solved by a Python code. The output of the code are the coordinates of all the points that have crossed the liquidus temperature of the clad tube material. It is shown that the area representing the resulting points resemble the shape of weld pool in the clad side.

Keywords Weld pool modeling · Finite difference method · Laser welding · TIG welding

Nomenclature

T   temperature at any given point and time
t   time variable
φ independent space variable for circumferential direction
z   independent space variable for axial direction
k   thermal conductivity of clad
ρ density of clad
q_c'' convective heat flux
h   heat transfer coefficient
T_∞ Ambient temperature
r   independent space variable for radial direction

B. Vikas Kumar Reddy (✉) · A. V. G. Reddy · A. C. Wali · D. Srivastava
Fast Reactor Facility, Nuclear Fuel Complex, Hyderabad, India
e-mail: wikasreddy@gmail.com

S. Murugan
Indira Gandhi Centre for Atomic Research, Kalpakkam, India

$\dot{q}$ heat generation
C_P specific heat of clad
q_r'' radiative heat flux
σ Stefan–Boltzmann constant

1 Introduction

Welding is an important metal-joining process that is widely used in industries. The structural components made of welding will be subjected to stresses depending on the loading conditions. A good weld design is needed for the safe application of load on the welded structures. Determining the optimal set of parameters for welding by carrying out actual experimental trials is time consuming and tedious. It is preferable to have a theoretical understanding of determining the optimal parameters of welding by numerical modeling.

Developing numerical models to study heat flow in and around the weld pool has been the interest of many researchers for the past few years. Ganesh et al. [1] employed FEM model using commercial software to predict residual stresses and distortion in TIG-welded stainless steel plates. Magalhaes et al. [2] used finite difference method to solve the numerical approximation of heat conduction equation to determine the cooling rates in GTA welding of stainless steel and aluminum. They modeled the heat source to be circular in nature with Gaussian distribution of heat flux. Kim and Na [3] solved the numerical approximations of heat and mass transfer equations employing finite difference method.

Nowadays, commercial software is generally used for solving heat transfer differential equations for welding [4]. In the present work, a simple model considering only heat conduction was developed to ascertain the size and shape of resulting weld bead for GTAW and Laser welding. The model developed is for tube to plug welding. In this simple model, the clad tube only has been modeled and the heat transfer to the end plug is not considered. This model can be used to determine the average power that gives the desired depth of penetration for tube to plug welding.

2 Numerical Modeling

2.1 Governing Equations

The final shape of the weld bead depends largely on the amount of heat input, component geometry, and resulting temperature distribution.

The following differential equation explains heat conduction in the clad tube (in cylindrical coordinates):

$$\frac{1}{r}\frac{\partial}{\partial r}\left(kr\frac{\partial T}{\partial r}\right) + \frac{1}{r^2}\frac{\partial}{\partial \varphi}\left(k\frac{\partial T}{\partial \varphi}\right) + \frac{\partial}{\partial z}\left(k\frac{\partial T}{\partial z}\right) + \dot{q} = \rho C_P \frac{\partial T}{\partial t}$$

Heat loss to the ambient by convective and radiative heat transfer is given by

$$q_c'' = h * (T - T_\infty)$$

$$q_r'' = \sigma * \left(T^4 - T_\infty^4\right)$$

2.2 Material Modeling

The material used was SS 316LN. Based on the available thermophysical properties at various temperatures, a linear fit with least error was obtained, which was used for modeling. Latent heat of fusion was incorporated into specific heat between solidus and liquidus regions. Heat convection by molten metal movement within the weld pool was accounted for by suitably increasing thermal conductivity.

2.3 Finite Difference Model

Energy balance was applied at each point to the discretized clad tube. Initially developed 3D model turned out to be computationally expensive. It was replaced with a 2D model for radial and axial directions by making suitable adjustments to account for heat loss in the circumferential direction. Also while solving for temperatures of nodes, only the first pulse is considered followed by cycle off time in case of laser welding.

Fine mesh was applied in and around the region where the weld pool is known to form, and a coarser mesh was applied to the rest of the clad tube.

The lower side of the rectangle, as shown in Fig. 1 represents the inner radius of clad tube and the other side represents outer radius. Tube to plug joint is on the left side while right side is end. Fine mesh is applied in the area of interest, i.e., around the joint area, while the coarse mesh is applied everywhere else to save computational time. Element size in the region with fine mesh is 0.02 mm in radial direction and 0.03 mm in axial direction. In the region with coarse mesh, the
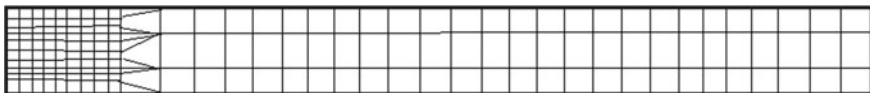

Fig. 1 Schematic of mesh applied over section of clad tube

element size is 0.1 mm in radial direction and 0.15 mm in axial direction. The total number of elements used is 90,000.

The heat source for both laser and GTA welding was modeled as a circular spot with a Gaussian distribution of energy. Furthermore, the heat input in laser welding is considered to be penetrating in nature, with intensity dropping exponentially with depth, while in GTA welding, it is placed on the surface. The term for heat flux distribution is taken as

$$q'' = q_0 e^{-f\frac{r^2}{R^2}}$$

where r is the radial distance from center of laser spot, R is the radius of laser spot, and f is the power distribution factor.

Explicit scheme was used to solve the resulting temperature relations at each node and the time step was chosen such that the solution is stable for all points.

A Python code was developed to model, mesh, and solve the simultaneous linear equations at nodes, by taking the required inputs from the user like tube dimensions, heat input, size of mesh, minimum time step, etc. Essentially, the temperatures at each nodal point are evaluated and the coordinates of points, which have crossed liquidus temperature (1730 K), are extracted. When plotted, these points resemble the weld bead after solidification since the weld bead itself is the set of all points which have crossed the liquidus temperature.

3 Experimental Procedure

The laser welding was carried out using pulsed mode Nd:YAG laser system attached with a rotary work handling mechanism. Speed of rotation of the tube can be adjusted along with laser welding parameters like peak power, pulse duration, pulse frequency, shape of pulse, etc. Square pulse is used in the current study.

TIG welding was carried out on an automated welding machine. The machine is customized by integrating the welding unit with a rotatable chuck. Heat input parameters like background current, peak current, etc., can be adjusted. The clad tube, end plug and joint configuration are shown in Fig. 2.

Experimental parameters used are the following:

TIG Welding	Laser Welding
Voltage: 6 V	Peak power: 1400, 1500, 1600 W
Current: 28 A	Pulse duration: 8 ms, Pulse frequency: 9
Time for one revolution: 15 s	Time for one revolution: 13 s
Shield gas: Argon	Shield gas: Argon
Shield gas flow rate: 6 l pm	Shield gas flow rate: 6 l pm

The welded samples were polished sequentially from 200-grade emery to 1200 grade. The polished samples were electro etched with 10% oxalic acid in deionized
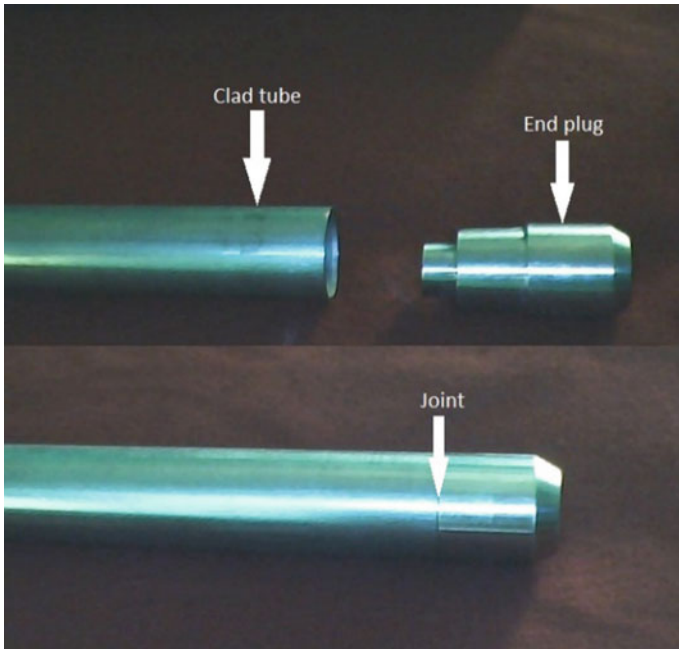
Fig. 2 Clad tube, end plug and joint configuration

water for 15–20 s. The samples were then observed under a microscope to determine the depth of penetration and bead width.

4 Results and Discussion

Clad tube of ID 13.13 mm, OD 14.33 mm, and length 100 mm was modeled. Many trials were made with the code by varying the parameters of heat source like surface heat input, penetrating beam, uniform distribution of intensity, and Gaussian distribution. The results were found to be different for each case.

The results of the simulation for laser and TIG welding are shown in Figs. 3 and 5, respectively. An average power of 108 W was applied for laser welding. For TIG welding, a power of 170 W was applied for a duration of 80 ms. Y-axis shows radial position and X-axis shows axial position. Thus, the leftmost point at bottom gives the depth of penetration and rightmost point at top gives bead width. It can be seen that the weld bead shape is concave for laser and convex for GTAW. This is in line with experimental observations because in laser welding, the bead is pointed in nature while that in TIG welding is circular in nature (Figs. 4 and 6). Since the clad tube alone is modeled, the result shows the region of weld pool that lies in clad tube. All the parameters are the same in the two cases, except the nature of heat

source. The effect of laser beam being modeled as "penetrating" into the metal can be seen in the depth of penetration and steep nature of weld pool. More energy reaching deeper regions caused increased depth of penetration. It can be observed from Fig. 3 that the weld bead is abruptly ending at the bottom. Had the plug been modeled too, the weld pool would have extended further downward. It can be inferred that deeper the weld pool, greater is its width at a given distance from surface. Thus, the width of weld pool at the inner side of clad tube is an indirect measure of the depth of penetration. That is, greater the width at bottom, greater would be the depth of penetration and vice versa.

Average power (W)	Bead width at OD of clad		Bead width near ID of clad		Attained temperature (K)
	Predicted (mm)	Actual (mm)	Predicted (mm)	Actual (mm)	
100	1.4	1.487	0.334	0.335	1790
108	1.4	1.643	0.534	0.476	1889
115	1.46	1.714	0.667	0.613	1953

It can be seen from Figs. 7, 8, 9 and 10 that increasing laser power increases the depth of penetration and bead width. Peak power of 1400, 1500, 1600, and 1700 W was used with 8 ms as pulse duration and pulse frequency of 9. In the first case, laser power is barely sufficient to get a penetration of 100%. When the average power is increased to 108 W, the weld pool has reached inner side of clad tube, but the actual depth of penetration cannot be measured directly. However as discussed previously, the width at inner side is a measure of the depth of penetration. The
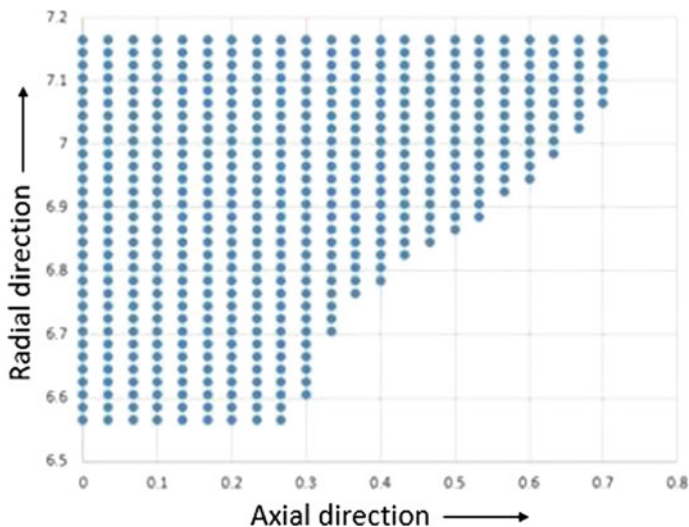
Fig. 3 Typical result of laser welding simulation
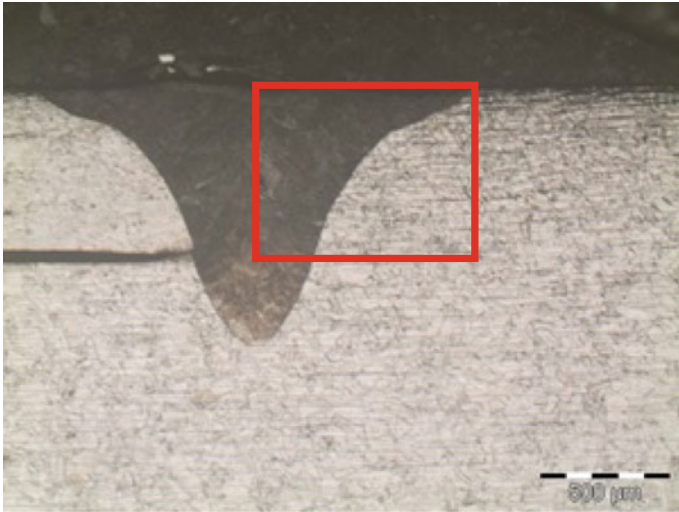
Fig. 4 Macrograph of a laser welded specimen
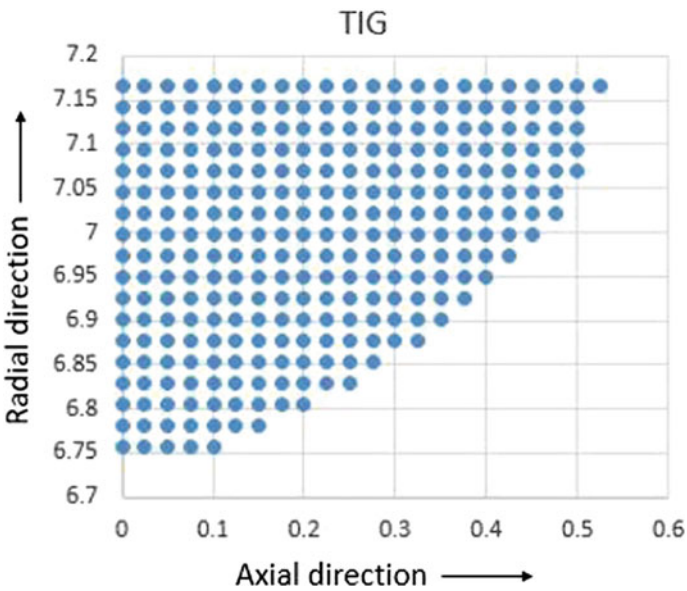
Fig. 5 Typical result of TIG welding simulation

widths at top and bottom (i.e., bead width at OD and ID of clad tube, respectively) are shown in the table alongside those obtained from actual welds. It can be seen that as the power is increased, the bead width at the ID of clad tube increases and
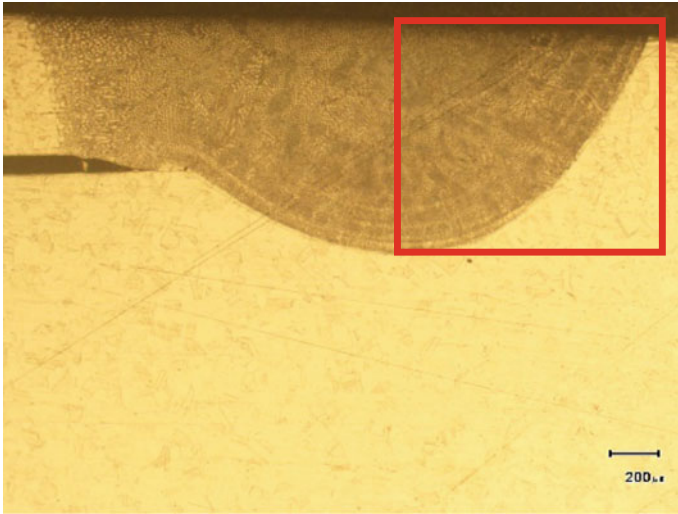
Fig. 6 Macrograph of a TIG welded specimen

the predicted bead widths closely match with experimental results. It can also be observed that for a given increase in power, the increase in bead width at ID (which is a measure of the depth of penetration) is significantly greater than the increase in bead width at OD.
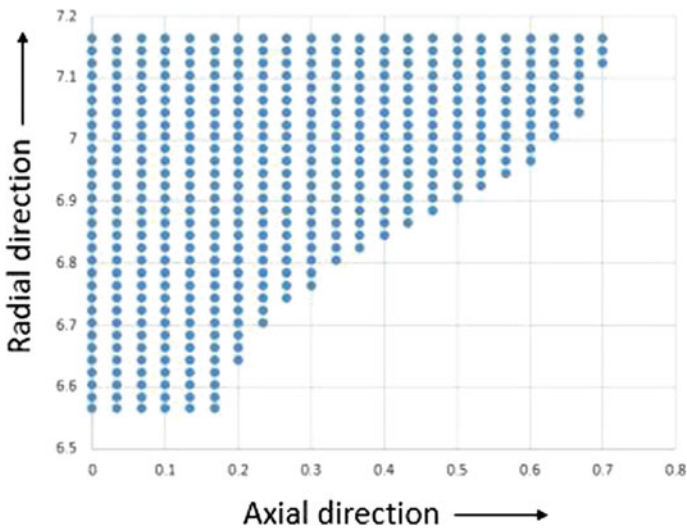
Fig. 7 Weld bead for laser welding with 100 W
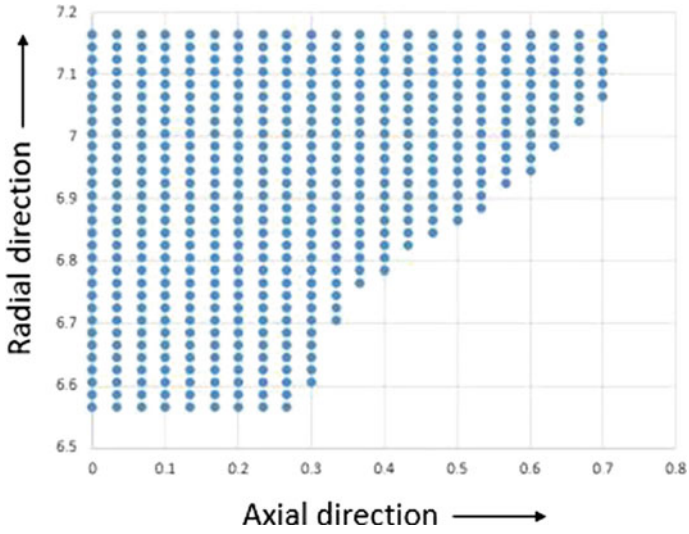
Fig. 8 Weld bead for laser welding with 108 W
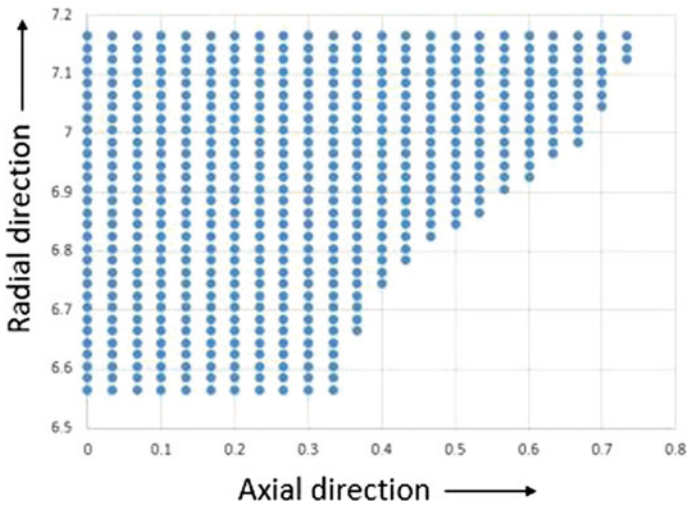
Fig. 9 Weld bead for laser welding with 115 W

This effect is not so predominant in case of GTA welding. Increase in bead width at top and bottom is 0.12 mm and 0.03 mm, respectively, as can be seen from Figs. 9 and 10. This could be the result of penetrating nature of the laser beam while TIG welding involves surface heat input (Figs. 11 and 12).
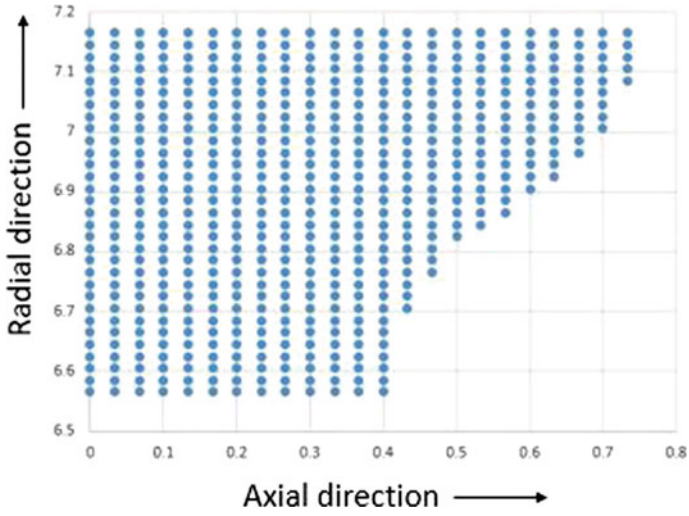
Fig. 10 Weld bead for laser welding with 122 W

Fig. 11 Weld bead for TIG welding with 150 W
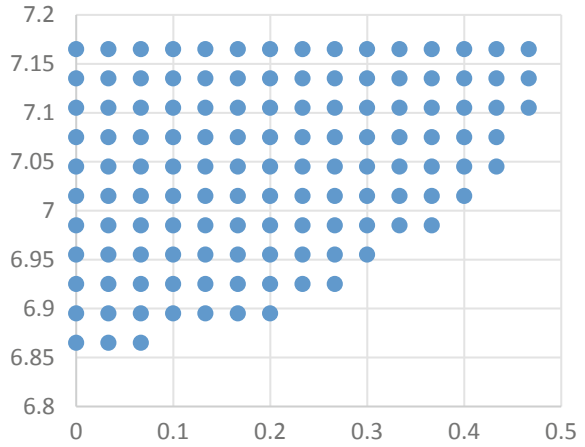
Fig. 12 Weld bead for TIG welding with 170 W
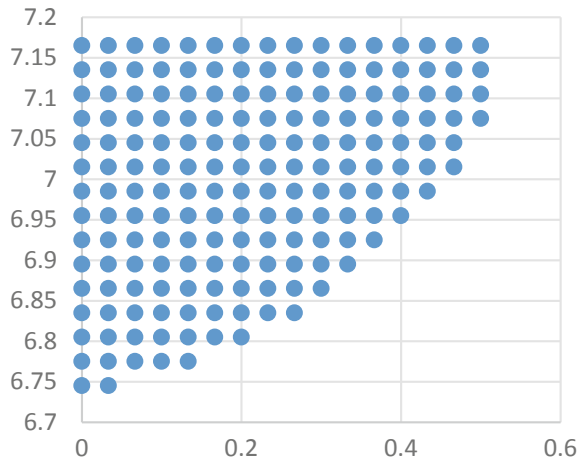
5 Conclusions

1. The developed conduction model employing finite difference method to obtain temperature relations was tested for different average powers and the predicted results match with the experimental results. Although the model did not take into account convection within weld pool, the predicted weld bead shapes are close to the actual welds.
2. The present model considers a 2D approximation of the joint configuration. Further studies could be done by considering the 3D model to account for the effects of welding speed and other parameters like pulse frequency.

References

1. S. Mahadevan, P. Vasantharaja, T. Jayakumar, Modeling, prediction and validation of thermal cycles, residual stresses and distortion in type 316 LN stainless steel weld joint made by TIG welding process. Procedia Eng. **86**, 767–774 (2014)
2. Elisan dos Santos Magalhaes, Ana Lúcia Fernandes de Lima e Silva and Sandro Metrevelle Marcondes Lima e Silva, A GTA welding cooling rate analysis on stainless steel and aluminum using inverse problems. Appl. Sci. **7**, 122 (2017)
3. W.-H. Kim, S.-J. Na, Heat and fluid flow in pulsed current GTA weld pool. Int. J. Heat Mass Transf. **41**, 3213–3227 (1998)
4. V.M. Joy Varghese, M.R. Suresh, D. Siva Kumar, Recent developments in modeling of heat transfer during TIG welding—a review. Int. J. Adv. Manuf. Technol. **64**, 749–754 (2013)

Deformation and Fracture Behavior of Cold-Drawn Pearlitic Steel Wires After Heat Treatment

Suprit P. Bhusare and Balila Nagamani Jaya

Abstract Cold-drawn pearlitic steel wires exhibit exceptionally high strengths in the range of 2–6 GPa due to extensive refinement in interlamellar spacing. They also exhibit a loss in ductility due to the high dislocation density and residual stresses that they accumulate during wire drawing. Hence, they are subjected to stress-relieving annealing treatments during which they undergo further microstructural changes. The aim of this work is to investigate the effect of annealing conditions on the mechanical properties and microstructure of the wires using tension, torsion, and notch toughness tests. The deformation and fracture behavior is then correlated to its evolving microstructure to determine strategies to enhance their damage tolerance.

1 Introduction

Cold-drawn pearlitic steel wires are used in suspension cables, tire beads, conveyors, and engineering springs in automobiles, due to their ability to be drawn into thin wires, while exhibiting exceptionally high strengths and toughness [1]. Manufacturing of pearlitic steel wires is carried out in a series of stages, which includes patenting, rough drawing, fine drawing, stress relieving, and copper coating. They have extraordinary strength but low torsional ductility, which is not desirable for their reliability as support cables in suspension bridges and elevators. For this, the wires are wrapped together as bundles to raise the strength but meanwhile torsion and tension forces act on these wires [2].

Different parameters in the wire drawing process can affect their microstructure and hence their mechanical properties. The microstructure of high-carbon steel wires consists of pearlite, which is a nanocomposite of ferrite and cementite phases. While ferrite is a low-strength ductile matrix phase having a body-centered cubic

S. P. Bhusare · B. N. Jaya (✉)
Department of Metallurgical Engineering and Materials Science, Indian Institute of Technology Bombay, Mumbai 400076, India
e-mail: jayabalila@iitb.ac.in

(BCC) crystal structure, cementite is a high-strength brittle reinforcement of iron carbide (Fe_3C) having an orthorhombic crystal structure. The final wire strength and ductility depend strongly on the morphology of ferrite and cementite present [1, 2]. With extensive wire drawing, the microstructure becomes increasingly nanocrystalline with a high dislocation density, followed by cementite dissolution [3]. The inherent texture and alignment of the ferrite/cementite interfaces along the drawing direction make these wires extremely anisotropic in their fracture behavior as well [4]. Further, these wires are subjected to a post-drawing annealing treatment for stress relief, during which they undergo age softening, loss of lamellar microstructure, and formation and coarsening of spherodized cementite [3]. These treatments include bluing at 300–400 °C and/or hot dip galvanizing at 450 °C [5].

Several studies have reported on the macro and micro-mechanical response of these steels which have been drawn to different extents [3, 4, 6]. The increase in strength is seen to plateau at higher drawing strains due to the dissolution of cementite and supersaturation of C in the dislocations cores of ferrite. This also leads to brittle fracture and low fracture resistance in heavily cold-drawn pearlite [4, 7]. There is a search for strategies to prevent or postpone this event by heat treatments during intermediate stages of wire drawing [8] or by post-annealing [9], some of which have demonstrated limited success. In the present study, we have investigated the correlation between microstructure–mechanical property of cold-drawn pearlite at increasing annealing temperatures well below the austenitization temperature. This will aid in evolving optimized strategies to improve the fracture toughness and overall damage tolerance of these wires while maintaining their strength and anti-corrosive properties.

2   Experimental Methodology

The as-drawn pearlitic steel wires (AD) (from TATA GLOBAL WIRES), having a diameter of 1.6 mm and an equivalent drawing strain of 2.47 were laboratory annealed at three different temperatures (200, 400, and 600 °C) for a time period of 30 min using muffle furnace. This was followed by air cooling at a surface cooling rate of 20 °C/s. The composition of the wires is given in Table 1. Basic microstructural characterization was carried out on polished and etched (4% Nital) wire samples using scanning electron microscopy (SEM) (Zeiss Auriga Compact SEM) at 5 kV. The samples were electropolished with a solution of 20% perchloric acid + 80% methanol at 10 V for 7 s, followed by colloidal silica polishing for

Table 1 Chemical composition of as-drawn sample

Element	C	Mn	S	Si	P
Composition (wt%)	0.82	0.52	0.01	0.19	0.01

45 min for electron backscatter diffraction (EBSD) measurement. EBSD scans were carried out at 30 kV within specimen area of 20 * 20 μm^2 with 15 nm step size.

To find out the stress–strain behavior under uniaxial stress state, tensile tests were performed on Tinius Olsen H25KS 25KN UTM, at room temperature. The test was carried along longitudinal direction at a constant strain rate of 8.33 * 10^{-5} s^{-1}, with a gauge length of 100 mm for all conditions. To calculate notch toughness, the same procedure was followed but with a reduced gauge length of 70 mm. The wire was notched perpendicular to the drawing direction having a/D ratio greater than ∼0.3 using electrical discharge machining. The a/D ratio was measured from the fracture surface micrographs taken after the fracture test. The notch toughness was calculated according to Eq. 1a,1b [4].

$$K = \sigma \sqrt{\pi a} * f(a/D) \tag{1a}$$

$$
\begin{aligned}
f(a/D) =& 1.4408 - 3.6364(a/D) + 19.35(a/D)^2 \\
& - 34.7849(a/D)^3 + 36.8446(a/D)^4
\end{aligned}
\tag{1b}
$$

where σ is the applied stress on the pearlitic steel wire and a is length of the transverse notch produced on the samples. In each case, maximum load converted to far-field stress was used to calculate K_C.

To determine the stress–strain behavior under shear, torsion tests were performed on Instron^{TM} torsion tester (model MT2). These tests were conducted at a maximum torque of 225 N and a constant speed of one rotation per minute. The gauge length was taken as 100 mm for all the conditions. All these tests were carried out at room temperature under ambient conditions.

3   Results and Discussion

The representative stress–strain graphs from tension and torsion tests are shown in Figs. 1 and 2. The 0.2% yield strength (YS) and ultimate tensile strengths (UTS), as well as, strain to failure from all the tests are summarized as a function of annealing temperature in Figs. 3 and 4. There is a plateau or minor increase in YS/UTS initially, followed by a drop, in both tension and torsion tests. This suggests age hardening in low-temperature annealed samples (at 200 °C), followed by age softening in high-temperature annealed samples (at 400 and 600 °C) [9]. The strain to failure remains fairly constant up to 200 °C, and then reduces drastically for the high-temperature annealed samples. Further microstructural characterization done using SEM and EBSD are shown in Figs. 5 and 6. The initial microstructure has a lamellar character with an interlamellar spacing of about 60 ± 10 nm up to 200 °C annealing. It is seen to coarsen for samples annealed at higher temperatures, while also losing the lamellar character. With evident reprecipitation of cementite
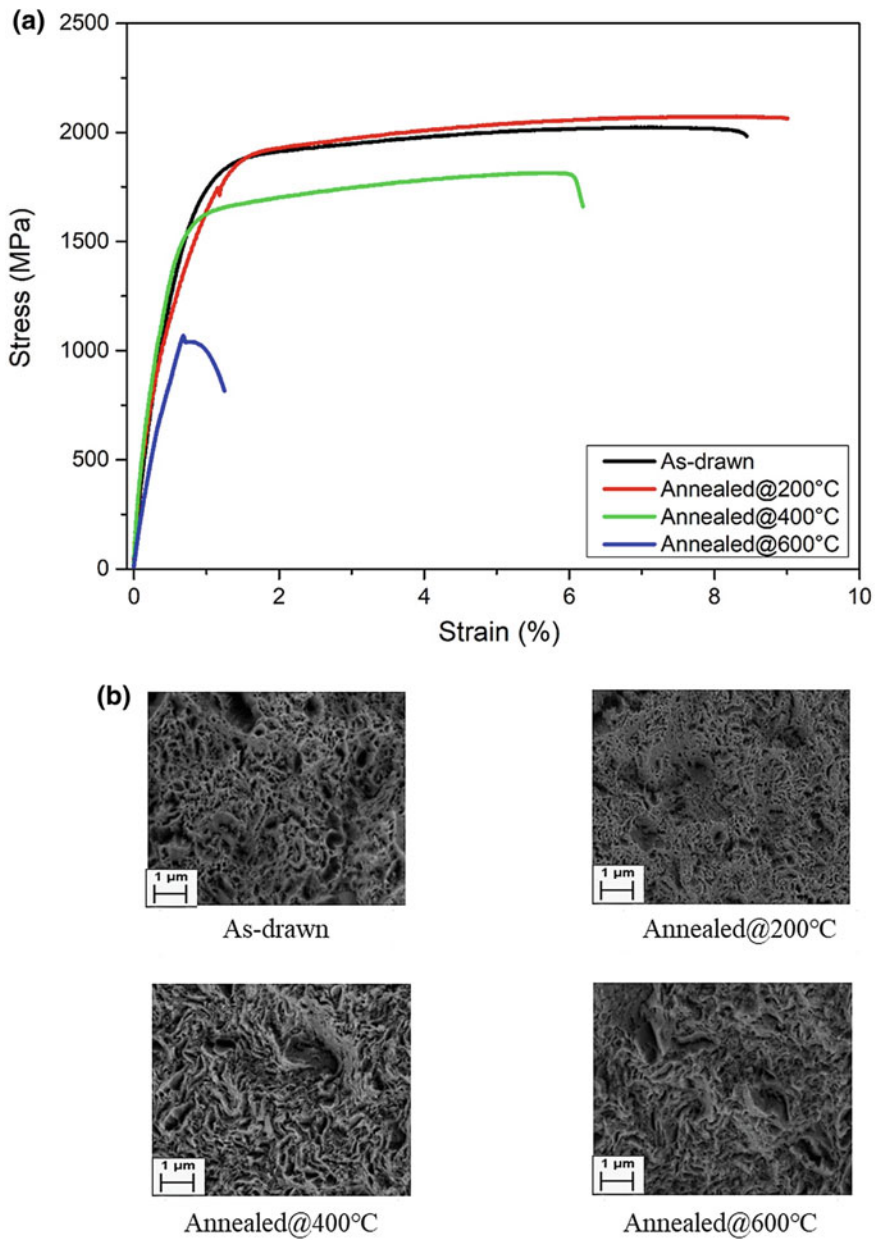
Fig. 1 a Stress–strain graph with b corresponding fracture surfaces under tension
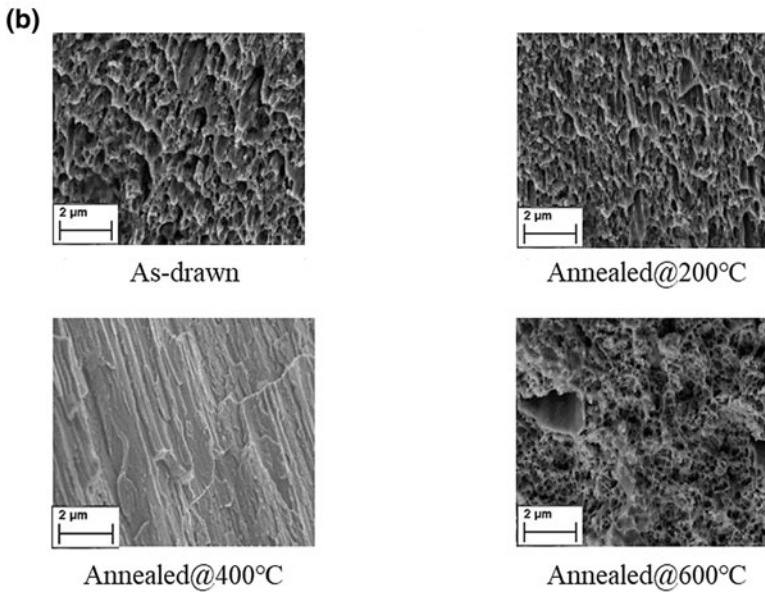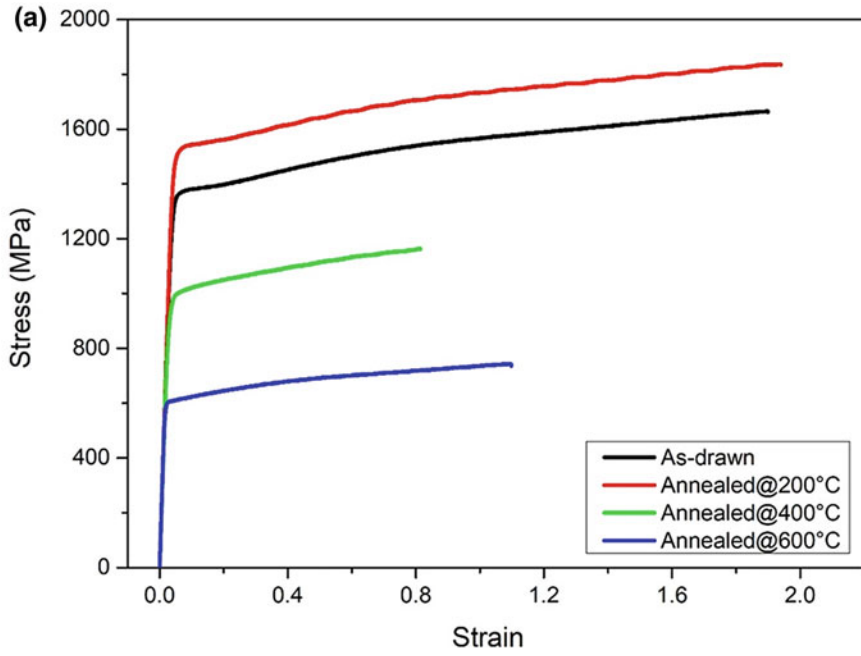
Fig. 2 **a** Stress–strain graph with **b** corresponding fracture surfaces under torsion
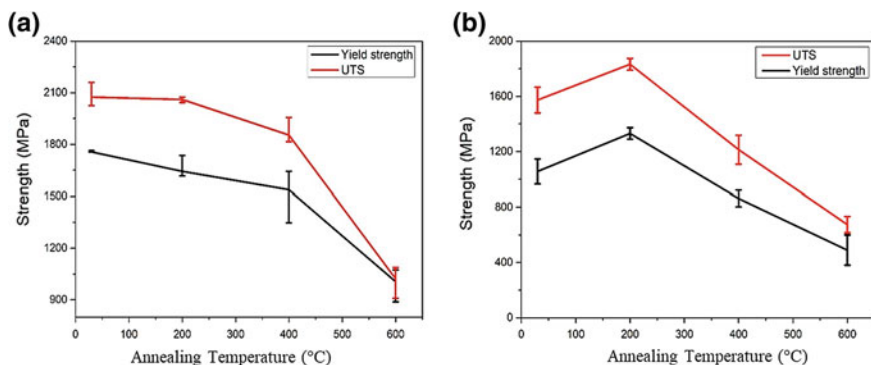
Fig. 3 Strength–temperature graph; **a** under tension, **b** under torsion
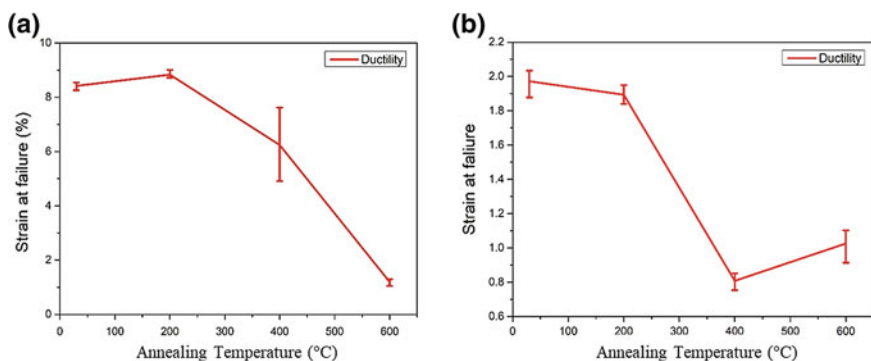
Fig. 4 Ductility–temperature graph; **a** under tension, **b** under torsion

particles at 400 °C and their coarsening into spherodized cementite at 600 °C (Fig. 5d), the grain size increases to 450 ± 50 nm. EBSD maps corresponding to 200 and 600 °C annealed samples are shown in Fig. 6. These maps and corresponding high-angle grain boundary fraction calculated from them show a clear dip in HAGB fraction (less than 50%) at 200 °C indicating recovery, while they increase again at 400 °C, pointing to the initiation of recrystallization, which is more obvious in the 600 °C sample (close to 70%). The lamellar structure is destroyed at higher annealing temperatures, instead, recrystallization and grain coarsening of ferrite, as well as reprecipitation of spherodized cementite and its coarsening are seen to occur.

Considerable cementite dissolution was reported in the as-drawn state in samples of a similar composition and drawing strain in an earlier work [8]. The excess C tends to occupy the dislocation cores in the ferrite, whose density is extremely high after the severe plastic deformation process. Post-annealing microstructural investigations indicate that the initial minor age hardening or plateau in strength occurs
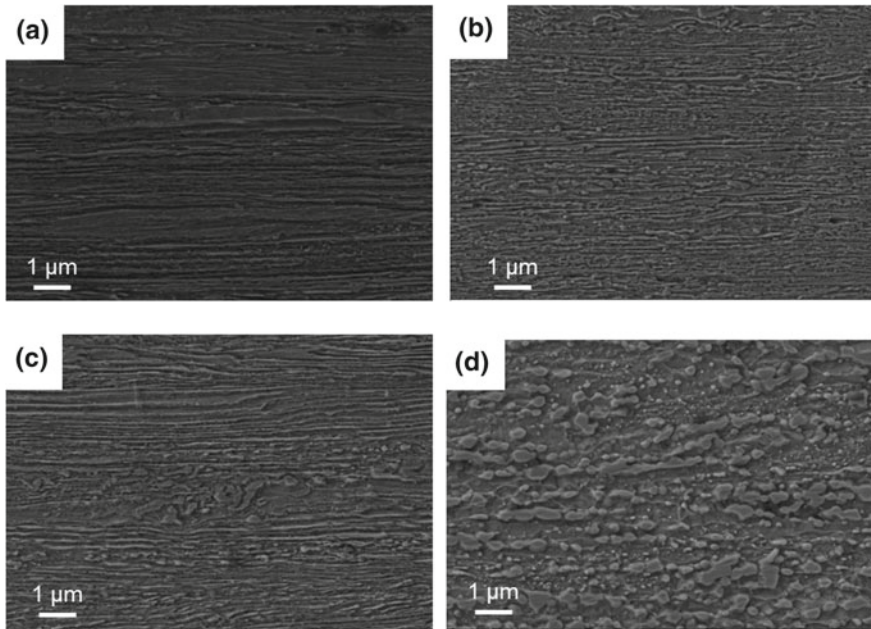
Fig. 5 SEM micrographs; **a** as-drawn, **b** annealed at 200 °C, **c** annealed at 400 °C, **d** annealed at 600 °C

due to the competing mechanisms of recovery in the ferrite and the resegregation of the C to the grain boundaries during low temperature annealing. This was also shown by Li et al. [6] using APT and TEM measurements in steel wires of a similar composition. As the dislocation density decreases during recovery, the C cannot remain dissolved in the ferrite and tends to segregate back to triple junctions and grain boundaries. The peak-aging conditions at 200 °C are followed by age softening that results due to the onset of recrystallization in the ferrite and precipitation and coarsening of the cementite particles. At higher annealing temperatures, the ferrite undergoes further grain coarsening and spherodization of cementite increases. The lamellar structure is destroyed and in its place, we have a heterogeneous microstructure. Although all failures were of cup and cone type in tension and revealed dimple fracture features, there is a significant decrease in the strain to failure at higher annealing temperatures. This is due to the irregular cementite precipitates acting as stress concentration points leading to early onset of void nucleation and cracking, as shown in Figs. 1 and 7. In torsion, this in fact leads to delamination fracture with cleavage fracture features in the 400 °C annealed samples (Fig. 2b).

This is mainly because of the obstruction caused by the reprecipitated cementite particles to the plastic flow in ferrite [10].
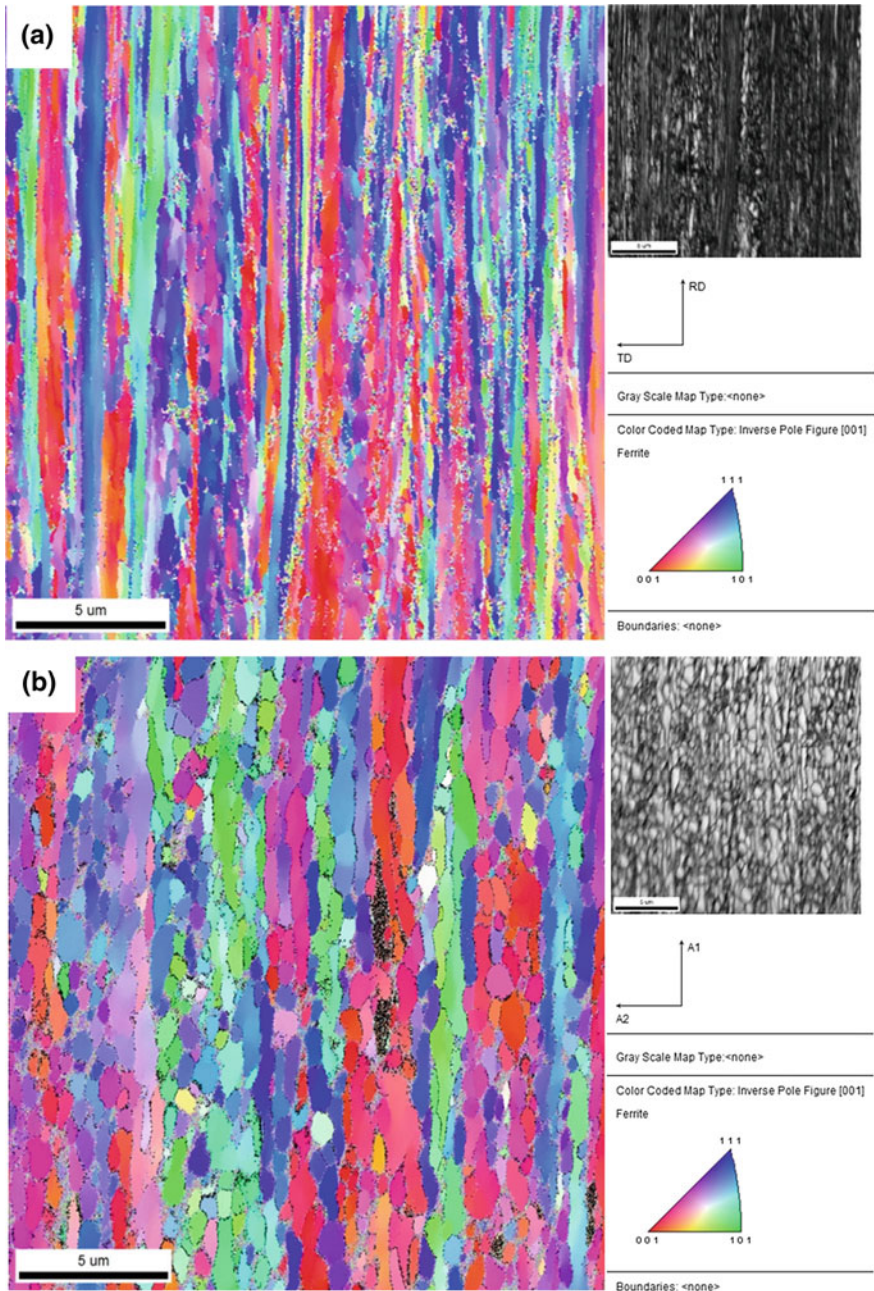
Fig. 6 EBSD analysis; **a** annealed at 200 °C, **b** annealed at 600 °C
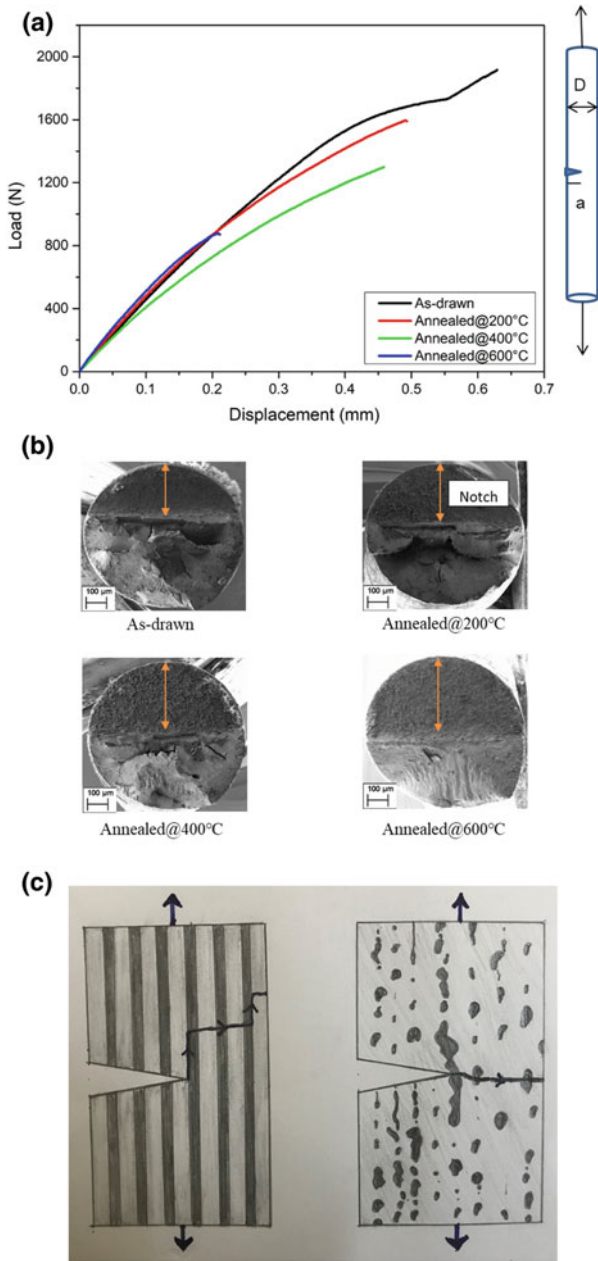
Fig. 7 a Load–displacement graph with **b** corresponding fracture surfaces for notched samples under tension **c** schematic for the propagation of crack of notched samples loaded in the transverse direction
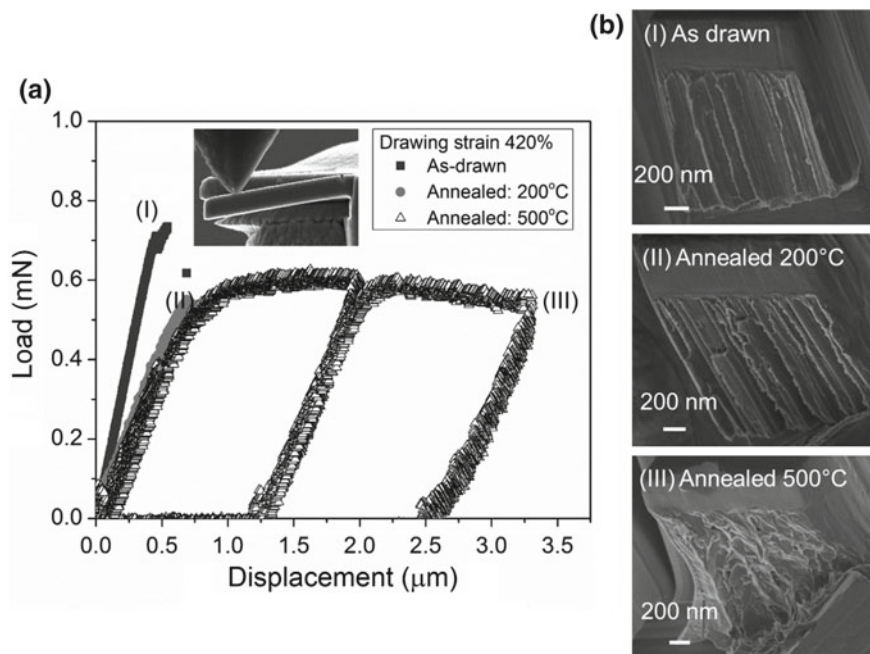
Fig. 8 **a** Fracture behavior of heavily cold-drawn pearlite in the longitudinal direction using microcantilever tests and **b** corresponding fracture surfaces for as-drawn and annealed wires (reproduced with permission from [7])

Further, notch toughness experiments with the notch plane transverse to the drawing direction were carried out to assess the impact of the evolving microstructure on the crack trajectory and overall fracture toughness of the wires. The notch toughness of the as-drawn samples, as well as those annealed at 200 and 400 °C, remained fairly high, in the range of 53 MPam$^{1/2}$ ± 2.4 MPam$^{1/2}$, while it drops considerably to 43.2 MPam$^{1/2}$ ± 1.2 MPam$^{1/2}$, for the sample annealed at 600 °C. The fracture surface also shows distinct differences. While the crack trajectory ahead of the notch tip is rough and wavy for the low-temperature annealed samples up to 400 °C, they become flat, with cleavage fracture features for the one annealed at 600 °C, (Fig. 7). The former shows extensive crack deflections before final failure, while the latter shows quasi-brittle fracture. An earlier work looked at fracture behavior of similar wire samples annealed at low and high temperatures in the longitudinal direction, with the crack plane parallel to the interlamellar boundary between the ferrite and cementite (Fig. 8) [7]. They showed that for as-drawn and low-temperature annealed samples, the fracture toughness along the longitudinal direction was very low, in the range of 4–5 MPam$^{1/2}$, while for high-temperature annealed samples, the fracture toughness recovers significantly with the signature of extensive plastic deformation before failure (Fig. 8). This seemingly opposite behavior in the longitudinal and transverse directions is

explained here. Weak interfaces in one direction help in crack deflection and enhancement of damage tolerance in the perpendicular direction. This is observed from the literature on other lamellar composites with soft–hard material combinations (e.g., bone and nacre) which demonstrate extreme anisotropies in fracture behavior. This counterintuitive notion that weak interfaces are actually better for enhanced fracture resistance is demonstrated in these pearlitic steel wires as well, as shown in the schematic in Fig. 7c. The low-fracture toughness in the longitudinal direction (Fig. 8) results in extensive crack deflection when loaded in the transverse direction for the low-temperature annealed samples, improving their notch toughness significantly. Crack deflection in the transverse direction is completely absent for the high-temperature annealed samples, because of their high toughness in the longitudinal direction. The absence of this extrinsic toughening mechanism at the process zone leads to a lower fracture resistance in them in the transverse direction. Further characterization of the interface structure in terms of TEM and APT will shed more light on the mechanism of fracture.

4   Conclusions

The deformation and fracture behavior of cold-drawn pearlitic steel wires after different stages of annealing, and its correlation to the evolving microstructure was studied. Tension and torsion tests reveal an initial age hardening followed by age softening with increasing annealing temperature. This is evidently due to initial resegregation of C to the grain boundaries during recovery in low-temperature annealed samples, followed by recrystallization, grain growth, and precipitation of spheroidized cementite at higher annealing temperatures. This, in turn, influences the fracture behavior differently, with higher fracture toughness achieved in samples subjected to lower annealing temperatures, due to weak interfaces along the interlamellar boundaries driving extensive crack deflection in the transverse direction. The fracture resistance is reduced at higher annealing temperatures owing to coarse spheroidized particles acting as crack nucleation sites. Therefore, it is proposed that annealing at low temperatures (~ 200 °C) is the optimum recipe for producing high-strength pearlitic wires with improved damage tolerance.

References

1. S. Goto, R. Kirchheim, T. Al-Kassab, C. Borchers, Application of cold drawn lamellar microstructure for developing ultra-high strength wires. Trans. Nonferrous Met. Soc. China (English Ed.) **17**(6), 1129–1138 (2007)
2. D. Raabe, P. Choi, Y. Li, A. Kostka, Metallic composites processed via extreme deformation: toward the, September 2014 (2010)
3. Y.J. Li, P. Choi, S. Goto, C. Borchers, D. Raabe, R. Kirchheim, Evolution of strength and microstructure during annealing of heavily cold-drawn 6.3 GPa hypereutectoid pearlitic steel wire. Acta Mater. **60**(9), 4005–4016 (2012)
4. A. Hohenwarter, B. Völker, M.W. Kapp, Y. Li, S. Goto, D. Raabe, R. Pippan, Ultra-strong and damage tolerant metallic bulk materials: a lesson from nanostructured pearlitic steel wires. Sci. Rep. **6**(1), 33228 (2016)
5. J.W. Lee, J.C. Lee, Y.S. Lee, K.T. Park, W.J. Nam, Effects of post-deformation annealing conditions on the behavior of lamellar cementite and the occurrence of delamination in cold drawn steel wires. J. Mater. Process. Technol. **209**(12–13), 5300–5304 (2009)
6. Y. Li, D. Raabe, M. Herbig, P. Choi, S. Goto, A. Kostka, H. Yarita, C. Borchers, R. Kirchheim, Segregation stabilizes nanocrystalline bulk steel with near theoretical strength. Phys. Rev. Lett. **113**(10), 1–5 (2014)
7. B.N. Jaya, S. Goto, G. Richter, C. Kirchlechner, G. Dehm, Fracture behavior of nanostructured heavily cold drawn pearlitic steel wires before and after annealing. Mater. Sci. Eng. A **707**(September), 164–171 (2017)
8. A. Durgaprasad, S. Giri, S. Lenka, S. Kundu, S. Mishra, S. Chandra, R.D. Doherty, I. Samajdar, Microstructures and mechanical properties of as-drawn and laboratory annealed pearlitic steel wires microstructures and mechanical properties of as-drawn and laboratory annealed pearlitic steel wires. Metall. Mater. Trans. A (August) (2017)
9. D.B. Park, J.W. Lee, Y.S. Lee, K.T. Park, W.J. Nam, Effects of the annealing temperature and time on the microstructural evolution and corresponding the mechanical properties of cold-drawn steel wires. Metals Mater. Int. **14**(1), 59–64 (2008)
10. L. Zhoua, F. Fanga, L. Wang, H. Chen, Z. Xie, J. Jianga, Torsion delamination and recrystallized cementite of heavy drawing pearlitic wires after low temperature annealing. Mater. Sci. Eng. A, 52–60 (2018)

Microstructure, Mechanical, and Magnetic Properties of Cold-Rolled Low-Carbon IF Steel

Siuli Dutta, Ashis K. Panda, Amitava Mitra, Subrata Chatterjee and Rajat K. Roy

Abstract The present work is focused on the effect of annealing on the magnetic, microstructure, and mechanical properties of 50% cold-rolled IF steel. The heat treatment is carried out at different temperatures ranging from 200 to 700 °C for 15 min holding time, to monitor the recovery and recrystallization process. The microstructure is observed by optical microscopy, and analyzed by image analysis software for quantification of recrystallization fractions and grain size. At 200–550 °C temperatures, no significant microstructural change is observed, indicating the dominancy of recovery at these temperatures. It is also confirmed by a nominal variation of hardness and tensile properties at the aforementioned temperature ranges. The magnetic parameters of coercivity (Hc) and remanent (Br) are measured through the electromagnetic sensing device, indicating a significant change during recovery. The recrystallization completion takes place at 660 °C, confirmed by mechanical and magnetic softening.

1 Introduction

The interstitial-free (IF) steel is widely used in automobiles as a material of car body due to a good combination of strength and formability. The manufacturing process of IF steel sheets is combined with hot rolling, cold rolling, and annealing. The annealing is an essential step for work-hardened steel sheets to soften the material. The main softening mechanisms are recovery and recrystallization taking place during annealing treatment [1]. Recovery is related to the annihilation and

---

S. Dutta (✉) · A. K. Panda · A. Mitra · R. K. Roy
Advanced Materials & Processes Division, CSIR-NML, Jamshedpur 831007, India
e-mail: siuli.dutta21@gmail.com

S. Dutta · S. Chatterjee
School of Materials Science and Engineering, IIEST, Shibpur, Howrah 711103, India

rearrangement of dislocation into low-energy configuration, while recrystallization is the formation of new strain-free grains structure and migration of high angle grain boundaries with a low dislocation density [2, 3]. The microstructure controlling is the most important criteria for obtaining desirable mechanical properties of the steel during processing. Microstructural features, viz., grain size, phases, and precipitate size play influential roles in controlling the steel properties. The conventional material characterization methods for the evaluation of microstructures are destructive techniques, such as optical microscopy, X-ray diffractions, scanning electron microscopy, and transmission electron microscopy [4, 5], delaying the total production time. Various electromagnetic nondestructive techniques were introduced over the past five decades for correlating the magnetic parameters to microstructure and mechanical properties of steels [6]. Several grades of ferromagnetic steel under different conditions such as creep, fatigue, residual stress, etc., have been studied by many authors and a good correlation have been observed between the mechanical properties and magnetic parameters like coercivity, permeability, remanent with microstructural features such as precipitates, volume fraction, dislocation density, grain and sub-grain size, hardness, and stress state of the materials [7, 8]. Though, a minimal discussion has been reported for microstructural changes on cold-deformed material by magnetic nondestructive evaluation (NDE). The present work is focused on the magnetic parameters derived from magnetic nondestructive, and its correlation with microstructural and mechanical properties after post-annealing treatment of cold-rolled IF steels.

2   Experimental Details

An industrial produced hot-rolled sheet of 5 mm thickness is 50% cold rolled to achieve 3 mm thickness in laboratory condition. The chemical composition (wt %) of cold-rolled steel sheet is C—0.003, N—70 ppm, S—0.01, Ti—0.002, Mn—0.195, Si—0.002, Cr—0.023, P—0.009, Cu—0.006, and Fe—99.61. The samples were cut in the dimension of (100×25) mm^2, parallel to the rolling direction (RD) of the steel sheet. The post-annealed samples were used for the determination of microstructure, magnetic, and mechanical properties of steel. The samples were put in a tube furnace for annealing at the temperature range of 200–700 °C for soaking time of 15 min and a heating rate of 15 °C/s. Cold rolled and annealed samples were subjected to tensile measurement (INSTRON 8862) using a strain rate of 0.5 mm/min. The mechanical hardness measurement was carried out using macro hardness tester (EconometVH-50MD) at a load of 30 kgf, with a dwell time of 15 s. Magnetic measurements were carried out using a laboratory-based magnetic nondestructive evaluation (Magstar) sensing device, as discussed elsewhere [9]. The magnetic measurement was taken on both sample surface (top and bottom), with an applied sinusoidal field of strength 1500Oe and frequency of 0.05 Hz for magnetic hysteresis loop measurement (MHL). Microstructure analysis was

investigated using an optical microscopy (LEICA DM 2500 M), and average grain size is measured by Leica image analysis software.

3   Results and Discussion

3.1   Microstructure Evolution of Cold Rolled and Annealed Samples

The optical micrographs of cold rolled and annealed samples are depicted in Fig. 1. The cold-rolled microstructure consists of deformed elongated grains of 21 μm size and 2.5 aspect ratio (Fig. 1a). The nucleation of strain-free grain is found at 580 °C, represented by arrow marks, as shown in Fig. 1b. At 600 °C, the large number of strain-free grains are observed (represented by white circular marks), known as partially recrystallized stage (Fig. 1c). The completion of recrystallization takes place after annealing at 660 °C, where equiaxed strain-free grains are found with a grain size of 16 μm and an aspect ratio of 1.31 (Fig. 1d).
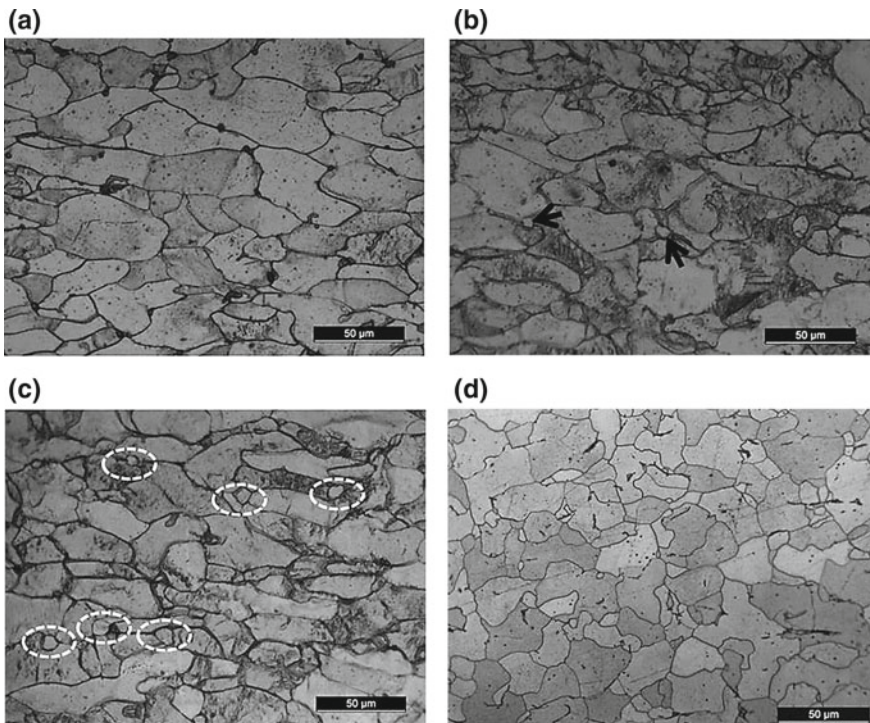
Fig. 1 Optical micrographs of cold rolled and annealed samples: **a** cold rolled 50%, **b** 580 °C, **c** 600 °C, **d** 660 °C/15 min

3.2 Mechanical Behavior

(a) **Hardness measurement**

The hardness changes are explained for cold rolled and annealed samples in Fig. 2. The hardness at post-annealing within 200–400 °C is mostly similar to the cold-rolled sample. With increasing annealing temperature within 400–550 °C, a small (192–183 HV) hardness change is due to recovery. Suddenly hardness value is dropped at a temperature of 580 °C, due to the onset (nuclei) of recrystallization. At 580 < T< 620 °C, hardness value continuously changes due to mechanical softening occurring at high annealing temperature. At T > 620 °C, hardness value is saturated due to the completion of recrystallization at 660 °C with the hardness softening of 95%.

(b) **Tensile measurement**

Mechanical properties of cold rolled and annealed samples are evaluated by the tensile test and the obtained values of yield strength (YS), ultimate strength (UTS), and elongation (EL) are presented in Table 1. The stress–strain curve of cold rolled and annealed samples are shown in Fig. 3a and strength and elongation values are plotted against the annealing temperature (Fig. 3b). The stored energy by the cold-rolling process results in strength (UTS) of 455 MPa and low ductility. Even no changes are observed in the stress–strain data after annealing at 200 °C. Upon increasing of annealing temperature at 580 °C, the start of nuclei in the deformed matrix results in the lowering of strength and increase of elongation (EL) to 18%. Further increasing annealing temperature from 600 to 660 °C, the completion of recrystallization is evidenced with an increase of EL from to 31 and 45%, and the decrease of YS and UTS from 217 to 206 MPa and from 309 to 304 MPa, respectively.

Fig. 2 Hardness variation as a function of annealing temperature
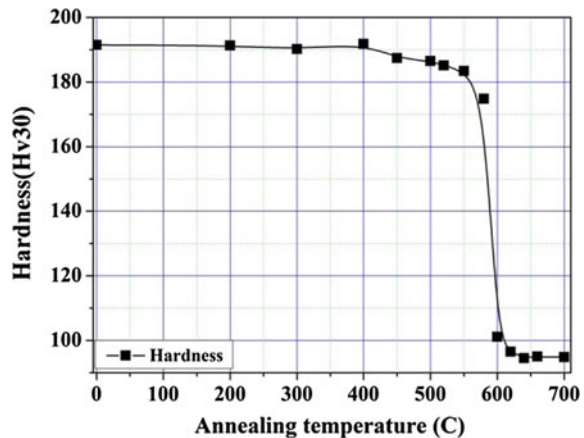
Table 1 Mechanical properties of cold rolled and different annealed specimens

Sample conditions	YS (MPa)	UTS (MPa)	Elongation (EL) %
Cold rolled 50%	455	455	0.41
200 °C/15 min	456	456	1.15
580 °C/15 min	356	395	18
600 °C/15 min	217	309	31
660 °C/15 min	206	304	45
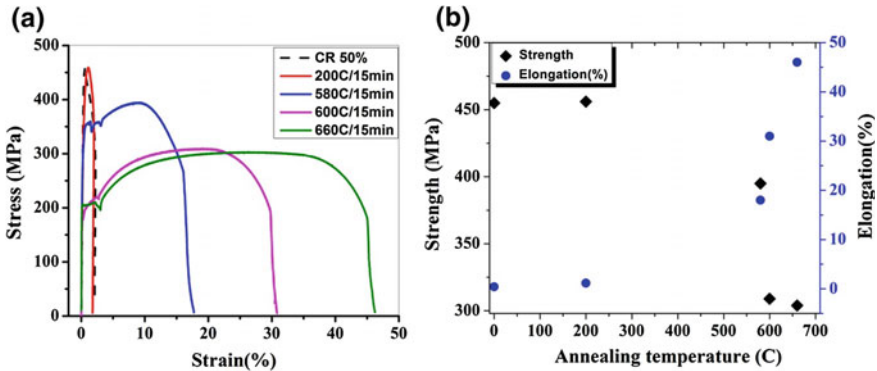
Fig. 3 **a** Stress–strain curves **b** tensile strength and elongation as a function of annealing temperature in cold-rolled IF steel

Figure 4 explains the fracture surface of the cold rolled and annealed samples, a typical ductile fracture with a mixture of large and fine dimples. With the increase of annealing temperature at 580 °C, dimple size increases slightly due to the onset of nucleation (Fig. 4b), and the dimple size becomes larger with the increase of annealing temperature at 660 °C (Fig. 4c). It indicates the ductility enrichment at the completion of recrystallization.

3.3 Magnetic Measurement

Figure 5 shows the variation of coercivity (Hc) and remanent induction (Br) as a function of annealing temperature. The cold-rolled material is magnetically harder with high coercivity and low remanent induction due to the deformed structures of high dislocation density. At low annealing temperature (200–550 °C), the gradual variation of decreasing coercivity and increasing remanent induction takes place with increasing annealing temperature, indicating the enhancement of magnetic softness at this temperature range. It occurs due to annihilation and rearrangement of dislocations at this recovery region. Martinez et al. reported the
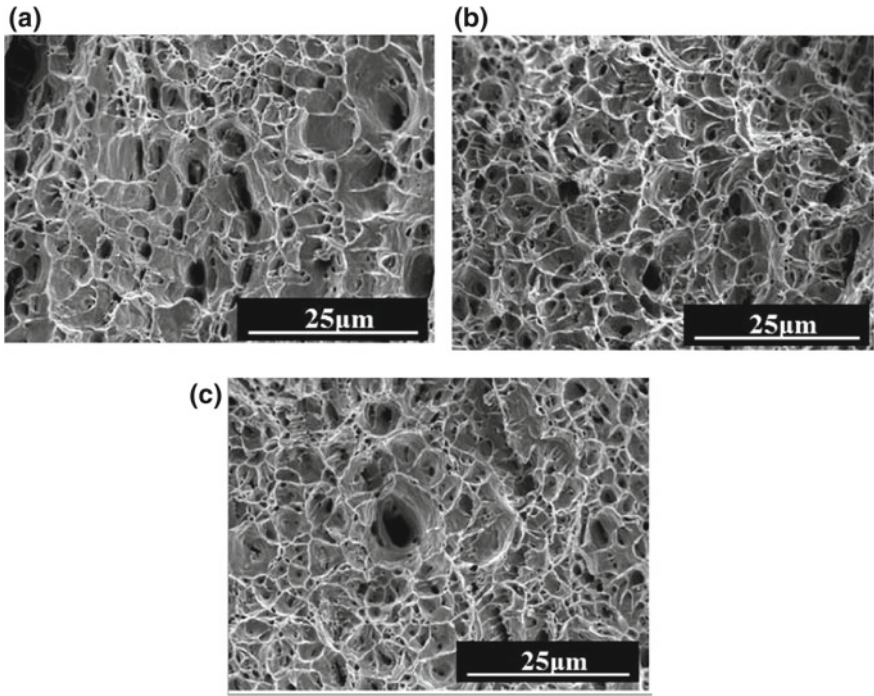
Fig. 4 Fracture surface of the cold rolled and annealed samples: **a** cold rolled 50%, **b** 580 °C, and **c** 660 °C/15 min
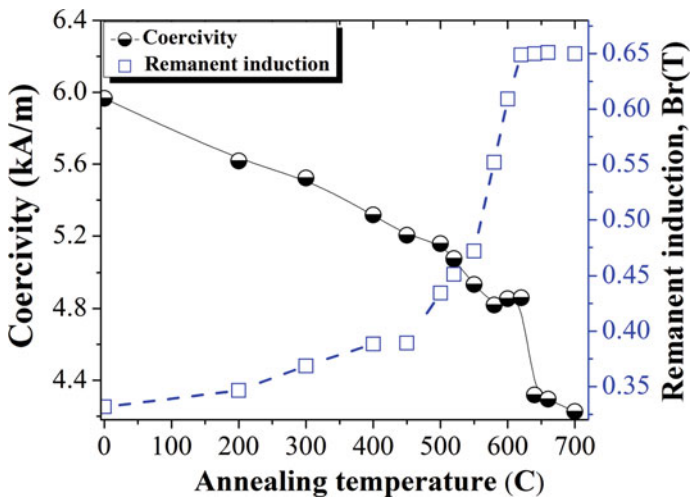
Fig. 5 Variation of magnetic parameters of cold-rolled IF steel as a function of annealing temperature

lowering of coercivity (Hc) with annealing time for low and extra low-carbon steel and discussed the phenomenon according to the linear proportionality of Hc with dislocation density (ρ) (Hc ∝ ρ) [10]. The reduction of dislocation density reduces the restraining sites for the magnetic domain wall movement inside the matrix. Further an increase of annealing temperature (550–620 °C), the coercivity becomes stagnant and a gradual increase of remanent induction owing to the onset of strain-free grains in the deformed matrix [11]. In earlier research, it is found the plateau in the coercivity variation occurs due to the occurrence of strain-induced boundary migration (SIBM) phenomenon before the onset of nucleation [12]. Upon the increase of annealing temperature (T > 620 °C), the high rate of recrystallization causes the lowering of coercivity for the hindrance of domain wall movement. The completion of recrystallization at 660 °C saturates coercivity. A probable growth of recrystallized grains reasons for the stagnancy of remanent induction (Br) and the lowering of coercivity beyond 660 °C.

4   Conclusions

In the present study, the microstructure, magnetic, and mechanical properties of 50% cold-rolled IF steel are investigated at different annealing temperature within (200–700 °C). The conclusions are as follows:

 i. At low annealing temperature, 200 < T< 550 °C, the recovery declines coercivity and intensifies remanent induction. A small change in hardness and tensile properties are observed in this region.
 ii. At high annealing temperature T > 550 °C, the strain-free grain generation corresponds to the decrease in hardness, YS, and UTS and the increase of elongation to 18%.
iii. The completion of recrystallization at 660 °C leads to more decrease of hardness and strength, and about 46% increase of elongation.
 iv. Magnetic nondestructive assessment such as magnetic hysteresis loop (MHL) is a prospective NDE tool to offline measurements for the recovery and recrystallization behavior of 50% cold-rolled IF steel.

References

1. X. Y-bo, Y. Y-mei, L. X-hua, W. G-dong, Prediction of rolling load recrystallization kinetics and microstructure during hot strip rolling. Iron Steel Res. **14**(6), 42–46 (2007)
2. F.J. Humphreys, M. Hatherly, *Recrystallization and Related Annealing Phenomena*, 2nd edn. (2004)
3. D. Raabe, *Recovery and Recrystallization Phenomena, Physics, Models, Simulation, Physical Metallurgy*, 5th edn. (2014), pp. 2291–2397
4. E. Gomaa, M. Mohsen, A.S. Taha, M.M. Mostafa, A study of annealing stages in Al–Mn (3004) alloy after cold rolling using positron annihilation lifetime technique and Vickers microhardness measurements. Mater. Sci. Eng. A. **362**, 274–279 (2003)
5. A.O.F. Hayama, H.R.Z. Sandim, Annealing behavior of coarse-grained titanium deformed by cold rolling. Mater. Sci. Eng. A. **418**, 182–192 (2006)
6. D.C. Jiles, Review of magnetic methods for nondestructive evaluation. NDT Int. **21**, 5 (1988)
7. A. Mitra, J.N. Mohapatra, A.K. Panda, A. Das, N. Narasaiah, D.C. Jiles, Effect of Plastic Deformation on the Magnetic Properties 304 Stainless Steel during Tensile Loading, ECNDT (2006)
8. V. Moorthy, S. Vaidyanathan, Baldev Raj, T. Jayakumar, B.P. Kashyap, Insight into the microstructural characterization of ferritic steels using micromagnetic parameters. Met. Mat Trans. A. **31**, 1053 (2000)
9. R.K. Roy, A.K. Panda, A. Mitra, An electromagnetic sensing device for microstructural Phase determination of steels through non-destructive evaluation, in *Proceeding of 6th International Conference on Sensing Technology*, IEEE Xplore (2012), pp. 226–229
10. A. Martinez-de-Guerenu, F. Arizti, M. Diaz Fuentes, I. Gutierrez, Recovery during annealing in a cold rolled low carbon steel. Part I: kinetics and microstructural characterization. Acta Mater. **52**, 3657–3664 (2004)
11. S. Dutta, A.K. Panda, A. Mitra, S. Chatterjee, R.K. Roy, Magnetic non destructive evaluation of softening of cold rolled low carbon IF Steel. Adv. Mater Res. **1148**, 187–192 (2018). https://doi.org/10.4028/www.scientific.net
12. R.K. Roy, S. Dutta, A.K. Panda, V. Rajinikanth, S.K. Das, A. Mitra, M. Strangwood, C.L. Davis, Assessment of recovery and recrystallisation behaviours of cold rolled IF steel through non-destructive electromagnetic characterization. Phil. Mag. **98**, 21 (2018)

Part IV
Composites

Optimization of Mechanical Characteristics of UHMWPE Composites Using Computational Intelligence

A. Vinoth and Shubhabrata Datta

Abstract Orthopaedic implant materials are chosen considering their favourable mechanical properties and their compatibility to the human body. This study aims at proposing a suitable implant material for the hip joint, one of the most vital synovial joints of the human body. The current practice involves the use of Ultra-High-Molecular Weight Polyethylene (UHMWPE) for acetabular cup replacements in the hip joint. The debris produced from the use of such acetabular sockets may trigger adverse tissue reactions, which may account to osteolysis in the course of time. This study aims at developing new UHMWPE composites with various reinforcements to improve its structural integrity in vivo, and other related performance. This study employs Artificial Neural Network (ANN) and Genetic Algorithm (GA) for the above-said purpose. Numerous experimental data that involves the usage of UHMWPE reinforced with carbon nanotube (CNT) and Graphene are compiled to develop three distinct models for Young's modulus, tensile strength and hardness using ANN. The fundamental relation between the composition and particle sizes of two different reinforcement materials were explored using simulation studies for all three models. The best established ANN model from each mechanical property is considered as an objective function and for optimization using GA with different constraints on the composition of reinforcements in tandem to obtain the appropriate composition and the particle sizes of reinforcements corresponding to the respective mechanical properties that led to designing UHMWPE composites reinforced with multiple nanoparticles having improved performance for its application as orthopaedic implant material.

Keywords Orthopaedic implant material · UHMWPE · CNT · Graphene · Artificial neural network · And genetic algorithm

A. Vinoth (✉) · S. Datta
Department of Mechanical Engineering, SRM Institute of Science and Technology, Kattankulathur, Kancheepuram 603203, Tamil Nadu, India
e-mail: vinoth.a@ktr.srmuniv.ac.in

1 Introduction

Polymers have an extensive range of applications in the field of orthopaedics, owing to their availability in a variety of compositions and forms which shall be instantly contrived into intricate shapes and structures. However, one challenge is their degree of flexibility which does not copiously meet the dynamic mechanical demands of certain implants in orthopaedic surgery [1]. In case of the ceramic or metallic implant materials, the problem of stress shielding exists, owing to stiffness mismatch between the bone and the implant. It has been identified that this effect could be minimized by matching the host tissues with that of the implant stiffness. Contrary to that, low modulus polymer materials also impair the potential use of bone, are not recommended for certain specific orthopaedic applications [2]. Charnley proposed polymers for making acetabular components in hip arthroplasty in the early 1960s, in an attempt to bring down frictional impacts and the metallic wear [3]. Charnley employed polytetrafluoroethylene (PTFE) as replacement of metals for acetabular components. However, extensive clinical research related to PTFE acetabular cups in the total hip replacement prosthesis exposed an alarming degree of wear and distortion [4]. Owing to which Ultra-High-Molecular Weight Polyethylene (UHMWPE) is considered to be a better substitute for PTFE. Even then, it is obvious that the debris produced by the UHMWPE socket, may trigger antagonistic biological tissue responses which may eventually lead to osteolysis. This condition results in the implant misalignment, thus paving way for a revision surgery of the acetabular cup. Owing to these reasons, the necessity for the perfection of the UHMWPE composites has kindled substantial interest in the scientific community, in the recent years. To improve the properties of UHMWPE, several particles have been used by several researchers as reinforcement to make UHMWPE composites reinforced with carbon fibre, carbon nanotube, graphene, hydroxyapatite (HA) nano particles, nano-Al_2O_3, fibre, nano-SiO_2 fibre [5]. Though some of these composites exhibited favourable mechanical properties, there is no unanimity about the composites performance. Hence, it can be said that studies on the polymer nanocomposites gained explicit momentum. Several measures have been formulated in an ardent effect to make UHMWPE composites with multiple nanoparticles since these nanoparticles greatly influence the enhancement of the favourable mechanical properties of these composites. The conventional experimental trial and error methods are quite tiresome, might consume much time and cost. On the contrary, untangling the mathematical links between the particle composition and size with that of its materialistic properties will assist in the computational design of UHMWPE composites that give out optimal results. The complex correlation between the composition, structure and property is challenging to be styled using physical models, data-driven models have been in extensive use in the field of materials engineering [6–9]. This study aims at designing a UHMWPE composite with ideal mechanical characteristics using multiple nanoparticles as reinforcement. Young's modulus, hardness and ultimate tensile strength are used for the purpose. Computational intelligence techniques like ANN

is employed to understand the influence of nanoparticles as reinforcements individually and in tandem on the mechanical properties of the composites. Genetic algorithm (GA), is employed for the optimization of the composite parameters. This is performed by utilizing the developed ANN models as objective functions, as ANN and GA have had multiple tandem applications in materials design wherein ANN is specifically used as objective functions in GA-based optimization [10, 11]. The optimum solutions obtained using GA provide choices for designing UHMWPE composites reinforced with multiple nanoparticles having superior performance for its application in the acetabular cup.

2   Database

153 numbers of data on the ultra-high-molecular weight polyethylene (UHMWPE) composites reinforced with carbon nanotube and graphene were collected from published literature [11–19]. The particle size and composition of the particles are used as seven input variables and three mechanical properties are used as output variables. This record is utilized for developing ANN models to which further assists in analysing the relationship between the input and output variables. ANN models are generated individually for the mechanical properties, viz., Young's modulus, ultimate tensile strength and hardness. Table 1 features the input and output variables, their respective symbols, the minimum and maximum values along with the standard deviations of each of the variables.

Table 1 List of input and output variables with their minimum, maximum, mean and standard deviation value for Young's modulus, ultimate tensile strength and hardness respectively

Variables	Symbols	Min	Max	Mean	Std. dev.
Molecular weight (Million g/mol)	M	1.2	6	3.86	2.03
Carbon nanotube (wt%)	CNT	0	5	0.32	0.76
CNT Fibre length (μm)	l_c	0	30	10.41	12.08
CNT Fibre OD (nm)	d_c	0	55	19.79	19.49
Graphene (wt%)	Grpn	0	5	0.49	1.05
Graphene sheet thickness (nm)	t_g	0	20	1.11	3.12
Graphene sheet length (μm)	l_g	0	40	2.72	9.20
Young's Modulus (MPa)	E	400	1400	899.46	304.55
Ultimate tensile strength (MPa)	UTS	3	101	38.81	22.59
Hardness (GPa)	H	0.047	0.1	0.07	0.02

3   Computational Methods

Two evolutionary algorithms are used in this work. ANN, for the development of data-driven models is used as an objective function for GA for the single-objective optimization of the mechanical properties. The role of ANN and GA are briefly explained as follows.

3.1   Modelling Using Artificial Neural Network (ANN)

Artificial neural network is a model that mimics the role of a human brain. The network of "neurons" constitutes the most significant functional unit in the human brain. The links between these elements determine the comprehensive function of the brain as a whole. The neural networks can be made to perform a desired function by fine-tuning these connections and the element weights. Thus, neural networks can be regulated in such a way that a specific input generates a particular target output. It can be seen that the output and the target values can be compared and adjustments are made until a perfect match is obtained. Characteristically, this results in the usage of multiple input/target pairs in the process of training a network for performing the desired task [20]. This study uses feed forward back propagation ANN with an input layer, one or more hidden layer and an output layer. Each of these layers comprises numerous neurons or nodes. As a general practice, the nodes number in the input and the output layer are taken from the application problem under evaluation whereas the number of nodes in the hidden layer is determined by the user. It should be noted that synaptic connections exist between the nodes of different layers. In this single-layer 7-N-1 type network structure, 7 denotes the input neurons number which is defined by the following parameters: Molecular weight of UHMWPE, CNT (wt%), CNT Fibre length, CNT Fibre OD, Graphene (wt%), Graphene sheet thickness, Graphene sheet length. N denotes the number of hidden neurons which can be extracted through trial and error method only. The output variables employed in this study are Young's modulus (E), ultimate tensile strength (UTS) and Hardness (H). The tan-hyperbolic (tan h) transfer function at the hidden layer and linear transfer function at the output layer are used in developing the interconnections between the layers. The calculated output of the node in the output layer is equated as follows [21].

$$y = \left[\sum_{1}^{j} w_j \left\{ tanh \left(\sum_{1}^{i} w_{ji} x_i + b_j \right) \right\} + b \right]$$

where y denotes the output of the node in the output layer; x_i denotes the ith node input of the input layer and w_{ji} denotes the connective weights between nodes in the inputs and hidden layer. W_j denotes the connection weights between the nodes in the hidden layer and the outputs; and b_j and b are biased expressions that symbolize

the transfer function threshold. The deviation between the intended or projected output and the real output is back propagated for the adjustment of weight and bias values. This study involves the development and training of three distinct ANN models that vary in architecture and the number of hidden units that ranges between 3 and 15 in one hidden layer. The best model is selected for each output and is used for extended study.

3.2 Genetic Algorithm (GA)

When it comes to solving optimization problems, be it constrained or unconstrained, genetic algorithm is the perfect choice, a method that thrusts biological evolution. Three operations, namely selection, crossover and mutation make up a simple genetic algorithm. GA implicates repeated modifications of a selected population of individual solutions. Each phase involves the selection of random individuals from a current population and designates them as parents so that they can be used in the production of the next-generation children. The process continues and after consecutive generations, an optimal solution is evolved [22]. This optimization is done in GA by specifying an objective function on a single- or multi-objective fashion with or without constraints. This study involves the individual optimization of each of the output parameters for their maximum value using single-objective genetic algorithm, by varying the molecular weight of the UHMWPE on the developed ANN model of each output as an objective function with the constraints and on varying the sum of the weight percentages of CNT and Graphene below 2, 4 and 6%, respectively.

4 Results and Discussion

4.1 ANN Modelling

Three different ANN models were built with all input variables and the mechanical properties as output variables. Taking into account the presence of 3–15 hidden nodes, many iterations were executed on the hidden nodes. The least error was picked as the best one for a model. Figure 1 shows the scatter plots for the prediction of the trained ANN models.

Surface plots were developed by fixing the input variables at their mean value and by considering two input variables and one output variable at a time to perceive the influence of input variables upon the final properties. The various input variable pairs are CNT wt%–graphene wt%, CNT wt%–fibre length, CNT wt%–fibre OD, Graphene wt%–sheet length and Graphene wt%–sheet thickness. Figure 2 shows the variation of the various input variables with respect to E. From Fig. 2a, it is
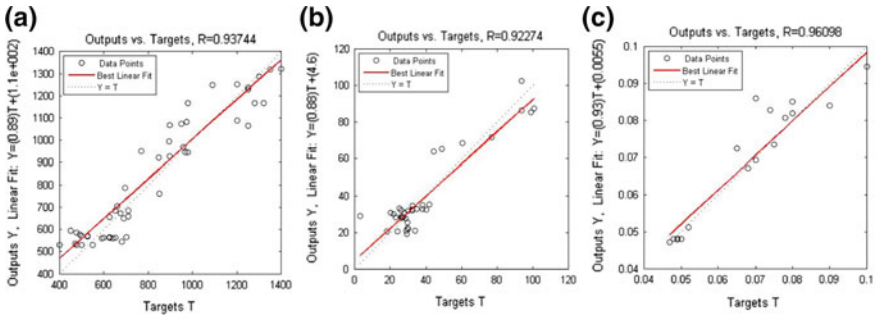
Fig. 1 ANN Model predictions with linear fit for **a** E, **b** UTS and **c** hardness
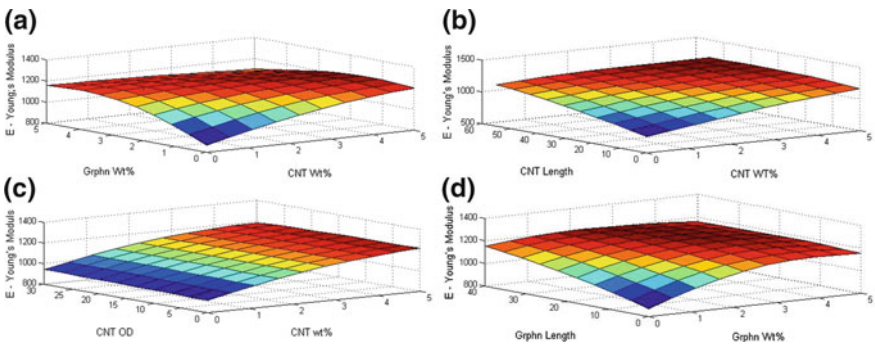
Fig. 2 Surface plots indicates the variation of E with **a** CNT–graphene wt%, **b** CNT wt%–fibre length, **c** CNT wt%–fibre OD and **d** Graphene wt%–sheet length

obvious that as CNT and Graphene wt% increases up to 3%, E also increases but the value of E decreases beyond 5%. Figure 2b indicates that on increasing the CNT fibre length and its wt%, there is an increase in E. Figure 2(c) shows that the value of E increases with increase in wt% and CNT fibre OD. Earlier, Bakshi [12] also proposed that higher the percentage of CNT tends to increase the value of Young's modulus. From Fig. 2d, it is evident that upon increasing the graphene sheet length and its wt%, there is an increase in the value of E.

Figure 3 depicts the surface plots generated from the simulation studies using the ANN model for UTS. From Fig. 3a, it is obvious that as CNT wt% and till 2% of graphene increases, UTS increases but it decreases with further increase in graphene. Figure 3b, indicates that for lesser CNT fibre length and higher wt%, there is an increase in UTS, but it decreases for higher length and higher wt%. Figure 3c shows that there is an increase in UTS with an increase in CNT fibre OD. From Fig. 3d, it is evident that the value of UTS is irregular on the addition of graphene. Earlier, Fan [23] inferred that graphene-reinforced composites indicated enhancement in the elastic modulus and hardness, but their values were uneven with
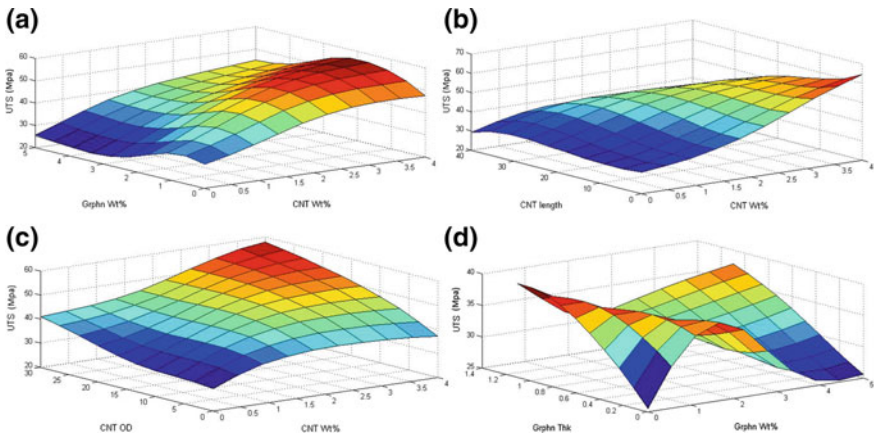
Fig. 3 Surface plots indicates the variation of UTS with **a** CNT–graphenewt%, **b** CNT wt%–fibre length, **c** CNT wt%–fibre OD and **d** Graphene wt%–sheet thickness

graphene contents addition as in tensile strength. Wang [24] have also reported that too high or too low percentage of graphene tends to decrease the value of UTS.

Figure 4 shows the simulation studies based on the ANN model of hardness. From Fig. 4a, it is obvious that as CNT wt% and graphene wt% increases, the value of hardness (H) also increases. Figure 4b indicates that on increasing the CNT fibre length and its wt%, there is an increase in H linearly. From Fig. 4c, we can understand that there is no substantial impact on H with an increase in CNT fibre OD and its wt% till 6 nm and 0.06%, respectively. From Fig. 4d, it is evident that on increasing the graphene sheet thickness and its wt% there is an increase in H. Earlier, Suner [13] has reported that higher the percentage of graphene tends to increase the value of hardness.
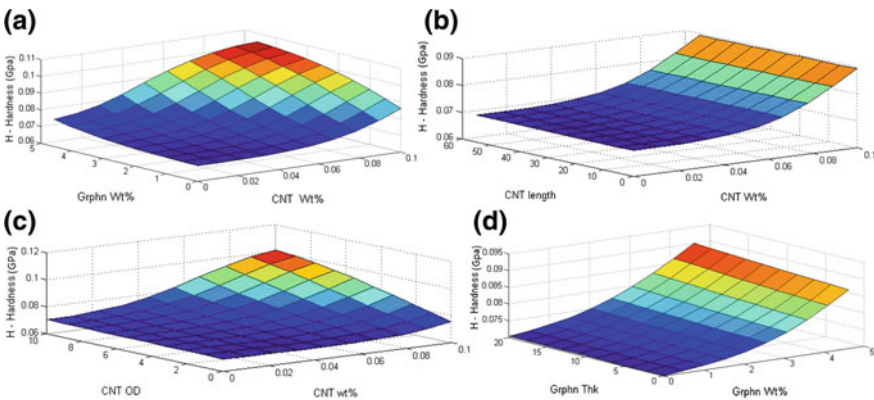
Fig. 4 Surface plots indicates the variation of H with **a** CNT–graphenewt%, **b** CNT wt%–fibre length, **c** CNT wt%–fibre OD and **d** Graphene wt%–sheet length

4.2 Single-Objective Optimization

Optimization was carried out using single-objective genetic algorithm for maximization of E, H and UTS separately with the developed ANN models as objective functions and the subsequent constraints were applied while performing optimization studies using GA for several times upon altering the molecular weight of UHMWPE between 2.5 and 4.5 (million gm/mol). This range was chosen from the collected data and the GA parameters, so that the results are not confined to suboptimal region. The summation of the compositional parameters like the nanoparticles weight percent is constrained at 4 wt%, considering the fact that the higher content of particles can cause irregularity of the mechanical properties which was observed from the simulation results. Table 2 lists the genetic algorithm parameters which are kept constant during optimization. The range of input parameters obtained from the optimization study using GA for different molecular weights are listed in Table 3.

It is evident that the optimum values obtained from GA have a substantial difference in values of each input parameters except fibre length and OD of CNT and sheet thickness of graphene for the optimization of "E". There is no significant difference in values of each input variables for the optimization of "H" except the

Table 2 Value of GA parameters

Parameters	Values
Number of generation	500
Number of population	500
Probability of mutation	0.1
Probability of crossover	0.95

Table 3 Range of input variables for different molecular weight

Properties	Molecular weight (million g/mol)	CNT			Graphene		
		wt%	Fibre length (μm)	Fibre OD (nm)	wt%	Sheet Thickness (nm)	Sheet length (μm)
Young's modulus —E	2.5	1.77	2	55	2.23	1	14.46
	3.5	1.99	2	55	2.01	1	6.30
	4.5	3.35	2	55	0.65	1	4
Ultimate tensile strength— UTS	2.5	2.88	30	33.83	0.87	0.78	–
	3.5	2.77	30	11.51	1.23	0.14	–
	4.5	2.52	30	11.50	1.48	0.11	–
Hardness —H	2.5	0.091	10	55	3.909	1	40
	3.5	0.084	10	55	3.916	1	40
	4.5	0.071	10	55	3.928	1	40

weight % of CNT and graphene. It is evident that there is a significant difference in all the input variables except fibre length of CNT for the optimization of UTS. From the table, it is evident that for achieving maximum Young's modulus, the preferred wt% of CNT and Graphene are almost equal. Whereas for maximizing UTS desired level of CNT is more, and for maximizing hardness more graphene is preferred.

5   Conclusions

The findings from this study are listed as follows:

- The ANN models are impeccable as objective functions for optimization using GA in a single-objective fashion.
- Computational intelligence based study using ANN and GA is found to be capable for developing a predictive model for the different mechanical properties to design UHMWPE composites with various nanoparticles as reinforcements in tandem.
- Graphene and CNT do not have a similar effect on the different mechanical properties.
- There is a scope for further experimentation with the optimum results obtained from the GA.

References

1. S. Ramakrishna, Compos. Sci. Technol. **61**, 189–224 (2001)
2. S.M. Lee, *Orthopaedic Composites* (VCH Publishers, New York, 1991), pp. 74–87
3. Z.D. Mikić, J. Acta Chir. Iugosl. **60**, 9–13 (2013)
4. J. Blumm, Int. J. Thermophys. **31**, 1919–1927 (2008)
5. J.F. Mano, Compos. Sci. Technol. **64**, 789–817 (2004)
6. S. Datta, Int. Mater. Rev. **58**(8), 475–504 (2013)
7. S. Sinha, J. Mater. Des. **46**, 227–234 (2013)
8. T. Bhattacharyya, Mater. Sci. Eng. A **565**, 148–157 (2013)
9. S. Kumar, *Neural Networks—A Classroom Approach* (Tata McGraw-Hill Publishing Company Limited, New Delhi, 2004)
10. I. Mohanty, Comp. Mater. Sci. **50**, 2331–2337 (2011)
11. P.-G. Ren, Macromol. Mater. Eng. **297**, 437–443 (2012)
12. S.R. Bakshi, Compos. Part A. **38**, 2493–2499 (2007)
13. S. Suner, Compos. Part B. **78**, 185–191 (2015)
14. R. Manoj Kumar, Compos. Part A-Appl. S. **36**, 62–72 (2015)
15. A. Chih, Tribol. Int. **116**, 295–302 (2017)
16. A.V. Maksimkin, Compos. Part B. **94**, 292–298 (2016)
17. Hivabahrami, Adv. Polym. Tech. **0**, 21508 (2015)

18. Y. Wang, Compos. Sci. **65**, 793–797 (2005)
19. A.V. Maksimkin, J. Alloy. Compd. **536S**, 538–540 (2012)
20. H. Demuth, M. Beale, *Neural Network Toolbox User's Guide Version* (The Mathworks, Inc., 2013)
21. S. Ganguly, Appl. Soft. Comput. **46**, 260–266 (2016)
22. *Global Optimization Toolbox User's Guide* (The Mathworks, Inc., 2016)
23. H.L. Fan, Biomacromolecules **11**, 2345–2351 (2010)
24. Y. Wang, Carbon **49**, 1199–1207 (2011)

Machining of Kevlar Aramid Fiber-Reinforced Plastics (K-1226) Using Solid Carbide Step Drill K44

R. Nagaraja, T. Rangaswamy and K. R. Channakeshava

Abstract Composite materials have found increasingly wider application in aircraft, space vehicles, offshore structures, piping, electronics, automobiles, boats, and sporting goods due to their superior properties and high strength to weight ratio. Among these, the aerospace industry is using composite materials for numerous components and structures. Many of these components require machining during its fabrication. Machining of composite materials is difficult to carry out due to the damage being introduced into the component in the form of delamination, fiber pullout, and local cracks. Further, rapid wear development in the cutting tool also takes place during the machining of composite materials. Conventional machining processes such as turning, drilling, or milling can be applied to composite materials, provided proper tool design and operating conditions are adopted. Kevlar Aramid Fiber-Reinforced Plastics (K-1226) is widely used in the industry due to its chemical stability at high temperature and resistance to wear. Studies show that conventional cutting of this laminates is extremely difficult due to the frictional force developed via thermal expansion of substrate material. This has restricted the Kevlar component usage. In this regard, the present paper describes the effective method for drilling K-1226 material with reduced machining defects and tool wear using solid carbide step drill K-44. The drilling operation is carried out on K-1226 composite laminates of thicknesses 8, 10, and 12 mm. K 44 step drill with varying cutting speed and feed rate are used for drilling holes. The drilled laminates are examined using C-Scan analysis. The results show dramatic improvements of the tool performance and surface quality. K44 is a single shot drill, designed to replace

R. Nagaraja (✉)
Helicopter MRO Division, HAL, Bangalore, Karnataka, India
e-mail: nagaraja65@yahoo.com

T. Rangaswamy
Department of Mechanical Engineering, Government Engineering College, Hassan, Karnataka, India
e-mail: ranga.hassan@gmail.com

K. R. Channakeshava
Smt L.V. Government Polytechnic, Hassan, Karnataka, India
e-mail: channakeshava.k.r@gmail.com

three conventional drills having diameters 6.5, 8.5, and 11.5 mm. The tool geometry detail of K44 drill is also presented in the paper.

Keywords K1226 · K44 · Radial drilling machine · C-Scan

1 Introduction

Kevlar fiber, due to its unique properties such as high strength to mass ratio and modulus, has become very popular as reinforcement in composite materials and its application has grown considerably. However, for enhancing Kevlar fiber composite usage in various applications, a proper characterization is very important. Many researches have been conducted in recent years, for characterization of Kevlar fiber and its composites [1]. Serval researchers have worked on hybridizing fibers to obtain new properties [2]. The attempts to machine Kevlar aramid fiber-reinforced plastics (KFRP) with conventional cutting tools have proven to be extremely difficult. This has somewhat restricted the material's usage by negating the advantages of its high strength to weight ratio and fatigue tolerance. The effects of various machining parameters such as workpiece temperature, cutting speed, and tool geometry on the machinability of KFRP are presented and analyzed in [3]. The curing process for Kevlar 49-Epoxy composites is evaluated in [4]. The effect of cutout hole on multilayer Kevlar-29/epoxy composite laminated plates was investigated for various fiber orientation angles. The ultimate load of failure for each Kevlar-29/epoxy-laminated plates had been determined and specified in [5]. Kevlar-reinforced polymer composites are always difficult to machine, characterized by poor, fuzzy surface finish with partially pulled out and crushed fibers.

In machining, drilling is essentially required to join different structures. But the drilling of Kevlar laminates may lead to different kinds of damages like surface delamination, fiber pull out, high surface roughness, local cracks. Many researches attempted to minimize machining problems and show that the defect is influenced by the selection of the machining parameters, the geometry of cutting tool tip and the nature of its material [6, 7]. The importance of drill point angle in high speed drilling is discussed in [8]. For drilling the composite laminates, the tool geometry is a very important parameter to be considered, the design of solid carbide step drill K44 is developed in [9]. The application of various drill bits have been reviewed in [10] and the influence of various factors on drill performance is experimented in [11]. The aim of this work is to study the performance of solid carbide step drill K44 to drill hole on K-1226 laminates and to reduce delamination factor.

2 Experimental Procedure

2.1 Design of Solid Carbide Step Drill (K44)

Table 1 shows the chemical composition used for solid carbide drill (K44) used for drilling the holes in KFRP composite laminates.

2.2 Tool Geometry of Solid Carbide Step Drill

The tool geometry of the solid carbide step drill K44 used for drilling composite laminate is shown in Fig. 1. It is consists of three steps at a distance of 20 mm (L1), 40 mm (L2), 30 mm (L3), and overall length including the holder is 110 mm having the diameters of d1 = 6.5 mm, d2 = 8.5 mm, and d3 = 11.5 mm, respectively. The point angle of 140º, rake angle of 4º, helix angle of 30º, gash angle 55º, and axial angle 4º is considered. The margin of 8% and land of 85% for each diameter is achieved.

2.3 Kevlar (K-1226) Laminate Fabrication

2.3.1 Materials Properties

Material properties of Kevlar fabric selected for the study is as tabulated in Table 2.

A batch of 913-54%-1226 Kevlar composite with a cross-ply 0º/90º or 45º stacking sequence Kevlar composites of 42 layer is produced by first preparing (13 + 13 + 14) layer specimen each layer of 0.18 mm thickness using hand lay-up technique. The pre-compaction is carried out in autoclave for 1 h at a temperature of 75º and 2.5 bar pressure. Three pre-compacted laminates are combined and carbon layer of 0.4 mm thickness is placed on top and bottom of the pre-compacted laminate as shown in Fig. 2a. Vacuum bagging is carried out at room temperature for one hour under −0.8 bar and further Autoclave processing is carried out as per

Table 1 Chemical composition of solid carbide drill (K44)

Material	Percentage
Tungsten (W)	87.3
Carbon (C)	8.59
Phosphorus (P)	2.37
Sulfur (S)	1.17
Chromium (Cr)	0.29
Nickel (Ni)	0.19
Iron (Fe)	0.1
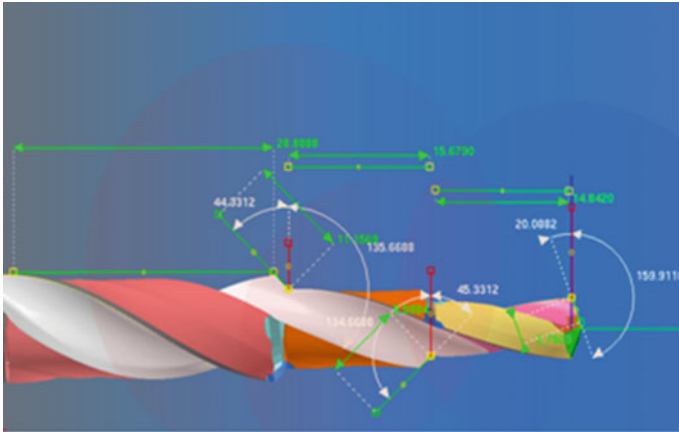
Fig. 1 3D model of solid carbide step drill K44

Table 2 Kevlar composite material specification

Material	Kevlar fabric
Material specification	913-54%-1226
Prepreg area weight (gsm)	245–275
Resin content (%)	51–57
DSC—Differential Scanning Calorimetry (Ts) (°C)	139–147
DSC—Differential Scanning Calorimetry Peak Temp (Tp) (°C)	149.5–56.5
Thickness in mm (T)	0.18 mm
Weight in gms/m^2	6240

the cure cycle dwell temperature between (75º, 60 min) and (135º, 30 min, and 5 bar) respectively. The specimen is cooled at 60º temperature for 3–4 h. The same process is adapted to achieve 10 and 12 mm thickness of Kevlar laminates (Fig. 2). The autoclave curing chart is shown in Fig. 3.
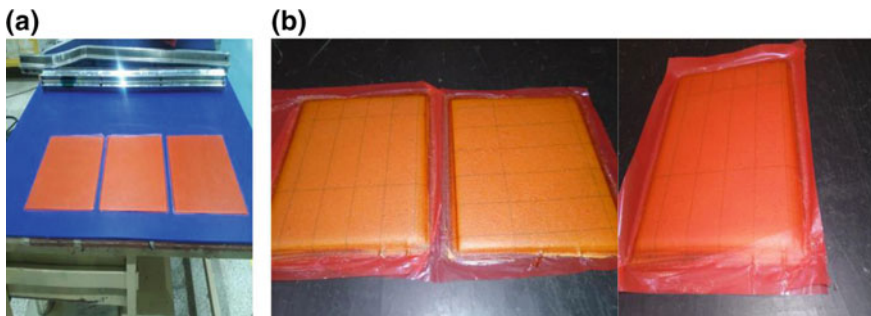
Fig. 2 **a** Pre-compacted Kevlar Laminates and **b** cured laminate thickness of (8, 10, and 12 mm)
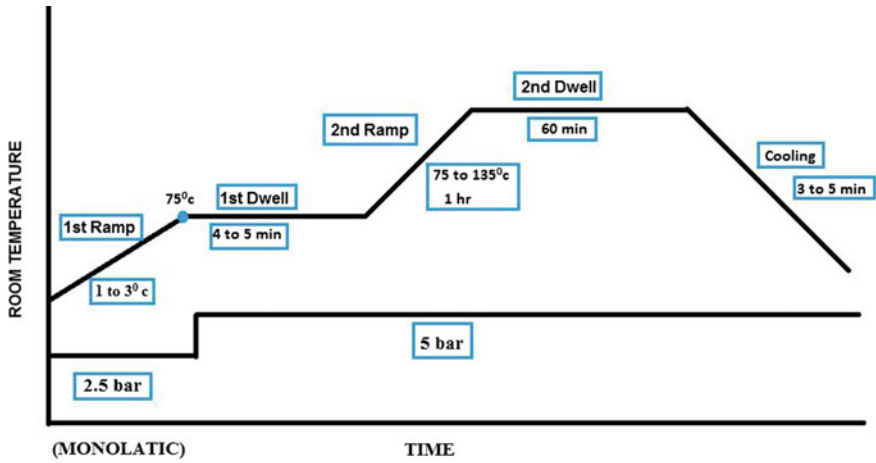
Fig. 3 Autoclave curing chart

2.3.2 Experimental Setup

The specimen is set on the jig, the solid carbide step drill is fixed to the spindle of radial drilling machine as shown in Fig. 4a. With varying spindle speed and feed rate, the drilling operation is carried out to drill holes of 11.5 mm diameter on a Kevlar laminate as in shown in Fig. 4b for varying thickness of 8, 10, and 12 mm using a solid carbide step drill. The drilled laminates are tested for delamination factor using ultrasonic C-Scan.
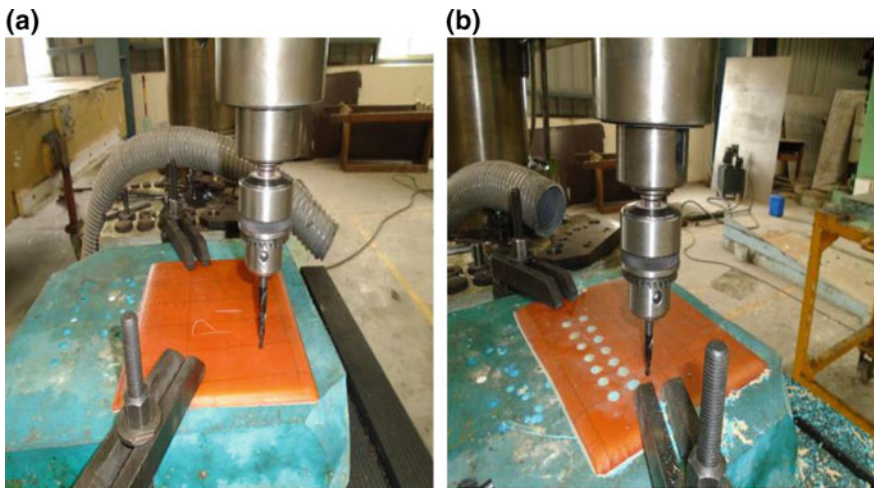
Fig. 4 **a** Kevlar Laminates setup and **b** drilled holes on Kevlar Laminates

3 Results and Discussion

The present study uses C-Scan analysis to determine the quality of holes drilled on the basis of presence of internal and surface defect, cracks, and delamination factor. The C-Scan analysis of the Kevlar laminate drilled for varying thickness of 8, 10, and 12 mm at a feed rate of 0.125, 0.25, and 0.5 mm/rev are shown in Fig. 5. Each image was computationally processed to identify and characterize the region of interest, namely hole, delaminated, and non-delaminated regions. The hole region corresponds to the central area, the delaminated region consists of a white border around the machined hole and the non-delaminated regions are colored areas located outside the damaged area. From these figures, it can be clearly observed that there is no delamination occurred at lower feed rates and cutting speed, whereas at
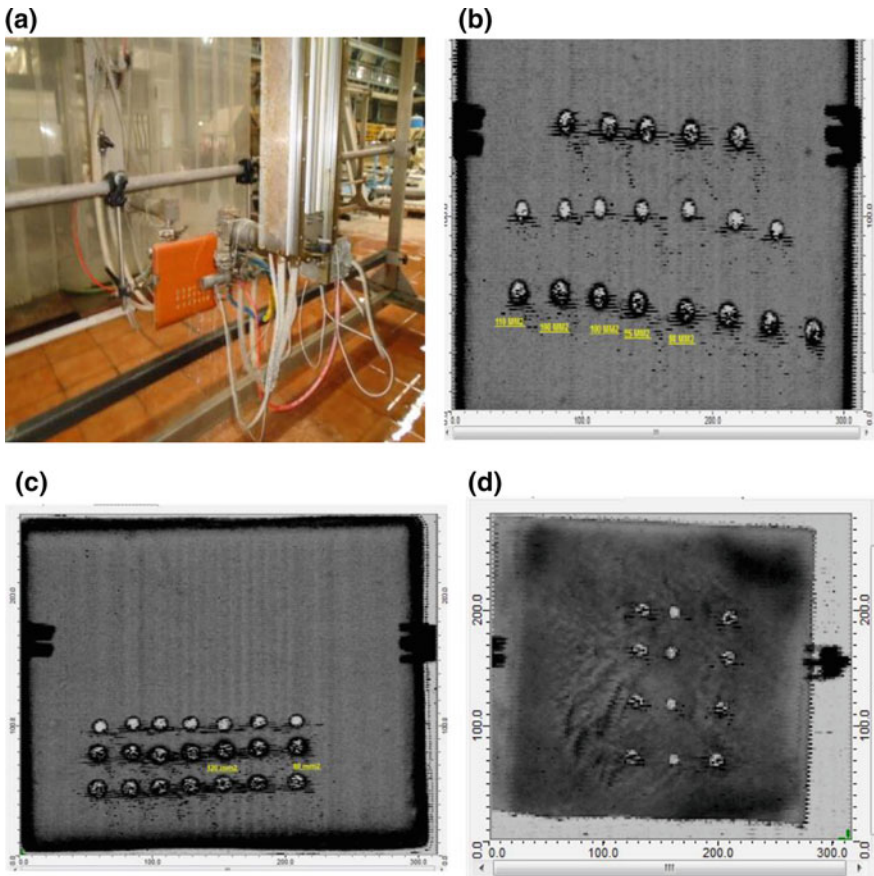
Fig. 5 a C-Scan setup. **b** Analysis for 8 mm thicknes. **c** Analysis for 10 mm thickness. **d** Analysis for 12 mm thickness

Fig. 6 a Kevlar Laminate 8 mm graph of Feed rate mm/rev versus cutting speed m/min. **b** Kevlar Laminate 10 mm graph of feed rate mm/rev versus cutting speed m/min. **c** Kevlar Laminate 12 mm graph of feed rate mm/rev versus cutting speed m/min

(a) kevlar laminate 10 mm thickness

	1	2	3	4	5	6
Feed rate (F) mm/rev.	0.125	0.125	0.25	0.25	0.5	0.5
Spindle speed (n) rpm	500	630	900	1250	1400	1400
Cutting speed (Vc)m/min	18	22	32	45	50	50

(b) kevlar laminate 12 mm thickness

	1	2	3	4	5	6
Feed rate (F) mm/rev.	0.125	0.125	0.25	0.25	0.5	0.5
Spindle speed (n) rpm	500	630	1000	1250	1400	1600
Cutting speed (Vc)m/min	18	22	35	45	50	57

(c) kevlar laminate 12 mm thickness

	1	2	3	4	5	6
Feed rate (F) mm/rev.	0.125	0.125	0.25	0.25	0.5	0.5
Spindle speed (n) rpm	500	630	1000	1250	1400	1600
Cutting speed (Vc)m/min	18	22	35	45	50	57

higher feed rates and cutting speed, top edge delamination was observed for 12 mm thickness Kevlar laminate. Therefore, it is concluded that the solid carbide step drill K44 designed was found more suitable for drilling the composite material. The graph of feed rate versus cutting speed and spindle speed is shown in Fig. 6.

4 Conclusion

From the performance study of solid carbide step, drill K44 has a diameter of 11.5 for machining of Kevlar K1226, and it concludes that:

Machining of higher thickness K1226 laminate with lower feed rate and higher spindle speed, cutting speed leads to delamination-free holes.

Whereas machining of higher thickness K1226 laminate with higher feed rate, spindle speed, and cutting speed leads to a minor top edge delamination which is in the acceptable range.

For lower thickness K1226 laminate with higher feed rate, spindle speed, and cutting speed, no delamination occurred.

Hence, it is be concluded from the study that the solid carbide step drill K44 was found suitable for machining of Kevlar K1226 laminates of 8, 10, and 12 mm thickness.

References

1. T.J. Singh, S. Samanta, Characterization of Kevlar fiber and its composites: a review. Mater. Today (Article) **2**(4–5), 1381–1387 (2015)
2. N. Shaaria, A. Jumahata, M.K.M. Razifa, *Impact Resistance Properties of Kevlar/Glass Fiber Hybrid Composite Laminates*, Jurnal Teknologi, May 2015
3. D. Bhattacharyya, D.P.W. Horrigan, A study of hole drilling in Kevlar composites. Mater. Manuf. Process. J. **8**(6) (1993)
4. A. Chennakesava Reddy, Evaluation of curing process for Kevlar 49-Epoxy composites by mechanical characterization designed for brake liners. Int. J. Sci. Res. **4**(4) (2015, April)
5. A.R. Abu Talib, A.A. Ramadhan, A.S. Mohd Rafie, R. Zahari, Influence of cut-out hole on multi-layer Kevlar-29/epoxy composite laminated plates. Mater. Des. J. **43**, 89–98 (2013, January)
6. J.A. Bencomo-Cisnero et al., Characterization of Kevlar-29 fibers by tensile tests and nanoindentation. J. Alloy. Compd. **536**, S456–S459 (2012). Elsevier
7. A.M. Abrao, P.E. Faria, P. Reis, J.P. Davim, Drilling of fiber reinforced plastics: state of the art. J. Mater. Process. Technol. **186**, 1– 3 (2007). Elsevier
8. K. Palani Kumar, A.J. Campos Rubio, M. Abroa, A. Esteves Correia, J. Paulo Davim, Influence of drill point angle in high speed drilling of glass fiber reinforced plastics. J. Compos. Mater., 1–14 (2008)
9. T. Rangaswamy, R. Nagaraja, *Design and Development of Solid Carbide Step Drill K44 for Machining of CFRP*, PFAM-XXVI, Chonbuk National University, Jeonju, Republic of Korea, October 2017
10. Hochenga, H. Tsao, The path towards delamination-free drilling of composite materials. J. Mater. Process. Technol., **167**, 251–264

11. D.F. Galloway, Some experiments on the influence of various factors on drill performance. Trans. ASME **79**, 191–237 (1957)
12. W.D. Callister, D. Rethnish, *Materials Science and Engineering: An Introduction* (New York, NY USA, 2010).
13. A. Mishra, Overview study of the machining of composite materials. Impact J. **4**(7) (2016, July)

Performance Enhancement of UHMWPE with Surface Functionalized Multiwalled Carbon Nanotubes/Graphite

P. Sarath Kumar, K. Sai Narendra Reddy, D. Unnikrishnan and Meera Balachandran

Abstract Carbon nanostructures have been effectively used to reinforce polymers due to their excellent mechanical properties. This paper investigates the thermal and mechanical properties of ultra-high-molecular weight polyethylene UHMWPE nanocomposites reinforced with acid-modified multi-walled carbon nanotubes (MWCNT) and graphite. The UHMWPE nanocomposites were prepared by melt mixing at 200 °C. The test specimens were compression moulded at 215 °C and 7.36 MPa and mechanical and thermal properties were studied with respect to nanofiller content. Evaluation of mechanical and thermal properties of the nanocomposites showed that the addition of up to 1% MWCNT to the UHMWPE significantly improved the tensile and flexural properties by 30%. In the case of graphite, tensile properties decreased while flexural property increased. While the thermal properties such as specific enthalpy and percentage of crystallinity increased with nanofiller content. These observed results are attributed to the nanofiller content as well as the dispersion of the nanofiller in the polymer, which was substantiated by morphological analysis using transmission electron microscopy. However, at higher concentration of carbon nanofillers, both mechanical and thermal properties showed a slight decline due to the formation of agglomerates.

P. Sarath Kumar · K. Sai Narendra Reddy · D. Unnikrishnan
Department of Mechanical Engineering, Amrita School of Engineering, Amrita Vishwa Vidyapeetham, Coimbatore, India

P. Sarath Kumar · M. Balachandran (✉)
Centre of Excellence in Advanced Materials and Green Technologies (CoE – AMGT), Amrita School of Engineering, Amrita Vishwa Vidyapeetham, Coimbatore, India
e-mail: b_meera@cb.amrita.edu

M. Balachandran
Department of Chemical Engineering and Materials Science, Amrita School of Engineering, Amrita Vishwa Vidyapeetham, Coimbatore, India

Nomenclature

U	Unfilled UHMWPE
UG-0.5	UHMWPE with 0.5 wt% of graphite
UG-1	UHMWPE with 1 wt% of graphite
UG-1.5	UHMWPE with 1.5 wt% of graphite
UC-0.5	UHMWPE with 0.5 wt% of carbon nanotube
UC-1	UHMWPE with 1 wt% of carbon nanotube
UC-1.5	UHMWPE with 1.5 wt% of carbon nanotube

1 Introduction

Polymer nanocomposites have a wide range of applications and advantages over conventional polymers and composites [1]. The properties of polymer nanocomposites can be tailored by altering the ratio of the polymer matrix and reinforcing elements as well as size, shape and type of nanoreinforcements [2, 3]. Ultra-high-molecular weight polyethylene (UHMWPE) is a semi-crystalline polymer having unique properties like very low coefficient of friction, low wear, high toughness, high impact resistance, low dielectric constant and high thermal conductivity that makes it suitable for a variety of applications like bearings, gears, liners, wear strips, fixtures, armour and radar domes, joint prosthesis, etc. [4, 5]. These applications require mechanical strength in addition to specific properties. The mechanical properties can be improved by either altering the polymer structure like crystallinity and cross-linking or by reinforcing the polymer with fillers [6]. Nanosized fillers are attractive options for reinforcement as they provide the large specific surface area necessary for polymer–filler interactions that tremendously improve polymer properties at filler contents much lower than conventional micro fillers. Carbon-based nanofillers like carbon nanotubes and graphite have unique properties. Carbon nanotubes (CNTs) have exceptional properties like very high tensile strength, stiffness, electrical conductivity, flexibility, elasticity and thermal conductivity, large aspect ratio and low thermal expansion coefficient making them a promising reinforcement for composites [7]. In modern engineering, both single-walled (SWCNT) and multi-walled (MWCNT) are used reinforcement in polymer composites [8, 9]. Most of the research is available UHMWPE–CNT nanocomposites focus on the tribological properties prepared by ball milling technique [10]. Graphite is a crystalline allotrope of carbon having layered arrangement of thick sheets of carbon. Its layered structure providing high surface area, aspect ratio and specific strength make graphite nanoparticles a potential reinforcement for high-strength composites [11]. Generally, carbon nanomaterials

have a tendency to agglomerate in a polymer matrix and the properties of nanocomposites depends on how well the nanotubes are dispersed in the polymer [12].

Arash Golchin et al. carried out an investigation of the tribological behaviour of UHMWPE reinforced with multi-walled carbon nanotube and graphene oxide (GO) in water-lubricated sliding contacts. It is found that irrespective of the treatment, GO/MWCNT reinforced composites invariably showed lower friction and higher wear resistance in comparison to the unfilled UHMWPE. This was mainly attributed to the lubricating action of the carbonaceous nanofillers in water-lubricated contacts [13]. Silvia Suñer et al. studied the wear rate, size and volume distributions, bioactivity and biocompatibility of the wear debris generated from UHMWPE/Multi-walled carbon nanotube (MWCNT) nanocomposites for total joint replacement. The studies showed that the addition of MWCNTs led to a significant reduction in wear rate and wear particles from the UHMWPE/MWCNT nanocomposite had lower osteolytic potential compared to those produced from the conventional polyethylene [14]. Investigations on nanotribological behaviour of UHMWPE with graphene nanoplatelet (GNP) reinforcement showed that as GNP content increased, the coefficient of friction decreased while wear resistance decreased by more than four times [15]. A. Bhattacharyya et al. made a detailed study of the improved tensile strength and creep resistance properties UHMWPE reinforced with graphene [16].

This paper investigates the morphological, thermal and mechanical properties of UHMWPE nanocomposites reinforced with acid-modified multi-walled carbon nanotubes and graphite nanocomposites prepared by melt compounding.

2   Experimental

2.1   Materials and Preparations

The UHMWPE used in the work was in powder form, with a molecular weight of 2–6 million amu [HIDEN, YUHWA Korea Petrochemical Ind. Co. Ltd.]. Carbon nanotube used as reinforcement was acid (-COOH) modified MWCNT with length 1–10 micron, outer diameter 5–10 nm and surface area 330 m^2/g [United Nanotech Innovations, Bangalore, India]. Graphite (Nano 27) having 99% carbon, surface area 250 m^2/g and lamella thickness index 10–11 was sourced from Asbury carbons, Asbury, USA.

UHMWPE–MWCNT/Graphite nanocomposites were prepared by melt mixing in a two roll mill at 200 °C at 40–50 rpm with varying weight percentages of MWCNT/Graphite (0, 0.5, 1 and 1.5%). The nanocomposite test specimens were compression moulded at 215 °C and 7.36 MPa.

2.2 Characterization

The tensile properties were evaluated as per ASTM D638 on INSTRON 4502Universal Testing Machine (UTM) at a crosshead speed of 1 mm/min. The flexural strength and modulus were evaluated on a 3 point UTM with a crosshead speed of 1.25 mm/min as per ASTM D790. The average value obtained for 5 specimens are reported. Differential scanning calorimetry was done on DSC Q20 V24.10 Build 122 in a nitrogen atmosphere at 10 °C/min in the temperature range −100–200 °C. Transmission electron micrographs of the nanocomposites were obtained from Jeol/JEM 2100 transmission electron microscope.

3 Results and Discussion

3.1 Morphology

The dispersion of MWCNT and nanographite in UHMWPE was analysed with transmission electron microscope. From the TEM images in Fig. 1, it was observed that both MWCNT and graphite were well dispersed/exfoliated in at nanofiller content of 0.5 and 1 wt%. In nanocomposites containing 1.5 wt% CNT/Graphite, dispersion as well as agglomeration was observed. One of the reasons for formation of agglomerates is the van der waals force between the CNT particles. At higher nanofiller content the interparticle distance is less and the van der waals force is greater causing agglomeration [17].

3.2 Mechanical Properties

The mechanical properties of UHMWPE nanocomposites are presented in Figs. 2 and 3. In CNT-reinforced UHMWPE, the tensile strength and modulus increased with increasing CNT content. The mechanical properties of the nanocomposite depend on dispersion state of the nanofiller in polymer matrix and the interfacial bonds. As evident from the TEM micrographs in Fig. 1b and d MWCNT was evenly dispersed in UHMWPE. The uniform dispersion of MWCNT and the resulting polymer–filler interfaces and interfacial interactions ensure efficient transfer of mechanical load/stress applied to the MWCNT–UHMWPE interface. The distribution of MWCNT efficiently hindered the chain movements during deformation resulting in improved tensile modulus. At 1.5%, as evident from the TEM images, slight agglomeration caused the interfacial area and interfacial interactions to decrease. The agglomerates of MWCNT also act as macro-particle like centres of friction and stress concentration. Hence, at 1.5% MWCNT, there was slight reduction in mechanical properties.
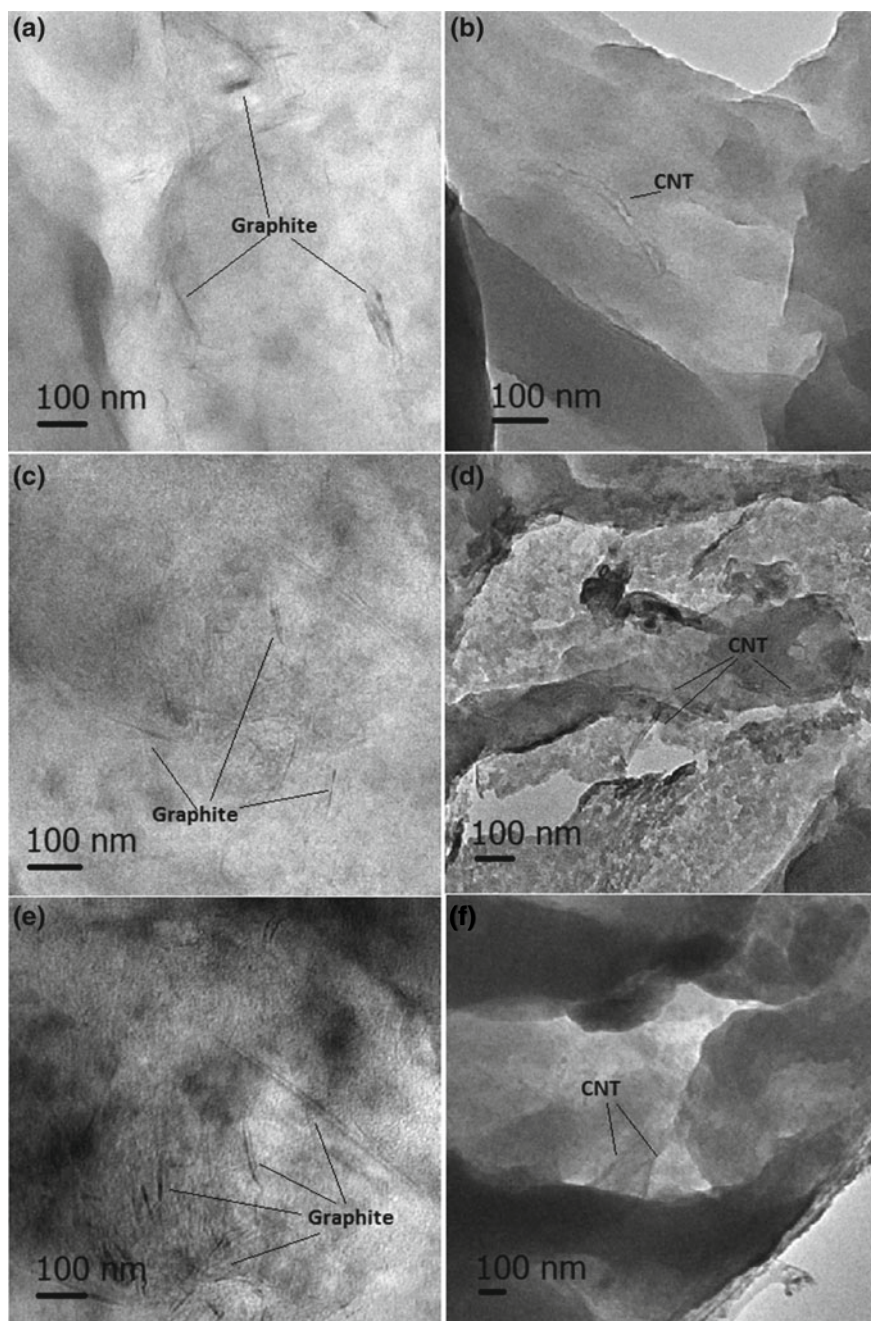
Fig. 1 TEM images (100 nm) of **a** UG-0.5 **b** UG-1 **c** UG1.5 **d** UC-0.5 **e** UC-1 **f** UC-1.5
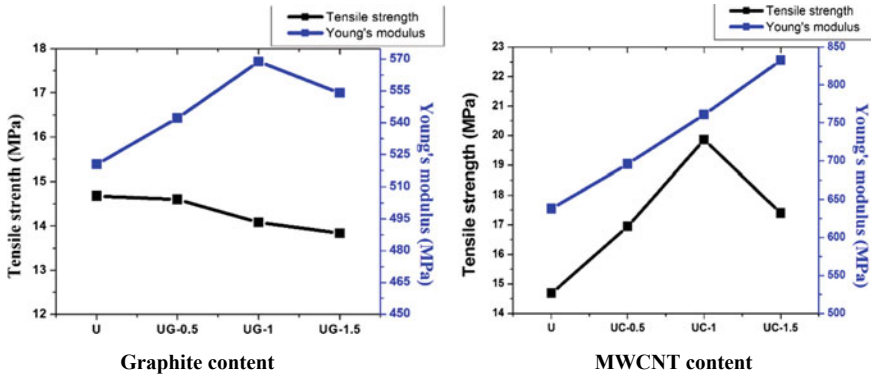
Fig. 2 Tensile properties of UHMWPE–graphite/MWCNT composites
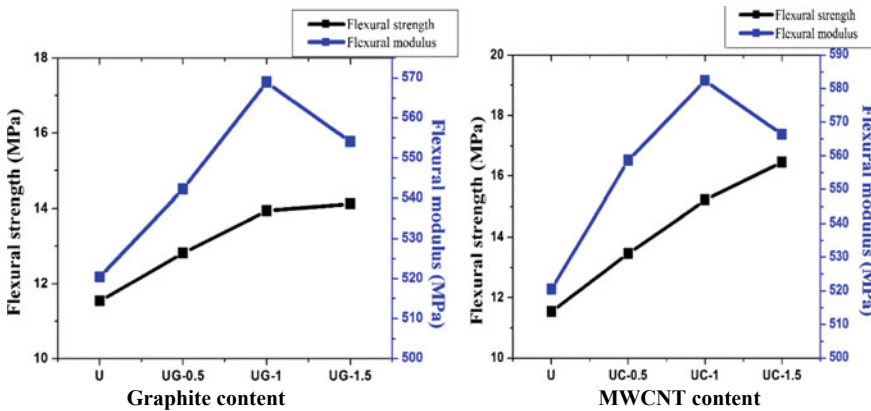
Fig. 3 Flexural properties of UHMWPE–graphite/MWCNT composites

The tensile strength of UHMWPE decreased marginally with the addition of graphite with a 5.7% decline for 1.5% of graphite. In several polymers, reduction in tensile properties with addition of graphite filler has been attributed to its restrictive effect and deformation of molecular chains [18].

Flexural modulus was calculated by the following equation:

$$\text{Flexural modulus} = \frac{FL^3}{4wdh^3} \tag{1}$$

where F = load applied on the middle of the beam

　　L = distance between the two outer supports

　　w = width of the beam

　　d = deflection due to the load

h = height of the beam

Flexural strength of UHMWPE was found to be 11.54 MPa. Figure 3 shows the flexural strength of UHMWPE increases with the addition of MWCNT/Graphite. The content of MWCNTs (0.5–1.5 wt%) enhances and increase the flexural strength from (11.54 MPa for the UHMWPE to 16.45 MPa). Addition of 1.5 wt% of MWCNT leads to increase the flexural strength by 42.54% compared with the UHMWPE and 20% increase by Graphite. Addition of carbon nanofillers creates attractive polar forces and van der Waals bonding between polymer chains. Hence it will increase the constraints between filler/UHMWPE chains and polymer chains itself. The nanofillers attributes a restrictive effect over the UHMWPE by deformation of their molecular chains and restricting the motion [19].

3.3 Thermal Properties

DSC gives us the results of melting, crystallization temperatures, specific enthalpies and degree of crystallinity. These results are tabulated in Table 1:

The percentage of crystallinity was calculated using the following equation:

$$\% \, crystallinity \, = \, ((\Delta Hm - \Delta Hc)/(\Delta Hm \, ^\circ)) * 100 \qquad (2)$$

where ΔH_m and ΔH_c are the specific enthalpy of melting and re-crystallization.

ΔH_m° = Reference value represents heat of melting if the polymer was 100% crystalline.

ΔH_m° for UHMWPE was taken as 293.6.

Table 1 shows that there is no change in both melting and crystallization temperatures in all compositions. In polymers, melting point is dependent on the structure of the polymer, primary and secondary bonding between chains, molecular weight, heat and entropy of fusion, etc., by addition of MWCNT there is no appreciable change in the above factors and hence, there is no change in melting point [20]. The specific enthalpies of both melting and recrystallization increased up

Table 1 DSC results

Sample	Melting temperature (°C)	Re-crystallization temperature (°C)	Specific enthalpy of melting ΔH_m (J/g)	Specific enthalpy of re-crystallization ΔH_c (J/g)
U	135	114	90	80
UG-0.5	135	114	156	139
UG-1	135	112	224	205
UG-1.5	136	114	216	201
UC-0.5	135	118	226	199
UC-1	134	118	381	352
UC-1.5	135	118	235	209

to 1 wt% of filler content, after which they decreased. The percentage crystallinity of the composites were calculated and plotted as a function of nanofiller content in Fig. 4. There was an increment of 212 and 108% in the degree of crystallinity with 1 wt% of MWCNT and graphite. Upon further increasing the composition of CNT/Graphite degree of crystallinity decreased. It may be concluded that the well-dispersed MWCNT/Graphite induces nucleation sites for crystallization [21]. The increase in crystallinity at 1 wt% of CNT may also contribute to the increase in tensile strength as observed in Fig. 2.

4   Conclusions

Nanocomposites of UHMWPE were prepared by melt mixing with MWCNT and nanoscale graphite as reinforcements. TEM results showed well dispersed MWCNT/Graphite at lower concentrations and agglomeration at 1.5 wt%. The tensile strength of UHMWPE is increased by 14% with 1 wt% of CNT which is attributed to the dispersion of CNT in the matrix as well as increase in percentage crystallization. Beyond this composition, the tensile strength decreased. Young's modulus increased continuously upon increasing the weight percentage of CNT. Tensile properties of the UHMWPE decreased continuously with the graphite content. Flexural strength of the nanocomposite improved with the addition of CNT/Graphite nanofillers. The addition of CNT/Graphite up to 1% to the UHMWPE significantly improved thermal properties such as specific enthalpy and percentage of crystallinity while the melting point was unaffected. At higher concentration of fillers, both mechanical and thermal properties showed slight decline due to the formation of agglomerates. The optimum composition for UHMWPE—MWCNT/Graphite nanocomposites is 1 wt%.
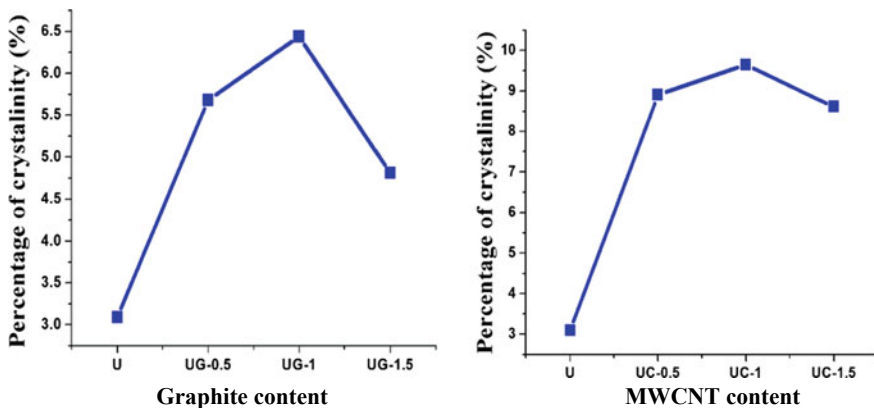

Fig. 4   Percentage crystallinity of UHMWPE–graphite/MWCNT composites

References

1. M. Remanan, R.S. Rao, S. Bhowmik, L. Varshney, M. Abraham, K. Jayanarayanan, Hybrid nanocomposites based on poly aryl ether ketone, boron carbide and multi walled carbon nanotubes: Evaluation of tensile, dynamic mechanical and thermal degradation properties. E-Polymers **16**(6), 493–503 (2016)
2. N. Ashok, M. Balachandran, F. Lawrence, N. Sebastian, EPDM–chlorobutyl rubber blends in c-radiation and hydrocarbon environment: mechanical, transport, and ageing behavior **45195**, 1–11 (2017)
3. M. Kumar, S. Bhowmik, M. Balachandran, M. Abraham, Composites: part A effect of surface functionalization on mechanical properties and decomposition kinetics of high performance polyetherimide/MWCNT nano composites. Compos. Part A **90**, 147–160 (2016)
4. M. Deng, S.W. Shalaby, Properties of self-reinforced ultra-high-molecular-weight poly-ethylene composites. Biomaterials **18**(9), 645–655 (1997)
5. J.A. Puértolas, UHMWPE matrix composites, 3rd edn. (Elsevier Inc., Amsterdam, 2016)
6. A.V. Maksimkin et al., Bulk oriented nanocomposites of ultrahigh molecular weight polyethylene reinforced with fluorinated multiwalled carbon nanotubes with nanofibrillar structure. Compos. Part B Eng. **94**, 292–298 (2016)
7. B.P. Grady, Effects of carbon nanotubes on polymer physics. J. Polym. Sci., Part B: Polym. Phys. **50**(9), 591–623 (2012)
8. B.J. Kim, J.H. Byun, S.J. Park, Effects of graphenes/CNTs co-reinforcement on electrical and mechanical properties of HDPE matrix nanocomposites. Bull. Korean Chem. Soc. **31**(8), 2261–2264 (2010)
9. D.C. Davis, J.W. Wilkerson, J. Zhu, D.O.O. Ayewah, Improvements in mechanical properties of a carbon fiber epoxy composite using nanotube science and technology. Compos. Struct. **92**(11), 2653–2662 (2010)
10. Y. Xue, W. Wu, O. Jacobs, B. Schädel, Tribological behaviour of UHMWPE/HDPE blends reinforced with multi-wall carbon nanotubes. Polym. Test. **25**(2), 221–229 (2006)
11. A. Avanzini, G. Donzella, D. Gallina, Fatigue damage modelling of PEEK short fibre composites. Procedia Eng. **10**, 2052–2057 (2011)
12. T. McNally et al., Polyethylene multiwalled carbon nanotube composites. Polymer (Guildf) **46**(19 Special Issue), 8222–8232 (2005)
13. A. Golchin, A. Wikner, N. Emami, An investigation into tribological behaviour of multi-walled carbon nanotube/graphene oxide reinforced UHMWPE in water lubricated contacts. Tribol. Int. **95**, 156–161 (2016)
14. S. Suñer, C.L. Bladen, N. Gowland, J.L. Tipper, Investigation of wear and wear particles from a UHMWPE/multi-walled carbon nanotube nanocomposite for total joint replacements. Wear **317**(1–2), 163–169 (2014)
15. D. Lahiri, F. Hec, M. Thiesse, A. Durygin, Tribology international nanotribological behavior of graphene nanoplatelet reinforced ultra high molecular weight polyethylene composites. Tribol. Int. **70**, 165–169 (2014)
16. A. Bhattacharyya, S. Chen, M. Zhu, Graphene reinforced ultra high molecular weight polyethylene with improved tensile strength and creep resistance properties. Express Polym. Lett. **8**(2), 74–84 (2014)
17. Y.-S. Zoo et al., Effect of carbon nanotube addition on tribological behavior of UHMWPE. Tribol. Lett. **16**(4), 305–309 (2004)

18. M.D.S. Hajar et al., Effect of graphite loading on the electrical and mechanical properties of Poly (Ethylene Oxide)/Poly (Vinyl Chloride) polymer films. J. Phys. Conf. Ser. **908**(1) (2017). IOP Publishing
19. Fan-Long Jin, Soo-Jin Park, A review of the preparation and properties of carbon nanotubes-reinforced polymer composites. Carbon Lett. **12**(2), 57–69 (2011)
20. J.A. Brydson, *Plastics Materials* (Elsevier, Amsterdam, 1999)
21. J.-F. Gao et al., Temperature-resistivity behaviour of CNTs/UHMWPE composites with a two-dimensional conductive network. Polym. Plast. Technol. Eng. **48**(4), 478–481 (2009)

Elastic Properties of Non-self-Similar Two Hierarchical Bio-inspired Unidirectional Composites

A. J. Abhirami and S. Anup

Abstract Mineralized natural structures such as bone, nacre and deep-sea sponges possess excellent mechanical properties even though they are composites made up of brittle and weak constituents. Advanced materials can be designed by studying the applicability of mechanical principles of such biological materials to engineering materials. Several methods have been developed for producing artificial materials very similar to nacre and bone. As a result, bio-inspired composites are developed with regularly and stairwise staggered arrangements of hard platelets in a relatively soft matrix. Load-bearing natural biological materials like bone and nacre exhibit two to seven levels of structural hierarchy based on their respective constituent materials (biominerals and proteins) of relatively poor mechanical properties. Motivated by the mechanical properties of mineralized natural structures, research on the synthesis of biomimetic hierarchical materials has been undergoing worldwide. However, there have been only a limited number of researches done on non-self-similar hierarchical structures, from a global hierarchical point of view. It is shown in Zhang et al. (J Mech Phys Solids, 58(10):1646, 2010, [1]) that regularly staggered composites possess better stiffness whereas stairwise staggered composites possess better strength. A combination of the above stated two types of staggering in a two hierarchical (2H) composite can give better mechanical properties. The present study is intended to find out the elastic properties of non-self-similar2Hcomposites. For this, two combinations are considered; 2H regularly staggered composite made with stairwise staggered composite as reinforcing platelets (RS) and 2H stairwise staggered composite made with regularly staggered composite as reinforcing platelets (SR). Results show that the Young's modulus for both the cases lies between that for stairwise and regularly staggered models for a certain range of aspect ratios of platelets.

Keywords Bio-inspired composites · Hierarchical · Mechanical properties · Stairwise staggered · Regularly staggered

A. J. Abhirami (✉) · S. Anup
Department of Aerospace Engineering, Indian Institute of Space Science and Technology, Trivandrum 695547, Kerala, India
e-mail: aj.abhirami@gmail.com

241

Nomenclature

2H	Two hierarchical
RS	Regularly staggered composite made with stairwise staggered composite as reinforcing platelets
SR	Stairwise staggered composite made with regularly staggered composite as reinforcing platelets
E	Modulus of Elasticity of composite
E_p	Modulus of Elasticity of platelet
E_R	Modulus of Elasticity of regularly staggered composite
E_S	Modulus of Elasticity of stairwise staggered composite
E_{RS}	Modulus of Elasticity of 2H RS composite
E_{SR}	Modulus of Elasticity of 2H SR composite
G_m	Shear modulus of matrix
φ_R	Volume fraction of regularly staggered composite
φ_S	Volume fraction of stairwise staggered composite
ξ	Overlapping ratio
ρ	Aspect ratio of platelet
ρ_R	Aspect ratio of platelet in regularly staggered composite
ρ_S	Aspect ratio of platelet in stairwise staggered composite
ρ_{RS}	Aspect ratio of platelet in 2H RS composite
ρ_{SR}	Aspect ratio of platelet in 2H SR composite
α_R	Parameter combining the effects of φ_R, ρ_R, G_m and E_p
α_S	Parameter combining the effects of φ_S, ρ_S, G_m and E_p
α_{RS}	Parameter combining the effects of φ_R, φ_S, ρ_S, G_m, E_p and α_S
α_{SR}	Parameter combining the effects of φ_R, φ_S, ρ_R, G_m, E_p and α_R

1   Introduction

For most of the biological materials, there exists an amazing relation between the structure and the mechanical properties by which they achieve superior mechanical properties compared to that of their constituents. Studying the physical mechanisms underlying their superior properties and functions is helpful for designing advanced biomimetic materials. Some examples for biological composites are nacre, bone, antler and teeth. Nacre, which is also known as 'the mother-of-pearl' is the pearly inner layer of mollusk shells, and is a typical example of staggered composite which is composed of about 95 vol% inorganic aragonite platelets and 5 vol% thin layers of protein-rich biopolymers in a multilayered 'brick-and-mortar' (B-and-M) architecture [2]. The 'bricks', called aragonite platelets are glued by the 'mortar', called protein; forming a B-and-M structure as shown in Fig. 1.

Several researches have reported that an important role is played by the staggering or alignment of platelets in the nano/microstructures in attaining the superior
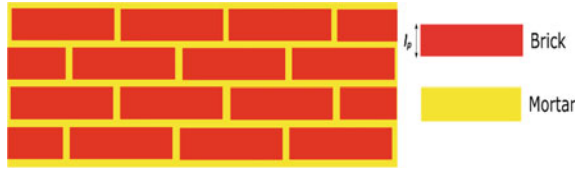
mechanical properties in Biological materials [3–6]. Gao et al. [7] and Ji and Gao [8] developed a tension–shear chain model as shown in Fig. 2 to demonstrate how the natural biological materials attain higher mechanical properties.

A regular staggered tension–shear chain model in which the overlapping length = L/2 where L is the length of the platelet, can be used to interpret many underlying mechanisms in biocomposites. However, there exist other patterns also like stairwise staggering, random staggering and continuous layering. Figures 3 and 4 show schematic diagrams of regularly and stairwise staggered nanostructures.

These structures produce the best mechanical properties compared to other distribution patterns; this can be a possible reason for why nature choose regular and stairwise staggering [1]. Synthetic composites, which mimics the design of the naturally occurring biocomposites are referred to as bio-inspired composites. In such composites, the structurally inferior building blocks when arranged in a

Fig. 2 Schematic illustration of Tension–Shear chain model proposed by Gao et al. [7] and Ji and Gao [8]
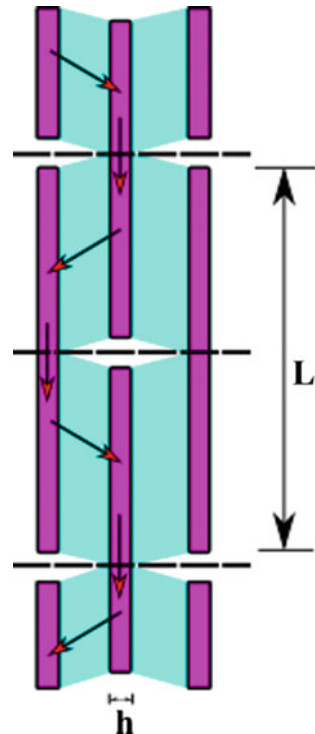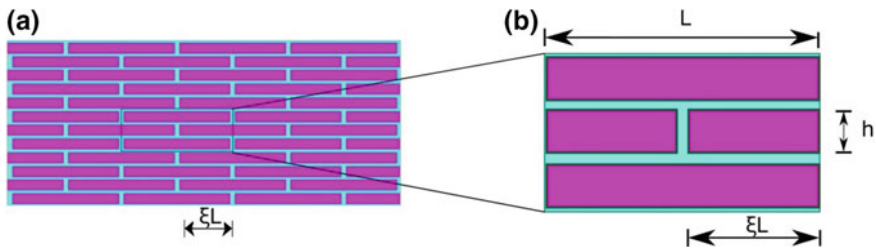
Fig. 3 Schematic diagram of a Regularly staggered nanocomposite structure with offset. **a** Overall composite **b** unit cell with platelets having L × h dimension and an overlapping distance of ξL
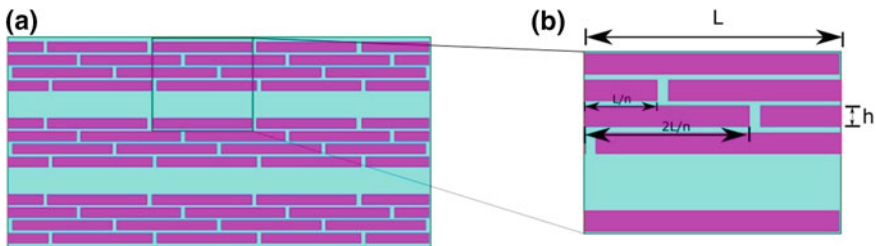
Fig. 4 Schematic diagram of a Stairwise staggered nanocomposite structure. **a** Overall composite **b** unit cell; n is the number of platelets within each period

multilevel hierarchy impart a significantly improved strength to the composite; compared to that of the constituents. For this, the geometry also plays an important role. For a broad domain of crack sizes, a stable crack propagation is enabled by introducing hierarchical structure due to its increased defect tolerance and toughness [9, 10]. In a study based on a quasi-self-similar hierarchical model, it is shown that there exists an optimal hierarchical structure with an optimal number of hierarchical levels for maximum material toughness [11]. Also, the characteristic size from the bottom to top structures varies from tens of nanometres to hundreds of micrometres within the optimal hierarchy.

Equations for finding out the mechanical properties of regularly staggered and stairwise staggered models have been developed in [1]. High stiffness and strength which are comparable to those of the reinforcing platelets are achieved in composites with stairwise staggering including regular staggering with the number of platelets in each period, n = 2 [1]. It was also found that these composites possess large failure strain and energy storage capacity compared to the soft matrix. Mirzaeifar et al. [12] explored the effect of adding both self-similar and dissimilar hierarchical levels to the material architecture and it was shown that the geometries with multiple hierarchical levels possessed higher defect tolerance. It was also found that the composites with more hierarchical levels dramatically improve the defect tolerance of the material.
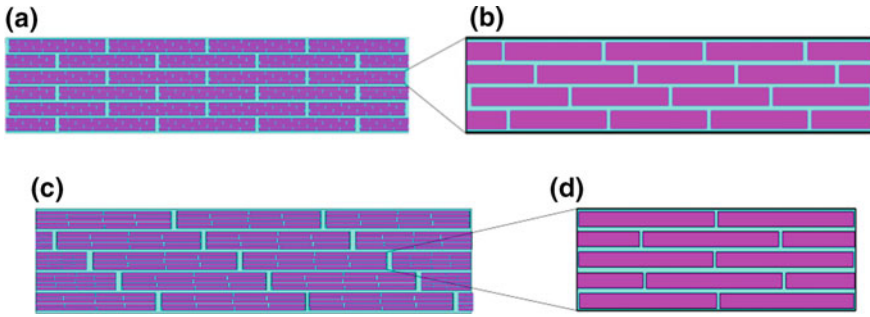
Fig. 5 **a** 2H Regularly staggered composite made with stairwise staggered composite as platelet; **b** Zoomed view of platelet; **c** 2H stairwise staggered composite made with regularly staggered composite as platelet; **d** Zoomed view of platelet

From a global hierarchical point of view, there have been only a limited number of researches done on bio-inspired composites. The studies conducted so far is even lesser when it comes to the case of non-self-similar hierarchical structures. From [1], it is seen that regularly staggered composites possess better stiffness whereas stairwise staggered composites possess better strength. Therefore, the combination of these two types of staggering in a two hierarchical (2H) composite can give better mechanical properties. The present study is intended to find out the elastic properties of a two hierarchical (2H) composite made with two combinations viz. 2H regularly staggered composite with stairwise staggered composite as reinforcing platelets (RS) and 2H stairwise staggered composite with regularly staggered composite as reinforcing platelets (SR). The inspiration to perform this study is that this could help for the innovation of biomimetic environment-friendly composite materials with excellent mechanical properties which can be used in aerospace applications. In this report, an attempt is made to evaluate the elastic properties of a non-self-similar 2H RS and 2H SR composites which are illustrated in Fig. 5.

2 Elastic Properties of Two Hierarchical Composites

The structural arrangements of platelets play a key role in the mechanical properties in unidirectional nanocomposites. Here, we review the elastic property, i.e. stiffness of a regularly staggered composite made and stairwise staggered composite with n = 5 [1].

For a regularly staggered composite, the modulus of elasticity E_R is given by [1] as

$$E_R = \frac{\varphi_R E_p}{\frac{4}{3} + \frac{1}{3\bar{\xi}(1-\xi)\alpha_R}} \tag{1}$$

where,

$$\alpha_R = \frac{\varphi_R \rho_R^2 G_m}{3(1 - \varphi_R)E_p} \tag{2}$$

is a parameter combining the effects of platelet volume fraction of the regularly staggered composite φ_R and aspect ratio of the regularly staggered composite ρ_R, as well as the shear modulus of matrix G_m and platelet elastic modulus E_p. Here, ξ is the overlap ratio which is equal to 1/2 for regular staggering.

Similarly, for a stairwise staggered composite with n platelets in each period, the modulus of elasticity E_S is given by [1] as

$$E_S = \frac{\varphi_S E_p}{\frac{n(3n-4)}{3(n-1)^2} + \frac{n^2}{3(n-1)\alpha_S}} \tag{3}$$

where

$$\alpha_S = \frac{\varphi_S \rho_S^2 G_m}{3(1 - \varphi_S)E_p} \tag{4}$$

is a parameter combining the effects of platelet volume fraction of the stairwise staggered composite φ_S and aspect ratio of the stairwise staggered composite ρ_S, as well as the shear modulus of matrix G_m and platelet elastic modulus E_p. Figure 6 shows the variation of normalized Young's modulus for regularly staggered composites and stairwise staggered for n = 5 and 10 with respect to aspect ratio as per Eqs. (1) and (3).

The stiffness, E_{RS} of a 2H RS composites is found out by substituting (3) for E_P in (1) and (2) after which the obtained expression for E_{RS} is normalized by dividing it by $E_P \varphi_R \varphi_S$ (since the volume fraction for the 2H composite is $\varphi_R \varphi_S$) as,

Fig. 6 Variation of normalized Young's modulus with respect to platelet aspect ratio for regular and stairwise staggered composites 5–150
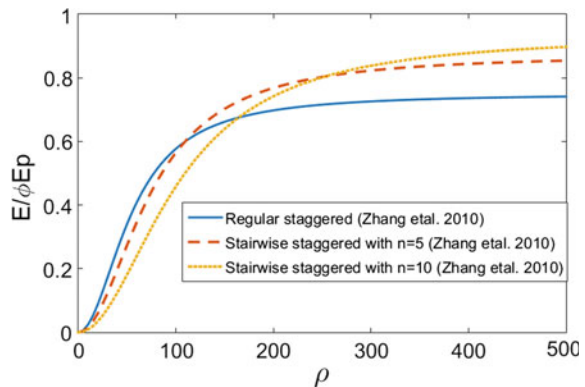
$$\frac{E_{RS}}{E_P \varphi_R \varphi_S} = \frac{1}{\left[\frac{4}{3} + \frac{1}{3\xi(1-\xi)\alpha_{RS}}\right]\left[\frac{n(3n-4)}{3(n-1)^2} + \frac{n^2}{3(n-1)\alpha_S}\right]} \tag{5}$$

where

$$\alpha_{RS} = \frac{\varphi_S \rho_S^2 G_m \left(\frac{n(3n-4)}{3(n-1)^2} + \frac{n^2}{3(n-1)\alpha_S}\right)}{3(1-\varphi_R)\varphi_S E_p} \tag{6}$$

Similarly, by substituting (1) for E_P in (3) and (4), the stiffness for a 2H SR composite is found out and then normalized as follows:

$$\frac{E_{SR}}{E_P \varphi_R \varphi_S} = \frac{1}{\left[\frac{4}{3} + \frac{1}{3\xi(1-\xi)\alpha_R}\right]\left[\frac{n(3n-4)}{3(n-1)^2} + \frac{n^2}{3(n-1)\alpha_{SR}}\right]} \tag{7}$$

Where,

$$\alpha_{SR} = \frac{\varphi_S \rho_S^2 G_m \left(\frac{4}{3} + \frac{1}{3\xi(1-\xi)\alpha_R}\right)}{3(1-\varphi_S)\varphi_R E_p} \tag{8}$$

3 Results and Discussion

The variation of normalized Young's modulus of the 2H RS and 2H SR composite with respect to the corresponding platelet aspect ratio at the second level of hierarchy (i.e. ρ_{RS} for 2H RS and ρ_{SR} for 2H RS) for different values of the platelet aspect ratio of the composite in the first hierarchical level (ρ_S for 2H RS ρ_R for 2H RS) and is shown in Fig. 7a and Fig. 7b respectively. For plotting the curves, an overlapping ratio of $\xi = 0.5$; volume fractions $\varphi_R = \varphi_S = 0.5$, moduli ratio $\frac{E_p}{G_m} = 2980$ and n = 5 are adopted.

It can be seen that the Young's modulus increases with increase in platelet aspect ratio at the second level of hierarchy (i.e. ρ_{RS} for 2H RS and ρ_{SR} for 2H RS) as well as the platelet aspect ratio of the composite in the first hierarchical level (ρ_S for 2H RS ρ_R for 2H RS). After reaching a particular value of platelet aspect ratio at the second level of hierarchy, it is seen that the Young's modulus tends to attain a constant value. The rate of increase in Young's modulus with respect to increasing values of the platelet aspect ratio of the composite in the first hierarchical level is also decreasing. Also, it is observed that for 2H SR composites, the increase in Young's modulus with respect to ρ_R is comparatively higher than that of the corresponding values of ρ_S in 2H RS composites. But, for the maximum value of platelet aspect ratio in the first level of hierarchy i.e. when ρ_R or ρ_S reaches 500,
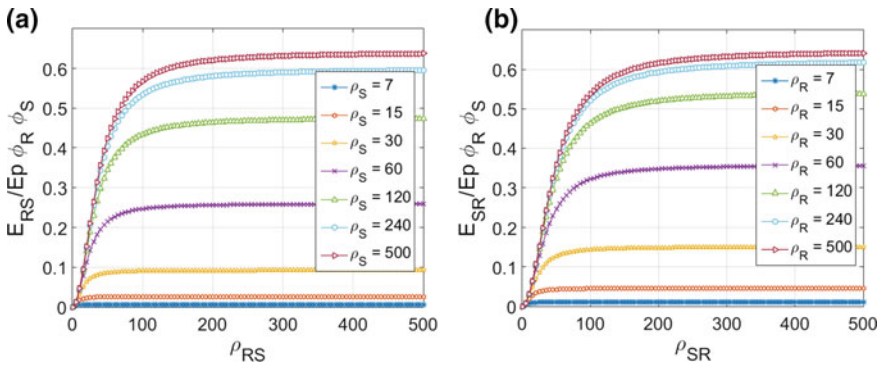
Fig. 7 a Variation of normalized Young's modulus of 2H RS composite with respect to ρ_{RS} for different values of ρ_S varying from 7 to 500; **b** Variation of normalized Young's modulus of 2H SR composite with respect to ρ_{SR} for different values of ρ_R varying from 7 to 500

the difference between Young's modulus of 2H RS and 2H SR composites seems to be inappreciable even though 2H SR composites possess a marginally higher value of Young's modulus.

4 Conclusions

From the results and discussions, it can be concluded that the elastic properties of 2H RS composites, as well as 2H SR composites, vary in a similar manner as that of for regular or stairwise staggered composites. The 2H SR composites are having a higher rate of increase in Young's modulus with an increase in platelet aspect ratio in the first level of hierarchy compared to that of 2H RS composites. Also, the maximum value of E_{RS} and E_{SR} attained is nearer to that of the corresponding maximum value for a regularly staggered composite (E_R). This implies that the elastic properties are not much affected by the introduction of a non-self-similar 2H in the composite. But, the variation of strength, strain and toughness are to be investigated to find whether it is possible to obtain a composite with improved mechanical properties. Finding an optimum level of hierarchy required to achieve the improved mechanical properties is also a problem to be addressed for.

References

1. Z.Q. Zhang, B. Liu, Y. Huang, K.C. Hwang, H. Gao, Mechanical properties of unidirectional nanocomposites with non-uniformly or randomly staggered platelet distribution. J. Mech. Phys. Solids **58**(10), 1646 (2010)
2. F. Barthelat, Biomimetics for next generation materials. Philos. Trans. R. Soc. A **365**, 2907 (2007)

3. S. Anup, S.M. Sivakumar, G.K. Suresh Kumar, Structural arrangement effects of mineral platelets on the nature of stress distribution in bio-composites. Comput. Model. Eng. Sci. **18** (2), 145 (2007)
4. J.D. Currey, Mechanical properties of mother of pearl in tension. Proc. R. Soc. Lond. B Biol. Sci. **196**(1125), 443 (1977)
5. J.D. Currey, *The mechanical adaptations of bones* (Princeton University Press, Princeton, 2014)
6. P. Fratzl, H.S. Gupta, E.P. Paschalis, P. Roschger, Structure and mechanical quality of the collagen–mineral nano-composite in bone. J. Mater. Chem. **14**(14), 2115 (2004)
7. H. Gao, B. Ji, I.L. Jäger, E. Arzt, P. Fratzl, Materials become insensitive to flaws at nanoscale: lessons from nature. Proc. Natl. Acad. Sci. **100**(10), 5597 (2003)
8. B. Ji, H. Gao, Mechanical properties of nanostructure of biological materials. J. Mech. Phys. Solids **52**(9), 1963 (2004)
9. D. Sen, M.J. Buehler, Structural hierarchies define toughness and defect-tolerance despite simple and mechanically inferior brittle building blocks. Sci. Rep. **1**, 35 (2011)
10. L.S. Dimas, M.J. Buehler, Influence of geometry on mechanical properties of bio-inspired silica-based hierarchical materials. Bioinspiration Biomim. **7**(3), 1 (2012)
11. Z. Zhang, Y.W. Zhang, H. Gao, On optimal hierarchy of load-bearing biological materials. Proc. R. Soc. Lond. B Biol. Sci. **278**(1705), 519 (2011)
12. R. Mirzaeifar, L.S. Dimas, Z. Qin, M.J. Buehler, Defect-tolerant bioinspired hierarchical composites: simulation and experiment. ACS Biomater. Sci. Eng. **1**(5), 295 (2015)

Part V
Computational Mechanics

Molecular Dynamics Simulations Study on the Grain Size Dependence of Deformation and Failure Behavior of Polycrystalline Cu

P. Rohith, G. Sainath and B. K. Choudhary

Abstract The tensile deformation and failure behavior of polycrystalline Cu nanowires have been examined using molecular dynamics (MD) simulations at 10 K. MD simulations have been performed on polycrystalline Cu nanowires with grain size ranging from 1.54 to 5.42 nm. The simulation results indicate that the yielding as well plastic deformation in all the Cu nanowires proceeds by the slip of Shockley partial dislocations irrespective of grain size. Interestingly, the formation of fivefold twin and deformation induced grain growth has been observed during the plastic deformation. The polycrystalline Cu with the grain size of 5.42 nm fails through shear along the grain boundary (intergranular failure), while the shear along the slip planes within the grain (intra-granular failure) has been observed for grain size less than 5.42 nm. The variations of yield strength and flow stress at 10% strain as a function of grain size follows inverse Hall–Petch relation.

Keywords Molecular dynamics simulations · Nanocrystalline Cu · Partial dislocations · Grain growth

1 Introduction

Nanocrystalline materials are promising materials for a large number of applications in nano/microelectromechanical (NEMS/MEMS) systems such as transparent electrodes, sensors, and flexible electronics [1, 2]. The optimal utilization and reliability of these materials critically depend on a thorough understanding of their mechanical properties and associated deformation mechanisms. Many experimental investigations and computer simulations have confirmed the superior mechanical properties of nanocrystalline materials and also their dependence on size, shape, strain rate and temperature [3–12]. These superior properties arise from their finite

P. Rohith (✉) · G. Sainath · B. K. Choudhary
Materials Development and Technology Division, Metallurgy and Materials Group Indira Gandhi Centre for Atomic Research, HBNI, Kalpakkam 603 102, Tamil Nadu, India
e-mail: rohith@igcar.gov.in

size resulting in high surface area and low defect density. For example, Cao and Ma [3] investigated the dependence of yield strength of FCC Cu nanopillars on specimen shape and temperature. It has been reported that yield stress and Young's modulus decreases with increase in temperature [3]. Park and Zimmerman [4] have simulated the tensile loading of Au nanowires of different size and various strain rates. They have observed that the yield stress increases with increasing strain rate and in ultrathin Au nanowires, they have reported the formation of atom-thick chains prior to fracture [4]. Similarly, Wu et al. [5] have reported that long Cu nanowires (1503 nm) exhibit brittle failure, while short nanowires fail in a ductile manner. These results suggest that the size effects in single-crystalline nanowire have been well understood [6–12].

Unlike the single crystalline nanowires, where only the sample size becomes important, the sample size along with grain size influence the strength and deformation mechanisms of polycrystalline nanowires. The size effects associated with sample size are known as extrinsic size effects, while that associated with grain size are known as intrinsic size effects. Many reports have shown that the coarse-grained materials can be strengthened by introducing grain boundaries. The high strength in these materials results from the interaction of dislocations with grain boundaries, which acts as barriers for dislocation motion. In coarse-grained materials, the yield strength as a function of grain size follows the Hall–Petch (HP) relation [13, 14] as follows

$$\sigma_Y = \sigma_0 + kd^{-1/2}$$

where σ_0 is the friction stress in the absence of grain boundaries, k is a constant, and d is the grain size. In other words, the yield stress increases with decreasing grain size. This is because the pile-ups in fine grain size materials contain fewer dislocations as a result, the stress at the tip of the pile-up is lower and thus, a larger applied stress is required to generate dislocations in the adjacent grain. Further in coarse-grained materials, the dislocations multiply by a well-known Frank–Read mechanism. However, as grain size decreases to few tens of nanometers, the HP relation will break down and also the Frank–Read mechanism no longer operates. A compilation of yield stress data taken by Meyers et al. [15] for Cu suggests that the critical grain size at which the HP relation breaks down is close to 20 nm. Below this grain size, the yield stress decreases with decrease in grain size. It has been observed that in this small grain size regime, the yield stress follows the inverse Hall–Petch relation. This inverse HP relation has been first observed by Chokshi et al. [16] in Cu and Pd. The inverse HP relation has been explained based on the diffusional creep occurring through the transport of vacancies along the grain boundaries, i.e., GB diffusional creep. However, Wolf et al. [17] reconciled GB diffusion creep and GB sliding as single deformation mechanism known as sliding accommodated grain boundary diffusion creep. In addition to sliding accommodating diffusional creep, grain rotation and coalescence of grains leading to grain growth has been observed as other dominant plastic deformation mechanisms [18].

In the past, MD simulations have been performed on the deformation behavior of nanocrystalline nanowires. Schiotz et al. [19] have performed MD simulations on nanocrystalline Cu with grain size varying from 3.3 to 6.6 nm at 300 K. An inverse HP relation with yield stress varying from 1 to 1.2 GPa for grain sizes of 3.3–6.6 nm has been reported. Similarly, Li et al. [20] have studied the effect of grain size on deformation behavior of nanocrystalline Mo nanowires. They have reported that the deformation and fracture behavior of Mo nanowires depends critically on the grain size. Cao et al. [21] have observed the significantly lower value of strength for polycrystalline Cu nanowire as compared to single crystalline Cu nanowire. These works suggest that grain size influences the mechanical properties, deformation mechanisms and also the fracture behavior of the nanocrystalline nanowires. Several studies on polycrystalline Cu have explained the variations in yield stress with grain size up to 6 nm [16, 22]. However, the operational deformation and failure mechanisms and yield stress of polycrystalline Cu nanowires with average grain size below 6 nm has not been reported earlier. In view of this, an attempt has been made in this paper to understand the grain size dependence of deformation and failure behavior of nanocrystalline Cu nanowires using MD simulations. The grain size has been varied in the range 1.54–5.42 nm with random grain orientations. The deformation behavior has been explained in terms of dislocation plasticity and grain growth. The failure mechanism as a function of grain size has also been reported.

2   MD Simulation Details

Molecular dynamics (MD) simulations have been performed using large-scale Atomic/Molecular Massively Parallel Simulator (LAMMPS) package [23] developed by Plimpton. To describe the interactions between Cu atoms, embedded atom method (EAM) potential developed by Mishin et al. [24] has been employed. This potential is widely used to study the mechanical properties and associated deformation mechanisms in Cu [6, 12].

The polycrystalline Cu nanowires have been prepared using the Voronoi algorithm with random grain orientation. All the nanowires used in the present study have a square cross section width (d) of 10.8 nm and length of 21.6 nm providing an aspect ratio of 2:1. In order to understand the effect of grain size on the deformation and failure behavior, the grain size has been varied from 1.54 to 5.42 nm. Periodic boundary conditions were chosen along length direction, while the other directions were kept free in order to mimic an infinitely long nanowire. Use of periodic boundary conditions removes the artificial effects associated with end grips, which acts as localized sites for defect nucleation and failure [25]. To relax the internal stress present in the nanowire particularly at grain boundaries, the model system was first heated to 300 K and then cooled back to 10 K, where the actual tensile loading has been carried out. Velocity Verlet algorithm has been used to integrate the equations of motion with a time step of 2 fs. Upon equilibration at 10 K, the nanowires were deformed under tensile loading at a constant strain rate of

1×10^9 s^{-1} along the axial direction. The strain rate considered in MD simulations is significantly higher than the experimental strain rates, which is due to the inherent time scale limitations from MD. The stress has been obtained using the Virial expression [26], which is equivalent to a Cauchy's stress in an average sense. The strain (e) has been obtained as e = $(l - l_0)/l_0$, where l is the instantaneous length and l_0 is the initial length after equilibration. The visualization of atomic configurations is accomplished in AtomEye [27] with common neighbor analysis (CNA) [28] parameter.

3   Simulation Results and Discussion

The tensile stress–strain behavior of polycrystalline Cu nanowires of grain size in the range of 1.54–5.42 nm has been presented in Fig. 1. It can be seen that all the nanowires undergo elastic deformation up to a peak stress followed by a marginal stress reduction. For clarity, the initial elastic regime has been shown in the inset. The values of the Young's modulus have been calculated from the elastic regime of stress–strain curve and they were found to be in the range of 45–60 GPa. The observed Young's modulus values are in agreement with the experimental results of Nieman et al. [29]. Following the elastic deformation, the flow stress decreases gradually along with marginal oscillations until failure. Interestingly, all the nanowire fails at approximately the same values of strain, irrespective of their grain size.

The peak stress values at the end of elastic regime have been considered as yield stress in all the nanowires. Figure 2a shows the variation of yield stress and flow stress at 10% as a function of grain size. It can be seen that both the yield stress and flow stress increases linearly with an increase in grain size. The obtained yield stress values in polycrystalline Cu nanowires (1.6–2.3 GPa) are much lower than the single crystalline nanowires (11.5 GPa) [12]. This is due to the heterogeneous

Fig. 1 Stress–strain curves for polycrystalline Cu nanowires (10.84 × 10.84 × 21.69 nm) with different grain size in the range of 1.54–5.42 nm at 10 K
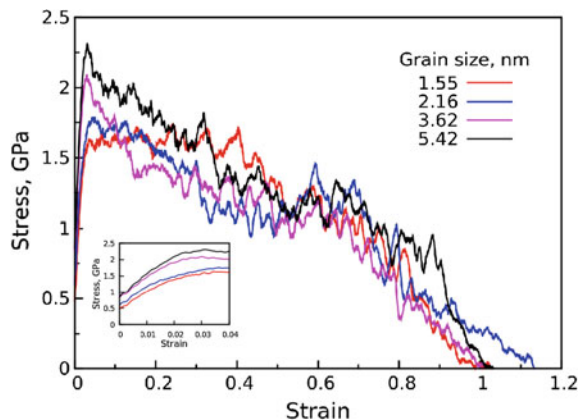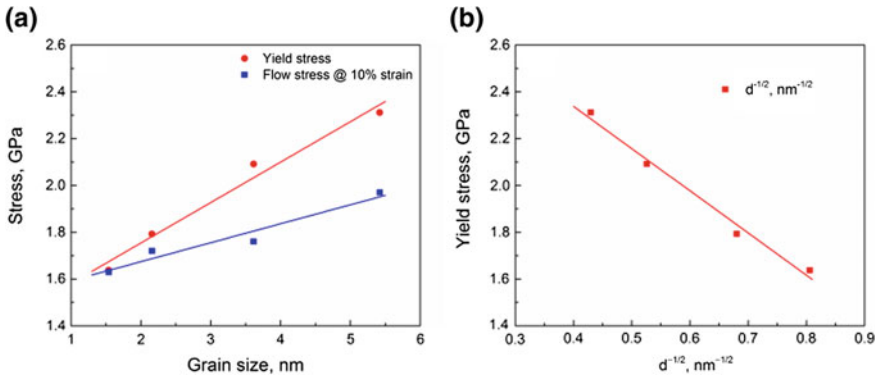
Fig. 2 a The variation of yield stress and flow stress at 10% strain as a function of grain size for polycrystalline Cu nanowire at 10 K. **b** Yield stress variation with the inverse square root of grain size ($d^{-1/2}$) in nm$^{-1/2}$ exhibiting inverse Hall–Petch (IHP) relation

behavior of grain boundaries, which results in high stress concentration and thus reduces the yield strength significantly [30]. Figure 2b shows the yield stress variation with the inverse square root of the grain size. By linear fitting of data, the slope is found to be negative. This negative slope (−1.80) indicates that the polycrystalline Cu nanowires with grain sizes in the range of 1.54–5.42 nm follows inverse Hall–Petch behavior. This inverse Hall–Petch behaviour at nanoscale has been reported for many polycrystalline materials [16–19, 30]. Saha et al. [31] have observed the similar slope exhibiting the inverse Hall–Petch relationship in polycrystalline W nanowires. The inverse Hall–Petch relation for polycrystalline Cu nanowire has been shown as follows:

$$\sigma_Y = 3.05832 - \frac{1.80192}{d^{0.5}}$$

where σ_Y is yield stress expressed in GPa and d is the grain size in nm. Many mechanisms have been proposed for this inverse Hall–Petch behaviour such as suppression of dislocation pile-ups [32], dislocation motion through multiple grains [33], sliding in the grain boundaries [34, 35], grain rotation [35], and enhanced diffusional creep in the grain boundaries [16]. The increase in strength with an increase in grain size (inverse Hall–Petch) in the present study can be attributed to the grain boundary sliding mechanism [19, 36]. However, the observed yield stress variation with grain size can be explained based on dislocation nucleation from grain boundaries. Due to higher fraction of grain boundary atoms in small grain size sample, the dislocation nucleation is easier leading to lower yield strength, while lower fraction of grain boundary atoms increases the stress required for dislocation nucleation at large grain sizes.

The atomic configurations during the tensile deformation of polycrystalline Cu nanowire with a grain size of 3.61 nm have been presented in Fig. 3. The stress

reduction following the elastic deformation of polycrystalline Cu nanowires is associated with nucleation of Shockley partial dislocation from the grain boundaries (Fig. 3a). Due to large number of the disordered atoms, the grain boundaries possess high energy as compared to the grain interior. The high energy of the grain boundaries makes them favorable sites for dislocation nucleation. The dislocation nucleation from grain boundaries rather than free surfaces is the reason for much lower yield stress of polycrystalline nanowires as compared to their single crystal counterparts [12]. The plastic deformation in Cu nanowires is dominated by the glide of 1/6 <112> partial dislocations nucleated from the grain boundaries. The 1/6 <112> Shockley partial enclosing the stacking faults have been found. The cyan colored atoms which represent the stacking fault atoms confirms the dislocation-mediated plasticity in polycrystalline copper. However, along with dislocation-mediated plasticity, deformation twinning is also observed. The observed twinning mechanism along with dislocation-mediated plasticity in poly-crystalline nanowires is in agreement with that observed in nanocrystalline Cu under tensile and torsion loading [30]. With increase in strain, the deformation induced grain growth has been observed (Fig. 3a–c). The traces of initial grain boundaries have been indicated by solid lines as shown in Fig. 3a. Following the grain growth with increasing strain, the trace line for each grain boundary has been shown as a dotted line. The grains with white colored trace line expands (Fig. 3a–d), while the grain with yellow colored trace line shrinks (Fig. 3a, b) and completely disappears in Fig. 3c. This indicates that the large grains expand at the expense of smaller grains. This grain coarsening/growth has been observed for all nanowires irrespective of their grain size. The grain growth in our MD simulations

(a) ε = 3.35 % (b) ε = 11.75 % (c) ε = 28.50 % (d) ε = 45.45 % (e) ε = 69.30 % (f) ε = 98.45 %
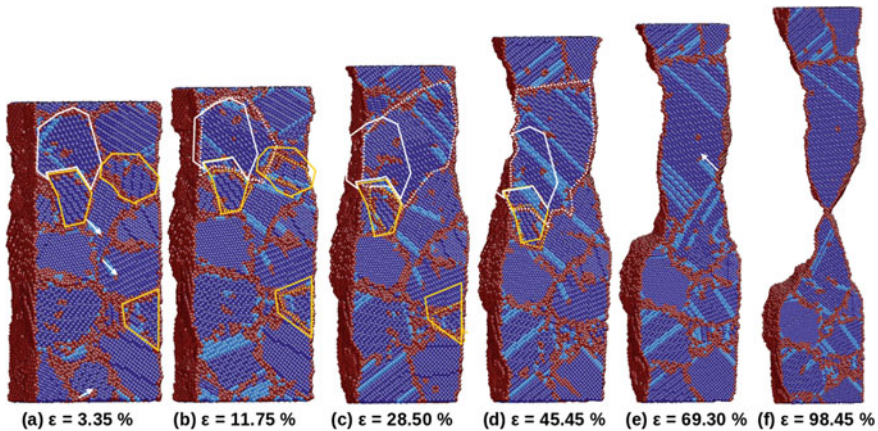
Fig. 3 Deformation behavior of polycrystalline Cu nanowire with grain size of 3.61 nm under tensile loading. The deformation through the slip of partial dislocations can be seen at all strains. The blue color atoms represent FCC atoms, cyan color atoms represent the stacking faults and the red color atoms indicate the surfaces, grain boundaries and dislocation cores. The solid (green, white, yellow and ash) curves represent the trace of initial grain boundaries, while the dashed curves represent the traces of instantaneous grain boundaries

occurs through grain boundary sliding. Usually, at high temperature, the thermal energy acts as a driving force for grain growth. However, at low temperatures, the applied stress, which is in the order of few GPa, acts as a driving force. Under external stress, the rotation of neighboring grains coupled with atomic shuffling from grain interior to grain boundary (order to disorder) or grain boundary to grain interior (disorder to order) results in grain growth. Similar grain growth mechanism has been reported in earlier studies [37, 38]. The continuous grain coarsening results in the formation of a single large grain (yellow colored dotted trace line in Fig. 3d), where the deformation localizes and nanowire fails through shear intra-granular failure.

An interesting phenomenon observed during the tensile deformation of poly-crystalline Cu nanowires is the formation of fivefold deformation twins near the grain boundaries as shown in Fig. 4. Successive emission of partial dislocations along the same glide plane from the grain boundaries results in the twin formation. This twin formation mechanism in polycrystalline Cu nanowires is similar to that in single crystalline Cu nanowires [39]. Formation of twin from grain boundaries relives the strain in the grain interior. Intersection of deformation twins with different Burgers vector leads to the formation of fivefold twin symmetry. Similar fivefold twin formation has been reported earlier through experimental investigations and MD simulations [30, 40–42].

As shown in Fig. 3, the plastic deformation is dominated by dislocation-mediated plasticity and deformation twinning irrespective of the grain size. However, it has been observed that the failure mechanism is different in nanowires of different grain size. In nanowires with a grain size up to 3.61 nm, the failure occurs by the shear along the slip plane of single grain, i.e., intra-granular failure (Fig. 5a–c). However in nanowire with a grain size of 5.42 nm, the failure has been observed along the grain boundary, i.e., intergranular failure (Fig. 5d).

Fig. 4 The fivefold deformation twin observed during tensile deformation of polycrystalline Cu nanowire with a grain size of 2.16 nm. The blue color atoms represent the perfect FCC atoms, the cyan color atoms represent the twin boundaries and the red color atoms represent the grain boundary
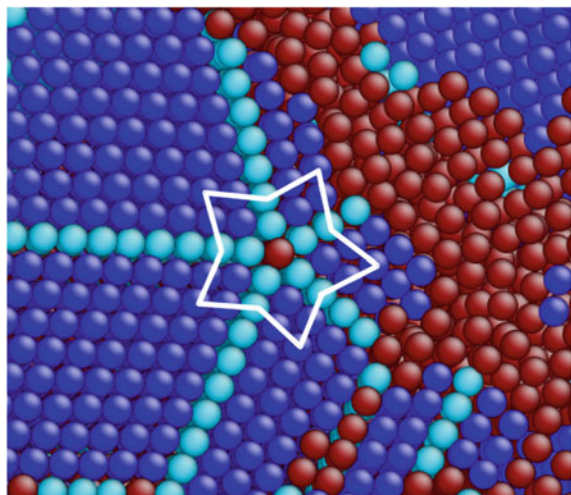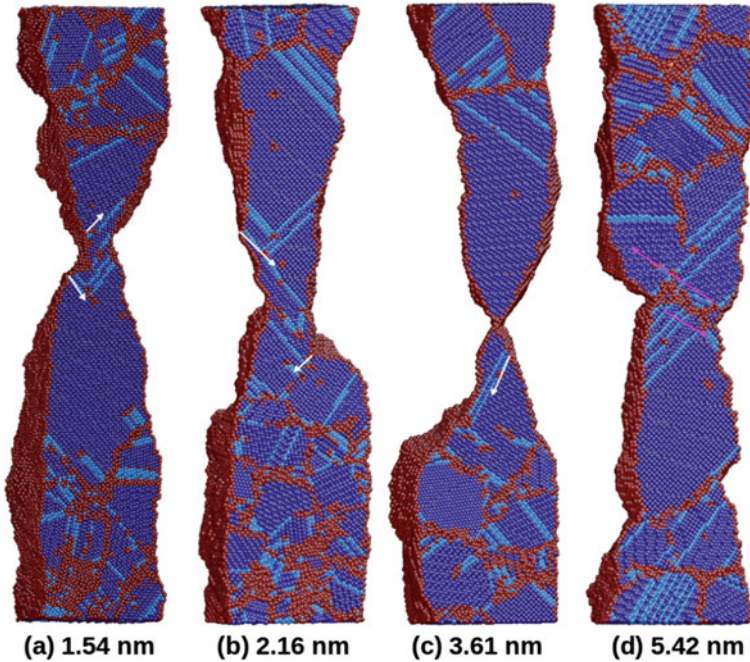
Fig. 5 Failure behavior in polycrystalline Cu nanowires with varying grain sizes in the range of 1.54–5.2 nm under tensile loading. Nanowires with grain sizes below than 3.61 nm fails through shear along the slip lines, while the nanowire with 5.42 nm fails through grain boundary sliding

Finally, all the nanowires irrespective of grain size, exhibit the same ductility (failure strain), which indicates that ductility is insensitive to grain size.

4 Conclusion

MD simulations have been performed to investigate the tensile deformation behavior of polycrystalline Cu nanowires of different grain size. The tensile stress–strain behavior is characterized by the initial elastic deformation up to peak stress followed by a gradual decrease in flow stress until failure. The variation of yield stress and flow stress follows the inverse Hall–Petch relation as a function of grain size. The deformation behavior under the tensile deformation is dominated by the glide of partial dislocations which nucleated mainly from the grain boundaries. Along with partial dislocation mediated plasticity, deformation by twinning has also been observed. Due to twinning on multiple and interacting twin systems, the formation of fivefold twin has been observed. During the plastic deformation, an extensive grain growth resulting in the formation of large grains has been observed. For nanowires of grain size up to 3.61 nm, the failure has been observed by the

shear along the slip planes, while, grain boundary failure has been observed in nanowire with a grain size of 5.42 nm. Irrespective of the grain size, all nanowires exhibit similar ductility (failure strain) indicating that ductility is insensitive to grain size.

References

1. Y. Xia, P. Yang, Y. Sun, Y. Wu, B. Mayers, B. Gates, Y. Yin, F. Kim, H. Yan, Adv. Mater. **15**, 353 (2003)
2. H.C. Postma, I. Kozinsky, A. Husain, M. Roukes, Appl. Phys. Lett. **86**, 223105 (2005)
3. A. Cao, E. Ma, Acta Mater. **56**, 4816 (2008)
4. H.S. Park, J.A. Zimmerman, Phys. Rev. B **72**, 054106 (2005)
5. Z. Wu, Y.W. Zhang, M.H. Jhon, H. Gao, D.J. Srolovitz, Nano Lett. **12**, 910 (2012)
6. H. Liang, M. Upmanyu, H. Huang, Phys. Rev. B **71**, 241403 (2005)
7. F. Sansoz, Acta Mater. **59**, 3364 (2011)
8. G. Richter, K. Hillerich, D.S. Gianola, R.M. Nig, O. Kraft, C.A. Volkert, Nano Lett. **9**, 3048 (2009)
9. C. Peng, Y. Zhan, J. Lou, Small **8**, 1889 (2012)
10. J. Han, L. Fang, J. Sun, Y. Han, K. Sun, J. Appl. Phys. **112**, 114314 (2012)
11. M. Yaghoobi, G.Z. Voyiadjis, Acta Mater. **121**, 190 (2016)
12. P. Rohith, G. Sainath, B.K. Choudhary, Comput. Mater. Sci. **138**, 34 (2017)
13. E. Hall, Proc. Phys. Soc. **B64**, 747 (1951)
14. N. Petch, J. Iron Steel Inst. **174**, 25 (1953)
15. M.A. Meyers, A. Mishra, D.J. Benson, Prog. Mater. Sci. **51**, 427 (2006)
16. A.H. Chokshi, A. Rosen, J. Karch, H. Glieter, Scr. Mater. **23**, 1679 (1989)
17. D. Wolf, V. Yamakova, S.R. Phillpota, A.K. Mukherjeeb, Z. Für. Met. **94**, 1091 (2003)
18. A.J. Haslam, D. Moldovan, V. Yamakova, D. Wolf, S.R. Phillpot, H. Gleiter, Acta Mater. **51**, 2097 (2003)
19. J. Schiøtz, F.D.D. Tolla, K.W. Jacobsen, Nature **391**, 561 (1998)
20. X. Li, W. Hu, S. Xiao, W.Q. Huang, Phys. E **40**, 3030 (2008)
21. A. Cao, Y. Wei, E. Ma, Phys. Rev. B **77**, 195429 (2008)
22. R.A. Masumura, P.M. Hazzledine, C.S. Pande, Acta Mater. **46**, 4527 (1998)
23. S. Plimpton, J. Comput. Phys. **117**, 1 (1995)
24. Y. Mishin, M.J. Mehl, D.A. Papaconstantopoulos, A.F. Voter, J.D. Kress, Phys. Rev. B **63**, 224106 (2001)
25. W. Cai, W. Fong, E. Elsen, C.R. Weinberger, J. Mech. Phys. Solids **56**, 3242 (2008)
26. J.A. Zimmerman, E.B. Webb, J.J. Hoyt, R.E. Jones, P.A. Klein, D.J. Bammann, Modell. Simul. Mater. Sci. Eng. **12**, S319 (2003)
27. J. Li, Modell. Simul. Mater. Sci. Eng. **11**, 173 (2003)
28. D. Faken, H. Jonsson, Comput. Mater. Sci. **2**, 279 (1994)
29. G.W. Nieman, J.R. Weertman, R.W. Siegel, Nanostruct. Mater. **1**, 185 (1992)
30. X. Tian, J. Cui, B. Li, M. Xiang, Modell. Simul. Mater. Sci. Eng. **18**, 055011 (2010)
31. S. Saha, M.A. Motalab, M. Mahboob, Comput. Mater. Sci. **136**, 52 (2017)
32. T.G. Nieh, J. Wadsworth, Scr. Met. Mater. **25**, 955 (1991)
33. J. Lian, B. Baudelet, A.A. Nazarov, Mater. Sci. Eng. A **172**, 23 (1993)
34. T.G. Langdon, Mater. Sci. Forum **189**, 31 (1995)

35. Z. Shan, E.A. Stach, J.M.K. Wiezorek, J.A. Knapp, D.M. Follstaedt, S.X. Mao, Science **305**, 654 (2004)
36. V. Yamakov, D. Wolf, S.R. Phillpot, A.K. Mukherjee, H. Gleiter, Nat. Mater. **3**, 43 (2004)
37. H. Van Swygenhoven, P.M. Derlet, Phy. Rev. B **64**, 224105 (2001)
38. F. Sansoz, V. Dupont, Appl. Phys. Lett. **89**, 111901 (2006)
39. G. Sainath, P. Rohith, B.K. Choudhary, Philos. Mag. **97**, 2632 (2017)
40. E.N. Hahn, M.A. Meyers, Mater. Sci. Eng. A **646**, 101 (2015)
41. X.Z. Liao, Y.H. Zhao, S.G. Srinivasan, Y.T. Zhu, R.Z. Valiev, D.V. Gunderov, Appl. Phys. Lett. **84**, 592 (2004)
42. A.J. Cao, Y.G. Wei, Appl. Phys. Lett. **89**, 041919 (2006)

Development of Hybrid Solid Element Using Hybrid Stress–Displacement Formulation

A. Amrutha, R. Marimuthu and Rajesh P. Nair

Abstract The hybrid elements are developed based on two-field variational formulation with the displacements and stresses interpolated separately. The hybrid solid elements are less susceptible to locking than standard displacement-based formulation and can be used to model any complicated structural configurations. This paper presents the development of hybrid solid hexahedral element using hybrid stress–displacement formulation. At the time of formulation of the element, the stress parameters which are developed based on suppression of zero energy mode, as given in the literature is considered. This stress parameter is condensed out at the element level and the element stiffness matrix is expressed. Because of this process, the system of equation only depends on the displacements and externally applied load vector. This hybrid solid element is superior to displacement based formulation and will work for thin structures as well as nearly incompressible materials. The structural configuration model based on this element will converge with less number of elements. The superiority of the present element will be demonstrated through various literature problems available.

Keywords Hybrid stress–displacement formulation · Hybrid element · Solid element

Nomenclature

u	displacement vector at any point within the element
u_S	displacement vector corresponding to the surface where traction force is applied
p_i	point load applied at the node a_i in the direction where p_i applied
$[B]$	strain–displacement matrix
N	shape function matrix

A. Amrutha (✉) · R. P. Nair
Department of Ship Technology, Cochin University of Science and Technology, Cochin 682022, India
e-mail: amrutha.agulal1993@gmail.com

R. Marimuthu
SMSD/STR, VSSC, Thiruvananthapuram, India

$[N_s]$ shape function corresponding to the surface where traction force t is applied

$[C]$ compliance matrix

S_n stresses defined in the natural coordinate

S_g stresses defined in the global coordinate

$\{\beta\}$ stress parameter

ε_a strain in terms of displacement

ε_s strain in terms of stress

A transformation matrix

J Jacobian matrix

$[P_g]$ interpolation function in global coordinate system

K_e stiffness matrix

f^e external force

E modulus of elasticity

v Poisson's ratio

1 Introduction

The main advantages of developing elements based on hybrid stress–displacement formulation over standard displacement formulation are such elements perform well irrespective of whether the material is compressible or almost incompressible, whether the geometry is thin or thick.

The hybrid stress displacement formulation is two variable functional having displacements and stress parameters. The stress parameters are expressed in natural coordinate system then transformed to global coordinate system using the Jacobian matrix at Gauss points. The stress function is developed for 20 node brick element which is compared with the 27 node hybrid brick element of Jog [1] and 8 node brick element of Pian and Tong [3] based on suppression of zero energy modes. The presently developed elements performance is compared with the other elements which are available in the literature [1]. The results obtained are compared and presented in a tabular form. The present element uses only 54 stress parameters which are optimally required for the element to be stable. This element is computationally less intensive compared to 27 node element and of course, performance is a little less superior compared 27 node brick element of Jog [1]. However, this element computationally less intensive balances by refining the mesh and matches well with the 27-node of Jog [1].

2 Finite Element Formulation

The virtual work expression for solid element is given as

$$\int_V \delta\varepsilon_a{}^T S_g \, dV = \int_V \delta u^T b \, dV + \int_S \delta u_S^T \bar{t} \, dS + p_i \delta a_i \tag{1}$$

$$\int_V \delta S_g{}^T (\varepsilon_a - \varepsilon_s) dV = 0 \tag{2}$$

The interpolation functions are obtained in global coordinate system using Jacobian matrix by transformation.

The details of each term are given as

$$\varepsilon_a^T = a^T [B]^T \tag{3}$$

$$\varepsilon_S = [C] S_g = [C] [P_g] \{\beta\} \tag{4}$$

$$u = [N]a, \quad u_S = [N_S]a \tag{5}$$

The stress function for solid element is written in natural coordinate system defined as

$$S_n = [P_n]\{\beta\} \tag{6}$$

$$[S_g] = A S_n \tag{7}$$

$$[P_g] = A P_n \tag{8}$$

$$S_g = [P_g]\{\beta\} \tag{9}$$

Substituting these equations in Eqs. (1) and (2) results in

$$[G]a = [H]\{\beta\} \tag{10}$$

where

$$[H] = \int [P_g]^T [C] [P_g] \, dV \tag{11}$$

$$[G] = \int [P_g]^T [B] \, dV \tag{12}$$

$$\{\beta\} = [H]^{-1} [G]a \tag{13}$$

Finally arriving at

$$[G]^T[H]^{-1}[G]a = f^e \tag{14}$$

where

$$K_e = [G]^T[H]^{-1}[G] \tag{15}$$

$$f^e = \int_V [N]^T b \, dV + \int_S [N_S]^T \bar{t} \, dS + \{p\} \tag{16}$$

Therefore,

$$K_e a = f^e \tag{17}$$

Stress can be found out using the equation

$$\text{Stress } S_g = P_g \beta = P_g H^{-1} G a \tag{18}$$

2.1 Stress Function for 20-Noded Hexahedral Element

Stress function for 20-noded hexahedral element is

$$
\begin{aligned}
\tau^{\xi\xi} &= \beta_1 + \beta_7\xi + \beta_{13}\eta + \beta_{19}\zeta + \beta_{25}\xi\eta + \beta_{31}\eta\zeta + \beta_{37}\xi\zeta + \beta_{43}\xi\eta\zeta + \beta_{49}\eta^2 + \beta_{52}\zeta^2 \\
\tau^{\eta\eta} &= \beta_2 + \beta_8\xi + \beta_{14}\eta + \beta_{20}\zeta + \beta_{26}\xi\eta + \beta_{32}\eta\zeta + \beta_{38}\xi\zeta + \beta_{44}\xi\eta\zeta + \beta_{50}\xi^2 + \beta_{53}\zeta^2 \\
\tau^{\zeta\zeta} &= \beta_3 + \beta_9\xi + \beta_{15}\eta + \beta_{21}\zeta + \beta_{27}\xi\eta + \beta_{33}\eta\zeta + \beta_{39}\xi\zeta + \beta_{45}\xi\eta\zeta + \beta_{51}\xi^2 + \beta_{54}\eta^2 \\
\tau^{\xi\eta} &= \beta_4 + \beta_{10}\xi + \beta_{16}\eta + \beta_{22}\zeta + \beta_{28}\xi\eta + \beta_{34}\eta\zeta + \beta_{40}\xi\zeta + \beta_{46}\xi\eta\zeta \\
\tau^{\eta\zeta} &= \beta_5 + \beta_{11}\xi + \beta_{17}\eta + \beta_{23}\zeta + \beta_{29}\xi\eta + \beta_{35}\eta\zeta + \beta_{41}\xi\zeta + \beta_{47}\xi\eta\zeta \\
\tau^{\xi\zeta} &= \beta_6 + \beta_{12}\xi + \beta_{13}\eta + \beta_{24}\zeta + \beta_{30}\xi\eta + \beta_{36}\eta\zeta + \beta_{42}\xi\zeta + \beta_{48}\xi\eta\zeta
\end{aligned} \tag{19}
$$

2.2 The Global Transformation Matrix

The global transformation matrix obtained from Jacobian matrix is given as

$$[P_g] = A[P] \tag{20}$$

where

$$A = \begin{bmatrix} a_1^2 & a_2^2 & a_3^2 & 2a_1a_2 & 2a_2a_3 & 2a_1a_3 \\ b_1^2 & b_2^2 & b_3^2 & 2b_1b_2 & 2b_2b_3 & 2b_1b_3 \\ c_1^2 & c_2^2 & c_3^2 & 2c_1c_2 & 2c_2c_3 & 2c_1c_3 \\ a_1b_1 & a_2b_2 & a_3b_3 & (a_2b_1 + a_1b_2) & (a_2b_3 + a_3b_2) & (a_1b_3 + a_3b_1) \\ b_1c_1 & b_2c_2 & b_3c_3 & (b_2c_1 + b_1c_2) & (b_2c_3 + b_3c_2) & (b_1c_3 + b_3c_1) \\ a_1c_1 & a_2c_2 & a_3c_3 & (a_1c_2 + a_2c_1) & (a_3c_2 + a_2c_3) & (a_3c_1 + a_1c_3) \end{bmatrix} \quad (21)$$

where Jacobian matrix is given as

$$J = \begin{bmatrix} \frac{\partial x}{\partial \xi} & \frac{\partial y}{\partial \xi} & \frac{\partial z}{\partial \xi} \\ \frac{\partial x}{\partial \eta} & \frac{\partial y}{\partial \eta} & \frac{\partial z}{\partial \eta} \\ \frac{\partial x}{\partial \zeta} & \frac{\partial y}{\partial \zeta} & \frac{\partial z}{\partial \zeta} \end{bmatrix} = \begin{bmatrix} a_1 & a_2 & a_3 \\ b_1 & b_2 & b_3 \\ c_1 & c_2 & c_3 \end{bmatrix} \quad (22)$$

2.3   Numerical Integration

Gaussian quadrature formula is used for the numerical integration and $2 \times 2 \times 2$ and $3 \times 3 \times 3$ integration schemes are used for stiffness computation of 8-noded element, 20-noded element, and 27-noded element respectively.

$$\boldsymbol{K_e} = [G]^T [H]^{-1} [G] \quad (23)$$

$$[G] = \sum_{i=1}^{ngauss} \sum_{j=1}^{ngauss} \sum_{k=1}^{ngauss} [P_g]_{ijk}^T [B]_{ijk} det J W_i W_j W_k \quad (24)$$

$$[H] = \sum_{i=1}^{ngauss} \sum_{j=1}^{ngauss} \sum_{k=1}^{ngauss} [P_g]_{ijk}^T [C] [P_g]_{ijk} det J W_i W_j W_k \quad (25)$$

Externally applied load was integrated for volume for body force and surface integration was made for traction load and point loads were applied in the direction at a particular node.

3   Results and Discussions

This section brings out the validation of the finite elements that are developed based on Hybrid stress–displacement formulation. Validated the accuracy of 8 node brick element and 27 node brick element, then 20 node brick element is developed. The intended purpose of the following set of problems is to ascertain the accuracy and convergence rate of the developed elements in various applications and thus evaluating the elements prior to actual use. Present elements are validated with a

standard set of problems that include straight cantilever beam, curved beam, and twisted beam. The results that are tabulated are obtained from the FEM solution with the theoretical results available in literature.

3.1 Straight and Curved Beam

A straight cantilever beam and curved beam (see Figs. 1 and 2), both of thickness 0.1 m and with material properties $E = 10^7$ N/m^2, v = 0.3 is loaded by 1N in-plane force at free end. Tables 1, 2 and 3 shows the displacement values obtained for three types of elements for different meshes. From Tables 1, 2, 3 and 4, the hybrid formulation gives better results compared to displacement formulation.

3.2 Clamped Rectangular Plate

A rectangular plate with material properties $E = 3.1 \times 10^9$ N/m^2, v = 0.3 is subjected to a central point load F, whose lateral dimensions is 2a × 2b. Due to symmetry of rectangular plate, only a quadrant is modeled as shown in Fig. 3.
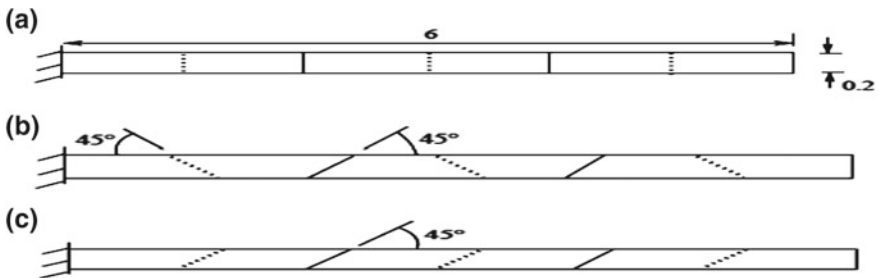
Fig. 1 Straight cantilever beam with **a** rectangular shape elements, **b** trapezoidal shape elements, **c** parallelogram shape elements

Fig. 2 Curved beam
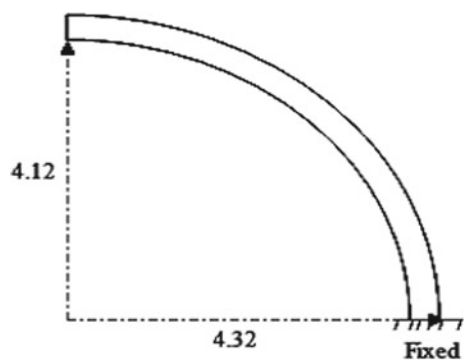
Table 1 Displacement results of cantilever beam for 1N in-plane force at free end

Theoretical value	Mesh	Displacement formulation	C.S Jog [1]	Hybrid stress–displacement formulation
0.108	*8 node*			
	6 × 2 × 2	0.104	0.105	0.105
	20 node			
	3 × 1 × 1	0.101	–	0.105
	27 node			
	3 × 1 × 1	0.102	0.107	0.107

Table 2 Displacement results of cantilever beam with trapezoidal shape elements for 1N in-plane force at free end

Theoretical value	Mesh	Displacement formulation	C.S Jog [1]	Hybrid stress–displacement formulation
0.108	*8 node*			
	6 × 2 × 2	0.066	0.005	0.066
	20 node			
	3 × 1 × 1	0.004	–	0.005
	27 node			
	3 × 1 × 1	0.004	0.068	0.068

Table 3 Displacement results of cantilever beam with parallelogram shape elements for 1N in-plane force at free end

Theoretical value	Mesh	Displacement formulation	C.S Jog [1]	Hybrid stress–displacement formulation
0.108	*8 node*			
	6 × 2 × 2	0.0661	0.0662	0.0662
	20 node			
	3 × 1 × 1	0.0539	–	0.0706
	27 node			
	3 × 1 × 1	0.0751	0.1033	0.1033

Table 4 Displacement results of curved beam for unit in-plane force at free end

Theoretical value	Mesh	Displacement formulation	C.S Jog [1]	Hybrid stress–displacement formulation
0.087	*8 node*			
	6 × 2 × 2	0.076	0.076	0.076
	20 node			
	3 × 1 × 1	0.080	–	0.086
	27 node			
	3 × 1 × 1	0.081	0.087	0.087

Fig. 3 A quadrant of
clamped rectangular plate
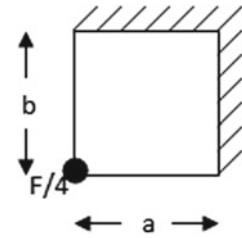
All degrees of freedom at edges are restricted. The purpose of this example is to see
whether shear locking occurs as the thickness of the plate h of the plate is reduced
in comparison to its lateral dimensions.

Four cases are considered:

Case 1. a = 1, b = 1, F = 4000, h = 0.02
Case 2. a = 1, b = 1, F = 4, h = 0.002
Case 3. a = 1, b = 2, F = 4000, h = 0.02
Case4.a = 1, b = 2, F = 4, h = 0.002.

It is found that 27-noded elements performance is superior compared to other two
elements. However, 20-noded elements results are very close to 27-noded element
(Tables 5, 6, 7 and 8).

3.3 Thick-Walled Cylinder Subjected to Internal Pressure

A thick-walled circular cylinder of inner radius 3, and outer radius 9 and unit length
is subjected to 1 N/m^2 pressure at the inner radius. The material properties are
E = 1000 N/m^2. A quarter of the domain is modeled due to symmetry. This

Table 5 Displacement results of case 1 of clamped rectangular plate for central point load

Theoretical value	Mesh	Displacement formulation	C.S Jog [1]	Hybrid stress–displacement formulation
0.0582	*8 node*			
	4 × 4 × 2	0.0318	0.0554	0.0532
	8 × 8 × 2	0.0543	0.0574	0.0547
	20 node			
	2 × 2 × 1	0.0128	–	0.0481
	4 × 4 × 1	0.0508	–	0.0562
	27 node			
	2 × 2 × 1	0.0407	0.0575	0.0550
	4 × 4 × 1	0.0531	0.0579	0.0567

Table 6 Displacement results of case 2 of clamped rectangular plate for central point load

Theoretical value	Mesh	Displacement formulation	C.S Jog [1]	Hybrid stress–displacement formulation
0.0582	*8 node*			
	4 × 4 × 2	0.0007	0.055	0.053
	8 × 8 × 2	0.0103	0.057	0.055
	20 node			
	2 × 2 × 1	0.0002	–	0.042
	4 × 4 × 1	0.0196	–	0.050
	27 node			
	2 × 2 × 1	0.0401	0.0573	0.043
	4 × 4 × 1	0.0524	0.0578	0.054

Table 7 Displacement results of case 3 of clamped rectangular plate for central point load

Theoretical value	Mesh	Displacement formulation	C.S Jog [1]	Hybrid stress–displacement formulation
0.07508	*8 node*			
	4 × 4 × 2	0.0301	0.0688	0.0657
	8 × 8 × 2	0.0655	0.0732	0.0695
	20 node			
	2 × 2 × 1	0.0121	–	0.0518
	4 × 4 × 1	0.0598	–	0.0713
	27 node			
	2 × 2 × 1	0.0427	0.0732	0.0518
	4 × 4 × 1	0.0646	0.0745	0.0710

Table 8 Displacement results of case 4 of clamped rectangular plate for central point load

Theoretical value	Mesh	Displacement formulation	C.S Jog [1]	Hybrid stress–displacement formulation
0.075088	*8 node*			
	4 × 4 × 2	0.0006	0.0686	0.0656
	8 × 8 × 2	0.0088	0.0730	0.0694
	20 node			
	2 × 2 × 1	0.0002	–	0.0450
	4 × 4 × 1	0.0180	–	0.0552
	27 node			
	2 × 2 × 1	0.0434	0.0730	0.0620
	4 × 4 × 1	0.0638	0.0743	0.0689

Fig. 4 Thick-walled circular cylinder
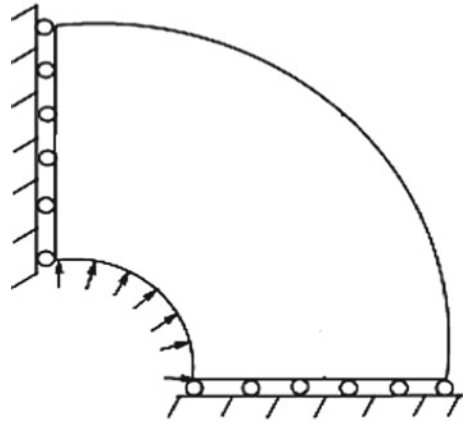
problem studies the performance of the developed elements when the material is almost incompressible, i.e., when $v \rightarrow 0.5$.

Case 1: Poison's ratio v = 0.499
Case 1: Poison's ratio v = 0.4999

The 20-node element and the 8-node element give erroneous result, but 27-noded element gives a good result (Fig. 4; Tables 9 and 10).

Table 9 Displacement results of case 1 thick-walled cylinder subjected to internal pressure

Theoretical value	Mesh	Displacement formulation	C.S Jog [1]	Hybrid stress–displacement formulation
5.060249E−03	*8 node*			
	4 × 4 × 2	0.0049	0.0049	0.0042
	8 × 8 × 2	0.0050	0.0050	0.0054
	16 × 16 × 2	0.0051	0.0050	0.0060
	20 node			
	2 × 2 × 1	0.0023	–	0.0044
	4 × 4 × 1	0.0044	–	0.0069
	8 × 8 × 1	0.0048	–	0.0079
	27 node			
	2 × 2 × 1	0.0030	0.0049	0.0049
	4 × 4 × 1	0.0046	0.0050	0.0050
	8 × 8 × 1	0.0050	0.0051	0.0051

Table 10 Displacement results of case 2 thick-walled cylinders subjected to internal pressure

theoretical value	Mesh	Displacement formulation	C.S Jog [1]	Hybrid stress–displacement formulation
5.062275E−03	*8 node*			
	4 × 4 × 2	0.00493	0.00480	0.0042
	8 × 8 × 2	0.00503	0.00501	0.0054
	16 × 16 × 2	0.00505	0.00505	0.0060
	20 node			
	2 × 2 × 1	0.0004	–	0.0044
	4 × 4 × 1	0.0024	–	0.0069
	8 × 8 × 1	0.0044	–	0.0079
	27 node			
	2 × 2 × 1	0.0021	0.0049	0.00385
	4 × 4 × 1	0.0025	0.0050	0.00504
	8 × 8 × 1	0.0050	0.0051	0.00506

4 Concluding Remarks and Scope for Future Works

It can be concluded that the developed 27-noded, 20-noded, 8-noded hexahedral elements based on hybrid stress–displacement formulation works better than a standard displacement based formulation. 20-noded hexahedral element gives more accurate result than 8-noded hexahedral elements, and 27-noded hexahedral element gives more accurate result than 20-node hexahedral element. These elements work well for compressible or nearly incompressible, regular or distorted mesh, thin or thick structures. These hybrid elements are less susceptible to locking problems than elements based on displacement formulation.

The developed 27 node based on hybrid stress–displacement formulation works for all ranges of poisons ratio except for 0.5. Hence, this can be very well used for very close incompressible material except for fully incompressible material such materials that being practically used are viscoelastic, rubber kind of material. The same element can be used for compressible materials also. Since developed elements works for thin to thick shell configuration without locking. The present linear FE formulation can be extended for nonlinear analysis also. Further, this can be extended for linear dynamic and nonlinear dynamic analysis.

References

1. C.S. Jog, A 27-node hybrid brick and a 21-node hybrid wedge element for structural analysis. Finite Elem. Anal. Design **41**, 1209–1232 (2005)
2. C.S. Jog, Improved hybrid elements for structural analysis. J. Mech. Mater. Struct. **5**(3) (2010)

3. T.H. Pian, P. Tong, Relations between incompatible displacement model and hybrid stress model. Int. J. Numer. Meth. Eng. **22**, 173–181 (1986)
4. K. Mallikarjuna Rao, U. Shrinivasa, A set of pathological tests to validate new finite elements. Sadhana **26**(6), 549–590 (2001)
5. R.H. MacNeal, R.L. Harder, A proposed standard set of problems to test finite element accuracy. Finite Elem. Anal. Design **1**, 3–20 (1985)
6. K.Y. Sze, A. Ghali, A hybrid brick element with rotational degrees of freedom. Comput. Mech. **12**, 147–163 (1993)
7. W. Chen, Y.K. Cheung, Three-dimensional 8-node and 20-node refined hybrid isoparametric elements. Int. J. Numer. Meth. Eng. **35**, 1871–1889 (1992)
8. J.A.T. Freitas, F.L.S. Bussamra, Three-dimensional hybrid-Trefftz stress elements. Int. J. Numer. Meth. Eng. **47**, 927–950 (2000)
9. T.H. Pian, D. Chen, On the suppression of zero energy deformation modes. Int. J. Numer. Meth. Eng. **19**, 1741–1752 (1983)
10. R.L. Spilker, S.P. Singh, Three-dimensional hybrid-stress isoparametric quadratic displacement elements. Int. J. Numer. Meth. Eng. **18**, 445–465 (1982)
11. K.Y. Sze, Stabilization schemes for 12-node to 21-node brick elements based on orthogonal and consistently assumed stress modes. Comput. Meth. Appl. Mech. Eng. **119**, 325–340 (1994)
12. R.L. Spilker, B.E. Engelmann, Hybrid-stress isoparametric elements for moderately thick and thin multilayer plates. Comput. Meth. Appl. Mech. Eng. **56**, 339–361 (1986)
13. S.W. Lee, J.J. Rhiu, A new efficient approach to the formulation of mixed finite element models for structural analysis. Int. J. Numer. Meth. Eng. **23**, 1629–1641 (1986)
14. K.Y. Sze, A novel approach for devising higher-order hybrid elements. Int. J. Numer. Meth. Eng. **36**, 3303–3316 (1993)
15. C.S. Jog, Higher-order shell elements based on a Cosserat model, and their use in the topology design of structures. Comput. Meth. Appl. Mech. Eng. **193**, 2191–2220 (2004)
16. K.Y. Sze, X.H. Liu, S.H.H. Lo, Hybrid-stress six-node prismatic elements. Int. J. Numer. Meth. Eng. **61**, 1451–1470 (2004)

Mixed-Mode Creep Crack Growth Simulations Using Continuum Damage Mechanics and Virtual Node XFEM

V. B. Pandey, M. Kumar, I. V. Singh, B. K. Mishra, S. Ahmad, A. Venugopal Rao and Vikas Kumar

Abstract In this work, mixed-mode elasto-plastic creep crack growth simulations are performed through virtual node extended finite element method. The continuum damage mechanics is combined with virtual node extended finite element method (VNXFEM) to avoid the requirement of fine mesh. The VNXFEM models the crack growth within an element using coarse mesh. J2 plasticity model is used to model the plasticity of isotropic and homogeneous material. To maintain the equilibrium in the elasto-plastic analysis, Newton–Raphson method is implemented. Creep strains and damage variable are computed from Liu–Murakami creep damage model. To solve the creep and damage equations, forward Euler method is applied. To reduce the local behavior of damage (mesh dependency of damage), mesh regularization schemes are adopted. P91 steel specimen at 650 °C is used and 2-D plane strain condition is assumed for simulating the mixed-mode crack propagation. The present study summarizes that VNXFEM is an effective method to model the crack propagation with a coarse mesh.

Keywords Creep crack growth · Continuum damage mechanics · Virtual node extended finite element method · Elasto-plastic · Nonlocal approach

1 Introduction

The accurate life estimation of components always remains a challenging task for the scientific community. The life prediction becomes more complicated when components are encountered to extreme environmental conditions. The components used in nuclear reactors, power plant, aero engines, and chemical plant are sub-

V. B. Pandey (✉) · M. Kumar · I. V. Singh · B. K. Mishra
Department of Mechanical and Industrial Engineering, IIT Roorkee, Roorkee 247667, Uttarakhand, India
e-mail: vibhuti.pandey27@gmail.com

S. Ahmad · A. Venugopal Rao · V. Kumar
Defence Metallurgical Research Laboratory, DRDO, Hyderabad 500066, Telangana, India

jected to high temperature and this high temperature encourages creep deformation. In the presence of cracks in such components (which usually occurs), the life of the components reduces dramatically. Therefore, the remaining life of these components needs to be estimated.

Over the years, various mathematical models [1–4] have been developed to predict the creep behavior. In the previous two decades, continuum damage mechanics (CDM) based creep models have obtained quite a reputation for creep life assessment. The models provided by [5–8] are popular in literature.

Numerical tools are essential for the life assessment of components under creep environment. The finite element method (FEM) is the most prominent numerical tool for creep and creep crack growth simulations [9–14] but it is computationally expensive. Therefore, to solve the crack growth problems accurately at coarser meshes, the extended finite element method (XFEM) has been used extensively [15]. Recently, the XFEM is combined with CDM to study the elastic, plastic and fatigue crack propagation simulations [16–19]. Pandey et al. [20] used XFEM and CDM to simulate the creep crack propagation in compact tension (CT) and C-shaped tension (CST) specimen. They concluded that the combined approach of CDM and XFEM easily models the creep crack growth at relatively coarser meshes.

It is observed by Kumar et al. [21] that XFEM uses a fine mesh to model kinks in the crack growth problems. To overcome this issue, they developed the virtual node extended finite element method (VNXFEM). The VNXFEM is a modification in standard XFEM that provides better and more efficient results at relatively coarser mesh. In VNXFEM, current tip element is separated into two virtual elements using virtual nodes [21].

It is well known that the crack propagates in a zigzag fashion when the CDM is used to model crack growth, and one has to use fine mesh in standard XFEM to solve the crack growth. Therefore, in this paper, VNXFEM is combined with CDM to study the mixed-mode creep crack growth simulation in P91 steel at 650 °C. The experimental results of P91 steel at 650 °C are obtained from [11]. To evaluate damage variable, Liu–Murakami creep damage model is used. Mesh regularization schemes are employed to reduce the effect of mesh size on the simulation.

2   Mathematical Formulation

An analytical and numerical formulation is provided in this section to solve the elasto-plastic creep crack growth problem.

2.1   *Elasto-Plastic Creep Analysis*

In this work, elasto-plastic analysis and creep analysis are performed separately. Creep strains are evaluated from the stresses, which are obtained from the

elasto-plastic analysis. For small strain problem, total strain field ε^{total} is decomposed into elastic ε^e, plastic ε^p, and creep strain ε^c parts,

$$\varepsilon^{total} = \varepsilon^e + \varepsilon^p + \varepsilon^c \tag{1}$$

Isotropic hardening and J2 plasticity model is selected to mimic the plasticity. For small strain problems, the total incremental strain is written as

$$d\varepsilon = d\varepsilon^e + d\varepsilon^p \tag{2}$$

The incremental part of elastic strain is computed as

$$d\varepsilon^e = \mathbf{C}\, d\boldsymbol{\sigma} \tag{3}$$

where $\mathbf{C}$ is the compliance matrix.

For associated flow rule of plasticity, the incremental part of plastic strain is computed as

$$d\varepsilon^p_{ij} = \Delta\lambda \frac{\partial F}{\partial \boldsymbol{\sigma}_{ij}} \tag{4}$$

where $\Delta\lambda$ is a scalar multiplier and F is the von-Mises yield function.

2.1.1 Creep Strain Relations

To calculate the creep strain rate, Liu–Murakami creep constitutive model is used and it is expressed in its multiaxial form as [11]

$$\dot{\varepsilon}^c_{ij} = \frac{3}{2} A \sigma^n_{eq} \frac{\mathbf{S}_{ij}}{\sigma_{eq}} \exp\left(\frac{2(n+1)}{\pi\sqrt{1+3/n}} \left(\frac{\sigma_1}{\sigma_{eq}}\right)^2 \omega^{3/2} \right) \tag{5}$$

where A and n are material constants. $\dot{\varepsilon}^c_{ij}, \omega, \mathbf{S}_{ij}, \sigma_1, \sigma_{eq}$ represents creep strain rate, damage variable, deviatoric stress, maximum principle stress, and von-Mises stress, respectively.

The damage evaluation equation is given as

$$\dot{\omega} = D \frac{(1-e^{-q})}{q} \sigma^p_r e^{q\omega} \tag{6}$$

where D, q, and p are material constants. σ_r is the rupture stress which is given as

$$\sigma_r = \alpha\sigma_1 + (1 - \alpha)\sigma_{eq} \tag{7}$$

where α is a multi-axiality parameter. To predict the value of α, either notched specimen or CT specimen can be used.

2.2 Extended Finite Element Method

To capture the discontinuities, enrichment functions are added in the standard FE approximation [15]. After adding enrichment functions, displacement approximation becomes,

$$
\begin{aligned}
\mathbf{u}(\mathbf{x}) = &\sum_{i=1}^{ne} N_i(\mathbf{x})\mathbf{u}_i + \sum_{j=1}^{np} N_j(\mathbf{x})\big[H(\mathbf{x}) - H(\mathbf{x}_j)\big]\mathbf{a}_j \\
&+ \sum_{k=1}^{nq} N_k(\mathbf{x})\left\{ \sum_{\alpha=1}^{4} [\gamma_\alpha(\mathbf{x}) - \gamma_\alpha(\mathbf{x}_k)]\mathbf{b}_k^\alpha \right\}
\end{aligned} \tag{8}
$$

where, ne is the set of standard FE nodes in the mesh, $\mathbf{u}_i$ is the standard FE nodal displacement vector, $N(\mathbf{x})$ is the standard FE shape function, np is the set of nodes associated with split elements and nq is the set of nodes associated with tip elements. $\mathbf{a}_j$ is the nodal displacement vector corresponding to Heaviside function $H(\mathbf{x})$ and $\mathbf{b}_k$ is the nodal displacement vector corresponding to the branch function $\gamma_\alpha(\mathbf{x})$.

To ensure the plasticity around the crack tip, HRR (Hutchinson, Rice, and Rosengren) singular enrichment functions are employed as branch functions [20].

$$\gamma_\alpha(\mathbf{x}) = r^{1/1+m}\left[\cos\frac{\theta}{2}, \sin\frac{\theta}{2}, \cos\frac{\theta}{2}\sin\theta, \sin\frac{\theta}{2}\sin\theta\right] \tag{9}$$

where (r, θ) are the local crack tip parameters and m is the power law hardening exponent.

2.3 Crack Propagation Strategy

For a crack to grow, two parameters are required: (i) crack direction and (ii) increment in crack length. To find the direction of crack, a semicircle is drawn around the crack tip as shown in Fig. 1. Then, some points are selected on the circumference of this semicircle. At each point, stress triaxiality is calculated from the known stress field. The point, which has the maximum value of stress triaxiality, provides the crack direction. To obtain the smooth crack path, some more

Fig. 1 Crack propagation
direction finding scheme

Virtual Split Element

Virtual Tip Element

Crack Tip

Gauss Point
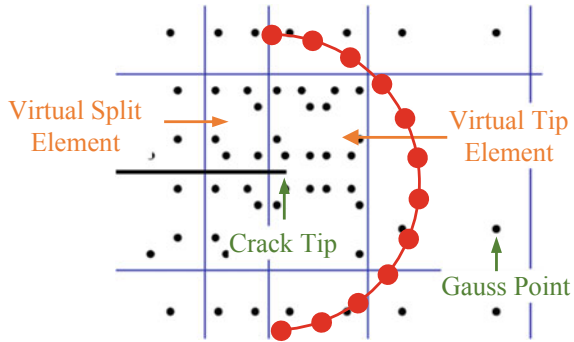
semicircles of slightly smaller and larger radius are also tested and then the direction is achieved by averaging the direction obtained from each semicircle. In the present work, for the sake of brevity in the simulation, the increment in crack length is considered a constant value. Pandey et al. [20] have shown that below $\Delta a = 0.25$ mm, the crack growth curve diverges significantly and the large value of the crack increment can't be justified physically. Therefore, in the present work, as the damage criterion satisfies, $\Delta a = 0.25$ mm is added to the previous crack tip in the obtained direction.

In VNXFEM, as the crack advances, the virtual tip element also shifts their position and hence, the number of Gauss points and their position changes in the element. As per Eq. (6), the damage is evaluated at the Gauss points. Since, the number of these Gauss points and their location changes with crack growth, it is essential to calculate the damage value on new points properly. For this reason, the data transfer technique is also used in the present simulation. To implement the data transfer technique, Gauss points are grouped in their respective elements and then by using extrapolation–interpolation function, the value of damage is estimated on the new Gauss points. To perform the data transfer technique, a built-in MATLAB function named *scatteredinterpolant* is used [22]. For the mathematical details of *scatteredinterpolant*, the interested readers are suggested to follow [23].

2.4 Mesh Regularization

Mesh regularization schemes (i.e., nonlocal integral damage model, reduction in the critical value of damage parameter and stress limitation approach) proposed by Murakami and Liu [10] are implemented in the present work to diminish the mesh dependency of the solution.

3   Results and Discussion

In this section, two cases are considered for the creep crack growth. In the first case, a CT specimen having straight crack is used for the validation of study. In the second case, an inclined cracked CT specimen is used to simulate the results of mixed-mode crack growth problem.

3.1   *Validation*

A compact tension specimen made of P91 steel subjected to 3600 N at 650 °C is used for the validation. The stress–strain curve for P91 steel at 650 °C is given in Fig. 2. The dimensions of CT specimen and crack orientation are shown in Fig. 3a.

Material properties and creep constants of P91 at 650 °C are provided in Table 1. The value of creep constants (i.e., A and n) and damage constants (i.e., D, p, and q) are evaluated from creep curves and stress versus rupture time plot. However, to evaluate the rupture stress, α is used. The value of α is predicted such that it can estimate the crack growth curves. Hence, this value can be different as it depends on the numerical approach [20, 24]. Once this value is obtained, it remains fixed for other studies. The effect of different values of α can be found in [20].

The experimental results are taken from [11]. A coarse mesh of 45×45 elements is used for simulating the results. To implement the nonlocal approach, apart from critical value of damage at each Gauss point (i.e., ω^C), two other numerical parameters are also required. The length scale parameter (i.e., l_c) and the damage parameter of nonlocal domain (i.e., Dcp) are implemented to reduce the mesh sensitivity. The details regarding to the implementation of these numerical parameters can be found in [20]. In the present work, the critical value of numerical

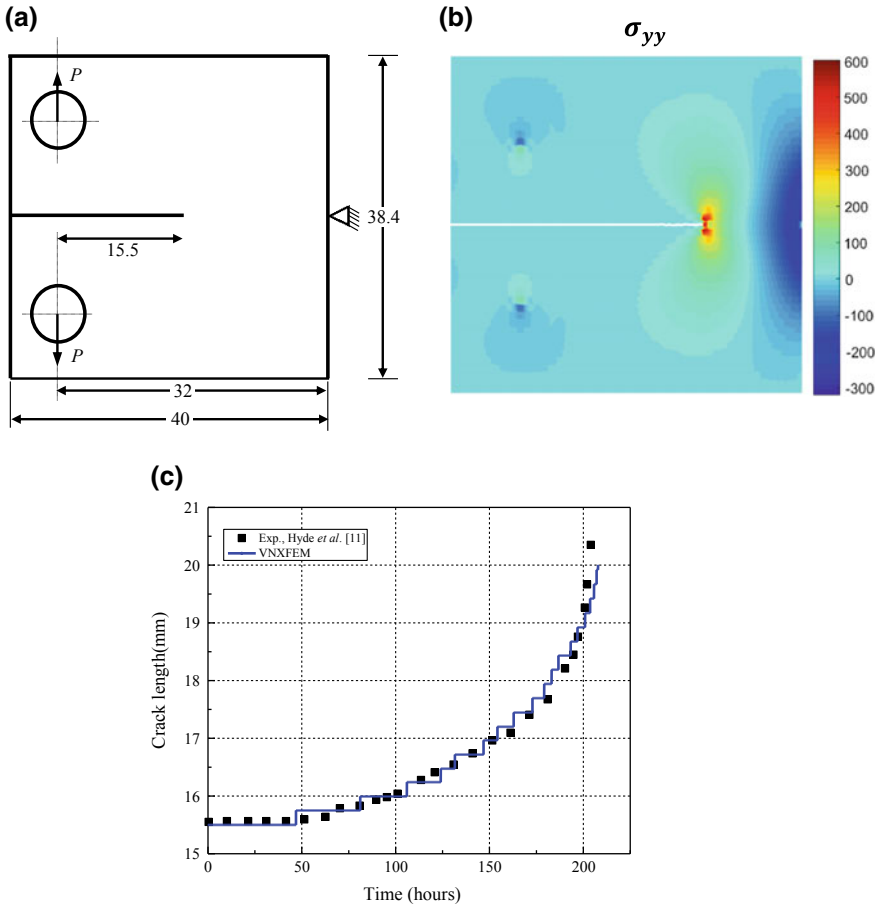**Fig. 2** Stress-strain curve for P91 steel at 650 °C [11]
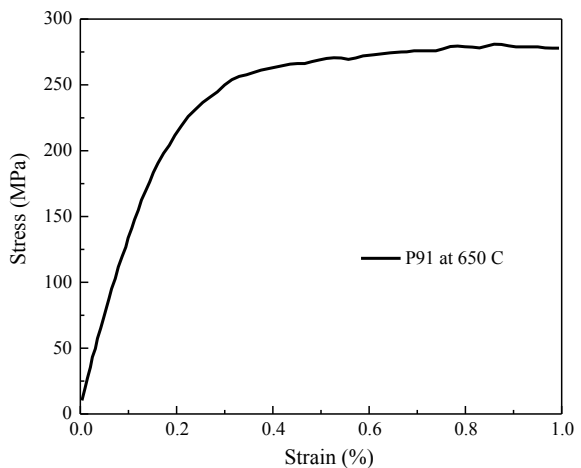
Fig. 3 Straight crack propagation. **a** Dimensions of CT specimen. **b** Stress contour plot. **c** *a* versus time curve

Table 1 Material properties, creep and damage constants of P91 steel [11]

E (GPa)	ν	σ_y (MPa)	σ_u (MPa)	A (MPa^{-n} h^{-1})	n	D (MPa^{-p} h^{-1})	p	q	α
132	0.3	262	281	1.092×10^{-20}	8.462	2.952×10^{-16}	6.789	3.2	0.48

parameters, i.e., $\omega^C = 0.99$ and $Dcp^C = 0.9$ is considered for crack growth. For reducing the mesh dependency, $l_c = 1.2$ mm is chosen. The value of these numerical parameters is selected such that they can mimic the crack growth curve. Once these values are selected for a specimen, they can be used for other studies (i.e., different applied loads and different geometries) on same temperature [20].

A plane strain condition is assumed for the simulations. The crack growth results are compared with the experimental data. Simulated results in the form of stress plot

and crack length versus time curve are shown in Fig. 3b, c, respectively. The present simulation shows good agreement with experimental results. Result reported in Fig. 3b indicates that the scheme (as discussed in Sect. 2.3) to predict the crack direction gives satisfactory results. The validation study also confirms that VNXFEM is an efficient approach to simulate the creep crack propagation with coarse meshes.

3.2 Mixed-Mode Crack Growth

In this case, a CT specimen with inclined crack is used to study of mixed-mode crack propagation. Dimensions of CT specimen and crack orientation are shown in
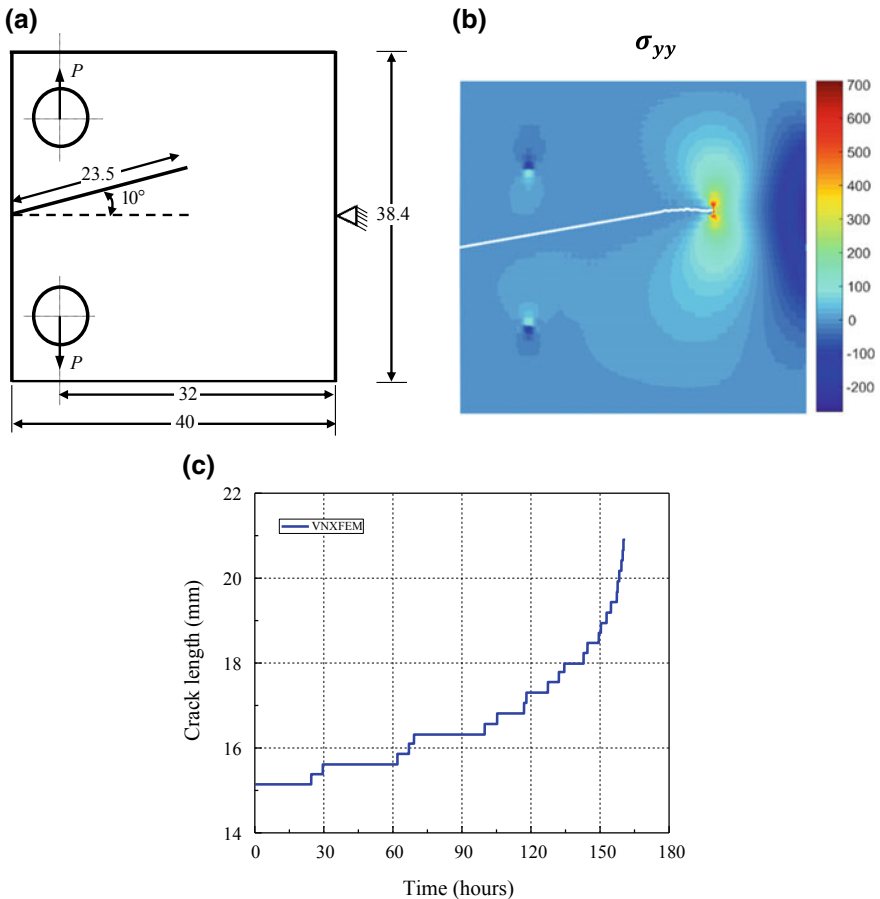

Fig. 4 Inclined crack propagation. **a** Dimensions of CT specimen. **b** Stress contour plot. **c** *a* versus time curve

Fig. 5 Comparison of *a* versus time curve of mode I and mixed mode loading
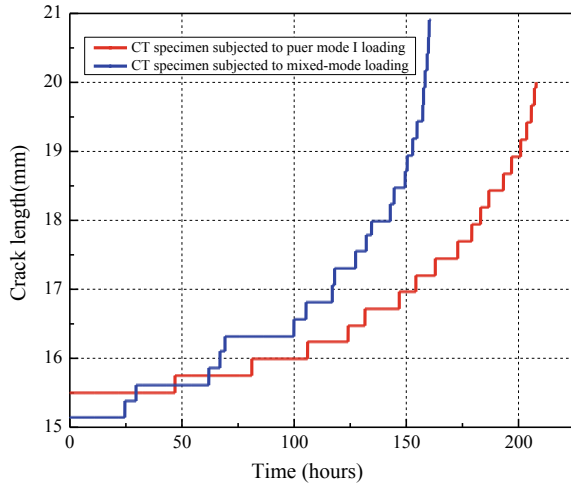

Fig. 4a. Applied load, material, and numerical parameters are taken same as the previous case. The simulated results are presented in the form of stress plot and crack length versus time graph in Fig. 4b, c, respectively. Figure 4b shows that the combination of CDM and VNXFEM can efficiently capture the direction for mixed-mode crack growth problems.

To study the effect of mixed-mode loading on crack growth rate, the crack growth curves obtained from straight cracked CT specimen and inclined cracked CT specimen are drawn in Fig. 5. It can be seen that the crack growth rate is higher in the inclined cracked CT specimen, which is due to less constraint condition in mixed mode as compared to pure mode I loading. Therefore, the von-Mises stresses near the crack tip are relatively higher in mixed-mode condition, which leads to higher damage evolution rate and consequently higher crack growth rates as compared to pure mode I loading.

4 Conclusions

In this paper, mixed-mode creep crack propagation is simulated by virtual node extended finite element method and continuum damage mechanics. Liu–Murakami creep damage model is implemented to evaluate the damage variable and creep strain. Compact tension specimen made of P91 steel subjected to 3600 N at 650 °C is used to perform the study. A plane strain condition is assumed for the crack propagation. Mesh regularization schemes are applied to reduce the mesh-dependent results. To predict the crack propagation direction, a semicircle and stress triaxiality-based approach are employed. Data transfer method is also used in this study to transfer the history-dependent variables from old Gauss points to new Gauss points. The present study shows that the proposed methodology is

capable enough to determine the remaining life of the cracked specimen. Simulation performed on an inclined cracked specimen predicts the crack growth direction efficiently. This study summarizes that the VNXFEM with coarse mesh is sufficient to predict the residual life of cracked specimen under creep environment.

References

1. F.H. Norton, *The Creep of Steel at High Temperatures* (McGraw-Hill Book Company Incorporated, New York, 1929)
2. A. Graham, K.F.A. Walles, J. Iron Steel Inst. Lond. **179**, 105 (1955)
3. R.W. Evans, B. Wilshire, *Creep of Metals and Alloys* (Institute of Metals, CRC Press, 1985)
4. M. Kumar, I.V. Singh, B.K. Mishra, S. Ahmad, A.V. Rao, V. Kumar, J. Mater. Eng. Perform. **25**, 3985 (2016)
5. L.M. Kachanov, Izvestia Akademi Nauk SSSR Otd. Tekhn. Nauk **8**, 26 (1958)
6. Y.N. Rabotnov, *Creep Problems In Structural Members* (North-Holland, Amsterdam, 1969)
7. K.M. Nikbin, D.J. Smith, G.A. Webster, Proc. R. Soc. Lond. A Math. Phys. Eng. Sci. **396**, 183 (1984)
8. Y. Liu, S. Murakami, JSME Int. J. Ser. A **41**, 57 (1998)
9. J.F. Wen, S.T. Tu, X.L. Gao, J.N. Reddy, Eng. Fract. Mech. **98**, 169 (2013)
10. S. Murakami, Y. Liu, Int. J. Damage Mech. **4**, 230 (1995)
11. M. Saber, Experimental and finite element studies of creep and creep crack growth in P91 and P92 weldments. Doctoral Dissertation, University of Nottingham (2011)
12. M. Yatomi, K.M. Nikbin, N.P. O'Dowd, Int. J. Pres. Vessels Pip. **80**, 573 (2003)
13. C.S. Oh, N.H. Kim, Y.J. Kim, C. Davies, K. Nikbin, D. Dean, Eng. Fract. Mech. **78**, 2966 (2011)
14. N.H. Kim, C.S. Oh, Y.J. Kim, C.M. Davies, K. Nikbin, D. Dean, Eng. Fract. Mech. **105**, 169 (2013)
15. T. Belytschko, T. Black, Int. J. Num. Meth. Eng. **45**, 601 (1999)
16. R. Larsson, M. Fagerstrom, Int. J. Num. Meth. Eng. **62**, 1763 (2005)
17. Y. Xu, H. Yuan, Comput. Mater. Sci. **46**, 579 (2009)
18. M.R. Seabra, P. Šuštarič, J.M. Cesar de Sa, T. Rodič, Comput. Mech. **52**, 161 (2013)
19. S.N. Roth, P. Léger, A. Soulaïmani, Comput. Methods Appl. Mech. Eng. **283**, 923 (2015)
20. V.B. Pandey, I.V. Singh, B.K. Mishra, S. Ahmad, A.V. Rao, V. Kumar, Int. J. Damage Mech. 1056789517737593, (2017)
21. S. Kumar, I.V. Singh, B.K. Mishra, T. Rabczuk, Comput. Methods Appl. Mech. Eng. **283**, 1425 (2015)
22. MATLAB and Statistics Toolbox Release 2012b, The MathWorks, Inc., Natick, Massachusetts, United States
23. I. Amidror, J. Elect. Imaging **11**, 157 (2002)
24. C.J. Hyde, T.H. Hyde, W. Sun, A.A. Becker, Eng. Fract. Mech. **77**, 2385 (2010)

Influence of Curvature Ratio on Perforation of 2024 Aluminium by Conical Impactor

K. Senthil, S. Rupali, M. A. Iqbal, A. Thakur and A. P. Singh

Abstract The impact resistance of 2024 aluminium alloy target plate of varying curvature ratio has been studied against conical impactor through numerical simulations using ABAQUS. The curvature ratio (h/r) of the target was varied as 0, 0.25, 0.5, 0.75 and 1.15 and the curvature ratio was calculated as the ratio between apex height (h) and radius (r) of the target. The apex height of the target (h) was varied as 0, 17.1, 34.2, 51.3 and 68.4 mm, whereas, the span (l) and radius (r) of the target are 119 and 59.5 mm, respectively. The material parameters for the Johnson–Cook model were employed to predict the material behaviour of target as well as projectile as available in literature [1–3]. The impact velocity of projectile was 605 and 180 m/s, considered against the chosen target configuration to study the influence of varying incidence velocity. The choice of 180 m/s incidence velocity is likely to be equivalent to the ballistic limit of 3.18 mm thick 2024 aluminium target, whereas, the 605 m/s incidence velocity was considered based on the assumption that hand guns were operated in the range of 500–820 m/s incidence velocity. It was observed that when the incidence velocity is 605 m/s, the resistance of target with varying curvature ratio is insignificant. However, the incidence velocity is 180 m/s, the resistance of the target was found to be increased significantly with increasing curvature ratio. Therefore, it is concluded that the incidence velocity is close to the limiting velocity, of 180 m/s, the resistance of the target with curvature ratio of 1.15 was found to be increased by 52% as compared to the target with curvature ratio of 0.

Keywords Curvature of target · Conical impactor · Aerospace alloy · Finite element analysis · Impact resistance

K. Senthil (✉) · S. Rupali · A. Thakur · A. P. Singh
Department of Civil Engineering, NIT Jalandhar, Jalandhar 144011, Punjab, India
e-mail: kasilingams@nitj.ac.in; urssenthil85@yahoo.co.in

M. A. Iqbal
Department of Civil Engineering, IIT Roorkee, Roorkee 247667, India

1   Introduction

Aluminium 2024 alloy seems to be monarch in aircraft construction, though new alloys have been applied in the field of aerospace industry. The 2024 aluminium alloy is used in wings and fuselage structures because of the tension they receive during its operation. Nowadays, designing aircraft skin against sharp fragments or projectile impact is very important. However, the ballistic studies on 2024 aluminium alloy are rarely available in the literature [4–7]. A majority of the studies on ballistic impact was focused on the flat target plate due to the fact that a certain incidence addresses the worst scenario for predicting the target performance. However, in most of the impact event, the target may be curvature in nature. Based on a detailed literature survey, it was observed that the ballistic performance of thin aluminium plates and shells were studied widely [1, 3, 8, 9]. However, the studies on shells and curved structures against sharp nose such as conical projectiles on potential and most widely used aerospace materials such as 2024 aluminium alloy are rarely available. In the present study, numerical investigations were carried out on 2024-O aluminium of 3.17 mm thick target of varying curvature against cylindroconical nose hard steel projectile of 12.7 mm diameter. The ABAQUS finite element code in conjunction with Johnson–Cook elasto-viscoplastic material model available in literature was employed to perform the simulation. Also, the numerical simulations were carried out for the ballistic evaluation of targets against conical projectiles at varying incidence velocities in order to obtain the response of target at varying conditions.

2   Constitutive Modelling

The strength and damage response of the 2024 aluminium target material has been predicted using the Johnson and Cook [10] elasto-viscoplastic constitutive equations are already available in ABAQUS FE-based commercial software. The constitutive behaviour and model was based on the von Mises stress laws. The von Mises flow rules takes the effect of yielding of material, linear thermoelasticity, plastic behaviour, strain hardening of material, strain rate hardening, softening of material and damage. Johnson and Cook [10] have extended the failure criterion proposed by Hancock and Mackenzie [11] by adding the effect of strain path, strain rate and temperature in the fracture strain equations, along with the stress triaxiality. The fracture criterion was based on the damage evolution wherein the fracture of the material was assumed to occur when the damage indicator, reaches one. The strain at failure was assumed to be dependent on a non-dimensional plastic strain rate, a dimensionless pressure-deviatoric stress ratio, (between the mean stress and the equivalent von Mises stress) and the non-dimensional temperature. As it was discussed already in Senthil and Iqbal [12] that, when material damage occurs, the stress–strain relationship no longer accurately represents the material behaviour,

ABAQUS [13]. The use of stress–strain relationship beyond ultimate stress introduces a strong mesh dependency based on strain localization and the energy dissipated decreases with a decrease in mesh size. In the present study, Hillerborg's [14] fracture energy criterion has been employed in order to reduce mesh dependency by considering stress–displacement response after the material reaches the ultimate strength, i.e. damage begins. In the present study, the fracture energy approach has been employed as a damage evolution criterion in conjunction with Johnson–Cook damage initialization criteria. The damage evolution criterion assumes that the damage is characterized by the progressive degradation of material stiffness leading to its failure. It also takes into account the combined effect of different damage mechanisms acting simultaneously on the same material. The material parameters proposed by Kay [2] are used to characterize the material behaviour of target as shown in Table 1. The material behaviour of the deformable conical projectile was also defined using the JC model available in ABAQUS [13]. In the present study, the projectile material was assumed to be similar to that of hardened steel core available in literature Iqbal et al. [1, 3]. The material parameters of hardened steel projectile and target employed for the JC model are shown in Table 1.

Table 1 Material parameters for target and projectile

Description	Notations	Parameters	
		Target [2]	Projectile [1, 3]
Modulus of elasticity	E (MPa)	71,000	200,000
Poisson's ratio	v	0.33	0.32
Density	ρ	2710	7850
Yield stress constant	A (MPa)	368.9	1657
Strain hardening constant	B (MPa)	683.9	20,855
	n	0.73	0.651
Viscous effect	C	0.0083	0.0076
Thermal softening constant	m	1.7	0.35
Reference strain rate	ε_o	1	0.0005
Melting temperature	Θ_{melt} (K)	893	1800
Transition temperature	$\Theta_{transition}$ (K)	293	293
Fracture strain constant	D_1	0.112	0.0301
	D_2	0.123	0.0142
	D_3	1.5	−2.192
	D_4	0.007	0
	D_5	0	0.35

3   Numerical Modelling

The finite element model of the target and the projectile was made using three dimensional modelling approach of ABAQUS. The projectile, as well as target, was modelled as deformable body. The total length (38.6 mm), the nose length (12.7 mm) and cylindrical length (25.9 mm) of the projectile, Senthil et al. [7, 15]. The mass of the projectiles was kept constant, 30 g. The target plate was modelled as a deformable body with a diameter of 119 mm. The surface-to-surface contact was assigned between the projectile and target using kinematic contact algorithm. The projectile was considered as the master surface and the contact region of the plate as slave surface, Senthil and Iqbal [12], Senthil et al. [16]. The effect of friction between the projectile and target was considered 0.04. The target plates were restrained at periphery with respect to all degree of freedom. The size of the element was considered 0.2 mm × 0.2 mm × 0.2 mm in the impact region of target of the all chosen target configuration. The total number of elements of target modelled against 0, 17.1, 34.2, 51.3 and 68.4 mm apex height was 104,921, 169,521, 176,471, 178,380 and 178,375, respectively. The size of element was considered based on a mesh convergence study performed in our previous study, Senthil et al. [7, 15]. The deformable projectile was meshed with four-node linear tetrahedron elements, C3D4. The size of the element was 1 mm in the whole body of the projectile and the total number of elements was 12,384. The typical finite element model of projectile, as well as target, were shown in Fig. 1. The simulations were performed up to 0.0005 s with 20 frames. When the damage parameter reaches 1, the element will be killed by default and are deleted from the system during the interaction of projectile and target of every steep time of 20 frames (0.0005/20 = 0.000,025 s).
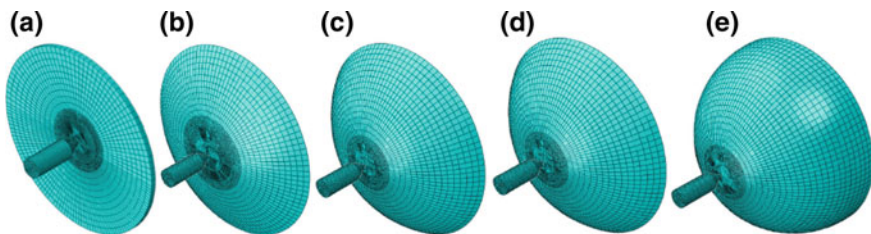

Fig. 1 Finite element modelling of impactor and target of curvature ratio **a** 0, **b** 0.25, **c** 0.5, **d** 0.75 and **e** 1.15

4 Results and Discussion

The ballistic resistance of 3.175 mm monolithic plate was studied against 12.7 mm diameter conical projectiles. The numerical results of the present study have been validated with the available experimental results, Senthil et al. [17]. The incidence velocities 605 and 180 m/s were employed in the present study. The impact and residual velocities of projectiles against the target of varying curvature are shown in Table 2. It is found that the residual velocity of projectile at high incidence, i.e. 605 m/s, the resistance of the target is almost same and it was concluded based on the residual velocity of projectile close to 589 m/s (in the range of 584–594 m/s). The reason may be due to the high incidence velocity of projectile and thin target and the variation of residual velocity of projectile was 584–594 m/s may be neglected. However, at lower incidence velocity, i.e. 180 m/s, the resistance of target affects significantly and the residual velocity of the projectiles was found to be varying in the range of 57–0 m/s. It was observed that in case of flat target, the ballistic performance was found to be inferior (Residual velocity 57 m/s) whereas the target with curvature ratio of 0.25 was found to be superior (Residual velocity 0 m/s) among the chosen target configurations. The flat target failed through tension and shear dominations along with compression and negligible bending compression. In case the target having curvature ratio 0.25, the target initially was influenced by significant out of plane bending due to their curvature and later the target was stretched significantly and failed through tension and shear dominations. The penetration and perforation of the target of varying curvature ratio against conical projectiles of 605 and 180 m/s incidence velocities were shown in Fig. 2a–e. Therefore, it is concluded that the incidence velocity close to limiting velocity, i.e. 180 m/s, the resistance of the target with curvature ratio of 1.15 was found to be increased 50% as compare to the target with curvature ratio of 0.

Figure 3 shows the von Mises stresses of target hit by conical projectile of incidence velocity 605 and 180 m/s. The projectile trajectory during perforation remains unchanged for each configuration of increasing curvature ratio and the target failed through petal formation. The intensity of global target deformation has been found to increase in case of target with 0.25 curvature ratio, see Fig. 3b. The von Mises stress at the target having curvature ratio of 0, 0.25, 0.5, 0.75 and 1.15 against 605 m/s incidence velocity was found to be 681, 599, 702, 719 and

Table 2 Ballistic response of target against 605 and 180 m/s incidence velocity

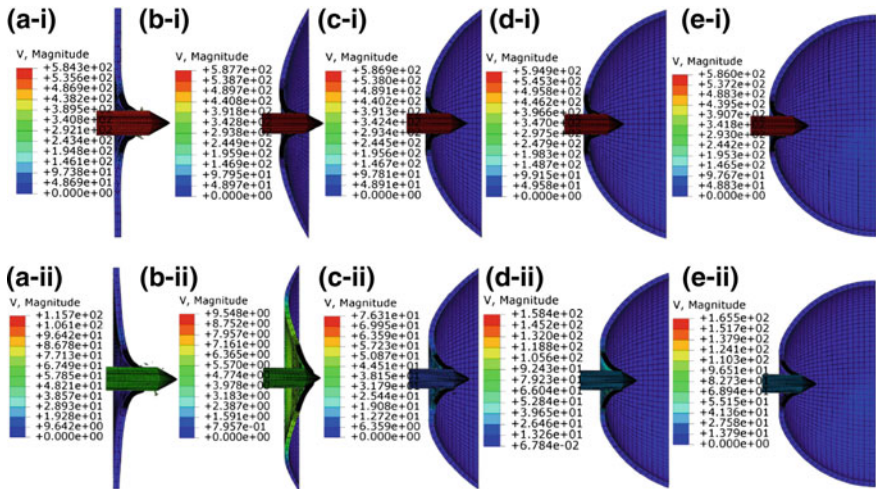| Curvature ratio	Residual velocity (m/s)	
	Incidence velocity 605 m/s	Incidence velocity 180 m/s
0	584	57
0.25	587	0
0.50	586	19
0.75	594	27
1.15	586	26

Fig. 2 Residual velocity (m/s) of projectiles against the target having curvature ratio **a** 0, **b** 0.25, **c** 0.50, **d** 0.75 and **e** 1.15 at (i) 605 and (ii) 180 m/s incidence velocity
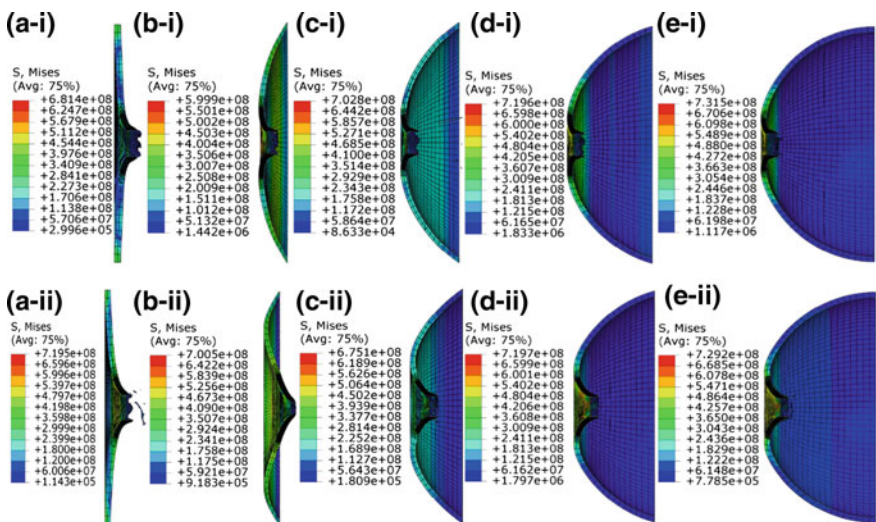

Fig. 3 Von Mises stresses (N/m^2) of target having curvature ratio **a** 0, **b** 0.25, **c** 0.50, **d** 0.75 and **e** 1.15 at (i) 605 and (ii) 180 m/s incidence velocity

731 MPa respectively. The von Mises stress at the target having curvature ratio of 0, 0.25, 0.5, 0.75 and 1.15 against 180 m/s incidence velocity was found to be 719, 700, 675, 719 and 729 MPa, respectively. It is observed that the stress developed in the target having curvature ratio of 0.75 and 1.15 were found to be almost same. In case of target curvature ratio 0 and 0.5, the Mises stress was found to be varied in the range of 5%. At target curvature ratio 0.25, the Mises stress was found to be varied in the range of 15%. At 605 m/s incidence velocity, the minimum stress was observed in the target having curvature ratio 0.25 was about 599 MPa and it is found to be more suitable. At 180 m/s incidence velocity, the minimum stress was observed in the target having curvature ratio 0.50 was about 675 MPa and it is found to be more suitable.

The influence of low and high incidence velocity of conical nose impactor on 2024 aluminium has been studied. Figure 4i–ii shows the effect of incidence velocity of 180 and 650 m/s on the target impacted by 30 g mass deformable conical nose impactor. The maximum forces developed in the target having curvature ratio of 0, 0.25, 0.5, 0.75 and 1.15 against 605 m/s incidence velocity was found to be 1949, 782, 763, 366 and 127 kg respectively. At 605 m/s velocity, all the target was found perforated. The maximum forces developed in the target having curvature ratio of 0, 0.25, 0.5, 0.75 and 1.15 against 180 m/s incidence velocity was found to be 1558, 661, 150, 111 and 161 kg respectively. At 180 m/s incidence velocity, the target having curvature ratio 0.25 offered resistance significantly without any perforation. It is observed that 0.25 curvature ratio has experienced global deformation due to less curvature, see Fig. 4b-ii. It is observed that the at low as well as high incidence velocity, the forces developed in the target
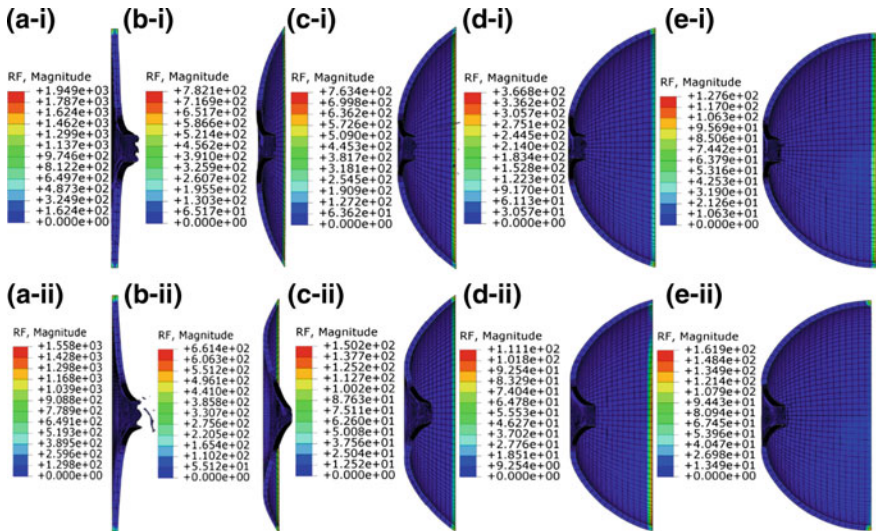

Fig. 4 Reaction forces (Kg) offered by target having curvature ratio **a** 0, **b** 0.25, **c** 0.50, **d** 0.75 and **e** 1.15 at (i) 605 and (ii) 180 m/s incidence velocity

found almost similar. Therefore, it is concluded that the resistance of target was found to be increased with increase of curvature ratio either of higher or lower the incidence velocity.

The influence of varying incidence velocity was studied on the failure mechanism of the target. The change in shape of petals was noticed due to increase in incidence velocity of projectile. At low incidence velocity, the material stretched equally when the nose of projectile comes out of the rear side after piercing the target and found five petals, see Fig. 5a. In case of high incidence velocity, the material stretched equally when the nose of projectile comes out of the rear side after piercing the target and found six petals, see Fig. 5b. Therefore, it is concluded that the failure mechanism of the target at high and low incidence velocity has been found to be not identical, Fig. 5. In the present study, the influence of varying incidence velocity against varying curvature ratio has not been discussed since the chosen incidence velocity of 180 m/s is close to ballistic limit.

The influence of varying curvature ratio was studied on the failure mechanism of the target, see Fig. 6. The change in shape of petals, as well as change in number of petals, were also noticed due to increase in curvature ratio of target. The number of petals though increased with an increase in the curvature ratio up to 0.50, however it remained smaller than that of Fig. 5a. The number of petals on target having curvature ratio of 0, 0.25, 0.50, 0.75 and 1.15 against 605 m/s incidence velocity is 6, 6, 7, 6 and 5 petals, respectively. The material stretched equally when the nose of projectile comes out of the rear side after piercing the target having curvature ration 0 and 0.25 and found six petals, see Fig. 6a, b. In case of curvature ratio 0.5, the number of petals were found seven and unequal in shapes and height, see Fig. 6c. It may be due to the reason that the radius and apex height of the target is responsible for the shape and sharpness of the petals. In case of curvature ratio 0.75 and 1.15, the number of petals were found six and five respectively, see Fig. 6d–e. It is also noticed that the gap between the petals are more in case of target having curvature ratio 1.15. Therefore, it is concluded that the failure mechanism of target changes significantly by varying the curvature ratio.
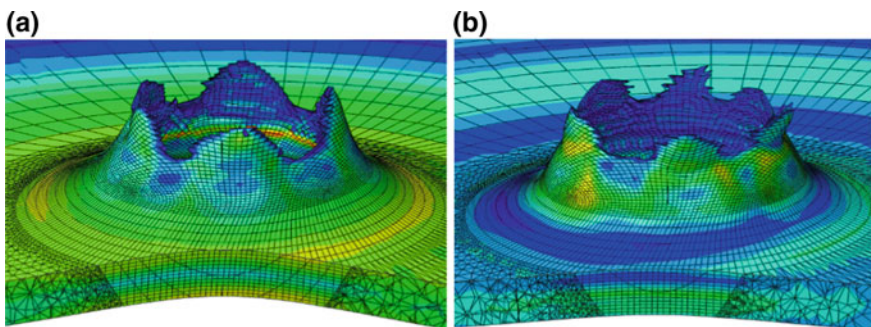

Fig. 5 Deformed profile of flat target against **a** 180 and **b** 605 m/s incidence velocity
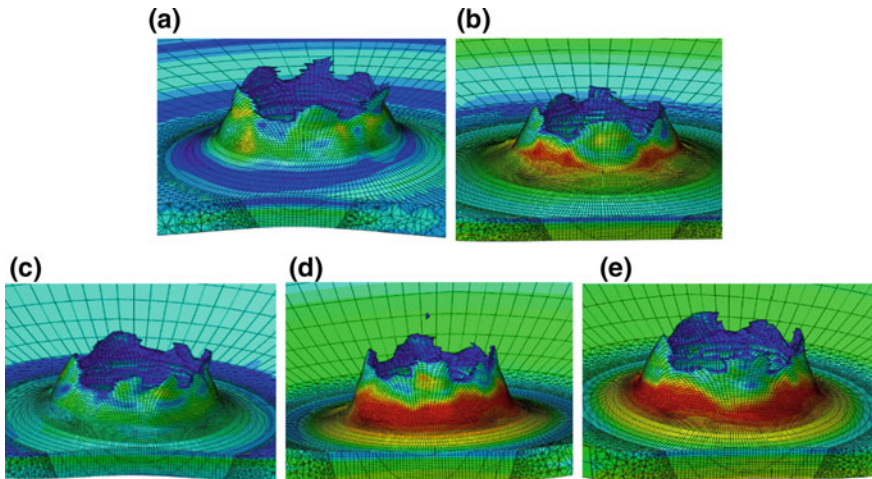
Fig. 6 Deformed profile of target having varying curvature ratio **a** 0, **b** 0.25, **c** 0.50, **d** 0.75 and **e** 1.15 against 605 m/s incidence velocity

5 Conclusions

The ballistic resistance of aerospace aluminium alloy of varying curvature ratio has been studied against conical impactor having mass of 30 g through numerical simulations using ABAQUS/Explicit commercial package. The curvature ratio of the target was varied as 0, 0.25, 0.5, 0.75 and 1.15 and the curvature ratio is calculated as the ratio between apex height (h) and radius (r) of the target. The material parameters for the Johnson–Cook model were employed to predict the material behaviour of target, as well as projectile, were available in the literature. The impact velocity of projectile 605 and 180 m/s was considered against the chosen target configuration to study the influence of incidence velocity. The results thus obtained in light of residual velocity, von Mises stresses and reaction forces were compared and the following conclusions were drawn.

It is concluded that the incidence velocity close to limiting velocity, i.e. 180 m/s, the resistance of the target with curvature ratio of 1.15 was found to be increased by 52% as compared to the flat target (curvature ratio of 0). At 605 m/s incidence velocity, the minimum stress was observed in the target having curvature ratio 0.25 was about 599 MPa and it is found to be more suitable. At 180 m/s incidence velocity, the minimum stress was observed in the target having curvature ratio 0.50 was about 675 MPa and it is found to be more suitable. In light of reaction forces, it is concluded that the resistance of target was found to be increased with increase of curvature ratio either of higher or lower the incidence velocity. The failure mechanism of the target at high and low incidence velocity has been found to be not identical. The number of petals on target having curvature ratio of 0, 0.25, 0.50,

0.75 and 1.15 against 605 m/s incidence velocity is 6, 6, 7, 6 and 5 petals, respectively. Therefore, it is concluded that the failure mechanism of target changes significantly by varying the curvature ratio.

References

1. M.A. Iqbal, G. Tiwari, P.K. Gupta, Euro. J. Mech. A/Solids **59**, 37–57 (2016)
2. G. Kay, FAA Rep. No. DOT/FAA/AR-03/57, Federal Aviation Administration, Washington, D.C. (2003)
3. M.A. Iqbal, K. Senthil, P. Sharma, N.K. Gupta, Int. J. Impact Eng. **96**, 146–164 (2016)
4. W. Goldsmith, S.A. Finnegam, Int. J. Impact Eng. **4**, 83–105 (1986)
5. M. Buyuk, S. Kan, M.J. Loikkanen, J. Aerospace Eng. **22**, 287–295 (2009)
6. D.R. Lesuer, Technical Report DOT/FAA/AR-00/25. Livermore: Lawrence Livermore National Laboratory (2000), pp. 1–41
7. K. Senthil, M.A. Iqbal, B. Arindam, R. Mittal, N.K. Gupta, Thin-Walled Struct. **126**, 94–105 (2017)
8. G. Tiwari, M.A. Iqbal, P.K. Gupta, Int. J. Crashworth, 1–16 (2018)
9. M.A. Iqbal, K. Senthil, V. Madhu, N.K. Gupta, Int. J. Impact Eng. **110**, 26–38 (2017)
10. G.R. Johnson, W.H. Cook, Eng. Fract. Mech. **21**, 31–48 (1985)
11. J.W. Hancock, A.C. Mackenzie, J. Mech. Phys. Solids **24**, 147–169 (1976)
12. K. Senthil, M.A. Iqbal, Theoret.Appl. Fract. Mech. **67–68**, 53–64 (2013)
13. ABAQUS/Explicit User's Manual, Version 6.8 (2008)
14. A. Hillerborg, M. Modeer, P.E. Petersson, Cem. Concr. Res. **6**, 773–782 (1976)
15. K. Senthil, B. Arindam, M.A. Iqbal, N.K. Gupta, Proc. Eng. **173**, 363–368 (2017)
16. K. Senthil, M.A. Iqbal, S. Rupali, Int. J. Prot. Struct. (2019). https://doi.org/10.1177/2041419618807493
17. K. Senthil, S. Rupali, M.A. Iqbal, *8th International Conference on Structural Engineering and Construction Management*, December 7–9, 2017, University of Peradeniya, Peradeniya, Kandy, Sri Lanka (2017)

Numerical Studies on Ratcheting Behaviour of Straight Pipes

M. Saravanan, S. Vishnuvardhan, P. Gandhi and G. Raghava

Abstract In order to simulate ratcheting behaviour in SA 312 Type 304 LN stainless steel straight pipes of 168 mm nominal outer diameter used in power plant systems, finite element studies were carried out under combined internal pressure and cyclic bending load. The length and average thickness of the pipe was 2700 mm and 14.5 mm, respectively. Reduced thickness in the gauge length portion of 200 mm at the centre of the pipe was 11.5 mm. Finite element (FE) analysis was carried out using ABAQUS software by direct cyclic method. A complete FE model of the specimen was generated using solid modelling with the dimensions equal to the dimensions of the pipe specimen on which ratcheting experiment was conducted earlier. Analysis was carried out for three different cases under different combinations of internal pressure and cyclic displacements. The internal pressure was varied from 25 to 45 MPa. The bending load was applied in the form of cyclic displacement which was varied from ±25 mm to ±45 mm. The elastic–plastic response of the pipe was simulated by using the Chaboche hardening parameters. Non-linear isotropic/kinematic hardening Chaboche model with three back stresses was used to study the effect of biaxial ratcheting. Ratcheting strain values were obtained at different locations in the gauge length portion of the pipes and significant ratcheting strain accumulation was observed in the circumferential and longitudinal direction. Details of the studies carried out and the results of the investigations are discussed in this paper.

Keywords Straight pipe · Finite element analysis · Ratcheting · Cyclic hardening parameters · Strain accumulation

M. Saravanan (✉) · S. Vishnuvardhan · P. Gandhi · G. Raghava
CSIR-Structural Engineering Research Centre, 600 113 Chennai, India
e-mail: sardirajm@serc.res.in

1 Introduction

Piping components are widely used in chemical and petroleum industries, military and power plant structures. These components are usually under high pressure subjected to large amplitude reverse cyclic loading during an earthquake event showing a strong possibility of plastic strain accumulation by ratcheting which reduces the fatigue life. The experimental investigations carried out on the ratcheting behaviour of pressurized piping resulted in valuable inputs to understand the general rule of ratcheting deformation and fatigue. In the existing experimental conditions, it should be noticed that the actual structure size and type, as well as loading conditions, are limited. For the design of actual complex structures, Finite Element Analysis (FEA) can be helpful to predict the ratcheting behaviour of pressurized piping based on appropriate constitutive models.

Progresses in constitutive models for simulation and prediction of ratcheting have been mainly reported by Ohno [1], Abdel-Karim [2], Kang [3] and Chaboche [4, 5]. So far, models available in commercial FEA software contain bilinear kinematic hardening (BKH) model [6], multilinear kinematic hardening (MKIN) model [7] and Chaboche (CH3) model. However, the existing models in available finite element packages require further advancement to increase accuracy in prediction [8]. The shortcomings of available finite element packages while simulating ratcheting behaviour accurately, is attributed to the choice of constitutive model. Hence, it is necessary to implement advanced constitutive models into FEA software to achieve better evaluation of structural ratcheting.

Software packages such as ANSYS or ABAQUS use advanced constitutive models for ratcheting simulation. Advanced constitutive models have been incorporated into ANSYS, ABAQUS, etc. In recent years, a number of advanced non-linear kinematic hardening constitutive models have been proposed by Chaboche et al. [9], Chen et al. [10], Jiang and Sehitoglu [11], Dafalias and Popov [12], Guionnet [13], Delobelle et al. [14], Hassan et al. [15], and many others for improving ratcheting simulation under multiaxial loading. There are two key points for the advance constitutive models which affect the accuracy of ratcheting prediction. One is that these models contain large number of parameters, many of which are determined through a trial and error curve fitting approach using several experimental responses at the material level [16]. Obviously, the process is tedious and might be erroneous. Then, Rahman overcame through developing an automated parameter optimization system using genetic algorithm. The other is a suitable integration algorithm, which should satisfy the requirements of accuracy, efficiency and stability. It is critical for the numerical calculation.

Suzuki [17] and Fujiwaka et al. [18] simulated the ratcheting behaviour of piping component under dynamic and static loadings with the general purpose FEM code ABAQUS. The results indicated that the moment–rotation relationship and time history of rotation showed good agreement with the experimental results. Kulkarni [19] predicted the ratcheting strain of the straight pipe under three-point and four-point bending modes with CH3 model in ANSYS. The results showed that

ratcheting strain only occurred in the circumferential direction, whereas no strain accumulation occurred in the longitudinal direction for three-point and four-point bend analysis. For three-point bending, the CH3 model over predicted the ratcheting strain. Whereas, for four-point bending, it was found that the CH3 model under predicted ratcheting strain in the initial cycles, but CH3 model performed the better in higher number of cycles.

Evaluation of cyclic plasticity models in ratcheting simulation of straight pipes under cyclic bending and steady internal pressure was carried out by Syed Rahman et al. [20]. This study evaluated seven cyclic plasticity models for structural ratcheting response. The models evaluated were bilinear, multilinear, Chaboche, Ohno-Wang, Abdel Karim-Ohno, modified Chaboche and modified Ohno-Wang. The first three models were already available in the ANSYS finite element package, whereas the last four were implemented into ANSYS for this study. It was demonstrated that when the model parameters were determined from the material response data, none of the models performed satisfactorily in simulating the straight pipe diameter change and circumferential strain ratcheting responses. The ratcheting rate of stainless steel pressurized piping branch under seismic loading was studied by Zakavi and Rahmani [21]. In this study, cyclic loading behaviour of stainless steel SS304 pressurized piping branch junction was described. Effects of internal pressure and quantity of moments on ratcheting strain were investigated. The non-linear kinematic hardening model was used for the assessment of plastic behaviour of the branch pipes. The constant parameters of the hardening model and stress–strain data were obtained from several stabilized cycles of specimens that were subjected to simulated seismic bending cycles. The results showed that the maximum ratcheting strain occurred in the direction of branch corner. The ratcheting strain rate increased with the increase of moment levels and constant internal pressure. The results showed that initially the rate of ratcheting was large and then it decreased with the increase of cycles.

Ratcheting deformation was studied on a straight pipe made of Z2CND18.12 N stainless steel with local wall thinning subjected to constant internal pressure and reversed bending using finite element analysis by Chen et al. [10]. The local wall thinning was located at the centre of the straight pipe; whose geometry was rectangular cross section. Three-dimensional elastic–plastic analysis with ANSYS was carried out on a Chen–Jiao–Kim (CJK) kinematic model to evaluate the structural ratcheting behaviour. The results indicated that the ratcheting strain was along the centre of the straight pipe extending to the two ends and the ratcheting strain occurred mainly in the hoop direction and was relatively small in the axial direction. The ratcheting strain of straight pipe with local inside or outside wall thinning increased with the increasing of depth, axial length and circumferential angle. The effect of depth and axial length of the local wall thinning on the ratcheting strain was larger than that of the circumferential angle.

This paper discusses numerical studies carried out on ratcheting behaviour of SA 312 Type 304LN stainless steel straight pipes subjected to combined internal pressure and four-point reversed cyclic bending.

2   Material Properties

The pipe specimens used in the present studies were made of Type 304LN stainless steel conforming to ASTM A312/A312 M-14 standard [22]. The chemical composition in weight for the steel was: C, 0.025%; Mn, 1.79%; P, 0.022%; S, 0.001%; Si, 0.357%; Ni, 9.35%; Cr, 18.98%; N, 0.092%. The yield strength and ultimate tensile strength of the elbow material were 251 MPa and 611 MPa, respectively. The percentage elongation was 68 and the Young's modulus was 183 GPa.

The elastic–plastic response of the material subjected to cyclic loading with a large amplitude is described by the constitutive models based on isotropic or kinematic hardening rules using cyclic hardening parameters. Cyclic hardening parameters evaluated earlier for Type 304LN stainless steel based on the results of strain-controlled fatigue studies carried out at six different strain amplitude values varying from ±0.20 to ±0.95% have been used in the present study [23, 24]. ASTM E 606-04 [25] was followed in preparing the test specimens and carrying out strain-controlled fatigue tests on Type 304LN stainless steel. Circular specimens having uniform gauge test section and straight-sided collet grip end connections were chosen for the studies. The test specimens had overall dimensions of length 220 mm and diameter 16 mm; the diameter in the gauge section was 8 mm. The strain-controlled fatigue tests were carried out under constant amplitude under fully reversed condition using a ±250 kN capacity fatigue rated UTM. A triangular wave pattern was employed during testing. Totally five specimens were tested, each at different amplitudes; the cyclic strain amplitude values during the tests were 0.20, 0.35, 0.65, 0.80 and 0.95%. The corresponding number of reversals to failure ($2N_f$) were 110710, 11132, 2534, 1766 and 794. The hardening parameters were evaluated based on the Chaboche model by decomposing the mid-life stabilized hysteresis curves into three segments as follows: (i) the initial modulus when yield starts, (ii) the non-linear transition of the hysteresis curve after yielding starts until the curve becomes linear again and (iii) the linear segment of the curve in the range of higher strain.

The hardening parameters include: (i) isotropic parameters Q and b and (ii) kinematic hardening parameters σ_o, C_1, C_2, C_3, γ_1, γ_2 and γ_3. Where Q is the maximum change in the size of the yield surface, b is the rate of change of yield surface during plastic deformation, σ_0 is the size of the yield surface, C is the hardening modulus and γ is the rate at which the kinematic hardening modulus decreases with the increase in plastic deformation. The values of kinematic hardening are defined by means of three back stresses, $\sigma_0 = 137.45$, $C_1 = 106137$ MPa, $\gamma_1 = 4407$, $C_2 = 71250$ MPa, $\gamma_2 = 366$, $C_3 = 4264$ MPa, $\gamma_3 = 9$, where $\sigma0$ defines the yield stress at zero plastic strain, C is the hardening modulus and γ is the rate at which the kinematic hardening modulus decreases with the increase in plastic deformation. The value of isotropic hardening parameters is defined by using cyclic hardening option by specifying the parameters $Q = 99.24$ MPa and $b = 0.0135$.
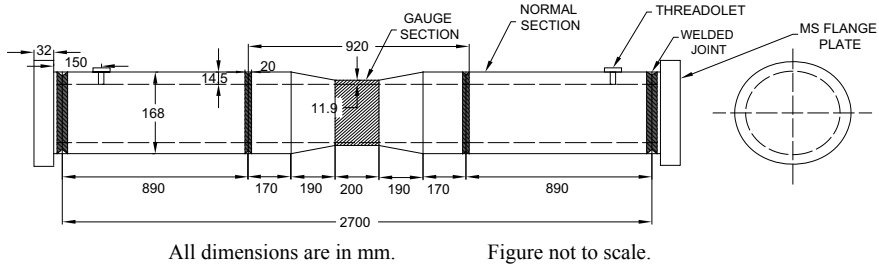
All dimensions are in mm. Figure not to scale.

Fig. 1 Details of a typical pipe specimen

3 Details of Pipe Specimens

Figure 1 shows the details of a typical pipe specimen. The total length of the pipe specimens was 2700 mm and average thickness at normal section was 14.5 mm. The pipe specimens were made by connecting three pieces of straight pipes of 168 mm outer diameter. The thickness of the pipe specimen was reduced to 12.0 mm in the gauge length portion of 200 mm at the centre of the pipe by machining. The pipe specimens were welded with blind flanges at both the ends. Figure 1 shows the details of a typical pipe specimen. Two threadolets were provided in the pipe specimens at a distance of 150 mm from the centre of the weld, as shown in Fig. 1.

This provision was used to apply and measure the desired internal pressure. The circumferential and axial length of the test area or gauge area was divided into twelve (pitch = 30°) and eight (pitch = 25 mm) equal segments along the circumferential and longitudinal directions respectively and grid lines were marked. The circumferential grid lines were numbered in sequence from 1 to 12. Similarly, the longitudinal grid lines were marked in sequence from 'A' to 'I' with grid line 'E' being at the centre of the pipe.

4 Experimental Investigations

Figures 2 and 3 show the ratcheting test setup for pipe specimen and close-up view of the pipe specimen. The pipe specimens were filled with water and pressurized. The pressure was maintained using an automated high-pressure hydraulic pump. The desired pressure could be maintained till a through-wall crack occurred in the specimen. Totally four numbers of straight pipes were tested. The tests were carried out under different combinations of internal pressure and cyclic displacement. The applied internal pressure was varied between 25 MPa to 45 MPa. The maximum applied cyclic displacements were varied from ±25 to ±45 mm and the frequency of loading was varied from one cycle in four minutes (0.0042 Hz) to one
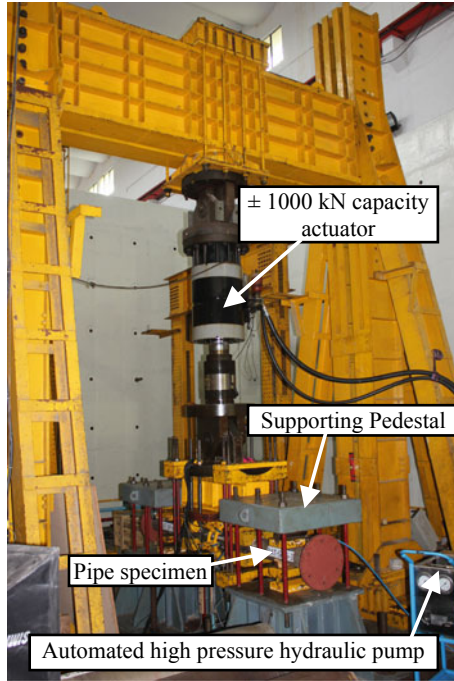
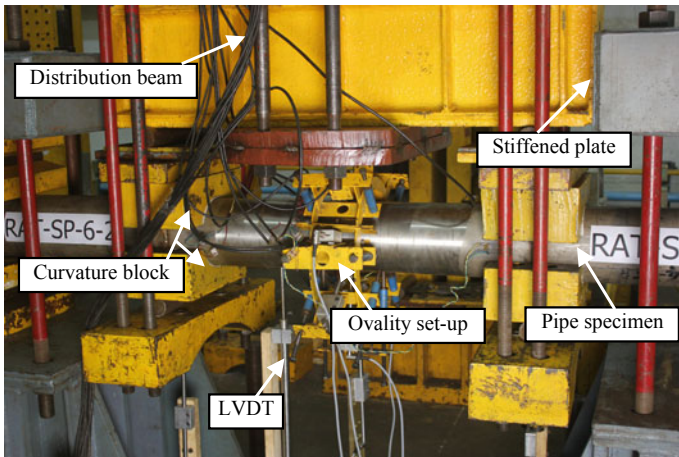**Fig. 2** Ratcheting test setup for pipe specimen

Fig. 3 Close-up view of the pipe specimen

Table 1 Results of ratcheting experimental investigations on stainless steel straight pipes

| Specimen ID	Internal pressure (MPa)	Applied load line displacement (mm)	Number of cycles to occurrence of through-wall crack	Number of cycles to final failure	Maximum load range (kN)
RAT-SP-6-1[a]	25	±45	54	62	1133
RAT-SP-6-2[a]	45	±25	195		1222
RAT-SP-6-3[a]	25	±35	83	95	1016
	30				1086
	35				1154
	40				1170
RAT-SP-6-4[a]	35	±25	105	112	948
		±30			1092
		±35			1221
		±40			1295

[a]Reference [26]

cycle in one minute (0.0500 Hz). The experiments were carried out at a very low frequency during the initial fatigue cycles and the test frequency was gradually increased towards the end of the experiments. In order to measure strains, sixteen numbers of two element rectangular post-yield rosette strain gauges were mounted in the test/gauge area in the case of pipe specimens. In order to measure the change in the circumference at the gauge length portion (in the case of pipes), ovality measurements were continuously obtained by using ovality setup. Three LVDTs were arranged at the bottom of the pipe specimen, one at the centre of the specimen and two at the inner span locations, to measure the pipe deflection.
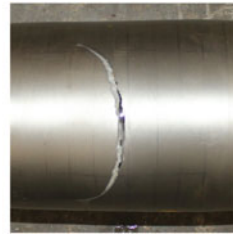
The applied load and load line displacement were obtained directly through the in-built load cell and LVDT in the actuators. Table 1 gives the results of ratcheting experimental investigations on stainless steel straight pipes. The pipe specimens failed either by the occurrence of through-wall crack accompanied by simultaneous ballooning or bursting with simultaneous ballooning. Figure 4 shows the occurrence of a through-wall crack indicated by a sharp water jet in a straight pipe which failed due to ratcheting. Figure 5 shows views of test sections of the pipe specimens at failure. Figure 6 shows the load versus load line displacement curve for the pipe

Fig. 4 Occurrence of through-wall crack indicated by a sharp water jet for the pipe specimen RAT-SP-6-1

Sharp water jet
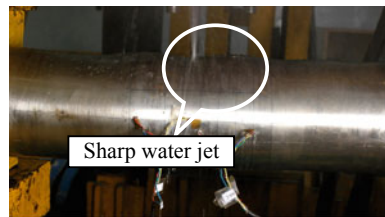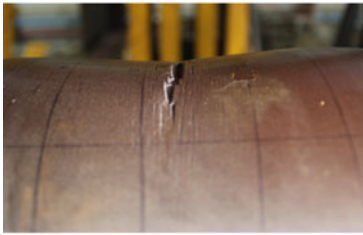
Specimen RAT-SP-6-1   Specimen RAT-SP-6-2

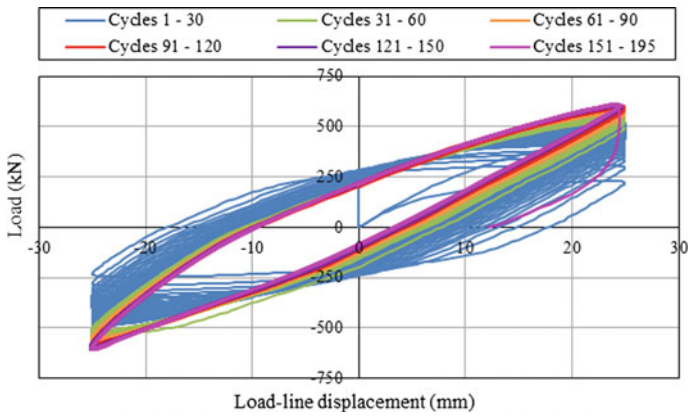**Fig. 5** Views of test sections of the pipe specimens at failure

Fig. 6 Load versus load line displacement curve for the pipe specimen RAT-SP-6-2

Fig. 7 Variation of longitudinal and circumferential strains at different grid points in the gauge length portion during the ratcheting experiment for the pipe specimen RAT-SP-6-3
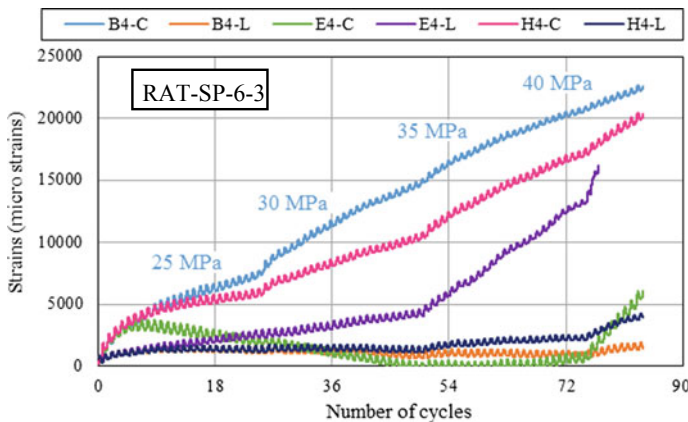
specimen RAT-SP-6-2. Figure 7 shows the variation of longitudinal and circumferential strains at different grid points in the gauge length portion during the ratcheting experiment for the pipe specimen RAT-SP-6-3.

5 Numerical Investigations

Analytical studies were carried out on straight pipes under combined internal pressure and cyclic bending using commercially available finite element (FE) software ABAQUS. Full model of the pipe was created. C3D8R element type is used to mesh the model of the pipe specimen. The C3D8R element is a general purpose linear brick element, with reduced integration. C3D8R is a continuum stress/displacement, three-dimensional, 8-node, reduced-integration element. The shape functions are the same as for the C3D8 element. The specimen was modelled with 2640 elements and 5328 nodes. Figure 8 shows the mesh modelling of the pipe specimen. Direct cyclic step was created with the cyclic time period of 1 using the displacement Fourier coefficients from the previous direct cyclic step. The automatic increment was used with the maximum number of increments which was 5000 and the increment size was 0.01 for the initial and 1 for the maximum. The maximum number of iterations used in this step was entered as 20 in order to get accurate results. The elastic–plastic response of the pipe specimens under combined internal pressure and cyclic bending load was simulated by using the Chaboche hardening parameters. Analysis was carried out for three different cases under different combinations of internal pressure and cyclic displacements; the combination was the same at which experiments were carried out on four pipes earlier by Saravanan et al. [23]. Analysis was carried out till the number of cycles to the occurrence of through-wall crack obtained during experiments. Figure 9 shows the details of the grid lines and the strain gauge locations in the pipe specimen. Numerical studies were carried out earlier on ratcheting behaviour of Type 304LN stainless steel straight pipes under combinations of internal pressure and cyclic displacements up to 50 cycles of loading [27].

**Fig. 8** Mesh modelling of the pipe specimen
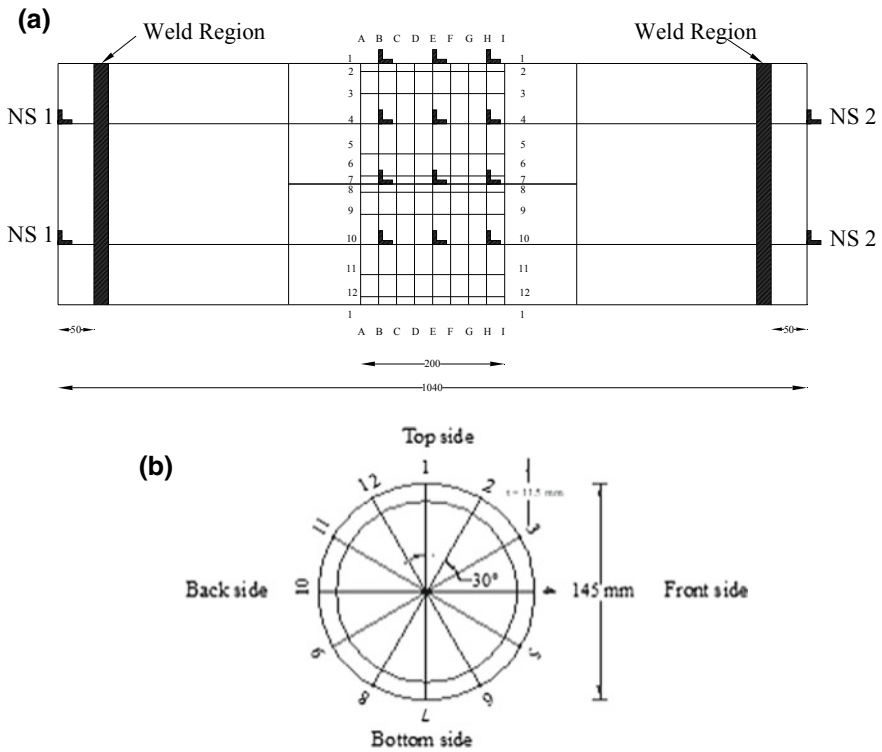
Fig. 9 Details of grid lines and strain gauge locations in a pipe specimen

6 Results and Discussion

In order to simulate ratcheting behaviour in SA 312 Type 304 LN stainless steel straight pipes of 168 mm nominal outer diameter, finite element studies were carried out under combined internal pressure and cyclic bending load. The elastic–plastic response of the pipe was simulated by using the Chaboche hardening parameters. Finite element analyses were carried out using ABAQUS software by direct cyclic method. Ratcheting strain values were obtained at different locations in the gauge length portion of the pipes. Internal pressure was applied on the inner surface of the pipe and loading was applied on the top of the inner span location of the pipe in Y-direction (upward). The applied cyclic displacement was defined by the sinusoidal waveform with peak displacements equal to the experimental values. The strain values were obtained in the circumferential and longitudinal directions at different locations for the two pipe specimens under combined internal pressure and cyclic bending.

Fig. 10 Load versus displacement curves
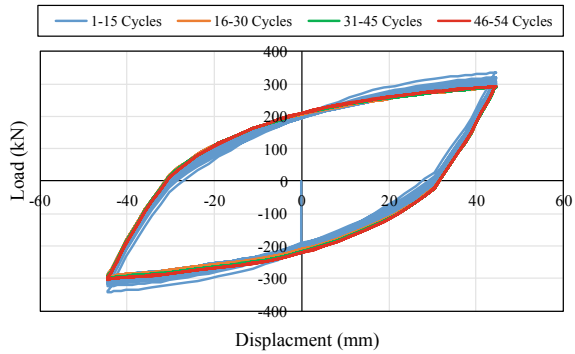
(a) Internal pressure of 25 MPa and cyclic displacement of ±45 mm
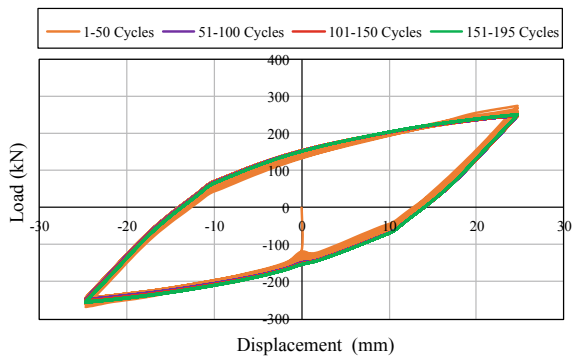
(b) Internal pressure of 45 MPa and cyclic displacement of ±25 mm

Figure 10a, b show the load versus displacement curves for typical cases of pipe specimens. The load was gradually increased with a constant applied displacement at the initial few cycles. After that, there was no variation in the load and it remained almost constant up to end of the tests. Figure 11 shows the variation of circumferential and longitudinal strains in the top and bottom of the gauge section for typical cases. Significant ratcheting strain was observed in the circumferential direction when compared to the longitudinal direction. Finite element analyses overestimated the circumferential strains compared with the experimental data. Figure 12 shows von Mises stress distribution in the pipe specimen obtained from the FE analysis.

From the experimental studies, it was observed that when the specimen was subjected to a multi-step internal pressure of 25, 30, 35 and 40 MPa (25 cycles for each step), the accumulation of plastic strains in the circumferential direction

(a) Internal pressure of 25 MPa and cyclic displacement of ±45 mm

(b) Internal pressure of 45 MPa and cyclic displacement of ±25 mm

(c) Internal pressure of 35 MPa and cyclic displacement varied from ±25 mm to ±40 mm

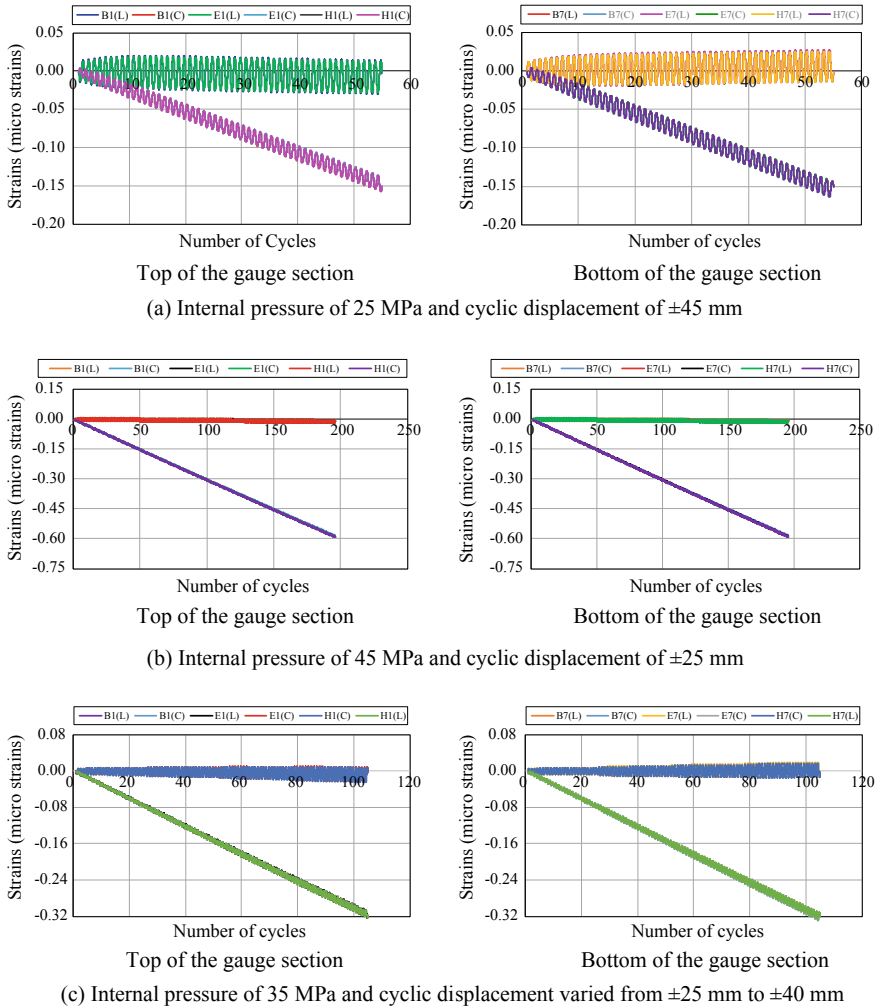**Fig. 11** Variation of circumferential and longitudinal strains at different grid points in the gauge length portion

substantially increased with increase in internal pressure. The cyclic bending load was gradually increased with the change in the applied cyclic displacement from ±25 to ±40 mm. The accumulation of plastic strains in the circumferential direction gradually increased with increase in applied displacement.
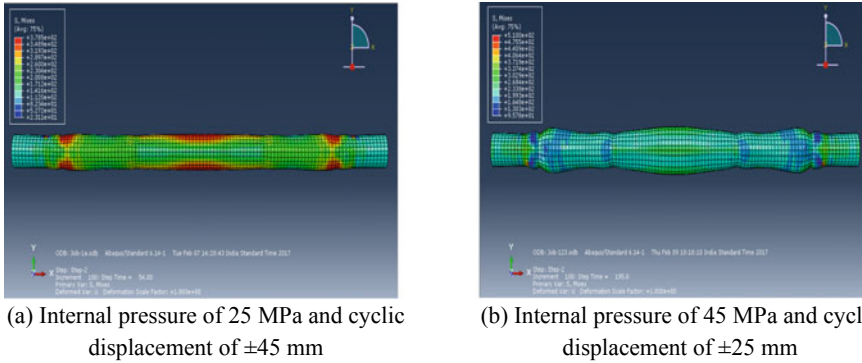
(a) Internal pressure of 25 MPa and cyclic
displacement of ±45 mm

(b) Internal pressure of 45 MPa and cyclic
displacement of ±25 mm

Fig. 12 Von Mises stress distribution in the pipe specimen

7   Summary and Conclusions

Finite element studies were carried out to simulate ratcheting behaviour in SA 312 Type 304 LN stainless steel straight pipes of 168 mm nominal outer diameter under combined internal pressure and cyclic bending load. Finite element analysis was carried out using ABAQUS software by direct cyclic method. A complete FE model of the specimen was generated using solid modelling with the dimensions equal to the dimensions of the pipe specimen on which ratcheting experiment was conducted earlier. Analysis was carried out for three different cases under different combinations of internal pressure and cyclic displacements. The internal pressure was varied from 25 to 45 MPa. The bending load was applied in the form of cyclic displacement which was varied from ±25 mm to ±45 mm. The elastic–plastic response of the pipe was simulated by using the Chaboche hardening parameters. Non-linear isotropic/kinematic hardening Chaboche model with three back stresses was used to study the effect of biaxial ratcheting. Ratcheting strain values were obtained at different locations in the gauge length portion of the pipes and significant ratcheting strain accumulation was observed in the circumferential direction. Finite element analyses overestimated the circumferential strains compared with the experimental data.

References

1. N. Ohno, Abdel-Karim, ASME J. Eng. Mater. Technol. 122(200) 35
2. M. Abdel-Karim, Int. J. Pres. Ves. Pip. **82**, 427 (2005)
3. G.Z. Kang, Int. J. Fat. **30**, 1448 (2008)
4. J.L. Chaboche, Euro. J. Mech. A/Solids. **13**, 501 (1994)
5. J.L. Chaboche, Int. J. Plast **24**, 1642 (2008)
6. W. Prager, J. Appl. Mech. **23**, 493 (1956)
7. Z. Mróz, J. Mech. Phy. Solids, 15 (195), p. 163
8. Tasnim Hassan, Yimin Zhu, Vernon C. Matzen, Int. J. Pres. Ves. Pip. **75**, 643 (1998)
9. X. Chen, R. Jiao, Int. J. Plast **20**, 871 (2004)
10. X. Chen, R. Jiao, K.S. Kim, Int. J. Plast **21**, 161 (2005)
11. Y.Y. Jiang, H. Sehitoglu, ASME Trans. J. Appl. Mech. **63**, 726 (1996)
12. Y. Dafalias, E. Popov, ASME Trans. J. Appl. Mech. **43**, 645 (1976)
13. C. Guionnet, ASME Trans. J. Eng. Mat. Tech. **114**, 56 (1992)
14. P. Delobelle, P. Robinet, L. Bocher, Int. J. Plast **11**, 295 (1995)
15. T. Hassan, E. Corona, S. Kyriakides, Int. J. Plast **8**, 117 (1992)
16. S. Bari, T. Hassan, Int. J. Plast **16**, 381 (2000)
17. K. Suzuki, *Proceedings of Ninenth International Conference Nuclear Engineering*, Nice, France, Paper No. 155 (2001)
18. T. Fujiwaka, H. Kobayashi, Y. Asada, C. Shitara, *Proceedings of ASME Press Ves Piping Conf*erence (Vancouver, Canada, 2002),p.
19. S.C. Kulkarni, Y.M. Desai, T. Kant, G.R. Reddy, P. Prasad, K.K. Vaze, C. Gupta, Int. J. Press. Ves. Pip. **81**, 609 (2004)
20. Syed M. Rahman, Tasnim Hassan, Edmundo Corona, Int. J. Plast **24**, 1756 (2008)
21. S.J. Zakavi, V. Rahmani, Int. J. Sci. Res. **3**, 191 (2014)
22. ASTM A 312/ A 312 M -14: *Standard Specification for Seamless, Welded and Heavily Cold Worked Austenitic Stainless Steel Pipes*, USA
23. Bhavana Joy, S. Vishnuvardhan, G. Raghava, P. Gandhi, Mathews M. Paul, *Proceedings of 2nd International Conference on Mater for the Future* (Thrissur, India, 2011)
24. G. Jenitha, M. Saravanan, S. Vishnuvardhan, G. Raghava, V. Naresh Babu, *Trans Tech Publications,* J. Appl. Mech. Mater, 592–594 (2014), 1200
25. ASTM E 606-04: *Standard Practice for Strain-Controlled Fatigue Testing*, USA
26. M. Saravanan, S. Vishnuvardhan, G. Raghava, P. Gandhi, *Ratcheting studies on stainless steel straight pipes under combined internal pressure and cyclic bending*, CSIR-SERC Research Report No. R&D 03-MLP 18141-RR-09, June 2016
27. G.G. Obuli, M. Saravanan, S. Vishnuvardhan, P. Gowthamramkarhik, Int. J. Innovat. Res. Sci. Eng. Tech. **4**, 1727 (2015)

A Comparison of Applied Element Method and Finite Element Method for Elastostatic Problems

D. Lincy Christy, T. M. Madhavan Pillai and Praveen Nagarajan

Abstract Finite element method (FEM) is a general numerical method to solve differential equations. Applied Element Method (AEM) is also a numerical method, but limited for structural analysis. Instead of node-to-node connection in FEM, applied elements are connected by springs. Stiffness matrix is for a pair of spring rather than for an element. A pair of spring consists of two springs to simulate normal stress (normal spring) and shear stress (shear spring) for a two-dimensional (2D) element. A comparison of AEM and FEM in terms of convergence and processing time is done in this paper. For this, 2D linear and non-linear analysis of structures is carried out. Although the processing time depends upon the features of the computer, the comparison of the results of AEM and FEM on the same system is done. In general, the analysis by AEM takes less time when compared to FEM. This is attributed to the lesser number of degrees of freedom per element in AEM. This reduces the memory requirement in AEM compared to FEM, for same meshing. In the case of linear analysis, AEM is found to be superior when compared to FEM with respect to accuracy. The results from both AEM and FEM converged at almost the same rate. Incremental method of non-linear analysis was attempted. To incorporate material non-linearity in AEM, the stiffness of the springs is varied according to its strain. Both AEM and FEM predicted similar load–deflection curve.

Keywords Applied element method · Finite element method · Linear analysis · Non-linear analysis · Convergence · Processing time

Nomenclature

α	Angle of inclination of the line connecting the centre of the element and spring from the x-direction
ε	Strain
σ	Stress
a	Centre–centre distance between elements

D. L. Christy (✉) · T. M. Madhavan Pillai · P. Nagarajan
Department of Civil Engineering, NIT Calicut, Kerala, India
e-mail: lincychristyd@gmail.com

b Width of beam
d Depth of beam
l Length of beam
n_l Number of elements along the length direction
n_d Number of elements along the depth direction
t Thickness of the element
A Area of cross section
E Young's modulus of the material
F Force vector
G Shear modulus of the material
I Moment of Inertia
K Stiffness matrix
K_n Stiffness of normal spring
K_s Stiffness of shear spring
L Distance of the spring from the centre of the element
U Displacement vector

1 Introduction

AEM and FEM are both numerical methods used for structural analysis. After the development of stiffness matrix, the procedure remains the same. Rigidity of elements, position of degrees of freedom and element connectivity is different in both the methods. One basic difference between AEM and FEM is that elements are rigid in AEM but deformable in the case of FEM. The degrees of freedom are located at the centre of the element in AEM. This keeps the elements rigid by simply straining the springs around it. Element connection is accomplished through springs along the face of the elements and by nodes in AEM and FEM respectively.

AEM is applicable to orthotropic and anisotropic materials. Although AEM is versatile, it is not popular. In this paper, the application of AEM to the analysis of elastostatic problems is highlighted. For this, 2D elastostatic problems are solved using AEM and FEM. These methods are compared with respect to the results and computational time.

1.1 Applied Element Method

AEM is a numerical method solely used for structural analysis. It was developed by Kimiro Meguro and Hatem Tagel-Din in 1997 [1–5]. In this method, the structure is made up of a number of rigid elements with springs around them connecting each other. There are only two types of elements in AEM—2D and 3D (Fig. 1).

Fig. 1 Elements in AEM
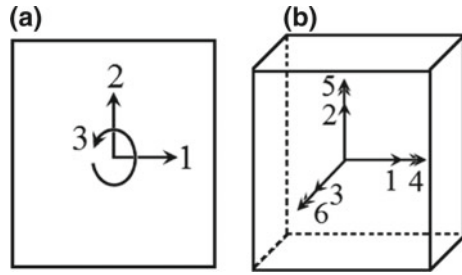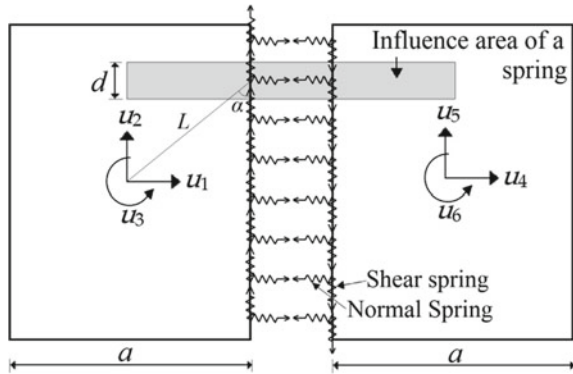**a** 2D element **b** 3D element

Fig. 2 Distribution of springs in AEM

A 2D element consists of two translational and one rotational degrees of freedom. A 3D element has three translational and three rotational degrees of freedom at the centre of the element. This paper discusses the analysis using 2D element. The distribution of springs and its properties are shown in Fig. 2.

L, α, d, a and t represent the distance between centre of the element and position of spring, the inclination of this length (L) with vertical, depth of the section represented by spring, length of the element and thickness of the element, respectively, as shown in Fig. 2. Each set of spring has one normal spring and shear spring, to take care of normal strain and shear strain, respectively. Their stiffnesses are denoted by K_n and K_s, respectively, and are given by Eq. 1.

$$K_n = \frac{Edt}{a} \quad ; \quad K_s = \frac{Gdt}{a} \tag{1}$$

For a pair of springs, Eq. 2 gives the equilibrium equation.

$$KU = F \tag{2}$$

$U = \{u_1; u_2; u_3; u_4; u_5; u_6\}$ and $F = \{f_1; f_2; f_3; f_4; f_5; f_6\}$

where U and F are the displacement vector and force vector, respectively. u_1, u_2, u_3, u_4, u_5 and u_6 are the displacements as shown in Fig. 2. The corresponding forces are represented by f_1, f_2, f_3, f_4, f_5 and f_6.

Every set of spring will have a stiffness matrix (K) of size 6×6 dependent on its stiffness and position as given by Eq. 3.

$$K = \begin{pmatrix} K_n & 0 & -K_n L\cos\alpha & -K_n & 0 & K_n L\cos\alpha \\ 0 & K_s & K_s L\sin\alpha & 0 & -K_s & K_s L\sin\alpha \\ -K_n L\cos\alpha & K_s L\sin\alpha & K_n L^2\cos^2\alpha + K_s L^2\sin^2\alpha & K_n L\cos\alpha & -K_s L\sin\alpha & -K_n L^2\cos^2\alpha + K_s L^2\sin^2\alpha \\ -K_n & 0 & K_n L\cos\alpha & K_n & 0 & -K_n L\cos\alpha \\ 0 & -K_s & -K_s L\sin\alpha & 0 & K_s & -K_s L\sin\alpha \\ K_n L\cos\alpha & K_s L\sin\alpha & -K_n L^2\cos^2\alpha + K_s L^2\sin^2\alpha & -K_n L\cos\alpha & -K_s L\sin\alpha & K_n L^2\cos^2\alpha + K_s L^2\sin^2\alpha \end{pmatrix}$$

$$(3)$$

This single equation forms the base of AEM. A glimpse into the formulation is given in [6]. The global stiffness matrix is obtained by assembling the stiffness matrices of all the springs.

1.2 Finite Element Method

FEM is a numerical method generally used in engineering and other fields to solve differential equations. In this paper, FEM is used for structural analysis. There are a number of elements in FEM based on the type and behaviour of the structure. Here, a rectangular 2D plane stress element shown in Fig. 3 is used.

It is seen that there are eight degrees of freedom in the 2D element of FEM compared to three degrees of freedom in AEM (Fig. 1). This will, of course, increase the size of stiffness matrix and hence the processing time. The procedure in AEM is much simpler than that of FEM. The stiffness matrix is determined by integration in FEM, whereas, it is directly available in AEM. In FEM, numerical integration is necessary when non-rectangular elements are used. The simplicity of AEM is explicit from the fact that only springs are used for modelling any type of

Fig. 3 Rectangular 2D element in FEM
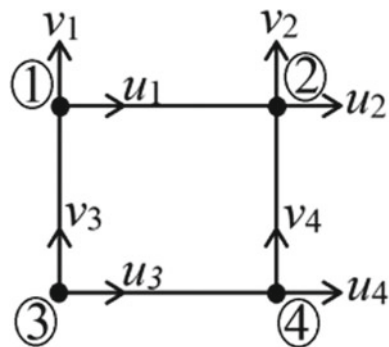
structure. Moreover, transition elements are not required in AEM to connect elements of different size. Therefore, smaller elements can be directly connected to bigger elements. Hence, computational complexities are much lesser in the case of AEM. But unlike FEM, the application of AEM is limited to structural mechanics.

2 Linear Analysis

To study the convergence and processing time of AEM and FEM, a cantilever beam with tip load is analysed by varying the number of elements. The beam is 2 m long and its cross section is 150 mm × 200 mm as shown in Fig. 4. The Modulus of elasticity and Poisson's ratio of the material are 25000 N/mm^2 and 0.2 respectively. 10 number of springs are provided along all faces in the case of AEM.

The analysis by AEM and FEM are done using MATLAB codes. The FEM code is developed according to [7–9]. They follow similar process and are done in the same system [Intel (R) Core (TM) i7 6500U CPU@ 2.5 GHz 2.6 GHz processor with 16.0 GB RAM].

The deflection at the tip of the cantilever, including the strain energy of shear is given by Eq. 4.

$$\text{Deflection at the tip of cantilever beam} = \frac{Pl^3}{3EI} + \frac{3Pl}{2AG} = 1.076 \, \text{mm} \qquad (4)$$

2.1 Convergence Study of AEM and FEM

Deflection at the tip of the cantilever beam is determined for different number of elements along length and depth directions (n_l and n_d, respectively) by both AEM and FEM. The convergence of deflection in the case of AEM and FEM are shown separately in Figs. 5a and b, respectively.

Figure 5 shows that the variation between the results for different number of elements along depth direction is very less for AEM when compared to FEM. This indicates that it is enough to use one element along depth to find deflection in the case of AEM. The discrepancy found in FEM when one element is used along the depth direction is attributed to the shear locking inherent in four noded quadrilateral elements. The convergence rate of both AEM and FEM is close enough.

Fig. 4 Cantilever beam considered for analysis
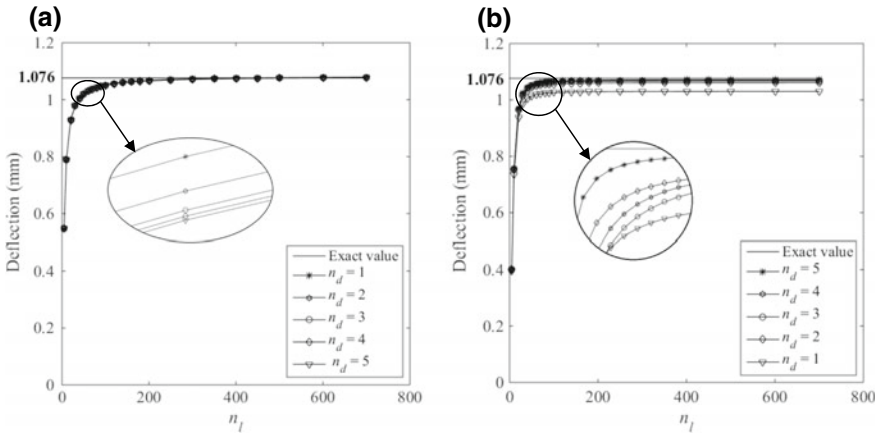

1 kN

2 m

200 mm

150 mm

(a)

(b)
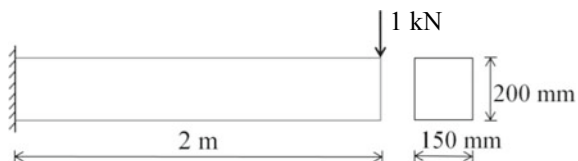
Fig. 5 Deflection versus No. of elements along the length for **a** AEM **b** FEM

Table 1 Comparison of deflection by AEM and FEM (for $n_l = 250$)

n_d	Deflection (mm)		Percentage difference (%)	
	AEM	FEM	AEM	FEM
1	1.071	1.029	−0.496	−4.356
2	1.070	1.060	−0.589	−1.495
3	1.069	1.067	−0.640	−0.881
4	1.069	1.069	−0.652	−0.657
5	1.069	1.070	−0.662	−0.551

The results are converged when 250 number of elements are taken along the length direction. Comparison of the deflection obtained by AEM and FEM at this stage is given in Table 1.

Table 1 shows that AEM gives more accurate results compared to FEM. As the number of elements is increased along the depth direction, the deflection determined increases in FEM, but decreases in the case of AEM.

2.2 Processing Time of AEM and FEM

Figure 6 illustrates how the ratio of time taken for analysis by FEM to that of AEM varies with the number of elements.

Figure 6 shows that the time taken by FEM is much higher than that of AEM when the number of elements along length and depth directions are less. One of the
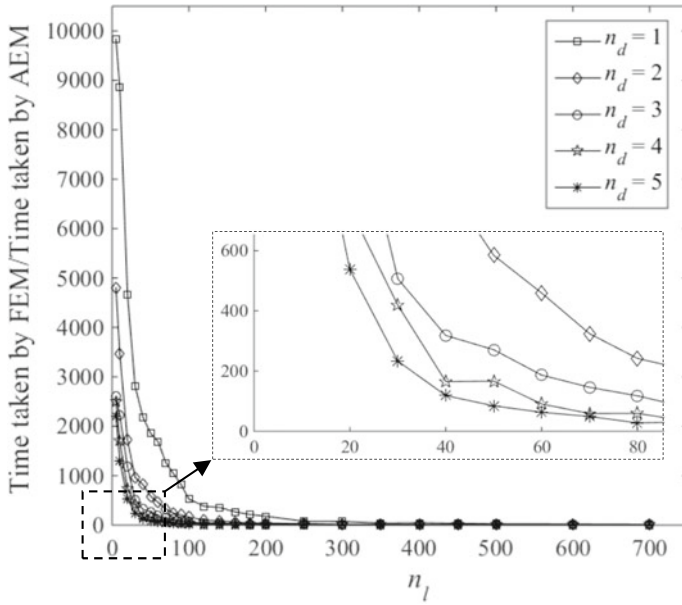
Fig. 6 Time taken by FEM/Time taken by AEM versus No. of elements along length for linear analysis

n_d	Processing time (s)		Ratio of processing time of FEM and AEM
	AEM	FEM	
1	0.08	6.05	77.57
2	0.38	10.65	27.86
3	1.42	14.90	10.52
4	3.32	20.20	6.08
5	6.83	25.40	3.72

Table 2 Comparison of processing time for linear analysis by AEM and FEM (for $n_l = 250$)

reasons for the increase in processing time in FEM is the more number of degrees of freedom per element compared to AEM. Table 2 gives the processing time of AEM and FEM when 250 elements are taken along length direction.

Table 2 ascertains that FEM requires more time for processing when compared to AEM. This variation reduces when more number of elements are used.

3   Non-linear Analysis

Cantilever beam studied in Sect. 2 is analysed considering material non-linearity. A typical stress–strain relation to model plain concrete in compression is used and is given by Eq. 5.

$$\sigma = 5 \times 10^8\, \varepsilon^3 - 9 \times 10^6\, \varepsilon^2 + 30000\varepsilon \tag{5}$$

where σ and ε are stress and strain, respectively. Here, stress is in N/mm^2.

The stress–strain curve is assumed to be linear in tension. The modulus of elasticity and Poisson's ratio are 30000 N/mm^2 and 0.2, respectively. A tip load of 22 kN is applied. Incremental method of non-linear analysis is adopted for analysis.

3.1   Incremental Method of Non-linear Analysis

In the Incremental method, the non-linear problem is divided into a number of linear problems. The load is divided into a number of increments. Initially, the stiffness matrix corresponding to the initial modulus of elasticity is used with the first load increment to determine the first displacement increment. The modulus of elasticity of various points in the structure is calculated based on the strain field determined from the displacement vector. The stiffness matrix thus obtained is used with the next load increment to obtain the next displacement increment. This procedure is repeated until all load increments are applied. The sum of all the load increments and displacement increments will give the final load and displacement vectors respectively. Here, the challenge lies in the determination of modified stiffness matrix when the structure is deformed.

3.2   Convergence Study of AEM and FEM

The variation of deflection with n_l and n_d for AEM and FEM in the case of non-linear analysis are shown in Figs. 7a and b, respectively.

From Fig. 7, it is seen that the deflection obtained from AEM and FEM converges as the number of elements increases. But there is a discrepancy in the result when one element is used along the depth direction for FEM. This is due to shear locking. The results in Fig. 7 are reframed to compare the results from AEM and FEM and are shown in Figs. 8a and b. This is for 1 and 5 number of elements along the depth direction.

AEM predicts larger deflection than FEM. In this problem, FEM predicts lesser deflection than AEM for a given load.
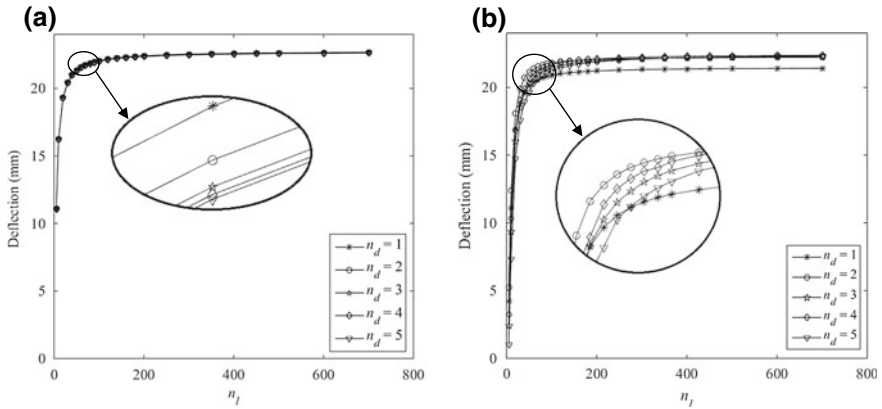
Fig. 7 Deflection versus No. of elements along the length for **a** AEM **b** FEM
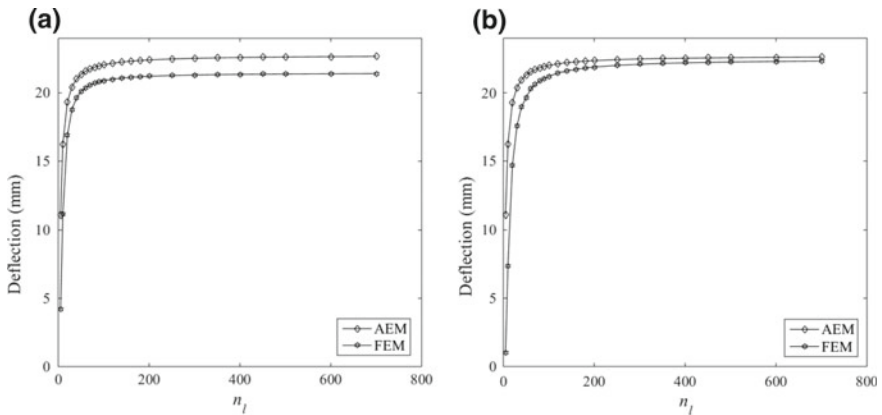
Fig. 8 Deflection versus No. of elements along the length for AEM and FEM with number of elements along depth as **a** 1 **b** 5

The same problem was analysed with 5–20 increments in load to study the effect of number of increments on convergence. The variation of deflection with number of increments for AEM and FEM are shown in Figs. 9a and b respectively. For this, n_l and n_d were 20 and 3, respectively. The slope at the load of 11000 N for the case of 20 increments are also shown in Fig. 9.

When the load is incremented in 20 steps, the deflection obtained by AEM and FEM are 20.1 mm and 16.5 mm, respectively. Figure 9a and b shows that the deflection obtained from AEM and FEM converges as the number of increments increases.

Fig. 9 Load versus deflection in **a** AEM **b** FEM

3.3 Processing Time of AEM and FEM
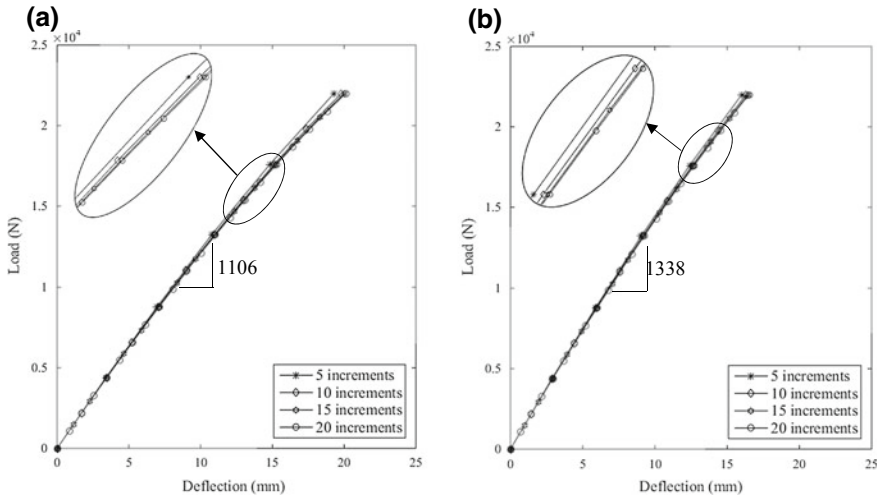
Figure 10 shows the ratio of processing time of AEM and FEM for different number of elements along length and depth directions.

In non-linear analysis also, FEM consumes more time than AEM.

Table 3 gives the ratio of time taken by FEM and AEM when the beam is meshed into 250 elements along the length direction.

Table 3 shows that FEM takes longer time than AEM for processing. In the case of non-linear analysis, this difference becomes more acute once convergence is attained. This is visible from Tables 2 and 3.

In the case of AEM, the strain in the springs can be determined from the displacement of the degrees of freedom of the elements connected by them. Using the strain, the modulus of elasticity and hence the modified stiffness of all the springs can be obtained. These steps do not involve intensive computations.

When it comes to FEM, the strain vector is obtained from the displacement vector using the strain–displacement matrix. As the strain–displacement matrix is dependent on the x and y coordinates, the strain vector also becomes dependent. Hence, the constitutive matrix which is dependent on the strain vector will no longer be a constant within the elements. The calculation of stiffness matrix which involves integration thus becomes cumbersome. Although the elements are identical, their stiffness matrices have to be separately determined. This increases processing time to a large extend.
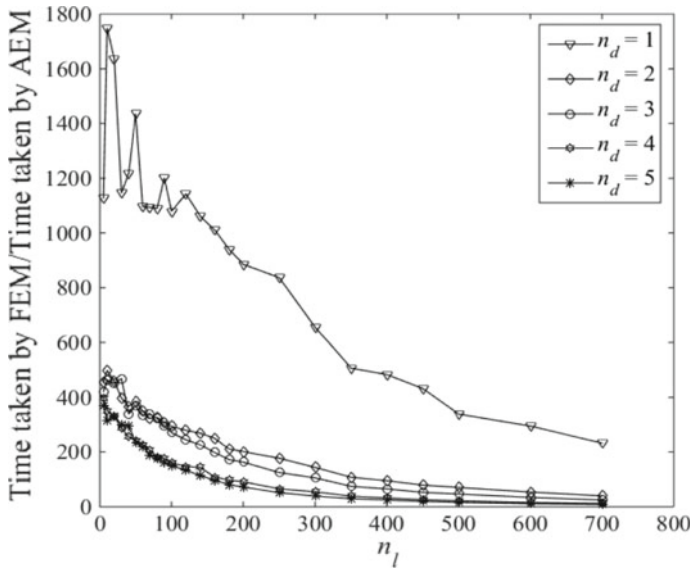
Fig. 10 Time taken by FEM/Time taken by AEM versus No. of elements along length for non-linear analysis

Table 3 Comparison of processing time for non-linear analysis by AEM and FEM (for n_l = 250)

n_d	Processing time (s)		Ratio of processing time of FEM and AEM
	AEM	FEM	
1	0.29	243.53	837.33
2	1.42	251.36	176.98
3	3.41	426.04	124.96
4	6.55	429.26	65.49
5	11.67	602.07	51.60

4 Conclusions

The study of some plane stress elastostatic problems with isotropic material is carried out. The conclusions arrived for this specific case are given below:

(i) AEM gives more accurate results than FEM for similar meshing in the case of linear analysis.

(ii) The convergence rate of AEM and FEM is close enough for both linear and non-linear analysis.

(iii) The processing time of FEM is much higher than that of AEM when lesser number of elements are used. This is attributed to the more number of degrees of freedom in an element in FEM than that of a similar element in AEM.

(iv) The load–deflection curve converges as the number of increments increases.

References

1. K. Meguro, H. Tagel-Din, A new efficient technique for fracture analysis of structures, Bull. Earthq. Resist. Struct. Res. Cent., IIS, Univ. Tokyo 103 (1997)
2. K. Meguro, H. Tagel-Din, A new simplified and efficient technique for fracture behavior analysis of concrete structures, in *Proceedings of the Third International Conference on Fracture Mechanics of Concrete and Concrete Structures* (1998), p. 911
3. K. Meguro, H. Tagel-Din, Struct. Eng./ Earthquake Eng. **17**, 21 (2000)
4. H. Tagel-Din, K. Meguro, Struct. Eng./Earthquake Eng. **17**, 137 (2000)
5. K. Meguro, H. Tagel-Din, J. Nat. Disaster Sci. **24**, 25 (2002)
6. D.L. Christy, T.M.M. Pillai, P. Nagarajan, Analysis of concrete beams using applied element method, in IOP Conference Series: Materials Science and Engineering, IOP Publishing (2018), p. 1
7. B. ANSYS, ANSYS Mechanical APDL Theory Reference, Release 15 (2013)
8. C.S. Desai, J.F. Abel, *Introduction to the Finite Element Method – A numerical method for engineering analysis*, Van Nostrand Reinhold Company (1972)
9. T.R. Chandrupatla, A.D. Belegundu, *Introduction to finite elements in engineering* (Upper Saddle River, Prentice Hall, NJ, 2002)

Part VI
Concrete

Seismic Behaviour of Steel–Fibre-Reinforced GGBS Concrete Beam-Column Joints

P. Saranya, Praveen Nagarajan and A. P. Shashikala

Abstract Beam-column joints play a crucial role in the structural behaviour of framed structures. Use of highly ductile material and addition of steel fibres to concrete will enhance the seismic resistance of beam-column joints. It has been observed that addition of Ground-Granulated Blast furnace Slag (GGBS), a byproduct from the steel industry, will provide more ductility and durability to concrete. Addition of GGBS as a partial replacement into concrete reduces the disposal issues and minimise the carbon footprint. The seismic studies reveal that in a reinforced structure, the failure of beam-column joint is critical during earthquakes. Ductile behaviour of GGBS concrete will enhance the seismic performance of beam-column joints This paper aims at investigating the feasibility of using GGBS as a partial replacement to cement in steel fibre reinforced concrete composites. Experimental investigations were conducted on exterior beam-column joints made of steel–fibre-reinforced GGBS concrete. Optimum percentage replacement of cement by GGBS is obtained as 40 by weight. Beam-column joints were tested under monotonic loading and behaviour of GGBS concrete (ultimate load, deflection and cracking) is compared with cement concrete. Effect of steel fibres on GGBS concrete by varying the percentage from 0.25 to 1 was also studied. The ultimate load for GGBS and steel–fibre-reinforced GGBS beam-column joint was obtained as 17 and 33% more than that of cement concrete beam-column joint. The experimental studies were compared with numerical method (ANSYS), and good agreements in the results are observed.

Keywords ANSYS · Beam-column joints · GGBS · Steel fibre

P. Saranya (✉) · P. Nagarajan · A. P. Shashikala
National Institute of Technology Calicut, Kozhikode 673601, Kerala, India
e-mail: saranyasankar81@gmail.com

1 Introduction

Concrete plays an important role in the infrastructure development of a country. Ordinary Portland Cement (OPC) is the most vital ingredient of concrete, as it binds the constituents together and enables the composite to attain strength. Since cement is a main contributor of carbon dioxide to the atmosphere (major reason for global warming), there is an urgent need to reduce the usage of cement [1]. This challenge can be addressed by using alternative materials having lower carbon footprint namely industrial by-products like fly ash, silica fume, cement kiln dust, rice husk ash, wood ash, ground-granulated blast furnace [2–4], etc. But the usage of cementitious materials may lead to a decrease in structural and durability properties of concrete composites which have to be studied in detail before using such materials [5–7].

In the case of seismic performance of a framed structure, beam-column joint plays an important role. This region is highly congested due to high percentage of reinforcement and there exists a complex variation of strain in this region due to the geometric discontinuity [8]. During earthquakes, the beam-column joint is subjected to large shear forces. Due to the formation of multiple cracks, the joint gets severely damaged. Studies have proved that the steel fibre reinforced concrete can resist the propagation of cracks to a certain extent [9, 10].

This research aims at investigating the feasibility of using GGBS as a partial replacement to cement in steel fibre reinforced concrete composites by experimental and numerical studies. Development of steel fibre-reinforced GGBS concrete may reduce the emission of greenhouse gases to the atmosphere.

2 Experimental Programme

Experimental investigations were carried out by adding GGBS as a partial replacement to cement at various percentages such as 30, 35, 40, 45 and 50 by weight of cement. Steel fibre was added at 0.5, 0.75 and 1% of total volume of concrete. The optimum percentage of GGBS and steel fibre for attaining maximum strength was estimated and the behaviour of beam-column joint was studied with this mix proportion.

2.1 Materials

Cement used for the study was ordinary Portland cement with a specific gravity of 3.05. The initial and final setting time was found to be 38 min and 450 min, respectively. Chemical composition of cement is given in Table 1

Table 1 Chemical compositions (%) of cement and GGBS

Chemical composition	CaO	SiO_2	Al_2O_3	Fe_2O_3	MgO	LOI
Cement	61.53	20.36	4.31	5.98	1.36	6.46
GGBS	38.9	33.5	10.68	2.35	9.45	5.12

GGBS was obtained from Mangalore Steel Industries (Pvt. Limited), India. Specific gravity was found to be 2.98. Chemical composition of GGBS is given in Table 1.

River sand which satisfies the code requirements (IS 2386-3 (1963)) was used as fine aggregate, which has a fineness modulus of 2.75. Coarse aggregates of size 10 mm were used. Water absorption of fine and coarse aggregates was obtained as 1.4% and 0.93%, respectively.

Crimped steel fibres having aspect ratio 60 were used for increasing the cracking resistance. Fibres having a length of 30 mm and diameter 0.5 mm was used.

2.2 Mix Design and Specimens

Mix design for getting a compressive strength of 25 N/mm² was carried out according to IS 10262-2009. Cubes and cylinders were cast by varying the percentage of GGBS and steel fibre. The details of different materials used for mix proportioning are given in Table 2. In the concrete mix, GGBS was added as a partial replacement for cement at various percentages of 30, 35, 40, 45 and 50 by weight of cement. Steel fibre was added at 0.5, 0.75 and 1% of total volume of concrete. Three specimens were prepared for each combination. Ingredients were mixed in a pan mixer and during mixing, fibres were sprinkled by hand for avoiding balling effect of fibres. Concrete was filled in each mould in three layers and compacted on a vibrating table. All the specimens were demoulded within 24 h and cured under water for 28 days.

Table 2 Mix proportioning of concrete

Sl. No	Material	Quantity (kg/m^3)
1	Binder content	350
2	Water	175
3	Fine aggregate	618.24
4	Coarse aggregate	1196.48
5	Steel fibre	58.86

2.3   Compressive Strength of Specimens

Compressive strength test was conducted on $150 \times 150 \times 150$ mm cubes cured for 28 days as per the procedure specified in IS 516:1959. Compression testing machine of capacity 3000 kN was used for testing the specimens. Strength of different mixes is summarised in Table 3.

The 7-day strength of GGBS concrete was found to be lower than that of ordinary portland cement concrete, because of the slow pozzolanic reaction of GGBS i.e. the calcium hydroxide formation takes longer time. At later stages, the compressive strength was more for GGBS concrete because of higher calcium silicate bond (C-S-H). The compressive strength increased by 2.55%, 7%, 16.53%, 9.97% and 9.84%, respectively, for 30, 35, 40, 45 and 50% replacement of cement with GGBS. The optimum percentage of GGBS and steel fibre obtained was 40 and 0.75, respectively, in terms of strength.

Table 3 Compressive strength of GGBS concrete at 7 and 28 days

| Mix no.	GGBS (%)	Steel fibre (%)	Compressive strength (N/mm²)	
			7 day	28 day
1	0	0	20.12	31.34
		0.5	20.56	32.95
		0.75	21.02	33.35
		1	20.97	32.98
2	30	0	17.09	32.19
		0.5	17.15	33.08
		0.75	17.96	33.94
		1	17.88	33.86
3	35	0	16.98	33.59
		0.5	17.06	33.97
		0.75	17.25	34.41
		1	17.22	33.99
4	40	0	17.29	36.58
		0.5	17.53	36.86
		0.75	17.62	37.45
		1	17.61	37.33
5	45	0	16.26	34.52
		0.5	16.31	34.95
		0.75	16.44	35.02
		1	16.41	34.98
6	50	0	15.44	34.48
		0.5	15.63	34.76
		0.75	15.78	35.23
		1	15.68	34.97
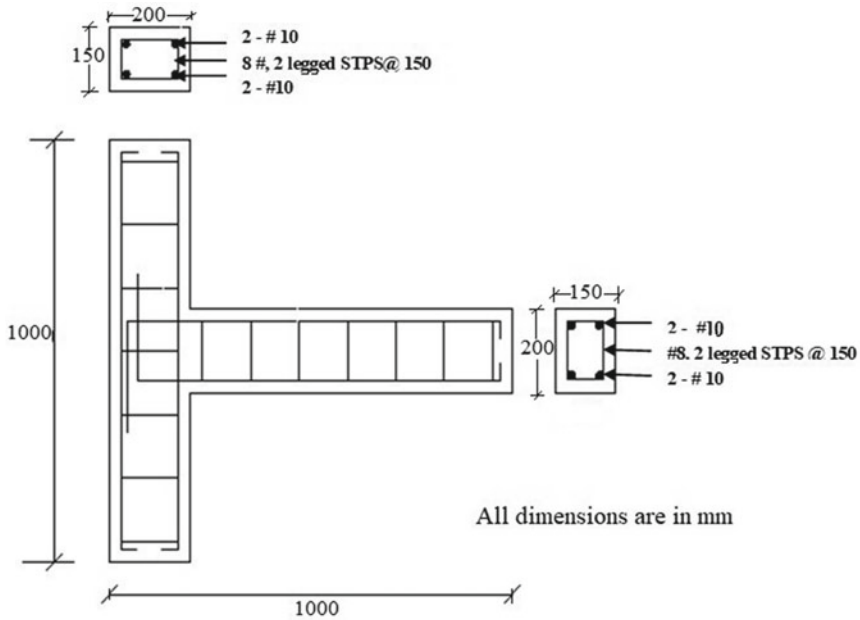
Fig. 1 Reinforcement details of beam-column joint

2.4 Details of Beam-Column Joint Specimen

In this present investigation, three exterior beam-column joint specimens were tested under monotonic loading. Reinforced cement concrete specimens were prepared by using M25 grade concrete. The second specimen was made by using concrete in which cement was replaced with an optimum percentage of GGBS. 0.75% of steel fibre (optimum percentage) was added in the third specimen and tested under monotonic loading.

Beam-column joint specimens were designed as per IS 456-2000 and IS 13920-2014 and having cross-sectional dimension of 150 mm × 200 mm. Height and clear span of the column and beam were 1000 mm and 800 mm respectively (Fig. 1) Column and beam were reinforced with four high yield strength deformed bars (HYSD) having 10 mm diameter and transverse ties of 6 mm diameter HYSD bars were provided.

2.5 Test Set Up

Test setup for the specimen is shown in Fig. 2. The specimen was tested in a compression testing machine under monotonic loading. A constant load of about

Fig. 2 Test set up for beam-column joints

20% of its axial capacity was applied to the column for holding the specimen in position and to simulate column axial load. At free end of the beam, hydraulic jack was used to apply load to the specimen. A load cell of 100 kN capacity was used to measure the applied load. A dial gauge was used to measure the beam displacement. Three numbers of LVDTs with a gauge length of 200 mm were used to measure the deformation at different locations. The load was applied continuously until failure occurred.

2.6 Numerical Analysis

Numerical analysis of the beam-column joint was carried out in ANSYS. SOLID65 element was used for representing concrete which has eight nodes with three degrees of freedom at each end. Similarly, 3D spar element LINK8 was used for representing reinforcements. Figure 3 shows the beam-column joint modelled in ANSYS. Effect of GGBS was included in the model by using constitutive relations of GGBS concrete in solid 65 elements. Effect of steel fibre was integrated into the model by providing material properties, volume ratio and orientation angle of fibres in real constant input of solid 65 elements.

Fig. 3 Modelling in ANSYS
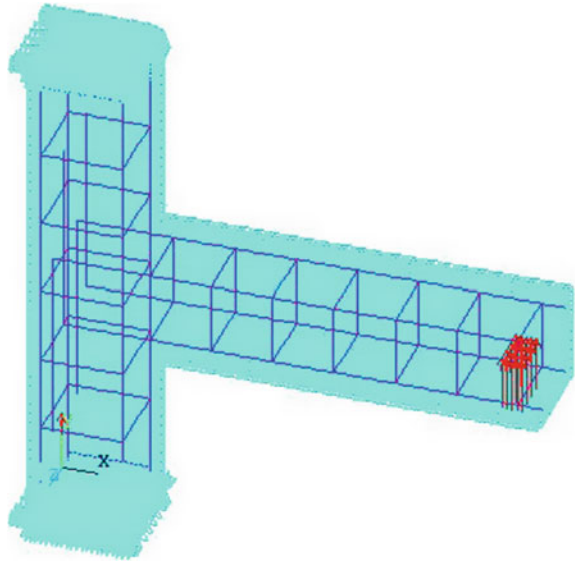
3 Results and Discussions

3.1 Behaviour of Beam-Column Joints

All beam-column joint specimens such as reinforced cement concrete (RCC BCJ), GGBS concrete (GGBS BCJ), steel–fibre-reinforced GGBS concrete (SFGGBS BCJ) were tested under monotonic loading. Failure of all beam-column joint specimens occurred in beams near to columns, while the first crack was observed in the interface between beam and column. More cracks were observed in the flexural span of the beam due to further increase in load. Joint shear failure was not observed in any of the specimens. More microcracks were observed in SFGGBS BCJ.

3.2 Ultimate Load and Deflection

Ultimate load of beam-column joint specimens are shown in Table 4. The ultimate load carrying capacity of GGBS BCJ and SFGGBS BCJ are found to be 17 and 33% more than RCC BCJ.

Deflection of beam-column joint specimens at ultimate load are shown in Table 5. SFGGBS BCJ has shown more deflection than RCC BCJ. Addition of steel fibre increased 27% more deflection than RCC BCJ. Fibres arrest the cracks by bridging across it and demand more energy for further propagation of crack or formation of new cracks elsewhere. This may cause an increase in deforming

Table 4 Ultimate load of BCJ by experimental and numerical studies

Beam-column joint (BCJ)	Ultimate load (kN)		Error (%)
	Experimental	Numerical	
RCC BCJ	18	18.6	3.33
GGBS BCJ	21	22	4.76
SFGGBS BCJ	24	24.5	2.08

Table 5 Deflection of beam-column joint specimen

BCJ	Deflection at ultimate load (mm)		Error (%)
	Experimental	Numerical	
RCC BCJ	22	21.6	1.82
GGBS BCJ	23	21.9	4.7
SFGGBS BCJ	28	27.6	1.42

capacity of the specimen. It is found that GGBS is not having much influence on the deformation capacity of concrete, this might be due to the fact that the engineering properties of GGBS concrete is similar to that of OPC concrete [11]. Good agreement was observed between experimental and numerical results.

3.3 Load–Deflection Characteristics

Load–deflection characteristics of beam-column joints is shown in Fig. 4.

The curve showed linear behaviour up to first crack load. Ductility factor can be calculated from the following equation $\mu = \Delta_u/\Delta_y$. where Δ_u and Δ_y are the maximum and yield displacements respectively [12]. Ductility factor for OPC concrete, GGBS concrete and SFGGBS concrete obtained are 11, 13 and 19, respectively. This indicates the SFGGBS concrete has higher ductility compared to OPC concrete.

3.4 Crack Pattern

Crack pattern observed on beam-column joints is shown in Fig. 6. Cracks were observed in flexural span of the beam near to column in both experimental and numerical studies. First cracks were developed near to joint. Due to further increase in loading, cracks were propagated up in the beam and with increased crack width. More cracks were observed in steel fibre reinforced beam-column joints. Good
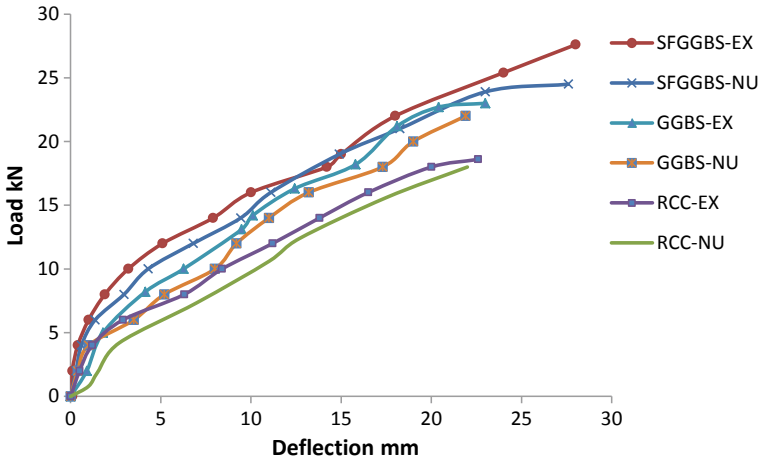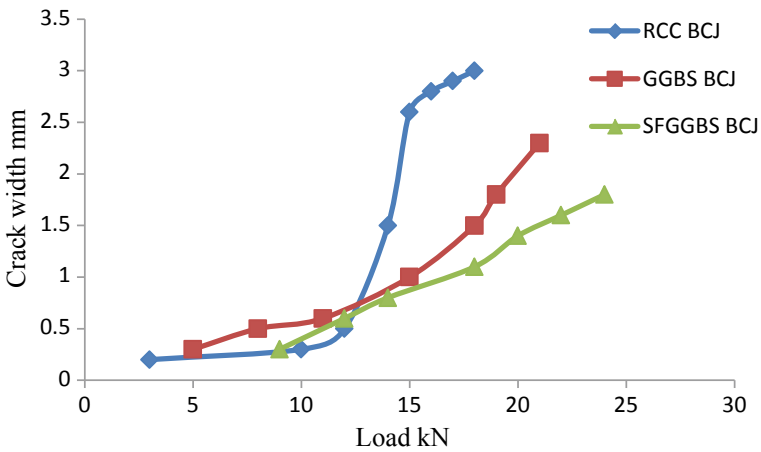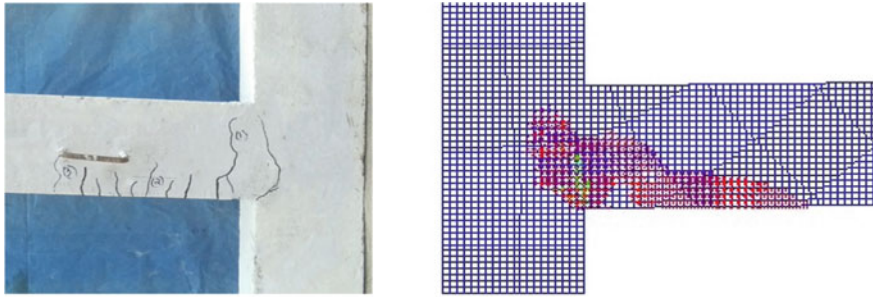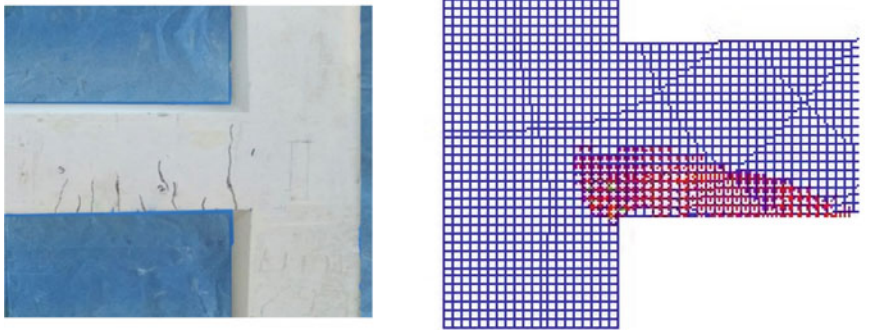
Fig. 4 Load–deflection curve

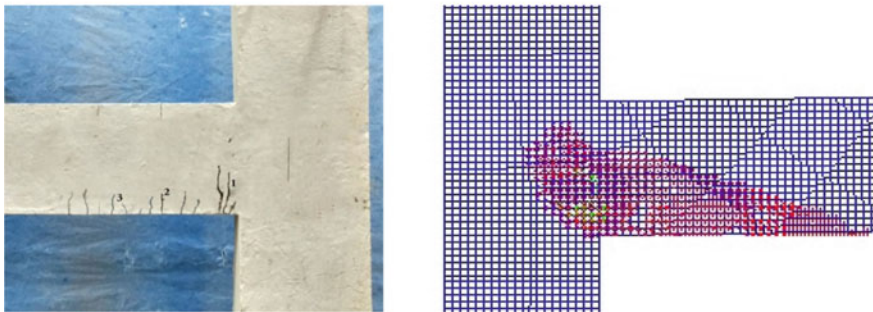**Fig. 5** Crack width versus load

agreement in crack pattern was observed in numerical and experimental studies. The increase in crack width along with load is shown in Fig. 5. Wider cracks were developed near to the joint in beams. Large crack was observed in RCC BCJ than GGBS and SFGGBS beam-column joints.

(a) RCC BCJ

(b) GGBS BCJ

(c) SFGGBS BCJ

Fig. 6 Crack pattern from experimental and numerical studies

4   Conclusions

The following conclusions are made from the above study,

1. The optimum percentage of replacement of cement with GGBS was obtained as 40% and steel fibre was 0.75% of total volume of concrete in terms of strength.

2. GGBS BCJ and SFGGBS BCJ have 17 and 33% more ultimate load carrying capacity than RCC BCJ.
3. GGBS BCJ has more deflection than RCC BCJ. Addition of steel fibre increases the deflections to more than 27% when compared to RCC BCJ.
4. Wider cracks were observed in RCC BCJ than GGBS and SFGGBS BCJ.
5. Good agreement in results was observed in ultimate load, deflection and crack pattern of beam-column joints by experimental and numerical studies.

The above results are obtained by considering limited test specimens. As the experimental results are found to be in good agreement with numerical results, the above numerical model can be used for further parametric studies.

References

1. J. Bijen, Constr. Build Mater. **5**, 309–314 (1996)
2. S. Teng, T.Y.D. Lim, B.S. Divsholi, Constr. Build Mater. **40**, 875–881 (2013)
3. P.J. Wainwright, N. Rey, Cem. Concr. Compos. **22**, 253–257 (2000)
4. A. Bouikni, R.N. Swamy, A. Bali, Constr. Build Mater. **23**, 2836–2845 (2009)
5. J.M. Gao, C.X. Qian, H.F. Liu, B. Wang, L. Li, Cem. Concr. Res. **35**, 1299–1304 (2005)
6. D. Higgins, Briefing. Proc. ICE – Constr. Mater. **160**, 99–101 (2007)
7. S. Kourounis, S. Tsivilis, P.E. Tsakiridis, G.D. Papadimitriou, Z. Tsibouki, Cem. Concr. Res. **37**, 815–822 (2007)
8. P.L. Maier, S.A. Durham, Constr. Build Mater. **29**, 428–437 (2012)
9. A. Oner, S. Akyuz, Cem. Concr. Res. **6**, 505–514 (2007)
10. G.J. Osborne, Cem. Concr. Compos. **21**, 11–21 (1999)
11. S.P. Sangeetha, J. Pure. Appl. Math. **118**, 867–879 (2018)
12. M.A.A. Siddique, A.A. El Damatty, A.M. El Ansary, Can. J. Civ. Eng. **41**, 17–31 (2013)

Experimental Investigation on the Fracture Behaviour of Polypropylene Fibre-Reinforced Rubcrete

Anand Raj, P. J. Usman Arshad, Praveen Nagarajan and A. P. Shashikala

Abstract Use of crumb rubber to replace fine aggregates has opened up new avenues to explore the trends to develop more robust and eco-friendly construction material (Rubcrete) when compared to conventional concrete. Research trends indicate an increase in toughness in concrete with the use of crumb rubber, and the addition of polypropylene fibres counters the development of microcracks. The brittle nature of concrete can be explained with respect to the fracture energy required to open unit area of the crack surface. The paper highlights the results of experiments carried out to ascertain the significance of polypropylene fibres on the fracture energy of M40 grade rubcrete. Using a notched three-point bending beam (3PBB) specimen based on RILEM TC 50 FMC, cracks in rubcrete are subjected to fracture under Mode I loading. Variation in the fracture energy was studied for the polypropylene fibre-reinforced rubcrete with the addition of fibres up to 0.3% of total volume of the mix starting from 0.1% with an increment of 0.1%. Analysis of results for toughness and energy absorption characteristics showed that the specimens reinforced with polypropylene fibres have lesser brittle behaviour than that of conventional concrete specimens and optimum results were obtained for the addition of 0.3% polypropylene fibres.

Keywords Rubcrete · Fracture energy · Polypropylene fibre-reinforced concrete

1 Introduction

Concrete has been the most favoured construction material that has been used in the past century. It has been used for the construction of the common houses to building the tall skyscrapers. Use of concrete has been accepted worldwide, mainly because of its ability to withstand compressive loads [1]. Despite its wide popularity

A. Raj (✉) · P. J. Usman Arshad · P. Nagarajan · A. P. Shashikala
Department of Civil Engineering, National Institute of Technology Calicut,
Kozhikode 673601, Kerala, India
e-mail: anandrajce@gmail.com

in the construction field, concrete lacks in its ability to withstand tensile loads and has poor toughness.

The lack of ability to absorb energy by concrete has been a cause of concern for its applications in areas that demand it. Concrete technologists and researchers have been trying to improve the ability of concrete in its areas of weakness. Use of worn out tyre rubber in concrete in many forms has improved its energy absorption capacity and ductility to varying degrees based on the form. Rubber has been used as a partial or full replacement of both fine and coarse aggregates in concrete. It is generally referred to as Rubcrete [2]. In this study, partial replacement of fine aggregates by volume has been carried out with crumb rubber graded to the same size of fine aggregates with a limit of 20%.

The mechanical properties of rubcrete have been studied by many researchers all across the globe. The compressive strength and tensile strength of rubcrete have shown a decreasing trend with the increased content of rubber. Improved ductility and impact absorption are, however, the highlight of rubcrete making it usable in structural elements demanding those traits [3, 4]. Fibres are added to concrete to improve the properties of concrete to suit specific purposes. Military research and applications have led to the development and use of fibre-reinforced concrete in combat areas and strategically essential places. Natural and synthetic fibres have been added to concrete, and the properties of fibre-reinforced concrete have been studied. Different fibres have different action on the behaviour of concrete matrix. Addition of polypropylene fibres into concrete, do not have a considerable impact on the compressive and tensile strength. However, they help in delaying the initial crack formation and propagation of cracks in concrete. The impact strength of concrete has been observed to increase with the addition of polypropylene fibres [5].

Development of cracks in concrete and their propagation can be studied based on fracture mechanics approach. The crack model of Hillerborg describes fracture energy as the energy needed to produce a unit area of a crack [6]. Determination of the fracture energy of a brittle material like concrete is governed by Technical Committee 50—Fracture Mechanics of Concrete (TC 50—FMC). It provides all the guidelines for the tests required to compute the fracture energy G_f. Estimation of fracture energy is essential to determine the design methodologies of the concrete variants. Fracture energy indicates the fracture toughness of the material and can be used to validate the energy absorption studies conducted by other means [7–11].

1.1 Need for the Study

Fracture energy is an important parameter that helps in establishing the design methodology for rubcrete and its variants as it has been deemed to be useful in a variety of applications like crash barriers, highway pavements, railway sleepers, etc. In all the afore-mentioned structures, the ability to absorb energy by rubcrete and its variants is the key feature. Failure of these structures is characterised by the

presence and propagation of cracks. It has been noted that limited studies have been reported on the fracture properties of rubcrete. A thorough understanding of the fracture behaviour of rubcrete is essential for its utilisation of structural elements.

2 Experimental Investigation

Three-point bend beam test is used to assess the fracture energy of eight variants of M40 grade concrete beams of size $60 \times 100 \times 500$ mm. Extensive trials had to be conducted to finalise the mix proportions conforming to the specified strength. This section provides details of the experimental programme conducted for the study.

2.1 Materials and Mix Proportions

Portland pozzolana cement along with coarse aggregates having a size less than 12.5 mm were used. The fine aggregate used for the study was manufactured sand belonging to zone 2 as per IS:383-1970 for conventional concrete. For the rubber concrete variants, volume replacements of fine aggregates up to 20% with an increment of 5% starting from 10% was carried out with crumb rubber procured from local tyre re-treading unit. The volume replacements of fine aggregate were carried out in such a way that the grain size distribution of the mixture of fine aggregates and crumb rubber matches with that of the available manufactured sand. Grain size distribution curve for the crumb rubber sand mixture is shown in Fig. 1. The specific gravities of fine aggregates, coarse aggregates and rubber were 2.61, 2.79 and 0.6, respectively.

In order to improve the workability of concrete, a sulphonated naphthalene-based superplasticiser was used. The crumb rubber used was pretreated with a polyvinyl alcohol solution of 2% by weight of water in which the rubber was mixed for about half an hour to improve the bonding of rubber with the concrete matrix. The mix proportions were finalised after conducting extensive trials using

Fig. 1 Grain size distribution curve for fine aggregate
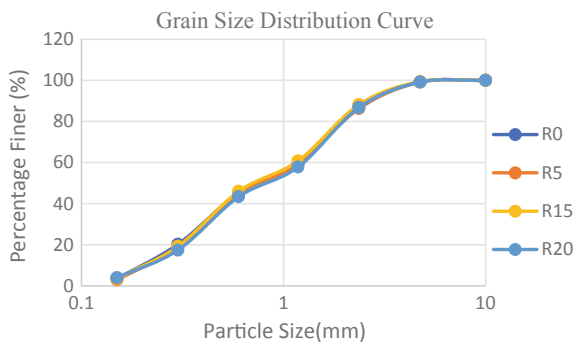
the trial mixes arrived based on IS 10262:2009. The mix proportions obtained for conventional concrete is shown in Table 1. When the slump of the mixes was observed, it was evident that there was a reduction in workability of concrete. Figure 2a shows the slump obtained for the concrete mixes with an increase in rubber contents. Figure 2b shows the compressive strength of rubcrete mixes when compared to the conventional mix. It was observed that the slump and compressive strength of rubcrete have reduced significantly for the mix with 20% crumb rubber. Hence, the study was limited to the mix with 15% crumb rubber and conventional mix. Polypropylene fibres were added to the mix as 0.1, 0.2 and 0.3 percentage of the total volume of the mix.

2.2 Specimen Details and Test Arrangement

Computation of fracture energy using three-point bend beam test is governed by Technical Committee 50—Fracture Mechanics of Concrete (TC 50—FMC). The

Table 1 Mix proportions for M40 grade conventional concrete

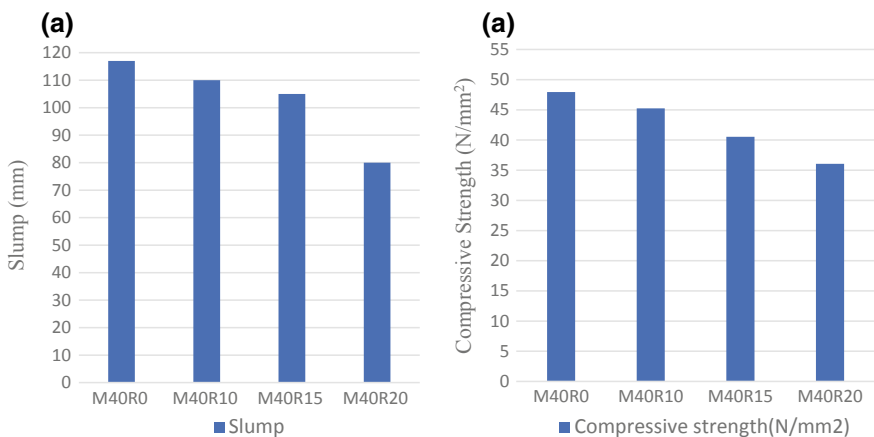| Mix ID	Rubber content (%)	Cement (kg/m^3)	Coarse aggregates (kg/m^3)	Fine aggregates (kg/m^3)	Rubber (kg/m^3)	Water (kg/m^3)	Superplasticiser (kg/m^3)
M40R0	0	446.65	992	829.57	0	178.66	2.73
M40R5	5	446.65	992	806.21	10.33	178.66	2.73
M40R10	10	446.65	992	763.78	20.66	178.66	2.73
M40R15	15	446.65	992	721.35	30.99	178.66	2.73
M40R20	20	446.65	992	678.91	41.32	178.66	2.73

Fig. 2 **a** Slump and reduction in slump for rubcrete **b** Compressive strength for rubcrete
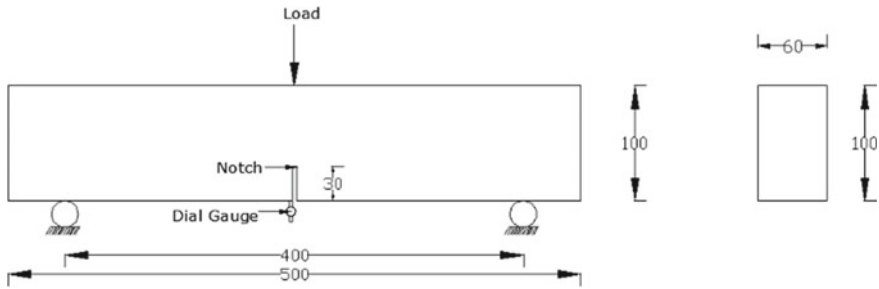
Fig. 3 Specimen details and testing arrangement (all dimensions in mm)

Table 2 Details of specimen cast

Specimen ID	Rubber content (%)	Polypropylene content (%)	Number of specimens
M40R0	0	0	3
M40R5	5	0	3
M40R10	10	0	3
M40R15	15	0	3
M40R0PP0.1	0	0.1	3
M40R0PP0.2	0	0.2	3
M40R0PP0.3	0	0.3	3
M40R15PP0.1	15	0.1	3
M40R15PP0.2	15	0.2	3
M40R15PP0.3	15	0.3	3

size of the beam used in the study has dimensions $60 \times 100 \times 500$ mm with span to depth ratio of 4 and notch depth to overall depth ratio of 0.3. A notch of 30 mm depth and width 4 mm is provided at the midspan. Figure 3 shows the details of the specimen and testing arrangement. Details of the specimen cast for the study is presented in Table 2.

2.3 Casting and Curing of Specimens

Wooden moulds were fabricated to cast the specimens. To prevent the water from being absorbed by timber, the interior portions of the mould were provided with a thin plastic film. Then moulds were then coated with shuttering oil to ensure easy removal of the specimen after casting. Mixing of the ingredients was carried out in a pan mixer of capacity 0.23 m³. For the casting of rubcrete, required crumb rubber was pretreated with polyvinyl alcohol (PVA) solution having a concentration of 2% PVA by weight of water in which rubber was soaked. Rubber was immersed in

Fig. 4 Cast beams

20% of the total water. Pretreated rubber was added to the mix immediately after the addition of aggregates. Care was taken to ensure uniform mixing of all ingredients. Then the concrete was placed on moulds placed on a vibration table, and proper vibration was provided. Figure 4 shows the cast specimen. The specimens were carefully removed from their moulds and curing was carried out.

2.4 Testing of Beams

Testing of the beams for three-point bend beam test was carried out on a servo-controlled machine at a constant rate of deformation to achieve stable failure of the specimens. A dial gauge having a least count of 0.01 mm was used to measure the deflection at a strain rate of 0.2 mm/minute. Figure 5 shows the testing of the specimen on a displacement control universal testing machine having a capacity of 10 kN.

Fig. 5 Testing of specimens on a displacement control machine

The fracture energy per unit projected area is calculated by Eq. 1 based on TC-FMC [7] λ

$$G_f = \frac{W_0 + 2P_w\delta_0}{(h - a_0)t}$$

(1)

where W_0 is the area below the load–deflection curve, P_w is the weight of the beam and δ_0 is the deflection at final fracture λ due to self-weight and applied load λ at midspan, h is the total depth of the beam, a_0 is the initial notch depth and t is the thickness of the beam.

3 Results and Discussion

This section deals with the representation of results of the three-point beam bend tests and the computed results of fracture energy.

3.1 Load–Deflection Curves

The load–deflection curves of the conventional concrete specimen and rubcrete specimen with 15% crumb rubber are shown in Fig. 6. It can be observed that the peak load has reduced in the case of rubcrete specimens. The softening effect has been reduced after crossing the peak load.

The load–deflection curves for the polypropylene fibre-reinforced concrete beams have been presented in Figs. 7 and 8. The polypropylene fibres are extremely flexible and easy to handle making their uniform distribution across the specimen easy. Due to their extremely wiry nature, they help in establishing bridges across the materials in the concrete matrix. Because of this bridging, they help in preventing the separation of voids during the application of loads. From the load–deflection curves of polypropylene fibre-reinforced concrete beams, it can be noted that there is a

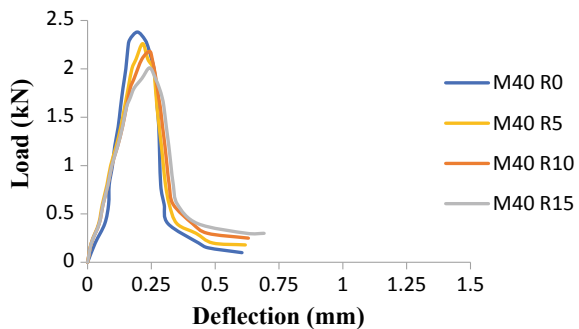**Fig. 6** Load–deflection curves for rubcrete beams

Fig. 7 Load–deflection curve for polypropylene fibre-reinforced concrete beams
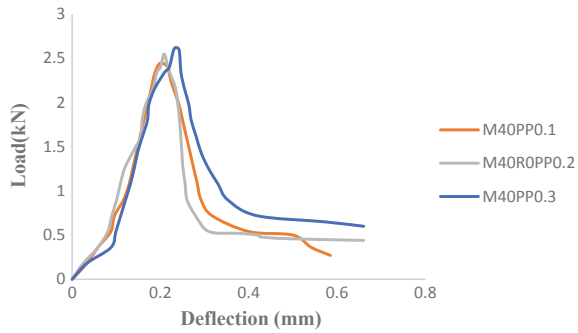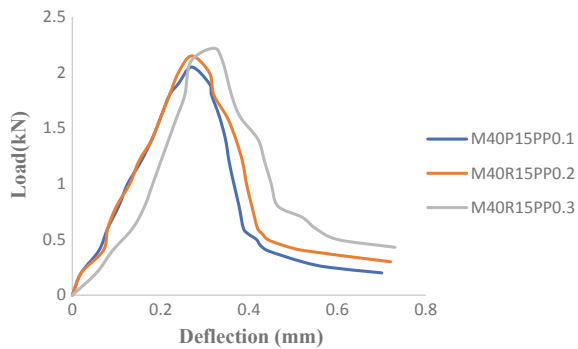

Fig. 8 Load–deflection curve for polypropylene fibre-reinforced rubcrete beams

reduction in softening behaviour of the beams with an increase in fibre content. This slight hardening behaviour may be the effect of prevention of initiation and propagation of microcracks due to the above-mentioned bridging effect. It should also be noted that addition of polypropylene fibres does not have a significant effect on the peak load in conventional concrete. Once the bridge between the particles is broken, then the role of polypropylene fibres is reduced. But in rubcrete, the addition of polypropylene fibres help in bridging those gaps and resulted in enhanced performance. The combination of polypropylene and rubcrete has a lesser softening effect resulting in a larger area under the load–deflection curve.

3.2 Fracture Energy of Beams

Figures 9 and 10 represent the fractured surface of conventional concrete beams, and polypropylene fibre-reinforced rubcrete beams, respectively. For conventional concrete specimen, the fractured surface is relatively smooth when compared to the polypropylene fibre-reinforced rubcrete specimen. This feature indicates the brittle failure of conventional concrete. In the case of polypropylene fibre-reinforced rubcrete, the rugged fracture surface with protruding rubber and polypropylene

Fig. 9 Fractured surface of conventional concrete beams

Fig. 10 Fractured surface of polypropylene fibre-reinforced rubcrete beams

fibres showcase greater resistance encountered by the propagating cracks due to the greater friction generated by the fibre–rubber–aggregate-cementitious material interfaces. As a result, greater energy has to be expended for crack propagation in polypropylene fibre-reinforced rubcrete beams when compared to the conventional concrete beams. The fracture energy of beams is computed using Eq. 1 represented in Sect. 2. Table 3 shows the fracture energy and the ratio of fracture energy to cost for various beam specimens. Figure 11 shows the variation of fracture energy with different volume fractions of polypropylene fibres.

It is evident from Fig. 11 and Table 3 that there is an increase in fracture energy of rubcrete when compared to conventional concrete. The fracture energy has increased from 4 to 13% for rubcrete with 5, 10 and 15% rubber content. An increase in the crumb rubber content has resulted in increased fracture energy. This may be due to the ability of crumb rubber to absorb the energy supplied by the load to propagate the crack. Addition of polypropylene fibres of volume fraction 0.1, 0.2 and 0.3% has enhanced the fracture energy by 4–31%. Polypropylene fibres may create an additional restraint on the debonding of atoms during the application of load because of their ability to hold the different ingredients of the heterogeneous concrete mix.

Table 3 Fracture energy of beams

Beam ID	Fracture energy G_f (Nm/m^2)	Increase in G_f with respect to M40R0 (%)	Fracture energy to cost ratio (Nm/m^2)/Rs)	Variation in fracture energy to cost ratio with respect to M40R0 (%)
M40R0	126.55	0	8.28	0
M40R5	131.45	3.87	7.93	−4.22
M40R10	139.07	9.89	7.88	−4.83
M40R15	143.14	13.11	7.61	−8.09
M40R0PP0.1	131.57	3.97	8.17	−1.32
M40R0PP0.2	139.40	10.15	8.24	−0.48
M40R0PP0.3	165.59	30.84	9.35	+12.92
M40R15PP0.1	146.07	15.42	7.45	−10.02
M40R15PP0.2	160.43	26.77	7.86	−5.07
M40R15PP0.3	172.24	36.10	8.11	−2.05

Fig. 11 The effect of polypropylene volume fraction V_f (%) on G_F for M40 rubcrete
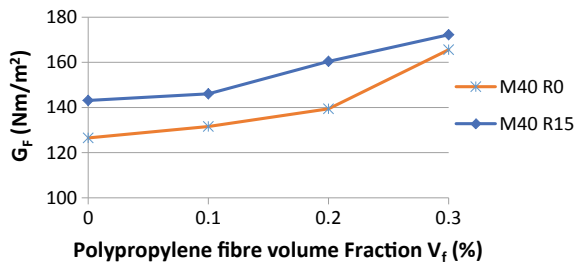
Analysis of fracture energy to cost ratio shown in Table 3 indicates that, as the rubber content increases, the energy to cost ratio decreases which means that the cost required to enhance energy absorption is reduced. M40R0, M40R5, M40R10 and M40R15 have fracture energy to cost ratio in (Nm/m^2)/(Rs) of 8.28, 7.93, 7.88 and 7.61, respectively which shows that cost required to enhance energy absorption is reduced. In the case of concrete with polypropylene concrete, the fracture energy to cost ratio in (Nm/m^2)/(Rs) is 8.17, 8.24 and 9.35, respectively. The energy to cost ratio for the polypropylene fraction of 0.3% is greater than for conventional concrete. In comparison with the normal concrete, the fracture energy of rubcrete with (15% rubber) and polypropylene fibres increases by 15.42, 26.77 and 36.10% for 0.1, 0.2 and 0.3% polypropylene content and the energy to cost ratio (Nm/m^2)/(Rs) is 7.45, 7.86 and 8.11, respectively. Above trends indicate that more energy is required for the propagation of cracks in polypropylene fibre-reinforced rubcrete and the cost encountered to achieve this feat is lesser than conventional concrete.

4 Conclusions

In this study, the results of experimental investigations of the three-point bend beam test on polypropylene fibre-reinforced M40 grade conventional concrete, and rubcrete is presented. Rubcrete specimen exhibited better performance with regard to deflection and energy absorption characteristics. Addition of polypropylene fibres enhanced the performance of both conventional concrete and rubcrete. Based on the study, the following conclusions have been derived.

Partial replacement of fine aggregates with rubber enhances the fracture energy of concrete. The optimum proportion of replacement of fine aggregates with crumb rubber was observed to be 15% as further addition of rubber significantly reduces compressive strength of concrete. Increase in rubber content in concrete enhances the fracture energy and reduces the fracture energy to cost ratio.

The fracture energy of conventional concrete and rubcrete increased with the addition of polypropylene fibres. The fracture energy to cost ratio of polypropylene fibre-reinforced conventional concrete and polypropylene fibre-reinforced rubcrete was less than that of conventional concrete except in the case of 0.3% volume fraction of polypropylene fibre-reinforced conventional concrete.

References

1. J.K. Wight, J.G. Macgregor, *Reinforced Concrete Mechanics and Design* (Pearson Education, New Jersey, 2012)
2. A.R. Khaloo, M. Dehestani, P. Rahmatabadi, Waste Manag. **28**, 2472–2482 (2008)
3. D. Li, Y. Zhuge, R. Gravina, J.E. Mills, Constr. Build. Mater. **166**, 745–759 (2018)
4. N.M. Miller, F.M. Tehrani, Constr. Build. Mater. **147**, 264–271 (2017)
5. A.M. Alhozaimy, P. Soroushian, F. Mirza, Cem. Concr. Compos. **18**, 85–92 (1996)
6. A. Hillerbrog, Mater. Struct. **18**, 407–413 (1985)
7. RILEM TC-50 FMC. Mater. Struct. **18**, 285–290 (1985)
8. M. Elices, G.V. Guinea, J. Planas, Mater. Struct. **25**, 327–334 (1992)
9. Y. Chen, P. Qiao, Proceedings of the Eleventh International Conference on Aerospace Division International Conference (Earth and Space 2008), CA, USA (2008), pp. 1–8
10. B.L. Karihaloo, *Fracture Mechanics and Structural Concrete, Longman Scientific and Technical* (Wiley, New York, 1995)
11. P. Kumar, *Elements of Fracture Mechanics* (McGraw Hill Education (India) Private limited, New Delhi, 2014)

Effects of Water to Cement Ratio on Concrete Fracture Parameters

Dinesh Kumar Samal, Sonalisa Ray and T. Hemalatha

Abstract This paper presents an experimental investigation of the influence of different water to cement ratios (w/c) on fracture properties of concrete. Water/cement ratio plays a vital role in governing the strength of concrete as well as the strength and thickness of interfacial transition zone (ITZ), which in turn affects the formation of fracture process zone and cracking behaviour in concrete. In this study, three-point bend tests have been performed on notched concrete beams with varying water to cement ratios between 0.35 and 0.5 to determine the fracture properties of concrete. Aggregates with a nominal maximum size of 12.5 mm have been used for this study. The size of the fracture process zone is one of the important parameters that determine the brittleness of concrete. Digital Image Correlation (DIC) has been used to obtain various fracture parameters such as crack opening displacement, length and width of the fracture process zone (FPZ). VIC-3D software has been utilized to process digital images to measure surface strains and displacements. A decrease in fracture energy has been observed with the increase in water to cement ratio from 0.35 to 0.45. This can be attributed to the modification of pore structure in ITZ with the increase in water to cement ratio. In addition, the paper also compares the variation of crack tip opening displacement at different stages of loading for the proposed water/cement ratios. Variation in characteristics of FPZ for different water to cement ratios, viz. length and width of the FPZ are also examined.

D. K. Samal · S. Ray (✉)
Department of Civil Engineering, Indian Institute of Technology Roorkee,
Roorkee 247667, Uttarakhand, India
e-mail: sonarfce@iitr.ac.in

T. Hemalatha
CSIR-Structural Engineering Research Centre, Chennai 600113, Tamil Nadu, India

1 Introduction

It has been long established that concrete is composed of three phases, viz. aggregates, bulk cement paste and interfacial transition zone. The role of water to cement ratio in influencing the ITZ properties is considerable, which in turn influences fracture parameters and cracking behaviour of concrete. Wu and his coworkers [1] used the DIC technique and found out that the length of the fracture process zone (FPZ) increases during crack propagation but decreases after the full growth of FPZ. Skarzynski et al. [2] proposed a method to determine the width of the localised zone using three-point bend tests on notched beams. Various researchers [3] have compared the results obtained through acoustic emission technique and DIC, and found DIC to be more effective in measuring fracture length. Trivedi et al. [4] proposed Optical Crack Profile (OCP) approach to measure process zone parameters such as its length and width using DIC. Shah and Chandra Kishen [5] used DIC to determine the fracture toughness and critical energy release rate for concrete–concrete-jointed interfaces. Alam and coworkers [6] used DIC to capture crack propagation and estimated the effective crack length from the crack opening profile. In this paper, the role of water to cement ratio on the fracture parameters, such as the size of the fracture process zone (FPZ), fracture energy and crack tip opening displacement is studied using DIC.

2 Experimental

2.1 Raw Materials

The cement used is ordinary Portland cement of 43 grade. Natural sand with a fineness modulus of 2.7 is used as fine aggregate. The coarse aggregates are the crushed limestone particles with a maximum size of 12.5 mm and a bulk specific gravity of 2.39.

2.2 Mix Design

Notched concrete beam specimens have been prepared using three mix ratios with varying water to cement ratios and are presented in Table 1 along with their mechanical properties.

Table 1 Mix designs and mechanical properties of concrete specimens

W/C	Cement (kg/m^3)	Fine aggregate (kg/m^3)	Coarse aggregate (kg/m^3)	Water (kg/m^3)	Compressive strength (MPa)	Tensile strength (MPa)	Modulus of elasticity (GPa)
0.35	413	657	1162	144.55	45.2	3.65	21.9
0.4	413	657	1162	165.2	40.5	2.84	17.88
0.45	413	657	1162	185.85	38.17	2.77	25.44
0.5	413	657	1162	206.5	34.62	2.56	24.9

2.3 Specimen Preparation

The moulds used for the casting of beams are made up of mild steel. Owing to the difficulties associated with making a notch in hardened concrete, the notch has been made in the mould itself as shown in Fig. 1. A schematic sketch of typical beam geometry used in this study is presented in Fig. 2. Three specimens of each mix are cast for the experimental programme. To obtain strain and displacement values over the beam surface upon loading, a speckle pattern is prepared over the area of interest on beam specimen. Speckle pattern can be prepared with self-adhesive, pre-printed patterns, stamps or paint speckles applied with air brushes or spray cans [7]. A white coloured enamel paint is applied on the beam surface after which a black speckle pattern is created by the spraying method.

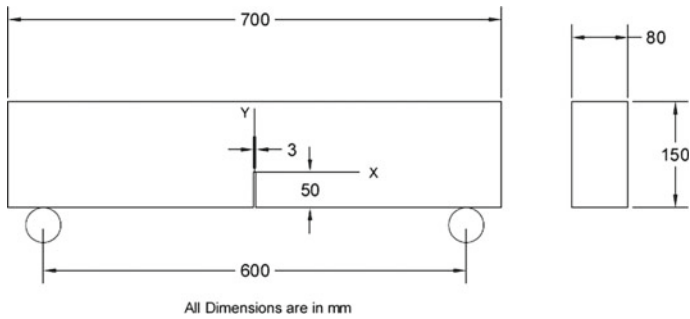**Fig. 1** Moulds for the casting of beams

Fig. 2 A typical geometry of beam specimen

2.4 Digital Image Correlation Technique

Digital image correlation technique is a non-contact optical measurement technique for displacements and strains in the Area of Interest (AOI) on the surface. A software for image correlation called 'VIC-3D' is used to analyse the speckle images. DIC uses a digital camera to take successive images of the surface under deformation at a particular time interval and later these images can be analysed to calculate displacement and strain field at any point. It utilizes a speckle pattern in the area of interest on the surface of the specimen.

2.4.1 Calibration

The calibration of the 3D system is done by analysing the images of a moving rigid calibration target taken in front of a stereo camera pair. Lens distortions are removed and the camera's position is triangulated while extrinsic and intrinsic parameters of cameras are calculated. This defines a three-dimensional coordinate system on the surface without any measurement bias. The accuracy of the intrinsic (focal length, principal point, distortion parameter) and extrinsic parameters (translation vector and rotation matrix) of the system defines the quality of the measurement. The calibration is done by taking images of a calibration plate under different perspective views.

2.4.2 Principle of Measuring Displacements

A stereoscopic sensor setup is used to focus on a specific pixel in the image plane of the respective sensor. The position of each object point in three dimensions is calculated using the imaging parameter for each sensor and the sensor orientation with respect to each other. Each object point position in the selected images at two

different stages of loading is identified by applying a correlation algorithm, which uses a stochastic intensity pattern on the speckled beam surface.

2.4.3 Correlation Algorithm

The correlation algorithm is based on the tracking of the grey value pattern (a set of pixels) of the object point. The maximum grey level of the image depends on its digitisation depth. In grey-scaled or coloured images, an object point can take on any value between 0 and 255. In a coloured image, the grey levels of any pixel can be computed using the following formula:

$$\text{Grey level} = 0.299 * C_R + 0.587 * C_G + 0.114 * C_B \tag{1}$$

where C_R, C_G and C_B are the red component, green component and blue component for the pixel, respectively.

During the loading process, the initial image is taken as the reference image or we can set a desired reference image for the analysis. The reference image function is assumed as f(x, y) and distorted image field function is f*(x*, y*). Theoretical relation between both discrete functions is presented in Eq. 2.

$$f^*(x^*, \, y^*) - f(x + u(x, y), \, y + v(x, y)) \, = \, 0 \tag{2}$$

where u(x, y) and v(x, y) represents the displacement field for a pattern. The cross-correlation coefficient acts as an index for the matchability of two subsets with an assumption of homogeneity in displacement field within the subset and is given as
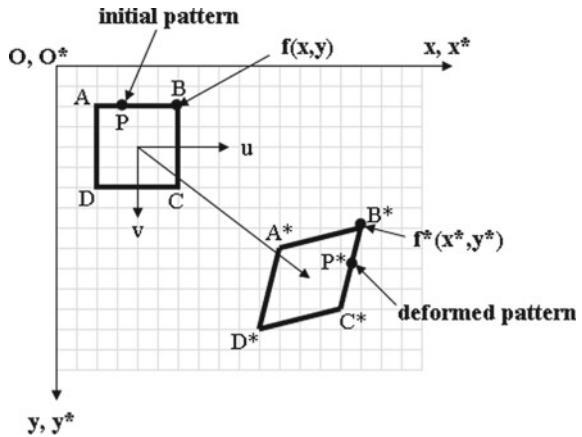
$$C = 1 - \frac{\sum [f(x, y).f^*(x^*, \, y^*)]}{[\sum \left(f(x, y)^2\right) . \sum (f^*(x^*, \, y^*)^2]^{\frac{1}{2}}} \tag{3}$$

where f(x, y) and f*(x*, y*) is the grey level values of the initial image and deformed image respectively. Arguments x, y, x*, y* are the coordinates on the speckled surface. The relation between the coordinates is given by

$$x^* \, = \, x + u + \frac{\partial u}{\partial x} \Delta x + \frac{\partial u}{\partial y} \Delta y \tag{4}$$

$$y^* = y + v + \frac{\partial v}{\partial x} \Delta x + \frac{\partial v}{\partial y} \Delta y \tag{5}$$

Fig. 3 Pattern under deformation [5]

where u and v are the displacement of the centres of the pattern in x and y directions, respectively, Δx and Δy are the distances between coordinate (x, y) and the centre of the pattern. The value of the coordinates (x, y), displacements (u, v) and their derivatives $(\frac{\partial u}{\partial x}, \frac{\partial u}{\partial y}, \frac{\partial v}{\partial x}, \frac{\partial v}{\partial y})$ can be calculated by performing an image correlation (Fig. 3).

2.5 Experimental Procedure

Three beam specimens of different water to cement ratios have been cast and cured for 28 days in water. After 28 days of curing, specimens are removed from water and surface is cleaned and painted with white paint. Speckle pattern is made over painted beam surface using black spray. A closed-loop servo-controlled controls testing machine with a load cell of 10 kN capacity is used for testing. The complete load–deflection curves are recorded for all the tests.

The beams are tested under Crack Mouth Opening Displacement (CMOD) control at a rate of 0.5 μm/s in accordance to RILEM 50-FMC guidelines. The CMOD values are recorded using clip gauge, which is placed between the knife edges. Before the test, calibration is done to ensure accurate strain and displacement calculations. Camera angle and focus has been fixed for the calibration and it is made not to change during the testing. Images of the plate are taken at different rotations to calibrate the system. For calibration, 7 mm size plate is used in this study. During testing, the images are taken at a fixed interval of 2 images per sec. Post-processing and analysis are done using a commercially available package 'VIC-3D'. Figure 4 shows the experimental setup of the test.

Fig. 4 Experimental setup

3 Results and Discussion

3.1 Fracture Energy

Experiments have been performed on concrete beam specimens under three-point bending for different w/c ratios. During testing, the load, CMOD and displacement values are recorded continuously until failure. The fracture energy has been calculated using the work of fracture method proposed by RILEM. The total energy dissipated in the test is given by $W = W_0 + mg\delta_f$, where W_0 is the area under the load–deflection curve, mg is the weight of the specimen and δ_f corresponds to the deflection when the beam fractures completely. Fracture energy thus calculated from the load versus displacement curve is plotted as shown in Fig. 5. It is observed that as expected the fracture energy is decreased when w/c is increased from 0.35 to 0.45. With an increase in w/c, the ITZ becomes weaker, the tortuosity of cracks will be less resulting in decreased fracture energy. However, with the w/c of 0.5, there is a marginal increase in fracture energy as compared to 0.45. The reason for this peculiar behaviour of specimens at a higher water to cement ratio needs to be investigated.

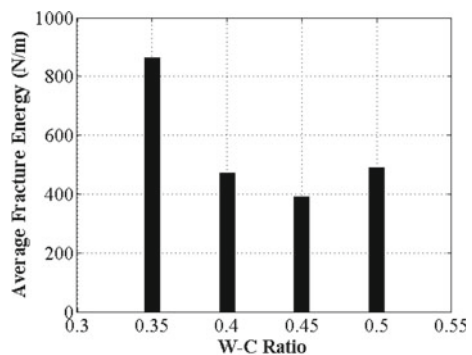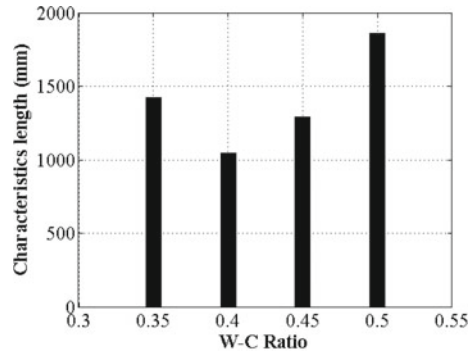**Fig. 5** Variation of fracture energy with w/c ratio

Fig. 6 Variation of
characteristic length with w/c
ratio

3.2 Characteristics Length (L_{ch})

Brittleness of concrete is evaluated by one of the parameters called characteristic length. As characteristic length is more, the brittleness is less. Characteristic length l_{ch} can be calculated using the relation, $l_{ch} = EG_F/f_t^2$ where E = modulus of elasticity, G_F = fracture energy, and f_t = tensile strength. Figure 6 shows the variation in characteristic length for different water/cement ratios. It can be seen that there is no trend in the characteristic length measured. With an increase in w/c from 0.35 to 0.4, l_{ch} decreases, however, it increases again in 0.45 and 0.5. As l_{ch} is directly proportional to elastic modulus and fracture energy and inversely proportional to the square of tensile strength, all these parameters determine the length which in turn affects brittleness. Further, it is noticed that some similarity in the trend of fracture energy and characteristic length with different w/c.

3.3 Development of FPZ

It is known that there exists a sizeable inelastic zone ahead of the crack tip which governs the fracture behaviour in concrete. Prediction of fracture process zone dimensions are important and challenging. In this work, the DIC technique has been utilized [4] to calculate FPZ dimensions. The overall response of the beam with W/C = 0.45 at different stages of fracture behaviour is described in Fig. 7a–e. The plots represent the growth of FPZ with strain levels. At 80% of pre-peak load, the strain close to the notch is around 650 μ and at the peak load of 4.443 kN, it is observed to be 1380 μ. At 80% of post-peak response, the strain level gets increased by a factor of around 4 from the strain level observed at peak load. Further, at 50% of post-peak load, the strain level increases by a factor of 6.8 ($\sim$7) from the strain level observed at peak load. At 25% of the post-peak load and 5% of the post-peak load, the size of FPZ increases significantly. In addition, the strain levels at these loads are observed to be 14000 μ.
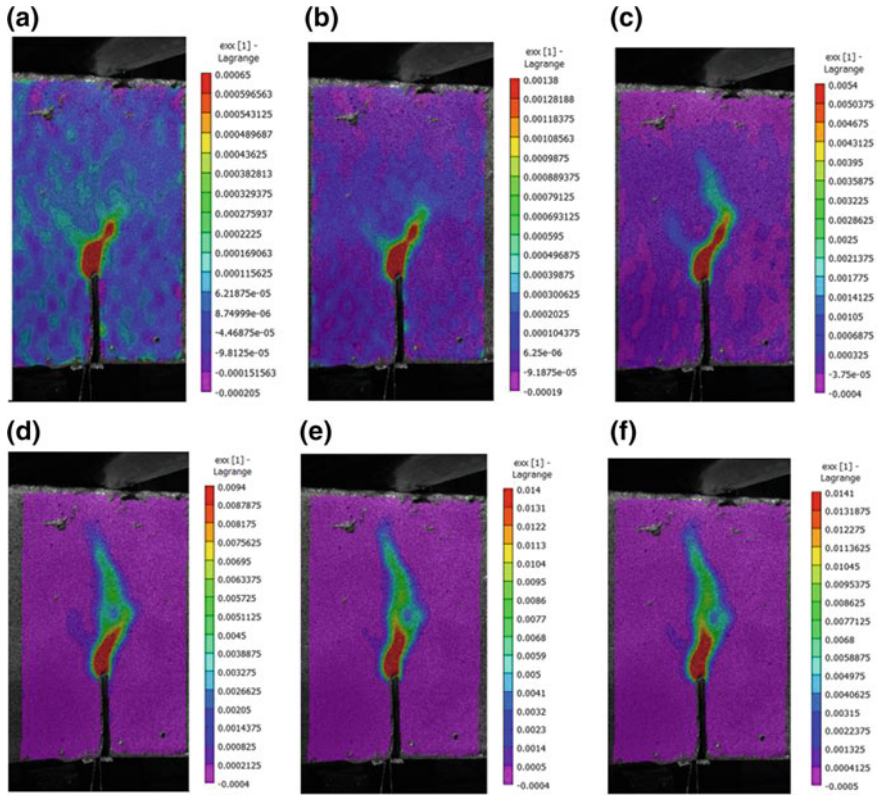
Fig. 7 FPZ growth by X-axis strain for W/C = 0.45 at load points (**a**) P1, (**b**) P2, (**c**) P3, (**d**) P4, (**e**) P5 and (**g**) P6

3.4 The FPZ Size

The size of fracture process zone (length and width of FPZ) have been calculated by a method called Optical Crack Profile (OCP) based on 'Digital image correlation' proposed by Trivedi et al. [4]. In concrete, the FPZ is complex and comprises two zones namely, inner strain softening zone and outer microfracture zone [8]. Outer microfracture zone cracks are not interconnected and thus do not contribute to the softening in concrete and therefore neglected in the calculation of FPZ dimensions. FPZ length and width are obtained by analysis of strain data obtained from DIC. FPZ width and length has been calculated along the X- and Y-axis, respectively, of the notched beam specimen (as shown in Fig. 2). In order to obtain FPZ length and width, variations of strains have been plotted as a function of distance along Y- and
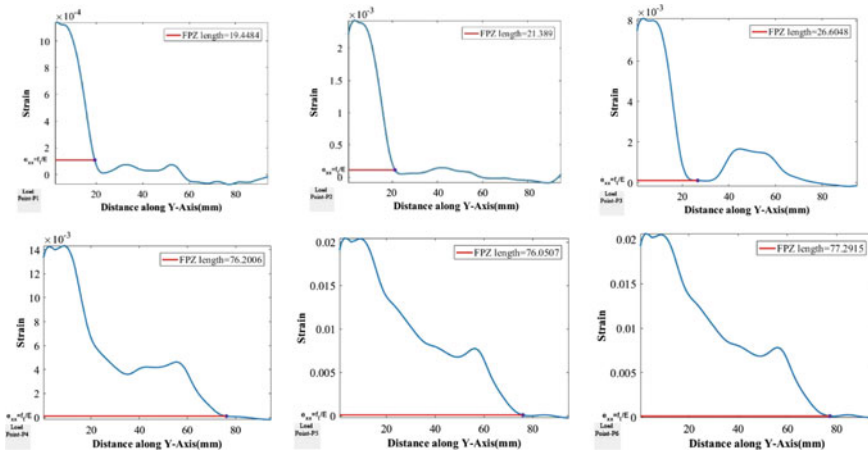
Fig. 8 FPZ length at various load points for W/C = 0.45

X-axes, respectively. In Fig. 8, the variation of strain (ε_{xx}) as a function of distance along the crack length have been presented at different load levels as described in Table 2. The strain values lower than f_t/E is considered to be the part of the outer softening zone. A line at strain equal to f_t/E in Fig. 8 to divide the inner and outer softening zone. Here f_t and E represents the tensile strength and modulus of elasticity of concrete. The region where strain (ε_{xx}) is greater than f_t/E represents the FPZ length or width depending on the curve under investigation. Figures 8 and 9 shows the calculated FPZ length and width respectively at various load points in the load–deflection curve. Description of various load shown in Fig. 10. It can clearly be seen that both FPZ length and width increases steadily until 50% post-peak load is reached and doesn't experience significant change afterwards for w/c = 0.45. Figure 11 shows the variation of FPZ length and width, respectively, for all the specimens with different water to cement ratios. FPZ length and width for w/c equal to 0.35 and 0.5 do not change much during the post-peak part but keep on increasing for w/c equal to 0.4 and 0.45.

Table 2 Description of various load points

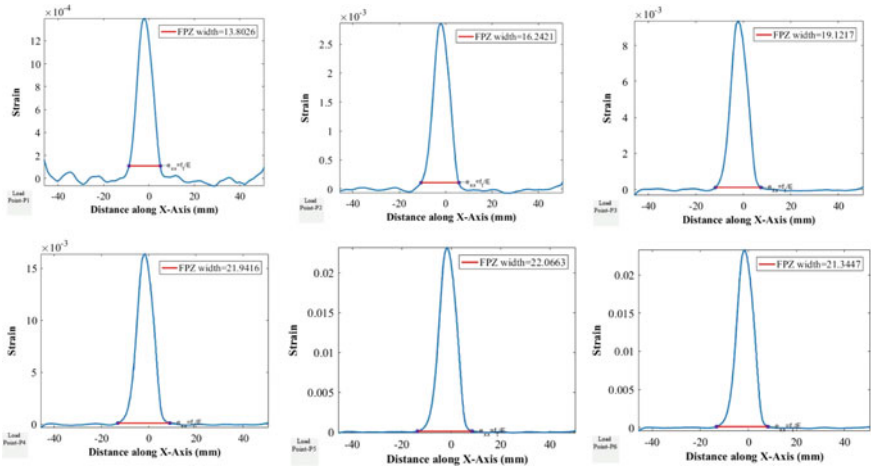| Load Points	Load
P1	80% Pre-peak load
P2	Peak load
P3	80% Post-peak load
P4	50% Post-peak load
P5	25% Post-peak load
P6	5% Post-peak load

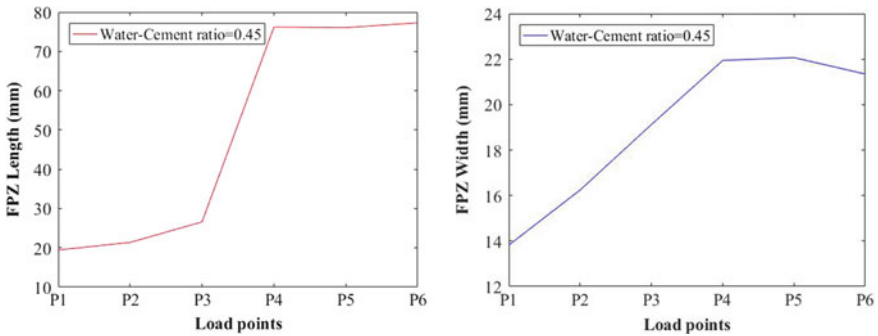**Fig. 9** FPZ width at various load points for W/C = 0.45

Fig. 10 Variation of FPZ length and width at various load points for W/C = 0.45
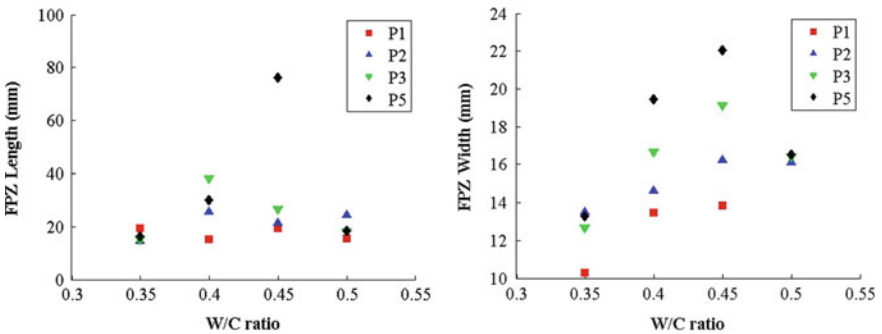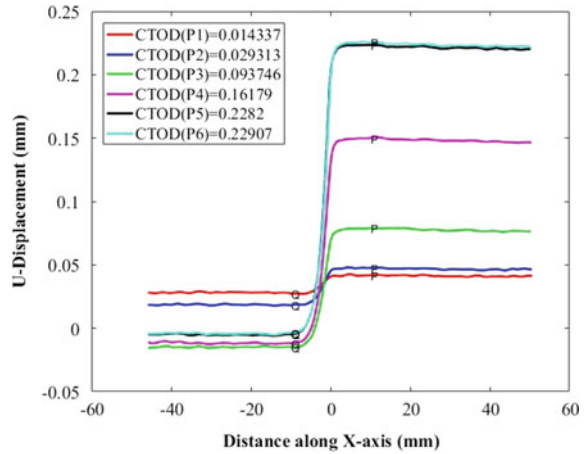

Fig. 11 Variation of FPZ length and width with water to cement ratio at different load points

Fig. 12 Crack tip opening displacements for W/ C = 0.45

3.5 Crack Tip Opening Displacement

The displacement values at the points in the area of interest along the length perpendicular to the crack

(Y) have been obtained by a correlation software 'VIC-3D'. X-direction displacements (u) at the points on the line perpendicular to the notch at the notch tip is calculated using the 'VIC-3D'. Variations of displacements as a function of distance along the X-axis at various load points for W/C = 0.45 are shown in Fig. 12. In the initial stage of loading, displacement is almost nearly horizontal. As the test progresses, the points on both the sides of the notch move in opposite directions. The crack tip opening displacement is calculated by measuring the displacement jump from Fig. 12.

4 Conclusions

Fracture energy is observed to be reduced with the increase in w/c ratio from 0.35 to 0.45. This could be attributed to the modified pore structure in the ITZ with the increase in w/c ratio. However, when the w/c ratio is increased to 0.5, an increase in the fracture energy is observed. The characteristic length is found to be more in the mix with w/c equal to 0.5. This increase in fracture energy and characteristic length with increased water to cement ratio is found to be peculiar and needs further investigations for finding the reasons for the behaviour. In case of concrete with water to cement ratios equal to 0.35 and 0.5, FPZ characteristics, i.e. its length and the width almost remained constant for the post-peak softening of the concrete whereas they increase for the water to cement ratios equal to 0.4 and 0.45. Influence of FPZ width on fracture energy can be observed from Figs. 5 and 11.

It is seen that a decrease in fracture energy for concretes with a water–cement ratio varying from 0.35 to 0.45 corresponds to increase in FPZ widths. Also, fracture energy for concrete with w/c ratio equal to 0.5 increased when compared to concrete with w/c equal to 0.45 which corresponded to a decrease in FPZ widths. Although the results about FPZ length and widths for w/c equal to 0.5 needs further investigation, the above result is indicative of correlation between fracture energy on the FPZ width.

References

1. Z. Wu, H. Rong, J. Zheng, F. Xu, W. Dong, An experimental investigation on the FPZ properties in concrete using digital image correlation technique. Eng. Fract. Mech. 2978–2990 (2011)
2. L. Skarżyński, J. Tejchman, Experimental investigations of fracture process using DIC in plain and reinforced concrete beams under bending. Strain 521–543 (2013)
3. S.Y. Alam, J. Saliba, A. Loukili, Fracture examination in concrete through combined digital image correlation and acoustic emission techniques. Constr. Build. Mater. 232–242 (2014)
4. N. Trivedi, R.K. Singh, J. Chattopadhyay, Investigation on fracture parameters of concrete through optical crack profile and size effect studies. Eng. Fract. Mech. 119–139 (2015)
5. S. Shah, J.M. Chandra Kishen, Fracture properties of concrete–concrete interfaces using digital image correlation. Exp. Mech. 303–313 (2011)
6. S.Y. Alam, A. Loukili, F. Grondin, Monitoring size effect on crack opening in concrete by digital image correlation. Eur. J. Environ. Civ. Eng. 818–836 (2012)
7. S. Bhavikatti, M. Bhat, C. Murthy, Fatigue crack growth monitoring in Ti-6Al-4 V alloy using acoustic emission technique and digital image correlation. J. Non-Destr. Eval. (2011)
8. K. Duan, X. Hu, F.H. Wittmann, Boundary effect on concrete fracture and non-constant fracture energy distribution. Eng. Fract. Mech. 2257–2268 (2003)

Mechanical and Dynamic Properties of Polypropylene Fiber Reinforced Concrete

Radhika Sridhar and Ravi Prasad

Abstract In this present study, static and dynamic properties of polypropylene fiber reinforced concrete (PPFRC) have been experimentally studied. The mechanical properties have been carried out by conducting compression, splitting tensile and flexural strength of PPFRCs. In addition to this, dynamic properties such as damping ratio and fundamental frequency of PPFRC beams in free–free conditions were also determined experimentally. In this paper, the influence of 0.1, 0.2, 0.3, and 0.4% variation of fiber contents by total fiber volume fraction of concrete was investigated. In order to determine the effect of polypropylene fibers in concrete and to compare, the properties of plain concrete have also been studied. The results emphasize that the addition of fibers reduces the fundamental frequency and increase the damping ratio of concrete. In the present study, damage assessment of PPFRC has also been experimentally studied. The test results emphasize that the addition of fibers reduces the fundamental frequency and increase the damping ratio of concrete. Damping of PPFRC beams increases with the increase of damage whilst the fundamental natural frequency decreases with an increase of damage. The changes of fundamental natural frequency and damping values have been correlated to the damage degree of the prismatic beam experimentally. The dynamic modulus of elasticity of PPFRC was lower than that of normal concrete. It has been found that polypropylene fiber reinforced concrete with a fiber content of 0.4% has the best properties.

Keywords Polypropylene · Damping · Frequency · Damage · Flexure

R. Sridhar (✉) · R. Prasad
Department of Civil Engineering, NIT-Warangal, Warangal, India
e-mail: radhika.sridhar2210@gmail.com

1 Introduction

Historically, concrete is the most commonly used construction material because of its versatility and availability all over the world [1–3]. Due to the environmental service conditions and complexity of structures such as high-rise buildings, dams, bridges, hydraulic structures, and offshore structures, any normal grade or ordinary concrete could no longer meet the requirements in generality. It is well known, nevertheless, the ratio between compressive strength and flexural strength or split tensile strength of ordinary concrete or high-strength concrete will be inevitably brittle in nature [4]. In order to overcome this drawback, researches have been focused on various necessary treatments such as adding fibers to concrete, use of supplementary mineral admixtures and externally strengthening the members with fiber reinforced polymers [5]. Amongst these, addition of fibers like steel, polypropylene, polyvinyl alcohol, natural, and synthetic fibers into concrete has been accepted widely because of its improved mechanical properties such as compressive strength, split tensile strength, flexural strength, and flexural toughness [6]. In recent years, mainly steel fibers have been used by numerous researchers especially in concrete industry. By adding steel fibers to concrete significantly increases the flexural strength, toughness, and its post–cracking behavior [7, 8]. Most of the synthetic fibers have a low modulus of elasticity such as polypropylene, polyethylene, polyester, and nylon. The main advantages of using synthetic fibers are its alkaline resistance, high melting point, and low cost of raw materials [9]. While steel fibers improve the hardened concrete properties whereas the synthetic fibers provide benefits even when the concrete is in plastic state. Besides, in the recent few decades, inclusion of nonmetallic polypropylene fiber has also become one of the most extensively used fibers in concrete which in turn enhances the dynamic as well as durability properties of the composite matrix [10]. Generally, the concrete structures will always be subjected to vibration forces such as impact loading on dynamic shock of moving vehicles. Depending on the type of structure and impact or dynamic load, harmonic excitation exists through the external force of a certain frequency applied to a system for given amplitude. Resonance can also occur when the external excitation has the same frequency as the natural frequency of the system. In this regard, it is necessary to study the dynamic property of any structure at typical modes which will be helpful in reducing resonance and attenuating vibration [11, 12]. The essential concept concealed with vibration monitoring technique for any concrete structure damage analysis would be based on dynamic characteristics and does not rely on the geometry of the structure; as a result, changes will occur in the dynamic response behavior [13]. The dynamic behavior of concrete is one of the important parameter which can be determined by its dynamic properties such as, dynamic modulus of rigidity, dynamic modulus of elasticity and dynamic Poisson's ratio which present different values compared to their static or mechanical properties [14]. Some of the aforementioned research work has been studied about the static properties of different composite matrix and there is a dearth of knowledge available on the study of dynamic properties of

fibrous concrete. Therefore, the main aim of the present experimental work is to study the effect of polypropylene fiber on mechanical and dynamic properties and also the effect under damaged and undamaged condition of polypropylene fiber reinforced concrete (PPFRCs).

2 Experimental Program

In the present experimental work, fiber dosages of 0.1, 0.2, 0.3, and 0.4% by volume fraction were considered to investigate the static properties including compressive, splitting tensile and flexural strength and dynamic properties of polypropylene fiber reinforced concrete.

2.1 Materials

Ordinary Portland cement with specific gravity of 3.15 was used in this present study. Good quality river sand was used as fine aggregate. The coarse aggregate which is used in this experimental work was of 20 mm size crushed angular shape. The sieve analysis of coarse and fine aggregates has been carried out as per Indian standards. The aggregates are free from dust before used in concrete. The differences and usage of fiber depend on the requirement of behavior and property for a concrete, allowing the increase in explicit effects and mechanical properties. The fibrillated polypropylene fiber which was used in this study is shown in Fig. 1 and its physical and mechanical properties are illustrated in Table 1.

Fig. 1 Typical view of polypropylene fiber

Table 1 Physical and material properties of Polypropylene fibers

Fiber type	Shape of fibers	Length (mm)	Diameter (mm)	Aspect ratio	Tensile strength (MPa)	Modulus of elasticity (GPa)	Density (kg/m^3)
PP	Straight	12	0.038	315	420	5	990

2.2 Mix Design

The determination of mix design for this research to obtain the desired strength of M25 grade of concrete was performed based on IS 10262:2009. Five mixtures of PPFRC were included in this experimental work in order to determine the mechanical, dynamic properties and damage assessment of PPFRCs. Control concrete specimens without fibers have also been cast to ascertain the effect of the polypropylene fiber reinforced concrete. Mix proportion of M25 grade concrete is shown in Table 2.

2.3 Casting Procedure

In this experimental work, a portable mixer has been used throughout the study. The following mix procedure was adopted, firstly the fine aggregates and coarse aggregates were added into the mixture machine and allowed to mix for 55 s to 1 min and the required amount of cement was added into it. Then the water was added gradually to the mixture and it has been continued in order to get the proper workability. Then the fibers were added gradually and it was mixed for another 2 min to get better performance in mechanical properties. In order to determine the mechanical and dynamic properties of PPFRC, three specimens of standard cubes (150 mm × 150 mm × 150 mm), cylinders (150 mm diameter and 300 mm height) and prisms (cross-section 100 mm × 100 mm and 500 mm length) were cast for each percentage variation of PP fibers as well as plain concrete (Reference

Table 2 Mix proportions of plain and polypropylene fiber reinforced concrete

Mix no	Designation	Fiber V_f (%)	Cement (kg/m^3)	Sand (kg/m^3)	Coarse aggregate (kg/m^3)	Water (kg/m^3)
1	M1	0	1	1.89	2.89	0.42
2	M2	0.1	1	1.89	2.89	0.42
3	M3	0.2	1	1.89	2.89	0.42
4	M4	0.3	1	1.89	2.89	0.42
5	M5	0.4	1	1.89	2.89	0.42

concrete) for comparison. A total of 15 cylinders, 15 prisms, and 15 cubes were cast and tested only for mechanical properties study.

2.4 Mechanical and Dynamic Properties Testing Procedure

All cubes and cylinders have been and tested in a compression testing machine of 2000 kN capacity to evaluate the compressive strength and splitting tensile strength as shown in Figs. 2 and 3 respectively. All the beams were tested in a dynamic universal testing machine of 1000 kN capacity under four-point loading condition to acquire modulus of rupture which is shown in Fig. 4. Cracking load is the load which would be taken by fibers and the part of concrete after the first visible crack is produced. The prismatic specimens of size (500 mm × 100 mm × 100mm) were cast for each percentage variation of PPFRC to examine their fundamental transverse frequency in free–free condition (According to ASTM C-215) [15]. A total of 15 prisms were cast and tested in order to evaluate the dynamic properties and vibration-based damage assessment of PPFRCs. All specimens were tested using dynamic analyzer and impact hammer technique which consists of the forced transducer which is used for excitation, accelerometer to collect the response from the analyzer which is used to carry out the frequency response function.. Fundamental resonant frequency between 1 and 4000 Hz has been considered in this present study. Schematic view of dynamic testing experimental set up is shown in Fig. 5.

Fig. 2 Typical view of compression test

Fig. 3 Typical view of splitting test

Fig. 4 Typical view of flexure test

2.5 Test Procedure for Damage Evaluation

Prismatic beams of aforementioned size were cast and tested at the age of 28 days for all mixtures to evaluate the damage characteristics of PPFRCs in free–free condition and its typical view is shown in Fig. 6. At the mid-span of the specimen, a small damage has been induced with the help of concrete cutter machine. Before
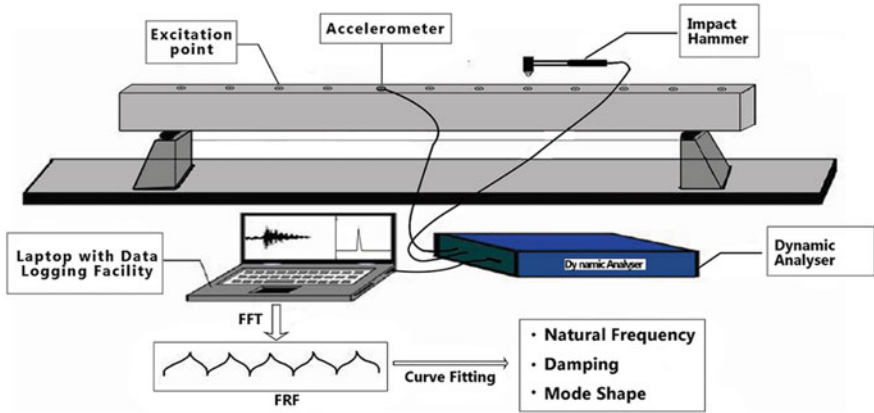
Fig. 5 Typical view of dynamic testing experimental set up

Fig. 6 Typical view of beam in free–free condition

inducing damage to the prismatic beams, all specimens were tested for its undamaged condition (free–free supports) in order to compare and assess the damage in concretes with polypropylene fibers inclusion. Figure 7 displays the specimen at first damage level. Totally four damage stages were considered in this present study,

(1) Undamaged beam (D_0)
(2) Damage-induced at the mid-span of width 10 mm and depth 10 mm (D_1)
(3) Damage-induced at the mid-span of width 10 mm and depth 20 mm (D_2)
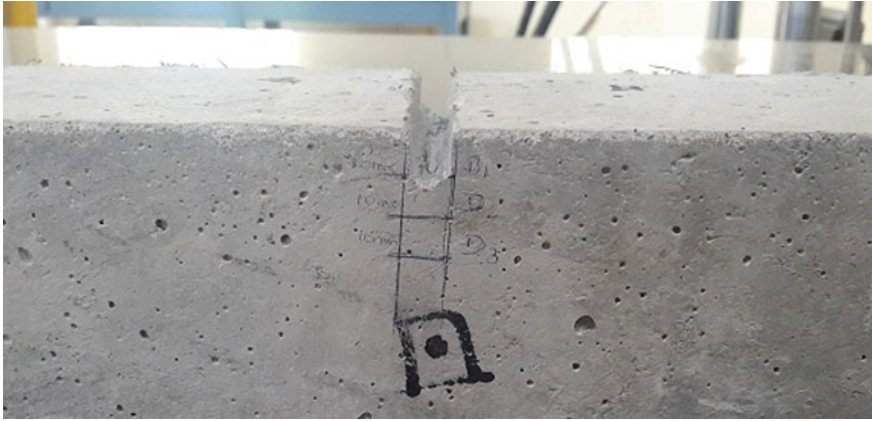(4) Damage-induced at the mid-span of width 10 mm and depth 30 mm (D_3)

Fig. 7 View of specimen at first damage level

3   Results and Discussion

The results acquired through experimental tests are discussed in this chapter. Static result shows the behavior of plain and fibrous concrete composites and the dynamic result shows the dynamic response behavior of the beams in both damaged and undamaged states under free–free constraints.

3.1   Mechanical Property Tests

The mechanical property tests have been carried out at the age of 28 days and the acquired results are shown in Table 3. The compressive strength of concrete is the most important strength parameter and it is a qualitative measure for other properties of hardened concrete. When the concrete fails under compressive load, it is a mixture of crushing and shear failure. Compressive strength results emphasize that the increase in percentage volume fraction of PP fibers led to 3.5% to 8% increases in compressive strength for M2 and M4 specimens, respectively when compared with plain concrete. The splitting tensile strength was carried out on a concrete cylinder specimens were cast for four sets of PP fibers and one set of plain concrete at the age of 28-days. From the results, the maximum load which was taken by the cylinder were considered for splitting tensile strength evaluation and the specimens were broken into two halves at the same load for plain concrete whereas for PPFRC, cylindrical specimens were held together after cracks and even when the test was continued up to more than the maximum load. Percentage increase of compressive strength, splitting tensile strength, and flexural strength with the comparison of plain concrete is shown in Fig. 8.

Table 3 Mechanical and dynamic properties of plain and PPFRC

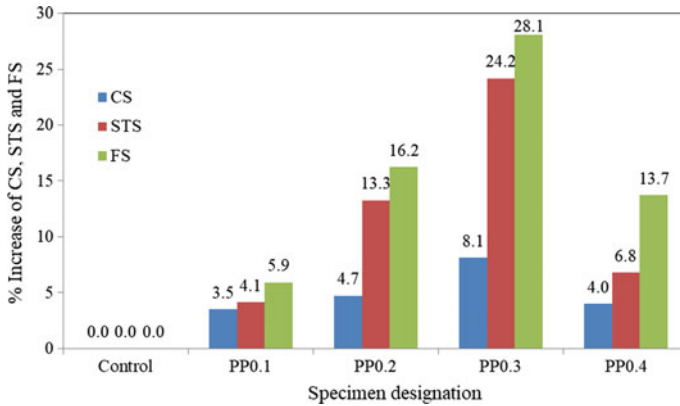| Mixes	Compressive strength (MPa)	Split tensile strength (MPa)	Flexural strength (MPa)	Transverse frequency (Hz)	Longitudinal frequency (Hz)	Torsional frequency (Hz)	Dynamic elastic modulus (GPa)
M1	34.87	3.39	4.74	1446	3446	2394	38.37
M2	36.09	3.53	5.02	1432	3432	2381	38.26
M3	36.52	3.84	5.51	1429	3426	2370	37.87
M4	37.70	4.21	6.07	1421	3411	2361	37.62
M5	36.26	3.62	5.39	1409	3398	2344	37.45

Fig. 8 Comparison of compressive, split tensile, and flexural strength of PPFRCs

3.2 Dynamic Property Tests

Table 3 shows the dynamic property values obtained for PPFRCs. Damping ratio of PPFRC prismatic beams increases with the addition of fiber content. Fundamental longitudinal, transverse, and torsional frequencies have been tested for all mixtures in three different directions according to ASTM C215 [15]. The test results emphasize that the highest fundamental natural frequency attained for nonfibrous concrete in all the three vibration modes when compared with PPFRCs.

The resonant transverse frequencies decrease with an increase in fiber content. It was observed that the fundamental transverse frequency decreased was about 1.7% for M4 mixture when compared to that the frequency of plain concrete. From the table, it can be clearly observed that the dynamic modulus of elasticity of PPFRCs have been decreased with the addition polypropylene fiber content. The value of dynamic modulus has been calculated from the fundamental transverse frequency according to the standards of ASTM.

$$\text{Dynamic modulus of elasticity, } E_{\text{dynamic}} = CMn^2 \qquad (1)$$

where,

M   = Mass of the specimen
n   = Transverse frequency
C   = $0.9464(L^3T)/bt^3$
L, b, t = Length, width and depth of the specimen
T   = Correction factor

3.3 Damping Ratio and Fundamental Frequency of PPFRC After Damage

Fundamental transverse frequency and damping ratio values obtained for undamaged and three different damage levels of PPFRCs are illustrated in Tables 4 and 5, respectively in free–free condition. The values of damping ratio have been decreased gradually for second mode when compared with first mode because of the increment in fundamental transverse frequency. PPFRC beam with 0.4% fiber content has the damping ratio for both first as well as second mode of vibration. From the table, it can be observed that the fundamental frequency decreases with increase in fiber content as well as structural damage, whereas damping increases with increasing in fiber content and damage when compared to the properties of undamaged stage. Percentage decrease of fundamental transverse frequency and damping ratio for three damage levels are shown in Figs. 9 and 10 of PPFRCs with the comparison of undamaged specimens for first and second mode, respectively. From these figures, it can be observed that the percentage decrease of transverse frequency in first mode is lower than that of the percentage decrease of frequency in second mode. The damping ratio value of first mode for all the mixtures was higher than that of the damping ratios in second mode because the fundamental frequency of second mode is always higher than first mode.

Table 4 Transverse frequency and damping ratio of plain and PPFRCs in undamaged condition

Designation of the mixture	Transverse frequency-1st mode (Hz)	Damping ratio-1st mode	Transverse frequency-2nd mode (Hz)	Damping ratio-2nd mode
M1	1446	0.48	3493	0.34
M2	1432	0.51	3486	0.38
M3	1429	0.54	3474	0.41
M4	1421	0.56	3462	0.43
M5	1409	0.59	3457	0.45

Table 5 Transverse frequency and damping ratio of plain and PPFRCs in damaged condition

Specimen designation	Damage 1					Damage 2					Damage 3				
	f-1st mode (Hz)	ζ-1st mode	f-2nd mode (Hz)	ζ-2nd mode		f-1st mode (Hz)	ζ-1st mode	f-2nd mode (Hz)	ζ-2nd mode		f-1st mode (Hz)	ζ-1st mode	f-2nd mode (Hz)	ζ-2nd mode	
M1	1431	0.51	3474	0.38		1410	0.54	3457	0.41		1396	0.56	3435	0.44	
M2	1422	0.54	3463	0.41		1403	0.56	3438	0.43		1384	0.59	3416	0.46	
M3	1408	0.56	3448	0.44		1394	0.59	3415	0.46		1376	0.61	3392	0.49	
M4	1401	0.59	3427	0.46		1383	0.61	3394	0.49		1362	0.62	3373	0.51	
M5	1384	0.62	3413	0.49		1365	0.64	3384	0.51		1348	0.65	3365	0.54	

Fig. 9 Percentage decrease of frequency-1st mode
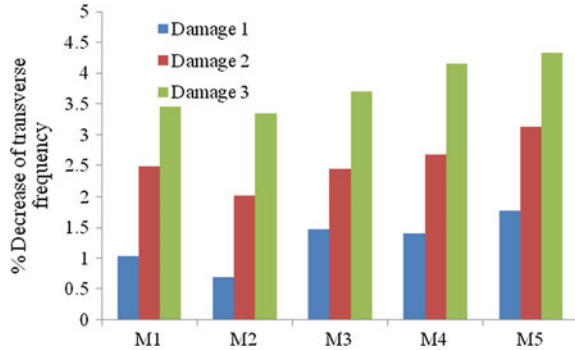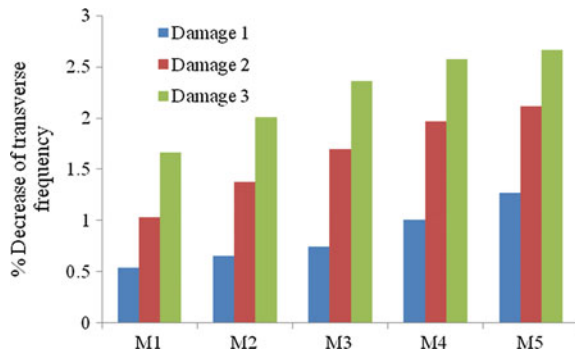

Fig. 10 Percentage decrease of frequency-2nd mode

4 Conclusions

Following conclusions are drawn from the present investigation:

1. The workability of concrete was largely affected by the inclusion of PP fibers for 0.3% fiber volume fraction and more.
2. The testing confirmed that PP fibers in concrete can improve its flexural strength considerably when compared with compression and splitting tensile strength.
3. The addition of PP fibers can significantly increase the compressive strength, splitting tensile strength and flexural strength of PPFRC. The result showed that 3.5–8% increase of compressive strength, 4–24% increase of splitting tensile strength and 6–28% increase of flexural strength for M2 and M4 mixtures, than that of plain concrete.
4. The fundamental transverse frequency of concrete specimens tends to slightly change with environmental effect such as (wind, humidity, temperature etc.).
5. From the result, it has been observed that the damping ratio increased with the addition of fibers.

6. The damping ratio increased with the addition of PP fiber content. Also, the damping ratio of PPFRC specimens increased with an increase in structural damage.
7. The fundamental resonant frequency of control concrete decreased when the damage increases and also decreased with the increase of PP fiber content.
8. Dynamic modulus of elasticity decreased with an increase in the fiber content as well as total volume fraction of fibers.

References

1. A. Sivakumar, N. Santhanam, A qualitative study on plastic shrinkage cracking in high strength hybrid fiber reinforced concrete. Cem. Concr. Compos. 575 (2007)
2. A. Senthil Kumar, S. Natesan, Effect of polypropylene addition on restrained shrinkage cracking of cement composites, J. Inst. Eng. Div. 100 (2004)
3. H. Tanyildizi, Statistical analysis for mechanical properties of polypropylene fiber reinforced light weight concrete containing silica fume exposed to high temperature. J. Mater. Des. 3252 (2009)
4. A. Bard, A.F. Ashour, A.K. Platten, Statistical variations in impact resistance of polypropylene fiber reinforced concrete. Int. J. Impact Eng. 1907 (2006)
5. M. Nili, V. Afroughsabet, The effects of silica fume and polypropylene fibers on the impact resistance and mechanical properties of concrete. Int. J. Impact Eng. 927 (2010)
6. Y. Mohammed, R. Azad, S. Singh, S. Kaushik, Impact resistance of steel fibrous concrete containing fibers of mixed aspect ratio. Constr. Build. Mater. 183 (2009)
7. M. Hsie, C. Tu, P.S. Song, Mechanical properties of polypropylene fiber reinforced concrete. Constr. Build. Mater. 153 (2008)
8. T. Gupta, R. Sharma, S. Chaudar, Impact resistance of concrete containing waste rubber and silica fume. Int. J. Impact Eng. 76 (2015)
9. P.S. Song, H. Hwang, B.C. Sheu, Strength properties of nylon and polypropylene fiber reinforced concrete. Cem. Concr. Compos. 1546 (2005)
10. O. Karahan, C. D. Atis, Durability properties of polypropylene fiber reinforced fly ash concrete. Mater. Des. 1044 (2011)
11. H. Mohammadhosseini, A.S.M.A. Awal, Influence of palm oil fuel ash on fresh and mechanical properties of self compacting concrete. Sadhana 1 (2015)
12. S. Orak, Investigation of vibration damping on polymer concrete with polyester resin. Cem. Concr. Res. 171 (2000)
13. L. Zheng, X.S. Huo, Y. Yuan, Experimental investigation on dynamic properties of rubberized concrete. Constr. Build. Mater. 939 (2008)
14. V.T. Giner, S. Ivorra, F.J. Baeza, E. Zornoza, B. Ferrer, Silica fume admixture effect on the dynamic properties of concrete. Constr. Build. Mater. 3272–3277 (2011)
15. ASTM C 215, Standard test method for fundamental transverse, longitudinal and torsional resonant frequencies of concrete specimens, Am. Soc. Test. Mater. (2008)

Part VII
Creep and Creep-Fatigue Interaction

Influence of Creep on Isothermal and Thermomechanical Low Cycle Fatigue of Type 316 LN SS Weld Joint

T. Suresh Kumar, A. Nagesha and R. Sandhya

Abstract Thermomechanical fatigue (TMF) behaviour of a type 316LN austenitic stainless steel weld joint under in-phase (IP) and out-of-phase (OP) temperature—mechanical strain combinations were investigated. IP TMF was generally found to be more detrimental compared to OP cycling. The interaction of creep deformation with TMF was studied by incorporating dwell periods of 1 min and 5 min at peak tensile strain under IP TMF. Isothermal low cycle fatigue (IF) and tensile hold creep-IF interaction tests were concurrently conducted at the maximum temperature (T_{max}) of TMF cycles. Results obtained were compared with the behaviour exhibited by the base metal. The cyclic stress response (CSR) of the base metal and weld joint under creep—TMF and creep—IF was found to depend on the hold period. The microstructural transformation in the weld metal played a significant role in the observed difference in CSR between the base metal and the weld joint. Creep-TMF resulted in a higher stress relaxation and consequently led to lower lives compared to creep-IF cycling. The crack initiation and propagation modes were characterized through detailed optical and scanning electron microscopy whereby, the dependence of fracture morphology on the testing conditions under continuous cycling and hold time conditions were established. The extent of intergranular damage was seen to increase with an increase in the hold period. A combined influence of creep and metallurgical transformations in the weld metal contributed to significant reduction in creep-TMF life with hold period.

Keywords Thermomechanical fatigue · Isothermal low cycle fatigue · Creep—TMF interaction · 316 LN SS weld joint

T. Suresh Kumar
Homi Bhabha National Institute, Kalpakkam, India

A. Nagesha (✉) · R. Sandhya
Materials Development and Technology Division, Indira Gandhi Centre for Atomic Research, Kalpakkam 603102, Tamil Nadu, India
e-mail: nagesh@igcar.gov.in

1 Introduction

Type 316LNaustenitic stainless steel (SS) is widely used for structural components designed to operate at elevated temperatures (673–923 K) in sodium-cooled fast reactors (SFRs) due to its excellent high temperature mechanical and chemical properties. Weld joints in such components pose a major challenge as they contain both metallurgical and mechanical heterogeneities that render them vulnerable to localized damage. Upon exposure to elevated temperatures, the δ-ferrite that is introduced in the weld deposit to mitigate the hot cracking and microfissuring gets transformed into various types of deleterious phases with attendant degradation in mechanical properties. It is well established that the performance of weld joint is significantly influenced by the transformation of δ-ferrite [1, 2]. In cases where creep and fatigue operate in tandem, the structural integrity of the weld joint is of major concern. Literature pertaining to elevated temperature cyclic deformation behavior of austenitic stainless steel weld joint (WJ) is largely restricted to isothermal low cycle fatigue (IF) [1–5]. However, thermomechanical fatigue (TMF) testing is a better representation of the actual service conditions (reactor start-up/shut-downs and operational transients) compared to IF tests conducted even at the maximum temperature (T_{max}) of the expected thermal cycle [6–8]. In addition, on-load periods at elevated temperatures introduce time-dependent creep effects and the resultant creep–fatigue damage is potentially more deleterious resulting in early failure compared to either of the mechanisms acting independently. Despite wide usage of austenitic SS and its welds, there are no reported studies on the TMF behaviour of 316 LN SS weld joint particularly at temperatures at which creep effects play a definitive role in the overall damage development in the material. Incorporation of creep damage into TMF cycles will provide a better insight into the deformation behaviour and damage evolution of the weld joint in actual service, thereby leading to a more reliable life estimation compared to conventional isothermal cycling. Considerable work has been performed to understand the creep–fatigue interaction behaviour under isothermal conditions for different grades of austenitic SS base metal [9–13] and welds [5, 14]. Introduction of hold at the peak tensile strain is generally reported to be more deleterious compared to the hold in the compressive part or both in the tensile and compressive parts of the cycle [9, 13, 14]. However, no literature exists on the creep–fatigue interaction behaviour of austenitic SS weld joints under thermal cycling conditions. The principal objective of the present study is to elucidate the influence of dwell times on the deformation behaviour, damage mechanisms, and lifetime variation of the 316 LN SS weld joint under IF and TMF cycling and to compare the results with data obtained under IF cycling at the T_{max}.

2   Experimental

The chemical compositions of the 316 LN SS base metal (BM) and the filler metal used for welding are presented in Table 1. The geometry of the weld joint and the welding procedure are explained elsewhere [1]. The in-phase (IP) and out-of-phase (OP) TMF experiments were conducted on tubular specimens with a gauge length of 25 mm and wall thickness of 1.5 mm using a ±100 kN servohydraulic fatigue testing machine, equipped with an induction heating facility, capable of imposing independently programmable temperature, and mechanical strain onto the specimen. The tests were carried out under strain control mode with a constant mechanical strain amplitude ($\Delta\varepsilon_{mech}/2$) of ±0.4%, using a temperature interval of 623–873 K under IP and OP temperature–mechanical strain combinations. A symmetrical triangular waveform with a constant mechanical strain rate ($\dot{\varepsilon}_{mech}$) of 6.4×10^{-5} s^{-1} was used for all the tests. The interaction of creep with TMF was studied by incorporating dwell periods of 1 min and 5 min at peak tensile strain under IP TMF. IF and tensile hold creep—IF interaction (conventional creep–fatigue interaction) tests were concurrently conducted at the T_{max} of TMF. A few TMF and creep–TMF tests were also performed on the base metal at a fixed temperature interval of 623–873 K. The number of cycles corresponding to a 20% drop in the saturation stress amplitude was used as a criterion to determine the number of cycles to failure, N_f. Crack initiation and propagation modes were studied using optical microscopy while the fracture surfaces were examined using scanning electron microscopy.

3   Results and Discussion

3.1   Cyclic Stress Response

The BM showed an initial pronounced cyclic hardening, followed by a stable cyclic stress response (CSR) as shown in Fig. 1a. Such a behaviour is typical of the alloy and has been adequately addressed and explained in the literature [9]. The WJ in contrast, displayed an extended softening stage following an initial hardening regime, Fig. 1a. However, the CSR shown by the WJ was higher compared to the BM owing to the presence of a relatively harder weld metal and a microstructurally altered heat affected zone (HAZ). With progressive cycling though, the stress

Table 1 Chemical composition of the E316-15 (modified) electrode and 316L (N) base metal in wt%

Material	C	Mn	Ni	Cr	Mo	N	S	P	Fe
Base metal	0.03	1.7	12.2	17.5	2.5	0.07	0.0055	0.013	Bal
Filler metal	0.05	1.4	11.1	18.9	2.3	0.12	0.009	0.02	Bal

response of the WJ shifts downward compared to that of the BM as shown in Fig. 1a. A significant reduction in the dislocation density as a result of their annihilation in the weld region has been established as the mechanism responsible for the observed cyclic softening in the weld joint [1–3, 14]. OP TMF cycling displayed a higher stress response and longer life in comparison with IP TMF as shown in Fig. 1a.

The extent of initial hardening was seen to be lower in the BM with hold time condition, compared to continuous cycling (Fig. 1a). Also, the peak tensile stress amplitude decreased with introduction of the hold period, as shown in Fig. 1a. Moreover, the period of stress saturation was seen to decrease with introduction of hold. It was also observed that with increasing hold period (i.e., 10 min), the saturation regime gets replaced by a gradual softening that culminates in a rapid stress drop due to macro-crack propagation. Decrease in CSR with introduction of hold time compared to continuous cycling in type 316 LN SS base metal has been attributed to enhanced substructural recovery and increase in the grain boundary damage accumulation during the stress relaxation period [9]. The CSR displayed by the WJ under hold condition was marked by an initial hardening to a maximum stress followed by a near-saturation regime and a rapid stress drop towards the end of the test. An interesting observation is that the CSR is higher under hold conditions compared to continuous cycling for the WJ as shown in Fig. 1a. This is in contrast to the behaviour exhibited by the BM, which showed a lower CSR under hold conditions as stated above. Another important finding related to the CSR of WJ is that the presence of a near-saturation regime under hold condition. This is in contrast with the continuous softening observed under continuous cycling condition and suggests a balance between the strengthening effect due to cyclic hardening and a softening effect due to a decrease in the dislocation density and the substructural recovery during hold period at the T_{max}. Detailed metallographic investigations are underway to ascertain the operative mechanism responsible for the observed CSR in hold time tests. A clear difference was observed in the CSR of the WJ under TMF
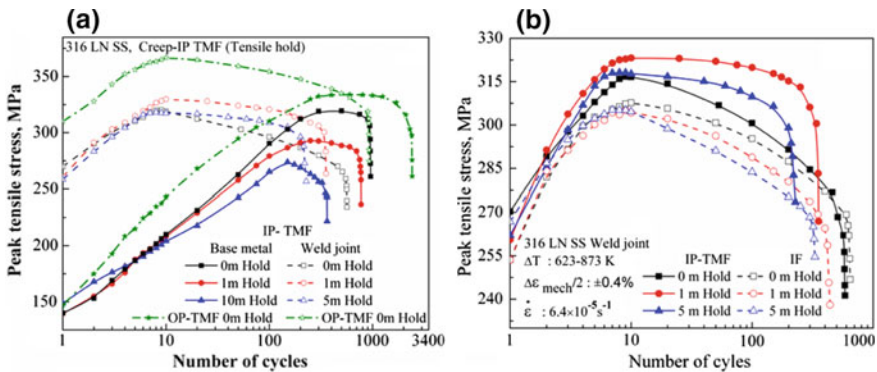

Fig. 1 **a**: Comparative CSR of the base metal and weld joint under TMF and creep—TMF, **b**: Comparative CSR of the weld joint under TMF and IF (623–873 K, $\Delta\varepsilon_{mech}/2 = \pm 0.4\%$)

and IF conditions with and without hold time, as shown in Fig. 1b. TMF cycling led to a consistently higher stress response under continuous cycling and hold time conditions in comparison with IF cycling at the same strain amplitude. Under TMF, additional factors such as cold work effects and recovery play significant roles at the lower and higher ends of the thermal cycles respectively. Due to the constant temperature throughout the IF cycle, the flow behaviour is identical throughout the cycle. The WJ displayed a lower CSR under isothermal conditions with hold period compared to continuous cycling, as shown in Fig. 1b. This is similar to the behaviour exhibited by the BM under hold conditions as shown in Fig. 1a.

3.2 Stress Relaxation

The stress relaxation as a function of time elapsed in hold time tests is a measure of the creep damage developed during constant strain hold tests. The amount of stress relaxation during the hold period was calculated by taking the difference between the stress values at the start and end of the hold period. The magnitude of relaxed stress is plotted against the hold time for BM and WJ under TMF cycling, as shown in Fig. 2a. The figure also shows the variation of relaxed stress with hold time under IF cycling of the WJ. An increase in the magnitude of the relaxed stress was noted with increasing duration of the hold, Fig. 2a. Incorporation of hold also led to build-up of additional plastic strain as reflected from Fig. 2a. An interesting observation is the higher amount of stress relaxation under creep—IP TMF compared to creep—IF cycling as shown in Fig. 2b, which clearly shows the difference in the damage evolution in the two cases. The strain rate associated with the stress relaxation is an important factor to be considered, as it demarcates the contribution of creep deformation from that of cyclic deformation. The inelastic relaxation strain rate ($\dot{\varepsilon}$) for the half-life cycle is calculated using the following relationship:
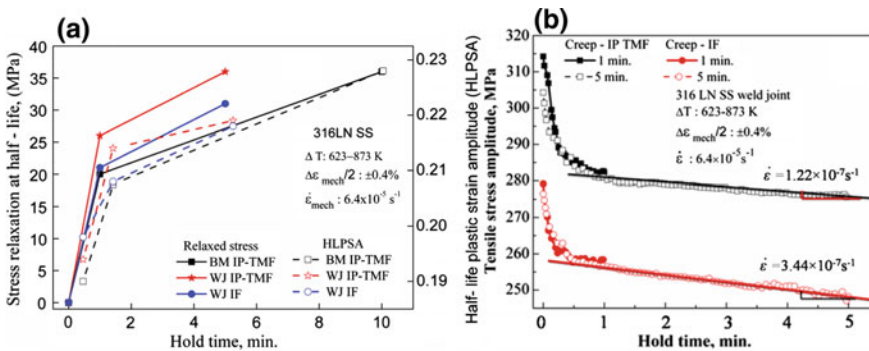

Fig. 2 a: Variation of half-life relaxed stress and plastic strain with hold time for BM and WJ under IF and TMF cycling. b: Tensile stress relaxation of the WJ during the hold as a function of time for 1-min and 5-min hold periods

$$\dot{\varepsilon} = \frac{d\sigma}{dt} \cdot \frac{1}{E}$$

where E is Young's modulus (which was calculated from the 1st cycle hysteresis loop of the IF cycle at 873 K and found to be 150 GPa), σ is the stress and t represents time. The minimum inelastic strain rates during stress relaxation were found to be 1.2×10^{-6} s^{-1} and 1.6×10^{-6} s^{-1} for 1 min hold test under creep—IP TMF and creep—IF cycling respectively. The corresponding strain rates with the hold time of 5 min were found to be 1.22×10^{-7} s^{-1} and 3.44×10^{-7} s^{-1} in the above (creep-TMF and creep-IF) testing conditions which clearly indicates an increase in the creep damage when thermal cycling occurs on either side of the strain hold.

3.3 Transformation of δ-Ferrite

The weld metal contained a duplex microstructure with vermicular δ-ferrite in the range 6.5–7 FN distributed uniformly within the austenite matrix. It is well established that the δ-ferrite in the weld metal acts as the nucleation site for all the transformations taking place during thermal exposure with [1, 2, 14–17] or without stress [18]. As seen from Fig. 3a, the percentage of δ-ferrite transformed increased with increasing hold period. As seen, IF resulted in a higher amount of δ-ferrite transformation than IP TMF under continuous cycling. Presence of stress is known to have a significant bearing on both the type and the amount of precipitate formation in 316 SS weld metal [15–17]. Moreover, the extent of δ-ferrite transformation at a given temperature is a strong function of the applied stress level, and
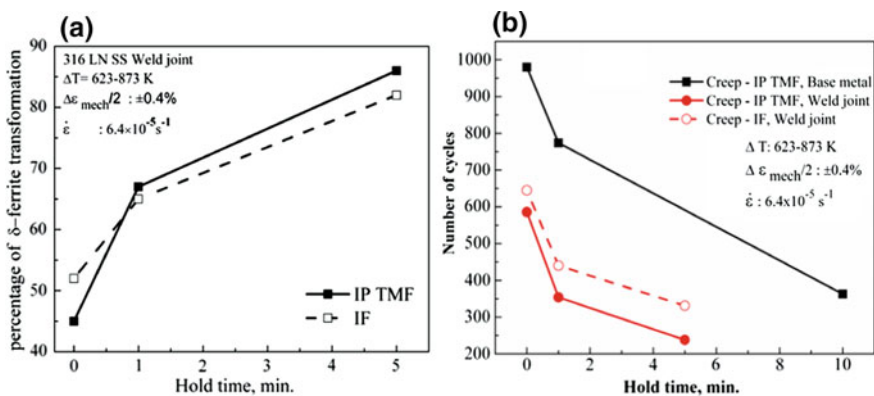

Fig. 3 a: The percentage of δ-ferrite transformation at different hold time, **b**: Variation in fatigue lives of the base metal and weld joint as a function of tensile hold period, under TMF and IF cycling

associated differences in the dislocation substructures [15]. Significant differences in the substructural evolution between TMF and IF cycling and the influence on the precipitation behaviours thereof, have been established from earlier studies on 316 LN SS base metal [19]. In the present study, the extent of δ-ferrite transformation was found to have a correlation with the test duration under continuous cycling. On the other hand, under hold time conditions, creep—TMF led to a higher amount of transformation of the δ-ferrite in comparison with creep—IF even though the test duration was shorter in the former case.

3.4 Fatigue Life and Fracture Behaviour

An important finding from the viewpoint of structural integrity was that the IP TMF cycling was more detrimental compared to the IF cycling at the T_{max} under both continuous cycling and hold time conditions, as can be seen from Fig. 1b. Figure 3b presents the variation in cyclic life of the BM and WJ with hold period. Reduction in cyclic life of the WJ in comparison with the BM is clearly seen, which may be attributed to the former's inherent microstructural heterogeneity [1, 2, 14]. Two important effects associated with increase in the amount of δ-ferrite transformation in the weld metal region are: (a) decrease in the strength of the weld metal (decrease in strength gradient across the weld joint) due to the loss of strengthening alloying elements from the matrix [18], thereby increasing the amount of deformation within the weld zone, (b) stress concentration along the austenite/σ-phase interface following the transformation of δ-ferrite, leading to early failure in the weld region of the joint [1–4, 21]. The introduction of a tensile hold period into the fatigue cycle has a marked detrimental effect on the cyclic life for both the BM and the WJ, as shown in Fig. 3b. The damaging effect associated with hold times is attributed to creep deformation which results in stress relaxation during the strain hold (Fig. 2b). The cyclic life was found to decrease considerably with an increase in the length of the hold period. Type 316LN SS is prone to creep damage at temperatures above 823 K in the form of grain boundary cavities/cracks at junctions of grain boundary triple points and grain boundary-second phase particles and grain boundary-slip band intersections [13]. Under creep-fatigue loading, the above steel is generally known to be more susceptible to creep damage under tensile strain hold cycling compared to compressive holds [9, 13, 14]. The IP TMF and creep—IP TMF waveforms were found to be more damaging and resulted in lower lives compared with the conventional IF and creep—IF cycling respectively, under identical testing conditions as shown in Fig. 3b. The reduction in life under IP TMF cycling has been attributed to the detrimental influence of creep damage in 316LN SS base metal [20]. The fracture surfaces of the failed samples were examined under optical microscopy and scanning electron microscopy (SEM) to gain a clear insight into the damage modes under different testing conditions. The cracks were generally seen to initiate in the base metal part of the WJ in continuous cycling and 1 min hold conditions under IF and IP TMF. It may be

noted that the base metal, due to low yield strength, experiences a higher amount of strain compared to the weld metal, leading to crack initiation in the former. The tensile properties of the BM and WM regions of the weld joint obtained from the automated ball indentation (ABI) technique are presented in Table 2 [1].

An increase in the hold period leads to an increased softening in the weld region, thereby increasing the amount of deformation within the weld zone. This results in the initiation of cracks in the weld metal part of the joint as shown in Fig. 4a which presents cracking in the weld region under creep—IF cycling with a tensile hold time of 5 min. This could also be associated with the higher amount of transformation of the δ-ferrite in the above case (Fig. 3a), leading to precipitation of carbides and σ-phase. The fractographs of the WJ samples are presented in Fig. 4b–e. The crack initiation and propagation occurred in transgranular mode with well-defined striations in continuous cycling under IP TMF in the base metal and weld joint as shown in Fig. 4b, c. Figure 4c also shows the presence of many short secondary cracks in

Table 2 ABI generated tensile properties of base metal and weld metal regions of weld joint at 873 K [1]

316LN SS weld joint		
Location	Yield strength (MPa)	Ultimate tensile strength (MPa)
BM	195	483
WM	318	477
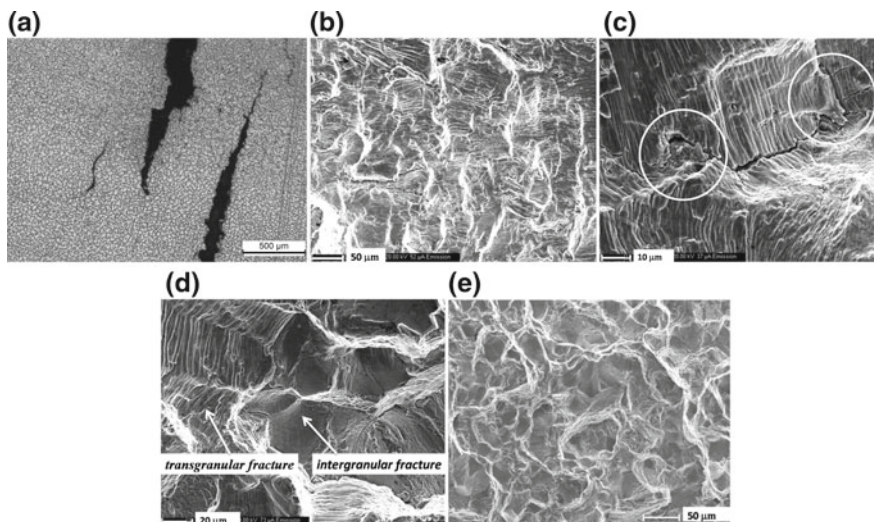
Fig. 4 a: Optical micrograph of the weld metal failure under creep—IF at 5 min hold, fractographic features illustrating **b**: Clear striations in BM, **c**: Joining of secondary cracks with major propagating crack, under IP TMF, **c:**, **d**: Mixed mode fracture in the BM region of WJ under 1 min creep—TMF, **e**: Predominantly intergranular fracture in weld region at 5 min creep—TMF

addition to the major crack, perpendicular to the loading direction. The shorter cracks were seen to join with the major propagating crack as indicated by circles in the figure. A significant contribution from the creep damage was evident in the form of intergranular damage upon introduction of peak tensile strain hold, as shown in Fig. 4d, e. The deformation under 1 min hold tests proceeds with the trans- plus intergranular mixed mode of failure, whereas 5 min samples showed predominantly intergranular damage as shown in the Fig. 4d, e respectively. The creep damage accumulated in IF cycling under tensile hold could get partially healed by the beneficial compressive ramp at the same temperature. It is well known that cracks propagate predominantly in the tensile part of the cycle. In the present case, a high stress range at high temperatures in IP TMF suggests that crack growth takes place more rapidly compared to IF cycling. It should be noted that tensile creep deformation occurs at 873 K and compressive deformation takes place at the 623 K under creep—IP TMF cycling in the temperature range of 623–873 K. The net accumulated creep damage under creep—IP TMF is seen to be higher than that occurring under creep—IF cycling, presumably on account of the minimal healing effects owing to the lower temperature deformation in the former case.

This is also reflected in the amount of stress relaxation and the half-life plastic strain amplitudes, as shown in Fig. 2a. Based on the above observations, the following factors emerge as plausible reasons for the lower lives obtained under creep —IP TMF compared to creep—IF:

(a) Higher stress relaxation inducing larger amount of creep damage,
(b) Enhanced accumulation of intergranular creep damage due to the development of higher tensile stresses under creep—IP TMF compared to creep – IF,
(c) The compressive deformation taking place at lower temperatures regime precludes damage reversal or healing effects unlike the case in IF conditions and
(d) Higher δ-ferrite transformation in the weld metal region under IP TMF with hold time.

4　Conclusions

1. TMF led lower lives compared to IF cycling at the maximum temperature of TMF.
2. TMF resulted in higher stress response compared to IF cycling at the T_{max} for both base metal and weld joint under continuous cycling and hold time conditions.
3. The δ-ferrite transformation under continuous cycling depends on the time of exposure, however, under hold conditions the stress range and thermal cycling plays a significant role in its transformation.
4. The weld joint displayed lower lives compared to the base metal under identical waveforms. The creep—IP TMF cycling was seen to yield lower lives for the base metal and weld joint in comparison with the conventional isothermal creep–fatigue cycling due to more tensile creep damage.

5. Crack growth takes place in transgranular mode under continuous cycling. Introduction of tensile hold time induced significant intergranularity to the mode of fracture.

References

1. T. Suresh Kumar, A. Nagesha, J. Ganesh Kumar, P. Parameswaran, R. Sandhya, Metall. Trans. A **49**(8), 3257 (2018)
2. M. Valsan, D. Sundararaman, K. Bhanu Sankara Rao, S.L. Mannan, Metall. Trans. A **26**, 1207 (1995)
3. G.V. Prasad Reddy, R. Sandhya, M. Valsan, K. Bhanu Sankara Rao, Int. J. Fatigue **30** (2008) 538
4. K. Bhanu Sankara Rao, M. Valsan, S.L. Mannan, Mater. Sci. Eng. A **130,** 67 (1990)
5. Vani Shankar, K. Mariappan, R. Sandhya, K. Laha, Int. J. Fatigue **82**, 487 (2016)
6. E.G. Ellison, A. Al-Zamily, Fatigue Fract. Eng. Mater. Struct. **17**(1), 39 (1994)
7. S.Y. Zamrik, D.C. Davis, L.C. Firth, Isothermal and Thermomechanical Fatigue of Type 316 Stainless Steel, in *Thermomechanical Fatigue Behavior of Materials: Second Volume*, ASTM STP 1263, ed. by M.J. Verrilli, M.G. Castelli (ASTM, Philadelphia, 1996), pp. 96–116
8. E. Yoshihisa, S. Ganesh Sundara Raman, Sci. Tech. Weld. Join. **5**(3), 174 (2000)
9. V.S. Srinivasan, A. Nagesha, M. Valsan, K. Bhanu Sankara Rao, S.L. Mannan, D.H. Sastry, Int. J. Press. Vessel. Pip.**76**, 863 (1999)
10. R. Hales, Fatigue Eng. Mater. Struct. **3**(4), 339 (1980)
11. D.S. Wood, J. Wynn, A.B. Baldwin, P.O'Riordan, Fatigue Fract. Eng. Mater. Struct. **3** (1980)
12. G.V. Prasad Reddy, R. Sandhya, S. Sankaran, P. Parameswaran, K. Laha, Mater Des. **88,** 972 (2015)
13. P. Rodriguez, K. Bhanu Sankara Rao, Nucleation and growth of cracks and cavities under creep–fatigue interaction, *Prog. Mater. Sci.* **37,** 403 (1993)
14. K. Bhanu Sankara Rao, R. Sandhya, S.L. Mannan, Int. J. Fatigue **15**(3), 221 (1993)
15. M.D. Mathew, G. Sasikala, S.L. Mannan, P. Rodriguez, Mater. Sci. Technol. 7(6), 533 (1991)
16. G. Sasikala, S.K. Ray, S.L. Mannan, Mater. Sci. Engg. A **359**, 86 (2003)
17. M.D. Mathew, G. Sasikala, T.P.S. Gill, S.L. Mannan, P. Rodriguez, Mater. Sci. Tech. **10**(12), 1104 (1994)
18. T.P.S. Gill, M. Vijayalakshmi, P. Rodriguez, K.A. Padmanabhan, Metall. Trans. A **20**, 1115 (1989)
19. A. Nagesha, R. Kannan, P. Parameswaran, R. Sandhya, K. Bhanu Sankara Rao, Vakil Singh, Mater. Sci. Eng. A **527,** 5969 (2010)
20. G.V. Prasad Reddy, A. Nagesha, R. Sandhya, S. Sankaran, M.D. Mathew, K. Bhanu Sankara Rao, Metall. Trans. A **46,** 695 (2015)
21. F. Liu, Y.H. Hwang, S.W. Nam, Mater. Sci. Eng. A **427**, 35–41 (2006)

Creep Deformation Behaviour of Modified 9Cr-1Mo Steel Clad Tubes

S. Latha, K. Laha, P. Parameswaran, G. V. Prasad Reddy,
G. Sasikala and Shaju K. Albert

Abstract Modified 9Cr-1Mo ferritic steel has been considered as the cladding tube material in Metallic Fuel Fast Reactor, in view of its inherent void swelling resistance. Creep studies were conducted on modified 9Cr-1Mo steel clad tubes at 823, 873 and 923 K at various stress levels. The resultant rupture lives ranged from 100 to 16,000 h. The creep curves exhibited a negligible loading strain, a small primary, and extensive tertiary regions at all the test conditions. A power law relationship was followed between minimum creep rate and applied stress, and the stress exponent obtained was characteristic of the precipitation hardened alloys. The stress exponent decreased with increase in temperature. Apparent activation energy for creep, in the present study, was estimated to be around 365 kJ/mol. An inverse power law relation was obtained between applied stress and rupture lives, and the corresponding stress exponent decreased with increase in temperature. The relation between deformation and fracture for these clad tubes was established using Monkman-Grant and Modified Monkman-Grant relationships. Scanning electron microscopic investigations revealed coarsening of precipitates after long term creep exposure. The creep properties generated in the current study compare well with the NIMS (Japan) clad tube data at 823 K and 873 K.

1 Introduction

Modified 9Cr-1Mo steel is being used for steam generator of fast nuclear reactor and fossil-fired power generating plants [1, 2]. Modified 9Cr-1Mo steel is currently being considered as the potential clad material for metallic fuel fast reactor even though the creep strength is lower than austenitic stainless steel by a moderate level.

S. Latha (✉) · P. Parameswaran · G. V. Prasad Reddy · G. Sasikala · S. K. Albert
Materials Development and Technology Division, Metallurgy and Materials Group, Indira
Gandhi Centre For Atomic research, Kalpakkam 603102, Tamil Nadu, India
e-mail: slatha@igcar.gov.in

K. Laha
AUSC Mission Directorate, Noida, New Delhi, India

This is because of its inherent resistance to damage caused by neutron irradiation than austenitic stainless steel. The creep-rupture behaviour of modified 9Cr–1Mo steel is widely reported [3, 4] and the steel has been included in the various codes and standards including French nuclear design code RCC-MR [5]. It is proposed to design and construct metallic fuel fast reactors in India. Though extensive creep studies have been conducted on Modified 9Cr-1Mo steel extracted from various product forms, very limited studies have been conducted in the form of thin tubes with wall thickness less than 0.5 mm. Hence, it is necessary to study the creep properties of this material in tubular form and in the present study, the creep behaviour of Modified 9Cr-1Mo steel clad tubes has been studied at 823, 873 and 923 K.

2   Experimental

Modified 9Cr-1Mo clad tubes of length about 3 m and outer diameter 6.6 mm, inner diameter 5.7 and 0.45 mm wall thickness were produced from Nuclear fuel complex, Hyderabad. These tubes were normalized in the temperature range 1313–1363 K and cooled in air, followed by tempering at 1053 K and cooled in air. The chemical composition of the clad tubes is given in Table 1.

The tubes were cut into lengths of 100 mm and welded with mandrels (holders). The specimen design for creep testing of clad tubes is shown in Fig. 1a. Creep tests were carried out in the temperature range 823–923 K which correspond to the temperatures experienced by the clad tubes during service. Creep tests were conducted, at stresses in the range 80–280 MPa, as per ASTM Standard E139. The creep elongation was recorded by a four-rod extensometer with Mitutoyo digimatic indicator, having a measurement resolution of ± 0.001 mm, and was continuously logged into a data logger.

The microstructure obtained in the normalized and tempered condition is shown in Fig. 1b. The microstructure consisted of tempered martensitic lath structure dispersed with precipitates. In this class of materials, the nature of precipitates has been well established and they belong to MX (VC and NbC) carbides mostly within the lath structure and $M_{23}C_6$ carbides on the lath boundaries and prior austenitic grain boundaries [6].

Table 1 Chemical composition (wt%) of modified 9Cr-1Mo steel clad tube

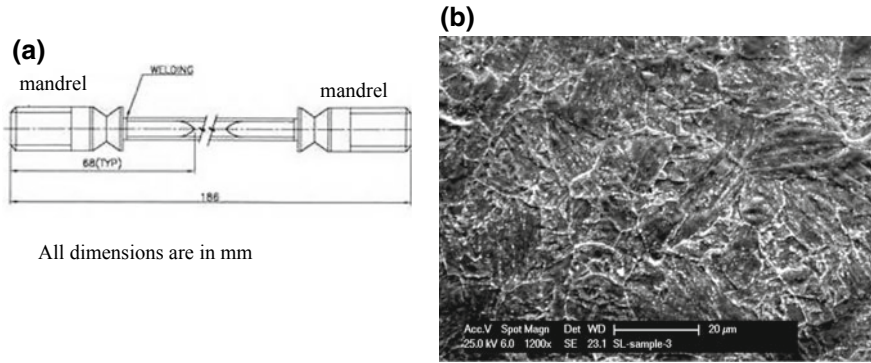| C	Si	Mn	Cr	Mo	Ni	P	S	Al	Cu	N
0.1	0.36	0.45	8.9	0.98	<0.03	<0.01	0.004	<0.03	0.09	0.09
Ti	V	Nb	Sn	Sb	N/Al					
<0.01	0.19	0.06	<0.01	<0.01	>3					

Fig. 1 **a** Creep Specimen and **b** Microstructure in the as—received (normalized and tempered) condition showing tempered martensitic structure dispersed with precipitates

3 Results and Discussion

3.1 Creep Curves

The Fig. 2a–b shows the creep curves obtained at various stress levels at 823 and 923 K. The creep curves consisted of a negligible instantaneous strain, a small primary, and extended tertiary regions, for most of the test conditions, except at low-stress levels. In the latter case, considerable secondary creep is also noticed. The Fig. 3a–b shows the variation of creep rate with time at 823 and 923 K. During primary creep, the creep rate decreases with increase in strain due to work hardening and in the secondary stage, the work hardening effect is balanced by the annihilation of dislocations and rearrangement of dislocations. The creep rate thereafter accelerates due to damage accumulation in the tertiary stage. In this
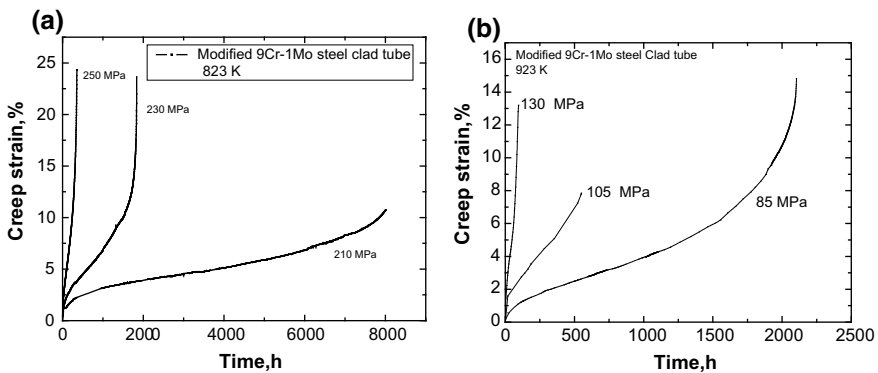
Fig. 2 Creep curves at various stress levels at **a** 823 K and **b** 923 K
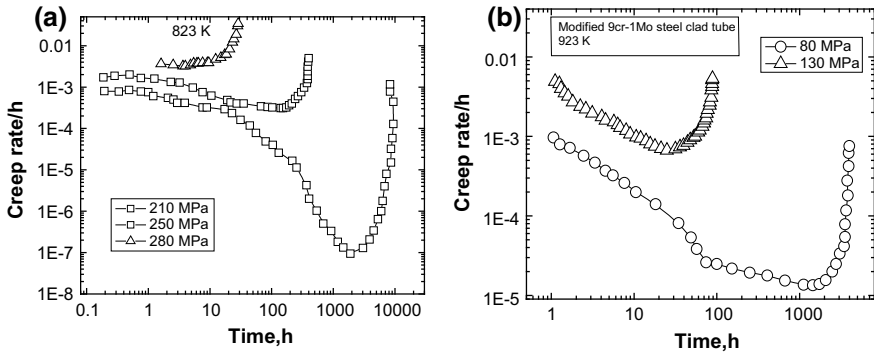
Fig. 3 Creep rate—time plots at various temperatures **a** 823 K and **b** 923 K

study, the variation of creep rate with time generally shows a decrease in primary region, a minimum and an increase in the tertiary region. As apparent from Figs. 2 and 3, the material accumulates large amount of strain in the tertiary stage at all the stress levels. Further, at low-stress levels, the strain accumulation in tertiary stage occurs over a longer period. The minimum in creep rate shifts to higher creep exposure times as the applied stress decreases. In general, increase in creep rate is observed with increase in stress. At 823 K, the minimum in creep rate increases by about four orders of magnitude with increase in stress from 210 to 250 MPa.

3.2 Minimum Creep Rate and Activation Energy

The Fig. 4 shows the variation of minimum creep rate with applied stress at 823 K. The relation between minimum creep rate and applied stress exhibited a power law in the form,

$$\dot{\varepsilon_m} = A\sigma^n \tag{1}$$

Fig. 4 Stress dependence of minimum creep rate and rupture life
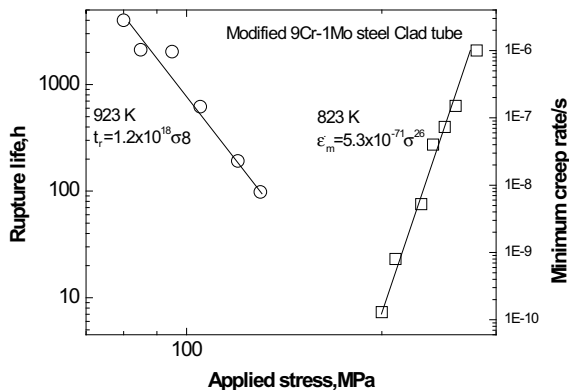
where $\dot{\varepsilon}$ is the minimum creep rate A is a constant. The stress exponent value of 26 at 823 K, 14 at 873 K and 13 at 923 K obtained in this study is a characteristic of precipitation hardened alloys. Stress exponent values exhibited a marginal decrease with increase in temperature from 873 to 923 K. The value of stress exponents are high compared to that of dislocation climb controlled models of power law creep wherein stress exponents of 3–7 are usually observed. A stress exponent of 15 at 873 K has been observed by Spigarelli and Quadrini [7] for Modified 9Cr-1Mo steel. Also, Kimura et al. [8] reported high values of stress exponent of 16 at 823 K and 12 at 873 K at high stress levels (similar to stress levels used in this study) for modified 9Cr–1Mo steel. The stress field produced by precipitates on the dislocations gives a high value of stress exponent. In addition to high "n" values in the high stress regime, decrease in stress exponent with increase in temperature in the range 823–923 K has been also reported for the Modified 9Cr-1Mo steel [9].

3.2.1 Activation Energy

Activation energy for modified 9Cr-1Mo steel clad tubes was estimated from the plot of minimum strain rate versus reciprocal of temperature. Creep tests were conducted at 210 MPa at temperatures of 823, 848, and 873 K and the minimum strain rates obtained from these tests were used for calculation of activation energy. The slope of the plot of minimum strain rate versus reciprocal of temperature gives the value of Q/R, where Q is the activation energy and R is the universal gas constant (Fig. 5). Activation energy for creep of Modified 9Cr-1Mo steel clad tube was estimated to be around 365 kJ/mol. The measured value is greater than the activation energy for self-diffusion in α iron. Similar values of activation energy were reported for Modified 9Cr-1Mo steel by Zhao et al. [10] and Krishna Guguloth et al. [11].

Fig. 5 Plot of minimum creep rate versus reciprocal of temperature
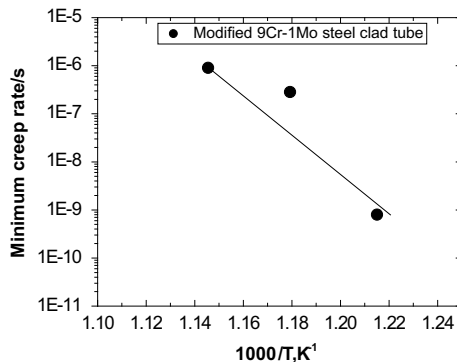
3.3   Rupture Life

The variation of rupture life with applied stress is shown in Fig. 4 for 923 K. The relation between rupture life and applied stress followed a power law,

$$t_r = B\sigma^{-m} \tag{2}$$

where t_r is the rupture life, B is a stress coefficient and m is the stress exponent. Similar to the variation in stress exponent values with temperature, m values also showed a decrease with increase in temperature. The power law coefficients and stress exponents for the stress dependence of minimum creep rate and stress dependence of rupture life are shown in Table 2.

The creep strength of Modified 9Cr-1Mo Steel clad tubes at 873 K are compared with NIMS Modified 9Cr-1Mo steel clad tubes [12], Japan and RCC-MR minimum, average strength values [13] Fig. 6. It is observed that the creep strength of Modified 9Cr-1Mo steel clad tubes (IGCAR tubes, used present study) is comparable to NIMS tubes and lie well above the RCC-MR minimum values. The rupture elongation of all the tubes is above 10% irrespective of the applied stress. Rupture elongation did not show a clear trend with rupture life.

Table 2 Power law coefficient and stress exponent for the dependence of minimum creep rate with stress and Power law coefficient and stress exponent for the stress dependence of rupture life

Temperature, K	$\dot{\varepsilon} = A\sigma^n$		$t_r = B^{-m}$	
	Power law coefficient, A	Stress exponent, n	Power law coefficient, B	Stress exponent, m
823	5.3×10^{-71}	26	5.13×10^{45}	18
873	5.2×10^{-39}	14	1.78×10^{28}	12
923	1.6×10^{-35}	13	1.22×10^{18}	8

Fig. 6 Comparison of creep strengths of IGCAR tubes with NIMS tubes and RCC-MR values at 873 K
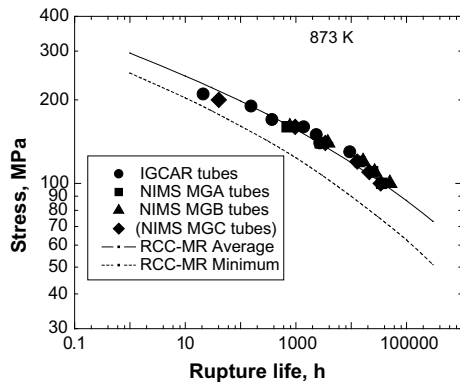
3.3.1 Relation Between Deformation and Fracture

The relation between minimum creep rate and rupture life proposed by Monkman-Grant [14] is given by

$$\dot{\varepsilon}_m{}^{\alpha} t_r = C \tag{3}$$

where α is the Monk man-Grant exponent and C is a constant. When α is unity, the constant C = C_{MG} is called as Monkman-Grant constant. For materials exhibiting small tertiary and large fraction of secondary creep, the product of ε_m and t_r would be an appropriate measure of strain to failure, and m and C will be independent of test temperature chemical composition of the alloy [14]. The Fig. 7a shows the variation of rupture life with applied stress. The Monkman-Grant exponent α, in this case, is around 0.8, which is near to unity and the Monkman-Grant constant C is 0.3. Tempered martensitic stainless steel (9Cr–Mo–Nb–V) indicates a Monkman–Grant exponent value, m = 0.94 [15]. Identical exponent value was also established for stainless steel Type 316L [16]. However, in a separate study, the same steel
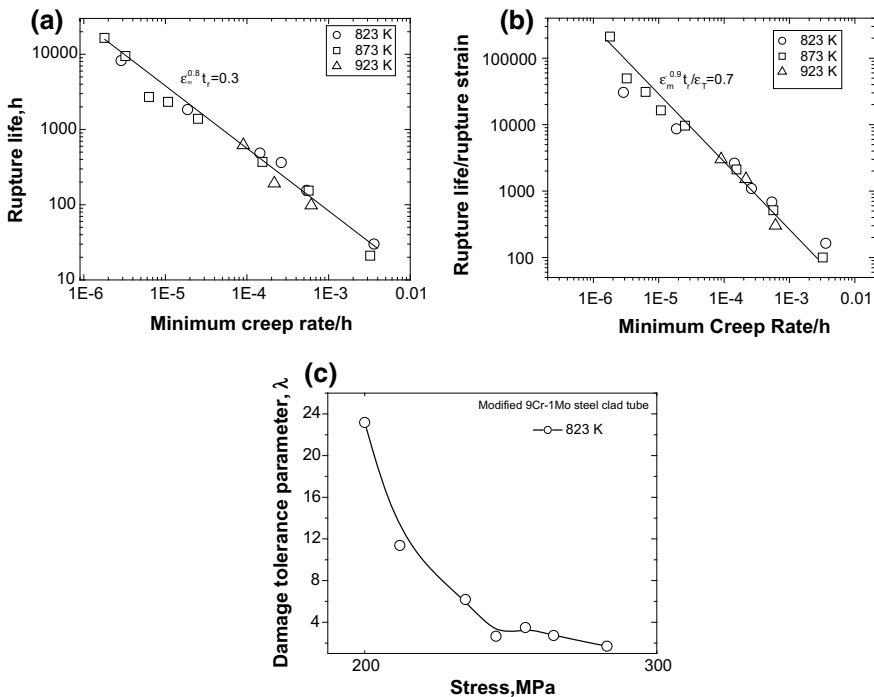
Fig. 7 **a** Monkman-Grant relationship **b** Modified Monkman-Grant relationship and **c** Variation of creep damage tolerance factor with stress at 823 K for modified 9Cr-1Mo steel tubes

exhibited a strain rate exponent, m = 0.6 [17]. When a material exhibits large tertiary creep and decrease in creep strain to failure with increasing rupture life, the scatter in data can be reduced by a relation proposed Dobes and Millika [18] by dividing rupture life with rupture strain as

$$\dot{\varepsilon}_m^{\alpha'} t_r / \varepsilon_T = C' \tag{4}$$

where α' and C' is are constants, and when α' is unity, $C' = C_{MMG}$, is the Modified Monkman-Grant Constant. The plot of Rupture ductility divided by rupture stain versus minimum creep rate is shown in Fig. 7b. In this relation also, also the value of α' around 0.9, which is close to unity and C' is around 0.7.

The inverse of modified Monkman-grant Constant is known as the damage tolerance parameter,λ, when α' is unity. Creep damage tolerance parameter indicates the ability of a material to withstand strain concentrations. The plot of versus λ versus stress at 823 K is shown in Fig. 7c. This shows that the values of λ depends on stress. The values of λ is high at low stresses and with increase in stress it shows a decrease. Similar behaviour was noticed for type 347 foils [19]. The high value of λ suggests that the contribution of secondary strain to the strain to fracture is very small. For $\lambda = 1.5$–2.5, the creep damage mechanism corresponds to cavitation, and for $\lambda = 2.5$ or more, it corresponds to microstructural degradation such as a coarsening of the precipitates and/or dislocation substructural softening. It is known that Grade 91 steel, typical heat resisting steel has λ values of 5 and more [20]. This indicates that at low stress levels due to long time creep exposure, the damage takes place by coarsening of precipitates.

4 Microstructural Studies

The scanning electron micrographs of the specimens creep tested at various temperatures and stress levels are shown in Fig. 8a–d. In comparison to Fig. 1b, the microstructures of the creep exposed specimens revealed considerable coarsening of the precipitates, particularly those on the prior austenite grain boundaries and on the lath boundaries. It has been reported that $M_{23}C_6$ precipitates on the above boundaries usually undergo coarsening during creep exposure and sets the instability of lath structure [21]. It can be seen from the images in Fig. 8a–b, at the same magnification, at 823 K gradual coarsening of precipitates takes place upon long creep durations (Fig. 8b). However, we could not quantify the coarsening kinetics which requires extensive TEM investigations. The coarsening kinetics appeared to increase with increase in temperature, for longer creep exposures, as shown in Fig. 8c. However, in the case of creep tests at high temperatures but for shorter rupture lives, the lath structure within the prior austenitic grain boundaries did not show much change on a macroscale.
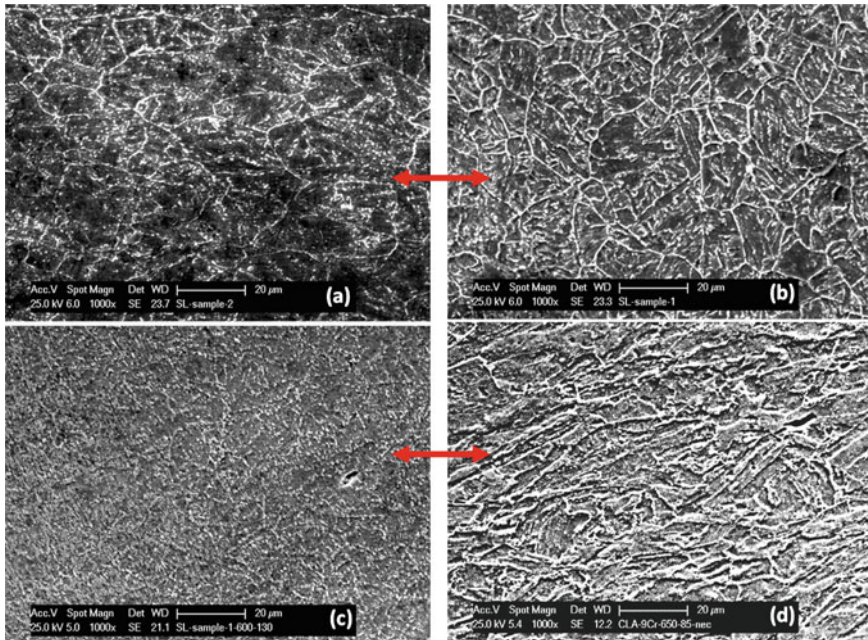
Fig. 8 a Scanning electron microstructure of creep tested specimen at 823 K/240 MPa: rupture life: 480 h and **b** 823 K/ 210 MPa: rupture life: 8000 h **c** Scanning electron microstructure of creep tested specimen at 873 K/130 MPa rupture life: 9000 h and **d** 923 K/85 MPa: rupture life: 2000 h

5 Conclusions

1. Creep curves of Modified 9Cr-1Mo steel clad tubes generally show a small primary and extended tertiary regions.
2. The variation of minimum creep rate and rupture life followed a power law. The creep strengths of Modified 9Cr-1Mo steel clad tubes are comparable to that of NIMS tubes, Japan and the values lie above RCC- MR minimum values.
3. Monkman-Grant relationship and Modified Monkman-Grant relationship were obeyed with the values of constants close to unity. Creep damage tolerance factor was high at low stresses due to precipitate coarsening.
4. Scanning electron microstructures of the tubes exhibited coarsening of precipitates and retention of lath structure after high-temperature creep exposure.

References

1. S.L. Mannan, S.C. Chetal, B. Raj, S.B. Bhoje, Trans. Indian Inst. Met. **56**, 155 (2003)
2. R.L. Klueh, Int. Mater. Rev. **50**, 287 (2005)
3. K. Kimura, H. Kushima, F. Abe, K. Yagi, Mater. Sci. Eng., A **234–236**, 1079 (1997)
4. S. Spigarelli, L. Kloc, P. Bontempi, Scripta Mater. **37**, 399 (1997)
5. Design and Construction Rules for Mechanical Components of FBR Nuclear Islands, *RCC-MR, Section 1, Subsection Z, Appendix A3*, 18S, 2002, pp. A3.18S/1-26
6. K. Guguloth, N. Roy, Mat. Sci. Eng. **A 680**, 388 (2107)
7. S. Spigarelli, E. Quadrini, Mater. Des. **23**, 547 (2002)
8. K. Kimura, H. Kushima and K. Swada, Mater. Sci. Engg., A **510–511,** 58 (2009)
9. V. Sklenicka, K. Kucharova, M. Svoboda, L. Kloc, J. Bursik, A. Kroupa, Mater. Charac. **51**, 35 (2003)
10. Y.R. Zhao, H.P. Yao, X.L. Song, J. Jia, Z.D. Xiang, J. Alloys Compd. **726**, 1246 (2017)
11. K. Guguloth, J. Swaminathan, N. Roy, R. N. Ghosh, Mater. Sci. Engg. A **684**, 683 (2017)
12. NIMS Creep Data Sheet, *Atlas of Creep Deformation property* No. D-1 (2007)
13. RCC-MR, *Section III tome I Subsection Z, Appendix A3*. 18AS, p. 14 (2010)
14. F.C. Monkman, N.J. Grant, Proc. Am. Soc. Test. Mater. **56**, 593 (1956)
15. V. Gaffard, J. Besson, A.F. Gourgues-Lorenzon, Int. J. Frac. **133**, 139 (2005)
16. W.G. Kim, S.H. Kim, W.S. Ryu, KSME Int. J. **11**, 1420 (2002)
17. B. Michel, Nucl. Eng Des. **227**, 161 (2004)
18. F. Dobes, K. Milicka, J. Mater, Science **10**, 382 (1976)
19. H.O. Ali, M.N. Tamin, J. Nucl. Mater. **433**, 74 (2013)
20. C. Phaniraj, B.K. Choudhary, K. Bhanu Sankara Rao, B. Raj, Scr. Mater., **48**, 1313 (2003)
21. B.K. Choudhary, E. Isaac Samuel, J. Nucl. Mater. **412**, 82 (2011)

Identifying the Creep Deformation Mechanism in P9 Steel at Elevated Temperatures

E. Isaac Samuel, Durga Prasad Rao Palaparti, S. D. Yadav, J. Christopher and B. K. Choudhary

Abstract Elevated temperature plastic deformation in metallic alloys and solids is often governed by various and alternative competing mechanisms such as diffusional flow, dislocation glide, and climb processes. In order to identify the creep deformation mechanism operating in P9 steel, creep rupture tests were carried out at 793 and 873 K employing stresses in the range of 50–300 MPa. Stress dependence of steady-state creep rate obeyed power law and exhibited two-slope behaviour characterised by different values of stress exponent and activation energy in the low and high stress regions. However, by invoking back stress concept, the variation of temperature compensated minimum creep rate with modulus compensated effective stress yielded single-slope power law behaviour with stress exponent of 4 and a true activation energy close to self-diffusion of iron. These observations suggested that the creep deformation in P9 steel is governed by climb of dislocations.

Keywords P9 steel · Steady-state creep · Back stress · Power law creep

1 Introduction

Creep is continuing plastic deformation of materials at elevated temperatures subjected to constant stress and occurs as a result of thermally activated migration of dislocation, grain boundary mobility and diffusion of vacancies. Uncovering the role of various factors that determine the physical mechanism underlying creep deformation had been exhaustively examined [1–9]. Apparent activation energy values for creep of metals and alloys with dilute solid solution had been observed to be independent of creep stress and strain, and were found to be in good agreement

E. Isaac Samuel (✉) · S. D. Yadav
Materials Development and Technology Division, Indira Gandhi Centre for Atomic Research, Kalpakkam 603102, Tamil Nadu, India
e-mail: isaac@igcar.gov.in

D. P. Rao Palaparti · J. Christopher · B. K. Choudhary
HBNI, Mumbai, Maharashtra, India

with the self-diffusion activation energy. The substructural changes that occur during creep are influenced by time, temperature and stress, however, the rate of change of substructure remains nearly constant during steady state. The secondary creep, described either by a steady state or minimum creep rate, has a special relevance with respect to engineering design and life prediction of in-service components. The influence of applied stress (σ_a) and temperature (T) on steady-state creep rate ($\dot{\varepsilon}_s$) has been widely described by Mukherjee, Bird and Dorn [2, 3] type relationship as,

$$\dot{\varepsilon}_s = A \frac{D\mu b}{kT} \left(\frac{\sigma_a}{\mu}\right)^n, \tag{1}$$

where A is a material constant, D is the diffusion coefficient, μ is the shear modulus, k is the Boltzmann's constant, b is the Burgers vector and n is the stress exponent. In Eq. 1, D is expressed as $D = D_0 \exp\left(-Q_C/RT\right)$, where D_0 is the frequency factor, Q_c is the activation energy and R is the universal gas constant. In pure metals and simple solid solution alloys, n has been observed close to 4 in the dislocation creep regime. In case of complex solid solution and precipitation hardened alloys, stress exponent values significantly higher than 4 have been observed [4, 10]. In addition to above, two-slope behaviour with different values of stress exponent and activation energy in the low and high stress regions has been also reported. The high stress exponent and activation energy values associated with two-slope behaviour have been rationalised by incorporating back stress (σ_b) into the creep rate relationship [2, 3] as

$$\dot{\varepsilon}_s = A \frac{D\mu b}{kT} \left(\frac{\sigma_a - \sigma_b}{\mu}\right)^{n_0}, \tag{2}$$

where n_0 is the modified stress exponent close to 4. The back stress is a measure of the resistance to deformation provided by microstructure. The origin of back stress arises from dominance of strengthening caused by solid solution, dislocations, precipitates and subgrains. In view of this, the back stress has also been referred to as friction stress/internal stress/threshold stress/resisting stress [4–9]. The term ($\sigma_a - \sigma_b$), referred as effective stress (σ_e) which is a part of the applied stress, is genuinely responsible for creep deformation. The true activation energy and the exponents evaluated from the power law dependence of temperature compensated creep rate with the effective stress serve as key indicators in identifying the underlying mechanism that control the creep deformation.

P9 steel is also known as 9Cr-1Mo steel belongs to the group of 9–12% Cr ferritic-martensitic steels with good resistance to deformation when exposed to creep and fatigue loading conditions at elevated temperatures [10–17]. The steel is commonly used as steam generator components in power generating industries and is also under active consideration for fast reactor core components under severe irradiation conditions [11, 14]. The strength of these materials relies on the complex and hierarchical microstructure with different interfaces such as prior austenitic

grain boundaries (PAGBs), blocks and sub-blocks, packets and laths/subgrains along with precipitates [10, 11, 13, 14]. These interfaces are generally pinned by the second phase particles present in the microstructure. In addition to the above, microstructural degradation results from enhanced recovery and coarsening of second phase particles. The synergistic effect of these processes leads to damage and eventually failure [17]. During service at elevated temperatures, these alloys undergo creep deformation controlled by various mechanisms.

In the present investigation, creep deformation behaviour characterised by two-slope behaviour with different values of stress exponent and activation energy in the low and high stress regions in P9 steel have been examined using effective stress dependence of steady-state creep rate described by Eq. (2) at 793 and 873 K. The back stress has been evaluated following Lagneborg and Bergman approach [4] and the mechanism responsible for the creep deformation is addressed.

2 Experimental

Creep rupture tests were conducted on P9 steel of 20 mm plate thickness with chemical composition (in wt%), 0.01C, 0.48Si, 0.45Mn, 0.002S, 0.008P 8.44Cr, 0.95Mo and balance Fe. The steel was normalised at 1223 K for 15 min followed by air cooling. Subsequently, it was tempered at 1053 K for 2 h and air cooled to achieve tempered martensitic microstructure. Creep tests were performed on 10 mm diameter and 50 mm gauge length cylindrical specimens machined from the normalised and tempered plate at stresses ranging from 50 to 300 MPa at 793 and 873 K. The initial microstructure was examined using optical and scanning electron microscopes.

3 Results and Discussion

Figure 1a, b show the microstructure of P9 steel in normalised and tempered condition observed through optical and scanning electron microscopy, respectively. The microstructure consisted of fine tempered lath martensite and precipitates. The boundaries of prior austenite grains and martensite laths were decorated with $M_{23}C_6$ precipitates and the intra-lath matrix regions contained fine M_2X precipitates (Fig. 1b). The microstructure of the P9 steel in normalised and tempered condition exhibited prior austenite grain size of about 25 μm.

P9 steel exhibited small primary creep followed by well-defined secondary creep characterised by steady-state creep rate, and prolonged tertiary creep regions in all test conditions. Figure 2a shows the typical creep curve and Fig. 2b depicts the variation of creep rate as a function of time, at 873 K/ 60 MPa. Dependence of steady-state creep rate on applied stress obeyed power law (Eq. 1) and exhibited two-slope behaviour at 793 and 873 K as shown in Fig. 3a. High values of stress
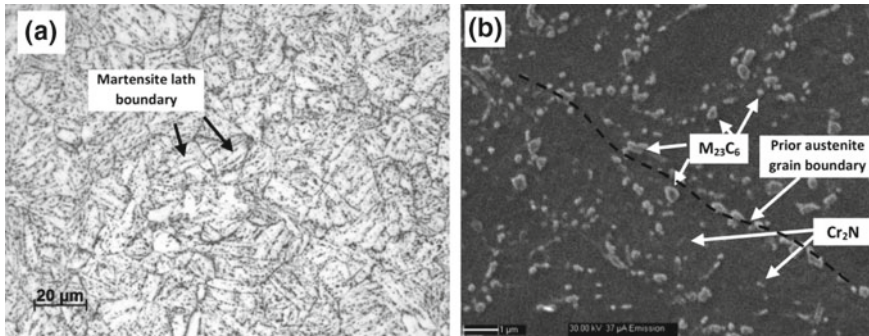
Fig. 1 As-received microstructure of P9 steel showing **a** tempered lath martensite and **b** precipitates on grain and lath boundaries and in the matrix region. Presence of $M_{23}C_6$ carbides and Cr_2N precipitates are shown by arrows in **b**
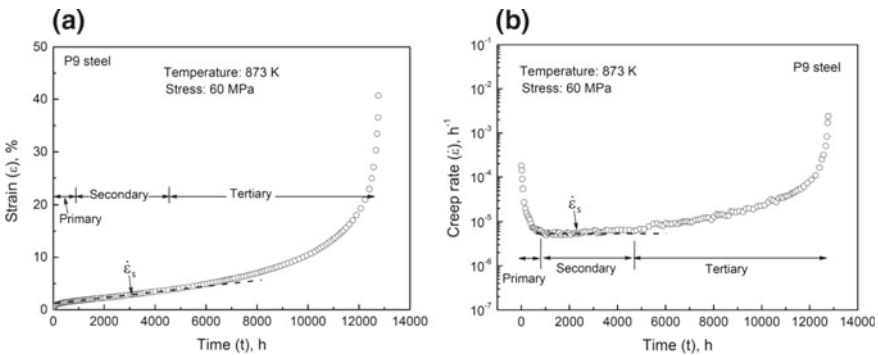

Fig. 2 Typical creep curve observed for P9 steel, represented as variation of **a** creep strain and **b** creep rate as a function of time at 873 K for 60 MPa

exponent $n = 10.8$ and 9.1 at 793 and 873 K, respectively, have been obtained in the high stress region. This was also associated with high activation energy values of 520 and 453 kJ mol^{-1} obtained for 150 and 175 MPa, respectively, as shown in Fig. 3b. An average value of activation energy of 486 kJ mol^{-1} can be assigned for high stress region. In the low stress region, stress exponent of $n = 4$ was observed at both temperatures, which is consistent with the recovery controlled models of creep [2, 3].

The two-slope behaviour and the observed high values of stress exponent and activation energy in the high stress region have been rationalised using back stress concept envisaged in the Lagneborg and Bergman [4] approach. In this approach, the back stress is evaluated by plotting fourth root of steady-state creep rate as a function of applied stress as shown in Fig. 4a for 873 K, as an example. Line LM passing through the origin represents low stress region and line PQ describes high stress region. The intersection of lines LM and PQ defines the transition stress (σ_T)
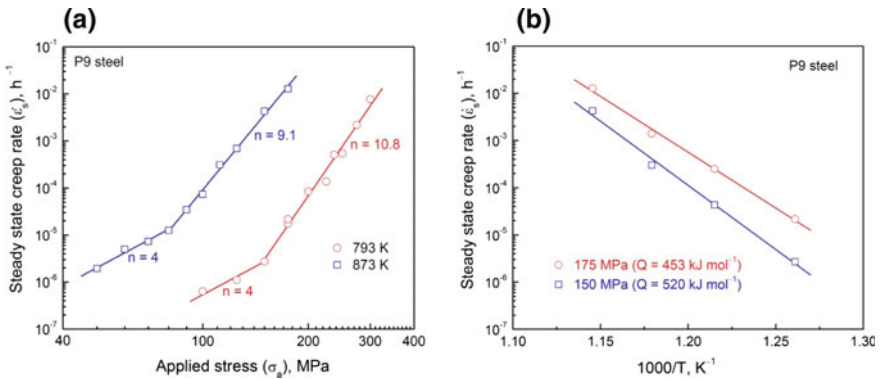
Fig. 3 **a** Stress dependence of steady-state creep rate at 793 and 873 K. **b** Apparent activation energy in the high stress region for the P9 steel

and the extrapolation of high stress data to zero creep rate at P provides the threshold stress (σ_H). In the high stress region, back stress is defined as $\sigma_b = \sigma_H$, whereas the back stress in low stress region is obtained as $\sigma_b = K.\sigma_a$, where K is the ratio of threshold stress and transition stress. Threshold stress (σ_H) values of 118.8 and 72.5 MPa and transition stress (σ_T) values of 154.3 and 94.5 MPa were obtained at 793 and 873 K, respectively. The proportionality constant $K = 0.77$ was obtained at 793 and 873 K in P9 steel, and this is in agreement with the values reported for precipitation hardened ferritic and austenitic steels and nimonic alloys [4]. The variation of σ_b with applied stress is typically shown for 873 K in Fig. 4b. It has been suggested that the transition of back stress from low stress to high stress region results from change in operative creep mechanism [4].
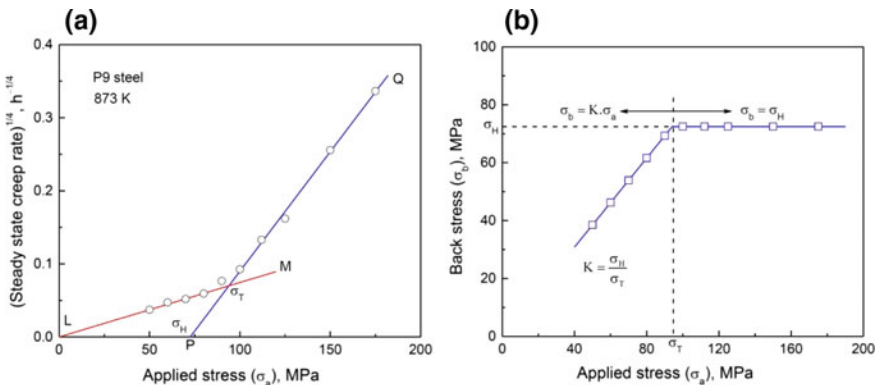
Fig. 4 **a** Determination of σ_H and σ_T from the plot of fourth root of steady-state creep rate versus applied stress, **b** variation of back stress with applied stress in the low and high stress regions at 873 K
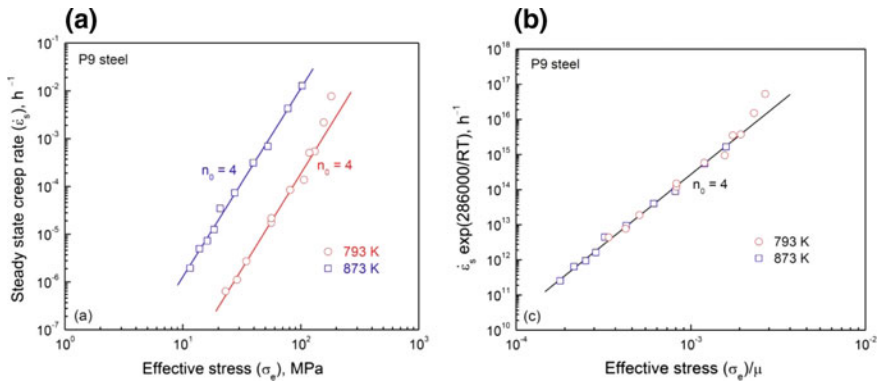
Fig. 5 a Steady-state creep rate versus effective stress at 793 and 873 K, **b** true activation energy and temperature compensated creep rate versus modulus compensated effective stress for both 793 and 873 K

By incorporating appropriate back stress in low and high stress regions in Eq. 2, a single-slope behaviour for effective stress dependence of steady-state creep rate with stress exponent $n_0 = 4$ has been obtained at 793 and 873 K as shown in Fig. 5a. Using least square optimisation of Eq. 2 to the variation of temperature compensated creep rate and effective stress normalised to modulus, true activation energy was iteratively evaluated as 286 kJ mol^{-1} with adjusted $R^2 = 0.996$. The obtained true activation energy value is observed to be close to self-diffusion in iron. By using optimised true activation energy in the temperature compensated creep rate, the plot of $\dot{\varepsilon}_s \exp\left(286000/RT\right)$ versus modulus compensated effective stress (σ_e/μ) resulted in a single-slope behaviour with unified stress exponent of 4 for both 793 and 873 K (Fig. 5b). These observations clearly suggest that the creep deformation in both low and high stress regions is controlled by climb of dislocations.

4 Conclusions

Detailed analysis has been performed to rationalise the observed two-slope behaviour associated with different low and high values of stress exponent and activation energy in the low and high stress regions, respectively, in the stress dependence of steady-state creep rate in P9 steel. The implementation of back stress concept into the creep rate relationship resulted in a single-slope behaviour with unified stress exponent of 4 for 793 and 873 K and true activation energy of 286 kJ mol^{-1}. Based on these observations, the governing creep deformation in both low and high stress regions has been ascribed to be dislocation climb controlled.

References

1. M.E. Kassner, M.T. Perez-Prado, *Fundamentals of Creep in Metals and Alloys* (Elsevier Ltd, Amsterdam, 2004), p. 11
2. J.E. Bird, A.K. Mukherjee, J.E. Dorn, *Qualitative Relation Between Properties and Microstructure*, ed. by D.G. Bandon, A. Rosan (Israel University Press, Jerusalem, 1969), pp. 255–342
3. A.K. Mukherjee, J.E. Bird, J.E. Dorn, Experimental correlation for high-temperature creep. ASM Trans. Quarterl **62**, 155–179 (1969)
4. R. Lagneborg, B. Bergman, The stress/creep rate behaviour of precipitation-hardened alloys. Met. Sci. **10**, 20–28 (1976)
5. K.R. Williams, B. Wilshire, Effects of microstructural instability on the creep and fracture behaviour of ferritic steels. Mater. Sci. Eng. **28**, 289–296 (1977)
6. D.A. Miller, A constitutive equation for creep deformation of 1CrMoV ferrritic steel at 823-838 K. Mater. Sci. Eng. **54**, 169–176 (1982)
7. D.O. Northwood, I.O. Smith, The stress exponent of steady-state creep in Al-Mg alloys. Mater. Lett. **2**, 339–343 (1984)
8. J. Wolfenstine, The existence of a threshold stress during creep of a Ti-53.4 mol.% Al alloy, Mater. Lett. 12 (1991) 203–206
9. S.D. Yadav, B. Sonderegger, M. Stracey, C. Poletti, Modelling the creep behaviour of tempered martensitic steel based on a hybrid approach. Mater. Sci. Eng., A **662**, 330–341 (2016)
10. B. Raj, B.K. Choudhary, A perspective on creep and fatigue issues in sodium cooled fast reactors. Trans. Indian Inst. Met. **63**, 75–84 (2010)
11. R.L. Klueh, Elevated temperature ferritic and martensitic steels and their application to future nuclear reactors. Int. Mater. Rev. **50**, 287–310 (2005)
12. Xingang Tao, Chuanwei Li, Lizhan Han, Gu Jianfeng, Microstructure evolution and mechanical properties of X12CrMoWVNbN10-1-1 steel during quenching and tempering process. J. Mater. Res. Technol. **5**, 45–57 (2016)
13. H. Ghassemi-Armaki, R.P. Chen, K. Maruyama, M. Yoshizawa, M. Igarashi, Static recovery of tempered lath martensite microstructures during long-term aging in 9–12% Cr heat resistant steels. Mater. Lett. **63**, 2423–2425 (2009)
14. B.K. Choudhary, Tertiary creep behaviour of 9Cr–1Mo ferritic steel. Mater. Sci. Eng., A **585**, 1–9 (2013)
15. Y.W. Xu, S.H. Song, J.W. Wang, Effect of rare earth cerium on the creep properties of modified 9Cr-1Mo heat-resistant steel. Mater. Lett. **161**, 616–619 (2015)
16. S.D. Yadav, S. Kalácska, M. Dománková, D.C. Yubero, R. Resel, I. Groma, C. Beal, B. Sonderegger, C. Sommitsch, C. Poletti, Evolution of the substructure of a novel 12% Cr steel under creep conditions. Mater. Charact. **115**, 23–31 (2016)
17. S.D. Yadav, U. Jäntsch, T. Scherer, M.R. Ahmadi, J. Rosc, C. Poletti, Investigation of creep cavities in a novel 12Cr-0.36Ta steel employing three-dimensional electron backscatter diffraction technique. Mater. Lett. **207**, 76–79 (2017)

Developments in Assessing Welds in High Temperature Conditions and Different Stress Triaxialities

T. Bender, A. Klenk and S. Weihe

Abstract This paper presents the current state of the assessment of similar ferritic-martensitic weld joints in creep or creep-fatigue conditions. Possibilities of the numerical modelling of failure are shown. Two different constitutive models, one for creep and one for creep-fatigue conditions, are presented. Microstructure simulated specimen is used to obtain numerical properties of the heat affected zone. The assessment of a P92 creep component test with weld is presented. The use of a strain-based failure criterion leads to a good prediction of the type 4 failure and the failure time. In addition, to explain the different failure locations of a low-cycle fatigue test with and without hold time, numerical simulations were performed. It is found that the hold times affect the local stress–strain hysteresis loops and may explain the different failure location. To obtain information about the creep-fatigue-crack behaviour of welds a test with a corner crack specimen was performed. The results show that the crack growth behaviour seems to be similar but the crack initiation times are different.

Keywords P92 · HAZ · Weld joint · Creep · Creep-fatigue

Nomenclature

q	Multiaxial factor
D	Damage parameter
p	Accumulated inelastic strain
$\boldsymbol{\varepsilon}_{in}$	Inelastic strain tensor
$\tilde{\varepsilon}$	Geometric sum of principal strains
$\boldsymbol{\sigma}$	Stress tensor
$\boldsymbol{\sigma}'$	Deviatoric stress tensor
$\boldsymbol{\varepsilon}_{in}$	Inelastic strain tensor
X	Kinematic hardening tensor
$\mathbf{X}'$	Deviatoric kinematic hardening tensor

T. Bender (✉) · A. Klenk · S. Weihe
Materials Testing Institute, University of Stuttgart, Pfaffenwaldring 32,
D - 70569 Stuttgart, Germany
e-mail: Thorben.Bender@mpa.uni-stuttgart.de

R   Isotropic hardening variable
Q   Limit of isotropic hardening
σ_{vis} Time-dependent stress (viscos-stress)
k   Yield stress
n   Norton-parameter

1 Introduction

Weld joints are indispensable for construction and repair of power plant compo-
nents, which are operated in the high-temperature regime. In general, weld joints
are distinguished between similar and dissimilar weld joints based on the chemical
properties of two connected materials. In this paper, a ferritic-martensitic steel of
the ASTM Grade P92 and similar weld joints of this steel grade are investigated.

During the welding process, the microstructure and mechanical behaviour
especially of ferritic and martensitic steels are changed. The weld joint is in contrast
to the parent metal a complex heterogeneous material. In general, a weld joint can
be divided into 5 different zones: The weld metal (WM) that consist of the electrode
material. The heat affected zone (HAZ) can be observed at the transition from the
WM to the parent metal (PM), which is not affected by the welding process. The
HAZ itself can be divided into three zones: (i) the HAZ1, usually shows slightly
larger grain size than the PM and better creep properties; (ii) the HAZ2 with similar
creep properties compared to the PM; (iii) HAZ3 close to the PM with poor creep
strength compared to the PM. A schematic representation of weld joint and an
optical microscopy microsection of P92 are shown in Figs. 1 and 2, respectively.

The weld joint is often the weakest link for static loads and especially for pure
creep loads. A comparison of creep tests with PM and crossweld specimens shows
that depending on temperature and runtime the failure location changes from PM to
the HAZ. Due to this effect, an "S-shaped creep curve" as shown in [2] is observed.
Especially martensitic steels show this behaviour. In practice, for the design of
components, weld reduction factors are used to determine the creep behaviour of
weld joints based on the PM behaviour. However, components exposed mainly to
creep loads show premature failure located in the HAZ as well. This failure type is

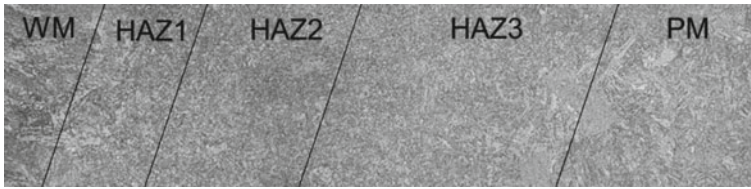**Fig. 1** Schematically shown
HAZ [1]
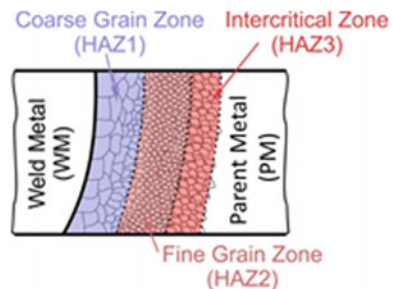
Fig. 2 Microsection of P92 weld

known as Type 4 cracking. The main difference between PM failure and Type 4/ HAZ failure is that the failure in the HAZ is primarily a local phenomenon, which cannot be predicted by using standard design methods like using the 1% creep limit.

Creep behaviour of weld joints is much better understood compared to the fatigue or creep-fatigue behaviour. The low-cycle fatigue (LCF) tests of P92 PM and crossweld specimen was performed by Veerababu et al. [3]. For the same nominal strain amplitude, the number of cycles to failure is lower for the weld joint compared to the PM. However, typical HAZ failure, except in one test, was not observed. The reason for the lower fatigue life of the weld joint can possibly be explained by the inhomogeneity of the material properties. The WM is usually stiffer than the PM [4]. In a strain controlled LCF test, the stiffer material will deform less than the softer PM; consequently, the local strain amplitude in the PM is larger than the nominal strain amplitude of the specimen. This larger local strain amplitude leads to faster failure.

In contrast to LCF tests, LCF tests with hold times usually lead to failure in the HAZ and to lower lifetime compared to PM tests. Takahashi [5] performed LCF and creep-fatigue interaction (CFI) tests on P91 material. For all CFI tests, failure in the HAZ and lower lifetime were observed. The effect of short and long holds during fatigue tests of a similar weld joint–Grade 91 material–were investigated by Shankar et al. [6]. The results show that the hold times decrease the fatigue life of the weld joint.

At the Material Testing Institute University of Stuttgart (MPA Stuttgart) the behaviour of Grade 92 welds in the creep, creep-fatigue regime as well as the behaviour of cracks in those welds are subjected to several research projects. In this paper, a short introduction to the research status is given. First, a short overview over numerical assessment methods is given then the numerical modeling of weld joints is discussed. In the fourth section some examples and results are discussed.

2 Numerical Modelling of Failure

For the assessment of specimen or components, different methods can be used. In this section, a quick overview of some methods is given and the applicability of these methods for weld joints is discussed. The discussed approaches are either strain-based or based on a phenomenological damage model.

For components in the creep regime, the standard design approach is the limitation of the global creep strain (1–2%) and consideration of the weld joint with a weld strength factor. However, since the failure of welds is a local phenomenon, a local failure criterion is essential. A strain-based criterion with consideration of the multiaxial stress state was used for the prediction of creep-crack initiation of ferritic-martensitic material in [7]. For the limit strain, which indicates failure of an element in the simulation the uniform elongation, ε_{gl}, was used. The uniform elongation can be determined by a detailed analysis of broken creep strain specimens. The approach seems suitable for the assessment of welds, but it has a drawback: ε_{gl} is mostly not known and difficult to determine without the fractured specimen. For this reason, a failure criterion, for the failure prediction of a P91 pressure vessel, was developed based on the uniform rupture strain $\varepsilon_{ur,uni}$, which can be calculated from creep–strain curves in [1, 8]. Both strain-based approaches seem suitable for the assessment of weld joints. The only disadvantage is need of various creep tests for the PM and HAZ and the values tend to scatter.

A more phenomenological approach is the use of a creep law with a damage parameter. At the MPA Stuttgart, a modified Graham–Walles (GWD) creep law with a damage parameter based on the principle of effective stress is used. The formulation with 12 parameters is shown in the Eqs. (1) and (2). For the parameter identification, creep tests are used. The procedure will be discussed in Sect. 3.

$$\dot{\varepsilon} = 10^{A_1} \cdot \left(\frac{\sigma_{mises}}{(1-D)} \right)^{n_1} \cdot \varepsilon_{eq}^{m_1} + 10^{A_2} \cdot \left(\frac{\sigma_{mises}}{(1-D)} \right)^{n_2} \cdot \varepsilon_{eq}^{m_2} \tag{1}$$

$$\dot{D} = 10^{A_{D1}} \cdot \left(\left(\frac{\sqrt{3}}{q} \right)^{\alpha} \cdot \sigma_{mises} \right)^{n_{D1}} \cdot \tilde{\varepsilon}^{m_{D1}} + 10^{A_{D2}} \cdot \left(\left(\frac{\sqrt{3}}{q} \right)^{\alpha} \cdot \sigma_{mises} \right)^{n_{D2}} \cdot \tilde{\varepsilon}^{m_{D2}} \tag{2}$$

The creep law allows the description of all three different creep stages as well the effect of stress multiaxiality, which is essential for the assessment of components and weld joints. In [9] the damage evolution in a thick-walled pipe (E911) under internal pressure was investigated. The results showed that the hypothetic creep damage concentrates in the HAZ3 and it is largest close to the external surface. This observation coincides with the typical damage symptoms of experimental component tests of ferric-martensitic steels.

For the assessment of specimens or components subjected to fatigue or creep-fatigue, an approach similar to the weld strength reduction factor is wanted. But a simple modification of the crack initiation curve, determined on PM tests, is due to the inhomogeneity of the weld not sufficient. The different assessment approaches of the standards (DIN, ASME, RCC, R5) will not be discussed in this paper, and only a phenomenological approach will be presented. To describe the cyclic behaviour a viscoplastic modified Chaboche model (CNOW) is used [10–12].The model consist of two flow rules, one for high stresses (3) and one for low stresses (4). The inelastic strain rates for the first flow rule is given in (6) and for the second flow rule in (7). The accumulated strain rate can be calculated with Eq. (8).

Kinematic and isotropic hardening is taken into account with the formulation (9), (11) and (12). For the parameter, identification creep tests and complex cycle fatigue tests are used. The procedure, particularly for weld joints, is presented in the following section.

$$\text{flow rule for high stresses} \quad f_1 = J_2(\boldsymbol{\sigma} - \boldsymbol{X}_1) - R - k - \sigma_{vis1} = 0 \qquad (3)$$

$$\text{flow rule for low stresses} \quad f_2 = J_2(\boldsymbol{\sigma} - \boldsymbol{X}_2) - \sigma_{vis2} = 0 \qquad (4)$$

$$\text{with } J_2(\boldsymbol{\sigma} - \boldsymbol{X}_{1,2}) = \sqrt{\frac{3}{2}(\boldsymbol{\sigma}' - \boldsymbol{X}'_{1,2}) : (\boldsymbol{\sigma}' - \boldsymbol{X}'_{1,2})} \qquad (5)$$

inelastic strain rate for high stresses
$$\dot{\boldsymbol{\varepsilon}}_{in1} = \frac{3}{2} \cdot \left\langle \frac{\sigma_{vis1}}{K_1} \right\rangle^{n_1} \cdot \frac{\boldsymbol{\sigma}' - \boldsymbol{X}'_1}{J_2(\boldsymbol{\sigma} - \boldsymbol{X}_1)} = \frac{3}{2} \dot{p}_1 \frac{\boldsymbol{\sigma}' - \boldsymbol{X}'_1}{J_2(\boldsymbol{\sigma} - \boldsymbol{X}_1)} \qquad (6)$$

inelastic strain rate for low stresses
$$\dot{\boldsymbol{\varepsilon}}_{in2} = \frac{3}{2} \cdot \frac{1}{1-D} \left\langle \frac{\sigma_{vis2}}{K_1(1-D)} \right\rangle^{n_2} \cdot \frac{\boldsymbol{\sigma}' - \boldsymbol{X}'_2}{J_2(\boldsymbol{\sigma} - \boldsymbol{X}_2)} = \frac{3}{2} \dot{p}_2 \frac{\boldsymbol{\sigma}' - \boldsymbol{X}'_2}{J_2(\boldsymbol{\sigma} - \boldsymbol{X}_2)} \qquad (7)$$

$$\text{accumulated inelastic strain rate} \quad \dot{p}_{1,2} = \sqrt{\frac{2}{3} \dot{\boldsymbol{\varepsilon}}_{in\,1,2} : \dot{\boldsymbol{\varepsilon}}_{in\,1,2}} \qquad (8)$$

two kinematic variables for high stresses (Ohno-Wang)

$$\dot{\boldsymbol{X}}_{1,i} = \frac{2}{3} c_{1i} a_{1i} \dot{\boldsymbol{\varepsilon}}_{in1} - c_{1i}\left(\phi_{1i} + (1 - \phi_{1i})e^{-d_{1i}p_1}\right) \boldsymbol{X}_{1i} \dot{p}_1 - \beta_{1i} \boldsymbol{X}_{1i} + \frac{d(c_{1i}a_{1i})}{dT} \frac{\boldsymbol{X}_{1i}}{c_{1i}a_{1i}} \dot{T} \qquad (9)$$

$$\boldsymbol{X}_1 = \sum_{i=1}^{2} \boldsymbol{X}_{1i} \qquad (10)$$

one kinematic variable for low stresses (Ohno-Wang)

$$\dot{\boldsymbol{X}}_{21} = \frac{2}{3} c_{21} a_{21} \dot{\boldsymbol{\varepsilon}}_{in2}(1 - D) - c_2 \boldsymbol{X}_{21} \dot{p}_2 + \frac{d(c_{21}a_{21})}{dT} \frac{\boldsymbol{X}_{21}}{c_{21}a_{21}} \dot{T} \qquad (11)$$

$$\text{isotropic variable} \quad \dot{R} = b(Q - R)\dot{p}_1(1 - D) + \gamma \, |Q_r - R|^{m-1}(Q_r - R) \qquad (12)$$

In [13] a damage approach of Lemaitre is used for the lifetime assessment of a thick-walled steam header. The total damage comprises of the fatigue damage and the creep damage. The damage variable is analogue to the damage variable in the GWD model based on the effective stress concept. The investigated header was

manufactured from Alloy 617 m and Alloy 263 and was part of a test loop in the project HWTII. The lifetime assessment with the CNOW model and the Lemaitre damage calculation led to the most realistic values.

3 Numerical Modelling of Weld Joints

To take the local effects of a weld joint into account in a numerical simulation, the different sections shown in Fig. 1 must be modelled numerically. In each section, different material parameters must be used. This is a simplification, which must be done to model the weld joint numerically. In reality, the material properties of the HAZ changes continuously with distance to the fusion line. However, it is important to use different material properties at least for the HAZ1 and HAZ3 to obtain the influence of the HAZ on the stress triaxialities. The width of the WM and the HAZ must be determined based on micro sections of the weld. In Fig. 3 on the left side, a typical numerical model for a weld creep specimen with one fusion line is shown.

To obtain the material parameters for the HAZ sections, microstructure simulated specimens were used. Those specimens were manufactured using PM rods, which were inductively heated to a characteristic peak temperature for each section and subsequently quenched in oil. The maximum peak temperatures were 1373 K for HAZ1, 1223 K for HAZ2 and 1148 K for HAZ3. In [14] it is shown that P92 develops the weakest creep strength with peak temperatures around 1173 K. The quenching is followed by annealing of weld joints according to VdTÜV. The advantage of this procedure is the usage of homogenous standard specimen for the characterisation of the HAZ material. The results of creep tests at 873 K with a stress of 160 MPa from [13] are shown in Fig. 4. The HAZ3 shows accelerated creep compared to the PM and HAZ2. The HAZ1 shows a slower creep behaviour. With those creep tests, material parameters for the GWD creep model for each

Fig. 3 Modelling of welds, left side: Full model, right side: Simplified model
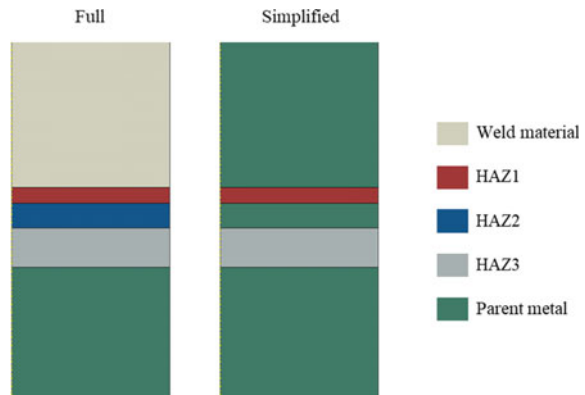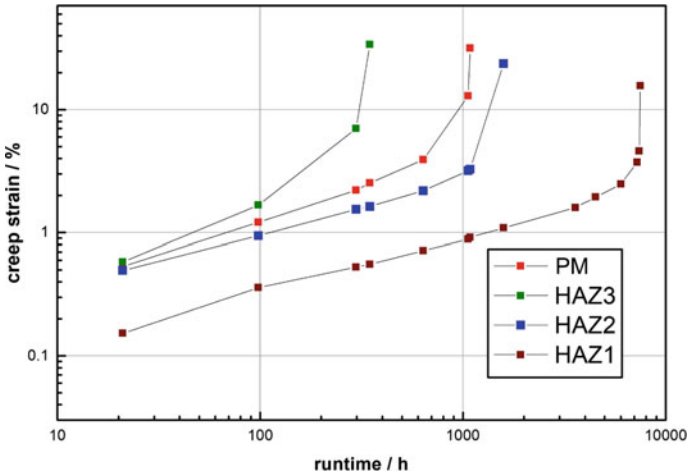
Fig. 4 Creep test parent metal and HAZ1-3, P92 [13]

section can be determined. Most of the times the creep behaviour of the WM is not known, but because most of the welds are overmatched, the WM has better creep properties than the PM. Therefore the usage of PM parameters is a conservative assumption. In Fig. 4 the HAZ2 shows similar creep behaviour as the PM, therefore the creep parameters would be similar. The error in the simulation by using PM parameters for HAZ2 is then negligible. As a result, the five-section model can be simplified to a three-section model, see Fig. 3 (right side). With the shown model and the GWD creep law the creep strain concentration and the stress multiaxially in the HAZ3 can be shown [9].

In addition to the creep properties, information about the cyclic behaviour is needed to identify the parameter of the viscoplastic CNOW. To obtain those information, fatigue tests with complex pre-program, so-called CLCF tests, are used. In the pre-program, different strain amplitudes and strain rates were tested. The first part is schematically shown in Fig. 7. The hold times were introduced to capture the relaxation behaviour of the material as well. Usually, after 3–4 iterations with different strain amplitudes, the pre-program is finished and followed by cyclic fatigue testing till failure of the specimen. As well as for obtaining the creep properties of the HAZ, CLCF tests with microstructure simulated specimen and with PM specimen were performed. The results for the complex pre-program are shown in Figs. 5 and 6 the results of the subsequent cyclic part are shown. A comparison of the different stress responses in the pre-program is difficult because slightly different programs were used.

On the basis of those test results and the creep tests results, the parameters for the PM and the HAZ were fitted using optimization tools. For a better comparison of the cyclic behaviour, the numerical results of the PM and the HAZ from an identical
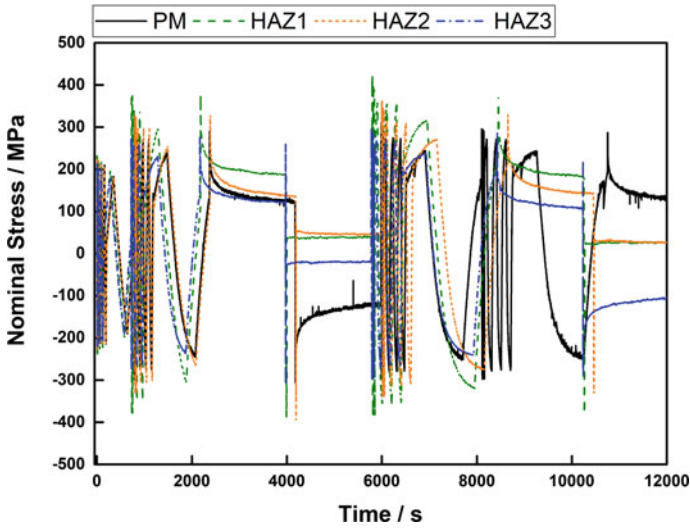
Fig. 5 Complex pre-program [13]
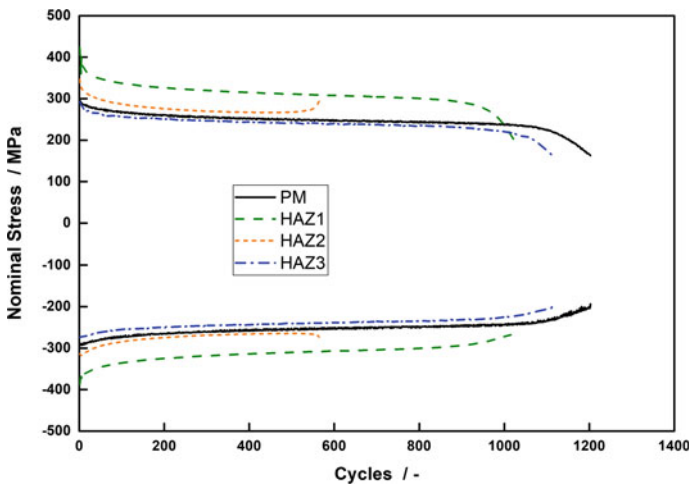
Fig. 6 Periodic part [13]

complex pre-program is shown in Fig. 8. Similar observation to the creep test can be obtained. The HAZ2 and the PM show nearly the same cyclic and relaxation behaviour, thus the effort to determine parameters for HAZ2 is not necessary as for the creep parameters. The HAZ1 responds with the highest peak stress values and little relaxation during the hold times. This observation suits the already known
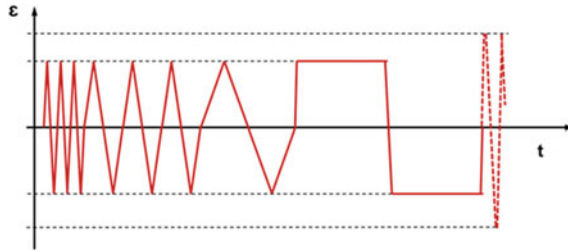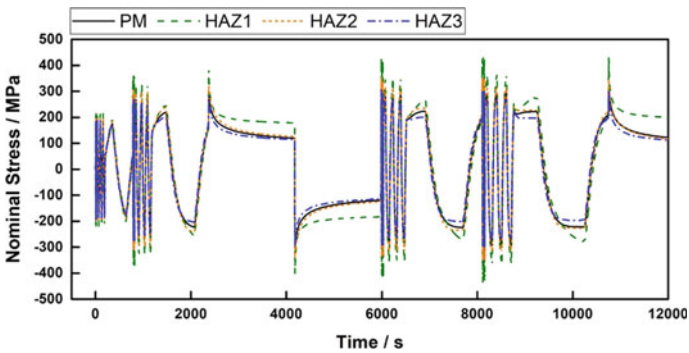
Fig. 7 First part of complex pre-program

Fig. 8 FEM results for parent metal and HAZ

creep behaviour. The smallest peak values were reached from the HAZ1 material which also shows the highest relaxation during the hold times. The same observation can be made with a comparison of the experimental results shown in Figs. 5 and 6. With those parameters, two different cross weld tests were simulated, the results and the comparison are shown in Sect. 4.2.

4 Experimental Results and Simulation of P92

In this section, two application examples of different methods, described in Sects. 2 and 3, are given. In Sect. 4.1 the assessment of a vessel subjected to internal pressure is shown, whereas in Sect. 4.2 an outlook in the assessment of weld joints subjected to creep-fatigue loads is presented. In the last subsection, some results of Creep-fatigue-crack and with corner crack specimen are shown.
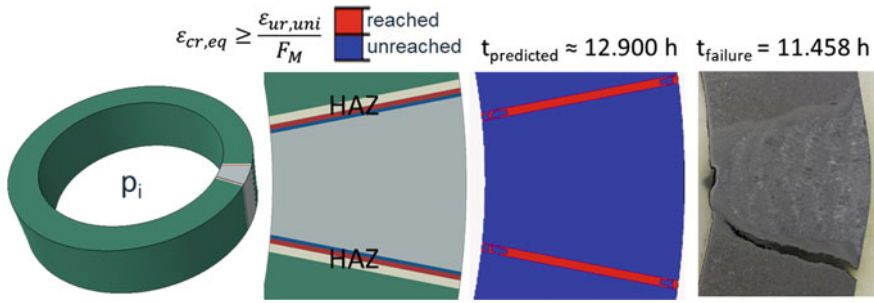
Fig. 9 Assessment of P92 vessel [1]

4.1 Vessel with Internal Pressure

The component test enables the possibility to verify assessment methods, material or weld joints in component like stress situations. At MPA Stuttgart, a component test with P92 material was performed to test a longitudinal weld. Even though longitudinal welds are not very common in the industry, this approach allows testing welds with only pure internal pressure without additional axial forces. The largest principal stress occurs vertical to the weld, which is the worst possible condition. The test temperature was 898 K and the pressure was 26.5 MPa. After 11.458 h, pressure dropped and a long longitudinal crack in the outer HAZ was found, as shown in Fig. 9 right. In [1] the assessment for this component test was presented. A section of the numerical model with weld can be seen in Fig. 9 left. For the simulation, the previously presented GWD creep law and the assessment method based on the uniform rupture strain ε_{ur} were used. Based on creep test of a different P92 melt, the uniform rupture strain, ε_{ur}, was determined. To apply the uniform rupture strain, $\varepsilon_{ur,uni}$, on a complex multiaxial stress state, the $\varepsilon_{ur,uni}$ is divided by a factor F introduced by [15, 16] The failure criterion, introduced by Schleyer in [1, 8] is reached when the equivalent creep strain, $\varepsilon_{cr,eq}$, is equal to or larger than $\varepsilon_{ur,uni}/F$. The results of the simulation are shown in Fig. 9. The criterion is first reached in HAZ3 close to the outer surface and expands then to the inner surface until the criterion is in the complete HAZ3 fulfilled. This time can be seen as the time of failure. With this assessment method, the failure time and failure location could be well predicted.

4.2 Fatigue and Creep-Fatigue Tests

In this section, one CLCF and one LCF test with strain controlled hold times on P92 similar welds at 873 K are simulated and compared. For the simulations, simplified weld model and the CNOW model are used. Figure 10 shows the result of the
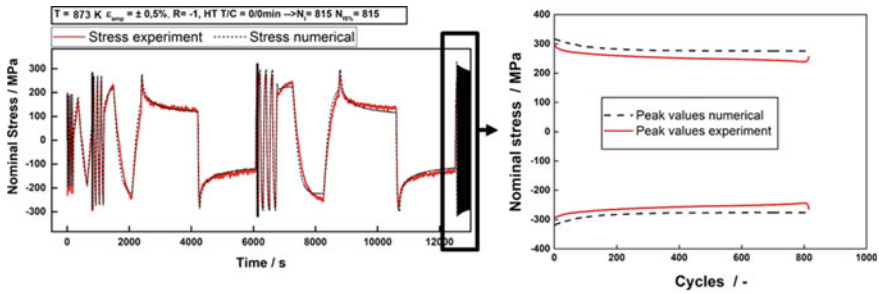
Fig. 10 Experimental and numerical results of CLCF test, P92 weld joint

complex pre-program and the cyclic part for both—experiment and simulation. A comparison between simulation and experiment shows that in the pre-program the conformity of simulation and experiment is very good. However, the stress peaks in the cyclic part are overestimated by the simulation. The specimen failed after 815 cycles. Several fine cracks were found in PM and HAZ. The failing crack is located in PM. The observed damage pattern is common for fatigue tests and the occurred failure can be interpreted as typical PM failure.

The test setup for the second investigated test was alternating between cyclic and hold time testing. After each hold time, the number of cycles were increased. The comparison between the simulation and the experiment is shown in Fig. 11 on the left. Since the cyclic damage parameters of the CNOW model are not used in this parameter set, the simulations show no cyclic softening. The peak stresses are overestimated at the end of the simulation. The relaxation behaviour for the first four hold times is well reproduced. After the test, only one crack in the HAZ was found.

For the assessment of weld joints, the investigation of local strain and stresses is essential. The equivalent strain plots in Fig. 11 on the right show the conditions before (B) and after (C) the fifth hold time. It can be easily seen that during the hold times the strain accumulates in HAZ3. This happens due to the weak creep strength and high triaxiality in HAZ3.
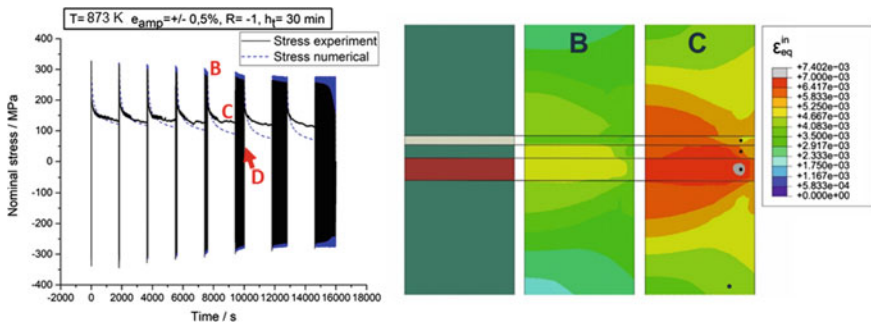
Fig. 11 Experimental and numerical results of LCF test with hold times, P92 weld joint
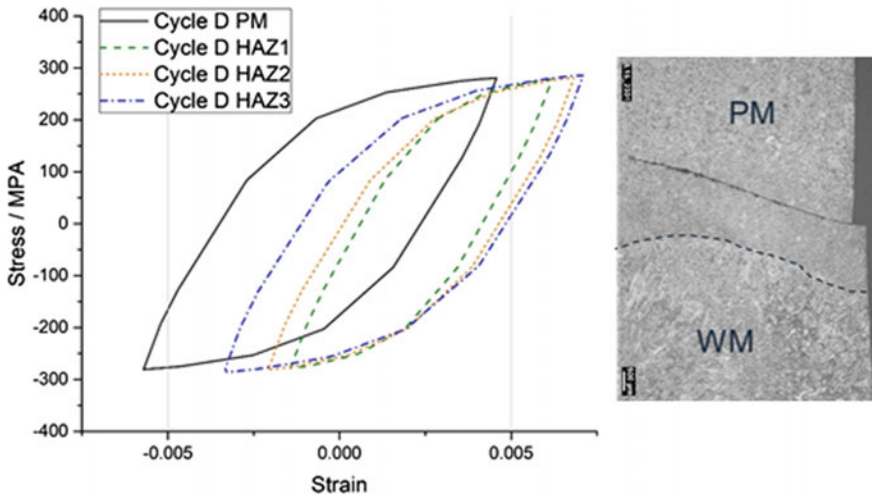
Fig. 12 Local hysteresis loops LCF test with hold time, microsection of specimen

In Fig. 12 the hysteresis loops for the element in the middle of each zone for the last cycle, cycle D, of the cyclic part after the fifth hold time is shown. The strain accumulation in the HAZ, especially in HAZ3, leads to a shift of the local hysteresis loops to larger strain values. The HAZ3 and HAZ2 show the largest strain at peak.

A comparison of the hysteresis loops of the CLCF tests at cycle $N_{f/2}$ is shown in Fig. 13. The HAZ1 and HAZ2 are subjected to the smallest hysteresis loops. The PM and HAZ1 on the other hand show larger and very similar, expect a slight shift, loops. The difference in the loops of the CLCF test is quite small. Without hold time a shift of the hysteresis loops of the HAZ does not occur.

A comparison of the different hysteresis loops behaviour with regards to the different failure location indicates that the shift in the hysteresis loops of the LCF test caused by the hold times could be a possible explanation for the different location. The largest strain at peak in the CLCF test simulation is in the PM Fig. 13. The simulation of the LCF test with hold times shows the largest strain at peak in the HAZ Fig. 12. During pure fatigue testing the HAZ1 seems to have some kind of supporting effect for the HAZ. This observation is, of course, a hypothesis and needs further investigations.

4.3 Experimental Results of Fracture Mechanic Tests

Only little is known of the creep-fatigue-crack behaviour of weld joints. This is topic of a research project at MPA Stuttgart. To allow a direct comparison of different crack location with one corner crack specimen a new test method was developed. Two cracks, with a slightly vertical offset, were eroded in opposite
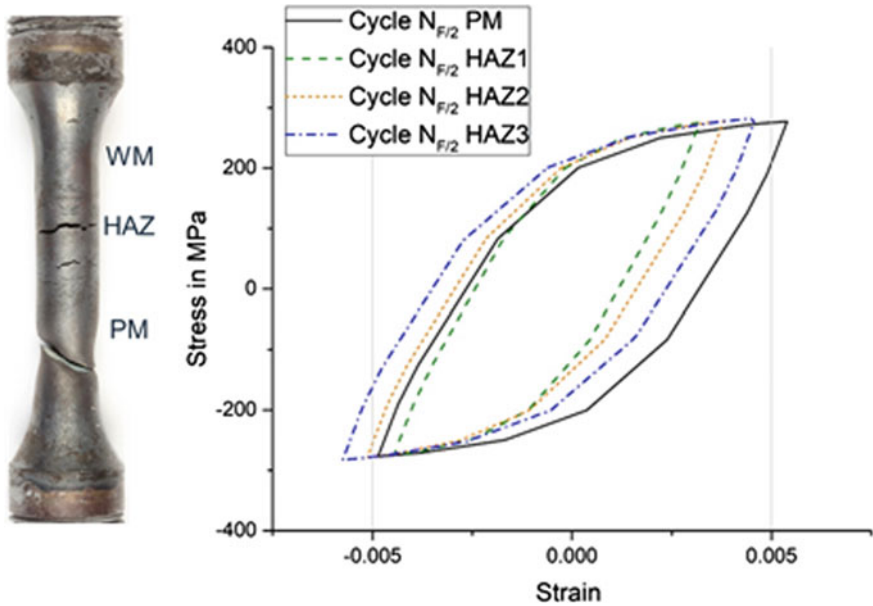
Fig. 13 Local hysteresis loops CLCF test, damage pattern of specimen

edges of the specimen. One starter crack was located in the HAZ and the other in the WM, see Fig. 14. After the instrumentation two with extensometers, potential measurements for both cracks and one thermocouple the specimen was heated to 898 K. The specimen was tested with a stress ratio of −1 and a hold time in tension of 10 min. The maximum nominal stress was 95.3 MPa. After 6791 cycles respectively 1170 h a rise in both potentials was observed and the test was stopped. For the crack in the HAZ a larger rise in the potential was measured. The test setup after testing is shown in Fig. 15.
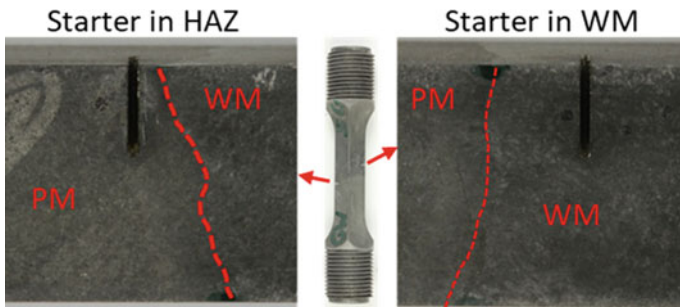
Fig. 14 Crack starter in 2 Crack specimen (CC)

Fig. 15 Test setup (after testing)

Both cracks were broken up and the crack length was measured. The fracture surfaces are shown in Fig. 16. The crack length in HAZ is 4.9 mm and in WM 3.71 mm. For the crack in the HAZ, a micro section through both crack surfaces was prepared and can be seen in Fig. 16.

The crack grows straight into the material at first but after some time the direction changes and the crack grows closer to the fusion line respectively deeper in the HAZ. Only in the region around the crack creep cavities were found. A comparison of the da/dN over the maximum stress intensity factor $K_{I,max}$ of both crack locations and another similar—but with a one crack specimen—PM test are shown in Fig. 17. Crack initiation (0.5 mm) occurred after 650 h for the crack in
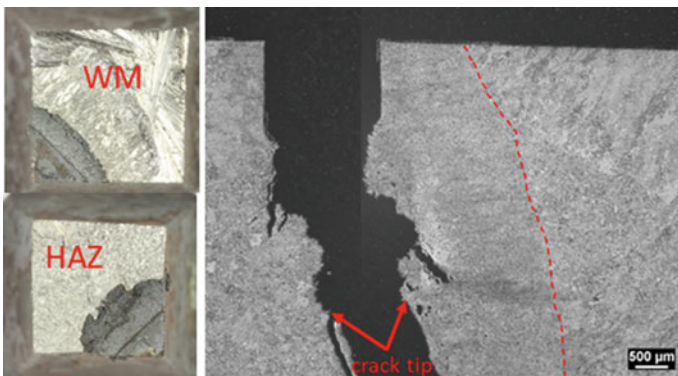
Fig. 16 Fracture surfaces and mircosection of HAZ crack
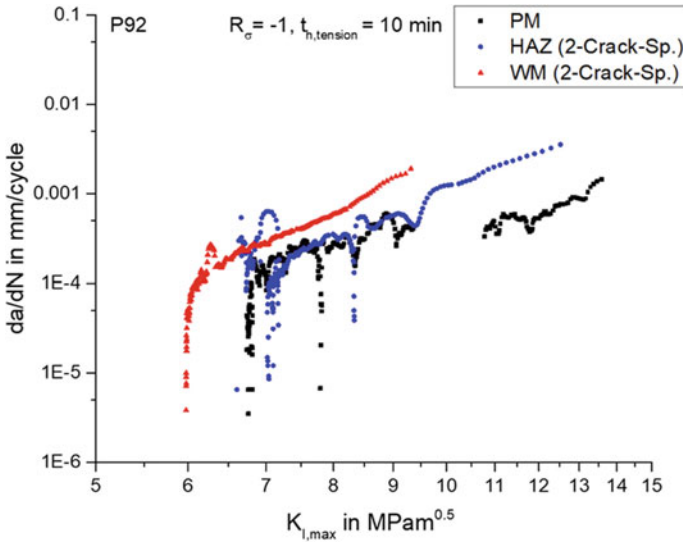
Fig. 17 Fatigue crack growth

HAZ, 960 h for the crack in WM and 800 h for the crack in the PM. The crack growth seems to be similar for all three crack locations but the crack initiation is different. Further experimental and numerical investigations of the creep-fatigue-crack behaviour of the different weld zones are planned.

5 Conclusions

Different methods for the assessment of weld joints were presented. Nowadays the creep behaviour and assessment are well known. It was shown that a strain-based failure criterion is a very well approach regarding the predicted failure time and location for a P92 creep component test. However, the creep-fatigue behaviour and assessment are still challenging tasks. Different failure locations have been observed for different test conditions in the literature and on tests performed at MPA. The reasons for the change in the failure location due to hold time is not fully understood. The numerical simulations were performed for better understanding. A shift in the local stress–strain hysteresis, which may be an explanation for the different failure locations was shown in simulations for the LCF test with hold time. However, this is still a topic of ongoing research. With a better understanding of the local behaviour, it may be possible to develop a strain-based assessment approach for welds under creep-fatigue loads. A complete assessment approach should include the assessment of cracks and defects but only little is known about the creep-fatigue-crack behaviour of welds. First test results show that the crack growth

behaviour of the different zones may be similar, but the HAZ shows the smallest crack initiation time. To verify this observation, further experiments and numerical simulations are needed.

References

1. J. Schleyer, T. Bender, A. Klenk, Developments in assessment of welds under creep, fatigue and creep-fatigue loadings, in *Conference on Power Plant Operation and Flexibility* (London, 2018) pp. 4–6
2. M. Bauer, *Optimierung der Schweißverbindung zur Verhinderung des vorzeitigen Kriechversagens in der Wärmeeinflusszone über die gezielte Festigkeitsauswahl des Schweißgutes*: MISMATCH. Abschlussbericht, AVIF Forschungsvorhaben Nr. A221, MPA Universität Stuttgart (2009)
3. J. Veerababu, S. Goyal, R. Sandhya, K. Laha, Low cycle fatigue behaviour of grade 92 steel weld joints. Int. J. Fatigue **105**, 60–70 (2017)
4. T.P. Farragher, S. Scully, N.P. O'Dowd, C.J. Hyde, S.B. Leen, High temperature, low cycle fatigue characterization of P91 weld and heat affected zone material. J. Press. Vessel Technol. **136**(2), 021403 (2014)
5. Y.Takahashi, M. Tabuchi, Creep and creep-fatigue behavior of high chromium steel weldment, Acta Metall. Sin. (Engl. Lett.) **24**, 175–182 (2011)
6. V. Shankar, K. Mariappan, R. Sandhya, M.D. Mathew, Evaluation of low cycle fatigue damage in grade 91 steel weld joints for high temperature applications. Procedia Eng. **55**, 128–135 (2013)
7. A. Hobt, Bewertung von Fehlstellen im Kriechbereich; Ph.D., IMWF and MPA Stuttgart (2015)
8. J. Schleyer, M. Speicher, A. Klenk, M. Seidenfuß; Assessment of welds in components with similar martensitic welds using cross weld data and numerical calculations, in *4th International ECCC Conference*, (Düsseldorf, Germany, 2017) pp. 10–14
9. A. Klenk, K. Maile, M. Bauer, Modelling and assessment of welds at high temperature; IIW (2008)
10. J.L. Chaboche, Viscoplastic equations for the description of cyclic and isotropic behavior of metal*s*, Bulletin de l'Académie Polonaise des Science, Série des Science techniques, vol. XXV, 1 (1977)
11. D. Nouailhas, Unified modelling of cyclic viscoplasticity, application to austenitic stainless steels. Int. J. Plast. 5 (1989)
12. N. Ohno, Constitutive modelling of cyclic plasticity with emphasis on ratchetting. Int. J. Sci. 40, 251/261 (1998)
13. P. Buhl, F. Baras, D. Hüggenberg, A. Klenk, Life assessment of Marten-sitic steels and nickel based alloys in the creep fatigue regime, in MPA Universität Stuttgart (Hg.), 41st MPA Seminar (Stuttgart, Germany, 2015), pp. 5–6
14. F. Abe, M. Tabuchi, S. Tsukamoto, T. Shirane, Microstructure evolution in HAZ and suppression of type IV fracture in advanced ferritic power plant steels. Int. J. Press. Vessels Pip. **87**, 598–604 (2010)
15. M.J. Manjoine, Ductility indices at elevated temperature. J. Eng. Mater. Technol. **97**(2), 156–161 (1975)
16. M.J. Manjoine, Creep-rupture behavior of weldments. Weld. J. **61**, 50–57 (1982)

Creep Rupture Behaviour of Alloy 625 Nickel-Base Superalloy Casting for Advanced Ultra Supercritical Power Plant Applications

Somnath Nandi, G. Jaipal Reddy, Dhirendra Kumar and Kulvir Singh

Abstract In the twenty-first Century, the world especially India faces the critical challenge of providing abundant, and cheap electricity to meet the needs of a growing global population, while at the same time, preserving environmental values which are very important. Traditional methods of coal combustion emit pollutants (including CO_2) at high levels relative to other power generating options. Maintaining coal as a generating option will require methods for addressing these environmental issues. To reduce CO_2 emissions, research and development on Advanced Ultra Super Critical (AUSC) power generation is ongoing to enhance the efficiency of a coal-fired power generation. In an AUSC plant, it is considered to use Nickel-base superalloys with higher strength capabilities at elevated temperature conditions in addition to conventional heat-resistant steel. Alloy 625 nickel-base superalloy is selected for the steam turbine casing in AUSC power plant applications because of its better properties. In higher temperature domain, Creep is one of the major properties to be assessed for the material to be used in AUSC power plants. Creep rupture tests along with other mechanical tests were conducted on Alloy 625 cast material at elevated temperatures to generate the data for design applications. In this paper, creep behaviour of Alloy 625 is presented at various stress and temperatures and microstructures are correlated along with other mechanical properties.

Keywords AUSC power plant · CO_2 emissions · Alloy 625 casting · Mechanical properties · Creep rupture

S. Nandi (✉) · G. Jaipal Reddy · D. Kumar · K. Singh
Metallurgy Department, Corporate R&D Division, BHEL, Hyderabad 500 093, India
e-mail: somnandi@bhel.in

1 Introduction

Energy security combined with lower carbon dioxide emissions is increasingly quoted to protect global environment by twenty-first century. In India, electric power generation by coal-fired power plants have increased to meet the needs of growing population and economy as coal is abundant. However, traditional coal-fired power plants emit harmful gases such as CO_2, NOx, SOx at high levels relative to other electric power generating options. Adaptation of the ultra supercritical power plants with increased steam parameters significantly improves efficiency, which reduces the fuel consumption and the emissions of gases responsible for environmental damage [1, 2]. Coal-fired supercritical-steam power plants are currently operating with steam temperatures at the inlet to the high-pressure turbine close to or slightly above 600 °C. The use of recently developed ferritic steel is expected to allow this temperature to be raised to 620 °C, which probably represents the inherent limit of capability of these advanced steels. Further increases in temperature will require the use of Ni-base alloys. The range of alloys used in steam turbines is relatively small, partly because of the need to ensure a good match of thermal properties, such as expansion and conductivity, and partly because of the need for high-temperature strength at acceptable cost. The use of commercial alloys depends upon the maximum temperatures and pressures to which specific components will be exposed, and these are heavily dependent upon the detailed design of the turbine, which can vary significantly among the various manufacturers. For higher temperatures, Ni-based alloys will be required, and the question will be whether adequate strengthening can be developed in cast alloys, or whether wrought alloys will be needed. Out of various materials in the pipe line, 625 superalloy is selected for the Indian Advance Ultra Supercritical (AUSC) power plant applications but the major materials needs are for Ni-based alloys for operation at 720 °C with (i) adequate creep rupture strength; (ii) abilities to cast them into the required size and shape, and to inspect for defects; and (iii) ability to perform initial fabrication, welding (on cast or wrought forms, including dissimilar metal welds), and to make repair welds on aged material. Creep is one of the major properties to be assessed for the material to be used in AUSC power plants. Studies on high-temperature material properties are being carried out in every parts of the world as Alloy 625 is identified as one of the major material for the Advanced Ultra Supercritical power plant applications. Creep plays a vital role in the selection of the material for high-temperature applications. In our present study, the microstructural analysis is carried out on the ruptured samples and observed that the precipitates are mostly rich in chromium, when analysed by energy dispersive X-ray analysis (EDS). The blocky particles M(C, N), are mainly composed of titanium, when analysed by EDS, and are randomly distributed in the matrix and at grain boundaries. The precipitation of intermetallic γ'' and Ni_2(Cr, Mo), inter and intragranular carbides impart high strength to the alloy for service exposed condition [3]. In similar manner, in as received condition the EDS result shows the precipitates to be Cr-rich $M_{23}C_6$ carbides, Niobium carbides and Ti(C, N). The

morphology of the precipitates was found to vary considerably from irregular geometries to a more symmetrical cubic geometry. The precipitates of Ti, Nb-rich/ carbides as well as Cr, Mo, Nb carbides form at grain boundaries in Alloy 625 [4].

This study investigates the creep behaviour of Alloy 625 at high temperatures along with tensile properties at high temperatures and microstructure correlation of the alloy using optical and Scanning Electron Microscopy analysis

2 Experimental

2.1 Materials

Alloy 625 casting used in this study has been procured as a cast step block from M/ s Voestalpine, Austria. The chemical composition of Alloy 625 is given in Table 1. The cast block was solution annealed at a temperature of 1200 °C for 10 h and subsequently, water quenched. The microstructure of the as received alloy is shown in Fig. 1.

2.2 Experimental Procedure

The cast step block (casting) as received from M/s Voestalpine, Austria as per the material data generation program for Indian Advance Ultra Supercritical (AUSC)

Table 1 Chemical composition of Alloy 625

Element, wt%	C	Mn	Si	P	S	Mo	Fe	Cr	Nb	Al	Ti	Ni
Alloy 625	0.018	0.147	0.241	0.009	0.004	8.319	2.481	21.00	3.266	0.206	0.209	Bal
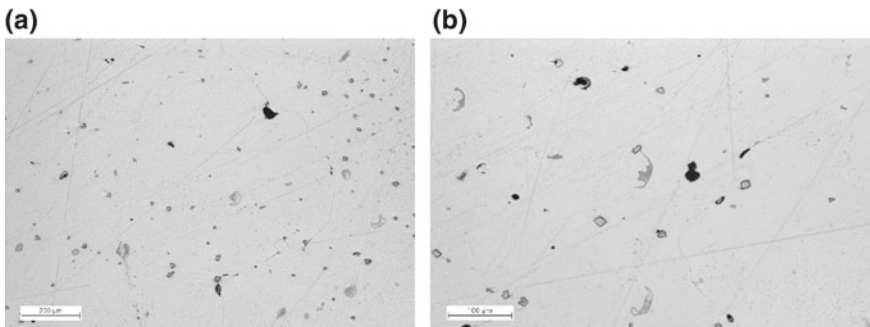
Fig. 1 Microstructure of as received Alloy 625 **a** 100X **b** 200X respectively

technology development, was cut down from the centre location of the step block of top portion of 300 mm × 300 mm × 300 mm into standard creep testing sample (M8) as per ASTM E139. The creep sample prepared and tested in a constant load Creep Testing machine (*Mayes* make) under different stresses and temperatures. The temperature ranges from 650 to 800 °C where as stresses are varied from 160 to 360 MPa. Apart from the creep testing, tensile tests were also carried out at different temperatures to study the mechanical behaviour of Alloy 625 for advance ultra-super critical power plant applications.

Microstructural analyses are also carried out on the tested samples to investigate and correlate the structural changes of the alloy with the mechanical properties of the alloy. Subsequently, hardness measurements are done to analyse the changes in hardness of the alloy on effect of various stresses and temperatures applied on the alloy.

The study is basically the initial work started for the material development program taken for Indian Advance Ultra Super critical power plant technology.

3 Results and Discussion

3.1 Creep

Creep is one of the important material properties for high-temperature applications, especially in thermal power plants. For AUSC power plants the operating temperatures are very high in the range of 720 °C where creep testing of the Alloy 625 is very much important. As for Alloy 625 superalloy (cast form) is concerned, creep rupture tests were performed at different stresses and temperatures and subsequently microstructural analyses were carried out to examine the effect on microstructure due to creep. The creep rupture testing was being carried out in the range of 650 to 750 °C with different stress condition ranging from 125 to 275 MPa. Figure 2
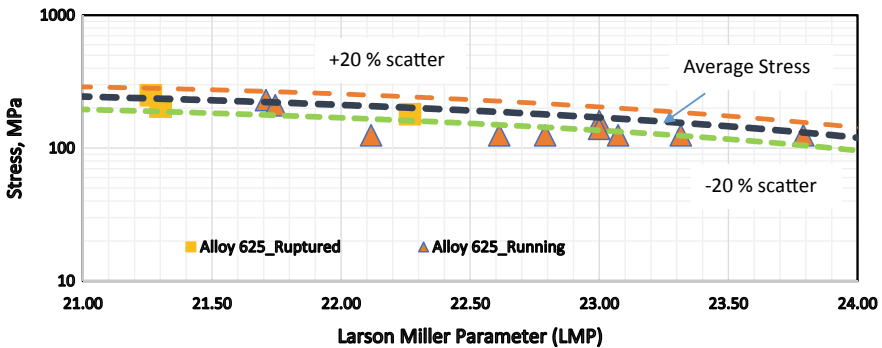
Fig. 2 Stress with LMP Plot for Alloy 625 casting

shows the plot between the stress applied and the Larson Miller Parameter (LMP) obtained from the creep rupture testing of the Alloy 625 at different stresses and temperatures. The majority of the creep tests are ongoing and they are in their secondary stages, hence it can be inferred that the LMP points obtained from their rupture values are expected to come in the average stress range as indicated in Fig. 2. The average stress has been calculated based on the various literature data and manufacturer's test data and compared with the testing data.

3.2 Effect of Creep on Microstructure

Creep rupture tests were carried out at temperatures 650 and 700 °C at different stresses to see the effect of creep behaviour on the microstructures. In this paper, two test conditions are discussed, one at 650 °C with 230 MPa and another one at 700 °C with 180 MPa of stress. In the first case, the rupture hours estimated around 200 h (early ruptured) whereas in second condition the rupture hour was around 768 h. Microstructural studies like optical and Field Emission Scanning Electron Microscopy were carried out along with EDS analysis where it revealed the isolated
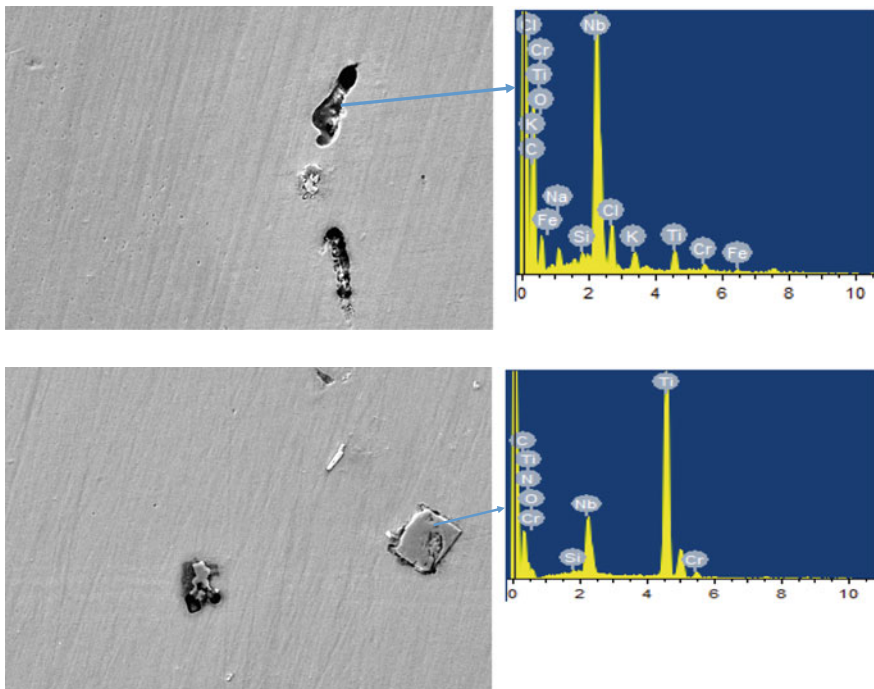
Fig. 3 SEM Micrograph at 2000X along with EDS Analysis of crept sample tested at 650°, 230 MPa

carbide precipitation which are Cr, Mo and Nb-rich in 650°. In 700° case, the carbide precipitates are small and evenly distributed over the matrix where as in 650°, the carbide precipitates are large in size and unevenly distributed over the matrix area.

The results of two creep test condition are very much the initial tests carried out for Alloy 625 casting. The test parameter for 650 and 700 °C with stress level of 230 and 180 MPa were expected for 3000 h but unfortunately it prematurely failed at 200 h and 768 h respectively. Both the crept samples were cut and scanning electron micrography was carried out along with Energy dispersive spectroscopy (EDS) on the precipitates found in the matrix as shown in Figs. 3 and 4 respectively. In Fig. 3, which shows isolated carbide and Ti precipitates, non-uniformly dispersed in the austenitic matrix causing for early failure. The microstructure appears similar to the microstructure of the re-solution annealed material before creep testing while in Fig. 4, which also shows carbide and Ti precipitates in smaller sizes and uniformly dispersed in the austenitic matrix as compared to Fig. 3. For Fig. 4, it appeared that a certain degree of precipitate dissolution has taken place, resulting in thinner precipitates. The degree of precipitate dissolution
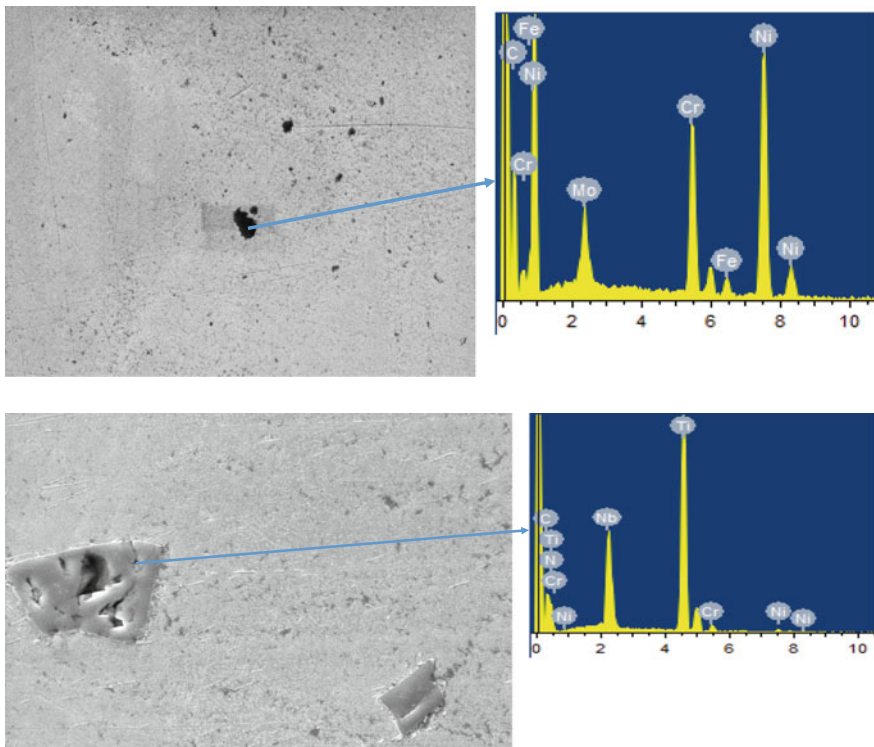
Fig. 4 SEM Micrograph at 2000X along with EDS Analysis of crept sample tested at 700°, 180 MPa

appeared to have increased on exposure to higher temperature as seen from the micrograph of the alloy after testing at 700 °C, although the 768 h test time was very less [5, 6].

Since, these are the initial crept samples which prematurely failed, hence detailed correlation will be made later. As per the other tests running at 650 and 700 °C with different stress levels, the Alloy 625 casting is showing better life and comparable to literature data (Fig. 2).

3.3 Mechanical Properties

Apart from creep testing on Alloy 625 casting, mechanical properties assessment in terms of tensile testing has been carried out in room temperature as well as elevated temperatures. Figure 5a, b shows the 0.2% Yield strength and Ultimate tensile strength data of Alloy 625 plotted against temperature. The tested data (0.2% yield
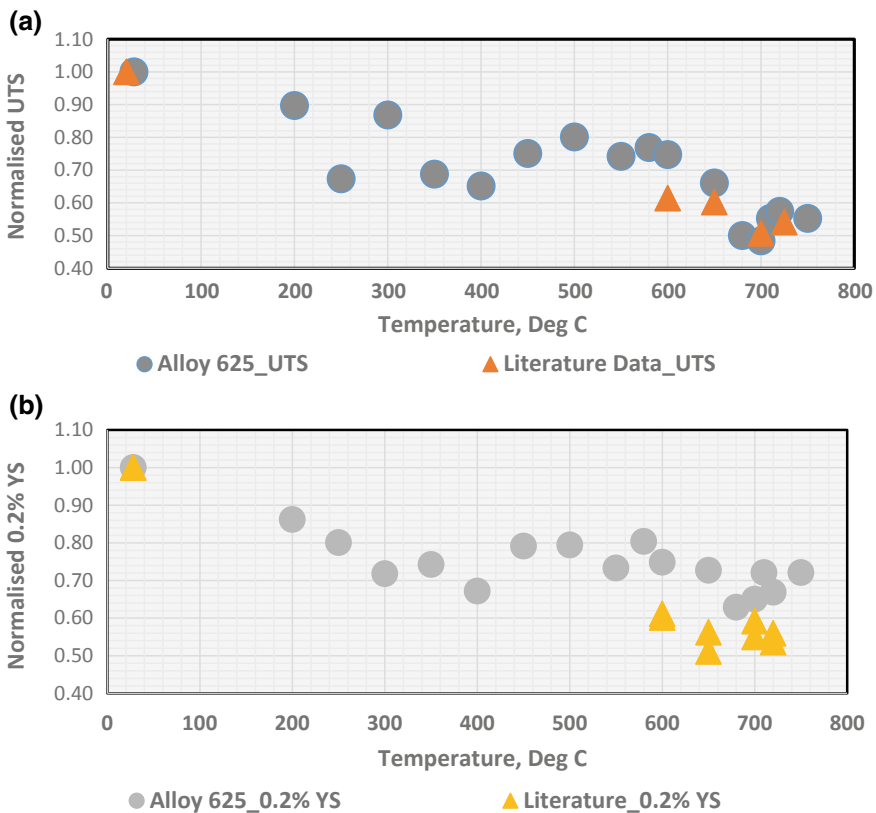
Fig. 5 a, b UTS & 0.2% YS plots at elevated temperatures for Alloy 625 casting

and UTS) are much higher than the literature data obtained from various alloy manufacturer and it gives the confidence for applications of casing component for AUSC power plant.

4   Conclusions

- Plotting the Larson Miller curve for the Alloy 625 casting indicated that the material shows good creep strength at high temperatures and stresses within the regime of 700 °C.
- The presence of carbides, especially the Cr-rich $Cr_{23}C_6$ type, Nb-rich & Ti precipitates were the important microstructural features which is thought to be precipitated mainly in the matrix.
- Mechanical properties data (0.2% YS & UTS) of Alloy 625 shows good strength at elevated temperatures especially in the domain of 700 °C
- The study is basically an initial work for the Alloy 625 casting for the material development program for Indian AUSC power plants, hence a detailed correlation of the creep strength and other mechanical properties with the microstructure are to be studied.

References

1. G. Wright, et al., Materials issues for turbines for operation ultra-supercritical steam
2. R. Viswanathan, Annual Progress Report, Steam turbine materials for ultra supercritical coal power plants
3. Vani Shankar et al., Microstructure and mechanical properties of Inconel 625 superalloy. J. Nucl. Mater. **288**, 222–232 (2001)
4. W. Yu, et al., Recent development in the characteristics of alloy 625 for A-USC steam turbine casting. *Energy Materials 2017, The Minerals, Metals & Material Series*. https://doi.org/10.1007/978-3-319-52333-0_20
5. M. D. Mathew, et al., Microstructural changes in alloy 625 during high temperature creep. Mater. Charact. **59**, 508–513 (2008)
6. M.D. Mathew, et al., Creep properties of service-exposed alloy 625 after re-solution annealing treatment. Mater. Sci. Eng. A **372**, 327–333 (2004)

Part VIII
Design, Analysis and Fabrication

Feasibility of ACI 318-14 Strut-and-Tie Provisions for the Analysis and Design of Rubcrete and Steel Fibre Reinforced Rubcrete Deep Beams

M. S. Sandeep, Praveen Nagarajan and A. P. Shashikala

Abstract The regions in a structure with linear strain distribution are generally called as Bernoulli's region (B-region) while the regions with nonlinear strain distribution are called Disturbed region (D-region). Most commonly used theories for the analysis and design of concrete structures are applicable only for B-regions since they are based on the assumption of linear strain distribution. This compels the structural designers to depend on empirical relations and thumb rules for the analysis and design of D-regions. Strut-and-Tie method is a newly developed design methodology that has the potential to analyse and design D-regions as well as B-regions with equal importance. The primary factor that influences the effectiveness of Strut-and-Tie method is the strut efficiency factor (βs). Even though Strut-and-Tie method is included in many of the International Standards like American code ACI-318-14, Canadian code CSA-A23.3-14, Australian code AS 3600-2009, Euro code EC2:2004, New Zealand code NZE 3101-1-2006, etc. the mentioned procedure is applicable only for conventional reinforced concrete. The paper highlights the development of strut efficiency factor (βs) for bottle-shaped strut in concrete deep beams (a D-region) with and without crumb rubber and steel fibre based on experimental and numerical studies. The obtained value of strut efficiency factor is used to check the feasibility of using the available value of βs for calculating the strength of concrete struts cast using rubcrete and steel fibre reinforced rubcrete (SFRR). Initially, the proposed method of analysis was validated using available experimental results. Good agreement was observed between the experimental failure load and deflection and that produced from numerical analysis.

Keywords Strut efficiency factor · Strength reduction factor · Rubcrete · SFRC · Ansys · Numerical analysis

M. S. Sandeep (✉)
Department of Civil Engineering, Muthoot Institute of Technology and Science,
Kochi 682308, Kerala, India
e-mail: sandeep.ms1986@gmail.com

P. Nagarajan · A. P. Shashikala
Department of Civil Engineering, National Institute of Technology Calicut,
Kozhikode 673601, Kerala, India

Nomenclature

B-regions	Bernoulli's region
β_s	Strut efficiency factor
SFRR	Steel fibre reinforced rubcrete
A_{cs}	Area of cross-section of strut
f'_c	Cylinder compressive strength
D-region	Disturbed region
STM	Strut-and-tie method
W_s	Width of strut
P_u	Peak Load
f_{ck}	Cube compressive strength

1 Introduction

Ductility is an important property for the material of any structural member that defines its seismic resistance. As far as normal concrete is considered it is brittle in nature. Hence, use of newly developed ductile construction material is always preferable. Rubcrete is a recently developed concrete which uses rubber particles taken from waste tyre, for partially replacing its aggregates. From the research works conducted on rubcrete it is found that the presence of rubber particles improves the ductility, toughness and impact resistance of the resulting concrete material. The major drawback of rubcrete is the reduction in compressive strength arising due to the presence of rubber particles. Mohamed et al. [1] studied the performance of full scale self-consolidating rubberized concrete beams and ordinary rubberized beams in flexure. It was observed that with increase in percentage of rubber content there was a reduction in compressive strength, concrete stiffness and first crack load. On the other hand, the deformation capacity, ductility and toughness of the tested beams were improved with the addition of rubber particles to a reasonable amount. Research conducted by Segre et al. [2] and Najim et al. [3] shows that pre-treatment of rubber particles with chemicals like NaOH, Polyvinyl Alcohol, etc. before its application in concrete will help in improving the bond between rubber particles and surrounding matrix. The addition of discrete fibres is another supplementing method by which the flexural and tensile strength of rubcrete can be enhanced. If pre-treated crumb rubber along with discrete steel fibre is added to concrete mix, the advantages of both rubcrete and steel fibre can be combined along with a control over the reduction of strength. Such a cementitious composite material containing crumb rubber along with steel fibre is termed and steel fibre reinforced rubcrete (SFRR).

During the design of high rise buildings and other major structures in earthquake prone areas, the shear predominant regions must be given due importance. The shear predominant behaviour of structural members like deep beams, beam-column joints, corbels, etc. will result in brittle mode of failure which is not preferred. If these shear predominant members are cast using SFRR, it is possible to bring in a better ductile mode of failure in comparison to the members cast using conventional concrete.

Structural members can be divided into two regions namely Bernoulli's region (B-region) and Disturbed region (D-region). This classification is done based on the variation of strain distribution existing in these regions. The conventional design methods are developed based on Bernoulli's hypothesis which assumes linear strain distribution. Such methods cannot be used for designing D-regions. As a result, the design of such regions is carried out based on past experience, thumb rules and empirical equations. Strut-and-tie method (STM) offers an alternative to such empirical method. Since STM is a realistic approach, many international codes like American code ACI-318-14, Canadian code CSA-A23.3-14, Australian code AS 3600-2009, Euro code EC2:2004, New Zealand code NZE 3101-1-2006, etc. have already adopted it.

The basic procedure in STM is to idealise the actual structure using an equivalent truss and to analyse it for the applied loads. A simple strut-and-tie model adopted for analysing a deep beam is shown in Fig. 1. STM consists mainly of three parts namely concrete strut, tension tie and nodes. The tension member provided in a STM which is used to represent the reinforcing steel is called tension tie. The member of a STM used to represent the compression zone is usually termed as a concrete strut and the point at which these members intersect are termed as nodes. These different components of a STM adopted for a deep beam are shown in Fig. 1.

The accuracy of STM greatly depends on the correct estimation of the strength of concrete strut. One of the main parameters that influence the prediction of the strength of concrete strut is the Strut efficiency factor. A lot of research work was done to establish the allowable strength of concrete strut for normal concrete. On the other hand, the work done to check the feasibility of existing models or work

Fig. 1 STM for a deep beam
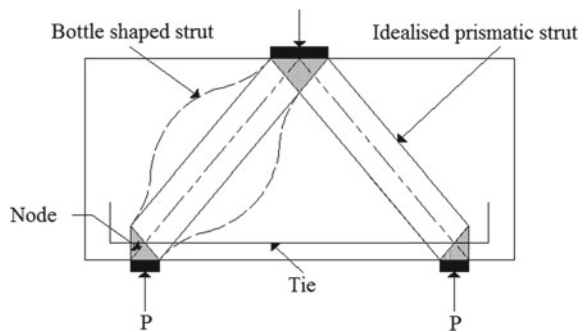
done to estimate the allowable strength of strut for concrete having fibres and rubber particles are limited. Sahoo et al. [4, 5] conducted studies on strut efficiency factor for bottle-shaped struts in deep beams. They concluded that the bottle-shaped strut have similar strength as that of prismatic strut. They also recommended revision of strut efficiency factor for bottle-shaped struts. Based on the investigation they proposed the following lower bound predictive model for efficiency factors of struts made of normal weight natural aggregate concrete having fc' up to 82 MPa.

$$\beta = \left(0.6 + \frac{0.05}{r_c} + 55\rho_T\right)\left(\frac{\alpha_s}{90}\right) \tag{1}$$

Yang and Ashour [6] have conducted an experimental study on continuous deep beams and a reduction in strut efficiency value was observed while the depth and strength of concrete were reduced. Brown et al. [7] and Quintero-Febres et al. [8] compared experimental data with the STM provisions in ACI code. The former found that the equation given in ACI for finding the amount of reinforcement required in a strut produced conservative but unpredictable results in comparison with test results. It was found that the results produced using a strut efficiency factor $\beta s = 0.60$ in high strength concrete were 10% higher than the experimental failure load. Quintero-Febres et al. [8] observed inconsistencies in ACI provisions for minimum reinforcement crossing a strut in comparison to the test data. Ashour and Morley [9] conducted an upper-bound analysis of reinforced concrete continuous deep beams. By calibration of the calculated failure load against the experimental failure load, they produced effectiveness factor for concrete in compression. They have proposed the following expression for the efficiency factor mainly applicable to bottle-shaped struts in continuous deep beams.

$$\beta s = 0.77 - \frac{f_c'}{110} - \frac{\rho}{0.85} \tag{2}$$

where ρ is the weighted reinforcement ratio for the horizontal and vertical reinforcement based on their relative contribution to the load capacity of continuous deep beams, βs is the strut efficiency factor and f_c' is the compressive strength of concrete.

Strut-and-tie provisions were first introduced in Building Code for structural concrete, by American Concrete Institute (ACI) in 2002. ACI 318-14 [10] uses strut efficiency factor for estimating the strength of concrete strut which in turn modifies the compressive strength of concrete. The present ACI code, ACI 318-14 recommends discrete values of strut efficiency factor for both strut and nodes. For example, a value of 0.75 is recommended for Bottle-shaped strut which have at least 0.3% effective transverse reinforcement.

The aim of the present investigation was to study the effect of rubber particles and steel fibre on the strut efficiency factor of concrete deep beams and to check the feasibility of using ACI 318-14 Strut-and-tie provisions for the analysis and design

of deep beams cast using rubcrete and SFRR. Numerical study along with experimental results was used for this purpose. Based on the failure load, the strut efficiency factor for different deep beam specimens was found out.

2 Nonlinear Finite Element Analysis Using Ansys

The present numerical investigation made use of Solid 65 element for modelling concrete. It is an element having eight nodes, available in ANSYS element library [11]. Each of these eight nodes have three degrees of freedom. This element has the ability to undergo plastic deformation, crushing and cracking in all three directions. It also has the ability to model rebar in required orientation.

The main reinforcement and side face reinforcement in the deep beams were modelled using link 180 elements present in ANSYS element library. It has two nodes with three degrees of freedom at each node. The steel plates provided at support and loading points were modelled with the help of Solid185 element. It also has eight nodes similar to Solid65 with three degrees of freedom at each of its node. Details of node locations and geometry of these elements are shown in Fig. 2.

Linear, as well as multi-linear isotropic material properties, need to be defined for Solid65 elements. Willam and Warnke model and von Mises failure criterion were used for defining the failure surface for multi-linear isotropic material. The stress–strain relationship for concrete was experimentally obtained by testing concrete cylinders having 300 mm height and 150 mm diameter. Stress–strain curves, Young's Modulus and Poisson's ratio obtained from experimental studies were used in defining the properties of concrete. Stress–strain relationship for main and shear reinforcements were defined using bilinear curves with a yield stress of 500 MPa and 250 MPa respectively. For steel fibre reinforced concrete, steel fibre was distributed uniformly in all the three orthogonal directions using the real constant parameters of solid65 elements. The load was gradually applied on both the top bearing plates utilising the automatic time stepping option available in ANSYS. Simply supported boundary condition was ensured by suitably restricting the possible movements at both the bottom bearing plates.
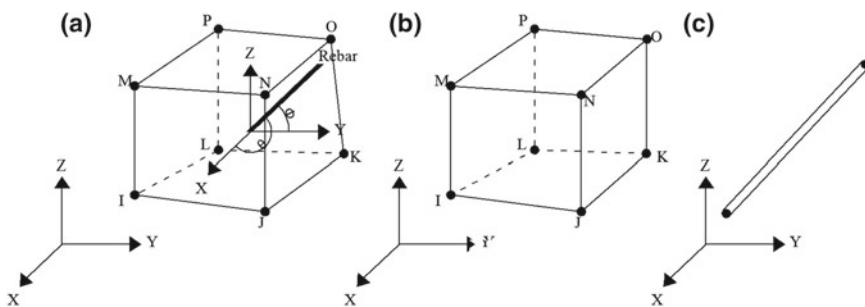

Fig. 2 **a** Solid 65 element. **b** Solid 185 element. **c** Link 180 element [13]

3 Validation of Finite Element Analysis Using Experimental Data

Four deep beams with different percentages of crumb rubber and steel fibre were cast and tested to validate the numerical analysis. The crumb rubber and steel fibre content were finalised so as to get a comparison of numerical and experimental results for conventional concrete, rubcrete and steel fibre reinforced rubcrete. Typical reinforcement details and dimensions of the test specimens are shown in Fig. 3. The deep beam specimens were designated as ES1 to ES4 as given in Table 1.

All the specimens were designed to fail in shear using the equation developed by Nagarajan and Pillai [12]. The specimens were tested under 2-point loading in an electro-hydraulic servo controlled UTM having 1000 kN capacity. The load was applied at a constant displacement rate of 2 mm per minute. Deflections were recorded at regular intervals with the help of dial gauge fixed at mid-span as shown in Fig. 4. The results of the tested beams along with the failure load obtained from numerical analysis are shown in Table 2.

It was observed that even though the addition of 10% crumb rubber resulted in a reduction of load carrying capacity by 5%, the load carrying capacity of steel fibre reinforced rubcrete specimens containing 0.50% and 0.75% steel fibre along with 10% crumb rubber were enhanced by 7% and 13% respectively. This can be
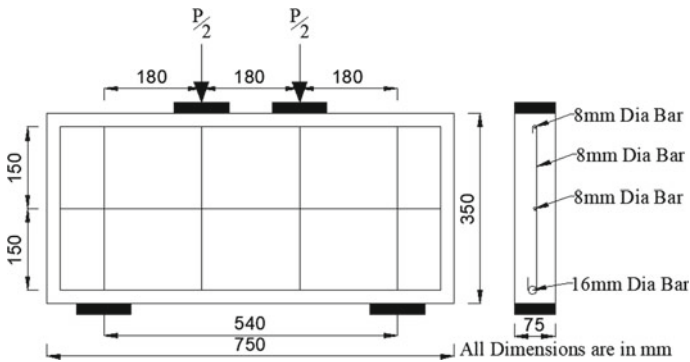
Fig. 3 Typical dimensions and reinforcement details of the test specimen

Table 1 Designation of specimens used for experimental study

Specimen	Rubber content (%)	Steel fibre content (%)
ES1	0	0
ES2	10	0
ES3	10	0.50
ES4	10	0.75
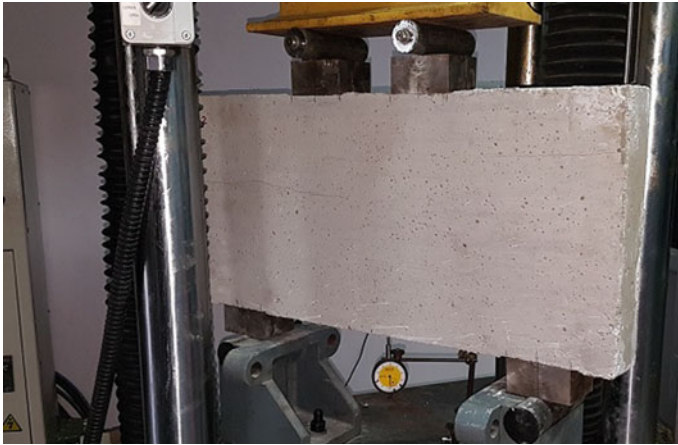
Fig. 4 Typical load setup

Table 2 Test results of specimens ES1 to ES4

No	Specimen	Compressive strength (MPa)	Failure load P_{ue} (experimental) (kN)	Failure load P_{un} (Numerical) (kN)	Percentage difference in failure load, P_{ue} and P_{un} (%)
1	ES1	45.56	406.68	396.00	2.63
2	ES2	42.53	387.05	368.00	4.92
3	ES3	44.53	435.94	447.00	2.54
4	ES4	43.54	460.89	483.00	5.02

attributed to the bridging action of steel fibres which has an important role in preventing and controlling the growth and width of cracks. The bridging action of steel fibre will help in enhancing the strength of weak interfacial zones in rubcrete and thereby help in improving its overall load carrying capacity.

As shown in Table 2, the variation in failure load obtained from numerical analysis in comparison to experimental results was well within the limits. A maximum variation of 5% was observed for specimen containing 10% crumb rubber and 0.75% steel fibre. It was also observed that the numerically obtained failure load for specimen containing steel fibre was slightly higher than that obtained from experiment. This is due to the heterogeneity of concrete and the uniform distribution of fibre in numerical analysis which is not possible to attain experimentally. The fibres will be fully effective when they are uniformly distributed in concrete matrix. Comparisons of the load-deflection response of experimental and numerical results are depicted in Figs. 5 and 6. Figure 7 shows a comparison of crack pattern obtained for specimen ES2 experimentally and numerically.
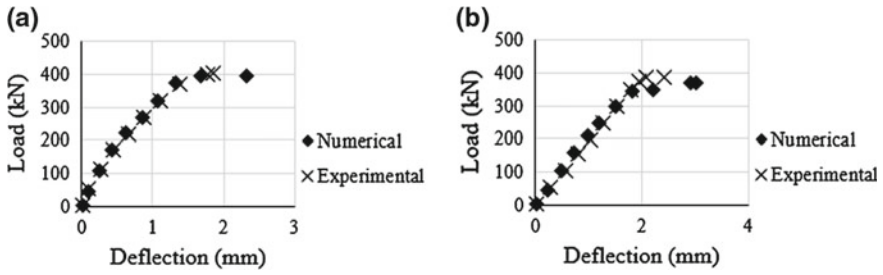
Fig. 5 Load-deflection response of ES1 (**a**) and ES2 (**b**)
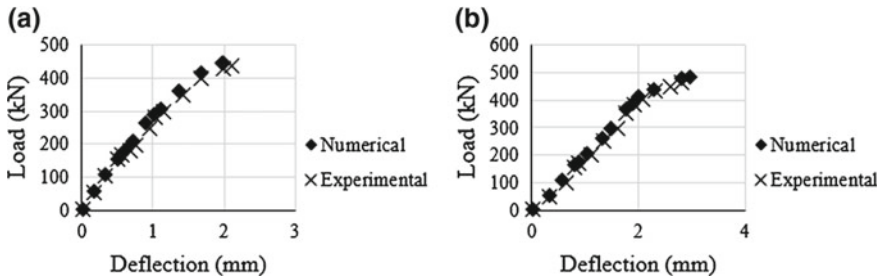
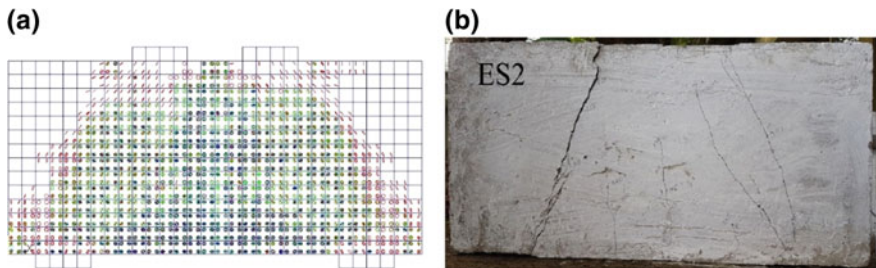Fig. 6 Load-deflection response of ES3 (**a**) and ES4 (**b**)

Fig. 7 Details of crack pattern. **a** Numerical. **b** Experimental

4 Strut Efficiency Factor Based on Collapse Load of Deep Beam

The procedure for calculating strut efficiency factor based on the load carrying capacity is shown below. Figure 8 shows a typical strut-and-tie model used for the calculation of strut efficiency factor. Based on the strut-and-tie model shown in Fig. 8, the least width of strut AB will be obtained at node A. The width of the strut is given by Eq. (3).

Fig. 8 Typical strut-and-tie model for analysis of deep beam [13]
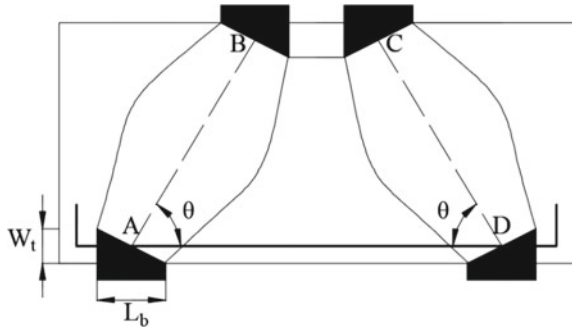
$$W_s = W_t \cos \theta + L_b \sin \theta \qquad (3)$$

where θ is the angle between tension tie and concrete strut

$$\theta = \tan^{-1}(\frac{300}{180}) = 59°$$

$$W_s = 56 \cos(59) + 100 \sin(59) = 114.56 \, \text{mm}$$

As the beam thickness, b, is 75 mm, the least cross-sectional area of the bottle-shaped strut is:

$$A_{cs} = 75 \times 114.56 = 8592 \, \text{mm}^2$$

The axial force acting (F) can be expressed in terms of peak load, P_u using the expression given below.

Force in strut,

$$F = \frac{0.5 \times P_u}{\sin(59)} = 0.58 \, P_u \qquad (4)$$

Therefore, based on Eq. 23.4.1a and Eq. 23.4.3 of ACI 318-14 [10], F_{ns} can be replaced by F and the strut efficiency factor, β_s, can be computed as:

$$\beta_s = \frac{0.58 \, P_u}{(0.85 f_c' Acs)} \qquad (5)$$

Based on the peak load obtained from experimental results of specimen used for validation, the strength reduction factor was calculated using Eq. (5) and is tabulated in Table 3.

Table 3 Strut efficiency factor for specimen ES1 to ES4

Specimen	Compressive strength (MPa)	Peak load (kN)	Strut efficiency factor (βs)
ES1	45.56	406.68	0.89
ES2	42.53	387.05	0.90
ES3	44.53	435.94	0.97
ES4	44.04	460.89	1.04

5 Numerical Analysis of Deep Beams

The result produced using numerical analysis presented a good agreement with the experimental results. So, the same procedure was adopted for analysing different specimen having varying crumb rubber and steel fibre content. The designations, content of crumb rubber and steel fibre for different specimen are shown in Table 4. Three different rubber contents varying from 0 to 20% and two different steel fibre content (0.50% and 0.75%) as shown in Table 4 were used for the analysis. Since most of the literatures reported significant reduction in strength beyond 20% crumb rubber addition the maximum limit for the same was fixed at 20% in this investigation. Also, the maximum steel fibre content was fixed at 0.75% because the chances of resulting in blowing effect were reported to be more on higher fibre contents. Typical dimensions and reinforcement details of the models used for the analysis were same as that shown in Fig. 3. The peak load and corresponding deflections obtained during the analysis are shown in Table 5. The strut efficiency factor for each of these specimens was obtained using Eq. (5) and is tabulated in Table 5.

From Table 5 it can be observed that the value of strength reduction factor increased with the steel fibre content. This implies that the steel fibre reinforced rubcrete strut have more strength in comparison to conventional concrete and plain rubcrete struts. The strength reduction factor obtained for rubcrete was same as that obtained for the conventional concrete deep beam. On comparing the strut efficiency factor obtained for conventional concrete, rubcrete and SFRR with the value

Table 4 Designation of specimens used for numerical analysis

No	Specimen	Rubber content (%)	Steel fibre content (%)
1	N1	0	0.00
2	N2	10	0.00
3	N3	15	0.00
4	N4	20	0.00
5	N5	10	0.50
6	N6	15	0.50
7	N7	20	0.50
8	N8	10	0.75
9	N9	15	0.75
10	N10	20	0.75

Table 5 Results of numerical analysis and strut efficiency factor

No	Specimen	Crumb rubber content (%)	Steel fibre volume (%)	Failure load P_u (kN)	Deflection at peak load (mm)	f_{ck} (MPa)	β_s
1	N1	0	0.00	396.00	2.34	45.56	0.86
2	N2	10	0.00	368.00	3.00	42.53	0.86
3	N3	15	0.00	334.00	3.24	38.64	0.86
4	N4	20	0.00	314.00	3.00	35.89	0.87
5	N5	10	0.50	447.00	2.00	44.53	1.00
6	N6	15	0.50	419.00	2.96	41.03	1.01
7	N7	20	0.50	372.00	1.98	36.93	1.00
8	N8	10	0.75	483.00	2.98	43.54	1.10
9	N9	15	0.75	441.00	3.07	40.00	1.09
10	N10	20	0.75	408.00	3.11	37.01	1.09

given in ACI 318-14 ($\beta_s = 0.75$) it can be seen that the code underestimates the strength of bottle-shaped concrete strut. Based on the results it can be found that steel fibre reinforced rubcrete bottle-shaped strut are not inferior to prismatic strut. The result of the analysis shows that the ACI provision for STM design can be safely used for the design of deep beams cast using rubcrete as well as SFRR.

6 Conclusions

An attempt was made to check the feasibility of using the strut efficiency factor provided in ACI 318-14 for the analysis and design of rubcrete and SFRR deep beams using the strut-and-tie method. The results of the study show that the strut efficiency factor obtained for conventional concrete was 15% higher in comparison to the value given in ACI 318-14. The strut efficiency factor obtained in all the case including rubcrete and SFRR were higher in comparison to the value provided by ACI 318-14. So, the provisions in ACI 318-14 can be safely used for the analysis and design of deep beams cast using rubcrete and SFRR. In the case of SFRR, the strut efficiency factor obtained was more than or equal to 1.00, which shows that SFRR bottle-shaped struts have similar behaviour as that of prismatic struts.

References

1. M.K. Ismail, A.A. Hassan. Performance of full-scale self-consolidating rubberized concrete beams in flexure. ACI Mater. J. **113**(2), 207 (2016)
2. N. Segre, I. Joekes, Use of tire rubber particles as addition to cement paste. Cem. Concr. Res. **30**(9), 1421–1425 (2000)

3. K.B. Najim, M.R. Hall, Crumb rubber aggregate coatings/pre-treatments and their effects on interfacial bonding, air entrapment and fracture toughness in self-compacting rubberised concrete (SCRC). Mater. Struct. **46**(12), 2029–2043 (2013)
4. D.K. Sahoo, B. Singh, P. Bhargava, An appraisal of the ACI strut efficiency factors. Mag. Concr. Res. **61**(6), 445–456 (2009)
5. D.K. Sahoo, B. Singh, P. Bhargava, Strut efficiency factors for structural concrete made from coarse recycled concrete aggregates. J. Struct. Eng. **37**(1), 49–54 (2010)
6. K.-H. Yang, A.F. Ashour, Effectiveness of web reinforcement around openings in continuous concrete deep beams (2008)
7. M.D. Brown, C.L. Sankovich, O. Bayrak, J.O. Jirsa, Behavior and efficiency of bottle- shaped struts. ACI Struct. J. **103**(3), 348–355 (2006)
8. C.G. Quntero-Febres, G. Parra-Montesinos, J.K. Wight, Strength of struts in deep concrete members designed using strut-and-tie method. ACI Struct. J. **103**(4), 577–586 (2006)
9. A.F. Ashour, C.T. Morley, Effectiveness factor of concrete in continuous deep beams. J. Struct. Eng. **122**(2), 169–178 (1996)
10. ACI 318-14, *Building Code Requirements for Structural Concrete and Commentary* (American Concrete Institute, USA, 2014)
11. ANSYS, Inc., ANSYS help, release 12.1, documentation, Copyright (2006)
12. P. Nagarajan, T.M.M. Pillai, Analysis and design of simply supported deep beams using strut and tie method. Adv. Struct. Eng. **11**(5), 491–499 (2008)
13. M.S. Sandeep, P. Nagarajan, A.P. Shashikala, S.A. Habeeb, Determination of strut efficiency factor for concrete deep beams with and without fibre. Adv. Comput. Des. **1**(3), 253–264 (2016)

Hot Bending of Large Size Seamless Primary Pipe for Sodium Cooled Fast Breeder Reactor

Gagan Gupta, Sriramachandra Aithal, R. Sritharan, S. Clement Ravi Chandar, S. Raghupathy, P. Puhtiyavinayagam, V. Balasubramaniyan, K. R. Ramasamy, Sakthivel Ramasamy and G. Vijayakumar

Abstract In a pool-type fast neutron reactor, the primary pipe supplies cold sodium from pump to grid plate. The primary pipe of Prototype Fast Breeder Reactor (PFBR) was made from pressing the plates by die and punch and joining the two h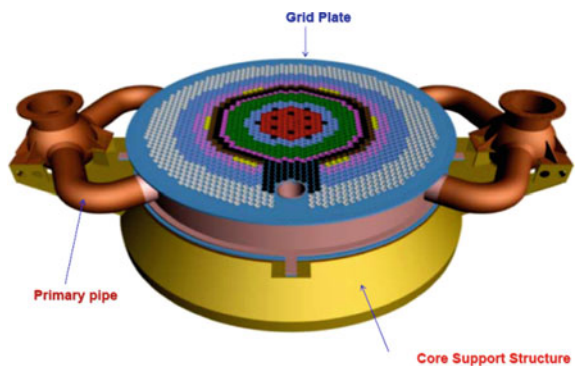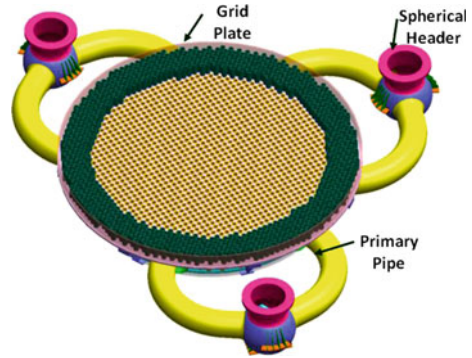alves by welding in longitudinal direction. Though weld joints are extensively used and acceptable, it is desirable to reduce the number of weld joints, which increases the reliability of the component. In this context, it is proposed to use seamless pipe for primary pipes of future FBRs. However, the large-sized seamless bends needed for meeting this objective are not readily available and hence, a technology development exercise was taken-up to bend a large size seamless austenitic stainless steel pipe (Outer diameter 457 mm and nominal thickness 14.27 mm) to a bend radius of 2 times its diameter for a bend angle of 110°. The objective of the development was to demonstrate the manufacturing feasibility of seamless pipe bend, with controlled dimensions, before its adoption in the design. This paper discusses the details of development activities carried out in various stages towards bending of a large size seamless pipe. The hot bending attempts through die and punch method involving large number of trials as well as through induction bending technique are detailed out. After many unsuccessful trials of hot bending on carbon steel pipe with various die and punch options (viz. end support die, full-length support die) and several challenges with induction bending, primary pipe bending has been successfully demonstrated, meeting the specification requirements. The paper also highlights various qualification tests,

G. Gupta (✉) · S. Aithal · R. Sritharan · S. Clement Ravi Chandar · S. Raghupathy · P. Puhtiyavinayagam
Indira Gandhi Center for Atomic Research, Kalpakkam 603102, Tamil Nadu, India
e-mail: gagan@igcar.gov.in

V. Balasubramaniyan
Safety Research Institute, Kalpakkam 603102, Tamil Nadu, India

K. R. Ramasamy · S. Ramasamy · G. Vijayakumar
M/S KRR Engineering Pvt. Ltd, Chennai 600058, India

which the primary pipe bend has met. The successful completion of hot bending of large diameter seamless pipe has demonstrated the indigenous manufacturing capability of such bends and has given confidence for its incorporation in the primary pipes of future FBR.

Keywords Seamless pipe · Fast reactor · Die and punch · Induction bending · Hydrostatic test · Non-destructive examination

1 Introduction

Primary pipe is one of the important components of reactor assembly in 500 MWe, Prototype Fast Breeder Reactor (PFBR) and future Fast Breeder Reactors (FBR). It supplies pressurized cold sodium (397 °C and 0.8 MPa) from the outlet of the primary sodium pump to grid plate and forms part of primary coolant boundary (Fig. 1). It also facilitates installation and removal of primary sodium pump from top of roof slab. There are total four primary pipes (two per pump) for supplying sodium (7200 kg/s) to the grid plate. It is designed as Class-1 component as per RCC-MRx-RB design code [1]. Utmost care, high-quality construction and inspection procedures are adopted in the manufacture of these primary pipes to prevent any leakage or rupture under all the reactor conditions. The material of construction is ductile austenitic stainless steel 316LN [2]. In future FBRs, since the reactor power has been increased from 500 to 600 MWe, it requires higher flow rate to remove the heat from the core. Hence, three primary sodium pumps are proposed to be used instead of two used in PFBR and accordingly, primary pipes have been increased from four to six numbers. The primary pipe configuration for future FBRs has been shown in Fig. 2. It also increases the safety margin in case of one pipe rupture event (increase in core flow up to 45% from 30% in PFBR) and flow uniformity inside the grid plate. In PFBR, primary pipe was manufactured by pressing the plates in a die and punch arrangement and joining the two halves by

Fig. 1 PFBR primary pipe layout

Fig. 2 Primary pipe layout in future FBR

welding in longitudinal direction. Though, weld joints are extensively used and acceptable, it is desirable to reduce the number of weld joints so as to avoid any weld joint related defects/deficiencies thereby increasing the reliability of the component and thus of primary heat transport system as a whole. In this context, it is proposed to use seamless pipe instead of welded pipe for primary pipe assembly of future FBRs. However, the large-sized seamless bends needed for this objective are not readily available and hence, a technology development exercise was taken-up to bend a large size seamless austenitic stainless steel pipe (Outer diameter 457 mm and nominal thickness 14.27 mm) to a bend radius of 2 times its diameter and for a bend angle of 110°. The objective of the development was to demonstrate the manufacturing feasibility of seamless pipe bend before its incorporation in the design.

In this paper, the details of developmental activities carried out in a stage-wise manner towards bending of a large size seamless pipe and the qualification tests conducted are discussed. The successful completion of hot bending of large diameter seamless pipe has demonstrated the indigenous manufacturing capability for such bends and has given confidence for its incorporation in the primary pipe of reactor assembly of future FBR.

1.1 Literature Review

Pipe bending using induction heating a local area is an advanced technique to produce large diameter pipe bend with a small to large bend radius and has been widely used. It has advantages such as low cost and time, higher quality production, high efficiency, etc. Many experiments on induction bending with small diameter pipes and simulation by FEM were carried out to improve and develop the process. Zutang et al. [3] has found that for pipe bend radius of 2.12 D, thinning in both analytical and experimental result were matching and error was 2.4% only. Ryu et al. [4] has given the process parameter for the induction bending based on elastic–plastic large deformation FEM for large diameter pipe. For bend angle of 100°, the ovality is less than 6%. Miyazaki et al. [5] has carried out monotonic

bending test of pipes with local thinning. Ovality or crack initiation/growth occurs at the tensile stress region and ovalization or local buckling occurs at compressive stress region. Hu [6] has proposed optimal process design for pipe bending using the dynamic reverse moment method. In the case of pipe bending with bend radius = 1.5D, the design factors that have the strongest effect on the thickness reduction ratio is the reverse moment, heating width, temperature, temperature gradient and feeding velocity. Data on experiments with large size induction bent pipe with smaller bend radius is rarely available.

1.2 Bending Methods

The bending procedure is determined by the diameter and wall thickness of pipe, bend radius, material of construction and the requirements after bending. There are two bending methods, hot bending and cold bending. Hot bending method has three bending procedures, i.e., Furnace bending, Incremental bending, Induction bending. In Furnace bending, the pipe is firmly packed and heated in a furnace. After removing from the furnace, pipe is restrained at one end and bending moment is applied at the other end. In incremental and induction bending, a narrow circumferential bend is heated to the required temperature and a force is applied by the hydraulic cylinder (in incremental bending) or a radial arm (in induction bending) to bend the small heated area. The heating device is moving in case of incremental bending along the job but fixed in induction bending. Cold bending method has several bending procedures, i.e., Rotary draw bending, Ram bending, Roll bending, etc. In Rotary draw bending, the pipe is secured to a rotary bending die by a clamp die. As the bending die rotates, it draws the pipe against the pressure die. In ram bending, the pipe is held by two supporting dies and a force is applied by means of a hydraulic ram to a forming shoe located at the centre of the work piece. In roll bending, forming rolls of same diameter arranged in a pyramid are used. Two fixed rolls oppose the adjustable centre roll. The pipe passed through the rolls to the required bend radius.

2 Technology Development

2.1 Bending Profile of Pipe

The bending profile of seamless primary pipe is shown in Fig. 3. It is a seamless pipe (Outer diameter 457 mm and nominal thickness 14.27 mm) bent into 2D bend radius and 110° bend angle. The specified dimensional requirements of the bent pipe are as per PFI standard [7] and given below.

Parameter	Specified values
Outside diameter	457 mm
Ovality	≤ 8%
Thickness	>10 mm after bending
Bend angle	±0.5 degree
Local buckling /wrinkles	Ratio of crest to depth > 12
	The maximum vertical height of any wave, measured from the averaged height of two adjoining crest to the valley, shall not exceed 3% of the nominal pipe size
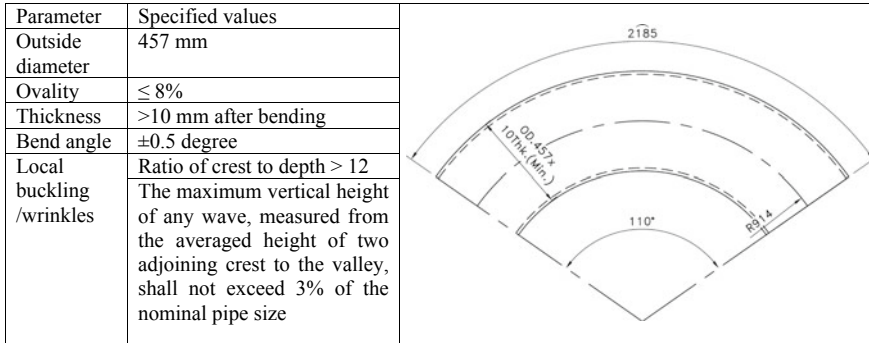
Fig. 3 Primary pipe profile

2.2 Raw Material

Two numbers of SS 304L large diameter seamless pipes as per ASTM A 312 (Outer diameter 457 mm and nominal thickness 14.27 mm, 4 m each) [8] were procured and supplied as free issue material to the industry for trial as well as for actual job after verification of the chemical composition and mechanical test reports. Though the material of construction of primary pipe in the reactor is SS316LN, SS 304 L was chosen for technology development considering matching tensile properties and forming behaviour with SS 316 LN while being cost effective and easily available.

2.3 Stages of Technology Development

The technology developmental activities were carried out in four stages. In first stage, hot bending using punch and die arrangement was adopted. Towards this, at first, end supported die and punch in carbon steel was chosen, developed and used for trial bending of hot carbon steel pipe (same dimensions as that of SS304L pipes) in hydraulic press. The pipe was blinded at one end, tightly packed with sand and closed by attaching dummy closure on the other side. Subsequently, the pipe was heated gradually up to 420 °C by using electrical resistance method and kept over the end supported die and bent gradually by punch using 4000 t hydraulic press. In case of 2D bend radius, hot bending is only recommended by the PFI standards [7]. The pipe was heated to 420 °C to reduce the yield strength of the material (<50% as compared to room temperature) so that material will easily deform/flow in the applied loading direction during forming. Further, for temperature less than 425 °C, creep in the material is negligible irrespective of holding time. After forming, the profile of the pipe was measured and it was observed that ovality is beyond the specified limits and thickness reduction was also high. Subsequently, the punch

profile was modified and instead of end supported dies, full-length die was man-
ufactured to control the ovality. Again, more trials bending with carbon steel pipe
was taken up with similar heating as adopted earlier. After several trials, it was
observed that **specified dimensions (ovality)/quality in bend cannot be achieved
by this method**. However, thickness reduction was not much. It was also observed
that pressing tool marks are appearing on pipe surface. The punch, full length die,
pressing of trail carbon steel pipe on end support and full-length support die are
shown in Fig. 4 and their schematic arrangement is shown in Fig. 5. The main
reason for not meeting the specified bend requirements was very small ratio of

Punch   Full Length Die

Fig. 4 Pressing of hot carbon steel pipe with end support die and full length die

Fig. 5 Schematic arrangement of die and punch for hot forming

thickness to diameter of the pipe due to which it was difficult to control the ovality of the pipe.

In the **second stage**, it was decided to use induction bending instead of die and punch method, as an alternate option as per manufacturing specification. In this stage, carbon steel pipe was bent in induction bending machine. Adjustable induction coil was used in the machine to heat a small width ∼25 mm of pipe continuously and maintain the temperature along the pipe circumference during bending. A layout of the specified bent pipe dimensions as per specification was marked on the floor to check the profile. Induction bending of carbon steel pipe and profile measurement on marked floor is shown in Fig. 6. The ovality of the pipe was measured at five circumferential locations along the length as shown in Fig. 7 and thickness was measured using ultrasonic thickness measurement gauge.

It was observed that the dimensions achieved with bent carbon steel pipe were meeting the specified requirements. **Ovality was less than 5% and minimum thickness was 13.6 mm. No wrinkles were observed on pipe surface. Pipe profile was within ±1%.** Based on successful trial of carbon steel bend, decision was taken to go ahead with bending of SS304L pipe in induction bending facility.

Bent Carbon steel pipe

Induction bending of carbon steel pipe   Profile measurement of bent pipe

Fig. 6 Induction bending machine, bent carbon steel pipe, and profile measurement
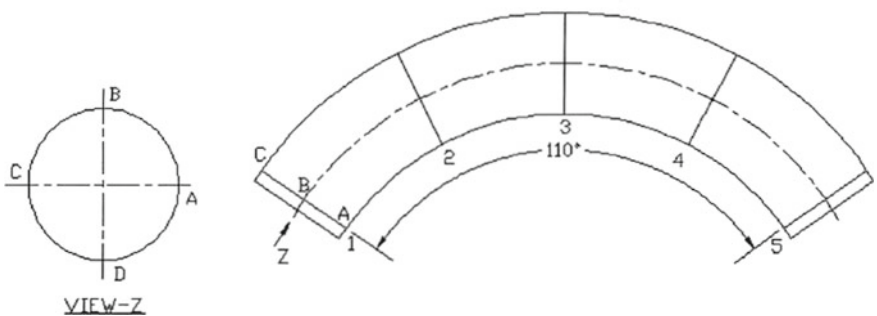
Fig. 7 Locations of ovality measurement on bent pipe along the length

Fig. 8 Crack at 40° bend angle

In the **third stage**, the trial SS304L pipe was fixed in the induction bending machine and bending operation was started. During half-way through the bending, a crack was appeared after bending for 40°, as shown in Fig. 8. The bending operation was stopped and pipe was removed from the bending machine for investigation. At first hardness measurement of the SS304L pipe was carried out and it was observed that the hardness measured was within the acceptable range. Subsequently, chemical analysis was carried out and it was observed that vanadium percentage in the material is high ($\sim$0.098%), which is not prescribed in ASTM also. Based on the literature review, it was observed that the vanadium increases the hot hardness of the material [9] and was concluded to be the reason for the pipe cracking as this information was not available apriori to set the bending parameters in the machine. Further, it was also concluded that the initial variation in thickness of the pipe along the circumference though within the limit as per ASTM standard, was also one of the parameter due to which heating was not uniform. Based on the above observations, machine parameters were identified (viz., heating rate, water flow rate, coil to pipe gap, air flow rate etc.), which needs to be fine tuned/varied as the bending progresses to account for the thickness variation as well as presence of vanadium. Subsequently, the trial bending was taken-up again with the balance material sufficient for 70° bend (Fig. 9). Based on the detailed inspection carried out, it was observed that the trial pipe bend met all the dimensional requirements as well as no crack was observed during both visual as well as surface examination of the pipe.

In the **fourth stage**, actual pipe bend of 110° was taken-up based on the finalized machine parameters and completed successfully (Ref. Fig. 10). Extra length of $\sim$100 mm was kept at both the ends for facilitating hydrostatic testing.

Fig. 9 70° trial bend during bending and unloading
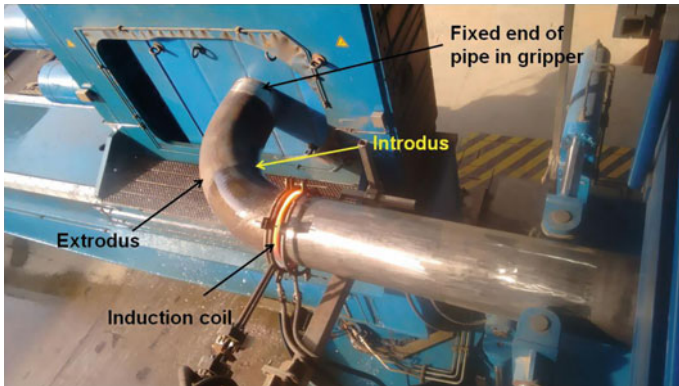
Fig. 10 Final primary pipe 110° bend after bending

The temperature of extrodus and introdus surfaces of pipe was maintained in the range of 900–1100 °C and was monitored by laser sensors. It is required to maintain the lower temperature at extrodus and higher temperature at introdus because introdus is under compression during bending and needs to be softer.

During bending, thinning will take place at extrodus and thickening (buckling/ wrinkles) takes place at introdus. Higher temperature at introdus reduces the yield strength, softens the material and thereby allows it to flow in all direction which inturn helps in reducing the buckling. Lower temperature at extrodus helps in increasing the ductility which will not allow material to crack. The feed rate of the pipe was automatically controlled to $\sim$20 mm/min. As the bent pipe segment moves out of the induction coil region, water was continuously sprayed in a controlled rate along the circumference of heated pipe for quenching the surface to reduce oxidation. The water, after quenching, is blown away from the induction coil using directed and controlled air flow. Bending load was applied continuously at one fixed end of the pipe by rotating the gripper assembly in the required bend radius. 'Induction bending is a complex process, involving 40 parameters which need to feed before starting the bend and are continuously monitored on two monitors simultaneously during bending to get quality product. Some of the crucial parameters were studied which are temperature of introdus and extrodus of the pipe, feed rate, coolant flow rate, air flow rate, induction coil movement etc.'

2.4 Heat Treatment of Trial and Actual Pipe

After induction bending of trial pipe and actual pipe, stress relieving heat treatment of bent pipe was carried out at 1050 ± 15 °C in electrical furnace. Heating rate, cooling rate, temperature difference between two thermocouples was within the specified limit.

Fig. 11 Hydrostatic test
setup
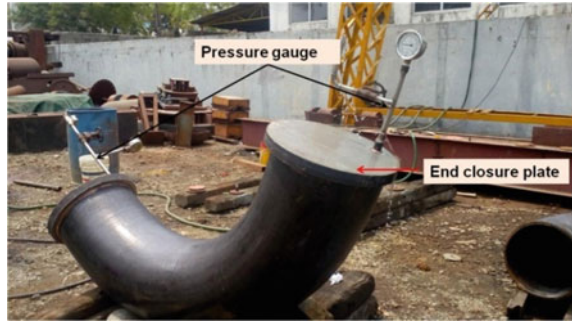
2.5 Hydrostatic Test of Actual Pipe

After heat treatment, the bent pipe was thoroughly cleaned with steel wire brush and a setup was made for hydrostatic test. Both the ends of the pipe were closed via welding of circular plates at both ends and it was filled with cleaned de-mineralized (DM) water. DM water was pressurized via reciprocating pump up to 1 MPa (1.25 times the design pressure 0.8 MPa) and held for ten minutes. The pressure was monitored at both the ends using pressure gauges. There was no leakage of water and no drop in pressure was noticed during test and result was satisfactory. The test setup is shown in Fig. 11.

2.6 Pickling and Passivation

After hydrostatic test, end closure plates and extra length at both the ends were removed by grinding and sharp edges were rounded off. The entire surface was cleaned, degreased. Pickling by nitric acid solution was carried out on entire surface. After pickling, the entire surface was cleaned with DM water and passivation was carried out.

2.7 Non-destructive Test

Visual examination of the actual and trial pipe was carried out after hot bending as well as after heat treatment and results were satisfactory. The bend was free from cracks, dents, objectionable flattening and any other injurious defects. Liquid Penetrant Examination (LPE) was carried out on entire outer surface and accessible portion of inner surface as per ASME BPV Code Section–V [10] after heat treatment of bend and again after hydrostatic test and no defects were observed in the bend. Ultrasonic testing (UT) was carried out for thickness measurement and

volumetric defect checking. UT of extrodus surface was carried out in accordance with ASTM A999-04a [11] and notch depth was 5% of wall thickness ($\sim$0.7 mm). The width of the notch was twice the depth ($\sim$1.4 mm). Two reference blocks were made for UT. In one block, the notches were made on inner and outer surface along longitudinal and circumferential direction and in another reference block, small drilled holes were made. The reference blocks are shown in Fig. 12. No defects were observed during UT of the pipe.

2.8 Metallographic Examination

After NDE examination, a small sample was cut from the end of the pipe and sent for metallographic examination as per ASTM E112 [12]. The average ASTM grain size observed was No. 5 and is within the specified limits.

2.9 Dimensional Inspection

Dimensional inspection of trial bend (70°) was carried out after hot bending. For actual 110° bend, dimensional inspection were carried out at two stages, first after hot induction bending and second after heat treatment and hydrostatic test to check for any variation in dimensions subsequent to hydro test. The diameter and thickness were measured at seven circumferential locations along the length to calculate the ovality and thinning as shown in Fig. 13. Pipe profile was checked on layout and found within 10 mm (2% of OD of pipe). The dimensional inspection report of trial and actual pipe bend are given in Table 1. After completion of developmental activities, actual bend, trial bend were packed in a steel frame, delivered and unloaded as shown in Fig. 14.

Fig. 13 Dimensional measurement of actual bend
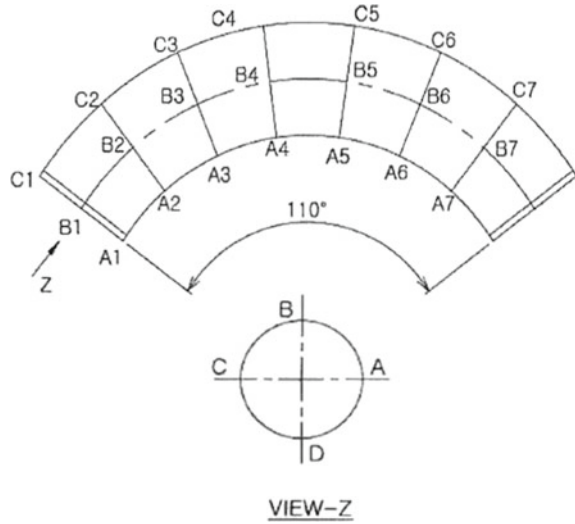
Table 1 Dimensional inspection report of actual pipe

Parameter	Specified values	After hot bending	After hydrostatic test
Outside diameter (mm)	As specified in para 2.1	432–463	432–463
Ovality (%) (Max. OD—Min. OD)/ nominal OD		1.09–6.78	1.09–6.78
Thickness (mm) (Minimum)		12.5	12.5
Bend angle (degree)		±0.32	±0.32
Local buckling/wrinkles		No wrinkles	No wrinkle

Fig. 14 Actual and trial bend

3 Result and Discussion

The dimensional requirement of actual primary pipe bend was achieved within the specified requirements. The ovality was minimum at the end and maximum at the centre. Maximum ovality of 6.78% was observed at A3-C3 section. Thickness of bend at introdus (A1-A7) was minimum near the centre A4 (15.3 mm) and for extrodus (C1-C7), minimum was at C5 (13.9 mm). Minimum and maximum thicknesses of bend were observed at B4 and D2 locations, which are 12.5 mm and 22.7 mm respectively.

4 Conclusions

Technology development of primary pipe was carried out successfully, meeting all the specified requirements. The successful completion of hot bending of large diameter seamless pipe has demonstrated the indigenous manufacturing capability for such bends and has given confidence for its incorporation in the primary pipe of reactor assembly of future FBR.

References

1. RCC-MRx Code 2012, Section III—Tome 1—Subsection B: class N1Rx reactor components and supports
2. S.C. Chetal, P. Chellapandi, *Improved primary pipe design concepts for future FBR (IAEA-TECDOC–1406)* (International Atomic Energy Agency (IAEA), 2004)
3. W. Zutang, H. Zhong, Theory of pipe-bending to a small bend radius using induction heating. J Mat. Proc. Technol. **21**, 275–284 (1990)
4. K.H. Ryu et al., Process design of the hot bending process using high frequency induction heating. J. Korean Soc. Precis. Eng. **18**(9) (2001)
5. K. Miyazaki et al., Fracture behavior of carbon steel pipe with local wall thinning subjected to bending load. Nucl. Eng. Des. **191**, 195–204 (1999)
6. J. Hu, Optimum design of pipe bending based on high frequency induction heating using dynamic reverse moment. Int. J. Precis. Eng. Manuf. **12**(6), 1051–1058 (2011)
7. PFI standard ES-24 Pipe bending tolerances—Minimum bending radii (2003)
8. ASTM A312-09, Standard Specification for Seamless, welded, and Heavily Cold worked Austenitic Stainless Steel pipes
9. http://www.substech.com/dokuwiki, Effect of alloying elements on steel properties
10. ASME BPV Code Section–V, Non-destructive Examination
11. ASTM A999-04a, Specification for General Requirements for Alloy and Stainless Steel Pipe
12. ASTM E112, Standard Test Methods for Determining Average Grain Size

Dynamic Response of Sacrificial Curved Steel Wall Under Blast Loading

P. Sreekanth and M. D. Goel

Abstract Due to increased frequency of terrorist attacks and blast threats all over the world, safety of personnel and structural integrity under blast loading is most important. This necessitates immediate research intervention to understand the behavior of various structures and structural components under such extreme loadings. In the present investigation, non-linear dynamic finite element (FE) analysis of sacrificial curved steel wall is carried out with varying angle of curvature (i.e. 0°–180°). Herein, non-linear dynamic analysis is carried out using ABAQUS® finite element package. ConWep formulation is used for defining blast loading and performance of the wall, in terms of peak deflection, is compared to understand the effect on curvature on peak deflection. For this purpose, three-dimensional deformable 4-node, reduced integration, hourglass control with finite membrane strains elements are employed for non-linear FE analysis of curved wall. Non-linear dynamic analysis is carried out with varying angle of curvature along top one-fourth length of the wall. Further, performance of curved walls is compared with that of straight vertical wall in terms of peak deflection. Deflection at various points along the height of wall is computed and analyzed. Based on this analysis, it is observed that a simple change in curvature of wall results in considerable improvement in blast resistance with all other conditions being same.

P. Sreekanth · M. D. Goel (✉)
Department of Applied Mechanics, Visvesvaraya National Institute of Technology, Nagpur 440 010, Maharashtra, India
e-mail: mdgoel@apm.vnit.ac.in

1 Introduction

Designing of the structures to resist blast loading has become a necessary criterion for special structures like oil-rigs, oil and gas storage houses, chemical industries and weapon storage houses, etc. A structure is composed of many components which include roofs, beams, columns, walls, foundations, etc. Further, there exists a boundary wall to protect the whole structure from any unwanted element at a safer distance. This boundary wall is the first level of security in blast resistant design of structures. Any blast threat has to clear this barrier and then only it will have interaction with the main structure/components. Thus, if designer is able to hold the blast well within this wall, then the main structure or component is safe. Hence, it can also be termed as sacrificial wall which protects the main structure/component. Thus, this requires design and analysis of walls considering various parameters under such extreme loadings. In year 2011, Goel and Matsagar [1] investigated the dynamics response of stiffened plates subjected to air blast [1]. They analyzed various stiffener layouts sandwiched between two steel plates to be used as energy absorption structure against blast. Later on, they carried their analysis on dynamic response of steel–sand composite stiffened plates under impulsive loading [2]. They used commercially available ABAQUS® package for finite element analysis of stiffened steel–sand composite plates. Further, Goel and Matsagar (2013) investigated the mitigation strategies in design of structures to exhibit improved blast resistance as well as with maintaining architecturally appealing appearance. In their research, they discussed the various blast mitigation strategies and presented a comprehensive assessment of blast response mitigation technologies [3]. Wu and Sheikh [4] investigated the mitigation of blast effects on reinforced concrete panel using foam cladding using finite element modeling [4]. In their analysis, they investigated the capacities of metallic foam cladding, which can absorb significantly high blast energy in protecting critical reinforced concrete slabs against blast loadings. Liskay et al. [5] analyzed the behavior of building and its key elements of blast resistant building design. In their research, they discussed essential elements within the structures, building materials and occupants of the structure interact with the building [5]. Later on, Matsagar [6] presented computation of stress and displacement response of composite plates under blast loading. He investigated the performance of composite plates as sacrificial blast walls subjected to impulsive loading [6]. Recently, Verma et al. [7] presented blast resistant design of structure, wherein, they reported various methods applied to different types of structure, such as masonry, concrete, steel and the effectiveness of each method. In their analysis, they discussed about unidirectional passive dampers in steel structures, FRP retrofit technique in masonry walls, varying core density in sandwich structures and composites materials [7]. Thus, it is observed that several researchers investigated the different structural components using various materials. However, investigation on the effect of geometrical design on wall response against blast load is not

presented in detail. Thus, in the present investigation, curved steel wall is analyzed under blast loading using ABAQUS® finite element package. Performance of steel wall with different angle of curvatures is compared with that of straight wall in terms of their peak deflection at various points along the height of the wall.

2 Finite Element Analysis

The wall is modeled using ABAQUS® package wherein, wall is considered to be bent with respect to the axis parallel to the wider plane of the wall and perpendicular to the support base of the wall (Fig. 1). In the present investigation, a wall is of 2 m × 2 m size is considered wherein, the top 0.5 m portion is bent towards the blast loading face. The wall thickness is 0.03 m and it is modeled as shell in ABAQUS® [8]. For FE modeling, deformable shell element of extrusion type has been selected for the analysis of curved steel wall. Wall is analyzed for various angles of curvatures varying from 0° to 180° at regular interval of 15°. Thus, total of 13 walls are analyzed under identical loading conditions. Further, FE models are developed to maintain equal mass in all angles of curvatures of structures so as to avoid the effect of additional mass. In order to understand the deformation pattern, different points are selected for the analysis of wall as shown in Fig. 1. The wall is modeled using S4R (a 4-noded doubly curved thin or thick shell, reduced integration, hourglass control, and finite membrane strains) with global part size 0.01 based on mesh convergence study.

   The wall is made of steel and material properties of steel are considered as reported by Goel et al. [1]. Here, steel has density, Young's modulus and Poisson's ratio as 7800 kg/m^3, 210 GPa, 0.3, respectively. For plastic behavior of wall, yield

Fig. 1 Observation points along the wall for computing the deflection
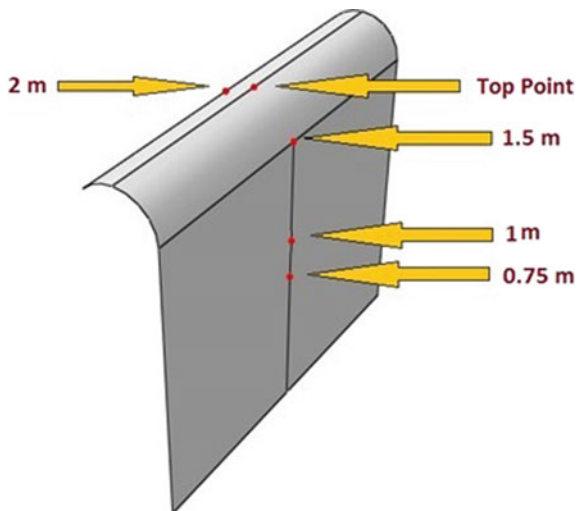
stress variation with plastic strains is considered. Plastic yield stress parameters of steel with corresponding plastic strain is already reported by Goel et al. [1] and the same are used in the present investigation. It is to be noted that base of the wall is considered as fixed with ENCASTRE (U1 = U2 = U3 = U4 = U5 = U6 = 0) boundary condition as available in ABAQUS®. Sides of wall are considered as hinged with displacement type (U2 = U3 = UR1 = 0) boundary conditions to model as the real wall structure. For the analysis of wall with various curvatures, ConWep blast function is applied wherein 1 kg of TNT is exploding at a standoff distance of 1 m from the face of the wall. ConWep is a collection of conventional weapons effects calculations from the equations and curves of TM 5-855-1. This is function can perform variety of conventional weapons effects calculations such as air blast, fragment, and projectile penetrations, breach, cratering, and ground shock, etc. Using this function, pressure, $P(t)$ is computed by the following equation:

$$P(t) = P_r \cos^2 \theta + P_i \left(1 + \cos^2 \theta - 2 \cos \theta\right) \tag{1}$$

This function considers the enhancement of pressure due to reflection of waves. The pressure $P(t)$ on door face is determined based on input amount of TNT, standoff distance, and angle of incidence "θ". Here, P_r and P_i is the reflected and incidence pressure, respectively. Final pressure, $P(t)$ is computed using above equation and is applied automatically to the wall surface.

3   Validation of Fe Scheme

In order to validate the present FE scheme, analysis and results reported by Varma et al. [9] are used. Varma et al. [9] carried out investigation on dynamic response of brick masonry panel walls under high explosive detonations. In their analysis, they considered wall of 3 m × 3 m × 0.345 m size for their experimental study under blast loading. This wall was enclosed in reinforced concrete frame of cross-sectional area 0.35 m × 0.345 m and same is considered in the present validation. Wall and frame are modeled in three-dimensional, deformable solid element models with same dimensions of walls used by Varma et al. [9]. Concrete damaged plasticity model is used for the design of reinforced concrete frame material model. Material properties of masonry as per Varma et al. [9] are used, wherein, concrete has yield strength, modulus of elasticity, cracking strain and Poisson's ratio of concrete as 20 MPa, 22 GPa, 1.2×10^6 and 0.15, respectively. Steel of grade Fe415 is used with yield strength, modulus of elasticity and Poisson's ratio of 415 MPa, 200 GPa and 0.3, respectively. 4.1% percentage of steel is used in the design of frame and same is applied herein. Contact of wall and frame is defined with general contact type with tangential behavior and penalty friction of coefficient 0.8 as per ABAQUS®. Wall is fixed with base of frame with ENCASTRE (U1 = U2 = U3 = UR1 = UR2 = UR3 = 0). ConWep blast function is considered to analyze the effect of blast loading.

Table 1 Validation of present FE scheme with experimental results of Varma et al. [9]

S. no.	Weight of charge (kg)	Standoff distance (m)	Peak deflection of wall (m)	
			Experimental result from Varma et al. [9]	Present finite element results
1	22.4	5.5	0.047	0.048
2	22.4	7	0.040	0.039
3	43.2	4.5	0.104	0.103
4	23.4	4	0.071	0.072
5	23.3	6	0.042	0.043
6	11.7	5	0.018	0.020

For meshing, C3D8R solid type with 5000 elements in wall and 1500 elements in frame is used. Deflection-time history is defined to compute the deflection of wall at midpoint of wall. Different models of walls are prepared with different loads of charge at different locations as considered in experimental analysis of Varma et al. [9]. Peak deflections of walls are evaluated using present FE scheme and the same are reported in Table 1 along with experimentally observed values of Varma et al. [9]. From this table, it can be observed that peaks deflection observed from experimental investigation of Varma et al. [9] are in close agreement with the results computed using present FE scheme, thus validating the present FE scheme. Further analysis is carried out using same scheme for the wall considered in the present investigation. It is important to note that any FE analysis is greatly influenced with the type of material model chosen and with the approximation of boundary conditions with the realistic one. These two parameters influence the results to a greater instant. Material model available for various materials are based on detailed investigation which in turn is based on the experimental and mathematical formulation of the physical behavior of material under a given condition. Herein, validation is done using concrete material model wherein results from experimental and numerical simulation were available in open literature as reported by Varma et al. [9]. The main reason for using concrete material model is to show that FE technique used in the present analysis is giving similar results as reported by other researchers based on their investigation.

4 Results and Discussions

In the present investigation, a steel wall with varying degree of curvature is analyzed using FE package ABAQUS®. To understand the behavior of the wall under blast load, deflection-time histories at various points along the wall with varying angle of curvature are computed. Blast load is applied using ConWep blast function

available in ABAQUS®. Further, to avoid the clumsiness of results deflection-time history response of straight wall and 180° curvature wall are plotted for better understanding of variation of deflection with time. Deflections of wall are calculated at the mid-line of its width and at 0.75, 1, 1.5 and 2 m from base to top vertically as already reported in Fig. 1. Figure 2 shows deflection-time histories of wall at selected points i.e. 2, 1.5, 1 and 0.75 m from the base of the wall (Refer Fig. 1) for straight and 180° curvature wall. From this figure, it can be observed that introduction of curvature results into considerable reduction in peak deflection for all the observation points considered in the present investigation. Further, for walls considered in the present investigation, it is observed that deflection is increasing with increase in height of observation point and maximum deflection is observed at top point (Refer Fig. 1 for locations). At top point, deflection is observed to be about 0.069 m whereas, at 2 m point it is found to be 0.067 m which is 2.8% lower than the top point deflection. It is important to note here that top point is the 2nd location facing the blast loading. Similarly, at 180° curvature, deflection at 1.5 m point, 1 m point and 0.75 m point is observed as 0.0275, 0.025 and 0.020 m, respectively. This peak deflection is 61.26, 64.79 and 71.83% lower than the deflection at top point, thus indicating the effect of provision of curvature into the wall geometry. Thus, based on this analysis it can be said that deflection of wall is varying along the height of the wall and maximum deflection is observed at top point of the wall.

Further, peak deflections are plotted for straight and curved plates at various selected locations of the wall. Peak deflection of each wall with varying angle of curvature is computed. Figure 3 shows the variation of peak deflection of wall with varying angle of curvature of wall at observation points i.e. at top point, 2, 1.5, 1, and 0.75 m. From this figure, it can be observed that peak deflection is decreasing with increase in angle of curvature for all the observation points considered in the present investigation except at 0.75 m point wherein, at curvature of 105° and 120° higher deflections are observed as compared to the deflection $\leq$ 90° curvatures. The reason for such a behavior may be attributed to the fact that this particular angle of curvature and location of observation point combination is experiencing severe reflection and thus resulting into the higher deflection. Further, variation of peak deflection with varying angle of curvature at 0.75 m may also be attributed to modal pattern of deflection of wall. Moreover, the rate of reduction in peak deflection is varying with the point of observation along the height of the wall. Additionally, it can be observed that with increase in curvature angle peak deflection reduces for all the point in comparison with straight wall (0° curvature). This shows the effectiveness of geometrical configurations on the blast response of the wall. Thus, it can be said that proper curvature of wall helps in improvement of blast resistance with all other conditions being same.
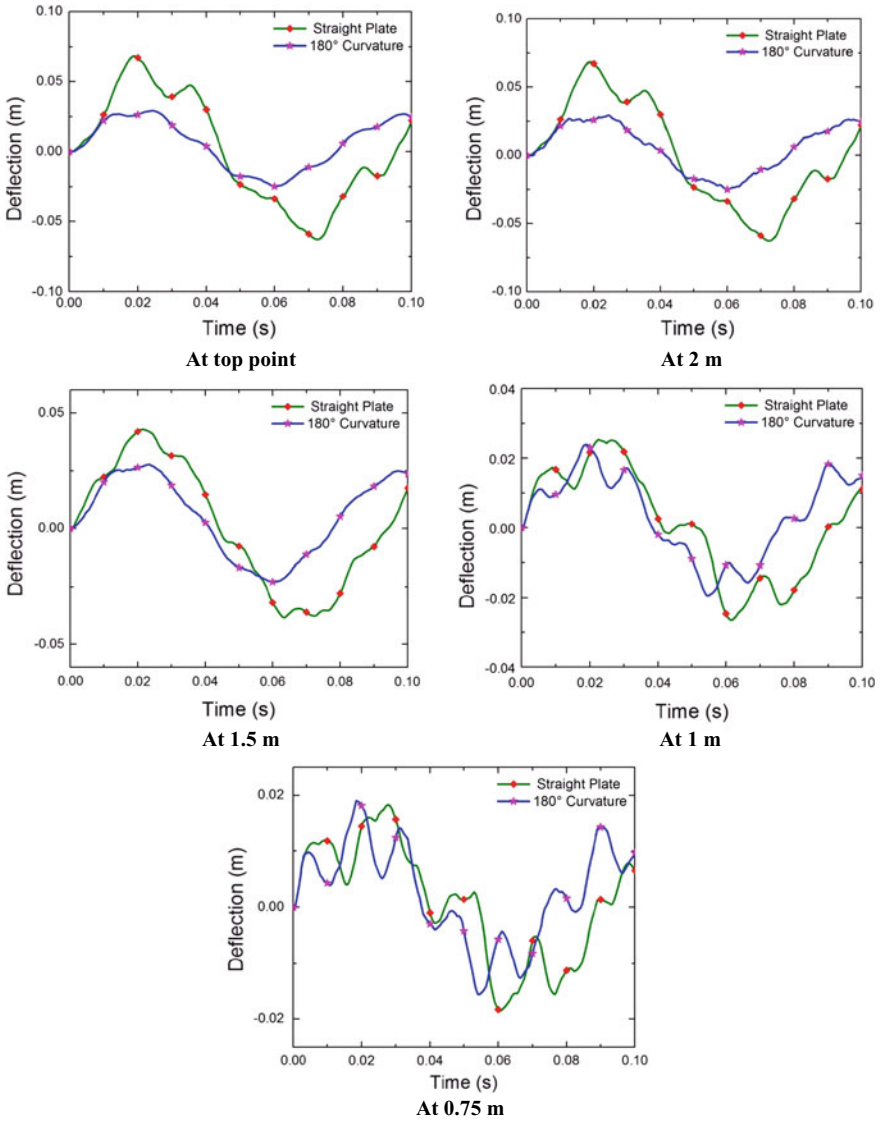
Fig. 2 Deflection-time histories of wall at various points along the wall height under blast loading
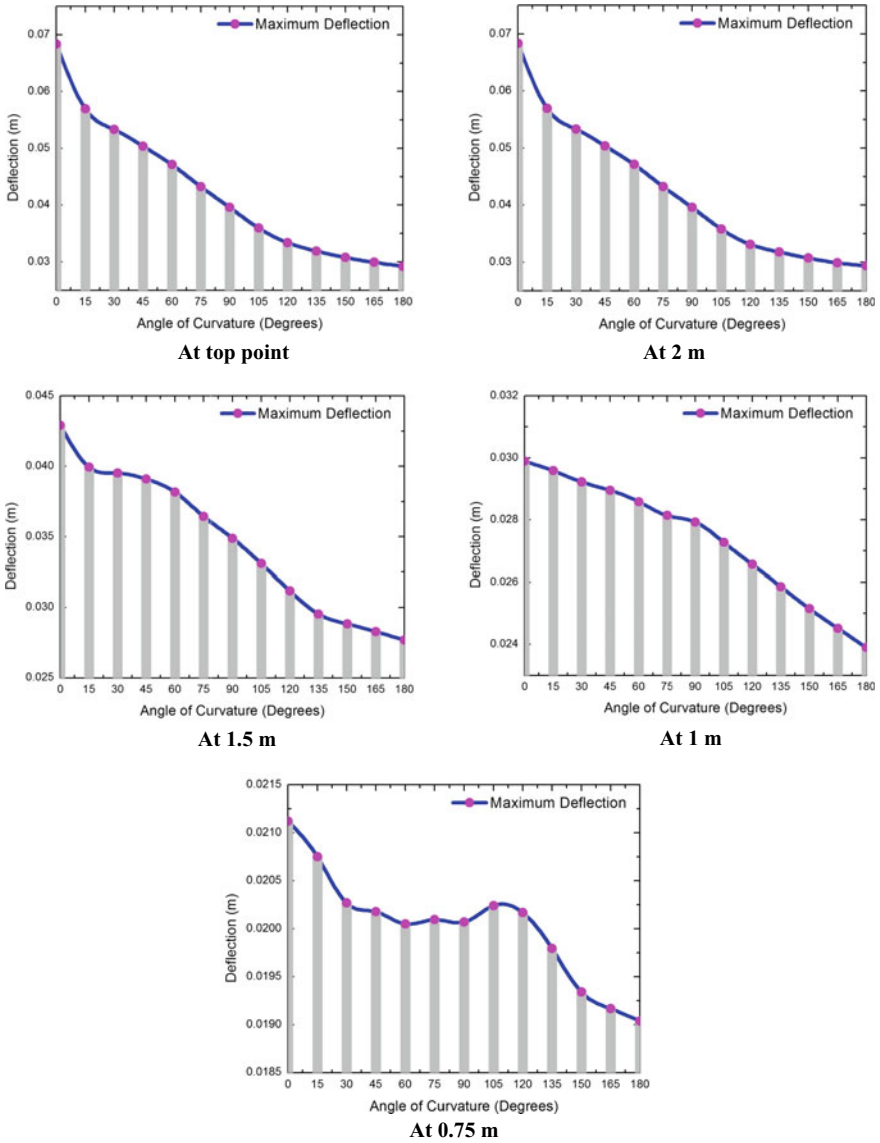
Fig. 3 Variation of peak deflection of wall with varying angle of curvature at various points along the wall height under blast loading

5 Conclusions

In the present investigation, non-linear dynamic finite element (FE) analysis of sacrificial curved steel wall is carried out with varying angle of curvature (i.e. 0°–180°). Herein, non-linear dynamic analysis is carried out using ABAQUS® finite element package. ConWep formulation is used for defining blast loading and performance of the wall, in terms of peak deflection, is compared to understand the effect on curvature on peak deflection. For this purpose, deformable 4-node, reduced integration, hourglass control with finite membrane strains elements are employed for non-linear FE analysis of curved wall. Non-linear dynamic analysis is carried out with varying angle of curvature along top one-fourth length of wall. Further, performance of curved walls is compared with that of straight vertical wall in terms of peak deflection. Deflection at various points along the height of wall is computed and analyzed. Based on this analysis, the following conclusions are drawn,

1. It is concluded that that introduction of curvature results into considerable reduction in peak deflection.
2. For straight wall, it is found that deflection is increasing with increase in height of observation point and maximum deflection is observed at top point.
3. It is found that introduction of curvature results in reduction of peak deflection. Thus, proper curvature of wall helps in improvement of blast resistance with all other conditions being same.
4. Peak deflection is decreasing with increase in angle of curvature for all the observation points considered in the present investigation except at 0.75 m point wherein, at curvature of 105º and 120º higher deflection are observed as compared to the deflection $\leq$ 90º curvatures.
5. Rate of reduction in peak deflection is varying with the point of observation along the height of the wall.

References

1. M.D. Goel, V.A. Matsagar, A.K. Gupta, Int. J. Prot. Str. **2**(1), 139 (2011)
2. M.D. Goel, T. Chakraborty, V.A. Matsagar, J. Batt. Technol. **15**(3), 1 (2012)
3. M.D. Goel, V.A. Matsagar. *Prac. Period. Str. Des. Const.*, **19**(2) 2014
4. C. Wu, H. Sheikh, Int. J. Impact Eng **55**, 24 (2013)
5. Z. Liskay, S. Rugg, C. Thompson, Lehigh Rev. **22**(5), 41 (2014)
6. V.A. Matsagar, Disaster Adv. **7**(1), 23 (2014)
7. S. Verma, M. Choudhury, P. Saha, Int. J. Res. Eng. Technol. **4**(13), 64 (2015)
8. ABAQUS® User's manual, *Dassault Systemes Simulia Corporation*, France (2011)
9. R.K. Varma, C.P.S. Tomar, S. Parkash, V.S. Sethi, ASME-Publications-PVP **351**, 207 (1997)

Free Vibration Analysis of Levy-Type Smart Hybrid Plates Using Three-Dimensional Extended Kantorovich Method

Susanta Behera and Poonam Kumari

Abstract In this research work, three-dimensional (3D) piezoelasticity solution is developed to analyze the free vibration behaviour of rectangular hybrid piezo-laminated plate using three-dimensional extended Kantorovich method (3D EKM). The partial differential equations (PDEs) of a bivariate problem is converted into two sets of ordinary differential equations (ODEs) in the two directions, by approximating the solution as a series of products of two separable functions. Following an iterative process which converges fast the free vibration frequency and other state variables are computed. The accuracy of this method is extensively verified by comparing the present prediction with previous analytical results published in the literature and with the finite element solutions wherever analytical solutions are not available. Benchmark results are presented for bimorph and hybrid composite plates for different boundary conditions. Effect of electric circuit conditions and plate aspect ratios (b/a) on the natural frequency are also investigated. The present results can serve as benchmark to assess the two-dimensional and numerical solutions.

Keywords Extended Kantorovich method · Free vibration · Hybrid plates · Analytical solution · Three-dimensional solution

Nomenclature

a,b	In-plane dimensions of the composite plate
d_{ij}	Piezoelectric constants
D_i	Electric displacement components ($i = x, y, z$)
h	Thickness of the composite plate
s_{ij}	Elastic compliance
S	Span-to-thickness ratio

S. Behera (✉)
Department of Mechanical Engineering, PMEC, Berhampur 761003, Odisha, India
e-mail: susantabc@gmail.com

P. Kumari
Department of Mechanical Engineering, IIT Guwahati, Guwahati 781039, Assam, India

t	Time variable
V	Volume of the plate
u, v, w	Displacement components along x, y and z axes, respectively
z_{k-1}, z_k	Z-coordinate of the bottom and top surfaces of kth layer, respectively
ε_{ij}	Dielectric coefficients
ϕ	Electric potential
σ_i	Normal stress components ($i = x, y, z$)
τ_{ij}	Shear stress components ($i, j = x, y, z$)
ξ_i, ξ_2	Dimensionless in-plane coordinates
$\zeta^{(k)}$	Local thickness coordinate for kth layer

1 Introduction

Laminated composite structures in the form of plates embedded or surface bonded with piezoelectric layers, known as smart hybrid structures, are extensively used for vibration control, structural health monitoring and many other sensing and control applications as multifunctional structures. Such structures are subjected to various types of static and dynamic loads. So, it is very important to understand how such smart hybrid laminated structures behave under the influence of free vibration which come under the scope of investigation of the present work. Recent review of literature on different two-dimensional (2D) and three-dimensional (3D) piezoelasticity theories [1, 2] for the static and dynamic analysis of composite and sandwich piezoelectric hybrid plates are available in the literature. The 3D solutions have advantage of predicting results in highest accuracy and hence can be used as benchmark solution for the assessment of other 2D theories. Yang et al. [3] and Heyliger and Brooks [4] presented the free vibration analysis of hybrid piezoelectric plates under cylindrical bending and extended further to the analysis of rectangular plates [5, 6]. Kapuria and co-workers [7, 8] presented the 3D harmonic analysis of hybrid piezoelectric plates and magnetoelastic angle-ply panels. The above-mentioned articles dealt with the all-round simply supported plates or panels. Applying state space finite element method (SSFEM) Quing et al. [9] presented the 3D static and free vibration solution for hybrid piezoelectric plates. In a recent paper, Feri et al. [10] presented 3D static and free vibration of piezo-layered cross-ply laminated plate. Extended Kantorovich method (EKM) proposed by Kerr [11] has been applied to plates [44] and shells based on 2D plate/shell theories. The 3D application of EKM has been carried out by Kapuria and Kumari [12, 13] based on 3D elasticity theory following a mixed formulation approach and has been extended to cylindrical bending of hybrid piezolaminated panels [14]. The multi-term 3D EKM has been applied for the bending analysis of Levy-type elastic laminated plates by Kumari and Kapuria [15] and later extended to multi-layered piezolaminated plates by Kumari et al. [16]. This 3D EKM has recently been applied for free vibration analysis of elastic laminated plates by Kumari and Behera [17].

In this paper, the free vibration analysis of piezoelectric bimorph plates and smart hybrid composite plates are presented using 3D EKM. Results are presented for different plate aspect ratios, various mechanical and electric boundary conditions and their effect on plate natural frequencies are investigated. The present results can be used as benchmark to assess the results of other 2D theories.

2 Formulation

As shown in Fig. 1, a cross-ply smart hybrid laminated composite plate with surface bonded piezoelectric layers at the top and bottom is considered for the study. The piezoelectric material bonded is orthorhombic with respect to principal material axes and has class mm2 symmetry. The reference plane lies at the plate mid-surface. The plate has L orthotropic layers and kth layer of the plate has thickness h^k. The plate is subjected to Levy-type boundary conditions at $y = 0, b$ and are subjected to any combination of boundary conditions ay $x = 0, a$.

The strains and electric field components from the 3D piezoelasticity relations are substituted into the modified Hamilton's principle for free vibration case of piezoelectric plate, without any body force and internal charge, to yield:

$$
\left.\begin{aligned}
&\int_t \int_V [\delta u(\tau_{xz,z} + \sigma_{x,x} + \tau_{xy,y} - \rho\ddot{u}) + \delta v(\tau_{yz,z} + \tau_{xy,x} + \sigma_{y,y} - \rho\ddot{v}) + \delta w(\sigma_{z,z} + \tau_{zx,x} + \tau_{yz,y} - \rho\ddot{w}) \\
&+ \delta\phi(D_{z,z} + D_{zx,x} + D_{yz,y}) + \delta\sigma_x(\bar{s}_{11}\sigma_x + \bar{s}_{12}\sigma_y + \bar{s}_{13}\sigma_z + \bar{d}_{31}D_z - u_{,x}) + \delta\sigma_y(\bar{s}_{12}\sigma_x + \bar{s}_{22}\sigma_y + \bar{s}_{23}\sigma_z \\
&+ \bar{d}_{32}D_z - v_{,y}) - \delta\sigma_z(w_{,z} - \bar{s}_{13}\sigma_x - \bar{s}_{23}\sigma_y - \bar{s}_{33}\sigma_z - \bar{d}_{33}D_z) - \delta\tau_{yz}(v_{,z} + w_{,y} - s_{44}\tau_{yz} - \bar{d}_{24}D_y) \\
&- \delta\tau_{zx}(u_{,z} + w_{,x} - s_{55}\tau_{zx} - \bar{d}_{15}D_x) + \delta\tau_{xy}(s_{66}\tau_{xy} - v_{,x} - u_{,y}) - \delta D_x(\phi_{,x} + \bar{\varepsilon}_{11}D_x - \bar{d}_{15}\tau_{zx}) \\
&- \delta D_y(\phi_{,y} + \bar{\varepsilon}_{22}D_y - \bar{d}_{24}\tau_{yz}) - \delta D_z(\phi_{,z} + \bar{\varepsilon}_{33}D_z - \bar{d}_{31}\sigma_x - \bar{d}_{32}\sigma_y - \bar{d}_{33}\sigma_z)]dVdt = 0, \\
&\hspace{6cm} \forall\, \delta u_i, \delta\phi, \delta\sigma_i, \delta\tau_{ij}, \delta D_i
\end{aligned}\right\}
$$

$$(1)$$
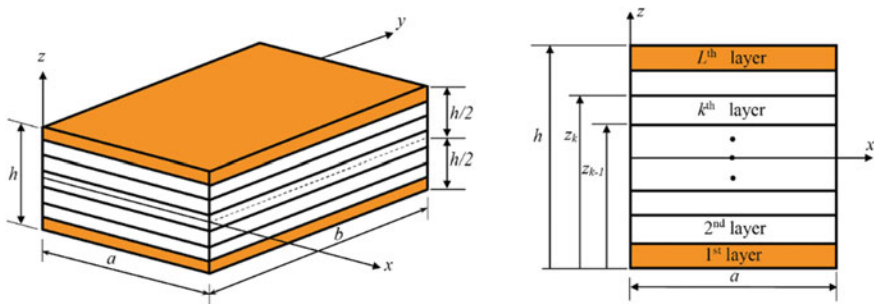
Fig. 1 Geometry and configurations of hybrid laminated plate

where V is $(a \times b \times h)$, $\bar{s}_{ij} = s_{ij} - d_{3i}\bar{d}_{3j}$, $\quad \bar{d}_{ij} = d_{3i}/\varepsilon_{33}$ for $(i,j) = 1, 2, 3$. $\bar{\varepsilon}_{11} = 1/\varepsilon_{11}, \bar{\varepsilon}_{22} = 1/\varepsilon_{22}, \bar{\varepsilon}_{33} = 1/\varepsilon_{33}$, $\bar{d}_{24} = d_{24}/\varepsilon_{22}, \bar{d}_{15} = d_{24}/\varepsilon_{11}$. Dimensionless coordinates $\xi_1 = x/a$, $\xi_2 = y/b$ and and $\zeta^{(k)} = (z - z_{k-1})/t^{(k)}$, which vary from 0 to 1. The outer top and bottom surfaces of piezo-layers are shear traction free and have prescribed ϕ i.e. close circuit (CC) condition or prescribed D_z i.e. open circuit (OC) condition. Mathematically, at $z = \pm h/2$, $\sigma_z = \tau_{yz} = \tau_{yz} = 0, \phi = 0$ or $D_z = 0$. Adjacent layers are assumed to have perfect bonding and hence $u, v, w, \sigma_z, \tau_{yz}, \tau_{zx}, \phi$ and D_z are continuous at the interfaces between kth and $(k + 1)$th layers. The piezo-elastic layer interfaces are grounded for effective actuation/sensing. On these interfaces, D_z is discontinuous, so ϕ is taken zero instead. The edges at $\xi_1 = 0$ and 1 are subjected to arbitrary boundary conditions among simply supported, clamped and free. The edges at $\xi_2 = 0$ and 1 are simply supported with $(u = \sigma_y = w = 0)$, and under close circuit (CC) condition with $\phi = 0$.

2.1 Fourier Series-Generalized Solution

The solution variables are expressed in terms of Fourier series in y, those satisfy the boundary conditions at the pair of simply supported edges identically.

$$(v, \tau_{xy}, \tau_{yz}, D_y) = \sum_{m=1}^{\infty} (v, \tau_{xy}, \tau_{yz}, D_y)_m \cos \omega t \cos m\pi\xi_2$$

$$(u, w, \sigma_x, \sigma_y, \sigma_z, \tau_{zx}, \phi, D_x, D_z) = \sum_{m=1}^{\infty} (u, w, \sigma_x, \sigma_y, \sigma_z, \tau_{zx}, \phi, D_x, D_z)_m \cos \omega t \sin m\pi\xi_2$$

$$(2)$$

where $(\ )_m$ denotes the mth Fourier term. The substitution of the above expressions into the variational Eq. (1) and using the orthogonality properties of cosine and sine for each m, we obtain the following field variables $\mathbb{X} = [u, v, w, \sigma_x, \sigma_y, \sigma_z, \tau_{xy}, \tau_{yz}, \tau_{zx}, \phi, D_x, D_y, D_z]_m^T$, which are functions of ξ_1 and ζ. The solution of the field variables X is assumed in terms of an n-term series of products of separable functions in ξ_1 and ζ. Solution of the jth variable $\mathbb{X}_j$ of $\mathbb{X}$ for the kth layer is taken as:

$$\mathbb{X}_j(\xi_1, \zeta) = \sum_{i=1}^{n} f_j^i(\xi_1)g_j^i(\zeta) \text{ for } j = 1, 2,\ldots, 13.$$ Functions $f_j^i(\xi_1)$ are valid for all layers, whereas $g_j^i(\zeta)$ corresponding to kth layer which is determined iteratively. In the first iteration, functions $f_j^i(\xi_1)$ are considered as known, while $g_j^i(\zeta)$ are determined for each layer. Functions $g_j^i(\zeta)$ are divided into two groups, a column vector

$\bar{G}$ for the eight variables those appear in the boundaries and $\hat{G}$ a column vector consisting of the remaining five variables. Then, the solution $\mathbb{X}_j$ is substituted back into Eq. (1) and performing integrating over ξ_1 direction and considering that the variations δg_j^i are arbitrary, the coefficients of δg_j^i are equated to zero individually which results in the following set of 8n ODEs and 5n algebraic equations for $g_j^i(\zeta)$ for the kth layer: $M\bar{G}_{,\zeta} = \overline{A}\bar{G} + \widehat{A}\widehat{G}$; $K\widehat{G} = \widetilde{A}\bar{G}$, where $M, \overline{A}, \widehat{A}, K$ and $\widetilde{A}$ are $8n \times 8n, 8n \times 8n, 8n \times 5n$ and $5n \times 8n$ matrices, respectively. Using the algebraic equation, $\hat{G}$ is eliminated from the ODE which further yields a system of $8n$ homogeneous first order ODEs with constant coefficients. These equations are solved analytically to reach at the final solution in the form $\sum_{i=1}^{8n} K_{di}(\zeta)C_i = 0$, where the coefficient matrix K_d depends on $\omega = \omega_m$. For non-trivial solution, it's determinant is zero and ω can be obtained by root finding of the equation $|det(K_d)| = 0$ using bisection method. The natural frequencies $\omega_{01} = \omega_m$ are obtained using the procedure of [19]. In the second iteration step, functions $g_j^i(\xi_1)$ are considered as known, while $f_j^i(\xi_1)$ is solved. This time, the integration is performed over the thickness direction ζ. Following the same procedure as in the previous section, a system of $13n$ differential-algebraic equations is obtained for $f_j^i(\xi_1)$.

3   Results and Discussion

At first, the results from the present method are validated by comparing with the results from other analytical solutions for two different configurations of plate (a) and plate (b) as shown in Fig. 2. The material properties mat.1, mat.2, mat.3… etc. are given as follows taken from ref. [16, 18].

$[(E_1, E_2, E_3, G_{12}, G_{23}, G_{31})$ GPa, (v_{12}, v_{13}, v_{23}), ρ kg/m³]=

mat.1: [(6.9, 6.9, 6.9, 1.38, 1.38, 1.38,), (0.25, 0.25, 0.25), 1578]

Fig. 2 Configurations of smart hybrid plate (**a**)

Plate (a)
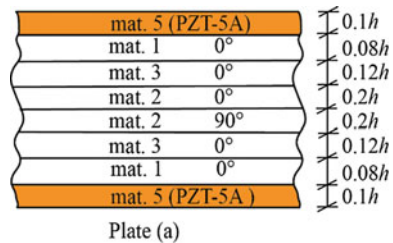
mat.2: [(224.25, 6.9, 6.9, 56.58, 1.38, 56.58), (0.25, 0.25, 0.25), 1578]
mat.3: [(172.5, 6.9, 6.9, 3.45, 1.38, 3.45), (0.25, 0.25, 0.25), 1578]
mat.4: [(181, 10.3, 10.3, 7.17, 2.87, 7.17), (0.28, 0.28, 0.33), 1578] and
mat.5: [(61.0, 61.0, 53.2, 22.6, 21.1, 21.1), (0.35, 0.38, 0.38), 7600], and
$[(d_{31}, d_{32}, d_{33}, d_{15}, d_{24})$ pm/V, $(\eta_{11}, \eta_{22}, \eta_{33})$ nF/m] = [(−171, −171, 374, 584, 584),
(15.3, 15.3, 15.0].

The natural frequency $\bar{\omega}_m$ is non-dimensionalized as: $\bar{\omega}_m = \omega a S \sqrt{\rho_0/E_0}$. Here,
$E_0 = 6.9$ GPa for plate (a) and 380.7 GPa for plate (c). $\rho_0 = 1578\,\text{kg/m}^3$ for plate
(a) and 7600 kg/m3 for plate (c).

3.1   Validation

The natural frequencies for a square plate with S values of 5, 10 and 20 are
presented in Table 1 for a square hybrid plate (a) of highly unsymmetrical lay-up
and are compared with the 3D exact [19] results. It is observed that the present
EKM results are exactly matching with the 3D exact results for thick to thin plates.

3.2   Benchmark Results

A rectangular piezoelectric bimorph plate (b) as shown in Fig. 3 which consists of
two identical layers of PZT-4 piezoceramics with poling along z-direction is con-
sidered here. The material properties of PZT-4 considered here is taken as given in
Ref. [18]:

Table 1 Natural frequencies $\bar{\omega}_{mn}$ of all-round simply supported (S-S) hybrid composite plate (a) with different S values

S	Entity	Present	3D Exact [19]
5	$\bar{\omega}_{11}$	7.4148	7.4148
	$\bar{\omega}_{21}$	14.714	14.714
	$\bar{\omega}_{22}$	18.643	18.643
	$\bar{\omega}_{31}$	23.621	23.621
10	$\bar{\omega}_{11}$	10.034	10.034
	$\bar{\omega}_{21}$	22.397	22.397
	$\bar{\omega}_{22}$	29.659	29.659
	$\bar{\omega}_{31}$	37.741	37.741
20	$\bar{\omega}_{11}$	11.418	11.418
	$\bar{\omega}_{21}$	29.024	29.024
	$\bar{\omega}_{22}$	40.137	40.137
	$\bar{\omega}_{31}$	53.580	53.580
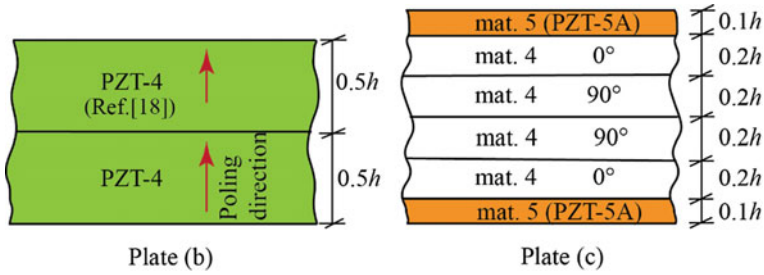
Fig. 3 Configurations of bimorph plate (**b**), smart hybrid plate (**c**)

$[(C_{11}, C_{22}, C_{33}, C_{12}, C_{23}, C_{31}, C_{44}, C_{55}, C_{66}] = [139, 139, 115, 77.8, 74.3, 74.3, 25.6, 25.6, 30.6]$ GPa

$[(e_{31}, e_{32}, e_{33}, e_{15}, e_{24}), (\eta_{11}, \eta_{11}, \eta_{33})] = [(-5.2, -5.2, 15.1, 12.7, 12.7)$ C/m^2, $(13.06, 13.06, 11.51)$ nF/m] and $\rho = 7600$ kg/m^3.

The interface between the two PZT layers is grounded. The natural frequencies $(\bar{\omega}_m)$ are obtained for the plate of span-to-thickness ratio, $S = 10$, for (i) top, bottom close circuit ($\phi = 0$), (ii) top, bottom open circuit conditions ($D_z = 0$) and (iii) top close, bottom open circuit conditions. The flexural natural frequencies for the first ten modes determined by the present 3D EKM are produced in Table 2 for F-F case. The side surfaces at $\xi_1 = 0, 1$ of the F-F plate are kept in open circuit condition for the cases (ii) and (iii). The 3D FE results obtained from ABAQUS are also presented for comparing the relative accuracy. For this 20-noded hexahedral solid element of type C3D20RE for piezo-layers with reduced integration is considered in the modelling. The model is discretized by (50 ×50 ×20) mesh size in length, width and thickness. The percentage difference (% diff.) is calculated as % diff. = [(3D EKM frequency—3D FE frequency)/3D EKM frequency] × 100. A maximum difference of 1.58% is noted for the sixth frequency in case (i) for plate aspect ratio, $b/a = 2$.

The benchmark frequencies of first ten flexural modes of a square smart composite plate (c) of top and bottom PZT-5A layers bonded on symmetric cross-ply graphite-epoxy (mat.4) substrate subjected to different sets of boundary conditions are presented in Table 3 for S values of 5, 10 and 20. All the side surfaces of piezoelectric layers, piezo-elastic interfaces and the outer surface of the top piezoelectric layer are grounded ($\phi = 0$) whereas the outer surface of the bottom piezoelectric layer is kept in open circuit condition. It is observed that the boundary conditions affect the lower mode frequencies significantly for the thick, moderately thick and thin plates, while its diminishing effect is observed at higher modes.

Table 2 Non-dimensional flexural natural frequencies of piezoelectric bimorph plate (b) with F-F boundary conditions for $S = 10$

b/a	Mode sequence	Top, bottom close		Top, bottom open		Top close, bottom open	
		Present	3D FE % diff.	Present	3D FE % diff.	Present	3D FE % diff.
1	1	2.905	−0.03	3.007	0.02	2.957	0.14
	2	4.649	−0.04	4.708	0.04	4.684	0.13
	3	10.490	−1.15	10.784	−0.62	10.522	−0.09
	4	11.195	−0.12	11.557	−0.12	11.389	0.29
	5	13.005	0.05	13.283	−0.11	13.248	0.82
	6	18.968	−0.24	19.571	−1.20	19.248	0.65
	7	20.564	−0.78	21.158	−0.24	20.587	−0.72
	8	23.522	−0.13	24.044	−0.09	23.763	0.04
	9	25.088	−0.12	25.480	−0.08	25.278	0.05
	10	28.485	−0.64	28.779	0.52	28.540	–0.21
2	1	0.729	−0.55	0.749	−0.13	0.737	0.13
	2	1.985	−0.05	1.994	0.0	1.990	0.10
	3	2.905	−0.03	3.007	0.03	2.958	0.17
	4	4.649	−0.04	4.708	0.04	4.684	0.14
	5	6.454	−0.12	6.650	0.37	6.575	0.30
	6	7.850	−1.58	8.137	−0.59	7.985	1.18
	7	8.317	−0.04	8.481	−0.14	8.387	−0.03
	8	10.490	−1.15	10.784	−0.62	10.554	0.21
	9	11.195	−0.12	11.557	−0.12	11.389	0.29
	10	13.005	0.05	13.283	−0.11	13.152	0.10

For instance, the percentage difference in the natural frequency in first mode between C-C and F-F is 48.92% calculated with respect to C-C frequency while it is 24.54% at the tenth mode for the thick plate, it is 60.89 and 26.62% at first and tenth mode for moderately thick plate and for the thin plate the difference is 69.93 and 34.37% at the first and tenth mode frequencies. Similar trend can be ascertained for other cases of boundary conditions also. The mode shapes for first three flexural frequencies of thick plates for various boundary conditions are illustrated in Fig. 4. In the figure, the numerical figures side by to the mode numbers denote the corresponding natural frequencies.

Table 3 The first ten non-dimensional flexural frequencies ($\bar{\omega}_m$) of smart composite plate (c) for different sets of boundary conditions

S	BCs	Mode sequences									
		1	2	3	4	5	6	7	8	9	10
5	S-S	7.181	13.594	13.821	18.367	20.931	21.632	24.523	24.884	28.817	29.448
	C-C	7.887	14.018	14.150	18.713	21.680	21.460	25.162	24.981	29.488	29.925
	C-S	7.476	13.901	13.838	18.514	21.160	21.656	24.708	25.057	28.890	29.513
	C-F	4.715	9.449	12.284	15.409	16.202	20.582	20.570	22.746	23.434	26.774
	F-F	4.028	5.514	11.314	11.851	13.081	17.234	17.745	20.330	21.135	22.581
10	S-S	9.369	19.614	21.236	28.724	34.047	35.019	40.796	40.876	49.491	50.098
	C-C	11.589	20.427	23.266	29.903	34.352	36.461	41.391	41.954	50.215	50.675
	C-S	10.551	20.000	22.251	29.292	34.187	35.716	41.076	41.375	50.156	50.047
	C-F	5.651	13.601	16.956	22.849	26.523	31.843	33.382	36.450	40.121	44.519
	F-F	4.532	6.706	16.120	16.659	17.666	25.695	30.240	31.422	32.679	37.183
20	S-S	10.433	22.930	27.833	37.474	43.185	51.659	54.923	59.448	68.796	73.865
	C-C	15.723	25.333	34.516	42.574	44.202	57.712	57.814	64.273	69.431	77.225
	C-S	12.830	24.007	31.336	40.042	43.650	54.750	56.289	61.887	69.065	75.548
	C-F	6.059	17.450	19.164	28.383	37.857	39.798	46.499	47.271	62.376	62.516
	F-F	4.727	7.169	18.352	19.542	20.958	31.527	39.071	41.063	41.412	50.680
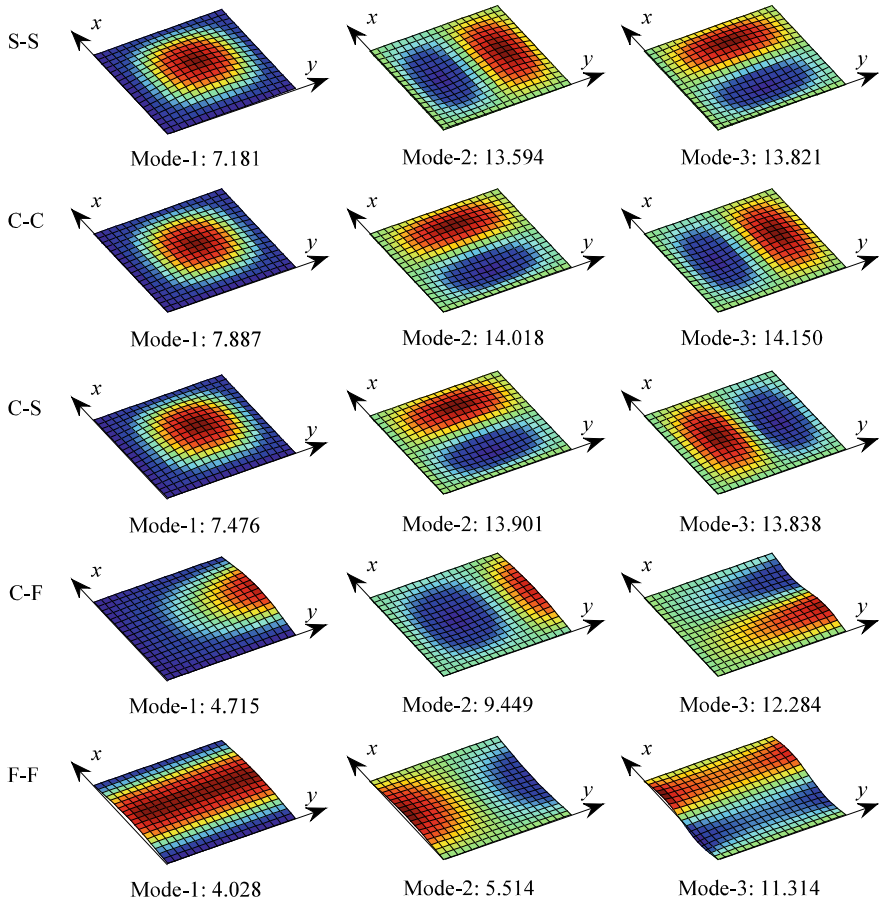
Fig. 4 First three flexural mode shapes for thick ($S = 5$) smart composite plate (c) subjected to arbitrary boundary conditions (S-S, C-C, C-S, C-F, F-F)

4   Conclusions

In this research work, the free vibration analysis of Levy-type hybrid composite plate is conducted by developing multi-term 3D EKM. Accuracy of the present method is extensively verified in comparison with other analytical results. The results for bimorph plate with different electrical boundary (close and open circuit) conditions and aspect ratios (b/a = 1 and 2) show good agreement with 3D FE results of ABAQUS. Benchmark natural frequencies are presented for hybrid composite plates subjected to different boundary conditions for different span-to-thickness ratios and are observed that influence of boundary conditions on plate frequencies are more significant at lower modes.

References

1. A.S. Sayyad, Y.M. Ghugal, On the free vibration analysis of laminated composite and sandwich plates: a review of recent literature with some numerical results. Compos. Struct. **129**, 177 (2015)
2. C.P Wu, K.H. Chiu and Y.M. Wang, A review on the three-dimensional analytical approaches of multilayered and functionally graded piezoelectric plates and shells. CMC Comput. Mater. Con., **8**, 93 (2008)
3. J.S. Yang, R.C. Batra, X.Q. Liang, The cylindrical bending vibration of a laminated elastic plate due to piezoelectric actuators. Smart Mater. Struct. **3**(4), 485 (1994)
4. P. Heyliger, S. Brooks, Free vibration of piezoelectric laminates in cylindrical bending. J. Appl. Mech. **32**(20), 2945 (1995)
5. R.C. Batra, X.Q. Liang, The vibration of a rectangular laminated elastic plate with embedded piezoelectric sensors and actuators. Comput. Struct. **63**(2), 203 (1997)
6. P. Heyliger, D.A. Saravanos, Exact free-vibration analysis of laminated plates with embedded piezoelectric layers. J. Acoust. Soc. Am. **98**(3), 1547 (1995)
7. S. Kapuria S and G.G.S. Achary, Exact 3D piezoelasticity solution of hybrid cross-ply plates with damping under harmonic electro-mechanical loads. J. Sound Vib., **282**, 617 (2005)
8. P. Kumari, J.K. Nath, P.C. Dumir, S. Kapuria, 2D exact solutions for flat hybrid piezoelectric and magnetoelastic angle-ply panels under harmonic load. Smart Mater. Struct. **16**, 1651 (2007)
9. G. Qing, J. Qiu, Y. Liu, A semi-analytical solution for static and dynamic analysis of plates with piezoelectric patches. Int. J. Solids Struct. **43**, 1388 (2006)
10. M. Feri, A. Alibeigloo, A.A.P. Zanoosi, Three dimensional static and free vibration analysis of cross-ply laminated plate bonded with piezoelectric layers using differential quadrature method. Meccanica **51**, 921 (2016)
11. A.D. Kerr, An extension of the Kantorovich method. Q. Appl. Math., **4**, 219 (1968)
12. A. Fereidoon, A. Mohyeddin, M. Sheikhi, H. Rahmani, Bending analysis of functionally graded annular sector plates by extended Kantorovich method. Compos. Part B-Eng. **43**(5), 2172 (2012)
13. A.R. Ranji, H.R. Hoseynabadi, A semi-analytical technique for bending analysis of cylindrical panels with general loading and boundary conditions. J. Mech. Sci. Technol. **26**, 1711 (2012)
14. S. Kapuria, P. Kumari, Extended Kantorovich method for coupled piezoelasticity solution of piezolaminated plates showing edge effects. Proc. R. Soc. A **469**, 20120565 (2013)
15. P. Kumari, S. Kapuria, R.K.N.D. Rajapakse, Three-dimensional extended Kantorovich solution for Levy-type rectangular laminated plates with edge effects. Compos. Struct. **107**, 167 (2014)
16. P. Kumari, S. Behera, S. Kapuria, Coupled three-dimensional piezoelasticity solution for edge effects in Levy-type rectangular piezolaminated plates using mixed field extended Kantorovich method. Compos. Struct. **140**, 491 (2016)
17. P. Kumari, S. Behera, Three-dimensional free vibration analysis of Levy-type laminated plates using multi-term extended Kantorovich method. Compos. Part B-Eng. **116**, 224 (2017)
18. S. Kapuria, S.D. Kulkarni, An efficient quadrilateral element based on improved zigzag theory for dynamic analysis of hybrid plates with electroded piezoelectric actuators and sensors. J. Sound Vib. **315**(1–2), 118 (2008)
19. S. Kapuria, G.G.S. Achary, Exact 3D piezoelasticity solution of hybrid cross-ply plates with damping under harmonic electro-mechanical loads. J. Sound Vib. **282**(3–5), 617 (2005)

Analysis of Orthotropic Variable Thickness Rotating Disc

Manoj Sahni and Ritu Sahni

Abstract The present paper deals with the study of annular disc made of orthotropic material in which the thickness varying from inner to outer radii of the disc and its influence on the stresses is investigated. Here, the disc is divided into two regions–inner plastic and outer elastic. With a variation in thickness, a significant impact on the stresses (radial and circumferential) is observed. The thickness is varying radially in an axisymmetric disc and the stresses–radial and circumferential in elastic region and plastic region are analytically derived. The results are numerically discussed and graphically represented.

Keywords Orthotropic · Thickness · Disc · Stresses · Strains

1 Introduction

In the current scenario, the scientists and engineers are concerned with the study of the behaviour of components under various external actions. The study of the components, made up of functionally graded materials, has vital importance in the research community. Further, the disc of various types such as thin and thick discs, annular and solid disc are used as components in various engineering applications such as in high-speed gears, compact discs, turbines, bullock-cart wheels, fly wheels and many more. The industrial uses of disc are disc brakes, Magneto cover, disc spring for heavy loads, pneumatic clutches, etc. A variable thickness thin or thick is used in technical applications such as in turbine blades, gears, and many more. It has advantage over the rotating disc with constant thickness firstly, in terms of reduced weight and lower rotating inertia. Second, the stress is distributed along the radius in such a way that the optimal use of a disc material can be done. FGM

M. Sahni (✉)
Department of Mathematics, SoT, PDPU, Gandhinagar 382007, Gujarat, India
e-mail: manojsahani117@gmail.com

R. Sahni
Institute of Advanced Research, Gandhinagar 382007, Gujarat, India

rotating thin or thick discs has other industrial applications such as in ship propellers, aerospace structures, flywheels and internal combustion engines.

Hence, in recent years, scientific study of functionally graded materials attracts many researchers to study behavior of discs under various parameters of influence. For example, in the structural analysis, the properties of the anisotropic material cannot be neglected. The analysis of the strength of the material becomes more complicated if a material is made up of more than one material. The analytical solutions of isotropic, transversely isotropic, orthotropic materials, etc. and elastic–plastic analysis is found in a book by Timoshenko and Goodier [1]. Due to broad engineering applications, lots of research has been carried out using these materials. Analysis of rotating disc and cylinder with variable density and variable thickness having these materials is an important issue found in various mechanical and engineering problems.

Many researchers have worked on the problems related to disc and cylinders using classical approach and Seth's transition theory (see for instance, [2–12]). Callioglu et al. [2] studied the stress analysis of the annual region of rotating disc by considering its elastic–plastic region made up of orthotropic material. Alexandrova and Real [3] calculated the stress distributions for an intermediate elastic–plastic and fully plastic regions and studied the effect of angular rotation, thickness variation for both the regions. Thermal stresses are obtained for an orthotropic aluminum metal matrix composite disc analytically by Altan et al. [4]. He developed an algorithm to calculate thermal stresses with temperature varying quadratically from inner to outer radii of the disc. In continuation of the above work, both analytical and numerical methods are used, to compare the results for rotating isotropic homogeneity disc by Kansal et al. [5]. The effects of variation in density and thickness on creep stresses and strains were studied by Sharma et al. [6] using Seth's transition theory. Under the effect of internal pressure, the analysis of functionally graded rotating disc is done by Sahni et al. [7]. A shooting method is used to develop solutions for stresses and deformation under the assumption of plane stress by Eraslan et al. [8]. The solutions are obtained for rotating annular disks by Eraslan et al. [9] in terms of hypergeometric functions, with the boundary conditions which are of the form—pressure at one boundary and the other boundary is free. The effect of density varying exponentially on an elastic–plastic rotating disk using Tresca yield criterion and its associated flow rule is studied by Sahni et al. [10] in 2017. Further, with variation in Young's modulus for an axisymmetric case an analytical solution is obtained by Sahni et al. [11], in 2018. With continuation of this work, the effects of two parameters–thickness and Young's modulus are studied simultaneously and analytical solutions are obtained by Sahni et al. [12] in the same year.

In this paper, we have studied the effect of thickness parameter, varying radially in an axisymmetric case. Also, the expressions of the stresses–radial and circumferential in outer elastic region and inner plastic region are analytically derived. The graphs are drawn for both radial and circumferential stresses in an elastic region.

2 Governing Equations

Consider an annular disc whose inner radii is $'a'$ and outer radii is $'b'$. Let $'c'$ be the surface between inner and outer radii which differentiates inner plastic and outer elastic region. The ordinary differential equation for 1D axisymmetric problem for a rotating disc with variable thickness is given as [12],

$$\frac{d(hrT_{rr})}{dr} - hT_{\theta\theta} + hrw^2 r^2 = 0, \tag{1}$$

where h is the thickness varying from inner to outer radii and ρ, ω is the density and angular speed, respectively of an orthotropic annular disc. Here T_{rr}, $T_{\theta\theta}$ are stresses along radial 'r' and circumferential θ directions, respectively.

With the geometrical consideration, the strain–displacement relations are defined as [12],

$$\varepsilon_r = \frac{du}{dr}, \; \varepsilon_\theta = \frac{u}{r}, \tag{2}$$

where u is the radial displacement. Here ε_r and ε_θ are the strains in radial and circumferential directions, respectively. The strain compatibility equation is derived from Eq. (2) given as follows:

$$\varepsilon_r = \varepsilon_\theta + r\frac{d\varepsilon_\theta}{dr}. \tag{3}$$

The stress function $S(r)$ satisfying the equilibrium Eq. (1) is defined as,

$$T_{rr} = \frac{S}{hr} \quad \text{and} \quad T_{\theta\theta} = \frac{S}{h} + \rho\omega^2 r^2 \tag{4}$$

For orthotropic materials, the strain–stress compliance matrix in terms of stress function is given as,

$$\varepsilon_r = a_{rr}\frac{S}{hr} + a_{r\theta}\left(\frac{S}{h} + \rho\omega^2 r^2\right) \quad \text{and} \quad \varepsilon_\theta = a_{r\theta}\frac{S}{hr} + a_{\theta\theta}\left(\frac{S}{h} + \rho\omega^2 r^2\right) \tag{5}$$

where a_{rr}, $a_{r\theta}$ and $a_{\theta\theta}$ are the components of the compliance matrix.

3   Solution in an Outer Elastic Region

In this paper, the profile of the thickness parameter is chosen as

$$h = h_0 \left(\frac{r}{a}\right)^\beta, \tag{6}$$

where β is the parameter index and thickness varying from inner to outer radii of the annular disc.

Substituting Eqs. (5) and (6) into compatibility Eq. (3), we get

$$r^2 S'' + rS'(1 - \beta) - S(m^2 + \beta v_{r\theta}) = \frac{h_0 \rho \omega^2 r^{\beta+3}}{a^\beta}(v_{r\theta} - 3) \tag{7}$$

where $m = \sqrt{\frac{a_{rr}}{a_{\theta\theta}}}$ and $v_{r\theta} = \frac{a_{r\theta}}{a_{\theta\theta}}$, and $v_{r\theta}$ is the Poisson's ration which is taken as constant.

The stress function S is calculated as

$$S = C_1 r^{n_1} + C_2 r^{n_2} + h\rho\omega^2 r^3 \frac{(v_{r\theta} - 3)}{3\beta + 9 - m^2 - \beta v_{r\theta}} \tag{8}$$

where $n_{1,2} = \frac{\beta \pm \sqrt{\beta^2 + 4m^2 + 4\beta v_{r\theta}}}{2}$.

The stress components—radial and circumferential can be obtained from Eq. (4) as

$$T_{rr} = \frac{C_1 r^{n_1 - 1}}{h} + \frac{C_2 r^{n_2 - 1}}{h} + \rho\omega^2 r^2 \frac{(v_{r\theta} - 3)}{3\beta + 9 - m^2 - \beta v_{r\theta}}, \tag{9}$$

$$T_{\theta\theta} = \frac{n_1 C_1 r^{n_1 - 1}}{h} + \frac{n_2 C_2 r^{n_2 - 1}}{h} + \rho\omega^2 r^2 + \rho\omega^2 r^2 \frac{(v_{r\theta} - 3)}{3\beta + 9 - m^2 - \beta v_{r\theta}}(3 + \beta). \tag{10}$$

The boundary conditions are taken as free–free, i.e. radial stress is zero at both inner and outer boundary. Using these boundary conditions, the arbitrary constants are calculated as,

$$
\begin{aligned}
C_1 &= -\frac{a^{-\beta}\left(a^{\beta+3}b^{n_2} - a^{n_2}b^{\beta+3}\right)h_0\rho\omega^2(v_{r\theta} - 3)}{(a^{n_2}b^{n_1} - a^{n_1}b^{n_2})(-3\beta - 9 + m^2 + \beta v_{r\theta})}, \\
C_2 &= \frac{a^{-\beta}\left(a^{\beta+3}b^{n_1} - a^{n_1}b^{\beta+3}\right)h_0\rho\omega^2(v_{r\theta} - 3)}{(a^{n_2}b^{n_1} - a^{n_1}b^{n_2})(-3\beta - 9 + m^2 + \beta v_{r\theta})}.
\end{aligned} \tag{11}
$$

4 Solution in an Inner Plastic Region

In classical theory, a yield criterion is used to match the solution in the elastic–plastic interface. Here, Tsai-Hill yield criterion is used and the equivalent stress is given as [2]:

$$\overline{\sigma} = \sqrt{T_{\theta\theta}^2 - T_{rr}T_{\theta\theta} + T_{rr}^2\frac{X^2}{Y^2}}, \tag{12}$$

where X and Y are the yield strengths in tangential and radial directions, respectively. With the help of Ludwik equation, the yield strength can be written as [2]:

$$\overline{\sigma} = \sigma_0 + K\varepsilon_p^n \tag{13}$$

Here constants K, n and ε_p are the plasticity constant, hardening parameter and plastic strain, respectively. The constant σ_0 is the yield strength in tangential direction. The total incremental strains are written as [2]:

$$d\varepsilon_r = a_{rr}d\sigma_r + a_{r\theta}d\sigma_\theta + d\varepsilon_r^p, \quad d\varepsilon_\theta = a_{r\theta}d\sigma_r + a_{\theta\theta}d\sigma_\theta + d\varepsilon_\theta^p. \tag{14}$$

For anisotropic materials, governing equation for plastic strain increments is defined as [2]:

$$f_{ij} = \overline{\sigma}. \tag{15}$$

The associated flow rule is defined as follows [2]:

$$d\varepsilon_{ij}^p = \frac{\partial f_{ij}}{\partial \sigma_{ij}}d\lambda. \tag{16}$$

where $d\lambda$ is a scalar quantity equivalent to plastic strain increment $d\varepsilon_p$. Using the equation of equilibrium (1), circumferential stress can be written as:

$$T_{\theta\theta} = \frac{1}{h}\frac{d}{dr}(hrT_{rr}) + \rho\omega^2 r^2. \tag{17}$$

Using Eqs. (6), (12) and (17), we get

$$r^2(T_{rr}')^2 + T_{rr}'(rT_{rr}(1+2\beta) + 2\rho\omega^2 r^3) + \rho\omega^2 r^2 T_{rr}(1+2\beta) + (T_{rr})^2\left(\beta^2 + \beta + \frac{X^2}{Y^2}\right) + (\rho\omega^2 r^2)^2 - (\overline{\sigma})^2 = 0 \tag{18}$$

From Eq. (18), one obtain

$$\frac{dT_{rr}}{dr} = \frac{-(rT_{rr}(1-2\beta)+2\rho\omega^2r^3)\pm\sqrt{(rT_{rr}(1-2\beta)+2\rho\omega^2r^3)^2-4r^2\begin{bmatrix}\rho\omega^2r^2T_{rr}(1+2\beta)\\+(T_{rr})^2\left(\beta^2+\beta+\frac{X^2}{Y^2}\right)\\+\left(\rho\omega^2r^2\right)^2-\left(\bar{\sigma}\right)^2\end{bmatrix}}}{2r^2}$$

(19)

Further, using Eq. (16), plastic strain increments can be obtained.

The incremental strain–elastic and plastic can be obtained from the integration of Eq. (14), which is given as:

$$\varepsilon_r = a_{rr}T_{rr} + a_{r\theta}T_{\theta\theta} + \varepsilon_r^p + I_1 \quad \text{and} \quad \varepsilon_\theta = a_{r\theta}T_{rr} + a_{\theta\theta}T_{\theta\theta} + \varepsilon_\theta^p + I_2.$$

(20)

It follows that the plastic yielding first starts at the inner surface of the disc and at this point the strain components for both regions (elastic and elastic–plastic) are equal and zero, i.e. $\varepsilon_r^p = \varepsilon_\theta^p = 0$. Using this, the integration constants, I_1 and I_2 are calculated as zero. When the inner plastic region is extended to radius 'c', i.e. where the plastic yielding starts the radial stress can be easily found from the Eq. (9).

At the intermediate surface $(r = c)$, the radial stress at the elastic boundary and plastic boundary are equal. Let T_{rr} is at p at the elastic–plastic interface, i.e.,

$$T_{rr} = p \text{ at } r = c \quad \text{and} \quad T_{rr} = 0 \text{ at } r = b$$

(21)

For the plastic region, the constants of integration are obtained as,

$$C_1 = \frac{h_0((\frac{b}{a})^\beta h_0)^0(-b^3(\frac{b}{a})^\beta c^{n_2}\rho\omega^2(-3+v_{r\theta})+b^{n_2}c(\frac{c}{a})^\beta(p(-9+m^2-3\beta)-3c^2\rho\omega^2+(p\beta+c^2\rho\omega^2)v_{r\theta}))}{(-b^{n_1}(\frac{b}{a})^\beta c^{n_2}h_0+b^{n_2}c^{n_1}((\frac{b}{a})^\beta h_0)^0)(m^2-3(3+\beta)+\beta v_{r\theta})}$$

$$C_2 = \frac{(\frac{b}{a})^\beta h_0(-b^3c^{n_1}\rho\omega^2((\frac{b}{a})^\beta h_0)^0(-3+v_{r\theta})+b^{n_1}c(\frac{c}{a})^\beta h_0(p(-9+m^2-3\beta)-3c^2\rho\omega^2+(p\beta+c^2\rho\omega^2)v_{r\theta}))}{(b^{n_1}(\frac{b}{a})^\beta c^{n_2}h_0-b^{n_2}c^{n_1}((\frac{b}{a})^\beta h_0)^0)(m^2-3(3+\beta)+\beta v_{r\theta})}$$

(22)

5 Results and Discussion

In this work, elastic–plastic stress analysis is calculated for a variable thickness orthotropic rotating annular disc. The graphs are plotted using MATHEMATICA software. The mechanical properties are taken for curvilinear steel fibers-reinforced by aluminum matrix: $v_{r\theta} = 0.28$, $E_r = 89500$ MPa, $E_\theta = 71500$ MPa, $h_0 = 2$ cm., $a = 20$ mm., $b = 50$ mm., $\rho = 3.4725$ g/cm^3 [2]. The stresses–radial and circumferential is calculated for different angular velocities $\omega = 70, 100$ rad/s, which is
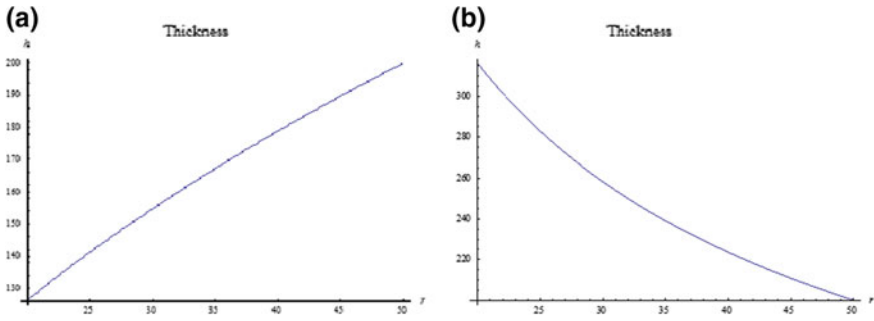
Fig. 1 Variation of Thickness profile from inner (r = a) to outer (r = b) radii for **a** $\beta = 0.5$, **b** $\beta = -0.5$

chosen arbitrarily and its effect is studied with increase in value of rotation. Also by taking different variable thickness parameter (β) the effect on stresses is analyzed.

In Fig. 1, the variation in disc profile for positive and negative values of β is shown. When β is positive the thickness is increasing from inner to outer surface of the disc. When it is negative, the thickness is decreasing from inner to outer radii. In Fig. 2, graphs are plotted for radial and circumferential stresses against radii in the elastic region. It is seen that with the increase in angular speed both the stresses show a sharp increase. The sharp increase from inner to outer is because of the centrifugal force acting outwards caused by rotation. The circumferential stress is maximum at the inner surface and minimum at the outer surface of the disc which can be seen from Fig. 2.

When the thickness is increasing from inner to outer radii of the disc, the circumferential stress is large as compared to the thickness when it is decreasing as
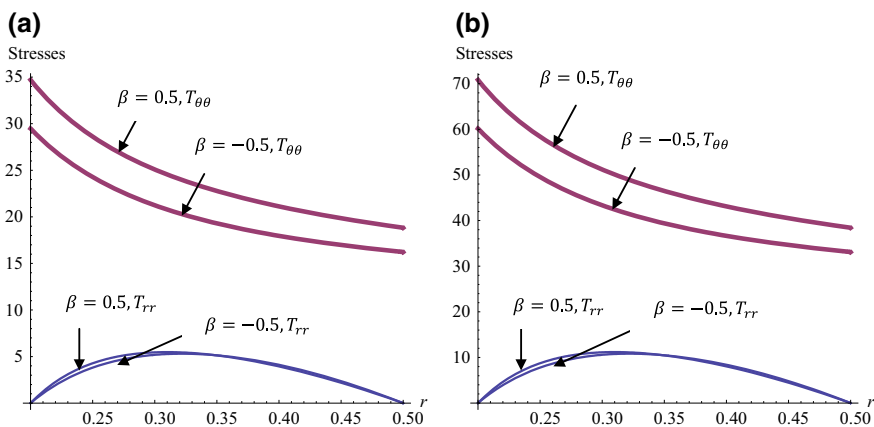
Fig. 2 Radial and circumferential stresses for variable thickness annular disk for angular speed **a** $\omega = 70\,\text{rad/s}$ and **b** $\omega = 100\,\text{rad/s}$

can be seen from Fig. 2. As the circumferential stress act as a restraining stress, hence for safety of the disc, it is better to manufacture disc with thickness varying radially in a non-linear fashion from inner to outer radii in a decreasing way. For constant thickness, i.e.$\beta = 0$, the results are verified with those available in literature [2].

6   Conclusions

The magnitude of the tangential stress component for elastic region is higher than the magnitude of the radial stress component. When the circumferential and radial stresses are lesser, the thickness decreases $(\beta = -0.5)$ as compared to thickness increases $(\beta = 0.5)$ at different angular speeds. Hence the disc with variable decreasing thickness from inner to outer radii is better to manufacture as compared to the disc with variable increasing thickness.

References

1. S. Timoshenko, J.N. Goodier, *Theory of Elasticity* (McGraw-Hill, New York, 1970)
2. H. Callioglu, M. Topcu, A.R. Tarakerlar, Int. J. Mech. Sci. **48**, 985 (2006)
3. N.N. Alexandrova, P.M.M.V. Real, Proc. IMechE, Part C: J. Mech. Eng. Sci. **221**, 137 (2007)
4. G. Altan, M. Topçu, N.B. Bektaş, B.D. Altan, J. Mech. Sci. Technol. **22**, 2318 (2008)
5. G. Kansal, M. Parvez, Int. J. Mod. Eng. Res. (IJMER) **2**, 3881 (2012)
6. S. Sharma, M. Sahni, Annals. Faculty Eng. Hunedoara–Int. J. Eng. 289 (2013)
7. M. Sahni, R. Sahni, Eng. Autom. Probl. **3**, 125 (2014)
8. A.N. Eraslan, Yaseminkaya and Busraciftcia, Math. Sci. Appl. E-Notes, **2** (2014)
9. A.N. Eraslan, Y. Kaya, E. Varli, Pamukkale University J. Eng. Sci. **22**, 24 (2016)
10. M. Sahni, S. Sharma, Res. Eng. Struct. Mat. **3**, 123 (2017)
11. M. Sahni, R. Sahni, Appl. Math. Comput. Intell. FIM 2015, **730**. Springer, Cham (2018), p. 26
12. M. Sahni, R. Sahni, Appl. Math. Comput. Intell. FIM 2015, **730** Springer, Cham (2018), p. 54

Shear Resistance Models of Girders with Corrugated Webs

Qazi Inaam and Akhil Upadhyay

Abstract Corrugated webs are increasingly used in many civil engineering applications especially in the girders of bridges. They offer increased out of plane stiffness and higher shear buckling capacities. The geometry of the corrugations alters the shear stress distribution in the webs when compared to flat webs. There are mainly two shear bucklings modes. Local buckling involves a single fold whereas global buckling involves many folds and extends over the entire depth of the web. Local buckling is calculated from classical plate buckling equations whereas global buckling is computed by treating corrugations as a flat orthotropic web. Recently a new method known as Direct Strength method (DSM) has also been applied to determine the shear capacity of beams with corrugated webs. In this paper various shear resistance models of girders with trapezoidal webs proposed by Lindner, Johnson and Cafolla, EN1993-1-5 and DSM are compared with experimental data to determine their efficiencies and applicability for design purposes.

Keywords Corrugated webs · Buckling · Shear design models

1 Introduction

Corrugated webs are used as girders for bridges in Germany, France, Japan, Korea and China. They constitute landmark bridges and are aesthetic in nature. Several models have been developed by various researchers [1–3] for calculating the shear capacities of corrugated beams involving various buckling checks. It is conventionally assumed that because of the corrugations in the web, it is unable to resist longitudinal stresses. Consequently, bending resistance is provided by the flanges of the girders. An increase in warping stiffness because of the corrugations has also been reported in the literature. Shear resistance of the corrugated girders is assumed to be provided by the webs. Thus, shear force is carried entirely by the webs

Q. Inaam (✉) · A. Upadhyay
Department of Civil Engineering, IIT Roorkee, Roorkee 247667, Uttrakhand, India
e-mail: inaamqazi@gmail.com

Fig. 1 Geometric configuration of the corrugated profile
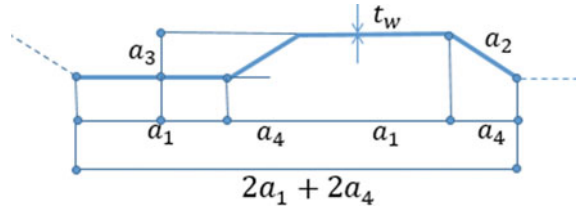
because of the accordion effect. As webs are incapable of resisting flexure, shear resistance of girders can be determined without moment–shear interaction. The average shear stress (τ) is constant and is calculated by:

$$\tau = \frac{V}{h_w t_w} \tag{1}$$

where V is the shear force, h_w and t_w are the web depth and web thickness respectively. The corrugation geometry and geometrical parameters are shown in Fig. 1.

DSM method [4] avoids lengthy effective width calculations and uses elastic buckling loads to calculate the design capacities.

2 Theoretical Background

Corrugated webs mainly fail in one of the following 3 shear modes: local buckling, global buckling and interactive buckling.

2.1 Local Shear Buckling

Local buckling involves individual folds of the web. This mode is significant as most of the practical girders used in bridges fall under this. From classical plate buckling theory we know that slenderness ratio of the subplate is the most important parameter. The individual sub folds are supported by horizontal flange edges at two edges and by adjacent folds at two vertical edges. The local shear buckling stress (τ_{cr}) [5, 6] is given by plate buckling theory:

$$\tau_{cr} = k_L \frac{\pi^2 E}{12(1 - v^2)} \left(\frac{t_w}{a_{\max}}\right)^2 \tag{2}$$

where v is the Poisson's ratio, E is Young's modulus of elasticity, a_{max} is the maximum fold with (maximum of a_1 and a_2), t_w is the thickness of the web panel and k_L is the local shear buckling coefficient. k_L depends on boundary conditions

Fig. 2 Local buckling of folds [7]
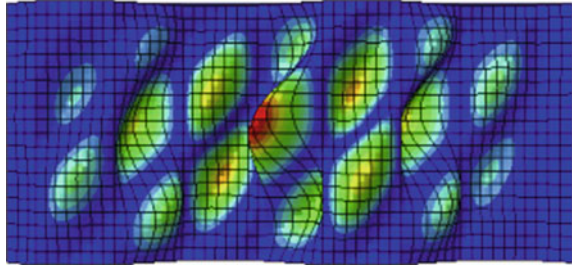
and fold aspect ratio. The value of k_L is 5.34 when the edges of the fold plate are assumed to be simply supported and 8.98 when the edges are assumed to be fixed supported. Figure 2 shows the local buckling failure mode of a sample corrugated web girder.

2.2 Global Shear Buckling

Global shear buckling stress is calculated by treating corrugated web as an orthotropic plate. Unlike local buckling the failure mode involves the entire depth of the girder. Easley [8] gave the formulae for calculating global buckling stress ($\tau_{cr,G}$) as:

$$\tau_{cr,G} = k_G \frac{D_x^{0.25} D_z^{0.75}}{t_w h_w^2} \tag{3}$$

$$D_x = \frac{E t_w^3}{12(1 - v^2)} \frac{a_1 + a_4}{(a_1 + a_2)} \tag{4}$$

$$D_z = \frac{E I_z}{w} = \frac{E t_w^3 a_3^2}{12} \frac{3a_1 + a_2}{(a_1 + a_4)} \tag{5}$$

where D_X and D_Z are the orthotropic plate bending stiffnesses in weak and strong axis, k_G is the global buckling shear coefficient. The value of k_G is assumed to be 32.4 for simply supported edges and 60.4 for clamped edges. Figure 3 shows the global shear buckling mode of corrugated web girder.

2.3 Interactive Shear Buckling

Interactive shear buckling modes have characteristics of both local buckling and global buckling modes. This type of failure involves buckling in multiple folds. Generalized interaction formulae is given by [1]:
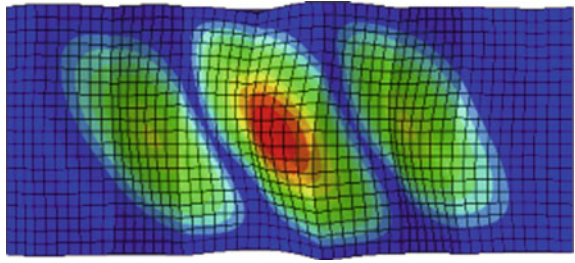
$$\frac{1}{\left(\tau_{cr,I}\right)^n} = \frac{1}{\left(\tau_{cr,L}\right)^n} + \frac{1}{\left(\tau_{cr,G}\right)^n}$$

$$\tau_{cr,I} = \frac{\tau_{cr,L} \cdot \tau_{cr,G}}{\left(\left(\tau_{cr,L}\right)^n + \left(\tau_{cr,G}\right)^n\right)^{\frac{1}{n}}} \tag{6}$$

where $\tau_{cr,I}$ is the interactive buckling stress, $\tau_{cr,L}$ is the local buckling stress and $\tau_{cr,G}$ is the global buckling stress. Various researchers have given different values of n based on experimental and empirical results. Figure 4 illustrates the interactive buckling stress of the corrugated web.

3   Shear Resistance Models

The characteristic shear resistance of beams having corrugated web [9] is given by:

$$V_R = \chi \frac{f_{yw}}{\sqrt{3}} h_w \cdot t_w \tag{7}$$

where χ is the minimum of the reduction factors computed for local buckling and global buckling. Slenderness parameter is defined as:
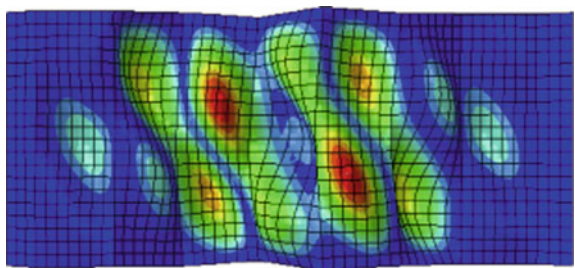
$$\lambda_i = \sqrt{\frac{f_{yw}}{\tau_{cri}\sqrt{3}}} \tag{8}$$

3.1 Lindner's Model [1]

Lindner proposed the reduction factor of

$$\chi_{i,L} = \frac{0.588}{\lambda_i} \tag{9}$$

$$\text{Where} \quad \lambda_1 = \sqrt{\frac{f_{yw}}{\tau_{cr1}\sqrt{3}}}$$
$$\lambda_2 = \sqrt{\frac{2f_y}{\tau_{cr2}\sqrt{3}}} \text{ if } 0.5 < \frac{\tau_{cr1}}{\tau_{cr2}} < 2 \tag{10}$$
$$\text{and } \lambda_2 = \sqrt{\frac{2f_y}{\tau_{cr2}\sqrt{3}}} \text{ for other } \frac{\tau_{cr1}}{\tau_{cr2}} \text{ values}$$

3.2 Johnson's Model [3]

Johnson's model involves checks for local buckling, global buckling and combined local and global buckling. The check for local buckling is predicted by:

$$\chi_{1J} = \frac{0.84}{\lambda_1} < 1 \quad where \quad \lambda_1 = \sqrt{\frac{f_{yw}}{\tau_{cr1}\sqrt{3}}} \tag{11}$$

Global buckling check involves

$$\chi_{2J} = \frac{0.61}{\lambda_2^2} \quad where \quad \lambda_2 = \sqrt{\frac{f_{yw}}{\tau_{cr2}\sqrt{3}}} \tag{12}$$

$$\tau_{cr,G} = 36\frac{D_x^{0.25}D_z^{0.75}}{t_w h_w^2} \tag{13}$$

$$where\ D_x = \frac{Et_w^3}{12(1-v^2)}\frac{a_1+a_4}{(a_1+a_2)} \ and\ D_z = \frac{EI_z}{w} = \frac{Et_w^3 a_3^2}{12}\frac{3a_1+a_2}{(a_1+a_4)} \tag{14}$$

The interaction check between classical local and global buckling is given by

$$\chi_{3J} = \frac{0.74}{\lambda_3^2} \tag{15}$$

$$where \ \lambda_i = \sqrt{\frac{f_{yw}}{\tau_{cri}\sqrt{3}}} \ and \ \frac{1}{(\tau_{cr,I})} = \frac{1}{(\tau_{cr,L})} + \frac{1}{(\tau_{cr,G})} \tag{16}$$

χ_J is taken as the lowest from all the 3 checks.

3.3 EN 1993-1-5 Model [10]

This model has 2 check each for local and global buckling. The reduction factors for local and global buckling respectively are given by:

$$\chi_{1,EN} = \frac{1.15}{0.9 + \lambda_1} < 1 \tag{17}$$

$$\chi_{2,EN} = \frac{1.5}{0.5 + \lambda_2^2} \leq 1 \tag{18}$$

Local buckling is desired as this mode of failure shows considerable post-buckling strength which is not expected for global buckling failure. Figure 5
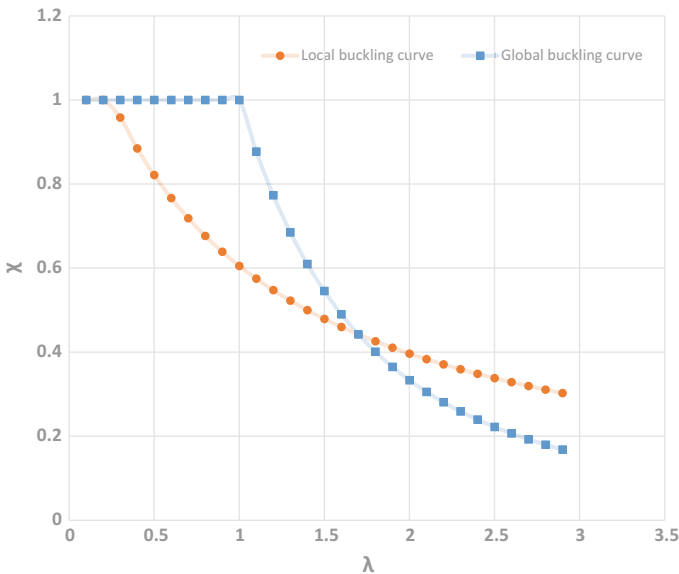
Fig. 5 Typical buckling curve as per EN 1993-1-5 [10]

shows the χ-λ curves for corrugated webs. It can be seen from the figure that the reduction factor for local buckling has a plateau until $\lambda_l = 0.25$.

3.4 DSM Shear Model

DSM method is only applied to filtered experimental results to include only those values where V_L or V_Y are very much less than global shear buckling force V_G.

The nominal shear capacity V_v for corrugated webs considering tension field action is calculated [11] as follows:

$$V_v = V_y \quad \text{for} \quad \lambda_v \leq 0.561 \tag{17}$$

$$V_v = \left[1 - 0.25\left(\frac{V_L}{V_Y}\right)^{0.6}\right]\left(\frac{V_L}{V_Y}\right)^{0.6} V_Y \text{ for } \lambda_v > 0.561$$
$$\text{where } V_L = \frac{k_L \pi^2 E A_w}{12(1-v^2)(w/t)^2}, k_L = 5.31 + 4\left(\frac{w}{h}\right)^2 \tag{18}$$
$$\lambda_v = \sqrt{\frac{V_y}{V_L}} \text{ and } V_G = \frac{k_G D_x^{0.25} D_y^{0.75} A_w}{th^2}$$

The design DSM curve incorporates the larger geometric imperfections and unavoidable residual stresses prevalent in corrugated beams.

The reduction factor is then calculated from:

$$V_v = \chi_{DSM} \cdot \frac{f_y . h t_w}{\sqrt{3}} \tag{19}$$

4 Results and Discussion

Table 1 shows the database of previous experimental results conducted by various researchers for calculating the experimental shear capacity V_u of corrugated webs having trapezoidal configuration. This table is expanded and reduction factors which are typical of Eurocode [10] have been calculated.

Table 2 shows the comparison of quotient $\left(\frac{\chi_u}{\chi_{model}}\right)$ for various shear resistance design methods as proposed by various researchers.

Table 1 Test results for the shear resistance of corrugated webs

S. NO	Original Test	h_w (mm)	t_w (mm)	f_{yw} (mm)	α	a_1 (mm)	a_3 (mm)	V_u (kN)	χ_u	χ_L	χ_J	χ_{EN}	χ_{DSM}
1	L1A	994	1.94	292	45	140	48	280	0.861	0.6168	0.6118	0.6205	0.7828
2	L1B	994	2.59	335	45	140	48	502	1.008	0.7306	0.8376	0.6907	–
3	L2A	1445	1.94	282	45	140	50	337	0.738	0.5243	0.5078	0.6261	–
4	L2B	1445	2.54	317	45	140	50	564	0.840	0.5289	0.6463	0.6933	–
5	L3A	2005	2.01	280	45	140	48	450	0.691	0.3718	0.3768	0.6385	–
6	L3B	2005	2.53	300	45	140	48	775	0.882	0.5381	0.4487	0.7008	–
7	B1	600	2.1	341	45	140	50	208	0.838	0.6178	0.7241	0.6210	0.7913
8	B2	600	2.62	315	45	140	50	273	0.955	0.8020	1.0000	0.7041	0.9339
9	B3	600	2.62	317	45	140	50	246	0.855	0.7994	1.0000	0.7031	0.9324
10	B4b	600	2.11	364	45	140	50	217	0.816	0.6008	0.6843	0.6121	0.7747
11	M101	600	0.99	189	45	70	15	53	0.818	0.5410	0.6673	0.6963	–
12	M102	800	0.99	190	45	70	15	79	0.909	0.4047	0.4804	0.6955	–
13	M103	1000	0.95	213	45	70	15	84	0.719	0.4280	0.3045	0.6283	–
14	M104	1200	0.99	189	45	70	15	101	0.779	0.3825	0.2699	0.5240	–
15	L1	1000	2.1	410	30	106	50	380	0.764	0.6357	0.7266	0.6804	–
16	L1	1000	3	450	30	106	50	610	0.783	0.6634	1.0000	0.7773	–
17	L2	1498	2	376	30	106	50	600	0.923	0.4378	0.5060	0.6787	–
18	L2	1498	3	402	30	106	50	905	0.868	0.6626	0.7216	0.7944	–
19	1	850	2	355	33	102	56	275	0.789	0.7915	0.9614	0.7000	0.9169
20	2	850	2	349	38	91	56	265	0.774	0.8533	1.0000	0.7385	–
21	V1/1	298	2.05	298	45	144	102	68	0.647	0.6272	0.8331	0.6259	0.8350
22	V1/2	298	2.1	283	45	144	102	70	0.685	0.6593	0.9202	0.6418	0.8635
23	V1/3	298	2	298	45	144	102	81	0.790	0.6119	0.7932	0.6180	0.8206
24	V2/3	600	3	279	45	144	102	235	0.810	0.9486	1.0000	0.7567	0.9916

(continued)

Table 1 (continued)

S. NO	Original Test	h_w (mm)	t_w (mm)	f_{yw} (mm)	α	a_1 (mm)	a_3 (mm)	V_u (kN)	X_u	X_L	X_J	X_{EN}	X_{DSM}
25	CW3	440	3.26	284	45	250	45	171	0.727	0.5885	0.7086	0.6055	0.8149
26	CW4	440	2.97	222	45	250	45	154	0.919	0.6064	0.7568	0.6151	0.8324
27	CW5	440	2.97	222	45	250	63	141	0.842	0.6064	0.7680	0.6151	0.8324
28	I/5	1270	2	331	62	171	24	260	0.536	0.3321	0.2560	0.5469	–
29	II/11	1270	2	225	62	171	24	220	0.667	0.4028	0.3766	0.6080	–
30	121216A	305	0.64	676	45	38	25	50	0.656	0.4927	0.4220	0.5493	0.6484
31	121221A	305	0.63	665	55	42	33	46	0.624	0.4424	0.3720	0.5159	0.5882
32	121221B	305	0.78	665	55	42	33	73	0.799	0.5477	0.5471	0.5827	0.7115
33	121232A	305	0.64	665	63	50	51	41	0.547	0.3701	0.2798	0.4621	0.4429
34	121232B	305	0.78	641	63	50	51	61	0.693	0.4595	0.4244	0.5276	0.5494
35	121809A	305	0.71	572	50	20	14	63	0.881	0.7059	0.8127	0.8094	–
36	121809C	305	0.63	669	50	20	14	55	0.741	0.6335	0.6183	0.7493	–
37	121832B	305	0.92	562	63	50	51	53	0.582	0.5788	0.6622	0.6002	0.6793
38	122409A	305	0.71	586	50	20	14	58	0.792	0.6974	0.7933	0.8058	–
39	122409C	305	0.66	621	50	20	14	58	0.804	0.6653	0.6976	0.7750	–
40	122421A	305	0.68	621	55	42	33	43	0.587	0.4869	0.4457	0.5456	0.6423
41	122421B	305	0.78	638	55	42	33	61	0.696	0.5592	0.5702	0.5893	0.7239
42	122432B	305	0.78	634	63	50	51	49	0.563	0.4620	0.4291	0.5293	0.5523
43	181209A	457	0.56	689	50	20	14	81	0.796	0.4045	0.2994	0.5741	–
44	181209C	457	0.61	592	50	20	14	89	0.934	0.4459	0.3732	0.6699	–
45	181216C	457	0.76	679	45	38	25	119	0.874	0.4837	0.4365	0.6030	–
46	181221A	457	0.61	578	55	42	33	62	0.666	0.4595	0.3558	0.5276	0.6071
47	181221B	457	0.76	606	55	42	33	98	0.806	0.5591	0.4865	0.5892	0.7214
48	181232A	457	0.6	552	63	50	51	52	0.595	0.3809	0.2828	0.4706	0.4527

(continued)

Table 1 (continued)

S. NO	Original Test	h_w (mm)	t_w (mm)	f_{yw} (mm)	α	a_1 (mm)	a_3 (mm)	V_u (kN)	χ_u	χ_L	χ_J	χ_{EN}	χ_{DSM}
49	181232B	457	0.75	602	63	50	51	80	0.672	0.4559	0.3914	0.5252	0.5415
50	181809A	457	0.61	618	50	20	14	82	0.824	0.4364	0.3575	0.6478	–
51	181809C	457	0.62	559	50	20	14	78	0.853	0.4607	0.4003	0.7046	–
52	181816A	457	0.63	592	45	38	25	75	0.762	0.4943	0.3816	0.5652	–
53	181816C	457	0.74	614	45	38	25	96	0.801	0.5053	0.4649	0.6105	–
54	181821A	475	0.63	552	55	42	33	56	0.610	0.4856	0.3933	0.5448	0.6385
55	181821B	457	0.74	596	55	42	33	93	0.799	0.5489	0.4740	0.5834	0.7105
56	181832A	457	0.61	689	63	50	51	53	0.478	0.3466	0.2337	0.4429	0.4107
57	181832B	457	0.75	580	63	50	51	79	0.688	0.4644	0.4062	0.5309	0.5513
58	241209A	610	0.62	606	50	20	14	71	0.537	0.3315	0.2104	0.4114	–
59	241209C	610	0.63	621	50	20	14	79	0.573	0.3288	0.2070	0.4056	–
60	241216A	610	0.63	592	45	38	25	76	0.579	0.3703	0.3022	0.5652	–
61	241216B	610	0.79	587	45	38	25	133	0.814	0.3935	0.4021	0.6385	–
62	241221A	610	0.61	610	55	42	33	77	0.588	0.4378	0.2891	0.5193	–
63	241221B	610	0.76	639	55	42	33	127	0.743	0.4520	0.3802	0.5808	–
64	241232A	610	0.62	673	63	50	51	69	0.470	0.3564	0.2299	0.4510	0.4218
65	241232B	610	0.76	584	63	50	51	101	0.646	0.4690	0.3772	0.5340	0.5552

The database of these results can be found at [9]

L = Lindner, J = Johnson, EN = European code (EN 1993-1-5), DSM = Direct Strength method

Table 2 Comparison of $\left(\frac{\chi_u}{\chi_{model}}\right)$ for various shear design proposals

Model	Lindner	Johnson	EN1993-1-5	DSM
Mean	1.46	1.58	1.22	1.04
Standard Deviation	0.301	0.538	0.141	0.141
CoV	0.207	0.34	0.115	0.135
Min	0.85	0.74	0.97	0.77
Max	2.25	2.89	1.49	1.31

5 Conclusions

From the observance of the test data and resistance models, it can be concluded that:

(1) The mean values of $\frac{\chi_u}{\chi_{model}}$ is 1.22 for EN 1993-1-5 and 1.04 For DSM and both of these methods give significantly accurate nominal shear capacities for girders with corrugated webs.

(2) The coefficient of variation is the least in the European code and DSM whereas the maximum for the Johnsons model. This is because of the discontinuities arising from the step function.

(3) The minimum resistance for the sample size computed by the EN 1993-1-5 code $\frac{\chi_u}{\chi_{EN1993-1-5,min}}$ is 0.97 which is the closest to the experimental values.

(4) While using EN 1993-1-5 model the designer should be aware that residual stresses, imperfections and interaction between moment, shear and transverse forces are not implicitly taken into consideration.

(5) DSM has limited application as the nominal shear strength is computed only from local buckling failure modes. But from practical considerations, local buckling failure governs failure modes for corrugated bridge girders.

References

1. J. Lindner, Granzschubtragfahigkeit von I-Tragern mit trapezforming profilierten Stegen. Stahlbau **57**, 377–380 (1988)
2. T. Höglund, Shear buckling resistance of steel and aluminium plate girders. Thin-walled Struct. **29**(1–4), 13–30 (1997)
3. R. P. Johnson, J. Cafolla, Corrugated webs in plate girders for bridges, in *Proceedings of the Institution of Civil Engineers: Structures and Buildings*, vol. 122, no. 2 (1997)
4. C.H. Pham, G.J. Hancock, Direct strength design of cold-formed C-sections for shear and combined actions. J. Struct. Eng. **138**(6), 759–768 (2012)
5. S.P. Timoshenko, *Theory of Elastic Stability, by S. Timoshenko*. (McGraw-Hill Book Company, Incorporated, 1936)
6. P. S. Bulson, *The Stability of Flat Plates*. Elsevier Publishing Company, 1969

7. M.F. Hassanein, O.F. Kharoob, Behavior of bridge girders with corrugated webs:(I) real boundary condition at the juncture of the web and flanges. Eng. Struct. **57**, 554–564 (2013)
8. J.T. Easley, Buckling formulas for corrugated metal shear diaphragms. J. Struct. Div. **101**(7), 1403–1417 (1975)
9. B. Johansson, R. Maquoi, G. al Sedlacek, C. Müller, D. Beg, Commentary and worked examples to EN 1993-1-5. Plated structural elements. JRC Sci. Tech. Rep. (2007)
10. C. E. N. (European C. for Standardization), Eurocode 3: design of steel structures—Part 1–5: plated structural elements (2006)
11. J. Papangelis, N. Trahair, G. Hancock, Direct strength method for shear capacity of beams with corrugated webs. J. Constr. Steel Res. **137**, 152–160 (2017)

Study and Comparison of Composite Shells with Metallic Shells for Underwater Vessel Application Using FEA

Lalwala Mitesh, Singh Neha and N. V. Datla

Abstract Submarines, underwater storage tanks, torpedo, and underwater pipelines come under the category of underwater vessels. Underwater vessels are subjected to hydrostatic pressure, depending on the depth at which they operate. This hydrostatic pressure causes buckling of the vessel, which can lead to failure of the vessel at the stress much lower than the ultimate strength of the material. This buckling failure limits the load carrying capacity and depth of operation of the underwater vessels. Composites due to their versatile and tailor-made properties can be effectively utilized for underwater vessel application. Hence, in the present work composite materials have been studied and compared with metallic materials for buckling failure for simplified underwater vessel application using the FEA. Weight of the shell for each material has been compared to identify the best material for vessel working at a depth of 1000 m from the sea level. In addition, the results of FEA analysis has been verified with the experimental results to validate the FEA model.

Keywords Underwater vessels · Buckling · Composites · FEA · Comparative analysis

1 Introduction

Submarines, underwater storage tanks, torpedo, and underwater pipelines come under the category of underwater vessels. These underwater vessels can be modeled as long cylinders with rigid-end closers [1]. These underwater vessels are subjected to hydrostatic pressure, which can cause buckling of the structure. This buckling occurs at much lower stresses than the ultimate strength of the material. Thus. buckling limits the load carrying capacity of underwater structures and the maximum

L. Mitesh · S. Neha (✉) · N. V. Datla
Department of Mechanical Engineering, Indian Institute of Technology Delhi, New Delhi 110016, India
e-mail: ineha.m27@gmail.com

depth of their operation. Hence, buckling is the most critical design consideration while designing the underwater vessels.

Only a few conventional metals can be used for the underwater application due to their poor corrosion resistance in seawater, high densities, or very high costs. Materials for submerged vessels must not solitary be capable of withstanding very high external pressures, but also well take on other properties such as good resistance to corrosion, high strength-to-weight ratio, good sound absorption qualities, formability, operating life span of the material, and economic considerations. Generally, metals like steel, aluminum alloys, and titanium alloys are used for the underwater vessels [2].

Composites due to their varied properties like high strength-to-weight ratio, tailor-made properties, good corrosion resistance, high life span and ease of formability has drawn the attention of many researchers for underwater application. It has been observed that the application of composites for underwater vessels can bring down their weight and expand the depth of operation. Hence, in the present work, we are planning to compare metallic and composite shells for underwater vessels aiming to operate at a depth of about 1000 m from buckling consideration using FEA (ANSYS) in terms of thickness of shell and mass of the shell.

2 Theoretical Concepts

Messager et al. [1] developed analytical expression for buckling of the composite shell using the third-order shear deformation theory (TOSD) in form of Eigenvalue buckling problem which is given by

$$([K] + P[L]) \begin{Bmatrix} a_u \\ a_v \\ a_w \\ a_{\varphi x} \\ a_{\varphi y} \end{Bmatrix} = \begin{Bmatrix} 0 \\ 0 \\ 0 \\ 0 \\ 0 \end{Bmatrix},$$

where K and L are stiffness matrices that depend on the material and boundary conditions of the system. Terms in the bracket are static displacement terms. As per definition, buckling load is the lowest value of P in the above equation that satisfies it.

Moreover, studies done by IFREMER (the French Research Institute for the Exploitation of the Sea) have suggested that buckling failure mode of the lengthy vessels can be characterized by two or three half circumferential sine waves called "type 2" and "type 3", respectively, as shown in Fig. 1.
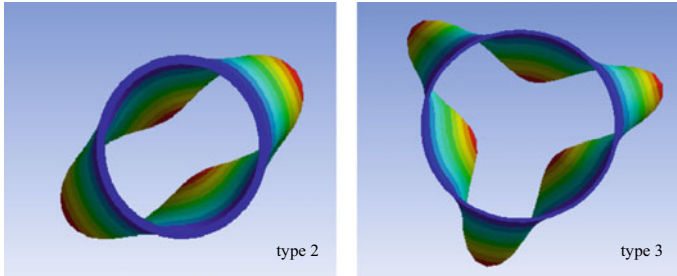
Fig. 1 Buckling mode of the underwater vessel (observed in the current study)

Messager et al. [1] also developed a methodology to determine the optimum laminate stacking sequence for the composite to achieve maximum buckling load for given material using the genetic algorithm techniques. They suggested that optimum lamina arrangement for the Carbon Epoxy composite is $(90_2/60/30_5/60/90)$ and that for Glass Epoxy composites is $(90_4/30_2/45/90_3)$ which gives a significant improvement in buckling load of the composite shells as compared to conventional ±55 orientation suggested by the IFREMER. They also validated their results using the experimental data.

Messager et al. [1] conducted buckling test on composite cylinders of Glass Epoxy having a mean diameter of 155 mm, length 400 mm, and thickness of 4.9 mm. They considered two cylinders, one having 55° fiber orientation with 7 laminate each having 0.7 mm thickness and another having $(90_3/15_2/90_2)$ stacking as determined by the optimization technique with each laminate of 0.7 mm thickness.

Govindraj et al. [3] carried out a comparative analysis of performance of metallic and polymer composite shell for typical underwater application of vessel having 1650 mm diameter and 350 mm length for 1000 m depth of application. From their study, they concluded that composite vessels have significant weight reduction as compared to metallic vessels for the same depth of operation. However, they used simplified orthotropic material properties of the composite, without taking into account the effect of lamina stack up as suggested by Messager et al. [1].

Hence, in the present study, comparative analysis of metallic and composite shell has been carried out with taking into account, lamina stack up of composite for the same application as used by Govindraj et al. [3]. We have used the similar methodology and boundary conditions as Govindraj et al. [3] for FEA. In addition, the methodology of FEA has been verified by comparing buckling pressure results from similar FEA model with the experimental load data provided by Messager et al. [1] for the two lamina arrangements described by him.

Table 1 Composite properties

Elastic constant	Carbon epoxy	Glass epoxy
E_1 (GPa)	156	45.6
E_2 (GPa)	9.56	16.2
E_3 (GPa)	6.57	16.2
υ_{12}	0.27	0.27
υ_{23}	0.492	0.49
υ_{31}	0.34	0.278
G_{12} (GPa)	5.47	5.83
G_{23} (GPa)	2.8	5.83
G_{31} (GPa)	3.92	5.78
Density(kg/m^3)	2100	1700

Table 2 Metal properties

Material	Steel-HY 80	Aluminum alloy	Titanium alloy
Young's modulus (GPa)	207	70	119
Poisson's ratio υ	0.29	0.33	0.32
Density (kg/m^3)	7850	2700	4400

3 Buckling Analysis of the Underwater Vessel Using Fea

Here for comparison, we are considering long cylindrical shell of the length 1650 mm and diameter 350 mm as a simplified model of the underwater vessel. We also assume that this vessel has to work at the depth of 1000 m from the sea surface. Hydrostatic pressure at this depth can be approximated as 10 MPa. Hence, the buckling pressure of the vessel should be more than 10 MPa for the given shell to survive the operation at this depth of operation.

We are comparing glass epoxy and carbon epoxy as composite with steel, aluminum alloy, and titanium alloy as metals for the vessel, whose properties are shown in Tables 1 and 2, respectively [3].

In the present work, we are using ANSYS 15.0 Workbench for analyzing buckling of the underwater vessel under hydrostatic load. The methodology to solve the problem using ANSYS is as shown in Fig. 2.

As discussed above, the first step is to define the mechanical properties of the materials under consideration. Mechanical properties of metals have been defined using the isotropic elastic model and that of composite have been defined using the orthotropic elastic model in ANSYS. The orientation of lamina for composite material has been defined using Advanced Composite Prep Post tool—ACP (Pre) of ANSYS, which is specially designed to define a composite laminar structure for the complex geometries. Using this tool, lamina orientation for glass epoxy and carbon
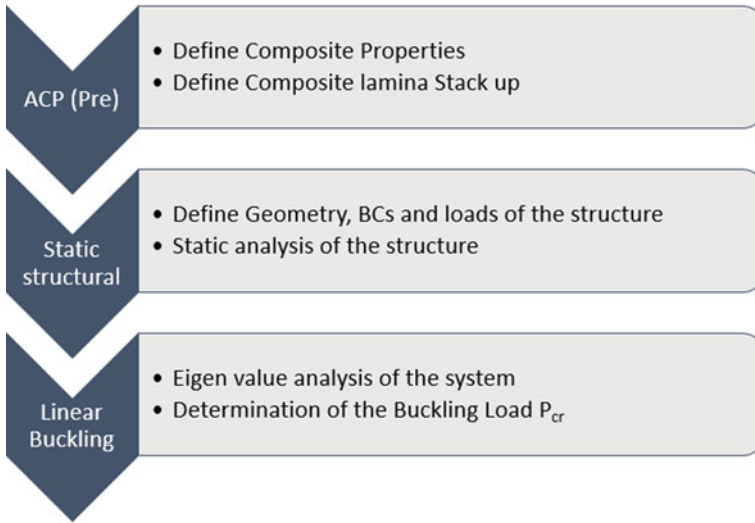
Fig. 2 Methodology of analysis using ANSYS
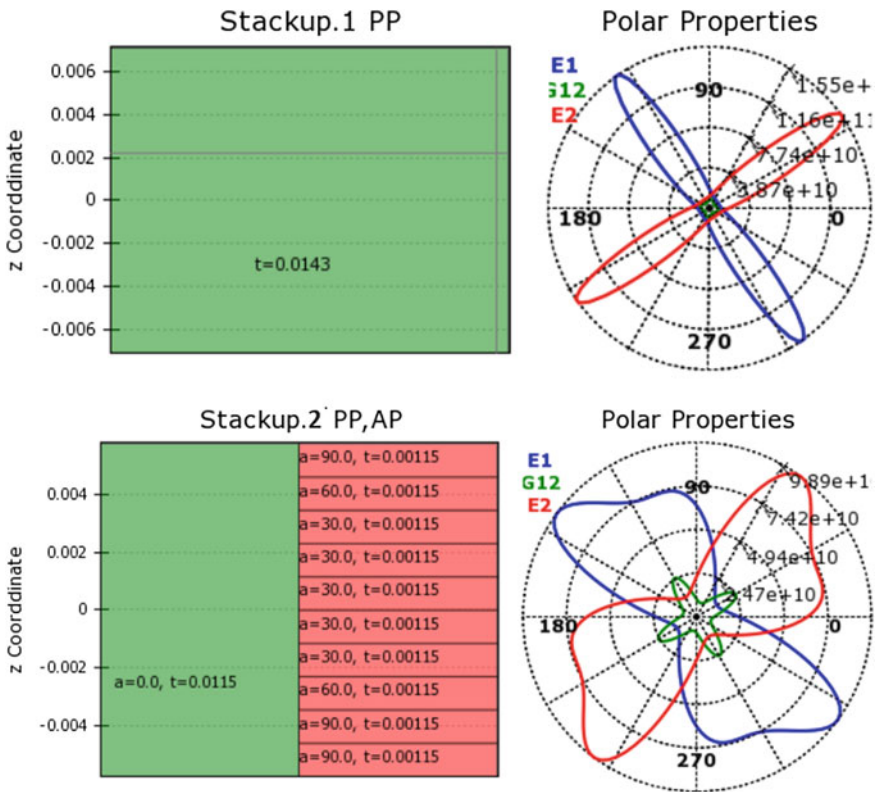
Fig. 3 Stack-up sequence and polar properties for carbon–epoxy composite

epoxy material has been defined for two orientations: 55° and optimal orientation suggested by Messager et al. for 10-ply lamination [1]—(90_2/60/30_5/60/90) for carbon epoxy and (90_4/30_2/45/90_3) for glass epoxy. Stack up sequence and its effective properties in polar coordinate for carbon epoxy for these two arrangements are shown in Fig. 3.

The vessel has been defined as a solid long cylinder with rigid end closers. Hence, in the present work, we have modeled underwater vessel as a cylindrical shell of diameter 350 mm and length 1650 mm using inbuilt modeling tool available in the ANSYS. It subsequently meshed with 4-node shell element with mesh refinement option to ensure that quality parameter such as warpage, aspect ratio, skew angle, Jacobian, minimum and maximum angles were satisfied. Shell elements are well suited for buckling analysis and each node of the shell element has 6 DOF. Meshed model of the vessel is shown in Fig. 3. The final meshed model consisted of 3456 elements made of 3504 nodes. The thickness of the vessel was controlled independently by shell thickness option in the shell element.

Since it is assumed that vessel is having rigid enclosures, fixed boundary conditions were applied at the two ends of the shell. Since hydrostatic pressure will be acting on the cylindrical surface of the shell. Hence, nominal pressure of 1 MPa has been applied on the cylindrical surface for the static structural analysis as shown in Fig. 4.
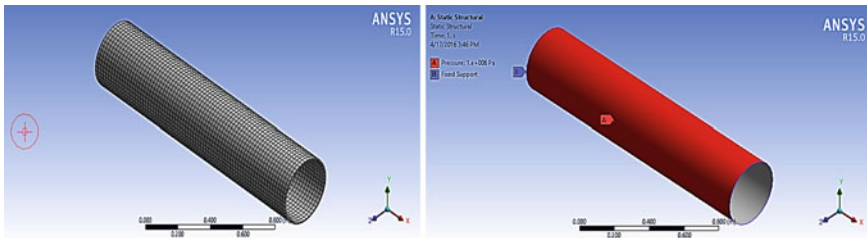
Fig. 4 Meshed model and boundary conditions for FEA
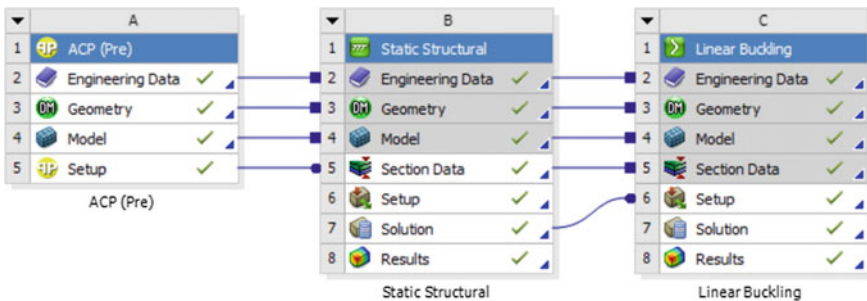
Fig. 5 Process flow chart for FEA

Flow diagram for analysis in ANSYS is shown in Fig. 5. As can be seen from the figure, first geometry and lamina stack up is defined using Ace (Pre), which will be transferred to the static structural unit for static deformation analysis. Results of this static analysis will be transferred to Linear buckling module, which will provide critical buckling pressure in terms of load multiplication factor. Since we have applied only pressure of 1 MPa, load multiplication factor will be the critical buckling pressure.

4 Reults and Discussion

4.1 Validation of FEA Model

FEA methodology has been verified by comparing FEA model results with experimental data published by Messager et al. [1] as discussed earlier. Comparison of experimental results with FEA results is given in Table 3. For this analysis, each vessel was modeled using the stack up of 7-ply lamination having lamina orientation of $(90_3/15_2/90_2)$ with each ply having 0.7 mm thickness, as was the case in the experimental test by Messager et al. [1].

As can be seen from Table 3, critical load values obtained from FEA are in good agreement with the experimental results value. As can be seen, there is a minor difference in the experimental test result values and simulation result values. This could be due to the simplification of the model and boundary conditions as compared to experimental test conditions, which are not exactly known. Moreover, in real-world experiments, hydrostatic buckling might be transforming from linear to nonlinear behavior under a given loading, which is not exactly known and hence not considered here for simplified study. However, this difference in the experimental value and simulation result value is consistent across all the models. Hence, the given methodology can be confidently applied for the comparative study of metallic and composite vessels for underwater application. But to obtain more accurate results, there is a need to identify whether nonlinear buckling will take place or not and also to successfully model it in FEA.

Table 3 Validation of FEA methodology results

Material	Critical buckling pressure P_{cr} (MPa)				% Error
	FEM analysis	Experimental analysis			
		Test1	Test2	Average	
Glass epoxy (55_7)	68.67	59.6	59.7	59.65	15.12
Glass epoxy $(90_3/15_2/90_2)$	94.36	85.8	82.7	84.25	12

Table 4 FEA results for different shells from buckling consideration

Material	Thickness (mm)	Mass of vessel (kg)	% Reduction in mass as compared to steel vessel	P_{cr}	Mode type
Steel-HY 80	6.85	97.558	0	10.194	3
Titanium alloy	8.60	68.652	29.63	10.025	2
Aluminum alloy	11.25	55.108	43.51	10.065	2
Carbon epoxy (55)	14.25	54.292	44.35	10.287	2
Carbon epoxy ($90_2/60/30_5/60/90$)	11.5	43.815	55.09	10.151	2
Glass epoxy (55)	17.5	53.974	44.67	10.21	2
Glass epoxy ($90_4/30_2/45/90_3$)	15.5	47.806	51.00	10.324	2

4.2 Comparative Study of Metallic and Composite Vessels

In the present study, the minimum thickness of the vessel required to sustain a buckling pressure of 10 MPa was calculated by FEA iterations. For these iterations value of the shell elements, thickness was manually changed until the value of load multiplication factor approached 10, which means buckling pressure of 10 MPa. Once the minimum thickness has been obtained, the weight of the vessel has been calculated using the thickness data. Weight and thickness for the shell of different materials to sustain buckling at depth of 1000 m have been tabulated in Table 4.
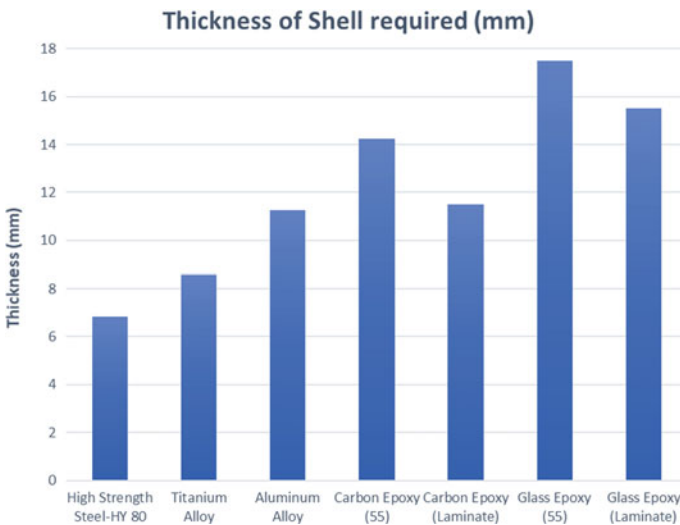
Fig. 6 Comparison of thickness for different shells
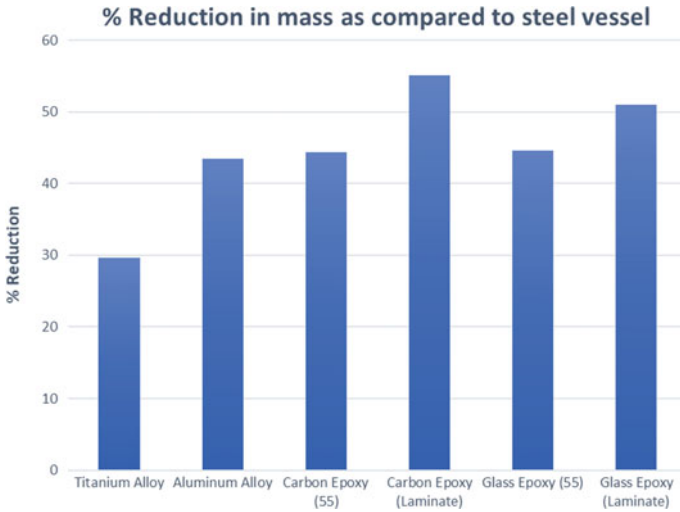
Fig. 7 Comparison of weight reduction (w.r.t steel vessel) for different shells

In addition, the mode shape of bucking—"type-2" or "type-3" has also been mentioned for each shell. As can be seen from the above table, the thickness of composite shell required is comparatively higher as compared to metallic shells. However, the low weight densities of composite materials counter the effect of these more thicknesses and hence their weights are significantly lower than metallic shells. Graphical comparison of thickness and weight for these vessels is given in Figs. 6 and 7, respectively.

As can be seen from the table and Figs. 6 and 7, results of FEA analysis are in good agreement with results provided by Messager et al. [1] and Govindaraj et al. [3], One point to note from the above table is, for given length and diameter, as the thickness of shell increases, buckling mode changes from "type-3" to "type-2". It can be observed that steel shell having minimum thickness experience "type-3" buckling, while all the other shells having more thickness experience "type-2" buckling.

5   Conclusion

From the above results, following conclusions can be drawn:

- Buckling pressure obtained from the Experimental test and FEA method conform to each other. FEA results are within 15% of the experimental data. This difference is also consistent across all the models. This difference could be due to the transition of linear buckling into nonlinear buckling at high pressure, which needs to be studied more in depth.
- Buckling Failure of the underwater vessel can be effectively studied using the FEA and buckling pressure can be found out for the given vessel.
- Thickness required for the composite shells is higher than the metallic shells for the same buckling pressure as can be seen from Fig. 6.
- For a given length, diameter and pressure application hydrostatic buckling mode of vessel depend on the thickness of the vessel. As the thickness of the vessel increases the buckling mode shift from "type-3" to "type-2". However, further study is required to determine critical thickness value at which buckling mode transit from "type-3" to "type-2" and on which parameters it depends.
- Even though the thickness of the composite shell is higher than the metallic shell, Composite shell provides significant weight reduction as compared to metallic shell due to their low weight densities as can be seen from Fig. 7.
- Around 55% reduction in weight can be obtained by using the composite carbon epoxy for underwater vessels.
- Laminate stacking also significantly affect the buckling load capacity of the composite material. Hence, it is necessary to select the optimum laminate stacking to maximize the depth of operation of the composite shell and reduce its weight.

References

1. T. Messager, et al., Optimal laminations of thin underwater composite cylindrical vessels. Compos. Struct. **58**(4), 529–537 (2002)
2. M. Govindaraj, et al., Buckling behaviour of underwater vessels by experimental, numerical and analytical approaches. J. Nav. Arch. Mar. Eng. **11**(1), 15–28 (2014)
3. M. Govindaraj, et al., Comparative study of metallic and polymer composite shells for underwater vessels using FEA. Int. J. Ocean. Syst. Eng. **3**(3), 136–141 (2013)

Part IX
Experimental Fracture Mechanics

Experimental Measurements of Interface Fracture Toughness Using Double Cantilever Bending

Ashwini Kumar Mishra, Sanjay Sampath, Gregory M. Smith and Nagamani Jaya Balila

Abstract Fracture properties at the interface of hard and brittle Alumina (Al_2O_3) coating over a soft Al (Al 6061) substrate are studied using the double cantilever bend (DCB) test. These coatings were thermally sprayed and included substantial porosity. Elastic properties of the Alumina layer were determined by three-point bending (3PB) of the coated specimens. Fracture energy of Alumina was determined using a notched sample of the free-standing Alumina coating. FEM analysis of DCB was performed to estimate the stress intensity factor at the crack tip along the Al/Al_2O_3 interface. The experimental results show mixed mode fracture behaviour in most of the coatings. Average fracture energy of the interface, 6.46 J/m^2, was estimated using these measurements.

Keywords Alumina · Interface strength · DCB test · 3 PB test

1 Introduction

Ceramic coatings applied over metal substrates have been widely used as thermal barrier coatings (TBCs), anti-corrosion coatings and abrasion resistant coatings [1]. Due to the inherently brittle nature of the ceramic layers, it is important to study their fracture behaviour. Most of the failures within these coatings are characterized by delamination modes during processing or service life. In cases where coating failure occurs by fracture, a large part of the crack's growth occurs during propa-

A. K. Mishra (✉) · N. J. Balila (✉)
Department of Metallurgical Engineering and Materials Science, Indian Institute of Technology Bombay, Mumbai 400076, India
e-mail: ashwini.mishra013@gmail.com

N. J. Balila
e-mail: jayabalila@iitb.ac.in

S. Sampath · G. M. Smith
Department of Materials Science and Engineering, Center for Thermal Spray Research, Stony Brook University, Stony Brook, NY 11790, USA

gation along the interface with the substrate. Various evaluation including uniaxial tensile testing [2], four point bend testing [3, 4] or three-point bend testing [5], peel test [6], scratch test [5] and nanoindentation test [5, 7, 8, 9] have been performed to determine fracture toughness of interfaces in order to evaluate their suitability in a given application [10, 11].

Film multilayers deposited by thermal spray are also useful in improving fracture toughness. These interfaces help in redistributing any stress concentration in front of a primary propagating crack. Most of the fractures within these systems occur or initiate at the interface of coating and substrate. In other cases, a weak interface helps to deflect the crack and enhances the damage tolerance. Either way, quantifying interfacial fracture toughness is important. DCB is the most commonly used interfacial fracture test geometry. In this work, interfacial fracture properties of an Alumina film (Al_2O_3) over an Al (Al 6061) substrate were determined by DCB test. To determine the elastic properties of the Alumina film, three-point bend (3PB) tests have been performed. Fracture toughness of the Alumina film is determined by single-edge notch bending of the free-standing film. We performed FEM simulation to analyse the DCB geometry in the presence of a notch with a finite root radius and compared it with analytical results.

2 Experimental Procedure

The deposition of the Al_2O_3 coating used a rod-based flame spray process. Alumina coatings were received from Stony Brook University, Center for Thermal Spray Research. The Alumina (Al_2O_3) coating was 2.07 mm thick while the substrate (Al 6061) thickness was 1.5 mm.

For determining Young's modulus of the coating, 3PB tests were performed with the film attached to the substrate. Dimensions for the 3PB test specimens are 44 ± 0.9 mm * 8 ± 1 mm * 3.58 mm (2.07 mm film +1.5 mm substrate). A span length of 30mm was used in the 3PB test. The experimental setup is shown in Fig. 1a.

Following the above determination of Young's Modulus, the same three-point bend setup was used with the notched free-standing Al_2O_3 film. The free-standing film was prepared by grinding away the metallic substrate. Dimensions of samples for these tests are 40 mm * 8 ± 1 mm * 2 mm. A 1 mm length edge notch was machined on these samples using a diamond saw at low speeds. A span length of 30mm was again used for the 3PB test.

For measurement of interface fracture toughness, DCB samples of dimension 19 mm * (8 ± 0.6) mm * 3.6 mm (2.07 mm film +1.5 mm substrate) were prepared. Sectioning of the samples was performed with a diamond coated blade. Small pieces of PMMA (10 mm * 8 mm * 3 mm) were pasted on these sample edges with a
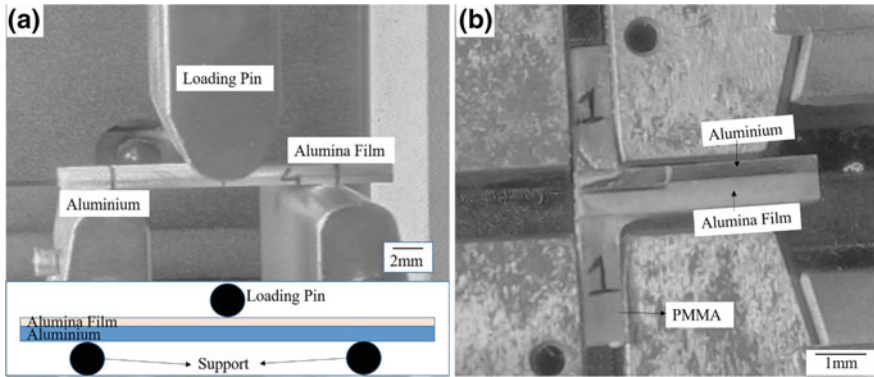
Fig. 1 **a** Three-point bend test of the coated sample **b** DCB experiment setup

strong adhesive to serve as grips for the DCB, as shown in Fig. 1b. The schematic in Fig. 2 shows the DCB specimen with dimensions. A crack of 7 mm length was machined at the interface of Alumina and Aluminium using a low speed saw with a diamond coated blade. DCB test was performed on 5 kN load capacity INSTRON 3345 universal testing machine at a cross-head displacement rate of 0.05 mm/min.
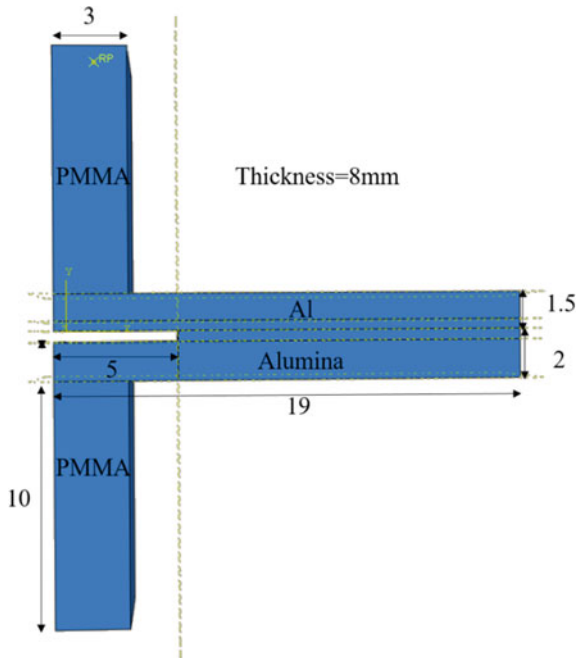
Fig. 2 3D model of DCB test (all dimensions in mm)

Table 1 Properties of material for FEM simulation

Material	$E(N/mm^2)$	Poisson's ratio (υ)	Maximum principal stress (N/mm^2)	Fracture energy (N/mm)
Al 6061 [12]	$68.9 * 10^3$	0.33	276	10.72
PMMA	3619 (Nanoindentation data from present study)	0.35 [13]		

2.1 Methodology for FEM

All the simulations were done in ABAQUS 6.14 assuming linear elastic fracture mechanics (LEFM) condition. Material properties are given in Table 1. The schematic in Fig. 2 shows the DCB geometry that was modelled. A notch of 5 mm length was created along the interface. Notch tip diameter is 0.45 mm and it was located completely in the Alumina film. A pre-crack of 0.1 mm was inserted by XFEM and located in front of the 5mm notch, 0.1 mm below the interface. The boundary condition for lower PMMA was 'encastered', i.e. displacement and rotation are fixed in all three directions. For the upper PMMA, boundary condition is given to restrict the motion in all directions, except in the y-direction. No interface properties were assigned between PMMA and specimen. Only elastic deformation of individual components was assumed. The test was carried out in displacement control, with a 0.15 mm displacement in y-direction imposed at the reference point. Total of 140568 elements of type C3D8R (8-node linear brick, reduced integration elements) were used with the 3D model.

2.2 Three-Point Bend Test for Film over Substrate

Young's moduli of the film can be calculated by three-point bend (3PB) test, using composite plate theory. It assumes that these are multilayers materials with isotropic behaviour. In 3PB test, for an applied load P, and span length L, deflection d of the beam is given by Eq. (1)–(3) [14]

$$d = \frac{PL^3}{48D} \tag{1}$$

where D is bending stiffness and given by [14]

$$D = \frac{1}{3}\sum_{k=1}^{n} Q_k\left(h_k^3 - h_{k-1}^3\right) \tag{2}$$

$$Q_k = \frac{E_k}{\left(1 - \upsilon_k^2\right)} \tag{3}$$

E_k and υ_k are Young's moduli and Poisson's ratio respectively, h_k is the vectorial distance from panel midplane, Q_k is plane strain reduced stiffness and n is the number of bonded layers.

In the present case of two material layers, D is given by Eq. 4 [14]

$$D = \frac{1}{3} \left[Q_f\left(-t_f^3\right) + Q_s\left(t_s^3\right) \right] \tag{4}$$

where t is thickness, f and s subscripts are used for film and substrate, respectively.

2.3 Fracture Toughness of Free-Standing Film

Fracture toughness of Alumina film is determined by 3PB flexural test. Stress intensity factor at the crack tip is given by Eqs. (5)–(6) [15]

$$K_I = \frac{6P\sqrt{a}}{tw} Y \tag{5}$$

where t, w and a are thickness, width and crack length, respectively, and Y is is the geometric factor.

$$Y = 1.99 - \left(\frac{a}{t}\right)\left(2.15 - 3.93\left(\frac{a}{t}\right) + 2.7\left(\frac{a}{t}\right)^2\right)\left(1 + 2\left(\frac{a}{t}\right)\right)\left(1 - \left(\frac{a}{t}\right)\right)^{3/2} \tag{6}$$

$$G_I = \frac{K_I^2}{Q_f} \tag{7}$$

2.4 Double Cantilever Beam Test for Film over Substrate

When a double cantilever beam is subjected to load P_0(per unit width), the energy release rate can be calculated by J-integral using Eqs. (8)–(11) [16]

$$J = P_0(\theta_f + \theta_s) = G \tag{8}$$

where θ_f and θ_s are the rotations of loading points at film and substrate. Both are taken as positive if they move away from the interface.

Rotation can be calculated by Euler–Bernoulli beam theory [17]

$$\theta_f = \frac{6P_0 a_0^2}{Q_f t_f^3} + \theta_{0f} \text{ and } \theta_s = \frac{6P_0 a_0^2}{Q_s t_s^3} + \theta_{0s} \tag{9}$$

where a_0 is crack length, θ_{0f} and θ_{0s} are root rotations for the two arms.

Combining equations, we get

$$G = P_0 \theta_0 + \frac{6P_0^2 a_0^2}{Q_s t_s^3} \left(\epsilon H^3 + 1 \right) \tag{10}$$

where $\theta_{0f} + \theta_{0s} = \theta_0$, $\epsilon = \frac{Q_s}{Q_f}$, H = t_s/t_f

For a linear system, root rotation can be calculated by dimensional arguments and is given by

$$\theta_0 = \frac{\theta_d P_0}{Q_s t_s} \tag{11}$$

where θ_d is a constant and its value depends on geometry, elastic properties and cohesive law. Its values in this paper are taken from Ref. [16].

3   Results and discussion

3.1   Young's Modulus by 3PB Test of the Coated Sample

Figure 3a shows load–deflection curve for 3PB test of the coated specimen. By measuring the overall bending stiffness of coating+substrate sample, Young's modulus of the coated film can be extracted using Eq. 1–4. The Young's moduli and Poisson's ratio of the substrate are taken from literature to be E (Al6061) = 68.9 GPa and v = 0.33 [12]. Initially, the load increases linearly with deflection. On reaching the maximum load, the Alumina fractures but the Al substrate continues to deform. Due to this, the load drop is gradual and not sharp. To obtain elastic properties and avoid nonlinear behaviour, bending stiffness of the system is calculated from the initial slope. Machine stiffness was calculated by performing a 3PB test on a material of known properties and was used to correct for cross-head displacement in order to obtain the actual displacement of the specimen. Poisson's ratio of the Alumina film is taken as 0.25 in this study. The elastic modulus of the Alumina film was found to be 27.05 ± 0.05 GPa. The low value of elastic modulus of Alumina is as expected since the coating has a lot of porosities caused by the formation of splats as shown in Fig. 3b. Average porosity fraction close to the interface was 27.5% as determined by image analysis.
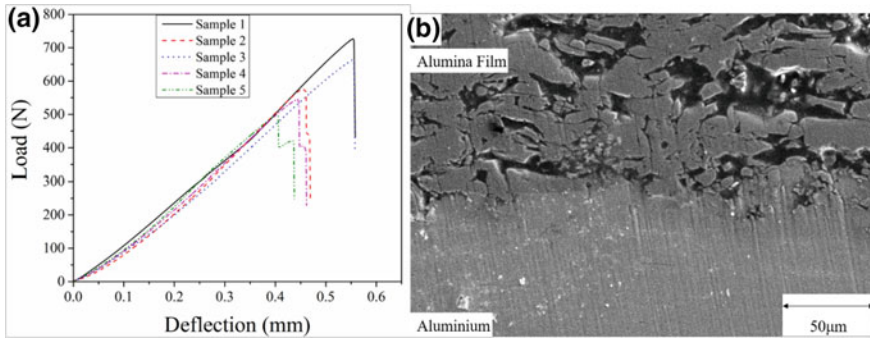
Fig. 3 a Load versus Displacement of 3PB test of the coated sample **b** SEM image of the film–substrate cross-section showing a wavy interface and porous nature of the Alumina film

3.2 Fracture Toughness of Alumina Film by 3PB Test

Fracture energy of the free-standing Alumina film was determined using a 3 PB test (Fig 4). The initial part of the load–displacement curve showed linear elastic behaviour. At maximum load (P_{max}), the sample failed (Fig 4a) albeit not catastrophically. The porosity in the Alumina causes crack deflections (Fig 4b, c) leading to some dissipation and gradual load drop. P_{max} was used to calculate the stress intensity factor using Eq. 5. The K_{IC} comes out to be 0.12 MPam$^{1/2}$, which is very low as compared to dense Alumina K_{IC} (3.5 MPam$^{1/2}$) [18]. Fracture energy (G) of the Alumina film was then determined using Eq 7, with its Young's modulus E_f from section 3.1 as input. Results of these test are shown in Table 2. The average value of G_C is 0.53 ± 0.17 J/m^2. The low fracture energy is a result of the high porosity in the film and the large scatter is a result of the heterogeneous shape and distribution of these pores.

3.3 Fracture Energy of Interface by DCB Test

Figure 5a shows the load–displacement curves of 4 samples of Al–Al$_2$O$_3$ from the DCB test. The initial response is again linear behaviour until reaching a maximum load (P_{max}), after which there is a gradual drop in force. The maximum load is the point at which the crack initiates from the notch tip along the interface. Fracture energy is, therefore, obtained from Eq. 10 using P_{max} for each sample. Table 3 summarises the results of each test. In most of the samples crack initially propagates along the interface, after which is kinks into the Alumina layer (Fig. 5b, c). Only in sample 2, the crack propagates along the interface throughout, leading to complete delamination, as shown in Fig. 6. Fracture energy G_c for this sample was calculated to be 4.80 J/m^2, while the average fracture energy for all the samples put together
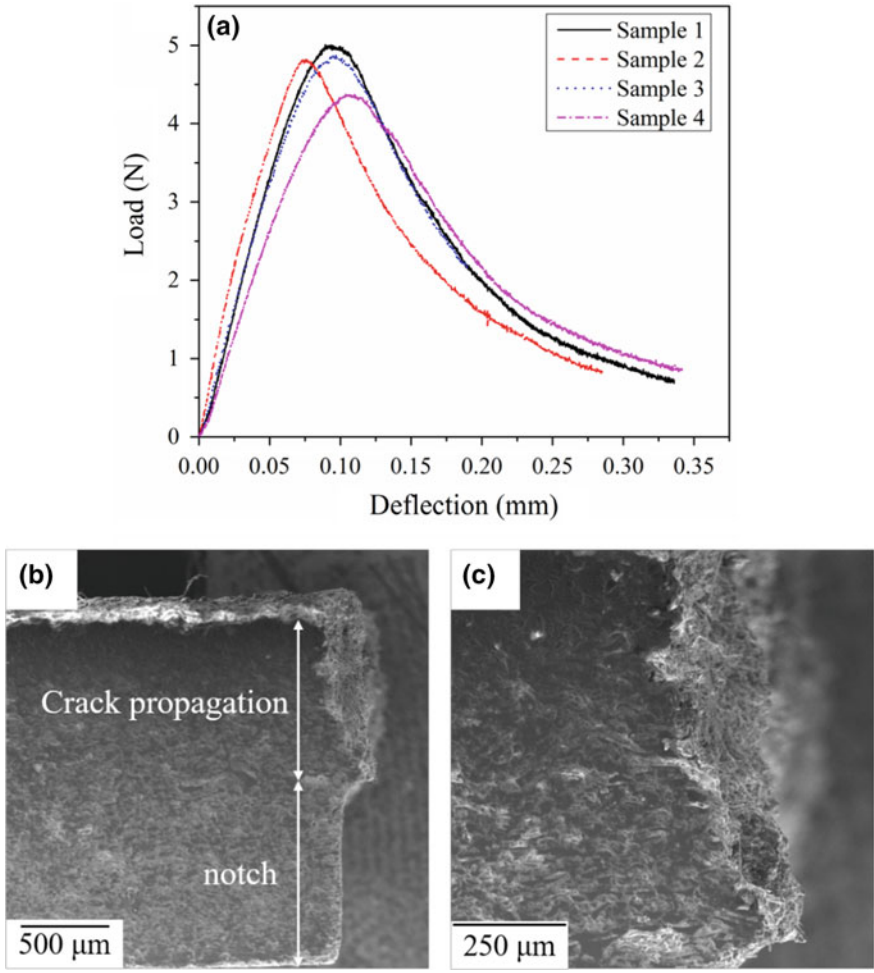
Fig. 4 **a** Load–Deflection curve for 3PB test of Alumina film **b** Crack path after 3PB test of Alumina film **c** Crack in front of the notch at high resolution

Table 2 Results of 3PB test of Alumina film

Sample	Crack length a (mm)	Width (mm)	Thickness (mm)	a/t	P_{max} (N)	K_{IC} (MPam$^{1/2}$)	G_C (J/ m^2)
1	1.13	9.07	2.06	0.55	5.007	0.15	0.82
2	0.81	8.34	2.01	0.40	4.83	0.10	0.37
3	0.92	7.53	2.12	0.43	4.87	0.12	0.52
4	0.84	7.28	2.05	0.41	4.38	0.10	0.40
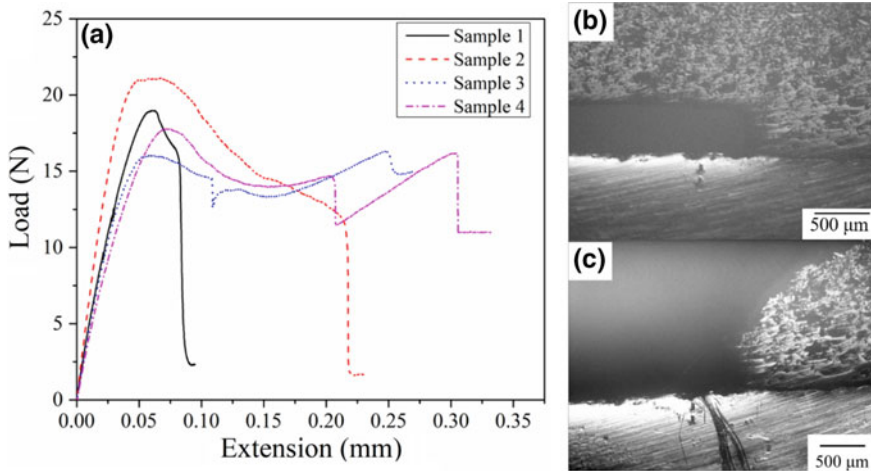
Fig. 5 **a** Load -Extension curve for DCB test, optical image of interface **b** before test **c** after test

Table 3 Results for DCB test

Sample	Width (mm)	P_{max}(N)	Critical load per unit length P_c(N/m)	a (mm)	Change in crack length (mm)	G(J/m^2)
1	7.66	19	2477	5.45	0.161	8.82
2	7.84	21	2694	3.58	13.90 mm (crack completely along interface)	4.80
3	8.59	16	1870	5.49	0.107	5.10
4	8.14	18	2187	5.56	0.198	7.14
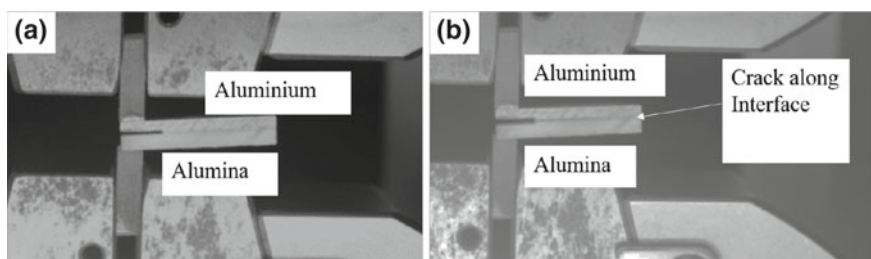
Fig. 6 Image of sample 2 **a** before DCB test **b** after test, showing complete interface crack growth

was found to be 6.46 J/m^2. A large variation in fracture energy was found in these samples (Table 3). This is possibly due to the large porosity and the extremely heterogeneous nature of the Alumina film, and the uncertainties in the extent of deformation in the PMMA and the adhesive used during the test. Therefore, most

samples showed a mixed mode of fracture. The fracture energy of the Alumina film
was found in Sect. 3.2 to be 0.53 J/m^2. Analytical calculations have shown that if
the ratio of G_f/G_i is less than 1.76, crack deflection into the film is expected [19]. In
the present case, this ratio comes out to 0.11. This explains why the crack deflects
into the Alumina in most cases.

3.4   Fracture Energy of Interface by FEM

The maximum principal stress as obtained from FEM simulations is shown in
Fig. 7a. Maximum principal stress is in front of the crack tip as expected. The
porosity in the Alumina layer was accounted for using the $E(Al_2O_3)$ determined
from the experiment. Fracture energy in terms of J integral versus force is plotted in
Fig. 7b. Experimentally measured P_{max} for sample 2, which fails completely along
the interface, was found to be 21.1 N. At this load value, fracture energy predicted
by simulation is 3.1 J/m^2. This value is comparable to the value obtained from
analytical formulations (4.8 J/m^2). Since fracture in the other experiments is not
completely along the interface, these were not simulated.
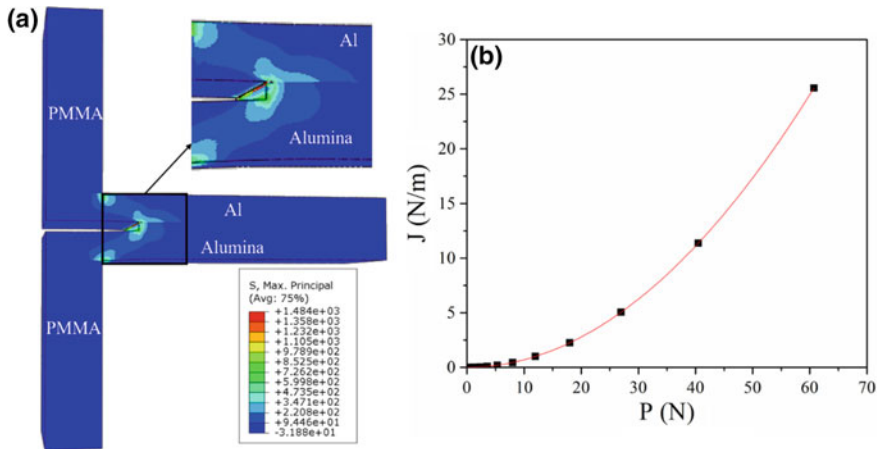
Fig. 7 **a** Stress contour of DCB specimen **b** Fracture energy versus Force curve for DCB test

3.5 Conclusion and Future Work

The objective of the present study was to determine the heterophase interface fracture energy of a thermal spray coated Alumina film over an Aluminium substrate. The DCB geometry was found the most suitable for the same. Since the film and substrate on either side of the interface have very different elasto-plastic properties and thicknesses, a modified DCB formulation proposed by Thouless [16] was used. This involved the accurate determination of the two unknown parameters: the elastic modulus and the fracture energy of the film itself. The elastic properties of the Alumina film were determined by a 3PB test of the bi-layered film-substrate system, from which Young's modulus of 27.05 GPa was found. Fracture energy of the Alumina film as measured from a 3PB of the free-standing coating specimen was found to be 0.53 J/m^2. Fracture energy of Alumina film is comparable to results obtained by Smith et al. [11]. The average fracture energy of the interface as determined from the DCB test was found to be 6.46 J/m^2. Mixed mode failure was observed in most DCB tests where the crack initially propagates along the interface and then kinks into the Alumina film, except on one occasion where complete delamination was recorded. The porosity of the Alumina film and its intrinsically brittle nature is responsible for this kinking, despite the fact that the maximum driving force for crack growth is along the interface. For the specimen which showed crack growth purely along the interface, FEM simulations were also used to extract the interface fracture energy. From the simulations, a G_c value of 3.1 J/m^2 was obtained which is comparable to the analytically determined value of 4.8 J/m^2 from the experimental data. The difference in the two is mainly because the FEM simulations did not account for the properties of the interface.

In order to model the crack growth better, cohesive zone modelling (CZM) of the interface will be carried out based on traction separation law in the future. CZM-based modelling will account more precisely for the properties of the interface, especially the interface strength and displacement at failure. This is important to understand the fracture behaviour of multilayers while quantifying the contribution of the interface on their damage tolerance.

References

1. C. Xie, W. Tong, Cracking and decohesion of a thin Al2O3film on a ductile Al-5%Mg substrate. Acta Mater. **53**(2), 477–485 (2005)
2. C. Edeleanu T.J. Law, Fracture of oxide films on strained aluminium. Philos. Mag. A J. Theor. Exp. Appl. Phys. **7**(76), 573–581 (1962)

3. R.H. Dauskardt, M. Lane, Q. Ma, N. Krishna, Adhesion and debonding of multi-layer thin film structures. Eng. Fract. Mech. **61**(1), 141–162 (1998)

4. M.S. Hu, A.G. Evans, The cracking and decohesion of thin films on ductile substrates. Acta Metall. **37**(3), 917–925 (1989)

5. D. Müller, E. Fromm, Mechanical properties and adhesion strength of TiN and Al coatings on HSS, steel, aluminium and copper characterized by four testing Methods. Thin Solid Films **270**(1–2), 411–416 (1995)

6. X. You, H. Zhao, Y. Wei, Determination of interfacial mechanical parameters for an Al/Epoxy/Al2o3system by using peel test simulations. Acta Mech. Solida Sin. **21**(3), 198–206 (2008)

7. N.G. Chechenin, J. Bøttiger, J.P. Krog, Nanoindentation of amorphous aluminum oxide films III. The influence of the substrate on the elastic properties. Thin Solid Films **304**(1–2), 70–77 (1997)

8. M.D. Kriese, D.A. Boismier, N.R. Moody, W.W. Gerberich, Nanomechanical fracture-testing of thin films. Eng. Fract. Mech. **61**(1), 1–20 (1998)

9. A. Abdul-Baqi, E. Van der Giessen, Delamination of a strong film from a ductile substrate during indentation unloading. J. Mater. Res. **16**(5), 1396–1407 (2001)

10. Y. Okajima, T. Nakamura, S. Sampath, Effect of powder injection on the interfacial fracture toughness of plasma-sprayed zirconia. J. Therm. Spray Technol. **22**(2–3), 166–174 (2013)

11. G.M. Smith, M. Resnick, K. Flynn, G. Dwivedi, S. Sampath, Nature inspired, multi-functional, damage tolerant thermal spray coatings. Surf. Coat. Technol. **297**, 43–50 (2016)

12. I. ASM Aerospace Specification Metals, "Aluminum 6061-T6; 6061-T651." http://asm.matweb.com/search/SpecificMaterial.asp?bassnum=ma6061t6

13. Bangs Laboratories, Material Properties of Polystyrene and Poly(methyl methacrylate) (PMMA) Microspheres, 1–2 (2015

14. J.N. Reddy, *Mechanics of Laminated Composite Plates and Shells: Theory and Analysis* (2003)

15. ASTM, ASTM—E1290 Standard Test Method for Crack-Tip Opening Displacement (CTOD) Fracture. ASTM. **03**(no. March), 1–13 (2003)

16. M.D. Thouless, Shear forces, root rotations, phase angles and delamination of layered materials. Eng. Fract. Mech. **191**, 153–167 (2018)

17. B.F. Sørensen, K. Jørgensen, T.K. Jacobsen, R.C. Østergaard, DCB-specimen loaded with uneven bending moments. Int. J. Fract. **141**(1–2), 163–176 (2006)

18. 94% Alumina Material Properties. Accuratus Ceramic Corporation (2002). https://accuratus.com/alumox.html

19. M.Y. He, J. W Hutchinson, Kinking of a crack out of an interface. J. Appl. Mech. 270–278 (1989)

Dynamic Fracture Behavior in HSLA Steel

Parul Sahu, H. N. Bar and Ashok Kumar

Abstract The influence of pre-straining process on dynamic fracture behavior of Cu-strengthened high-strength low-alloy (HSLA) of varied amount of pre-straining has been investigated in the current study. The influence of pre-straining on deformation due to tensile loading and on ductile fracture behavior of the steel has been carried out with the help of instrumented Charpy test and standard fracture test. Study of microstructure, its hardness, and tensile properties has been done to understand and correlate these properties with Charpy and dynamic fracture behavior of the investigated steel. Prior to the machining of the specimen, the stock materials are pre-strained at different levels. All the Charpy V notch (CVN) specimens are fatigue pre-cracked to generate natural crack. The pre-crack length was restricted to 5 mm (a/w = 0.5). Force–time behavior curve and the force–displacement curve is determined by double numerical integration of force–time curve. In the investigated steel, normalized energy increased slightly up to a level of 2% pre-strain and then decreased by increasing pre-strain level greater than 2%. The dynamic fracture toughness first increases up to 2% and then decreases beyond 2% pre-strain indicating the influence of pre-strain on dynamic fracture toughness behavior of steel. The fracture surface of investigated steel has been examined under scanning electron microscopy. This study has been also focused to understand (i) The nature of the stretch zone—a featureless band that forms prior to initiation of ductile fracture and (ii) the micromechanism of slow stable crack growth.

Keywords Pre-strain · Fracture toughness · Pre-cracking · Dynamic fracture behavior

P. Sahu
Department of Mechanical Engineering, MNNIT Allahabad, Prayagraj 211004, India

H. N. Bar
MST Division, National Metallurgical Laboratory, Jamshedpur 831007, India

A. Kumar (✉)
Department of Metallurgical and Materials Engineering, NIT Jamshedpur,
Jamshedpur 831014, India
e-mail: akumar.met@nitjsr.ac.in

523

1 Introduction

The naval structural application demands high strength, toughness, and good weldability, which are provided by low carbon, Cu-strengthened HSLA steels [1, 2]. It is mainly due to the reduction in carbon content and additional hardenability through age hardening and quenching. Several fabrication methods are available for naval structures but cold forming is the most favorable process. In cold forming of naval structures, rolled plates are heat treated and then deformed at ambient temperature into desired shapes and then finally welded together. One of the major advantages is that it does not require hot working due fabrication in quenched and tempered condition for structural application and material used as it is in cold deformed state. In any material, cold deformation can be given by pre-straining processes which produce the fresh dislocation substructure. Fracture mechanics of any material is also controlled by dislocation substructure present in the material. It is anticipated that cold deformation can have a strong effect on the material behavior of fracture. Several authors have investigated the effect of heat treatment on the microstructure and mechanical properties of Cu-strengthened HSLA steels. Majority of the study is limited to the microstructural characterization and effect on tensile properties and impact strength of the current materials [3]. A brief outline of these studies is available in the literature [4–10].

Materials used in marine condition should have the ability to resist fatigue loading and corrosive environment due to which assessment of fracture and fatigue behavior of these materials in the adverse marine environment is in demand and required.

2 Experimental

HSLA steel is available in the form of a plate having a thickness of 25 mm with rolling direction marked. The chemical compositions of steel are shown in Table 1.

In the scope of the study, the microstructure, hardness and chemical composition of current material examined and reported. In course of study, the effect of pre-straining on dynamic fracture behavior of pre-strained Charpy notched specimen is machined and fatigue pre-cracked to maintain uniform crack length (a/w = 0.5) according to ASTM 399-09 [11]. K_{jd} can be calculated by using the following equations:

Table 1 Chemical composition of HSLA steels in wt%

Steel	C	Mn	P	S	N	Si	Cr	Mo	Al	Nb	Ni	Cu
HSLA 100	0.06	0.84	0.01	0.003	0.008	0.25	0.74	0.58	0.023	0.03	3.47	1.54

$$K_Q = \frac{P_Q S}{\sqrt{BB_N} W^{3/2}} f\left(\frac{a}{w}\right)$$

where

$$f\left(\frac{a}{w}\right) = 3\sqrt{\frac{a}{w}} \cdot \frac{1.99 - \left(\frac{a}{w}\right)\left(1 - \frac{a}{w}\right)\left[2.15 - 3.93\frac{a}{w} + 2.7\left(\frac{a}{w}\right)^2\right]}{2\left(1 + 2\frac{a}{w}\right)\left(1 - \frac{a}{w}\right)^{3/2}}$$

The specimens are tested at Charpy impact tester at hammer speed of 5 m/s. The computerized data acquisition system has been used to capture force–time response.

In present work, pre-strained Charpy notched samples are fatigue pre-cracked to maintain uniform crack length using the computerized data acquisition system in order to capture the force–time response. The stress distribution is symmetrical throughout the specimen thickness during fatigue pre-cracking for uniform growth of the crack.

All the specimens have been pre-cracked in three-point bending using fatigue pre-cracking procedure in order to achieve the force–time curve. Force–displacement curve was obtained by double integration of force–time curve. Dynamic fracture toughness was calculated using ASTM E1820 [12]. As per recommendation, the calculation has to be made both for elastic J and plastic J (as in conventional J calculation) and have to be summed up. Total J refers to this only here.

The crack length was calculated in compliance method and compared with data measured from fractography. The force–time data have processed and it is observed that application of pre-strain resulted in the retention of dynamic fracture toughness up to 2% pre-strain However, there is rapid deterioration thereafter. The variation of maximum dynamic fracture toughness and total dynamic fracture toughness with the pre-strained situation has been reported.

3 Results and Discussion

3.1 Force–Time Behavior

See Fig. 1.

3.2 Force–Displacement Behavior

See Fig. 2.
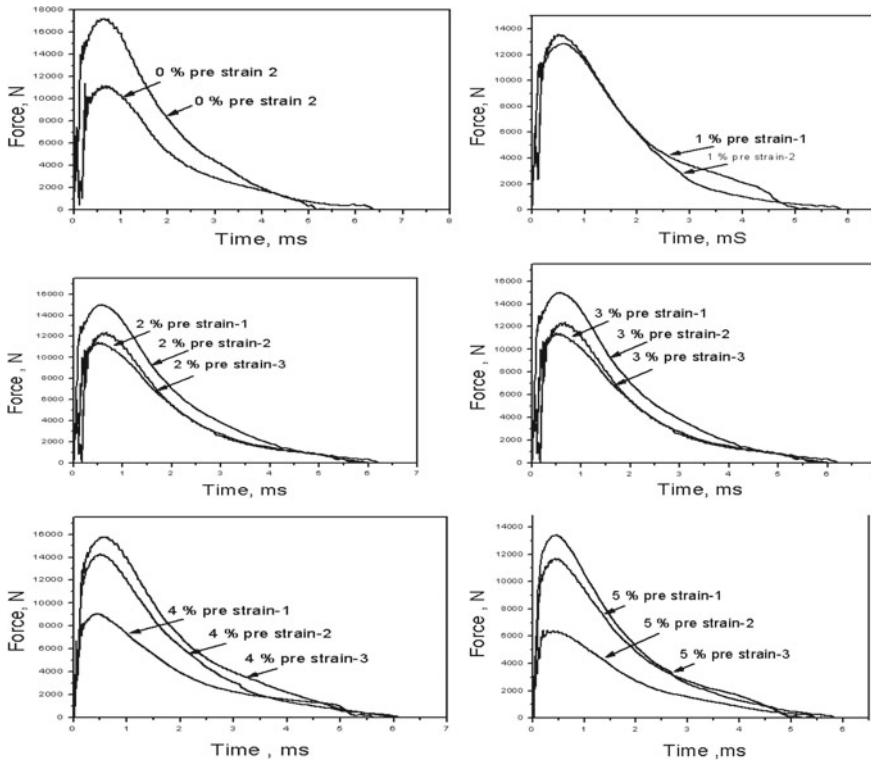
Fig. 1 Force–time behaviour curve of prestained samples with pre-strain level (0–5%)

3.3 Energy Variation Due to Pre-strain

Impact energy is an indication of toughness. Energy variation occurs due to the different pre-crack length. Therefore, it is required to normalize the energy by remaining ligament area.

$$\text{Remaining ligament area} = B \times \left(wa_{avg}\right)$$

3.4 Normalized Energy Versus Pre-strain

Normalized energy of all pre-strained sample is shown in Table 2. Normalized energy is defined as the impact of energy divided by the remaining ligament area. Variation of normalized energy with prestaining in steel is presented in Fig. 3. In this investigation, it can be seen that the normalized energy did not deteriorate, but increased slightly up to a 2% pre-strain level and beyond this, it decreased deleteriously (Fig. 4).
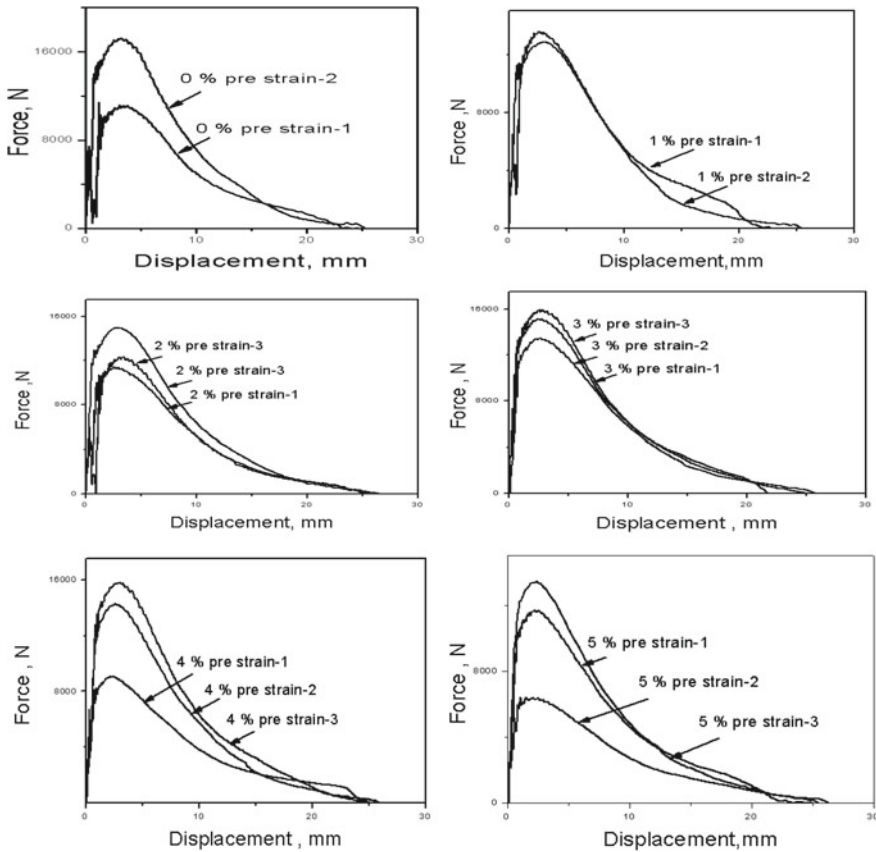
Fig. 2 Force displacement behaviour curve of samples with prestrain level (0–5%)

3.5 Variation of Dynamic J Versus Pre-strain

In this investigation, influence of pre-strain on dynamic fracture toughness has been conducted. It was observed that dynamic fracture toughness shows a rising trend for pre-strain value ranging from 0 to 2% This increase in fracture toughness for the pre-strained material is four times compared to that of 0% pre-strain. The fracture toughness values decrease for more than 2% pre-strained samples and it reached a value which is lower than for 0% pre-strain (undeformed material) for 10% pre-strained samples. The variation of dynamic fracture toughness (J_d) with pre-strain has been represented in Fig. 5. No decrease in fracture toughness was observed for both the investigated steels for 0–2% pre-strain, whereas it deteriorates for higher values of pre-strain up to 10%. This increased values of fracture toughness. The initial values of fracture toughness, which is almost constant up to 2% pre-strain is very important for the structural fabrication with the grades almost

Table 2 Average pre-crack length, ligament, area, energy, and energy/area of various pre-strained (0, 1, 2, 3, 4, and 5%) specimens

Specimen	a_{avg} (mm)	Ligament (mm)	Area (mm^2)	Energy (J)	Energy/Area (J/mm^2)
0p-1	4.74	5.26	52.60	112.26	2.134
0p-2	4.27	5.73	57.30	163.75	2.857
1p-1	4.38	5.62	56.20	130.01	2.313
1p-2	4.629	5.37	53.71	122.06	2.270
2p-1	3.98	6.02	60.2	115.45	2.083
2p-2	4.70	5.30	53.00	148.90	2.542
2p-3	4.158	5.49	54.90	116.35	2.195
3p-1	4.152	4.152	5.848	58.48	2.496
3p-2	4.154	4.154	5.846	58.46	2.260
3p-3	3.809	3.809	6.191	61.91	2.419
4p-1	5.406	4.594	45.94	94.35	2.053
4p-2	3.72	6.28	62.8	131.93	2.100
4p-3	3.77	6.23	62.3	151.01	2.423
5p-1	4.972	5.028	50.28	110.57	2.199
5p-2	6.07	3.93	39.30	65.95	1.668
5p-3	4.228	5.772	57.72	120.05	2.079

Fig. 3 Effect of prestrain on normalized energy
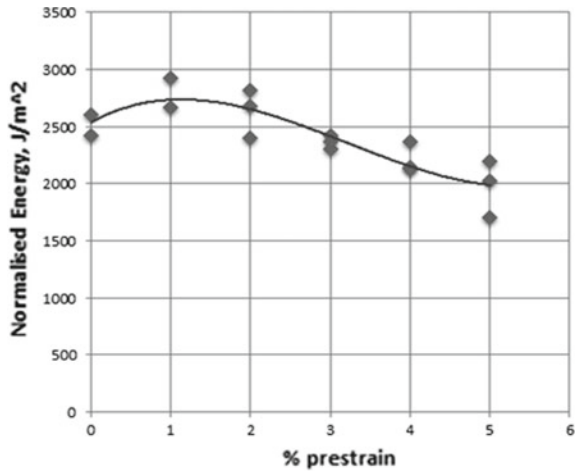
similar to the investigated high-strength low-alloy steels. These investigated steels indicate that fracture toughness values do not decrease with the pre-strain level given to the steels.

Fig. 4 Effect of prestrain on maximum dynamic J
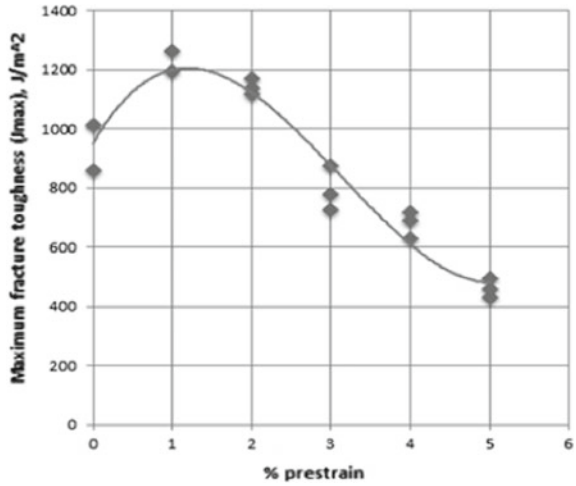
Fig. 5 Effect of prestrain on total dynamic fracture toughness
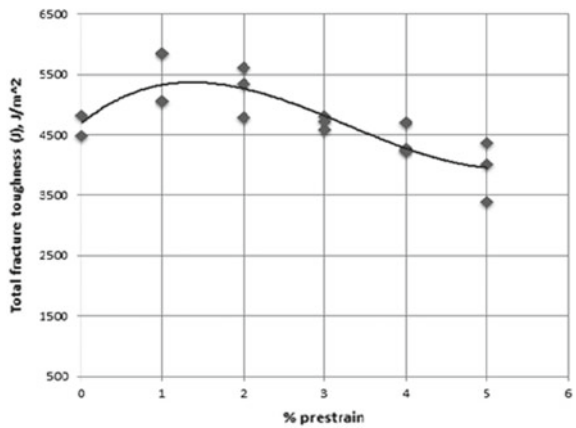
3.6 Total Dynamic Fracture Toughness Versus Pre-strain

The dynamic fracture toughness values in ductile materials are controlled by the plastic strain region around the crack tip. The plastic region developed by plastic strain depends on the factors like yield stress which indicates the start of plastic deformation and strain hardening index which takes into account the area covered by the plasticity due to the strain. The yield stress and strain hardening index also known as strain hardening exponent may change due to the pre-straining given to the material, and as a result, it changes the dynamic fracture toughness. Variation of dynamic fracture toughness with pre-straining is shown in Fig. 6. Assuming, there is approximately no crack extension up to maximum load. Initiation fracture

Fig. 6 Effect of prestrain on maximum dynamic fracture toughness
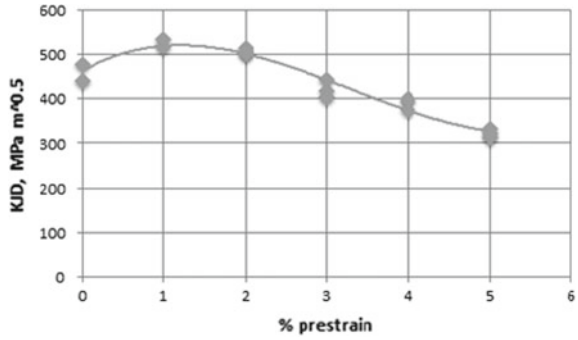
toughness (resistance to crack initiation) occurs under dynamic loading. So, total dynamic fracture toughness was measured. The total crack extension defines the energy absorbing tendency (Figs. 7, 8, 9, 10 and 11 and Table 3).

Fig. 7 Effect of prestrain on normalized energy and total energy
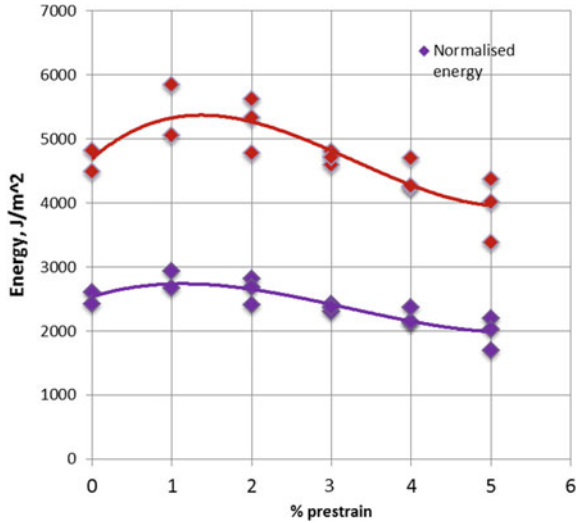
Fig. 8 Ratio of total energy to normal energy vs prestrain level
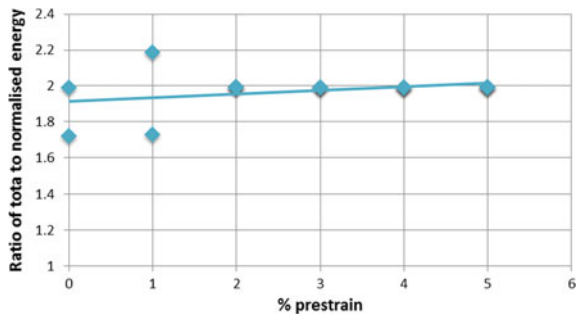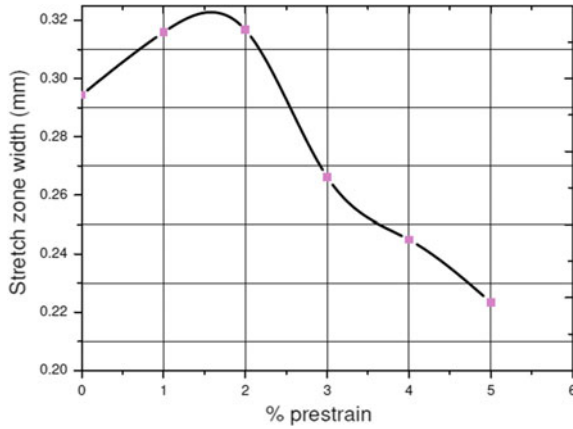
Fig. 9 Stretch zone width with various prestrain level
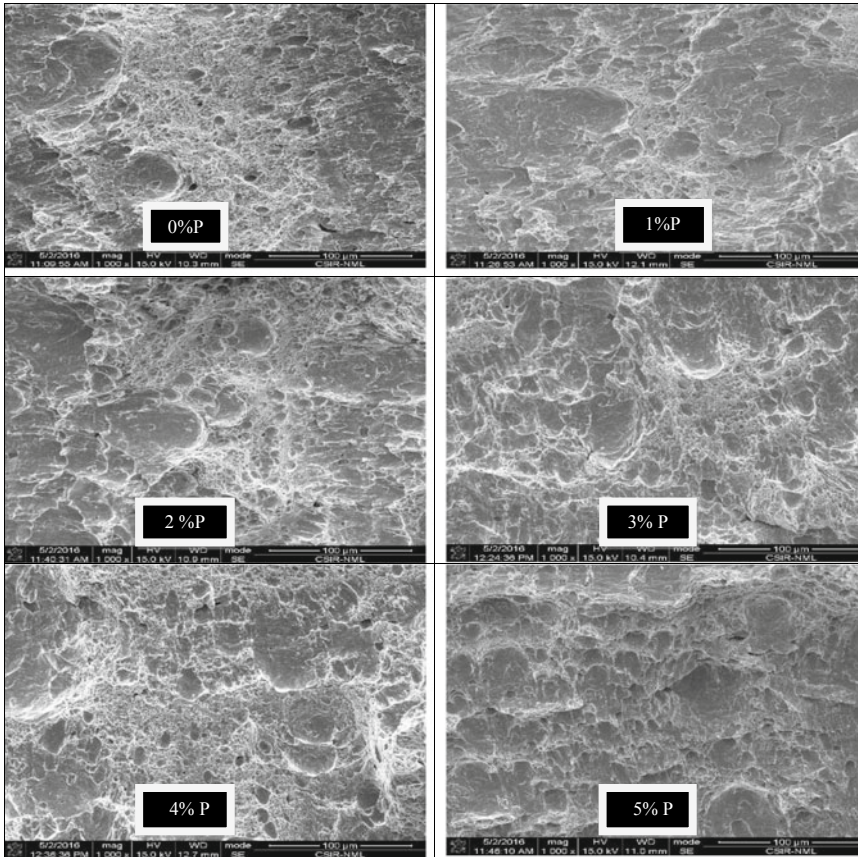
Fig. 10 Fracture surface of prestrained HSLA-100 steel after precracking

Fig. 11 Stretch zone formation of HSLA steel

Fracture surface

Stretch zone width

Precrack area
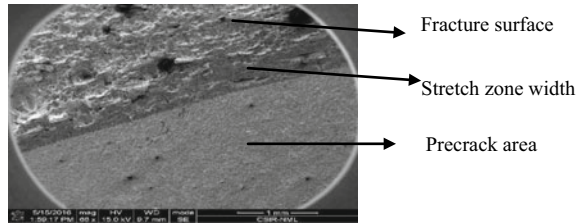
Table 3 Indicates the stretch zone width with various pre-strain level

Pre-strain	Stretch zone width (mm)
0	0.2944
1	0.3159
2	0.3167
3	0.26619
4	0.2449
5	0.2234

3.7 Factography

The fractured surface was ultrasonically cleaned and then examined under a scanning electron microscope (JEOL 850A Model).

3.8 Stretch Zone Formation

The fracture surface of HSLA-100 steel has been examined under scanning electron microscopy. The main focus in these studies has been made to understand (i) The nature of the stretch zone and (ii) the micromechanism of slow stable crack growth.

In HSLA, the stretch zone was very distinct, continuous and had an almost uniform width throughout the thickness of the specimen.

4 Conclusions

1. The force–displacement curve is determined by double numerical integration of force–time curve.
2. In the HSLA steel, it was observed that normalized energy did not deteriorate, and perhaps increased slightly, up to a pre-strain level of 2%, beyond which it decreased deleteriously.

3. The dynamic fracture toughness gets decreased when the material is pre-strained and more than 2% strain level is shown in Fig. 6.
4. Comparison of normalised and total energy and their ratio with pre-strain, Slope of normalized energy curve is twice of the slope the total energy curve. Ratio of the total to normalized energy is neat at about 1.8–1.9. $\eta pl = 1.9$ if the load–line displacement is used for *Apl*.
5. Stretch zone width of HSLA-100 steel has been examined under scanning electron microscopy.

References

1. E.J. Czyryca, R.E. Link, R.J. Wong, D.A. Aylor, T.W. Montem, J.P. Gudas, Nav. Eng. J. **102**, 63 (1990)
2. J.P. Christein, J.L. Warren, *Newport News Shipbuilding*, VA (1993)
3. S. Sivaprasad, S. Tarafder, V.R. Ranganath, K.K. Ray, Mater. Sci. Eng. A **284**, 195 (2000)
4. K.F. Amouzouvi, M.N. Bassim, *Fracture Problems and Solutions in Energy Industry* (Pergamon, Oxford, 1982), p. 179
5. K.F. Amouzouvi, M.N. Bassim, Mater. Sci. Eng. **60**, 1 (1983)
6. M.N. Bassim, M.R. Bayoumi, Mater. Sci. Eng. **81**, 317 (1986)
7. J.Q. Clayton, J.F. Knott, Met. Sci. **10**, 63 (1976)
8. K.F. Amouzouvi, Mater. Sci. Eng. **78**, 65 (1986)
9. P.K. Liaw, J.D. Landes, Metall. Trans. A **17**, 473 (1986)
10. L. Banks-Sills, I. Dunye, Eng. Fract. Mech. **57**, 67 (1997)
11. ASTM E-399-09: Standard Test Method for Linear Elastic Plain Strain fracture Toughness of Metallic Materials, ASTM, Philadelphia, PA (2009)
12. ASTM E-1820-15: Standard Test method for measurement of fracture Toughness, ASTM, Philadelphia, PA (2015)

Fracture Toughness Characterization of Mod.9Cr-1Mo Welds

B. Shashank Dutt, G. Shanthi and A. Moitra

Abstract The fracture toughness of the weld metal is crucial for the integrity of components as it is often been identified as the region prone to easy crack initiation and growth. To this end, fracture toughness characterization of Mod.9Cr-1Mo welds have been carried out, where the TIG and A-TIG processes were adopted as the welding procedures. The J–R curves at room temperature were determined using CT specimens, fabricated from the weld pads as well as from the base material. The average $J_{0.2}$ value for the base material and the TIG weld were 180 kJ/m^2 and 177 kJ/m^2, respectively. For A-TIG welds, a brittle fracture was observed with a negligible crack extension (less than 0.1 mm). Signatures of cleavage fracture, as observed in the SEM fractographs of the A-TIG weld, corroborates well with the above observation. In contrast, the fractographs of the TIG weld has shown dimples indicating a ductile fracture. For A-TIG welds, since valid J–R curves could not be obtained, average fracture stress was determined to be ~ 2 kN m^{-2}.

Keywords Modified 9Cr-1Mo steel · Welds · Fracture toughness · Heat treatment

1 Introduction

Mod.9Cr-1Mo steel is selected as the material for steam generator (SG) components of the fast breeder reactor. These components are subjected to operating temperatures from 370 to 550 °C. The mechanical properties of this class of steels including tensile, low cycle fatigue, fatigue crack growth and impact toughness properties were previously reported [1–7]. For fabrication of steam generator components welding is the major manufacturing process. In this class of steels and other

B. Shashank Dutt (✉) · G. Shanthi · A. Moitra
Metallurgy and Materials Group, Indira Gandhi Centre for Atomic Research,
Kalpakkam 603102, India
e-mail: shashank@igcar.gov.in

materials, it is well established that the microstructure and mechanical properties of welds, including heat-affected zone, differ from the base metal. In this class of welds, the heterogeneous microstructures of the welds are prone to embrittlement resulting in degradation of fracture toughness. To ensure the structural integrity of the components fabricated from welds, evaluation of elastic–plastic fracture toughness (J_{1c}) and J–R curves is of immense importance. Very few investigators [8] have reported J_{1c} in this class of welds (SMAW).

For welding of Mod.9Cr-1Mo steels, various welding processes including shielded metal arc welding (SMAW), Tungsten inert gas welding (TIG) processes are employed. It is well established that high quality of welds can be produced by TIG welding process and this welding process is recommended as one of the welding processes for Modified 9Cr-1Mo steels for SG components. Some of the limitations of TIG welding include (a) restricted depth of penetration (b) uncontrolled weld penetration and (c) requirement of several numbers of passes for thick sections. Previous investigators [6, 7] have reported that by A-TIG welding process welds can be produced with lesser number of passes. Previous investigators have reported a significant reduction of welding cost by employing A-TIG welding process instead of TIG welding process [9]. The higher depth of penetration is achieved in A-TIG welds by application of a thin layer of flux coating on the metal surface before welding. The advantages of A-TIG welding process compared with TIG welding include (i) higher productivity due to the increased depth of penetration, (ii) reduced distortion and (iii) consistent weld penetration can be achieved. It was also reported [6, 7] that impact toughness of A-TIG and TIG welds vary with the type of post-weld heat treatment (durations). Previous investigators [8] have reported fracture toughness of SMAW welds. In this investigation, TIG and A-TIG welding processes (including the base material) were selected for evaluation of fracture toughness (J_{1c}).

2 Experimental

In this study base metal of Modified 9Cr-1Mo plate of dimensions $390 \times 250 \times 12$ mm in normalised (1080 °C, 1 h) and tempered condition (760 °C, 2 h) was chosen for fabrication of the welds. The chemical composition of the base material is mentioned in Table 1.

Table 1 Chemical composition (wt%) of Modified 9Cr-1Mo steel (base)

Element	C	Si	Mn	Cr	Mo	V	Nb	Ni
wt%	0.08	0.50	0.39	9.4	1.0	0.25	0.09	0.13

Table 2 Parameters used for welding of Modified 9Cr-1Mo steel

Parameter	TIG welding	A-TIG welding
Electrode	EW-2%Th	EW-2%Th
Polarity	DCEN	DCEN
Shielding gas	Commercially pure argon (99.9%)	Commercially pure argon (99.9%)
Flow rate (l/min)	10	10
Heat input (kJ/mm)	0.8	1.04

The parameters used for TIG and A-TIG welding are given in Table 2. For both welding processes, pre-heating was done at 250 °C and the inter-pass temperature was maintained at 200 °C by using oxy-acetylene (neutral) flame. After welding, the weld pads were inspected by X-ray radiography to ensure defect-free welds. The defect-free welds were subjected to post-weld heat treatment (PWHT) at 760 °C for 2 h. The microstructures of the welds after PWHT were examined after polishing and etching by Vilella's etchant. Vickers hardness measurements were carried out for welds (including base metal) after PWHT and load of 500 g was applied. Averages of 10 readings were considered for hardness.

From the weld pads (after PWHT) of dimensions $324 \times 62 \times 12$ mm weld blanks of dimensions $70 \times 65 \times 12$ mm were fabricated. From the weld blanks, compact specimens (CT) of dimensions $62.5 \times 60 \times 10$ mm (10 mm thickness) were fabricated as per ASTM E1820 [10] specifications. The CT specimens were subjected to pre-cracking and side grooving for determination of J–R curves. The initial crack lengths (a_o) after pre-cracking were between 25 and 26 mm. The pre-cracking was carried out at room temperature (RT) using resonant fatigue machine by subjecting the CT specimens under fatigue loading. The initial frequency of load cycle was ~ 75 Hz. The loading range (stress intensity factor K) of 10–5 kN was applied. The initial frequency of load cycle was ~ 100 Hz and loading range of 10–5 kN was applied. After pre-cracking, the CT specimens were side-grooved to 20% net depth (2 mm deep grove on either surface). The *J*-tests were carried out for TIG and A-TG weld specimens including base material. The *J*-tests were carried out in a 100 kN servo-hydraulic machine having automated test control and data acquisition system. The *J*-tests were carried out at room temperature (RT) and at load line displacement rate of 0.01 mm/s. For both welds and base material, the *J*-tests were carried out in duplicate.

For *J*-testing, load (*P*), load line displacement (LLD) data were recorded and direct current potential drop (DCPD) technique was used for online determination of crack length. The LLD was monitored using crack opening displacement gauges. The tested specimens were heat-tinted (400 °C) and then pulled to fracture (room temperature). The initial (a_o) and final crack lengths (a_f) were optically determined by the nine-point average method. The fracture surfaces were examined in the Scanning Electron Microscope (SEM).

3   Results and Discussion

The microstructure (optical) of the base and welds after PWHT are shown in Fig. 1a–c. The microstructures revealed tempered martensite with prior austenite grain boundaries and lath boundaries. The microstructures revealed the uniform distribution of precipitates. It is widely reported that Modified 9Cr-1Mo steel has tempered martensite (metastable) microstructure with main precipitates as $M_{23}C_6$ (Cr rich) and MX (M = V, Nb, Cr; X = C, N) types. The presence of various precipitates can be confirmed for both the welds as shown in Fig. 2a, b. The EDX (elemental) analysis (Fig. 2c) indicated presence of MX type of precipitate. The precipitates were comparatively coarser in TIG welds as shown in Figs. 1b and 2a. For A-TIG welds, a few pockets of delta ferrite (darker phase) was observed as shown in Fig. 2b.

For the base material, hardness was 200 VHN and for TIG weld after PWHT hardness was 205 VHN. For A-TIG weld after PWHT the hardness was 270 VHN. For A-TIG welding process due to higher cooling rates and peak temperatures, the carbon content of martensite is expected to be higher, compared to the TIG welding

(a)

(b)

(c)
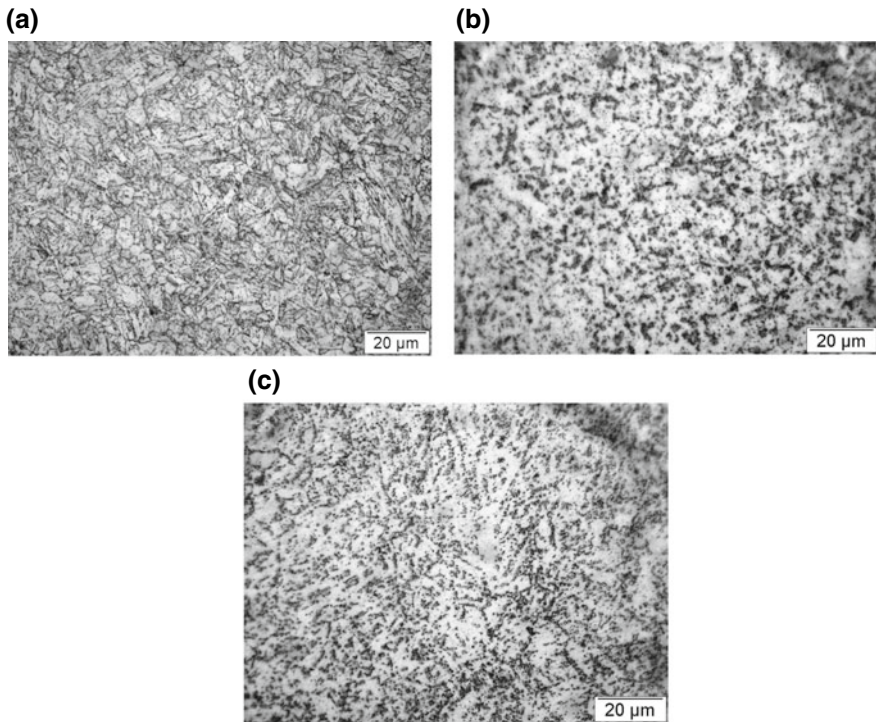
Fig. 1   a Microstructure of base metal. **b** Microstructure of TIG weld. **c** Microstructure of A-TIG weld

(a)

(b)

(c)
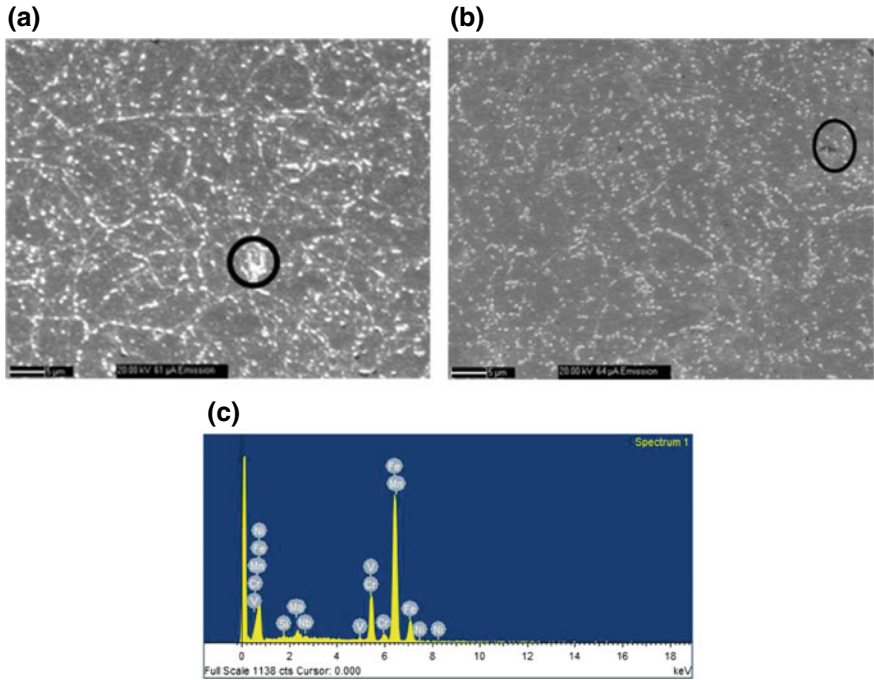
Fig. 2 a Microstructure of TIG weld. **b** Microstructure of A-TIG weld. **c** EDX result of precipitate in TIG weld

process. Due to higher carbon contents, the hardness of A-TIG welds is higher compared to TIG welds. Similar differences in hardness between A-TIG and TIG welds were reported by previous investigators [6, 7].

The load–displacement plots of base and TiG weld revealed ductile fracture as shown in Fig. 3. For A-TIG weld, no significant deformation was observed. For base material and TIG weld, plastic deformation was observed (Fig. 3), indicating ductile crack extension. For A-TIG welds, a negligible amount of plastic deformation was observed (less than 1 mm). This indicates a negligible amount of energy for crack extension (initiation) and crack propagation or tendency for brittle fracture.

The *J* values were computed following ASTM E 1820 [10] using Eqs. (1–6) as shown below:

$$J = J_{el} + J_{pl} \tag{1}$$

$$J_{(i)} = \frac{K_{(i)}^2(1 - v^2)}{E} + J_{pl(i)} \tag{2}$$

Fig. 3 Load–displacement
plots
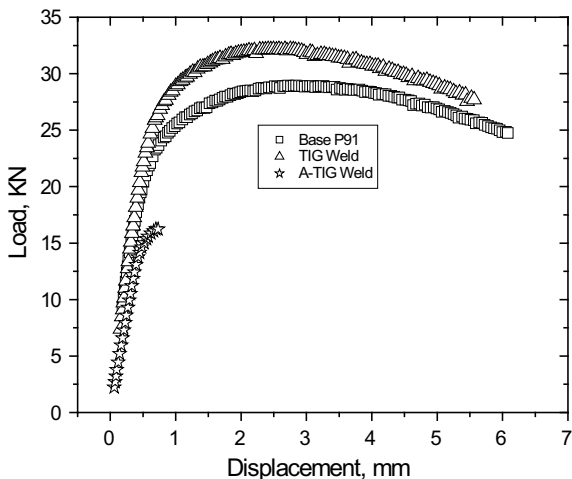
$$J_{pl(i)} = \left\{ J_{pl(i-1)} + \left(\frac{\eta_{(i-1)}}{b_{(i-1)}}\right) \cdot \frac{A_{pl(i)} - A_{pl(i-1)}}{B_N} \right\} \cdot \left[1 - \gamma_{(i-1)} \frac{a_{(i)} - a_{(i-1)}}{b_{(i-1)}} \right] \qquad (3)$$

$$\eta = 2.0 + 0.522 \frac{b}{W} \qquad (4)$$

$$\gamma = 1.0 + 0.76 \frac{b}{W} \qquad (5)$$

$$J = M\sigma_f(\Delta a) \qquad (6)$$

where J_{el}, J_{pl}—the elastic and plastic components of J, K—the stress intensity factor, ν—Poisson's ratio, A_{pl}—Instantaneous area under load–displacement curve and b = uncracked ligament (W-a), σ_{YS} = Yield strength (YS), σ_f = flow stress = (YS + UTS)/2, UTS = ultimate tensile strength, Δa = crack extension, M = blunting line equation constant = 2.

The J–R curves determined as per ASTM E1820 [10] are shown in Fig. 4a, b. Form the J–R curves, elastic–plastic fracture toughness (J_{1c}) values were determined. The fracture toughness (J_{ic}) value for base metal was ∼180 kJ/m² and for TIG weld fracture toughness was ∼177 kJ/m². The authors have previously reported [11] similar fracture toughness for a similar type of steel (base material). For A-TIG weld ductile fracture was not observed. From Fig. 3, it can be observed for A-TIG weld no significant crack extension (less than 0.1 mm) occurred due to brittle fracture. For A-TIG weld, a valid J–R curve was not possible to be determined. The average fracture stress (K_q) calculated based on initial crack length (∼25 mm) and corresponding to maximum load (Fig. 3) as per ASTM 1820 [10] was ∼2 kN/m². The fractographs of base metal (Fig. 5a) and TIG weld (Fig. 5b) revealed dimples of various sizes indicating a ductile fracture. The precipitates of
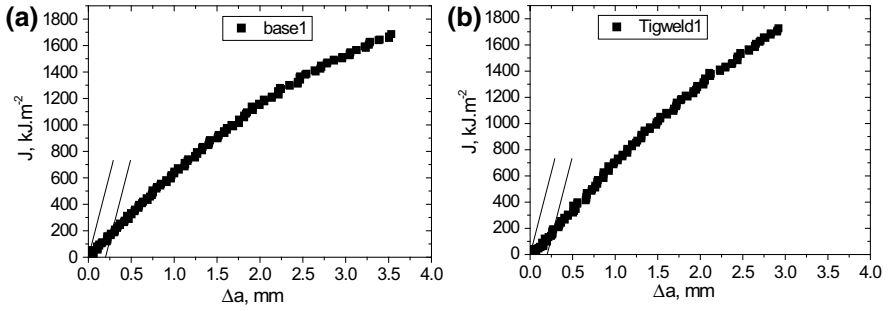
Fig. 4 a J–R curve of base metal. b J–R curve of TIG weld
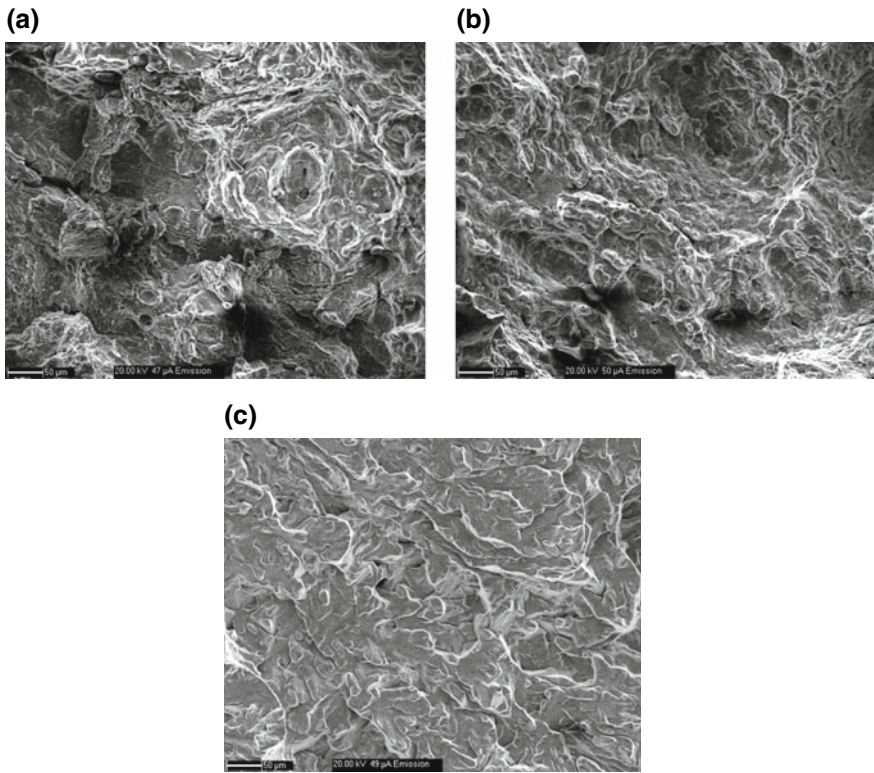
Fig. 5 a Fractograph of base metal. b Fractograph of TIG weld. c Fractograph of A-TIG weld

varying sizes act as the predominant sites for void nucleation and growth. For A-TIG weld, signatures of cleavage fractures were observed as shown in Fig. 5c. For A-TIG welds due to higher hardness or strength of matrix (martensite) resulted in cleavage crack initiation and propagation.

In this class of welds after cooling, martensite formation occurs. For TIG welds, martensite is tempered during each welding pass. The tempering of martensite after PWHT results in decreased dislocation density of the martensite. The tempering or PWHT also results in precipitation of various carbides. These changes in the microstructure are dependent on the temperatures during subsequent passes. Previous investigators [6, 7] have reported higher impact toughness for TIG welds compared to A-TIG welds. In this class of welds, it was also reported that toughness of welds is dependent on the quality of welds. Considering that toughness is dependent on strength and ductility, the optimum toughness can be achieved by controlling the factors affecting the microstructure of any steel (base or weld). Previous studies in this type of steels (base and welds) also mentioned [12] that the presence of delta ferrite in the microstructure results in significant degradation of toughness. Previous investigators [6] reported presences of delta ferrite (volume fraction of 0.5%) in A-TIG welds (as weld condition) and absence of delta ferrite in TIG welds. In this investigation, delta ferrite was not observed for TIG welds. For A-TIG welds, a few pockets of delta ferrite were observed (Fig. 2b).

Previous investigators [6] reported higher hardness for A-TIG welds compared to TIG welds. In this investigation, similar trends in hardness values were observed. For TIG welds [6], higher Charpy impact toughness was reported compared to A-TIG welds. In this investigation, both welds were subjected to similar PWHT (760 °C, 2 h) condition. The reasons for higher impact toughness of TIG welds [6] were explained based on enhanced tempering effects due to the multiple numbers of passes and due to the absence of delta ferrite. In this investigation, a similar mechanism [6] is applicable to explain the differences in fracture toughness between TIG and A-TIG welds. The higher hardness of A-TIG welds compared to TIG welds can be attributed to incomplete tempering effects.

In a related study for a similar class of welds [7], higher strength was observed for A-TIG welds after PWHT at 760 °C (6 h) compared to TIG welds after similar PWHT. The impact toughness [7] was observed to increase with the duration (2–8 h) of PWHT. The A-TIG welds [7] after PWHT at 760 °C for 6 h had fully tempered martensite microstructure and the weld after PWHT at 760 °C for 4 h contained partially tempered martensite. Previous studies [7] also mentioned the presence of delta ferrite in the microstructure of A-TIG welds [7]. The presence of delta ferrite was attributed to higher cooling rates after welding. It can be noted that similar [7] changes in microstructures are expected in this investigation, considering a similar type of steels (base) and similar PWHT of A-TIG welds. In this investigation, brittle fracture observed in A-TIG welds can be explained based on incomplete tempering effects of martensite.

4 Conclusions

The microstructure and fracture toughness of A-TIG and TIG welds (including base material) was evaluated. The higher hardness observed for A-TIG welds was due to partial tempering of martensite. The fracture toughness of TIG weld and base metal were comparable and ductile fracture was observed as revealed by fractographs with dimples. For A-TIG welds, brittle fracture was observed and this can be explained based on incomplete tempering effects after PWHT at 760 °C for 2 h.

References

1. M. Vani Shankar, Valsan. Mater. Sci. Eng. A **437**, 413 (2006)
2. A. Nagesha, M. Valsan, Int. J. Fatigue **24**, 1285 (2002)
3. M.N. Babu, G. Sasikala, Int. J. Fatigue **43**, 242 (2012)
4. Y. Asada, K. Dozaki, Nucl. Eng. Des. **139**, 269 (1993)
5. K. Aoto, R. Komine, Nucl. Eng. Des. **153**, 97 (1994)
6. B. Arivazhagan, J. Manuf. Process **16**, 305 (2014)
7. V. Maduraimuthu, Trans. Indian Inst. Met. **68**, 181 (2015)
8. X. Long, Mater. Sci. Eng. A **270**, 260 (1999)
9. M. Vasudevan, Sci. Technol. Weld. Join. **15**, 117 (2010)
10. ASTM Standard test method for measurement of fracture toughness, ASTM E1820 (2009), pp. 1–49
11. B.S. Dutt, Mater. Sci. Technol. **27**, 1527 (2011)
12. J. Onoro, J. Mater. Process. Technol. **180**, 137 (2006)

Effect of Microstructure on the Fatigue Crack Growth Behavior in Al–Zn–Mg–Cu Alloy

M. S. Nandana, Bhat. K. Udaya and C. M. Manjunatha

Abstract High-strength Al–Zn–Mg–Cu alloys are used in airframe structures, such as bulk heads, wing spars, and lug joints. In this investigation, the effect of RRA microstructure on the fatigue crack growth rate (FCGR) behavior is studied. The 7010 aluminum alloy was heat treated to two different conditions, i.e., T6 and RRA. The microstructure of the heat-treated alloy is characterized by using transmission electron microscope (TEM). The FCGR tests were performed as per ASTM E647 standard by using a 100 kN servo-hydraulic test machine. The tests were performed using standard compact tension (CT) specimens with a stress ratio, R = 0.7 using a sine wave form at 10 Hz in a standard laboratory air environment. The matrix microstructure of the RRA-treated alloy consists of fine scale η' ($MgZn_2$) precipitates with increased interparticle spacing when compared to closely packed η' precipitates in the standard T6-treated alloy. The grain boundary precipitates are coarsened and discrete in the RRA-treated alloy, while it is continuous in T6 condition. An improvement in the threshold stress intensity factor range (ΔK_{th}) by about 0.65 MPa$\sqrt{m}$ is observed in RRA-treated alloy compared to the T6-treated alloy. The FCGR was observed to be lower by 2 times in RRA-treated alloy compared to T6-treated alloy over the major portion of FCGR curve. The increased free slipping distance between the matrix precipitates in RRA-treated alloy is correlated to the improved fatigue crack growth resistance of the RRA-treated aluminum alloy.

Keywords Heat treatment · Fatigue · Microstructure · Crack growth

M. S. Nandana · Bhat. K. Udaya (✉)
Department of Metallurgical and Materials Engineering,
National Institute of Technology Karnataka, Surathkal, Mangalore 575025, India
e-mail: udayabhatk@gmail.com

C. M. Manjunatha
Structural Technologies Division, CSIR-National Aerospace Laboratories,
Bangalore 560017, India

1 Introduction

7xxx aluminum alloys composing Zn–Mg–Cu as main alloying elements, find wide application in structural members of the aircraft due to their superior mechanical properties and better corrosion resistance properties [1, 2]. These properties are influenced by the microstructural features, such as secondary phase particles, that get nucleated during aging treatment [3]. Owing to their good damage tolerance capabilities, with established processing methods and damage detection techniques these aluminum alloys still pose a good competitor for polymer composites [4, 5]. The major drawbacks of 7xxx alloys are that they are prone to corrosion and stress corrosion cracking (SCC) at the grain boundaries, when they are used in peak aged (T6) condition [5, 6]. Higher SCC resistance is imparted, when the alloy is treated in over aged (T7) condition, but with an inevitable loss of the peak strength by 10–15% [7, 8]. A novel heat treatment called retrogression and re-aging (RRA) proposed by Cina [9], retains the peak strength of the alloy along with SCC resistance similar to T7 condition.

The recent investigations reveal that the microstructural features, such as grain size, grain boundary precipitates, and second phase matrix precipitates influence the fatigue crack growth behavior in high-strength aluminum alloys [10, 11]. An increase in the FCGR was observed as the aging is prolonged. Desmukh et al. [12] observed that the crack growth rate was higher in overaged condition when compared to single-step aged and two-step near peak aged conditions in 7010 alloy. The wider precipitate-free zones (PFZ) and the presence of nonshearable precipitates in the matrix were responsible for the increased FCGR.

The FCGR behavior of the 7010 aluminum alloy in RRA-treated condition is not much reported in the literature. The present study aims at comparing the FCGR behavior of T6- and RRA-treated aluminum alloys, both exhibiting equivalent tensile strength and yield strength. The influence of the microstructural modifications on the reduced FCGR and increased threshold stress intensity factor range (ΔK_{th}) in RRA-treated alloy is highlighted.

2 Experimental

2.1 Material

A rolled plate received in T7451 condition was used for the present research work. The alloy was composed of 6.3Zn2.21Mg1.65Cu0.124Zr0.21Fe0.073Si with the balance of aluminum (wt%). The rolled microstructure of as received alloy is presented in Fig. 1.
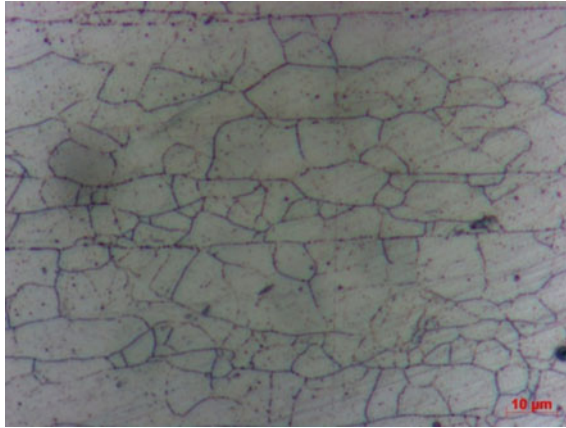
Fig. 1 Optical microscope image of the AA7010 in as received condition

2.2 Heat Treatment

The T6 treatment involves artificial aging at 120°C for 24 h, following the solution treatment and water quenching. The RRA treatment involves subjecting the T6-treated alloy to retrogression, i.e., high-temperature heating at 200°C for 20 min. The retrogression treated alloy is re-aged to peak aging condition to complete the process of RRA treatment. The details of the heat treatment steps are presented in Table 1.

2.3 Mechanical Testing

Round tensile test samples of gauge length 30 mm and gauge diameter of 6 mm were machined according to ASTM E8 Standard with the tensile axis being parallel to the rolling direction. The tensile tests were performed on a universal testing machine (Shimadzu make, AG-X Plus model) operated at a crosshead speed of 1 mm/min. Three trials were performed for each tempering conditions and the

Table 1 Heat treatment schedule adopted on AA7010

Aging conditions	Heat treatment steps
Peak aging (T6)	Solution treatment at 490°C for 6 h + aging at 120°C for 24 h
Retrogression and re-aging (RRA)	Solution treatment at 490°C for 6 h + aging at 120°C for 24 h + Retrogression at 200°C for 20 min + re-aging at 120°C for 24 h

average results were reported. Fracture toughness measurements were done according to ASTM E399 standard using 100 kN servo-hydraulic machine (Instron make). CT specimens of $50.5 \times 60 \times 25$ mm were used for fracture toughness estimation. Three trials were conducted and the average value is reported.

Fatigue crack growth rate (FCGR) tests were performed on the standard compact tension (CT) specimens as per ASTM E647. The CT samples with 50.5×60 12.5 mm (W $\times$ H $\times$ B) were adopted for performing FCGR tests. A sinusoidal loading pattern with a stress ratio (R = $\sigma_{min}/\sigma_{max}$) of 0.7 was applied with a cycle frequency of 10 Hz. A higher stress ratio is selected to overcome the effect of crack closure effect on the crack growth rate. The CT specimens were initially pre-cracked and a decreasing ΔK test was carried until the crack growth rate reached threshold value i.e., 1×10^{-6} mm/cycle. Further, the same sample was subjected to a constant load, increasing ΔK test until failure of the sample to get the entire Paris regime and high ΔK regime of FCGR curve. The crack length was continuously measured as per compliance technique using a crack mouth opening displacement (CMOD) gauge attached to the CT sample.

2.4 Microstructural Characterization

The microstructure of the alloy was characterized by using transmission electron microscope (TEM: JEOL, JEM2100) operated at 200 kV. The TEM samples were prepared by punching 3 mm diameter discs from the mechanically thinned (80 μm) section of the heat treated sample. The thin samples were further dimple ground to 15 μm thick by using dimple grinder (Gatan make). Ion milling was performed on the dimpled region by using Gatan PIPS instrument operated at a beam energy of 5 keV with a beam angle of 5° top and 5° bottom.

3 Results and Discussion

The bright-field TEM micrographs of the AA7010 in T6 and RRA-treated conditions are shown in Fig. 2. The precipitates (3–5 nm) were found to be homogeneously distributed in the matrix of both T6- and RRA-treated samples. The selected area electron diffraction patterns (SAED) in $[111]_{Al}$, with diffused spots at 1/3 and 2/3 of (220) aluminum plane highlights the presence of the η´ precipitates in the RRA matrix [13]. The RRA-treated sample also exhibits disc shaped larger sized η´ precipitates (10–12 nm) in the matrix. The partial dissolution of the matrix precipitates during retrogression, which grow upon re-aging step leads to the formation of the larger sized precipitates in the RRA-treated alloy [14]. The RRA-treated alloy exhibits an increase in the interparticle spacing of the matrix precipitates when compared to the T6-treated alloy. The interparticle spacing observed is about 6.1 nm in RRA compared to the observed 3.3 nm in the standard T6-treated alloy. The grain
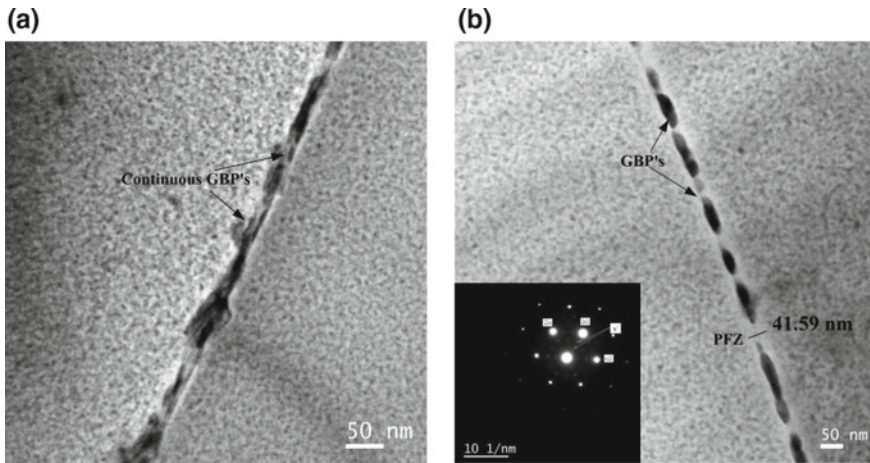
Fig. 2 Bright-field TEM micrographs of AA7010. **a** T6 **b** RRA

boundary precipitates η (MgZn$_2$) which are observed to be continuous (Fig. 2a) in the T6 condition, gets discontinuously arranged in RRA-treated sample, similar to the observations reported by other researchers [15]. The precipitate-free zone (PFZ) size was observed to be widened in RRA-treated alloy due to high-temperature retrogression. The average width of the PFZ in the RRA-treated sample is observed to be of 35–40 nm as compared to 25–35 nm in the T6 alloy.

3.1 Tensile Properties

The results of the tensile tests performed on T6- and RRA-treated alloy is presented in Table 2. The alloy in RRA treatment resulted in an ultimate tensile strength of 586 MPa which is similar to the strength of the T6-treated alloy. Reduction in elongation at the failure by 3% is observed in RRA-treated sample compared to T6-treated alloy. The fracture toughness of the RRA-treated sample is 41 MPa√m, which is reduced by a unit value when compared to that of the T6-treated alloy. This is due to the increase in the PFZ size (35–40 nm) in RRA-treated alloy compared to T6-treated alloy.

Table 2 Tensile and fracture toughness properties of the AA7010

Heat treatment condition	Ultimate tensile strength, MPa	Yield strength, MPa	Elongation at break %	Fracture toughness MPa√m
T6	581	495	14.4	42
RRA	586	506	11.3	41

3.2 Fatigue Crack Growth Behavior

The fatigue crack propagation rate (da/dN) plotted against applied stress intensity factor range (ΔK) for AA7010 in T6- and RRA-treated conditions is presented in Fig. 3. The typical three regimes of FCGR curve, i.e., near-threshold, linear Paris regime, and high ΔK regime could be observed in both heat treatment samples. The FCGR measured in the RRA-treated alloy is lower when compared to that in the T6-treated alloy at near-threshold and for the major portion of the Paris regime as observed in Fig. 3a. The near-threshold regime of FCGR curve is magnified and shown in Fig. 3b, that highlights the increase in threshold value (ΔK_{th}) in the RRA-treated alloy. The ΔK_{th} observed in RRA- and T6-treated samples are 5.78 MPa$\sqrt{m}$ and 5.13 MPa$\sqrt{m}$ respectively. The material constants C, m, and FCGR at different stress intensity range (ΔK) are tabulated in Table 3.

The near-threshold fatigue crack growth behavior in aluminum alloys is influenced by the microstructures such as grain size, matrix precipitates, and PFZ surrounding the grain boundary precipitates [12]. TEM microstructure of the RRA-treated alloy clearly reveals the growth of the matrix precipitates. The growth
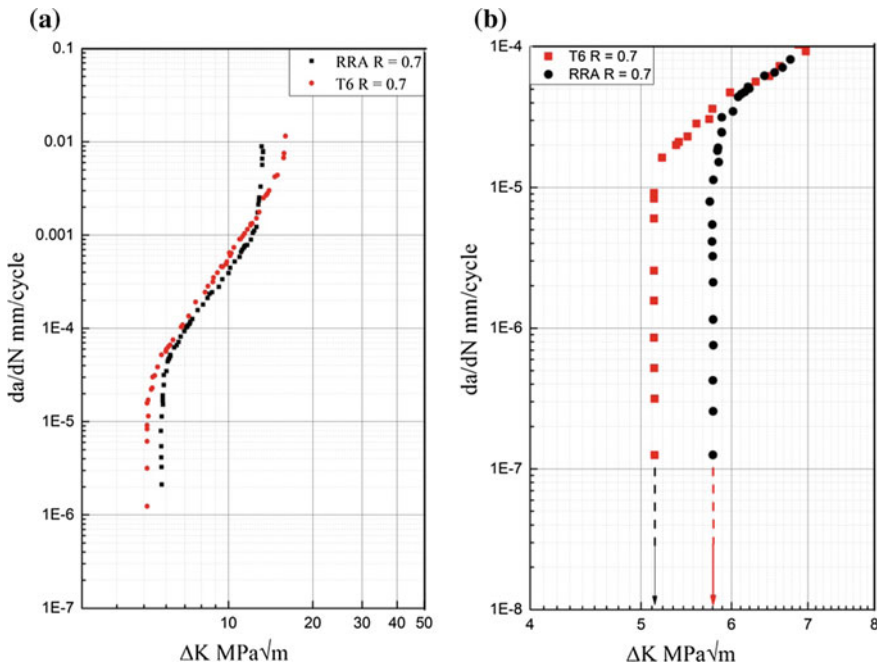
Fig. 3 FCGR curves of theT6- and the RRA-treated AA7010. **a** Complete FCGR curve, **b** Near-threshold regime

Table 3 Material constants C, m, and FCGR, da/dN corresponding to various ΔK levels

Alloy	C	m	da/dN = C(ΔK)^m mm/cycle		
			ΔK = 8 MPa√m	ΔK = 10 MPa√m	ΔK = 12 MPa√m
RRA	4.37×10^{-8}	4.06	1.79×10^{-4}	3.89×10^{-4}	8.91×10^{-4}
T6	2.52×10^{-8}	4.41	2.43×10^{-4}	6.03×10^{-4}	1.32×10^{-3}

of undissolved precipitates during retrogression, nucleation, and growth of the newly formed precipitates during re-aging lead to the increase in interparticle spacing of the matrix precipitates. The interspace between the matrix precipitates are found to be about 3.3 nm in T6 alloy, which is increased to about 6.1 nm in RRA-treated sample. In the near-threshold regime of FCGR, the crack tip plastic zone size is generally small compared to the grain size [16], indicating the average free slipping distance for a dislocation to be small. Hence during cyclic loading, there exists low chance, for a dislocation to interact with precipitates for every cycle, since the particles are way apart in RRA-treated sample compared to T6 alloy [16]. Moreover, during fatigue loading, reversible cyclic slip is promoted at the crack tip; thereby decreasing the damage accumulation per cycle. Unlike RRA, T6-treated alloy with densely populated matrix precipitates promote faster crack growth rate. At high ΔK regime, the plastic zone size at the crack tip is large, microstructural influence on FCGR is nullified, also the fracture toughness of RRA-treated alloy is slightly lower than that of T6, hence the crack growth rate in RRA alloy is higher at high ΔK regime.

The fractography reveals the formation of large facets in RRA-treated sample (Fig. 4d) when compared to smaller facets (Fig. 4a) formed in standard T6-treated alloy observed in the near-threshold fatigue fracture surface, which is similar to the earlier reports [17, 18]. The fracture surfaces in the Paris regime of both T6 and RRA samples exhibited ductile striation patterns as shown in Fig. 4b, e. The width of the striation patterns measured on the fractured surfaces matched quite well with the FCGR data (measured at ΔK = 10 MPa√m). A ductile dimple type (Fig. 4c, f) of fracture is observed at high ΔK regime in both T6- and RRA-treated samples.
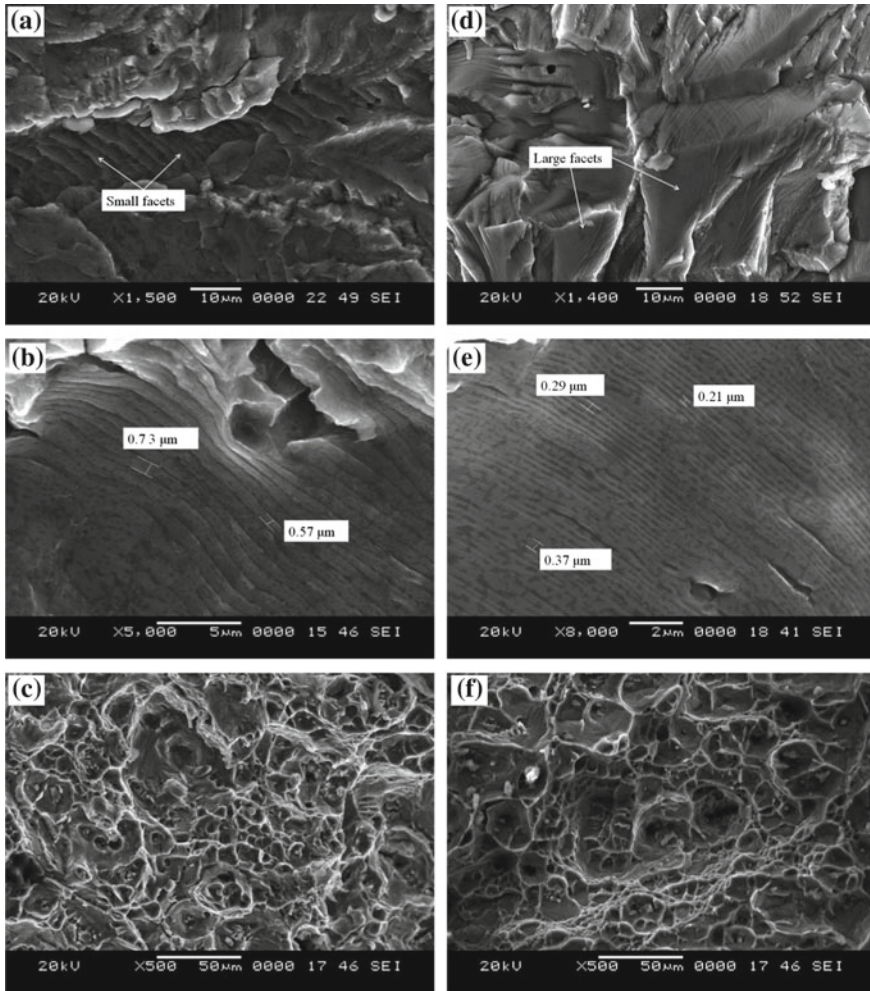
Fig. 4 SEM fractographs of the AA7010, at near-threshold, Paris regime, and final fracture: (**a**, **b**, **c**: T6), (**d**, **e**, **f**: RRA)

4 Conclusions

- RRA treatment with retrogression (200°C, 20 min) on AA7010 imparts equivalent tensile properties as that of the T6-treated sample.
- Decreased fatigue crack growth rate by about 2 times has been observed in RRA-treated alloy compared to that of T6 alloy at near-threshold and a major portion of the Paris regime.

- The microstructural modification during RRA treatment resulted in increased interparticle spacing of matrix precipitates that lead to the decrease in FCGR compared to the T6-treated alloy.

References

1. T. Warner, Recently developed aluminium solutions for aerospace applications. Mater. Sci. Forum **519–521**, 1271–1278 (2006)
2. A. Heinz, A. Haszler, C. Keidel, S. Moldenhauer, R. Benedictus, W.S. Miller, Recent development in aluminium alloys for aerospace applications. Mater. Sci. Eng. A **280**, 102–107 (2000)
3. T. Ram Prabhu, An overview of high-performance aircraft structural al alloy-AA7085, Acta Metall. Sin. **28**, 909–921 (2015)
4. P.A. Rometsch, Y. Zhang, S. Knight, Heat treatment of 7xxx series aluminium alloys - some recent developments. Trans. Nonferrous Metals Soc. China **24**, 2003–2017 (2014)
5. J.C. Williams, E.A. Starke, Progress in structural materials for aerospace systems. Acta Mater. **51**, 5775–5799 (2003)
6. S.J. Findlay, N.D. Harrison, Why aircraft fail. Mater. Today **5**, 18–25 (2002)
7. P.K. Rout, M.M. Ghosh, K.S. Ghosh, Microstructural, mechanical and electrochemical behaviour of a 7017 Al-Zn-Mg alloy of different tempers. Mater. Charact. **104**, 49–60 (2015)
8. X. Fan, D. Jiang, Q. Meng, Z. Lai, X. Zhang, Characterization of precipitation microstructure and properties of 7150 aluminium alloy. Mater. Sci. Eng. A **427**, 130–135 (2006)
9. C. B, Reducing the susceptibility of alloys, particularly aluminium alloys, to stress corrosion cracking, US3856584 A (1974)
10. Y. Xue, H. El Kadiri, M.F. Horstemeyer, J.B. Jordon, H. Weiland, Micromechanisms of multistage fatigue crack growth in a high-strength aluminum alloy. Acta Mater. **55**, 1975–1984 (2007)
11. H. Jian, F. Jiang, L. Wei, X. Zheng, K. Wen, Crystallographic mechanism for crack propagation in the T7451 Al-Zn-Mg-Cu alloy. Mater. Sci. Eng. A **527**, 5879–5882 (2010)
12. M.N. Desmukh, R.K. Pandey, A.K. Mukhopadhyay, Effect of aging treatments on the kinetics of fatigue crack growth in 7010 aluminum alloy. Mater. Sci. Eng. A **435–436**, 318–326 (2006)
13. J. Buha, R.N. Lumley, A.G. Crosky, Secondary ageing in an aluminium alloy 7050. Mater. Sci. Eng. A **492**, 1–10 (2008)
14. M.S. Nandana, K. Udaya Bhat, C.M. Manjunatha, Effect of retrogression heat treatment time on microstructure and mechanical properties of AA7010. J. Mater. Eng. Perform. **27**, 1628–1634 (2018)
15. X. Chen, Z. Liu, P. Xia, A. Ning, S. Zeng, Transition of crack propagation from a transgranular to an intergranular path in an overaged Al-Zn-Mg-Cu alloy during cyclic loading. Met. Mater. Int. **19**, 197–203 (2013)
16. P. Xia, Z. Liu, S. Bai, L. Lu, L. Gao, Enhanced fatigue crack propagation resistance in a superhigh strength Al–Zn–Mg–Cu alloy by modifying RRA treatment. Mater. Charact. **118**, 438–445 (2016)

17. V.K. Gupta, S.R. Agnew, Fatigue crack surface crystallography near crack initiating particle clusters in precipitation hardened legacy and modern Al–Zn–Mg–Cu alloys. Int. J. Fatigue **33**, 1159–1174 (2011)
18. Y.L. Wang, Q.L. Pan, L.L. Wei, B. Li, Y. Wang, Effect of retrogression and reaging treatment on the microstructure and fatigue crack growth behavior of 7050 aluminum alloy thick plate. Mater. Des. **55**, 857–863 (2014)

Rate Dependence of Dynamic Fracture Toughness of 20MnMoNi55 Low-Carbon Steel Using Two Methods on Instrumented Drop Weight Test of PCVN

Swagatam Paul, Sanjib Acharyya, Prasanta Sahoo and Jayanta Chattopadhyay

Abstract Earlier Charpy V-notch (CVN) specimens were used to determine the nil ductility temperature (NDT) with the help of the impact test. NDT is the measure of embrittlement of material at temperature scale. CVN energy is gross energy supplied to the specimen which includes fracture energy, energy loss due to friction and inertia. So, CVN energy is not a proper characterization of fracture behavior. Thus, the determination of fracture toughness is required. Fracture toughness can be evaluated from quasi-static loading as well as dynamic loading conditions. Fatigue pre-cracked Charpy V-notch (PCVN) specimens are used to find dynamic fracture toughness. Dynamic fracture mechanics differs from quasi-static fracture mechanics in three complex features: rate-dependent material properties, the effect of inertia and reflected stress wave. To overcome the effect of inertia and stress waves, the evaluation of dynamic fracture toughness needs some special technique. In this study, two different methods are used to evaluate the dynamic fracture toughness, one is impact response curve method and another is the J-integral method. For impact response curve method, there is no time constraint present at calculation process but for the J-integral method, there is some condition regarding fracture time to be satisfied to get the valid dynamic fracture toughness data. In this work, Pre-cracked Charpy V-notch (PCVN) specimens of 20MnMoNi55 low-carbon reactor pressure vessel steel are used for impact testing in Pendulum testing machine and Drop weight machine for 7 different velocities ranging from 1 m/s to 9 m/s at cryogenic temperature (−70 °C). Calibration between the test results from the impact test on pendulum type and Drop weight test is done and found to be matching. Dynamic fracture toughness at each velocity is evaluated and compared using two different methods namely impact response curve method and J-integral

S. Paul (✉) · S. Acharyya · P. Sahoo
Department of Mechanical Engineering, Jadavpur University, Kolkata 700032, India
e-mail: kgec.swagy@gmail.com

J. Chattopadhyay
Bhaba Atomic Research Centre, Mumbai 400085, India

method. Based on the results found, it is observed that two methods yield the same results if the time constraint referred is maintained for J-integral method.

Keywords Dynamic fracture toughness · Impact testing · RPV steel

1 Introduction

In a nuclear power plant, high neutron irradiation causes material embrittlement. Material loses its ductility and becomes brittle. The service life of critical components degrades rapidly, so, frequent inspection and maintenance of reactor pressure vessel (RPV) components is highly required. This type of embrittlement phenomenon can also be found in steel in sub-zero temperature. Steel loses its ductility with the decreasing temperature and becomes completely brittle below a certain sub-zero temperature, similarly above certain temperature steel shows completely ductile nature. But in ductile to brittle transition (DBT) zone fracture toughness of steel is scatter and probabilistic [1]. Earlier days simple Charpy v-notch (CVN) impact tests were done in different temperatures to find out the nil ductility temperature (NDT). NDT is the temperature where steel loses its ductility and becomes fully brittle. But NDT was not sufficient to characterize the scatter of DBT zone. Wallin [2] proposed a methodology based on three-parameter Weibull distribution to capture this scatter and probabilistic nature of DBT zone. This curve is called master curve which can be characterized by a single parameter named reference temperature (T_0). Basically, the master curve is the same for all ferritic steel and T_0 is the measure of embrittlement. T_0 is dependent on several factors like geometry, crack length, and loading rate [3]. Loading rate can be categorized into three different ranges, (1) Quasi-static, (2) Dynamic, (3) Impact. Up to 1–2 MPa$\sqrt{m}$/s the loading range is considered as quasi-static range, above 2 MPa$\sqrt{m}$/s the loading rate is dynamic range and above 10^5 MPa$\sqrt{m}$/s loading rate is considered as impact range. In this study, the main focus of the work is given on the evaluation process of dynamic fracture toughness from instrumented Charpy impact experiment results. Basically, the difference between quasi-static fracture mechanics and dynamic fracture mechanics is based on three major factors like (1) inertia effect, (2) rate-dependent material property, (3) propagation of stress wave [4]. So, evaluation of dynamic fracture toughness from impact testing requires some precise measurement techniques, advanced data acquisition process.

In literature, there are several techniques available to find out dynamic fracture toughness [5]. Some of them are based on experimental work like optical methods [6], electrical strain gauge method [7], and numerical methods like finite element analysis [8]. Several researchers proposed some cracked beam theory and vibration models [9] to the analysis of dynamic response curve. Dynamic response curves obtained from the instrumented impact test are of four types in nature, depending upon the fracture mechanism. Type I and II curves do not exhibit any general yield point on the load–displacement curve and the fracture process is unstable but type III

and IV show a stable crack growth after general yielding. Calculation methods for determining dynamic fracture toughness are different for four types of curves. In this study, two different techniques are used to evaluate dynamic fracture toughness from instrumented drop weight results. The techniques are (1) Impact response curve method (2) J-integral method. For impact response curve method, dynamic fracture toughness is calculated from machine compliance (C_m) and fracture time (t_f) whereas for J-integral method dynamic fracture toughness is calculated from fracture load (P_f) when the fracture occurs before general yielding. Impact response curve is a curve where pre-experimented dynamic stress intensity factor is plotted with time for ferritic steel of the same class. From the experiment, only fracture time is required and at the time of fracture, corresponding dynamic stress intensity factor is taken as a measure of dynamic fracture toughness for the tested material. But in the J-integral method, there is a validity criterion regarding fracture time. When the fracture occurs before a certain time, it can be said that the effect of inertia plays a crucial role and the energy which is measured from load–displacement curve is more than the energy required to fracture of the specimen. In Impact response curve there is no such validity criterion for fracture time. All the experiments are done at −70 °C temperature for 20MnMoNi55 RPV steel and the obtained load–displacement curves are type I curve. Experiments are done in two different machines. In the pendulum impact machine, the range of impact velocity is 1–5 m/s and for drop weight testing, machine impact velocities are 7 m/s and 9 m/s. Before going to do the experiments at −70 °C, calibration of two different test results is done at room temperature values. Both the results from two different methods are compared with the help of correlation coefficient study.

2 Experimental

The experimentation part consists of two steps, (1) fatigue pre-cracking of Charpy specimen (2) instrumented impact testing of pre-cracked Charpy specimen. Fatigue pre-cracking is done according to ASTM E647 and Impact testing is done according to ASTM E23. Impact testing is done in two different machines, (1) Pendulum-type Charpy impact machine (1–5 m/s) and (2) Drop weight machine (7 m/s and 9 m/s), because, in pendulum-type impact machine, maximum 5 m/s impact velocity can be achieved, for higher velocity, spring loaded drop weight machine is required. To calibrate results from both the machines, one set of experiments are done in five different impact velocities (1 m/s–5 m/s) at room temperature and compared for peak load, energy, and fracture time. All the impact testing is performed at −70 °C temperature. To achieve −70 °C temperature, liquid nitrogen is used during the test. The temperature soaking time is kept on an average of 15 min for each testing. Specimen dimension, picture of pendulum impact testing machine and drop weight machine (CEAST 9350 INSTRON) are shown in Figs. 1, 2, and 3, respectively.

Fig. 1 Charpy notch
Specimen Geometry
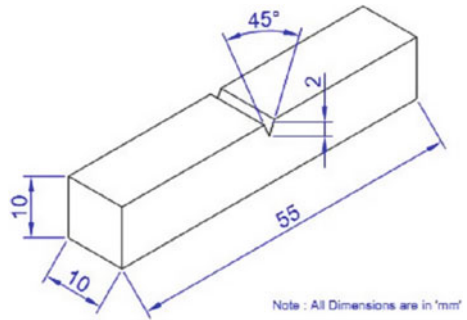
Fig. 2 Pendulum impact
testing machine
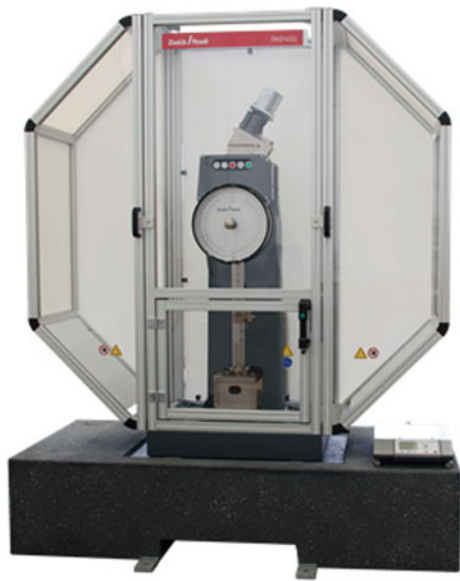
3 Fracture Toughness Evaluation

From instrumented Charpy impact tests, four types of load response curves can be found [10]. In Fig. 4, four types of load response curves are shown. Displacement is linearly proportional to the time because striking velocity is kept constant. In Fig. 3, type I and Type II curves have no general yielding point. The fracture occurs suddenly after reaching the maximum load. This type of fracture process has no stable crack growth. But in Type III and Type IV curves, stable crack growth is visible.

In this study, two different procedures are followed to evaluate the dynamic fracture toughness (K_{ID}). First one is the J-integral method and the second is impact

Fig. 3 Drop weight machine
(Instron Ceast 9350)

response curve method. Both methods have some advantages and disadvantages. A detailed procedure of two methods is discussed below.

3.1 J-Integral Method

In quasi-static fracture process, the inertia effect is neglected. But at higher loading rate, effect of inertia is a crucial factor and should be treated carefully. Before going to calculate dynamic fracture toughness with J-integral approach, it is necessary to check whether inertial oscillation is sufficiently damped or not. The time period of inertial oscillation of specimen is given by Ireland [11] in the following Eq. (1):

$$\tau = \frac{1.68(SBWC_sE)^{1/2}}{v_s} \tag{1}$$

where

S   = Span of support (40 mm)
B   = Thickness of specimen (10 mm)
W   = Width of specimen (10 mm)
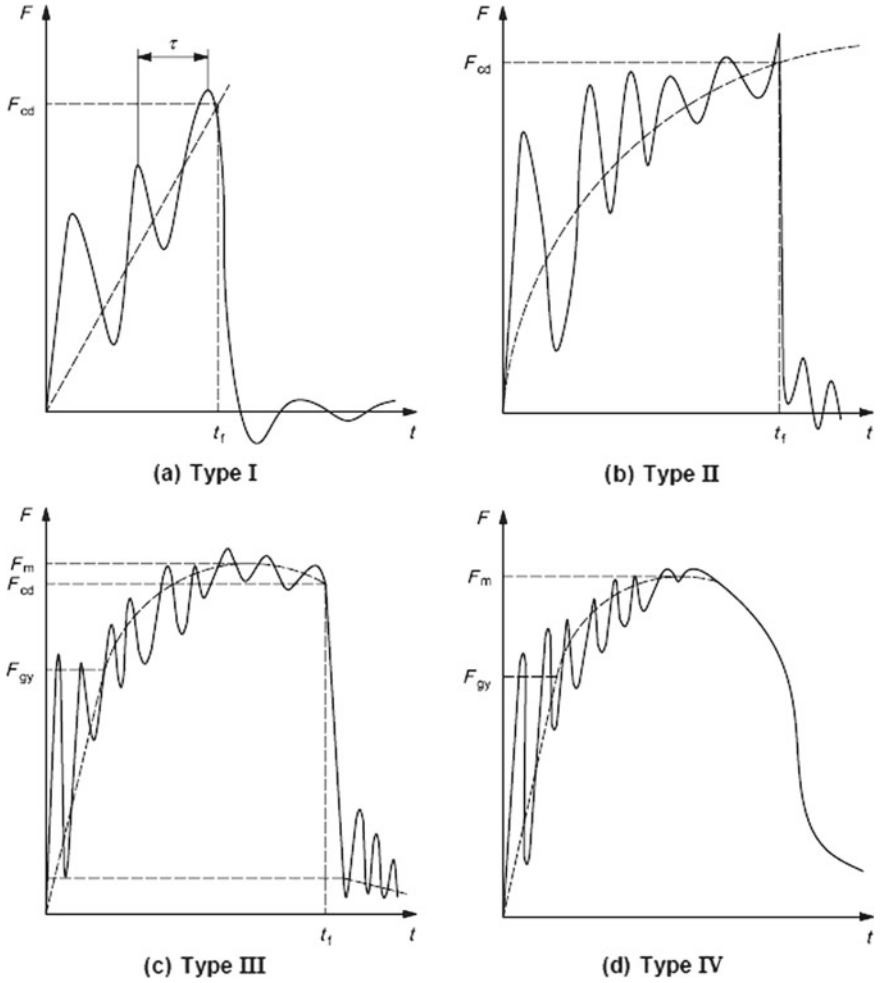
Fig. 4 Types of response curve obtained from Charpy Impact testing

C_s = Specimen compliance
E   = Young's modulus (210GPa)
v_s = Speed of sound wave steel (5000 m/s for steel)

$$C_s = \frac{S^3}{4EBW^3}\left[1 + 2.85\left(\frac{W}{S}\right)^2 - 0.84\left(\frac{W}{S}\right)^3\right] \qquad (2)$$

The condition for sufficient damping of inertial oscillation is $t_f \geq 3\tau$, where t_f is fracture time. If this condition is satisfied, dynamic fracture toughness can be

evaluated from the following equations. Equation (3) is used when fracture occurs before general yielding. It is a linear elastic fracture toughness.

$$K_{ID} = \frac{P_f S}{BW^{3/2}} f\left(\frac{a}{W}\right) \tag{3}$$

where

P_f = fracture load
a = initial crack length

$$f\left(\frac{a}{W}\right) = \frac{3\sqrt{\frac{a}{W}}}{2\left(1+2\frac{a}{W}\right)} \frac{1.99 - \left(\frac{a}{W}\right)\left(1-\frac{a}{W}\right)\left[2.15 - 3.93\left(\frac{a}{W}\right) + 2.7\left(\frac{a}{W}\right)^2\right]}{\left(1-\frac{a}{W}\right)^{3/2}} \tag{4}$$

When a prominent stable crack growth is visible in load response curve and fracture occurs after general yielding, elastic–plastic fracture toughness is evaluated in terms of J-integral following Eq. (5)

$$J_{ID} = J_e + J_P \tag{5}$$

where

$$J_e = \frac{K_e^2}{E'} \tag{6}$$

K_e is an elastic component which is calculated from Eq. (3), E' = E/(1-v²), plain strain Young's modulus. Plastic component of J is given by

$$J_P = \frac{2A_p}{B(W-a)} \tag{7}$$

where

A_p = Plastic area under the load–displacement curve

$$A_p = A_{total} - \frac{1}{2} C P_f^2 \tag{8}$$

C   = Reciprocal of initial elastic slope
A_{total} = Total area under the load–displacement curve

3.2 Impact Response Curve Method

Impact response curve is a relationship curve of dynamic stress intensity factor (K_I^{dyn}) and response time (t) for a certain class of material, e.g., steels. This K_I^{dyn} is determined from the shadow optical caustic method [12]. Pre-experimental K_I^{dyn} is plotted with the time (t) for a fixed test conditions (i.e., specimen geometry, hammer mass, impact velocity, etc.) and at the time of fracture (t_f), the corresponding value of K_I^{dyn} represents the value of dynamic fracture toughness (K_{ID} (t_f)). The K_I^{dyn} can be calculated from the following Eq. (9).

$$K_I^{dyn} = Rvt''$$ (9)

where

R   = constant (301 GN/m$^{5/2}$)

$t'' = f(t')$ Correction factor is given in Table 1, t' can be calculated using Eq. (10)

Table 1 Correction factor for determination of K_I^{dyn}

t' μs	$t'' = f(t')$ μs	t' μs	$t'' = f(t')$ μs	t' μs	$t'' = f(t')$ μs
0	0	40	45	80	69
2	0	42	46	82	70
4	2	44	47	84	75
6	4	46	46	86	81
8	6	48	45	88	88
10	0	50	45	90	94
12	13	52	46	9	100
14	17	54	49	94	106
16	20	56	53	96	111
18	24	58	57	98	116
20	28	60	61	100	118
22	30	62	65	102	119
24	33	64	69	104	118
26	35	66	72	106	117
28	36	68	73	108	115
30	38	70	73	110	115
32	39	72	72		
34	40	74	70		
36	42	76	69		
38	43	78	68		

$$t' = t_f \left[1 - 0.62 \left(\frac{a}{W} - 0.5 \right) + 4.8 \left(\frac{a}{W} - 0.5 \right)^2 \right] \tag{10}$$

t_f = measured physical fracture time
t' = modified time which compensates initial crack length in the range of $0.45 < \frac{a}{W} < 0.55$

The correction factor (t'') is less than 5% for $t' > 110\,\mu s$, thus when t' appears greater than 110 μs $t'' = t'$

The value of R is dependent on machine compliance (C_m). C_m can be calculated from following Eq. (11)

$$C_m = \frac{2E_p}{P_f^2} - C_s \tag{11}$$

E_p = Energy at fracture load (Pf).

The equivalent R for the specific machine can be evaluated by the given in Eq. (12)

$$Req = R \frac{1.276}{\left(1 + 0.276 \frac{C_m}{8.1*10^{-9}}\right)} \tag{12}$$

4   Results and Discussion

At room temperature, Charpy impact testing is conducted in two different machines at five different impact velocities (1 m/s to 5 m/s). Obtained values of peak load, energy, and fracture time in different impact velocities from two different machine data are compared in Table 2. From Table 2, it can be seen that peak load, energy, and fracture time results from pendulum impact testing (PCM) and drop weight testing machine (DWM) are closely matching to each other.

Dynamic fracture toughness is calculated from two different methods and some sample toughness results are given in Table 3, Figs. 5 and 6. From the results, it is evident that the dynamic fracture toughness increases with increasing impact velocity.

It is seen in Figs. 5 and 6, the value of dynamic fracture toughness is increasing with the increasing velocity. There is a scattered nature found in dynamic fracture toughness at a fixed impact velocity.

Correlation study is done for two different methods at different velocities within two sets of evaluated dynamic fracture toughness using Pearson's correlation

Table 2 Peak load, total energy, fracture time data from two different machines at room temperature in different impact velocities

Impact velocity (m/s)	Peak load (kN)		Total energy (J)		Fracture time (ms)	
	PCM	DWM	PCM	DWM	PCM	DWM
1	6.246	5.831	11.893	12.192	2.5	2.62
2	6.009	6.652	46.993	50.728	1.07	1.88
3	6.882	6.197	66.740	66.023	0.81	0.16
4	6.701	6.171	52.866	61.392	0.64	0.64
5	6.784	6.085	67.519	64.475	0.49	0.60

Table 3 Dynamic fracture toughness from two different methods with variation of impact velocity

a/w	Velocity (m/s)	Fracture time(μs)	Time for inertial damping 3τ (μs)	Load (P_f) (kN)	f(a/w)	t'' (μs)	J-Integral $K_{ID}(P_f)$ (MPa√m)	Impact response curve method $K_{ID}(t_f)$(MPa√m)
0.5	1	235	87	4.551	2.6625	235	48.462	42.515
0.5		310	87	3.779	2.6625	310	40.247	46.645
0.5		185	87	4.401	2.6625	185	46.871	35.308
0.5	2	155	87	3.622	2.6625	155	38.5827	30.672
0.5		130	87	3.915	2.6625	130	41.695	41.449
0.5		110	87	3.752	2.6625	115	39.966	35.516
0.5	3	105	87	4.579	2.6625	117.5	48.776	49.352
0.5		110	87	4.462	2.6625	115	47.522	41.023
0.5		100	87	4.471	2.6625	118	47.623	39.739
0.5	4	60	87	5.422	2.6625	61	57.754	44.695
0.5		60	87	4.923	2.6625	61	52.436	41.331
0.5		70	87	4.846	2.6625	73	51.616	48.106
0.5	5	60	87	5.982	2.6625	61	63.711	51.141
0.5		65	87	5.819	2.6625	70.5	61.982	48.968
0.5		70	87	6.273	2.6625	73	66.809	58.213
0.5	7	50	87	6.124	2.6625	45	65.221	42.683
0.5		200	87	3.869	2.6625	200	41.207	52.494
0.5		50	87	5.542	2.6625	45	59.029	40.657
0.5	9	20	87	7.109	2.6625	28	75.721	62.788
0.5		40	87	6.968	2.6625	45	74.211	67.496
0.5		40	87	7.493	2.6625	45	79.806	64.157

coefficient (r) formula (given in Table 5). The formula is given in Eq. 13 and a sample data set to study of correlation coefficient between two different methods for 1 m/s velocity is given in Table 4.

Fig. 5 Dynamic fracture toughness from the maximum load (P_f) with different impact velocity
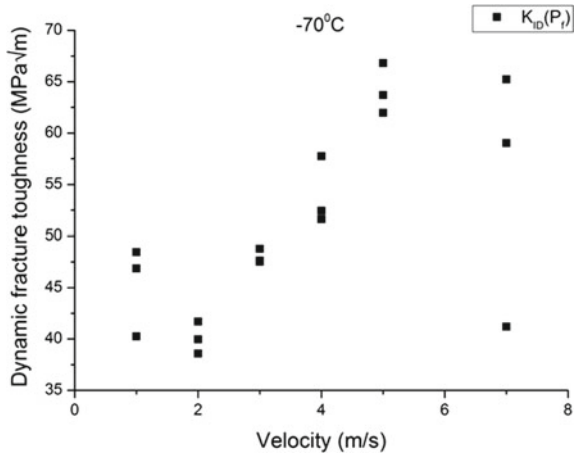
Fig. 6 Dynamic fracture toughness from impact response curve with different velocity
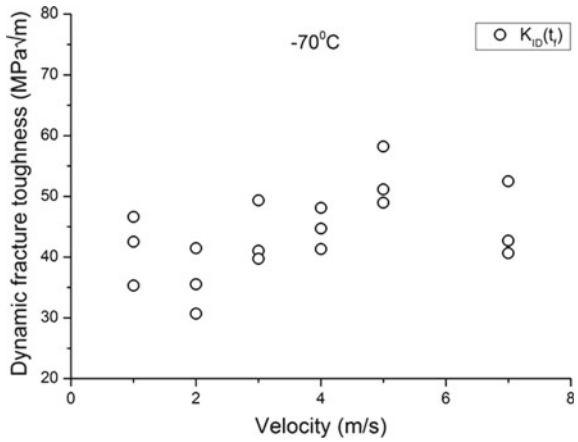
Table 4 Correlation study between two methods for 1 m/s impact velocity

Impact velocity (m/s)	x (MPa√m)	y (MPa√m)	r
1	56.044	45.79891	0.7029
	48.462	42.51566	
	32.814	26.44226	
	40.247	46.64591	
	46.87	35.30897	
	42.201	33.14874	
	36.612	32.03368	

Table 5 Correlation study between two methods for different impact velocity

Impact velocity (m/s)	1	2	3	4	5	7	9
r	0.7029	0.9291	0.8073	0.3314	0.5864	0.6436	0.4853

$$r = \frac{n(\sum xy) - (\sum x)(\sum y)}{\sqrt{\left[n\sum x^2 - (\sum x)^2\right]\left[n\sum y^2 - (\sum y)^2\right]}} \qquad (13)$$

where

r   = Correlation coefficient
n   = Number of samples
x   = Fracture toughness results from the J-integral method
y   = Fracture toughness results from impact response curve method.

5   Conclusions

In Figs. 5 and 6, it is showing that evaluated dynamic fracture toughness values are scattered in nature, because at −70 °C temperature 20MnMoNi55 steel is in ductile to brittle transition zone.

For J-integral method, the validity criteria for the dynamic fracture toughness are that, the fracture time (t_f) should be thrice greater than the time required for sufficient damping of the inertial oscillation (3τ). But for the impact response curve method, there is no such criterion present. So, in Table 5, it is seen where the fracture time is not greater than 3τ, the value of the correlation coefficient between the two methods is low. With the increase of striking velocity, the effect of inertia gets increased. Effect of inertia has not been accounted for in the J-integral method, but in Impact response curve method there is no need for inertia correction. So, the mismatch in fracture toughness results between two different methods is obvious and hence the correlation coefficient is much lower in higher impact velocity. Impact response curve method has one disadvantage that, it is applicable only for small-scale yielding, no large plastic deformation at the crack tip is allowed for this method. Since, at −70 °C temperature, all the obtained load–displacement curves are type I in nature and there is no stable crack growth present, thus impact response curve method is more appropriate than J-Integral method for our study.

References

1. S.H. Kim, Y.W Park,, J.H. Lee, S.S. Kang., *15th International Conference on Structural Mechanics in Reactor Technology* (SMiRT 15), Seoul, Korea (1999), pp. 15–20
2. K. Wallin, Eng. Fract. Mech. **69**, 451–481 (2002)
3. International Atomic Energy Agency, IAEA-TECDOC-1631, Vienna (2009)
4. L.B. Freund, *Dynamic Fracture Mechanics* (Cambridge University Press, Cambridge 1990)
5. F. Jiang, A. Rohatgi, K.S. Vecchio, J.L. Cheney, Int. J. Fract. **127**, 147–165 (2004)
6. J.W. Dally, D.B. Barker, Exp. Mech. **28**, 298–303 (1988)
7. J.W. Dally, R.J. Sanford, Exp. Mech. **27**, 381–388 (1987)
8. W.G. Guo, Y.L. Li, Y.Y. Liu, *Theor. Appl. Fract.* **26**, 29–34 (1997)
9. G.E. Nash, *Int. J. Fract. Mech*. **5**, 269–286 (1969)
10. International Standard ISO/FDIS 26843, (2009)
11. D.R. Ireland, Comments on EPRI instrumented impact procedures. Technical Report TR-75–37 (EPRI Fracture Toughness Program Information Meeting 1975)
12. J.F. Kalthoff, Int. J. Fract. **27**, 277–298 (1985)

Part X
Experimental Mechanics

Hardened Materials Material Deformation Study Using Digital Image Correlation Technique for Nuclear Power Plant Applications

S. Babu, S. Veeraragavan and T. Ramesh

Abstract This paper investigates the results of tensile tests to estimate the mechanical properties of the hardened work material. The proposed Digital Image Correlation (DIC) technique has been applied to estimate the mechanical properties of hardened bearing steels (AISI 52100, AISI 4140) that is used in the slewing ring for special applications in nuclear reactors, cranes, excavators, wind turbines, etc. Through this non-contact technique estimation of the mechanical properties in both elastic and plastic regions with significant strains becomes comparatively easy with tensile testing. Tensile tests have been conducted for each specimen of hardness (HRC) 50 and 60. Based on the results, Engineering sample Stress–Strain curves are plotted for hardened steel specimens. Then these results are used for the design and the development of large diameter slewing bearing in the fuel handling unit for fast breeder reactor because through DIC technique accuracy of strain rate value gets increased in comparison to UTM results. The scope of the research is to study the contact stress, load versus deformation curves, temperature distribution, and any FEM analysis for higher accuracy.

Keywords Digital image correlation · High-strength steel · Stress–strain curve

S. Babu (✉) · S. Veeraragavan
Department of Mechanical Engineering, PSG College of Technology,
Coimbatore 641004, Tamilnadu, India
e-mail: sjsham@gmail.com

S. Veeraragavan
e-mail: veeraragavan1020@gmail.com

T. Ramesh
Department of Civil Engineering, PSG College of Technology, Coimbatore 641004,
Tamilnadu, India

1 Introduction

In hardened material, stress–strain curve is an extremely essential graphical measurement in both materials of En19 and En31 for defining their mechanical properties. The hardness value is the prevailing parameter of mechanical properties of these materials compared to the strain rate effect. In high strain-rate of tension tests, the necking seems to be a function of the loading rate [1]. Tarigopula et al.'s [2] study stated that high rates of strain using digital image correlation can be measured through the strain localization in the tensile specimens. During non-uniform deformation of the gauge, this technique is able to obtain the in-plane displacement, strain fields sections and accordingly, the strains associated with diffused and localized necking may also be estimated. Chu et al. [3] presented a digital image processing approach with a unique hive triangle pattern for non-contact measurement of structural dynamic response data by integrating sub-pixel analysis. Feasibility of the suggested approach is established based on the numerical simulation of a photography investigation. According to these final results, the numerical solution associates nicely with the measured values of the displacement of the simulated image.

In bearing steel combination of AISI 4140–AISI 52100, AISI 4140 thermal contact resistance values increased notably with a surface roughness of the material due to three-layer combinations, which result in heat dissipation to the atmosphere. So experimental methodology of the material behaviour and the deformation characteristics to elevated temperatures is the inevitable parameter in design with AISI 4140, 52100 hardened materials [4, 5].

This survey shows that no one has measured strain localization and deformation of hardened bearing at heavy loading condition in comparison with DIC approach. Owing to the fact that strain maps are important for performing new investigations with digital image correlation, which provides a contour map of strains of a complete specimen surface subject which is being subjected to mechanical tests. This paper focuses on the AISI 52100, AISI 4140 (bearing steel), which is widely used in engineering applications and to develop a systematic, reliable, and productive approach to obtain material properties of AISI 52100, 4140 steel by using non-contact technique DIC successfully.

2 Digital Image Correlation Technique

Digital image correlation has become a widespread approach for measurements related to solid mechanics. DIC is a simple and cost-effective method because it takes advantage of the natural speckle pattern which sprays over the specimen-surface and Charge Coupled Device (CCD) camera are to be used to capture and process the digital images taken by them. DIC method is used to measure the deformation or principal strain during the compression and tensile testing. Bearing ball with the stochastic pattern, photogrammetric principle and Systematic DIC apparatus setup are shown in Fig. 1.
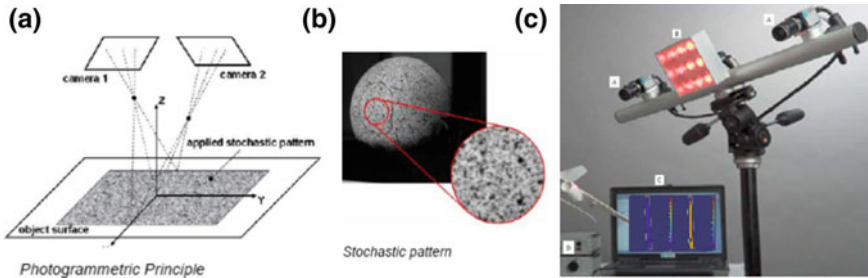
Fig. 1 **a** Photogrammetric principle, **b** Steel balls with a stochastic pattern and **c** Systematic DIC apparatus setup-(A-CCD camera, B-Calibrating High beam light, C-System Monitor and D-Data logger)

2.1 Displacement and Strain Measurements

To estimate the displaced field on the specimen-surface of the deformed image with respect to a reference image, the region of interest (ROI) is divided into a many numbers of sub-images and each sub-image is referred to as a zone of interest (ZOI). In this procedure of diagnosing displacements, the correlation principle helps to compare the ZOI in both images. The methodology compares the gray value pattern in small sub-images and attempts to develop a correlation value using standard procedures of cross-correlation algorithm [3], and that estimated value indicates the level of resemblance between the reference image and the deformed sub-images. Challenging is the precise matching of zones of interest (ZOI) which is essential for a good assessment of the movement prior to further improvements. To measure large displacements and strains, coarse-graining technique [6] is used to get an assessment of displacements. As a concern, the core centres of the ZOI in the deformed object surface are relocated by the preliminary valuations and then additional cross-correlation is executed to obtain estimations for sub-pixel displacements. At this time, a methodology is used for investigating any two selected images captured at different loading stages to estimate displacement fields. [3] Small subset on the object which is centred and named as P before deformation, after deformation new point P* arises by displacement of the subset both points are shown in Fig. 2.

The displacement zone on the specimen is decomposed into continuous determinate elements so that the measured displacement field is consistent with FE analysis computations. For equal distribution and division, apt to choose either a rectangular or square shape for each element since the image is divided into pixels, which leads to choosing linear shape functions. Because of this interaction, numerical modelling is used between the measurement of the displacement field by the correlation method and the predicted displacement field. Finally, if necessary, the sub pixel/sub image displacement is obtained using the modulation properties of the Fourier Transforms.
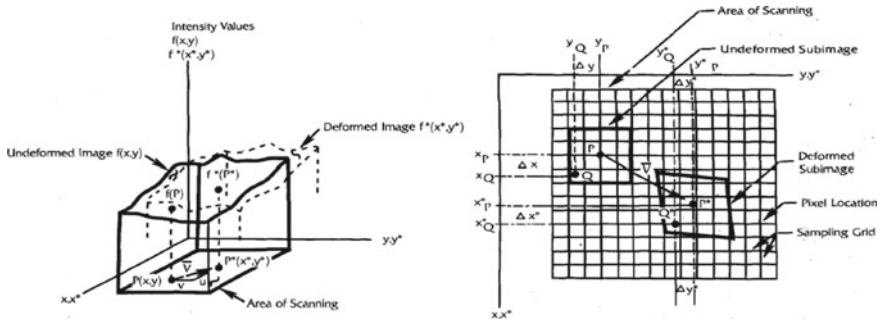
Fig. 2 Distortion of subset image and deformation of a sub-image in a sampling grid [3]

In hardened bearing, localized strain rate and raceway relative approach on steel ball are done already using the DIC technique and is a comparatively effective approach than LVDT and screw gauge measurements by which the localized deformation value of steel ball can be evaluated by simply extrapolating the data from this approach [7].

Displacements Assumptions: Assumptions should be considered when using DIC digital image processing: First, assume that the out-of-plane displacement does not influence the in-plane deformation; Second, the gradients of the out-of-plane displacement are assumed to be negligible when compared with the gradients of the in-plane displacements; Third, the effect of the out-of-plane displacements on the in-plane deformations of the ROI is assumed to be negligible.

3 Experimental

Generally, material properties in the elastic and plastic regions can be predicted from tension or compression tests under room temperatures. In our case tensile test is suitable, so for each of the 5 specimens for AISI4140, AISI52100 with and without hardened materials-totally 20 prepared and tensile experiments are conducted in which threaded, unthreaded and knurled sample specimens are used as shown in Fig. 3.

The annealed 15 mm diameter AISI 52100, AISI 4140 steel bar were machined into tensile specimens 5 mm diameter and 70 mm long and also verify the AISI 52100, AISI 4140 steel chemical composition as per in Tables 1 and 2. The measured hardness of the specimen is 62 ± 2 HRC. The specimens were cleaned gently using the sandpaper after heat treating. To ensure that specimens had the design hardness, the hardness of the specimen was rechecked after cleaning. At room and low temperatures, the hardened 52100 steel $\sim 62 \pm 1$HRC is brittle in nature; fracture resulting from surface cracks in tensile testing may create difficulty in determining the strain gauge location and also affects the testing results. The impending surface cracks
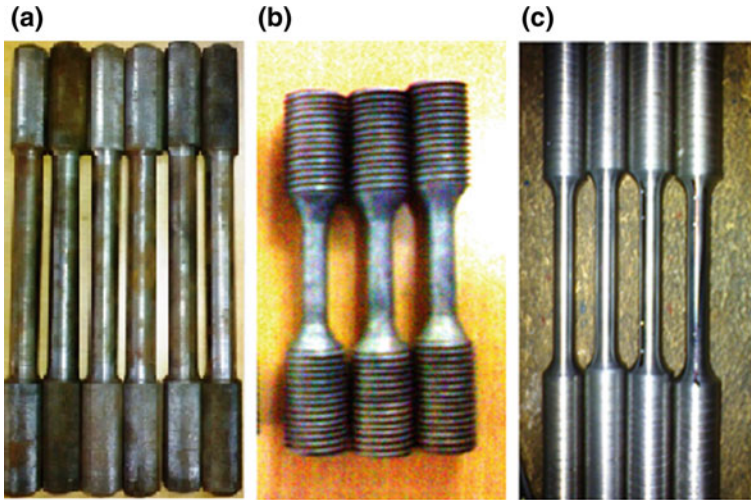
Fig. 3 Tensile specimen: **a** Knurled, **b** Threaded, and **c** Unthreaded

Table 1 Chemical Composition of AISI 4140 steel

C	Si	Mn	P_{max}	S_{max}	Cr	Mo
0.38–0.45%	0.1–0.40%	0.6–0.9%	0.015 max	0.015 max	0.9–1.20%	0.15–0.90%

Table 2 Chemical composition of AISI 52100 Steel

C	Si	Mn	P_{max}	Cr	S
0.98–1.10%	0.15–0.35%	0.25–0.45%	0.015%	1.30–1.60%	0.015 max

were minimized by gentle grinding, polishing and cleaning after heat treatment to attain a high surface finish maintained as per ISO 1608. In addition to forming a stochastic pattern the surfaces were sprayed with a white base colour and spattered with black colour on the top like shown in the Fig. 1b and CAD modelling along with dimensions of the specimen is shown in Fig. 4.

After the threaded ends of the specimens were fixed tightly with holder (Specimen needs a separate fixture to avoid slipping from UTM holder because of the holder hardness is close to tensile specimen hardness) and a tensile test was conducted based on ASTM (E4). The stepped diameter design was preferred for limiting stressful location and reducing the fracture load of the specimen. A curvature at the diameter reduction provides smooth size transition instead of sharp ends. Burrs were removed and sharp edges of the specimen were chamfered. These standard specifications of the specimen should reduce stress concentrations in the tensile testing specimen. As the material is brittle, minimizing surface cracks and stress concentration on the specimen surface was essential for successful tensile
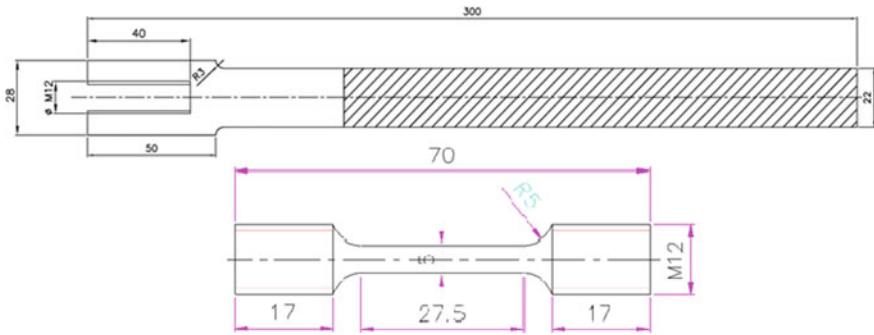
Fig. 4 CAD modelling of the specimen

testing at room temperature. In addition, straightness and roundness were also quantified to reduce the bending effects during tensile testing. Before loading, the calibration plate was used as a reference image and this image was taken with a distance of 320 mm between the specimen and the camera lens. As per the application of specimen size, lighting effect and location of calibration plate, focal length could be varied. Then, three tensile tests at each hardened and unhardened material were conducted to decrease the experimental miscalculations.

Figure 5 shows the experimental setup at room temperatures, which are recorded and controlled with the help of a digital load cell, an extensometer and these signals with data were provided for PC-based data sampling and investigation unit. To ensure lateral rigidity, the system should have a sliding plate and the sample is fixed so that the backlash effect is successfully eliminated. The Load was applied through UTM and for each and every ladder of the loading condition; high-quality cameras were used to take images of the specimen while loading and this image is correlated with the previous image as well as a reference image to estimate the displacement field.

Fig. 5 Experimental setup of UTM &tested specimen

4 Results and Discussion

The test was conducted by UTM (extensometer); DIC techniques and results were compared. The test was repeated three times and it was found that data of engineering stress–strain of AISI 4140 specimens 58 ± 1 HRC has a very minimal deviation at each testing which represents that the testing outcomes have good repeatability. No necking was detected in atmospheric temperature during the tensile tests. The diameter deviation before and after testing is negligible. In atmospheric temperature condition, the result shows that AISI 4140 steel 58 ± 1 HRC is brittle in nature. DIC technique is not supported to measure mechanical properties under elevated temperature condition because the high-quality cameras cannot focus on the specimen. The yield stress and strain analogous to the point on the curve that deviates from the straight line would be found from Fig. 6. Though stress at 0.2% offset strain was not taken as the yield stress and strain for the material under atmospheric temperature as the definition is applicable for ductile materials because at atmospheric temperature there is slight deformation before breakage in a very short time that the plastic deformation cannot be witnessed under a microscope. By UTM experiment, stress was found to be 887.77 N/mm^2, strain percentage was 1.025 from the results, that are shown in Figs. 6 and 7, the maximum elongation is 0.02 mm with respect to 10.96 kN load and this elongation value significantly matches with DIC results as shown in Fig. 7 wherein the round mark gives the extensometer impression, so DIC cameras do not capture that portion.

During UTM testing of the unthreading specimen, the results are deviated up to 18 ± 2% due to slip occurence between the extensometer holders. Even though threaded specimens were held tightly with extensometer, the results had varied up to 8 ± 2% because of stability and tolerance of UTM and their jaws of the testing machine.
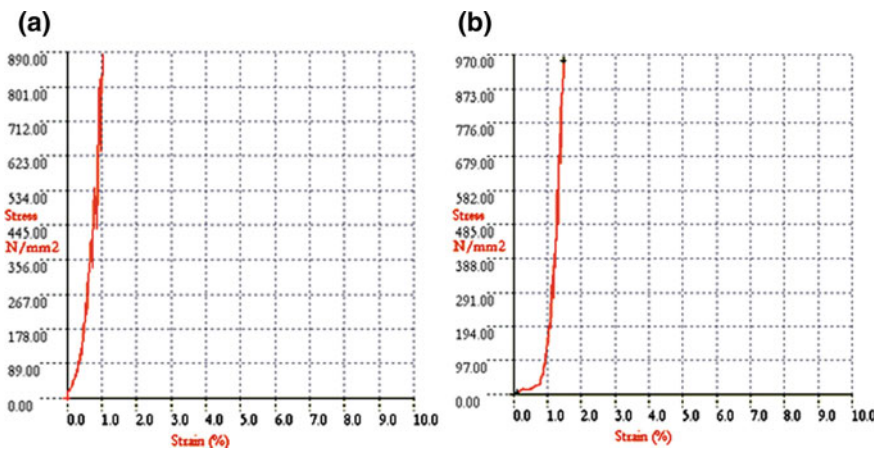
Fig. 6 Stress–strain curve: **a** Hardened AISI 4140& **b** Hardened AISI 52100
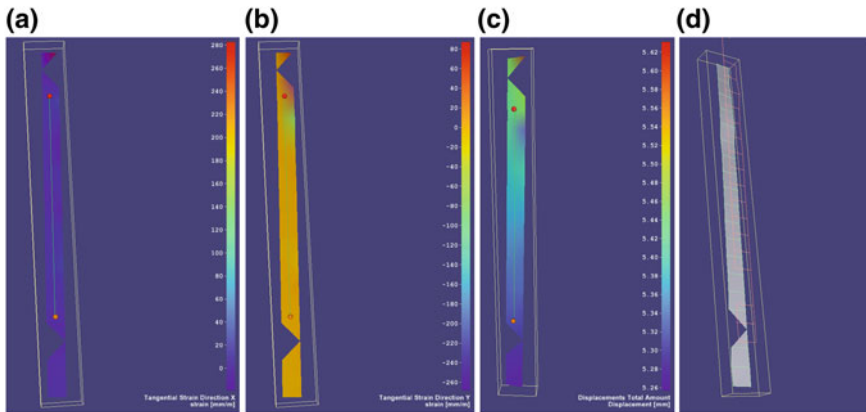
Fig. 7 Tangential Strain rate: **a** X-direction, **b** Y-direction by DIC, **c** Total Displacement & **d** Mesh of selected ZOI size of tensile specimen

From the DIC results, the average tangential strain rate was 1.255 mm/m tensile in y-direction and −0.077 mm/m compression x-direction—this means area reduction is negligible. So, these results recognize that the specimen does not undergo neck formation. The engineering stress–strain data from the undertaken experiments can be easily transformed to its true counterpart. Therefore, it is sensible to believe that the modification in microstructure will certainly influence the testing. Total cross travel or displacement of the specimen and selected ZOI of DIC is shown in Fig. 7.

5   Conclusion

Principally, the hardened material does not undergo neck formation, also the strain and strain rate measurement are too difficult. But, DIC technique is easy for measuring and is a simple method to calculate. So in this work, the DIC technique is applied successfully with tensile testing and provides significant results on hardened materials which is widely used with precise data and is compared to traditional UTM testing. Most significant problems in conventional testing are slip on holders, the stability of UTM and tolerance in measurements—from this results itself, we have found a deviation of $18 \pm 2\%$ (Unthreaded specimen) and $8 \pm 2\%$ (Threaded specimen). But DIC is a non-contact type and it results in the reduction of error and is an accurate measurement technique, especially for tensile testing. Stress–strain relation of materials and their properties are also essential inputs for any FEM simulation. So this hardness related strain values are useful for design and development of bearing in larger size especially in nuclear power plants. The hardened material properties are vital to know the surface integrity constraints such

as residual and contact stress. Finally, results obtained from DIC technique are comparatively good and accurate with UTM results.

References

1. Y.B. Guo, C.R. Liu, *Mechanical Properties of Hardened AISI 52100 Steel in Hard Machining Processes.* School of Industrial Engineering, Purdue University, West Lafayette, IN 47907
2. V. Tarigopula, O.S. Hopperstad, A Study of Localization in Dual-Phase High-Strength Steels Under Dynamic Loading Using Digital Image Correlation and FE Analysis (2006)
3. T.C. Chu, W.F. Ranson, M.A. Sutton, W.H. Peters, Applications of digital-image-correlation techniques to experimental mechanics. Exp. Mech. **25**, 232–244 (1985)
4. S. Babu, K. Manisekar, S. Kalaiselvi, Heat transfer analysis of slewing ring bearing for high thermal applications. ASME J. Thermal Sci. Eng. Appl. **9** (2017)
5. S. Babu, F. Paul Gregory, Heat distribution studies on slewing ring bearings using FLOTHERM software, in *IEEE International (biennial) Conference on "Technological Advancements in Power & Energy– TAP Energy 2017*, IEEE Xplore
6. F. Hild, B. Raka, M. Baudequin, S. Roux, F. Cantelauble, Multiscale displacement field measurements of compressed mineral wool samples by digital image correlation. Appl. Opt. **41** (32), 6815–6828 (2002)
7. S. Babu, K. Manisekar, *Static and local Strain Analysis of High Hardened Linear Model Mock-Up Bearing for Fast Breeder Reactor.* Materials Science Forum, vols. 830–831, pp. 223–226 (2015)

An Experimental Study on Adhesion, Friction and Stick-Slip Phenomena

Arun K. Singh, Avinash A. Thakre and Nitish Sinha

Abstract Stick-slip vibration is an important mode of failure in many structural and mechanical systems and that generally seen in the form of jerking, chattering, squeaking, etc. It is shown experimentally that similar to friction, adhesion is also dynamic in nature and that depends on slip velocity and relaxation or hold time. Fracture mechanics analysis of a soft and hard solid interface in the direct shear sliding reveals that energy release rate (*ERR*) varies periodically during stick-slip motion. However, in the steady sliding regime, *ERR* first increases to a maximum value at static strength, becomes constant during dynamic sliding and finally, the *ERR* reaches at the residual strength to a constant value known as work of adhesion. It is also observed during stick-slip motion that a crack always nucleates from the rear end of the block and traverses the entire interface before the slip and is followed by healing of the same interface begins from the front edge of the block. The present study establishes that a relative competition between the crack growth rate and interface healing rate basically controls the frictional behavior of sliding surfaces.

Keywords Adhesion · Friction · Interfacial fracture · Stick-Slip · Stress relaxation

1 Introduction

Stick-slip (SS) vibration is a mechanical instability that is generally observed in low-velocity regime wherein the sliding mass undergoes jerky or intermittent motion [1–9]. Examples of SS include squealing of brakes and also chattering during the metal cutting operations [1–3]. The intermittent motion disappears and steady sliding follows at a threshold velocity known as critical velocity [10–12]. According to frictional mechanics, SS motion occurs because of mechanical

A. K. Singh (✉) · A. A. Thakre · N. Sinha
Department of Mechanical Engineering, VNIT, Nagpur 440010, Maharashtra, India
e-mail: aksinghb@gmail.com

interaction between friction force and elasticity of the sliding mass [1, 3–5]. Friction is basically a shear force that resists the relative motion between two contacting surfaces, while elasticity is a property of a deformable mass to store mechanical energy [1, 2]. Consequently, elasticity of the sliding mass stores mechanical energy during a stick phase, this energy dissipates during the following slip phase [1, 2]. Various theories of friction have been proposed in the literature for hard materials such as rocks and metals [1–5]. Friction at hard solid surfaces arises due to plastic deformation of micro asperities and interlocking phenomena [1, 4]. The classical model argues that difference between static and dynamic gives rise to SS motion [1]. Rabinowicz [4] discovered a critical distance of the order of the size of micro asperities that basically determines the nature of frictional sliding. A velocity-dependent friction law is necessary for SS motion, wherein frictional strength must reduce with velocity but at the same time the surfaces must heal sufficiently to regain its strength in order to repeat the next cycle of SS motion [4]. Persson [1] has shown theoretically that derivative of velocity-dependent friction law yields the characteristic critical velocity of the sliding interface.

Frictional properties of the soft solids such as gels, rubbers, and elastomers are qualitatively similar to the hard surfaces, yet their basic mechanism of friction is different. For instance, in the case of soft solids, friction and adhesion result from the bonding and debonding of the dangling chains at the sliding interface [9–12]. Further strength and the density of these molecular chains are dependent on normal stress, sliding velocity, relaxation time as well as nature of the substrate [10–12].

Figure 1 shows the schematic sketch of the direct shear specimen subjected to a normal load σ_n and being pulled at sliding velocity v_0. In Fig. 1a, it is assumed that the sliding specimen is completely attached with the substrate and friction force develops along the slip interface in the opposite direction of v_0. Figure 1b, in contrast, shows that a crack always nucleates at the rear end of the block and propagates to the leading edge due to constant v_0.

The sliding problem in Fig. 1a has been analyzed using frictional mechanics approach [9–12]. Accordingly, frictional properties are characterized in terms of static, dynamic, and residual strengths in steady sliding regime [10–12]. Stick-slip, in contrast, occurs in the unstable regime and below a critical velocity in which the specimen shows jerky or intermittent motion [1]. The concept of fracture mechanics
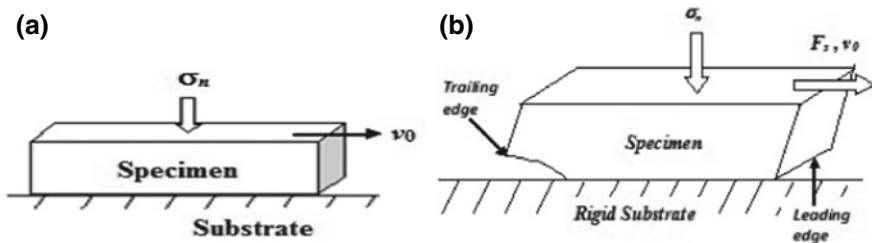
Fig. 1 Schematic diagrams of the direct shear sliding in slide-hold-slide (SHS) using friction and fracture approaches [17]

is also used for the same to understand the interfacial rupture of the specimen that gives rise to friction force as in Fig. 1b.

In recent years, both experimental and theoretical studies have intended to correlate the relationship between adhesion and friction processes at a slip interface [13–18]. Friction is fundamentally an interfacial shear rupture that occurs via fracture mode II/mode III or both [13–18]. However, opening mode (I) of fracture also contributes to magnitude of friction [17, 18]. Adhesion, on the other hand, is the just opposite process of interfacial rupture wherein two ruptured surfaces merge again [1]. In other words, adhesion is a precursor of friction or interfacial fracture but both are opposite in process. Rubinstein et al. [13] have reported crack-like fronts at the sliding interface of two hard and roughened polymer surfaces [13]. David and Rubinstein [14] have also investigated experimentally the frictional strength during stick-slip motion. Svetlizky and Fineberg [15] have examined the microscopic rupture behavior of the same surfaces in stick-slip regime. Thakre and Singh [17] have established that crack length at static, dynamic and residual strengths and these signify unstable, dynamic and static strengths, respectively [16–18]. They have also claimed that static strength corresponds to the Griffith crack while dynamic and residual strengths are characterized by measuring steady and residual crack lengths, respectively [16–18]. The direct shear sliding experiment enables one to measure work of rupture, work of steady sliding and work of adhesion in steady sliding regime [16]. Griffith's fracture criterion states that for the crack propagation, energy release rate (ERR) signifies the energy flowing into the tip of the crack must be equal to the energy needed to create two new surfaces [19, 20]. Thus, energy release rate (ERR) is generally defined as the change in total potential energy (Π) per unit increase in the crack area ($A_c = b\Delta a$) and $ERR = -\partial\Pi/b\partial(\Delta a)$ which may be expressed in light of Fig. 1b in terms of elastic modulus (E), thickness (h) of a plane stress specimen [16] as

$$ERR = \left[\frac{6F^2 h^3}{Eb^2(\ell - \Delta a)^4} + \frac{1.8F^2 h}{Eb^2(\ell - \Delta a)^2}\right] \tag{1}$$

Equation (1) enables on to estimate ERR by measuring the interfacial crack length and corresponding frictional shear strength [16–18].

2 Experimenal Procedure

A low-velocity linear tribometer is used to study both adhesion and shear fracture of the sliding surfaces [12, 16]. Direct shear mode (Fig. 1) is generally preferred on a gelatin hydrogel and glass interface to measure the interfacial shear strength by using slide-hold-slide (SHS) experiments [12, 16–18]. The gel blocks were prepared using gelatin hydrogel of concentration ($c = 15\%$) in distilled water. And the

sliding experiments were conducted on a smooth glass substrate at a fixed temperature of 20 °C and 60% humidity. Other details of the sample preparation and friction experiments are reported in detail [12, 16–18].

3   Results and Discussion

Typically, a solid slides steadily or undergoes unsteady or stick-slip motion on a substrate (Fig. 2). During the steady sliding, the gel block moves on the substrate smoothly and indicates almost a constant frictional force after peak or static friction [12]. It is evident that shear stress varies periodically between momentary static and dynamic points. At the same time, the first SS cycle depends on history but subsequent cycles depend on external pulling rate v_0. It is also obvious that in a "stick" phase, the interface ruptures with shear stress and reaches to the critical value at static strength to become unstable. It is followed by a "slip" phase wherein healing of the sliding interface begins from the front edge to the trailing edge in Fig. 2. In other words, the sliding interface regains its energy during stick period but loses during the slip period of a SS cycle. This observation is in conformation with the theory of frictional mechanics [10–12].

Figure 2 also presents that for a pulling velocity larger than the critical velocity, after the unstable rupture at static strength (τ_{max}), healing of the interface begins from the leading edge in the direction opposite to the sliding. But the rate of strengthening during healing or relaxation is not enough to stop the sliding block, thus resulting in dynamic motion as steady strength (τ_{std}). Further, when the steadily sliding block stops, the shear stress reduces with time to a nonzero magnitude known as residual strength (τ_{res}) (Fig. 2). This is because of the relative competition between adhesion force at the slip interface and elastic force (stiffness) of the gel block [16]. Hence, time-dependent stress relaxation of the sliding interface indicates that adhesion is dynamic in nature. This is similar to the

Fig. 2 Variation of frictional stress vs. time in both stick-slip and steady sliding regimes for varying pulling velocity
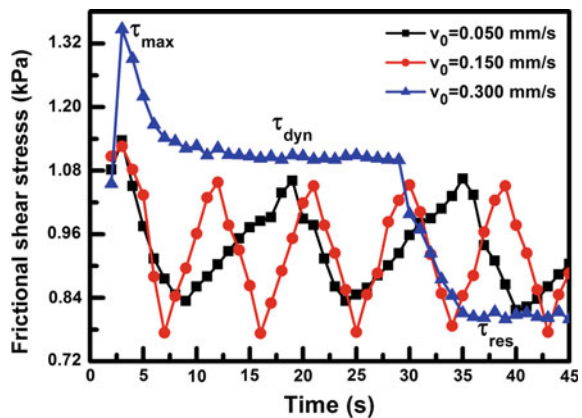
Fig. 3 Variation of interfacial crack length with time for different pulling velocity
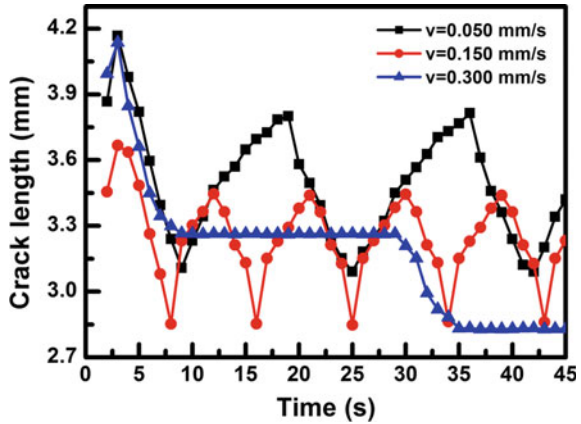
interfacial strengths which also increase with relaxation time and pulling velocity [10–12].

Figure 3 illustrates the experimental result that interfacial crack also seen nucleating from the trailing edge and propagate in the sliding direction. In SS regime, the interfacial crack shows a periodic increase and decrease during stick and slip phase respectively. The velocity of the interfacial crack also varies accordingly [17, 18]. However, the periodic trend disappears in a steady sliding regime as in Fig. 3. Consequently, the crack length decreases continuously and reaches a constant value τ_{std} and decreases to a minimum value of crack length at the τ_{res}. Interestingly at the τ_{max} interfacial crack (Δa) reaches the critical value and results in the complete rupture of the interface. The critical value of Δa at the τ_{max} represents Griffith's critical crack length which leads to rupture of the interface [16].

Figure 4 presents the results concerning the variation of energy release rate (*ERR*) versus time using Eq. (1) and experimental data in view of Figs. 2 and 3. The results show that the *ERR* also varies periodically in stick-slip motion but in a

Fig. 4 Variation of energy release rate (ERR) with time for different pulling velocity
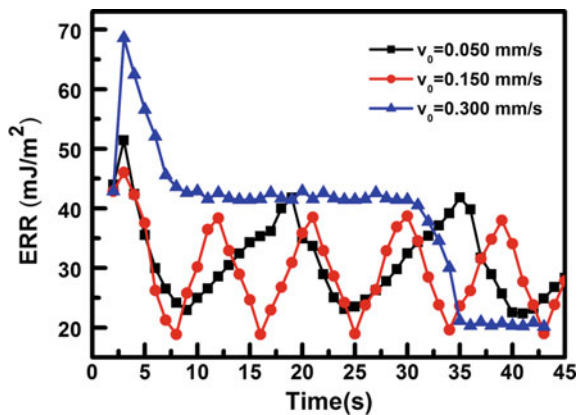
stable regime, the *ERR* is characterized at τ_{max}, τ_{std}, and τ_{res}. The qualitative nature of variation of *ERR* with time is similar to the results in Figs. 2 and 3.

Finally, it is believed that the present study should be useful for understanding the sliding behavior of soft and hard as well as hard and hard solids interfaces in rock slope failure, earthquake process as well as in the failure of structural and mechanical components. Another interesting conclusion that a living animal like geckos generates large adhesion force by adjusting the stiffness of its toes and legs [1].

4 Conclusions

The present study analyzes the sliding behavior of soft and hard solids using friction and fracture mechanics approaches. Both the approaches confirm that adhesion and rupture of the sliding surfaces are dynamic in nature and a relative competition between them gives rise to stick-slip or steady sliding motion. The present study also establishes that sliding behavior is basically controlled by rupture as well as healing of the interfacial crack via the mixed mode (I and II) of fracture. Thus, friction properties are also the manifestation of the relative competition between interfacial rupture (crack growth) and adhesion (crack healing) along the sliding surfaces.

References

1. B.N.J. Persson, *Friction of elastic solids* (Springer, Heidelberg, 2002)
2. R.A. Ibrahim, Appl. Mech. Rev. **47**, 209 (1994)
3. J.R. Rice, A.L. Ruina, J. Appl. Mech. **50**, 343 (1983)
4. E. Rabinowicz, Proc. of the Phys. Soc. **71**(4), 668 (1958)
5. A. Ruina, J. Geophys. Res.: Solid Earth **88**, 10359 (1983)
6. T. Baumberger, C. Caroli, O. Ronsin, Euro. Phys. J. E **11**, 85 (2003)
7. T. Yamaguchi, S. Ohmata, M. Doi, J. Phys.: Condens. Mat. **21**, 205105 (2009)
8. A.D. Berman, W.A. Ducker, J.N. Israelachvili, Langmuir **12**, 4559 (1996)
9. A.E. Filippov, J. Klafter, M. Urbakh, Phys. Rev. Lett. **92**, 135503 (2004)
10. A.K. Singh, V.A. Juvekar, Soft Matter **7**, 10601 (2011)
11. A.K. Singh, V.A. Juvekar, arXiv preprint arXiv:1412.0099, (2014)
12. V. Gupta, A.K. Singh, Int. J. Mod. Phys. B **30**, 1650198 (2016)
13. S.M. Rubinstein, M. Shay, G. Cohen, J. Fineberg **140**, 201 (2006)
14. O. B. David, S.M. Rubinstein, Nature, **463**(2010), 76–79 (2010)
15. I. Svetlizky, J. Fineberg, Nature **509**(7499), 205 (2014)

16. A.A. Thakre, A.K. Singh, J. Adhes. Sci. Tech. **32**, 1899 (2018)
17. A.A. Thakre, A.K. Singh, Mat. Res. Exp. **5**(8), (2018)
18. A.A. Thakre, Ph.D thesis, VNIT Nagpur (2018)
19. A.A. Griffith, Proc. Royal Soc. Lond. **221**, 582 (1921)
20. D. Maugis, *Contact* (Adhesion and Rupture of elastic solids, Springer, Heidelberg, 2000)

Experimental Investigation of Material Constant for Perforated Plate

Gagan Gupta, Sriramachandra Aithal, Kulbir Singh, R. Suresh Kumar, K. Velusamy and P. Puthiyavinayagam

Abstract RCC-MR (2007) has been used as a design/manufacturing code for intermediate heat exchanger (IHX) in **P**rototype **F**ast **B**reeder **R**eactor (PFBR). The code uses equivalent solid plate (ESP) methodology for modeling a tube sheet to carry out stress analysis. Structural integrity assessment of tube sheets with ESP concept is the same as that of solid plate except that it uses an effective elastic constant (E* and ν*) in place of the actual material constants, E and ν. In the latest version of design code RCC-MR$_x$ (2012), values of effective elastic constants are provided for circular pitch pattern. Effective Young's modulus E* and Poisson's ratio ν* values are provided for the ligament efficiency (η) range between 0.1 to 0.6 and 0.3 to 0.6, respectively. In case of PFBR-IHX and IHX of future reactors, ligament efficiency of tube sheet is ∼0.255 for which effective Poisson's ratio ν* value is not available in design codes as well as in the open literature and also it cannot be extrapolated. Hence, an experiment was conducted to obtain the load–deflection curve, extract the values of strain and subsequently estimate the effective elastic constant (ν*). Toward this, scaled down IHX tube sheet models (3 Nos. perforated plates) of desired ligament efficiency were employed. In this paper, the experimental setup, load–deflection curve for IHX tube sheet scaled-down models, strain in tube sheet, estimation of ν*, comparison of experimental results with Finite Element(FE) analysis results are discussed. It is observed that (i) the measured deflection values near the inner edge are higher than the FE analysis values in actual model and, (ii) in ESP model, for material constants of E* and ν* (calculated from experiment), the achieved deflection values at various radial locations closely match with the experimental results and hence, can be used for modeling of equivalent solid plates.

Keywords Perforated plate design · Load–deflection curve · Material constants · Equivalent solid plate

G. Gupta (✉) · S. Aithal · K. Singh · R. Suresh Kumar · K. Velusamy · P. Puthiyavinayagam
Reactor Design Group, Indira Gandhi Center for Atomic Research, HBNI, Kalpakkam
603102, Tamil Nadu, India
e-mail: gagan@igcar.gov.in

Nomenclature

E	Young's Modulus of the actual material of the plate
E*	Effective Young's Modulus for the perforated plate in directions perpendicular to perforation axes
v	Poisson's ratio of material
v^*	Effective Poisson's ratio for the perforated plate in directions perpendicular to perforation axes
Ligament efficiency	Ratio of the nominal width of the minimum ligament (L) to the nominal distance between centers of the two holes or pitch (p), L/p

1 Introduction

In PFBR 500 MWe, IHX is used to transfer heat from primary sodium to secondary sodium. It is a vertical shell and straight tube type counter flow heat exchanger with primary sodium on the shell side and secondary sodium on tube side as shown in Fig. 1. Total 3600 straight tubes (outer diameter 19 mm and thickness of 0.8 mm) are arranged in 25 concentric rows around the inner shell between the top and bottom tube sheet and enclosed by an outer shell in order to direct the primary sodium flow downward [1]. Annular outlet header, which works as a collector for hot secondary sodium is welded to the top tube sheet. The tubes are rolled and welded to 150 mm thick annular top and bottom tube sheets at both ends. Tube sheets have circular holes arranged in a circular pattern. The radial and circumferential pitch between the holes is 25 mm and ~ 26.2 mm, respectively. The material of construction for IHX is austenitic Stainless Steel SS316 LN. The arrangement of the holes in IHX tube sheets is shown in Fig. 2.

Modeling of perforated tube sheets as Equivalent Solid Plate (ESP) with modified material properties E*and v* in FE analysis is a commonly used methodology. The effective elastic constants of the ESP used to represent the perforated area of the tube sheet, are derived for a condition of generalized plane strain and their values are dependent on the type of hole and their patterns in the perforated plate. O'Donnell et al. have given E* and v* values for the perforated plates having circular holes in triangular pitch patterns and subjected to in-plane and bending loading and for any thickness respecting h/p $\geq$ 2, which partly based on theory and partly on experiment [2]. Porowski et al. developed a general approach to the analysis of circular perforated plates with circular holes in triangular or square penetration patterns, including thickness direction properties differing from the in-plane properties. This implies that orthotropic material is best suited instead of isotropic properties based on equivalent solid properties [3]. Slot et al. has given a formulation of the relationship between the effective elastic constants for thick and thin perforated plates and have developed a new theory and formulae for thick
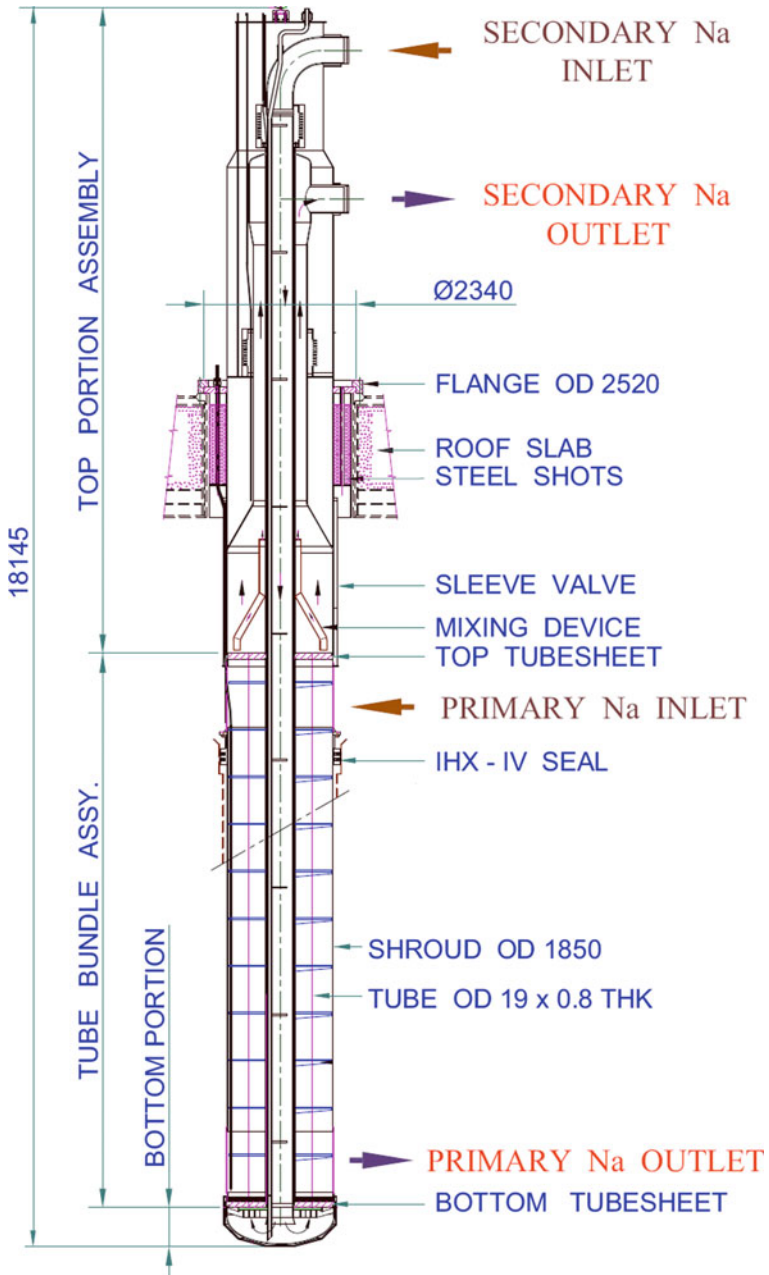
Fig. 1 Intermediate heat exchanger of PFBR

Fig. 2 Top view of IHX tube sheet (90° sector)
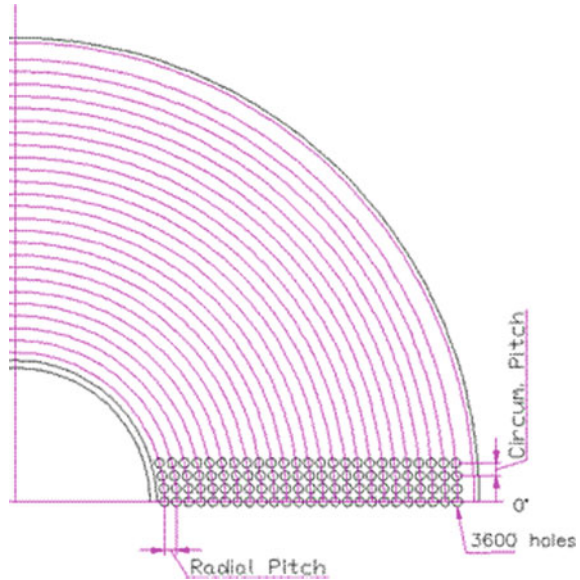
perforated plates with square and triangular pitch patterns, subjected to uniform in-plane loading, based on a generalized plane strain condition [4]. Srinivasan et al. [5] had modeled the perforated plate of IHX as anisotropic equivalent solid plate and assumed circular pitch pattern holes as square pitch pattern holes as per RCC-MR design code 1993. He has also explained that anisotropic equivalent solid plate results will be near to the actual perforated plate [5]. Suman Gupta et al. have analyzed the sodium to sodium heat exchanger in PFBR as per RCC-MR 2007 and modeled the tube sheet with effective elastic constants [6]. Effect of small solid rim area and groove on the interface of the perforated and un-perforated region were studied and practical guidelines were provided to accurately derive the primary stress intensities particularly at the interface, the most critical in the design of tube sheets. In ASME Boiler and Pressure Vessel Code ASME (2015), ESP properties for flat plates with triangular patterns and square patterns are included [7]. In fast-reactor-specific design and construction code, RCC-MRx 2012 [8], the effective elastic constant values E* and ν* are provided for the ligament efficiency (η) range between 0.1 to 0.6 and 0.3 to 0.6, respectively. In case of IHX for PFBR as well as future FBRs, ligament efficiency of tube sheet is ∼0.255. Hence, effective Poisson's ratio ν* value is not available for the tube sheet of Indian FBRs in design codes as well as in the open literature and also it cannot be extrapolated. Hence, an experiment was planned and executed on scaled down models of IHX tube sheet (3 Nos. perforated plates) of required ligament efficiency to obtain the load–deflection curve, extract the values of strain and subsequently estimate the effective elastic constant (ν*).

In this paper, the experimental setup, load–deflection curve obtained for IHX tube sheet models, strain in plate, estimation of v*, comparison of experimental results with FE analysis results are discussed.

2 Experimenal Setup

The perforated scaled down specimen (1:5) of IHX tube sheet (hereafter referred as test specimen) is an annular plate having seven rows of circular holes (Dia. 10 mm) and made of austenitic stainless steel grade SS304L. The radial distance between the holes, circumferential distance between the holes, thickness to pitch ratio (h/p) and ligament efficiency are 13.5 mm, 14 mm, ≥ 2, and 0.25 respectively. The hole's pattern and ligament efficiency in the test specimen are kept similar to that in tube sheet of IHX. The load on the IHX tube sheet is uniformly distributed but in the experiment the load was applied at the inner edge of specimen, which is conservative.

To apply the load and obtain the load–deflection curve of test specimens, an experimental setup was designed and fabricated. A rigid carbon steel support structure (self-balanced structure, i.e., both applied and reaction forces are absorbed within the structure) was manufactured with structural sections like beams, channels, and plates (Fig. 3). A schematic arrangement for the entire experimental setup is shown in Fig. 4. To simulate the actual boundary condition at the inner and outer edges, i.e., simply supported (free to rotate), the test specimen was supported on
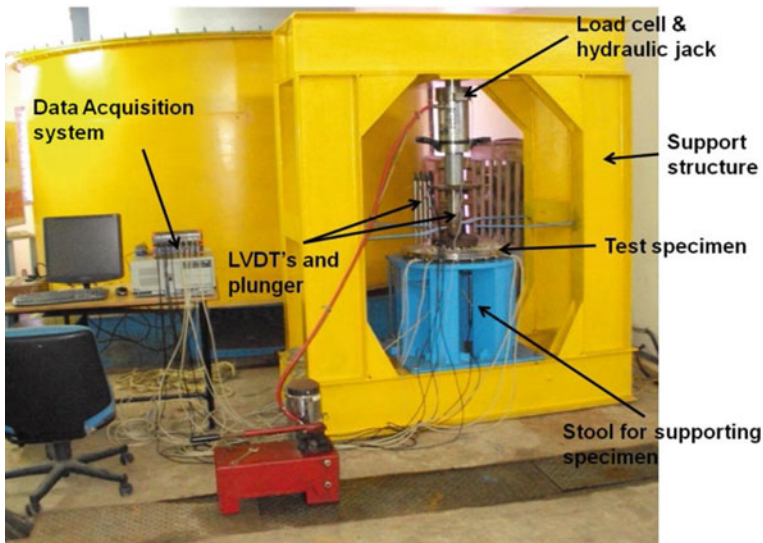
Fig. 3 Experimental setup for perforated plate
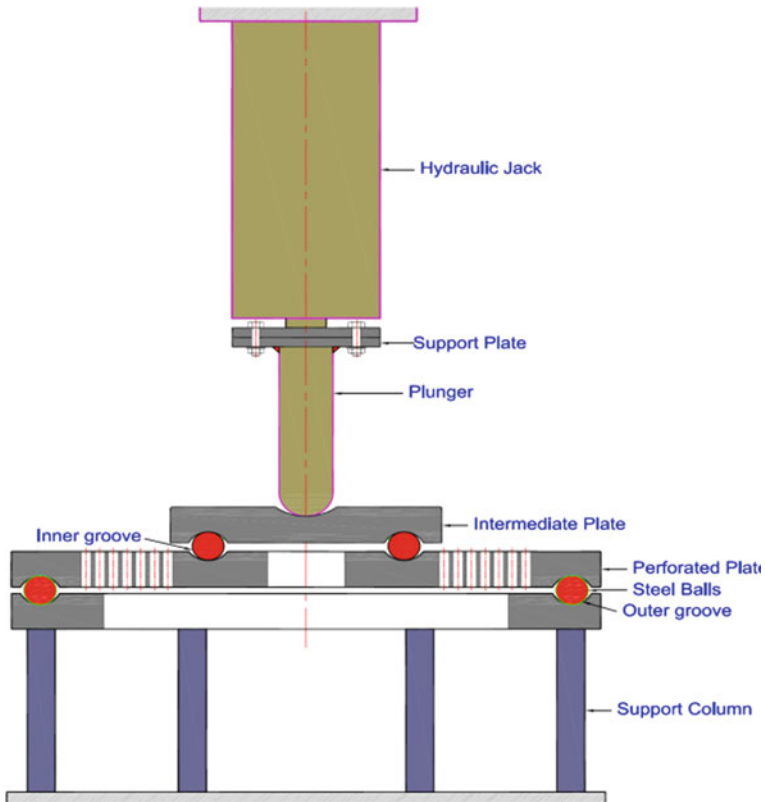
Fig. 4 Schematic arrangement for the experiment

high-strength hardened steel balls, which were placed within the spherical grooves on the plates in the experimental test setup (Fig. 5). Hydraulic jack was used to load the test specimen. Following instruments were identified and provided to extract the relevant experimental data:

- Load cell to measure the applied load was placed in-between the jack and specimen.
- Six numbers of LVDTs were provided along the radial direction at a distance of 72, 120, 142, 169, 196, and 228 mm from the center to record deflection (Fig. 6)
- Four Nos. of LVDTs were provided along the circumferential direction at 0°, 90°, 180°, and 270° to record circumferential variation in deflection, sequentially (Fig. 7).
- Bidirectional strain gauges on the top surface of one of the test specimens (specimen No. 2) at a radial location of 117.5 and 252.5 mm from the center of specimen, to extract strains in the top surface (Fig. 8). Since sufficient space was not available in the perforated region, the strain gauges were fixed very close to
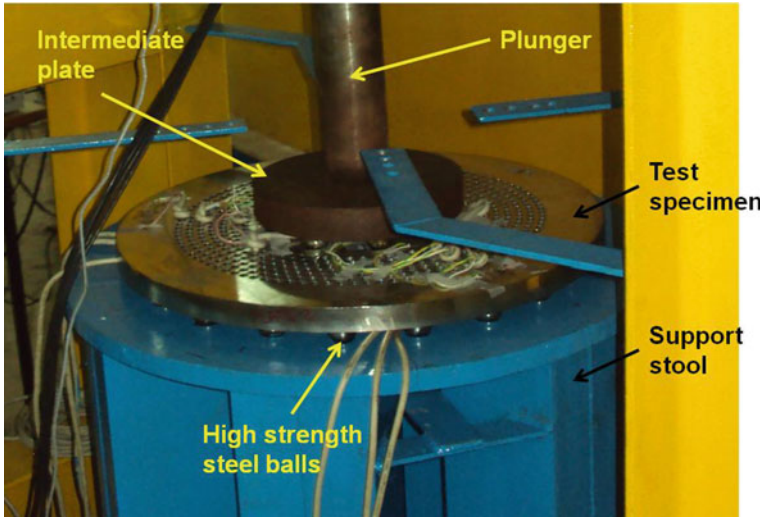
Fig. 5 Details of the test specimen, intermediate plate, and steel balls

Fig. 6 Six LVDTs in the radial direction, four on top and two on the bottom surface of the test specimen

the holes at the periphery. This would represent the strain in the perforated region also due to its proximity.

A data acquisition system was installed to record the readings from the load cell, strain gauges, and LVDTs (Fig. 9). The load was applied gradually on the intermediate plate in three steps, i.e., 5, 10, and 15 T (where T is tons) via plunger and transferred to test specimen's inner periphery region via high strength steel balls provided at eight locations.
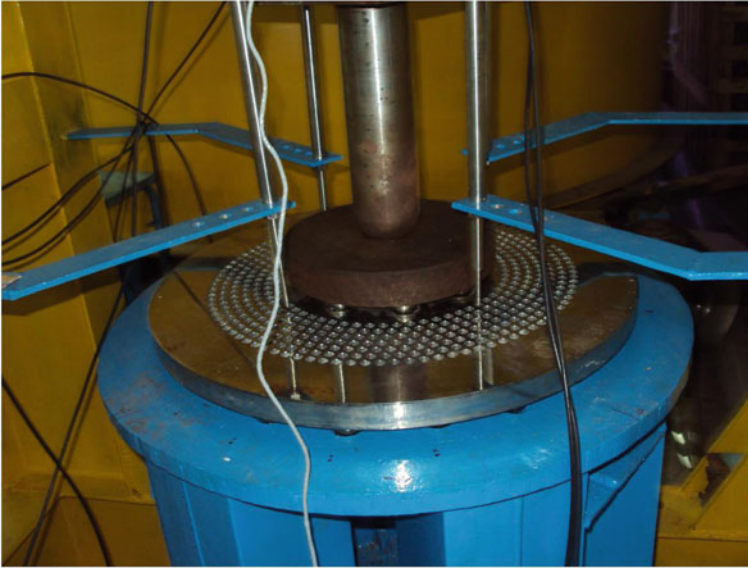
Fig. 7 LVDTs at four angular locations in the circumferential direction

Fig. 8 Bidirectional strain gauges pasted on specimen No. 2
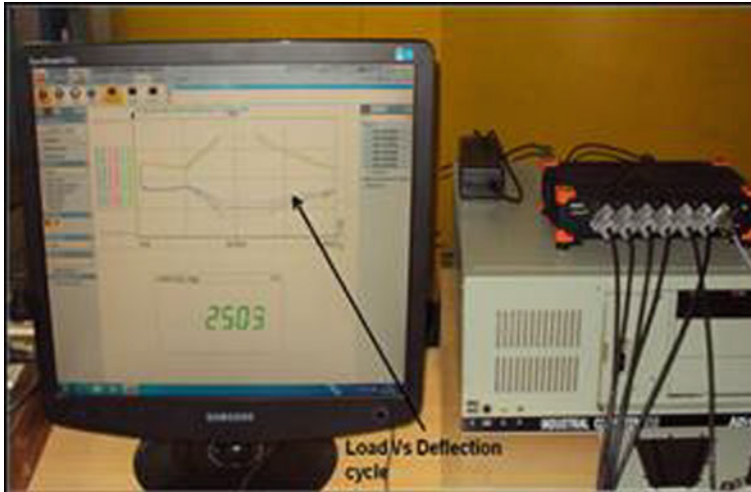
Fig. 9 Data acquisition system

3 Finite Element Analysis of Specimens

Three-dimensional FE model of 90° sector of the actual specimen and ESP model is generated and an elastic analysis was carried out for different loadings (5, 10.2, and 15.2 T). Load was applied at inner groove location and vertical deflection of the plate was restricted at outer groove location. The contact boundary condition at the ball locations as in the experiment was not enforced to reduce computation time. In the actual model (Fig. 10), the material properties, E (200 GPa) and ν (0.3) were taken from design code RCC-MRx. In ESP model (Fig. 11), for perforated region, the material is assumed as isotropic (conservative assumption [9]), E* (43.3 GPa) is taken from RCC-MR code and ν* ($\varepsilon_R/\varepsilon_H$) is calculated from the experimentally obtained strain value and averaged.

4 Results and Discussion

Deflection pattern of test specimen No. 2 along the radial direction (at LVDTs locations) with respect to loading is shown in Fig. 12. The radial locations of different LVDTs are also indicated in the graph. A similar pattern was observed for the other two specimens also.

It is observed that the deflections of perforated plates are nearly linear in the applied load range of 5–15 T. The maximum deflection value was observed in LVDT close to the center of the test specimen and it reduces gradually in the radial direction. The readings of LVDTs provided circumferentially for test specimen-3

Fig. 10 Actual specimen
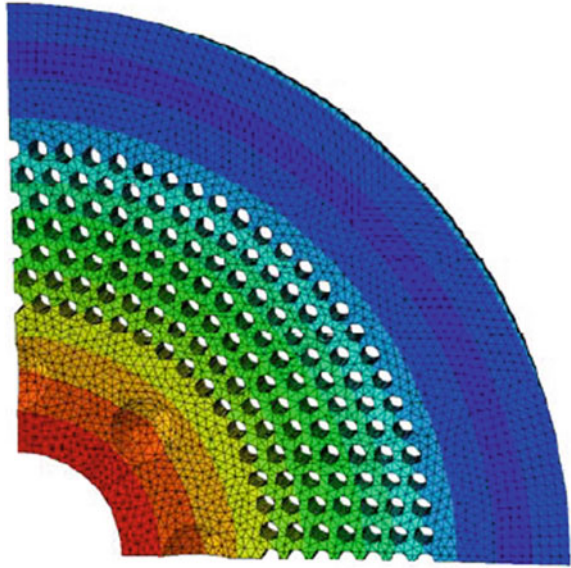
Fig. 11 ESP model
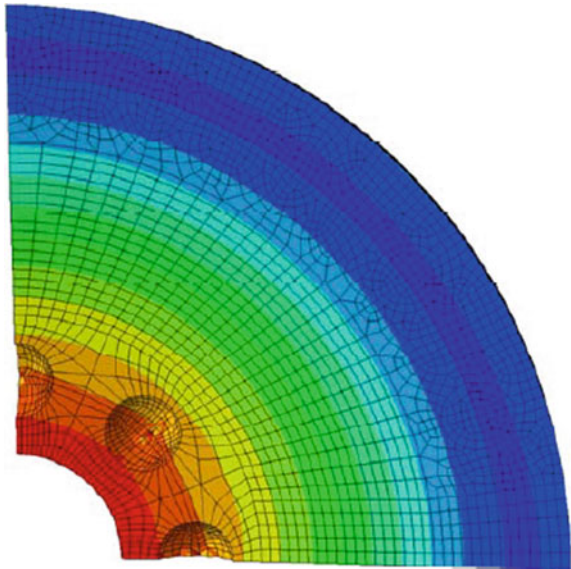
(shown in Table 1) shows that there is negligible variation in deflection values along the circumferential direction.

Strain values in test specimen at various radial locations (μm/m) are given in Table 2 where ε_R and ε_H are strain in radial and hoop directions, respectively. The strain values increase proportionately with the increase in load.

The averaged v^* at locations 117.5 and 252.5 mm from the experiment are obtained to be 0.20 and 0.21, respectively. Comparison between deflection values
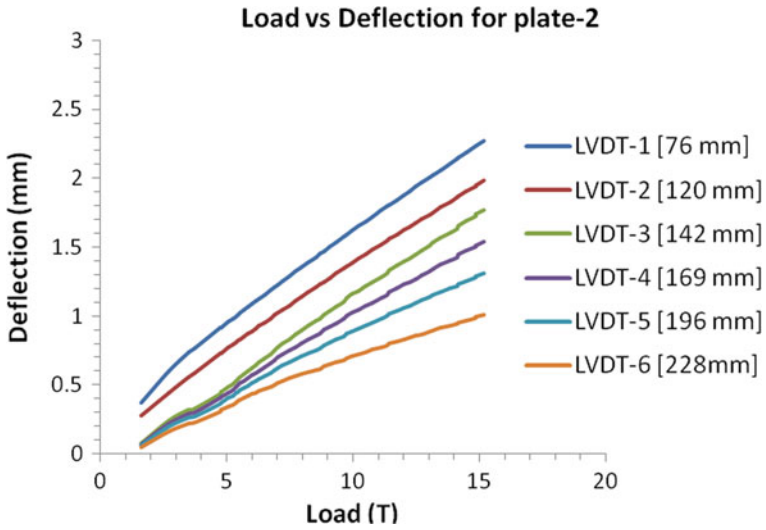
Fig. 12 Load versus deflection of test specimen-2

Table 1 Vertical deflection of test specimen-3 at four angular locations(mm)

Radial location from center (mm)	Load [T]	Angular orientation of LVDTs			
		0°	90°	180°	270°
76	5	0.87	0.92	0.89	0.87
	10.2	1.54	1.61	1.59	1.50
	15	2.39	2.27	2.22	2.33
120	5	0.76	0.76	0.76	0.79
	10.2	1.40	1.34	1.34	1.33
	15	2.02	2.10	2.06	1.97
142	5	0.51	0.63	0.51	0.70
	10.2	0.89	1.13	0.96	1.19
	15	1.26	1.35	1.56	1.60
169	5	0.40	0.33	0.47	0.39
	10.2	0.80	0.63	0.86	0.71
	15	1.07	1.17	0.95	0.98
196	5	0.45	0.39	0.42	0.53
	10.2	0.76	0.70	0.73	0.84
	15	1.04	0.93	0.97	1.06
228	5	0.36	0.25	0.38	0.35
	10.2	0.58	0.46	0.60	0.53
	15	0.79	0.61	0.75	0.65

Table 2 Strain values in test specimen (μm/m)

Load [T]	Angular orientation of strain gauge					
	90°				180°	
	Radial distance from the center of the plate (mm)					
	117.5		252.5		117.5	
	ε_R	ε_H	ε_R	ε_H	ε_R	ε_H
5	34	−274	51	−253	79	−294
10	94	−540	109	−509	169	−583
15.2	123	−841	181	−807	218	−908

as per experiment and FE analysis is tabulated in Table 3. It is observed that the deflection values obtained in experiments closely matches (within 2–12%) near to inner edge and middle region for ESP model. However, though the actual numerical model results are 20–25% higher than the FE analysis results, but are close to ESP model. This difference may be attributed to the boundary conditions considered in FE analysis as fixed in vertical direction, which nearly simulates actual condition. However, in experiment, since the specimen is supported over steel balls, these balls allow the plate to rotate at point of contact without any translation in the vertical direction. Further, though the support structure is designed to be a very rigid structure, there may be a marginal deflection of the support as against 100% rigid BC applied in FEM. In ESP model, (with material constants, E*—43.3 GPa and ν*—0.2), the achieved deflection values at various radial locations closely matches with the experimental results, and hence can be adapted for modeling the ESP model.

Table 3 Vertical deflection of test specimens (plates) in radial direction at six location

Plate-1	Load (T)	Distance from center (mm)					
		76	120	142	169	196	228
	5	0.91	0.77	0.45	0.41	0.37	0.32
	10.2	1.60	1.41	1.11	0.99	0.87	0.71
	15.2	2.22	1.96	1.76	1.55	1.33	1.06
Plate-2	5	0.96	0.77	0.54	0.50	0.45	0.38
	10.2	1.65	1.41	1.22	1.08	0.94	0.75
	15.2	2.28	1.99	1.78	1.55	1.32	1.01
Plate-3	5	0.88	0.77	0.60	0.56	0.51	0.45
	10.2	1.56	1.40	1.23	1.11	0.98	0.82
	15.2	2.18	1.95	1.89	1.67	1.45	1.17
Vertical deflection of FE models in radial direction at six location							
ESP model	5	0.81	0.67	0.59	0.47	0.35	0.19
	10.2	1.51	1.25	1.09	0.87	0.65	0.36
	15.2	2.18	1.80	1.58	1.26	0.93	0.52
Actual numerical model	5	0.65	0.52	0.44	0.36	0.36	0.14
	10.2	1.20	0.96	0.83	0.76	0.48	0.25
	15.2	1.76	1.38	1.18	0.94	0.67	0.37

5 Conclusions

An experimental investigation of scaled-down IHX tube sheet model was carried out for estimating the ESP material constants. The experimental results are compared with FE analysis results. It is observed that

 (I) The deflection values (near to the inner edge) obtained from the experiment are 20–25% higher than the values obtained from FE analysis of actual model,
(II) Regarding ESP model, with material constants of E* (43.3 GPa) and ν* (0.2), the achieved deflection values at radial locations near to inner edge and middle portion are within 2–12%, to that obtained from experiment and hence, can be adapted for modeling the equivalent solid plates.

References

1. R. Gajapathy, K. Velusamy, P. Selvaraj, P. Chellapandi, S.C. Chetal, T. Sundararajan, Thermal hydraulic investigations of intermediate heat exchanger in a pool-type fast breeder reactor. Nucl. Eng. Des. **238**, 1577–1591. http://dx.doi.org/10.1016/j.nucengdes.2008.01.005
2. W.J. O'Donnell, B.F. Langer, Design of perforated plates. ASME J. Eng. Ind. **84**, 1047–1060 (1962)
3. J.S. Porowski, W.J. O'Donnell, Elastic design methods for perforated plates. J. Eng. Power **100** (2), 356–362 (1978)
4. T. Slot, W.J. O'Donnell, Effective elastic constants for thick perforated plates with square and triangular penetration patterns. J. Eng. Ind. **93**(4), 1081–1088 (1971)
5. R. Srinivasan, A. Gupta, P. Chellapandi, S.C. Chetal, S.B. Bhoje, Structural mechanics analysis of intermediate heat exchanger for prototype fast breeder reactor, in *Transactions of the 17th International Conference on Structural Mechanics in Reactor Technology (SMiRT 17)*, 17–22 August 2003, paper F03-7, Prague, Czech Republic
6. S. Gupta, P. Chellapandi, Application of RCC-MR for the structural design of tube sheet of intermediate heat exchanger for a sodium cooled fast reactor. Nucl. Eng. Des. **280**, 181–200 (2014)
7. ASME SEC VIII Div 1. 'Rules for Construction of Pressure Vessels, NMA APP A Basis for establishing allowable loads for Tube to tubesheet joints' 2010
8. RCC-MRx Code 2012, Section III – Tome 1 – Subsection B: class N1Rx reactor components and supports, RB – 3900: Design rules for heat exchanger, Figure RB 3944.3c: E* and ν* for circular plates - constant circular pitch pattern
9. K. Singh et al., Assessment of simplified tube sheet analysis based on three dimensional finite element simulation, in *Structural Mechanics in Reactor Technology (SMiRT-21)*, New Delhi, India (2011)

Assessment of Speckle Pattern for Use in Digital Image Correlation Analysis Using Simulated Displacement Field

Abhishek Kumar, S. Vishnuvardhan and P. Gandhi

Abstract Local stresses and strains near the crack tip control fatigue crack growth process. Calculation of elastic–plastic strains and stresses at the crack tip requires solving the nonlinear boundary value problem of a cracked body. Analytical solutions of such problems for varied structural geometry are rarely attainable. A popular method of structural integrity assessment involves stress field characterization ahead of the crack tip. Stress Intensity Factor (SIF) calculation using full-field displacement from digital image correlation (DIC) results is a popular experimental method. Reliable estimation of displacement field from successive images of a specimen under deformation relies largely on intensity profile and its gradient on the specimen, known as speckle patterns. Application of DIC in integrity assessment of structural components of infrastructure and power plant systems should begin with speckle pattern characterization. Speckle pattern characterization can be carried out using two images without any motion or images with rigid-body motions (rigid-body translation and rotation) or images obtained using constant strain tests. The goal of speckle pattern characterization is to quantitatively compare the imposed motion with the recovered motion from DIC and estimation of minimum displacement resolution. Although characterizing speckle pattern using the methods suggested above is relatively straightforward, reproducing representative speckles for multiple cases is a challenge. To overcome this challenge, a speckle pattern assessment procedure, which uses simulated displacement field, is proposed in the present study. A rigid transformation and constant strain condition are simulated and the effectiveness of speckle pattern in capturing simulated displacement from DIC analysis is observed. Error distribution in the estimation of displacement is plotted. For quantitative evaluation of error in length, image calibration is also carried out.

A. Kumar (✉) · S. Vishnuvardhan · P. Gandhi
CSIR – Structural Engineering Research Centre, Chennai, India
e-mail: abhishek@serc.res.in

A. Kumar · S. Vishnuvardhan
Academy of Scientific and Innovative Research (AcSIR), New Delhi, India

Keywords Digital image correlation · Speckle pattern · Image deformation · Crack-tip · Fracture characterization · Stress intensity factor

Nomenclature

a	crack length
K	stress intensity factor
K_{max}	maximum stress intensity factor
ΔK	applied stress intensity range
$\{r, \varphi\}$	polar coordinates
$\sigma_x, \sigma_y, \tau_{xy}$	stress components in plane stress
v	poisson's ratio
W	width of specimen
B	breadth of specimen
σ_{YS}	Yield stress

1   Introduction

Evaluation of fracture parameter from experimental technique requires appropriate measuring techniques for strain field near the crack tip. Full-field measurement techniques are suitable for such cases. The full-field measurement technique is a metrology technique, which allows estimation of displacement, strain or stress over the surface of the tested specimen or component. Use of advanced materials and complex structures demand full-field noncontact measurement and investigation techniques for analysis. Traditionally, point wise strain gauge technique measurement has been used in such a scenario. This method is tedious, requires elaborate instrumentation, and is not very suitable for either in situ or real-time applications. Optical methods are a very popular and widely used alternative as they are nonintrusive, noncontact, and nondestructive [1]. All full-field noncontact optical metrologies are broadly classified into interferometric techniques and non-interferometric techniques as shown in Fig. 1 [2].

Interferometric metrologies use the difference in phase of scattered light waves from test object surface before and after deformation. Because of the working principle, these techniques require a coherent light source. The results are in the form of fringe patterns and to obtain the field variables (displacements, strains, or stresses) from fringe pattern, phase analysis, and fringe processing has to be carried out. Due to the abovementioned reasons, measurements are to be taken in a vibration-free isolated optical bench in the laboratory. Interferometric techniques cannot be used for real-time applications. Non-interferometric techniques determine the surface deformation from the difference in grayscale intensity of object surface before and after deformation. Grid methods [3, 4] and digital image correlation (DIC) [5, 6] are two popular non-interferometric techniques. These techniques work
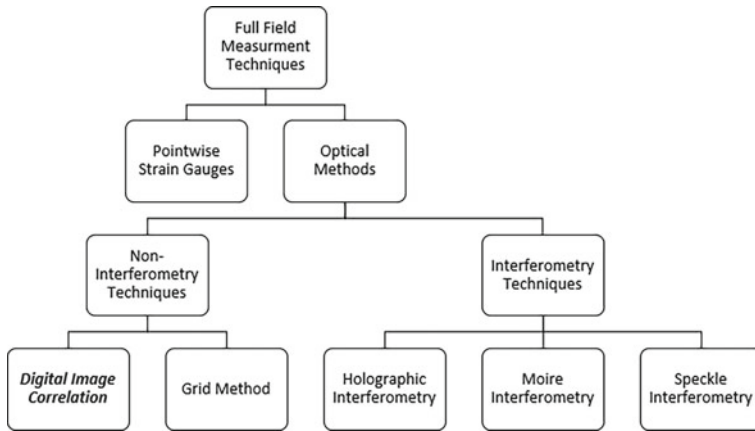
Fig. 1 Classification of full-field measurement techniques

with ordinary white light and surface preparation just involves the creation of high contrast speckle. Over a period, the method has grown and been used with other concepts like stereovision, extended finite element methods, X-ray tomography which allows the application of DIC to newer problems [7–12]. It is useful to see DIC as a technique, which borrows elements from digital image processing, numerical computing, and the domain where it has to be applied, in present case mainly solid mechanics and fracture mechanics (Fig. 2).

It reduces the instrumentation and is not intrusive to make DIC a perfect experimental technique to obtain parameter of constitutive models for biomaterials and composites or dynamic fracture characterization. In 2D-DIC technique, it is possible to determine the in-plane displacement field on the surface of the specimen or component undergoing deformation by taking successive images at different load steps. Typical set-up for a 2D DIC experiment is shown in Fig. 3. In the paper, a brief introduction of DIC is given and details of subset based DIC used in present

Fig. 2 Digital image correlation
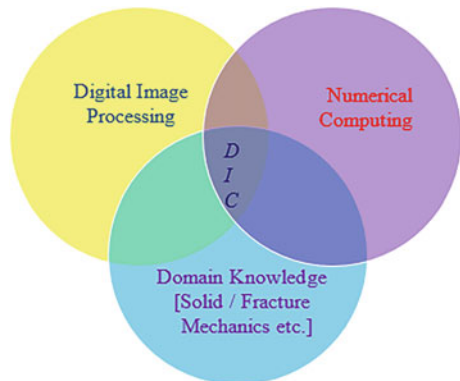
Fig. 3 Typical experimental set-up for a 2D-DIC experiment
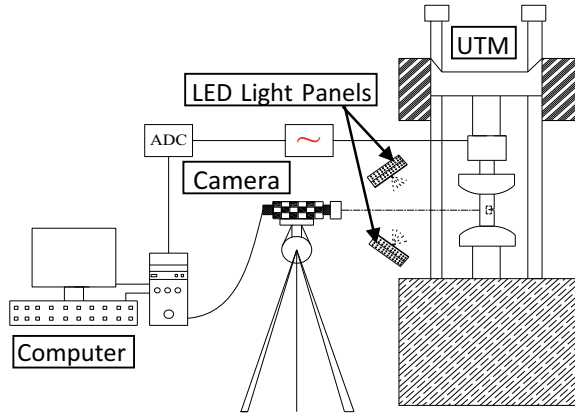
work is provided. The paper discusses the need for assessment of speckle pattern and simulated deformation for better reliability of DIC for displacement estimation. The speckle pattern used for assessment is used for evaluation of stress intensity factor.

2 Digital Image Correlation

The overall goal of DIC is to obtain displacement and strain fields within a region of interest (ROI) for a material sample undergoing deformation. To achieve this goal implementation of a displacement mapping function, a correlation criterion and a scheme for subpixel interpolation are requires. In a DIC experiment, images of a sample are taken as it deforms; these images are used as inputs to a DIC program. The idea is to obtain a one-to-one correspondence between material points in the reference (initial undeformed picture) and current (subsequent deformed pictures) configurations. DIC does this by taking small subsections of the reference image, called subsets, and determining their respective locations in the current configuration. The center of the subset is called 'marker'. Once the location of the subset in the current configuration is located which is carried out by establishing the best correspondence between the square area of the subset in the reference image and the square area in a subsequent image. A correlation criterion is used for establishing best correspondence. For each subset, we obtain the displacement of the marker information through the transformation used to match the location of the subset in the current configuration. Many subsets are picked in the reference configuration, often with a spacing parameter to reduce computational cost (also note that subsets typically overlap as well). The end result is a grid of points with displacement information with respect to the reference configuration, also referred to as Lagrangian displacements/strains. The displacement/strain fields can then either be reduced or interpolated to form a "continuous" displacement/strain field.

In order to allow the deformation of the subset and therefore improving the correlation, different shape functions (mapping functions) may be used. Deformation is assumed homogenous and to establishing deformation continuity a transformation coordinate in form of Eq. 1 is assumed. ξ and η are shape functions, primed variables are coordinate in the deformed state.

$$
\begin{aligned}
x_i^{'} &= x_i + \xi(x_i, y_i) \\
y_i^{'} &= y_i + \eta(x_i, y_i)
\end{aligned}
\tag{1}
$$

In the present work, a second-order transformation function is used to map reference subset to the deformed subset, which allows depicting of complicated deformations. The mapping transformation [13] is given by Eq. 2. u and v are rigid-body displacements along x-axis and y-axis, respectively. The mapping function is given as

$$
\begin{aligned}
x_i^{'} &= x_i + u + \frac{\partial u}{\partial x}\Delta x + \frac{\partial u}{\partial y}\Delta y + \frac{1}{2}\frac{\partial^2 u}{\partial x^2}\Delta x^2 + \frac{1}{2}\frac{\partial^2 u}{\partial y^2}\Delta y^2 + \frac{1}{2}\frac{\partial^2 u}{\partial x \partial y}\Delta x \Delta y \\
y_i^{'} &= y_i + v + \frac{\partial v}{\partial x}\Delta x + \frac{\partial v}{\partial y}\Delta y + \frac{1}{2}\frac{\partial^2 v}{\partial x^2}\Delta x^2 + \frac{1}{2}\frac{\partial^2 v}{\partial y^2}\Delta y^2 + \frac{1}{2}\frac{\partial^2 v}{\partial x \partial y}\Delta x \Delta y
\end{aligned}
\tag{2}
$$

In subset-based DIC algorithms, the reference image is partitioned into smaller regions referred to as subsets. The deformation is assumed to be homogeneous inside each subset, and the deformed subsets are then tracked in the current image. To evaluate the similarity degree between the reference subset and the deformed subset, a cross-correlation criterion is defined. The matching procedure is completed through searching the peak position of the distribution of correlation coefficient. In the present study, for assessment of speckle efficiency a subset-based DIC analysis is carried with subset size and subset spacing kept as 64 pixels and 16 pixels, respectively.

3　Simulated Deformation Fields

Reliable estimation of displacement fields from successive images of a specimen under deformation relies in large part on the particular subset intensity profiles and their gradients on the specimen, known as speckle patterns [14, 15]. Generally, the possible application of Digital Image Correlation (DIC), in this case, structural integrity assessment of structural components of infrastructure and power plant systems, should begin with speckle pattern characterization. The test involves two images without any motion, rigid-body motions (rigid-body translation and rotation), constant strain tests and similar simple tests. The goal is to quantitatively compare the simulated imposed motion with the recovered motion from DIC. Estimation of minimum displacement resolution is also an outcome of the tests.

(a) Original RGB image

(b) Converted grey scale image

(c) Image of cropped speckle pattern

(d) Cropped speckle pattern
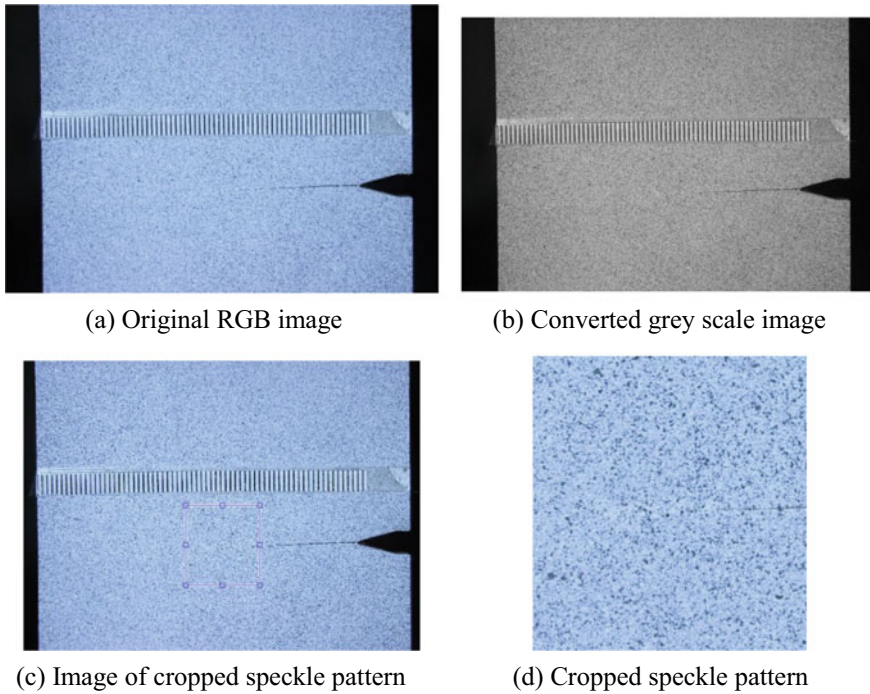
Fig. 4 Images used for speckle pattern assessment

Although the tests themselves are relatively straightforward, many times depending on the material in use and significant amounts of time and effort for conducting these benchmarking experiments are not feasible. The other biggest challenge is to reproduce the same representative speckle for multiple tests. To overcome these problems a speckle pattern assessment procedure is proposed which uses simulated displacement field. In the present study, we utilize an adapted code developed by Flank Lab of Brown University in the present study [16]. Figure 1 shows image earlier used for evaluation of stress intensity factor for a specimen made of IS 2062 Gr. E300 steel. Location of the speckle pattern, which is assessed shown in Fig. 4c. Figure 4d shows the speckle pattern assessed in the present work.

The cropped section is simulated to undergo various deformations. Figure 5 gives simulated images of cropped speckle under translation, pure shear, and uni-axial strain. These images are analyzed using DIC to evaluate the efficiency of the speckle pattern to capture the respective deformation modes. A rigid-transformation of 20 pixels in the lateral direction (X-displacement) is provided and the results of DIC analysis on the simulated image is shown in Figs. 6 and 7. X-displacement,
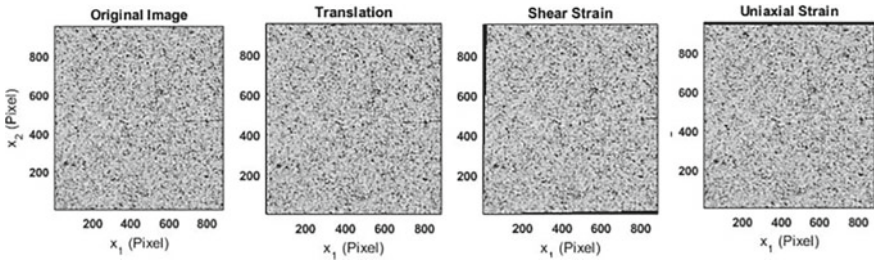
Fig. 5 Simulated images for various deformation modes

Fig. 6 X-displacement for translation case
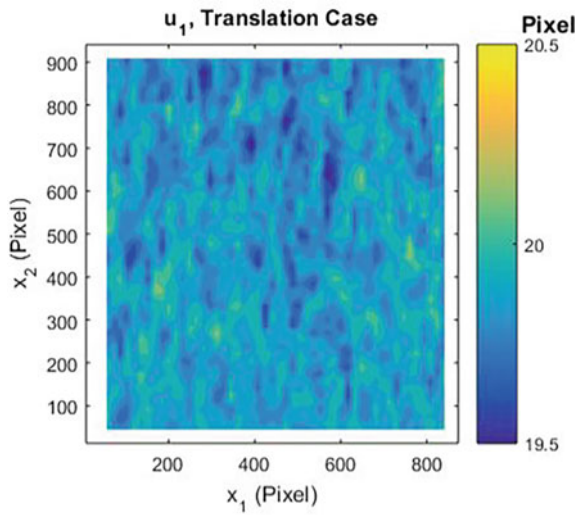
Fig. 7 Y-displacement for translation case
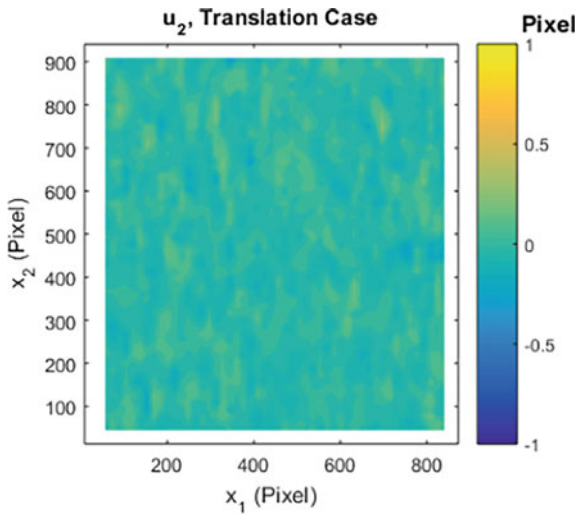
which is taken horizontal axis and Y-displacement, which is taken vertical axis evaluated from DIC of the simulated image is shown in Figs. 6 and 7, respectively.

For simulating displacement and strain field in cases of deformation Poisson's ratio of 0.3 and Young's modulus of 200 GPa is assumed.

4   Results and Discussion

Displacement fields recovered from DIC algorithm are shown in Figs. 8 and 9.

Error distribution in recovered error in X-Displacement from DIC is represented in Fig. 10 for the case of translation and in Fig. 11 for the case of uniaxial strain.

For quantitative evaluation of error in length, image calibration is carried as shown in Fig. 12. An error of 2 pixels will correspond to an error of 0.033 mm. The image in the present study has been used for stress intensity factor evaluation. Digital image processing based technique is used for locating crack-tip. Simple DIP algorithms like image inversion, filtering, and the fact that crack starts from the left side of the image are used. The steps involved in the image processing program are shown in Fig. 13.

Digital image correlation gives full-field displacement as output. Stress intensity factor (SIF) is one of the important fracture parameters required for structural integrity evaluation. SIF is evaluated from post-processing of the displacement field. The evaluation of SIF involves two steps, (1) location of crack tip and (2) fitting displacement data into stress field equation to evaluate SIF [17]. Fatigue crack growth (FCG) studies are carried out on an eccentrically-loaded single edge notch tension (ESE(T)) specimen made of IS 2062 Gr. E 300 steel. ASTM E 647-13: "Test method for measurement of fatigue crack growth rates" is followed in

Fig. 8 X-displacement for uniaxial strain case
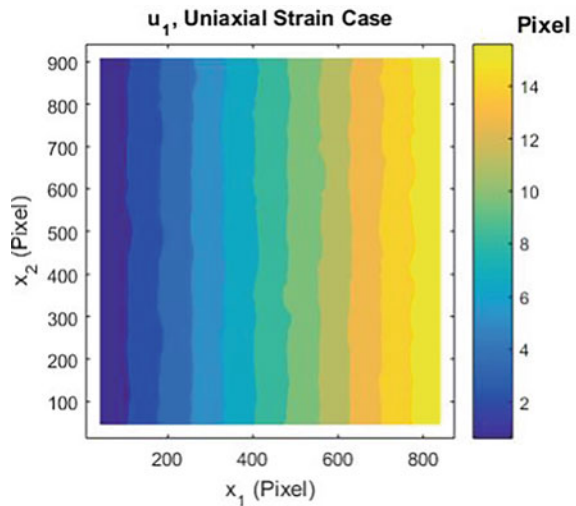
Fig. 9 Y-displacement for
uniaxial strain case
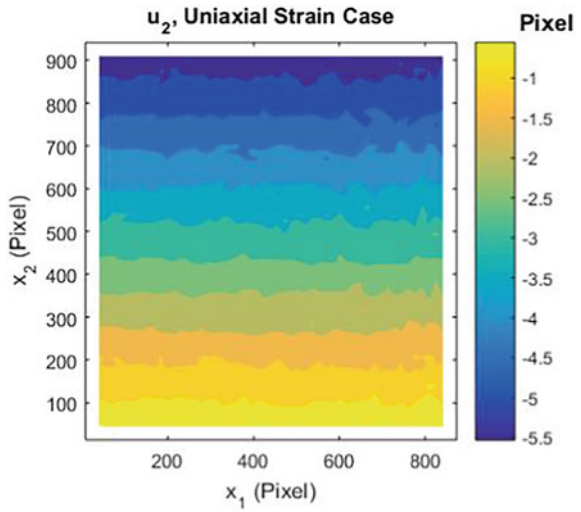
Fig. 10 Error in
X-displacement for translation
case
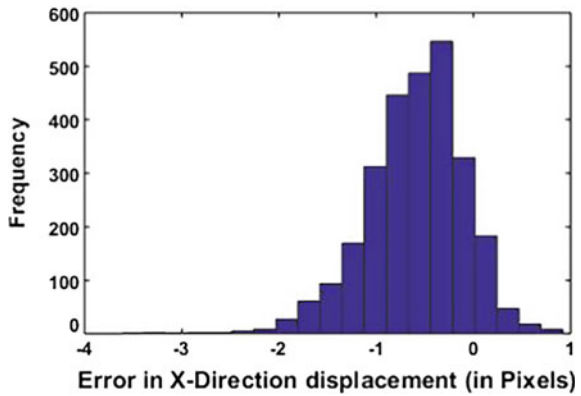
Fig. 11 Error in
X-displacement for uniaxial
tension case
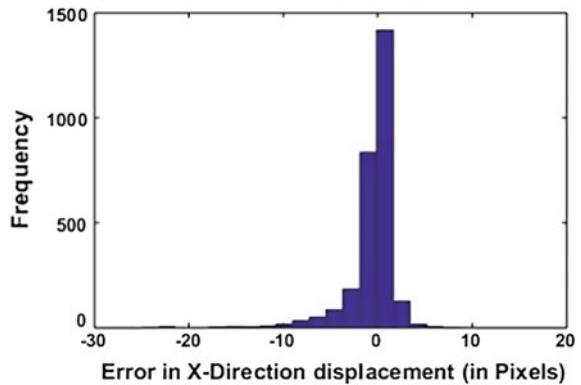
Fig. 12 Calibration for a
pixel to the length scale
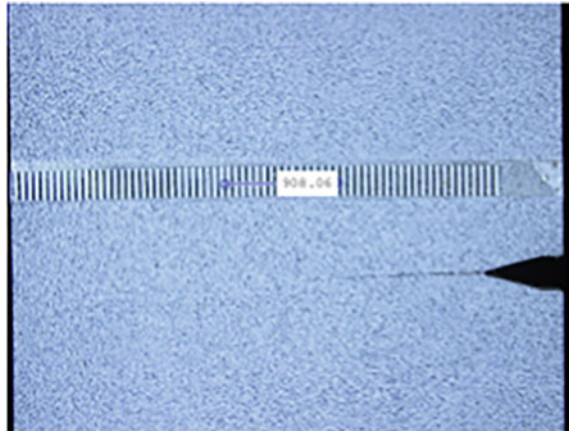
Fig. 13 Image processing to
locate crack-tip
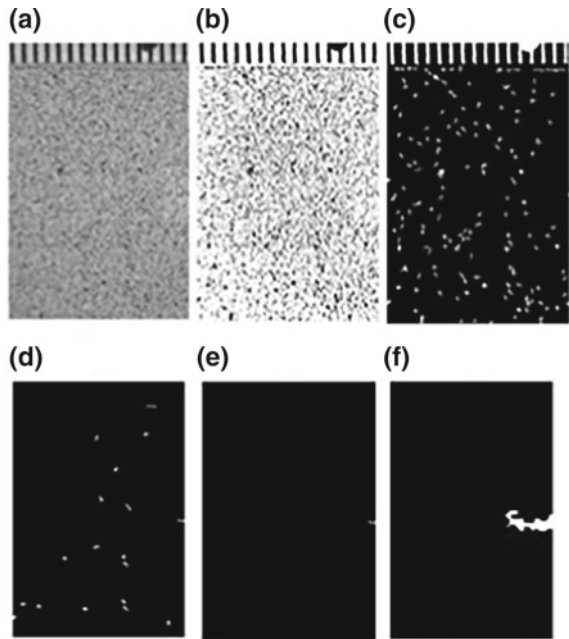
preparing the test specimen and carrying out the fatigue experiment. Constant
amplitude sinusoidal cyclic load is applied using a ±250 kN capacity fatigue rated
UTM. The stress ratio is 0.1. The maximum and minimum load values are 15 kN
and 1.5 kN, respectively. The MATLAB code is written to locate the crack-tip
using image processing methodology.

For generating the ROI, the area over which DIC has to be carried out, a
MATLAB program is written (see Fig. 14a, b). The size of ROI is obtained from

(a) ROI

(b) ROI superimposed over the specimen

(c) Strain field obtained using DIC
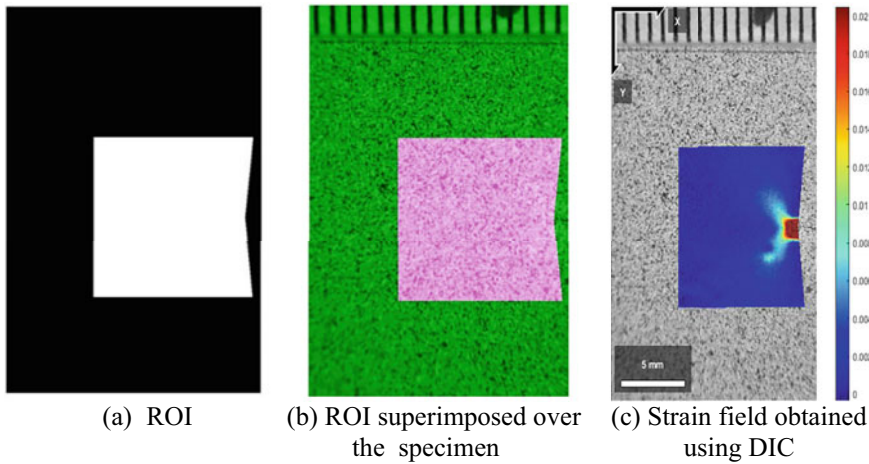
Fig. 14 ROI and strain field obtained from DIC

the user using the interactive program. DIC analysis is performed to obtain the displacement and strain fields using a MATLAB based open source software. SIF is computed using elastic strain field and stress field equations (Eq. 3) of Atluri and Kobayashi [18] for the mixed mode case in a general form. Strain field obtained from DIC analysis is shown in Fig. 14c. To obtain the stress field parameter, a set of over deterministic linear equations are solved using linear least squares method. The value of SIF for Mode I is obtained for a typical case with a crack length of 38.2 mm. The value of the stress intensity factor obtained is 47.54 $\boldsymbol{MPa \sqrt{m}}$. Figure 14c shows strain field obtained using DIC. ASTM E647-13 a gives closed form equations to evaluate stress intensity factor range for ESE(T) specimen for a given load range and crack length. SIF range evaluated for Pmin as zero gives stress intensity factor, the value of SIF obtained was 49.12 MPa√m. The result is in close agreement with the SIF obtained from DIC which is 47.54 MPa√m.

$$
\begin{Bmatrix} \sigma_x \\ \sigma_y \\ \tau_{xy} \end{Bmatrix} = \sum_{n=1}^{\infty} \frac{n}{2} A_{In} r^{\frac{n-2}{2}} \begin{pmatrix} \left\{2 + (-1)^n + \frac{n}{2}\right\}\cos\left(\frac{n}{2} - 1\right)\theta - \left(\frac{n}{2} - 1\right)\cos\left(\frac{n}{2} - 3\right)\theta \\ \left\{2 - (-1)^n + \frac{n}{2}\right\}\cos\left(\frac{n}{2} - 1\right)\theta + \left(\frac{n}{2} - 1\right)\cos\left(\frac{n}{2} - 3\right)\theta \\ -\left\{(-1)^n + \frac{n}{2}\right\}\sin\left(\frac{n}{2} - 1\right)\theta + \left(\frac{n}{2} - 1\right)\sin\left(\frac{n}{2} - 3\right)\theta \end{pmatrix}
$$
$$
- \sum_{n=1}^{\infty} \frac{n}{2} A_{IIn} r^{\frac{n-2}{2}} \begin{pmatrix} \left\{2 - (-1)^n + \frac{n}{2}\right\}\sin\left(\frac{n}{2} - 1\right)\theta - \left(\frac{n}{2} - 1\right)\sin\left(\frac{n}{2} - 3\right)\theta \\ \left\{2 + (-1)^n - \frac{n}{2}\right\}\sin\left(\frac{n}{2} - 1\right)\theta + \left(\frac{n}{2} - 1\right)\sin\left(\frac{n}{2} - 3\right)\theta \\ -\left\{(-1)^n - \frac{n}{2}\right\}\cos\left(\frac{n}{2} - 1\right)\theta - \left(\frac{n}{2} - 1\right)\cos\left(\frac{n}{2} - 3\right)\theta \end{pmatrix}
$$

$$(3)$$

where, {r, φ} are polar coordinates and σ_x, σ_y, and τ_{xy} are stress components in plane stress.

5   Conclusions

The presented speckle pattern assessment is a simple and effective methodology for quantitatively determining the efficiency of a speckle pattern to recover displacement values from DIC analysis. Speckle pattern assessment is carried on speckle on an ESE(T) specimen, which is used for evaluation of stress intensity factor. Simulated deformation field for cases of translation, shear, and uniaxial tensile strain is generated. DIC analysis is performed on the images to recover the displacement and strain fields. Error distribution in the computation of displacement field is also provided. The methodology will useful for judiciously imparting a speckle pattern for DIC applications.

References

1. P. K. Rastogi, (ed.), *Photomechanics*, vol 77 (Springer, Berlin, Heidelberg, 2000)
2. B. Pan, K. Qian, H. Xie, A. Asundi, Two-dimensional digital image correlation for in-plane displacement and strain measurement: a review Meas. Sci. Technol. **20**(6), 062001 (2009)
3. H.T. Goldrein, S.J.J.P. Palmer, J.M. Huntley, Automated fine grid technique for measurement of large-strain deformation maps. Opt. Lasers Eng. **23**(5), 305–318 (1995)
4. J. S. Sirkis, T. J. Lim, Displacement and strain measurement with automated grid methods. Exp. Mech. **31**(4), 382–388 (1991)
5. W. Peters, W. H. Ranson, Digital imaging techniques in experimental stress analysis. Opt. Eng. **21**(3), 427–431 (1982)
6. H. A. Bruck, S. R. McNeill, M. A. Sutton, W. H. Peters, Digital image correlation using Newton-Raphson method of partial differential correction. Exp. Mech. **29**(3), 261–267 (1989)
7. P. F. Luo, Y. J. Chao, M. A. Sutton, W. H. Peters, Accurate measurement of three-dimensional deformations in deformable and rigid bodies using computer vision. Exp. Mech. **33**(2), 123–132 (1993)
8. B. K. Bay, T. S. Smith, D. P. Fyhrie, M. Saad, Digital volume correlation: Three-dimensional strain mapping using X-ray tomography. Exp. Mech. **39**(3), 217–226 (1999)
9. R. Julien, From pictures to extended finite elements : Extended digital image correlation (X-DIC) Correlation d' images num 'eriques' etendue (CIN E). Science **335**(80), 1–8 (2007)
10. S. Roux, F. Hild, Digital image mechanical identification (DIMI). Exp. Mech. **48**(4), 495–508 (2008)
11. H. Tippur, C. Periasamy, A digital gradient sensor for nondestructive evaluation and stress analysis. *SPIE Newsroom* (2013)
12. F. Hild et al., Toward 4D mechanical correlation. Adv. Model. Simul. Eng. Sci. **3**(1), 17 (2016)
13. H. Lu, P. D. Cary, Deformation measurements by digital image correlation: Implementation of a second-order displacement gradient. Exp. Mech. **40**(4), 393–400 (2000)
14. X.-Y. Liu et al., Quality assessment of speckle patterns for digital image correlation by Shannon entropy. Opt. Int. J. Light Electron Opt. **126**(23), 4206–4211 (2015)

15. Z. Chen, X. Shao, X. Xu, X. He, Optimized digital speckle patterns for digital image correlation by consideration of both accuracy and efficiency. Appl. Opt. **57**(4), 884 (2018)
16. J. B. Estrada, C. Franck, Intuitive interface for the quantitative evaluation of speckle patterns for use in digital image and volume correlation techniques. J. Appl. Mech. **82**(9), 095001 (2015)
17. P. Lopez-Crespo, A. Shterenlikht, E. A. Patterson, J. R. Yates, P. J. Withers, The stress intensity of mixed mode cracks determined by digital image correlation. J. Strain Anal. Eng. Des. **43**(8), 769–780 (2008)
18. S. N. Atluri, A. S. Kobayashi, Mechanical responses of materials. Handb. Exp. Mech. 1–37 (1993)

Part XI
Failure Analysis

Failure Investigation of an Industrial Turbine Blade

A. H. V. Pavan, M. Swamy, G. Jayaraman and Kulvir Singh

Abstract A 30 MW industrial turbine set suffered failure during operation. The unit was shutdown and the turbine casing was opened to realize that a blade failed at the root. The root portions of the failed blade which were locked in the rotor were dismantled and sent to the laboratory for detailed failure analysis. Chemical analysis indicated that blades were manufactured as per specification. Microstructural characterization confirmed the presence of uniform tempered martensite, which was in conformance with the material standards. Visual examination and stereomicroscopic examination were carried out and it was observed that one of the root portions showed crack propagation features originating from the clamping pin location while the other portions indicated overload failure kind of features. Field Emission Scanning Electron Microscopic (FESEM) investigation confirmed the location of crack origin at the interface of clamping pin. Fretting debris was not observed at the crack origin eliminating the possibility of fretting fatigue failure mechanism. Elemental analysis using Energy-Dispersive X-ray spectroscopy (EDS) at the crack origin revealed the presence of elements such as Cl, S, Ca, etc. This led to suspicion on the chemistry of water utilized for generation of steam for running the turbine. Upon detailed review of water chemistry, it was confirmed that the same deviated from specified values. It can, therefore, be concluded that crack origin location being a highly stressed region in conjunction with the presence of elements such as Cl, S, Ca, etc., could have caused stress corrosion cracking leading to crack initiation. Subsequent load hunting of the turbine led to fast propagation of this crack to failure. The comprehensive procedure followed for carrying out failure investigation and detailed results obtained are discussed in this paper.

Keywords Industrial turbine · Stress corrosion cracking · Water chemistry · Turbine root failure · Load hunting

A. H. V. Pavan (✉) · M. Swamy · G. Jayaraman · K. Singh
Metallurgy Department, Corporate R&D Division, Bharat Heavy Electrical Limited, Vikasnagar, 500 093 Hyderabad, Telangana, India
e-mail: pavanahv@bhel.in

1 Introduction

Industrial turbines are very important equipment for generation of power either for captive needs (i.e., electricity will be utilized by the same industry) or for supplying it to the grid. In a typical industrial scale, they are of the following three types: (1) Gas turbines which use fuel from the industry to produce electricity; (2) Steam turbines which operate by pressurized steam obtained by burning fuel in a small scale boiler; (3) Steam turbines which operate in combined cycle generation mode, i.e., by utilizing hot flue gas from gas turbine output as heat input for production of steam using a heat exchanger. In general, industrial turbines have a typical operation capacity of less than 100 MW. There are various reasons reported for the failure of turbine blades at root section of which fretting fatigue, corrosion fatigue and stress corrosion cracking are the major ones [1–6].

In the present work, details are provided regarding failure analysis of turbine blade at root section. It was observed that during shutdown of a 30 MW industrial turbine set employed at a refinery, severe load hunting was observed. Upon opening the casing, it was observed that a blade failed at the root section as shown in Fig. 1. Damage to seal fins was also observed. Profile portion of the failed blade fractured and it underwent damage after detachment due to its impact with the turbine casing and subsequent stages of blades. Therefore, after dismantling the casing and blades, the following components were provided for root cause analysis: fractured root sections, damaged profile section of the fractured blade and an intact blade.

This work elucidates procedure for inferring the reason for failure of the blade and it is organized as follows: Sect. 2 provides (i) details of samples received, (ii) chemical analysis results, (iii) various equipment utilized for experimentation; Sect. 3 presents results obtained from tests such as visual examination, stereomicroscopic examination, microstructural examination, fractographic analysis, operation, and water chemistry related analyses along with discussion; Conclusions
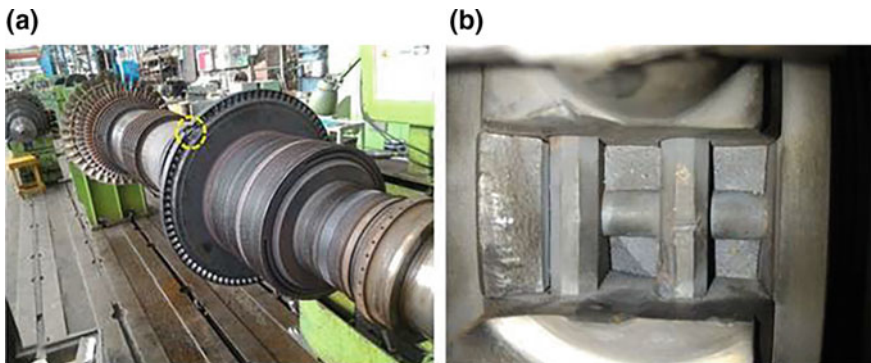
Fig. 1 **a** Failed location of the blade on the rotor; **b** Magnified view of the intact root portion below the clamping pins

deduced from current work and recommendations to prevent failures related to the present work are indicated in Sect. 4.

2 Materials and Experimentation

2.1 Details of Samples Received

Three numbers of failed blade root portion samples, damaged profile section of the failed blade and one number. of the intact blade were provided for carrying out metallurgical investigation and failure analysis. Failed blade portion samples were utilized for chemical analysis, stereomicroscopic examination, microstructural examination, and fractographic analysis while healthy blade sample was subjected to microstructural examination only.

2.2 Chemical Analysis

Chemical analysis was carried out at two locations on the damaged profile section of the failed blade using Optical Emission Spectrometry (OES). The results obtained are presented in Table 1. It was observed that the results are in agreement with the required material specifications.

2.3 Experimentation

Visual examination was carried out on all 3 portions of the failed blade root. The stereo-microscopic examination was carried out using Leica Z6 APO stereomicroscope. For understanding distribution of inclusions in the failed blade root sample and intact blade samples, grinding was carried out with a series of emery papers and they were subsequently polished with a suspended diamond particulate solution of 1 μm. Microstructural characterization studies were carried out using

Table 1 Chemical analysis of failed blade material (in wt%)

	C	Si	Mn	P	S	Cr	Mo	Ni	V
Min. specified	0.18	–	0.4	–	–	11	0.8	0.3	0.25
Max. specified	0.24	0.5	0.9	0.025	0.015	12.5	1.2	0.8	0.35
Location 1	0.23	0.3	0.69	0.02	0.01	11.98	0.93	0.53	0.34
Location 2	0.21	0.3	0.71	0.011	0.008	12.07	0.93	0.5	0.34

light optical microscopy by Leica DMI 5000 M Inverted Metallurgical Microscope. Detailed analysis of the fractured surface of failed blade root was carried out using Zeiss Supra 55VP Field Emission Scanning Electron Microscope (FESEM) coupled with Energy-Dispersive X-Ray Spectroscopy (EDS). All the results obtained are indicated in the subsequent sections of this work.

3 Results and Discussion

3.1 Visual Examination

Visual examination of all the three portions of the failed blade root was carried out. All the three blade root portion samples were marked or identified as sample 1, 2, and 3 (as presented in Fig. 2). It was observed that there were some metallic copper colored marks on the fractured surface of the blade root portion samples. Also, it appeared from surface morphology that Sample 1 was typical overload failure case.

Since fractured blade root portion samples might yield fruitful information which might explain the root cause for failure, detailed stereomicroscopic, and Scanning Electron Microscopic (SEM) studies for obtaining detailed information at higher magnifications were carried out on failed blade root samples which are elucidated in the following sections.

3.2 Stereomicroscopic Examination

Stereo-microscopic studies were carried out on all three sections of the failed blade root. Prior to stereomicroscopic analysis, the as-received samples were subjected to ultrasonication in fresh ethanol for 15 min duration in order to remove grease,

Fig. 2 Nomenclature and as-received fractured surfaces of blade root sections for failure analysis

debris, etc., from the fractured surface. This was carried for exposing various features on the fractured surface.

Typical overload failure (fast/final fracture) features observed in the case of sample 1 as shown in Fig. 3a. This part of the root is the last portion of the root to fail. Rust was observed even after cleaning the sample.

In case of sample 2, failure took place from the hole through which the clamping pin was inserted for holding the blade to the rotor firmly. No beach marks were observed over the fracture surface of this sample. The fractured surface was found to have copper colored deposits. A region marked over the fractured surface in Fig. 3b indicates overload features suggesting that sample 2 is an intermediate section of the root to fail.

Sample 3 also failed from the hole where clamping pin passes through. A few dent-like features were observed on the fractured surface possibly due to improper handling of the sample or during removal of samples from the rotor. Fractured surface in this case also was found to have copper colored deposits. Beach marks like features observed in region 1 as shown in Fig. 3c and the crack origin was identified in the same region of the fractured surface.

Since no copper-colored marks/deposits were present during the inspection of the fractured samples in the assembled condition in the rotor, it can be concluded that they might have come up during removal of samples from the rotor. Hence, these are ignored in further analysis and are not the cause for failure.
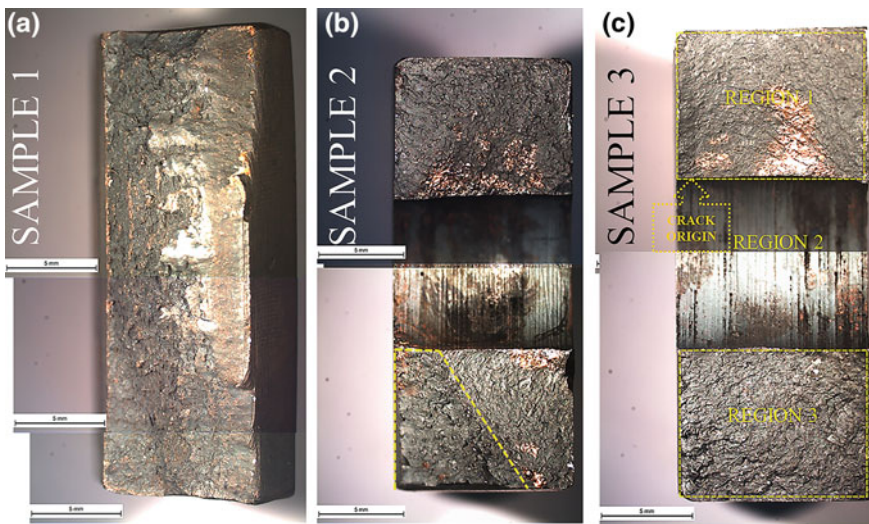
Fig. 3 Stitched stereomicrographs of fractured surface of as-received root sections. **a** Sample 1 indicating overload fracture kind of features. **b** Sample 2 indicating copper colored deposits on fractured surface with a marked region indicating overload fracture kind of features. **c** Sample 3 indicating beach mark features with crack origin in region 1 as indicated over the fractured surface

3.3 Microstructural Examination

Shroud portion of the healthy blade (i.e., the top surface of the blade) and root section of sample 1 (from the failed blade) were subjected to microstructural investigation. Samples were observed in as-polished condition for the analyzing distribution of inclusions. A very few inclusions were observed. Subsequently, etching was carried out on these specimens using Vilella's reagent. The microstructures obtained from the shroud portion of the healthy blade indicated a tempered martensitic structure. Similarly, those obtained from sample 1 are presented in Fig. 4 which also indicate the same. This is in compliance with the specified microstructure requirement.

3.4 Fractographic Analysis Using Field Emission Scanning Electron Microscope (FESEM)

Higher magnification stereomicrograph indicating the origin of the crack and direction of propagation over the fractured surface of sample 3 is presented in Fig. 5a. FESEM investigation with EDS was carried out on this sample for a better understanding of fracture features and surface chemistry at crack origin location. This sample for fractographic analysis was prepared by ultrasonic cleaning in ethanol medium for 15 min and vacuum drying for 48 h. Fractograph showing crack origin location and direction of propagation is presented in Fig. 5b.

During fractography, it was observed that the fractured surface was covered with rust and region close to crack origin showed the presence of a dent due to mechanical damage probably caused while removing the sample portion from the root. The fractured surface showed transgranular features indicating that the propagation occurred under higher stress levels. This dent is not a cause for failure. No fretting debris was observed. Hence, failure is not attributed to the fretting mechanism. EDS studies indicated that the fractured surface, especially at origin location, contained Cl, S, Ca, etc. (Figure 6). This raised suspicion on water/steam
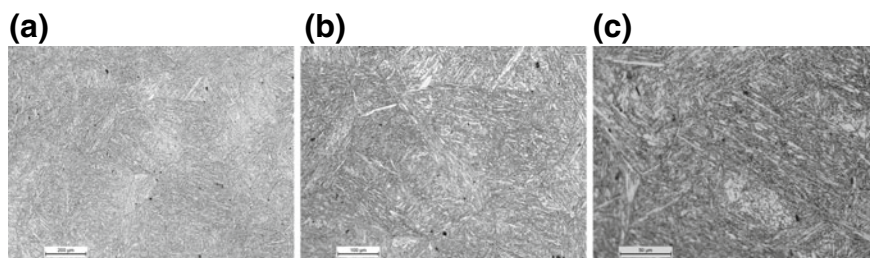
Fig. 4 Optical micrographs of root portion (from Sample 1) indicating tempered martensite structure at the following magnifications, **a** 100X, **b** 200X, **c** 500X
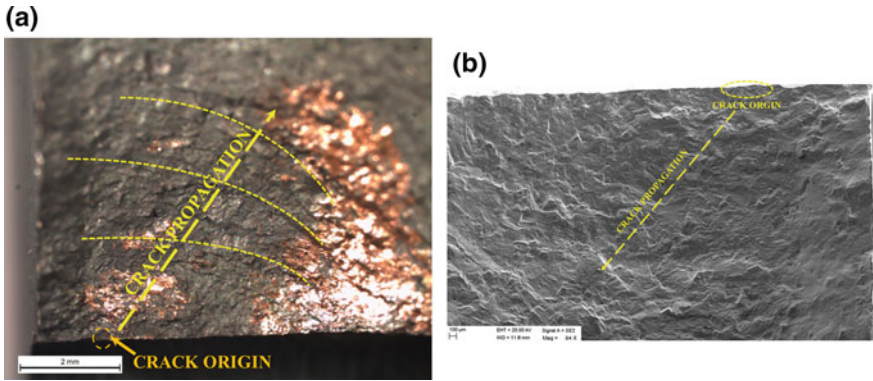
Fig. 5 **a** Stereomicrograph indicating the enlarged view of Region 1 of Sample 3 (as shown in Fig. 3) indicating the origin of crack, propagation direction, and beach mark like features; **b** Identification of crack origin on the same sample using FESEM
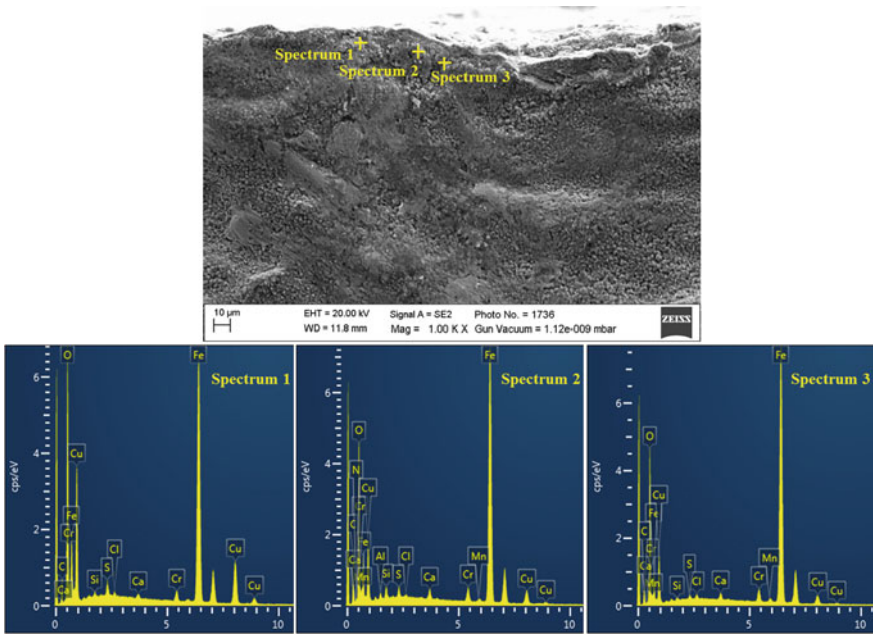
Fig. 6 EDS spectra corresponding to various locations shown in FESEM fractograph at 1000X showing the presence of Cl, S, Ca, etc., at crack origin region of Sample 3

chemistry which is reviewed in the following subsection of this work. It was also observed that significant amount of Cu was observed on fractured surface and this can be attributed to the procedure followed while removing the fractured portions of root from the rotor which was indicated in Sect. 3.2 of this work.

3.5   Water/Steam Chemistry

Water/Steam chemistry data obtained from the site of working was thoroughly reviewed and analyzed for deviations which can lead to corrosion. It was observed that pH values and/or conductivity values of demineralized water, feed water, condensate from the steam turbine, saturated steam and superheated steam of various components are higher than the specified limits. Also, it was observed that chlorides were present in condensate from the steam turbine. Higher pH and conductivity may be caused by a higher presence of hydroxide ions which lead to deposition of alkaline elements such as Ca, etc. over the crack origin location and fractured surface. These alkaline elements were observed over the fractured surface. Higher chloride leads to increased susceptibility to pitting which is a discontinuity [5] and can lead to crack initiation and growth when load abnormalities exist [7–9].

3.6   Operation Related Details

After reviewing the load and operation related details of the turbine, it was understood that the steam turbine was manually stopped on a specific day due to internal requirements. The extraction drain was also choked during this incident. Hence, this incident led to severe load hunting which persisted for more than one minute until the steam turbine tripped manually. Also, the shaft vibration of turbine went up during this event.

3.7   Discussion

Stereomicroscopic observation revealed that (a) Sample 3 is the first section to fail due to crack propagation like features over its fractured surface, (b) Sample 2 is the intermediate section to fail due to presence of small overload (fast fracture) features, (c) Sample 1 is the last section to fail due to overload (fast fracture) failure features on it. This happens when the blade is supported only by one section of root. In addition to the above, stereomicroscopic analysis of sample 3 inferred that crack origin was observed within the hole on the root meant for inserting the clamping pin as shown in Fig. 3c. FESEM examination of sample 3 at crack origin confirmed the presence of deposits which when analyzed by EDS were confirmed them to be rich in Cl, S, Ca, etc., over the fractured surface as shown in Fig. 6.

Upon review of water chemistry it was observed that pH (alkalinity) and/or conductivity were higher than required values. Higher alkalinity also depicts that alkaline elements such as Ca, etc. would have deposited on the cracked surface. Also, the steam condensate showed the presence of chloride ions. These chloride ions can cause pitting [5, 8]. These pits act as crack initiation sites where most of

the life fraction for a crack is spent and they tend to propagate in the presence of higher loads which takes significantly lower life fraction [7–9]. In the present case, crack origin can be attributed to the presence of Cl, S, Ca, etc. in the steam condensate. It was also observed in Fig. 5b that the fractured surface is transgranular and this occurs when a crack propagates at higher stress levels. From the operation history, it can be understood that when load hunting took place during shutdown of the turbine due to choking of extraction drain, loads over the blades would have increased tremendously. This might have led to fast propagation of crack as observed by a few beach marks on the fractured surface radiating into the blade root from the crack origin.

4 Conclusions

The following can be concluded from the investigations carried out as a part of this work:

1. Chemical composition and microstructure of the material were as per the required specifications.
2. Visual inspection indicated (a) damage to fractured surfaces as observed from a few dent-like features and (b) the presence of copper-colored marks (confirmed to be rich in copper from EDS analysis). These might have originated during the removal of failed root portions from the rotor and are not responsible for failure.
3. Fractography of Sample 1 by FESEM clearly indicated that fractured surface was covered by rust and there is damage close to the crack origin. The fractured surface consisted of transgranular features indicating higher stresses. No fretting debris was observed near the crack origin or in the surface of the pinhole ruling out the possibility of crack origin by the fretting mechanism. The beach marks (propagation lines) are observed to be faint, lesser in number and with a wide gap between them, as observed by both FESEM and stereomicroscope which indicate faster propagation of crack and failure. EDS studies indicated that the fractured surface consisted of Cl, S, Ca deposits.
4. Water/steam chemistry clearly indicated the presence of chlorides in steam turbine condensate on a few days. It also indicated that water and/or steam, as applicable, deviated from pH and conductivity requirements. This was observed to be more alkaline, therefore indicating higher dissolved oxygen content and hydroxide content, leading to deposits formation in the long run. Also, chlorides lead to increased susceptibility to pitting of the components which lead to crack initiation and propagation under the action of load variations. The same might have contributed to crack initiation in this case. This might have led to Cl, S, Ca deposits over the fractured surface and also at the crack initiation location.

5. Load hunting was observed, which occurred due to extraction blockage, thus, increasing load on the blades bypassing all the steam through the turbine to the condenser. This might have increased load over the blades, leading to faster crack propagation as observed from the transgranular fracture features.
6. Therefore, the blade failure can be attributed to stress corrosion cracking coupled with load hunting.

The following recommendations are to be followed in general for averting these kinds of failures:

1. Fitting procedure and clearances of the tapering pin must be followed as per design requirements. This is required to ensure no gap between the pin and the hole in the blade root segment such that no condensate nor deposit can enter/settle during start-up or shutdown and hence, prevents susceptibility to crack initiation by chloride, sulfide, or alkaline elements.
2. Water chemistry requirements have to be followed stringently.
3. Load hunting must be avoided by following the detailed procedure for start-up/shutdown as indicated in the operation manual.
4. Drains and strainers should be prevented from choking. This is due to that fact that if choking occurs, the load over the turbine increases and will lead to increased load on the blades.

References

1. N.K. Mukhopadhyay, S. Ghosh Chowdhury, G. Das, I. Chattoraj, S.K. Das, D.K. Bhattacharya, An investigation of the failure of low pressure steam turbine blades. Eng. Fail. Anal. **5**, 181–193 (1998)
2. M.C. Antony Harison, M. Swamy, A.H.V. Pavan, G. Jayaraman, Root cause analysis of steam turbine blade failure. Trans. Indian Inst. Met. **69**, 659–663 (2016)
3. D. Ziegler, M. Puccinelli, B. Bergallo, A. Picasso, Investigation of turbine blade failure in a thermal power plant. Case Stud. Eng. Fail. Anal. **1**, 192–199 (2013)
4. L.K. Bhagi, P. Gupta, V. Rastogi, Fractographic investigations of the failure of L-1 low pressure steam turbine blade. Case Stud. Eng. Fail. Anal. **1**, 72–78 (2013)
5. W. Tianjian, P. Yubing, G. Zhenhuan, F. Hua, Y. Gongxian, Stress corrosion behavior of 12Cr martensite steel for steam turbine LP blade, in Proceedings of the Energy Materials 2014, CSM and TMS, TMS, pp. 327–332 (2014)
6. G. Das, S. Ghosh Chowdhury, A. Kumar Ray, S. Kumar Das, D. Kumar Bhattacharya, Turbine blade failure in a thermal power plant. Eng. Fail. Anal. **10**, 85–91 (2003)
7. R. Ebara, Corrosion fatigue crack initiation in 12% chromium stainless steel. Mater. Sci. Eng. **468–470**, 109–113 (2007)

8. J.R. Donahue, J.T. Burns, Effect of chloride concentration on the corrosion-fatigue crack behavior of an age-hardenable martensitic stainless steel. Int. J. Fatigue **91**, 79–99 (2016)
9. H.P. Seifert, S. Ritter, The influence of ppb levels of chloride impurities on the stain-induced corrosion cracking and corrosion fatigue crack growth behavior of low-alloy steels under simulated boiling water reactor conditions. Corros. Sci. **108**, 148–159 (2016)

Fault Diagnosis and Root Cause Failure Analysis of Press Roller Mill for Heavy Industry

S. Babu, N. Murugan, M. Amudhan and T. S. Lagnesh

Abstract This case study is to identify and evaluate the root cause for failure of a roller press mill. Cement plant has a heavy crushing operation the roller's top surface is eroded, which is replaced by hard metal deposition by welding. In manufacturing, most of the steel metals are failing by either fatigue or by hard deposition through welding. In this case, repair welding has been used for several years. But there is no specific welding procedure adapted to repair the large size of the rolling parts as it is very difficult to operate in that situation and constraints of the welding operation. In this connection, the plant was inspected, their log book was verified, and the complete procedure of welding was checked. Further study was done by cutting the small piece of the press roller mill's material by using diamond abrasive cutter and it was used to prepare the test specimen using wire cut EDM. Further composition of the welding rod and base material were found by SEM study. Subsequently, their hardness values were also measured. From this study, it is concluded that the welding procedure was not followed properly and oxidation took place during the time of weld, because of the large variations of the weldability of the material over the surface of the base metal and also the presence of blue patches in the weld metal during SEM analysis.

Keywords Failure analysis · Roller press mill · Clinker · SEM · Fracture · Case study

S. Babu (✉) · M. Amudhan · T. S. Lagnesh
Department of Mechanical Engineering, PSG College of Technology, Coimbatore 641004, Tamil Nadu, India
e-mail: sjsham@gmail.com

N. Murugan
Department of Robotics and Automation Engineering, PSG College of Technology, Coimbatore 641004, Tamil Nadu, India

1 Introduction

The failure analysis is one of the important fields of mechanical engineering and it is becoming unavoidable in almost all the applications of engineering. In the work carried out by N. Venkatesh on "Design and Analysis of a Hydraulic Roller Press frame assembly", the frame assembly was optimized and redesigned in terms of overall weight reduction [1]. Jean-Luc Desir studied the fatigue failure of steel sections and proposed a specific welding procedure for large size of the parts in his paper "Examples of repair welding of heavy machinery subject to breakage due to low frequency alternated stresses" [2]. J. D. Buch studied and analyzed about the foundation of a cement mill and proposed the structural arrangement in his paper, "Foundation for roller press in a cement plant: A case study" [3]. Ernst Worrell and Christina Galitskyin their paper "Energy efficiency improvements and cost saving opportunities for cement making", discussed the substantial potential for energy efficiency improvement in the cement industry [4]. The repair of chill cast roll bodies are discussed in the Polycom machine manual.

From the above literature survey, it is evident that the study of failure analysis of a cement roller mill's base material and the repair weld is limited to a little. This study by the author has been done on the failure analysis of the base material and the repair weld material.

2 Background

The scope of the case study is to identify and evaluate the reasons for analysis of root cause for failure of Roller Press mill and submit a technical evaluation report providing the causes of the failure and suggestions to avoid the chances of such failures in near future. This roller press machine is used to grind the clinkers. The bulk material is fed to the gap between two rollers which are driven in counter rotation as shown in Fig. 1. The necessary press force is created by a hydraulic—pneumatic system which works like a spring. The movable roller is actuated towards the static roller with the help of a hydraulic cylinder to grind the clinkers fed from the vertical chute/hopper over the rollers. The roller comprises of a steel shaft and a mounted tire made of "bainite". In a roller press, clinker material is subjected to entrance pressure between opposing roller for a short time. The moveable roller can be positioned by about 45 ± 10 mm laterally to adjust the space between rollers depending on the size of materials to be rolled between the rollers. As such rollers are subjected to low frequency alternated repeated stresses. Failure by fatigue has been considered during the design. A repair welding technique has been developed and used on several such rollers. A specific welding procedure, to be adapted to such large size rolling parts, is very difficult to apply in in situ condition due to the constraints of the welding operation/procedure.

Fig. 1 Roller press used in a cement plant
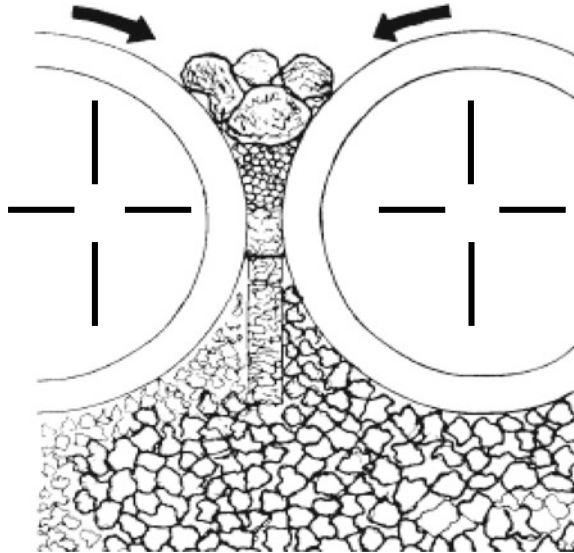
3 Maintenance Work

From the information collected, it was observed that the plant is stopped during the second week of each and every month, for scheduled maintenance to be carried out for rebuilding the rolls. The grinding surface/profile of the bainite tires are filled with metal by welding in a zigzag pattern, using special welding equipment and wires supplied/recommended by the OEM, to manage the wear/loss of surface metal of the bainite tire as well as to maintain the grinding efficiency. From the information available, the roller press was stopped for monthly maintenance. After leaving the machine for cooling, the doors were opened for maintenance (allowing 08:00 h. cooling period). The profile welding was started at about 05.00 p.m. after sandblasting the surface. The welding process was stopped at about 21:00 h. The welding technicians heard abnormal sound from the roller and noticed longitudinal crack throughout the fixed roller tire body from profile surface to seating ends of the shaft. The crack was fresh over the welded surface of the cylinder body/bainite tire and the shaft was not affected. Both the rollers were replaced with the spare rollers in the mill. The old rollers were kept in open near the roller press plant. The Faculty members of PSGCT inspected failed roller and found the same type of longitudinal crack in the movable roller (removed from the machine and kept in open), while they were in the process of removing the water jacket from the failed movable roller, to fix with the new roller replaced in the machine. The crack in the floating/movable roller was also fresh and over the newly welded area (welding is done as per the maintenance practice).

4 General Observations

From the visual inspections of the failed roller, the following points were observed that weld deposit consists of full of porous welds containing gas pockets. This may be due to inadequate shielding during the hard deposition which may be carried out under an open environment or under the industrial fan. This might have led to oxidation of the deposit as shown in Fig. 2.

It was found that the combination of welding filler material and base material was not a suggested pair as referred in welding manual which might have resulted in the formation of surface crack as shown in Fig. 2. A lot of pores are visible on the hard deposited as shown in the same figure. It is also observed from that the clearance of about 7 cm between roller edge and weld deposits as per the Repair Manual is not maintained.

From the above observation, it is very clear that the crack was initiated due to thermal stress, which occurred because of improper welding [4, 5]. A certain cement plant had undergone a problem in the roller in which the treads were subjected to frequent wear. The plant was inspected, their log book was verified, and the complete procedure of welding was checked. Crack was formed on the roller mill's base material because of being subjected to high subsurface thermal stress. A sample of the base material was taken for analysis. In order to retread the base material, a welding procedure was followed which is described in the following section.
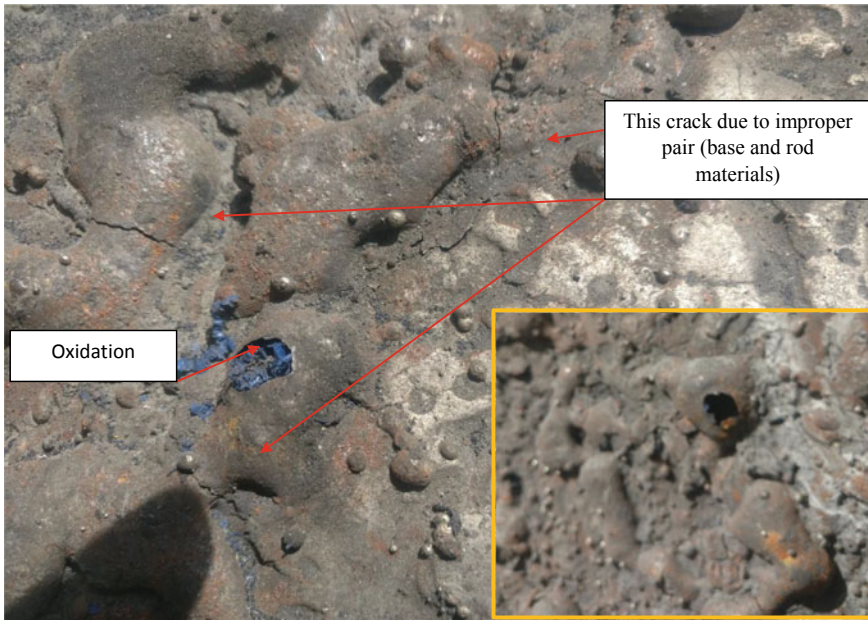
Fig. 2 Press roller surface with oxidation

5 Experimental Analysis

To analyze the material composition and properties of the weld, a sample (which has a flat surface) is necessary.

Composition Analysis: After the preparation of the sample, to determine the composition, two methods are there namely scanning electron microscope and optical emissive spectroscopy. We went for the latter because of certain advantages. Scanning electron microscope needs a larger sample piece. The sample should also have flatness with reference to the base. But our sample was small. So optical emissive microscopy was selected.

Optical Emissive Spectroscopy: The optical emissive spectroscopy is the method used to find the composition of the material by applying electric energy in the form of spark generated between the electrode and our sample which vaporizes the atoms. The atoms which are brought to higher energy state are called discharge plasma. And this excited atoms and ions generate emission spectrum lines. These spectral lines are unique to a particular element. By viewing these spectral lines, we can find the composition of the sample. The results obtained from the optical emissive spectroscopy are discussed in the results and discussion section.

Hardness Determination: Once the composition of the material was found out, the next objective was to determine the hardness. The hardness scale for stainless steel was C. But for conducting the hardness test, the sample was required to be flat on both the sides in order to mount. In addition to this, a well-finished surface was also needed other than the one used for material analysis. So, the opposite face of the analyzed surface was decided to be the surface to be used for hardness testing.

6 Results and Discussions

Weld Defects: The defects found in the weld are blowholes, oxidation, etc. Initially, the blowhole that is formed in the tread is due to the entrapped gases during the welding process as shown in Fig. 3. These gases are entrapped because of the

Fig. 3 Welded spot below hole

differential solidification of the welded tread. So these blowholes are the main reason for the formation of the crack in the welded tread. But these blow holes are not the reason for the wear of the tread. Wear is a material property which can be caused due to the inclusions present in the welded sample. So in order to avoid the problem of wear, we must choose better electrode and better welding procedures such as proper shielding, proper filler material with better strength, etc. The weld defects were found to be due to the thermal residual stress which is created due to shrinkage of hard deposition. Proper preheat and post heat treatment should be made.

SEM with EDS Results: The results obtained from the optical emissive spectroscopy are given below. (1) ZAF Method Standard less Quantitative Analysis (Fitting Coefficient: 0.35), (2) ZAF Method Standardless Quantitative Analysis (Fitting Coefficient: 0.25), (3) ZAF Method Standardless Quantitative Analysis (Fitting Coefficient: 0.26). Sample results are shown in Fig. 4.

It is clearly evident from the microstructure that the failure is due to some kind of ductile cum brittle failure. Ductile failure can be seen as dimple-like structure in the microstructure. Ductile kind of failure is initially happening and then the brittle failure happens. The white patches in the specimen indicate some kind of inclusions and rust is formed in the given sample to us. This can lead to brittleness which ultimately leads to wear and failure of the tread. In order to increase the wear resistance, proper welding procedure must be followed. Wear can be reduced by doing a proper surface treatment.

Rockwell Hardness Test Results: The prepared mold was then supposed to be undergoing hardness tests. The main types of indentation hardness test available are Vicker's, Brinell, and Rockwell hardness test. Among them, the Brinell hardness test makes use of a larger ball indenter (10 mm diameter) as shown in Fig. 5. So this method was not suitable for our small sample. In the Vicker's hardness test, the indenter was designed in such a way that it gives an impact force to the sample. Since our sample was very light, it would slip from the setup if we go for Vicker's hardness. So the only available test was Rockwell hardness test, which is also widely used in industries.
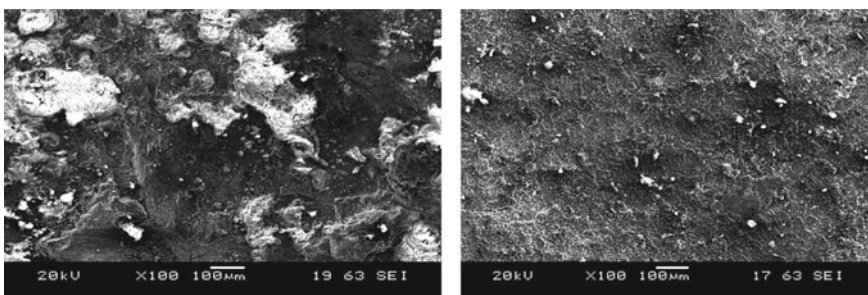
Fig. 4 Optical emissive spectroscopy image

Fig. 5 Hardness test specimen image
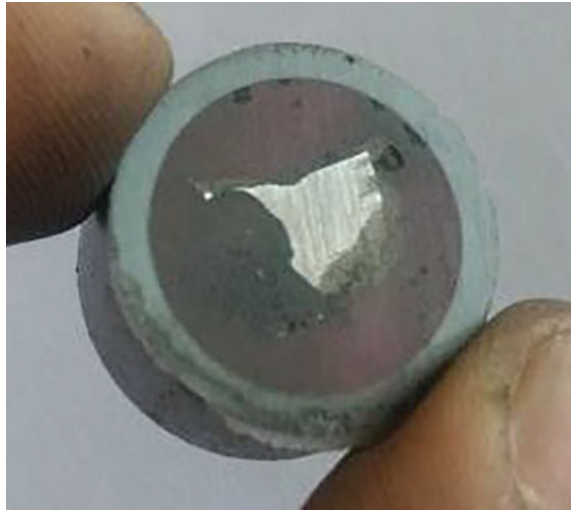
The results from the Rockwell hardness test of the weld sample are tabulated below.

Trial	Scale	Load applied (in kg f)	Hardness Value
1.	C	30	58
2.	C	30	59
3.	C	30	58

7   Conclusions

Thus, a failure analysis was carried out on a roller press base. Material and the weld material used for the repairing and the reasons for failure are identified. Based on the results of SEM with EDS and the hardness test, it is found that the given filler material is a low-alloy steel. The hardness of the steel is nearly found to be 58HRC, which clearly indicates that the tread is in the Martensite state which can lead to crack. So they must do welding by following the Welding Procedure Qualification. A suitable electrode must be chosen and proper shielding has to be provided. So based on this electrode, a suitable strength filler material, welding current, and temperature has to be chosen. For stainless steel, there is no need for preheating. From our sample, it is clear that the sample is a low-alloy steel for which the preheating is mandatory. But here the preheating is not done so there is a fast cooling which results in the formation of martensite state which leads to the crack formation. So we have to do preheating and then we have to slow cooling so that we have no martensitic structure in our tread.

References

1. Welding manual of "*Repair of chill cast roll bodies of the POLYCOM*"
2. J.- L. Desir, Examples of repair welding of heavy machinery subject to breakage due to low frequency alternated stresses. in Case History on Integrity and Failures in Industry, pp. 109–120
3. A. A. Omar, Effect welding parameters on hard zone formation at dissimilar metal. weld. J. **77** (2) (1998)
4. Manual of Fundamentals of Hard facing arc welding, welding alloy group; www.welding-alloys.com
5. http://www.lincolnelectric.com/en-us/support/welding-how-to/pages/cracks-hardfacing-welds-detail.aspx

Fatigue Failure of a Spiral Bevel Gear in a Typical Low-Bypass Turbofan Engine

P. M. Shantiswaroop, S. A. Savanur, Benudhar Sahoo and Chinmay Beura

Abstract In a twin spool turbofan engine, power gets transmitted from the HP (high pressure) rotor to the engine accessories gearbox (EAGB) to drive various accessories through a pair of spiral bevel gears. Over the years, straight bevel gear assembly has been modified to spiral bevel gear configuration for providing a smooth operation. This case study deals with failure analysis of a spiral bevel gear having 1.5 module, 28 numbers of teeth, rotating at approximately 16,000 RPM and transmitting a power of approximately 350 KW. The gear has logged 1341.19 h after installation against the specified life of 1400 h. Failure of the gear has resulted in excessive generation of metallic particles leading to the seizure of high-pressure rotors during flying. This gear is manufactured from a low-alloy steel 12Х2НВФА-ВД of Russian origin by forging route with surface hardened by carburizing with a case depth of 0.6–1.0 mm. The spiral bevel gear has broken into three fragments approximately 120° apart. Stereomicroscopic examination reveals fatigue striations which could be observed distinctly with the help of Scanning Electron Microscope at a magnification of 3000×. The fatigue failure has progressed at the root of the gear across the tooth thickness and with initiation at an under-filling having an approximate size of 10 μm by 30 μm on the working side. No metallurgical abnormality is attributed to the failure of gear. As the subjected gear failed during flag end of its specified technical life in a progressive mode with a flaw near surface, magnetic particle inspection of the gear has been introduced during overhaul.

P. M. Shantiswaroop · S. A. Savanur · B. Sahoo (✉)
RCMA(KPT), CEMILAC, DRDO, Sunabeda, India
e-mail: bsahoo543@gmail.com

C. Beura
HAL, Koraput, India

1 Introduction

A gas turbine consist of mainly five modules namely intake, compressor, combustion chamber, turbine, and jet nozzle. These five module work on the principle of Brayton Cycle to produce the desired work output plus the thrust. The work output in terms of shaft power is divided into two parts, one is used to sustain its own working cycle and the other part is utilized to run the accessories fitted in the aircraft. The shaft power produced by the engine gets transmitted through an engine mounted gearbox to drive various accessories such as fuel pumps, hydraulic pumps, starter generator, etc. The gearbox is the main linkage between the core engine and the accessories. Any failure or malfunction of gearbox can lead to loss of drive resulting in flameout of the engine leading to a single engine landing in twin-engine aircraft. This is a case study of the failure of a spiral bevel gear in the main transmission line of a low-bypass turbofan twin-engine aircraft resulting in the emergency landing.

Gearbox comprises of various gears of different shape, size and type and its function is to transmit power from a source to different components by dividing the total available power. Gearbox mainly is meant to step down or step up the speed of the source and supply to various accessories for the intended speed by selecting the proper gear ratio.

A gear transmits power or motion and force from one element in a working unit to another element in the same unit or to another working unit in the same plane or to a completely different plane. If the power transmission is in the parallel plane then spur gear is chosen, while for intersecting plane, bevel gear. Factors influencing the design and selection of gear are speed, gear ratio, availability of space, strength, smooth operation and to counter vibration.

Gear design is also a process of synthesis in which gear geometry, material, heat treatment, manufacturing methods, and lubrication system are selected to meet the requirements of a given application. The designer must design the gear with adequate strength, wear resistance, and scuffing resistance.

A gear at the surface must be sufficiently hard to resist wear and the core must be tough enough to resist shock. Carburized case hardened gears are best suited for heavy duty service and it also offers high resistance to wear, pitting, and fatigue. Case-hardened gear can withstand higher loads than thorough hardened gear, in spite of the latter are less noising and less expensive. The following factor must be considered when selecting a case hardened gear [1].

- High tooth pressure will crack a thin case (the case hardening must be of sufficient depth to prevent case crushing)
- Too soft a core will not provide proper backing for a hard case.
- Compressive stresses in the case improve fatigue durability and a high case hardness increases wear resistance.
- If the ratio of case depth to core thickness is too small excessive stresses in the subsurface layer can produce poor fatigue life.

- Residual tensile stresses are highest with low core hardness and increase with increasing case depth. These stresses can be relieved by tempering.

Gear failure can be classified into different ways. The American Gear Manufacturers Association (AMGA) has classified 36 modes of Gear failure under the broad categories of Wear, Scuffing, Plastic Deformation, Contact Fatigue, Cracking Fracture and Bending Fatigue [1]. L. E. Alban has classified gear failure into four groups—fatigue, impact, wear, and stress rupture [2].

2 Design and Manufacturing of the Failed Gear

This case study deals with the main bevel gear, which transmits about 300 kW at more than 15,000 rpm from the HP rotor to the engine accessories gearbox. This is a spiral bevel gear having 28 numbers of teeth with a module of 1.5 having a direction of inclination of the tooth towards left, pitch circle diameter (PCD) of 21, pressure angle of 20°. The gear is made of Russian-origin low-alloy steel 12Х2НВФА-ВД with an average carbon content of 0.12 wt% having melted through VIM (vacuum induction melting) + VAR (vacuum arc remelting) and refined by ESR route (Table 1).

Basic manufacturing route followed for manufacturing the gear is closed die forging while the finished shape is achieved by hobbing and grinding. This gear is case hardened up to a depth of 0.6–1.0 mm along the profile of teeth and for the remaining surfaces, it is hardened up to a depth of 0.6–1.2 mm. The hardness of case hardened surface is HR_C 60–64 while that of the core is HR_C 32–42.5. To have a tempered martensite structure, it undergoes low-temperature tempering at a temperature of 200 °C for one hour. To reveal the flaw if any, the gear gets subjected to various NDE such as red dye penetrant inspection and MPI (magnetic particle inspection). The assembly of the gear is checked by the contact pattern of both the meshed gears. Generally, there are two ways of checking the contact pattern, i.e., with no-load and under load. In both the cases, usually a Prussian blue of thickness approximately 8–10 μm is applied at the pinion and the mesh is rotated to get a contact pattern on the other gear. The geometry of the contact pattern along with its position indicated the wrong dimension/assembly which necessitates correction. This method is known as a blue check because of the use of Prussian blue. Ideally, a smooth transfer of load is indicated by a typical fishtail pattern.

Table 1 Specified chemical composition of gear material

	C	Cr	Ni	Mn	Si	W	V
Wt (%)	0.09–0.16	1.90–2.40	0.80–1.20	0.30–0.70	0.17–0.37	1.00–1.40	0.18–0.28

3   Methodology Followed for Failure Analysis

Although the sequence of failure analysis is subject to variation, depending upon the nature of a specific failure, the principal steps that comprise the investigation and analysis are as follows [3].

3.1   Background Data and Selection of Samples

HP (high pressure) RPM of the incident engine wound down from 93 to 0% in 2 s. The pilot switched off the right engine and carried out a single engine landing.

The incident engine has accrued 1341.19 h since new and 236.44 h since the last overhaul. Visual examination and FDR (flight data recorder) analysis of the last sortie was carried out. FDR analysis did not reveal any trend of RPM drop in the previous sorties and no abnormality was observed in any of the engine performance parameters. The oil sample was checked and metal particle was found. Manual cranking of RH (right hand) engine was carried out and it was found that LP rotor was free. This initial observation indicated a failure in the HP rotor and gearbox. Gearbox was dismantled from the engine. After removal of the gearbox rotation of the aero engine was carried out and HP rotor rotation was found smooth. Further during checking of gearbox, no smooth rotation of gear train was observed implying failure is within the gearbox. During strip examination of gearbox, broken main spiral bevel gear could be found.

During stripping, bevel gear found was broken from the base of the shank into three pieces at approximately 120° apart. The three pieces are marked as 1, 2, and 3, respectively, while the shank of the failed gear is marked as 4 as shown in Fig. 1. All the teeth of the bevel gear were found to be rubbed. Mounting bracket holding the bevel gear assembly was found deformed and circlip was dislodged from its position.

Fig. 1 Photograph of failed gear and serviceable gear

3.2 Visual Examination

The bevel gear was broken into three pieces and one tooth was dislodged from the gear and was separated from its place as shown in Fig. 1. The teeth of the gear and the disc portion were heavily damaged. All the teeth of the gear were heavily rubbed with some hard object and that might be secondary in nature. The root portion of the gear shows the presence of crack which might have caused further damage if it were in service. All the cracks are along a particular position of the root area.

3.3 Chemical Analysis

The semi-quantitative analysis of the chemical composition of the broken gear was done with the help of X-ray fluorescence spectroscopy. Chemical compositional analysis revealed Mn:0.4%. Si:0.27%, Cr:2.1%, Ni:1.0%, W:1.2%, and V:0.20%, which conformed to the specified material 12X2HBΦA.

3.4 Hardness Check

Hardness is a measure of the case carburizing and microstructural features such as tempered martensite. Both bulk hardness and variation in hardness from surface to core have been made to characterize the microstructure of case and the core of the failed gear.

3.4.1 Bulk Hardness

The bulk hardness of the case and core of the failed gear is measured using Rockwell hardness tester C-scale and is placed at Table 2, which conforms to specification requirements.

3.4.2 Hardness Survey

A piece was cut from the failed gear and was subjected to grinding of 3 mm and was further subjected to microhardness check at a distance of 0.1 mm each up to a

Table 2 Hardness of case and the core of the failed gear

Properties	Damaged gear
Case hardness	59–61 (HR$_C$)
Core hardness	34–36 (HR$_C$)

Microhardness survey of failed gear showing gradual decrease in hardness from case to core indicating there is no decarburization of the gear teeth

Fig. 2 Microhardness survey of failed gear showing gradual decrease in hardness from case to core indicating there is no decarburization of the gear teeth
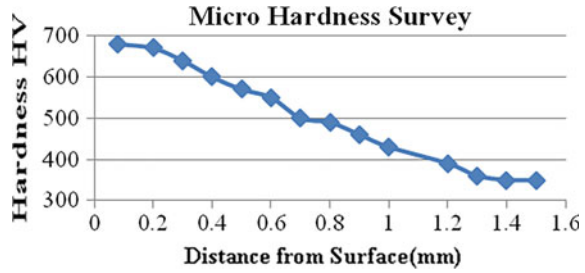
depth of 1.5 mm. During the hardness survey, the microhardness value gradually decreased from 690 $HV_{0.5}$ to 340 $HV_{0.5}$ at a depth of 1.5 mm from the root of the gear tooth indicating that there is no decarburization of the gear tooth. The microhardness survey report of the failed gear is shown in Fig. 2.

3.5 Optical Microscopy

The microstructural study of the failed gear indicated the presence of case carburized layer free from cementite network while the core microstructure shows a uniform distribution of tempered martensite.

The microstructure of both core and case of the failed gear as observed under the optical microscope are placed in Fig. 3a, b, respectively. From the above microstructure study and hardness of the damaged gear, it may be concluded that there is no metallurgical abnormality with the failed gear.

3.6 Fractography

The fracture surfaces of the broken pieces of the gear were observed with the help of a stereo binocular microscope of make Leica. All the fracture surfaces having a
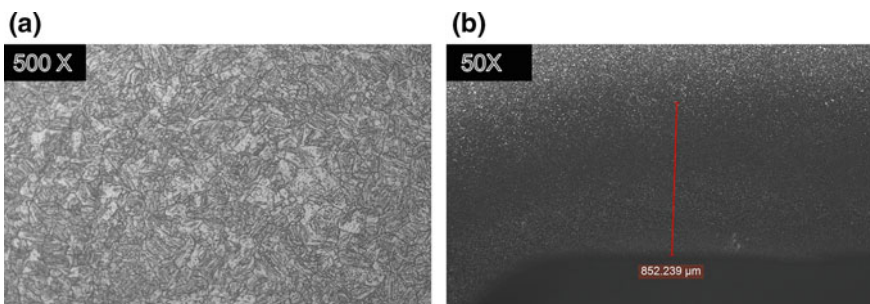
Fig. 3 Microstructural analysis **a** tempered martensite of the core, **b** carburized layer in the case
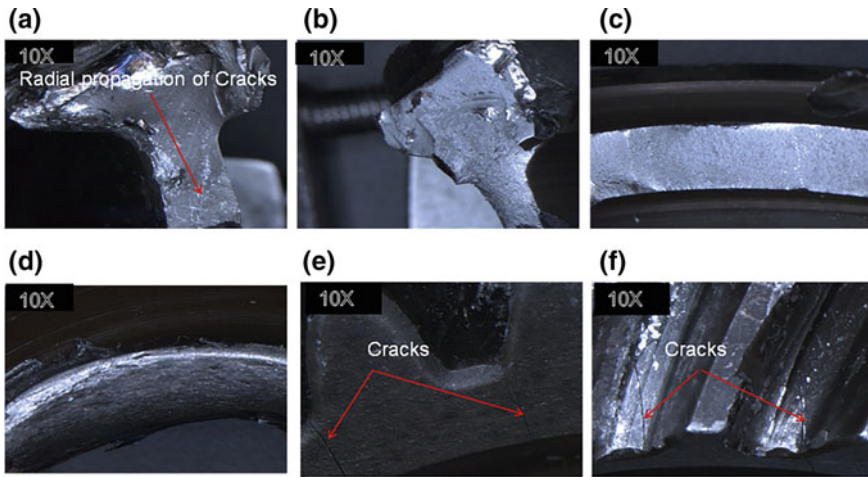
Fig. 4 View of fracture surfaces of failed gear in various orientations **a** propagation of cracks along radial direction **b** view of fracture surface indicating brittle mode of failure **c** flat fracture surface near shaft/hub, **d** showing one of the damaged fracture surface near the hub/shaft area **e** cracks in the root web region and **f** cracks in the tooth profile

signature of the brittle mode of failure as shown in Fig. 4a, b indicating propagation of crack in a very fast manner. A large portion of the fracture surface was also found to be in damaged as shown in Fig. 4c, d. Secondary cracks are observed on the flank and tooth of gear as shown in Fig. 4e, f, respectively. Breakage of the shank from the gear is secondary damage.

The broken piece of gear containing the fracture surface revealed fatigue striations as shown in Fig. 5a. The tooth adjacent to the fracture surface in Fig. 5b–c also contain fatigue striations on it. However here the fatigue crack has initiated at more than one locations showing multiple fatigue crack front. These multiple fatigue cracks might be secondary in nature. The root portion of the broken gear was also examined under stereo binocular microscope and development of a number of cracks were found. The position of all the cracks with respect to the gear
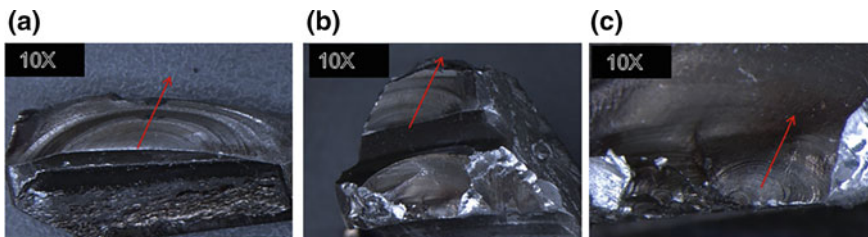
Fig. 5 Presence of fatigue striations on one of the tooth from the broken gear **a** half moon cut showing striations **b** presence of striations and **c** broken gear teeth at low magnification
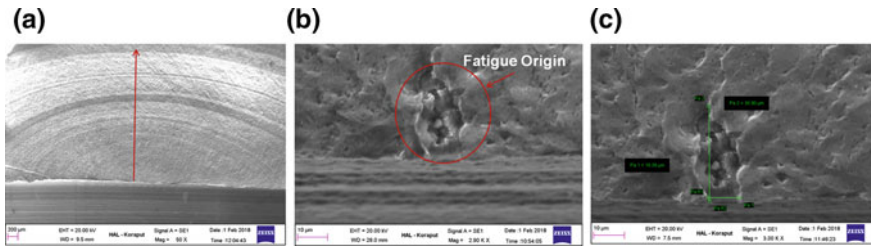
Fig. 6 Fatigue striations observed under SEM. **a** Arrow showing eye of fatigue **b** defect from where the crack has initiated and **c** crack initiation point with approximately defect size

tooth is found to be similar. Also, the fatigue cracks as seen in Fig. 5a, b are also formed along the same particular location with respect to the gear tooth.

The fracture surface containing the fatigue striations was further subjected to investigation with the help of Scanning electron microscope at magnification starting from $50\times$ to gradually increasing to $500\times$, $1500\times$ and then $3000\times$ magnification. The fatigue crack appeared to have developed from the center of the teeth. The area was seen under higher magnification to find out the origin of crack.

The SEM image of the fracture surface is shown in Fig. 6. The striation marks are concentric and the eye of the failure appears to be from the point as shown in Fig. 6a. The eye was found to be a small defect which was measured to be of width approximately 10 μm and length 30 μm as shown in Fig. 6c. The crack initiation portion was subjected to EDXS analysis. The EDXS analysis of the defect location could not reveal the presence of any nonmetallic inclusions like alumina, silicates, etc., which are generally found in case of alloy steel.

4   Stress Analysis of Failed Gear

Static structural analysis was carried out by FEM using ANSYS Version R15.0 to estimate the stress developed in the gear during its operation (Fig. 7).

Number of nodes were 75,101 while the number of elements was 46,088. It gets supported on the bearing which has been considered as a frictionless surface. The major load are its rotation of 4000 rpm approximately and bending load. Gear is made of low alloy hardened and tempered steel and having a minimum ultimate tensile strength of 900 MPa and yield strength of 700 MPa. The maximum principal stress is estimated to be 291.38 MPa near the root of the gear tooth profile as shown in Fig. 7.
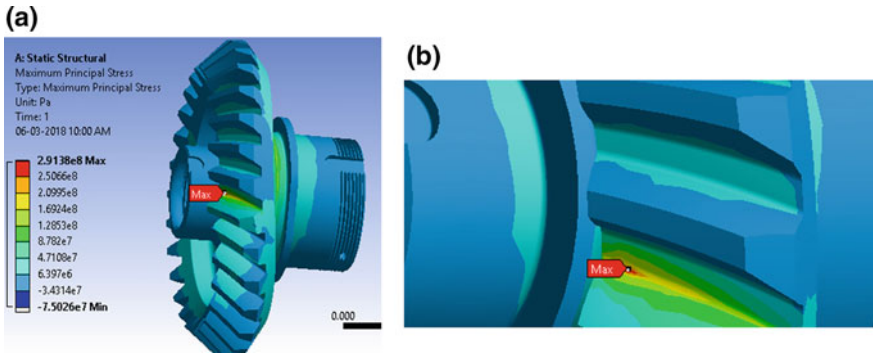
Fig. 7 Stress analysis of the failed gear **a** maximum principal stress **b** magnified view of max stress location

5 Residual Stress Measurement

Gears are designed against HCF, therefore, compressive residual stress at the surface enhances fatigue life. Shot penning is usually adopted to introduce compressive residual stress at the surface during the manufacturing of gear. Reduction of compressive residual stress during operation is an indication of fatigue life consumption. Residual stress was measured using X-ray diffraction method on the new gear and on a gear having operated for about 1400 h as that of failed gear. Full profile of the gear is covered by measuring residual stress at three points both on the convex and concave profile as in sketch in Fig. 8a. The residual stresses at various locations of the gears are plotted in Fig. 8b and it is found that there is a reduction of approximately. 100–150 MPa compressive residual stress on the Cat-B gear, i.e., operated for about 1400 h which in turn reduces the fatigue life.
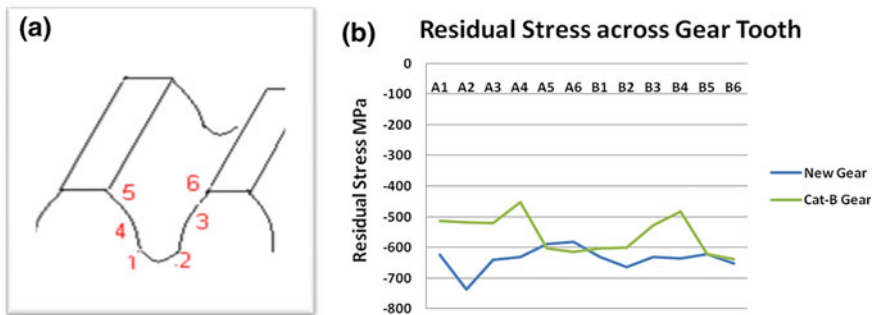
Fig. 8 Residual stress measurement **a** sketch showing the points on the gear teeth **b** Stress across various sections of gear tooth on new and cat-B gear

6   Discussion on the Results

From the metallurgical investigation, it may be concluded that a fatigue crack has developed near the center of the root of one of the tooth and subsequently it has propagated along the tooth. This tooth might have dislodged and caused severe damage to the adjacent tooth and resulted in breaking of the gear into three pieces. The origin of the fatigue crack was found to be a defect which was measured to be of size 10 μm × 30 μm approximately.

The failed spiral bevel gear is made of low alloy steel refined through ESR (electro-slag refining) route. The semi-quantitative chemical analysis, microstructural study and hardness check could conform to the specified material and processing. Further, as the alloy is manufactured through ESR route followed by ultrasonic inspection of the billet, a significant metallurgical flaw could be ruled out. This also could be confirmed by the EDXS analysis of the origin of fatigue indicating absence of any nonmetallic inclusion. As the gear is manufactured by forging, development of any unfilling cannot be ruled out. However, during the manufacturing of the gear, in the finished stage, gear gets subjected to MPI (magnetic particle inspection) to reveal any subsurface flaw which is more than 7 μm in size. A flaw having lower size than the sensitivity of MPI may remain undetected during manufacturing which might have grown into a critical size due to loading of gear in its operation. However, during subsequent overhaul, the failed gear gets only subjected to FPI (fluorescent penetrant inspection) which mainly reveal surface defects. The subsurface defect observed under SEM can't be detected by FPI during overhaul. Reduction in compressive residual stress on Cat-B gear is a measure of fatigue damage which further lead to the development of a flaw/or extension of the existing flaw to a higher size with each cyclic loading. As the origin of fatigue failure is with a flaw size of 10 μm × 30 μm, it can be easily detected by magnetic particle inspection during overhaul.

Gears are classified as safety-critical components and are designed against HCF. Static stress analysis of the gear states that the stress developed is well within the yield strength of the material under specified operating conditions. Also, the gears assembled in other engines having logged equivalent operating hours are subjected to FPI and MPI, and no abnormality could be revealed. Further, the same gear has worked for about 1400 h in other engines, therefore the failure may not be attributed to poor design. Now, MPI has been introduced during overhaul, which could detect any subsurface cracks, thereby such failure can be avoided in future.

7   Conclusion

The gear has failed in fatigue mode which is of progressive in nature and the origin is at the subsurface with an un-filling of 10 μm × 30 μm size located at the subsurface.

Gears are made of low-alloy steel for their toughness and followed by surface hardening to achieve the wear resistance against the mating gear. Carburising is generally adopted for providing wear resistance to the surface. FEM analysis reveals that under given operating conditions, the stress experienced by the gear is much lower to its yield strength, therefore, design lacunae may be ruled out. Further, the raw material being processed through ESR followed by sensitive NDE such as ultrasonic in billet and FPI and MPI on gear, the possibility of flaw developed in the material during its manufacturing is of less possibility. However, during operation in aero-engine, due to cyclic loading, a flaw might have developed which could lead to failure of the gear. Further, this can be explained by a reduction in compressive residual stress on the gear having operated for about 1400 h.

The failure of the main bevel gear is the primary reason for the engine failure. The gear has failed in fatigue mode. The origin of fatigue is at the subsurface with a defect of size which has developed a fatigue crack and which eventually led to the breaking of the gear. Magnetic particle inspection (MPI) has been introduced during overhaul in line with manufacturing technology. This failure is a classic example of tooth bending fatigue at mid-length of the tooth at the root radius.

References

1. J.R. Davis & Associates, *Gear materials, Properties and Manufacture* (ASM International, 2005)
2. L.E. Alban, *Systematic Analysis of Gear failures* (American Society for Metals, 1985)
3. Metal Handbook (Ninth Edition), *Failure analysis and Prevention*, vol. 11 (ASM, 1986)

Part XII
Fatigue

Low Cyclic Fatigue Behavior of Alloy 625 at Ambient and Elevated Temperatures

Mubashir Bashir, R. Kannan, R. Sandhya and G. A. Harmain

Abstract Nickel base superalloy, alloy 625 is chosen to be the candidate material for the casing of the rotor in the Advanced Ultra Supercritical (AUSC) power plant, being developed in India. The casing of the rotor is subjected to repeated thermal stresses as a result of temperature gradients that occur on heating and cooling during start-ups and shutdowns or during temperature transients that leads to the Low-Cycle Fatigue (LCF) deformation. The present study deals with LCF behavior of the alloy 625. LCF tests were conducted on the alloy in the temperature range 300–973 K at strain amplitudes in the range $\pm$ 0.25 to $\pm$ 1%, employing a constant strain rate of 3×10^{-3} s^{-1} using a completely reversed (R = −1) triangular waveform on a servo-electric fatigue machine as per ASTM E606. The cyclic stress response of the alloy was characterized by a continuous hardening before the onset of failure under all testing conditions. The fatigue life was found to decrease with an increase in the test temperature and the applied strain amplitude. Dynamic Strain Aging is found to influence the fatigue deformation of the alloy and was characterized by the serrations in the stress–strain hysteresis loops, a negative dependence of half-life stress amplitude and plastic strain amplitude. The results obtained are correlated with the detailed optical and scanning electron microscopic investigations.

Keywords Alloy 625(as-cast) · Low cycle fatigue · DSA · Cyclic stress response

M. Bashir · G. A. Harmain
Department of Mechanical Engineering, NIT Srinagar, Srinagar, India

R. Kannan (✉) · R. Sandhya
Metallurgy and Materials Group, Indira Gandhi Centre for Atomic Research, 603102 Kalpakkam, TN, India
e-mail: rkannan@igcar.gov.in

1   Introduction

Alloy 625 is a nickel base solid solution strengthened superalloy having good combinations of high-temperature mechanical properties, microstructural stability, corrosion/oxidation resistance, good castability, significant damping resistance as well as excellent creep and fatigue resistance [1, 2]. The castability is difficult to achieve with precipitation strengthened alloys having high Ti and Al alloying elements, however, Europe has gained a success to produce the solid solution strengthened alloy with good castability [3]. The high strength and good thermal stability of equiaxed cast alloy are attributed to: solid solution strengthening with additions of refractory alloying elements such as Mo and Nb, strengthening of grain boundaries by carbides, precipitation strengthening by γ' precipitate [Ni$_3$ (Al, Ti)] due to the addition of Al and Ti. Moreover, the addition of Nb leads to strengthening by precipitation of metastable γ'' phase [Ni$_3$ (Nb, Al, Ti)] [4, 5]. The top priority of indigenous AUSC power plant is material development for the design of various components to provide highly efficient, highly reliable, affordable, and environment-friendly electricity. Alloy 625 is treated as the most potential candidate material for the complex casing of AUSC turbine rotor. The casing of the rotor encounters intermittent thermal stresses as a result of temperature gradients that occur on heating and cooling during start-ups and shutdowns or fluctuating temperature transients during the service, that introduces the low-cycle fatigue (LCF) deformation. Hence, in the present study, LCF tests have been conducted on Alloy 625 in the cast form. The material has exhibited cyclic hardening and DSA phenomena. The casting defects introduce a significant scatter in LCF data.

2   Experimental

The 100 mm × 11 mm × 11 mm rectangular blanks were taken out from as-received cast block, from which cylindrical specimens of 6 mm gauge diameter and 12.5 mm gauge length was machined out. The chemical composition of nickel base superalloy, alloy 625 (as-cast) used in this investigation is shown in Table 1. LCF tests were performed in air, using a servo-electric fatigue testing machine equipped with a high-temperature furnace. The axial strain controlled LCF tests were carried out as per ASTM E606. The LCF tests were conducted at various strain amplitudes ranging from ± 0.25% to 1% at 300, 573, 873, and 973 K, employing triangular waveform with a constant strain rate of 3×10^{-3} s^{-1}.

Table 1   Chemical composition of alloy 625, wt%

Elements	P	S	C	Mn	Si	Al	Ti	Fe	Nb	Mo	Cr	Ni
wt.%	0.005	0.007	0.02	0.17	0.18	0.18	0.19	2.86	3.53	8.63	21.34	Bal.

Metallographic examination was done on tested and untested specimens using electrolytic etching (10% perchloric acid in methanol) for 3 min. Fractography of the failed samples were studied in a scanning electron microscope.

3 Results and Discussion

3.1 Microstructure

The initial microstructure of alloy 625 is shown in Fig. 1. The grain boundary was not visible as the grain was quite big. However, the micrograph clearly shows dendritic structure with Nb and Mo interdendritic dark field [3]. Optical micrograph of the tested specimen showed carbides and precipitates both within grains and along the grain boundaries (Fig. 2).

Fig. 1 Initial microstructure of alloy 625
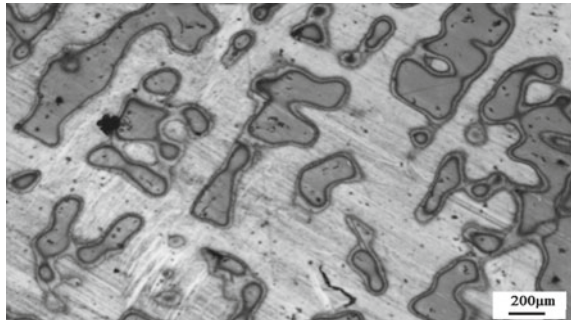
Fig. 2 Micrograph of the tested sample
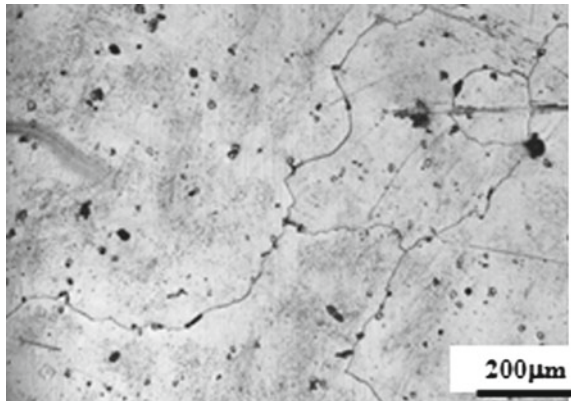
3.2 Cyclic Stress Response Behavior

3.2.1 Effect of Strain Amplitude

The cyclic stress response of alloy 625 with the change in applied strain amplitude for a given temperature is portrayed in Fig. 3a–d. The general observation is that there is a continuous increase in the stress values from the first cycle onwards followed by a drastic decrease in the same due to initiation and propagation of macrocracks. There is an overall upward shift of CSR curves with an increase in strain amplitude at all four temperatures. The cyclic hardening in alloy 625 can be attributed to (a) dislocation multiplication and accumulation within the slip band [6], (b) heterogeneous precipitation of fine $M_{23}C_6$ carbides at the dislocations [7], (c) in situ precipitation of γ' and (d) dislocation and solute atom interactions (dynamic strain aging, DSA).
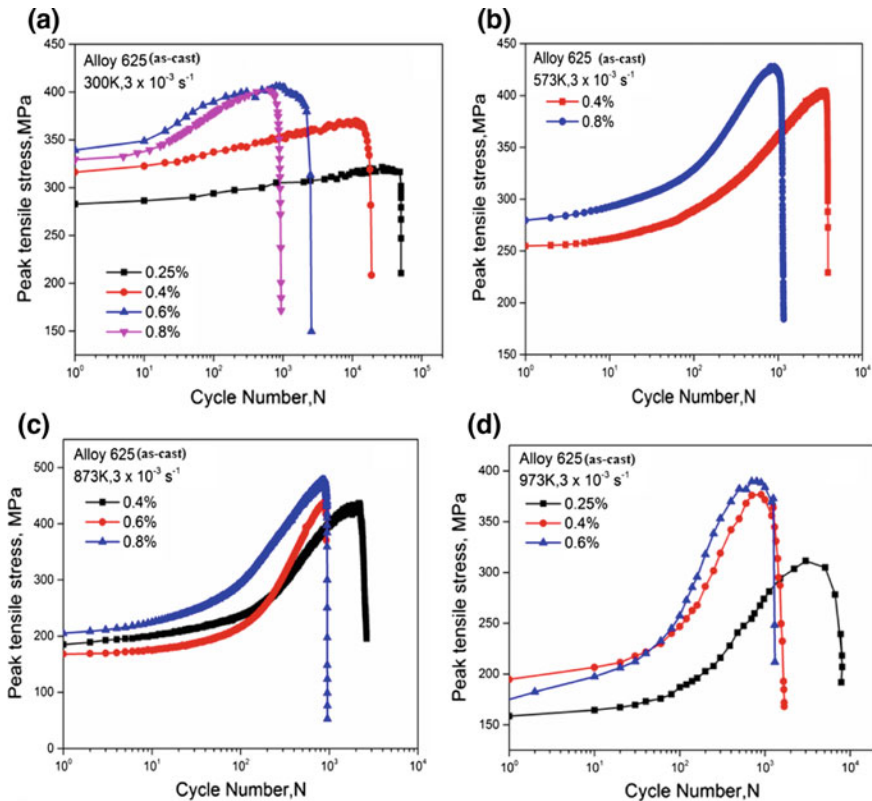
Fig. 3 Effect of strain amplitude on the cyclic stress response of alloy 625 at **a** 300 K, **b** 573 K, **c** 873 K and **d** 973 K

Fig. 4 Effect of temperature on the cyclic stress response of alloy 625 at strain amplitude of ±0.4%
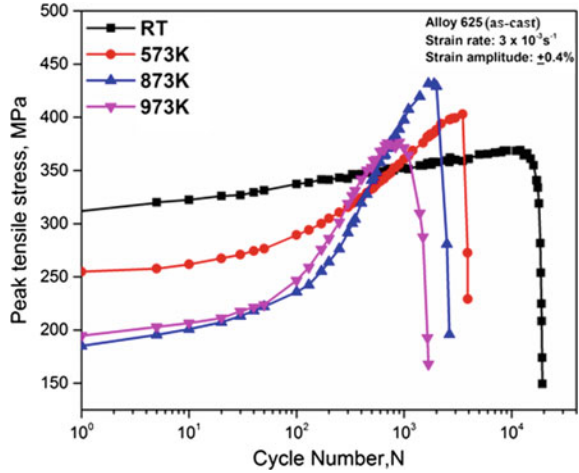
3.2.2 Effect of Temperature

Figure 4 illustrates the cyclic stress response as a function of temperature for a constant strain amplitude (±0.4%). It has been observed that the cyclic hardening increases linearly at 300 K whereas at higher temperatures the increase is steep until failure. It has been observed that peak tensile stress decreases with increase in temperature during the initial part of cycling, typically, about 100 cycles. At higher number of cycles the stress response is higher for higher temperatures, showing a steep hardening effect, in comparison to 300 K. These observations point to the fact that there is a difference in the underlying deformation mechanisms under different temperature–strain amplitude combinations that affect the cyclic stress response of alloy 625.

Figure 5 shows the Coffin–Manson plot for alloy 625 at different temperatures and the parameters obtained from the linear regression method are given in Table 2. The slope of Coffin–Manson plot is sharper at 873 K and above, indicating greater damage in the material leading to the lowering of fatigue life at these temperatures.

3.3 Dynamic Strain Aging and Its Manifestations During Low-Cycle Fatigue Deformation

In the present study, serrations have been observed in the plastic portions of stress–strain hysteresis loops at a strain amplitude of ±0.6% and at temperatures 873 and 973 K, shown in Fig. 6a, b and the plastic portions are enlarged in Fig. 7a, b. This has been attributed to the occurrence of DSA. However, the absence of serrations in hysteresis loops does not imply absence of DSA [8]. Furthermore, the anomalous stress response, i.e. increase in cyclic stress with an increase in temperature has
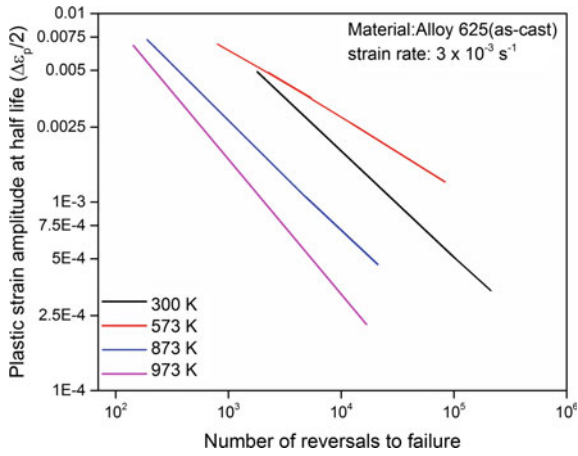
Fig. 5 Coffin–Manson plot of alloy 625 tested at various temperatures

Table 2 Effect of temperature on Coffin–Manson constants for alloy 625

Temperature, K	Fatigue ductility coefficient, ε_f'	Fatigue ductility exponent, c
300	0.3364	−0.5638
573	0.0754	−0.3551
873	0.1644	−0.5941
973	0.2369	−0.7157
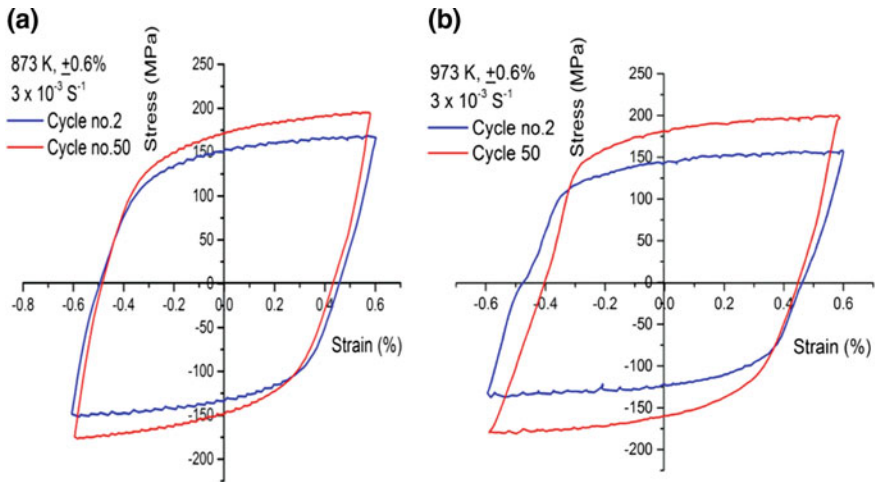
Fig. 6 Representation of the evolution of hysteresis loops at **a** 873 K and **b** 973 K
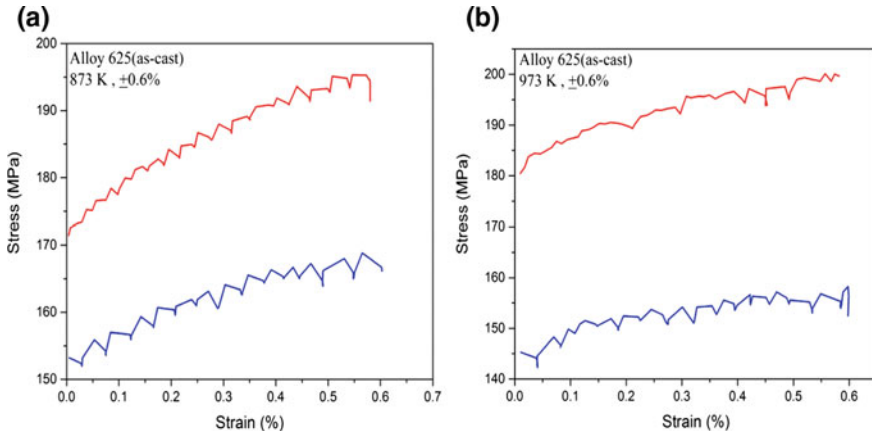
Fig. 7 Serrations observed in alloy 625 in stress–strain hysteresis loops at **a** 873 K and **b** 973 K

Fig. 8 SEM fractograph of the sample tested at 973 K and at a strain amplitude of ±0.4% showing extensive oxidation of the fracture surface
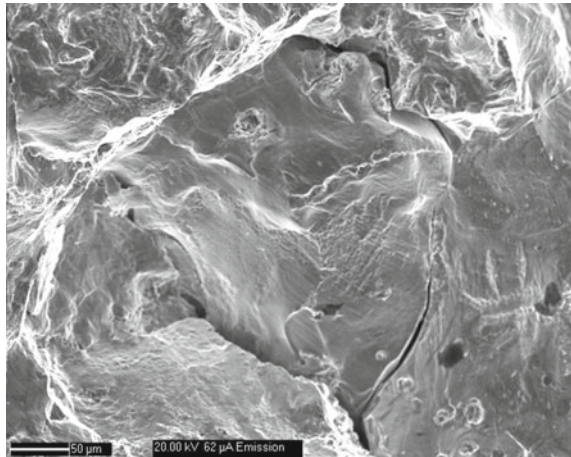
been observed at temperatures of 873 and 973 K. While serrations are present at 973 K, the effect of DSA does not seem to be very predominant at this temperature. The hardening at 973 K could have a contribution from precipitation. DSA fundamentally results from attractive interaction between solute species and mobile dislocations, either during their glide [9] or temporary arrest at local obstacles in the glide plane [10]. Consequently, the unlocking of dislocations or generation of new dislocations results in increased stress response, for maintaining the imposed strain.

Fig. 9 SEM fractograph of the sample tested at 973 K and at a strain amplitude of ±0.4%
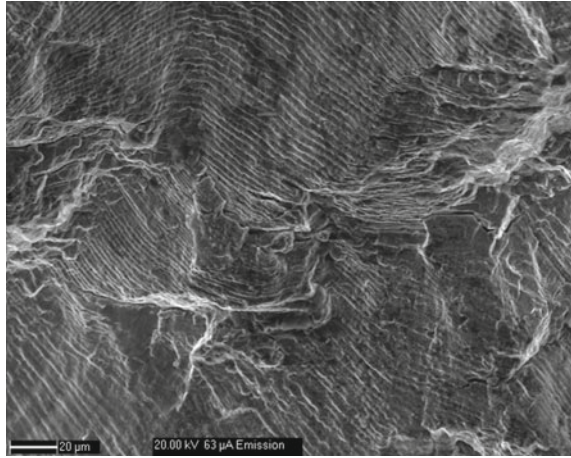
Fig. 10 SEM fractograph of the sample tested at 873 K and at a strain amplitude of ±0.4% showing extensive casting defects (Shrinkage Cavities)
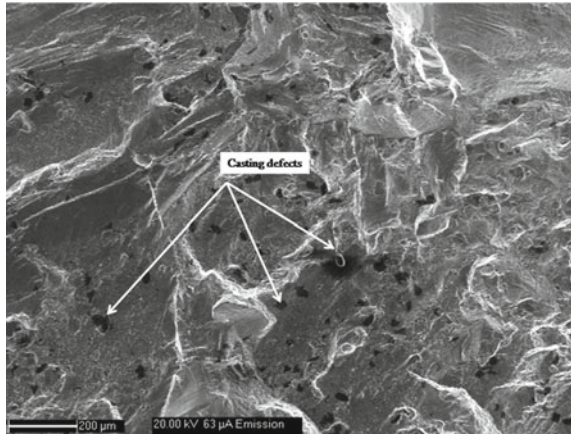
3.4 Fractographic Studies

The effect of oxidation leading to lower life can be clearly seen at 973 K, Fig. 8. As seen from the representative fractography in Fig. 9, the fatigue failure was typically by transgranular mode evidenced by striations on the fracture surface. The scatter in the LCF properties can be attributed to the casting defects as is evident in Fig. 10.

4   Conclusions

1. alloy 625 exhibited intense cyclic hardening at all temperatures of investigation and the rate of hardening is more at 873 and 973 K.
2. LCF life decreased with increase in temperature and strain amplitude.
3. Evidence for the operation of dynamic strain aging was obtained in the form of serrations, increased hardening and a minima in the plastic strain. The peak DSA temperature in the range of temperatures studied was 873 K.
4. The fracture mode was predominantly transgranular, as evidenced by striations on the fracture surface. Oxidation also played a role in the fracture at 973 K.
5. It was shown that the scatter in the LCF properties can be attributed to the casting defects (shrinkage cavities) present in the material, as observed by scanning electron microscopy.

References

1. J.M. Rakowski, C.P. Stinner, M. Lipschutz, J.P. Montague, E.A. Loria (eds.), *The Minerals, Metals and Materials Society* (2005), pp. 271–286
2. L.E. Shoemaker, E.A. Loria (eds.), *The Minerals, Metals and Materials Society* (2005), pp. 409–418
3. W. Yu, S. Liu, Y. Wang, L. Sun, *Energy Materials* (2017), pp. 213–223
4. C. Yuan, X. Sun, Fengshi Yin, Y. Yu, J. Mater. Sci. Technol. **17**, 425–428 (2001)
5. A. Nagesha, P. Parameswaran, Niraj Kumar, R. Sandhya, M.D. Mathew, Mater. High Temp. **29**, 49–53 (2012)
6. G. Chai, P. Liu, J. Srodigh, Mater. Sci. **39**, 2689 (2004)
7. W.l. Mankins, J.C. Hosier, T.H. Bassford, Microstructure and phase stability of Inconel 617. Metall. Trans. **5**, 2579–2590 (1974)
8. K.K. Ray, K. Dutta, S. Sivaprasad, S. Tarafder, Procedia Eng. **2**, 1805–1813 (2010)
9. A.H. Cottrell, *Oxford University, London* (1953)
10. A.W. Sleeswyk, Acta Metall. **6**, 598–603 (1958)

Comparison of LCF Performance of a Ferritic Steel Strengthened with Nanoprecipitates with that of a Conventional HSLA Steel

Shrabani Majumdar, Kumar Sadanand Arya, Ashok Kumar and P. V. Dilip

Abstract Recently, there is a drive to substitute conventional ferrite-pearlite HSLA steel sheets (7–9 mm thick) of TS 550 MPa by high-strength ferritic steels (TS $\sim$ 800 MPa) in thinner gauges (5 or 7 mm) in long and cross member of trucks. In the new ferritic steel, the chemical composition and thermomechanical processing parameters are optimized to minimize the formation of coarse cementite and promote the formation of fine precipitates of nanometer size to strengthen the ferrite. Automotive components are subjected to cyclic loading in service but reports on fatigue behavior of high-strength ferritic steel of 800 MPa TS, are limited in the literature. In this investigation, the low-cycle fatigue (LCF) performance of a ferritic steel strengthened with nanometer-sized precipitates (referred henceforth as HS-800) has been compared with that of a conventional HSLA steel (BSK-46). It emerges that under elasto-plastic strain, HS-800 steel exhibits cyclically stable behavior in sharp contrast to BSK-46 steel which predominantly exhibits continuos cyclic softening especially at lower strain amplitudes of ±0.2 to ±0.5%. It emerges from C–M plot that at lower strain amplitudes of ±0.2 to ±0.4%, HS-800 steel exhibits much lesser cyclic plastic strain. The cyclically stable behavior and the lower amount of cyclic plasticity lead to superior LCF performance of HS-800 steel.

Keywords Ferritic steel · Nanometer-sized precipitates · HSLA steel · Low-cycle fatigue (LCF) · Cyclically stable behavior · Cyclic softening

S. Majumdar (✉) · P. V. Dilip
R&D Division, Tata Steel Ltd., Jamshedpur 831001, Jharkhand, India
e-mail: shrabani@tatasteel.com

K. S. Arya · A. Kumar
Department of Metallurgical and Materials Engineering, National Institute of Technology, Jamshedpur 831014, India

1   Introduction

Recently, there is a drive to substitute conventional HSLA steels (ferrite-pearlite, TS $\sim$ 550 MPa) in heavy vehicle components by high-strength formable steel (ferritic, TS $\sim$ 780–800 MPa) leading to significant weight reduction. The new steel, referred here as HS-800, is a low-carbon Ti-Mo-bearing steel, strengthened with nanometersized Ti-Mo-C precipitates. It is possible to achieve thermally stable nanometersized carbide precipitates of primarily Ti-Mo-C type by lowering the austenite to ferrite transformation temperature (through the addition of $\sim$ 1.7 wt% Mn) and by retarding the formation of pearlite and large cementite (through the addition of $\sim$ 0.25 wt% Mo) in HS-800 steel [1]. Automotive-components are subjected to cyclic loading in service but the report on fatigue-behavior of HS-800-steel is scarce in the literature. In this paper, fatigue performance of HS-800 steel has been compared with that of conventional HSLA steel (BSK-46) in terms of cyclic stress response, strain–life curves, Coffin–Manson plots and damage at the microstructural level. The objective is to correlate the results with the performance of the above steels during end use or service.

2   Experimental

The chemical compositions of the selected steels are shown in Table 1. The selected steels are low-carbon steels, strengthened with Manganese. Mn content of HS-800 is almost double of that of BSK-46 steel. Mn imparts solid solution strengthening in both the steels. But in HS-800 steel, Mn is also required to lower the austenite to ferrite transformation temperature. BSK-46 contains microalloying elements Nb and V while HS-800 is micro-alloyed with Ti and Nb. The microalloying elements help to refine the ferrite GS and impart grain boundary strengthening. Additionally, HS-800 is alloyed with molybdenum, which retards the growth of cementite and other large carbide particles in the steel to achieve fine nanometer-sized TiC and Ti-Mo-C in the steel.

Tensile properties are determined using longitudinal samples designed as per ASTM E08 M standard [2]. The tensile tests were carried out at cross-head speed was 10 mm/min. The results are shown in Table 2. The yield strengths and tensile strengths of BSK-46 (ferrite and pearlite) and HS-800 steel (ferrite) are 497 and 730 MPa and 536 and 800 MPa respectively.

The microstructures of the selected steels are shown in Fig. 1. The microstructure of BSK-46 steel comprises of around 85% ferrite and 15% pearlite. The average ferrite GS of BSK-46 steel is 10 ± 3 μm. The microstructure of HS-800 steel comprises of ferrite with average GS of 4 ± 2 μm.

Low-cycle fatigue samples were designed as per ASTM E 606 standard [3]. The tests were carried out under fully reversed strain amplitudes ($\Delta\varepsilon_t/2 = \pm 0.2\%$ to $\pm 1.0\%$) at a constant strain rate of 0.002 s^{-1}. The failure of the specimens was

Table 1 Chemical compositions of selected steels (wt%)

	BSK-46	HS-800
C	0.060	0.077
Mn	0.83	1.70
S	0.005	0.007
P	0.020	0.020
Si	0.39	0.024
Al	0.040	0.047
N_2 ppm	50	52
Nb	0.035	0.017
V	0.033	–
Ti	–	0.117
Mo	–	0.25

Table 2 Tensile properties of selected steels

	Yield strength (MPa)	Tensile strength (MPa)	Uniform elongation (%)	Total elongation (%)
HS-800	730	800	9	20
BSK-46	497	536	14	29
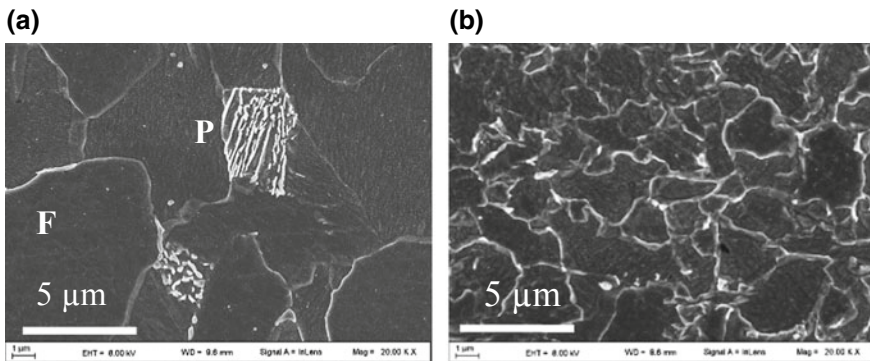
Fig. 1 Microstructure of **a** BSK-46 and **b** HS-800

defined as a state when the stress amplitude dropped to 20% when referred with respect to stable stress amplitude. The variation in cyclic stress amplitude with the number of loading cycles were recorded for each test. Strain–life curves are expressed as (i) plot of total strain amplitude ($\Delta\varepsilon_t/2$) versus the number of reversals to failure and (ii) as a plot of plastic strain amplitude ($\Delta\varepsilon_p/2$) versus the number of

reversals to failure. The latter is also known as Coffin–Manson (C–M) plots. TEM of as received and fatigued HS-800 steel samples was carried out to reveal the associated dislocation structures.

3 Results and Discussion

Results of LCF tests are summarized in Fig. 2 wherein cyclic stress response of the selected steels (Fig. 2a, b), strain–life curves (Fig. 2c) and Coffin–Manson plots (Fig. 2d) are shown. It emerges that HS-800 steel predominantly exhibits cyclically stable behavior (Fig. 2a). The above phenomenon is of great benefit from the application point of view. In sharp contrast, BSK-46 steel exhibits continuous cyclic softening till $\Delta\varepsilon_t/2 \leq \pm 0.5\%$. At $\Delta\varepsilon_t/2 \geq \pm 0.6\%$, a moderate amount of cyclic hardening is noticed at $\Delta\varepsilon_t/2 \geq \pm 0.9\%$, some amount of secondary cyclic hardening is also noticed prior to failure. The strain–life curves in Fig. 2c shows that the LCF life of HS-800 steel is superior. It emerges from Fig. 2d that the amount of plastic strain experienced by HS-800 steel is much lesser especially at $\Delta\varepsilon_t/2 \leq \pm 0.4\%$. The superior fatigue performance of HS-800 steel can be
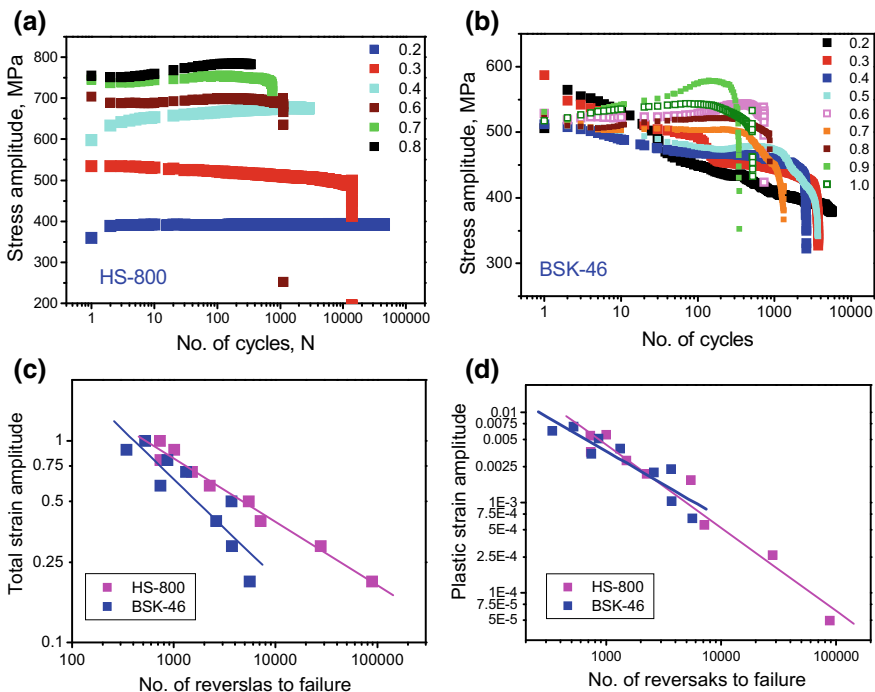
Fig. 2 Cyclic stress response **a** HS-800 and **b** BSK-46, **c**, **d** Strain–life plots

attributed to its stable cyclic stress response and the lower amount of cyclic plasticity experienced by this steel.

The dislocation structure of as received and fatigued HS-800 steel is shown in Fig. 3. In as received steel, mostly areas of low dislocation density and some dislocation–precipitate interaction is noticed. At some locations, a moderate amount of dislocation clusters is also found. In samples fatigued at low strain amplitude ($\Delta\varepsilon_{t/2} = \pm 0.20\%$), many long and straight dislocations are noticed which can possibly be attributed to the difficulty in dislocation mobility and predominance of planar-slip (Fig. 3b, c). The dislocation cells formed in a sample fatigued at higher $\Delta\varepsilon_t/2 = \pm 0.7\%$ is shown in the representative micrograph shown in Fig. 3d.

The nature of cyclic stress response exhibited by the selected steels can be examined in the light of dislocation substructures observed in the present work as well as that reported in earlier investigations [4–6]. It is possible that the solid solution strengthening provided by Mn and the precipitation strengthening provided by the nanometer-sized precipitates (presence of Mo promotes the formation of nanoscale precipitates) enhances the cyclic yield strength of HS-800. As a result, there is limited cyclic plasticity and lesser generation of dislocations at lower $\Delta\varepsilon_t/2$. However, at $\Delta\varepsilon_t/2 > \pm 0.2\%$; deformation mode possibly changes to multiple slip, leading to remarkable increase in (a) dislocation density and (b) number of dislocation tangles/clusters along with (c) formation of dislocation cells. With an increase in dislocation density and formation of dislocation clusters, it is expected that there will be an increase in the dislocation–precipitate interaction. All the above phenomenon lead to a significant amount of cyclic hardening. However, it is possible that at $\Delta\varepsilon_t/2 > \pm 0.2\%$; the newly generated dislocations also start to rearrange themselves in low-energy stable dislocation structures, e.g., dislocation walls, channels, and large subgrains leading to some amount of cyclic softening. Hence, at $\Delta\varepsilon_t/2 \geq \pm 0.3\%$, there is a balance between cyclic hardening and cyclic softening leading to cyclically stable behavior.

In BSK-46, uninhibited dislocation movement at low $\Delta\varepsilon_t/2$ causes faster formation of low-energy-stable dislocation structures, e.g., dislocation walls, channels and large sub-grains leading to cyclic softening as evident from Fig. 2b. It is
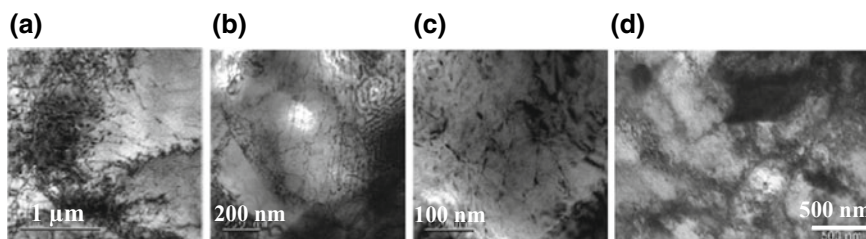
Fig. 3 Dislocation structure in HS-800 steel **a** as received steel, **b**, **c** fatigued at $\Delta\varepsilon_t/2 = \pm 0.20\%$ and **d** fatigued at $\Delta\varepsilon_t/2 = \pm 0.7\%$

possible that at higher $\Delta\varepsilon_t/2 \geq \pm 0.6\%$, sub-grains becomes progressively smaller along with the formation of dislocation cells leading to a significant amount of cyclic hardening.

4   Conclusions

The fatigue performance of a conventional micro-alloyed steel (BSK-46) with that of a novel high-strength ferritic steel strengthened with nanometer-sized precipitates (HS-800) has been compared. The main conclusions are as follows:

- The selected steels are low-carbon steels, solid-solution strengthened with manganese while grain-size strengthening is provided by the microalloying elements. In HS-800 steel, the higher amount of Mn is required to lower the austenite to ferrite transformation temperature. HS-800 is alloyed with Molybdenum which retards the growth of cementite and other large carbides to achieve fine nanometersized precipitates in the steel required for additional precipitate strengthening. The microstructure of BSK-46 steel comprises of 85% ferrite (GS $\sim 10 \pm 3$ μm) and remaining perlite. HS-800 is a predominantly ferritic steel with finer GS (4 ± 2 μm). The yield strengths and tensile strengths of BSK-46 and HS-800 steel are 497 and 730 MPa and 536 and 800 MPa, respectively.
- HS-800 steel predominantly exhibits cyclically stable behavior. The above phenomenon is of great benefit from the application point of view. The cyclically stable behavior is a desirable attribute for application of the steel in heavy vehicle component which is subjected to cyclic loading in service.
- In sharp contrast, BSK-46 steel exhibits continuous cyclic softening till $\Delta\varepsilon_t/2 \leq 0.5\%$. The continuous cyclic softening is an unfavorable attribute and softening is not desirable in any component during service as it may lead to faster failure. However, in BSK-46, at $\Delta\varepsilon_t/2 \geq \pm 0.6\%$, a moderate amount of cyclic hardening is noticed and at $\Delta\varepsilon_t/2 \geq 0.9\%$, some amount of secondary cyclic hardening is also noticed prior to failure.
- The LCF-life of HS-800 steel is superior which can be attributed to its stable cyclic stress response and a lesser amount of cyclic plasticity exhibited by the steel.

References

1. Y. Funakawa, T. Shiozaki, K. Tomita, T. Yamamoto, E. Maeda, ISIJ Int. **44**, 1945 (2004)
2. ASTM E8 M-04, *Standard Test Methods for Tension Testing of Metallic Materials* [*Metric*] (ASTM, Philadelphia, PA, 2004), p. 86

3. ASTM E606-92, *Standard Practice for Strain Controlled Fatigue Testing* (ASTM, Philadelphia, PA, 1998, 2004), p. 592
4. S.G.S. Raman, K.A. Padmanabhan, Int. J. Fatigue **17**, 271 (1995)
5. S. Sankaran, V.S. Sarma, K.A. Padmanabhan, Mater. Sci. Eng. **345**, 328 (2003)
6. W. Chen, T. Kitamura, M. Feng, Int. J. Fatigue **112**, 70 (2018)

Fatigue Life Estimation of Welded Plate Girder of Railway Bridge

Suhasini N. Madhekar and Dinesh Shewale

Abstract Fatigue failure of steel member connections is a well-known failure mechanism for railway steel bridges, which sustain heavy cyclic loads. Their structural members and connections are prone to damage caused by repeated loading of trains, moving at varying speeds. Fatigue damage due to cyclic loads leads to crack formation in members and failure of joints. The designs in Indian Railway Standard (IRS) Bridge Rules are according to the Working Stress Method (WSM). In the present study, fatigue analysis of standard RDSO Heavy Mineral Loading steel plate girder of 24.4 m span is carried out using (i) provisions of IS 800 (2007): Limit State Method, and (ii) software ANSYS. The fatigue life has been estimated for the three cases. For the case study, data of an experimentally tested I-girder available in the literature (Gang et al, ASCE J Compos Construct 16 (2), 2000) [1] is considered. The maximum equivalent stresses, deformations, and fatigue life in terms of the number of cycles, are evaluated. In LSM the governing factor for capacity estimation is elastic Lateral Torsional Buckling Moment. Correction for stress range given in IS 800 (2007) estimates lower fatigue life compared to working stress method (IRS bridge rules); as the effect of lateral torsional buckling is not considered in IRS bridge rules. Fatigue life estimated in terms of the number of cycles, using ANSYS is less than that obtained from the provisions of IS 800. It is concluded that the governing criteria for designing long span plate girder bridges are the lateral torsional buckling moment.

Keywords Welded plate girder · Fatigue life estimation · Railway bridges · Bridge rules

S. N. Madhekar (✉) · D. Shewale
Department of Civil Engineering, Applied Mechanics, College of Engineering Pune,
Pune 411 005, Maharashtra, India
e-mail: suhasinimadhekar@gmail.com; snm.civil@coep.ac.in

S. N. Madhekar · D. Shewale
Water Resources Department, Government of Maharashtra, Mumbai, India

1 Introduction

If repeated cyclic loading is applied on a structural element, it fails after a certain number of loading–unloading cycles, even when the maximum cyclic stress level applied is much lower than its ultimate strength, and in fact, much lower than the yield stress. Steel bridges commonly contain structural elements that are prone to damage caused by repeated loading from vehicular traffic. Fatigue damage due to these cyclic loads tends to accumulate over time, with the primary adverse consequence being the formation of cracks in the steel structures and failure of joints. Fatigue is the phenomenon of gradual decrease of resistance of the material to repeated loading and failure takes place at the magnitude of stresses well below the ultimate/yield strength of the material. Connections and damaged locations attribute to stress concentrations. It starts with crack initiation at points of stress concentration, then crack growth and finally the member fails in fatigue due to not much area of cross section left to sustain any further load. Different types of fatigue loading are distinguished by using load ratio 'R': (i) Repeated and Reversed Load (R = 1), (ii) Partially Reversed Load (0 < R < 1) and (iii) Repeated-One Direction Load (R = 0). In this study partially reversed loading is applied, considering load ratio R = 0.2.

2 Fatigue Analysis: Experimental Testing on Steel I-Section [1]

2.1 Specimen Details

Standard hot-rolled steel beams of length 3 m were tested experimentally for studying their fatigue behavior, when strengthened with different fiber-reinforced composite plates [1]. The height and flange width of the beam cross section were 350 mm and 175 mm, respectively, and the web thickness and flange thickness were 7 mm and 11 mm, respectively. For simulating damage caused, two U-shaped notches with a width of 8 mm were cut on both sides of the tension flange at the midspan of beam, serving as the damage-sensitive region, as shown in Fig. 1. The depth of the notches was maintained at 21.8 mm, with ±0.1 mm tolerance. A steel cover plate of the length of 3 m and of the cross section of 240 mm × 12 mm was welded on the exterior surface of the top flange of the steel beams, to provide equivalency of dead load of the concrete deck. 80 mm × 6 mm stiffeners were welded on both sides of the web at the loading and supporting points.

(a) Notch at the mid-span of beam section

(b) Sectional details of the notch provided
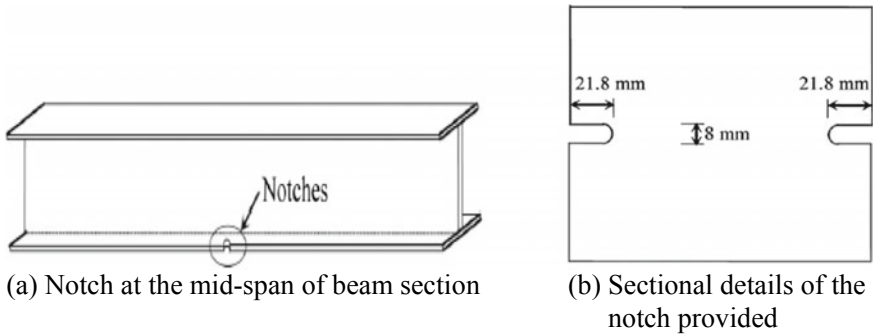
Fig. 1 Details of the test specimen

2.2 Fatigue Test

The experimental results presented in reference [1] are used for validation purpose in the present analytical study. In the test, maximum and minimum values of load were 200 kN and 40 kN respectively. The specimens were gradually loaded till 200 kN and then gradually unloaded till the load reached 40 kN. This variation of load, with the constant amplitude of 120 kN, was maintained until the failure of the specimens due to fatigue, caused by repetitive cycles of loading till 200 kN and unloading till 40 kN. The upper and lower limits of the loads simulate practical conditions of loading and unloading, causing fatigue of bridge girders. It is assumed that when trains pass over railway bridges, they move with constant speed. Thus, the fatigue test results at constant amplitude, imply that the fatigue life of railway bridges can be estimated using the experimental results as a basis for validation.

The specimen was tested as a simply supported beam with a span of 2.8 m. It was loaded in two-point bending [4]. The two-point loads were applied using the spreader beam on the top flange at a distance of 250 mm from the mid-span of beam section, as shown in Fig. 2a. The fatigue test was conducted under constant amplitude cyclic load of 60% (120 kN) of the calculated yield load of the un-strengthened midspan notched section of the beam, with a frequency of 4 Hz.

(a) Schematic of the test setup

(b) Fatigue cyclic load time history
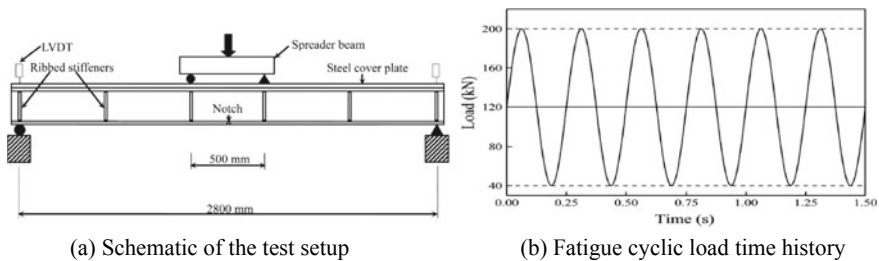
Fig. 2 Experimental set up for the beam specimen

The loading time history is shown in Fig. 2b. The maximum load applied for fatigue was P_{max} (200 kN) to simulate the combined effect of actual dead load and live load. 20% of the maximum load was adopted as the lower limit value P_{min} (40 kN) for fatigue load, to simulate the effect of dead load with the load ratio R = 0.2. Before the fatigue test, a monotonic load was applied at increments of 10 kN until the maximum value of fatigue load P_{max} was reached.

In the specimen, crack propagated to a visible size of approximately 5 mm when 10×10^4 load cycles were reached. After 15.6×10^4 cycles, the tension flange completely cracked, leading to instantaneous fracture of the steel beam, utilizing its full capacity to bear any further load cycles.

3 Fatigue Analysis: IS 800 (2007) [2]

In the experimental program, constant load range (stress range) was assumed. The current fastest train in India is the Gatimaan Express with a top speed of 160 km/h. Indian Railway aims to increase the speed of passenger trains to 160–200 km/h on dedicated conventional tracks. However, in practical situations, different trains passing on various steel welded plate girder railway bridges, move with quite different speeds. Also, while moving on curved tracks, the train speed is much less. India's most dangerous bridge constructed over the Sea, Pamban Bridge at Rameswaram, connects the mainland to the Island of Rameswaram. While moving on the 2.3 km long plate girder bridge built over the sea, the train speed is restricted to 15 kmph, because of the pretty high wind speed. Considering low, medium and high-speed trains moving on different bridges, the analytical study of fatigue assessment was carried out for variable stress range.

Provisions given in IS 800 (2007) are applicable for high-cycle fatigue. Low cycle fatigue is that when the structure is subjected to $\leq 10^3$ cycles. High-cycle fatigue is that when the structure is subjected to 10^3 to 10^9 cycles, and cycles $\geq 10^9$ are considered as ultra-high-cycle fatigue. In the present study, high cycle fatigue analysis was done. For the purpose of design against fatigue, different details of members and connections are classified under different fatigue class. The design stress ranges corresponding to various numbers of cycles are given for each fatigue class in IS 800 (2007). Members which are subjected to cyclic loads at an expected particular stress range are designed referring to the fatigue classes. In the present case, the steel I-beam of the section specified in Sect. 2 of the paper is analyzed.

3.1 Analysis Steps

(i) The values of stress range obtained from standard S-N curve shall be modified by a capacity reduction factor (μ)

$$\mu = \left(25/t_p\right)^{0.25} \leq 1.0 \tag{1}$$

where t_p is the plate thickness. Capacity reduction factor given in Eq. (1) is applicable for plates of thickness greater than 25 mm.
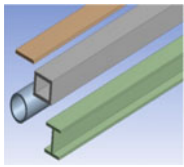
(ii) Partial safety factor for fatigue shall be based on the consequences of fatigue failure:

    (a) Fail-safe structural component/detail is the one where the local failure of one component due to fatigue crack does not result in the failure of the structure due to the availability of alternate load path (redundant system).

    (b) Non-fail-safe structural component/detail is the one where the local failure of one component leads rapidly to failure of the structure due to its non-redundant nature.

(iii) Table 1 presents the classification of detail category for the purpose of assessing fatigue strength.

    Table 2 presents constructional details for detail category 118. The beam under study is I-beam, which falls in this category.

(iv) Fatigue assessment for variable stress range.

Fatigue assessment at any point in a structure, wherein variable stress ranges f_{fi} or τ_{fi} for n_i number of cycles (i = 1 to r) are encountered, shall satisfy the following:

Table 1 Partial safety factors for fatigue strength (Υ_{mft}) [2]

S. no.	Consequence of failure		
	Inspection and access	Fail-safe	Non-fail-safe
1	Periodic inspection, maintenance, and accessibility to detail is good	1.00	1.25
2	Periodic inspection, maintenance, and accessibility to detail is poor	1.15	1.35

Table 2 Detail category classification—non-welded details [2]

Constructional detail		
Detail category	Illustration	Description
118 (f_{fn} = 118 N/mm^2)		Rolled and extruded products (a) Plates and flats (b) Rolled sections (c) Seamless tubes Sharp edges, surface and rolling flaws to be removed by grinding in the direction of applied stress

(a) For normal stress:

$$\frac{\sum_{i=1}^{\gamma_s} n_i f_i^3}{5 \times 10^6 \left(\frac{\mu f_{fn}}{\gamma_{mft}}\right)^3} + \frac{\sum_{j=\gamma_s}^{r} n_j f_j^5}{5 \times 10^6 \left(\frac{\mu f_{fn}}{\gamma_{mft}}\right)^5} \leq 1 \tag{2}$$

(b) For shear stress:

$$\sum_{i=1}^{r} n_i \tau_i^5 \leq 5 \times 10^6 \left(\frac{\mu f_{fn}}{\gamma_{mft}}\right)^5 \tag{3}$$

where Υ_s is the summation upper limit of all the normal stress ranges (f_i), having magnitude lesser than ($\mu \cdot f_{fn}/\Upsilon_{mft}$) for that detail and the lower limit of all the normal stress ranges (f_j), having a magnitude greater than ($\mu \cdot f_{fn}/\Upsilon_{mft}$) for the detail. In the above summation all normal stress ranges, f_i and f_j having a magnitude less than $0.55\ \mu \cdot f_{fn}$ and $0.55\ \mu \cdot \tau_{fn}$ may be disregarded.

3.2 Sectional Properties

For calculation of section properties, notched section, i.e., reduced section due to the provision of notches, is considered, since it will provide the least section modulus to resist the externally applied forces. For shear stress calculation, the moment of inertia considered is I = 131.23 × 10^6 mm^4 since there is no notch provided at the location of maximum shear stresses, i.e., at supports and at loading points. The data considered for fatigue analysis is

Section Modulus (Z)	$= 614.137 \times 10^3 \text{mm}^3$
Moment due to 200 kN load (M$_1$)	$= 115$ kNm
Moment due to 40 kN load (M$_2$)	$= 46$ kNm
Bending stress, σ_1 due to M$_1$ (f_1)	$= 187.25$ N/mm^2
Bending stress, σ_2 due to M$_2$ (f_2)	$= 74.9$ N/mm^2
Shear stress, τ_1 due to 2 − 100 kN loads	$= 45.9$ N/mm^2
Shear stress, τ_1 due to 2 − 40 kN loads	$= 18.306$ N/mm^2

For calculating shear stress near supports, the area without stiffener is considered; since it will provide lesser cross-sectional area to carry shear stress (Fig. 3).

Fig. 3 Properties of beam section

$$bf_1 = 175 \text{ mm}$$
$$bf_2 = 131.4 \text{ mm}$$
$$t_w = 7 \text{ mm}$$
$$t_f = 14 \text{ mm}$$
$$d = 322 \text{ mm}$$
$$D = 350 \text{ mm}$$
$$I = 116.28 \times 106 \text{ mm}^4$$
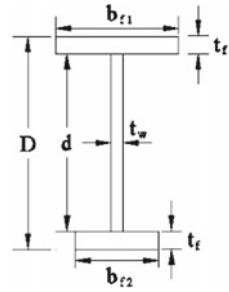
3.3 Fatigue Analysis

Capacity reduction factor is given by, $\mu = (25/t_p)^{0.25} \leq 1.0$.

However maximum thickness is 14 mm which is less than 25 mm, therefore μ is taken equal to 1.0. γ_{mft} is considered = 1.25, for non-fail safe detail; with periodic inspection, maintenance and good accessibility to detail. As mentioned in Sect. 1, for partially reversed loading, the load ratio, R lies in between 0 and 1 $(0 < R < 1)$. In the present study, R = 0.2 (R = 40/200). Following procedure shows fatigue life estimation as per IS 800:2007, for R = 0.2.

$$\frac{\sum_{i=1}^{\gamma_s} n_i f_i^3}{5 \times 10^6 \left(\frac{\mu f_{fn}}{\gamma_{mft}}\right)^3} + \frac{\sum_{j=\gamma_s}^{r} n_j f_j^5}{5 \times 10^6 \left(\frac{\mu f_{fn}}{\gamma_{mft}}\right)^5} \leq 1$$

As mentioned in Sect. 3.3, $\mu = 1$, $\gamma_{mft} = 1.25$ and $f_{fn} = 118 \text{ N/mm}^2$, thus, $\frac{\mu f_{fn}}{\gamma_{mft}} = 94.4 \text{ N/mm}^2$.

Bending stress, σ_1 due to M_1 (f_1) = 187.25 N/mm^2 (For 200 kN load) > 94.4 N/mm^2 ($n_i = n_1$).

Bending stress, σ_2 due to M_2 (f_2) = 74.9 N/mm^2 (For 40 kN load) < 94.4 N/mm^2 ($n_j = n_1$).

This considers the load ratio (40/200) = 0.2. Substituting these values in Eq. (2),

$$\frac{n f_2^3}{5 \times 10^6 (94.4)^3} + \frac{n f_1^5}{5 \times 10^6 (94.4)^5} \leq 1$$

$$\frac{n(74.9)^3}{5 \times 10^6 (94.4)^3} + \frac{n(187.25)^5}{5 \times 10^6 (94.4)^5} = 1$$

Solving, fatigue life 'n' = 16.2 × 10^4 Cycles. Following the same procedure, fatigue life can be estimated for other load ratios.

Using Variable stress range formulae for:

(a) Normal stress range using Eq. (2), N = 16.20 × 10^4 cycles
(b) Shear stress range using Eq. (3), N = 18.14 × 10^6 cycles

Therefore actual fatigue life of I-section is least of above two, i.e., 16.20 × 10^4 cycles.

4 Fatigue Analysis: Using ANSYS 15.0

The 3D model of the steel I-beam section is generated in ANSYS design modeler. The same section which was used for experimental test [1] and for analysis using IS 800 (2007) was modeled in ANSYS. Small elementary areas having negligible thickness were created to apply point loads on the top flange. To simulate the support conditions used in experimental test [1], support sections were modeled. Two notches with a width of 8 mm were cut on both sides of the tension flange at the midspan of the beam. The length of the notches was maintained at 21.8 mm. In actual test to simulate a dead load of deck slab, plate of length of 3 m and of cross section of 240 mm × 12 mm was welded on the external surface of the top flange. However, in ANSYS, pressure producing the same intensity of load i.e. 9.42 × 10^{-3} N/mm^2 was applied [3]. Figure 4 shows the particulars of section modeled in ANSYS.

4.1 Design Parameters

Two-point loads of 100 kN each with a loading ratio of 0.2 were applied 250 mm away from the midspan on both sides, as shown in Fig. 5. Maximum equivalent Von Misses stress developed was 185.15 N/mm^2. Figure 6 shows the equivalent Von Mises stress distribution.

In ANSYS for fatigue analysis, Soderberg's fatigue theory is used. Soderberg theory gives conservative results compared to Goodman theory and Gerber theory [5]. Equation of Soderberg's theory is given as

(a) 3D Model of Section   (b) Notches at Midspan   (c) Elementary Areas Modeled
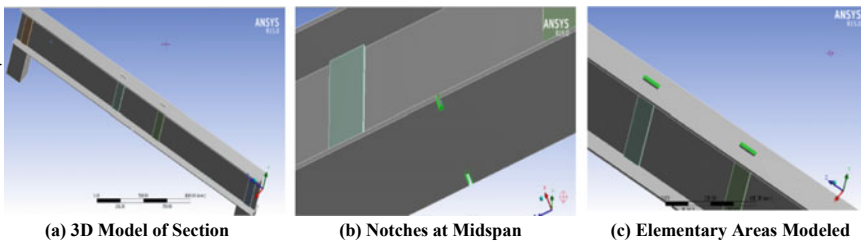
Fig. 4 Particulars of section modeled in ANSYS

Fig. 5 Point loads applied at A & B
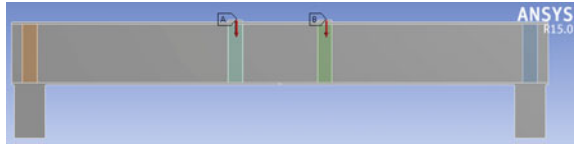
Fig. 6 Von Mises stress distribution
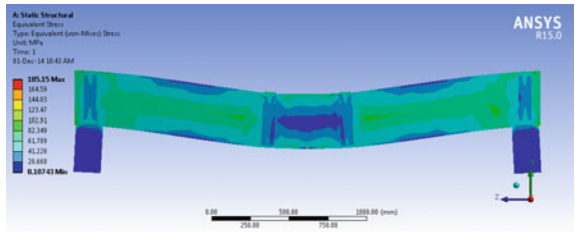
$$\left(\frac{\sigma_a}{\sigma_e}\right) + \left(\frac{\sigma_m}{S_y}\right) = 1 \quad \left(\frac{\tau_a}{\tau_e}\right) + \left(\frac{\tau_n}{S_{ys}}\right) = 1 \tag{4}$$

where

σ_a/τ_a	amplitude of normal/shear stress
σ_m	mean cycle stress
σ_e/τ_e	endurance limit at constant strength
τ_m	shear yield strength
S_y	yield tensile strength
S_{ys}	S_y to $0.5S_y$ depending on material type ($0.577S_y$ for steel).

It is observed that the specimen fails at 14.74×10^4 cycles.

5 Results and Discussions

The graph presented in Fig. 7 shows the variation of fatigue life with respect to variation in load ratio. As the load ratio goes on increasing the stress range goes on decreasing and hence the fatigue life goes on increasing. As the load ratio goes on decreasing the stress range goes on increasing and hence the fatigue life goes on decreasing. Generally, in case of bridges, the load ratio is never below zero for self-weight and applied live load i.e. the bridges are normally subjected to the compressive type of loading. Also, bridges may be subjected to load reversal due to wind and earthquake forces, for limited period. It means that the loading cycles to which bridge will be subjected in case of load reversal will be very low, leading to low-cycle fatigue.

Table 3 presents fatigue life results by IS 800 (2007) and by ANSYS. The results are in close agreement.
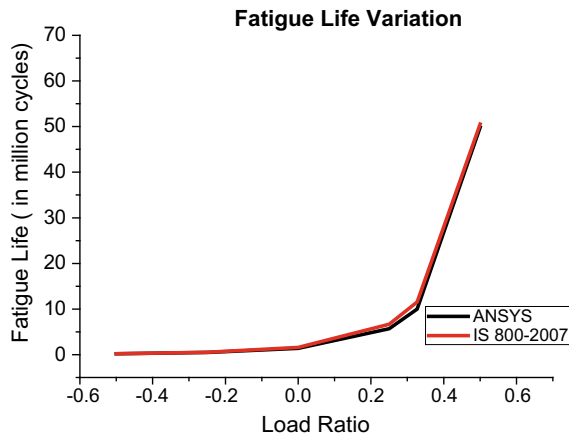
Fig. 7 Variation of fatigue life with load ratio

Table 3 Fatigue life results in number of cycles

S. no.	Method of evaluation	Fatigue life (number of cycles)
1	Experimental fatigue test	15.6×10^4
2	Analysis according to IS 800:2007 provisions	16.20×10^4
3	Analysis using finite element tool ANSYS	14.74×10^4

6 Conclusions

The paper presents a study on the fatigue analysis, based on the ANSYS finite element analysis, and comparing the results with the results of experimental tests and also with the results based on IS 800 (2007) provisions. High-cycle fatigue analysis on steel I-section which is commonly used in steel bridges is performed. A lot of experimental and statistical data are considered for developing clauses IS 800 (2007). There can be a lot of variation in the experimental results, performed in different laboratories under different environments, due to testing limitations. Hence, welded plate girders should be designed using the recommendations of IS 800 (2007). The clauses and factors used in the code are based on actual experimentations, thus they indirectly consider the experimental evaluation as well.

Fatigue life given by IS 800 (2007) is higher (by 5.2%) compared to that of the experimental test results. Fatigue analysis using ANSYS 15.0 based on Soderberg's theory of fatigue analysis predicts life lesser (by 4.31%) compared to the experimental test results. The fatigue life estimated for the selected section in shear stress fatigue is more, compared to normal stress fatigue. Due to normal stress fatigue failure before the final rupture of the section, significant yielding resulting in crack propagation is observed. This ensures the ductile failure of the section which is advantageous in repair and restoration of structures. The only variable factor used in the analysis according to IS 800 (2007) provisions is a partial factor of safety for

fatigue strength (Υ_{mft}). It is felt that there should be the inclusion of additional variable factors on which fatigue strength of structure would depend. Also in the case of welded structures, the weld generally fails due to stress concentration in the welding process and applied cycles of load. In welded structures, experimental fatigue testing should be done for sections having similar sectional properties by varying weld size of connections.

References

1. W. Gang, H.-T. Wang, Z.-S. Wu, H.-Y. Liu, Y. Ren, Experimental study on the fatigue behavior of steel beams strengthened with different fiber-reinforced composite plates. ASCE J. Compos. Construct. **16**(2) (2012)
2. IS 800 *General Construction in Steel—Code of Practice* (2007)
3. Goel Ravindra Kumar, *Fatigue Design of Welded Connections for Railway Bridges* (International Seminar, Indian Institute of Welding, Mumbai (February), 2005)
4. H.-B. Sim, C.-M. Uang, Experimental fatigue evaluation of welded connections in cantilevered steel sign structures. J. Struct. Eng. **129**(12) (2013)
5. H.P. Iraj, H. P. Mamaghani, C. Shen, E. Mizuno, T. Usami, Cyclic behavior of structural steels. J. Struct. Eng. **121**(11) (1995)

Fretting Fatigue Behavior of Aluminum Alloy

**M. Jayaprakash, Kulkarni Achyuth, Mahesh Patel
and Sangam Sangral**

Abstract In this study, the fretting fatigue behavior of aluminum alloy was studied by carrying out experimental fretting fatigue tests and fretting wear test using Al–Si–Mg (2024-T6) alloy. For fretting wear test, both the pin and plate are made of Al–Si–Mg alloy. In fretting fatigue test, both the specimens and contact pads (bridge type) are made of Al–Si–Mg alloy. Fretting wear tests were conducted to get basic friction properties. Fretting fatigue tests were carried out at various contact pressures (100, 150 and 200 MPa). Finite element analysis was carried out to obtain the stresses at the contact, i.e., tangential stress and compressive stress. The relation between tangential stress, compressive stress, and fretting fatigue lives has been plotted for the Al–Si–Mg alloy. Based on the plot, the fretting fatigue strength prediction of Al–Si–Mg alloy was discussed.

Keywords Fretting wear · Fretting fatigue · Al alloys · Tangential stress · Contact pressure

1   Introduction

Al–Si–Mg alloy is widely used in automotive applications, especially in automotive engine components due to their moderate strength, lightweight, wear resistance, and good corrosion resistance. In automotive engine, the parts are clamped together mostly by bolted joints. During service, due to engine vibration fretting wear occurs which leads to the accumulation of the wear debris at the contact transfer of materials from one surface to another occurs, which can cause surface damage and cracking at the contact interface. Under the cyclic loading, it leads to unexpected failure due to fretting fatigue. To mitigate these kinds of failure, it is important to study and understand more clearly the mechanisms of fretting wear and fretting fatigue in aluminum alloy contacts.

M. Jayaprakash (✉) · K. Achyuth · M. Patel · S. Sangral
Discipline of Metallurgy Engineering and Materials Science, IIT Indore, Indore 453552, India
e-mail: jayaprakash@iiti.ac.in

So far, a good number of research works has been carried out on fretting wear and fretting fatigue [1, 2], a number of fretting fatigue strength prediction methods have been developed [3, 4]. In particular, a number of reports were published on fretting fatigue and fretting wear behavior of Al alloys [5–10]. Szolwinski et al. [5] have investigated the fretting fatigue of 2024 Al alloy and proposed a strength prediction considering wear at the contact. Considering the fretting wear aspects, Zu et al. and Blanchard et al. [6, 7] have investigated the fretting fatigue behavior. However, the wear shows two complex effects on fretting fatigue behavior. First one is wear at contact causes more surface damage, which degrades fretting fatigue strength. In second case, if wear rate is high there is chance to erode the initiated cracks due to fretting fatigue [9]. It might enhance fretting fatigue strength. Also, Newman proposed strength prediction methods of Al alloys based on fracture mechanics approach [10].

Because of the interaction of multiple variables on fretting wear and fretting fatigue behavior, a more appropriate method to predict the fretting fatigue strength of actual structural components is yet to be identified. Considering this, in the earlier studies, a fretting fatigue strength prediction method based on stress distribution at the contact edge has been developed [11, 12], which is called as fretting fatigue design curve. It has also been confirmed that this method can be successfully used for the appropriate prediction of fretting fatigue strength of both simple geometry and actual complex geometries regardless of contact geometry, load, and material strength for steel.

This proposed design curve is a material property and is applicable only to the material for which it has been developed, i.e., for steel. Aluminum alloys are also widely used in critical components parts, where fretting wear and fretting fatigue failure occurs. It is equally important to study the fretting wear and fretting fatigue behavior of aluminum alloys and based on that it could be possible to develop a most appropriate strength prediction method.

In this study, fretting wear and fretting fatigue behavior of Aluminum alloy has been investigated at different contact loads/contact pressures. Finite element analysis (FEA) is also carried out to calculate the stress distribution at the contact during fretting fatigue. The method used for plotting the fretting fatigue design curve is the same as that used for steels, which is given in Ref. [2]. The fretting fatigue design curve is obtained for Al–Si–Mg alloys successfully. It can be used as a tool for the prediction of fretting fatigue strength for the components made of Al–Si–Mg alloy irrespective of loading condition, contact pressure, and contact geometry.

2 Experimental

2.1 Materials

The material used both for fretting wear and fretting fatigue was 2024-T6 aluminum alloy (Al–Si–Mg alloy). The yield strength and ultimate tensile strength of the aluminum alloy (2024-T6) used in the present study are 340 MPa and 480 MPa, respectively. For fretting wear test, the pin used was of 10 mm diameter. The flat plate used was $30 \times 15 \times 10$ mm. For fretting fatigue test, flat-on-flat contact was used. The dimensions of specimen for fretting fatigue test and contact pad used in the present study are shown in Fig. 1. The schematic of fretting fatigue test setup is shown in Fig. 2. The contact surfaces of both the specimens and contact materials (for both fretting wear and fretting fatigue tests) were polished up to 1500 grit emery paper and then washed with acetone sonically before each test.
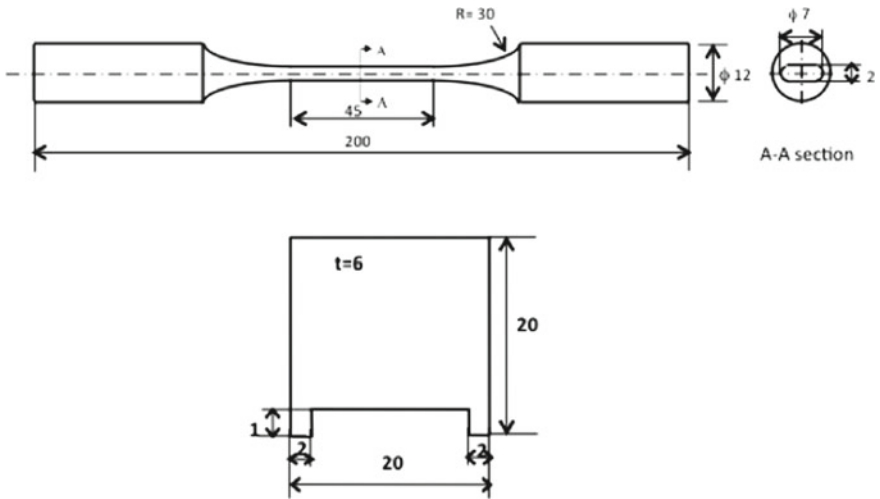
Fig. 1 Dimensions of fretting fatigue test specimen and contact pad

Fig. 2 Schematic of fretting fatigue test setup
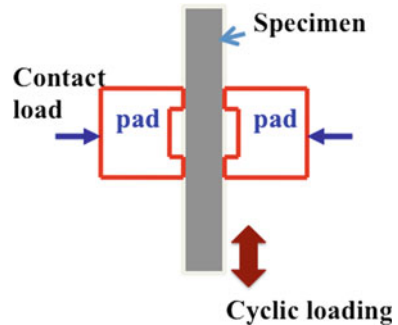
2.2   Fretting Wear and Fretting Fatigue Tests

Fretting wear test was carried out at a frequency of 5 Hz, with displacement amplitude of 0.5 mm at three different loads (10, 20, and 30 N).

Fretting fatigue tests were done using a servo-hydraulic fatigue testing machine at a stress ratio (R) of −1 and with a frequency of 10 Hz in laboratory air. The fretting fatigue test was conducted as per JSME standard S015. A calibrated stainless steel ring was used to apply and maintain constant contact pressures during fretting fatigue test. The fretting fatigue tests were carried out at different contact pressures (100, 150, and 200 MPa).

2.3   Finite Element Analysis

The finite element analysis (FEA) was used to calculate the stress distributions along the contact interface during fretting. Three-dimensional FEA was carried out using ANSYS software. The coefficient of friction used was 0.3, which is obtained from fretting wear test experimentally using same pair of materials. The photograph of FEA model used in present study is shown in Fig. 3.

3   Results and Discussion

3.1   Evaluation of Coefficient of Friction from Wear Test

The relation between coefficient of friction (μ) and number of cycles obtained from fretting wear tests at different contact loads is given in Fig. 4. At the initial cycles, the coefficient of friction steeply increased and attains a stabilized value for all the

Fig. 3 FEA model
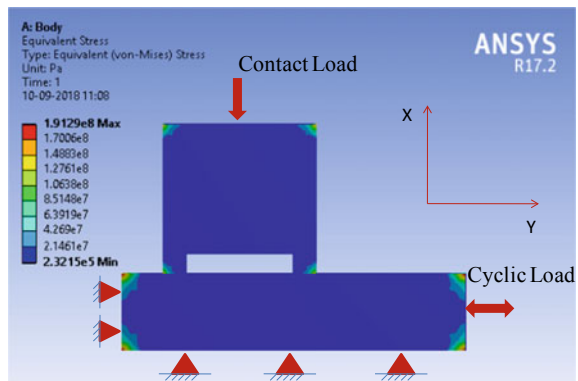
Fig. 4 Plot between coefficient of friction and number of cycles for fretting wear test
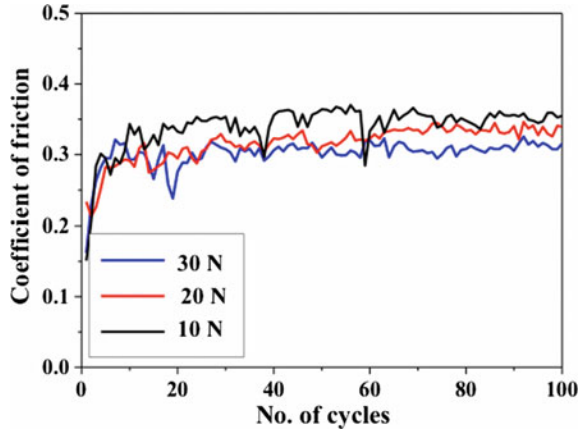
contact loads applied, which is the usual characteristics in fretting wear. The stabilized values of coefficient of friction values were in the range of 0.28–0.32. Based on the values obtained from fretting wear test, for the FEA value of 0.3 was used as coefficient of friction.

3.2   Fatigue Behavior of Al–Si–Mg Alloy Under Fretting

Figure 5 shows the plain fatigue and fretting fatigue test results of aluminum alloy used in present study. From the figure, it can be observed that fretting has a significant effect on fatigue strength. Because of fretting, the fatigue strength of Ai–Si–Mg alloy was reduced by more than 40%.

It has been reported that in fretting fatigue, due to fretting the friction stress was generated at the contact interface which leads to the surface damage and early crack

Fig. 5 The plain fatigue and fretting fatigue test of 2024-T6 aluminum alloy
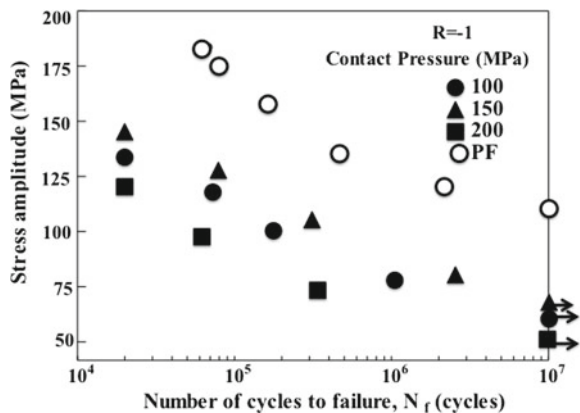
nucleation. This is the primary reason behind the huge reduction in fatigue strength in fretting fatigue compared to plain fatigue (without fretting) [4, 11]. In general, if the contact pressure is increased, the friction stress will also increase and hence the surface damage will increase and accelerate the crack nucleation process. At the same time, with an increase in contact pressure more compressive stress will generate at the contact, which might retard the crack propagation. The contact pressure might show complex behavior with fretting fatigue strength, which mainly depends on materials and domination of other fretting fatigue variables like relative slip, etc. [9].

Figure 5 shows S–N curve of Al–Si–Mg alloy for plain fatigue test and fretting fatigue tests at different contact pressures. As observed from Fig. 5, contact pressures have a significant effect on fretting fatigue behavior of aluminum alloy. Also, it has been seen from Fig. 5, the fretting fatigue strength of Al–Si–Mg alloy showed a mixed behavior with an increase in contact pressure. That is, initially with an increase in contact pressure, the fretting fatigue strength increased, and then drastically reduced. This mixed behavior was due to the combined effect of tangential stress and compressive stress at the fretting contact edge. That is, there is competition between the tangential stress, which accelerates the crack initiation, propagation, and the compressive stress that resists the propagation of initiated crack.

3.3   Evaluation of Stresses at Contact Using FEA

In general, the fretting fatigue crack initiates at the contact where the friction stress (i.e., the tangential stress) is maximum [13–16]. The propagation/growth rate of initiated crack is highly influenced by compressive stress generated at the contact during fretting fatigue. Therefore, the final fretting fatigue life/strength is highly affected by these two stress parameters. Based on these two important stress parameters in the previous study, a new fretting fatigue strength prediction method has been proposed using TSR-CSR diagram for various steel [11, 12].

In this study, the tangential stress range and compressive stress range at the contact during fretting fatigue test of aluminum alloy were evaluated using FEA at various stress amplitudes and were shown in Fig. 6. From the S–N curve, the stress amplitude corresponds to a particular fretting fatigue life extrapolated for various contact pressures. The stress amplitude and the corresponding contact pressures were applied to FEA model in steps. Then the tangential stress range and compressive stress values were evaluated and plotted as shown in Fig. 7. The method for evaluation of tangential stress, compressive stress, and the plotting of TSR-CSR diagram was the same as that mentioned in previous studies in Ref. [11, 12]. Tangential stress range–compressive stress range curve has been plotted for Al–Si–Mg alloy and is shown in Fig. 7. As seen from Fig. 7, the plot between tangential stress range and compressive stress range showed a linear relation with respect to particular fretting fatigue lives, regardless of contact pressures. Using this tangential stress range and compressive stress range plot shown in Fig. 7, the fretting fatigue
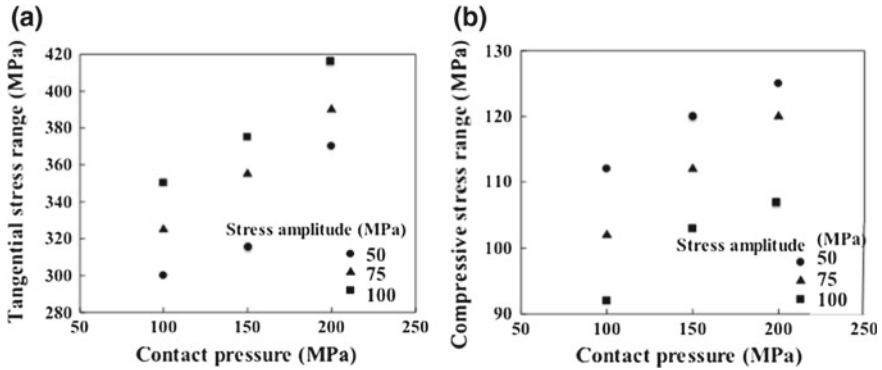
Fig. 6 Tangential stress range and compressive stress range at contact edge during fretting fatigue for 2024-T6 Al alloy evaluated using FEA

Fig. 7 Plot between tangential stress range and compressive stress range corresponding to various fretting fatigue lives for 2024-T6 aluminum alloy
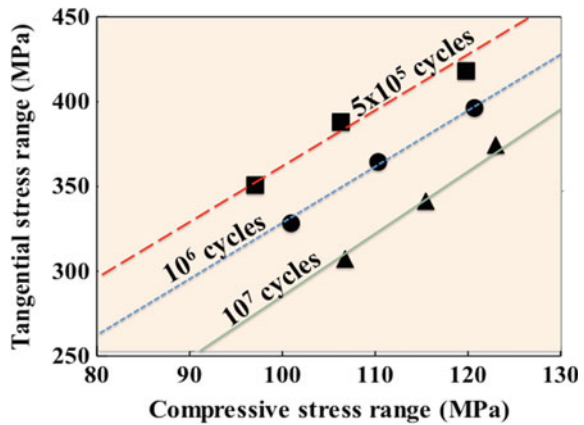
strength of aluminum alloy (2014-T6) with any contact geometry and loading conditions can be predicted appropriately. The procedure for strength prediction based on this figure is the same as mentioned in Ref. [11].

4 Conclusions

In this study, the fretting wear and fretting fatigue of aluminum alloy (Al–Si–Mg alloy) were studied by conducting fretting wear test and fretting fatigue tests. From the results, the following conclusions were drawn:

I. The coefficient of friction of the Al alloy used in the present study was about 0.3, which is obtained by fretting wear test.

II. In the Al alloy used, fatigue strength was reduced drastically (more than 40%) due to fretting.

III. Fretting fatigue of Al alloy used in present study showed a complex behavior with respect to contact pressure. Initially, with an increase in contact pressure fretting fatigue strength increased, and then drastically decreased.

IV. Tangential stress and compressive stress play a significant role in deciding fretting fatigue strength.

V. The plot between tangential stress range and compressive stress range with respect to fretting fatigue lives showed a linear relationship.

VI. The fretting fatigue lives of the aluminum alloy used in this study can be successfully estimated using the tangential stress range–compressive stress range diagram regardless of loading conditions and contact pressure.

References

1. Y. Mutoh, J.Q. Xu, Fracture mechanics approach to fretting fatigue and problems to be solved. Tribol. Int. **36**, 99 (2003)
2. R.B. Waterhouse, Fretting at high temperature. Tribol. Int. **14**(4), 203 (1981)
3. D.A. Hills, D. Nowell, Mechanics of fretting fatigue—Oxford's contribution. Tribol. Int. **76**, 1 (2014)
4. M. Jayaprakash, S. Ganesh Sundara Raman, Effect contact pressure on fretting fatigue behavior of AISI 304 stainless steel. Trans. Indian Inst. Metals **59**, 431 (2006)
5. M.P. Szolwinski, T.N. Farris, Observation, analysis and prediction of fretting fatigue in 2024-T351 aluminum alloy. Wear **22**(1), 24 (1998)
6. Z.R. Zhou, S.R. Gu, L. Vincent, An investigation of the fretting wear of two aluminium alloys. Tribol. Int. **30**(1), 1 (1997)
7. P. Blanchard, C. Colombie, V. Pellerin, S. Fayeulle, L. Vincent, Material effects in fretting wear: application to iron, titanium, and aluminum alloys. Metall. Mater. Trans. A **22**(7), 1535 (1990)
8. Z.R. Zhou, L. Vincent, Cracking induced by fretting of aluminium alloys. J. Tribol. **119**(1), 36
9. M. Jayaprakash, S. Ganesh Sundara Raman, Influence of pad span on fretting fatigue behavior of AISI 304 austenitic stainless steel. J. Mater. Sci. **42**, 4305 (2007)
10. J.C. Newman Jr., E.P. Phillips, M.H. Swain, Fatigue life prediction methodology using small crack theory. NASA Report (Jan 1997)
11. Y. Mutoh, M. Jayaprakash, Tangential stress range—compressive stress range diagram for fretting fatigue design curve. Tribol. Int. **44**(11), 1394 (2011)
12. M. Jayaprakash, Y. Mutoh, K. Asai, K. Ichikawa, S. Sukarai, Effect of contact pad rigidity on fretting fatigue behavior of NiCrMoV turbine steel. Int. J. Fatigue **32**(11), 1788 (2010)
13. N. Ali Bhatti, M. Abdel Wahab, Fretting fatigue crack nucleation: a review. Tribol. Int. **121**, 121 (2018)
14. Z.B. Xu, J.F. Peng, J.H. Liu et al., Effect of contact pressure on torsional fretting fatigue damage of 316L austenitic stainless steel. Wear **376–377**, 680 (2017)
15. M. Jayaprakash, M. Okazaki, Y. Miyashita, Y. Otsuka, Y. Mutoh, Fretting fatigue behavior of austenitic stainless steel considering the mean stress and overload effect. Trans. Indian Inst. Metals **70**, 597 (2017)
16. T. Daisuke, K. Masanobu, K. Ryosuke et al., Effect of contact pressure on fretting fatigue failure of oil-well pipe material. Int. J. Fatigue **101**, 67 (2017)

Role of Stacking Fault Energy on Symmetric and Asymmetric Cyclic Deformation Behavior of FCC Metals

Jayanta Kumar Mahato, Partha Sarathi De, Amrita Kundu and Pravash Chandra Chakraborti

Abstract The present investigation is aimed towards an understanding on cyclic deformation behavior of two FCC metals having different stacking fault energy (SFE); annealed copper and annealed aluminium. Symmetric cyclic loading tests under strain-control mode have been conducted over strain amplitude from 0.2 to 1.0 pct until complete failure of the specimens. Asymmetric cyclic loading tests under stress-control mode, i.e. ratcheting tests, have also been conducted with various combinations of mean stress and stress amplitude till complete failure of the specimen. During symmetric cyclic loading, cyclic hardening response is followed by a stress saturation stage for both FCC metals. Whereas in case of copper, this saturation stage continues till failure, a secondary hardening stage appears at the end of stress saturation stage and continues till complete failure in case of aluminium. Such difference in cyclic hardening phenomenon of two different FCC metals is linked with the different values of SFEs. Asymmetric cyclic loading under stress-control mode results in continuous elongation of specimen in the direction of mean stress for both FCC metals. However, in case of aluminium such accumulation of inelastic strain ceases due to plastic shakedown after certain amount of ratcheting strain during asymmetric cyclic loading with stress combinations having maximum stress of 80 MPa or lower.

Keywords Ratcheting · Low cycle fatigue · Stacking fault energy · Dislocation cell structure

J. K. Mahato (✉) · A. Kundu · P. C. Chakraborti
Metallurgical and Material Engineering Department, Jadavpur University,
Kolkata 700032, India
e-mail: jayanta.mahato@gmail.com

P. S. De
Department of Engineering Design, IIT Madras, Chennai 600036, India

1 Introduction

Fatigue behavior of material is commonly studied under completely reversed cyclic straining or stressing. Material damage caused by cyclic loading is also studied under stress-control asymmetric cyclic loading, i.e. cyclic loading with non-zero mean stress. In this case, final failure of specimen occurs due to combined effect of fatigue damage and cycle-by-cycle inelastic strain accumulation. Such inelastic strain accumulation in the direction of applied mean stress is known as "ratcheting deformation". Therefore, the damage occurring due to ratcheting deformation deteriorates the cyclic life of specimens and components as compared to what happened in case of pure fatigue deformation. In this regard, the study of both symmetric and asymmetric cyclic loading behavior of materials is essential for safety and structural integrity purpose of cyclically loaded components and structures.

In FCC metals and alloys, stacking fault energy (SFE) plays important role in cyclic plastic deformation process, mainly at stress saturation stage. One of the basic mechanisms in cyclic deformation process of FCC metals is related to the cross slip of screw dislocations or climb of edge dislocations. This cross slip and climb mechanisms are controlled by stacking fault energy [1–5]. Higher SFE material makes secondary slip easier and increases the probability of cross slip. As the ability of dislocation to cross slip favors the formation of dislocation cell structure, dislocation cell structures are formed in case of higher SFE materials [6]. As for example, the cross slip in case of aluminium is higher, and hence dislocation cell structure forms at stress saturation stage even at low strain amplitude [6]. Such cell structure developed in high SFE metals influences the fatigue crack growth rate as cell boundaries offer the preferred route of cracks [7]. Awatani et al. [7] suggested that since in case of higher SFE metals dislocations can move through cell boundaries mobility of dislocations contributing to crack extension decreases with decreasing value of SFE. Kang et al. [8] have experimentally observed the strain-control symmetric cyclic hardening/softening behavior of three different FCC metals. They have reported that hardening behavior caused by symmetric cyclic loading depends on the value of stacking fault energy of material. They found that the extent of cyclic hardening is low in case of higher SFE material (pure aluminium) compared to the moderate SFE material (pure copper).

Similar to symmetric cyclic loading behavior, asymmetric cyclic loading behavior i.e. ratcheting deformation also depends on stacking fault energy (SFE). In this regard, Kang et al. [8] have experimentally observed the uniaxial ratcheting behavior of different FCC metals having different stacking fault energies, e.g. SS304, pure copper and pure aluminium. They have pointed out that in case of stress-control asymmetric cyclic loading the ratcheting strain does not decrease with decreasing value of stacking fault energy, but decreases with decreasing extent of cyclic hardening of the material. Over the past three-to-four decades many researchers studied uniaxial and multi-axial ratcheting behaviors of different materials, like medium carbon steel, 1Cr18Ni9Ti stainless steel, 25CDV4.11 steel,

SS304 stainless steel, SS316L stainless steel, SA333 Gr 6 piping steel, 9Cr–1Mo steel, IF steel, SA333 Grade 6 C-Mn Steel, Inconel 718, Cu alloy [9–21] and many others. However, the role of stacking fault energy (SFE) of single-phase materials on both symmetric and asymmetric cyclic loading behavior is limited in the open literature domain.

The objective of present investigation is to study the effect of stacking fault energy on both low cycle fatigue and ratcheting deformation behavior of two different FCC metals.

2 Experimental Procedure

Present investigation has been carried out on commercial purity polycrystalline copper (99.97 wt%) and aluminium (98.48 wt%) supplied in the rod form. Cylindrical specimen blanks of copper were annealed at 850 °C for 2 h and then quenched in normal water. In case of aluminium, the specimen blanks were heated at 500 °C for 2 h and then slowly cooled in the furnace. Small metallographic specimens were taken from the heat-treated specimen blanks and polished following usual metallographic procedure. After polishing, etching of copper and aluminium specimens was done with $FeCl_3$ solution and Keller's reagent, respectively. The polished and etched specimen surfaces were observed in an inverted optical microscope, Leica DMILM. Microstructure of different fields of view was grabbed using a digital camera, Leica DC300. Linear intercept method following ASTM E112 standard has been used to measure the grain size of annealed specimens.

Cylindrical tensile specimens of 30 mm parallel length and 6.25 mm gauge diameter were fabricated out of heat-treated specimen blanks. Tensile tests were performed at room temperature in a computer-controlled servo-hydraulic universal testing machine, Instron of ± 100 kN load capacity. Tests were done under strain-control mode using an extensometer of 25.00 mm gauge length at a strain rate of 10^{-3} s^{-1}.

In case of symmetric cyclic loading, tests were performed on specimens having 15.00 mm parallel length and 7.00 mm gauge diameter. Strain-control cyclic loading at different strain amplitudes (0.20–1.0%) was done until complete failure of the specimens. Tests were done using a triangular strain waveform at strain rate of 5×10^{-3} s^{-1}. All the tests were done at room temperature (~ 300 K) in a computer-controlled servo-electric universal testing machine, Instron 8862, of ± 100 kN load capacity. An extensometer of 12.50 mm gauge length and $\pm 20\%$ full range capacity was used for constant strain amplitude cyclic tests. A general-purpose fatigue testing software, Instron WaveMatrix 1.5, has been used for controlling the tests and acquiring test raw data.

In case of asymmetric cyclic loading, tests were performed on specimens having 28.00 mm parallel length and 7.0 mm gauge diameter. Stress-control cyclic loading at different combinations of mean stress and stress amplitude has been done until

complete failure of the specimens. Tests were done under engineering stress-control mode at a stress rate of 200 MPa s^{-1}. A triangular stress waveform has been used for the purpose of cyclic loading. All the tests were done at room temperature ($\sim$300 K) in the same machine as that has been used for symmetrical cyclic loading purpose under strain-control mode. In this case also, tests were controlled and data acquisition was accomplished using a general-purpose fatigue testing software, Instron, WaveMatrix 1.5. An extensometer of 25.00 mm gauge length and -10 to 100% full range capacity was used to record cycle-by-cycle strain response during asymmetric cyclic loading. In most cases, tests were continued until complete failure of the specimens.

3　Results and Discussion

3.1　Microstructure and Tensile Properties

Microstructure of annealed copper and aluminium specimens is shown in Fig. 1a, b. It is found that microstructure of annealed copper specimens consists of polyhedral grains with annealing twins interspersed in some grains. But in case of aluminium, it is found that microstructure only consists of equiaxed grains. The difference between the microstructure of copper and aluminium specimen is that while the microstructure of annealed copper consists of annealing twins, the microstructure of annealed aluminium does not consist of any such annealing twin due to its higher SFE value. The measured two-dimensional average grain size of annealed Cu and annealed Al was obtained as 175 and 82 µm respectively. Tensile properties of annealed copper and aluminium have been listed in Table 1. It is found that strength, ductility and work hardening exponent values are more in case of annealed copper due to its low SFE (SFE of Cu $\sim$80 mJ m^{-2}) in comparison to annealed aluminium (SFE of Al $\sim$200 mJ m^{-2}).
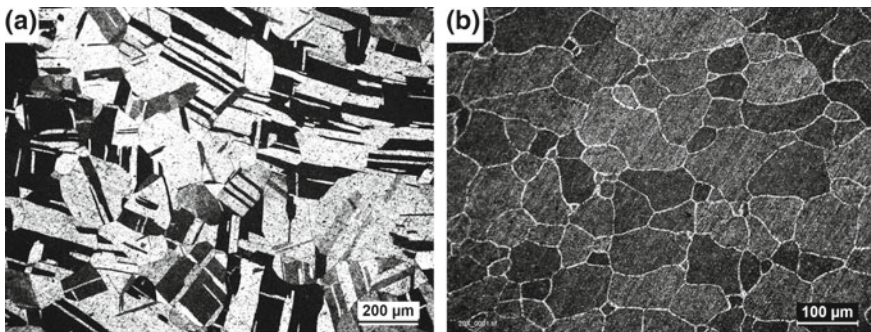
Fig. 1 Optical micrographs of **a** annealed copper and **b** annealed aluminium

Table 1 Tensile properties of annealed copper and annealed aluminium

Specimen	YS (MPa)	UTS (MPa)	Uniform strain (%)	Total strain (%)	n	K (MPa)	Reduction in area (%)
Copper	60.0	221.0	33.0	49.0	0.39	485	77.55
Aluminium	48.0	103.0	16.0	31.0	0.24	196	92.91

3.2 Symmetric Cyclic Behavior

The cyclic hardening or softening during strain-control symmetric cyclic loading can be identified in terms of the variation of true stress amplitude with the number of cycles. The true stress amplitude variation with number of cycles for annealed copper and aluminium is shown in Fig. 2a, b, respectively. It is observed that with increase of strain amplitude, true stress amplitude response increases for both annealed copper and aluminium. It is also observed that irrespective of applied strain amplitude the cyclic hardening followed by cyclic stability occurred for both FCC metals. In case of annealed Copper, hardening continued up to about 100 cycles followed by cyclic stable behavior. Such stable cyclic stress response happens due to the formation of stable dislocation cell structure [22]. It is found that with increase of strain amplitude the stress saturation region is gradually decreased and finally becomes insignificant at higher applied strain amplitudes.

In case of annealed aluminium, the initial hardening is first stabilised within few cycles and the stress saturation condition does not prevail for large number of cycles; instead, further hardening (secondary hardening) occurred very rapidly and extensively at the end of stress saturation stage, Fig. 2b. Such different cyclic stress response of annealed copper and aluminium can be attributed to the dislocation cell structure formation. The stable dislocation cell structure formation depends on stacking fault energy (SFE) of materials; higher SFE material have more tendency to form stable dislocation cell structure because higher SFE material makes secondary slip easier and increases the probability of cross slip which favors the
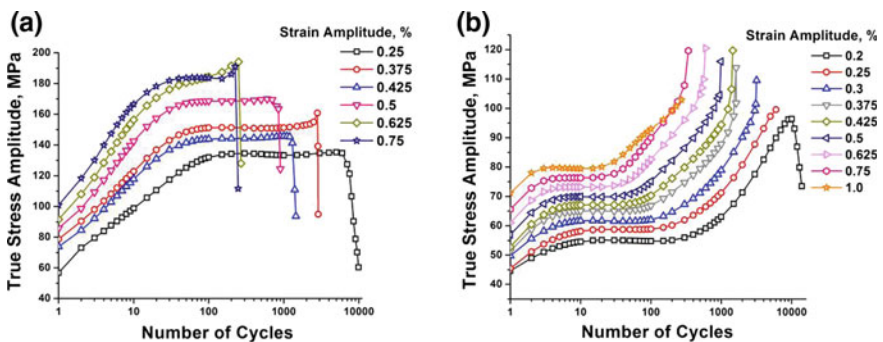
Fig. 2 Stress response variation with number of cycles for **a** annealed copper and **b** annealed aluminium at different strain amplitude levels

formation of dislocation cell structure [6]. It has also been reported by Oh et al. [22] that during the early cyclic hardening stage of type 347N stainless steel (SFE ~ 20 mJ m^{-2}) dislocations develop into a loosely tangled structure due to less interaction of dislocations. On continued cycling beyond the early hardening stage, i.e. during stress saturation period, the dislocations are rearranged into a dislocation substructure (weak cell structure). Further cycling results in the transformation of dislocation substructure into a distinct cell structure and increases the dislocation cell density, and thereby secondary hardening occurs in type 347N stainless steel [22]. Similar to the early investigation [22] in the present study also secondary hardening occurred at the end of stress saturation stage in case of annealed aluminium.

It is found that at lower strain amplitude the fatigue life is less for annealed aluminium compared to annealed copper. This is attributed to the effect of SFE on dislocation dynamics involving dislocation movement, multiplication of dislocation and their interactions. In case of high SFE material, dislocations easily cross slip around obstacles. Due to easy cross slip, the high stacking fault energy material promotes the formation of slip bands and large plastic zones at the crack tips, which assists the initiation and growth of fatigue cracks [23]. But in case of low SFE material, cross slip of dislocations is difficult. This restricts fatigue crack initiation and propagation [23]. Therefore, fatigue crack initiation and propagation are more difficult in case of low SFE materials compared to high SFE materials. Therefore, SFE of copper being low as compared to aluminium both fatigue crack initiation and propagation become more difficult compared to aluminium and more fatigue life observed in case of copper at lower strain amplitude.

Figure 3a shows the experimentally obtained saturated stress–strain hysteresis loops of both copper and aluminium under fully reversed uniaxial strain-control cycling. In case of annealed copper, the half of the numbers of cycles to failure is considered as saturated cycle but in case of aluminium, the number of cycles at the middle of saturation stage is considered as saturated cycles. This was done due to secondary hardening behavior of annealed aluminium. It is clear in the present investigation that both the FCC metals exhibit non-masing behavior, Fig. 3a.
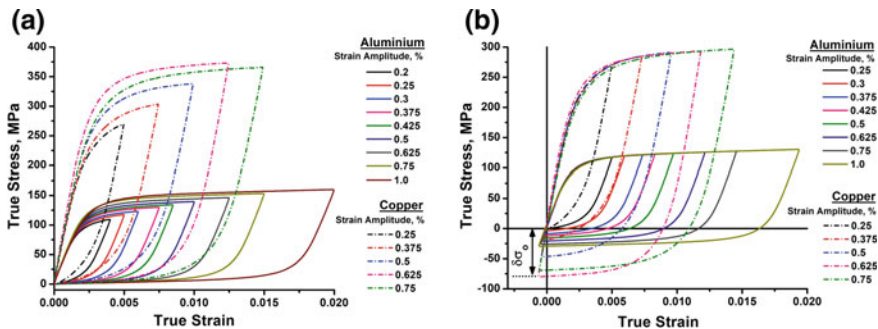
Fig. 3 Plot of **a** half-life/saturated life stress–strain hysteresis loop and **b** master curve for determining non-masing stress of both annealed copper and aluminium

Table 2 Measured non-masing stress ($\delta\sigma_o$) of annealed copper and aluminium

	Non-masing stress ($\delta\sigma_o$) (MPa)							
Strain amplitude (%)	0.25	0.3	0.375	0.425	0.5	0.625	0.75	1.0
Annealed copper	0		44		48	82	137	
Annealed aluminium	0	4	9	12	16	21	26	29

To account the non-masing behavior, stable hysteresis loops have been plotted by translating the loading branches of different strain amplitudes in such a way that they overlap in a master curve, Fig. 3b. The extension of the linear region for any total strain range (taking origin as reference) is considered as the magnitude of the non-masing stress ($\delta\sigma_o$) which is an additional quantity that is required to shift the corresponding tip to the origin. The non-masing stress represents the increase in proportional stress range due to non-masing behavior of the material. The measured non-masing stress for investigated annealed copper and aluminium is listed in Table 2. It is observed that non-masing stress is more in case of annealed copper compared to annealed aluminium and it increases with increase of strain amplitude. The less non-masing stress observed in case of annealed aluminium is due to its higher stacking fault energy compared to annealed copper. During cyclic loading, easy cross slip occurs in case of aluminium due to its higher stacking fault energy; therefore, less amount of non-masing stress is required to overlap loading branches in a master curve.

3.3 Asymmetric Cyclic Behavior

Engineering stress-control ratcheting curves of annealed copper and annealed aluminium at different stress combinations are shown in Fig. 4a, b, respectively. It is observed that during ratcheting deformation, irrespective of applied stress
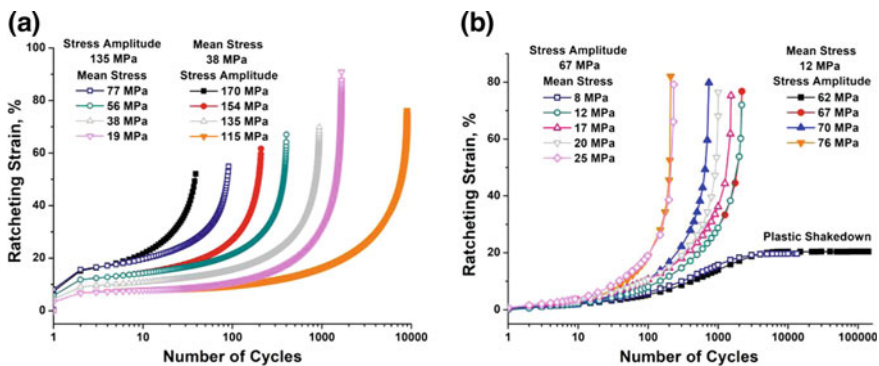
Fig. 4 Ratcheting curves of annealed **a** copper and **b** aluminium at different stress combinations

combination the inelastic strain accumulation in the specimen occurs except in case of plastic shakedown effect due to the presence of non-zero mean stress. It is also observed from Fig. 4a that in case of annealed Cu the ratcheting strain is accumulated in three different stages. In the first stage, irrespective of stress combinations the ratcheting strain evolution increases rapidly followed by almost a steady-state condition. Finally, in the last stage, ratcheting strain accumulation occurs very rapidly due to increase of true stress caused by large reduction of specimen cross-sectional area accompanied by specimen elongation.

Similar to annealed copper the ratcheting curves of annealed aluminium shown in Fig. 4b also reveal different stages of deformation. The interesting observation is that plastic shakedown occurs at certain stress combinations for which the maximum stress is at or below 80 MPa. Hysteresis loops showing plastic shakedown have been shown in Fig. 5. In these cases, after accumulation of about 17–20% ratcheting strain no further strain is accumulated with progression of cyclic loading and thus tests were terminated. Such plastic shakedown at a maximum stress of 80 MPa or below can be linked with the magnitude of saturated stress during strain-control cyclic loading even at higher strain amplitude of 1.0%. The occurrence of plastic shakedown in case of annealed aluminium specimen is attributed to the higher SFE value of aluminium. It has already been mentioned that secondary hardening occurs during strain-control cyclic loading at the end of stress saturation stage in case of aluminium due to the formation of stable dislocation cell structure at stress saturation stage [22, 24]. The probable formation of similar stable dislocation cell structure in case of asymmetric cyclic loading of aluminium specimens hinders the ratcheting deformation after accumulation of certain amount of ratcheting strain for lower stress combinations, e.g. 12 ± 62 MPa and 8 ± 67 MPa.

Interestingly, it is observed that amount of strain accumulation for both FCC metals is more in case of ratcheting deformation compared to the tensile deformation irrespective of stress combinations excepting plastic shakedown cases. It is known that after nucleation of voids, void growth and void coalescence limit the

Fig. 5 Hysteresis loops showing plastic shakedown during ratcheting of aluminium at 67 ± 8 MPa stress combination
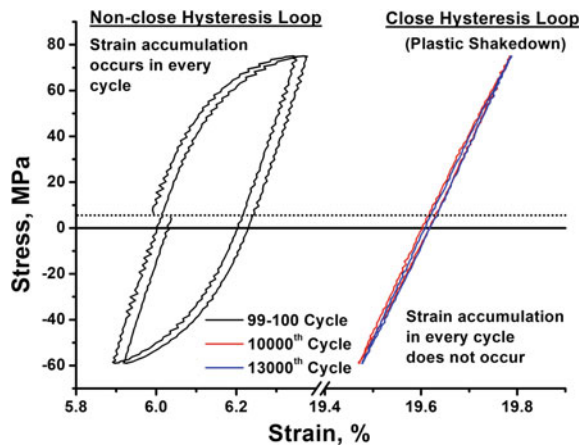
uniform strain during tensile loading of ductile materials. It is believed that the compressive stress present during ratcheting deformation retards nucleation of voids and void growth and thus accumulation of higher amounts of uniaxial strain occurs during ratcheting deformation as compared to monotonic deformation.

It is observed that irrespective of stress combinations the ratcheting strain rate evolution varies with number of cycles in three different stages for both FCC metals. In the first stage, ratcheting strain rate decreases rapidly within first few cycles, followed by accumulation of ratcheting strain at an almost steady (constant) rate. Finally in the last stage, ratcheting strain rate again increases until complete failure of the specimens due to increase of true stress caused by substantial reduction in cross-sectional area along with the elongation of specimen. It is also observed that the initial as well as although the ratcheting deformation, ratcheting strain rate is more for higher stress amplitude (s_a) or higher mean stress (s_m) and decreases with decrease in s_a or s_m. As ratcheting strain rate increases with increase of either s_a or s_m, the ratcheting life decreases with increase in either s_a or s_m. In case of aluminium, the ratcheting strain rate falls down at steady-state region and tends to be zero at stress combination of 12 ± 62 and 8 ± 67 MPa due to the plastic shakedown effect.

The average steady-state ratcheting rate has been calculated from the ratcheting strain rate curves of both FCC metals, Fig. 6a, b. It has been found that increase of either s_a or s_m at constant s_m or s_a respectively, the average ratcheting strain rate increases for both FCC metals. Interestingly it is also observed that irrespective of applied stress combinations the average ratcheting strain rate follows a power relationship with the number of cycles to failure (N_f) for both FCC metals, Fig. 7. In the present study the ratcheting life can be fairly estimated from this power relationship as the steady-state ratcheting deformation stage constitutes the major fraction of the cyclic life. From Fig. 7, it can be said that for a certain steady-state ratcheting rate, the number of cycles to failure is more in case of annealed aluminium compared to annealed copper. However, the effect of stacking fault energy
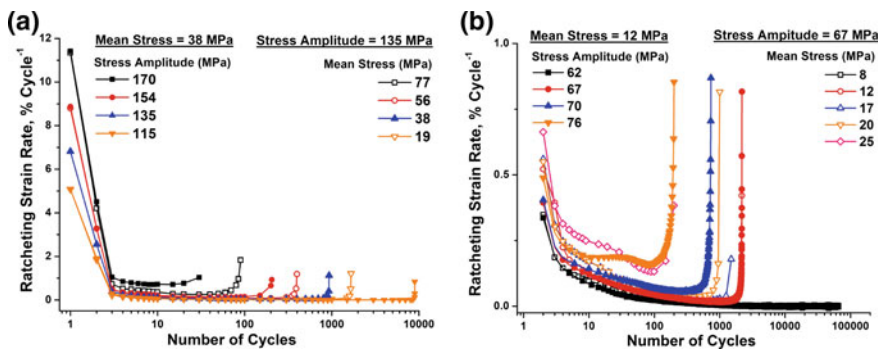
Fig. 6 Ratcheting strain rate variation with number of cycles at different stress combinations for **a** annealed copper and **b** annealed aluminium specimens

Fig. 7 Co-relationship between average steady-state ratcheting rate with cycles to failure irrespective of stress combination for both FCC metals
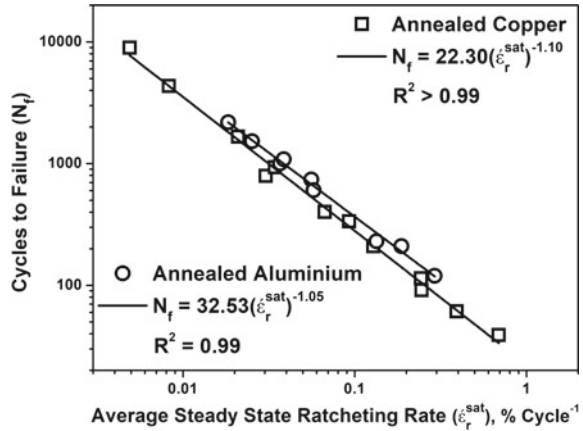
on steady-state ratcheting strain rate could not be directly correlated as the applied stress components (mean stress and stress amplitude) were different in both FCC metals.

3.4 Fractography

The fracture morphologies of annealed copper and aluminium failed under symmetric cyclic loading condition are presented in Figs. 8a–c and 9a–c respectively. It is observed that irrespective of applied strain amplitudes fatigue striations are formed for both annealed copper and annealed aluminium specimens. Therefore, it seems that the whole fracture process is governed by stage II crack growth during symmetric cyclic loading condition. As each fatigue striation represents a single stress cycle [23] the spacing of fatigue striations reflects the fatigue crack propagation rate. It is found that the average striation spacing increases with increase of strain amplitude. This corroborates well with the LCF lives of both FCC metals (Fig. 2). It is also found that irrespective of applied strain amplitude the average
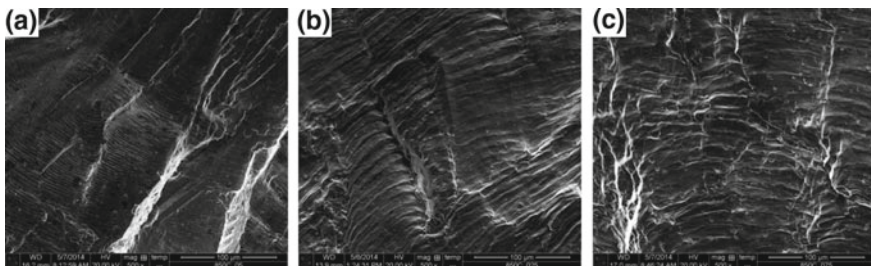
Fig. 8 Fractographs of copper fatigued at **a** 0.25, **b** 0.5, **c** 0.75% strain amplitude levels
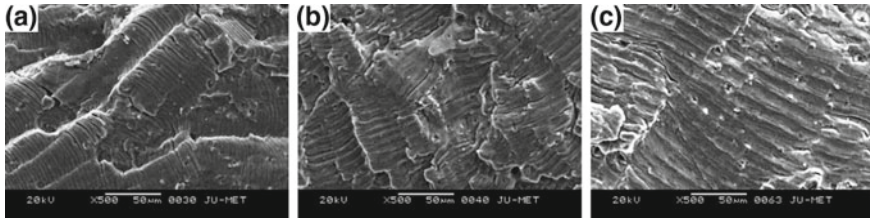
Fig. 9 Fractographs of aluminium fatigued at **a** 0.25, **b** 0.5, **c** 0.75% strain amplitude levels

striation spacing is more in case of annealed aluminium as compared to annealed copper. This happens due to the more SFE value and higher cross slip propensity of aluminium.

4 Summary

From the present investigation the following conclusions have been drawn:

1. In case of symmetric cyclic loading condition the cyclic stress response of annealed aluminium is completely different from that of annealed copper. In case of aluminium, the secondary hardening appeared at the end of stress saturation stage. This is attributed to the easy formation of stable dislocation cell structure at saturation stage due to its higher SFE values. More non-masing stress is needed in case of annealed copper compared to annealed aluminium to overlap all the loading branches in a master curve. This is attributed to the lower SFE values of annealed copper.
2. During strain-control symmetric cyclic loading both FCC metals failed by formation of fatigue striations. The spacing between striations formed during LCF test depends on applied strain amplitude and stacking fault energy of material.
3. Stress-control asymmetric cyclic behavior of both FCC metals occurred in different stages: ratcheting strain evolution increases rapidly followed by a steady state and finally again increases very rapidly. In case of annealed aluminium plastic shakedown occurred after accumulation of certain amount ratcheting strain at stress combinations for which maximum stress is at or below 80 MPa. Such plastic shakedown at a maximum stress of 80 MPa or below can be linked with the magnitude of saturated stress during strain-control cyclic loading. The occurrence of plastic shakedown in case of annealed aluminium specimen is attributed to the higher SFE value of aluminium.

References

1. A.S. Argon, W. Moffatt, Acta Metall. **29**, 293 (1981)
2. Q. Kong, Y. Li, Philos. Mag. A **68**, 113 (1993)
3. V.S. Sarma, J. Wang, W. Jian, A. Kauffmann, H. Conrad, J. Freudenberger, Y. Zhu, Mater. Sci. Eng. A **527**, 7624 (2010)
4. Y. Zhao, Y. Zhu, X. Liao, Z. Horita, T. Langdon, Appl. Phys. Lett. **89**, 121906 (2006)
5. G. Sande, Softening Behaviour of Selected Commercially Pure Aluminium Model Alloys (Norwegian University of Science and Technology, 2012)
6. Y. El-Madhoun, A. Mohamed, M. Bassim, Mater. Sci. Eng. A **359**, 220 (2003)
7. J. Awatani, K. Katagiri, K. Koyanagi, Metall. Trans. A **10**, 503 (1979)
8. G. Kang, Y. Liu, Y. Dong, Q. Gao, J. Mater. Sci. Technol. **27**, 453 (2011)
9. S. Bari, T. Hassan, Int. J. Plast **18**, 873 (2002)
10. X. Chen, R. Jiao, K.S. Kim, Int. J. Plast **21**, 161 (2005)
11. X. Chen, R. Jiao, Int. J. Plast **20**, 871 (2004)
12. G. Kang, Y. Li, J. Zhang, Y. Sun, Q. Gao, Theoret. Appl. Fract. Mech. **43**, 199 (2005)
13. G. Kang, Q. Kan, J. Zhang, Y. Sun, Int. J. Plast **22**, 858 (2006)
14. X. Feaugas, C. Gaudin, Int. J. Plast **20**, 643 (2004)
15. C. Gupta, J. Chakravartty, G. Reddy, S. Banerjee, Int. J. Press. Vessels Pip. **82**, 459 (2005)
16. M. Yaguchi, Y. Takahashi, Int. J. Plast **21**, 43 (2005)
17. K. Dutta, K. Ray, Mater. Sci. Eng. A **575**, 127 (2013)
18. S.K. Paul, S. Sivaprasad, S. Dhar, S. Tarafder, Int. J. Press. Vessels Pip. **87**, 440 (2010)
19. S.K. Paul, S. Sivaprasad, S. Dhar, S. Tarafder, J. Nucl. Mater. **401**, 17 (2010)
20. S. Park, K. Kim, H. Kim, Fatigue Fract. Eng. Mater. Struct. **30**, 1076 (2007)
21. C.-B. Lim, K. Kim, J. Seong, Int. J. Fatigue **31**, 501 (2009)
22. Y.-J. Oh, T.-B. Hwang, B.M. Shin, Mater. Trans. **46**, 317 (2005)
23. G.E. Dieter, in *Mechanical Metallurgy* (SI Metric Ed, McGraw-Hill, 1988), p. 396
24. Y. Sun, S.-L. Shen, X.-H. Xia, Z.-L. Xu, Mater. Des. **47**, 106 (2013)

Ratcheting Behavior of SA333 Gr-6 C–Mn Steel at Elevated Temperatures

Girendra Kumar, H. N. Bar, S. Sivaprasad and Ashok Kumar

Abstract Experiments were carried out on SA333 C–Mn steel at 300 °C for different mean stress (σ_m) and stress amplitude (σ_a) combinations. The temperature varying tests were carried out at fixed load condition. It was observed that ratcheting strain accumulation and plastic strain amplitude increases, whereas ratcheting life decreases with the increase of mean stress and stress amplitudes. With an increase in temperature, ratcheting life increases and strain accumulation decreases up to 300 °C, whereas on further increase in temperature ratcheting strain accumulation increases with reduction in ratcheting life. It was interesting to note that the minimum ratcheting rate was observed at 250 and 300 °C. The dynamic strain aging (DSA) phenomena lead to the hardening of material at these temperature regimes. The investigated steel shows DSA temperature regime lies between 250 and 300 °C.

Keywords Ratcheting · Temperature · Ratcheting rate · Dynamic strain aging (DSA)

1 Introduction

SA333 Gr-6 C–Mn steel is used in engineering structures due to its favorable properties like higher thermal conductivity and lower thermal expansion. This material is commonly available and can be fabricated by welding and bending process. In Indian Nuclear Power Plants, this material is used as a primary heat transport piping system for pressurized heavy water reactor PWHR. The piping

G. Kumar (✉) · A. Kumar
Department of Metallurgical and Materials Engineering, N. I. T. Jamshedpur, Jamshedpur 831014, India
e-mail: imgirinit2012@gmail.com

H. N. Bar · S. Sivaprasad
Materials Engineering Division, CSIR- National Metallurgical Laboratory, Jamshedpur 831007, India

structures may be formed as T joints, elbow joint, and straight pipes. These structures must be designed against failure under cyclic symmetrical or asymmetrical loading in service. In such piping structure, cyclic plastic deformation can occur during start-up and shutdown as well as variation in operating condition or seismic event. This leads to permanent accumulation of plastic strain in the material. To overcome these problems, ratcheting study is an important criterion for the successful design of these engineering structures.

Ratcheting can be defined as the directional and progressive accumulation of strain under an asymmetrical stress-controlled cycling. To understand this phenomenon, several research works have been carried out at uniaxial cyclic loading with nonzero mean stress. Various works on uniaxial ratcheting for 304 and 316 stainless steel at room and high temperatures have been reported by Yoshida et al. [1], Chaboche and Nouailhas [2], Ruggles and Krempl [3, 4], and Delobelle [5, 6]. Majority of available literature on ratcheting behavior pertains to studies on piping materials like SA333 [7, 8] and austenitic steels [9–20]. Mean stress and stress amplitude are the two parameters which govern the ratcheting behavior studied by several authors [7, 13, 14, 17, 20–24]. Sarkar et al. [24–26] studied the ratcheting behavior at elevated temperatures and investigated the DSA phenomenon on 316LN stainless steel. The studies on ratcheting behavior of SA333 Gr-6 C–Mn steel are mainly available at ambient temperature [7, 8, 13, 14] and at various loading conditions. However, there is lack of ratcheting behavior studies at elevated temperatures in this material (SA333). The service temperature of this material is about 300 °C and it may vary during start-up and shutdown. Thus, it is crucial to understand the ratcheting behavior of material at different temperatures.

In this investigation, an attempt has been made to study the engineering stress-controlled ratcheting behavior of the material at 300 °C with various combinations of mean stress and stress amplitude. To evaluate the effect of temperature, tests were carried out at a fixed load of 100 and 350 MPa mean stress and stress amplitude, respectively, with temperature varying from RT to 350 °C. For all the tests, a stress rate of 115 MPa/s was kept constant. In order to evaluate the effect of mean stress, stress amplitude and temperature on the deformation behavior of the material various aspects of analysis were done in terms of ratcheting life, ratcheting strain accumulation, plastic strain amplitude, and ratcheting rates.

2 Experimental

The material used in this investigation was SA333 Gr-6 C–Mn steel pipe which has an outer diameter and a wall thickness of 320 and 55 mm, respectively. The chemical composition (in wt%) was C 0.18%, Mn 0.9%, Si 0.02%, P 0.02%, and balance Fe. The microstructure of the raw material was depicted in Fig. 1. It consists of a ferrite–pearlite banded structure. The widths of ferrite and pearlite band were 19 and 15 μm, respectively. The gage diameter and length of the specimen were 8 and 15 mm, respectively. Engineering stress-controlled ratcheting
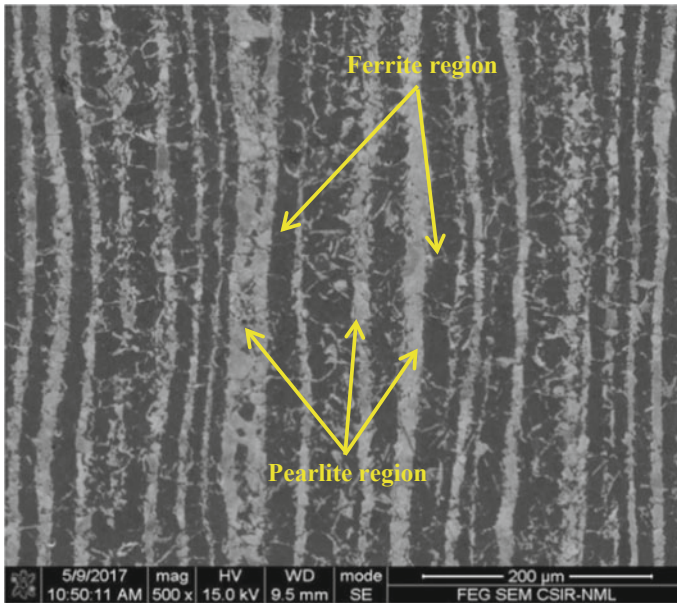
Fig. 1 Ferrite–pearlite banded structure of SA 333 steel in SEM

tests were carried out at (a) fixed mean stress 100 MPa and varying stress amplitudes between 300 and 400 MPa (b) fixed stress amplitude 400 MPa and varying mean stress between 0 and 75 MPa, and (c) varying temperature between RT and 350 °C at fixed load. A loading rate of 115 MPa/s was kept constant for all tests. Ratcheting tests were conducted in closed-loop servo-electric test system.

A 12.5 mm gage length high-temperature extensometer with 100% travel was used to measure the strain accumulation during tests. Tests were continued until failure and load-strain data acquired throughout the tests to obtain minimum 200 data points in each stress cycle. Tests were conducted under software control running on a computer interfaced to the control system of the testing machine.

3 Results and Discussion

Ratcheting is a secondary deformation and induces an accumulation of strain in one direction during cyclic loading with nonzero mean stress. Non-closure of the hysteresis loop, during asymmetrical cyclic loading results in shifting of hysteresis loop along the strain axis. The amount of opening of the loop depends on the loading condition, such as stress level, stress rate, loading path, and loading history [27]. Axial ratcheting strain accumulation ε_r for the individual cycle can be mathematically denoted as follows [7]:

$$\varepsilon_r = \frac{1}{2}\left(\varepsilon_{\max} + \varepsilon_{\min}\right) \tag{1}$$

where ε_{max} is the maximum strain and ε_{min} is the minimum strain of a particular hysteresis loop, ε_r is the progressive increase in strain cycle by cycle and it can be accelerated by the increase of mean stress and stress amplitude, $d\varepsilon_r/dN$ is ratcheting strain rate defined as the increment of ratcheting strain ε_r over each cycle, where N is the number of cycles. The ratcheting strain accumulation is also dependent on temperature.

3.1 Influence of Mean Stress σ_m and Stress Amplitude σ_a on Ratcheting Behavior

The influence of σ_m and σ_a on ratcheting behavior of SA333 Gr.6 C–Mn steel has been studied at 300 °C. Figure 2 represents the ratcheting response curves at various combinations of σ_m and σ_a. It was observed that ratcheting strain increases with the increase of mean stress or stress amplitude. Initially, ratcheting strain curves were stable up to few cycles after that there was slow increase in strain accumulation and finally a rapid increment was observed till the failure of the material. Ratcheting strain curves remain constant until the termination of tests at the other load conditions. For fixed σ_a, with an increase in σ_m, σ_{max} increases which leads to increase in ratcheting strain accumulation (ε_r).

Again Fig. 2 shows that ratcheting life decreases and ratcheting strain accumulation increases with an increase in σ_m or σ_a. The decrease in life with increasing σ_m can be explained in terms of increase in plastic strain amplitude as well as the hysteresis loop area. Some authors [23, 26] shown an increase in life with an increase in σ_m. Paul et al. [7] shown decreasing life even when plastic strain amplitude decreases. Resistance to ratcheting strain accumulation due to dynamic

Fig. 2 Ratcheting strain accumulation versus a number of cycles at various combinations of mean stress and stress amplitude at 300 °C
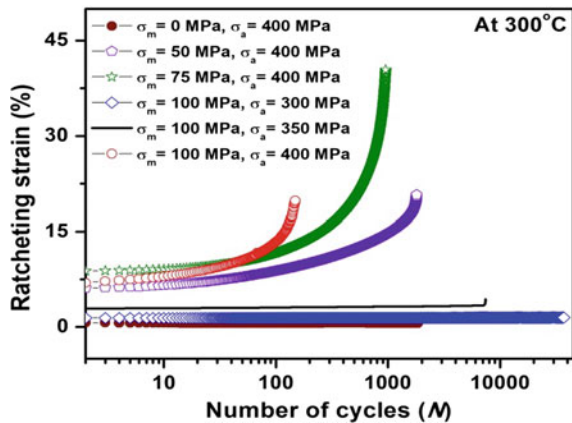
Table 1 Ratcheting tests result at 300 °C for different σ_m and σ_a combinations

σ_a (MPa)	σ_m (MPa)	Number of cycles (N_f)	Ratcheting strain (%)	Plastic strain at half-life (%)	Loop area at half-life (MJ/m^3)
400	0	7000 (test stopped)	0.5	0.069	1.521
400	50	1795	20.7	0.186	4.207
400	75	950	40.5	0.201	4.56
300	100	35,000 (test stopped)	1.49	0.0023	0.743
350	100	7386	4.39	0.022	0.937
400	100	150	19.6	0.145	2.88

strain aging is a consequence of locking–unlocking of mobile dislocations by solute atoms [22, 28]. At 300 and 350 MPa stress amplitudes, it was observed that no strain accumulated due to an elastic shakedown as the locking of mobile dislocation by solute atmosphere (carbon or nitrogen) associated with DSA, which was highly prominent in these load combinations. It was also observed that in these load combinations plastic strain amplitude reduces almost to zero. The observation of fracture surface reveals that fracture mode was transgranular with micro-cracks at 100 MPa mean stress and 350 MPa stress amplitude. Again from Fig. 2, it can be seen that lowest ratcheting life was observed at a mean stress of 100 MPa and 400 MPa stress amplitude, because of rapid strain accumulation in the material as σ_{max} was near about UTS of the material (512 MPa). The failure of the material was ductile in nature. All the results of ratcheting tests at 300 °C are represented in Table 1.

3.2 Ratcheting Strain Rate with Mean Stress and Stress Amplitude

The ratcheting strain rate response represents the hardening–softening characteristic of the material. If ratcheting rate increases or decreases, then this signifies the softening and hardening behavior of the material, respectively. The ratcheting rate can be defined as the difference in ratcheting strain between two consecutive cycles [7, 17, 23].

Figure 3 shows the three regimes in ratcheting rate curve. In regime I, the ratcheting rate decreases gradually with number of cycle (N): termed as primary ratcheting; in regime II, ratcheting rate remains constant: known as secondary ratcheting; while in regime III, ratcheting rate increases rapidly with the increase in number of cycles: called tertiary ratcheting, and results in large ratcheting strain in limited cycles [29]. The ratcheting rate curve is similar to conventional creep curve, but the deformation mechanism is different. The ratcheting is governed by the movement of dislocations, their interaction, and cell formation, whereas creep is related to dislocation glide, diffusion and grain boundary sliding [7, 27]. The

Fig. 3 Variation of ratcheting strain rate $d\varepsilon_r/dN$ with number of cycles
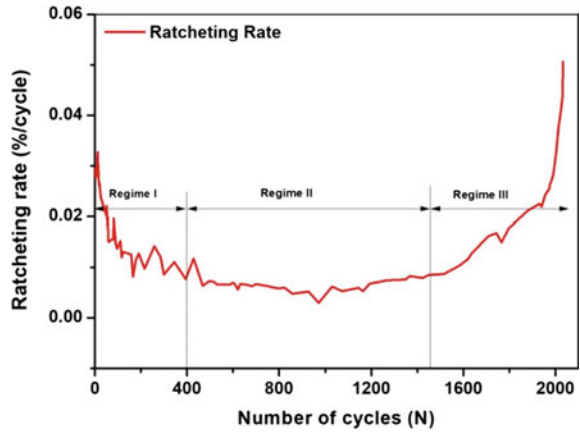
ratcheting strain rate at half-life with the variation of mean stress and stress amplitude is plotted in Fig. 4a, b, respectively. It was found that ratcheting rate increases with the increase in mean stress and stress amplitudes. For $\sigma_a = 300$ and 350 MPa, ratcheting rate at half-life was nearly zero. This may be due to pronounced hardening induced by DSA which leads to very slow ratcheting rate. Some authors [23, 29] shown the strain burst phenomena indicating the release of dislocations from the solute atmosphere.

3.3 Temperature Effect on Ratcheting Strain Accumulation and Cyclic Life

The effect of temperature on ratcheting behavior of the material was studied at 100 MPa σ_m, 350 MPa σ_a and temperature range RT to 350 °C. Figure 5a
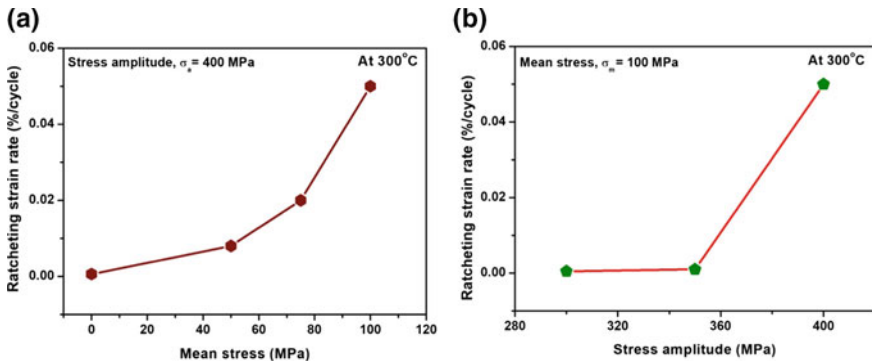
Fig. 4 Variation of ratcheting strain rate **a** with mean stress (σ_m) for constant stress amplitude ($\sigma_a = 400$ MPa) and **b** with stress amplitude (σ_a) for a constant mean stress ($\sigma_m = 100$ MPa)
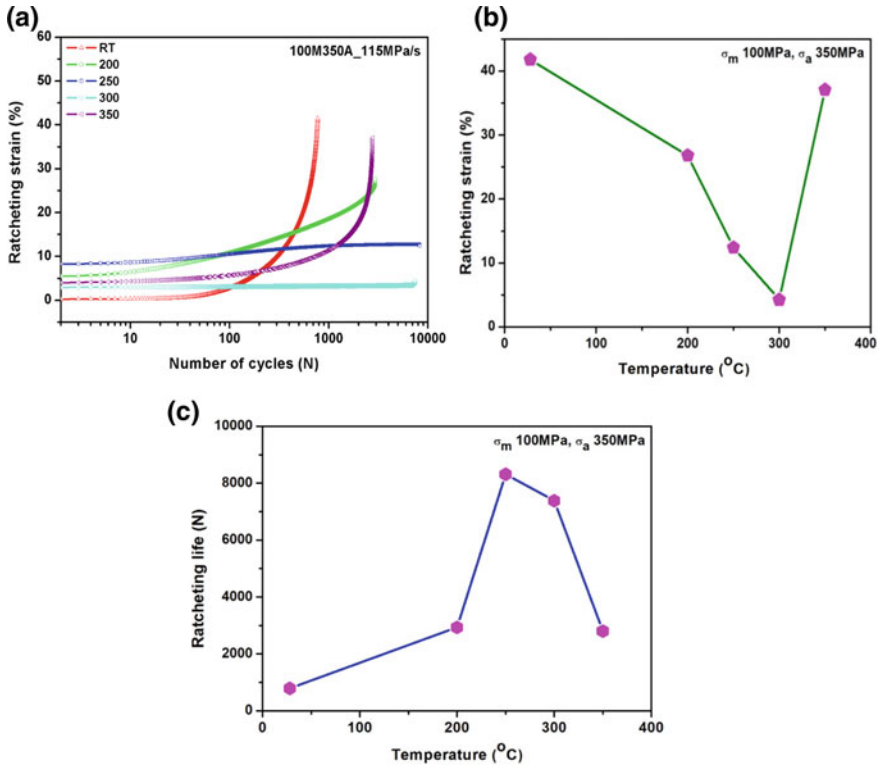
Fig. 5 **a** Ratcheting strain accumulation versus number of cycles at different temperatures, **b** total ratcheting strain versus temperature and **c** ratcheting life of the material versus temperature

represents the ratcheting strain accumulation curves for various temperatures. Results reveal that at room temperature ratcheting strain accumulation was slowly increasing up to about thirty-fifth cycle and after that there was rapid strain accumulation. The rapid strain accumulation leads to thinning of cross-sectional area resulting into failure of material at very less number of cycles. Figure 5a indicates a very slow increment in the ratcheting strain response curve at 250 °C temperature, while at 300 °C a steady-state response throughout the life. This may be due to the locking of mobile dislocations by a solute atom (carbon or nitrogen) which is activated at particular temperature regime and stress rate. Again there is a further increase in the temperature, and initial cycles show a constant response after that slow increment in strain, and finally a rapid strain accumulation takes place. Dynamic strain aging phenomena lead to hardening of material which influence the ratcheting behavior.

In general, with the increase of temperature material shows softening characteristic, but here material gets hardened at certain range of temperature, which delays the strain accumulation. Figure 5b shows that with the increase of temperature, ratcheting strain accumulation decreases up to 300 °C and with a further

Table 2 Ratcheting tests result at σ_m 100 MPa and σ_a 350 MPa at various temperatures

Temperature (°C)	Total number of cycles (N_f)	Ratcheting strain (ε_r) %	Ratcheting rate at half-life ($d\,\varepsilon_r/dN$)
RT	790	41.8	0.0393
200	2935	26.8	0.008
250	8310	12.4	−6.985E−4
300	7386	4.25	−8.5029E−4
350	2800	34.07	0.00628

increase in temperature, ratcheting strain again increases due to the recovery of material. On the other hand, the life of the material increases with the increase in temperature up to DSA regime and further increment in temperature leads to a reduction in life shown in Fig. 5c. The failure mode of the material at 300 and 350 °C was completely different. At 300 °C, the sudden failure of the material occurs due to embrittlement, while at 350 °C the failure of material was due to rapid strain accumulation which leads to early damage of material. Results of ratcheting tests at 100 MPa mean stress and 350 MPa stress amplitude are represented in Table 2. It reveals that maximum life was observed at 250 °C, whereas minimum ratcheting strain accumulates at 300 °C. Here, sudden failure of material at 300 °C results in slightly shorter life than that of 250 °C.

3.4 Influence of Temperature on Ratcheting Strain Rate

To understand the effect of temperature on ratcheting strain rate, a graph has been plotted between ratcheting rate and number of cycles. Ratcheting strain rate represents the amount of strain accumulation with a successive number of cycles. It can be observed from Fig. 6a that at all the temperatures initial ratcheting rate curve shows decreasing trends. It was also found at RT and 350 °C that after a certain number of cycles a rapid ratcheting rate was observed. The ratcheting strain rate was constant until the failure of the material at 250 and 300 °C. Initially, maximum ratcheting rate was observed at 200 °C. In overall, it reveals that with the increase of temperature ratcheting strain rate is found decreasing till the DSA temperature regime and again there is a further increase in temperature ratcheting rate. This may due to recovery process taking place.

With the increase of temperature, ratcheting rate at half-life cycle is found to be continuously decreasing up to temperature 300 °C and then there is a further increase in temperature ratcheting rate. These results are represented in Fig. 6b. Rapid increase in ratcheting rate indicates the release of dislocations from the solute atoms atmosphere [29] and the free movement of dislocations during cyclic loading.
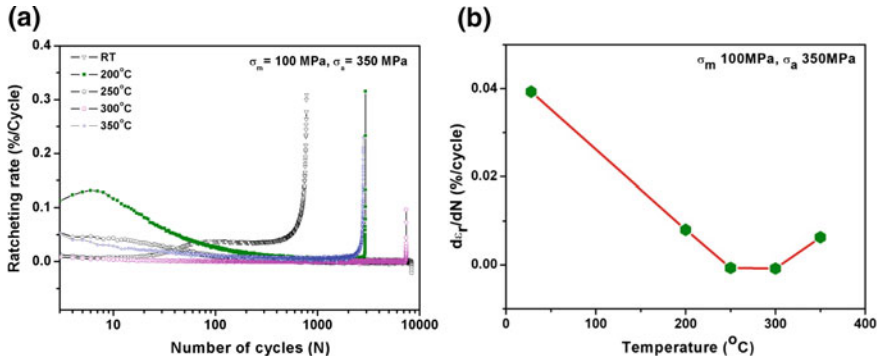
Fig. 6 a Ratcheting strain rate versus number of cycles and **b** ratcheting rate with a variation of temperatures at half-life

4 Conclusions

In this investigation, ratchetingtests of SA333 Gr. 6 C–Mn steel at 300 °C with various combinations of stress amplitude and mean stress and variation of temperature (RT to 350 °C) at fixed load conditions were conducted, and conclusions arrived as follows:

- The ratcheting life and strain accumulation decreases and increases, respectively, with the increase of mean stress and stress amplitude.
- Ratcheting strain rate increases with the increase of mean stress and stress amplitudes.
- The ratcheting life increases whereas ratcheting strain accumulation decreases up to 300 °C. Further increase in temperature leads to increase and decrease in ratcheting strain and life, respectively. The maximum ratcheting life and minimum strain were observed at 250 °C and 300 °C, respectively, due to dynamic strain aging (DSA) phenomena.
- In DSA regime, the ratcheting rate was found minimum due to hardening of the material.

References

1. F. Yoshida, J. Kondo, Y. Kikuchi, Trans. JSME Ser. A **54**, 1151 (1988)
2. J.L. Chaboche, D. Nouailhas, ASME J. Eng. Mater. Technol. **111**, 384 (1989)
3. M.D. Ruggles, E. Krempl, ASME J. Eng. Mater. Technol. **111**, 378 (1989)
4. M.D. Ruggles, E. Krempl, J. Mech. Phys. Solids **38**, 575 (1990)
5. P. Delobelle, Int. J. Plast **9**, 65 (1993)
6. P. Delobelle, P. Robinet, L. Bocher, Int. J. Plast **11**, 295 (1995)
7. S.K. Paul, S. Sivaprasad, S. Dhar, S. Tarafder, J. Nucl. Mater. **401**, 17 (2010)

8. S. Sivaprasad, S.K. Paul, S.K. Gupta, V. Bhasin, N. Narasaiah, S. Tarafder, Int. J. Press. Vessels Pip. **87**, 464 (2010)

9. X. Feaugas, C. Gaudin, Int. J. Plast **20**, 643 (2004)

10. G.Z. Kang, Y.G. Li, J. Zhang, Y.F. Sun, Q. Gao, Theor. Appl. Fract. Mech. **43**, 199 (2005)

11. L. Bochet, P. Delobelle, P. Robinet, X. Feaugas, Int. J. Plast **17**, 1491 (2001)

12. X. Yang, Int. J. Fatigue **27**, 1124 (2005)

13. S.K. Paul, S. Sivaprasad, S. Dhar, S. Tarafder, Theor. Appl. Fract. Mech. **54**, 63 (2010)

14. S.K. Paul, S. Sivaprasad, S. Dhar, S. Tarafder, Mater. Sci. Eng. A **528**, 4873 (2011)

15. L. Taleb, G. Cailletaud, Int. J. Plast **27**, 1936 (2011)

16. M.B. Ruggles, E. Krempl, J. Mech. Phys. Solids **38**(4), 575 (1990)

17. K.K. Ray, K. Dutta, S. Sivaprasad, S. Tarafder, Proc. Eng. **2**, 1805 (2010)

18. G. Kang, Q. Gao, in *Proceedings of 18th International Conference on Structural Mechanics in Reactor Technology (SMiRT 18),* Beijing, China (2005)

19. G. Kang, Q. Gao., L. Cai, Y. Sun, Nucl. Eng. Des. **216**, 13 (2002)

20. J. Polak, J. Man, M. Petrenec, J. Tobias, Int. J. Fatigue **39**, 103 (2012)

21. G. Kang, Y. Liu, Z. Li, Mater. Sci. Eng. A **436**, 396 (2006)

22. P. Rodriguez, Bull. Mater. Sci. **6**, 653 (1984)

23. A. Sarkar, A. Nagesha, R. Sandhya, M.D. Mathew, Mater. High Temp. **29**(4), 351 (2012)

24. A. Sarkar, A. Nagesha, M.D. Mathew, Proc. Eng. **55**, 650 (2013)

25. A. Sarkar, A. Nagesha, P. Parameswaran, R. Sandhya, M.D. Mathew, Mater. Sci. Eng. A **564**, 359 (2013)

26. A. Sarkar, A. Nagesha, R. Sandhya, M.D. Mathew, High Temp. Mater. Proc. **32**(5), 475 (2013)

27. A. Sarkar, B.K. Kumawat, J.K. Chakravartty, J. Nucl. Mater. **467**, 500 (2015)

28. A.H. Cottrell, in *Dislocations and Plastic Flow in Crystals* (Oxford University, 1953)

29. S.-J. Hong, S.B. Lee, J. Nucl. Mater. **340**, 307 (2005)

Stress–Strain Behaviour of Modified 9Cr–1Mo Steel in Asymmetric Cyclic Stressing at Room Temperature

Prerna Mishra, R. S. Rajpurohit, N. C. Santhi Srinivas and V. Singh

Abstract Asymmetric cyclic stressing of structural components causes accumulation of plastic strain known as ratcheting. It is an important factor in design of nuclear power plants as the accumulated plastic strain causes severe reduction in life of the structural components. Operating variables such as the rate of stressing ($\dot{\sigma}$), mean stress (σ_m) and amplitude of stress (σ_a) control the ratcheting fatigue behaviour. Fatigue tests were conducted with σ_m from 190–210 MPa, σ_a from 400 to 420 MPa and the $\dot{\sigma}$ from 50 to 450 MPa/s. The accumulation of plastic strain and its influence on cyclic life of the modified 9Cr–1Mo steel was studied. Increase in the σ_m and σ_a led to the increase in the accumulated plastic strain and reduction in fatigue life. On the other hand, increase in the $\dot{\sigma}$ caused increase in fatigue life because of less plastic strain accumulation. There was cyclic softening with increase in σ_m and σ_a, whereas there was cyclic hardening from rise in the $\dot{\sigma}$.

Keywords Modified 9Cr–1Mo steel · Asymmetric stress cycle · Ratcheting strain · Stress–strain behaviour · Plastic strain

1 Introduction

The modified 9Cr–1Mo steel is one of the very important materials for steam generators and wrapper tubes in liquid metal fast breeder reactors (LMFBR) due to its excellent properties like void swelling resistance, higher conductivity, lower coefficient of thermal expansion, higher strength in tension, fatigue and creep, superior weldability, good oxidation resistance, microstructure stability, and stress corrosion cracking resistance in water steam systems [1–5]. Its high strength is derived from its typical microstructure consisting of lath martensite and high

P. Mishra (✉) · R. S. Rajpurohit · N. C. Santhi Srinivas · V. Singh
Department of Metallurgical Engineering, Indian Institute of Technology
(Banaras Hindu University), Varanasi 221005, India
e-mail: prernam.rs.met16@iitbhu.ac.in

density of dislocations in it along with Cr, V, and Nb carbides in the normalized (1060 °C) and tempered (780 °C) state [6].

During service, structural components experience both symmetric and asymmetric cyclic stressing. Accumulation of plastic strain resulting from asymmetric cyclic stressing due to nonzero mean stress is called ratcheting/ratcheting fatigue or cyclic creep [7, 8]. Ratcheting plays dominant role in reduction of cyclic life. The important variables for the process of ratcheting are σ_m, σ_a, and $\dot{\sigma}$.

A number of investigators have carried out experimental and numerical analysis related to ratcheting fatigue of various materials such as steels, alloys of aluminium, copper, and zirconium [9–11]. However, there is no report on ratcheting behaviour of the modified 9Cr–1Mo steel, an important material of power plants.

The cyclic stress response of the components in cyclic strain controlled mode reflects their hardening/softening behaviour. On the other hand, cyclic hardening and softening of a material under stress control is displayed by decrease and increase in the plastic strain range, respectively. The behaviour of a metallic component subjected to cyclic strain controlled loading may exhibit cyclic hardening, softening, or no change in the stress response depending upon the initial condition of the material as well as the test conditions [12, 13]. The work reported here examines stress–strain behaviour of the modified 9Cr–1Mo steel under asymmetric cyclic loading (Fig. 1) at room temperature.

2 Experimental

The modified 9Cr–1Mo steel was obtained from the IGCAR, Kalpakkam, India in the form of plate of 25 mm thickness following normalizing (1060 °C-1 h) and tempered (780 °C-1 h) treatment (Table 1).

Cylindrical fatigue samples were prepared having gauge diameter of 5.5 mm, gauge length of 15 mm, and threaded ends of 12 mm diameter and length of 35 mm on either side of the specimen. The radius of curvature of the shoulder was 25 mm (Fig. 2). The gauge section was polished with emery papers of 1/0–4/0 grades and finally with paste of alumina powder. Using the three operating parameters (σ_m, σ_a, and $\dot{\sigma}$) and keeping two of them constant at a time, ratcheting fatigue tests were conducted at room temperature, using a 50KN servo-hydraulic MTS^{TM} (Model 810) equipped with fully automatic test star IIs controller. Strain was accurately measured mounting the MTS extensometer of 12 mm gauge length (Model: MTS 632.53E) over gauge section of the samples. Thin slices were sectioned ≈2 mm from the fractured end of the fatigue tested samples and were further reduced to ≈50 µ by mechanical polishing and discs of 3 mm diameter were punched out from them. TEM foils were prepared from these discs using twin jet

Table 1 Composition of the modified 9Cr–1Mo steel (mass%)

C	Si	Mn	P	S	Cr	Mo	Ni	Al	Nb	N	V	Fe
0.1	0.26	0.41	0.018	0.002	9.27	0.95	0.33	0.013	0.074	0.044	0.21	Balance
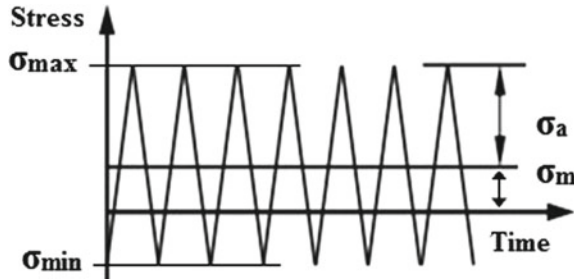
Fig. 1 Asymmetric stress cycling with tensile σ_m and σ_a
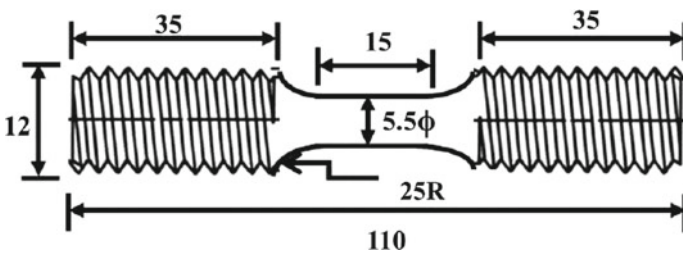
Fig. 2 Geometry of the test sample used for ratcheting fatigue (Dimensions in mm)

electro polisher (Model: Struers Tenupol 5) in the electrolyte containing 6% perchloric acid, 34% n-butanol in methanol, at 22 V, cools to −40 °C. The deformation behaviour and dislocation substructure were analysed by transmission electron microscopy.

3 Results and Discussion

Variation of plastic strain

Plastic strain accumulates due to asymmetric loading. A number of researchers have investigated cyclic stress–strain behaviour and found that it depends not only on the material but also on the magnitude of the stress and stress profile. Materials such as stainless steels and pure copper display cyclic hardening, while 1070 steel exhibits cyclic softening. In general, hardened material (cold worked, quenched) undergoes cyclic softening and soft materials (annealed) exhibit cyclic hardening [14]. With the aid of hysteresis loop (HL) width, cyclic stress–strain behaviour of the modified 9Cr–1Mo steel was evaluated, for the various combinations of σ_m, σ_a and $\dot{\sigma}$. Figure 3 shows the translation of HL for $\sigma_m = 190$ MPa at $\sigma_a = 410$ MPa and $\dot{\sigma} = 150$ MPa/s. The HL for the first cycle shows maximum amount of plastic strain with tensile mean stress.
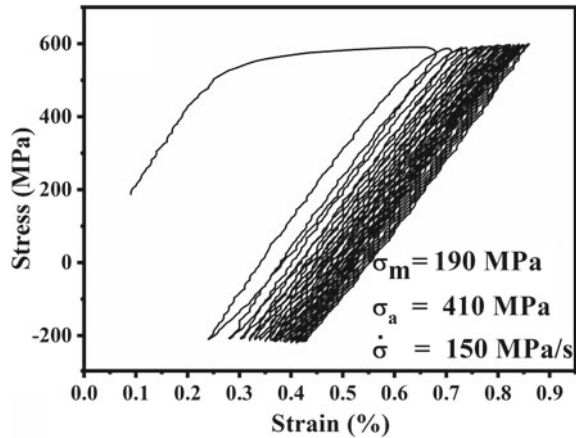
3.1 Impact of Mean Stress on Stress–Strain Behaviour During Asymmetric Cyclic Stressing

Keeping a particular combination of the three variables, comparison was made of the HLs in terms of their width at different number of cycles. In Fig. 4, the effect of σ_m from 190 MPa to 210 MPa at constant σ_a of 410 MPa and $\dot{\sigma}$ of 150 MPa/s is presented at different number of cycles 5, 50 and 500. The general rule is that more the HL area, more amount of energy is absorbed by the material and this lowers the fatigue life.

As shown in Fig. 4, at the constant σ_a = 410 MPa, the width of HLs increased with increase in σ_m from 190 to 210 MPa. The increase in the width of HL with increase in σ_m can be attributed to increase in cyclic softening of the material. Figure 5 shows variation of the HL energy with σ_m. It may be seen that the PSE decreases with increase in the number of cycles at all the three levels of σ_m. In general, the PSE increases with increase in σ_m at 5, 50 and 500 cycles. However, at σ_m of 200 and 210 MPa, the PSE at 500 cycles is higher than that at 50 cycles. This shows that cyclic softening increases at 500 cycles and the effect is more pronounced at the highest σ_m of 210 MPa. Similarly, Fig. 6 shows variation of PSE with number of cycles up to failure at different σ_m illustrating cyclic hardening/ softening of the material. It is evident from Table 2 that at σ_m = 210 MPa, PSE in the first cycle was very high (3.92 MJ/m^3) and drastically reduced to (0.52 MJ/m^3) in the second cycle. There was continued decrease in the PSE (Table 2) till the 90th cycle (0.21 MJ/m^3); however, it started increasing during further cycles and at 500 cycles reached to 0.27 MJ/m^3. Thus, it is obvious that plastic deformation in the first cycle occurred easily; however, cyclic hardening occurred during the subsequent cycles up to the 90th cycle and beyond that there was cyclic softening of the material at slow rate. There is similar trend in variation of the PSE with number of cycles also at the σ_m of 190 and 200 MPa. From the TEM micrograph,
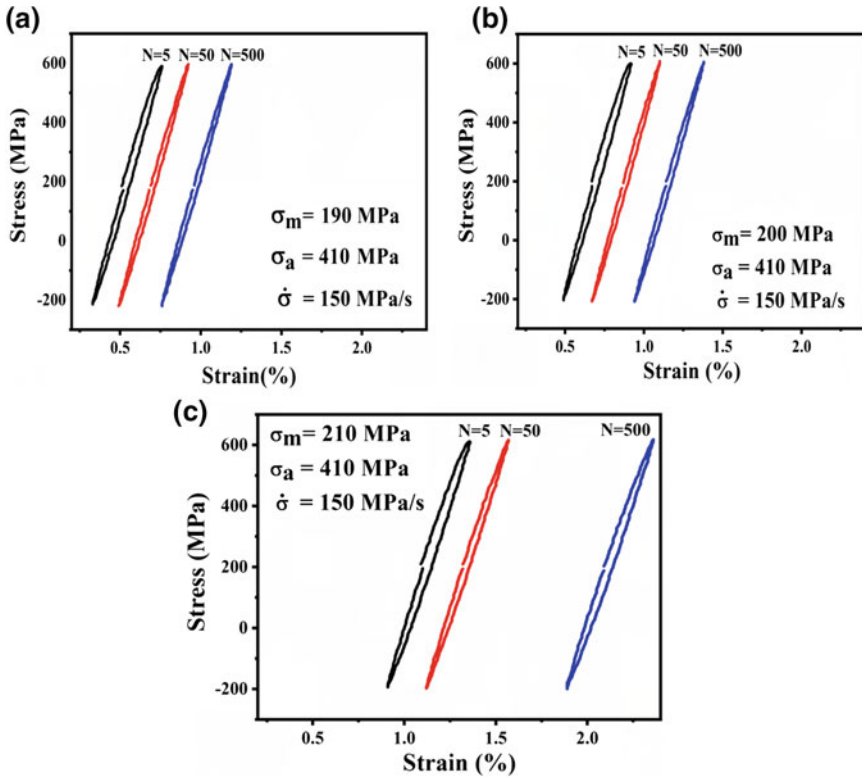
Fig. 4 HL's corresponding to cycle number 5, 50 and 500 stress cycles at various σ_m: **a** 190 MPa, **b** 200 MPa, **c** 210 MPa at σ_a = 410 MPa and $\dot{\sigma}$ = 150 MPa/s

Fig. 5 Effect of σ_m on HL energy at different number of cycles at constant σ_a = 410 MPa and $\dot{\sigma}$ = 150 MPa/s

Fig. 6 Variation of plastic strain energy (PSE) with number of cycles at different σ_m, at constant $\sigma_a = 410$ MPa and $\dot{\sigma} = 150$ MPa/s
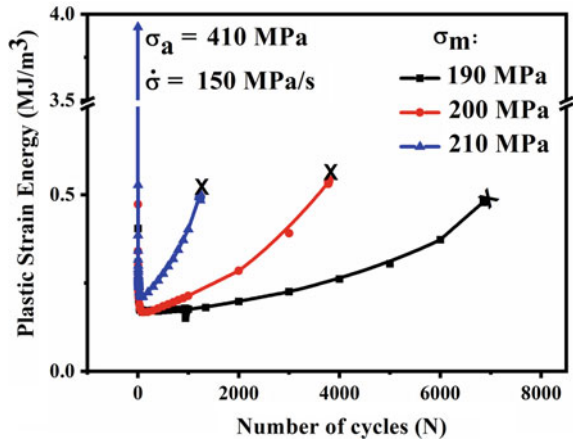
Table 2 Data showing variation of plastic strain energy with mean stress and the number of cycles

Cycle no.	Plastic strain energy (PSE) (MJ/m^3)		
	$\sigma_m = 190$ MPa	$\sigma_m = 200$ MPa	$\sigma_m = 210$ MPa
1	1.72	2.23	3.92
2	0.40	0.47	0.52
90	0.16	0.16	0.21
500	0.17	0.18	0.27
1000	0.18	0.21	0.40

Fig. 7a second phase particles are observed which are indicated by circles and there is easy movement of dislocations resulting in softening. The cyclic hardening after the first cycle resulted from interaction between the dislocations and precipitates of different carbides ($Cr_{23}C_6$, VC, NbC) along the boundary, indicated by arrows and also due to pinning of dislocations marked by circles in Fig. 7b. The relatively large extent of cyclic softening during the later stage of cycling, at all the σ_a may be attributed mainly to smaller subgrains formed by the process of dynamic recovery as shown in the TEM micrograph in Fig. 7c resulting in decrease in hardness or in softening. These features of the TEM micrographs are similar to those observed earlier by Preeti et al. in this steel during symmetrical loading (R = −1) in strain-controlled mode [15].

3.2 Impact of Stress Amplitude on Stress–Strain Behaviour During Asymmetric Cyclic Stressing

The impact of σ_a on HL's at $\sigma_m = 200$ MPa and $\dot{\sigma} = 150$ MPa/s is shown in Fig. 8. The increase in the width of HLs with increase in σ_a may be seen to be similar to that observed for the effect of σ_m and this behaviour may be attributed to the role of
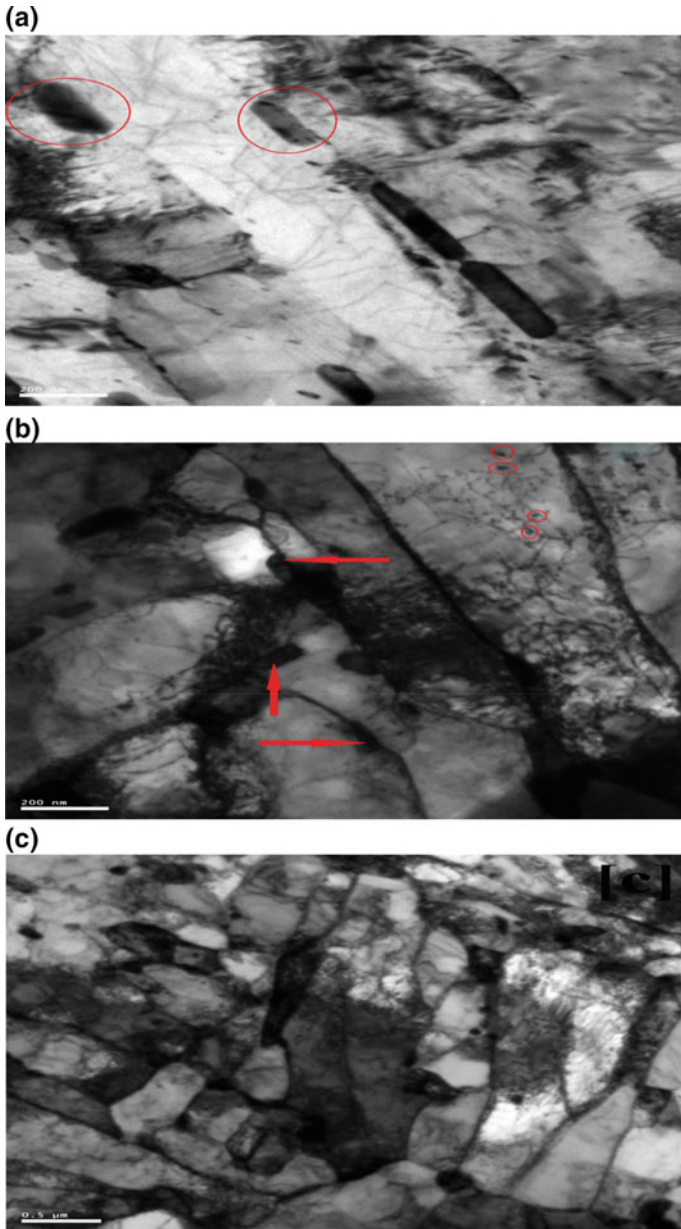
Fig. 7 TEM micrographs of the modified 9Cr–1Mo steel: **a** normalized and tempered, showing easy movement of dislocations, **b** arrows show interaction of dislocations and precipitates whereas circles show pinning of dislocations, **c** formation of smaller subgrains by the process of dynamic recovery in the specimen tested at $\sigma_m = 210$ MPa, $\sigma_a = 400$ MPa and $\dot{\sigma} = 150$ MPa/s
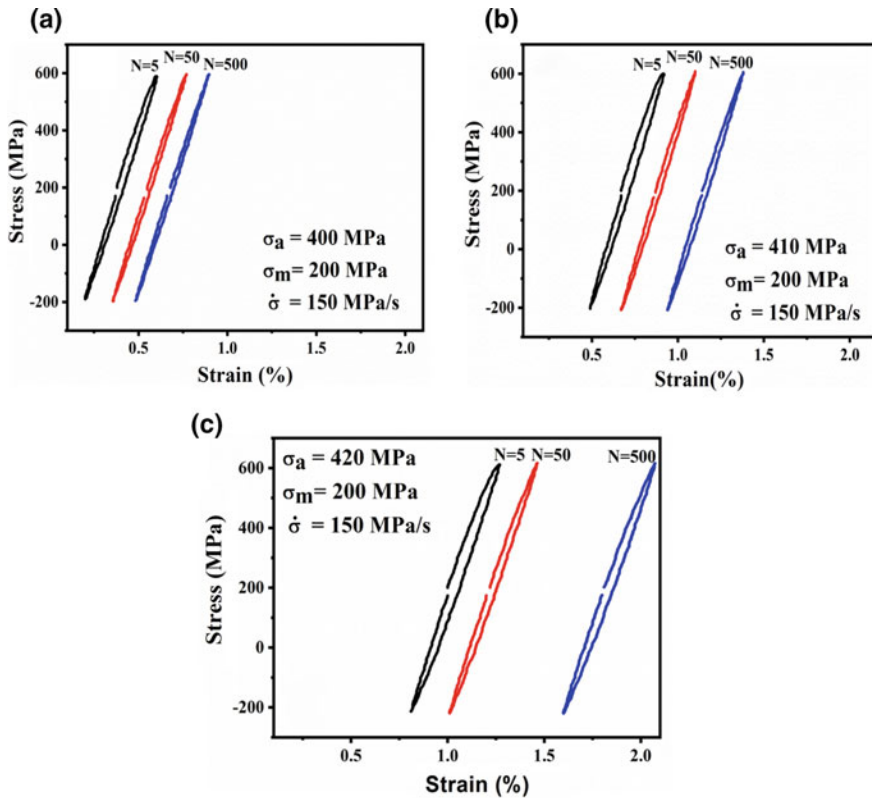
Fig. 8 HLs corresponding to cycle number 5, 50 and 500 at various σ_a: **a** 400 MPa, **b** 410 MPa, **c** 420 MPa at the σ_m = 200 MPa and $\dot{\sigma}$ = 150 MPa/s

dislocations during the initial hardening and the later stage of softening as discussed in the case of σ_m effect.

In general, larger the width of the HL, higher is the extent of softening and decrease in the width of the loops signifies increase in cyclic hardening of the material. It may be noticed from Fig. 8 that with increase in σ_a the width of HLs increases, and thus there is an increase in the degree of softening with increase in this parameter.

Figure 9 shows variation of PSE with σ_a for different number of cycles. The PSE is highest during the 5th cycle as compared to those in the 50th and 500th cycles, at all the three levels of σ_a. Likewise, there was maximum softening during the initial stage and was followed by hardening during the subsequent cycles at all the three levels of σ_a. Further, the degree of softening increased with σ_a.

It is evident from Fig. 9 that with increase in σ_a the absorbed PSE increased reflecting softening of the material. Figure 10 illustrates variation of PSE with number of cycles to failure at various σ_a, and its cyclic hardening/softening behaviour affected by σ_a.

Fig. 9 Effect of σ_a on HL energy at different number of cycles at constant σ_m = 200 MPa and $\dot{\sigma}$ = 150 MPa/s

Fig. 10 Variation of PSE with number of cycles at different σ_a at constant σ_m = 200 MPa and $\dot{\sigma}$ = 150 MPa/s

The variation of PSE at different σ_a with number of cycles up to failure is shown in Fig. 10. The absorbed PSE increased with σ_a, causing softening and larger accumulation of plastic strain with consequent decrease in fatigue life.

3.3 Impact of Stress Rate on Stress–Strain Behaviour During Asymmetric Cyclic Stressing

The impact of stress rate on the HL at σ_m = 200 MPa and σ_a = 410 MPa is shown Fig. 11.

It may be observed from Fig. 11a that at the $\dot{\sigma}$ of 50 MPa/s the width of the HL is more at 50 cycles than that at 5 cycles; however, the loop width is decreased at
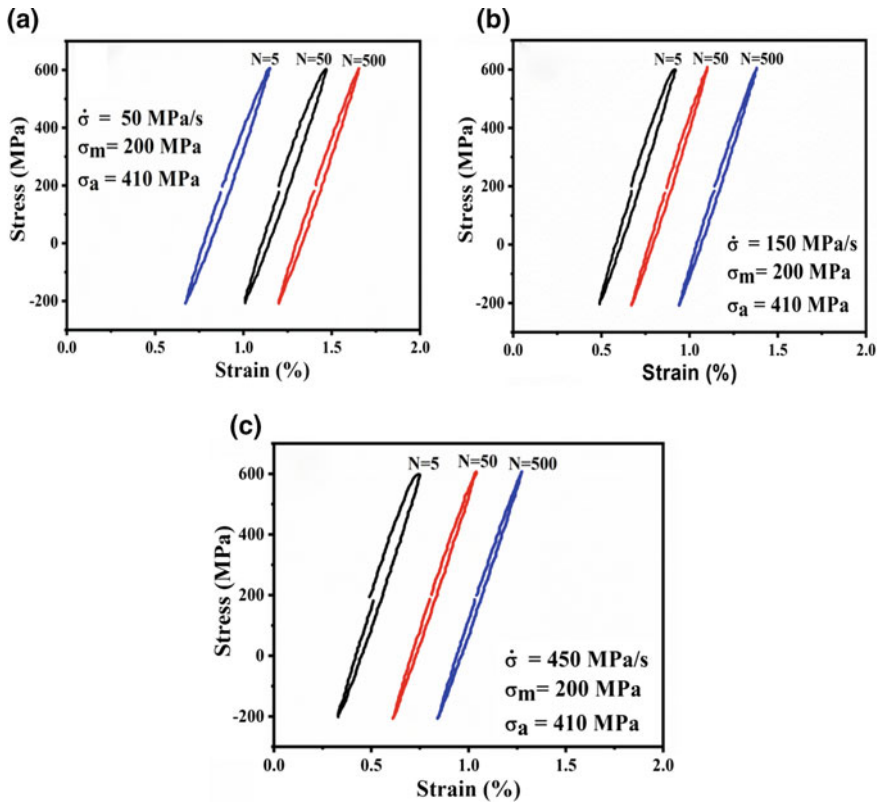
Fig. 11 HLs corresponding to cycle number 5, 50 and 500 at different $\dot{\sigma}$: **a** 50 MPa/s, **b** 150 MPa/s, **c** 450 MPa/s at $\sigma_m = 200$ MPa and $\sigma_a = 400$ MPa

500 cycles. On the other hand, at the higher $\dot{\sigma}$ of 150 and 450 MPa/s, the loop width continuously decreases from the 5th to 500th cycle (Fig. 11b, c). Thus, with increase in the $\dot{\sigma}$ there is an increase in the degree of hardening.

Figure 12 displays variation in PSE of HLs at different number of cycles, with stress rate. The PSE is highest at the lowest $\dot{\sigma}$ of 50 MPa/s, and it decreases at the higher $\dot{\sigma}$ of 150 MPa/s and again increases during the later stage (N = 500 cycles). The variation in PSE of the HLs corresponding to 50th and 500th loops shows continuous decrease in PSE with increase in $\dot{\sigma}$ from 50 MPa/s to 450 MPa/s. Thus, with increase in $\dot{\sigma}$ the absorbed PSE decreased and reflected cyclic hardening of the material.

Fig. 12 Effect of $\dot{\sigma}$ on HL energy at different number of cycles at constant $\sigma_m = 200$ MPa and $\dot{\sigma} = 150$ MPa/s
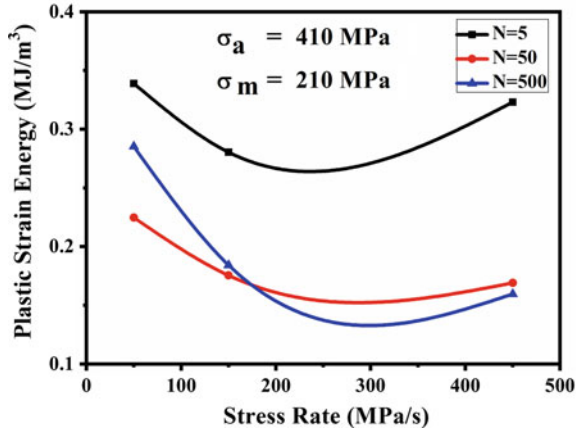
4   Conclusions

The cyclic hardening/softening behaviour of the modified 9Cr–1Mo steel under asymmetrical stress loading was analysed from variation in the width of the HLs and the PSE, with all the three operating parameters (σ_m, σ_a and $\dot{\sigma}$) as well as with number of cycles till failure. The following inferences are drawn from this investigation:

1. Cyclic hardening is observed during the initial cycles, up to 90 cycles, and is followed by cyclic softening during the subsequent cycles till failure with increase in the σ_m from 190 to 210 MPa. It is mainly because of formation of dislocation cell structure.
2. Cyclic hardening occurs during the initial 90 cycles, and is followed by cyclic softening during the subsequent cycles till failure, with increase in the σ_a from 400 to 420 MPa.
3. Cyclic hardening occurs with increase in $\dot{\sigma}$ from 50 MPa/s to 450 MPa/s and in general the extent of hardening increased with increase in the number of cycles.
4. There is an increase in the cumulative plastic strain with increase in σ_m and σ_a, whereas there is a decrease in the cumulative plastic strain with increase in the $\dot{\sigma}$.

References

1. S.L. Mannan et al., Selection of materials for prototype fast breeder reactor. Trans.-Indian Inst. Metals **56**(2), 155–178 (2003)
2. R.E. Stoller, A.S. Kumar, D.S. Gelles., in *Effects of Radiation on Materials: 15th International Symposium*. ASTM (1992)

3. R.L. Klueh, A.T. Nelson, Ferritic/martensitic steels for next-generation reactors. J. Nucl. Mater. **371**(1), 37–52 (2007)
4. R.L. Klueh, Chromium-molybdenum steels for fusion reactor first walls—a review. Nucl. Eng. Des. **72**(3), 329–344 (1982)
5. Srinivas, N.C. Santhi, P. Verma, V. Singh, Dynamic strain ageing behaviour of modified 9Cr-1Mo Steel under monotonic and cyclic loading. Procedia Eng. **184**, 765–772 (2017)
6. Paul, V. Thomas, S. Saroja, M. Vijayalakshmi, Microstructural stability of modified 9Cr–1Mo steel during long term exposures at elevated temperatures. J. Nucl. Mater. **378**(3), 273–281 (2008)
7. K. Dutta, K.K. Ray, Ratcheting strain in interstitial free steel. Mater. Sci. Eng. A **575**, 127–135 (2013)
8. R.S. Rajpurohit, N.C. Santhi Srinivas, V. Singh, Ratcheting strain accumulation due to asymmetric cyclic loading of Zircaloy-2 at room temperature. Procedia Struct. Integr. **2**, 2757–2763 (2016)
9. J. Zhu et al., Bending ratcheting tests of Z2CND18. 12 stainless steel. Int. J. Fatigue **35**(1), 16–22 (2012)
10. S. Vishnuvardhan et al., Ratcheting failure of pressurised straight pipes and elbows under reversed bending. Int. J. Press. Vessels Pip. **105**, 79–89 (2013)
11. R.S. Rajpurohit et al., Effect of ratcheting on tensile behavior of Zircaloy-2 at room temperature. Trans. Indian Inst. Met. **71**(5), 1149–1160 (2018)
12. S.K. Paul et al., Key issues in cyclic plastic deformation: experimentation. Mech. Mater. **43** (11), 705–720 (2011)
13. G.E. Dieter, *Mechanical Metallurgy*, SI Metric edn. (McGraw-Hill Book Company, Singapore, 1987)
14. S.K. Paul et al., Cyclic plastic deformation and cyclic hardening/softening behavior in 304LN stainless steel. Theor. Appl. Fract. Mech. **54**(1), 63–70 (2010)
15. P. Verma, et al., Low cycle fatigue behavior of modified 9Cr–1Mo steel at room temperature. Mater. Sci. Eng. A **652**, 30–41 (2016)

High Cycle Fatigue Behaviour of a 10 wt% Cr Steel at Ambient and Elevated Temperatures

Rukhsana Mehdi, Aritra Sarkar, A. Nagesha, R. Sandhya and G. A. Harmain

Abstract The present investigation deals with the high cycle fatigue (HCF) behaviour of a 10 wt% Cr steel at ambient as well as elevated temperatures (300–853 K). S–N curves were generated at different temperatures employing an R-ratio of −1. Influence of mean stress was established through Haigh diagram at 853 K using different R-values. Fatigue life was found to decrease with increase in test temperature and stress amplitude. Prediction of fatigue life was attempted using Basquin equation. Detailed fracture surface analysis was performed to study the crack initiation and propagation modes towards understanding the mechanisms of failure at different temperatures.

1 Introduction

10 wt% Cr steel belongs to series of 9–12 wt% ferritic steels, with a typical microstructure comprising of martensitic laths decorated with Cr-rich precipitates. Compared to austenitic steels, 10 wt% Cr steel has a higher strength, lower coefficient of thermal expansion and a higher thermal conductivity. Due to martensitic structure and the balance in chemical composition, the steel possesses a good ductility and toughness, in combination with adequate high temperature strength. The steel is intended for use in the low-pressure turbine section of the indigenous advanced ultra-supercritical power plants (AUSC-PP) which are expected to mitigate the CO_2 emissions and thereby help preserve the coal deposits in India for longer usage [1–5]. Components of low-pressure turbines in the AUSC-PP are subjected to severe flow-induced vibrations and thermal pressure fluctuations leading to considerable HCF damage. This necessitates a detailed study on the HCF

R. Mehdi · G. A. Harmain
Department of Mechanical Engineering, NIT Srinagar, Srinagar, India

A. Sarkar (✉) · A. Nagesha · R. Sandhya
Metallurgy and Materials Group, Indira Gandhi Centre for Atomic Research,
Kalpakkam 603 102, Tamil Nadu, India
e-mail: aritra@igcar.gov.in

behaviour of 10 wt% Cr steel. The present investigation is based on the HCF behaviour of 10 wt% Cr steel over a wide range of temperature (300–853 K) and establishes important constant life diagrams that are necessary for the design of these components against HCF.

2 Experimental

The chemical composition of the 10 wt% Cr steel is shown in Table 1. HCF specimens with hourglass geometry with a minimum diameter of 6 mm were machined from the wire-cut blanks extracted from the cylindrical forging of diameter 200 mm (Fig. 1). HCF tests were conducted under engineering stress-controlled mode on an electromagnetic resonance machine operating at a frequency of $\sim$55 Hz with dynamic load capacity of $\pm$50 kN and static load capacity of $\pm$100 kN. Tests are conducted over a wide range of temperature from 300 to 853 K employing different values of alternating stress (σ_a) and mean stress (σ_m), keeping the maximum stress (σ_{max}) below the yield stress (YS). Tests were conducted in accordance with ASTM standard E466-15 [6]. Two repeat tests were carried out for selected combination of σ_a and σ_m. The variation of yield strength with temperature, based on in-house unpublished data [7], is shown in Table 2. Failed specimens were examined using scanning electron microscope (SEM) to understand the fracture modes. The fracture surfaces of the failed specimens were studied using Philips EM 502 SEM to study the variation in crack initiation and propagation behaviour and the striation features.

Table 1 Chemical composition of 10 wt% Cr steel

Element	C	Si	Mn	P	S	N	Al
wt%	0.11–0.13	0.12 max	0.40–0.50	0.012 max	0.005 max	0.045–0.060	$\leq$0.010
Element	Cr	Mo	Nb	Ni	V	W	
wt%	10.2–10.6	1.0–1.10	0.04–0.06	0.70–0.80	0.15–0.25	0.95–1.05	
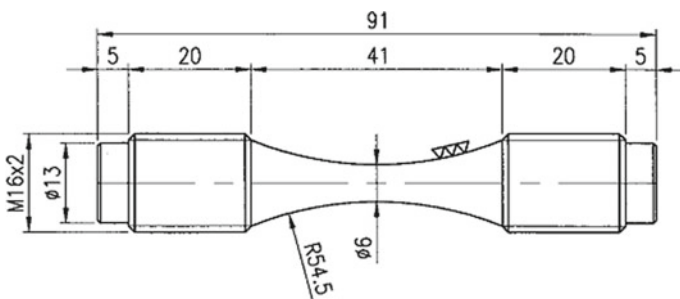
Fig. 1 Specimen geometry for HCF testing

Table 2 Variation of YS, UTS and *endurance limit* with temperature (K)

T (K)	YS (MPa)	UTS (MPa)	Endurance limit (MPa)	Endurance limit (% of YS)	Endurance limit (% of UTS)
300	783	899	400	51	44
673	641	714	300	46	42
853	483	500	220	45	44

3 Results and Discussion

3.1 Initial Microstructure

The untested 10 wt% Cr steel has a tempered martensitic structure which is presented in Fig. 2. Lath structure with high dislocation density induced by martensitic transformation during normalisation heat treatment is observed predominantly with lath boundaries as well as prior austenite grain boundaries being decorated with carbides.

3.2 S–N Behaviour of 10 wt% Cr Steel at Different Temperature

Figure 3 shows the comparative S–N behaviour of the 10 wt% Cr steel at all temperatures ($R = -1$). The plot shows a gradual increase in cyclic life with decrease in stress amplitude. The specimens which have not failed after 10^7 cycles are indicated as *run-out* (indicated by an arrow in Fig. 3). The corresponding stress amplitude is taken as the *endurance limit* or *fatigue limit* of the material at that temperature. Two repeat tests were carried out for selected combinations of σ_a and

Fig. 2 Typical microstructure of 10 wt% Cr steel in as-received condition

Martensitic laths
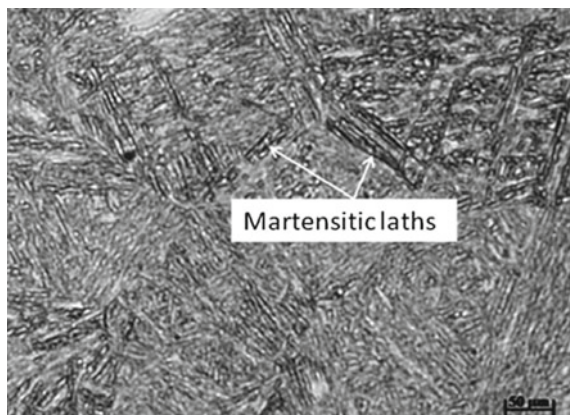
Fig. 3 Stress–life plot for 10 wt% Cr at different temperatures
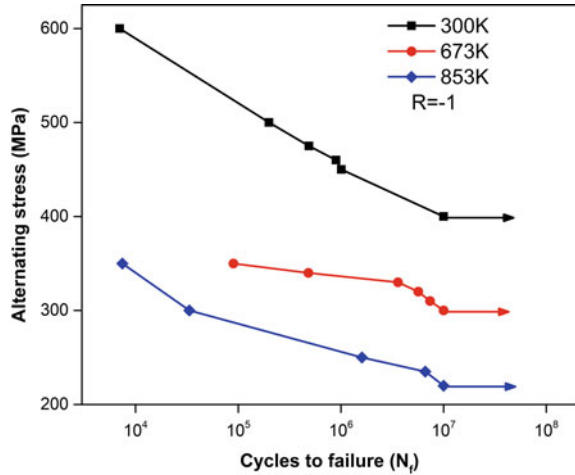
σ_m, both in the shorter and longer life regimes which show a scatter of ±50%. The amount of scatter is found to be well within the scatter band of two as is typical of HCF. It is clear from the plot that fatigue life also decreases with increase in temperature, irrespective of the applied stress. This eventually leads to a lower value of the *endurance limit* with an increase in temperature. This is also evident from Table 2 which shows a decrease in endurance limit (as % of YS and UTS) from 51 to 45% when the temperature is increased from 300 to 853 K, indicating a strong temperature sensitivity of HCF behaviour. This suggests that the deformation mechanisms may be different at higher temperatures where the applied stress alone may not be the sole responsible factor in dictating the fatigue life. This is also corroborated by previous findings on similar steels highlighting the effect of oxidation or internal inclusions on fatigue life at high temperatures [8, 9]. Basquin equation is the well-known linear relationship between σ_a and the number of reversals to failure [10] which is represented as $\sigma_a = \sigma'_f (2N_f)^b$ where σ_a, and $2N_f$ are alternating stress and the number of reversals to failure, respectively. σ'_f is the fatigue strength coefficient and b is the fatigue strength exponent (or Basquin's exponent). The HCF test data is plotted using the Basquin's equation to determine the fatigue parameters (shown in Table 3). It is clearly depicted from Table 3 that fatigue parameters, especially $\sigma_{f'}$ varies widely with temperature, indicating that the fatigue life at elevated temperatures (853 K) may be dictated by factors like creep or oxidation apart from the applied stress, compared to room temperature (RT) where the applied stress may be the sole factor governing the fatigue life. These fatigue parameters are further used for prediction of fatigue life at RT and

Table 3 Fatigue parameters derived from Basquin equation

Temperature (K)	σ_f (MPa)	B
853	594.55	−0.05809
300	1026.67	−0.05609

Fig. 4 Comparison of predicted and experimental life using Basquin's fatigue parameters at 300 and 853 K
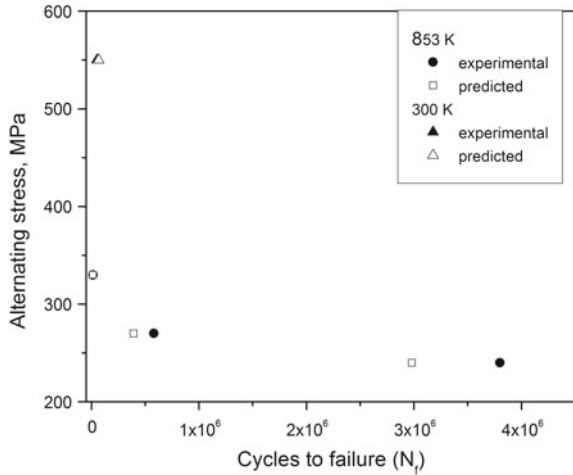
Table 4 Comparison between predicted and experimental life using fatigue parameters

Temperature (K)	Alternating stress (σ_a) (MPa)	Experimental life	Predicted life	Factor of safety
853	240	3799657	2980135	1.27
	270	579785	392340	1.47
	330	15000	12400	1.20
300	550	52219	68035	0.76

853 K. The comparison between the predicted and experimental lives is shown in Fig. 4 and Table 4 and a reasonable agreement within a scatter band of two was obtained.

3.3 Generation of Constant Life Diagram (N_f: 10^7) at 853 K

Based on tests conducted with different $\sigma_a - \sigma_m$ combination at 853 K, a constant life diagram is generated by plotting (σ_a) against (σ_m) for a particular constant life of 10^7 cycles (specimens which went for *run-out* up to N_f: 10^7 cycles), shown in Fig. 5. Figure 6 shows the comparison of constant life diagram generated using the test data, with Soderberg and Goodman lines. Soderberg and Goodman lines are constructed by joining the *endurance limit* at $R = -1$ with YS and UTS, respectively [10]. Constant life diagrams are constructed by joining data points corresponding to approximately same life through different contours/curvatures which also intersect different R-ratios (Fig. 5). The numbers indicated adjacent to the life contours are the minimum lives corresponding to particular domain. It may be

Fig. 5 Generation of constant life diagram of 10 wt % Cr steel at 853 K (N_f: 10^7)
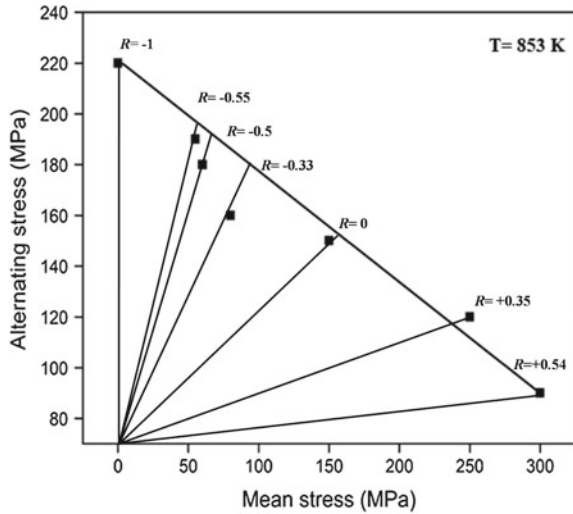
Fig. 6 Comparison between constant life diagram (using experimental data) with Soderberg and Goodman lines, 853 K
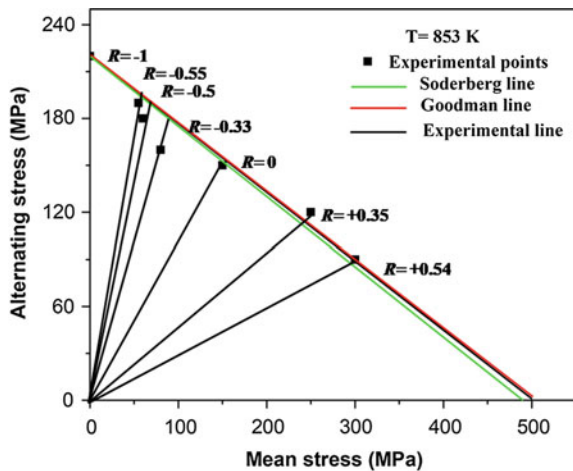
noted here that for a given constant life contour, the stress amplitude required for a given value of mean stress is termed as 'allowable stress' [11]. The term allowable is used to indicate the maximum (safe) value of the stress amplitude that can be tolerated for a particular mean stress so that the resulting life corresponds to the specific life contour as defined by Fig. 5. As shown in Fig. 5, the allowable σ_a decreases with increase in σ_m. The experimental constant life diagram shows an excellent agreement with the Soderberg and Goodman lines. The constant life diagram generated for N_f: 10^7 cycles is further extended to N_f: 10^6 cycles, in the form of Haigh diagram in Fig. 7, which indicates the safe region of operation (in terms of σ_a and σ_m) for a given life. The safe regime corresponding to N_f: 10^7 cycles

Fig. 7 Generation of Haigh diagram for 10 wt% Cr steel at 853 K
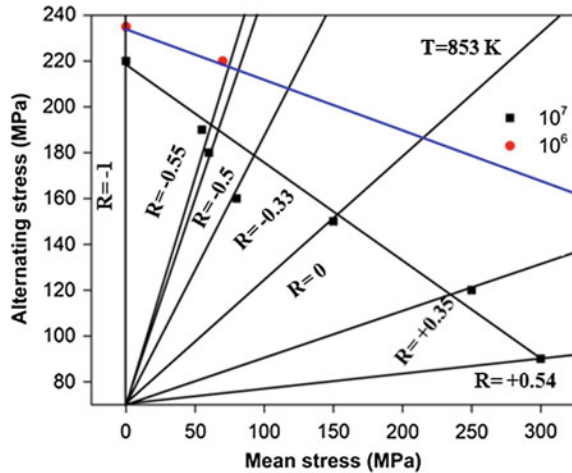
and N_f: 10^6 cycles are marked by black and blue lines in the figure, respectively. The above diagram therefore assumes importance in ensuring structural integrity, providing important inputs to the designer. It may be noted that literature on fatigue behaviour of ferritic steel is extremely scant [8, 9] and the evolution of Haigh diagram is not reported till date.

3.4 Fractographic Investigations

Fracture surfaces of the failed specimens under HCF at different temperatures ranging from 300–853 K ($R = -1$) are presented in Fig. 8a–c. Figure 8a ($\sigma_a = 450$ MPa, 300 K) shows transgranular fatigue crack propagation marked by striations (indicated in the figure). With an increase in the test temperature, crack propagation changes from transgranular to mixed mode with traits of intergranularity. This is clearly depicted in Fig. 8b pertaining to HCF testing at 673 K (σ_a: 340 MPa) showing the overall view of the fracture surface where grain boundary facets as a signature of intergranular crack propagation are clearly seen. This is also reflected in Fig. 8c which shows a closer view from Fig. 8b, where large intergranular cracks were observed apart from striations, underlining strong influence of creep on HCF. Cr-rich precipitates are also found to be present (Fig. 8c), as revealed from the corresponding EDS analysis. A marked effect of oxidation is observed at 853 K (Fig. 8d–e) which pertains to HCF testing at a σ_a of 235 MPa. It was observed that oxidation plays a crucial role in crack initiation, particularly at 853 K where the initiation region is found to be masked by oxide scales. Ingress of oxygen into the slip bands initiated many secondary cracks (marked in Fig. 8d) which further aids the overall crack propagation. The process is also facilitated by formation of intergranular cracks at 853 K, under the influence of creep (marked in
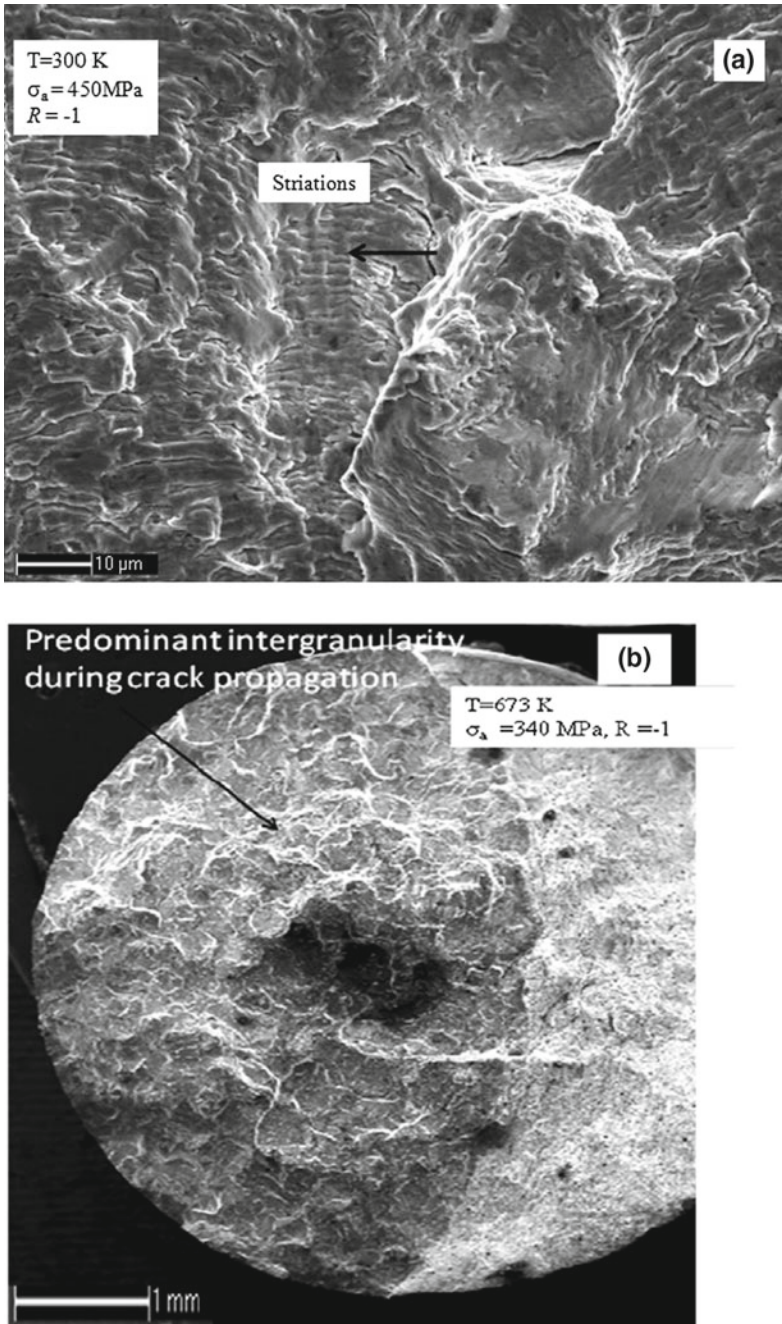
Fig. 8 SEM fractographs pertaining to HCF tests at **a** 300 K, σ_a = 450 MPa, **b** 673 K, σ_a = 340 MPa and **c** 853 K, σ_a = 235 MPa
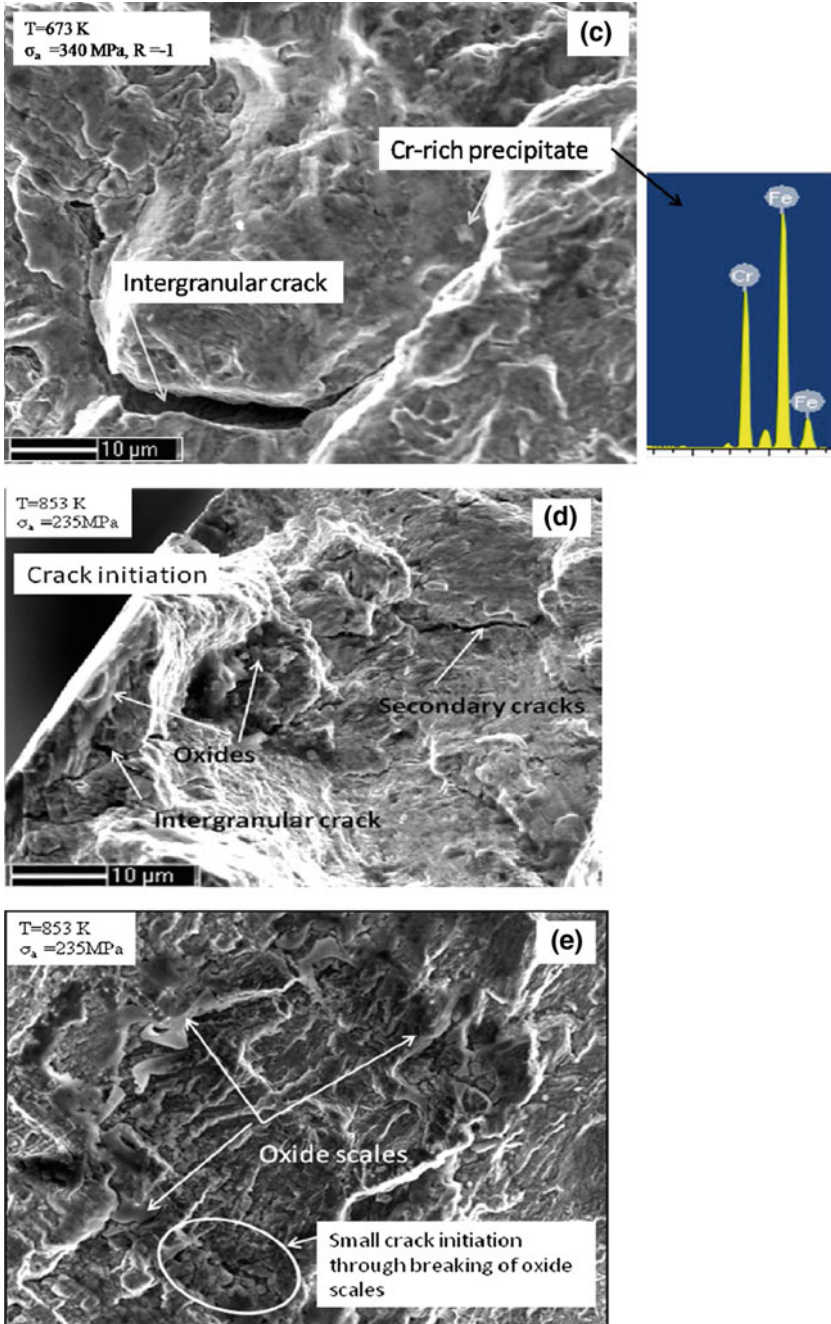
Fig. 8 (continued)

Fig. 8d). This clearly depicts the effect of creep and oxidation on fatigue crack initiation at high temperatures, apart from slip. The effect of oxidation at 853 K is further corroborated from Fig. 8e which shows the fracture surface being heavily masked by oxide scales. Breaking of these oxide scales through the process of cycling has induced many secondary cracks which are also observed from the figure (marked in Fig. 8e). The above features observed through the SEM images shown at 673 and 853 K clearly establish the fact that fatigue life at these temperatures is significantly affected by creep and oxidation, as mentioned earlier. This also explains the decrease in the endurance limit and fatigue parameters with temperature, as shown in Table 3.

4   Summary

HCF behaviour of the 10 wt% Cr steel is studied which showed a gradual increase in cyclic life with decrease in stress amplitude and temperature. This resulted in a lowering of the endurance limit with increase in temperature. The HCF behaviour is correlated with fracture surface analysis and the importance of creep and oxidation on HCF at higher temperatures is highlighted. Using test data for different $\sigma_a - \sigma_m$ combinations, constant life Haigh diagram is generated at 853 K. The information generated assumes importance in ensuring structural integrity, providing important design inputs.

References

1. J. Fujio Abe, J. Engg. **1**, 211–214 (2015)
2. N.C. Bhatt, M. Batrani, J. Mohan, V. Gopalakrishnan, M.K. Verma, Int. J. Engg. Res. Tech. **4**, 291–293 (2015)
3. R. Mishnev, N. Dudova, R. Kaibyshev, Mater. Sci. Forum **879**, 1311–1316 (2016)
4. N. Dudova, R. Kaibyshev, ISIJ Intl. **51**, 826–831 (2011)
5. E. Saito, N. Matsuno, K. Tanaka, S. Nishimoto, R. Yamamoto, S. Imano, Mitsubishi Heavy Ind. Tech. Rev. **52**, 39–46 (2015)
6. ASTM E-466-15, Standard Practice for Conducting Force Controlled Constant Amplitude Axial Fatigue Tests of Metallic Materials (2015)
7. T. Sakthivel, G.V. Prasad Reddy, Unpublished data (IGCAR)
8. Kobayashi, N. Yoshikawa, K. Sugimoto, ISIJ Inter. **53**, 1479–1486 (2013)
9. Y. Matsumori, J. Nemoto, Y. Ichikawa, I. Nonaku, H. Miura, *ASME Mechanical Engineering Congress and Exhibition* 8, Houston, Texas, USA (2012), pp. 85–89
10. G.E. Dieter, *Mechanical Metallurgy*, 3rd edn. (McGraw-Hill Education Publications, New Delhi) ISBN-10:1-25-906479-4
11. Aritra Sarkar, A. Nagesha, R. Sandhya, M.D. Mathew, High Temp. Mater. Proc. **35**, 361–368 (2016)

Part XIII
Structural Health and Condition Monitoring

Detection of Multiple Flaws in Steam Generator Tubes of PFBR Using Ultrasonic Guided Waves

M. M. Narayanan, Anish Kumar and C. K. Mukhopadhyay

Abstract An ultrasonic guided wave-based methodology is developed for the detection of multiple flaws in steam generator tubes of the prototype fast breeder reactor. To this end, axisymmetric longitudinal mode (L(0,2)) at the frequency of 250 kHz is selected using dispersion curves based on its modal nature. It is observed that L(0,2) at 250 kHz detects multiple defects such as circumferential, axial, and partial pinholes and combination of them lying in the same line of sight with good sensitivity. Then, 3D-finite element (FE) simulations with circumferential defects are performed to understand the shadowing effect of one circumferential defect by another in its vicinity. FE results show that detection sensitivity of one circumferential defect behind another circumferential defect is affected and the amplitude reduction turns out to be around 4.7 dB.

Keywords Axisymmetric longitudinal mode (L(0,2)) · Circumferential · Axial, and pinhole defects · 3D-FE simulation

1 Introduction

Heat exchanger tubes of a steam generator (SG) in prototype fast breeder reactor (PFBR) are of great importance, as they carry water/steam inside the tubes with hot liquid sodium counterflowing on the outside to transfer heat to water. As the sodium–water reaction is highly exothermic with the evolution of highly corrosive products, it will cause huge damage and affect the routine operation of the reactor. Hence, it is necessary to ensure that the SG tubes are defect-free. To ensure this, a periodic examination and assessment of the integrity of the tubes must be done using a suitable and rapid nondestructive testing (NDT) method. PFBR is a 500 MWe sodium-cooled pool-type reactor being commissioned at Kalpakkam, India. It has

M. M. Narayanan (✉) · A. Kumar · C. K. Mukhopadhyay
Non-Destructive Evaluation Division, Metallurgy and Materials Group, Indira Gandhi
Center for Atomic Research, HBNI, Kalpakkam 603102, Tamil Nadu, India
e-mail: mmn@igvar.gov.in

eight steam generators of 1.2 m diameter and vertical height of 25 m [1]. Each SG has 547 heat exchanger tubes made of modified 9Cr–1Mo ferritic steel. The length of an SG tube is 23 m with the outer diameter and the wall thickness being 17.2 and 2.3 mm, respectively. Presently used NDT technique for the inspection of SG tubes is remote field eddy current technique (RFEC) [2]. The technique involves a low-frequency sinusoidal excitation of an exciter coil that generates eddy currents in the tube and the receiver coil then picks up the secondary magnetic fields generated in the tube with permeability variations averaged out. The amplitude and the phase of the induced voltage bear the information of presence of defects. However, in conventional eddy current testing of SG tubes (Ferromagnetic), the impedance changes sensed by the coil are very random and high due to the variation in permeability. Hence, every point of inspection needs to be magnetically saturated and demagnetized after a measurement, which is both time-consuming and cumbersome. For instance, it can provide a sensitivity of 10%WT deep circumferential and axial notches and 0.1 mm diameter through pinhole. Even RFECT is very time-consuming, because it requires the insertion of the coil assembly into tube all along the length of 23 m of the tube and is of low sensitivity as well. To overcome the difficulty, ultrasonic guided wave-based inspection methodology has been developed which can provide rapid inspection of the whole SG tube from one end without the insertion of the probe all along the 23 m length of the tube.

The use of low-frequency ultrasonic guided waves propagating in tubes has become very popular because of their nearly uniform strain energy density, less dispersion, and attenuation. For instance, axisymmetric longitudinal modes (L(0, m)) and torsional modes (T(0,m)) at low frequencies (50–100 kHz) are used in tubes for detection of small defects and a long range [3]. The present study utilizes L(0,m) modes (m refers to order of the mode) for detection of multiple defects such as circumferential, axial and pinhole defects lying in the same line in SG tubes. L(0, m) can be easily excited using direct coupling of an ultrasonic transducer to the end of a tube [4]. For instance, Cheong et al. [5] used L(0,1) mode at 500 kHz for detecting axial and circumferential notches in a feeder pipe of thickness 6.5 mm, the diameter of 63.5 mm, and the length of 1.5 m in a pressurized heavy water reactor. Rose et al. [6] used L(0,4) mode at fd = 4.4 MHz-mm for the detection of multiple cracks at different locations at the OD of a tube of about 1 m length. Yoon et al. [7] used L(0,1) mode at 2.25 MHz to detect axial notches in SG tubes of length 1.8 m, outer diameter 19.05 mm, and the wall thickness 1.09 mm of Korean nuclear power plant. Further, the ultrasonic guided wave-based inspection methodology has been developed for the inspection of steam generator tubes of PFBR by the authors of the paper [8]. The present study is the extension of the detailed work presented in reference [8].

The paper is organized as follows: Sect. 1.1 theory, Sect. 1.2 selection of an ultrasonic guided wave mode using dispersion curves, Sect. 2 details of experiments, specimen, and finite element (FE) models with circumferential defects, Sect. 3 results and discussion, and Sect. 4 conclusions.

1.1 Theory

Ultrasonic guided waves are elastic waves guided by boundaries. The propagation of ultrasonic waves in a solid is governed by Navier's equation of motion [9], as shown in Eq. 1:

$$(\lambda + 2\mu)\nabla\nabla.\bar{U} - \mu\nabla \times \nabla \times \bar{U} = \rho\frac{\partial^2\bar{U}}{\partial t^2} \tag{1}$$

where λ and μ are Lamé constants, ρ is the density of the solid, and $\bar{U}$ is the displacement vector. When solved in an infinitely long, homogeneous, and isotropic hollow cylinder with traction-free boundary conditions, Navier's equation yields three different families of guided waves. The three families are termed the longitudinal (L(0,m)), torsional (T(0,m)), and flexural (F(n,m)) modes, where "n" is the circumferential order and "m" is the mode number. These modes are entirely determined by material properties, the inner and outer radii of the tube, and the frequency-wall thickness (fd) product. The zero-order (n = 0) longitudinal and torsional modes are axisymmetric while $n \neq 0$ mode (flexural) is anti-symmetric. These modes are represented using dispersion curves plotted between phase velocity and frequency. A point on the dispersion curves represents a valid mode that can exist in a tube.

1.2 Mode Selection Using Disperse Software

The SG tubes of PFBR are made of modified 9Cr–1Mo material with the density of 7800 kg/m^3, Young's modulus of 220 GPa, and Poisson ratio of 0.2805 [10]. The inner and outer diameters of the tube are 12.6 mm and 17.2 mm, respectively, and the wall thickness is 2.3 mm. With the inner radius, wall thickness, and the elastic properties of the material of the tube, the phase velocity and the group velocity dispersion curves were obtained using Disperse software [11]. Figure 1a, b shows the phase velocity and the group velocity dispersion curves, respectively. L(0,2) at 250 kHz has been chosen for the study, in comparison to other modes, because of its highest group velocity, good separation from neighboring modes, non-dispersive nature, and easy excitability. The markers in Fig. 1a, b indicate the L(0,2) mode at the frequency of 250 kHz. The group velocity of this mode is 5380 m/s. The mode shape of L(0,2) is shown in Fig. 1c. Since most of the strain energy density is available in the axial direction, it can propagate for a long range of distances.
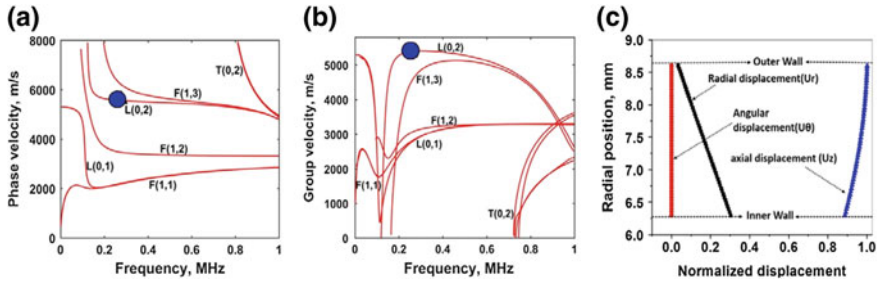
Fig. 1 **a** Phase velocity dispersion curves, **b** group velocity dispersion curves for SG tubes of PFBR, and **c** mode shape of L(0,2) at 250 kHz

2 Experimental and FE Simulation Details

To generate the L(0,2) mode, an ultrasonic transducer of frequency 250 kHz and the diameter of 40 mm was directly coupled to the one end of the tube and excited by a high power pulser–receiver, using a 5-cycled toneburst. The ultrasonic transducer generates ultrasonic waves in the tube and receives the reflected waves propagating back to the transducer. The received signals were then transferred to the oscilloscope through the pulser–receiver. The signals were sampled at 2.5 MHz and averaged 16 times. Figure 2 shows the schematic of the experimental setup.

2.1 Specimen Details

Four types of defects that can possibly occur in heat exchanger tubes are circumferential and axial defects due to stress-corrosion cracking, pinholes due to pitting corrosion, and wear scars due to fretting. The first three defects have been considered for the study and they have been machined using EDM technique. The dimensions of the defects are chosen based on our requirement. All the defects are deliberately chosen to lie along the same line. Figure 3 shows the respective defects
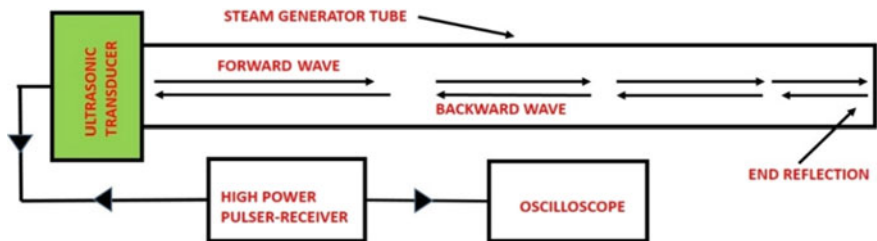
Fig. 2 Schematic of the experimental setup
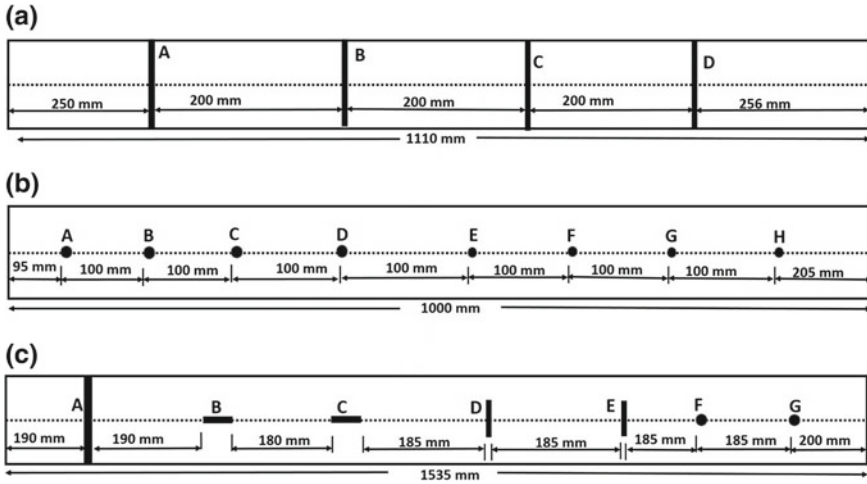
Fig. 3 **a** Full circumferential defects (CD) **b** pinholes (PH), and **c** combination of CD, axial, and PH defects

with their inter-separation. Table 1 shows the type of the defects, size, and the respective distances from the left ends of the tubes. Experiments were conducted on all the specimens, as discussed above.

2.2 Finite Element Simulation

In the present study, the finite element simulation software ABAQUS/Explicit was used to simulate the wave propagation utilizing explicit time-domain algorithm. The explicit scheme is a direct time stepping scheme based on the central-difference method [12, 13]. Toward this, a 3D-finite element model was developed in ABAQUS to simulate L(0,2) mode propagation in a 1.0 m long SG tube with full circumferential defects of depth 0.92 mm and width 1 mm at the locations: 250, 350, 400, 450, 500, 550, 650, and 750 mm, taken one at a time. Further, to study the shadowing effect of the defects, a circumferential defect was fixed at 250 mm and the circumferential defects were placed at the locations: 252, 257.5, 260, 275, 300, 325, 350, 400, 450, 500, 550, 650, and 750 mm. Therefore, in one model, two defects were taken at a time. Figure 4a, b shows the FE models with a single circumferential defect and two circumferential defects, respectively. The model was assigned the elastic properties, as given in Sect. 1.2. The spatial and the time steps were chosen as 0.48 mm and 5e−8 s, respectively. Figure 4 shows the excitation signal along the z-axis of the tube and the mesh used in the model. Both steps were

Table 1 Type of defects, locations, and their dimensions

S. No.	Defect label	Circumferential defects (1 mm width)			Pinhole defects (partial)			Combination of circumferential defect (CD), axial defect (AD) and pinholes (PH)
		CE (mm)	D (mm)	OL (mm)	Dia. (mm)	D (mm)	OL (mm)	
1	A	Full	0.23	250	2	0.23	95	CD: Full, 3 mm width, 0.23 mm D
2	B	Full	0.46	451	2	0.46	195	AD: 10 mm AL, 2 mm Width, 0.92 mm D
3	C	Full	0.69	652	2	0.69	295	AD: 10 mm AL, 2 mm Width, 1.38 mm D
4	D	Full	0.92	753	2	0.92	395	CD: 10 mm CE, 3 mm Width, 0.92 mm D
5	E				1	0.92	495	CD: 10 mm CE, 3 mm Width, 1.38 mm D
6	F				1	1.15	595	PH: 3 mm dia., 0.92 mm D
7	G	–	–	–	1	1.38	695	PH: 3 mm dia., through-and-through hole
8	H	–	–	–	1	1.61	795	–

CE circumferential extent, *D* depths of axial, circumferential or pinhole defect, *AL* length of axial defect, *Dia.* diameters of pinholes. The locations of the respective defects w.r.t the left ends, as shown in Fig. 3

sufficient to meet the convergence criterion. The number of through thickness elements was chosen to be 6. The geometry was meshed with six-node linear triangular prism elements (C3D6). To excite L(0,2) at 250 kHz, the excitation pulse was applied on the end face of the tube axi-symmetrically, as an axial displacement (Uz) with a five cycle Hanning-windowed toneburst of 250 kHz center frequency, as shown in Fig. 5.
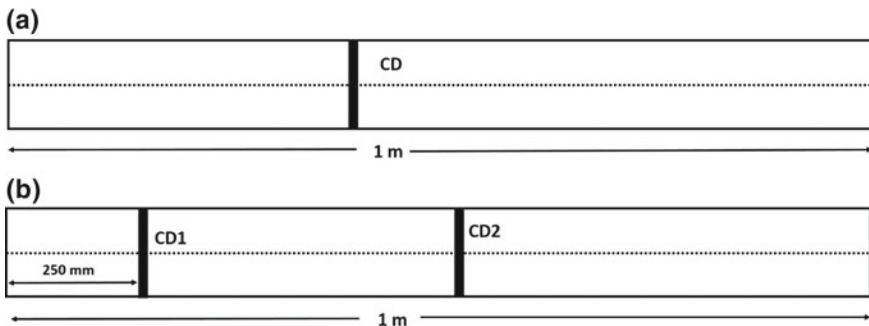
Fig. 4 FE models with **a** a full circumferential defect (CD) and **b** CD1 fixed at 250 mm and CD2 at different locations
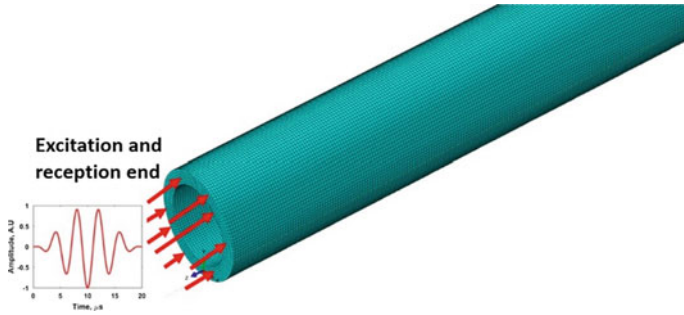
Fig. 5 Excitation signal along the z-axis of the tube and the mesh

3 Results and Discussion

Figure 6a–c shows the experimental time signal obtained in the tubes with full circumferential defects, pinholes, and the combination of circumferential, axial, and pinhole defects. In Fig. 6a–c, all the amplitudes were normalized w.r.t. the maximum response from defects. It can be observed that all the circumferential, axial, and pinhole defects were detected with good SNR. For the case of eight pinholes, all but the 1 mm diameter and 0.92 mm deep pinhole and 2 mm diameter and 0.23 mm deep pinhole were detected with good SNR. It can be observed in Fig. 6b that the echo corresponding to 2 mm dia. and 0.23 mm deep pinhole merges with the initial ringing. In the case of the combination of different defects, all seven defects are detected with good sensitivity without much mode conversion occurring. It indicates that irrespective of the nature of defects and their order, L(0,2) mode is able to detect them. It can also be noticed in Fig. 6c that the defect signals B and C corresponding to axial defects of the same length but different depths are of low amplitude because of less area of interaction presented by the defect. It can also be observed in Fig. 6a–c that the amplitudes increase and decrease in accordance with the size of the defect. In other words, the area of the defect governs the
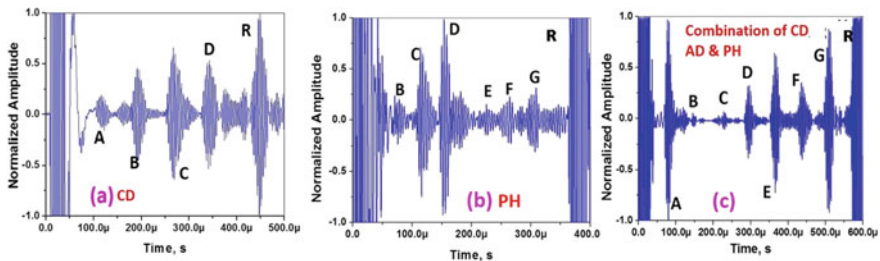
Fig. 6 Experimental signals obtained **a** for circumferential defects (CD), **b** for pinhole defects (PH), and **c** in a tube with the combination of CDs, axial defects (AD), and PHs. Labels A–G represent defects and R represents end reflection

amplitude of reflection. It can be observed that the defects detected by L(0,2) mode at 250 kHz are all of the size much less than the wavelength of the mode (~21 mm), due to the directed flow of wave energy and high axial stresses. Unlike bulk waves, guided waves can detect defects much smaller than the wavelength. For instance, the detection of axial defects of the given dimensions could be achieved because of the high axial stresses, presented by L(0,2) mode on the face the defects, on which the reflection coefficient depends fundamentally. In comparison with a circumferential defect of the same size as an axial defect, the reflection coefficient will be smaller due to smaller area presented by the axial defect but will never go unseen by the wave. Such reflections can be amplified to manifolds experimentally by high power toneburst system used.

Next, the influence of one circumferential defect on the reflected amplitude from the second circumferential defect has been studied using FE simulation. Toward this, FE models were first designed with full circumferential defects of the dimensions and the locations, as given in Sect. 2.2. Second, FE models with a circumferential defect fixed at 250 mm and with another circumferential defect (Fig. 4b) at different locations were considered to understand the shadowing of a second defect by the first defect. Figure 7a, b shows the averaged time signals for the cases of a circumferential defect (CD) at 500 mm and circumferential defects (CD1 and CD2) at 250 and 600 mm in 1 m long tubes, respectively. The reflected amplitude for CD2 at 600 mm is reduced in the presence of CD1 at 250 mm, as shown in Fig. 7b, due to the partial reflection from CD1. Figure 8 shows the maximum reflected amplitudes for CD at various locations and the maximum reflected amplitudes for CD2 at various locations in presence of CD1 at 250 mm. In Fig. 8, it can be seen that there is a reduction of the reflected amplitude as the distance of the CD increases due to the attenuation of the L(0,2) mode. It is, further, seen that (the red curve in Fig. 8) there is a reduction in the reflected amplitude corresponding to CD2, which is partly due to the presence of CD1 and attenuation.
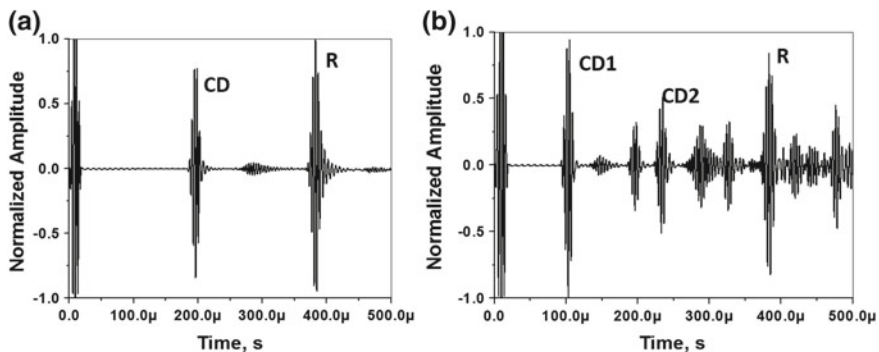
Fig. 7 FE time-domain signals **a** for the case of circumferential defect (CD) at 500 mm and **b** for circumferential defect (CD1) at 250 mm and CD2 at 600 mm in a 1 m long tube. **R** denotes the tube end reflection
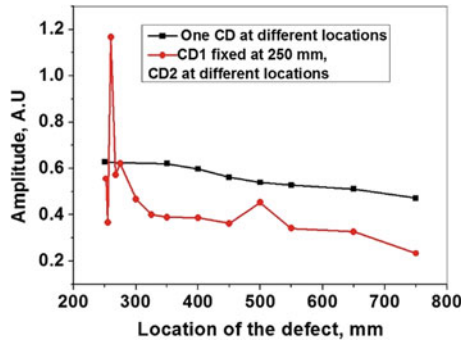
Fig. 8 a Maximum reflected amplitudes obtained for the case of a single circumferential defect (CD) at various distances and **b** maximum amplitudes obtained for the case with a circumferential defect (CD1) fixed at 250 mm and with the second circumferential defect (CD2) moved for different distances in 1 m long tubes. The dimensions of the CD are 0.92 mm depth, 1 mm width, and full circumference

However, the reduction is not smooth as compared to that of the first case. The regions far away from CD1 (300 mm) follow the trend observed as in the first case (black curve). And in the regions close to the defect CD1, the reflected amplitudes corresponding to CD2 are much lower than the reflected amplitudes corresponding to a single CD at respective locations followed by a sudden peaking of the reflected amplitude with CD2 at 260 mm due to interference. The distance at which the constructive superposition happens turns out to be 10 mm away from CD1. For instance, the drop in the amplitude due to CD2 to 252 mm w.r.t CD at 250 mm (Fig. 4a) is 4.7 dB due to shadow effect. It indicates that if a circumferential defect is in the neighborhood of another, it may be masked by the presence of the first defect for a distance of about 10 mm. The technique is limited by the shadowing effect due to inter-spacing of the defects. Hence, in such cases, a complimentary localized ultrasonic technique of higher sensitivity, namely, internal rotary inspection system (IRIS) can be used. IRIS is an ultrasonic technique of a little higher sensitivity than that of guided wave techniques. The technique uses the portion of the tube filled with couplant (water) for inspection. To inspect a tube, the transduction mechanism has to be taken all along the length of the tube. The technique has the scope of sizing defects and presents defect profile (namely axial or circumferential or pinhole) in image formats (B-scan and C-scan). The axial and spatial resolution of defects will be good. However, IRIS technique is highly time-consuming.

4   Conclusions

In this paper, ultrasonic guided wave propagation and the detection of multiple defects such as circumferential, axial, and pinhole defects in steam generator tubes of PFBR have been presented. An axisymmetric longitudinal mode L(0,2) was selected at 250 kHz using dispersion curves based on its modal nature. The mode exhibited negligible dispersion. The detection of multiple defects namely, circumferential, axial, and pinholes and their combination lying in the same line of sight was examined using experiments. The defects were detected with good sensitivity. The detection of the combination of circumferential, axial, and pinhole defects brings out a fact that the detection of such defects with good sensitivity is possible irrespective of the combination. The sensitivity for the case of full circumferential defects was 0.23 mm (10%WT) depth and 1 mm width. The sensitivity for the case of axial defects was 0.92 mm (40%WT) depth, 10 mm axial length, and 2 mm width. The sensitivity for the case of pinhole defects was 1.15 mm (50%WT) depth. However, the sensitivities for RFEC technique are 20% WT deep defects with the same extensions as given above and 2.3 mm through pinhole. Thus, the guided wave technique provides higher sensitivity. FE simulation was performed to study the shadowing effect presented by one circumferential defect on another for various distances. The results indicated that there is a shadowing effect for the range of around 10 mm from the first circumferential defect masking the presence of the second circumferential defect. The reduction of the reflected amplitude in the region of shadow turned out to be approximately 4.7 dB. It indicates the use of a complimentary localized technique in the neighborhood of a defect, after its detection. However, the mode is sensitive enough to capture all possible defects and at the same time, it can propagate for long range of distances, and thus it meets our entire requirement with respect to defect detection in SG tubes of PFBR. The guided wave technique developed requires only the placement of an ultrasonic transducer at a point for the inspection of the whole length of the tube. The technique is less time-consuming and does not involve much labor. But, the characterization of defects will be difficult with guided waves unless focusing is done. Further, the axial resolution will be low ($\sim$50 mm) because of low-frequency guided waves used for long-range inspection. However, the technique proves to be quite rapid and robust.

References

1. T.K. Mitra, A. Pai, P. Kumar, Challenges in manufacture of PFBR steam generators. Energy Proc. **7**, 317–322 (2011)
2. S. Vaidyanathan, S. Thirunavukkarasu, B.P.C. Rao, T. Jayakumar, P. Kalyanasundaram, B. Raj, Development of remote field eddy current technique for in-service inspection of ferromagnetic steam generator tubes. J. Non-Destr. Test. Eval. **4**(1), 26–30 (2005)

3. M.J.S. Lowe, P. Cawley, Long range guided wave inspection usage–current commercial capabilities and research directions. Technical report, Department of Mechanical Engineering, Imperial College, London, UK (2006), pp. 1–40, https://www3.imperial.ac.uk/pls/portallive/docs/1/55745699.PDF
4. D.N. Alleyne, P. Cawley, The excitation of Lamb waves in pipes using dry-coupled piezoelectric transducers. J. Nondestr. Eval. **15**(1), 11–20 (1995)
5. B. Yoon, S. Yang, H. Lee, Y. Kim, Detection and mode identification of axial cracks in the steam generator tube of the nuclear power plant using ultrasonic guided wave. J. Nucl. Sci. Technol. **47**(8), 754–759 (2010)
6. Y.-M. Cheong, D.-H. Lee, H.-K. Jung, Ultrasonic guided wave parameters for detection of axial cracks in feeder pipes of PHWR nuclear power plants. Ultrasonics **42**, 883–888 (2004)
7. J.L. Rose, J.J. Diriti, A. Pilarski, K. Rajana, F. Carr, A guided wave inspection for nuclear steam generator tubing. NDT&E Int. **27**(6), 307–310 (1994)
8. M.M. Narayanan, A. Kumar, S. Thirunavukkarasu, C.K. Mukhopadhyay, Development of ultrasonic guided wave inspection methodology for steam generator tubes of Prototype Fast Breeder Reactor (under review in Ultrasonics)
9. J.L. Rose, *Ultrasonic Guided Waves in Solid Media* (Cambridge University Press, USA, 2014)
10. A. Kumar, Correlation of microstructure and mechanical properties with ultrasonic parameters in metallic materials. Ph.D. thesis, Indian Institute of Technology, Kharagpur, India (2005)
11. Disperse Software, User's manual, Version 2.0 (2000)
12. M.B. Drozdz, Efficient finite element modelling of ultrasonic waves in elastic media. Ph.D. thesis, Imperial College of Science, University of London, UK (2008)
13. Abaqus Analysis User's Manual 6.10

Structural Health Monitoring of Cantilever Beam, a Case Study— Using Bayesian Neural Network and Deep Learning

Rahul Vashisht, H. Viji, T. Sundararajan, D. Mohankumar and S. Sumitra

Abstract The advancement of machine learning algorithms has opened a wide scope for vibration-based Structural Health Monitoring (SHM). Vibration-based SHM is based on the fact that damage will alter the dynamic properties, viz., structural response, frequencies, mode shapes, etc. of the structure. The responses measured using sensors, which are high dimensional in nature, can be intelligently analysed using machine learning techniques for damage assessment. Neural networks employing multilayer architectures are expressive models capable of capturing complex relationships between input–output pairs, but do not account for uncertainty in network outputs. A Bayesian Neural Network (BNN) refers to extending standard networks with posterior inference. It is a neural network with a prior distribution on its weights. Deep learning architectures like Convolutional Neural Network (CNN) and Long Short-Term Memory (LSTM) are good candidates for representation learning from high-dimensional data. The advantage of using CNN over multilayer neural networks is that they are good feature extractors as well as classifiers, which eliminates the need for generating hand-engineered features. LSTM networks are mainly used for sequence modelling. This paper presents both a Bayesian-multilayer-perceptron and deep-learning-based approach for damage detection and location identification in beam-like structures. Raw frequency response data simulated using finite element analysis is fed as input of the network. As part of this, frequency response was generated for a series of

R. Vashisht (✉) · H. Viji · S. Sumitra
Indian Institute of Space Science and Technology, Thiruvananthapuram 695547, India
e-mail: rahulvashisht290@gmail.com

H. Viji
e-mail: viji.narayan@gmail.com

S. Sumitra
e-mail: sumitra@iist.ac.in

H. Viji · T. Sundararajan · D. Mohankumar
Vikram Sarabhai Space Centre, ISRO, Thiruvananthapuram 695022, India
e-mail: t_sundararajan@vssc.gov.in

D. Mohankumar
e-mail: d_mohankumar@vssc.gov.in

749

simulations in the cantilever beam involving different damage scenarios (at different locations and different extents). These frequency responses can be studied without any loss of information, as no manual feature engineering is involved. The results obtained from the models are highly encouraging. This case study shows the effectiveness of the above approaches to predict bending rigidity with an acceptable error rate.

Keywords Bayesian neural network · Deep learning

1 Introduction

Deep learning models are being used on a daily basis to solve different tasks in vision, linguistics, and signal processing [1–5]. Understanding whether the model is under-confident or falsely overconfident can help get better performance out of the model. Recognising that test data is far from training data, one could easily augment the training data accordingly. In deep neural networks, usage of softmax to get probabilities is actually not enough to obtain model uncertainty. Standard neural network, with probability distribution over each of its weights is called BNN [6–11]. BNN gives the uncertainty estimates over the network outputs and can also help in model selection. Probabilistic backpropagation (PBP) is the learning technique used to train BNN in place of standard backpropagation.

This paper presents both a Bayesian-multilayer-perceptron-based approach and deep-learning-based approach (using architectures, viz., CNN and LSTM) for damage detection and location identification in cantilever beam. Raw frequency response data simulated using finite element analysis is fed as input of the network. Conventional data-driven approaches make use of statistical techniques for feature extraction from raw signals, in which case, data transformation has to be done accordingly for new data. The present approach models on raw data, which makes it ideal for real-time monitoring as it eliminates the need for data transformation. Details of each of the approaches are given in the following sections.

2 Experimental

2.1 Bayesian Neural Networks

Bayesian modelling is a powerful method to investigate the uncertainty in deep learning models [4]. Bayes theorem tells us about how to do inference from data. It follows the rule below to calculate conditional distribution of hypothesis given observed data.

$$P(\text{hypothesis}|\text{data}) = \frac{P(\text{data}|\text{hypothesis}) * P(\text{hypothesis})}{P(\text{data})}$$

Thus, learning and predictions can be seen as inference problems. Here, P (hypothesis) represents the prior beliefs over the hypothesis and P(data|hypothesis) represents likelihood of data given hypothesis which can be obtained from observed data. P(data) can be obtained by marginalising over the space of hypothesis and thus is considered as normalisation constant with respect to the hypothesis parameters.

Given training inputs $\mathbf{X} = \{x_1, x_2, \ldots, x_N\}$ and their corresponding outputs $\mathbf{Y} = \{y_1, y_2, \ldots, y_N\}$, in Bayesian (parametric) regression we would like to find the parameters ω of a function $y = f^\omega(x)$ that are likely to have generated the outputs. Following the Bayesian approach, some prior distribution is put over the space of parameters, $p(\omega)$. Prior distribution represents our belief as to which parameters are likely to have generated the data before we observe any data points. Once some data is observed the prior can be combined with the likelihood of the observed data to obtain the posterior which can be used for prediction of new data. The likelihood distribution $p(y|x, \omega)$ generates the output given the input and parameters ω. For regression, Gaussian likelihood is assumed which is as follows:

$$p(y|x, \omega) = N\big(y; f^\omega(x), \tau^{-1}I\big) \tag{1}$$

where τ is the model precision, which corresponds to adding observation noise to model output with variance τ^{-1}.

Using Bayes theorem, we can define the posterior as follows:

$$p(\omega|X, Y) = \frac{p(y|x, \omega)p(\omega)}{p(Y, X)} \tag{2}$$

This distribution captures the most probable function parameters given our observed data. For prediction of new input x^*, the posterior distribution and likelihood of new data x^* are combined and the parameters can be marginalised to obtain the predictive distribution for the new input, which is known as inference.

$$p(y^*|x^*, X, Y) = \int_\omega p(y^*|x^*, \omega)p(\omega|X, Y)d\omega \tag{3}$$

For most of deep learning models, the posterior distribution is intractable. Hence, posterior will be approximated by some approximating distribution $q(\omega|X, Y)$, which is obtained by minimising the KL-divergence between the posterior distribution and the approximating distribution [6].

Applying the Bayesian modelling gives the probabilistic interpretation of deep learning models by inferring distribution over model weights. Standard neural networks lack the capability of uncertainty measurement, as it only offers point

estimates. BNN offers robustness to overfitting, uncertainty estimates, and can easily learn from small datasets. We have used the probabilistic backpropagation to train the neural network which is discussed in the next section.

2.2 Probabilistic Backpropagation

Probabilistic backpropagation [8] (technique to train BNN) works similar to standard backpropagation (which is a technique to train a standard neural network). PBP uses a collection of one-dimensional Gaussians in place of point estimates for the weights, each one approximating the marginal posterior distribution of all the weights in the respective layer. In the forward pass, input data is propagated forward through the network. Since the weights are random, the activation produced in each layer is random, and results in intractable distributions. It sequentially approximates each of these distributions with the collection of one-dimensional Gaussians that match their marginal means and variances. At the end of this phase, PBP computes the logarithm of the marginal probability of the target variable instead of prediction error.

$$m^{a_l} = M_l m^{z_{l-1}} / \sqrt{n_{l-1} + 1}$$
$$v^{a_l} = [(M_l \circ M_l)v^{z_{l-1}} + V_l(m^{z_{l-1}} \circ m^{z_{l-1}}) + V_l v^{z_{l-1}}]/(n_{l-1} + 1)$$

where M_l and V_l are $n_l \times n_{l-1} + 1$ matrices whose entries are given by mean and variance of weight distribution. In the backward pass, the gradients of marginal distribution, Z is propagated backwards using reverse mode differentiation as in classical backpropagation. These derivatives are then used to update the means and variances of the posterior approximation.

The normalisation constant Z of posterior is obtained using approximation of integral as a normal distribution of the following form:

$$Z = N(y_n | m^{z_l}, vfinal)$$

where y_n is the actual output and m^{z_l} and is mean obtained after the forward pass, *vfinal* is variance obtained after forward pass and incorporating the prior information.

2.3 CNN

CNN [12] model can be described as the recursive application of convolution and pooling layer, followed by inner product layer, commonly called as dense layers, at the end of the network. Convolutional layer, which is the core layer of CNN is a

linear transformation that preserves the spatial information of the input space. Convolutional layer can be considered as a feature extraction layer. Pooling layers (optional) simply take the output of the convolutional layer and reduce its dimensionality. Intuitively, it is capable of bringing shift and distortion invariance to the input and to avoid overfitting to some extent. A convolutional layer's output shape depends on the shape of its input, shape of kernel, zero padding, and strides. The nonlinearity is incorporated in the network by applying activation functions such as relu, tanh, sigmoid, etc. after the convolution layer. A simple CNN, also known as ConvNet, is a sequence of layers. Every layer of a ConvNet transforms one volume of activations to another through a differentiable function. Convolutional layer does the convolution operation, which computes the output of neurons that are connected to local regions in the input. The pooling layer operates independently on every depth slice of the input and resizes it spatially. The layers used to build ConvNets are detailed below.

Convolutional Layer

This layer is the core building block of CNN. This layer does the convolution operation, which computes the output of neurons that are connected to local regions in the input. The CONV layer's parameters consist of a set of learnable filters. Every filter (also known as kernel) is small spatially (along width and height), but extends through the full depth of the input volume. During the forward pass, each of the filters is convolved with the input volume and dot products are computed between the entries of the filter and the input at any position. For the convolution layer, there are four hyperparameters, viz., number of filters K, the spatial extent of the filter F, the stride S, and the amount of zero padding P.

An input volume of size $W1 \times H1 \times D1$ produces a volume of size $W2 \times H2 \times D2$, where

$$W2 = (W1 - F + P)/S + 1$$
$$H2 = (H1 - F + P)/S + 1$$
$$D2 = K$$

The backward pass for a convolution operation is also a convolution (but with spatially flipped filters).

Pooling Layer

The pooling layer operates independently on every depth slice of the input and resizes it spatially. The depth dimension remains unchanged. The pooling options available are maximum pooling, average pooling, L2-norm pooling, etc. More generally, the pooling layer accepts a volume of size $W1 \times H1 \times D1$. The hyperparameters of this layer are their spatial extent F and the stride S. The resulting operation produces a volume of size $W2 \times H2 \times D2$, where

$$W2 = (W1 - F)/S + 1$$
$$H2 = (H1 - F)/S + 1$$
$$D2 = D1$$

The backward pass for a max(x, y) operation has a simple interpretation as only routing the gradient to the input that had the highest value in the forward pass. This layer is not mandatory and in some cases they are discarded.

Fully Connected Layer

Neurons in a fully connected layer have full connections to all activations in the previous layer, as seen in standard neural networks. The backward pass for FC layer can be done similar to CONV layer, where the spatial extent of the filter is the same as that of input volume.

Unlike traditional filters that have predefined parameters, the parameters of the 2D filter kernels in CNNs are automatically optimised by backpropagation.

2.4   LSTM

LSTM is a special kind of Recurrent Neural Network (RNN), capable of learning long-term dependencies [13]. They were introduced by Hochreiter and Schmidhuber. The core idea behind LSTMs lies that at each time step, a few gates are used to control the passing of information along the sequences that can capture long-range dependencies more accurately. LSTM has a chain of repeating modules of neural network, each having four neural network layers. The key to LSTMs is the cell state. The cell state runs straight down the entire chain, with only some minor linear interactions. LSTM consists of structures called gates, through which information is added or removed to the cell state. Gates are a way to optionally let the information through, composed out of a sigmoid neural network layer and a pointwise multiplication operation. At each time step t, hidden state h_t is updated by current data at the same time step, hidden state at previous time step, input gate, forget gate, output gate, and a memory cell. The decision regarding what information is to be through away from cell state is made by the forget gate layer. The forget gate accepts input at the current time step and hidden state at previous time step and outputs a number between 0 and 1 for each number in the cell state c_{t-1}. If the value is 0, it means to completely get rid of the information, while 1 means to completely retain (Fig. 1).
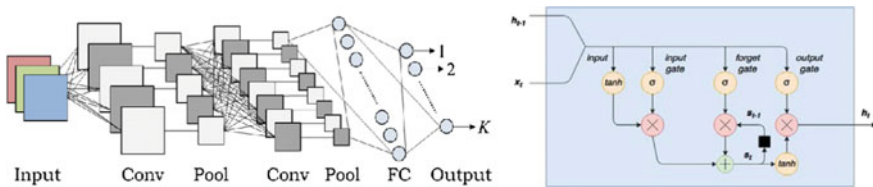
Fig. 1 Sample CNN [14] (left) and LSTM [15] architecture (right)

The basic LSTM equations are

$$a_t = \tanh(W_a x_t + U_a h_{t-1} + b_a)$$
$$i_t = \sigma(W_i x_t + U_i h_{t-1} + b_i)$$
$$f_t = \sigma(W_f x_t + U_f h_{t-1} + b_f)$$
$$o_t = \sigma(W_o x_t + U_o h_{t-1} + b_o)$$
$$c_t = f_t c_{t-1} + i_t \tanh(W_c x_t + U_c h_{t-1} + b_c)$$
$$h_t = o_t \tanh(c_t)$$

where model parameters including all $W \in R^{d \times k}$, $U \in R^{d \times d}$ and $b \in R^d$ are shared by all time steps and learned during model training, σ is the sigmoid activation function, denoting the element-wise product, k is a hyperparameter that represents the dimensionality of hidden vectors. The basic LSTM is constructed to process the sequential data in time order and the output at the terminal time step is used to predict the output.

2.5 Case Study

A cantilever beam structure of circular cross section having a length of 1 m is considered for the study. The structure is divided into four beam elements as shown in Fig. 2, where N stands for node and E stands for element [16–18]. Each element is having initial diameter of 0.01 m. Euler–Bernoulli beam element is used to idealise the structure. The nodal variables are transverse deflection and slope.
where EI is the beam rigidity and l is the length of the element. The stiffness and mass matrix of the beam element are as follows:

Fig. 2 Cantilever beam
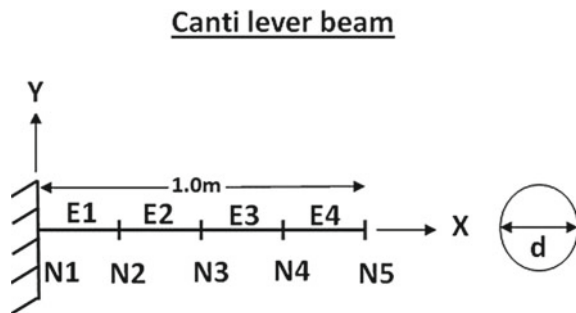
$$K = EI/l^3 \begin{bmatrix} 12 & 6l & -12 & 6l \\ 6l & 4l^2 & -6l & 2l^2 \\ -12 & -6l & 12 & -6l \\ 6l & 2l^2 & -6l & 4l^2 \end{bmatrix}$$

$$M = \rho Al/420 \begin{bmatrix} 156 & 22l & 54 & -13l \\ 22l & 4l^2 & 13l & -3l^2 \\ 54 & 13l & 156 & -22l \\ -13l & -3l^2 & -22l & 4l^2 \end{bmatrix}$$

where ρ is the mass density, A is the area and l is the length of the element. Damage is simulated by changing the diameter of the individual elements. Frequency response analysis is carried out from 0.1 to 10,000 rad/s for 1N excitation by varying the diameter of the beam element from 0.005 to 0.015 m. The excitation force is applied at node number 5 in Y direction. The acceleration response is monitored at node numbers 2, 3, 4 and 5 in the Y direction.

3 Results and Discussion

Response from each node is of length 10,000. Here, a single data point is obtained by concatenating responses in the order 5, 4, 3, 2 forming a vector of length 40,000. Sample input is shown in Fig. 3, where x-axis represents four responses (where each omega is varying from 1 to 10000) and y-axis corresponds to normalised acceleration. The output for each data point is a vector of length 4 corresponding to four diameter of the elements E1, E2, E3 and E4. Total input data points are 14,641.

For training model using deep learning architectures, data was divided into training–testing with a split of 70:30. Training data was further split into training–

Fig. 3 Sample input of cantilever beam study, frequency versus acceleration
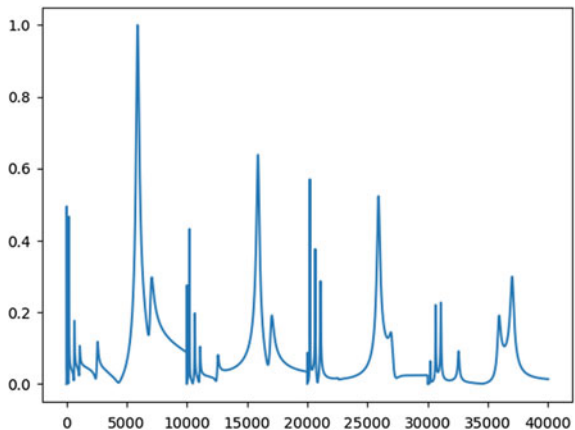
validation in the ratio 70:30. Adam was used as the optimiser. Mean squared error was used as the loss function.

3.1 CNN Model Architecture

To make the input data compatible for applying 2D CNN, each data point of length 40,000 is reshaped to 200×200. To predict diameter for each element, four neural network models were developed. The number of convolution and pooling layers used in each network with the respective hyperparameters are given in Table 1. After each convolution layer, RELU [19] nonlinearity is applied. Only for the first convolution, zero padding is done for all models. The last two layers for all models are Global average pooling and Dense layer (with one neuron). The R-squared score for this model is 0.9862 (Fig. 4).

Table 1 Hyperparameters used in 2D CNN architecture for each beam element

	Conv1	MaxPool1	Conv2	MaxPool2	Conv3	MaxPool3	Conv4
Element E1	32 (3,3)	(4)	32 (3,3)	(2)	32 (3,3)	(2)	8 (3,3)
Element E2	64 (5,5)	(4)	32 (3,3)	(2)	32 (3,3)	–	–
Element E3	64 (5,5)	(4)	32 (3,3)	(2)	16 (3,3)	–	–
Element E4	16 (3,3)	(2)	32 (3,3)	(2)	–	–	–
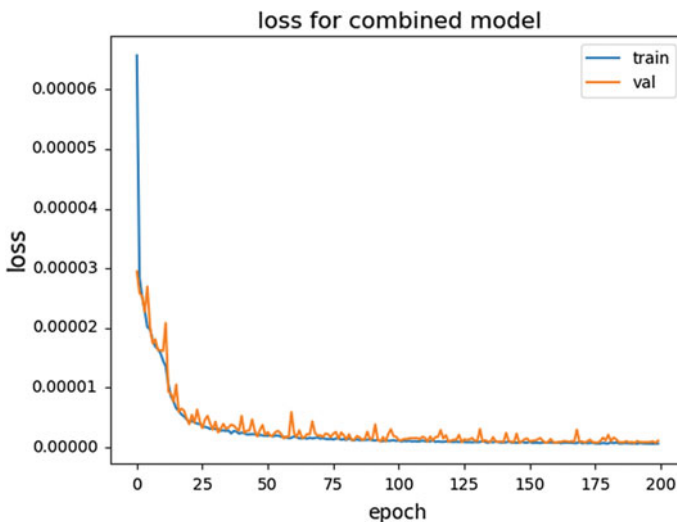
Fig. 4 2D CNN loss curve for cantilever beam

3.2   LSTM Model Architecture

To make the input data compatible for applying LSTM, each data point of length 40,000 is reshaped to (4, 10,000), where four represents the number of time steps. The data is modelled using a stack of three LSTM layers with 32, 16 and 4 hidden neurons, respectively. The loss curve is given in Fig. 5. The R-squared score for this model is 0.9910.

3.3   PBP Model Architecture

We have used the multilayer perceptron architecture with single hidden layer and 64 hidden units. It is trained using probabilistic backpropagation for 10 epoch with train test split of 50. The R-squared score for this model is 0. 9967.

3.4   Model Evaluation

To evaluate the efficiency of the model, R-squared score is used as the metric. The R-squared metric provides an indication of the goodness of fit of a set of predictions to the actual values. It is a statistical measure that measures how close the data are to predictions. $R^2 = 1 - SSE/SST$, where SSE is the sum of squares of difference
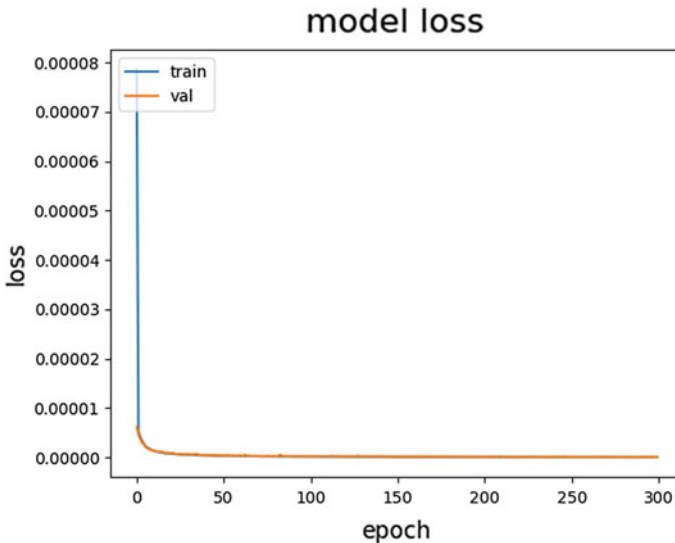
Fig. 5 LSTM validation loss for cantilever beam

Table 2 R-squared score of all architectures for cantilever beam

Algorithm	Test score
PBP	0.9967
LSTM	0.9910
2D-CNN	0.9862

between actual values and predicted values and SST is the sum of squares of difference between actual values and mean value.

R-squared statistic is defined as the percentage of the response variable variation that is explained by a linear model. It is always between 0 and 1. Here, we want our predicted values to be as close as possible to the actual values, and hence R-squared statistic should be close to 1. All the three models have given R-squared score, close to 1, which indicates the effectiveness of these algorithms to be applied on vibration-based SHM (Table 2).

3.5 Visualisation Using CNN Model

In regression outputs, one could visualise attention over input that increases, decreases or maintains the regressed filter index output. In this case study, this only tells us parts of the input that contribute towards to increase, decrease or maintaining the output value [20]. By default, Activation Maximisation loss yields positive gradients for inputs regions that increase the output and negative gradients that decrease the output. To visualise what contributed to the predicted output, gradients that have very low positive or negative values have to be considered. This can be achieved by performing grads = abs(1/grads) to magnifies small gradients.

A random test case taken for the study is shown in Fig. 5. The actual versus predicted output for the same is given in Table 3.

For our case study, we have to take top 10 gradients, which are shown in Figs. 6 and 7. The green lines show the top 10 features that maintain/contribute to the prediction. The blue lines show those features that can contribute to increase in the predicted value and orange lines are the ones that can contribute to decrease in the predicted value.

By visualising the gradients, it is evident that the first few modes are only required for identifying the damage near the fixed end whereas higher modes are required for identifying the damage near the free end, which is clearly reflected in gradient visualisation.

Table 3 Predicted and actual values for a test case of cantilever beam

	E1	E2	E3	E4
Actual diameter	0.011	0.008	0.015	0.015
Predicted diameter	0.01130249	0.00846803	0.01471727	0.01560052
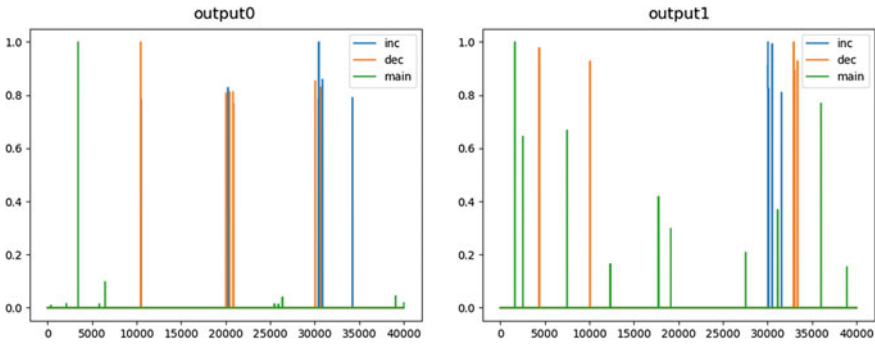
Fig. 6 Visualisation for outputs E1 and E2
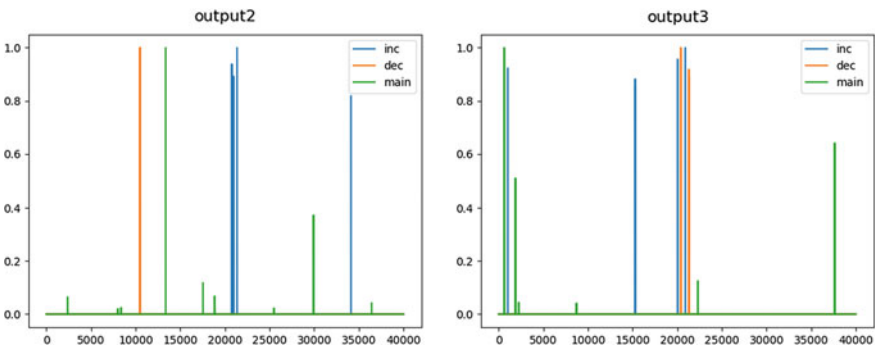
Fig. 7 Visualisation for outputs E3 and E4

4 Conclusions

The R-squared score obtained from all the three models are close to 1 for the unseen data, which shows that predictions are close to actuals and hence their generalisation capability. The R-squared score reflected by Bayesian model appears to outperform all the models. Moreover, gradient visualisation has demonstrated that neural networks are not just black boxes. It also gives us an intuition of the learning process, which closely associates with the underlying theory. The capability of deep learning architectures has shown their feature engineering capability, which could provide good predictions from raw vibration signals. This makes it ideal for real-time monitoring as it eliminates the need for data transformation.

References

1. A. Krizhevsky, I. Sutskever, G.E. Hinton, Imagenet classification with deep convolutional neural networks. Adv. Neural Inf. Process. Syst. (2012)
2. J. Wu, *Introduction to Convolutional Neural Networks* (Nanjing University, China, 2017)
3. A. Karpathy, Convolutional Neural Networks (2016)
4. A. Krizhevsky, I. Sutskever, G.E. Hinton, Imagenet classification with deep convolutional neural networks. In: Advances in Neural Information Processing Systems (2012)
5. Y. LeCun, Y. Bengio, G. Hinton, Deep learning. Nature (2015)
6. J.M. Hernández-Lobato, R.P. Adams, Probabilistic backpropagation for scalable learning of Bayesian neural networks, in *Proceedings of the 32nd International Conference on Machine Learning*, vol. 37, ICML'15
7. S. Ghosh, F.M. Delle Fave, J. Yedidia, Assumed density filtering methods for learning bayesian neural networks, in Disney Research, Association for the Advancement of Artificial Intelligence (AAAI) (2016)
8. T.P. Minka, A family of algorithms for approximate Bayesian inference. Ph.D. thesis (2001)
9. R.M. Neal, Bayesian learning for neural networks. Ph.D. thesis (1995)
10. D.J.C. MacKay, Bayesian methods for adaptive models. Ph.D. thesis (1992)
11. A. Graves, Practical variational inference for neural networks, in *Advances in Neural Information Processing Systems* (2011)
12. K. Simonyan, A. Zisserman Very deep convolutional networks for large-scale image recognition. CoRR (2014)
13. Bearings fault diagnosis based on convolutional neural networks with 2D representation of vibration signals as input
14. https://www.researchgate.net/figure/An-example-of-CNN-architecture_fig1_320748406
15. http://adventuresinmachinelearning.com/keras-lstm-tutorial/
16. O. Abdeljaber, O. Avci, S. Kiranyaz, M. Gabbouj, D. Inman, Real-time vibration-based structural damage detection using one-dimensional convolutional neural networks. J. Sound and Vib. **388**, 154 (2017)
17. R. Zhao, R. Yan, Z. Chen, K. Mao, P. Wang, R.X. Gao, Deep learning and its applications to machine health monitoring: a survey. arXiv preprint arXiv:1612.07640 (2016)
18. K. Simonyan, A. Vedaldi, A. Zisserman, Deep inside convolutional networks: visualising image classification models and saliency maps (2013)
19. V. Nair, G.E. Hinton, Rectified linear units improve restricted Boltzmann machines, in *Proceedings of the 27th International Conference on Machine Learning* (2010)
20. Y. Gal, Uncertainty in deep learning. Ph.D. thesis (2015)

Effect of Boundary Conditions in Damage Detection of Aluminum Beams Using PZT

Mohammed Aslam, Praveen Nagarajan and Mini Remanan

Abstract Structural Health Monitoring (SHM) and damage detection of engineering structures are always having great scientific and economic importance. Piezoelectric transducers have recently found its application in damage detection using wave propagation technique. Every finite element domain has a boundary. It is necessary to choose suitable conditions to be applied at the boundaries based on certain assumptions. The boundary of the finite element model will cause the elastic waves to be reflected and disturb the waveform. In this paper, a three-dimensional finite element analysis is performed on an aluminum beam with surface-bonded piezoelectric actuator and sensor under different boundary conditions. Piezoelectric patches operating in d_{31} and d_{24} modes are used as transducers for wave generation in pitch-catch configuration. Five different boundary conditions, namely, free-free, fixed-fixed, hinged-hinged, fixed-free, and fixed-hinged are considered to study its effects on wave characteristics. Signal processing techniques are then used for extracting the features of the sensed voltage signal to make an inference on the existence of damage.

Keywords SHM · PZT · Boundary condition · FEM · Guided wave

1 Introduction

Early detection of faults or damages in any structural systems due to harmful environmental effects helps in evading catastrophic failures. Structural Health Monitoring (SHM) systems and damage detection methods help to guarantee safety and stability of structures. Among the available transducers for SHM techniques, piezoelectric materials like Lead Zirconium Titanate (PZT) are found to be far superior to other sensors due to its distinct features such as lightweight, lower

M. Aslam (✉) · P. Nagarajan · M. Remanan
Department of Civil Engineering, National Institute of Technology Calicut, Kozhikode, Kerala, India
e-mail: pcaslam4@gmail.com

power consumption, ease of implementation, a broad range of bandwidth, low cost, and high sensitivity [1].

Recently, wave-propagation-based damage detection technique has added importance in SHM applications. During propagation, the elastic waves interact with discontinuities or damages present in the structures and get transmitted/ reflected which are detected by PZT transducers. These elastic waves are usually called as guided waves. The elastic wave that propagates through a waveguide is called a guided wave. A waveguide is a structure with boundaries that help elastic waves to propagate from one point to another [2]. A broad review on the use of guided wave in SHM systems can be found in [3, 4].

Finite element method has been extensively used as a mathematical tool for wave-propagation-based damage detection techniques [5]. This method has been successfully implemented in plates, pipes, and beam-like structures [6, 7]. Peng et al. [8] analyzed characteristics of wave propagation in thick beams. The numerical simulation of elastic wave propagation was also validated by experiments for both uncracked and cracked beams. A numerical study on crack detection of a cantilever steel beam was conducted by Wang et al. [9]. The crack location and its severity were identified by the additional wave packet and its amplitude. Soleimanpour and Ng [10] studied scattering and mode conversion analysis of guided waves at delaminations in laminated composite beams. The numerical simulations showed additional wave packet produced due to the interaction of incident wave with boundaries. The wave propagation in H-beam with/without a hole/notch was examined by Fucai et al. [11] using the finite element method. The damage was then localized using geometric-average-based reconstruction algorithm.

Numerical simulation of ultrasonic waves in structures requires too much computational time. Since these waves travel over long distances, a large part of the structural component must be included in the analysis. Also, the numerical model requires very fine mesh size for spatial resolution and very small time step to avoid numerical instability [12]. Therefore, it is necessary to reduce the finite element domain. This cannot be done by merely eliminating the parts of the model. The analyst generally chooses appropriate conditions to be applied at the boundaries based on certain assumptions. In wave propagation analysis, the boundary of the finite element model will cause the elastic waves to be reflected and superimpose with the propagating waves by making the wave field more complex. Sometimes absorbing boundaries can also be provided in the model to extend the model to an infinite domain. Absorbing boundaries can be provided using the infinite element method. It uses only one layer of special elements around the boundary to absorb the incident waves. This procedure is available in commercial software package Abaqus [13].

Effective damage detection necessitates the proper use of signal processing techniques. Fourier transform and wavelet transform are two common signal processing techniques that are used for damage detection and characterization [14]. Hossein and Hojjat [15] conducted a comparative study of different signal processing techniques that are used for SHM. In this paper, numerical simulation of

elastic waves generated by surface-bonded PZT for detecting damage in beam-like structures under different boundary conditions is discussed. The study also shows how the signal processing technique like Fourier transforms influences the damage detection process. Here, signal processing is done by the use of Matlab software.

2 Numerical Study

The geometry of the healthy and damaged aluminum beam with surface-bonded PZT used in this paper is shown in Fig. 1a and b, respectively. Two PZT transducers are placed at a distance of 35 mm from center of the beam on either side. One of the PZT acts as an actuator and the other as a sensor. The numerical models of the PZT transducers and the aluminum beam created in software Abaqus is shown in Fig. 2a and b, respectively. The aluminum beam model was modeled with the 3-D quadratic tetrahedral element (C3D10) finite elements and the PZT was modeled with 3-D piezoelectric quadratic tetrahedral elements (C3D10E). The fully coupled transient analysis was performed to simulate the piezoelectric effect.

The transducers were excited with a sinusoidal toneburst modulated with Hanning window. The equation used for the excitation is shown in Eq. 1.
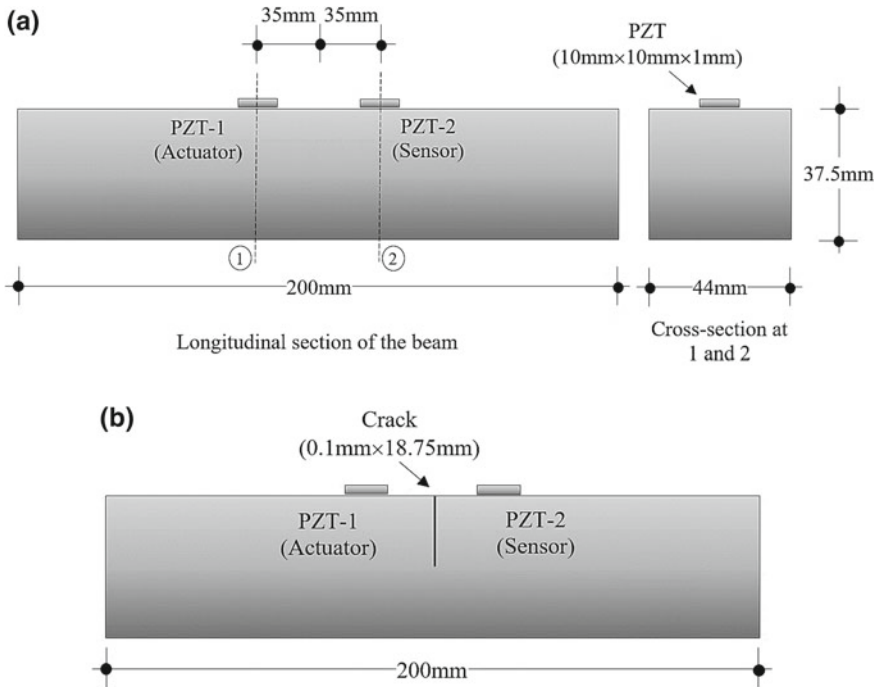
Fig. 1 PZT-bonded aluminum beam **a** healthy **b** damaged

(a) Healthy   (b) Damaged
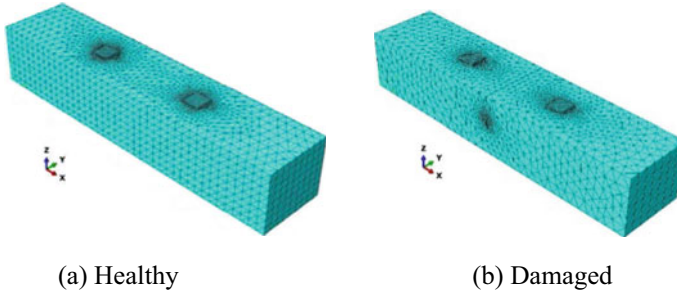
Fig. 2 The finite element model of PZT-bonded aluminum beam

$$V(t) = V\,Sin(2\pi f_c t)\frac{1}{2}\left[1 - \cos\left(\frac{2\pi f_c t}{N}\right)\right] \tag{1}$$

where V is the peak voltage, f_c is the central frequency, and N is the number of cycles. Here, the peak amplitude of the wave is taken as 10 V and N as 5.

As guided waves are dispersive, particularly in thick beams where more reflections are produced from the boundaries, the excitation frequency should be chosen such that the dispersion can be minimized. It was revealed that the dispersion curve obtained by Timoshenko beam theory and the Rayleigh–Lamb equations is identical for the fundamental A_0 mode [16]. Hence, for the present study, the dispersion curve of Lamb waves for an aluminum plate is used. To minimize the effect of dispersion, a low frequency of 50 kHz is selected. The Guided wave propagation was simulated in the time interval of 550 μs. Implicit integration scheme is used for the analysis because explicit analysis is not available for piezoelectric elements in Abaqus. The time step (Δt) for implicit integration is chosen "automatic" on the basis of the "half-step residual" method. Based on the convergence, the time step is modified at each step automatically. This procedure is explained in [17]. Large time step can be used in implicit schemes as they are unconditionally stable. However, the maximum increment is taken to be less than $T/$ 10 for obtaining reliable results, where T is the fundamental period [17, 18]. The mesh size is selected such that the maximum element size is less than 10% of the longitudinal wavelength in the material [18]. Five different boundary conditions, namely, free-free, fixed-fixed, hinged-hinged, fixed-free, and fixed-hinged are considered for the study. The boundary conditions are shown in Fig. 3. The material properties of aluminum and PZT are given in Table 1.
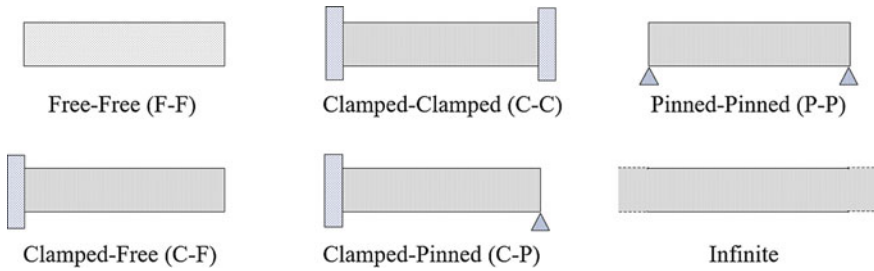
Fig. 3 Beams with different boundary conditions

Table 1 Material properties of the composite beam

Material properties	Density (kg/m^3)	Elastic constants		Piezoelectric constants		Dielectric constants	
		Notation	(GPa)	Notation	(C/m^2)	Notation	(nF/m)
PZT-4	7800	c_{11}	129.22	e_{31}	−3.3831	k_{11}	11.068
		c_{12}	86.402	e_{33}	16.520	k_{33}	6.6406
		c_{13}	83.062	e_{15}	15.149		
		c_{33}	116.90				
		c_{44}	28.830				
		c_{66}	21.410				
Material properties	Density (kg/m^3)	Elastic constant	Poisson's ratio				
Aluminum	2700	70 GPa	0.33				

3 d_{31} and d_{24} Mode Piezoelectric Transducer

In general, the poling direction of PZT is taken along the z-direction (or 3-direction). In the d_{31} mode, PZT is poled along the thickness, and the electrodes are placed at the top and bottom face of PZT as shown in Fig. 4a. Note that here 3-direction is oriented along the thickness. We apply an electric field in the z-direction and utilize the stress and strain produced in the x-direction to create an extension or bending in the material. In the d_{24} mode, 3-direction is oriented along the length of PZT, and the electrode is placed in a plane perpendicular to 2-direction as shown in Fig. 4b. Pure face shear deformation is obtained in this case.
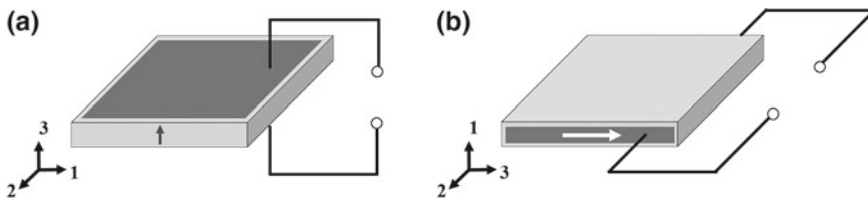
Fig. 4 Schematic diagram of **a** d_{31} PZT transducer **b** d_{24} PZT transducer

4 Results and Discussion

The transient response of the excited voltage signal was recorded by the PZT sensor for both healthy and damaged case. The voltage response of the PZT sensor for healthy and damaged beam obtained using the finite element method are compared with Boundary Element Method (BEM) solutions obtained by Zou et al. [19]. Figure 5a and b shows the comparison of sensor signals for the healthy and damaged beam, respectively. These signals are for F-F boundary condition and d_{31} mode excitation. The results obtained using FEM are in good agreement with the solutions obtained by Zou et al. [19]. Hence, the current finite element model is used for further studies.

The study is then extended for beams with different boundary conditions and under two different exciting modes of PZT. The transient voltage response of the PZT sensor for healthy and damaged beam under d_{31} and d_{24} mode excitation is shown in Fig. 6a and b, respectively. It can be observed that for most cases the wave packet signals in the time domain is more complex and distorted, which increases the difficulty in determining the incident and reflected wave packets. The signal waveform for C-C case under d_{31} mode is recognizable, whereas for other cases it is complex. It may be due to multi-mode and dispersive nature of waves.
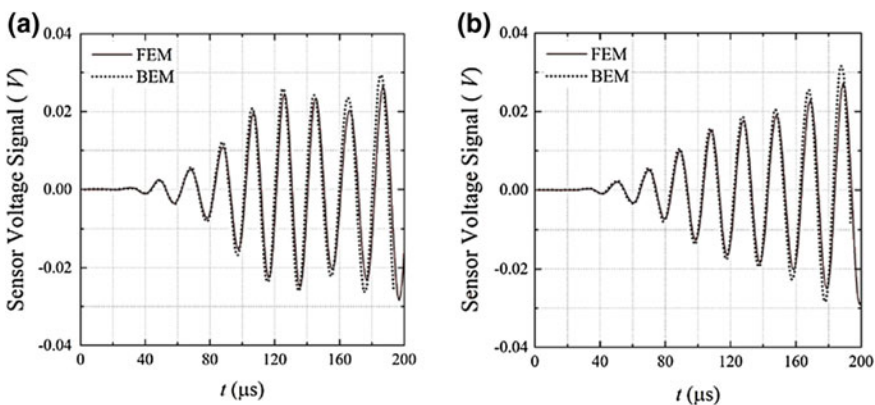
Fig. 5 Comparison of sensor voltage signal **a** healthy **b** damaged
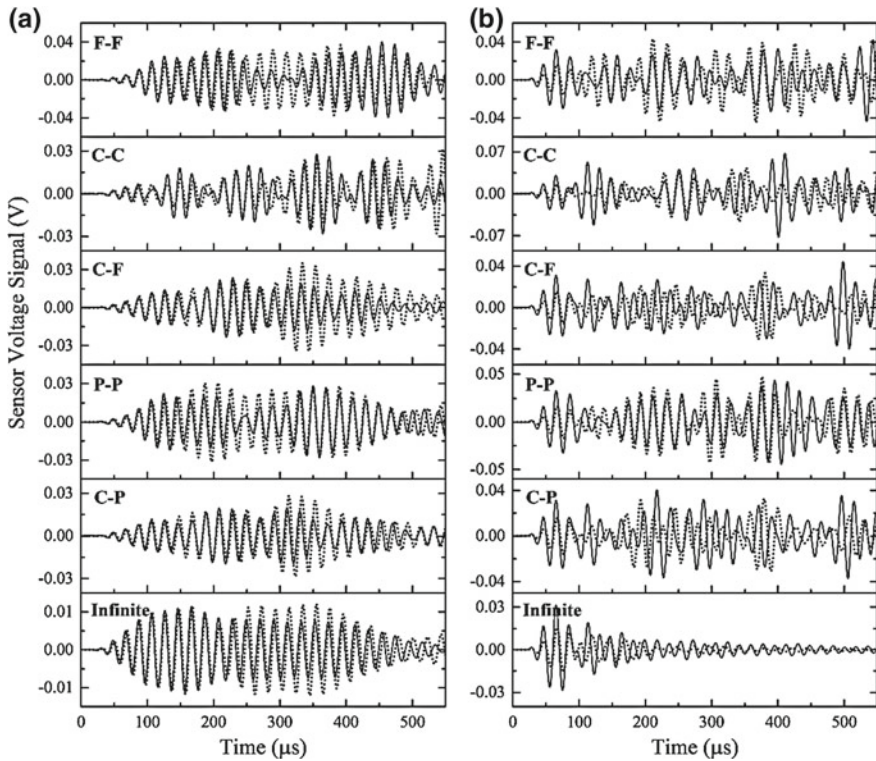
Fig. 6 Transient response of PZT sensor voltage signal under **a** d_{31} mode **b** d_{24} mode excitation (solid line—healthy, dotted line—damaged)

Under d_{24} mode excitation, the signal waveform for most of the cases is visible. It is observed that for infinite boundary condition, the signals get attenuated faster in the d_{24} mode as compared to d_{31} mode. This is because of the nondispersive nature and less mode conversion of fundamental shear horizontal (SH0) wave. The group velocity obtained from the numerical study under d_{24} mode excitation was 3181 m/s which is close to the bulk shear wave speed ($\sqrt{(G/\rho)}$, where G is the shear modulus and ρ is the density of the material). Also, for each boundary conditions, the waveform of the signals is different. This is because the transmitted and reflected waves become less isolated since the sensors are located close to the boundaries. It is noted that the amplitude of the transient signal corresponding to the d_{24} mode is comparatively higher than d_{31} mode excitation.

The other way of observing a transient signal is in its frequency domain. Fourier transform converts a signal in the time domain to the frequency domain (spectrum). The Fourier transform of sensor signal under d_{31} and d_{24} mode excitation is shown in Fig. 7a and b, respectively. The maximum Fourier amplitude under d_{31} mode excitation was obtained for a damaged beam with F-F boundary condition, while under d_{24} mode excitation maximum amplitude was observed in the healthy beam

with C-C boundary condition. These values are normalized with respect to their maximum values. All the other plots corresponding to d_{31} are normalized with respect to same normalizing factors used for generating a graph of F-F boundary condition. The plots corresponding to d_{24} are normalized with respect to same normalizing factors used for creating a graph of C-C boundary condition. As the
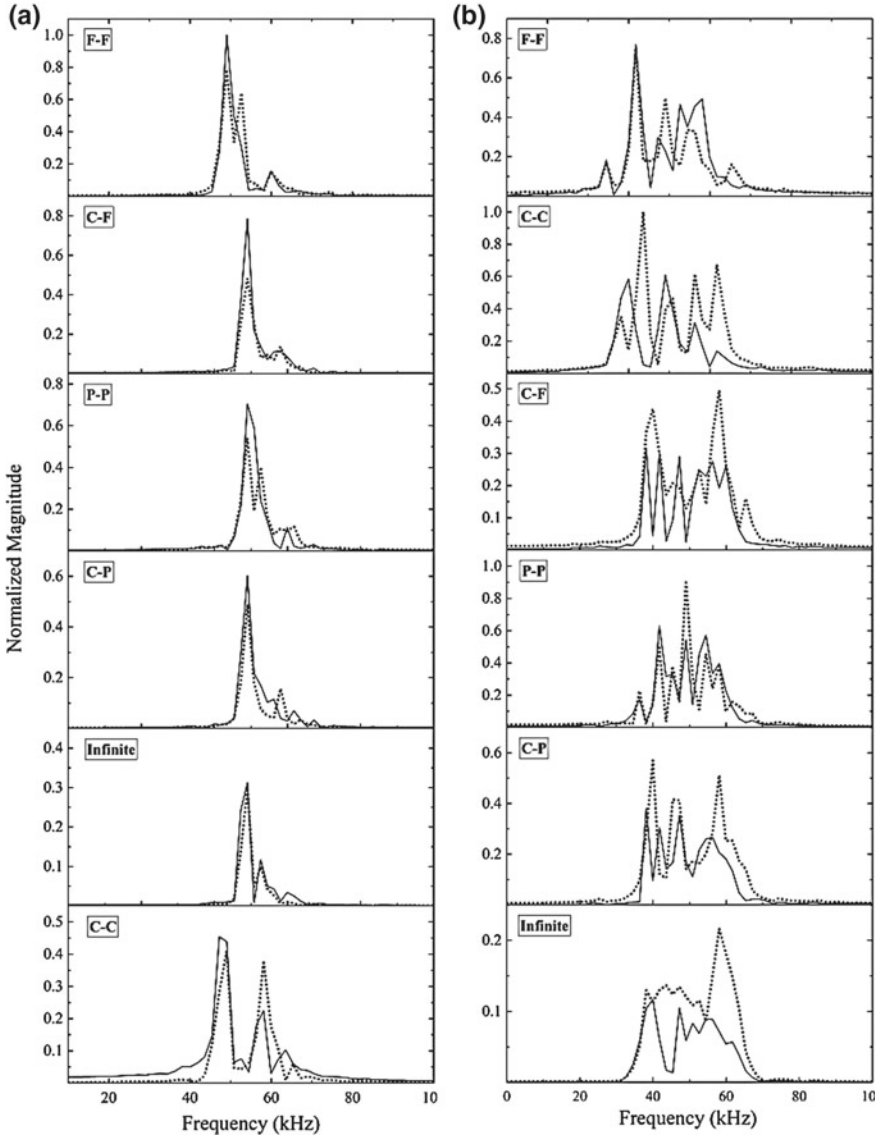
Fig. 7 Fourier transform of the sensor voltage signal under **a** d_{31} mode **b** d_{24} mode excitation (solid line—damaged, dotted line—healthy)
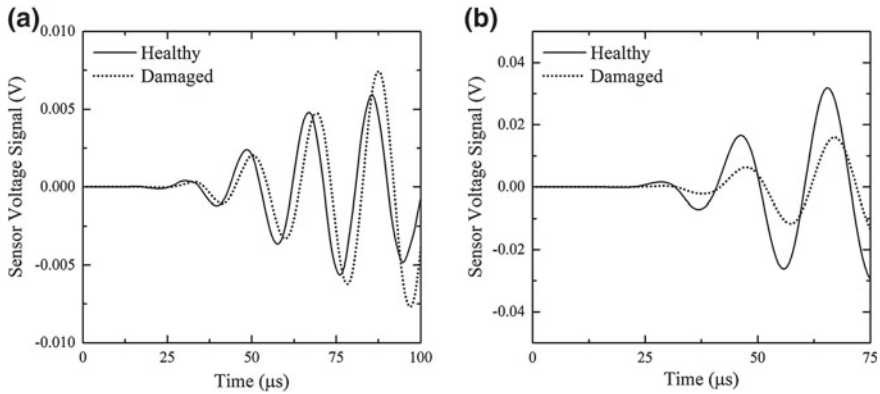
Fig. 8 The delay in arrival time **a** d_{31} mode **b** d_{24} mode

excitation is a narrow band pulse with a 50 kHz central frequency, the frequency of the voltage signal spreads in a finite bandwidth with most components near the central frequency. The difference in the Fourier magnitude represents the presence of damage. Increase in magnitude due to the presence of a crack is observed under d_{31} mode excitation. This might be due to the superposition of scattered/reflected wave with the progressing wave. The number of peaks in d_{24} mode excitation is more compared to d_{31} mode. This could be due to the presence of a number of wave packets as observed in Fig. 6b.

The presence of damage leads to delay in the arrival time of the signal. The delay in arrival time between healthy and damaged voltage signal is obtained by considering the first few portions of the signal. The delay in arrival time for F-F boundary condition under d_{31} and d_{24} mode excitation is depicted in Fig. 8a and b, respectively. The delay in arrival time for all boundary conditions under d_{31} excitation is 1.8 µs, whereas for d_{24} it is 1.2 µs.

5 Conclusions

The paper investigates the importance of considering the boundary condition in detecting damages in aluminum beams. From the numerical study, it is observed that the waveform of the transient signals is different for different boundary conditions. This is because the nature of the reflected wave from the boundary depends on the boundary condition. Two different PZT transducers were used for the study, d_{13} mode, and d_{24} mode. Under d_{31} mode, most of the signals are distorted due to dispersion, reflection, and mode conversion, while for d_{24} mode the wave packets are somewhat recognizable. Fourier transforms of the transient signal are also plotted to get information regarding the propagating modes and presence of damages. The presence of damage delayed the arrival time. For all boundary conditions

under d_{31} excitation, the time delay is 1.8 µs, whereas for d_{24} excitation it is 1.2 µs. Further processing of the signals is necessary to get information regarding wave reflection from the boundaries. These simulation results may be helpful for the researchers for interpreting the experimentally obtained wave signals.

References

1. V. Giurgiutiu, *Structural Health Monitoring with Piezoelectric Wafer Active Sensors* (Academic Press, Elsevier, 2008)
2. T. Kundu, *Ultrasonic Nondestructive Evaluation: Engineering and Biological Material Characterization* (CRC Press, New York, 2003), p. 224
3. E.H. Ling, R.H. Abdul Rahim, Aust. J. Mech. Eng. (2017)
4. M. Mitra, S. Gopalakrishnan, Smart Mater. Struct. **25** (2016)
5. C. Willberg, S. Duczek, J.M. Vivar-Perez, Z.A.B. Ahmad, Appl. Mech. Rev. **67**, 010803 (2015)
6. A. Raghavan, Shock Vib. Dig. **39**, 91 (2007)
7. R. Guan, Y. Lu, W. Duan, X. Wang, Struct. Control Health Monit. **24** (2017)
8. P. Haikuo, L. Ye, G. Meng, K. Sun, F. Li., J. Theor. Appl. Mech. **49**, 807 (2011)
9. D. Wang, H. Song, D. Shen, H. Zhu, in *IEEE Symposium on Piezoelectricity, Acoustic Waves and Device Applications* (2011), p. 90
10. S. Reza, C.-T. Ng, Struct. Monit. Maint. **2**, 213 (2015)
11. L. Fucai, H. Li, J. Qiu, G. Meng, Struct. Control Health Monit. **24** (2017)
12. M. Friedrich, L.J. Jacobs, J. Qu, NDT E Int. **32**, 225 (1999)
13. S. Yanfeng, V. Giurgiutiu, Wave Motion **58**, 22 (2015)
14. A. Rais, T. Kundu, Adv. Civ. Eng. 2012 (2012)
15. Q. Hossein, H. Adeli, J. Vibroeng. **18**, 2186 (2016)
16. C.H. Wang, L.R.F. Rose, J. Sound Vibr. **264**, 851 (2003)
17. V. Abaqus, *6.14 Documentation* (Dassault Systemes Simulia Corporation, 2014), p. 651
18. A.V. Pivkov, A.M. Lobachev, V.A. Polyanskiy, V.S. Modestov, St. Petersburg Polytech. Univ. J. Phys. Math. **2** (2016) 337
19. F. Zou, I. Benedetti, M.H. Aliabadi, Smart Mater. Struct. **23**, 015022 (2013)

A Novel Hybrid Technique to Identify the Minor Cracks in the Structure During Online Health Monitoring

K. Lakshmi and A. Rama Mohan Rao

Abstract The basic hypothesis of a structural health monitoring (SHM) system is that the global parameters like stiffness, mass, and damping of a structure are modified by damage and so the dynamic response. Nevertheless, in the case of subtle incipient damage, the changes in the dynamic characteristics of the structures developed in the structure alter only a few modal responses that too in a very mild manner, while all other modal responses remain intact. The damage features present in the modal responses of those few modes will be hidden in the measured total raw dynamic signatures. Often they get buried in the measurement noise. Keeping this in view, in this paper, a hybrid damage diagnostic algorithm combining a multivariate analysis technique called blind source separation (BSS) with time series analysis to identify and locate the minor cracks in structures is proposed. BSS decomposes the measured acceleration time-history responses into modal responses. We use an automated algorithm to isolate the modal responses which are sensitive to the presence of minor/subtle damages. These isolated modal responses are then reconstructed using the mixing matrix to obtain a new time-history data which is enriched with the minor damage features. The presence and spatial location of damage are obtained by processing the reconstructed time-history data using autoregressive–autoregressive with exogenous input (AR-ARX) model, using a Density Function of Probability (PDF), of the prediction errors. Both the numerical simulation studies and experimental studies are carried out to test and evaluate the proposed damage diagnostic algorithm and their capability in identifying minor/incipient damage like subtle cracks under noisy measurements.

Keywords Structural health monitoring · Blind source separation · Time series analysis · Damage diagnostics · Signal decomposition · Second-order blind identification (SOBI) · Autoregressive–autoregressive with exogenous input (AR-ARX) model

K. Lakshmi (✉) · A. Rama Mohan Rao
CSIR-Structural Engineering Research Centre, CSIR Campus,
Taramani, Chennai, Tamil Nadu, India
e-mail: lakshmik@serc.res.in

1 Introduction

Structural health monitoring provides reliable information on the actual condition of a structure to be captured and monitored, in the sequence of operations, namely, detection, localization, and evaluation of damage and prediction of remaining life. Among the vibration-based methods, damage diagnostic techniques using natural modes of the structure are proposed extensively in the past two decades. The modal-based damage detection methods exploit the global parameters of the whole structure and these global damage features are insensitive to the local and minor or incipient damage. Also, it is complex to handle the environmental variability, while using modal-based approaches. Further, they need an updated finite element model at every stage of damage. On the other hand, non-modal-based methods or signal-based analysis even though do not give a quantitative assessment, and are gaining popularity. Techniques based on time-frequency analysis [1], multi-variant analysis [2, 3], and time series algorithms [4–7] are found to be more promising.

Time-series-based methods are gaining popularity among structural health monitoring community in the recent past due to their inherent merits over other vibration-based methods. Time series models are modal free, amenable to real-time monitoring of structures, and can be advantageously used in wireless sensor networks [8, 9]. However, there are possibilities that the damage features built using the coefficients/errors become insensitive to reflect the damage due to various reasons like the low intensity of damage, the incompleteness of the damage information in coefficients/errors, and high measurement noise contamination in the signal. Also, typically, when the initiating damage is minor like trivial cracks, the minor changes in the dynamic characteristics of the structures developed in the structure alter only some specific modal responses while other modal responses remain unaltered. Hence, the damage features present in the modal response of specific modes due to the minor incipient damage will be masked in the overall response (i.e., the measured dynamic signature). Therefore, the modal responses which are sensitive to the presence of damage need to be extracted and used for damage diagnosis to increase the sensitivity of the damage features.

In this paper, we use second-order blind identification (SOBI) algorithm for modal decomposition of the signals (i.e., sources and weighting matrix) in order to isolate the modal responses containing significant damage features. These isolated modal responses are used to recreate the signal with enhanced damage features. These newly constructed signals are then used for damage diagnostics using time series models. The PDFs of prediction errors from AR-ARX models fitted to data from pristine and the unknown state of the structure are used as a damage index to discover the instantaneous time and location of damage. Numerical simulation studies and experimental studies are conducted to test the potency of the proposed algorithm for detecting a small incipient crack in the structure with measurement noise.

2 Blind Source Separation

The separation of original source waveforms from the sensor signals, without the knowledge of the system characteristics and the sources, is known as blind source separation, which is formulated as an inverse problem. Based on the observed records of sensor signals, x, in discrete time, from an unknown multiple-input multiple-output (MIMO) mixing system, A, an inverse system is identified to estimate the primary source signals, S. It can be expressed by the simple matrix factorization problem:

$$x(t) = As(t) \tag{1}$$

$$\hat{s}(t) = y(t) = W x(t) \tag{2}$$

where A is the mixing matrix denoted by $[a_{ij}]_{n \times n}$; $W_{n \times n} = A_{n \times n}^{-1}$ is the un-mixing matrix, and the pseudo-inverse of A; $s(k) = \{s_j(k)\}$ for j = 1, 2, … N are the sources (input to the system); $x(k) = \{x_i(k)\}$ for i = 1, 2, … N are sensor signals (system output), and $y(k) = \{y_j(k)\}$ for j = 1, 2, … N are the estimated sources. Then y gives the estimate of the sources $\hat{s}(t)$. BSS methods exploit the information in x only, to evaluate the un-mixing matrix, W.

According to the literature, the two popular approaches of BSS are independent component analysis (ICA) [10] which is based on the higher order statistics (HOS), and second-order blind identification (SOBI) [11] which exploits the time structure and uses second-order statistics (SOS). While ICA uses the properties of non-Gaussianity and statistical independence of sources, SOBI exploits second-order statistics by establishing multiple covariance matrices from the responses. There are no initial assumptions on statistical independence or the non-Gaussian nature of sources in the methods based on SOBI. Instead, they depend on the temporal statistics of second order. We exploit the second-order blind identification algorithm in a slightly different fashion in order to identify the small incipient damages present in the structure. We isolate the modal responses which are sensitive to the damage present in the structure using the improved SOBI technique and discard rest of the modal responses which do not really possess features related to the damage.

3 Methodology of Proposed Hybrid Technique

A hybrid damage detection technique combining blind source separation technique with time series analysis is proposed to detect the damage in the structural system at its earliest stage of incipience. The proposed technique is an output-only damage

detection method and utilizes the acceleration time-history response from the sensory system placed on the structure. The process of damage detection is carried out in two phases, namely, preliminary phase and testing phase.

3.1 Preliminary Phase

In the preliminary phase, the data from the structure when it is in a pristine state is utilized.

3.1.1 Database Formation

The baseline data is basically the acceleration time-history signal produced when the condition of the structure is healthy and there are only the effects of ambient variability and noise in the measurements present. A collection of baseline acceleration time history generated with the variability and measurement noise is compiled. These data corresponding to each node is segregated into various subsets. The subsets are formed to simulate a huge collection of samples corresponding to varying operational conditions and unknown environmental states. It also represents the statistical uncertainty which affects the estimation of time series models used further in the process.

3.1.2 AR Model

The acceleration responses of each sensor, in the form of time series x(t) in each baseline subsets, are fitted to AR model as

$$x(t) = \sum_{j=1}^{p} \phi_{xj} x(t-j) + e_x(t) \tag{3}$$

where "p" AR order, ϕ are the coefficients, and the fitting errors are given by e_x. The AR order is determined with a partial auto-correlation analysis [12].

3.2 Testing Phase

3.2.1 Data Formation

The current data subsets collected from the unrevealed condition of the structure (either healthy or damaged state) are established. Employing the new current time

series, y(t), collected from the system of the unrevealed structural state, the AR model is constructed as

$$y(t) = \sum_{j=1}^{p} \phi_{yj} y(t-j) + e_y(t) \tag{4}$$

In most of the damage diagnostic techniques, the structural responses are exploited directly to derive the damage features. The disadvantage of using the responses directly is that it becomes hard to differentiate between damage and the effect of another variability due to environmental/operational conditions, as the variability also cause changes in the dynamic response. This may give rise to the false alarms and remarkably influence the damage diagnostic schemes. In order to tackle this problem, a strategy called normalization is adopted. In the process of normalization, every subset of the current data is paired to a subset of the baseline data, such that they have arisen from closely similar conditions of unmeasured variability, if not the same.

3.2.2 Normalization

In the proposed technique, the process of normalization is performed by monitoring the coefficients of the AR models of baseline and current data subsets. Every subset of y(t) is paired with any one of the subsets of the baseline data, x(t) using the AR coefficients, on the basis of their correlation values. The correlations are evaluated using Eq. (5) that diminishes the difference between the coefficients ϕ_x and ϕ_y with order "p".

$$\text{Difference} = \sum_{j=1}^{p} \left(\phi_x^j - \phi_y^j \right)^2 \tag{5}$$

These two subsets are now matched and they are used further in the testing phase.

3.2.3 Modal Decomposition Using SOBI and Reconstruction of Time Series

The acceleration data of the matched subsets from the baseline and the current data is processed by the proposed improved version of SOBI to obtain the corresponding mixing matrices and sources. The estimated sources of the current subset are expected to possess the information of damage. Therefore, these sources and their corresponding vectors from the mixing matrix of the current subset are used further to reconstruct the current time-history response, $\tilde{y}_i(t)$ (i = 1, 2, … ns; ns: number of sensors) using the damage rich sources and the corresponding elements of the

mixing matrix. Similarly, the matched reference time series $\tilde{x}_i(t)(i = 1, 2, \ldots ns)$ is reconstructed based on the vector indices obtained from the current data subset and their corresponding interesting sources. Thus by this process, only the damage information is retained and the contribution of noise is getting eliminated. This new healthy and current time series blocks of all the sensors are used further to calculate the damage indices to locate the damage. In order to choose the appropriate sources of the current data to reconstruct the time-history responses with rich damage features, we use the following procedure:

i. The dynamic signatures, i.e., acceleration time-history responses, obtained from the current state of the structure, y(t) (i.e., with damage) are decomposed into M sources using SOBI. The modal time-history responses can be computed using the corresponding coefficients in the mixing matrix. The modal responses obtained are denoted as $C_m(t)$ (m =1, 2, … M).

ii. Similarly, the reference dynamic signatures x(t), i.e., responses from a healthy state of the structure, chosen using the matching technique discussed earlier are also decomposed into sources and mixing matrix using SOBI. The modal time-history responses computed are denoted as $R_m(t)$ (m =1, 2, … M) and mixing matrix as Ar.

iii. Compute the correlation coefficients γ_m^j (m = 1, 2, … M; j = 1, 2, 3,… ns) of the current modal responses, $C_m(t)$, and measured time-history responses x(t) of the reference condition.

iv. Similarly compute the correlation coefficients η_m^j (m = 1, 2, … M; j = 1, 2, 3, … ns) of the current modal responses, $C_m(t)$, and measured time-history responses y(t) of the current state.
Compute damage feature (DF) index of each current modal time-history response for each modal response (m = 1, 2, … NM)

$$DF(m) = MAX(\eta_m^j - \gamma_m^j)(m = 1, 2, \ldots M; \; j = 1, \; 2, \ldots ns) \qquad (6)$$

v. Sort the DF vector and choose the sorted top few modal time-history responses with higher values of damage feature index based on user-defined cutoff. The user-defined cutoff controls the process of reconstruction.

vi. Similarly reconstruct the reference and current time-history responses, $\tilde{x}_i(t)$ and $\tilde{y}_i(t)$ (i = 1, 2, 3 … ns) by choosing the modal time-history responses of the modes chosen in step v.

vii. Use these reconstructed current time-history data, $\tilde{y}(t)$ and reference time-history data, $\tilde{x}(t)$ for computing the spatial damage in the structure using the probability density function (PDF)-based damage index, DI_PDF, evaluated from the fitting errors of AR-ARX model presented in Lakshmi and Ram Mohan Rao [13].

The process described in Sect. 3.2.3 is shown in the form of a flowchart in Fig. 1.
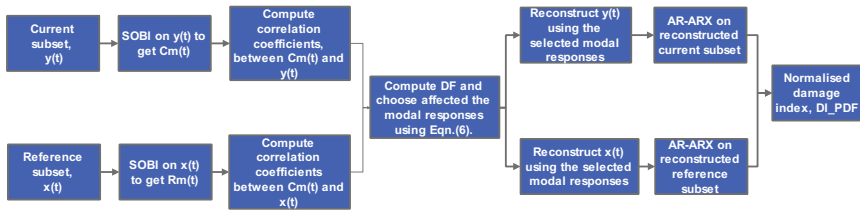
Fig. 1 Flowchart of modal decomposition using SOBI and reconstruction of time series

4 Verification Studies

4.1 Numerical Simulation Studies

The simulated numerical example used for validation studies is a beam with simply supported end conditions, shown in Fig. 2, with dimensions of 4000 mm × 450 mm × 500 mm, which is in a healthy state initially. The beam is approximated into 20 elements for the simulation studies. The beam is assumed to carry accelerometers on 19 nodes, eliminating the nodes at the supports.

The finite element module for the numerical simulation studies is developed in MATLAB environment. Standard one-dimensional Euler–Bernoulli beam elements are employed to model the beam and shear deformation is neglected. There are two nodes per element and each node has three degrees of freedom: longitudinal displacement, translational displacement, and bending rotation. Simply supported boundary conditions are imposed as shown in Fig. 2. A stochastic random dynamic loading is simulated for exciting the beam. Newmark's time marching scheme is used in finite element analysis to compute the acceleration time-history response with a sampling rate of 2000 Hz. Initially, acceleration time-history data for a duration of 5 s is synthesized with random loads and varied temperature recordings. In order to simulate the presence of noise in the measurements, Gaussian noise (white) is added to the acceleration response as signal-to-noise ratio (SNR). SNR describes the amplitude of the measurement noise with respect to the uncorrupted signal and is expressed as
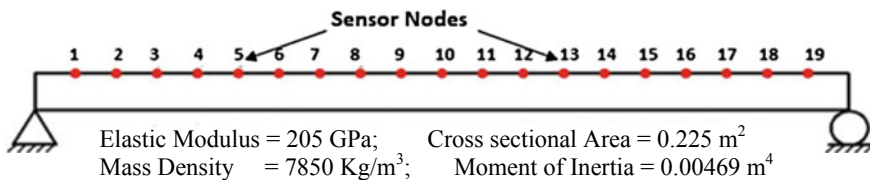
Fig. 2 A simply supported beam

$$SNR = 10 \, \log_{10} \frac{\sigma_{us}^2}{\sigma_{mn}^2} \, \text{dB} \tag{7}$$

where σ_{mn} and σ_{us} indicate the variance of the measurement noise and the original uncorrupted signal, respectively. This healthy data generated with simulated varied ambience/temperature conditions and noise (SNR-35) is segmented into 20 subsets with 500 samples in each.

In the same way, the acceleration response for the present state of the structure, with damage in the 16th element, by simulating a crack of 10 mm long, is synthesized and divided into subsets. For this purpose, the finite element formulations of the cracked beam are exploited in this numerical study to generate the acceleration responses after the simulation of damage. The modeling of crack uses elasto-plastic fracture mechanics (EFEM), where the plasticity at the crack tip is taken into account. The acceleration responses are generated to form the current data in a fashion that originally the structure is healthy and the damage is initiated after a few instants of time. To simulate this scenario, the damage is instigated after 2 s (i.e., exactly in 10th subset of current data).

Initially, the acceleration response is preprocessed with SOBI algorithm to extract the sources and the mixing matrix. From the extracted modal responses (sources and mixing matrix), damage-enriched modal responses are selected using the automated procedure presented in the earlier section. The new current time series is reconstructed using these damage-enriched modal responses. In the similar fashion, the new baseline time series is also reconstructed using the already selected modal responses. Once the current data subset and the baseline subset are reconstructed using the extracted sources and vectors of mixing matrix, AR-ARX model is used to determine the damage indices using DI_PDF discussed in Lakshmi and Ram Mohan Rao [13]. The details of the extracted sources, of both the dynamic signatures obtained from the healthy structure (baseline) and with damage (current data), are shown in Fig. 3(i) and (ii), respectively. The typical reconstructed signals of healthy (baseline) and current data (with damage) at the node (sensor) closer to the damage location (node 16) and the damage indices assessed for each sensor are shown in Fig. 4. The results presented in Fig. 4 clearly indicates that the proposed method based on BSS-AR-ARX is effective for detecting as well as locating the spatial damage present in the structure in the form of a subtle crack. Manipulating the index of the subset being analyzed, the precise time instant of damage is easily found out. In this numerical example, the instant of damage is established as 2 s.
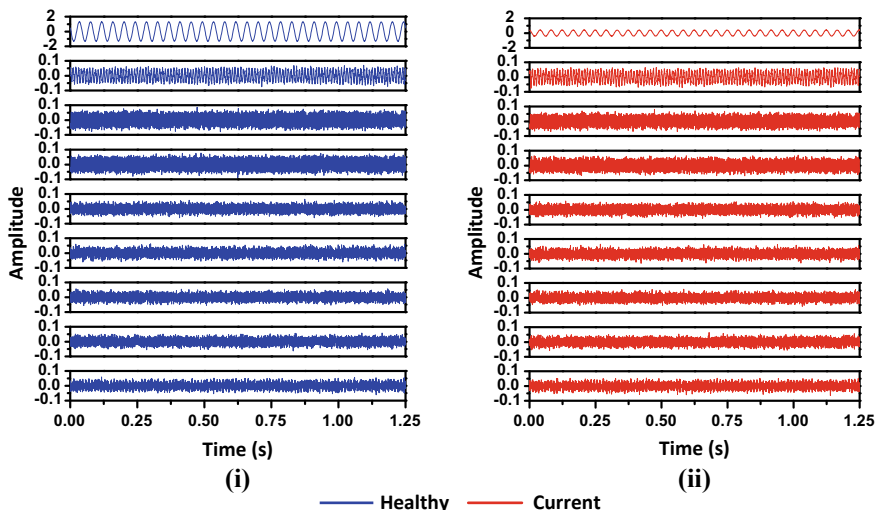
Fig. 3 Extracted sources from the responses of the simply supported beam using SOBI: (i) extracted sources of healthy data, (ii) extracted sources of current data
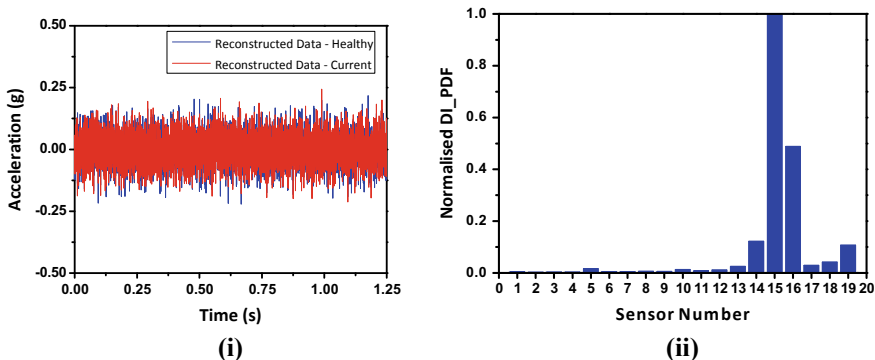
Fig. 4 Damage detection of simply supported girder: (i) superimposed reconstructed signals of current and healthy data, (ii) DI_PDF, computed as discussed in Lakshmi and Ram Mohan Rao [13], using AR-ARX model of reconstructed data

4.2 Experimental Verification

The structure considered for testing is a reinforced cement concrete simply supported beam. The dimensions of the beam are length of span-3 m, width of cross section—0.165 m, and depth—0.20 m. The longitudinal reinforcement in bottom was 2# 16 ϕ and in top was 2# 12 ϕ with 25# 6 ϕ stirrups. The initial few frequencies of the beam are as follows: 28, 112, 252, and 448 Hz.
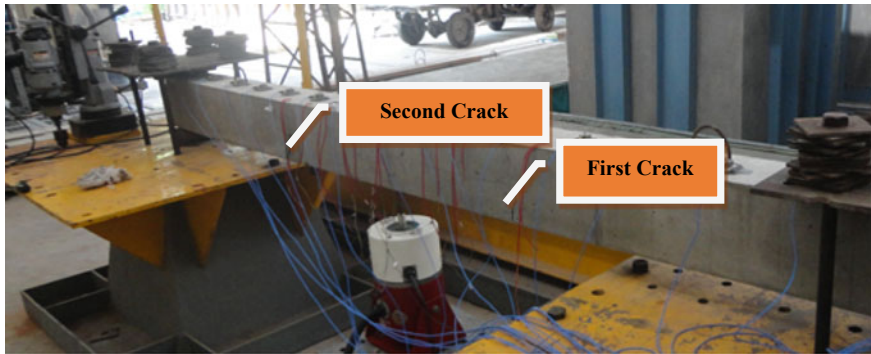
Fig. 5 Scenario of damage

The instrumentation of the beam is with 16 numbers of micro-electromechanical systems (MEMS) accelerometers with the measurement range of ± 2 g and frequency range of 0–350 Hz, placed equidistantly on the beam to collect the acceleration time-history signals. The excitations are performed by a modal shaker of sine peak force capacity of 200 N and the tests were carried out in the frequency range of 0–1000 Hz, for harmonic and random excitations. The variations in loading frequencies and amplitude are provided during every set of recordings to simulate variability due to operational loads. First, acceleration responses for 19 s, with a sampling rate of 3000 Hz, are recorded at 16 sensor nodes for the healthy state of the beam. This data set is referred to as "DATA SET-H".

The minor damage is instigated at about one-third span from both supports (i.e., in element no. 5 and element no. 12) of the beam, by applying the static loads in small increments. The minor cracks appear when the applied static load is nearly 12KN. The experiment with dynamic excitation force is conducted to fabricate test data (i.e., acceleration response) of the beam with inflicted minor damage and is mentioned as "DATA SET-D". The scenario of damage induced in the beam is shown in Fig. 5.

The acceleration data of "DATA SET-H" and "DATA SET-D" are used as a baseline and current data, respectively. The modal sources and mixing matrices for the baseline and current data are extracted using SOBI and the critical sources are selected using the correlation coefficient method and are used to reconstruct the new signal. The typical reconstructed new signals of DATA SET-H and DATA SET-D, corresponding to sensor number 12, are shown in Fig. 6(i). It can be seen from Fig. 6(i) that the change of dynamics due to minor damage cannot be inferred directly from the time-history data. To capture the damage information, AR-ARX model is constructed with the new reconstructed signals and DI_PDF is computed for each sensor node. The normalized values of damage indices of DI_PDF are shown in Fig. 6(ii). The higher peaks in Fig. 6(ii) clearly mirror the spatial position of damage (i.e., at one-third of the beam from both the supports).
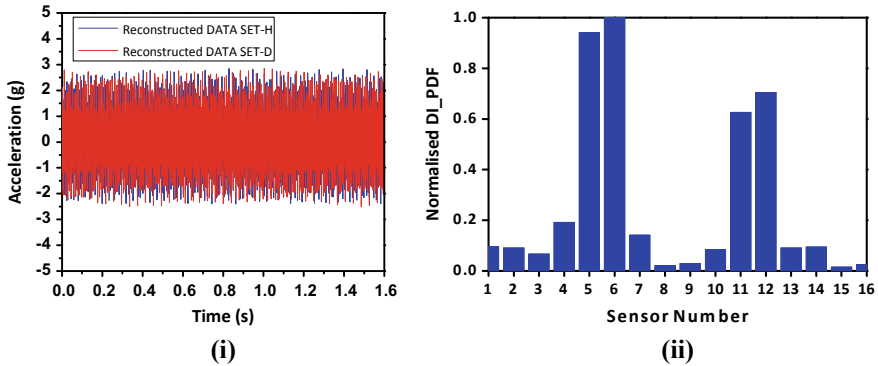
Fig. 6 Experimental studies on RCC beam: (i) superimposed reconstructed signals of DATA SET-H and DATA SET-D case signals of sensor-12, (ii) DI_PDF, computed as discussed in Lakshmi and Ram Mohan Rao [13], using AR-ARX model of reconstructed data

5 Conclusions

In the paper, a novel hybrid technique to recognize the location of the minor damage like minor cracks is presented. As the minor damage creates feeble changes in the dynamic characteristics of only a few modes of the structure, the damage features present in those modal responses get hidden in the overall response (i.e., the measured dynamic signature). Additionally, measurement noise and environmental variability also play their role in masking the minor damage features in the overall response of the structure. In view of this, in this paper, an attempt has been made to isolate these damage-sensitive modal responses and reconstruct a new signal accordingly using blind source separation using SOBI. The damage-enriched signals isolated by SOBI are further used for damage diagnosis using the AR-ARX model, employing a damage index, denoted as DI_PDF, constructed from the probability density function of AR-ARX prediction errors. The numerical simulation studies have been conducted by considering a simply supported beam with minor cracks. Laboratory experimental studies are performed by considering an RCC beam to complement the numerical simulations and also demonstrate its practical applicability in the field.

References

1. A.R.M. Rao, K. Lakshmi, Meccanica **50**, 1551–1578 (2015)
2. A.R.M. Rao, K. Lakshmi, V. Dhanya, Comput. Struct. **106–107**, 228–244 (2012)
3. A.R.M. Rao, K. Lakshmi, S. Krishnakumar, Adv. Eng. Softw. **86**(1), 85–106 (2015)
4. H. Zheng, A. Mita, Struct. Control Health Monit. **15**(7), 992–1005 (2008)
5. K. Lakshmi, A.R.M. Rao, Non-Destr. Test. Eval. **29**(4), 357–376 (2014)
6. K. Lakshmi, A.R.M. Rao, J. Non-Destr. Test. Cond. Monit. **57**(10), 580–588 (2015)

7. K. Lakshmi, A.R.M. Rao, N. Gopalakrishnan, Struct. Control Health Monit. **24**, e1960 (2017)
8. A.B. Noel, A. Abdaoui, T. Elfoulym, M.H. Ahmed, A. Badawy, M.S. Shehata, Commun. Surv. Tutor. **19**(3), 1403–1423 (2017)
9. Q. Ling, Z. Tian, Y. Yin, Y. Li, IEEE Sens. J. **9**(11), 1596–1604 (2009)
10. A.K.J. Hyvarinen, E. Oja, *Independent Component Analysis* (Wiley, New York, 2001)
11. A. Belouchrani, K.A. Meraim, J. Cardoso et al., IEEE Trans. Signal Process. **45**(2), 434–444 (1997)
12. G.E.P. Box, G.M. Jenkins, G.C. Reinsel, *Time Series Analysis: Forecasting and Control* (Prentice Hall, 1994)
13. K. Lakshmi, A.R.M. Rao, N. Gopalakrishnan, Struct. Infrastruct. Eng. 1–20 (2018)

Part XIV
Structural Integrity Assessment

Experimental Studies on Qualification of Structural Integrity of Eddy Current Flow Meter

**S. Suresh Kumar, Sudheer Patri, R. K. Sharma, R. Punniamoorthy,
Vishal D. Paunikar, Ranjith Jovin Cyriac, S. Harishkumaran,
P. Vasudevan, Ranga Ramakrishna, S. D. Sajish, V. A. Suresh kumar,
S. Chandramouli, C. Meikandamurthy, B. K. Sreedhar,
K. Sathishkumar, I. B. Noushad, S. Murugan and P. Selvaraj**

Abstract An eddy current flow sensor (ECFS) is used for measuring the sodium flow through the reactor core in prototype fast breeder reactor (PFBR). Being a safety critical system, ensuring the structural integrity of the sensor and associated support systems has a direct bearing on the safety and the availability of the reactor. The sensor operates in a harsh environment with maximum sodium temperature up to 525 °C, subjected to thermal shocks, seismic-induced loading, and flow-induced vibrations. The sensor employs special materials, components (MgO coil) which are not covered by codes. Due to non-availability of design guidelines in design codes for these sensors, the structural integrity of this sensor was demonstrated experimentally. Codal guidelines were extended wherever possible to aid in the experimental program. All the experiments done, other than FIV, are presented in the paper. During these tests, in addition to integrity, other functional checks were also carried out. The tests demonstrated the structural integrity of the ECFM and provided basis for obtaining regulatory clearance for ECFM.

Keywords Eddy current flow meter · Thermal shock testing · Seismic testing · Structural integrity

S. Suresh Kumar (✉) · S. Patri · R. K. Sharma · R. Punniamoorthy · V. D. Paunikar ·
R. Ramakrishna · V. A. Suresh kumar · S. Chandramouli · C. Meikandamurthy ·
B. K. Sreedhar · I. B. Noushad · S. Murugan · P. Selvaraj
Fast Reactor Technology Group, IGCAR, Kalpakkam 603102, Tamil Nadu, India
e-mail: sskr@igcar.gov.in

R. J. Cyriac · S. D. Sajish
Reactor Design Group, IGCAR, Kalpakkam 603102, Tamil Nadu, India

S. Harishkumaran · P. Vasudevan · K. Sathishkumar
Structural Engineering Research Centre, CSIR, Chennai 600036, Tamil Nadu, India

1 Introduction

An eddy current flow sensor (ECFS) is used for measuring the sodium flow through the reactor core in prototype fast breeder reactor (PFBR). It is a safety critical component as it provides signal for core under cooling incidents to reactor protection system, which triggers safety action. Thus, ensuring the structural integrity of the sensor and associated support systems has a direct bearing on the safety and the availability of the reactor.

The sensor is positioned in a sodium pipeline through which the part of sodium from pump outlet flows to the suction. It is subjected to thermal loading due to high-temperature operation (up to 525 °C), thermal shock loading during reactor transients, and the seismic-induced loading during design basis events like earthquakes, loss of decay heat removal system, etc.

Only superficial data is available in open literature on the studies related to the structural integrity of similar sensors. The design of an in-core flow meter, developed in Japan, was validated against thermal shocks, flow-induced vibrations, and seismic-induced loadings [1]. Similarly, many experimental studies were carried out for qualifying the sodium flow sensor developed for measuring the sodium flow in FFTF reactor [2].

In the sensor construction, certain magnetic and ceramic materials and components are employed. These materials are not covered in any of the design and construction codes, such as ASME and RCC-MR, followed for the design of FBRs. Moreover, no specific guidelines/design procedures are available for designing and qualifying these types of sensors in the design codes. Hence, experimental methods are resorted for demonstrating the structural integrity of the sensor. The codal guidelines were extended, wherever possible, to aid in the experimental program.

The present paper focuses on the experimental studies carried out for demonstrating the integrity of the sensor.

2 Constructional Features of ECFS

The schematic ECFS is shown in Fig. 1. It consists of a bobbin made of soft iron, with a primary and two secondary coils wound over it. The coils are made of SS-sheathed MgO-insulated copper conductor of 0.5 mm overall diameter. The bobbin has a central hole for routing the cables and two steps are machined on the bobbin to aid in coiling. The bobbin is screwed to a SS inner guide tube and is enclosed in an outer guide tube, which protects the sensor from sodium.

In PFBR, each probe assembly consists of two sensors, as shown in Fig. 2. The probe assembly along with the guide tube is called as eddy current flow meter. The schematic arrangement of ECFM installation in PFBR and the schematic of probe
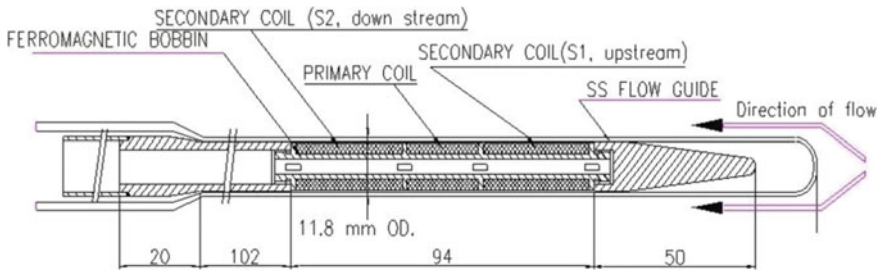
Fig. 1 Schematic of ECFS

Fig. 2 ECFM probe
assembly

assembly are shown in Fig. 3a and Fig. 3b, respectively. The guide tube and the SS pipe are supported at the top, approximately 9.4 m above the sensor. The inner guide tube has an ID and OD of 17.08 mm and 21.3 mm, respectively, which reduces toward the bottom for a length of 425 mm to an ID and OD of 12.0 mm and 14.0 mm, respectively. The inner guide tube is attached along with the outer guide tube to the pump shell box by flange joint at the top (Fig. 3). The inner guide tube is also supported through guides attached to the pump shell at the middle and suction casing at the bottom portion of the pump as shown in Fig. 3.

The normal operating temperature of the flow meter is 400 °C and the temperature may rise to 525 °C during a particular condition, when the decay heat removal by normal mode fails and a safety grade system takes over. The sensor is also subjected to thermal shocks during the takeover of the safety grade system, the expected shock is found to be 5 °C/s, by numerical analysis. The temperature of the sensor reduces to 200 °C during reactor cold shutdown condition. In addition, owing to its long slender nature of the sensor and its support arrangement, it is susceptible to seismic loadings and flow-induced vibrations. The studies for FIV are under progress and are not covered in this paper.

3 Experimental Program

The experimental program is designed to cover all the possible loading modes independently, which is as follows:

- High-temperature testing in sodium from 200 up to 525 °C.
- Thermal shock testing in sodium–argon to simulate the anticipated thermal shocks from 400 to 525 °C.
- Seismic testing simulating operation basis earthquakes and safe shutdown earthquakes in air and in sodium (simulated by aluminum tube around ECFM).

All the experiments were carried out with the same sensor. The qualification criteria of the sensor is that (i) the ECFM shall function satisfactorily under these loading conditions, (ii) the probe assembly shall not undergo any gross plastic deformation which precludes the retrieval of the sensor for replacement, (iii) there shall not be any structural damage like crack initiation, breakage, etc. on any of the items of the assembly, and (iv) the insulation resistance of the coils shall not be lowered to unacceptable values.

3.1 High-Temperature Testing in Sodium

High-temperature testing was carried out in a sodium test facility called steam generator test facility (SGTF) [3]. A section of sodium pipeline in SGTF is modified
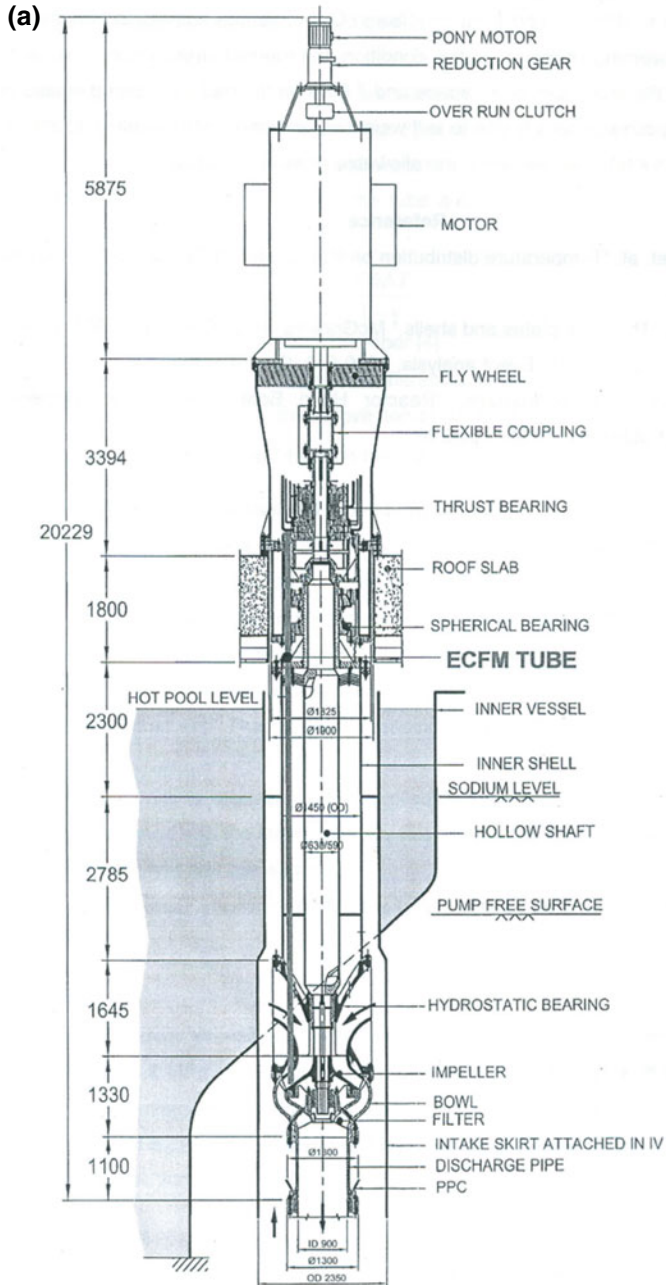
Fig. 3 a Schematic arrangement of sensor installation in PFBR (with primary sodium pump)
b Schematic of ECFM probe assembly in PFBR, shown in horizontal orientation

(b)
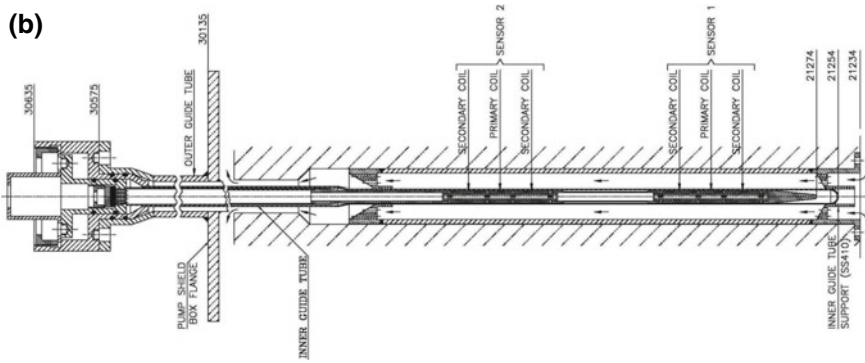
Fig. 3 (continued)

to create a test section for ECFS. The location is identified so as to obtain maximum sodium temperature of 525 °C. General assembly details of ECFM test section in SGTF is shown in Fig. 4. The experiment involves testing of sensor for different

Fig. 4 General assembly details of ECFM test section in SGTF
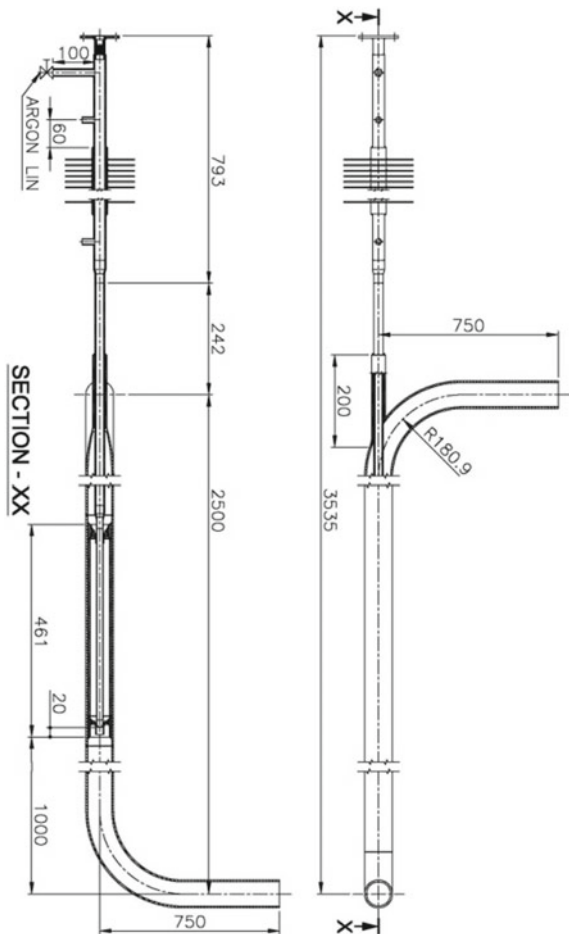
temperatures ranging from 250 to 525 °C in steps of 50 °C for sodium flow rates of static to 25 m³/h. through the test section. The test duration is around 50 days. The normal operating temperature of the sensor is 400 °C, which is below the creep temperature (425 °C) for the material of construction of the sensor. Hence, no separate creep test has been carried out.

3.2 Thermal Shock Testing

Thermal shock testing was carried out in Test pot-2 (TP-2) of Silverina sodium loop. TP-2 is a cylindrical vessel with approximately 400 mm diameter. The vessel is filled with sodium and heated to 525 °C using heaters. The ECFM assembly, with
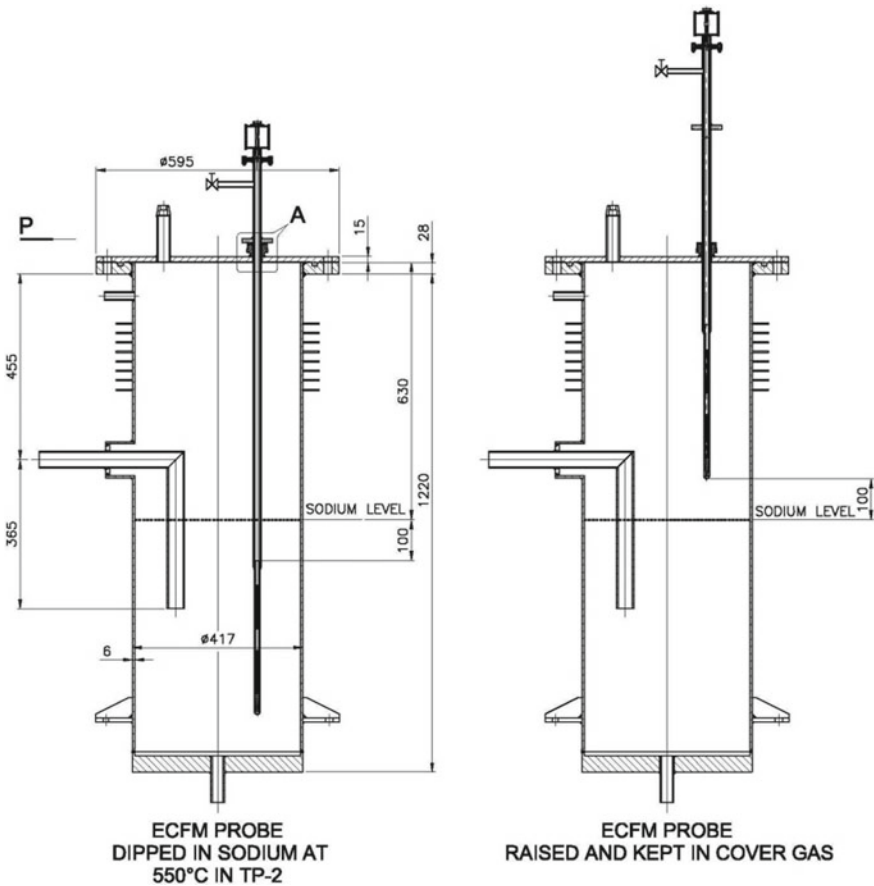
Fig. 5 Arrangement for testing of ECFM for thermal shocks

a thermocouple fixed to the bobbin, is inserted into TP-2, as shown in Fig. 5. Once the temperature of ECFM stabilizes at 525 °C, it is lifted to cover gas space and allowed to cool. As soon as the temperature reaches to 400 °C, it is plunged into the hot sodium subjecting to thermal shock.

The required number of thermal shocks to qualify the ECFM is arrived at based on the ASME guidelines [4]. These guidelines were originally prescribed for experimental fatigue qualification and were adapted to thermal shock loadings [5]. Accordingly, it is necessary to test a component for 4.6 times the operating cycles for structural qualification. Total number of demands for SGDHR in plant life is estimated to be 207; hence, total required thermal shocks are worked out to be 953. Creep–fatigue interaction is not considered in the present study.

3.3 Seismic Testing

The natural frequency analysis of the primary pump shows predominant mode at 9 Hz frequency [6]. This mode shows the primary sodium pump (PSP) shell to deform as simply supported beam supported at the top and at the bottom. The PSP being symmetric responds independently in each of the three orthogonal directions. In other words, it has very low cross coupling among all the axes. Hence, single axis test for the seismic qualification is proposed [7] with a specially designed support structure to simulate the PSP shell. Seismic excitations at the two support locations are extracted from the seismic analysis of reactor assembly. Out of the two horizontal excitations for each location, the excitation with higher peak acceleration is selected as the input time history for the qualification experiments.

Demonstration of structural integrity and functionality of ECFM after operation basis earthquake (OBE) is to ensure that it will not call for its replacement after OBE, while test for safe shutdown earthquake (SSE) is to ensure its structural integrity.

The experiments were carried out at the Advanced Seismic Testing and Research Laboratory (ASTaR) of Structural engineering Research Center (SERC), Chennai. Test model for seismic testing of ECFM has two components, namely, test support structure ($\sim$13 m), which simulates the primary pump shell and on 1:1 scale model of ECFM with inner guide tube. The mounting details are exactly simulated as in reactor. Figure 6 shows the test facility with test model mounted in position. The design of test support structure is carried out in such a way that the fundamental frequency of the structure matches with that of primary pump mode corresponding to 9 Hz. The input excitation is provided by two independent actuators connected at locations corresponding to the roof slab and grid plate of PFBR.

Fig. 6 SERC test facility with test model in position

Strain gages and accelerometers were pasted at different locations of the inner guide tube. Accelerometers are required to capture the dynamic properties of the structure and response during seismic excitation. Strain gages are required to measure the local strain on the components.

4   Results and Discussion

The following tests are carried out after in all the above experiments:

  (i) Visual examination of ECFM probe and inner guide tube to check for gross structural damage.
 (ii) Die penetrant inspection (DPI) was carried out on ECFM probe and inner guide tube to check for surface defects like porosity, cracks, etc.
(iii) Insertability of ECFM probe on inner guide tube and inner guide tube on test support structure.
 (iv) Measurement of insulation resistance IR and resistance values of individual coils.

ECFM is tested at 200, 250, 300, 400, 500, and 525°C as part of high-temperature testing. The ECFM has passed all the above tests and the performance of the ECFM is satisfactory before, during, and after testing.

ECFM has been subjected to 953 cycles of thermal shock loading. The obtained shock rate is ~12°C/s, which is higher than the desired value. The evaluations of temperature and ECFM signal during a typical shock are shown in Fig. 7. In this figure, SA1, SA2, SB1, and SB2 represent the output voltages of secondary coils. It can be seen that the temperature of the sensor rises, subjecting it to thermal shock, once it is plunged into the hot sodium from argon environment. Simultaneously,
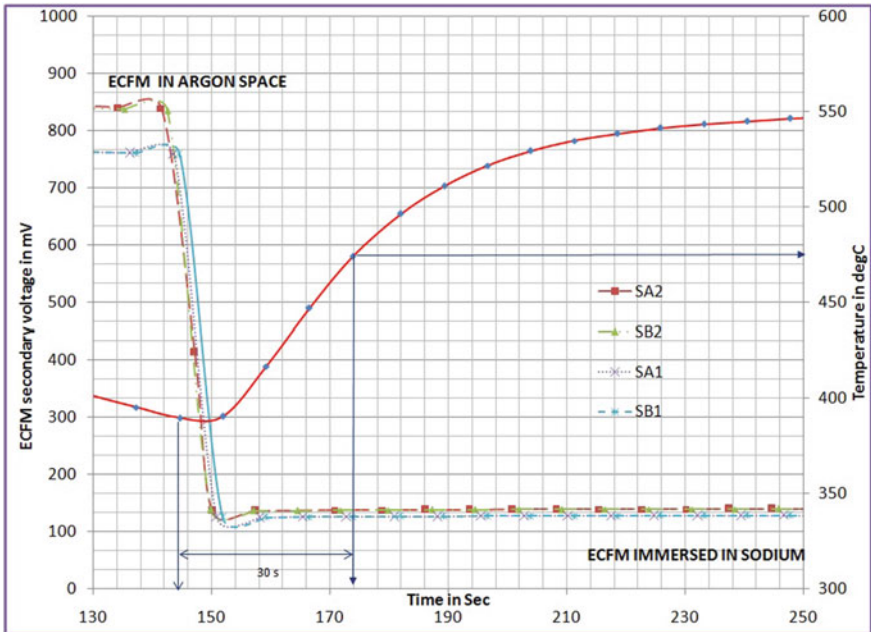
Fig. 7 Temperature and ECFM signal evolution during a thermal shock from 400 to 550 °C
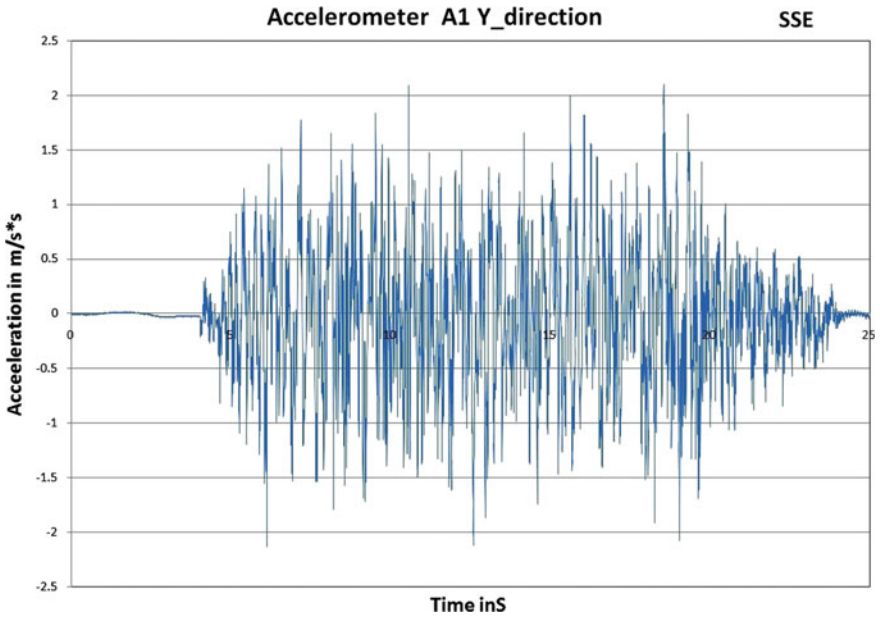
Fig. 8 Typical accelerometer reading during SSE
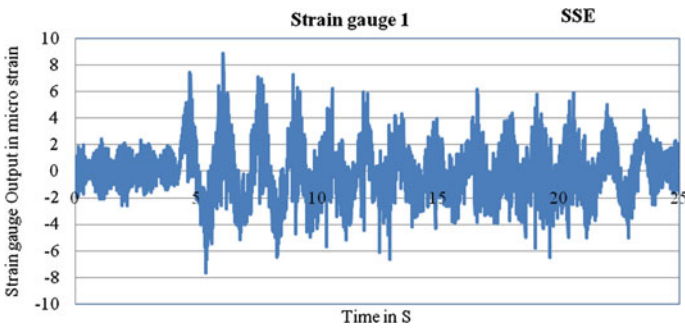
Fig. 9 Typical strain gage reading during SSE

the output voltage of secondary coils reduces. The outputs of sensors were stable and repeatable during all the 953 thermal shocks. The variation in output is less than 1%. All the components of ECFM probe are intact and no damage is noticed. IR values measured before commencing the experiment, during the experiment, and after completing the experiment have shown that the coils are healthy. The testing has qualified the ECFM for full design life of 40 years against thermal shocks, as per the ASME guidelines.

As part of seismic testing, totally 20 OBEs and 6 SSEs were carried out. Initially, trials are made to ensure the obtained response spectra match with the required response spectra. Typical accelerometer and strain gage readings recorded during SSE are shown in Figs. 8 and 9, respectively.

Salient observations of the seismic tests are given below:

- The insertion and removal of the ECFM were demonstrated after each OBE by mechanically lifting the ECFM from inner guide tube and inner guide along with ECFM probe from test supporting structure.
- Sensor coil healthiness was satisfactory and no degradation of IR and resistance values was noticed.
- DP inspection on inner guide tube and ECFM probe doesn't show any defects even after SSE.
- The maximum stress recorded was recorded during SSE and measured to be 3.33Mpa.
- Variation in ECFM sensor output during seismic excitations was insignificant.

With the above observations, it can be concluded that ECFM is qualified against design basis seismic loading.

5   Conclusion

The comprehensive test program to demonstrate the integrity of the ECFM against high-temperature sodium operation, thermal shocks, and seismic-induced loading has successfully met its goal. The demonstration against FIV is under progress. The tests demonstrated have enhanced our confidence in safe and reliable operation of ECFM and provided basis for obtaining regulatory clearance for ECFM.

References

1. A. Dohi, M. Oda, S. Iida, Development of an in-core flow meter for the LMFBR, in *International Conference on Liquid Metal Technology in Energy Production* (1976)
2. J. Brewer, R.A. Jaross, R.L. Brown, Eddycurrent probe-type sodium flow sensor for FFTF reactor fuel channel monitoring. IEEE Trans. Nucl. Sci. NS-**18**(1), 372 (1971)
3. V.A. Suresh Kumar, I.B. Noushad, K.K. Rajan, Steam generator test facility—A test bed for steam generators of Indian sodium cooled fast breeder reactors. Nucl. Eng. Des. **248**, 169–177 (2012)
4. *ASME Sec. III, Division 1, Appendices, Para II-1500* (2004)
5. S. Patri, R. Vijayashree, V. Rajan Babu, S. Suresh Kumar, S. Chandramouli, C. Meikandamurthy, V. Prakash, K. K. Rajan, G. Srinivasan, Experimental qualification of mechanical and electrical subsystems of a complex mechanism against fatigue failure. Trans. Indian Inst. Met. **69**(2), 549–554 (2016)

6. P. Chellapandi, et al., *Seismic analysis of Primary Sodium Pump*, PFBR/32110/DN/1074/R-A, Feb 2003 (Internal report)
7. IEEE 344 - 2004 recommended practice for seismic qualification of class 1E equipment for nuclear power generating stations

Seismic Performance of Nine-Story Self-centering Buckling-Restrained Braced Frames

Ahmad Fayeq Ghowsi and Dipti Ranjan Sahoo

Abstract Buckling-restrained braces (BRBs) are the special type of braces used in lateral force-resisting systems in structures located in high-seismic regions worldwide. The main advantages of BRBs are the symmetrical hysteretic response, high ductility, and excellent energy dissipation potential as compared to the conventional steel braces. Past studies have shown that the lack of re-centering capability of BRBs may result in the excessive post-earthquake residual displacement of the braced frame, which may not be cost-effective for repair and retrofit. To minimize the residual drift response of buckling-restrained braced frames (BRBFs), the self-centering mechanism should be fitted in braces. Such braces are termed as SC-BRBs. The shape memory alloy (SMA) rod which uses along with the BRB is relatively costly, to optimize the use of SMA rod along the BRB with effective re-centering capability is the aim of the present study. The evaluation of present study is focused on the seismic response of BRBFs with shape-memory-alloy-based SCBRBs under the near-field earthquake ground motions. A nine-story building has been considered for this numerical study. The present study frame is designed in accordance with current American seismic code (AISC 341 in Seismic provisions for structural steel buildings 341, [1]) and is modeled and analyzed using a computer software *OpenSees* (Mazzoni et al. in OpenSees command language manual, [2]). Forty near-field ground records are selected in the nonlinear dynamic analysis. The main parameters investigated are inter-story drift response and residual drift response with varying SMA uses. The analysis results for more use of SMA in the SC-BRBFs showed the better re-centering capability with marginally higher inter-story drift response.

Keywords Drift response · Buckling-restrained braces · Nonlinear modeling · Self-centering braces · Seismic analysis

A. F. Ghowsi (✉) · D. R. Sahoo
Department of Civil Engineering, Indian Institute of Technology Delhi,
New Delhi 110016, India
e-mail: faieq.ghowsi@gmail.com

1   Introduction

Buckling-restrained braces (BRBs) capable of exhibiting the symmetrical hysteretic behavior, the higher energy dissipation, and brace ductility are preferred in structural systems to the conventional steel brace systems (CBFs). Past studies, e.g., [3, 4] have shown that the lack of re-centering capability of BRBs may result in the excessive post-earthquake residual displacement of the braced frame, which may not be cost-effective for repair and retrofitting [5–7]. In order to minimize this effect, some modifications may be carried out in the development of BRBs so as to develop self-centering BRB (SC-BRB) systems which can provide the re-centering capability to the buckling-restrained braced frames (BRBFs) [8, 9].

The application and using post-tensioned (PT) on the structure for the purpose of self-centering capability have been proved to effectively control residual drift of on the structure [10–14]. A self-centering energy dissipative (SCED) brace using friction devices and a dual-tube self-centering with aramid-fiber PT tendons have been recently developed [5, 15]. A lightweight dual-tube SC-BRB, in which the BFRP, was adopted as pretension tendons material and the quasi-static experiments for three specimens were conducted by [16, 17]. The rocking behavior systems also developed for the purpose of self-centering capability by using pretension tendons along the height of the building. However, the energy dissipated device provided on base column for the purpose of dissipating energy of the system [18].

Reference [19] conducted a finite element analysis of dual-tube SC-BRB with composite tendons using polymer pretension. Reference [20] carried out a numerical study to evaluate the design parameters of SC-BRB using a rheological model. The present study is focused on the evaluation of seismic performance of a nine-story steel building with self-centering BRB. Shape memory alloy (SMA) rods are used along with BRB core segments to provide the self-centering capacity. The main goal is to verify the self-centering capabilities of BRBs in controlling the residual drift and inter-story drift response of BRBFs by varying the parameters of BRB core and SMA rod ratio for the same brace lengths. SC-BRBFs are modeled and analyzed using an open-source software *OpenSees* [2]. The main parameters investigated are the time-history drift response, inter-story drift, and residual drift response of the study frames.

2   Concept of SC-BRB

Self-centering BRB (SC-BRB) consists of a BRB brace used for dissipating energy and ductility. SMA rods add the self-centering capability to the brace. Rigid segments along the SMA rod are included to limit the length of SMA based on requirement. Outer and inner tubes are used to keep the SMA and rigid rod under tension all the time irrespective of the shortening and elongation of BRBs under the cyclic loading. Figure 1 shows the different components of a SC-BRB system.
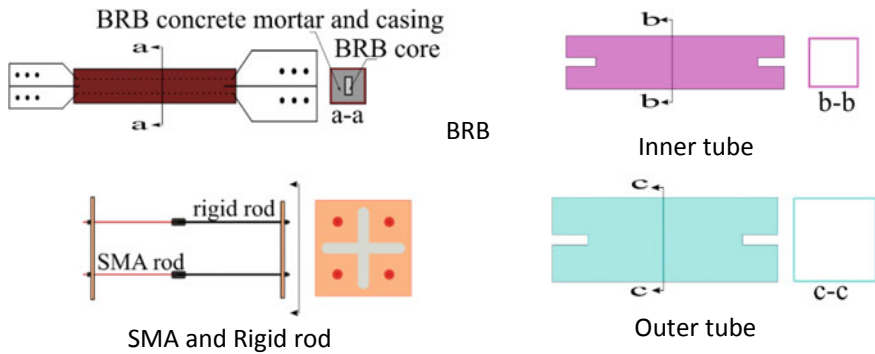
Fig. 1 Different components of SC-BRB system

Figure 2 describes the SC-BRB, the core component of SC-BRB, and two additional tubes covering the BRB. BRBs under cyclic loading work independently as the conventional BRB. Additional tubes are welded to the end elastic segments of BRB and carry the load from rods through the floating plates over the end elastic zones. The floating plates are connected through rods under pretention and unbounded with elastic zone of BRB ends.

Figure 2a shows the SC-BRB at the neutral position under no demand with pre-stress in the rods. The cruciform end zone has been catted in the movable plates to cross the cruciform end zone of the plate through the plate, as shown in Fig. 2b the compressive and tension loading in the SC-BRB, the movable plates, outer, and inner plates takes place as described in Fig. 2c, the SMA rod is going under tensile stress, either the assembly is under elongation or shortening. The gap between movable plate and outer/inner tubes is zero while brace is under zero loading, and there would be some gap is the BRB core is either shortening or elongation.
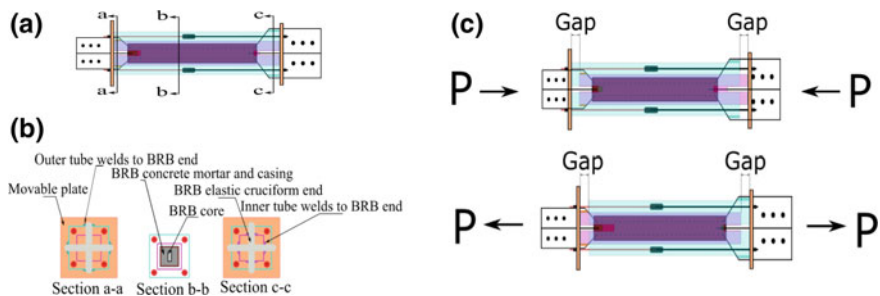
Fig. 2 A Typical SC-BRB assembly

3 Details of Study Building

The second generation of SAC steel projects building of nine-story benchmark buildings has been considered in this study. This building is assumed to exist in Los Angeles, California, for the medium-rise building. This design is actually not used in construction and it has been designed for the purpose of seismic code evaluation for low-, medium-, and high-rise buildings in Los Angeles, California region. The building is redesigned for BRBF and SC-BRBF by considering same gravity loading as well as seismic loading condition. The width of nine-story building is 45.73 m with five bay of each 9.15 m center to center and length of 45.73 m with five bay of each 9.15 m center to center, and height of the building is 37.19 m. Each floor height is 5.49 m at the first floor and 3.96 m above the first floor. Beam-to-column connections are considered as non-moment resisting in all floors. All column bases are considered as perfectly fixed. Figure 3 shows the plan and elevation of the building considered in this study. Material yield strength is considered 345 MPa for beams and columns in the design. The designed section details for BRB as well as SC-BRB are summarized in Table 1.

As the preliminary design, the design axial strength of BRB can be expressed as follows:

$$p_{u-BRB} = \phi p_{yBRB} \tag{1}$$

where P_{yBRB}= yield strength of BRB core. The ultimate strength of SC-BRB is given by Eqs. 2 and 3.

$$p_{u-SC-BRB} = \phi p_{yBRB} + \phi p_{i-SMA} \tag{2}$$

$$p_{u-SC-BRB} = 0.9 F_{ysc} A_{core} + 0.9 F_{i-SMA} A_{SMA} \tag{3}$$

where F_{ysc} = yield strength of steel BRB core, F_{i-SMA}= initial pre-stress in the SMA, A_{core} = area of BRB steel core, and A_{SMA}= area of SMA bar.
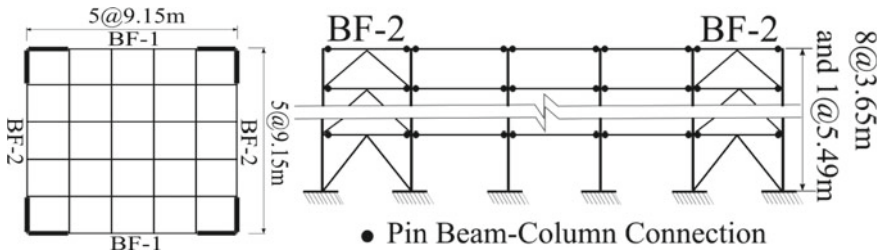
Fig. 3 Plan and elevation view of the study building

Table 1 Design details of nine-story SC-BRB

Story Level	BRB	SC-BRB		Columns	Braced bay columns	Beams	Braced bay beams
		(BRB) 24.5%	SMA (75.5%)				
	Area (mm^2)	Area (mm^2)	Area (mm^2)				
9	689.4	168.9	520.5	W10X100	W14X283	W10X68	W12X96
8	1238.6	303.5	935.2	W10X100	W14X283	W10X68	W12X96
7	1704.3	417.5	1286.7	W10X100	W14X283	W10X68	W12X96
6	2089.6	511.9	1577.6	W14X82	W14X455	W10X77	W12X106
5	2398.3	587.6	1810.7	W14X82	W14X455	W10X77	W12X106
4	2634.6	645.5	1989.1	W14X82	W14X455	W10X77	W12X106
3	2803.3	686.8	2116.5	W10X112	W14X500	W12X79	W12X120
2	2910.3	713.0	2197.3	W10X112	W14X500	W12X79	W12X120
1	3501.0	857.7	2643.3	W10X112	W14X500	W12X79	W12X120

4 Analytical Modeling

A nonlinear modeling has been developed in *OpenSees* [2] software. Beams and columns of the frame are modeled as nonlinear beam–column elements. Nonlinear plastic hinges are considered at each end of members and distributed plasticity considered within the entire beam and column elements. The SC-BRB parts have been individually modeled and validated with the experimental results of a past study by [9]. Stress–strain behavior of SMA rod material is validated with the coupon test result. The force-based beam–column element is selected for BRB core with fiber section, and higher moment of inertia has been assigned to the section to prevent from the buckling. A hysteretic material selected from the *OpenSees* library for the BRB element and the plastic cyclic hardening in tension and compression has been adjusted with the hysteretic material. The material degradation is also considered on the brace, after reaching maximum tensile strain. For considering the degradation after the fracture within the brace element, a hysteretic material selected for BRB element and validated with the experimental result. An assembly of SC-BRB has been developed by combining individual element in parallel. The nonlinear force-deformation behavior of SC-BRB assembly is adjusted to match the hysteretic behavior of SC-BRB.

The numerical model of SMA material was first developed by [21] not considering the residual strain. For the unloading, the reverse slope was considered to be parallel to the loading slope. Later, this material model was modified by [8] The parameters used in this material are shown in Fig. 4a, which considered modulus of elasticity on austenite phase, (E_{SMA}), yield stress (F_{SAS}), austenite slope (R_S), the ultimate slope in austenite (R_m), and similar variables for negative loading regions. Figure 4b shows the comparison of predicted stress–strain and force-deformation response of SMA coupons with test results. SMA coupons are of 21.6 mm in
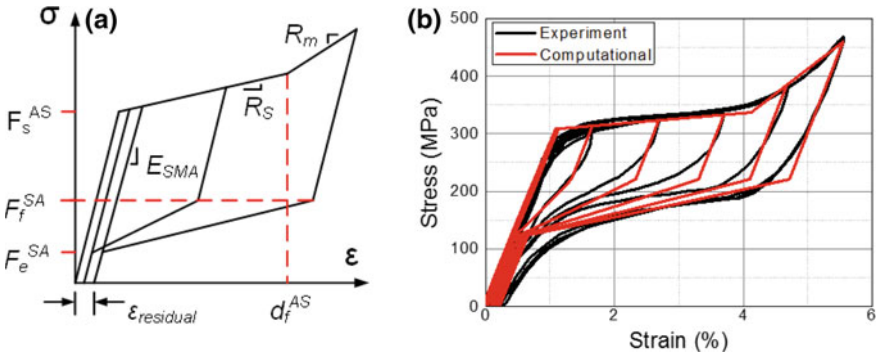
Fig. 4 **a** Modified material model used in this study **b** SMA coupons validation

diameter and of 122 mm in gage length. The numerical models successfully predicted with less than 10% stress error and better matched than the previous material which has been written by [21] for the material response of SMA rods.

Figure 5a shows the comparison of the force–strain response of SMA rods used in SC-BRB specimen. The outer and inner tubes have been used over the BRB to keep the SMA rod under pretension and preventing the BRB from SMA pretension demand. The movable plates are kept in contact on both ends of outer and inner tubes. The SMA rods are connected from one end to other in between outer and inner tubes. The material for outer and inner tubes are selected as in HSS standard section. The SMA rod properties of E_{SMA}, F_{sAs}, Rs, and Rm for SMA are assumed as 28,650 MPa, 308 MPa, 3.3%E_{SMA}, and 20%E_{SMA}, respectively. The results of the numerical study for SMA rods of SC-BRB specimen well matched by less than 10% error with the experimental results. The numerical modeling diagram of SC-BRB assembly is shown in Fig. 6. Individually elements are modeled and the appropriate section and material have been assigned for each element. BRB core is
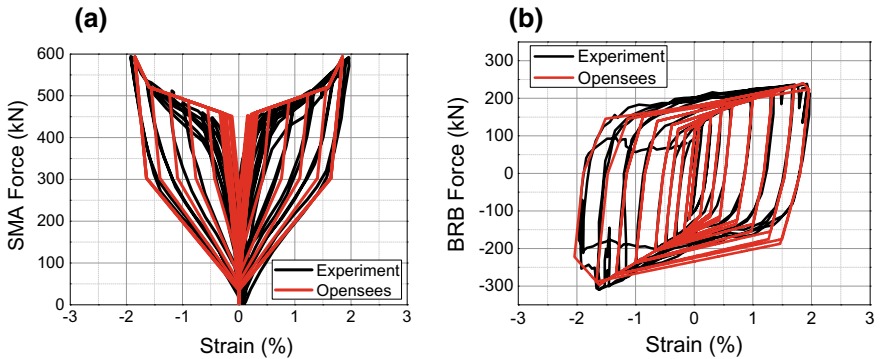
Fig. 5 Validation of numerical models with experimental results **a** SMA within SC-BRB **b** BRB within SC-BRB
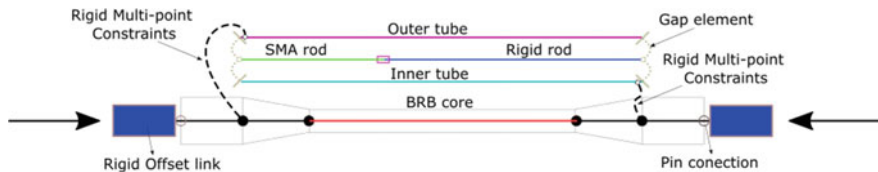
Fig. 6 Numerical modeling of SC-BRB assembly

modeled as displacement beam–column element with fiber sections with the higher moment of inertia to preventing the element from buckling, and the hysteretic material is selected from *OpenSees* library to capture the hardening parts on both tension and compression as well as the degradation after reaching to maximum ductility. Hysteretic result validation with experimental is shown in Fig. 5b.

The outer and inner tubes are modeled as an elastic beam–column element, the tubes connected to the BRB's elastic end zones through the rigid link zero length element in one end and unconnected in another end. The rigid rod used as an elastic element along the SMA rod, to minimize the use of SMA in length as per design requirement. Since there is no perfect material in *OpenSees* library to match with the real experimental result with less than 10% stress error, a UMAT code has been developed and implemented in the *OpenSees* suspended library. Figure 5a represents the loading/unloading response of SMA rod in SC-BRB assembly. The gap between outer/inner tubes and movable plates modeled as zero link element. The material for the gap element is selected as an elastic compression and small force for tension, to represent the gap behavior. Since the maximum ductility is very high in SMA, the overall degradation on the SC-BRB assembly is obtained from the BRB element.

Figure 7 shows the validation of SC-BRB assembly with experimental findings. The result showed a very well match between the numerical modeling and experimental result with less than 10% stress error indicating its capability of

Fig. 7 Numerical validation of SC-BRB assembly
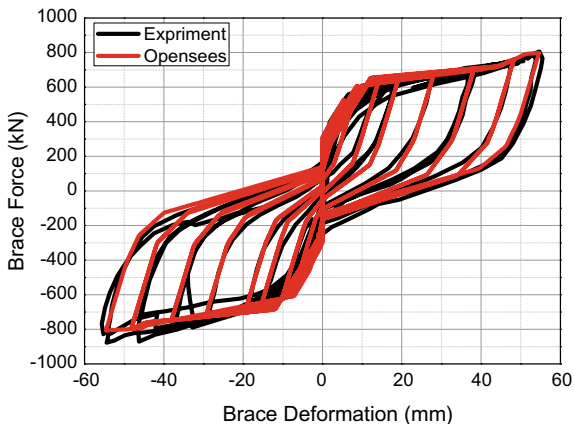
capturing perfectly loading and unloading as well as degradation. Thus, the numerical model for the combined assembly of SC-BRB can be extended for large-scale SC-BRB to validate with the experimental result.

5   Selection of Ground Motions

Nonlinear dynamic analyze is carried out for this study frame, for a set of ground motion developed by Somerville et al. [22] for SAC projects. This set consists of 20 ground motions with two-component near-fault time-history ground motions, the first suite of ten two-component (NF01-20) acceleration time histories are derived from the historical recordings, whereas the second set of ten two-component (NF21-40) time histories are developed from the physical simulations of fault rupture and seismic wave propagation through soil strata. The individual components of each ground motion are rotated 45° away from the fault-normal and fault-parallel orientations. These 40 ground motions represent different fault mechanisms in the magnitude range of 6.75–7.5 with a source-to-site distance varying from 0 to 18 km. These ground motions form a set that provides a reasonable representation of the median and variability of the ground motions that a given site may experience from a nearby earthquake of magnitude 7.0 at a distance about 5 km. This magnitude–distance pair controls the 10% in 50-year ground motions in many regions of California, USA [22]. Figure 8 shows the response spectra of all the selected near-fault ground motions selected in the previous study, the NF23 has been selected for this building time-history analysis. This NF23 ground motion has appeared to be critical for the study frame in past research by [4]. The scale factor multiplied to scale down the earthquake on the bases of average NF response spectrum to the design response spectrum, and the time period of the design frame is 1.18 s. The designed spectral acceleration for building location is based on 5% damping.

Fig. 8 Comparison of response spectrum of near-fault ground motion
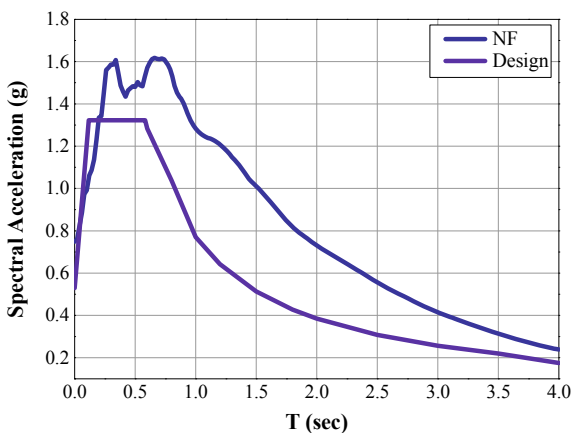
6   Analysis Results

Numerical model is validated by comparing the brace force-deformation response and SMA force–strain response measured in the past experiment. In this study, the ratio of using SMA rods is varied in the range of 0–100% of SMA rod. The varying detail of SC-BRB, the ratio varied based on preliminary design, as shown in Table 2. The zero percentage of SMA is indicated that no SMA used along the BRB braces, and it is only BRB frame. 100% of SMA is indicated that the brace is used only SMA, and no contribution of BRBs in the frame. The SC-BRB is designed as such that total strength will remain same while changing the ratio of SMA in SC-BRB.

SMA material is the most appropriate material which is significantly reducing the residual drift in the structure [23]. Unlikely, less energy can be dissipating. The BRBFs is having the most significant energy dissipation, unlikely, high residual drift is in these devices [24] noted as disadvantages in the BRBFs systems. To optimize the ratio of SMA rod in SC-BRB with minimum inter-story drift and achieving the maximum reduction of residual drift, the time-history analysis carried out with varying the ratio of SMA in SC-BRB.

Figure 9a–f shows the history drift of each floor under each ratio of SMA rod. In Fig. 9a with non-SMA, i.e., only BRB is used in the structure, the result showed a permanent drift at each floor after a peak drift. A drastic change in Fig. 9b time-history drift response in each story level while using 20% of SMA. Figure 9c–e shows that as the use of SMA is increasing, the peak drift is changing, most likely the drift close to zero while crossing the positive and negative peaks. In Fig. 9f while using 100% of SMA, the structure is likely to experience permanent drift after the extreme peak drift of the structure. Even though the SMA is 100% as SMA brace used with no BRB contribution, the maximum inter-story drift seems in this types of braces this indicates the probable failure of the beam and column elements.

Figure 10 shows the inter-story and residual story drift ratio variation at all story levels of SC-BRBF. The results showed a maximum inter-story drift of 3% at third story level of BRBF with zero percent of SMA, in which it causes 0.83% residual drift. For other cases of using SMA 20–100%, the inter-story drift increases as much as SMA% increases. Overall, the maximum inter-story drift is remaining same up to third floor for the SMA with ratio of 0–80%, third to sixth floor for the SMA with ratio of 20–80%, and relatively increasing inter-story drift with increasing SMA contributions from sixth to ninth floor level. The inter-story drift increasing significantly in 100% use of SMA; in other words, the SMA rod is acting to be as brace. Since there is the SMA rod is as ductile devices with less energy dissipation capability can significantly increase the inter-story drift of the structures. The residual drift of the structured shown in Fig. 10b can significantly reduce by increasing the SMA contributions in SC-BRB. BRB with 0% of SMA can significantly reduce the residual drift by adding 20% of SMA in SC-BRBFs. The SC-BRB with 40% of SMA contributions can reduce the residual drift of the structure close to the zero. The residual drift of SMA brace with no contributions of

Table 2 SMA ratio in SC-BRB assembly

Story level	Without SMA	20%SMA		40%SMA		60%SMA		80%SMA		100%SMA	
	BRB (mm^2)	BRB (mm^2)	SMA (mm^2)	BRB (mm^2)	SMA (mm^2)	BRB (mm^2)	SMA (mm^2)	BRB (mm^2)	SMA (mm^2)	BRB (mm^2)	SMA (mm^2)
9	71267	57013	14253	42760	28506	28506	42760	14253	57013	0.0001	71267
8	128048	102439	25609	76829	51219	51219	76829	25609	102439	0.0001	128048
7	176183	140946	35236	105709	70473	70473	105709	35236	140946	0.0001	176183
6	216015	172812	43203	129609	86406	86406	129609	43203	172812	0.0001	216015
5	247930	198344	49586	148758	99172	99172	148758	49586	198344	0.0001	247930
4	272359	217887	54471	163415	108943	108943	163415	54471	217887	0.0001	272359
3	289803	231842	57960	173882	115921	115921	173882	57960	231842	0.0001	289803
2	300864	240691	60172	180518	120345	120345	180518	60172	240691	0.0001	300864
1	306608	245286	61321	183965	122643	122643	183965	61321	245286	0.0001	306608
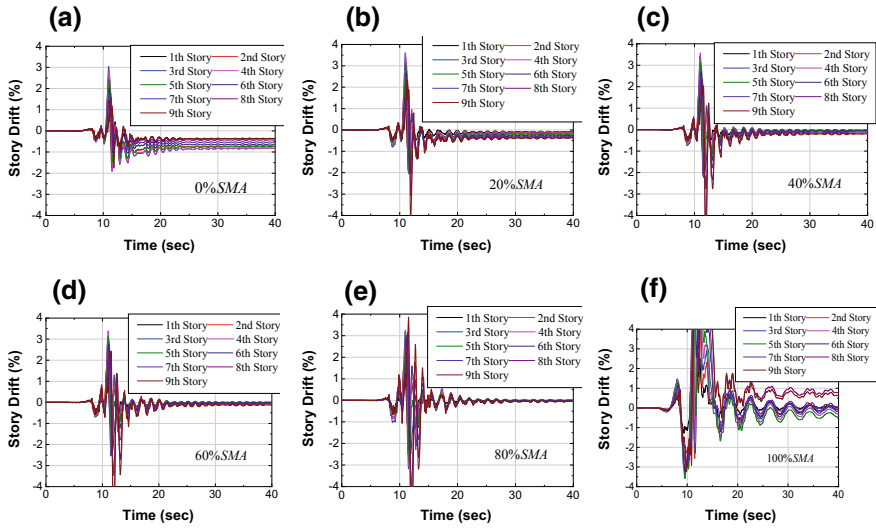
Fig. 9 Time-history drift response SC-BRBFs under NF23 ground motion
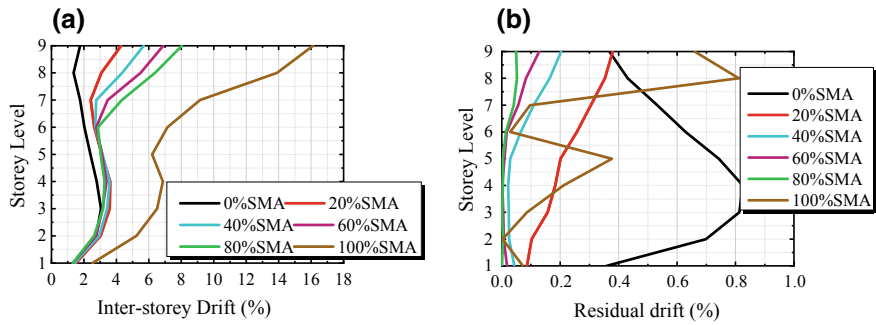
Fig. 10 **a** ISDR; and **b** RDR response of BRBFs under NF23 ground motion

BRBs is increased significantly, and this is due to significant drift on the frame which induced inelasticity and degradation on the beams and columns elements.

The comparative study of inter-story drift and residual drift has provided interesting results in which we can visualize the optimum SMA contribution and it can be cost-effective as well. The frame is designed based on first mode lateral load distributions. Since the inter-story drift is relatively higher on the sixth to ninth floor level on SC-BRB frame, either the SMA ratio has to be considered according to the floor level or the response spectra analysis is required to consider higher mode for the design of SC-BRB frame.

7 Conclusions

Based on this numerical study, the following conclusions can be drawn from this study:

- Using SMA in BRB frame caused a drastic change in time-history drift response and reduced the residual drift response.
- Using higher percentage of SMA may increase the peak inter-story drift response, which can the cause of failure in non-structural elements of the building.
- The increased peak drift response can cause damage in beam and column element of the structure. Thus, an optimum ratio of SMA to BRB is required to get the controlled drift response and better ductility of frame.
- Increase in the ratio of SMA in SC-BRB can reduce the energy dissipation due to flag shape of SC-BRB and at the same time, it is reducing the residual drift response due to nearly zero strain at zero loading. The energy due to earthquake has to dissipate on the building through the ductile element, to dissipate the same value energy with most like flag shape of SMA type, and it needed higher ductility on the brace to dissipate the same energy.

References

1. AISC 341, Seismic provisions for structural steel buildings AISC 341–10. *AISC 341* (2010)
2. S. Mazzoni, F. McKenna, M.H. Scott, G.L. Fenves, OpenSees command language manual (2006)
3. P.W. Clark, I.D. Aiken, K. Kasai, I. Kimura, Large-scale testing of steel unbonded braces for energy dissipation. Adv. Technol. Struct. Eng. 1–5 (American Society of Civil Engineers, 2000). https://doi.org/10.1061/40492(2000)12
4. A.F. Ghowsi, D.R. Sahoo, Performance of medium-rise buckling-restrained braced frame under near field earthquakes. in *Advances in Structural Engineering: Dynamics, Volume Two* (2015). https://doi.org/10.1007/978-81-322-2193-7_66
5. C. Christopoulos, R. Tremblay, H. Kim, M. Lacerte, Self-centering energy dissipative bracing system for the seismic resistance of structures. 96–107 (2008)
6. M. Dolce, D. Cardone, Theoretical and experimental studies for the application of shape memory alloys in civil engineering. J. Eng. Mater. Technol. **128**, 302 (2006)
7. S. Chao, M. Asce, N.B. Karki, A M. Asce, D.R. Sahoo, Seismic behavior of steel buildings with hybrid braced frames. J. Struct. Eng. **139,** 1019–1032 (2013)
8. M.R. Eatherton, L.A. Fahnestock, D.J. Miller, Self-centering buckling restrained brace development and application for seismic response mitigation. NCEE 2014 - 10th U.S. Natl. Conf. Earthq. Eng. Front. Earthq. Eng. (2014). https://doi.org/10.4231/d3hm52k7q
9. D.J. Miller, L.A. Fahnestock, M.R. Eatherton, Development and experimental validation of a nickel–titanium shape memory alloy self-centering buckling-restrained brace. Eng. Struct. **40,** 288–298 (2012)
10. M.J.N. Priestley, S. Sritharan, J.R. Conley, S. Stefano Pampanin, Preliminary results and conclusions from the PRESSS five-story precast concrete test building. PCI J. (1999). https://doi.org/10.15554/pcij.11011999.42.67

11. J.M. Ricles, R. Sause, M.M. Garlock, C. Zhao, Posttensioned seismic-resistant connections for steel frames. J. Struct. Eng. **127**, 113–121 (2001)
12. C. Christopoulos, A. Filiatrault, C. Uang, B. Folz, Posttensioned energy dissipating connections for moment-resisting steel frames. J. Struct. Eng. **128**, 1111–1120 (2002)
13. M.M. Garlock, J.M. Ricles, R. Sause, M. Asce, Experimental studies of full-scale posttensioned steel connections. 438–448 (2005)
14. H. Kim, C. Christopoulos, Friction damped posttensioned self-centering steel moment-resisting frames. J. Struct. Eng. **134**, 1768–1779 (2008)
15. J. Erochko, C. Christopoulos, R. Tremblay, Design and testing of an enhanced-elongation telescoping self-centering energy-dissipative brace. J. Struct. Eng. **141**, 04014163 (2015)
16. Z. Zhou, X.T. He, J. Wu, C.L. Wang, S.P. Meng, Development of a novel self-centering buckling-restrained brace with BFRP composite tendons. Steel Compos. Struct. **16**, 491–506 (2014)
17. Z. Zhou, Q. Xie, X.C. Lei, X.T. He, S.P. Meng, Experimental investigation of the hysteretic performance of dual-tube self-centering buckling-restrained braces with composite tendons. J. Compos. Constr. **19**, 04015011 (2015)
18. M.R. Eatherton et al., Design concepts for controlled rocking of self-centering steel-braced frames. J. Struct. Eng. **140**, 04014082 (2014)
19. Q. Xie, Z. Zhou, J.-H. Huang, S.-P. Meng, Influence of tube length tolerance on seismic responses of multi-storey buildings with dual-tube self-centering buckling-restrained braces. Eng. Struct. **116**, 26–39 (2016)
20. Z. Zhou, Q. Xie, S.P. Meng, W.Y. Wang, X.T. He, Hysteretic performance analysis of self-centering buckling restrained braces using a rheological model. J. Eng. Mech. **142**, 04016032 (2016)
21. B. Taftali, Probabilistic seismic demand assessment of steel frames with shape memory alloy connections. Ph.D. Dissertation, Georgia Institute of Technology, 2007
22. P.G. Somerville, N.F. Smith, R.W. Graves, N.A. Abrahamson, Modification of empirical strong ground motion attenuation relations to include the amplitude and duration effects of rupture directivity. Seismol. Res. Lett. **68**, 199–222 (1997)
23. A. Kari, M. Ghassemieh, S.A. Abolmaali, A new dual bracing system for improving the seismic behavior of steel structures. Smart Mater. Struct. **20**, 125020 (2011)
24. A.F. Ghowsi, D.R. Sahoo, Seismic performance of buckling-restrained braced frames with varying beam-column connections. Int. J. Steel Struct. **13** (2013)

Numerical Study on the Structural Integrity of Built-up Cold-Formed Steel Battened Columns

M. Adil Dar, Dipti Ranjan Sahoo and Arvind K. Jain

Abstract This paper presents the nonlinear behavior of cold-formed steel (CFS) built-up battened columns formed by connecting two channel sections toe to toe with pin-ended support conditions. Concentric axial load was applied at the loading end. The finite element model was developed using ABAQUS software, and was later validated against the test results available in the literature. A parametric study was conducted by varying the overall column slenderness and the toe-to-toe spacing. Numerical investigation on the structural integrity of such a built-up CFS column configuration was the main objective of this study. The North American Specifications (NAS) for cold-formed steel structures were used to quantify the design strengths of these built-up columns, and were later compared with the results obtained from the numerical study. This design strength predictions using NAS matched well with the numerical study results except for short columns.

Keywords Built-up column · Batten plates · Finite element analysis · Cold-formed steel

List of Symbols

CFS	Cold-formed steel
F	Flexural buckling
F + L	Combined local and flexural buckling
L	Local buckling
P_{FEA}	Ultimate FEA predicted strength
P_{NAS}	Design strength predicted by AISI-S100
P_{Exp}	Ultimate test strength
DSM	Direct strength method
EWM	Effective width method
MPC	Multi-point constraint

M. A. Dar (✉) · D. R. Sahoo · A. K. Jain
Department of Civil Engineering, IIT Delhi, New Delhi 110016, India
e-mail: dar.adil89@gmail.com

FEA   Finite element analysis
$(l/r)_{unbr}$ Unbraced chord slenderness
(l/r) Overall column slenderness

1   Introduction

The construction of cold-formed steel (CFS) structures has been rising since the last decade, mainly due to its faster cost-effective construction features. Innovative sectional profiles and stiffening arrangements for CFS sections have successfully contributed in delaying/eliminating various modes of premature buckling, thus considerably improving their load-carrying capacities as well as stiffness characteristics [5]. Properly designed CFS sections have the capability to reach their plastic moment capacity [9]. Selective partial stiffening of CFS sections fetches higher strength to weight ratio [6]. With easy fabrication and better economy, properly designed CFS timber composite sections perform better than conventional CFS sections [7]. High axial force demands often lead to the use of built-up members. The past studies on CFS built-up columns have focused on investigating the effect of numerous parameters like sectional compactness, column slenderness ratio, effect of spacers on the ultimate strength, etc. Vijayanand and Anbarasu [11] studied the influence of spacers on the behavior of CFS built-up columns composed of lipped channel sections. Overall slenderness, depth, and the number of spacers were the parameters that were varied. When the slenderness ratio increased, it was observed that the corresponding loads dropped. The ultimate strength of the built-up columns predicted by using DSM and EWM was conservative. From the failure modes, it was seen that for lower slenderness ratio, the proportions are un-conservative for the built-up battened columns which fail mainly by local buckling and conservative for columns which fail by elastic flexural buckling in case of higher slenderness ratio. Dabaon et al. [4] performed tests on battened CFS built-up columns comprising of two channels connected back to back at a varied spacing with pin-ended support condition. The strength obtained from the tests was compared against the design strengths predicted by North American Specification, Australian/New Zealand Standard, and European Code for cold-formed steel structures. It was confirmed that these specifications were un-conservative for the built-up battened columns failing mainly by local buckling, while the specifications were conservative for the built-up columns failing mainly by elastic flexural buckling. With the increase in channel spacing from 25 to 50 mm, the column slenderness dropped and collapse mechanism was driven by combined flexural and local buckling failure modes. By further increase in channel spacing from 50 to 75 mm, failure was dominated by local buckling. Anbarasu et al. [3] carried out an investigation to study the behavior of CFS web stiffened built-up battened columns. The column slenderness was varied from 30 to 120. The column strength

predictions calculated using DSM-1 were found to be conservative and this trend intensified in columns with higher slenderness ratio. Use of modified slender ratio in DSM-2 produced un-conservative results for built-up columns. The relationship between ultimate strength and column slenderness ratio was inversely proportional. Intermediate stiffening of the web eliminated the local buckling completely. Dar et al. [8] conducted an experimental study on CFS built-up laced columns and their results proved that built-up CFS columns (when designed properly) have potential to produce higher compression members with higher strength and desirable modes of failure.

Due to lack of research on built-up battened columns composed of channel sections connected toe to toe, there is a need to carry out an investigation on the same to study its behavior under axial loading. There are various parameters that affect the behavior of a battened built-up column like sectional compactness, column slenderness, the ratio of unbraced chord slenderness to the column slenderness, etc. The upper limit on the ratio of unbraced chord slenderness to the column slenderness for built-up CFS columns specified by the North American Specifications [2] is 0.5.

Accordingly, in this paper, the effect of variation in the ratio of unbraced chord slenderness to the column slenderness on the behavior of battened built-up CFS columns has been studied. A total of 46 finite element analyses were carried out on battened built-up columns with varying overall slenderness ratio and toe-to-toe spacing. The design strengths of these built-up columns were quantified by using North American Specifications [2] and compared with the results obtained from the numerical study.

2 Finite Element Modeling and Validation

2.1 Finite Element Modeling

For simulating the behavior of CFS built-up battened columns tested by [4], ABAQUS 6.14 [1] was used for developing the numerical models. Both the local and global buckling modes were suitably considered during numerical modeling. S4R5-type shell element was adopted for the modeling of built-up columns. The length of the channel section is 2210, width of the flange is 30 mm, depth of the web is 100 mm, and thickness of the section as 2 mm. Mesh convergence studies were conducted for better results. The size of mesh was 10×10 mm^2. The type of material model adopted was elastic perfectly. The Young's modulus (E) and the yield stress (f_y) adopted for CFS were 2×10^5 MPa and 450 MPa, respectively. Pin-ended support condition was simulated by restricting both rotation and translations in the relevant directions at both ends. Multi-Point Constraints (MPCs) were located at the geometric centroid of the cross section and were used for the application of these boundary conditions. The axial loading was applied in terms of

an axial displacement at the master node at the column's loaded end. For modeling the fasteners, mesh independent fastener option that is available in ABAQUS was used. To incorporate the geometric imperfections in the nonlinear analysis, eigen buckling analysis was conducted. The recommendation of Schafer and Pekoz [10], i.e., $0.006 \times w \times t$. was adopted for local imperfections. In addition, the global imperfection of 1/500 of the column height at its mid-height was taken to start the nonlinear analyses.

2.2 Validation

The test results presented by Dabaon et al. [4] were used to validate the finite element model developed. All the five specimens were modeled and analyzed. The results of FEA are compared with the test results as shown in Table 1. Figure 1 shows the comparison of load *versus* displacement response for specimen B2B25-300. Furthermore, Table 1 indicates that the FE models matched well with the experimental results, and hence the model can be confidently used for parametric studies.

Table 1 Comparison of FEA and test results

Model	P_{Exp} (kN)	P_{FEA}(kN)	P_{Exp}/P_{FEA}
B2B25-300	109.9	106.7	1.03
B2B50-300	119.1	122.5	0.97
B2B75-300	125.3	122.4	1.02
B2B50-150	133.1	131.6	1.01
B2B50-400	112.3	108.9	1.03

Fig. 1 Comparison of load versus displacement response for specimen B2B25-300
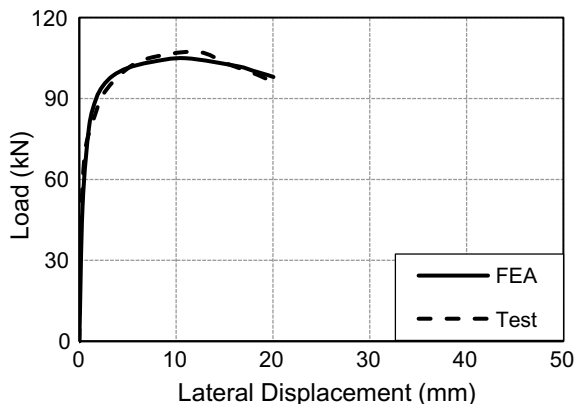
Fig. 2 Section details of the
built-up column
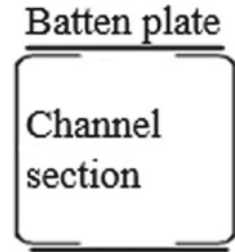
3   Sectional Details

Two plain channel sections were connected toe to toe with batten plates to construct
the cross section of the built-up column as shown in Fig. 2. The depth of the web
and the width of the flange of the individual channel section are 100 mm and
30 mm, respectively. The thickness of the channel section and the batten plate is
2 mm and 6 mm, respectively. The depths of end batten and intermediate batten are
150 mm and 100 mm, respectively. The clear spacing between the battens is
300 mm.

4   Parametric Study

The parametric study constituted of 33 pin-ended built-up CFS columns being
analyzed both numerically and theoretically. The slenderness ratio of the built-up
column was varied from 20 to 175 and the toe-to-toe spacing from 0 to 40 mm as
mentioned in Table 2. Design strengths were quantified using North American
Specifications for cold-formed steel structures [2] and later compared with the FEA
predicted strengths shown in Table 2. The specimens were labeled such that
channel arrangement, toe-to-toe spacing, and height of the column. For example,
the label "T2T-20-600" defines the following. T2T indicates that channels are
connected toe to toe, 20 indicates 20 mm spacing is provided between the channels
and 600 indicates the height of the column is 600 mm. Table 2 and Fig. 3 sum-
marize and compare the FEA predicted strengths and design strengths predicted by
North American Specifications for cold-formed steel structures, respectively, [2].
Figure 3 shows that AISI-S100 design strength predictions for the columns failing
by elastic flexural buckling match well with the FEM results but the same standard
predicts the design strength un-conservatively for the short built-up columns failing
predominantly by local buckling. The ultimate capacity of the columns reduced
with the increase in column slenderness and the same increased with the increase in
toe-to-toe spacing. Three types of failure modes were observed, viz., local buckling
(L) for short columns, flexural buckling for long columns (F), and combined
local + flexural buckling (F + L). Figure 4 shows local buckling in T2T-40-1400.

Table 2 Comparison of FEA results and design strengths for built-up columns

Specimen	P_{FEA}(kN)	P_{NAS}(kN)	P_{FEA}/P_{NAS}	Failure Mode
T2T-0-600	162.68	193.78	0.84	L
T2T-0-1000	162.28	182.65	0.89	L
T2T-0-1400	138.9	167.1	0.84	F + L
T2T-0-1800	121.18	148.32	0.82	F + L
T2T-0-2200	97.75	126.77	0.78	F + L
T2T-0-2600	83.25	104.82	0.8	F + L
T2T-0-3000	68.54	74.48	0.93	F + L
T2T-0-3400	56.56	59.14	0.96	F + L
T2T-0-3800	46.99	48.01	0.98	F + L
T2T-0-4200	39.6	39.71	1	F
T2T-0-4600	33.65	33.37	1.01	F
T2T-20-600	164.62	196.81	0.84	L
T2T-20-1000	161.69	190.69	0.85	L
T2T-20-1400	151.03	181.86	0.84	L
T2T-20-1800	143.49	170.7	0.85	F + L
T2T-20-2200	129.41	157.67	0.83	F + L
T2T-20-2600	110.44	143.05	0.78	F + L
T2T-20-3000	102.5	127.19	0.81	F + L
T2T-20-3400	85.33	111.15	0.77	F + L
T2T-20-3800	77.37	85.66	0.91	F + L
T2T-20-4200	66.96	71.44	0.94	F + L
T2T-20-4600	57.99	60.4	0.97	F
T2T-20-5000	50.65	51.69	0.98	F
T2T-20-5400	44.88	44.71	1.01	F
T2T-20-5800	39.62	39.03	1.02	F
T2T-20-6200	35.03	34.35	1.02	F
T2T-40-600	168.19	198.15	0.85	L
T2T-40-1000	159.97	194.34	0.83	L
T2T-40-1400	155.69	188.74	0.83	L
T2T-40-1800	153.79	181.53	0.85	F + L
T2T-40-2200	140.49	172.89	0.82	F + L
T2T-40-2600	130.78	163.04	0.81	F + L
T2T-40-3000	125.8	152.23	0.83	F + L
T2T-40-3400	114.45	140.36	0.82	F + L
T2T-40-3800	103.98	127.88	0.82	F + L
T2T-40-4200	92.87	115.28	0.81	F + L
T2T-40-4600	80.65	102.57	0.79	F + L
T2T-40-5000	74.33	80.81	0.92	F + L
T2T-40-5400	66.71	70.24	0.95	F + L
T2T-40-5800	59.71	61.57	0.97	F

Table 2 (continued)

Specimen	P_{FEA}(kN)	P_{NAS}(kN)	P_{FEA}/P_{NAS}	Failure Mode
T2T-40-6200	53.65	54.38	0.99	F
T2T-40-6600	44.02	48.35	0.92	F
T2T-40-7000	42.05	43.26	0.98	F
T2T-40-7400	39.96	38.92	1.03	F
T2T-40-7800	36.91	35.19	1.05	F
T2T-40-8200	33.58	31.97	1.06	F
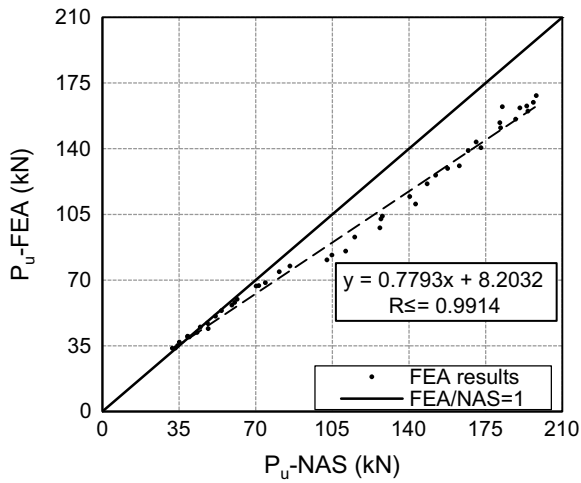
Fig. 3 Comparison of FEA results with NAS predicted design strengths

Figure 5 that plotted the load *versus* ratio of unbraced chord slenderness to the column slenderness $((l/r)_{unbr}/(l/r))$ shows that the relationship is approximately linear up to $((l/r)_{unbr}/(l/r)) = 0.75$. Therefore, for built-up columns with sectional compactness, $((l/r)_{unbr}/(l/r))$ up to 0.75 can be adopted instead of 0.5.
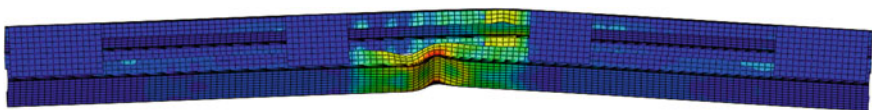
Fig. 4 Failure mode in T2T-40-1400
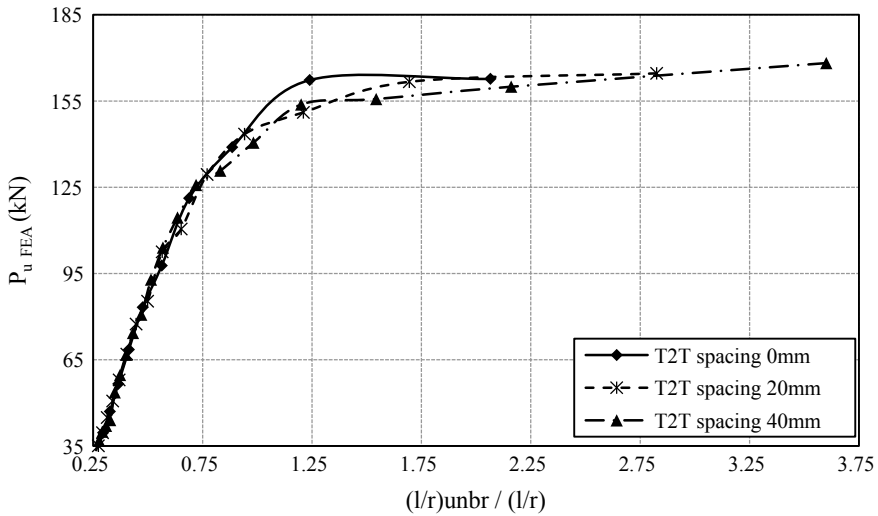
Fig. 5 Relationship between strength and ratio of unbraced chord slenderness to the column slenderness

5 Conclusions

A numerical study was carried out on CFS built-up battened pin-ended columns under axial loading. A total of 46 built-up columns comprising two plain channels toe to toe were analyzed. Parameters like column slenderness and the toe-to-toe spacing were varied. Following are the main conclusions drawn out of this study:

1. The finite element models developed in ABAQUS were in reasonable agreement with the test results available in the literature; therefore, ABAQUS can be used to simulate battened built-up columns.
2. AISI-S100 design strength predictions are reliable for the columns failing by elastic flexural buckling but un-conservative for the short built-up columns failing predominantly by local buckling.
3. With reference to the upper limit of 0.5 specified on the ratio of unbraced chord slenderness to the column slenderness by AISI S-100, for built-up columns with sectional compactness, $((l/r)unbr/(l/r))$ up to 0.75 can be adopted.
4. The ultimate capacity of the columns reduces with the increase in column slenderness and the same increases, with the increase in toe-to-toe spacing. From the parametric study, it is ascertained that ratio of unbraced chord slenderness to the column slenderness affects the behavior of battened built-up CFS columns.

References

1. ABAQUS User's Manual: Version 6.14 Hibbit, Karlsson, and Sorenson, Inc., Providence, RI (2004)
2. AISI S-100: (2016), North American specification for the design of cold-formed steel structural members. AISI Standard, Washington, DC (2016)
3. M. Anbarasu, K. Kanagarasu, S. Sukumar, Investigation on the behaviour and strength of cold-formed steel web stiffened built-up battened columns. Mater. Struct. **48**(12), 4029–4038 (2015)
4. M. Dabaon, E. Ellobody, K. Ramzy, Experimental investigation of built-up cold-formed steel section battened columns. Thin Walled Struct. **92**, 137–145 (2015)
5. M.A. Dar, M. Yusuf, A.R. Dar, J. Raju, Experimental Study on Innovative Cold-formed Steel Beams. Steel Compos. Struct. **19**(6), 1599–1610 (2015)
6. Dar, M.A., Subramanian, N., Dar, A.R., Anbarasu, M., Lim, J.B.P., Mir, A.: Behaviour of partly stiffened cold-formed steel built-up beams: Experimental investigation and numerical validation. Advances in Structural Eng. Epub ahead of print 28 June 2018. https://doi.org/10.1177/1369433218782767 (2018)
7. M.A. Dar, N. Subramanian, A.R. Dar, M. Anbarasu, J.B.P. Lim, Structural performance of cold-formed steel composite beams. Steel Compos. Struct. **27**(5), 545–554 (2018)
8. M.A. Dar, D.R. Sahoo, S. Pulikkal, A.K. Jain, Behavior of laced built-up cold-formed steel columns: Experimental investigation and numerical validation. Thin Walled Struct. **132**, 398–409 (2018)
9. N. Kumar, D.R. Sahoo, Optimization of lip length and aspect ratio of thin channel sections under minor axes bending. Thin Walled Struct. **100**, 158–169 (2016)
10. B.W. Schafer, T. Pekoz, Computational modelling of cold-formed steel: characterizing geometric imperfections and residual stress. J. Construct. Steel Res. **47**, 193–210 (1998)
11. S. Vijayanand, M. Anbarasu, Effect of spacers on ultimate strength and behaviour of cold-formed steel built-up columns. Proc. Eng. **173**, 1423–1430 (2017)

Seismic Performance of Shutdown System of Indian Pressurized Heavy Water Reactors

V. Chaudhry, D. K. Jain, S. M. Ingole, A. K. Balasubrahmanian and U. C. Muktibodh

Abstract Shutdown System constitutes a part of reactor safety system of Indian Pressurized Heavy Water Reactor (IPHWR). The system is required to be seismically qualified to demonstrate its capability of functioning and maintaining structural integrity during and after a seismic event. Experimental studies have been carried out on full-scale shutdown system assembly to evaluate the responses under multi-support excitation. Dynamic characterization and functionality test of the assembly have been carried out simulating rock site and alluvium soil condition. Critical parameters, viz. added mass coefficient and damping factor have been evaluated for the submerged structure from the experiments, and analytical studies have been carried out incorporating these parameters. Dynamic responses from experimental and analytical studies have been compared and are found to be in good agreement. Studies concluded that shutdown system can perform its intended safety function even when subjected to extremely strong earthquake motion.

Keywords Shutdown system · Seismic · Submerged perforated tubes · Added mass coefficient · Damping factor

1 Introduction

Indian Pressurized Heavy Water Reactors (IPHWRs) core primarily consists of a horizontal cylindrical calandria vessel. Calandria is pierced by coolant channels assemblies which comprise calandria tube, pressure tube, fuel bundles and heavy water coolant. Two independent fast-acting shutdown systems of diverse design exist in IPHWRs to bring the reactor in safe shutdown condition. Each of these systems is separately and independently capable of safely terminating any reactivity transient from various operating state of the reactor [1]. Shutdown System-1 (SDS-1) makes use of mechanical shut-off rods and Shutdown System-2 (SDS-2)

V. Chaudhry (✉) · D. K. Jain · S. M. Ingole · A. K. Balasubrahmanian · U. C. Muktibodh
Nuclear Power Corporation of India Ltd, Mumbai 400094, India
e-mail: vchaudhry@npcil.co.in

uses liquid poison to shutdown the reactor. In SDS-1, a reactor trip signal de-energizes an electromagnetic clutch which leads to insertion of shut-off rod inside the reactor core. The rod drops into the core under gravity inside a perforated zircalloy guide tube which is immersed in moderator. The rod is provided with initial thrust by pre-compressed spring. The performance of the system is required to be demonstrated during and after Safe Shutdown Earthquake (SSE) or S2 level earthquake [2].

Response of any Structure, System and Component (SSC) under seismic excitation depends on the characteristics of the earthquake ground motion, and the dynamic characteristics of the SSC itself. The characteristic of earthquake ground motion is greatly influenced by the local subsurface conditions, i.e. soil/rock [3]. A comparison of normalized ground response spectral shape of a typical soil site and rock site is shown in Fig. 1 [4]. It can be seen that the frequency content of rock site is in higher frequency range in comparison to soil site, and the spectrum does not become asymptotic even at 100 Hz, unlike soft soil spectrum which gets asymptotic at 25–35 Hz. In the present study, same response spectral shapes have been used as design basis ground motion.

Dynamic responses of submerged structures are entirely different as those observed in air. It has been observed [5] that structural component when submerged exhibits reduction in the frequency and increase in the damping values. A reduction in the natural frequency has been attributed to the added mass of fluid surrounding the submerged structure. A member submerged in water, when accelerated in a stationary fluid, induces the fluid in its immediate vicinity to move. The accelerating fluid, in turn, induces an added mass effect on to the member. The added mass phenomenon can be quantified based on added mass coefficient, C_m defined as [5]

$$C_m = \frac{added\ mass\ of\ fluid}{reference\ fluid\ mass} \tag{1}$$

where the reference fluid mass is the mass of the fluid cylinder having diameter equal to the dimension perpendicular to the direction of motion.

Fig. 1 Typical normalized ground response spectral shape for rock site and soil site [4]
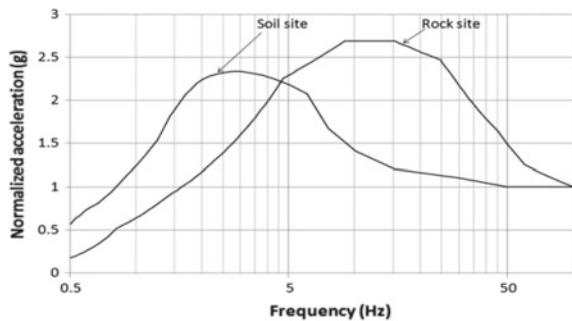
Various studies have been performed for estimation of the added mass coefficient and damping of the submerged structure. Sinha et al. [6] carried out experimental and analytical studies on various configurations of perforated tubes to evaluate the added mass coefficient. One of the submerged bodies considered in Sinha et al. [6] study was that of shutdown system guide tube which is geometrically similar to the perforated guide tube considered in the present study. For this tube, the added mass coefficient was evaluated to be 1.89.

Muto et al. [7] evaluated dynamic characteristics of perforated and non-perforated tube assemblies under submerged condition simulating 1/5 scale model of CANDU core. The study of perforated tubes indicated damping values of about 5% and 30% in air and water, respectively. Kuroda et al. [8] carried out shut-off rod insertion capability test with actual assembly. The assembly was subjected to sinusoidal motion (sweep test) and seismic input motion. Test results indicate higher damping value from 10 to 30% for the perforated guide under submerged condition. Further, maximum delay in the drop time of shut-off rod due to seismic excitation was observed as 200 ms.

The present paper brings out the details of experiment test setup, instrumentation provided and the studies carried out to evaluate the performance of SDS-1 assembly under multi-support seismic excitation of full-scale reactor grade assembly. Typical seismic motions representing rock site and alluvium soil site conditions are used to study the performance of the assembly. The performance of the assembly has been evaluated based on the variation in drop time of the shut-off rod from parked out condition to fully in condition of the reactor core, during the seismic event, as the drop time may get effected due to interaction of shut-off rod with the guide tube. Any lateral deflection of the guide tube during seismic excitation can affect the drop time, if the deflection of the guide tube is more than the radial clearance between the shut-off rod and guide tube. Emphasis has also been made to evaluate the dynamic characteristics of the assembly, specifically, for the submerged perforated guide tube The paper also brings out the numerical studies carried out to evaluate the responses of the submerged perforated guide tube under seismic excitation for rock site and its comparison with experimental results.

2 Experimental Studies

2.1 Test Setup

Multi-support seismic excitation tests of the shutdown system assembly have been carried out in the pseudo-dynamic test facility at Advanced Seismic Testing and Research (ASTaR) test facility of CSIR-SERC. Figure 2 shows the schematic view and typical arrangement of the components of the assembly. The assembly is supported on linear bearings at three locations, simulating the support conditions as exist in the reactor, and the seismic excitation is provided at these locations with the help of hydraulic actuators. Guide tube, which is a perforated zircalloy tube of
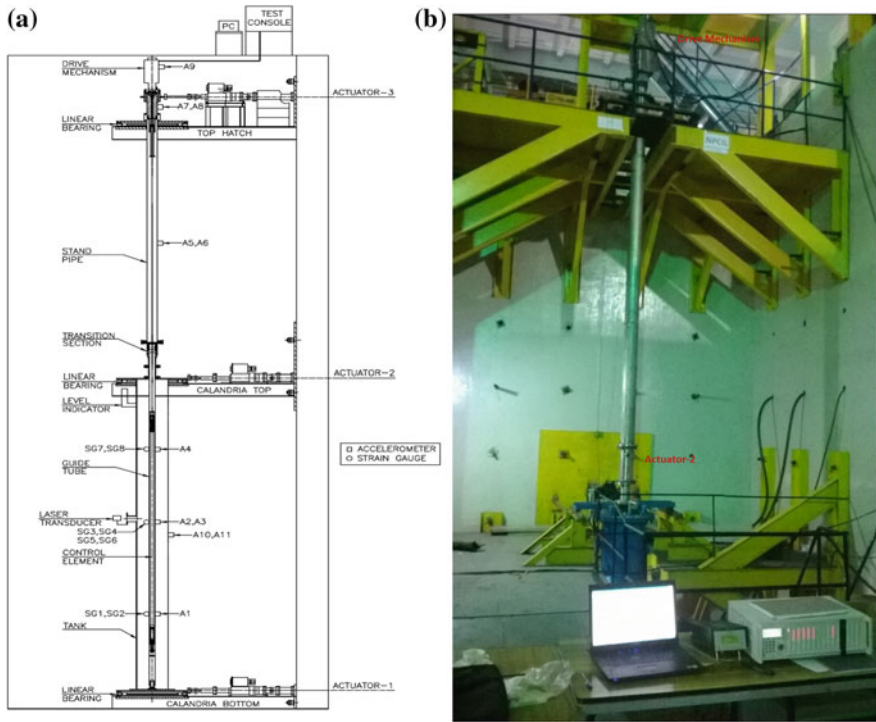
Fig. 2 **a** Schematic experiment setup of SDS-1 assembly along with transducers details **b** Test setup

91 mm outer diameter and 6708 mm long, is enclosed in a tank filled with water to simulate the submerged condition. The top end of the guide tube is supported in a self-aligning cup and the bottom end is supported in the lateral directions through a bayonet coupling. The shut-off rod assembly consists of a hollow cadmium sandwiched stainless steel rod called control element, which is kept above the tank top. At the top, the shut-off rod is held against a push spring which provides initial acceleration to the shut-off rod during its insertion. The rod is hung with the help of a wire rope, which is wound on a sheave in the drive mechanism of the SDS-1 assembly. The rod moves inside a perforated zircalloy guide tube which remains submerged under operating condition. The drive mechanism is mounted on the reactor nozzle extension called standpipe thimble, which is guided and supported at top hatch beam. The total height of the assembly is around 12 m.

3   Instrumentation

The important parameters which need to be evaluated in the multi-support excitation test of the assembly are modal parameters, viz. frequency and modal damping; displacement at the centre location of the guide tube; stress/strain at identified locations; drop time and displacement profile of shut-off rod. In order to evaluate the modal parameters, accelerometers and strain gauges have been mounted at various locations of the assembly in the perpendicular lateral directions (Fig. 2). Underwater accelerometers and strain gauges have been mounted on guide tube at different locations, viz. at the centre location of the tank and at 1500 mm from the bottom and top end of the guide tube. Accelerometers have been also mounted on standpipe, water tank and drive mechanism. In order to measure the relative displacement between the tank and guide tube, laser-based displacement transducer has been used. To measure the drop time and displacement profile of shut-off rod, four sets of triplicate limit switches have been provided in the drive mechanism. In addition to this, a Rotary Variable Differential Transformer (RVDT) has been used to indicate the position of the rod continuously. In order to study the effect on the drop time at different time instant of the seismic excitation, delay timer was deployed to actuate the drop of the shut-off rod.

4   Seismic Input Motion

Simulated seismic motions have been given to the assembly at three support locations, viz. calandria bottom, calandria top and calandria vault top, using three hydraulic actuators mounted at these elevations. The seismic input motions for the testing have been generated by carrying out time-history analysis of the building using design basis ground motion corresponding to rock and soil site. Typical design input motions used for seismic testing of the assembly for rock and soil site are shown in Figs. 3 and 4, respectively. In order to check the performance of the assembly for higher seismic levels, scaled up tests have been carried out up to 140% and 200% of design seismic input motion for rock and soil site, respectively.

4.1   Test Results

The assembly has been subjected to sinusoidal motion (sine sweep) and random motion corresponding to design input motion. Numbers of tests have been carried out in air and water to check the consistency in the experimental results. Modal parameters have been evaluated from sine sweep tests in air and under submerged condition. Seismic performance of the assembly has been evaluated based on the variation in the drop time of the shut-off rod under seismic excitation in comparison to drop time under static condition.
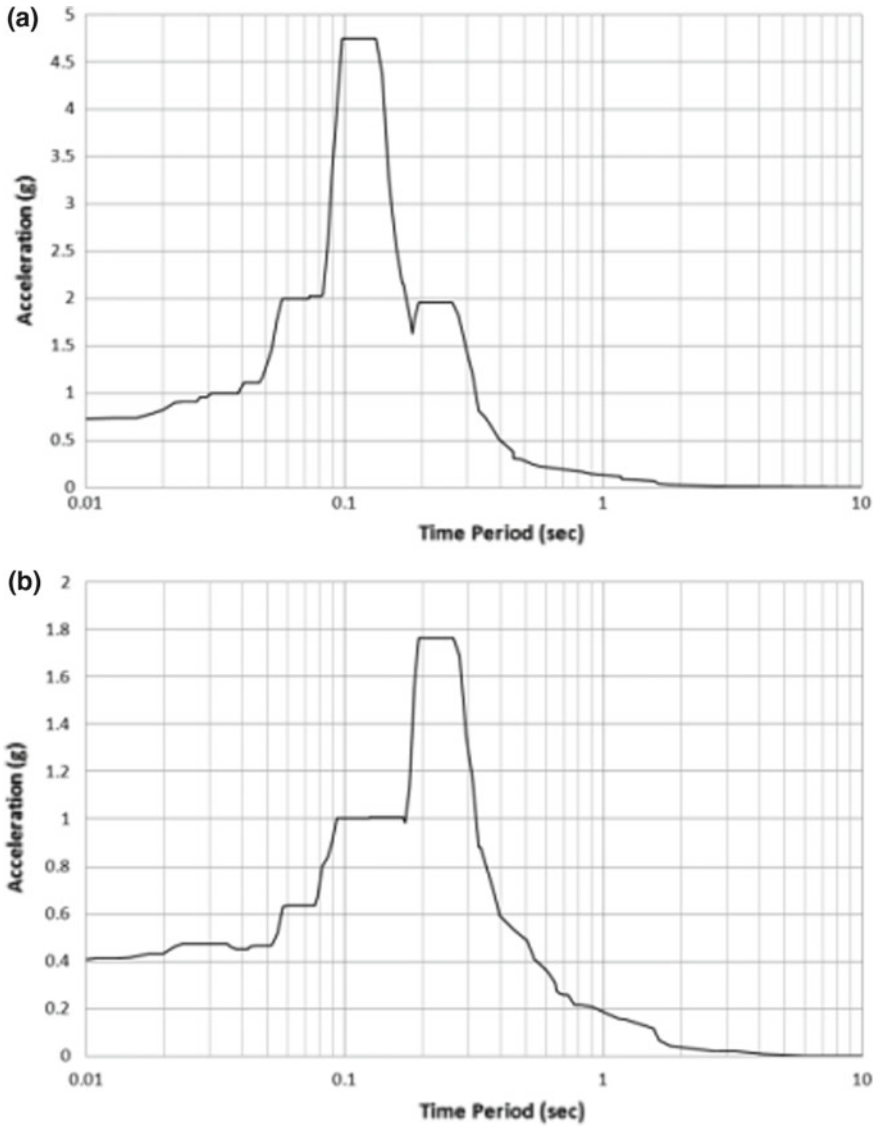
Fig. 3 Input motion for rock site at **a** tank top and bottom **b** top of the assembly

4.1.1 Modal Parameters

To evaluate the dynamic characteristics of the assembly, sine sweep tests have been carried out at sweep rate of less than 0.5 Hz per minute and acceleration levels of less than 0.15 g. The modal parameters of the guide tube have been evaluated from the responses obtained from accelerometer/strain gauges mounted at the centre
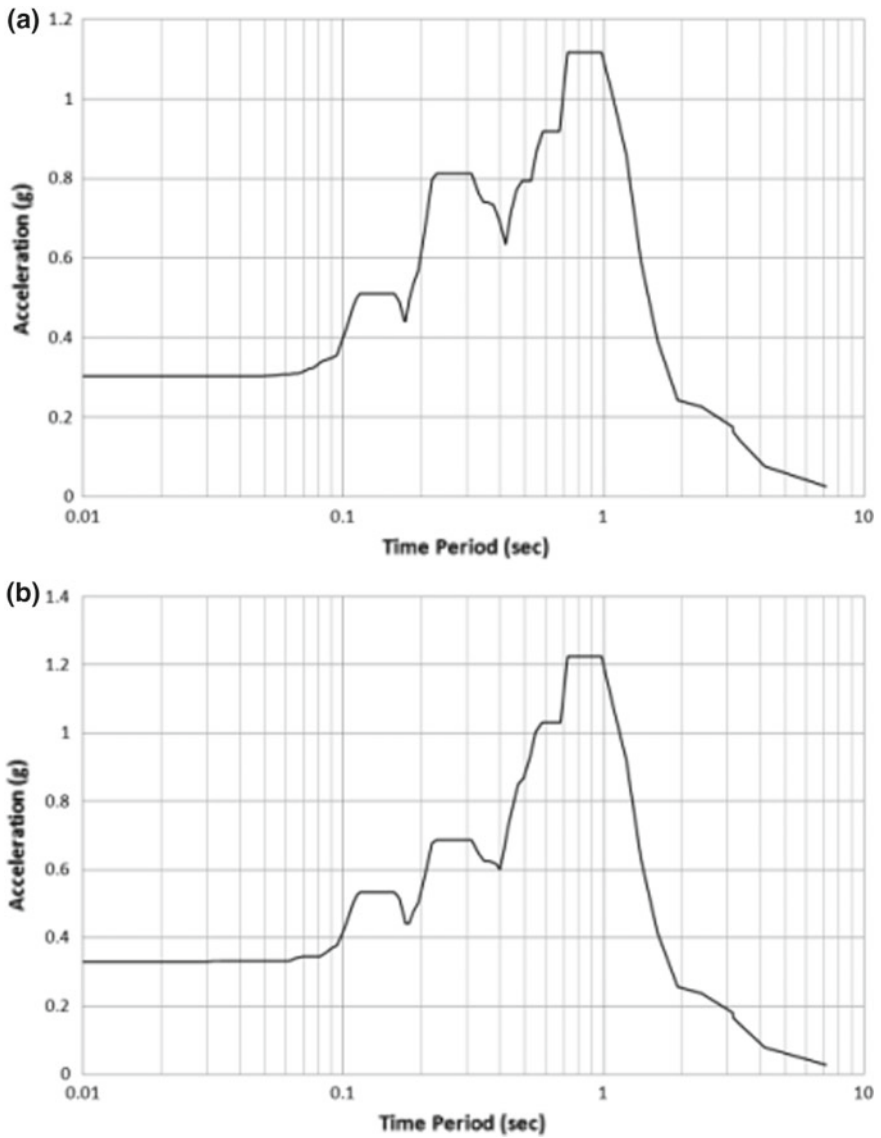
Fig. 4 Input motion for soil site at **a** tank top and bottom **b** top of the assembly

location of the guide tube using FFT analyzer (model no. 3524). The tests have been carried out both in air and water. The natural frequencies of perforated guide tube in air and water have been evaluated and are given in Table 1. The fundamental frequencies of the guide tube in air and water are 6.55 Hz and 2.7 Hz, respectively.

Table 1 Natural frequencies of guide tube

Mode	Air		Water	
	Experiment (Hz)	Analysis (Hz)	Experiment (Hz)	Analysis (Hz)
First mode	6.55	6.73	2.7	2.878
Second mode	21.1	21.76	9.4	9.375

The damping values have been evaluated using half-power bandwidth method. Damping ratio is given by,

$$\xi = (f_2 - f_1)/(f_2 + f_1) \times 100 \tag{2}$$

where f_1 and f_2 are the frequencies at $1/\sqrt{2}$ of the peak amplitude, i.e. half-power points. Using Eq. (2), the mean damping values for perforated guide tube in air and water are found to be 6.77% and 16.58%, respectively, with a standard deviation of 1.3 and 2.1%.

The added mass coefficient and the damping factor for the perforated submerged guide tube have been evaluated from experimental responses obtained in both air and water [9]. The added mass coefficient has been evaluated assuming that the structure guide tube stiffness remains constant when it is submerged in the fluid. Thus, the change in the frequencies in air and water exhibits the effect of added mass.

Stiffness in air,

$$K_a = \omega_{n,a}^2 M_a \tag{3}$$

Stiffness in water,

$$K_f = \omega_{n,f}^2 M_f = \omega_{n,f}^2 (M_a + M_{f_2}) \tag{4}$$

Equating Eq. (2) and (3) we have,
Added mass factor,

$$\frac{M_{fa}}{M_a} = \left(\frac{\omega_{n,a}}{\omega_{n,f}}\right)^2 - 1 \tag{5}$$

where K_a, M_a, $\omega_{n,a}$ and K_f, M_f, $\omega_{n,f}$ are the modal stiffness, modal mass and natural frequency of the guide tube in air and fluid, respectively. M_{fa} is the modal added mass. Eigenvalue analysis shows first mode as the dominant mode of vibration. The added mass factor considering first mode of vibration for the submerged perforated guide tube has been evaluated as 4.89. Added mass of fluid (M_{fa}) is given by 4.89 M_a (Eq. 5) and is equal to 78.24 kg. Reference fluid mass (the mass of the fluid cylinder having diameter equal to the dimension perpendicular to the direction

of motion) has been evaluated as 40.38 kg. Using Eq. (1), added mass coefficient for submerged perforated guide tube has been evaluated as 1.9.

Damping factor accounting the added mass effect has been evaluated as under, Damping coefficient in air,

$$C_a = 2\xi_a \omega_{n,a} M_a \tag{6}$$

Damping coefficient in water,

$$C_a + C_f = 2\xi_f \omega_{nf}(M_a + M_{fa}) \tag{7}$$

From Eq. (5) and (6) we have,
Added damping factor,

$$\frac{C_f}{C_a} = \frac{\omega_{n,a}\xi_f}{\omega_{nf}\xi_a} - 1 \tag{8}$$

where C_a, ξ_a and C_f, ξ_f are the modal damping and critical damping in air and water, respectively. Added damping factor for the perforated submerged guide tube has been evaluated as 4.94. Higher damping factor has been attributed to higher damping values observed for the perforated guide tube under submerged condition.

4.1.2 Responses of the Tube Under Seismic Excitation

As discussed earlier, the shut-off rod drops inside the perforated guide tube. Typical displacement responses at mid-location of guide tube measured using laser displacement transducer are shown in Fig. 5a, b for design input motion of rock site
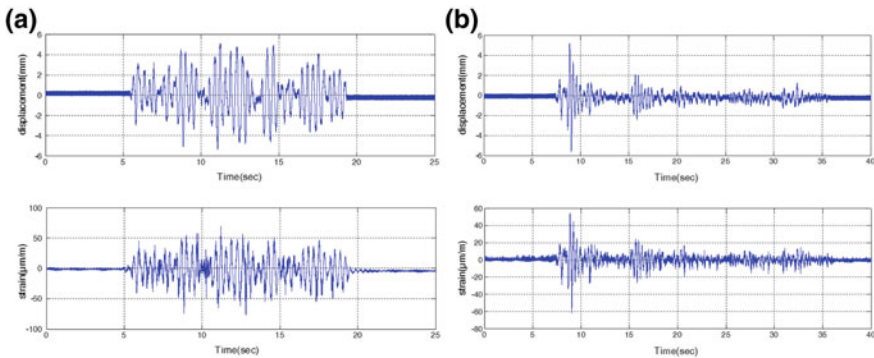
Fig. 5 a Displacement and strain gauge responses at mid-location of guide tube for design input motion of rock site. b Displacement and strain gauge responses at mid-location of guide tube for design input motion of soil site
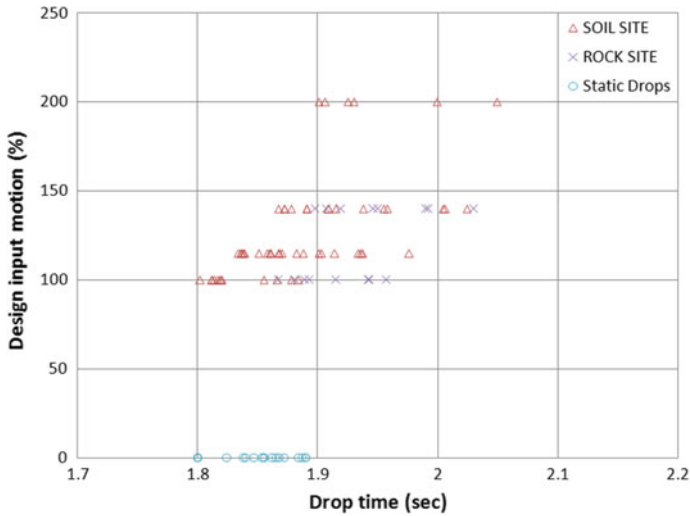
Fig. 6 Drop time for rock site and soil site under static and seismic excitation

and soil site, respectively. Initially, static drop tests have been performed in order to establish baseline data, followed by the drop tests under seismic excitation. In order to evaluate the performance of the assembly at various instants of strong motion, drop tests have been carried out by dropping the shut-off rod at different time intervals from the start of the seismic excitation, using delay timer (discussed in Sect. 2.2). Delay timer delays the time of release of the shut-off rod by a predefined value, so as to study its effect on the drop time during the seismic excitation. Figure 6 shows the variation in the drop time under static and seismic excitation for design and scaled up input motion for rock and soil sites. The maximum displacements measured at mid-location of guide tube have been 5.76 mm and 5.43 mm, for rock site and soil site, respectively. Maximum strains at guide tube mid-location are observed as 77.2 μm/m and 60 μm/m for rock site and soil site, respectively.

5 Numerical Studies

Finite Element (FE) analyses of the guide tube assembly have been carried out to evaluate the modal parameters and the seismic responses, specifically, displacements of the guide tube under seismic excitation using the same input motion as that used in the experimental studies. The modal parameters have been evaluated from eigenvalue analysis, whereas the seismic responses have been evaluated using time-history analysis.

Table 2 Maximum displacement of guide tube for design input motion for rock site

Design input motion (%)	Experiment	Analysis		
		5% damping	15% damping	30% damping
Rock site	5.76	39.95	14.77	5.82

The perforated guide tube has been modelled using three-dimensional beam element having six degree of freedom of commercial code Numerically Integrated elements for System Analysis (NISA). At bottom, the tube is constrained in all three translations simulating bayonet coupling and at the top all degrees of freedom are constrained as per the actual support conditions. For mass modelling, consistent mass approach has been adopted. The model has been validated by comparing the fundamental frequency using the following analytical solution [10],

$$\omega_1 = 15.42 \left(EV/ML^4\right)^{1/2} \tag{10}$$

where E is the Young's modulus, M is the mass, I is the moment of Inertia and L is the length of guide tube.

Accounting for the added mass coefficient (discussed in Sect. 2.4.1), the frequencies obtained from the analysis are found to be in good agreement with the experiment results (Refer Table 1).

Linear time-history analysis using Newmark time stepping method [11] has been used to find the responses of the submerged guide tube. The Newmark parameters 'β' and 'γ' considered in the analysis are 1/6 and ½, respectively. The analysis has been carried with time step of one millisecond using Raleigh damping of 5, 15 and 30% of critical damping. The maximum displacements of the guide tube for these damping values are brought out in Table 2. It has been observed that the numerical response of the guide tube corresponding to 30% of critical damping matches closely with the experiment results.

6 Discussion

Multi-support seismic tests have been performed on full-scale reactor grade shutdown system assembly. Seismic motion representing rock site and alluvium soil site conditions have been used to study the performance of the assembly under a seismic event. Testing of the assembly implicitly evaluate the performance of the structural components, drive mechanism and various instrumentation and control systems. The Shutdown System-1 (SDS-1) has performed satisfactorily meeting all the intended functional requirements including drop time of shut-off rod for all the tests which also include scaled up seismic input motion. The maximum variations in the drop time of the shut-off rod have been observed to be 155 ms and 247 ms

for design input motion and scaled up design seismic input motion, respectively (Fig. 6). The variations have been observed to be well within the acceptable limits of reactor safety requirements.

Interesting observations have been made from the experimental and numerical studies with regard to the response of the submerged perforated guide tube under seismic excitation. The modal parameters and the added mass coefficient are found to be in good agreement with the studies carried out on the geometrically similar perforated guide tubes by Sinha et al. [6]. The mean damping values from sine sweep tests for the perforated guide tube are observed to be 6.77% and 16.58% in air and water, respectively. The higher damping values in air in comparison to the material damping values (generally limited to 1–2%) have been attributed to the friction and joint slippage in the assembly, and thus can be categorized under structural damping. Damping values of the perforated guide tube under submerged condition have been observed to be further higher due to resistance offered by the surrounding water to the movement of the tube.

Time-history analysis using direct step-by-step time integration method has been carried out to find the displacement of the guide tube for various damping values ranging from 5% to 30% of critical damping, simulating the experimental conditions. It has been observed that the numerical response corresponding to 30% of critical damping matches closely with responses as those observed during experiments.

Mean damping values observed from sine sweep tests for the submerged perforated tube has been observed as 16.58%, which is lower than the damping value (30% of critical damping) evaluated from numerical studies by matching the experimental responses. Sine sweep tests have been carried out at sweep rate of less than 0.5 Hz per minute with acceleration levels of less than 0.15 g, whereas the acceleration level under seismic excitation is around 1 g (at dominant mode of 2.7 Hz). This has resulted in lower damping values for sine sweep test in comparison to the test under seismic excitation.

In present study, damping values observed under seismic excitation are found to be consistent with the damping values observed by Muto et al. [7] in their experimental studies carried out on the perforated tubes assemblies under submerged condition, simulating 1/5 scale model of CANDU core. Further, Kuroda et al. [8] also observed similar high damping values in the range of 10–30% for submerged perforated tubes.

7 Conclusion

Comprehensive experimental and numerical studies have been carried out to study the performance of Shutdown System-1 (SDS-1) of Indian Pressurized Heavy Water Reactors under seismic excitation. Typical seismic motion representing rock site and alluvium soil site conditions has been used in the study. Dynamic characteristics have been evaluated for the submerged guide tube. For the submerged

tube, the added mass coefficient is found to be 1.9, whereas the mean damping value observed is 16.58%. The functionality and structural integrity of the assembly has been demonstrated for seismic input motion up to 140% and 200% of design input motion for rock site and soil site, respectively. A maximum variation of 247 ms (200% motion for soil site) in the drop time of shut-off rod has been observed and is well within the acceptable limits. Responses from the experimental and numerical studies have been compared and are found to be in good agreement. Further, studies conclude that shutdown system of Indian Pressurized Heavy Water Reactors can perform its intended safety function even when it is subjected to extremely strong earthquake motion.

References

1. IAEA technical reports series no 407, Heavy water reactors: Status and project development (2002)
2. AERB: Safety guide No. AERB/NPP-PHWR/SG/D-23 (2009)
3. Silva, W.J., Youngs, R.R., Idriss, I.M.: Development of design response spectral shapes for Central and Eastern US (CEUS) and Western US (WUS) rock site conditions. In: Proceedings of the OECE-NEA Workshop on Engineering Characterization of Seismic Input 1999 NEA/CSNI/R(2000)2, Vol. 1, pp. 185–268 (1999)
4. Chaudhry, V., Pandey, J.K., Kumaran, H., Ingole, S.M., Sinha, S.K., Balasubrahmanian, A. K., Muktibodh, U.C.: Influence of gap size on the dynamic behavior of perforated tube under seismic excitation. Proc. Eng. **173C**, 1816–1824 (2017)
5. Dong, R.G.: Effective mass and damping of submerged structures, UCRL-52342 (1978)
6. J.K. Sinha, R.I.K. Moorthy, Added mass of submerged perforated tubes. Nucl. Eng. Des. **93**, 23–31 (1999)
7. Muto, K., Kuroda, K., Kasai, Y.: Forced vibration test of 1/5 scale model of CANDU core. In: 5th SMiRT Conference, K 12/3, pp. 1–10 (1979),
8. T. Kurado, C.G. Duff, *Experimental and analytical studies on the seismic behaviour of CANDU-PHW cores. International Meeting on Thermal Nuclear Reactor Safety* (American Nuclear Society, Chicago, 1982)
9. Vu, V.H., Thomas, M., Lakis, A.A., Marcouiller, L.: Effect of added mass on submerged vibrated plates. In: 25th Seminar on Machinery Vibration. Canadian Machinery Vibration Association (2007)
10. Thomson, W.T., Dahleh, M.D.: Theory of Vibration with Applications. Pearson Education, London (1998)
11. Chopra, A.K.: Dynamics of Structures. Prentice Hall of India Pvt. Ltd., New Delhi (2002)

Parametric Studies on the Seismic Behavior of Irregular Structures

E. Siva Naveen, Nimmy Mariam Abraham and S. D. Anitha Kumari

Abstract Irregular structures subjected to earthquake loads demand attention as they behave differently from regular ones. The number of irregular buildings being constructed is increasing yearly. Irregularities are unavoidable in certain cases, whereas in some other cases they are architecturally planned. Design of frame configurations incorporating such irregularities without compromising the performance of the structure needs detailed investigation on the parameters that influence the structural behavior. In this study, parametric studies are carried out in order to understand the effect of the type, degree, and location of irregularity on the behavior of structures. All these factors are found to affect the response of the structures significantly. The parameters such as mass, total cross-sectional area of columns, and storey height are considered for this study.

Keywords Irregularity · Configuration · Response · Degree of irregularity · Location of irregularity

1 Introduction

Existing structures and the ones to be constructed require assessment of their response under various loads. The response depends mainly on the arrangement of structural elements present in it. If these structural elements are arranged in an irregular manner, the structure behav'es differently. When a building is subjected to dynamic loads, inertia forces are developed and get concentrated at the center of mass of the structure. Usually, the vertical members such as columns and shear walls resist the horizontal inertia forces and the resultant of these forces gets concentrated at a point called center of stiffness. When the center of mass does not

E. Siva Naveen · N. M. Abraham (✉) · S. D. Anitha Kumari
Department of Civil Engineering, M. S. Ramaiah University of Applied Sciences,
Bangalore 560058, Karnataka, India
e-mail: nimmy555@gmail.com

coincide with the center of stiffness, eccentricity develops in the structure. Structures having such eccentricity are referred to as the irregular ones [1].

Structural irregularities can be attributed to the nonuniformity in the distribution of mass, stiffness, and geometry along the structure. If the nonuniformity is in the elevation of the structure, the same is called as vertical irregularity. The nonuniform distribution of the aforementioned parameters in the plan results in horizontal/plan irregularity. The magnitude of variation in response depends on the type, degree, and location of irregularities present. The incorporation of irregularities in the structure needs careful analysis before implementation.

Many researchers have studied the effect of response on structures having various irregularities. Varadharajan et al. [1] have reported a detailed review on different types of structural irregularities. They have discussed the criteria and limits specified for various irregularities by different codes of practice (IS 1893:2002, EC8:2004). They have concluded that the inelastic dynamic analysis methods yield accurate results compared to other methods like pushover analysis. Herrera and Soberón [2] have summarized the important seismic events from 1980 to 2008. The authors have attributed the reason for damage in buildings as different irregularities and concluded that irregular structures are more vulnerable than the regular ones. According to Sadashiva et al. [3], past research on irregularities does not justify the appropriateness of irregularity limits. Hence, they have developed a simple equation to estimate the increase in inter-storey drift due to mass irregularity which can be used to set irregularity limits. They have observed that increased mass, when present at either the first-floor level or at the roof, produced higher drift demands than when located at the mid-height.

Nafday [4] has discussed the definition of structural irregularity given by seismic codes. He has commented that it is not practical to cover exhaustively all the diverse irregularities that may arrive in practice. The author has also claimed that there is no guarantee on the reasonability of the limits stipulated by codes as they do not result from proper detailed analysis. Ahmed et al. [5] have investigated the effect of seismic response of L-shaped buildings. Equivalent static and response spectrum methods were performed using ETABS software. They have observed that the response of L-shaped building is higher than that of the regular frame due to torsion. Dutta et al. [6] have performed response spectral as well as nonlinear time-history analyses for different configurations of irregular structures. They have reported that higher stress concentration and higher ductility demand in the members around the irregularity may trigger early damage of these members, leading to early damage propagation resulting in progressive collapse of the entire or a major part of the structure.

It is observed from the existing literature that researchers have studied different types of irregularities. Moreover, it is seen that the presence of irregularity affects the behavior of structures. It is also inferred that the present standards give only approximate guidelines regarding various irregularities which results in the need for further investigations. Hence, in the present work, variation in structural response of reinforced concrete (RC) frames with change in type, degree, and location of

irregularity is analyzed. Mass and stiffness irregularities are considered for this particular study. The results of this study would help in designing irregularities in frames without compromising the performance of the structure.

2 Methodology and Validation

In this work, seismic response of a regular frame is obtained numerically and is validated with the experimental results reported in literature. Time-history analysis adopting modal superposition method is carried out using a finite element (FE)-based software, ETABS, and the maximum value of top storey displacement is determined. After validation, response time history of frames for different configurations is obtained in terms of top storey displacement, base shear, and overturning moment using the same software. The major inputs are geometry of the frame including dimensions of storeys and columns, total mass of each floor, modulus of elasticity, damping ratio, and earthquake data. The modulus of elasticity for the material is taken as $20,000 \times 10^6$ Pa. Rayleigh damping is assumed with a damping ratio of 4%. It is also assumed that the structure starts from rest on load application. Further, uncracked section properties are considered for geometric modeling.

Moehle [7] has conducted experiments on a small-scale nine-storeyed test structure subjected to scaled El Centro North-South 1940 ground motion. The results reported are used to validate the model developed for the present study. Two frames having nine storeys and three bays were placed opposite and parallel to each other. The frames together carry a total weight of 460 kg at each floor level. The typical storey height is 0.229 m and the frame has three bays in the direction of length and one bay in the direction of width. The dimensions of each bay in the direction of length and width are 0.305 m and 0.914 m, respectively. Frames were subjected to simulated earthquake base motion in horizontal direction parallel to the plane of the structure. The same test structure is modeled numerically using ETABS and the model is shown in Fig. 1.

Fig. 1 Numerical model of the regular frame used for validation
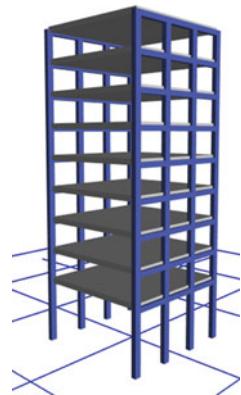
Table 1 Validation of the numerical model

Particulars	Literature [7]	Obtained
First natural frequency (Hz)	4.5	2.4
Second natural frequency (Hz)	14.4	15.3
Third natural frequency (Hz)	28.3	29.5
Top storey displacement (mm)	16.1	16.9

Modal properties are extracted for the first nine modes, out of which second, fifth, and ninth modes displayed lateral vibration. A comparison between the numerical and experimental values of natural frequencies and the top storey displacement is given in Table 1. The numerically obtained natural frequency values for the second and third modes are found to be slightly more than the experimental results due to the higher stiffness of the FE model. A difference is observed between the numerical and experimental values of first natural frequency. The numerical model underestimates the same and this could be due to the inability of the FE model to accurately model the support stiffness. However, the maximum top storey displacement obtained is in good agreement with the experimental results reported in literature.

3 Seismic Analysis of RC Frames

A nine-storeyed regular structure with six bays in the direction of length and three bays in the direction of width is considered. Other dimensions are kept same as that of Moehle's model [7]. Irregularities are introduced by varying parameters such as mass, total cross-sectional area of columns, and storey height at different locations. All the frames are analyzed to obtain response in the form of top storey displacement, base shear, and overturning moment.

3.1 Frame Configurations Considered for Analysis

In the present work, the effect of mass and stiffness irregularities on the seismic behavior of the chosen RC frame is analyzed. According to IS 1893:2016 (Part 1) [8], mass irregularity is to be considered when the mass of any storey is more than 150% of the adjacent storey. Stiffness irregularity is to be considered when the lateral stiffness of any storey is less than that of adjacent storey. The regular frame analyzed is shown in Fig. 2a. Figure 2b–d shows one configuration each from various types of irregularities considered in this study. Mass irregularity is present in Fig. 2b, whereas stiffness irregularity is present in Fig. 2c, d. The degree and location of irregularity are varied for the configurations given in Fig. 2b–d for parametric studies.
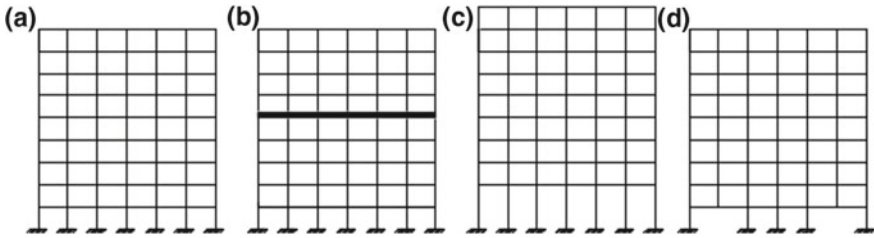
Fig. 2 Frame configurations: **a** regular, **b** irregular with respect to mass, **c** irregular with respect to storey height, and **d** irregular with respect to column cross-sectional area

3.2 Analysis of Regular Frame

The regular frame was modeled and was subjected to scaled north-south component of 1940 El Centro Imperial Valley earthquake. The same is shown in Fig. 3a. Time history of the response of the regular frame obtained in terms of top storey displacement, base shear, and overturning moment are depicted in Fig. 3b–d, respectively. The maximum values of top storey displacement, base shear, and overturning moment are obtained from these graphs and are used for parametric studies.
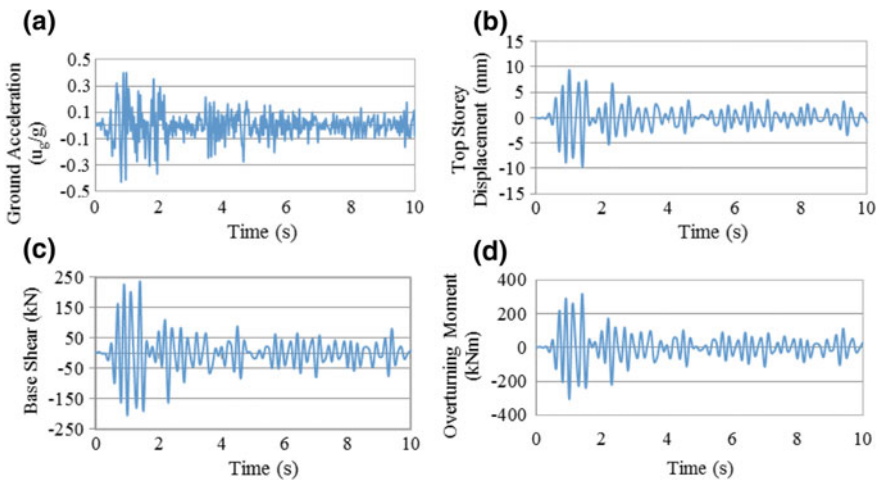
Fig. 3 Time history of **a** input ground acceleration, **b** top storey displacement, **c** base shear, and **d** overturning moment for regular frame

3.3   Parametric Studies

The natural frequencies of structures depend on their mass and stiffness. For any change in these parameters, frequencies of the structure change, resulting in change in response due to change in the accelerations attracted. Parametric studies are performed to understand the effect of type, degree, and location of irregularity on the structural response. In order to study the effect of degree of irregularity, parameters such as mass, storey height, and total cross-sectional (C/S) area of columns are considered. The total C/S area of columns captures the details of the total number of columns and the area of cross section of each column in the storey. The parameters are represented in the form of ratios of their magnitude in irregular structure to that of in regular structure. For example, mass ratio represents the ratio of storey mass of an irregular structure to the storey mass of a regular structure. A mass ratio of 1 represents the regular frame. The frames are analyzed for different values of these ratios. In order to study the effect of these parameters on the response, time-history analysis is done for each frame configuration and the maximum displacement at top storey, maximum base shear, and maximum overturning moment are obtained. The corresponding variation in the different forms of structural response for the variation in parameter ratios is studied. For this study, mass is varied at the fifth storey and total cross-sectional area of columns and storey height are varied at the first storey. Further, the effect of location of irregularity is studied by introducing irregularity at different storeys. The same is done by obtaining the variation in response by varying the location of both mass and stiffness irregularities separately. Mass irregularity was included at different locations by increasing the mass of the storey by a factor of 2. Stiffness irregularity was incorporated by reducing the storey height by a factor of 2.

Three lateral modes of vibration are obtained for each case analyzed. The mode shapes for the first three lateral modes of regular frame are depicted in Fig. 4. Other configurations also gave similar mode shapes. The natural frequencies and the corresponding mass participation for some of the cases analyzed are reported in Table 2. It is observed that natural frequency decreases with increase in mass ratio, increase in storey height ratio and decrease in total column C/S area ratio for all the
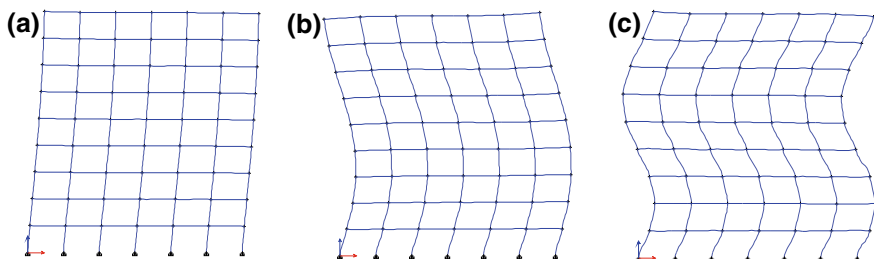
Fig. 4   Modes shapes obtained for the first three lateral modes of regular frame

Table 2 Natural frequencies (f) and corresponding mass participation factors (MPF) of some of the frame configurations analyzed

Configuration	Mode 1		Mode 2		Mode 3	
	f	MPF	f	MPF	f	MPF
Regular	6.016	0.8268	18.164	0.1074	31.011	0.0355
Mass ratio = 1.5	6.009	0.7971	17.947	0.1212	29.967	0.0440
Mass ratio = 2.0	6.004	0.7785	17.782	0.1357	29.177	0.0590
Mass ratio = 2.5	5.998	0.7583	17.559	0.1526	28.132	0.0688
Storey height ratio = 1.13	5.810	0.8489	17.515	0.1034	30.079	0.0280
Storey height ratio = 1.26	5.581	0.8714	16.841	0.0954	29.237	0.0215
Storey height ratio = 1.39	5.333	0.8930	16.185	0.0844	28.538	0.0155
Total column C/S area ratio = 0.92	5.977	0.8315	18.033	0.1068	30.811	0.0326
Total column C/S area ratio = 0.85	5.929	0.8372	17.874	0.0959	30.573	0.0136
Total column C/S area ratio = 0.78	5.870	0.8440	17.677	0.1040	30.298	0.0121

three lateral modes. The values of mass participation factor indicate that the first three modes considered here are sufficient for the accurate estimation of lateral response of the frames analyzed.

4 Results and Discussion

The results of the parametric study are shown graphically in Figs. 5, 6, 7, 8 and 9. Figures 5, 6 and 7 depict the influence of degree of irregularity on the seismic response of the structure. The variation of maximum response for varying mass ratio is given in Fig. 5. Maximum top storey displacement, maximum base shear, and maximum overturning moment have displayed similar trend in the range of mass ratio analyzed. It is observed that the response increases with increase in mass ratio, reaches maximum, and then decreases. Maximum response is observed at a mass ratio of around 3.5, whereas minimum response is observed for the regular configuration. These results are helpful in designing buildings where mass irregularity is expected. Factory with heavy machinery at one of the floors and an educational institution with a library at one floor level are examples that come under the case of mass irregularity.

The variation of maximum response in different forms for varying storey height ratio is shown in Fig. 6. Maximum top storey displacement, maximum base shear, and maximum overturning moment are minimum at a height ratio of 1.65. It is to be noted that this height ratio gives the values of both maximum base shear and maximum overturning moment less than those for the regular configuration. Maximum top storey response is seen to be increasing with increase in height ratio
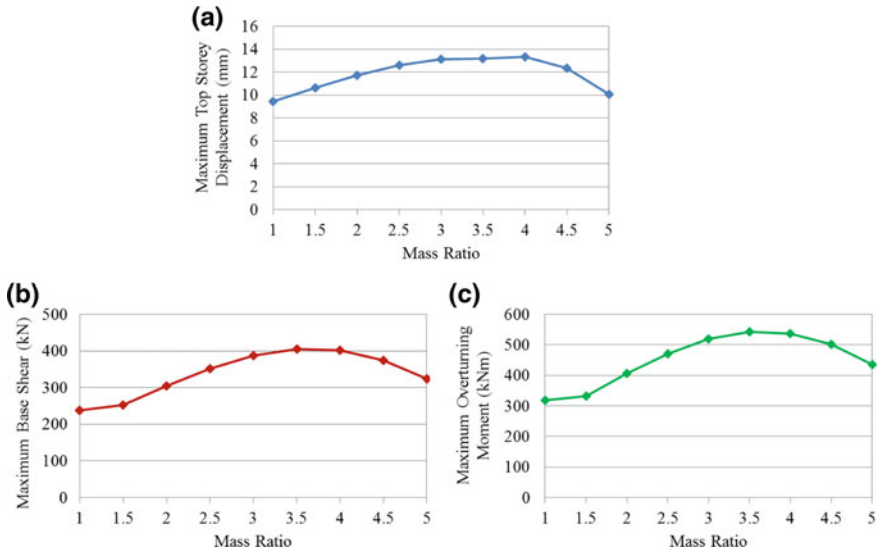
Fig. 5 Variation of **a** maximum top storey displacement, **b** maximum base shear, and **c** maximum overturning moment for varying mass ratio
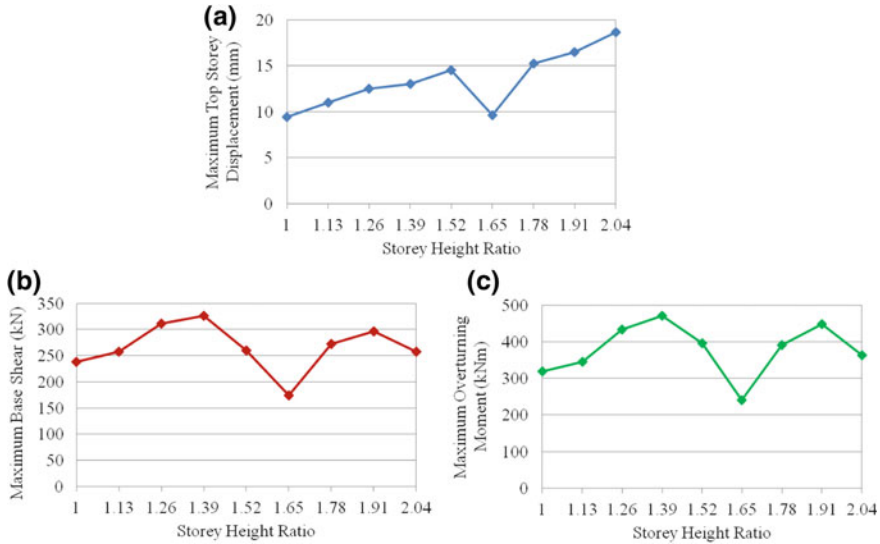
Fig. 6 Variation of **a** maximum top storey displacement, **b** maximum base shear, and **c** maximum overturning moment for varying storey height ratio
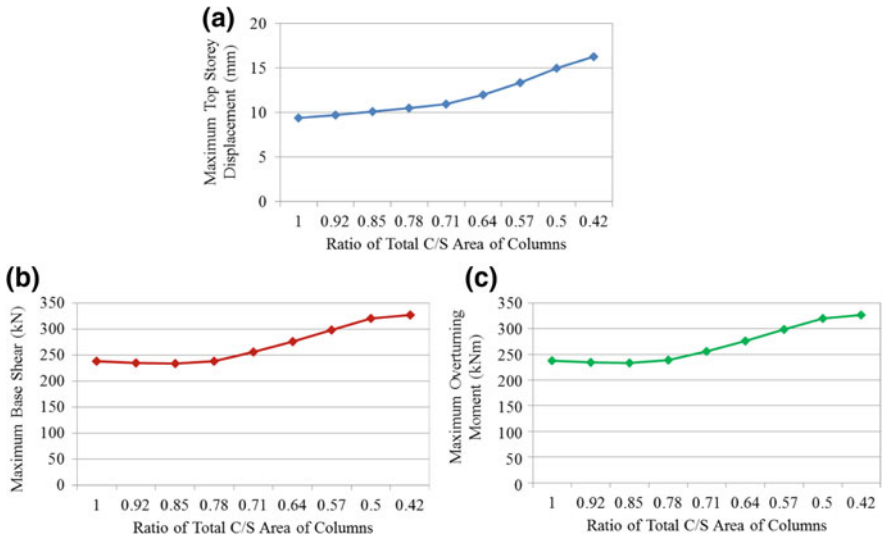
Fig. 7 Variation of **a** maximum top storey displacement, **b** maximum base shear, and **c** maximum overturning moment for varying total cross-sectional area of columns
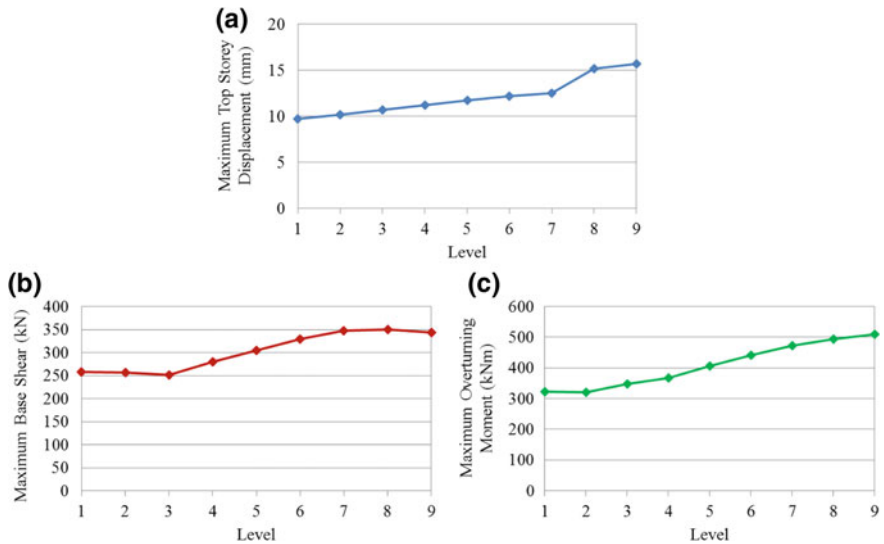
Fig. 8 Variation of **a** maximum top storey displacement, **b** maximum base shear, and **c** maximum overturning moment for varying location of mass irregularity

except for height ratio of 1.65. Variation of maximum base shear and maximum overturning moment follows similar pattern in the range of height ratio analyzed, with peaks at height ratios 1.39 and 1.91. The cases, where height of certain storeys
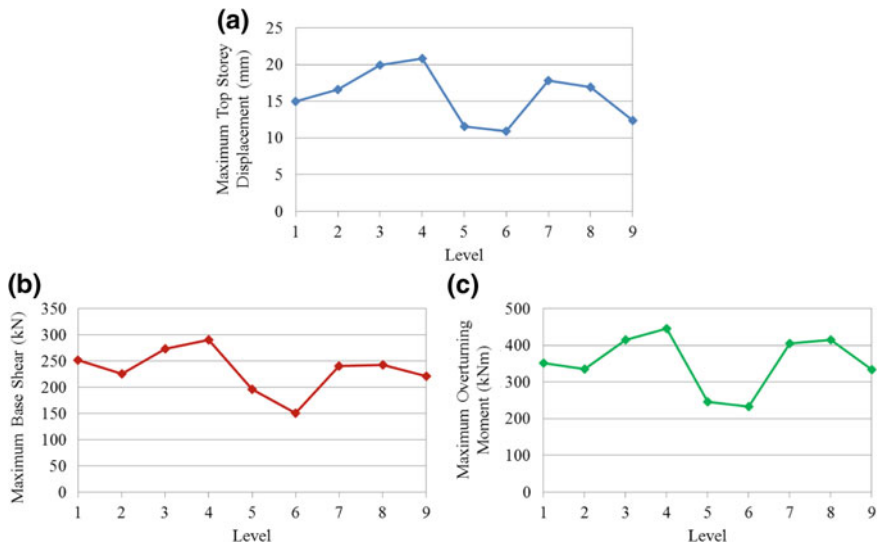
Fig. 9 Variation of **a** maximum top storey displacement, **b** maximum base shear, and **c** maximum overturning moment for varying location of stiffness irregularity

differs for specific utility like auditoriums in educational institutions, parking area at specific floors, etc., come under stiffness irregularity.

The variation of maximum top storey displacement, maximum base shear, and maximum overturning moment for decreasing total cross-sectional area of columns is shown in Fig. 7. All the three response quantities have shown similar trend. The response increases in a sigmoidal fashion from minimum at regular configuration with decrease in the ratio of column cross-sectional area. The slope of the curves is observed to increase from column cross-sectional area ratio 0.78. For ratio values more than 0.78, the slope of the curve is close to zero. Examples include certain convention halls, luxurious restaurants, etc., where the number of columns is significantly reduced at certain storeys.

Figures 8 and 9 show the influence of location of irregularity on the seismic response of the frame considered. Parametric study on location of irregularity helps in incorporating irregularities in structures at the most appropriate locations. For example, position of heavy machinery, space for library, location of auditorium, parking space, etc. may be decided on the basis of parametric studies on the location of irregularities. The variation of maximum top storey displacement, maximum base shear, and maximum overturning moment for varying location of mass irregularity is shown in Fig. 8. Sigmoid curves are obtained for all the three forms of response. It is observed that the least response is shown by the configuration in which mass irregularity is located at the first level. The response is seen to increase with the increase in the height of location of irregularity.

Figure 9 shows the variation of maximum top storey displacement, maximum base shear, and maximum overturning moment for varying location of stiffness irregularity. All the three forms of response have shown similar trend with two peaks each in their variation. The maximum response is observed when the stiffness irregularity is located at the fourth level, whereas the minimum response is observed when it is at the sixth level. It is further inferred that the maximum response occurs when stiffness irregularity is located at the quarter or three-quarter height of the frame. The response is minimum, when stiffness irregularity is located at the first, middle, or top levels of the frame.

5   Conclusions

Analyses are carried out to understand the effect of the type, degree, and location of irregularities on the behavior of RC frames subjected to earthquake loads. Seismic response is analyzed in terms of top storey displacement, base shear, and over-turning moment. All the three forms of response have shown similar trend for each case studied. The plots indicate that for a given location of irregularity, the change in degree of irregularity results in change in magnitude of response of the frame. Further, the plots show that for a given degree of irregularity, the change in location of irregularity affects the magnitude of response. It is also observed that the shape of curves showing variation of response for variation in magnitude of parameter differs for different parameters. Hence, it is inferred that the type of irregularity affects the seismic response of structures along with degree and location. Moreover, it is observed that the response is not always the minimum for regular configuration. Certain type, degree, or location of irregularity results in lower magnitude of structural response. Hence, the best possible structural design requires determination of the most appropriate parameters of irregularity satisfying aesthetical as well as utility demands without compromising the performance of the structure. In this study, analysis is carried out for a specific earthquake load and the site amplification effects are not taken into account. Further studies can be conducted by incorporating the effect of site conditions on the behavior of irregular structures.

References

1. S. Varadharajan, V.K. Sehgal, B. Saini, Review of different structural irregularities in buildings. J. Struct. Eng. **39**(5), 538–563 (2013)

2. R.G. Herrera, C.G. Soberón, Influence of plan irregularity on buildings, in *The 14th World Conference on Earthquake Engineering*, Beijing, China (2008)
3. V.K. Sadashiva, G.A. MacRae, B.L. Deam, Determination of structural irregularity limits—mass irregularity example. Bull. N. Z. Soc. Earthq. Eng. **42**(4), 288–301 (2009)
4. A.M. Nafday, Definition of structural irregularity in seismic codes. Structure Magazine, Structural Forum (2011), pp. 34–35
5. M.M.M. Ahmed, S.E.A. Raheem, M.M. Ahmed, A.G.A. Abdel-Shafy, Irregularity effects on the seismic performance of L-shaped multi-story buildings. J. Eng. Sci. **44**(5), 513–536 (2016)
6. S.C. Dutta, P.K. Das, P. Sengupta, Seismic behaviour of irregular structures. Struct. Eng. Int. **27**(4), 526–545 (2017)
7. J.P. Moehle, Seismic analysis of R/C frame wall structures. J. Struct. Eng. ASCE **110**, 2619–2634 (1984)
8. IS 1893 (Part-1), *Criteria for Earthquake Resistant Design of Structures*, Part 1, General Provision and Building, 5th Revision, Bureau of Indian Standards, New Delhi (2016)

Author Index

Subject Index